WESTERN PACIFIC INTERNATIONAL MEETING AND WORKSHOP ON TOGA COARE

Nouméa, New Caledonia
May 24-30, 1989

PROCEEDINGS

edited by

Joël Picaut *
Roger Lukas **
Thierry Delcroix *

* ORSTOM, Nouméa, New Caledonia
** JIMAR, University of Hawaii, U.S.A.

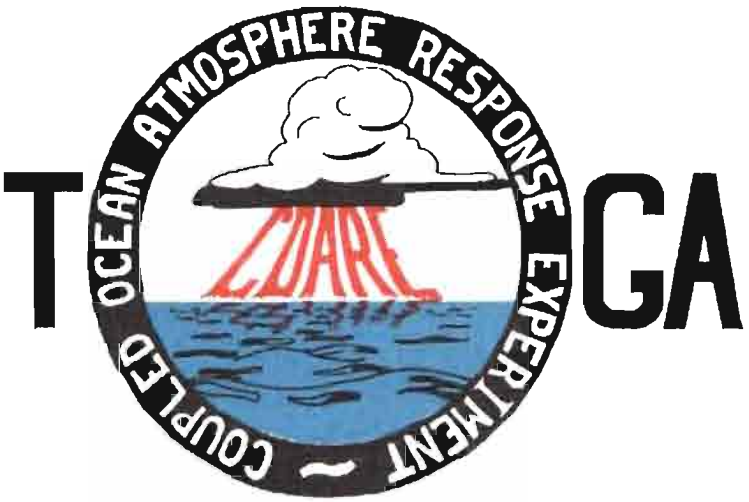

INSTITUT FRANÇAIS DE RECHERCHE SCIENTIFIQUE
POUR LE DÉVELOPPEMENT EN COOPÉRATION

ORSTOM

Centre de Nouméa

PROCEEDINGS OF THE WESTERN PACIFIC INTERNATIONAL MEETING AND WORKSHOP ON TOGA COARE

held at Centre ORSTOM de Nouméa, New Caledonia
May 24-30, 1989

compiled and edited by

Joël Picaut*
Roger Lukas**
Thierry Delcroix*

(December 1989)

* *Institut Français de Recherche Scientifique pour le Développement en Coopération, Centre ORSTOM de Nouméa, New Caledonia*
** *Joint Institute for Marine and Atmospheric Research, University of Hawaii, Honolulu, Hawaii, U.S.A.*

Participants at the end of the Meeting-Workshop

The Centre ORSTOM in front of Anse Vata beach,
with its 289 seats octagonal conference room.

ABSTRACT

The Western Pacific International Meeting and Workshop on TOGA COARE, held at Centre ORSTOM de Nouméa, New Caledonia during May 24-30, 1989, brought together more than one hundred scientists from Australia, Chile, China, France, Indonesia, Japan, New Zealand, the United Kingdom and the United States. The assembly was composed of a good mixture of oceanographers and meteorologists who specialize in tropical circulation or air-sea interaction problems. The main purpose of this combined Meeting/Workshop was to review the status of western tropical Pacific TOGA-related research, coordinate the growing multinational research efforts in the warm pool region, and cooperate in the planning of a major international air-sea interaction experiment, the TOGA Coupled Ocean-Atmosphere Response Experiment (COARE).

The first three days were devoted to the Western Pacific International Meeting, with 80 high quality scientific presentations on the following themes:

- Water masses, sea surface topography and circulation.
- El Nino/Southern Oscillation 1986-87.
- Theoretical and modeling studies of ENSO and related processes.
- Momentum, heat and moisture fluxes between atmosphere and ocean.
- Empirical studies of ENSO and climate variability.

Each of the five sessions was introduced by an invited speaker who provided a review or detailed an important aspect of the session subject.

From the large number of papers presented at the Meeting/Workshop and their vigorous discussion, it is clear that there has been a significant increase over the last years in attention given to problems of oceanic and atmospheric circulation and interaction in the western tropical Pacific. As a result, there have been some major advances in our understanding of the region.

With now more than 40 recent TOGA-related cruises in the western tropical Pacific, our knowledge about oceanic circulation in this region has grown. In particular more is known about the relation of the equatorial currents to those at the western boundary. The Indo-Pacific throughflow has been the subject of increasing modeling studies and it apparently does not show much of an interannual signal related to the occurrence of ENSO events. Linear analytical results concerning the reflection of Rossby waves off the gappy western boundary are now in hand, and long equatorial Rossby waves (which have been definitively observed through XBT, BT, altimetry, and CTD/ADCP measurements) do not appear to lose much energy, because of the gaps, when they reflect.

Several ideas have been presented about the formation and variations of the warm pool region. Its cooling during El Nino appears more due to evaporation than advection, though the role of entrainment is still not certain. One-dimensional models suggest that the hydrological cycle plays an important role in the coupling of the atmosphere and ocean in the warm pool region, and observations show substantial variations of the salinity structures within the warm pool, leading to the conclusion that salinity effects must be included in models of the warm pool region.

It has been shown that the difficulties which modelers had previously in simulating the mean SST in the warm pool can be finessed in stand-alone ocean models. Coupled models suggest that the annual average net heat flux between atmosphere and ocean is small (< 20 W/m^2) in the warm pool region, which is at odds with climatological analyses. However, new results point out problems with the bulk formulations used in the climatologies, as well as probable biasing of the observations used in the analyses. These problems may be unique to the high SST/low mean wind regime of the western Pacific warm pool.

The importance of the 30-60 day atmospheric oscillation and westerly wind bursts during the development of ENSO has been discussed. It has not been possible to be definite on this matter, but real progress on the statistics and dynamics of these fluctuations has been achieved. The relationship of these phenomena to fluctuations in deep convection, precipitation, and heat fluxes seems to be strong, and thus they are important in their own right.

Space-based observations are promising. The prospects for obtaining some of the large-scale, low-frequency fields needed for understanding the coupled system are good, however there are some substantial calibration and validation efforts that are needed. A greater challenge lies in obtaining high spatial and temporal resolution fields using remote sensing data.

A recurring conclusion among both observers and modelers was that the sparsity of observations of momentum, heat and moisture fluxes, and in some cases the quality of the observations, are a major limitation in our pursuit of understanding of the processes involved in the ocean-atmosphere coupling in the western Pacific warm pool region.

The subsequent Workshop on TOGA COARE started with a presentation of a draft of the U.S. COARE Science Plan. Following the recommendation of the Intergovernmental TOGA Board, this plan was discussed, amended and finally adopted as a first draft of an International TOGA COARE Science Plan by the multinational community present in Noumea. This was made possible through separate and plenary discussions of the following working groups:

- Air-sea fluxes and boundary layer processes.
- Regional scale atmospheric circulation and waves.
- Regional scale oceanic circulation and waves.

In addition, the working groups started the development of an Implementation Plan for COARE. During the plenary sessions, several presentations were also made on COARE-related programs and relevant observational technologies. The proposed TOGA COARE will be able to address many of the important unresolved issues that were highlighted at the meeting. In particular, COARE offers a unique opportunity for the calibration/validation of satellite observations, and for the development/validation of improved models of the oceanic and atmospheric planetary boundary layers, as well as a hierarchy of coupled models. Strong enthusiasm for TOGA COARE was expressed at the Meeting/Workshop. Modelers and observers have identified interesting and challenging problems relating to the coupling of the ocean and atmosphere in the warm pool of the western tropical Pacific. The scientific planning for COARE was advanced to near completion, and a healthy start on implementation planning was made. Cooperation and coordination between the oceanographic and atmospheric components of COARE appears to be vigorous, with plans from the three working groups converging toward an effective warm pool air-sea interaction experiment.

RESUME

Le Symposium International sur le Pacifique Ouest et Réunion de Travail TOGA COARE, qui s'est tenu en Nouvelle Calédonie au Centre ORSTOM de Nouméa du 24 au 30 mai 1989, a réuni plus d'une centaine de scientifiques d'Australie, Chili, Chine, Etats Unis, France, Indonésie, Japon, Nouvelle-Zélande et du Royaume Uni. L'assemblée était composée d'un savant mélange d'océanographes et de météorologues, spécialistes des problèmes de circulation tropicale ou d'interactions océan-atmosphère. Le but principal de cet ensemble Symposium/Réunion de Travail était de faire le point des recherches du programme international TOGA dans tout le Pacifique Tropical Ouest, de coordonner les efforts croissants de recherches multinationales dans le réservoir d'eaux chaudes de cette région et de préparer au niveau international l'importante expérience TOGA COARE d'interactions océan-atmosphère.

Les trois premiers jours ont été consacrés au Symposium International sur le Pacifique Ouest, avec 80 présentations scientifiques de haute qualité sur les thèmes suivants:

- masses d'eaux, topographie de surface et circulation.
- El Nino/Oscillation Australe (ENSO) 1986-87.
- études théoriques et modélisation des ENSO et de ses processus.
- flux de quantité de mouvement, de chaleur et de vapeur d'eau entre atmosphère et océan.
- études empiriques des ENSO et de la variabilité climatique.

Chacune des cinq sessions était introduite par un orateur invité qui a effectué une revue de synthèse ou détaillé un aspect important du thème de la session.

Le nombre très important de communications présentées durant le Symposium/Réunion de Travail et les nombreuses discussions associées, ont fait apparaître, depuis ces dernières années, un intérêt marqué pour les problèmes de circulation océanique et atmosphérique et les interactions dans le Pacifique Ouest. De ce fait, de sérieux progrès dans la compréhension de cette région ont été réalisés.

Avec maintenant plus de 40 croisières récentes en rapport avec TOGA, dans le Pacifique Tropical Ouest, notre connaissance sur la circulation dans cette région s'est améliorée. En particulier, la liaison entre les courants équatoriaux et ceux de la frontière ouest est mieux connue. Les échanges d'eaux entre le Pacifique et l'Océan Indien ont été le sujet d'un nombre croissant de modèles et apparemment ne sont pas soumis à une importante variabilité interannuelle en rapport avec les événements ENSO. Les études analytiques linéaires, sur la réflection des ondes de Rossby sur la frontière perméable (chaîne d'îles) du Pacifique Ouest, sont maintenant au point. Les ondes longues équatoriales de Rossby (qui viennent d'être définitivement mise en évidence grâce à des mesures XBT, BT, altimétrique et CTD/ADCP) ne semblent pas trop perdre d'énergie en se réfléchissant sur cette frontière perméable.

Plusieurs idées ont été présentées à propos de la formation et des variations du réservoir d'eaux chaudes du Pacifique Ouest. Son refroidissement durant El Nino semble dû plus à l'évaporation qu'à l'advection, quoique le rôle de l'entraînement ne soit pas encore certain. Les modèles uni-dimensionnels suggèrent que le cycle hydrologique joue un rôle important dans le couplage entre l'atmosphère et l'océan dans la région du réservoir d'eaux chaudes.

Les observations montrent des variations considérables de la structure de salinité dans ce réservoir et mènent à la conclusion que les effets de salinité doivent être pris en compte pour sa modélisation.

Il a été montré que les difficultés rencontrées auparavant par les modélisateurs pour simuler la température de surface moyenne du réservoir d'eaux chaudes, pouvaient être réduites par des modèles uniquement océaniques. Les modèles couplés suggèrent que la moyenne annuelle du flux de chaleur entre l'atmosphère et l'océan est petite (< 20 W/m^2) dans la région du réservoir d'eaux chaudes, ce qui n'est pas en accord avec les résultats d'études climatologiques. Par contre de nouvelles études mettent en évidence des problèmes avec les formules empiriques utilisées pour les climatologies, ainsi qu'un biais probable des observations utilisées pour ces analyses. Ces problèmes sont peut être uniques au réservoir d'eaux chaudes du Pacifique Ouest de par ses fortes températures de surface et son régime de vent faible.

L'importance de l'oscillation atmosphérique à 30-60 jours de période et de celle des coups de vent d'ouest pour le développement des ENSO a été discutée. Il n'a pas été possible d'aboutir à une conclusion à ce sujet, mais des progrès réels sur les statistiques et la dynamique de ces fluctuations ont été réalisés. Les relations entre ces phénomènes et les fluctuations de convection atmosphérique profonde, des précipitations et des flux de chaleur apparaissent marquées et de ce fait elles sont importantes en elles mêmes.

Les observations à partir de satellites sont prometteuses. Les perspectives sont bonnes pour obtenir quelques uns des champs basse fréquence et grande échelle, nécessaires à la compréhension du système couplé océan-atmosphère. Cependant il sera indispensable de faire un effort particulier dans l'étalonnage et la validation de ces observations. Un défi plus important est l'obtention de champs à haute résolution spatio-temporelle, à partir de capteurs satellitaires.

Une des conclusions, qui revenait régulièrement à l'esprit des observateurs et des modélisateurs était que la limitation principale à la compréhension des processus de couplage océan-atmosphère dans la région du réservoir d'eaux chaudes du Pacifique Ouest, vient du faible nombre d'observations de quantité de mouvement, de chaleur et de vapeur d'eau, et dans quelques cas de la qualité des observations,

La Réunion de Travail TOGA COARE, succédant au Symposium, a commencé par une présentation du document préliminaire du projet scientifique U.S. COARE. En suivant les recommandations du Bureau Intergouvernemental TOGA, ce document a été discuté, amélioré et finalement adopté, comme base pour un projet international TOGA COARE, par la communauté scientifique présente à Nouméa. Cela a été possible grâce aux séances plénières et séparées des groupes de travail ci-aprés:

- Processus des flux d'échanges air-mer et des couches interfaces.
- Circulation régionale atmosphérique et ondes associées.
- Circulation régionale océanique et ondes associées.

De plus, les groupes de travail, ont ébauché un plan de mise en oeuvre pour l'expérience COARE. Durant les sessions plénières, plusieurs communications ont aussi été présentées sur les programmes et les techniques d'observations pouvant se rapporter à COARE. L'expérience TOGA COARE proposée devrait être capable de répondre à de nombreuses questions non résolues qui ont été mises en avant durant le Symposium/Réunion de Travail. En particulier, l'expérience COARE va offrir une occasion unique pour l'étalonnage et la validation des observations et pour développer et valider, aussi bien les modèles océaniques et atmosphériques à couche limite que toute la gamme de modèles

couplés. Un enthousiasme marqué pour l'expérience TOGA COARE a été exprimé lors du Symposium/Réunion de Travail. Les modélisateurs et les observateurs ont identifié des problèmes très intéressants en rapport avec le couplage océan-atmosphère dans la région du réservoir d'eaux chaudes du Pacifique Ouest. Le projet scientifique pour COARE est presque achevé et un premier projet de mise en oeuvre a été bien avancé. La coopération et la coordination, entre les parties océanographique et atmosphérique de COARE, semblent se développer harmonieusement en suivant les projets des trois groupes de travail qui convergent vers une expérience efficace d'interaction air-mer sur le réservoir d'eaux chaudes du Pacifique Ouest.

ACKNOWLEDGMENTS

The Western Pacific International Meeting and Workshop on TOGA COARE was hosted by the Groupe SURTROPAC in the Centre ORSTOM de Nouméa.

Funding for the organization of the Meeting/Workshop and travel support were provided by the following agencies: Ministère de la Recherche et de la Technologie, Institut Français de Recherche Scientifique pour le Développement en Coopération (ORSTOM), International TOGA Project Office, Comité National Français pour la Commission Océanographique Intergouvernementale, Ministère des Affaires Etrangères, and Institut Français de Recherche pour l'Exploitation de la Mer. Major travel support for U.S. participants was provided by the U.S. TOGA Project Office. Additional U.S. travel support was provided by the National Aeronautics and Space Administration and the National Science Foundation.

Jean Fages, Director of the Centre ORSTOM de Nouméa, and his collaborators were of great help for this Meeting/Workshop. The success of this conference was mainly due to the excellent logistic support provided by the members of the Groupe SURTROPAC namely, Bruno Camusat, Anne Dandine, Yves Dandonneau, Thierry Delcroix, Gérard Eldin, Jacques Grelet, Christian Hénin, Marie José Langlade, François Masia, Yves Montel, Yves du Penhoat, Pierre Rual, Laurence Sombardier, Pierre Waigna, Sela Waigna and Henri Walico. Marie Françoise de Greslan, Véronique Maridet, Philippe Ribère and Marie Louise Touboul were also of great assistance. Jean Pierre Mermoud helped tremendously in the preparation of the proceedings. The Chairmen of the Workshop working groups, Antonio Busalacchi, Charles Eriksen, Greg Holland, William Lau, Timothy Liu, John Young together with Richard Carbone and Eric Lindstrom, helped in preparing the workshop proceedings.

The contribution of all these individuals and agencies is gratefully acknowledged.

Finally we would like to thank all attendees for their participation and contribution to the Meeting/Workshop.

Joël Picaut and Roger Lukas
Co-Chairmen
Western Pacific International Meeting
and Workshop on TOGA COARE.

TABLE OF CONTENTS

ABSTRACT i

RESUME iii

ACKNOWLEDGMENTS vi

INTRODUCTION

1. Motivation 1
2. Structure 2

LIST OF PARTICIPANTS 5

AGENDA 7

WORKSHOP REPORT

1. Introduction 19
2. Working group discussions, recommendations, and plans 20
   a. Air-Sea Fluxes and Boundary Layer Processes 20
   b. Regional Scale Atmospheric Circulation and Waves 24
   c. Regional Scale Oceanic Circulation and Waves 30
3. Related programs 35
   a. NASA Ocean Processes and Satellite Missions 35
   b. Tropical Rainfall Measuring Mission 37
   c. Typhoon Motion Program 39
   d. World Ocean Circulation Experiment 39
4. Presentations on related technology 40
5. National reports 40
6. Meeting of the International Ad Hoc Committee on TOGA COARE 40

APPENDIX: WORKSHOP RELATED PAPERS

Robert A. Weller and David S. Hosom: Improved Meteorological Measurements from Buoys and Ships for the World Ocean Circulation Experiment 45

Peter H. Hildebrand: Flux Measurement using Aircraft and Radars 57

Walter F. Dabberdt, Hale Cole, K. Gage, W. Ecklund and W.L. Smith: Determination of Boundary-Layer Fluxes with an Integrated Sounding System 81

MEETING COLLECTED PAPERS

WATER MASSES, SEA SURFACE TOPOGRAPHY, AND CIRCULATION

Klaus Wyrtki: Some Thoughts about the West Pacific Warm Pool 99
Jean René Donguy, Gary Meyers, and **Eric Lindstrom**: Comparison of the Results of two West Pacific Oceanographic Expeditions FOC (1971) and WEPOCS (1985-86) 111
Dunxin Hu, and **Maochang Cui**: The Western Boundary Current in the Far Western Pacific Ocean 123
Peter Hacker, Eric Firing, Roger Lukas, Philipp L. Richardson, and **Curtis A. Collins**: Observations of the Low-latitude Western Boundary Circulation in the Pacific during WEPOCS III 135
Stephen P. Murray, John Kindle, Dharma Arief, and **Harley Hurlburt**: Comparison of Observations and Numerical Model Results in the Indonesian Throughflow Region 145
Christian Henin: Thermohaline Structure Variability along 165°E in the Western Tropical Pacific Ocean (January 1984 - January 1989) 155
David J. Webb, and **Brian A. King**: Preliminary Results from Charles Darwin Cruise 34A in the Western Equatorial Pacific 165
Warren B. White, Nicholas Graham, and **Chang-Kou Tai**: Reflection of Annual Rossby Waves at The Maritime Western Boundary of the Tropical Pacific 173
William S. Kessler: Observations of Long Rossby Waves in the Northern Tropical Pacific 185
Eric Firing, and **Jiang Songnian**: Variable Currents in the Western Pacific Measured During the US/PRC Bilateral Air-Sea Interaction Program and WEPOCS 205
John S. Godfrey, and **A. Weaver**: Why are there Such Strong Steric Height Gradients off Western Australia ? 215
John M. Toole, R.C. Millard, Z. Wang, and **S. Pu**: Observations of the Pacific North Equatorial Current Bifurcation at the Philippine Coast 223

EL NINO/SOUTHERN OSCILLATION 1986-87

Gary Meyers, Rick Bailey, Eric Lindstrom, and **Helen Phillips**: Air/Sea Interaction in the Western Tropical Pacific Ocean during 1982/83 and 1986/87 229
Laury Miller, and **Robert Cheney**: GEOSAT Observations of Sea Level in the Tropical Pacific and Indian Oceans during the 1986-87 El Nino Event 247
Thierry Delcroix, Gérard Eldin, and **Joël Picaut**: GEOSAT Sea Level Anomalies in the Western Equatorial Pacific during the 1986-87 El Nino, Elucidated as Equatorial Kelvin and Rossby Waves 259
Gérard Eldin, and **Thierry Delcroix**: Vertical Thermal Structure Variability along 165°E during the 1986-87 ENSO Event 269
Michael J. McPhaden: On the Relationship between Winds and Upper Ocean Temperature Variability in the Western Equatorial Pacific 283

John S. Godfrey, K. Ridgway, Gary Meyers, and Rick Bailey: Sea Level and Thermal Response to the 1986-87 ENSO Event in the Far Western Pacific 291
Joël Picaut, Bruno Camusat, Thierry Delcroix, Michael J. McPhaden, and Antonio J. Busalacchi: Surface Equatorial Flow Anomalies in the Pacific Ocean during the 1986-87 ENSO using GEOSAT Altimeter Data 301

THEORETICAL AND MODELING STUDIES OF ENSO AND RELATED PROCESSES

Julian P. McCreary, Jr.: An Overview of Coupled Ocean-Atmosphere Models of El Nino and the Southern Oscillation 313
Kensuke Takeuchi: On Warm Rossby Waves and their Relations to ENSO Events 329
Yves du Penhoat, and Mark A. Cane: Effect of Low Latitude Western Boundary Gaps on the Reflection of Equatorial Motions 335
Harley Hurlburt, John Kindle, E. Joseph Metzger, and Alan Wallcraft: Results from a Global Ocean Model in the Western Tropical Pacific 343
John C. Kindle, Harley E. Hurlburt, and E. Joseph Metzger: On the Seasonal and Interannual Variability of the Pacific to Indian Ocean Throughflow 355
Antonio J. Busalacchi, Michael J. McPhaden, Joël Picaut, and Scott Springer: Uncertainties in Tropical Pacific Ocean Simulations: The Seasonal and Interannual Sea Level Response to Three Analyses of the Surface Wind Field 367
Stephen E. Zebiak: Intraseasonal Variability - A Critical Component of ENSO ? 379
Akimasa Sumi: Behavior of Convective Activity over the "Jovian-type" Aqua-Planet Experiments 389
Ka-Ming Lau: Dynamics of Multi-Scale Interactions Relevant to ENSO 397
Pecheng C. Chu and Roland W. Garwood, Jr.: Hydrological Effects on the Air-Ocean Coupled System 407
Sam F. Iacobellis, and Richard C.J. Somerville: A one Dimensional Coupled Air-Sea Model for Diagnostic Studies during TOGA-COARE 419
Allan J. Clarke: On the Reflection and Transmission of Low Frequency Energy at the Irregular Western Pacific Ocean Boundary - a Preliminary Report 423
Roland W. Garwood, Jr., Pecheng C. Chu, Peter Muller, and Niklas Schneider: Equatorial Entrainment Zone : the Diurnal Cycle 435
Peter R. Gent: A New Ocean GCM for Tropical Ocean and ENSO Studies 445
Wasito Hadi, and Nuraini: The Steady State Response of Indonesian Sea to a Steady Wind Field 451
Pedro Ripa: Instability Conditions and Energetics in the Equatorial Pacific 457
Lewis M. Rothstein: Mixed Layer Modelling in the Western Equatorial Pacific Ocean 465
Neville R. Smith: An Oceanic Subsurface Thermal Analysis Scheme with Objective Quality Control 475
Duane E. Stevens, Qi Hu, Graeme Stephens, and David Randall: The hydrological Cycle of the Intraseasonal Oscillation 485
Peter J. Webster, Hai-Ru Chang, and Chidong Zhang: Transmission Characteristics of the Dynamic Response to Episodic Forcing in the Warm Pool Regions of the Tropical Oceans 493

MOMENTUM, HEAT, AND MOISTURE FLUXES BETWEEN ATMOSPHERE AND OCEAN

W. Timothy Liu: An Overview of Bulk Parametrization and Remote Sensing of Latent Heat Flux in the Tropical Ocean 513
E. Frank Bradley, Peter A. Coppin, and **John S. Godfrey**: Measurements of Heat and Moisture Fluxes from the Western Tropical Pacific Ocean 523
Richard W. Reynolds, and **Ants Leetmaa**: Evaluation of NMC's Operational Surface Fluxes in the Tropical Pacific 535
Stanley P. Hayes, Michael J. McPhaden, John M. Wallace, and **Joël Picaut**: The Influence of Sea-Surface Temperature on Surface Wind in the Equatorial Pacific Ocean 543
T.D. Keenan, and **Richard E. Carbone**: A Preliminary Morphology of Precipitation Systems In Tropical Northern Australia 549
Phillip A. Arkin: Estimation of Large-Scale Oceanic Rainfall for TOGA 561
Catherine Gautier, and **Robert Frouin**: Surface Radiation Processes in the Tropical Pacific 571
Thierry Delcroix, and **Christian Henin**: Mechanisms of Subsurface Thermal Structure and Sea Surface Thermo-Haline Variabilities in the South Western Tropical Pacific during 1979-85 - A Preliminary Report 581
Greg. J. Holland, T.D. Keenan, and **M.J. Manton**: Observations from the Maritime Continent : Darwin, Australia 591
Roger Lukas: Observations of Air-Sea Interactions in the Western Pacific Warm Pool during WEPOCS 599
M. Nunez, and **K. Michael**: Satellite Derivation of Ocean-Atmosphere Heat Fluxes in a Tropical Environment 611

EMPIRICAL STUDIES OF ENSO AND SHORT-TERM CLIMATE VARIABILITY

Klaus M. Weickmann: Convection and Circulation Anomalies over the Oceanic Warm Pool during 1981-1982 623
Claire Perigaud: Instability Waves in the Tropical Pacific Observed with GEOSAT 637
Ryuichi Kawamura: Intraseasonal and Interannual Modes of Atmosphere-Ocean System Over the Tropical Western Pacific 649
David Gutzler, and **Tamara M. Wood**: Observed Structure of Convective Anomalies 659
Siri Jodha Khalsa: Remote Sensing of Atmospheric Thermodynamics in the Tropics 665
Bingrong Xu: Some Features of the Western Tropical Pacific: Surface Wind Field and its Influence on the Upper Ocean Thermal Structure 677
Bret A. Mullan: Influence of Southern Oscillation on New Zealand Weather 687
Kenneth S. Gage, Ben Basley, Warner Ecklund, D.A. Carter, and**John R. McAfee**: Wind Profiler Related Research in the Tropical Pacific 699
John Joseph Bates: Signature of a West Wind Convective Event in SSM/I Data 711
David S. Gutzler: Seasonal and Interannual Variability of the Madden-Julian Oscillation 723
Marie-Hélène Radenac: Fine Structure Variability in the Equatorial Western Pacific Ocean 735
George C. Reid, Kenneth S. Gage, and **John R. McAfee**: The Climatology of the Western Tropical Pacific: Analysis of the Radiosonde Data Base 741

Chung-Hsiung Sui, and Ka-Ming Lau: Multi-Scale Processes in the Equatorial Western Pacific 747
Stephen E. Zebiak: Diagnostic Studies of Pacific Surface Winds 757

MISCELLANEOUS

Rick J. Bailey, Helene E. Phillips, and Gary Meyers: Relevance to TOGA of Systematic XBT Errors 775
Jean Blanchot, Robert Le Borgne, Aubert Le Bouteiller, and Martine Rodier: ENSO Events and Consequences on Nutrient, Planktonic Biomass, and Production in the Western Tropical Pacific Ocean 785
Yves Dandonneau: Abnormal Bloom of Phytoplankton around 10°N in the Western Pacific during the 1982-83 ENSO 791
Cécile Dupouy: Sea Surface Chlorophyll Concentration in the South Western Tropical Pacific, as seen from NIMBUS Coastal Zone Color Scanner from 1979 to 1984 (New Caledonia and Vanuatu) 803
Michael Szabados, and Darren Wright: Field Evaluation of Real-Time XBT Systems 811
Pierre Rual: For a Better XBT Bathy-Message: Onboard Quality Control, plus a New Data Reduction Method 823

INTRODUCTION

1. Motivation.

The physical oceanography group of the Centre ORSTOM de Nouméa (named SURTROPAC in 1980 for SURvey of the TROpical PACific) has a long history of research measurements and discoveries in the western tropical Pacific. One of the most reproduced figures in equatorial oceanography is the temperature section along the equator from 86°W to 160°E resulting from measurements made during the 1964-65 boreal winter, and originally published by Lemasson and Piton (1968). The corresponding hydrological section was made during the maiden voyage of the R/V Coriolis from France to its permanent port of attachment in Nouméa. About 50 physical oceanography cruises were carried out in the Pacific until the end of its research vessel career with the January 1989 SURTROPAC-TOGA #11th cruise, regularly made along 165°E. During this quarter century of research work, 150-200 papers and reports were published. As time goes, the SURTROPAC group got more and more involved in multinational research activities (e.g. the tropical Pacific XBT network in 1979) and recently dedicated all of its activities to the TOGA programme. Most of the effort of the TOGA international scientific community is concentrated in the tropical Pacific and largely in its western part. As a consequence more than 40 cruises from seven different countries have been conducted in the western tropical Pacific since 1985.

With the growing interest of the TOGA programme in the warm pool region, the accumulation of consequent scientific results, and the fact that most of these activities at sea were relatively uncoordinated, it appeared necessary to organize an international meeting on air-sea interactions in the western tropical Pacific. This had been recognized as early as December 1986 during the first WESTPAC Symposium in Townsville, Australia. National or bilateral symposia have already dealt with such matters. The U.S. community held an important TOGA Western Pacific Air-Sea Interaction Workshop in Honolulu in September 1987, where it was strongly recommended to design a Coupled Ocean-Atmosphere Response Experiment (COARE) in the western tropical Pacific. Air-sea interactions in the Tropical Western Pacific was the purpose of the US/PRC symposium held in Beijing in November 1988. Given the comfortable facilities of the Centre ORSTOM de Nouméa and of its surroundings, Joël Picaut and Roger Lukas had decided to organize, with the cooperation of John Marsh of the International TOGA Project Office, the joint Western Pacific International Meeting and Workshop on TOGA COARE in Nouméa on May 24-30, 1989. The main purpose of this combined Meeting/Workshop was to review the status of western tropical Pacific oceanic and atmospheric research, coordinate the multinational research efforts in the warm pool region, and cooperate in the planning of a major international air-sea interaction experiment, TOGA COARE.

The goals of the Western Pacific International Meeting were to document results of recent TOGA modeling and data analyses that pertain to the western tropical Pacific ocean-atmosphere system. This was done by a combination of 80 invited and contributed presentations covering the following areas of research:

- Water masses, sea surface topography and circulation.
- El Nino/Southern Oscillation 1986-87.
- Theoretical and modeling studies of ENSO and related processes.
- Momentum, heat and moisture fluxes between atmosphere and ocean.
- Empirical studies of ENSO and climate variability.

The multi-national participation at the Meeting/Workshop provided the first real opportunity for the coordination of ongoing western tropical Pacific field efforts, and also provided an important opportunity for coordination of the many national plans for future research in the western tropical Pacific.

The Workshop on TOGA-COARE brought together scientists from a number of nations with interests in the problems of the western Pacific warm pool. A draft of the U.S. TOGA COARE Science Plan was presented for discussion, and the subsequent comments and revisions were incorporated. One important objective was to develop an internationally acceptable TOGA COARE Science Plan for consideration by the TOGA Scientific Steering Group (SSG) at its meeting in Hamburg in September 1989.

In early 1989, Peter Webster, chairman of the TOGA SSG formed an International Ad Hoc Committee on TOGA COARE, and the Meeting/Workshop in Nouméa offered an ideal venue for its first meeting. This group is to represent the scientific interest of the nations participating in COARE, both in the revision of the COARE Science Plan, and in the development of the COARE Implementation Plan.

2. Structure.

Based on the large number of participants gathering in Nouméa, two other meetings were held in Nouméa. The CCCO Pacific Panel held their annual meeting on May 20-23. The TOGA XBT Ad Hoc Panel of Experts met for the first time on May 31-June 1.

At the opening ceremony of the Meeting/Workshop, the 106 scientific participants were welcomed by a representative of the High Commissioner for New Caledonia and by the President of ORSTOM, the latter having travelled from France for the occasion. Each of the five sessions of the Western Pacific International Meeting was introduced by an invited speaker, who in 45 min. either provided a review or detailed an important aspect of the corresponding session topic. Due to the large number of abstracts received after the first announcement, the meeting was divided into an equal number of 25 min. oral presentations (including 5 min. discussion) and into two one-and-a-half day poster sessions. In addition, a miscellaneous poster session was added for a few presentations not directly related to air-sea interaction in the western tropical Pacific (such as ENSO-related productivity variability or XBT improvement techniques).

The Workshop on TOGA COARE started with a presentation of the U.S. TOGA COARE Science Plan. The workshop was then divided into three working groups:

- Air-Sea Fluxes and Boundary Processes.
- Regional Scale Atmospheric Circulation and Waves.
- Regional Scale Oceanic Circulation and Waves.

The corresponding reports were discussed in plenary session and led to recommendations regarding mostly implementation plans for COARE. Related programs, such as NASA Ocean Processes and Satellite Missions, Tropical Rainfall Measuring Mission, Typhoon Motion Program and World Ocean Circulation Experiment were presented, as well as two papers on related technology. In the last Workshop plenary session, scientists of seven nations (Australia, China, France, Indonesia, Japan, United Kingdom and United States) presented their informal reports related to tentative plans for national participation in TOGA COARE.

Finally, well-prepared social events helped to compensate for the unusual rainy weather which prevailed during most of the Meeting/Workshop as a consequence of the Pacific-wide cold event.

The remainder of these proceedings does not follow the order of the Meeting/Workshop. With most of the oral and poster presentations resulting in more than 700 pages of collected papers, it has been decided to present first the report of the TOGA COARE Workshop.

LIST OF PARTICIPANTS

Alexiou, Arthur	CCCO/IOC, Paris, France
Anderson, David	Clarendon Lab., Oxford, United Kingdom
Arkin, Phillip	NOAA/NMC/CAC, Washington D.C., U.S.A.
Bailey, Rick	CSIRO, Hobart, Australia
Blanchot, Jean	PROPPAC/ORSTOM, Nouméa, New Caledonia
Bradley, Frank	CSIRO, Canberra, Australia
Busalacchi, Antonio	NASA/GSFC, Greenbelt, U.S.A.
Buizer, James	NOAA/USTPO, Rockville, U.S.A.
Cadet, Daniel	INSU/CNRS, Paris, France
Camusat, Bruno	SURTROPAC/ORSTOM, Nouméa, New Caledonia
Carbone, Richard	NCAR, Boulder, U.S.A.
Clarke, Allan	Florida St. Univ., Tallahassee, U.S.A.
Coppin, Peter	CSIRO, Canberra, Australia
Dabberdt, Walter	NCAR, Boulder, U.S.A.
Dandonneau, Yves	SURTROPAC/ORSTOM, Nouméa, New Caledonia
Delcroix, Thierry	SURTROPAC/ORSTOM, Nouméa, New Caledonia
Donguy, Jean Rene	ORSTOM, Brest, France
Douillet, Pascal	ORSTOM, Nouméa, New Caledonia
Du Penhoat, Yves	SURTROPAC/ORSTOM Nouméa, New Caledonia
Dupouy, Cecile	PROPPAC/ORSTOM ,Nouméa, New Caledonia
Eldin, Gerard	SURTROPAC/ORSTOM, Nouméa, New Caledonia
Eriksen, Charles	University of Washington, Seattle, U.S.A.
Espinoza, Felix	Vina del Mar, Chile
Fairall, Chris	Penn. State Univ. University Park, U.S.A.
Firing, Eric	JIMAR/Univ. Hawaii, Honolulu, U.S.A.
Fonseca, Tomas	Universidad Catolica, Valparaiso, Chile
Gage, Kenneth	NOAA/ERL, Boulder, U.S.A.
Gal-Chen, Tzvi	University of Oklahoma, Norman, U.S.A.
Garwood, Roland	Naval Postgraduate School, U.S.A.
Gautier, Catherine	SIO, La Jolla, U.S.A.
Gent, Peter	NCAR, Boulder, U.S.A.
Godfrey, Stuart	CSIRO, Hobart, Australia
Graham, Nicholas	SIO, La Jolla, U.S.A.
Gutzler, David	Atm. and Environ. Res. Inc., Cambridge, U.S.A.
Hadi, Wasito	Meteor. and Geophys. Agency, Jakarta, Indonesia
Hagan, Denise	JPL, Pasadena, U.S.A.
Harjanto, Hery	Meteor. and Geophys. Agency, Jakarta, Indonesia
Hayes, Stanley	NOAA/PMEL, Seattle, U.S.A.
Henin, Christian	SURTROPAC/ORSTOM, Nouméa, New Caledonia
Hildebrand, Peter	NCAR, Boulder, U.S.A.
Holland, Greg	BMRC, Melbourne, Australia
Hu, Dunxin	Inst. of Ocean., Qingdao, People's Republic of China
Hurlburt, Harley	NORDA, Bay St. Louis, U.S.A.
Jarrige, Francois	ORSTOM, Paris, France
Kakar, Ramesh	NASA/H.Q., Washington D.C., U.S.A.
Kawamura, Ryuichi	Environ. Res. Center, Tsukuba, Japan
Khalsa, Siri Jodha	CIRES, Boulder, U.S.A.
Kessler, William	University of Washington, Seattle, U.S.A.
Kindle, John	NORDA, Bay St. Louis, U.S.A.
Lau, Ka-Ming	NASA/GSFC, Greenbelt, U.S.A.
Lagerloef, Gary	NASA/H.Q., Washington D.C., U.S.A.
Le Borgne, Robert	PROPPAC/ORSTOM, Nouméa, New Caledonia

Le Bouteiller, Aubert	PROPPAC/ORSTOM, Nouméa, New Caledonia
Lee, Valerie	ITPO, Geneva, Switzerland
Lindstrom, Eric	CSIRO, Hobart, Australia
Liu, Timothy	JPL, Pasadena, U.S.A.
Lukas, Roger	JIMAR/Univ. Hawaii, Honolulu, U.S.A.
Mangum, Linda	NOAA/PMEL, Seattle, U.S.A.
Marsh, John	ITPO, Geneva, Switzerland
McCreary, Julian	Nova University, Dania, U.S.A.
McPhaden, Michael	NOAA/PMEL, Seattle, U.S.A.
Meyers, Gary	CSIRO, Hobart, Australia
Miller, Laury	NOAA/NOS, Rockville, U.S.A.
Moncrieff, Mitchell	NCAR, Boulder, U.S.A.
Mooney, Kenneth	NOAA/USTPO, Rockville, U.S.A.
Morliere, Alain	ORSTOM, Paris, France
Motard, Jean Luc	Serv. Météo., Nouméa, New Caledonia
Mullan, Brett	New Zeland Met. Serv., Wellington, New Zealand
Murray, Stephen	CSI/Louisiana St. Univ., Baton Rouge, U.S.A.
Patzert, William	JPL, Pasadena, U.S.A.
Perigaud, Claire	JPL, Pasadena, U.S.A.
Pianet, Renaud	ORSTOM, Nouméa, New Caledonia
Picaut, Joël	SURTROPAC/ORSTOM, Nouméa, New Caledonia
Planton, Serge	CNRM, Paris, France
Radenac, Marie H.	PROPPAC/ORSTOM, Nouméa, New Caledonia
Rebert, Jean Paul	ORSTOM, Brest, France
Reid, George	NOAA/ERL, Boulder, U.S.A.
Reverdin, Gilles	LODYC, Paris, France
Reynolds, Richard	NOAA/NWS/NMC, Washington, U.S.A.
Rodier, Martine	PROPPAC/ORSTOM, Nouméa, New Caledonia
Rothstein, Lewis	University of Washington, Seattle, U.S.A.
Rual, Pierre	SURTROPAC/ORSTOM, Nouméa, New Caledonia
Sawyer-Crouch, Karyn	UCAR, Boulder, U.S.A.
Smith, Neville	BMRC, Melbourne, Australia
Sombardier, Laurence	SURTROPAC/ORSTOM, Nouméa, New Caledonia
Somerville, Richard	SIO, La Jolla, U.S.A.
Stephens, Graeme	Colorado St. Univ., Fort Collins, U.S.A.
Stevens, Duane	Colorado St. Univ., Fort Collins, U.S.A.
Sui, Chung-Hsiung	NASA/GSFC, Greenbelt, U.S.A.
Sumi, Akimasa	University of Tokyo, Tokyo, Japan
Takeuchi, Kensuke	Hokkaido University, Sapporo, Japan
Theon, John	NASA/H.Q., Washington D.C., U.S.A.
Thiele, Otto	NASA/GSFC, Greenbelt, U.S.A.
Tournier, Rolande	SURTROPAC/ORSTOM, Nouméa, New Caledonia
Voituriez, Bruno	IFREMER, Paris, France
Waliser, Duane	SIO, La Jolla, U.S.A.
Webster, Peter	Penn. State Univ., University Park, U.S.A.
Webb, David	IOS, Godalming Surrey, United Kingdom
Weickman, Klaus	NOAA/ERL/CRD, Boulder, U.S.A.
White, Warren	SIO, La Jolla, U.S.A.
Woodward, William	NOAA/NOS, Rockville, U.S.A.
Wyrtki, Klaus	University of Hawaii, Honolulu, U.S.A.
Xu, Bingrong	Snd. Inst. Ocean., Hangzhou, People's Republic of China
Young, John	University of Wisconsin, Madison, U.S.A.
Zebiak, Stephen	Lamont. Dorherty Geol. Obs., Palisades, U.S.A.
Zhou, Xiaoping	Inst. of Atm. Phys., Beijing, People's Republic of China

AGENDA

WESTERN PACIFIC INTERNATIONAL MEETING AND WORKSHOP ON TOGA COARE

Centre ORSTOM de Nouméa, New Caledonia

May 24-30, 1989

Wednesday, May 24

07H30: Registration/Poster setup

08H30: Official Welcome and Opening Remarks

Charles ERIKSEN (Session Chairman)

WATER MASSES, SEA SURFACE TOPOGRAPHY, AND CIRCULATION

09H15:
Invited speaker: Klaus WYRTKI: Some thoughts about the West Pacific Warm Pool

09H45 - 10H15: Coffee Break/Posters

Jean-René DONGUY, Gary MEYERS and Eric LINDSTROM: Comparison of results of two pre-COARE cruises: FOC (1971) and WEPOCS (1985-86).

Dunxin HU: Interannual Variability of the Western Boundary Current in the Pacific Ocean.

Peter HACKER, Eric FIRING and Roger LUKAS: Observations of the Low-Latitude Western Boundary Circulation in the Pacific during WEPOCS III.

Stephen MURRAY, Dharma ARIEF and John KINDLE: Throughflow between the Western Pacific and the Indian Ocean: Comparison between model and observations.

12H00 - 13H45: Lunch

Dunxin HU (Session Chairman)

13H45:
Christian HENIN: Thermohaline structures variability along 165°E in the Western Tropical Pacific Ocean (January 1984-January 1989).

Linda J. MANGUM and Stanley P. HAYES: Zonal scales of thermohaline variability in the Western Equatorial Pacific.

David J. WEBB and Brian A. KING: A survey of the Western Equatorial Pacific in September 1988.

15H15 - 15H45: Coffee Break/Posters

Poster session: Wednesday morning through Thursday midday

Eric FIRING and Jiang SONGNIAN: Variable currents in the Western Pacific measured during the USA-PRC bilateral TOGA Project.

John Stuart GODFREY: Steric height gradients, the Indonesian throughflow and the Leeuwin current.

Phillip L. RICHARDSON and Curtis A. COLLINS: Preliminary results from WEPOCS Drifters.

John M. TOOLE, Robert MILLARD, Maggie FRANCIS, Zongshan WANG and S. PU: On the bifurcation of the North Equatorial Current at the Philippine coast.

Rolande TOURNIER and Joël PICAUT: Thermal and current structure variabilities in the Western and Central Tropical Pacific during 1979-85.

Xiaoping ZHOU: An introduction of the four year expedition on West Pacific conducted by China Academy of Sciences.

EL NINO/SOUTHERN OSCILLATION 1986-87

15H45:

Invited speaker: Gary MEYERS (and Rick BAILEY, Eric LINDSTROM and Helen PHILIPS): Air-Sea interaction in the Tropical Pacific ocean during 1982-83 and 1986-87.

Laury MILLER and Robert CHENEY: GEOSAT observations of sea level in the Tropical Pacific and Indian oceans during the 1986-87 El Nino event.

Thierry DELCROIX, Gerard ELDIN and Joël PICAUT: Major GEOSAT sea level anomalies in the Western Tropical Pacific during the 1986-87 El Nino, elucidated as equatorial Kelvin and Rossby waves.

Gerard ELDIN and Thierry DELCROIX: Vertical thermal structure variability along 165°E during the 1986-87 ENSO event.

Michael J. McPHADEN and Stanley P. HAYES: Westerly wind forcing and SST variations in the Western Pacific during the 1986-87 event.

Poster session: Wednesday morning through Thursday midday

John Stuart GODFREY, Ken RIDGWAY, Gary MEYERS and Rick BAILEY: Sea level and thermal response to the 1986-87 ENSO event in the far Western Pacific.

Joël PICAUT, Bruno CAMUSAT, Thierry DELCROIX, Michael J. McPHADEN, and Antonio J. BUSALACCHI: Surface equatorial flow anomalies in the Pacific ocean during the 1986-87 ENSO using GEOSAT altimeter data.

18H30: Official reception at ORSTOM Hall

Thursday, May 25

John Stuart GODFREY (Session Chairman)

WATER MASSES, SEA SURFACE TOPOGRAPHY, AND CIRCULATION (continued)

08H15:
Warren B. WHITE, Chang-Kou TAI and Stephen PAZAN: The study of thermocline development in the Western Tropical Pacific during El Nino using TOGA XBT's GEOSAT altimetry, and the FSU Tropical Pacific model.

William S. KESSLER: Observations of long Rossby waves in the Northern Tropical Pacific.

THEORETICAL AND MODELING STUDIES OF ENSO AND RELATED PROCESSES

09H00:
Invited Speaker: Julian P. McCREARY: Coupled Ocean-Atmosphere models of El Nino and the Southern Oscillation.

09H45 - 10H15: Coffee Break/Posters

10H15:
Kensuke TAKEUCHI: On warm Rossby waves and their relation to ENSO events.

Yves du PENHOAT and Mark A. CANE: Effect of low latitude western boundary gaps on the reflection of equatorial motions.

Harley E. HURLBURT, John KINDLE, Joseph E. METZGER and Allan WALLCRAFT: Results from a global ocean model in the Western Tropical Pacific.

John KINDLE, Harley E. HURLBURT and Joseph E. METZGER: The dynamics of the Pacific to Indian ocean throughflow.

12H00 - 14H00: Lunch and poster changeover

Daniel CADET (Session Chairman)

14H00:

Nicholas E. GRAHAM and Warren WHITE: A simple 2-dimensional coupled model of the Equatorial Pacific.

Antonio J. BUSALACCHI, Michael J. McPHADEN, Joël PICAUT and Scott SPRINGER: Sensitivity of wind driven Tropical Pacific Ocean simulations on seasonal and interannual time scales.

Stephen E. ZEBIAK: Intraseasonal variability - a critical component of ENSO ?

Akimasa SUMI: Behavior of convective activity over the "Jovian-type" aqua-planet model.

15H45 - 16H15: Coffee Break/Posters

16H15:

Ka-Ming LAU: Dynamics of multi-scale atmosphere-ocean Interactions over the Tropical Western Pacific.

Edmund D. HARRISON and Benjamin S. GIESE : Some OGCM studies of the oceanic response to westerly wind episodes.

Roland W. GARWOOD and Pecheng C. CHU: Hydrological effects on the air-ocean coupled system.

Sam F. IACOBELLIS and Richard C.J. SOMERVILLE: A one-dimensional coupled air-sea model for diagnostic studies during TOGA/COARE.

Poster session: Wednesday morning through Thursday midday

Allan J. CLARKE: On the reflection and transmission of low frequency energy at the irregular Pacific Ocean boundary.

Roland W. GARWOOD, Peter MULLER, Pecheng CHU and Niklas SCHNEIDER: The equatorial mixed layer system: mean state and diurnal modulation.

Peter R. GENT: The sensitivity of the annual cycle in the Tropical Pacific Ocean to vertical mixing parameterizations.

Wasito HADI and NURAINI: The steady state response of Indonesian sea to a steady wind field.

Pedro RIPA: Instability conditions and energetics in the Equatorial Pacific.

Lewis ROTHSTEIN: Modeling the warm pool of the Western Equatorial Pacific Ocean.

Neville R. SMITH: An oceanic subsurface thermal analysis scheme with objective quality control.

Duane STEVENS, Qi HU and Graeme STEPHENS: The hydrologic cycle of the intraseasonal oscillation.

Peter J. WEBSTER, Hai-Ru CHANG and Chidong ZHANG: Some new insights on the joint interaction of the tropics and the extratropics.

Friday May 26

Akimasa SUMI (Session Chairman)

MOMENTUM, HEAT, AND MOISTURE FLUXES BETWEEN ATMOSPHERE AND OCEAN

08H00:
Invited Speaker: Timothy W. LIU: A brief review on the bulk parameterization and remote sensing of latent heat flux in tropical oceans.

Frank E. BRADLEY, Peter A. COPPIN and John S. GODFREY: Measurements of heat and moisture fluxes from the Western Tropical Pacific Ocean.

Richard W. REYNOLDS and Ants LEETMAA: Evaluation of NMC's operational surface fluxes in the Tropical Pacific.

Stanley P. HAYES, P. Michael J. McPHADEN, John M. WALLACE and Joël PICAUT: The influence of sea surface temperature on surface wind in the Equatorial Pacific Ocean.

09H15 - 10H15: Coffee Break/Posters

10H15:
Peter J. WEBSTER: The hydrology cycle: Interlocking processes between the ocean and the atmosphere.

T. KEENAN and Richard E. CARBONE: A preliminary morphology of convective systems in Tropical Northern Australia.

Phillip A. ARKIN: Estimation of large-scale oceanic rainfall for TOGA.

Catherine GAUTIER and Robert FROUIN: Surface radiation processes in the Tropical Pacific.

Poster session: Thursday midday through Friday evening

Thierry DELCROIX and Christian HENIN: Mechanisms of subsurface thermal structure and sea surface thermohaline variabilities in the South Western Tropical Pacific Ocean during 1979-85.

Greg J. HOLLAND, T.D. KEENAN and M.J. MANTON: Observations from the Maritime Continent: Darwin, Australia.

Roger LUKAS: Observations of air-sea interaction in the Western Pacific warm pool during WEPOCS.

M. NUNEZ and K. MICHAEL: Satellite derivation of ocean-atmosphere heat fluxes in tropical environment.

12H00 - 14H00: Lunch

William PATZERT (Session chairman)

EMPIRICAL STUDIES OF ENSO AND SHORT-TERM CLIMATE VARIABILITY

14H00:

Invited Speaker: Klaus M. WEICKMANN (and Siri Jodha S. KHALSA): Fluctuations of convection and circulation over the oceanic warm pool during September-December 1981.

Claire PERIGAUD: 30 days oscillations in the Tropical Pacific Ocean observed with GEOSAT altimeter.

Ryuichi KAWAMURA: Air-Sea interactions in the Tropical Western Pacific on interannual and intraseasonal time scales.

David S. GUTZLER and Tamara M. WOOD: Observed structure of convective anomalies.

15H45 - 16H15: Coffee Break/Posters

16H15:
Siri Jodha S. KHALSA: Remote sensing of atmospheric thermodynamics in the tropics.

Bingrong XU: Some features of the Western Tropical Pacific: Surface wind field and its influence on the upper ocean thermal structure.

Brett A. MULLAN: Influence of Southern Oscillation on New Zealand weather.

Kenneth S. GAGE, Ben B. BALSLEY, Warner L. ECKLUND, D.A. CARTER and J.R. McAFEE: Wind profiler related research in the Tropical Pacific.

Poster session: Thursday midday through Friday evening

John J. BATES: Signature of a west wind convective episode in special sensor microwave imager (SSM/I) data.

Daniel L. CADET, Gerard BELTRANDO and Richard PASCH: Interannual variability of the Indian Ocean surface fields.

John K. EISCHEID, Siri Jodha S. KHALSA and Klaus M. WEICKMANN: Relationships between the 30-60 day oscillation in the tropics and the varying frequency of atmospheric angular momentum oscillations.

David S. GUTZLER: Seasonal and interannual variability of the Madden-Julian oscillation.

Edmund D. HARRISON: Westerly wind anomalies from Central Pacific islands 1950-1980.

Marie-Helene RADENAC: Fine structure variability in the Equatorial Western Pacific Ocean.

George C. REID, Kenneth S. GAGE and John R. McAFEE: The climatology of the Western Tropical Pacific analysis of radiosonde data base.

Chung-Hsiung SUI and Ka-Ming LAU: Multi-scale processes in the Equatorial Western Pacific.

Stephen ZEBIAK: Diagnostic studies of Pacific surface winds.

Miscellaneous posters: ***Thursday midday through Friday evening***

Rick BAILEY: Relevance to TOGA of systematic XBT errors.

Jean BLANCHOT, Robert LE BORGNE, Aubert LE BOUTEILLER and Martine RODIER: ENSO events and consequences on the nutrients, planktonic biomass and production in the Southwestern Tropical Pacific Ocean.

Yves DANDONNEAU: Abnormal bloom of phytoplankton around 7°N in the Western Pacific during the 1982-83 ENSO.

Cecile DUPOUY: Sea surface chlorophyll concentration in the Southwestern Tropical Pacific as seen by NIMBUS CZCS from 1978 to 1984.

Pierre RUAL: A better data reduction method for XBT bathymessage.

William E. WOODWARD, Michael SZABADOS and Darren WRIGHT: Field evaluation of real-time XBT systems.

18H30: ORSTOM Dinner at Club Med

Sunday, May 28

08H00: Phare Amedee coral island trip (meeting point at Club Med pier, return at sunset)

Monday, May 29

08H00:
Overview of COARE Science Plan (plenary)

Working Group Discussions on Science Plan

12H00-14H00: Lunch

14H00:
Working Group Discussions on Science Plan

Presentations on Related Technology for COARE (plenary)

Tuesday, May 30

08H00:
Implementation Considerations and Related Programs (plenary)

Working Groups on Experimental Design

12H00-13H45: Lunch

13H45:
Working Group Reports (plenary)

National Reports (plenary)

Closing (plenary)

WORKSHOP REPORT

1. Introduction.

a. Historical Perspective.

Peter Webster, Chairman of the International TOGA Scientific Steering Group, presented the following overview of the development and planning for TOGA/COARE.

The U.S. TOGA Workshop on Western Pacific Air-Sea Interaction was held in Honolulu in September 1987 (Lukas and Webster, 1988), and the idea for a TOGA Coupled Ocean-Atmosphere Response Experiment (COARE) was outlined there in response to the need for new observations to answer many of the important questions raised at that Workshop.

A draft of a COARE Science Plan was prepared by Webster and Lukas (1988) following the Honolulu Workshop, and presented to the U.S. National Academy of Sciences TOGA Advisory Panel in April 1988, to the Joint Scientific Committee of WMO and ICSU in June 1988, and to the TOGA Scientific Steering Group at Cairns in July 1988.

The U.S. TOGA Panel, at its August 1988 meeting, endorsed the concept of a TOGA warm pool process experiment, and authorized the formation of a U.S. COARE Science Working Group (SWG) to continue the planning of COARE. This SWG met for the first time in Seattle in mid-September 1988, and again in Anaheim, California in late January 1989.

A revised version of the Science Plan was distributed in January 1989, which incorporated suggestions from the scientific community. The U.S. COARE SWG suggested further revisions, and a third draft of the COARE Science Plan was finished just prior to the present Meeting/Workshop, and distributed to all participants. It has been proposed as the first draft of an International TOGA/COARE Science Plan.

b. Presentation of Science Plan.

Roger Lukas gave an overview of the scientific background and tentative plans for TOGA/COARE, as contained in this draft Science Plan. The goals of the program were discussed, and it was emphasized that the exchange of heat, moisture, and momentum between the atmosphere and the ocean in the western Pacific warm pool region is the primary focus of COARE. The interactions among processes responsible for these fluxes, acting on a hierarchy of time and space scales, give rise to the complex and vigorous coupling of the atmosphere and ocean in the warm pool region; this hierarchy suggests a research strategy which is the foundation of the COARE. The nested time and space observational strategy proposed for COARE was illustrated, and it was emphasized that COARE will be embedded within the large scale TOGA monitoring program.

c. Discussion of Science Plan.

A general discussion of the draft COARE Science Plan was conducted in plenary. Numerous scientific and logistical issues were raised, and it was pointed out that the purpose of having the Workshop was to resolve these issues.

2. Working group discussions, recommendations, and plans.

The Workshop was then subdivided into three working groups:

- Air-Sea Fluxes and Boundary Layer Processes
- Regional Scale Atmospheric Circulation and Waves
- Regional Scale Oceanic Circulation and Waves

These groups were asked to address the draft COARE Science Plan on the first day of the Workshop, and to suggest additions and modifications as appropriate. For the second day of the Workshop, the groups were asked to address implementation considerations, such as array design and logistics. The working groups reconvened in plenary following each day's working sessions and at the beginning of the second day in order to hear presentations on related programs and relevant technologies.

The following charge to these working groups was given by Lukas:

- Make written contributions.
- Build on the existing framework.
- Translate COARE goals into specific scientific objectives and questions to be answered by COARE.
- Consider linkages among time and space scales for the Science Plan and for implementation. Specify needs from other working groups. State assistance that can be given to other working groups.
- Consider resolution, precision, accuracy, and duration requirements for observations.
- Begin to consider cost/benefit of particular observations.
- Planning letters from PI groups are welcomed.

The following subsections are intended to provide the substance of these working group deliberations and recommendations. The Science Plan contributions from these working groups have since been incorporated into the post-Noumea revision of the Science Plan. Recommendations regarding implementation are discussed in some detail. The bulk of the material is from the write-ups provided by the leaders of the various working groups.

a. Air-Sea Fluxes and Boundary Layer Processes.

co-Chairs: John Young, U. of Wisconsin/Madison, U.S.A.
Timothy Liu, JPL/Cal. Tech., U.S.A.

This group met together briefly, then broke down into smaller working groups in order to concentrate on particular aspects of the air-sea fluxes and boundary layer problems.

Before subdividing, J. Young urged the participants to consider the current status of our understanding of the air-sea fluxes, and to make sure that the mesoscale observations contribute to the goals of TOGA/COARE. An extended discussion of the draft COARE Science Plan then took place. The primary focus of discussion was the relative importance of the annual average heat flux into the warm pool versus the variability of the fluxes.

P. Gent said that the present COARE document overemphasizes the western Pacific climatological heat fluxes, and that present ocean numerical modeling results support the Newell hypothesis of near-zero net heat flux. In his model, Gent finds that

vertical diffusion in the upper ocean accounts for 9.4 Wm^{-2}, while horizontal advection can only account for 3.9 Wm^{-2}. These balance the net heat flux through the sea surface which was 13.5 Wm^{-2}. D. Anderson agreed that models show near-zero net heat flux, but that this result depends on model physics. Should the models be trusted? Anderson suggested that they must be verified.

When the minimum wind speed used in Gent's latent heat flux formulation is changed from 4 ms^{-1} to 3 ms^{-1}, the SST increases from 29.5°C to 32°C, and the net heat flux increases to 18 Wm^{-2}. SST in the warm pool thus appears to be quite sensitive to small changes in the net heat flux, and as R. Reynolds pointed out, SST might therefore be used as an observational constraint on flux estimates.

With regard to the radiative fluxes, C. Gautier pointed out the importance of understanding the contribution of mesoscale systems in reducing the incoming solar radiation, while S. Godfrey mentioned problems with the parameterization of the longwave radiative flux. G. Stephens expressed concern in relation to our ability to measure fluxes, including radiative fluxes, in the required range of 0-20 Wm^{-2}.

R. Lukas expressed the opinion that COARE will not measure the climatological net heat flux of O(0-20 Wm^{-2}), rather the day-to-day variations in the fluxes. R. Garwood echoed this, saying that it is the range of the fluxes and their variances that are needed for understanding of the coupling. D. Anderson maintained that air-sea fluxes have no special significance in coupled models, only in stand-alone models.

M. Moncrieff discussed the role of mesoscale processes (spatial scales of 2-2000 km) in COARE, and suggested that the super cloud cluster is the response of convection rather than the scale of energy input. There is a total lack of quantitative knowledge of scale interaction, though convective transports are apparently important. Moncrieff felt that the best strategy for obtaining information on the fluxes during COARE is to make observations both remotely and *in situ*, on a limited scale, and to use modeling systems to analyze the observations. This amounts to data assimilation on the mesoscale, which will involve interactive nested models, one of which will need to be a non-hydrostatic mesoscale model, while the other will need to be a regional scale hydrostatic model.

1) PBL/Mesoscale Subgroup. (reporter, R. Carbone, NCAR, U.S.A.)

Observing Domain.

The domain for the PBL/mesoscale observations is defined as an area with observations sufficient in spatial and temporal resolution so as to close sensible and latent heat, precipitation, radiation and momentum budgets in the circumstance of large amplitude mesoscale variability usually caused by atmospheric convection. This domain corresponds to the intensive flux area (IFA) of the draft COARE Science Plan.

Since mesoscale convective forcing is both frequent (every 1-6 days) and relatively short-lived (3-24 hrs), it was deemed sufficient and practical to obtain comprehensive flux data sets in 1-3 day bursts (FIOPs) less than 10 times during the 4-month-long IOP. For those observing systems and platforms for which it is practical, observations will be taken continually during the IOP.

It was judged unlikely that budgets could be closed over an area larger than 500 x 500 km. This task becomes more tractable with smaller domains (e.g. 100 x 100 km) but less relevant in its relationship to larger scales of atmospheric forcing. It was the sense of the sub-group that COARE should strive to devise a measurement/analysis strategy which would be effective at the 500 km scale while recognizing that resources and sensor limitations may eventually require a reduction in the size of the flux domain.

The range of domain sizes considered does not permit flux measurements on the scale of a convective supercluster or a large westerly wind burst. The observing strategy calls for representative sampling and determination of structure within such phenomena. Soundings and airborne and land-based radar observations outside the flux domain together with satellite imagery will permit the FIOP data to be placed in the larger scale, longer period context.

The flux experiment would rely on the larger COARE domain observations to schedule FIOPs. The concept of flexible scheduling may be extended to flexibility in location. Compromises would be required for a "floating domain" implementation, since several key observing systems would be land-based. A hybrid implementation should be examined whereby some of the FIOPs are conducted at alternate locations as required. Because of the heavy reliance on ships and aircraft, some degree of mobility is possible.

The primary domain location was not discussed in detail. One alternative to equatorial symmetry was advanced based upon a climatological maximum of precipitation south of the equator. Since organized convection appears to be frequent throughout the COARE domain, the importance of this point may be secondary to issues of oceanic circulation symmetry about the equator. Logistical matters, including island locations, further complicate these considerations since some instrumentation will need to be on land. Finally, there is consideration of the phase relationship of the flux domain to the larger scale atmospheric circulations in a potential El Nino onset event.

Observational Platforms.

The sense of the group, taking resource limitations into account, was that 4 long-range research aircraft and 4 research vessel stations (which likely means eight vessels over the 4 month period) are a minimum requirement for the flux domain. In addition, the availability of one or two land "platforms" is essential. The research vessels would steam around drifting marker buoys to minimize advection terms with continuous Seasoar CTD profiling and Doppler current profiling. In addition to hosting eddy correlation and dissipation *in situ* flux measurements and rawinsonde sounders, research vessels should be of sufficient size and capability to accommodate the needs of shipboard remote sensing devices such as lidar, UHF wind profiler, passive thermodynamic profiler and microwave radar in order to permit continual monitoring of precipitation, and wind and thermodynamic profiles during the FIOPs. These devices generally require precise platform attitude and position information.

The research aircraft are assumed to include the NASA DC-8, 2 NOAA P-3s and the NCAR Electra as a minimum set. While not discussed explicitly in the sub-group, the CSIRO F-27 could also make significant contributions to the flux domain program. The NASA ER-2, if logistically feasible, would also contribute greatly to the radiative flux component. In addition to standard flight level eddy correlation data, the primary aircraft would include three airborne Doppler radars (which can double as scatterometers), Doppler lidar, full long- and short-wave radiation packages, GPS dropsondes, AXBTs, AXCPs and possibly AXCTDs.

Land-based systems should include Doppler radars, and various atmospheric sounding stations (including surface observations and radiation) as site availability permits. At least six 5-cm Doppler radars are potentially available including NCAR(2), CRPE(2), US TOGA(1) and MIT(1). The TOGA and MIT systems are most amenable for shipboard installation. Two land-based systems would complete the flux domain network for precipitation and momentum flux estimation. The remaining two Doppler radars would be placed at equatorial land-based sites several hundred km east and west of the flux domain for precipitation climatology and morphology objectives.

Ocean moorings, including meteorological sensors on a surface buoy and supplemented with high vertical resolution thermistor chains in the upper few tens of meters, are considered highly desirable bounding and within the flux domain. For the oceanic boundary layer, it is important that Kelvin and Rossby wave-induced vertical motions be distinguished from thermodynamic changes below the mixed layer. Thus, the PBL domain should be sited within a carefully designed array of moorings.

Observational Strategy.

FIOPs will be short in duration as a consequence of the short residence time of organized convective systems (10 h) and expected rapid response of the ocean mixed layer. Three days will be a typical FIOP duration. This is close to the staffing resource limits on research vessels and research aircraft.

The guiding principle, in the conduct of observations from all measurement platforms will be to characterize the oceanic-atmospheric state according to phase of the mesoscale forcing event. We will seek to identify and quantify the "pre-storm" undisturbed state; the highly disturbed state in the heart of the aggregate mesoscale disturbance; and the "wake" state following the passage of large amplitude events.

Within each FIOP, there are several potential applications of the aircraft owing to their mobility and wide range of instrumentation. Some FIOPs will require 24 h sequential use of the P-3s and the Electra for the purpose of continual ABL flux, precipitation measurement and ocean response studies. Other FIOPs may be envisioned where these aircraft, together with the DC-8, are flown simultaneously at the expense of 24 h coverage. The optimal use of aircraft resources is a most challenging aspect of the flux domain experiment design.

Precipitation Estimation.

No single instrument or observing platform can adequately address the precipitation estimation problem so crucial to the success of COARE. Implicit in our discussions was a hybrid approach which employs latent heating budgets, rain gauges on ships, aircraft, moorings and islands; ground-based and airborne Doppler radar reflectivity and kinematic techniques; airborne and space-based radiometric techniques.

An area as large as 500 x 500 km will require contributions from all methods and this will be a major consideration in the final determination of the flux domain size. The higher time/space density of tropospheric soundings in the flux domain should permit time-resolved latent heating profiles which serve to separate convective and stratiform components of the precipitation. Latent heating profiles also serve as an integral constraint for more highly time-resolved analyses from the direct measurements of precipitation by means of radar.

2) Remote Sensing Subgroup. (reporter, T. Liu, JPL/Cal. Tech., U.S.A.)

Determination of Wind Stress from Satellite.

The requirement for an accurate and detailed wind stress product for the initialization of models will probably be met only in an adequate manner through a combination of *in situ* and satellite measurements.

The NASA Scatterometer (NSCAT), which measures at the Ku-band, will not be launched in time for COARE. But the AMI on ERS-1 will be in operation during COARE and could measure surface wind vectors at C-band when put in the scatterometer mode. However, there are serious sampling problems because it has only

half the swath width of NSCAT and can only operate in scatterometer mode for part of the time. The sensitivity of C-band radar to surface wind is not as well studied as Ku-band. A useful product may be derived from an atmospheric GCM with assimilated ERS-1 scatterometer observations.

The algorithms relating scatterometer observations to surface wind vectors are empirical and should be tested for a large range of conditions. For this purpose NASA has built aircraft-borne Ku-band and C-band scatterometers and has deployed them in various field experiments. The scatterometer geophysical algorithms have not been adequately tested in low wind conditions and scatterometer measurements were found to be sensitive to sea surface temperature and atmospheric stability (Liu, 1984; Freilich, 1986). The western Pacific, with its unique conditions of light winds, high sea surface temperature, and high instability, provides an ideal location to extend these aircraft studies. COARE will have high quality *in situ* measurements and the aircraft scatterometer will provide mesoscale area coverage of wind vectors in return.

Determination of Heat and Moisture Fluxes from Satellite.

There were studies in the central and eastern tropical Pacific using latent heat flux and shortwave radiation derived from satellite data during the 1982-83 ENSO and in the Tropic Heat Experiment (Liu,1988; Liu and Gautier 1989). It would appear natural to extend these efforts to the warm pool regions of the western Pacific ocean. Only data from operational spaceborne sensors, DMSP/SSMI, NOAA/AVHRR, GMS/VISSR are required. They could be supplemented by other operational sensors such as NOAA/TOVS and DMSP/SSMT. Intense efforts in algorithm development and retrieval techniques are underway.

The establishment of *in situ* monitoring of surface shortwave radiation, longwave radiation and atmospheric humidity, in addition to routine meteorological reports will help to solve the validation problem. The retrieval of surface heat flux from satellite data could be conducted in close cooperation with the International Satellite Cloud Climatology Project, the Surface Radiation Budget Program and the Global Precipitation Climatology Project to produce surface thermal and buoyancy forcing on the ocean.

b. Regional Scale Atmospheric Circulation and Waves.

co-Chairs: William Lau, GSFC/NASA, U.S.A.
Gregg Holland, BMRC, Australia

1) Science Plan discussions.

During the morning session of the first day of the Workshop, discussions were focused on the revisions of the TOGA Science Plan. It was felt that there should be more emphasis of the connection between TOGA/COARE with other current national and international climate research programs and initiatives such as Global Change, GEWEX. The large scale atmospheric component is a vital link of TOGA/COARE to the climate community. It was generally felt that the section of the science plan on global teleconnections, particularly the section on modeling was seriously deficient. In particular, the relationship of COARE in improving climate predictability through improvement of flux parameterization or other means need to be addressed. Each of the Workshop participants were asked to put in writing their recommendations to the Science Plan.

Gregg Holland suggested there needs to be a clear concise statement at the beginning of the document to point out the need for coupled ocean atmosphere studies. It was agreed that understanding of global climate change, the El Nino/Southern Oscillation, and intraseasonal oscillations requires a better specification of the coupling of the ocean and atmosphere. The lack of understanding of basic mechanisms and errors in general circulation models have the largest potential impact in Pacific warm pool region.

There are two specific concerns that need to be brought out clearly. These are:

- The sensitivity of the large scale climate system to the warm pool air-sea interaction,
- The convective/mesoscale feedback to the surface fluxes.

The traditional gap between the large scale atmospheric component and the convective/mesoscale component has to be bridged by TOGA/COARE. This is directly related to the fourth goal of COARE.

S. Zebiak and N. Graham pointed out that there is very little discussion of the state-of-the-art coupled model development in the Science Plan. It was felt very strongly by this subgroup that such a discussion be included. One of the main uses of the COARE data set will be for diagnostic purposes and for initialization and validation of coupled models. A hierarchical approach to coupled modeling should be adopted. At present, coupled models have demonstrated a rich variety of interannual modes of the coupled system. However, it is not clear which one of these theoretical modes can be applied to the real system. Observations from COARE will help to resolve some issues regarding the origin of these coupled modes.

While coupled GCMs are the ultimate tool for coupled ocean-atmosphere studies, intermediate and simple coupled models also play important roles for hypothesis testing and for elucidating certain phenomenological aspects of coupled ocean-atmosphere interaction. Given the high data density from COARE, one class of process-oriented models should be emphasized. These are coupled boundary layer models. Sensitivity to various input parameters can be first tested in one-dimensional models and then on to more sophisticated models. These models will be very useful in improving the parameterization of the coupling between atmosphere and ocean in GCMs. For data assimilation purposes, mesoscale models embedded in regional scale models or GCMs will be most useful.

It was agreed that the Science Plan should contain specific discussions of the possible mutual influences of teleconnections on phenomena of the western Pacific. It was pointed out that there is observational evidence to suggest that atmospheric teleconnections may indeed be important for the development of ENSO-related westerly wind anomalies in the western tropical Pacific. The subgroup agreed that most of the sources of problems arising from current GCMs in simulating intraseasonal oscillations and teleconnections may lie in the uncertainty in the convective and surface flux parameterization. It seems that a careful set of measurement in the warm pool is necessary both for diagnostic and forecasting purposes. In addition to the specific objectives for the Atmosphere component listed in the present version of the Science Plan, the following objectives should be included:

- To study the transition of the tropical planetary boundary layer from the descending regions of the eastern Pacific Ocean to the convective western Pacific Ocean region, and to identify how it relates to the changes in wind regimes during westerly wind burst.
- Apply the knowledge gained from the pursuit of the objectives above to improvements in operational forecasting models and global climate models.

Much of the remaining time of the morning session was devoted to the discussion of beefing up the COARE modeling component of the Science Plan. It was felt that, to approach the goals of TOGA/COARE, a major developmental program of ocean, atmosphere and coupled system models is necessary. The modeling component of TOGA/COARE should emphasize those aspects of modeling relative to the warm pool regions of the tropics and will cover the extended period from 1989-1996. It is crucial that this component of the program should consist of a hierarchy of modeling approaches ranging from simple conceptual models, process models, nested mesoscale models to atmosphere-GCM, ocean-GCM and coupled ocean-atmosphere GCM. Some of the phenomenological aspects and simple hypotheses discussed in the Science Plan are best tested with simple conceptual or process models. They will aid in the interpretation of data and results from more complex global models. The use of GCMs is essential to study the far-field influence or teleconnections associated with the multi-scale processes in the western Pacific warm pool region. Process models and mesoscale models will provide the needed detailed information for improving parameterization in GCMs. The coupling between ocean and atmosphere, and the scale interaction between processes with short (order of days), intermediate (order of months) and long (order of years) time scales will require coupled ocean-atmosphere GCMs.

Issues related to data management were also discussed. TOGA/COARE will provide the scientific background for designing an observing and data transmission system for operational prediction. In order to adequately represent the multi-scale phenomena in TOGA/COARE and to assimilate the diverse observing facilities in a spatially and temporally coherently fashion, the use of both atmosphere-GCM and ocean-GCM are necessary. For the atmosphere, nested mesoscale models may be needed to resolve the hierarchical structures found in the superclusters to scales of 500 km or smaller. The two-way interaction between mesoscale models and large scale models is needed to incorporate scale interactions and interactive feedback between convection, radiation and dynamics in the assimilation system. The 4-dimension assimilation of the full TOGA/COARE data including remote and *in situ* measurements in the atmosphere and ocean, and surface fluxes at the interface, will be the key to the development of future ocean-atmosphere prediction systems and will be a challenge to coupled ocean-atmosphere modelers.

It was also felt by the working subgroup, that the original Table 1 on the modeling elements of COARE was inadequate. A new table was developed, and incorporated into the final version of the Science Plan.

2) Implementation Plan discussions.

Discussions of the Implementation Plan took place in the afternoon session of the Workshop. The scientific justifications for reconsidering the COARE regional scale domain were discussed. It was pointed out that by moving the domain by 10° of longitude to the east, the domain would cover more of the region of large SST gradients while still keeping the domain within the region of SST greater than 28°C. It was also pointed out that most of the air-sea interactions associated with the 30-60 day oscillation occur at the eastern edge of the warm pool and the eastern-most extent of the 28°C appears to define the limit of the eastward penetration of convective activities associated with the 30-60 day oscillation. Shifting the large scale domain to the east is especially important in case a warm event should occur during the IOP of COARE. It was therefore recommended that a contingency plan be developed whereby the regional domain of COARE can be shifted by 10° east in case a warm event occurs during the IOP. This will complement the TOGA-TAO II ATLAS moorings at the eastern edge of the warm pool.

The working group felt that a large scale domain covering 30°N to 30°S, 120°E to 160°W should be included as part of the overlapping observation strategy of COARE. Six-hourly synoptic scale upper air and surface observations and at least 24 hour temperature reports are needed at all available stations within the domain. It is essential to ensure that operational wind and temperature data are reported and transmitted through the regular GTS or the TOGA enhanced monitoring facilities. G. Holland discussed the possibility of enhancing all the weather stations of the southern hemisphere near Australia and the possibility of installing portable sounding units at remote island sites. The Gilbert Islands were mentioned as sites where more observing stations are desirable. It was agreed that an eventual goal of the large scale component COARE is to obtain an unprecedented atmosphere-ocean data with high spatial and time resolutions. It is suggested that a mesoscale model embedded within large scale regional model or GCM should be adopted to assimilate all the atmosphere and surface information for later analyses. A real time data assimilation system with feeds to operational and research centers are highly desirable and the COARE data system should work with that goal in mind.

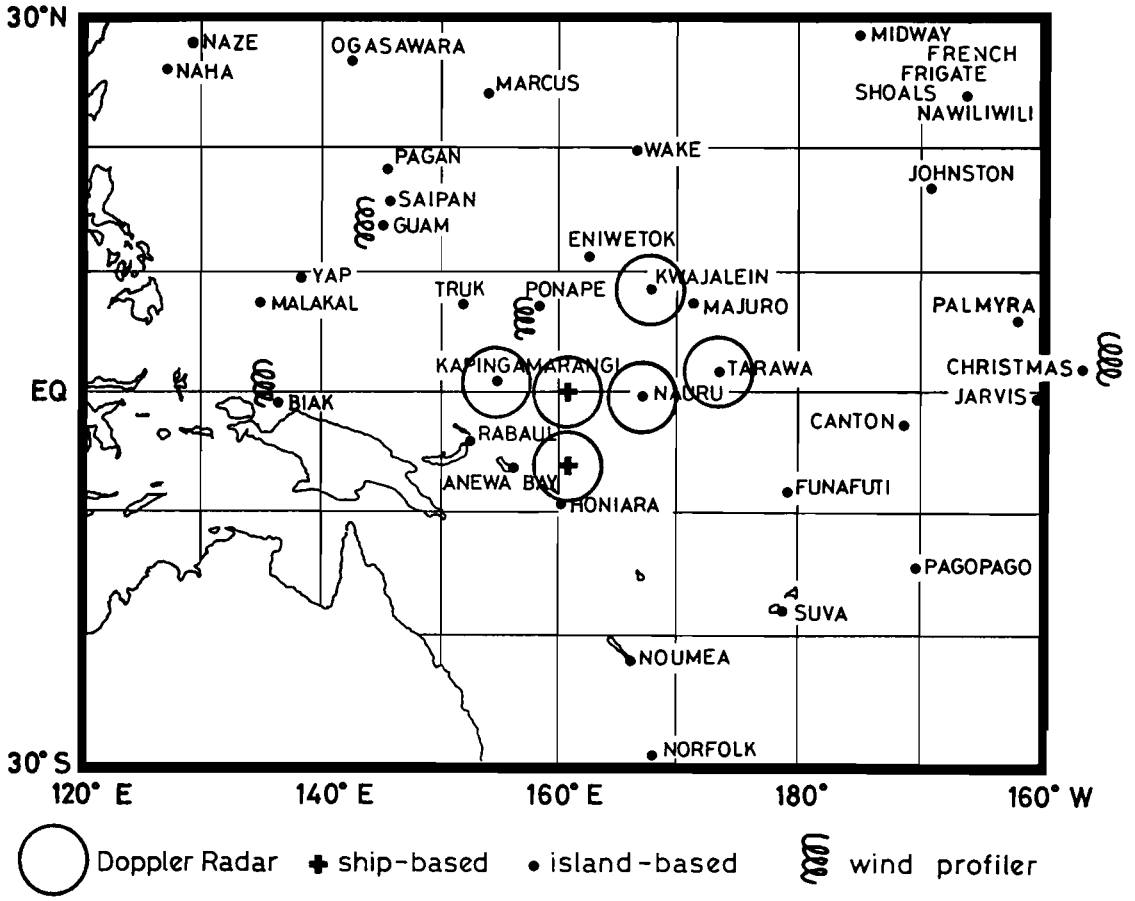

FIG.1. Suggested positions of ship- and island-based Doppler radars for the COARE Intensive Observation Period. Wind profiler locations are also suggested.

There were considerable discussions of the implementation plan with respect to the resources available. On a first count, there will probably be 2 ships available from the US, two from China and two from Japan, and possibly 4 from the Russians if they actually participate in the COARE IOP. The NCAR Electra, two NOAA P3s, 1 NASA DC-8 and ER-2 are suggested as possible aircraft that would participate in COARE. The NCAR Electra with its new radar system and the NOAA P3's are the minimal set that is needed to carry out some of the detailed boundary layer and flux measurements for COARE. There will be six or seven radars available for the IOP. They should be deployed with an overlapping strategy whether on ships or on islands to achieve maximum coverage of the order of 50 km and should be aimed at the major convective complex associated with super-cloud clusters (See Figs. 1 and 2). Individual PI instruments and measurements from pilot studies should complement and lead into the IOP.

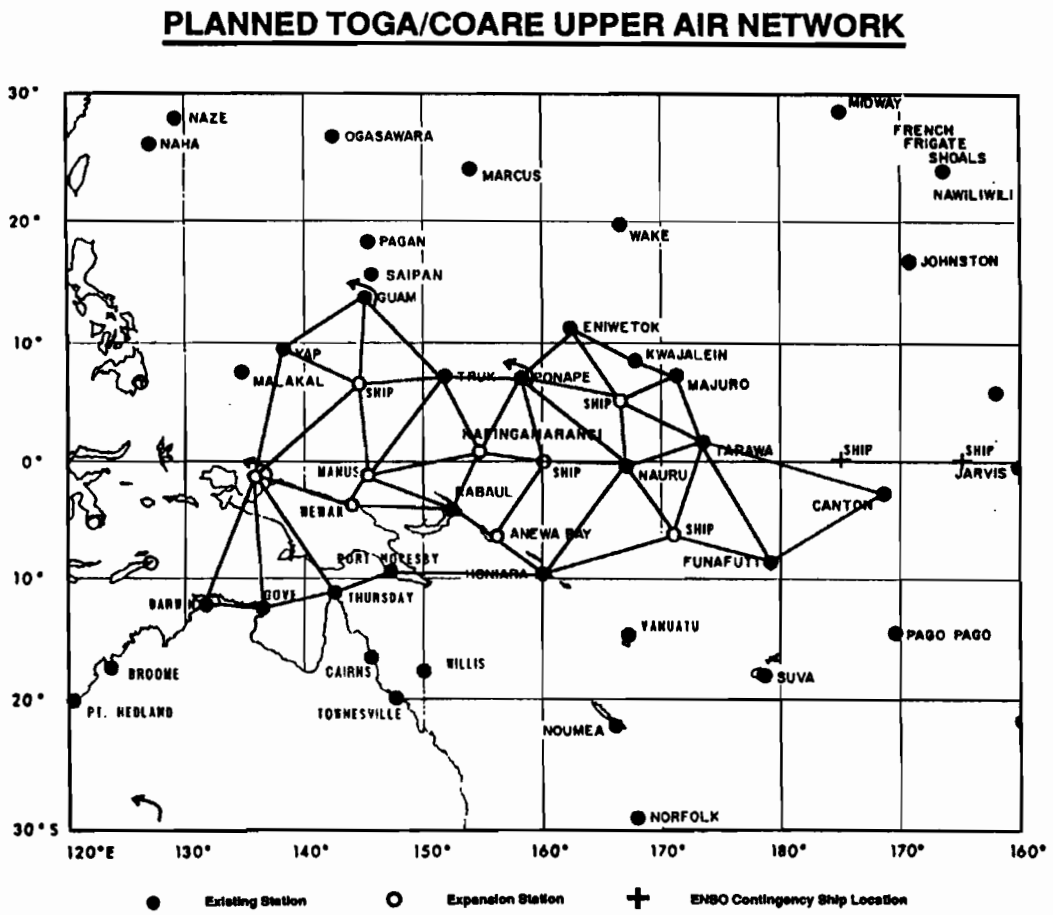

FIG.2. Planned upper air network for COARE enhanced monitoring. During the IOP, ships (indicated by +) would fill in the network.

The need to leave behind key instruments after the IOP (the "care-taker" array) was also discussed. It was suggested that certain automated systems or systems that required minimum maintenance should be left behind. Since intense observations can only be taken for periods of weeks, the synoptic scale monitoring together with the satellite monitoring will provide the needed continuity for the large scale parameters. For the care-taker array, the TOGA Radar, enhanced monitoring over the Gilbert Islands, the Kwajalein radars and NOAA integrated sounding systems including wind profilers should be considered.

The site of the operation center for the IOP was also discussed. The choice is going to be severely constrained by the available ground facilities, proximity to the convective centers and the intensive flux domain, and above all, humane living conditions for crews and field scientists. Tarawa and Nauru were mentioned as possible sites. The concept of multiple centers was also discussed but was considered unsatisfactory because of the difficulty of logistical coordination. These issues need to be resolved in coordination with other working subgroups.

In order to monitor the large scale aspects of phenomena over the warm pool region of the tropical western Pacific, the Atmospheric Circulation and Waves subgroup recommended the following implementation strategy for the enhanced monitoring and intensive observation phase:

- The proposed COARE domain (10°N-10°S, 140°E-180°) should be embedded in a larger domain (30°N-30°S, 120°E-160°W). Observations from the existing radiosonde network should be enhanced and, where possible, new portable stations should be set up on strategic island sites (See Fig. 1).
- Six hourly wind, moisture and temperature profiles are needed within the large scale domain. These observations should be coordinated with the TOGA-TAO II ATLAS moorings with enhancement at the eastern edge of the warm pool.
- There should be an "ENSO contingency plan" to shift the COARE domain eastward during the Intensive Observing Period. This involves changing the deployment of mobile units (e.g. ships, aircraft, etc.) of the observing system.
- Proposed radar, ship, and enhanced surface observation sites (including advanced surface radiation measurements and rain gauges) are shown in Fig. 2. Sites have to be chosen to facilitate 4-D assimilation of COARE observations into a mesoscale grid mesh (50 x 50 km) over the COARE domain embedded in a large scale domain (500 x 500 km, see Fig. 3).
- A real-time satellite communication system, in particular with links to GTS, should be set up so that there will be continuous coverage of the COARE domain and the large scale domain. We recommend the installation of an on-site 4-D assimilation center where real-time COARE observations can be ingested into models and distributed to operational centers such as NMC and ECMWF.
- An IOP operation center should be chosen close to the eastern part of the COARE domain to facilitate deployment of ships and aircraft in case the ENSO contingency plan needs to be implemented. The IOP center should also provide adequate landing facilities and hospitality for the crews. Tarawa or Nauru were suggested as possible candidates.
- There should be a "care-taker array" consisting of specific observation elements that can be left behind for an extended period after the IOP. Suggested arrays include:
  - . the TOGA Radar,
  - . Upper air and surface stations including the NOAA Integrated Sounding System,
  - . the Kwajalein Radar,
  - . Wind Profilers.

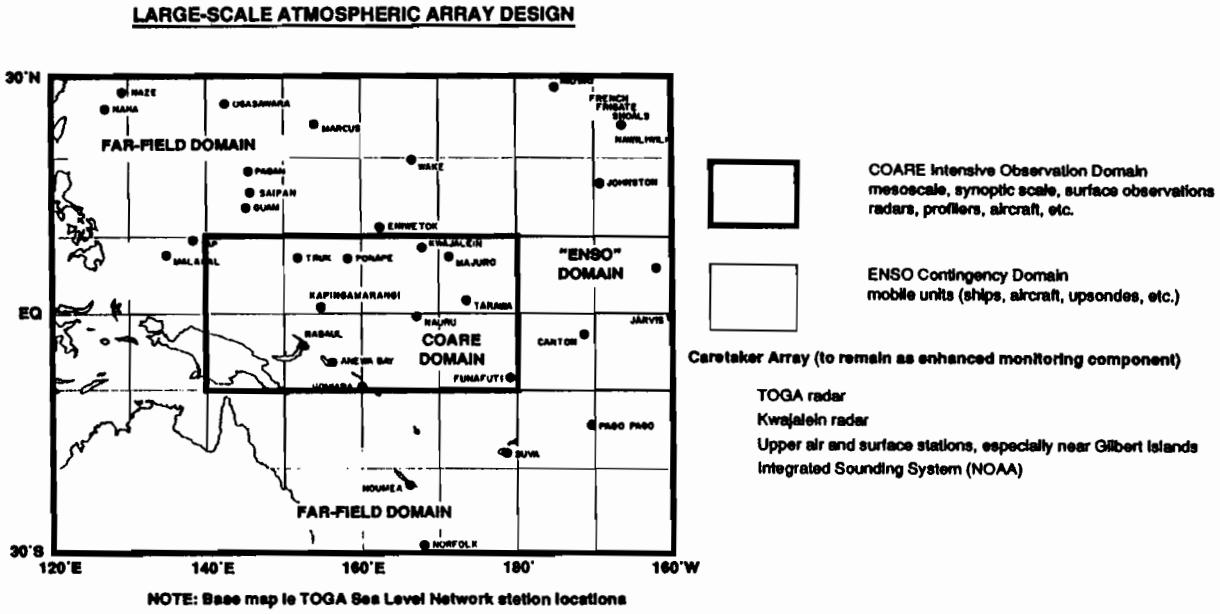

FIG.3. Large-scale atmospheric array design for COARE. The far-field domain requires an enhancement of the TOGA atmospheric observing system.

c. Regional Scale Oceanic Circulation and Waves.

co-Chairs: Charles Eriksen, University of Washington, U.S.A.
Antonio Busalacchi, GSFC/NASA, U.S.A.

Discussions during the first day's morning session were not well focused and reflected the collective uncertainty/concern/doubt with the primary goals of the TOGA/COARE oceanographic component (and the balance between the oceanographic and meteorological components in general), as expressed in the Science Plan.

Some of the early discussions considered questions regarding the role of horizontal advection in the upper 100 m of the COARE domain, particularly during westerly wind bursts and at the eastern edge of the warm pool. During such episodes, 1-dimensional mixed layer models are not likely to be adequate. This pointed to the need for a hierarchical approach to the oceanographic modeling. There is also a need for models that resolve the halocline and subduction. The early consensus was the oceanographic component of COARE would be along the lines of a 3-dimensional mixed layer experiment. The observations must be capable of observing the subduction of saline water from the east under the less saline water in the west, and the two different time scales for dynamic and thermal response of the warm pool.

COARE provides an opportunity for enhanced Western Pacific observations. By 1991-92, all TOGA-TAO moorings are to be in place west of the dateline. The exact placement of the ATLAS moorings west of the dateline is open to discussion and modifications in support of COARE.

The French plan to continue their occupation of the 165°E section twice per year. France plans on providing two research vessels during the IOP of COARE. The possibility exists that a Sea Soar may be able to be used for underway CTD profiling on one of these ships.

Fundamental questions were then raised with respect to westerly wind bursts (WWBs). Concern was expressed that WWBs were not necessarily directly correlated with SST, and that they are not necessarily more frequent prior to or during ENSO. Concern was expressed that COARE had the appearance of a high frequency/WWB experiment.

The following questions were posed as the motivation for *in situ* observations for the oceanographic component of COARE:

- What is the space-time structure of sea surface temperature (and sea surface salinity) in the western Pacific warm pool?
- What processes contribute to SST and SSS variability on time scales of days to months to years in the warm pool?
- How does mixing of heat, salt, and momentum occur in the upper western tropical Pacific Ocean?
- What is the net mass, heat, and salt flux into the COARE domain?
- What far-field processes affect the upper ocean in the warm pool and vice versa?

The issue of the location of the COARE domain was raised. After consideration of R. Weisberg's equatorial mooring at 170°W, the planned Japan/Australia mooring at 147°E, present and proposed ATLAS moorings, climatological distributions of highest SST and largest SST gradients, there were no compelling arguments for modifying the COARE domain.

Early on during this session it became clear, based on Sea Soar (towed CTD) sections, that at least two possible IOP regions were of interest or required; one near the equator where the thermocline is shallow and the other off the equator near the North Equatorial Countercurrent where the thermocline is relatively deep. Sea Soar profiles indicated meridional scales such that there was not much change in temperature or salinity within $\pm$ 2° of the equator yet there was also evidence of small scale fronts, especially in salinity.

In the time domain, the shortest time scales of interest may range anywhere from the passage of individual squall lines on up to the passage of WWBs. There is a clear need for a Sea Soar type instrument to map the halocline structure.

In order to facilitate the detailed planning, there needs to be an effort to analyze the existing data, especially the high resolution Sea Soar data, to see what can be learned.

The end result was the consensus that there is a broad spectrum of space and time scales that need to be considered by the oceanographic component of COARE, similar to the space-time partitioning present in the planning for the atmospheric component:

	space scale	time scale
Fine Scale T-S	10 km	1 month
Westerly Wind Burst	100-1000 km	day-month
Large-scale, Far Field	>1000 km	year

1) Oceanographic observations for COARE

Overall Strategy.

The observations in support of the oceanographic component of COARE must balance intensive surveys with long time series. This requires a combination of enhanced monitoring and the IOP. The enhanced monitoring for the oceanographic component should be in place at least 4 months prior to the IOP; one year is preferable. In order to place the IOP in a proper context, the duration of the enhanced monitoring should be 1-2 years. Strong concern was expressed that there be an intense oceanographic component capable of complementing the atmospheric component.

Intensive surveys during the IOP.

The scientific objectives of the intensive surveys are to quantify the vertical mixing of heat, salt, and momentum; to quantify the horizontal advection of temperature and salinity; and to quantify the air-sea fluxes of heat, moisture, and momentum. The observations must resolve the diurnal cycle and convective events.

The basic strategy for these month-long experiments is to have a central mooring which is boxed in (on two space scales) by two research vessels. The inner box would be roughly 10 km on a side, and would take 4 hours to sample. The outer box would be 100 km on a side, and would take 2 days to repeat. Figure 4 illustrates this strategy.

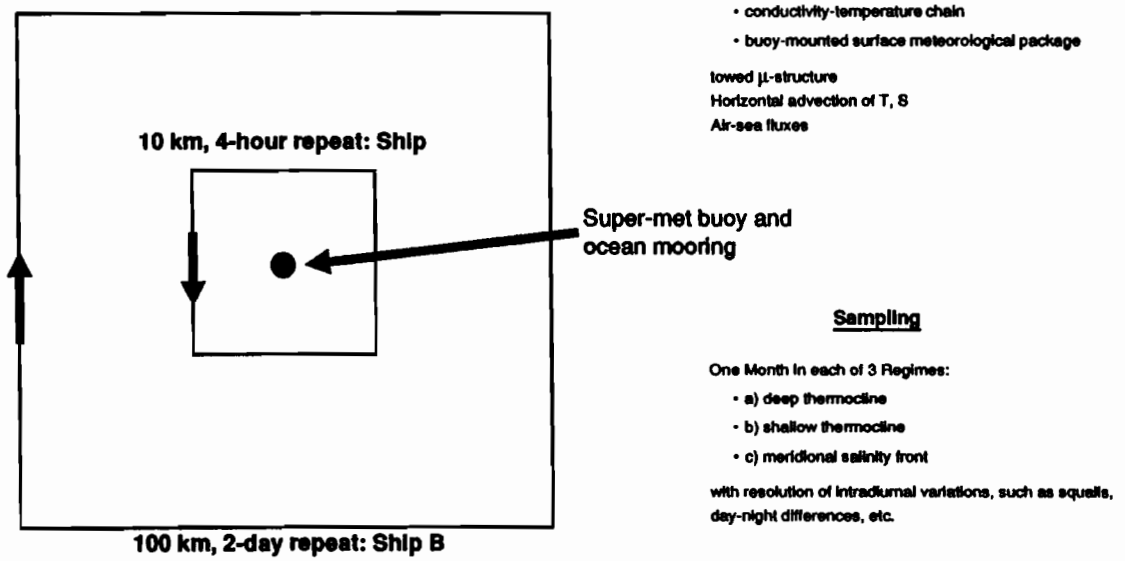

FIG.4. COARE IOP ocean mixed layer experimental design.

It was considered important to conduct intensive surveys in different regimes where one could expect either lateral or vertical processes to dominate. The three regions suggested were 1) where the thermocline is deep, 2) where the thermocline is shallow, and 3) where there is zonally-oriented salinity front near the equator.

The one month duration of each intensive survey is a compromise between the research vessel logistics and the desire to sample during a wide range of meteorological forcing.

Moored observations during the intensive surveys are important to provide high-resolution time series at fixed points. Currents will be measured using an acoustic Doppler current profiler, and temperature and salinity profiles will be estimated by discrete sensors on a thermistor/conductivity chain. A WHOI-type meteorological package on the surface buoy of the mooring will provide high-resolution time series of wind, air and sea temperature, humidity, barometric pressure, short- and long-wave radiation, and rain (see paper by Weller and Hosom, in the Appendix).

Shipboard measurements should be made while the ship is underway in order to maximize spatial coverage within a time frame over which the measurements might be considered synoptic. Observations should include currents measured by acoustic Doppler current profiler, as well as towed CTD and microstructure measurements. It will be necessary to stop the ship occasionally for standard CTD stations for calibration purposes and to get deeper into the water column. High-resolution meteorological observations, including those needed to estimate air-sea fluxes, should be made wherever possible. A shipboard Doppler weather radar is needed to estimate precipitation and wind stress over the experimental region.

Enhanced Monitoring: Regional long time series.

The objective of the enhanced oceanographic monitoring is to place the intensive observations properly within the context of the large-scale, low-frequency evolution of the warm pool. The existing TOGA monitoring is not sufficient: the variability of currents and thermohaline structure of the upper ocean in the warm pool must be observed with sufficient spatial resolution to resolve the response to monsoon and wind burst forcing.

The basic strategy for the enhanced monitoring is to augment the moored ATLAS array of thermistor chain moorings in conjunction with TAO-II to provide better spatial coverage of the thermal structure variations of the warm pool, and to enhance these observations with conductivity sensors to obtain time series of salinity at key locations. Also, current meter moorings are needed along the equator to resolve the vertical and zonal structure of current variations over at least two seasonal cycles. A special array of profiling current meters (PCMs) should be considered to obtain time series of temperature, salinity, and velocity profiles on and near the equator in the middle of the enhanced array.

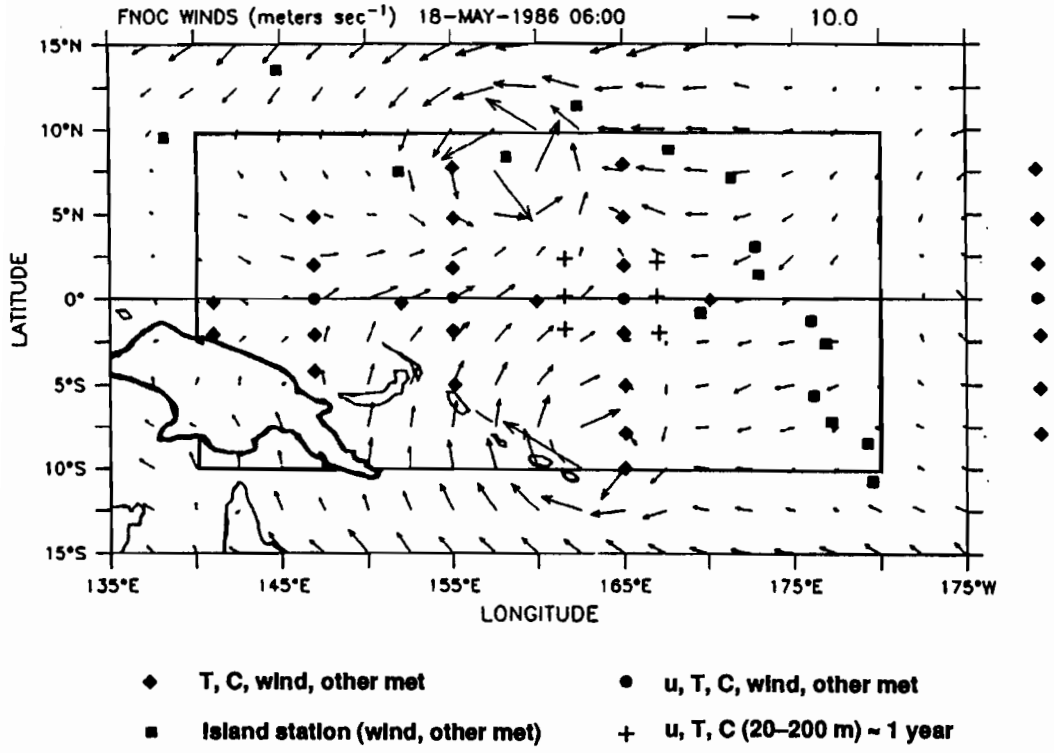

FIG.5. COARE ocean enhanced monitoring array.

The locations suggested for the elements of the oceanic enhanced monitoring for COARE are shown in Fig. 5. The zonal separation of 5° is dictated by the scales of observed energetic variability in the wind field, and the meridional separation of 2-3° is determined by both the meridional scales of wind variability and the dynamics of the equatorial waveguide. Some elements were suggested to observe boundary-related processes.

The duration of the enhanced monitoring should be two seasonal cycles, preferably one before the COARE IOP and one after. Some elements of the enhanced monitoring array should be considered for inclusion in the long-term, post-TOGA monitoring, on the basis of the results of the COARE IOP observations.

2) Oceanographic modeling for COARE.

Since the modeling component of COARE extends through the entire lifetime of the experiment, there will be a great deal of synergy between the modeling and observational elements of the experiment. Hence, the modeling will be evolutionary in nature. Going into COARE, TOGA-TAO together with improvements to operational AGCMs should lead to better estimates of the surface wind field over large areas and over long time scales. However, evaporation-precipitation estimates will remain uncertain and until they are certain, it will be difficult to include salinity effects properly in the OGCMs. In the mean time, much work needs to be done in order to include buoyancy fluxes in a whole suite of ocean models including the requisite idealized and sensitivity studies to buoyancy forcing.

The ocean modeling element of COARE will proceed with a hierarchical approach that considers both buoyancy fluxes and the large-scale ocean circulation of the western Pacific warm pool. In regions where horizontal gradients are small, 1-dimensional mixed layer models will be employed. Process-oriented models will be used to perform sensitivity studies to idealized specifications of buoyancy fluxes. The upstream and downstream effects of remote forcing, particularly the role of the western boundary, or the large-scale circulation in the warm pool will be addressed with process models. The sensitivity of the oceanic response to westerly wind bursts as a function of various thermohaline states will be considered by process and OGC models. OGCMs will also prove invaluable in interpreting the large-scale state of the warm pool and providing a context for the small scale oceanographic experiments within COARE. This will be accomplished via budget studies of mass, heat, and salt within the COARE domain, through the assimilation of the *in situ* and space-based measurements of the enhanced monitoring and IOP. The end result of the model development, intercomparison with *in situ* data, and incorporation of *in situ* data will be new ocean models that consider the effects of buoyancy forcing, that resolve both the thermal and haline structure, improved mixed layer parameterizations, and ultimately improvements to OGCMs and operational modeling capabilities.

3. Related Programs.

a. NASA Ocean Processes and Satellite Missions.

Gary Lagerloef of NASA Headquarters described the NASA Oceanic Processes program and satellite missions that relate to TOGA/COARE. He noted that about 20% of the program is devoted to developing spaceborne techniques and evaluating their utility for observing the oceans, while the application of these techniques to advancing our understanding of the oceans comprises the bulk of the program.

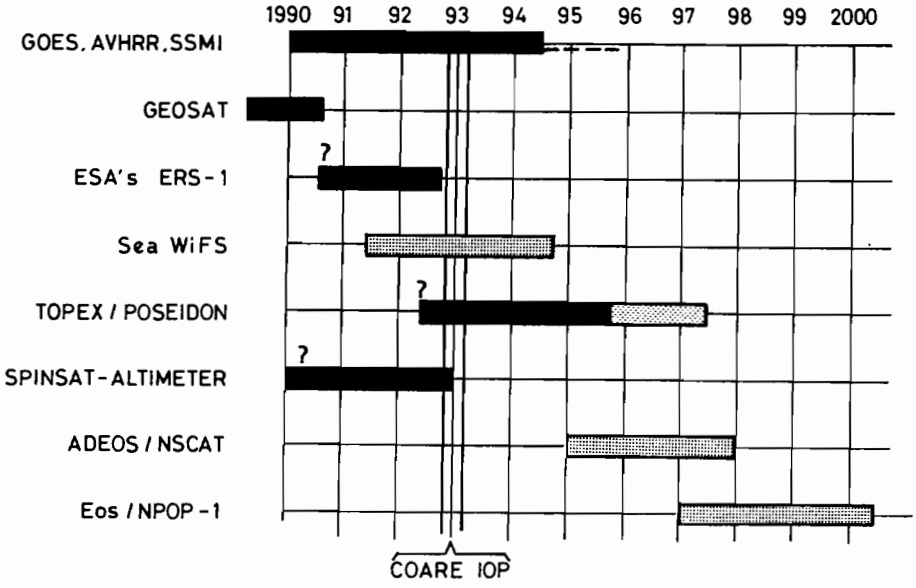

FIG.6. Timing for proposed satellite missions for ocean process studies. Operational satellites are indicated at the top. The timing of the COARE IOP is indicated.

Figure 6 shows the current status of a variety of ocean-related satellite missions. Light shading indicates that the mission is not yet funded; question marks indicate launch dates that are uncertain. It was noted that the intersection of these missions with the COARE IOP is presently only certain for the operational satellites (GOES, DMSP, NOAA polar orbiters).

The Oceanic Processes program can contribute to COARE by providing access to NASA and non-NASA ocean satellite data, and by providing airborne remote sensing observations during field experiments. One of the sensors that could be flown during COARE are the NUSCAT scatterometer, which can yield high spatial resolution vector winds over an area comparable to that of the outer box of the ocean mixed layer experiments (Fig. 7).

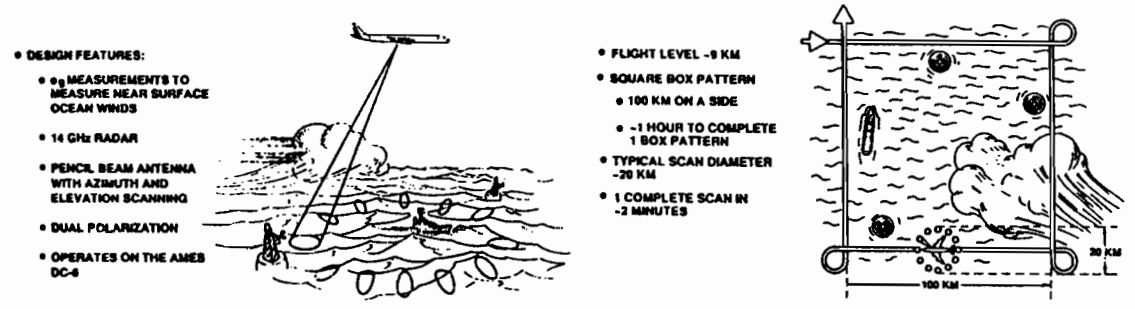

FIG.7. Overview of NUSCAT airborne scatterometer measurement capability. This observing system could become available for use during the COARE IOP.

The ESTAR-0/SFMR microwave radiometer (Fig. 8), which can provide SST and scalar wind speed estimates, is also a candidate for research aircraft flights. It is also possible that sea surface salinity might be inferred from these radiometer observations (Fig. 9).

MEASUREMENT CHARACTERISTICS OF THE AIRBORNE MICROWAVE RADIOMETERS FOR NASA OCEAN PROCESSES

L-BAND ESTAR-0	**C-BAND - MODIFIED SFMR**
SWATH FOR 10 KM ALTITUDE (H):	SWATH:
SWATH WIDTH (2.8xH) = 28 KM	15° SINGLE BEAM, 2.6 KM WIDTH
NUMBER OF CELLS CROSS TRACK = 13	
CELL SIZE : 1x2 KM (average);	SENSIVITY:
1x1 KM (center);	BRIGHTNESS TEMPERATURE ~0.3°K
1x4 KM (edge)	EQUIVALENT SST ~1.0°C OR BETTER
	EQUIVALENT WIND SPEED ~1.4 M/S
SENSIVITY:	
BRIGHTNESS TEMPERATURE ~0.3°K	VIEWING GEOMETRY:
EQUIVALENT SALINITY (@25°C SST) ~0.5°/..	VERTICAL INCIDENCE ANGLE 60°(AFT)
	VERTICAL POLARIZATION

FIG.8. Measurement characteristics of the airborne microwave radiometers for NASA's Ocean Processes studies. Airborne sensors may complement *in situ* and satellite-based observations, providing coverage on an intermediate space scale.

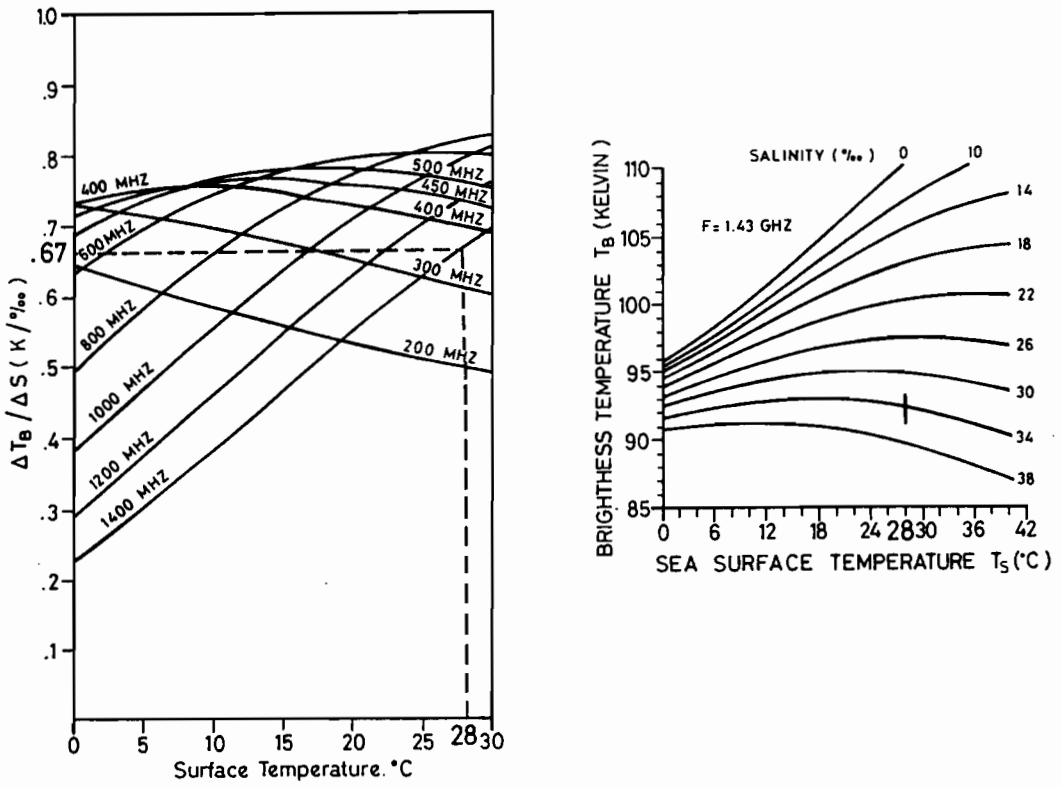

FIG.9. Sensitivity of emissivity of seawater with salinity, as a function of SST (left), and brightness temperature as a function of SST for various surface salinities (right).

Other instruments that could be flown on research aircraft missions include the C-SCAT C-band scatterometer, and a lidar which measures chlorophyll/primary productivity.

COARE will contribute to the Oceanic Processes program by providing high quality surface data for improving geophysical algorithms. If the TOPEX/Poseidon mission is launched in time, COARE will provide an excellent regional validation in view of the dense sea level network and the supporting environmental data that will be obtained.

b. Tropical Rainfall Measuring Mission.

Otto Thiele of Goddard Space Flight Center/NASA described the Tropical Rainfall Measuring Mission's status and the preflight activities that are related to TOGA/COARE. Phase-A studies by U.S. and Japan were completed in May, 1988. Japan's Science and Technology Agency approved initiation of Phase-B in May, 1989. NASA approved Phase-B studies to start in June 1989 with completion by September 1990. A decision will be made before 1 October 1990 for a FY91 new start for TRMM, with a planned launch in early 1996 from Tanegeshima, Japan.

The Kwajalein atoll groundtruth facility was highlighted for its contribution to pre-COARE studies, as well as its obvious contribution to the observing system for the COARE IOP. It was suggested that an intensive groundtruthing experiment using three

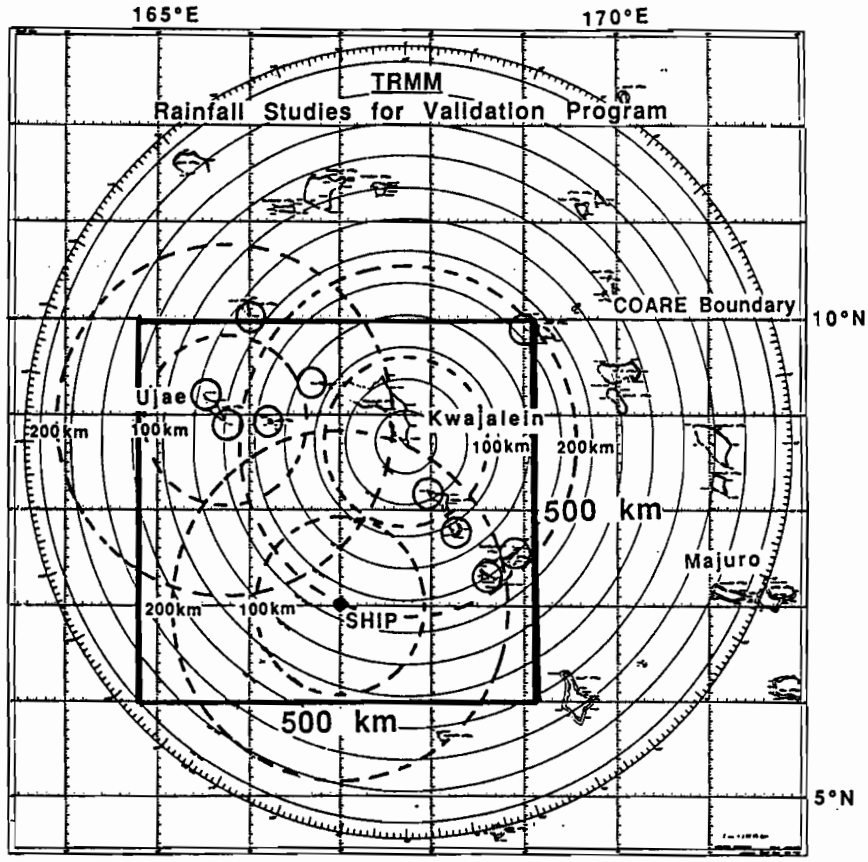

FIG.10. A suggested *in situ* rainfall measurement program for NASA's Tropical Rainfall Measurement Mission validation program.

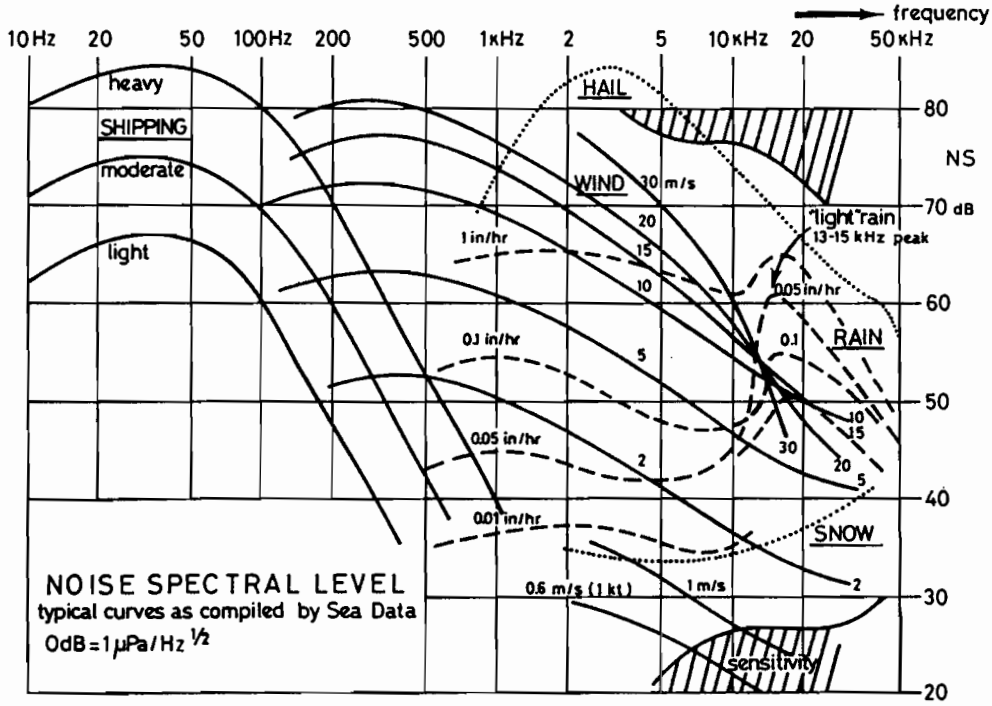

FIG.11. Typical oceanic frequency spectra for various noise sources. Rainfall has a narrow and relatively stable peak at relatively high frequencies due to bubble collapse. This might be exploited on oceanic moorings to get open ocean rain rates during COARE.

radars (including Kwajalein) could be conducted in conjunction with COARE (Fig. 10) such that a 500 km square box was covered by radar precipitation estimates, and where there are sufficient rain gauges to calibrate the radar estimates.

Another area of research being conducted as part of pre-TRMM efforts is in using acoustic signatures of rainfall on the ocean surface to estimate area-averaged precipitation rates. Figure 11 shows an ocean noise spectrum; the rain peak is around 14 kHz, which does not vary much with rain rate. TRMM researchers will conduct an experiment off-shore of Florida with a WOTAN acoustic system at a depth of 45 m.

c. Typhoon Motion Program.

Gregg Holland of the Bureau of Meteorology Research Center (Melbourne, Australia) presented the field program plans for the U.S. Office of Naval Research Tropical Cyclone Motion Initiative. This multinational effort is focusing on the off-equatorial tropical atmosphere to the east of the Philippines, though some oceanographic observations will be made during the program. The time frame for the observational effort will be August-September 1990.

This program is a large, multinational field effort in the western Pacific involving a large variety of observing systems and platforms. It therefore will provide valuable experience relative to COARE planning and implementation.

d. World Ocean Circulation Experiment.

Eric Lindstrom of the Commonwealth Scientific and Industrial Research Organization (CSIRO), on assignment to the U.S. WOCE Project Office, presented aspects of the WOCE plans that bear on COARE objectives and/or the western equatorial Pacific ocean circulation.

The areas where there is substantial overlap of WOCE and TOGA interests are:

- Meteorological sensors for air-sea flux measurements on ships and buoys (*)
- Improving models for estimating air-sea fluxes (*)
- Low-latitude western boundary currents (*)
- Surface drifters (design and deployments)
- Pacific Volunteer Observing Ship network (XBT, ADCP, MET)
- Sea level array
- Indonesian throughflow (*)
- Reanalysis
- Data management
- Satellites (*)

(* : areas with the greatest intersection with COARE)

Robert Weller of Woods Hole Oceanographic Institution is funded by WOCE to develop a package of air-sea interaction sensors that can be used to make high quality flux estimates from moored buoys or ships (a description of this effort is attached in the following appendix.) The results of this research will be of great benefit to the moored flux estimates made during COARE.

The improvement of atmospheric GCM boundary layer formulation for better estimation of air-sea fluxes is a high priority for WOCE and for COARE. The intensive observations made during COARE will aid in algorithm development, and will provide excellent validation of those algorithms.

Low-latitude western boundary currents in the western Pacific likely influence the size and location of the warm pool. These currents are also potentially important in the cross-equatorial transport of heat, so WOCE plans include moored measurements in some of these currents, such as the Mindanao Current. If these measurements can be coordinated with COARE observations, then the combined dataset will have even more value to the two programs. It will then be possible to calculate the correlation between fluctuations of the boundary currents and the near-equatorial currents.

The Indonesian throughflow is important to WOCE for the heat and mass budgets associated with the global ocean circulation. It is possible that changes in the air-sea interaction over the western Pacific warm pool influence the throughflow, and it is likely the case that the throughflow influences the size and location of the warm pool to some degree. If WOCE scientists are able to make observations within the Indonesian seas coincident with COARE, then the analysis of throughflow fluctuations and warm pool variations will be most useful for model validation studies.

4. Presentations on related technology.

Because many Workshop participants were generally unfamiliar with recent advances in the technology for measuring air-sea fluxes, two invited presentations were made. P. Hildebrand (NCAR/U.S.A.) spoke on, "Flux Measurements Using Aircraft and Radars", and W. Dabberdt (NCAR/U.S.A.) talked about "Determination of Boundary-Layer Fluxes With an Integrated Sounding System". These papers are included in the following appendix.

5. National reports.

Reports were made in the final plenary session by the scientists from the following nations:

Australia (E. Lindstrom)
China (X. Zhou)
France (D. Cadet)
Indonesia (H. Harjento)
Japan (A. Sumi)
United Kingdom (D. Webb)
United States (K. Mooney)

These reports were not official statements regarding TOGA/COARE, but were instead intended to communicate to the international group a sense for the areas of interest (related to COARE) by scientists from these nations, and some idea of the future plans that these groups will try to undertake. It was clearly stated that the official forum for commitments to COARE can only come through the international TOGA mechanism of the Intergovernmental TOGA Board, which will consider COARE at its January 1990 meeting in Geneva.

6. Meeting of the International Ad Hoc Committee on TOGA/COARE.

Members of this group are: P. Webster (Chairman), R. Lukas, J. Picaut, A. Sumi, J.S. Godfrey, G. Holland, D. Anderson, X. Zhou. A short organizational meeting was held the evening of May 29th.

The committee approved the suggestion by Webster that Lukas and Webster revise the existing version of the Science Plan, and distribute it as the second draft International TOGA/COARE Science Plan prior to the September TOGA SSG meeting. The hope was that a final Science Plan (SP) could be presented at that meeting. The revised draft SP was to be distributed by 15 July. *[Editor's note: This deadline was met.]*

Data management issues were raised. Some concern was expressed about priority for data usage given large personal and national investments in the collection of COARE datasets. It was agreed that explicit arrangements concerning exchange of data among nations should be developed. The suggestion was made to include some statements of principle concerning data management and exchange in the next revision of the SP, and to develop a considered policy of data management and exchange for the TOGA/COARE Implementation Plan.

The development of the Implementation Plan (IP) was discussed. The results of the present Workshop represent a good start on the IP, but there is clearly a need for much more input. In the U.S., plans are to issue a program announcement around the end of August, and to solicit planning letters from PIs or PI groups to address aspects of the program as outlined in the SP. These planning letters will provide important information for the IP, and will begin the process of matching scientists with specific tasks within COARE. This raised the question of how other nations intend to handle the development of national plans for participation in COARE, and any associated review/funding cycles.

The intention is to develop a draft IP for presentation to the International TOGA Board at least one month prior to its January 1990 meeting. Hopefully, this will allow time for national discussions and feedback at the the Board meeting.

WORKSHOP RELATED PAPERS

Improved Meteorological Measurements from Buoys and Ships for the World Ocean Circulation Experiment

Robert A. WELLER and David S. HOSOM

Woods Hole Oceanographic Institution,
Woods Hole, MA 02543 - U.S.A.

ABSTRACT

The World Ocean Circulation Experiment (WOCE) is directed at understanding ocean circulation and its interrelation to climate. During WOCE, moored buoys and ships will provide attractive platforms from which to make accurate in-situ measurements of the basic observables-- sea surface temperature, air temperature, wind velocity, barometric pressure, solar and longwave radiation, humidity and precipitation. From these measurements accurate estimates of the air-sea fluxes can be made. Drifting or moored air-sea interaction buoys will also be needed in WOCE for the verification of the surface data collected by remote sensing.

The overall goal of the "Improved Meteorological Measurements from Ships and Buoys" (IMET) effort is to develop accurate and reliable means of making meteorological measurements from ships and buoys during WOCE. Work being done at the University of Southern California concentrates on improving longwave radiation sensors. Scripps Institution of Oceanography is evaluating the effect of platform motions on radiometers, anemometers, and heading sensors. The work at the Woods Hole Oceanographic Institution includes development and evaluation of improved sensors, testing to quantify errors associated with present sensors, development of prototype data loggers capable of supporting intelligent data acquisition algorithms that reduce measurement error, and testing of sensors and data loggers on local moorings and on research ships.

Prototype buoy and ship data loggers are complete. Prototypes of some of the sensor modules are also complete. An optical WORM (Write Once, Read Many times) disc for storage has been working well even during rough weather testing on OCEANUS (Prada,1988) .Test buoy deployments began in January 1989 and test ship installations will be in operation later in 1989. Sensors for all variables are under test on land. Testing of the most promising of these will be continued on the test buoy and ship installations beginning in 1989.

1. Introduction.

Vertical exchange across the air-sea interface of horizontal momentum and of buoyancy, including heat and freshwater, couples the ocean and atmosphere. Observing this coupling is a fundamental need if WOCE is to understand ocean circulation and its interrelation to climate. During WOCE moored buoys and ships will provide especially attractive platforms from which to make accurate in-situ measurements of the basic observables -- sea surface temperature, air temperature, wind velocity, barometric pressure, solar and longwave radiation, humidity and precipitation -- and from which to make accurate estimates of the air-sea fluxes. They are attractive because they provide the means to make a direct measurement in situ and because sensors and electronics are returned periodically for calibration. The pre- and post-calibration procedure, along with an understanding of sensor performance in the field, provide the methodology to

ORSTOM
CENTRE DOCUMENTATION
Montpellier

F 30196

maintain and quantify the accuracy of the measurements. To obtain such high quality measurements in support of objectives of the Core 1 (the global description), Core 2 (the Southern Ocean), and Core 3 (ocean process studies) projects, the plan during WOCE is to deploy moored buoys equipped with meteorological instrumentation and to similarly equip a subset of the ships involved in WOCE.

The overall goal of the "Improved Meteorological Measurements from Ships and Buoys" (IMET) effort is to develop accurate and reliable means of making meteorological measurements from ships and buoys during WOCE. Work being done at the University of Southern California concentrates on improving longwave radiation sensors and determining the accuracy of net longwave flux estimates. Scripps Institution of Oceanography is evaluating the effect of platform motion on radiometers, anemometers, and heading sensors and investigating methods of reducing that error. The work at the Woods Hole Oceanographic Institution includes development and evaluation of improved humidity sensors; testing to quantify errors associated with present sensors for precipitation, sea and air temperature, and barometric pressure; participation with Scripps in the work on platform motion effects; development of prototype data loggers capable of supporting intelligent data acquisition algorithms that reduce measurement error; and testing of sensors and data loggers on local moorings and on research ships. Testing will include a variety of sensors (spanning various measurement techniques and a range of costs) in order to be able to quantify the trade-offs between accuracy, reliability, and initial expense.

2. Required measurements.

The basic meteorological quantities that need to be measured include sea surface temperature (SST), air temperature, wind speed and direction, barometric pressure, humidity (which may be obtained through wet bulb depression), incoming solar and longwave radiation, and precipitation. Stress, sensible heat flux, latent heat flux and evaporation are determined from these basic data using bulk formulae. Net shortwave radiation and net longwave radiation are also calculated. Accuracies of 10 watts per square meter are sought in the estimates of the mean values (averaged over monthly and longer time scales) of each of the four components of heat flux (sensible, latent, shortwave, longwave); accuracies of approximately 1 millimeter per day are sought in evaporation and precipitation; and an accuracy of 10% or 0.01 Pa is sought in stress.

Table of Desired Measurements.

Variable	Units	Min	Max	Res
Wind Speed	m/s	0.7	50	0.1
Wind Direction	deg	0	360	0.7
Air Temp.	degC	-40	45	0.001
Sea Surface Temp.	degC	-5	45	0.001
Solar Insolation	W/m2	0	1400	0.1
Barometric Press.	mb	850	1050	0.1
Relative Humidity	%RH	0	120	0.1
Longwave Radiation	W/m2	0	600	0.1
Precipitation	mm/hr	0	600	0.1

The majority of conventional surface meteorological data are provided by observations from the Volunteer Observing Ships (VOS). These data contain random errors due to inadequate sampling, poor instrument calibrations, ship air flow disturbance, etc. Effects such as heat contamination from the ship and salt contamination

of wet bulbs result in systematic biases. Random errors can be reduced by averaging but systematic biases must be identified by comparison of the VOS data with higher quality data from meteorological buoys, research ships, or an improved subset of the VOS. Drifting or moored air-sea interaction buoys will also be needed in WOCE for the verification of the surface fluxes of heat and momentum which have been determined from remote sensing or from atmospheric general circulation models and to obtain data from regions away from regular ship tracks. Data at the original sampling rate will be stored in the buoys for later recovery; averaged data will be telemetered via ARGOS for immediate use.

Net short wave radiation is estimated by measuring downwelling short wave radiation with a pyranometer and multiplying by (1-alpha), where alpha is the albedo (as from Payne 1972 for example). Instruments must be carefully calibrated and gimbal mounted to compensate for ship and buoy motion. Downward long wave radiation is measured by a similar sensor fitted with an opaque dome. Errors due to the radiative heating from parts of the ship in the field of view can be large and are additional to error due to motion and sensor deficiencies. Upwelling long-wave radiation must be inferred as the graybody emission of the sea surface plus the reflection of downwelling long wave radiation by the sea surface and by modelling dependence on air temperature and humidity (Siegel and Dickey 1986). Errors in measuring SST will enter in the graybody formula and are thus potentially large, but there are also uncertainties in the sea surface emissivity, sea surface reflectance, and the empirical model dependence on air temperature and humidity. However, it is difficult to make a good measurement of the sea surface temperature of the ocean. With diurnal heating, SST may be up to 3 degrees C warmer than the temperature at a depth of 1 meter; and, during a shower, relatively fresh water can be found at the surface that is cooler than the water below. Further, sensors placed on a ship or buoy hull may be affected by the thermal mass of the hull and, if not shielded, may be directly heated by the penetrating radiation. Such radiative heating is also the primary problem with air temperature measurements although aspirated air temperature sensor shields can be used to attempt to bring the error in air temperature down to approximately 0.2 degrees C. Humidity measurements of the desired accuracy will require the development of new sensors. Errors in the buoyancy flux will be associated with errors in both total heat flux and precipitation estimates.

3. Meteorological instrumentation.

Meteorological packages and sensor sets for use on both ships and buoys during WOCE are now under development. Air-sea fluxes will be computed using stability dependent algorithms for momentum, sensible heat, and latent heat (Large and Pond 1981,1982) and computing net shortwave using an albedo look-up table, and net longwave by estimating outgoing longwave with an improved graybody algorithm now being developed. Raw data and original sampling rate (as fast as every minute for one year) fluxes will be stored: several-hour averaged surface variables and fluxes will be telemetered via ARGOS. ARGOS data will be monitored (and quality checked so it will qualify for distribution via GTS) and archived at an accessible (dial-up and/or Ethernet) data base.

Prototype buoy and ship data loggers are complete. Prototypes of some of the sensor modules are also complete. An optical WORM (Write Once, Read Many times) disc for storage has been working well even during rough weather in a test installation on OCEANUS (Prada and Baggeroer 1988). Test buoy deployments began in January 1989, and test ship installations will be in operation later in 1989. Sensors for all variables, including precipitation, are under test on land. Testing of the most promising of these will be continued on the test buoy and ship installations beginning in 1989. Special

efforts are being made to develop relative humidity and precipitation sensors, to reduce errors in sea surface and air temperatures, to reduce errors in short and longwave radiation measurements associated with platform motion, to develop an improved wind /vane/ compass sensor, and to establish a reliable system configuration for use on ships and buoys.

4. Shipboard system.

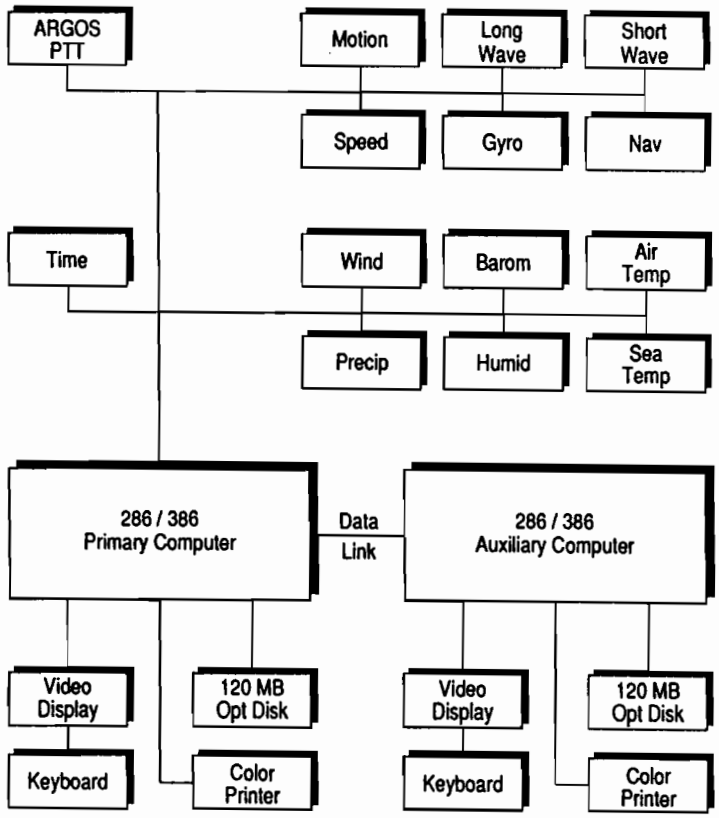

FIG.1. Shipboard system block diagram

The ship data logger/controller is an NEC APC-IV personal computer, as shown in Figure 1. Software development is carried out using standard MS-DOS compatible programs. The primary computer collects the data from the various sensors via a digital interface built into each sensor. It then stores the raw data on the optical disk, displays the data on a real time operator display, performs calculations and transmits longer term average data and calculated data via ARGOS. There is a color printer for hard copy data in a strip chart form and a keyboard for operator interaction. There are two basic sensor groupings, one that collects one minute averages and one that is capable of high speed

sampling of motion and radiation if desired. There is an auxiliary computer that is capable of accessing the primary optical disk and doing data analysis and evaluation without disturbing the primary data collection.

5. Buoy system.

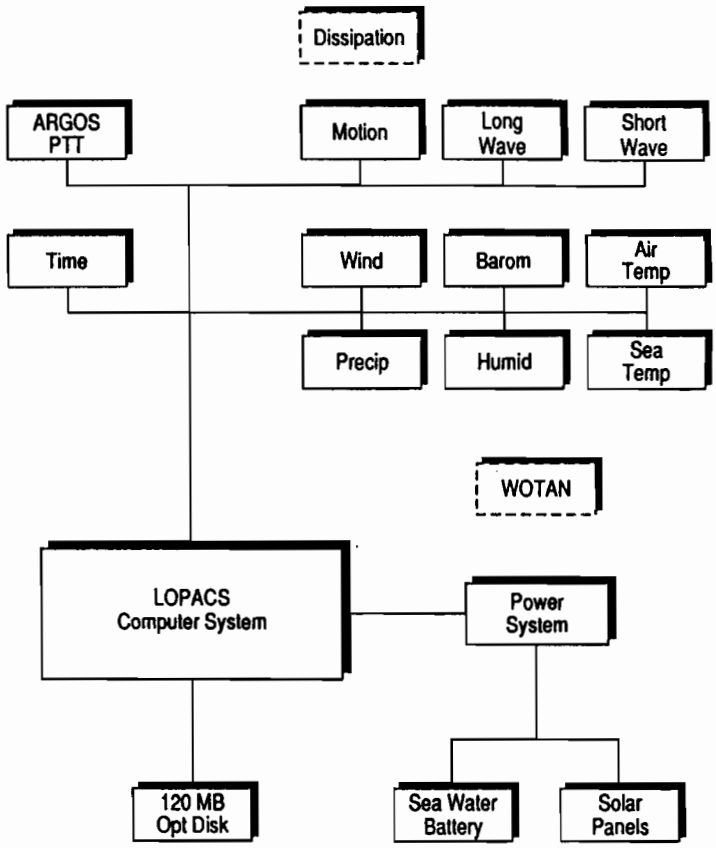

FIG.2. Buoy system block diagram

The buoy data logger/controller is based on a low-powered processor unit called LOPACS as shown in Figure 2. This controller is a CMOS based, IBM compatible, commercially available unit that is described in Reference 6. The software development is carried out using standard MS-DOS compatible programs that would be similar but not the same as the ship system. The system functions in the same way as a ship system except there is no operator display or interaction. The electronics is housed in a watertight area on the buoy and can be controlled via a watertight connector to a remote terminal.

6. Sensor modules.

The sensor set will provide measurement of wind velocity, air temperature, sea temperature, barometric pressure, relative humidity, incoming shortwave radiation, incoming longwave radiation and precipitation. Various alternate sensors for each variable are being tested to establish reliabililty, accuracy, and cost versus performance information for each type of measurement. The sensor modules being designed and built to work with the system are the current choice for sensors to satisfy the measurements required and are referred to as the "strawman" sensor set. The following figures and paragraphs describe the strawman sensor configurations.

Each sensor will be mated to a microprocessor based module that will perform some sampling tasks, convert the raw sensor output to engineering units, and send the data digitally over RS-485 (ship) or RS-232 (CMOS open drain) (buoy) link to the data logger/controller. Refer to Figure 3. for the configuration of the Digital Data Module. Each digital module is housed in a plastic, watertight 4.5" diameter housing with a 4 wire underwater connector providing power and data. In the development modules, there are two aluminum chassis, one of which contains one or more custom front end interface printed circuit cards while the other contains at least three cards, including a power and communications board, a digital module processor (DMP) card (currently a Basicon 2i unit) and an integrating 15 bit plus sign, analog to digital converter,parallel and counter I/O card. The (DMP) is typically programmed in BASIC 52 with 'C' as an alternative. This modular approach permits development of future sensor modules by investigators in other laboratories that will be compatible with the data collection system.

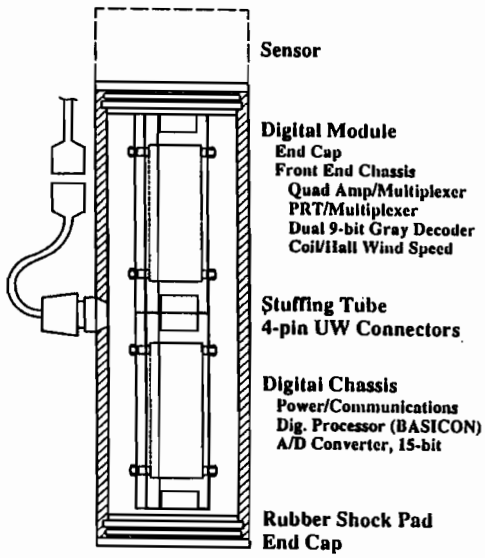

FIG.3. Digital data module

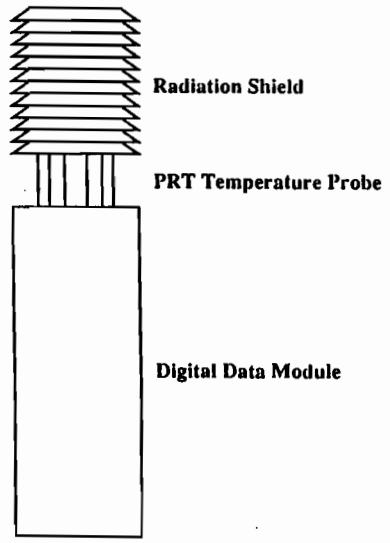

FIG.4. Air temperature module

The air temperature module uses a PRT (Platinum Resistance Thermometer) inside of an R. M. Young radiation shield shown in Figure 4. An autoranging, ratiometric measurement will be made to provide as high an accuracy as possible. The PRT offers a

linear, ultra low drift sensor. Close coupling of the sensor and the shielded front end electronics will provide a stable, low noise analog section and the DMP will be programmed to provide corrections based on stored calibration data.

Sea Surface Temperature is electronically very similar to the Air Temperature module but will be housed in an aluminum underwater housing for mounting under the buoy and is shown in Figure 5. The ship mounting is being evaluated but will probably be custom for each ship that the system is installed on.

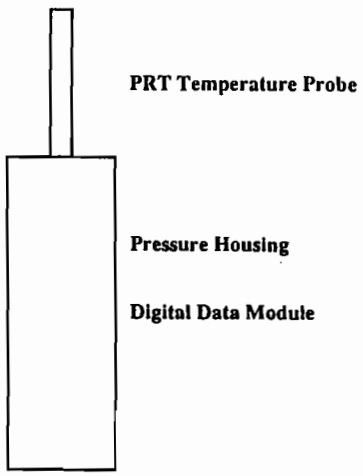

FIG.5. Sea surface temperature module

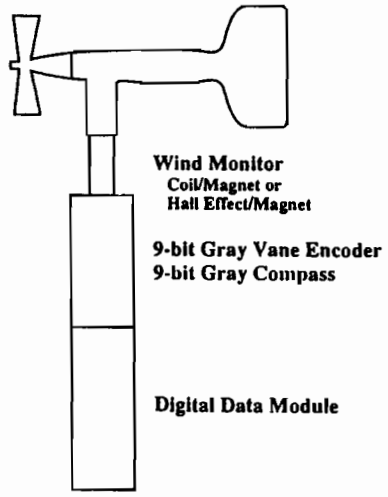

FIG.6. Wind speed and direction module

The wind speed and direction module is shown in Figure 6. An R. M. Young Wind Monitor has been selected since it has a proven record and uses a propeller to measure speed. The potentiometer is removed and the vane shaft extended down into the top of the data module housing addition. A commercially available 9 bit Gray Code shaft encoder is coupled to the vane. A Digicourse Model 226 gimbaled compass with a 9 bit Gray Code output is in the same housing . The wind speed will be measured with either the standard coil and magnet or with a Hall Effect unit and magnet. The front end electronics include a dual 9 bit Gray code to binary decoder and electronics to process either of the speed signals. The DMP will be programmed to sample, store and process the standard vector averaged wind data over a one minute time period.

The Short Wave Radiation module will consist of an Eppley PSP (Precision Spectral Pyranometer) mounted on an aluminum housing which provides a reference mass for the PSP. This is fastened to a standard digital module and the combination is mounted in a 2 axis gimbal as shown in Figure 7. This gimbal has low corrosion, sealed bearings that are filled with a lubricant. This provides extended life and some damping. The sensor can be adjusted in the gimbal to minimize acceleration sensitivity. The low level signal from the sensor is amplified by a low noise amplifier and sampled by the A/D card under DMP control.

Long Wave Radiation is measured by a Foot thermopile (Foot 1986) and has two compensating thermistors. The low level signals are amplified, multiplexed and stored by the DMP, where the compensation is accomplished by software rather than analog electronics. The long wave sensor also has a two axis gimbal as shown in Figure 8.

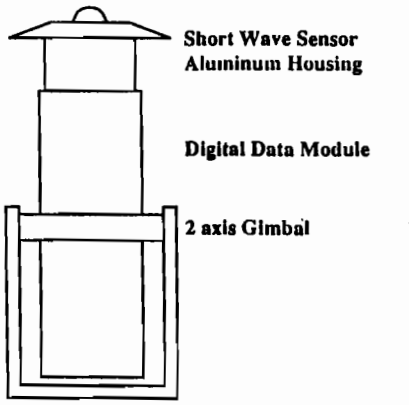

FIG.7. Short wave radiation module

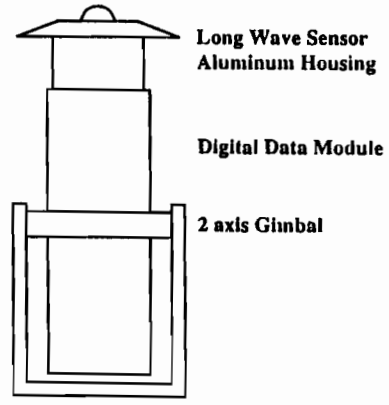

FIG.8. Long wave radiation module

The Barometric Pressure and Relative Humidity module shown in Figure 9 uses a common digital data module. The barometric pressure gage is an AIR (Atmospheric Instrumentation Research Inc.) Model DB-1A with a parallel digital output that goes directly to the DMP. The relative humidity unit is a Rotronics Model MP-100-F that has analog outputs for both relative humidity and local temperature. These are multiplexed into the A/D card and controlled by the DMP.

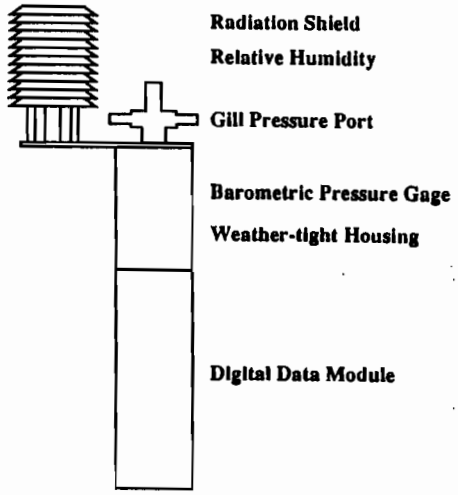

FIG.9. Barometric pressure and relative humidity module

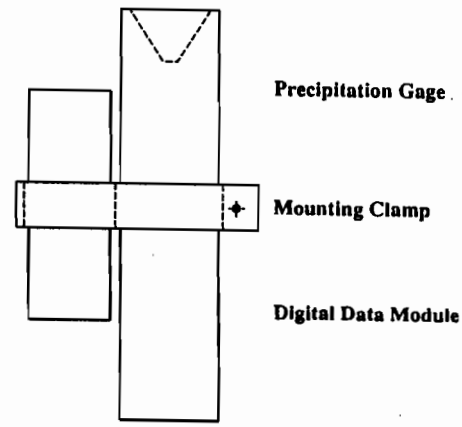

FIG.10. Precipitation module

The Precipitation sensor is an R. M. Young Model 50102 Rain Gage with a 0 to 50 millimeter capacity unit that automatically empties and repeats the measurement and is shown in Figure 10. The unit has a 0 to 5 volt output that is converted in the A/D board. The DMP makes measurements and keeps track of the emptying cycles. There is a heater for cold weather use but this would only be used on ships for power reasons. The digital data module will be mounted beside the rain gage.

7. Deployments during WOCE.

Potential deployments of the IMET systems in moored arrays and on ships in WOCE are discussed below. The primary goal of these deployments would be to provide data needed for the validation of the air-sea flux and meteorological data fields to be produced during WOCE. Detailed reasons for the deployments are given elsewhere; but briefly, these deployments would:

- Provide, at the site of a moored array embedded in a Core 3 or Core 1 or 2 data field, a point with time series of the surface variables and air-sea fluxes of the highest possible accuracy, both for examining response to local forcing and for reducing the error in the larger scale field.
- Validate routine products of atmospheric models, serving as a diagnostic point to check the performance of coupled atmosphere-ocean models.
- Provide very accurate input data or provide a means to validate/estimate the error in the air-sea flux fields used to force ocean or atmosphere models.
- Provide, at selected sites, accurate time series of surface variables and air-sea fluxes to assess the accuracy of existing climatologies (such as the Levitus data) and, if not assimilated, of the data fields being produced during WOCE.
- Validate satellite products and methodology, including wind, SST, rainfall (during the Tropical Rainfall Measurement Mission, TRMM), the use of microwave radiometers (SSM/I) to measure total water content in the atmospheric column and infer surface humidity, and radiation products from polar orbiting satellites.
- Provide the means to assess systematic errors in the data fields collected by the Volunteer Observing Ships (VOS).
- Lay the groundwork for a methodology and network of moored buoys that will replace the weather ships and for a method of maintaining a near real-time watch on oceanic locations where good surface data would, because of teleconnections, be a diagnostic to change in global circulation/climate.

Moored Buoy

The buoy deployments would be as follows:

- 1991-1993: Eight moored surface buoys, in the Ekman/Subduction process study in the Azores-Canary area.
- 1993-1997: Up to ten moorings at special locations and in arrays with a minimum of 3 elements for the purpose of calibration and validation of the WOCE air-sea flux fields. These arrays would be maintained at their sites for two years.

The large scale air-sea flux fields that might be provided by satellites and models will not be sufficient to address the needs of the planned Ekman Subduction experiment in the eastern North Atlantic in 1991 -1993. Accurate, in situ measurements are needed to provide the most accurate estimates of the wind stress and buoyancy forcing of the upper ocean. An array of eight surface moorings, each with meteorological instrumentation and each supporting current meters is under discussion.

For WOCE the plan is to build 10 surface meteorological mooring hardware sets by 1993 and thus to be able to maintain (with back to back one year deployments equipment at 2-3 sites in any year. Coordination will be sought with other investigators to add current meters to each mooring to examine local ocean response to atmospheric forcing,

to quantify the division between geostrophic and ageostrophic wind-driven flows, and to add data points with details of the vertical structure to the fields of ocean circulation being constructed during WOCE.

Ship Deployments

The ship deployments would be of three types:

- Research Ship System (RSS): Research Vessels participating in the WOCE Core 1, 2, and Core 3 activities with science parties seeking high quality meteorological observations.
- WOCE Hydrographic Program Ship System (WHPSS): Research Vessels participating on the WOCE Hydrographic Program.
- Ship of Opportunity System (SOS): Volunteer Observing hips (VOS) making repeated XBT and/or ADCP sections.

The RSS installation on U.S.Research Vessels would include three sensor installations (port, starboard, and bow mast) and a sensor suite designed to provide the best possible measurements of the surface variables and best possible estimates of the air-sea fluxes at reasonable cost (thus excluding as standard items an infrared hygrometer, optical rain gauge, and sonic anemometer). Two NEC APC-IV's would be used to provide redundancy and real-time access for the science party to the meteorological data. One APC-IV would carry on ARGOS telemetry and data logging at the standard rate and in the format to be provided by the other ships and buoys; the second APC-IV would be menu-driven and available to the science party and/or resident technician. This underway sampling would be coordinated with other underway sampling efforts. The optical disks would be returned after one or more legs to be quality-checked and read into the data base. Five RSS would be built in order to maintain four at sea. Targeted are the research ships where collection of meteorological data will be of direct scientific interest. Also, it is planned that one RSS be installed temporarily on a U.K. ship involved in WOCE for purposes of intercomparison. It is hoped that the five RSS will remain in operation following WOCE and that their data will continue to be distributed via GTS and archived.

The research ships involved in the WHP are the second focus of attention because they will provide platforms that will provide ship velocity data (via GPS), permitting true wind to be determined, and because the installation of a semi-permanent meteorological package (WHPSS) would benefit from the attention of the resident technician/science party on board. Port and starboard installation would be done and a single APC-IV would be installed. This would support ARGOS telemetry of several-hour averaged surface variables and fluxes, recording of raw data and raw sampling rate fluxes on optical disk, and simple strip-chart display (on video terminal and/or printer) of the data. Prime candidates are those ships in the WHP making sections in data sparse regions and/or sections that pass thru regions in particular need of calibration/validation.

The VOS making the repeat XBT sections would be the third choice. This SOS package will be a self-contained , unit similar to the package used on buoys. A single sensor set will be installed on a temporary mast. When possible, one sensor module will be used to link to ship's navigation, permitting determination of absolute wind and momentum flux. Internal logging on optical disk of raw data and raw sampling rate fluxes and ARGOS telemetry of several-hour averaged data will be supported. Primary targets for the planned installations will be ships equipped for WOCE to collect XBT and/or ADCP data, especially those transiting regions with otherwise sparse coverage of

surface meteorology and air-sea fluxes and/or locations where the modelling and remote sensing efforts need validation data. Four SOS will be built and used in a cooperative effort involving the investigators collecting the XBT/ADCP data.

Acknowledgments. This work was supported by the Ocean Sciences Division of the National Science Foundation, Grant No. OCE-8709614. Cooperating investigators are Rob Pinkel at Scripps Institution of Oceanography and Tom Dickey at the University of Southern California.

REFERENCES

Foot, J.S. ,1986: A New Pyrgeometer. J. Atmos. Oceanic Tech., **3**, 363-370 .

Large, W.G. and S., Pond, 1981: Open Ocean Momentum Flux Measurements in Moderate to Strong Winds. J. Phys. Oceanogr., **11**, 324 -336.

Large, W.G. and S., Pond, 1982: Sensible and Latent Heat Flux Measurements Over the Ocean. J. Phys. Oceanogr., **12**, 464 -482.

Payne, R.E. , 1972: Albedo of the Sea Surface. J. Atmospheric Sciences, **29**, 959-970.

Prada, K.E., 1988: Optical Disk Use and Evaluation in Harsh Field Environments. WHOI Contribution No. 6908. EOS December 8,1988.

Prada, K.E. and A.B., Baggeroer, 1988: An Artic Remote Autonomous Measurement Platform. WHOI Contribution No. 6608, January 1988. Proceedings of a Workshop on Instrumentation and Measurements in the Polar Regions ; also Oceans 87 with the same title.

Siegel, D.A. and T.D., Dickey, 1986: Variability of Net Longwave Radiation of the Eastern North Pacific. J. Geophys. Res., **91**, 7657 -7666.

Flux Measurement Using Aircraft and Radars

Peter H. HILDEBRAND

National Center for Atmospheric Research
P.O. Box 3000, Boulder CO 80307-3000 - U.S.A.

1.0 Measurement Goals

Aircraft are excellent platforms for measuring atmospheric turbulence. Due to their mobility and instrumentation, aircraft can make a wide variety of measurements over a large domain in a short length of time, and the aircraft flight pattern can be easily adjusted to accommodate to changes in the atmosphere and new measurement techniques.

This paper will discuss the use of instrumented aircraft to measure bulk and turbulent atmospheric transport of heat, moisture, and momentum over large distances. The paper will cover flux measurement from aircraft, the design of aircraft flight patterns. and the measurement accuracies which can result from these measurement techniques.

The measurement techniques include the use of in-situ and remote sensors. The discussion will cover aircraft instrumentation, instrumentation accuracies, the eddy correlation technique for measurement of atmospheric turbulence, and aircraft flight patterns. The discussion will be directed to particular problem of measuring the variability of atmospheric transport within an inhomogeneous atmosphere. This problem is of particular importance to TOGA COARE.

Most experiments which are designed to measure atmospheric transport of heat, moisture, and momentum have had smaller measurement domains than TOGA COARE. The TOGA-COARE time and space scales (Table 1) range from the diurnal cycle (24h and a cluster scale of about 500km), through the cloud cluster scale (1-3 days and up to 1700 km movement) to the meso-scale convective super cluster (MCC) scale (about 10 days and up to 4000 km movement). Making airborne in-situ and Doppler radar measurements over these large time and space scales will require new approaches to the collection and analysis of aircraft data.

---

[1] The National Center for Atmospheric Research is supported by the National Science Fountation.

ORSTOM
CENTRE DOCUMENTATION
Montpellier

F 30197

Table 1. The TOGA-COARE observational domains.

Large Scale: (LSA)	10°N - 10°S by 140°-180°E or ≈ 2200x4400 km. Over this area the large scale convective and precipitation events are to be described and the net fluxes of heat, moisture and momentum are to be measured.
Equatorial-Synoptic: (ESA)	5°N - 5°S by 150°-175°E or ≈ 1100x2800 km. Over this area the detailed structure of convective and episodic wind events and associated precipitation fields and broad scale heat, moisture and momentum fluxes are to be measured.
Intensive Flux: (IFA)	5°N - 5°S by 155°-170°E or ≈ 1100x1700 km. This area will include very detailed determination of the surface fluxes as well as the Equatorial Synoptic area measurements.

2.0 Measurement Techniques

Aircraft are ideally suited for measuring atmospheric phenomena over large distances. Aircraft in-situ and remote probing instrumentation, coupled with long aircraft flight tracks can provide high resolution measurements over large areas. The principle measurements which can be made from aircraft include in-situ measurements of temperature, moisture, winds, pressure, cloud particles, and many atmospheric chemical constituents. In addition, research aircraft typically include measurements of short and long wave radiation, and radiative earth surface temperature. Typical in-situ aircraft instrumentation and measurement accuracies are listed in Table 2. For more information on aircraft in-situ instrumentation see Research Aviation Facility (1987a,b, 1988a,b,c).

The aircraft in-situ measurement of temperature, moisture and winds readily lend themselves to evaluation of heat and momentum fluxes within the atmospheric boundary layer. However, due to limitations on sensor sensitivity, measurements of turbulent fluxes are generally limited to boundary layer and in-cloud measurements. The concentrations and turbulent transport of some chemical species have also been evaluated (e.g. see Lenschow, et al., 1982).

Currently available remote probing measurements from research aircraft include in-cloud precipitation and wind measurements from Doppler radars, boundary layer structure and wind measurements from lidar, and sea surface properties measured using

Table 2. HAPEX King Air instrumentation for turbulence measurements.

Variable	Instrument	Manufacturer and Model	Performance Accuracy	Resolution
In-situ Instrumentation				
Position	Inertial Navigation	Litton LTN-51	≤1.0 Nml / flt hour	0.0014°
Static Press.	Oscillation Freq.	Rosemont 1501	± 1 mb	0.034 mb
Airspeed	Variable Capacitance	Rosemont 1221	± 0.7 mb	0.006 mb
Air Temp.	Platinum Resistance	NCAR Fast Resp	± 0.05 °C	0.006 °C
Air Temp.	Platinum Resistance	Rosemont 102	± 0.5 °C	0.006 °C
Humidity	Lyman-alpha Hygrometer	NCAR LA-3	± 5 %[2]	0.2 %
Humidity	Thermoelectric Hygrometer	EG&G 137-C3-S3	± 0.5 °C if T>0 °C[3] ± 1.0 °C if T<0 °C	0.006 °C
Horiz. Winds	Gust Probe and INS	NCAR	± 0.1 m/s, t<0.6 h ±(1.0+0.5t) t in hrs	0.012 m/s
Vertical Winds	Gust Probe and INS	NCAR	± 0.1 m/s	0.012 m/s
Geometric Alt.	Radio Altimeter	Collins ALT-55	± 2-3%	0.1 m
Infrared Rad.	Pyrgeometer 4-45μm	Eppley PIR	---	0.4 W/m^2
Visible Rad.	Pyranometer 0.285-2.8 μm	Eppley PSP	---	0.4 W/m^2
Surface Temp.	Bolometeric Radiometer	Barnes PRT-5	± 1 °C	0.005 °C
Radar Measurements				
Rainfall Rate	Airborne Doppler Radar	NCAR	factor of 2	
Air Velocity	Airborne Doppler Radar	NCAR	± 1 m/s	
Ocean sfc winds	Airborne Doppler Radar	NCAR	± 2 m/s	

[2] with periodic baseline calibration.

[3] if relative humidity is > 11%

radar scatterometers. For a discussion of airborne Doppler radar measurement capabilities, see Hildebrand and Moore (1989). Airborne Doppler radar capabilities are currently under development (Hildebrand et al., 1988) and significant improvements in these capabilities are anticipated by the time of TOGA COARE.

2.1 Boundary layer fluxes of heat, moisture, momentum and passive constituents.

Measurement of atmospheric flux transport using aircraft in-situ instrumentation requires making a number of assumptions about the representativeness of the measurements to the actual state of the atmosphere. Specific assumptions include:

1) the turbulent fluctuations can be separated into mean and turbulent components from which the turbulent fluxes can be calculated,

2) the measurement of boundary layer turbulence must be an accurate sample of the domain of interest and thus representative of the true average atmospheric state within that domain,

3) the domain to be sampled must be sampled instantaneously within the domain, thus removing diurnal or temporal trends from the data.

Since most in-situ aircraft instrumentation is only capable of measuring turbulent intensities characteristic of the atmospheric boundary layer or convective storms, the following discussion will center primarily on sampling the atmospheric boundary layer.

2.1.1 Separation of in-situ measurements into mean and turbulent components.

The decomposition of turbulence measurements into mean and turbulent components (Wyngaard, 1986) is based on the assumption that for any measurements of turbulent flow, that any measured value (P) can be decomposed into mean (p) and turbulent (p') portions using the relation $P = p + p'$. This decomposition assumes that some representative mean value (p) exists and that there is process whereby the mean values (p) can be separated from the turbulent (p') portions of the flow.

Once the total flow is decomposed into mean and turbulent components, the turbulent fluxes can be calculated from averages of the turbulent components, appropriately manipulated to produce the needed products. For example, the vertical fluxes of any quantity (e.g. temperature) can be calculated as the product of T' and w' values, averaged over an appropriate interval. This technique also produces true variance

and covariance values for the means of any products such as $v_1'v_1'$ and $v_1'v_2'$, respectively, where the subscripts 1 and 2 denote different variables.

Classical use of this decomposition has assumed the atmosphere to be horizontally homogeneous, and that a single mean value or linear trend will be representative of the mean state of the atmosphere. In the undisturbed atmosphere, this assumption holds well and extensive measurements of convective boundary layer fluxes have been made. For example, temperature and moisture flux profile measurements from AMTEX (Wyngaard, et al., 1978) are shown in Fig. 1 and illustrate temperature and moisture flux measurements made using 60 km flight legs and a succession of altitudes within a 1.2 km deep boundary layer. In calculations such as this, mean values of the full flight data set were used to decompose the data into mean and turbulent portions.

The problem with the "mean value" eddy correlation technique arises when the mean value or the turbulent intensity changes along the flight track. An improved method of decomposition of the data into turbulent and mean components can be through the use of spectral decomposition or filtering of the data (Hildebrand, 1988). Using this technique, the data can be decomposed into short wavelength "turbulent" components and long wavelength "mean" components. This technique is schematically illustrated in Fig. 2 (top) where the variance of the total sample (0.27) is distributed between the variance of the mean (0.25) and the variance of the turbulent component (0.02). If the decomposition were made using the assumption of a "constant" mean value (Fig. 2 bottom), the total variance (0.27) would have been erroneously attributed to turbulence. This decomposition technique enables separating the turbulence from the mean state measurements. In its application to TOGA COARE, this technique will allow for measurement of the mean and turbulent conditions along very long flight paths which include both Meso-scale Convective Systems as well as clear areas.

Eddy correlation flux measurements have been extended to some chemical species for which there exists fast response instrumentation for sampling the chemical species. For example, Lenschow, et al., (1982) have sampled vertical ozone flux over land and over the oceans.

2.1.2 Accuracy of in-situ turbulent flux measurements.

The spectrum of turbulence can be divided into components or ranges (Wyngaard, 1986). The large-scale, energy-containing eddies perform the majority of the turbulent transport in the convective boundary layer and have spectral peaks typically at about 1.5h, where h in the boundary layer depth. These large eddies are highly variable in intensity, space, and time. Accurate measurement of boundary layer turbulence requires sampling

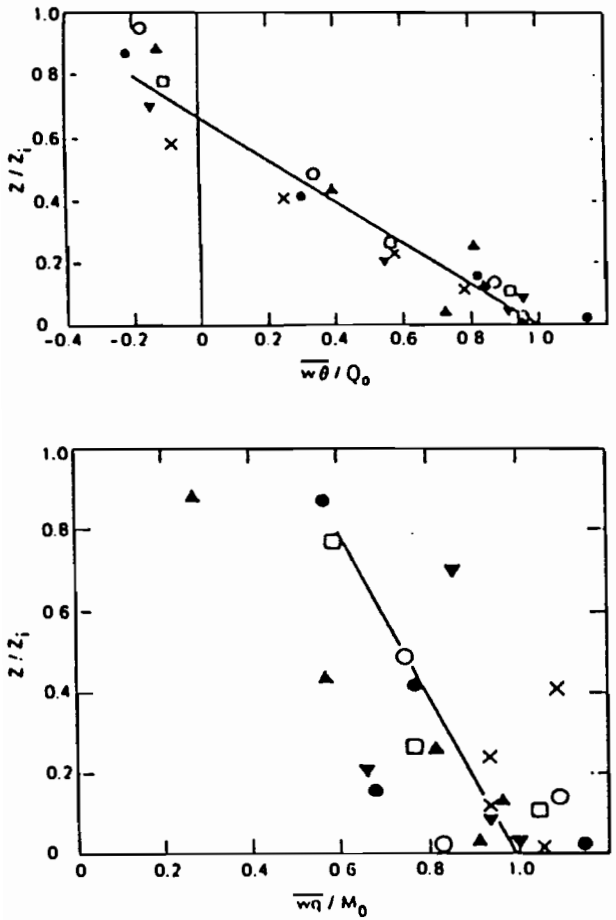

FIG.1. Measurements of the temperature and moisture flux profiles from the AMTEX experiment (after, Wyngaard et al., 1978).

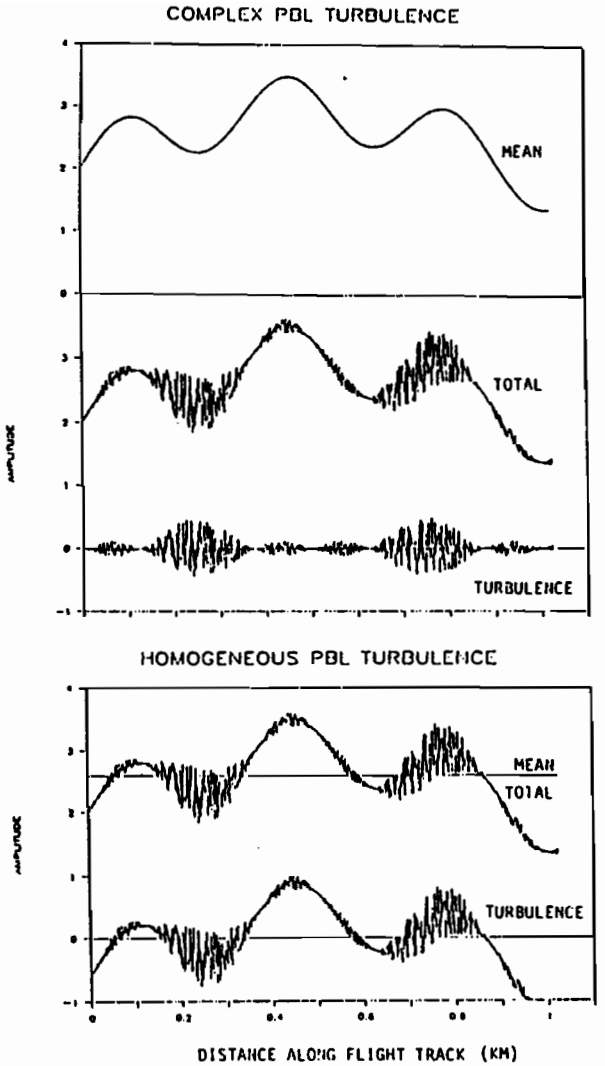

FIG.2. Top: Simulation of turbulent flow showing decomposition of the total flow into a constant mean value, plus a turbulent component having large and small scale deviations from the mean. Bottom: simulation of turbulent flow showing decomposition of the total flow through filtering into a variable mean value, plus a turbulent component only small scale deviations from the mean.

a reasonably large number of these large eddies in order to attain an accurate measurement of the boundary layer turbulence. Due to the size of the large eddies and the need to sample a number of them, flight tracks need to be fairly long if accurate turbulence measurements are to be made. This is because the turbulence measurements along the narrow flight path must be representative of a true mean value over the full boundary layer. Lenschow and Stankov (1986) evaluate the accuracy of boundary layer turbulence estimates due to random sampling error as a function of aircraft flight path length. Their relations are plotted in Fig. 3 for $0.1<z_*<.9$ and for errors ranging from 10% to 50%. These curves show that flight path lengths of 10 to 100 times the convective boundary layer depth are needed to achieve a 20% error in measurement of w'T' for measurements made between altitudes of 0.1h and 0.7h. For measurements of w'q', path lengths of about 20 to 30h will be needed to achieve 20% error.

For the AMTEX observations presented in Fig. 1, the w'T' measurements should have been accurate to about 10% at 0.1h, and to about 30% at 0.7h. The moisture flux measurements should have been accurate to 10-20% throughout the boundary layer. These error estimates are in general agreement with the scatter seen in Fig 1.

For the complex terrain, HAPEX experiment (Andre, et al., 1986), some evaluations of flux measurement accuracy were calculated as a function of sample path length (Hildebrand, 1988). Turbulence and fluxes were evaluated from 10 km block averages of the high frequency filter output. Based on a very limited sample, the HAPEX analysis (Fig. 4) shows the latent and sensible heat flux errors to drop below 20% at flight path lengths of >6h to 8h, and to drop below 10% error for flight path lengths of >15h to 18h. These results are about a factor of 2 to 3 better than the results of Lenschow and Stankov (1986).

Problems with the Lyman-alpha humidity sensor produced biases of about 5-25% difference in the measured latent heat fluxes as measured by two identical sensors in HAPEX (Hildebrand, 1988). It is likely that improvements in humidity instrumentation, currently underway in the research aviation community, should correct this problem.

On the basis of this discussion, a rough guideline is that aircraft flight tracks of about 10 times the boundary layer depth will produce measurements accurate to at least 20% for low boundary layer altitudes. Flight tracks of 30h to 50h should reliably produce heat flux measurements accurate to about 10%. For adequate sampling of turbulence at higher altitudes, track lengths will have to be longer. In the context of TOGA COARE, these restrictions do not represent a problem, and measurement accuracies of 10% to 20% should be possible.

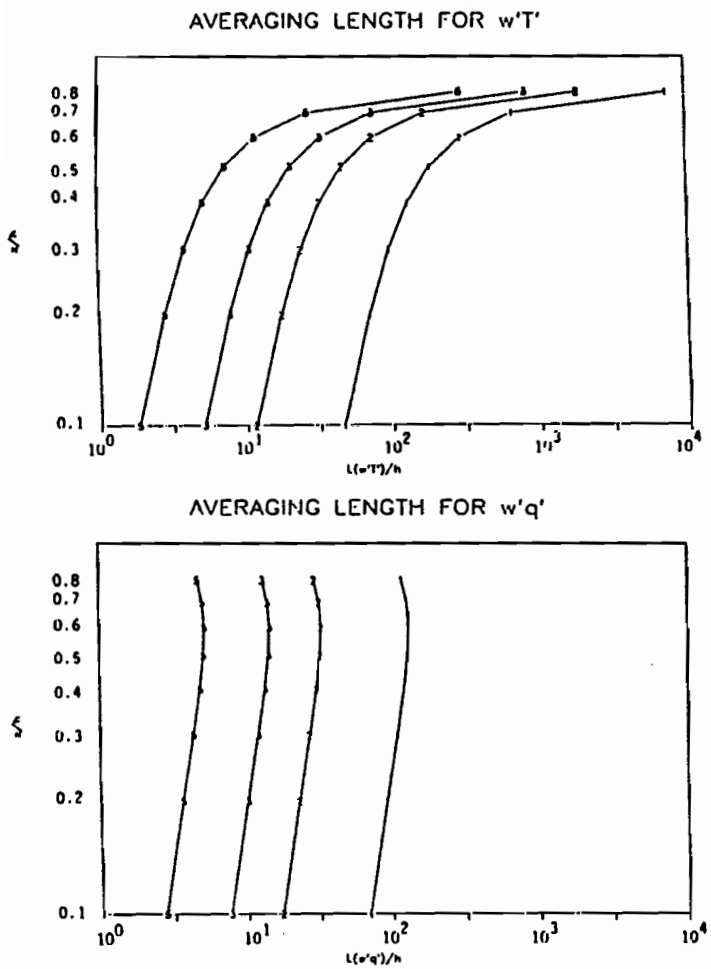

FIG.3. Vertical temperature and moisture flux accuracy as a function of flight path length and altitude in the boundary layer. The vertical scale is normalized boundary layer depth. The horizontal scale is flight path length, normalized by boundary layer depth. The curves of constant standard error of the temperature and moisture flux include 10%, 20%, 30% and 50% error curves, denoted by the number 1 through 5, respectively.

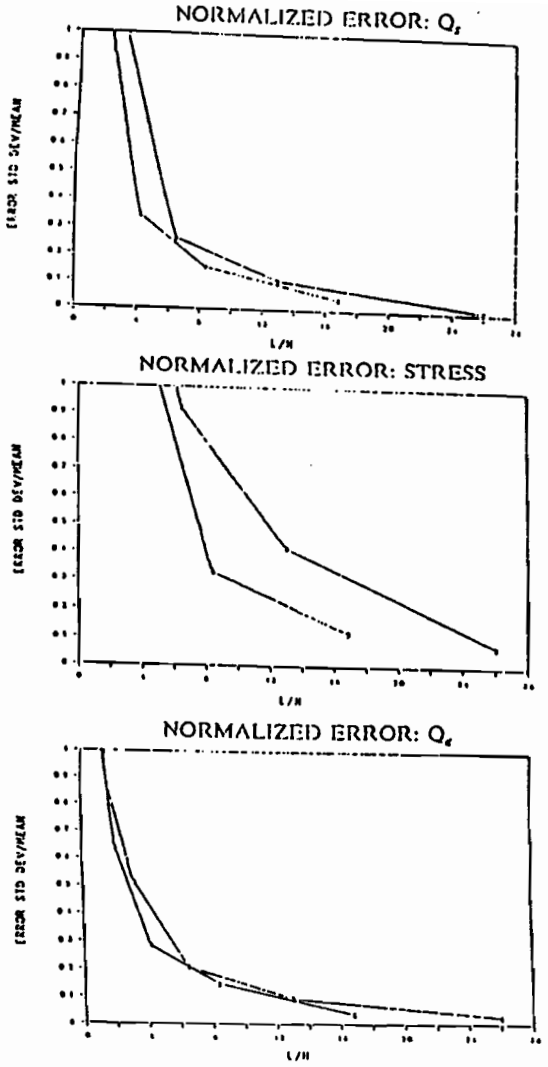

FIG.4. Measurement error plots for latent and sensible heat flux from HAPEX flight 21, for altitudes of 0.11-0.17h. The measurement error normalized by the mean value is plotted versus measurement path length normalized by the boundary layer depth.

2.1.3 Temporal effects.

During the time while observations are being made, the boundary layer is changing. This rate of change of the boundary layer is such that it can be assumed to be stationary for periods of 10 to 20 minutes. At the typical aircraft flight speeds of 120 to 150 m/s, the aircraft can fly 70 to 180 km in 10 to 20 min, depending on flight speed. The aircraft measurements can therefore be taken as approximating an instantaneous realization boundary layer turbulent flow for flight legs on the order of 30 to 100 times the typical horizontal scale length of boundary layer turbulence. For longer flight legs or repeated passes, e.g. at differing altitudes, stationarity cannot be assumed because the time required to fly the long flight leg can be long with respect to the rate of change of the boundary layer, either as the result of diurnal or other temporal forcing. This problem will have to be addressed in the design of TOGA COARE aircraft flight patterns.

2.2 Surface fluxes over the ocean

When the wind blows over the ocean surface it generates surface waves. These waves are the result of the coupling between the water surface and the drag of the wind. The surface roughness is apportionately proportional to the wind velocity. The radar backscatter cross-section of the roughened ocean surface is Bragg scattering from the surface capillary waves. This back-scattering is related to the wind speed, the incidence angle, the angle between the wind and the radar beam and radar parameters including polarization and wavelength (Ulaby et al., 1982; Elachi, 1988). The back-scatter cross section, σ_o, is given by

$$\sigma_o(U,\phi,\Theta) = A\ U^{\alpha}\ (1 + B \cos \phi + C \cos 2\phi)$$

where: U is the wind speed at 19.5 m msl, ϕ is the angle between the radar beam and the wind direction, Θ is the incidence angle, α is an exponent which is a function of ϕ. The constants α, A, B and C are empirically determined. Because σ is a function of U and ϕ, more than one measurement is necessary to determine the wind. Measurements from at least two orthogonal pointing angles are used to provide estimates of U with 4-fold ambiguity. This ambiguity can be resolved using synoptic meteorological analyses to select the correct quadrant. Addition of a third pointing angle at 45° to the other two can provide a measurement with a 180° ambiguity.

This technique has been used to derive surface winds over large areas of ocean. Figure 5 shows wind vector aliases for the Seasat SASS dual-beam scatterometer in the north Atlantic (Brown, 1983). Empirical evaluations of this technique (e.g. Jones, et al.,

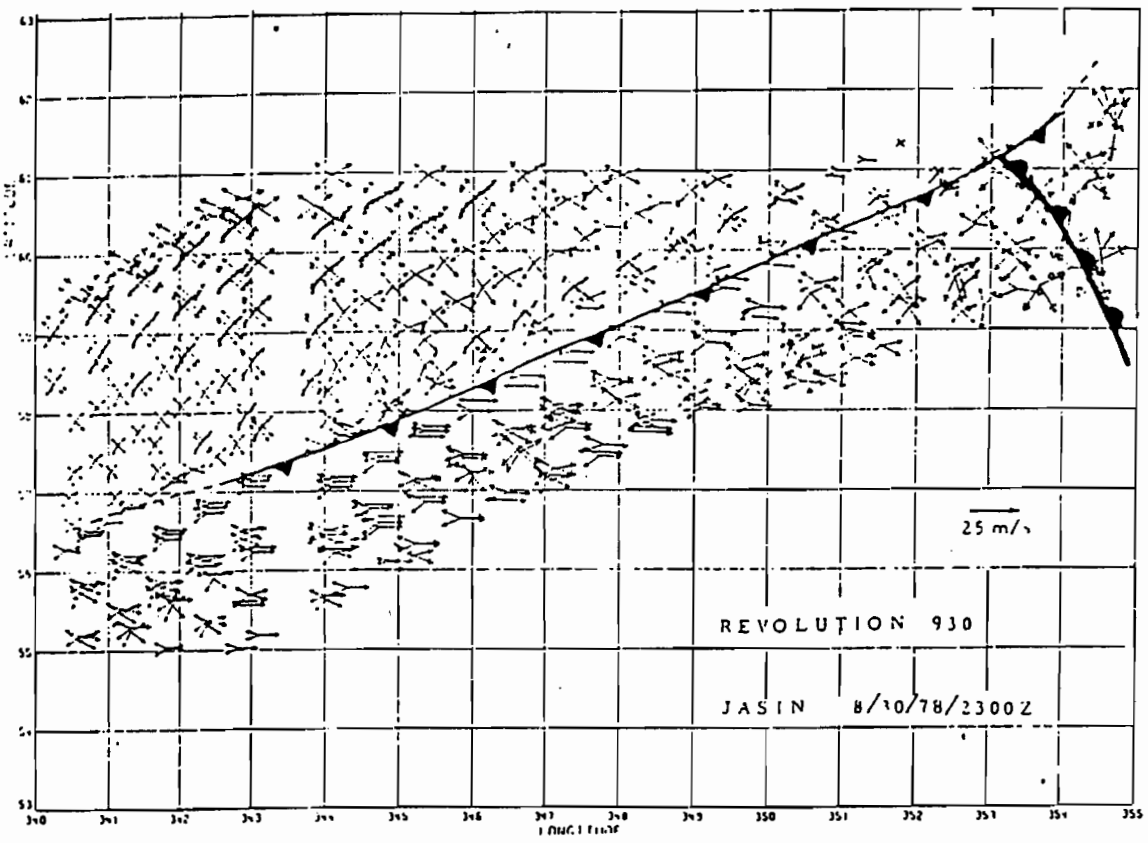

FIG.5. Wind vector alaises for the Seasat SASS dual-beam scatterometer in the north Atlantic (after Brown, 1983).

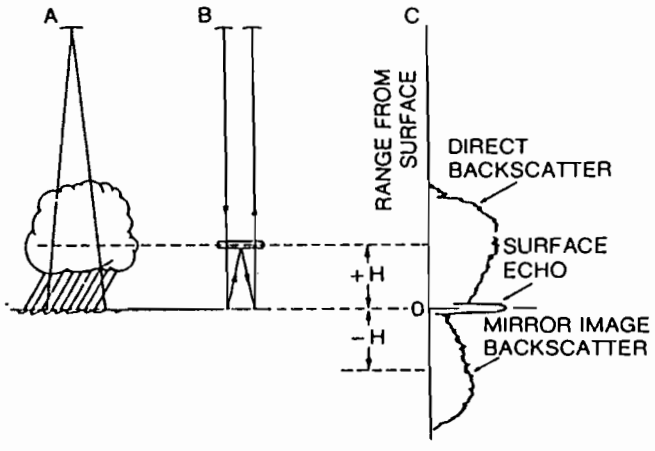

FIG.6. Use of sea surface reflection of radar measurements in rainfall to determine rainfall rate, attenuation and sea surface radar cross section. (after Meneghini and Atlas, 1984).

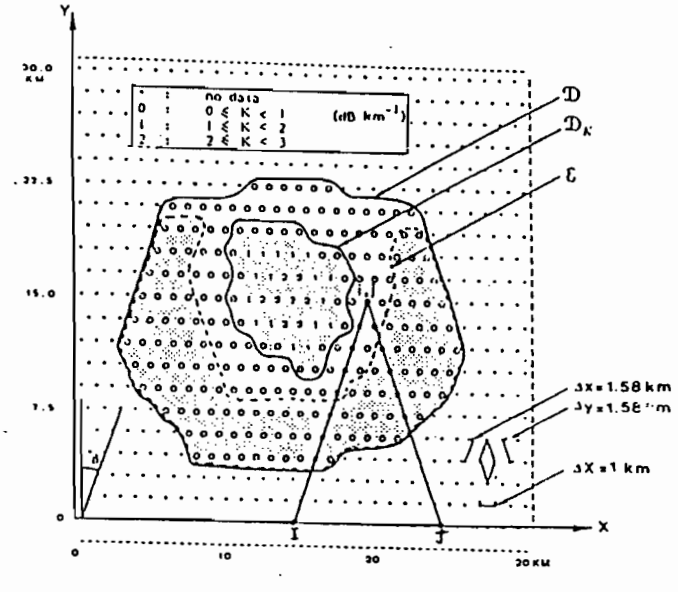

FIG.7. Stereoradar dual beam measurement of attenuation. (after Testud and Amayenc, 1988).

1978) have demonstrated that wind speeds within ±2 m/s (or about ± 10 %) and wind directions within ±20° are possible for winds of about 2 to 16 m/s. Over the ocean, the surface roughness can be related to the wind speed on the basis of simple empirical relations. The surface wind stress can therefore be derived from the 19.5m wind speed measurements. Additional research is needed, for measurement inconsistencies have been noted for high and low wind speeds and also resulting from sea surface temperature effects on viscosity (Woiceshyn, et al., 1986).

Using an airborne Doppler radar such as the ELDORA system (Hildebrand et al., 1988), surface wind and wind stress measurements can be obtained at all locations below the aircraft flight track. The data from within about ± 45° away from nadir can be used to formulate estimates of U and u* along the flight track. Such estimates can be mapped out away from the flight track to a distance approximately equal to the aircraft altitude.

Since the airborne radar also will include measurements of precipitation, it may be possible to correct the surface cross-section and wind measurements for rainfall and high wind surface spray. Additionally, the aircraft will provide radiometric surface temperature measurements, T_{SFC}. The measurements of surface temperature may enable correcting the relationship between the surface wind speed and the sea surface radar cross section for changes in T_{SFC}.

2.3 Large scale atmospheric transport through advective processes.

The advective transport of heat, moisture, and momentum can be evaluated from aircraft measurements, provided diurnal and temporal changes can be accommodated. The base measurements of atmospheric state parameters are measured accurately enough to provide quite meaningful evaluations of atmospheric gradients and advection. The temperature, humidity, and wind speed measurement accuracies (Table 2) provide advective transport measurements with accuracies of 10% to 20% for typical values of Q_s, Q_l and momentum flux. These values are comparable to the basic vertical flux measurement accuracies. However, due to the use of mean values in these calculations, the representativeness problem of the turbulent flux measurements does not affect these measurements.

The major problem in providing such measurements is related to development of a measurement technique which provides for adequate measurements and modeling of diurnal and temporal changes. For any long flight track the time required to fly the track will be long with respect to significant diurnal changes. This will require the use of fixed point measurements of diurnal or temporal changes.

2.4 Convective/MCS scale transport of heat, moisture and momentum.

Significant atmospheric heating occurs as a result of precipitation occurring in Meso-scale Convective Systems, particularly in the tropics. Measurement of precipitation production and distribution, both spatially and with altitude is therefore an important component of the TOGA COARE measurement program. The instrumented aircraft can provide accurate in-situ measurements of atmospheric dynamics and precipitation along the fight path; however, these measurements are hardly representative of the full Meso-scale Convective System transport. Therefore, use of airborne Doppler radars is essential to this measurement goal.

2.4.1 Precipitation measurement

The measurement of rainfall using radar involves use of radar reflectivity (Z) - rainfall (R) relationships in which it is assumed that $Z = aR^b$, where a and b are empirically derived constants which depend heavily on the rainfall dropsize distribution. Although these relationships are useful, they are inherently inaccurate due to the sensitivity of these relationships to the rainfall dropsize distribution. Additional radar rainfall measurement problems include incorrect radar rainfall algorithms, attenuation of the radar signal, contamination of the radar data due to partial beam filling, and the effects of ground clutter and incorrect calibration of the radar. Without additional calibration, radar rainfall measurements are subject to at least factor of two errors. Use of additional calibration (e.g. rain gages, aircraft, etc.) can provide measurements which may be as good as 10% or better for large area, long term precipitation measurement accuracies.

Improved rainfall estimation can be obtained using measurements of the attenuation (A) of the radar signal as it passes through the rainfall. This is because the A-R relations are insensitive to the rainfall particle size distribution, whereas the Z-R relations are quite sensitive to the dropsize distribution. Meneghini and Atlas (1984) have developed a technique of measuring rainfall rate and ocean surface cross section (Fig. 6). Another technique has been suggested by Testud and Amayenc (1988) in which the attenuation is determined from a dual beam airborne Doppler radar (Fig. 7). Both techniques make use of dual path precipitation observations to measure the attenuation. Either technique will enable measurement of A; hence, measurements of R of improved accuracy. A great deal of research has been devoted to development of improved remote rainfall measurement capabilities (Simpson, 1988). A major component of TOGA COARE will therefore include evaluation of these and other algorithms for improved accuracy radar rainfall measurement.

2.4.2 Storm cell/core transport processes.

Studies of cumulonimbus transport in GATE (LeMone and Zipser, 1980) and TAMEX (Jorgensen and LeMone, 1989) showed that the majority of convective drafts and cores are of scales of less than 2 km, and the primary mass transport in Meso-scale Convective Systems, also occurs at small scales (Fig. 8). In TAMEX, GATE and hurricanes only a rather small fraction of mass transport is associated with cores of >2 km or >3m/s (Jorgensen, 1984; Jorgensen and LeMone, 1989). Thus, for these cases, the narrow and weak cores are important to the vertical transport of mass.

2.4.3 Doppler radar measurement techniques

The current airborne Doppler measurements are principally suited for measurements of storm scale motions. Due to the slow scanning rate of the current airborne Doppler radar systems, the analysis of convective scale features of tropical convection has depended largely on aircraft in-situ measurements of air motions.

Measurement of the small scales of transport in tropical convection requires improvements in the resolution capabilities of airborne measurement systems. The NCAR ELDORA Airborne Doppler Radar Development Program (Hildebrand, et al., 1988) will include the improved spatial resolution as well as improved velocity and reflectivity measurement accuracy. The scanning techniques for the P-3 and ELDORA radars are illustrated in Fig. 9. The current NOAA P-3 aircraft are equipped with Doppler radars which make measurements every 1 km along the flight path (Fig. 10, bottom). A major needed improvement currently underway at NCAR will provide sampling data densities at up to 0.3 km (Fig. 10, top). The relative abilities of the P-3 and ELDORA radars to collect dual Doppler measurements of storm motions are illustrated in Fig. 11, where the areas covered in three hour flights are illustrated for the two radar systems. In large storm systems, such as the tropical storm illustrated in the lower left, some areas may be to intense to fly through. This may prohibit data collection, particularly for the P-3 radar.

3.0 Flight Patterns for Large Scale Atmospheric Flux measurements over the tropical ocean.

The seemingly diverse goals for the airborne flux measurements can very likely be accomplished with only a modest number of flight plans. The major constraints will include the flight range and duration of the aircraft, the range of operating altitudes, and the location of airports which are capable of supporting the aircraft. The flight

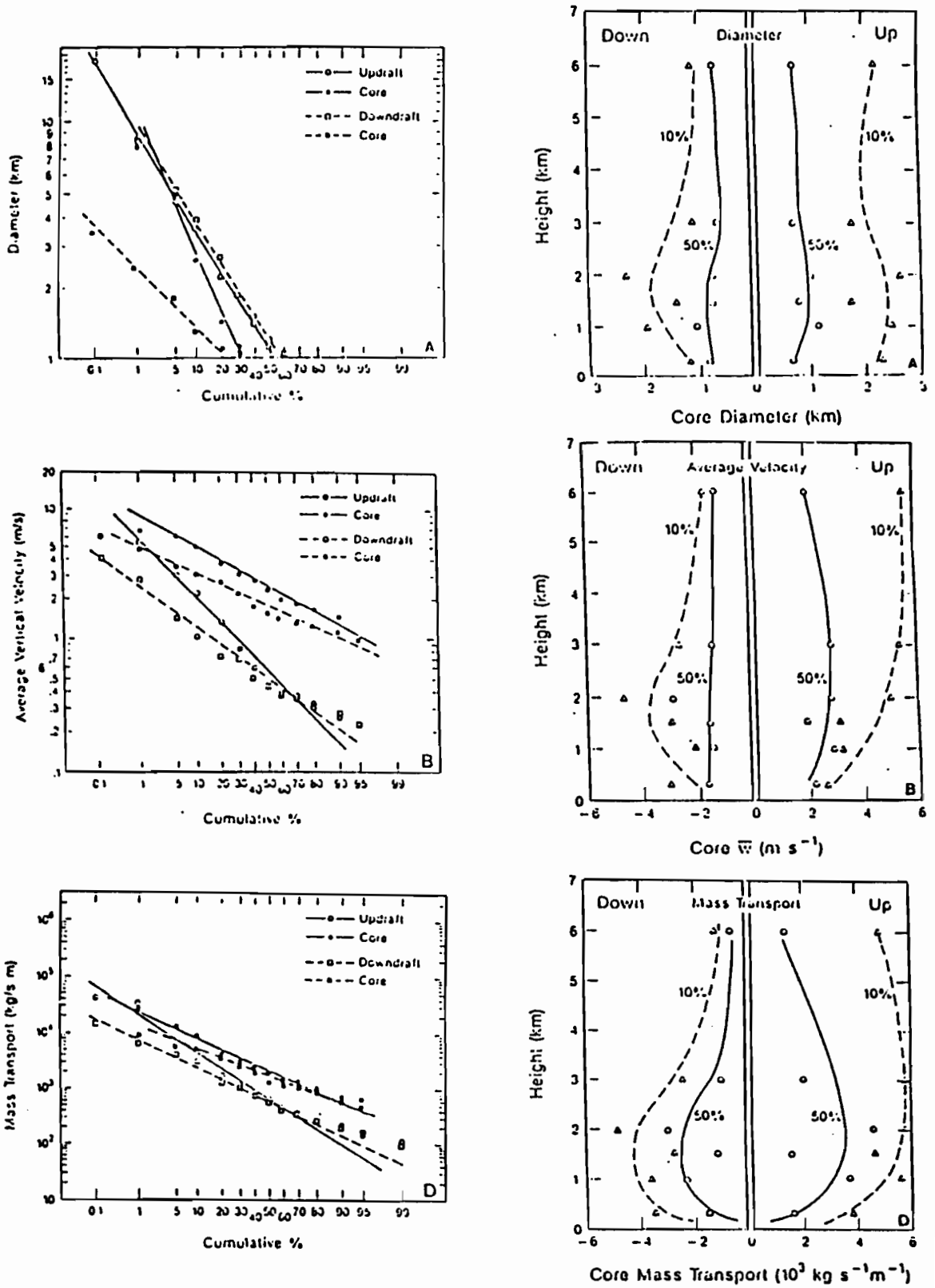

FIG.8. Left: Log-normal plots of cumulative distributions of (a) diameter, (b) average vertical velocity and (c) mass transport for MCSs. Right: Variation with altitude for the same three variables. (after Lemone and Zipser, 1980).

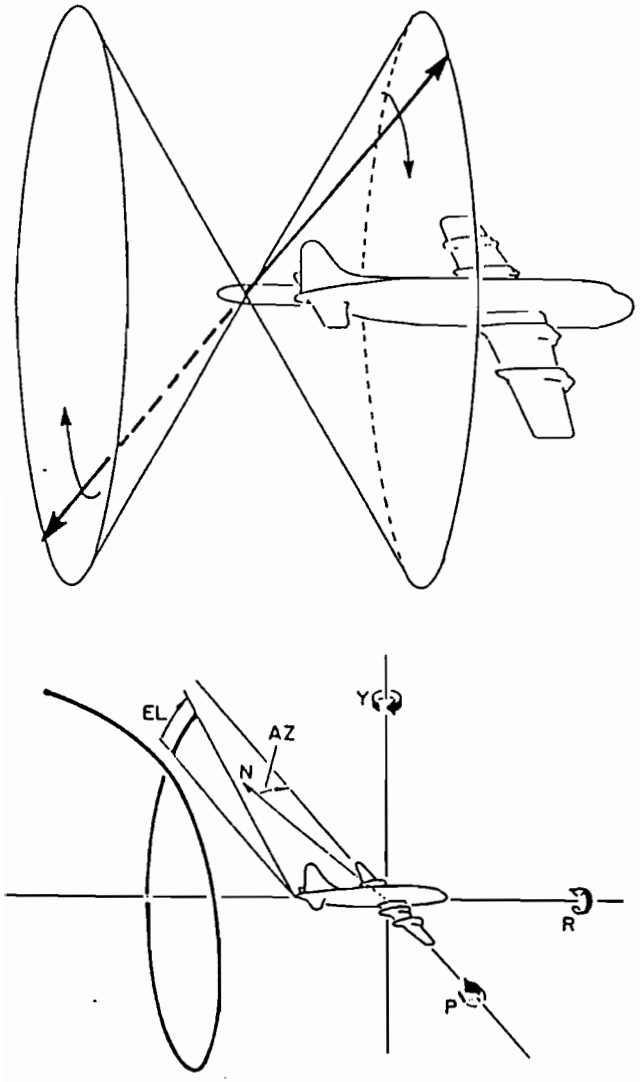

FIG.9. Scan techniques for the NCAR ELDORA (top) and NOAA P-3 airbone Doppler radars (bottom).

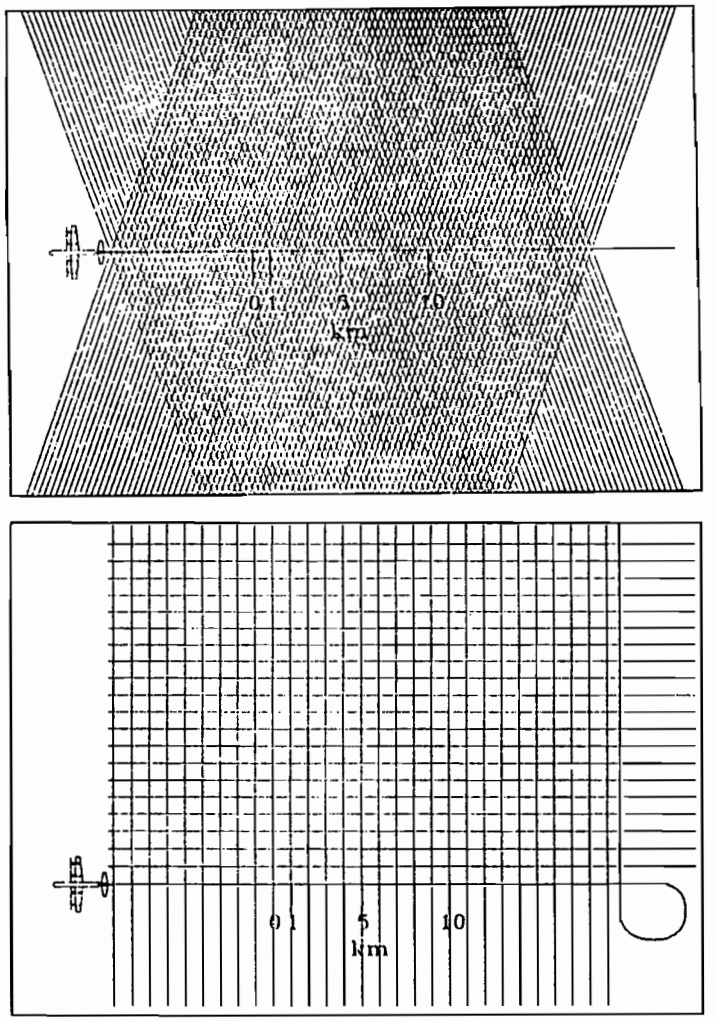

FIG.10. Horizontal measurement data density for the NCAR ELDORA (top) and NOAA P-3 airborne Doppler radars (bottom).

characteristics of the NCAR Electra and NOAA P-3 aircraft are listed in Table 3. Identification of which airfields in the TOGA COARE area have facilities which are suitable for the NCAR Electra or NOAA P-3 aircraft will be determined by NCAR and NOAA. While many of the larger islands will have airfields capable of handling the aircraft, some of these airfields may have several facilities.

Table 3. The flight characteristics of the NCAR Electra and NOAA P-3 aircraft.

Aircraft	Altitude (km)	Range (km)	Endurance (h)	Payload (kg)	Power (kw)
NCAR Electra	7.8	4,800	8	10,500	70
NOAA P-3	7.8	6,000	10	5,500	14.3

3.1 Large scale flight patterns for in-situ flux measurements

These flights will be oriented toward measurement of large scale atmospheric fluxes and gradients. Accordingly, long flight paths will be flown over large areas. These flight paths will include both Meso-scale Convective System and clear areas.

For the purpose of flux measurement, the flights will primarily be flown at altitudes in the boundary layer. Typical flights for boundary layer flux measurements (Fig. 12) will include flight leg lengths on the order of >100 km, soundings through the altitudes of interest, possible repeated flight legs at differing altitudes within the boundary layer, use of two aircraft to assess flux divergences along long flight tracks, use of multiple aircraft to assess diurnal changes over fixed flight tracks, and use of multiple aircraft to map large areas in reasonable short lengths of time. The use of cross-wind flight legs is illustrated in Fig. 12. Past studies of convective scales and sampling in the boundary layer have shown that convective large eddy scale sizes are frequently smaller in the cross-wind direction. Data collection in the cross-wind direction therefore improve sampling.

For the purpose of measuring Meso-scale Convective System structures with in-situ instrumentation or with radars, the aircraft will operate at a variety of altitudes from near sea surface to the maximum operating altitude of the aircraft. Typical flights for Meso-

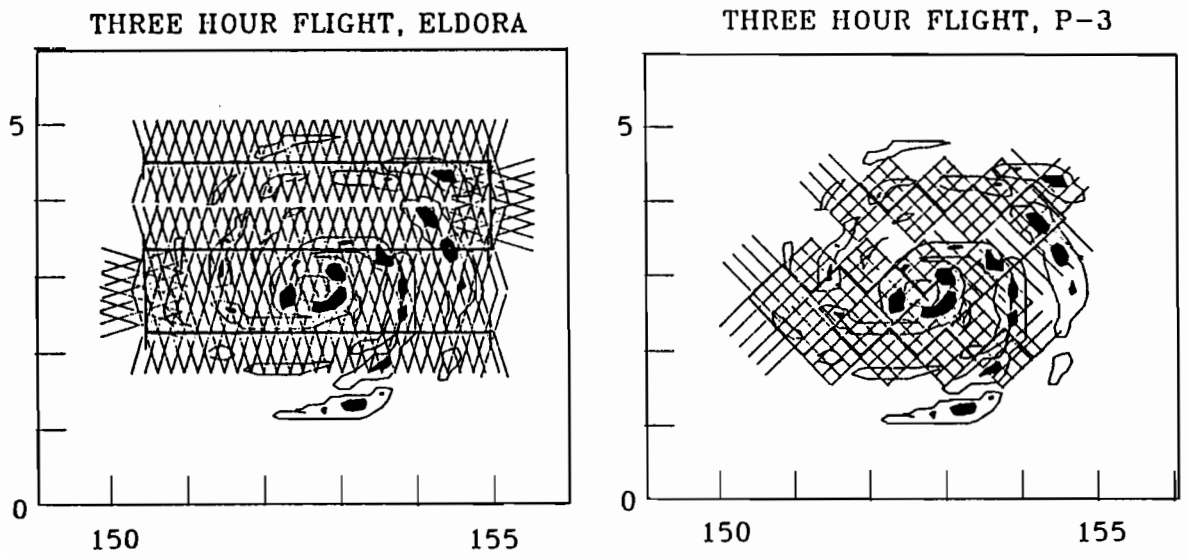

FIG.11. Three hour data collection areas for the NCAR ELDORA (right) and NOAA P-3 airborne Doppler radars (left).

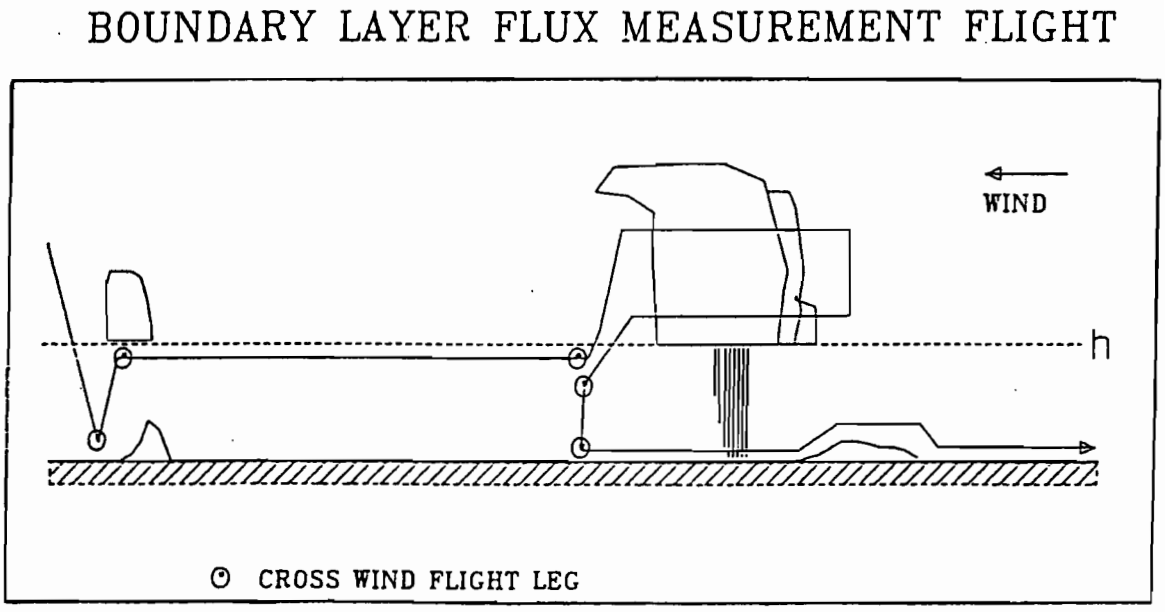

FIG.12. TOGA-COARE boundary layer flux measurement flight patterns.

scale Convective System structure measurement will include the same types of flights as for the flux measurement; however, the range of operating altitudes will be shifted to include all altitudes from the sub-cloud layer to the maximum operating altitude of the aircraft.

3.2 Airborne Doppler measurements of storm structure.

Use of the airborne Doppler radars for measurements of storm structure will vary some between the NCAR Electra and NOAA P-3 aircraft. For either type of airborne Doppler radar system, the flights can be made at a variety of altitudes according to other measurement needs (Fig. 13).

Due to the design of the NCAR ELDORA system, the Electra will be able to fly in simple straight lines through Meso-scale Convective Systems (Fig. 11). Such measurements can be made either in single paths past the storms, or in repeated flights through the storms. Since the radar only makes measurements out to about 60 km on either side of the flight track, multiple passes will be required to approach full coverage of large Meso-scale Convective Systems.

Flights using the NOAA P-3 aircraft for airborne Doppler radar measurements can be very much the same as the NCAR Electra flights, providing only single Doppler data are needed. However, the P-3 flights will be somewhat more complicated when dual Doppler data are desired. As is the case with the NCAR Electra, multiple passes will be needed to cover large Meso-scale Convective System areas.

A likely mode of operation will be to use the two aircraft in different modes. The ELDORA measurements can be directed toward dual Doppler radar and precipitation measurements of fine scales of Meso-scale Convective System motions which are related to Meso-scale Convective System transport mechanisms. The P-3 measurements can be directed toward radar measurements in which the higher resolution of ELDORA is not necessary and toward in-situ measurements. This complementary use of the aircraft will greatly enlarge the area observed in a given length of time.

3.3 Airborne radar measurement of backscatter cross-section.

The NCAR ELDORA radar, with its dual beam scanning, will provide measurements of near sea-surface (19.5m) winds and surface stress. Such measurements will be available in a swath under the aircraft extending away from the flight track

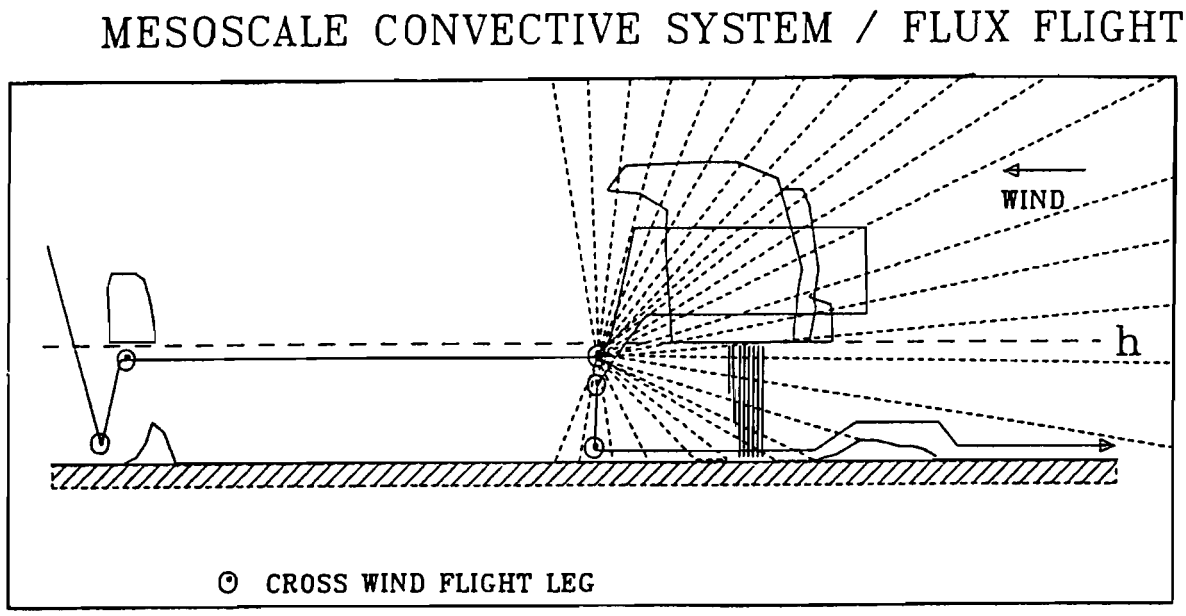

FIG.13. TOGA-COARE MCS measurement flight patterns.

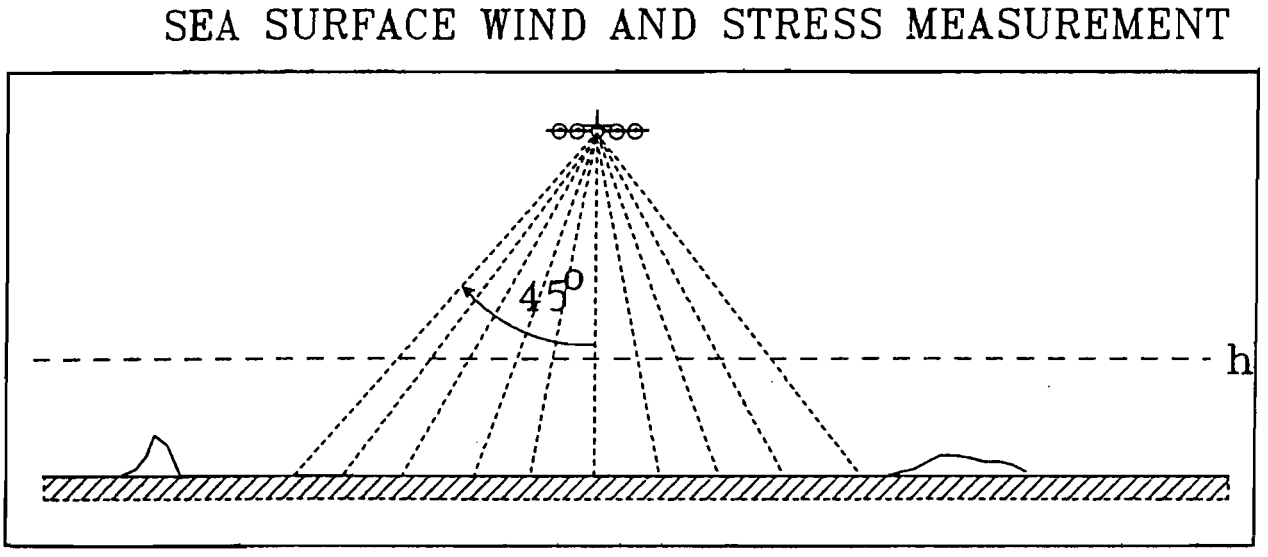

FIG.14. Airborne radar measurement of sea surface winds and stress.

approximately by the aircraft altitude (Fig. 14). The NOAA P-3 system will have some similar, but reduced accuracy abilities. There are some conflicting aspects of the use of both radar systems. Attenuation of the radar signal between the aircraft and the sea surface will deteriorate the quality of the wind and stress estimate. This error may, to some extent, be corrected by the mirror image technique of Meneghini and Atlas (1984). This possible attenuation may provide the impetus to fly fairly close to the sea surface. On the other hand, an increased altitude will widen the swath width for surface winds and stress. This goal will strongly advocate a higher altitude for radar observations.

In Meso-scale Convective System areas, the Doppler radar data are probably best collected at altitudes of 5-6 km. These altitudes will provide good swath widths. When the aircraft are being used for flux measurements, the typical 0.1-1.5 km flight altitudes will only provide surface wind and stress measurements along and very near to the flight track.

3.4 Measurements of atmospheric chemical constituents and transport.

Both the NCAR Electra and the NOAA P-3 aircraft routinely fly a wide variety of user-supplied instrumentation, much of it related to measurement of atmospheric chemistry. It is anticipated that the background state and transport of atmospheric chemical constituents may be an important ancillary role for these aircraft.

REFERENCES

Andre, J.C., J.P. Goutorbe and A. Perrier, 1986: HAPEX-MOBILHY: A Hydrologic Atmospheric Experiment for the Study of Water Budget and Evaporation Flux at the Climatic Scale, Bull. Amer. Meteor. Soc., 67, 138-144.

Brown, R.A., 1983: Surface wind analysis for SEASAT. J. Geophys. Res., 88, 1663-1673.

Elachi, C., 1988: Spaceborne Radar Remote Sensing: Applications and Techniques, IEEE Press, New York, N.Y. 254pp.

Hildebrand, P.H., C.L. Frush and C. Walther, 1988: Design of the ELDORA airborne Doppler radar. NCAR Technical Note NCAT/TN-325+EDD, 137 pp. (Category #5).

_____, 1988: Eddy correlation turbulence measurements from aircraft. Preprints, Workshop on Measurement and Parameterization of Land-Surface Evaporation Fluxes Workshop, Banyuls, France, 10-21 October 1988.

_____ and R. Moore, 1989: Meteorological radar observations from mobile platforms. Proceedings, Battan Memorial Radar Meteorology Conference. Amer. Meteor. Soc., Boston, MA, USA. (in press)

Jones, W., F. Wentz, and L. Schroeder, 1978: Algorithm for inferring wind stress form SEASAT-A. AIAA J. Spacecraft Rockets, 15, 368-374.

Jorgensen, D.P., 1984; Mesoscale and convective scale characteristics of mature hurricanes. Part I: General observations by research aircraft. J. Atmos. Sci., 42, 839-856.

Jorgensen, D.P. and M.A. LeMone, 1989: Characteristics of convective vertical velocity events observed by P-3 aircraft during TAMEX. Preprints, 18 Conf. on Hurricane Forecasting and Tropical Meteorology, San Diego., Amer. Meteor. Soc., Boston.

LeMone, M.A. and E. J. Zipser, 1980: Cumulonimbus vertical velocity events in GATE. Part I: diameter, intensity and mass flux. J. Atmos. Sci., 37, 2444-2457.

Lenschow, D.R. Pearson and B. Stankov, 1982: Measurement of Ozone vertical flux to ocean and forest. J. Geophys. Res., 87, 8833-8837.

_____ and B. Stankov, 1986: Length scales in the convective boundary layer, J. Atmos. Sci., 43, 1198-1209.

REFERENCES CONT'D

Meneghini, R. and D. Atlas, 1984: Simultaneous ocean cross-section and rainfall measurements from space with a radar pointed radar. NASA Tech. Memo. 86167, 42pp.

Research Aviation Facility, 1987a: Airborne Humidity Measurements, Research Aviation Facility, Bulletin 22, NCAR, Boulder, Co., 7pp.

Research Aviation Facility, 1987b: Measurements Techniques: Air Motion Sensing, Research Aviation Facility, Bulletin 23, NCAR, Boulder, Co., 49pp.

Research Aviation Facility, 1988a: The King Air: Overview and Summary of Capabilities, Research Aviation Facility, Bulletin 2, NCAR, Boulder, Co., 13pp.

Research Aviation Facility, 1988b: Flight Planning : King Air, Research Aviation Facility, Bulletin 5, NCAR, Boulder, Co., 7pp.

Research Aviation Facility, 1988c: Standard Output Data Products from the NCAR Research Aviation Facility, Research Aviation Facility, Bulletin 9, NCAR, Boulder, Co., 70pp.

Simpson, J., Ed., 1988: Report of the science steering group for a tropical rainfall measurement mission (TRMM), NASA Goddard Space Flight Center, Greenbelt, MD., 94pp.

Testud, J. and P. Amayenc, 1988: Stereoradar meteorology: A promising technique to observe precipitation from a mobile platform. J. Atmos. and Ocean. Technol., 6, 89-108.

Ulaby, F., R. Moore and A. Fung, 1982: Microwave Remote Sensing Vol II: Radar Remote Sensing and Surface Scattering and Emission Theory. Addisen-Wesley, Reading MA, 1064pp.

Wyngaard, J., 1986: Measurement Physics. Probing the Atmospheric Boundary Layer, ed. D. Lenschow, Amer. Meteor, Soc., Boston, 5-18.

_____, W. Pennell, D. Lenschow and M. LeMone, 1978: The temperature-humidity covariance budget in the convective boundary layer. J. Atmos. Sci., 35, 47-58.

REFERENCES CONT'D

Woiceshyn, P.M., M.G. Wurtele, D.H. Boggs, L.F. McGoldrick, and S. Peteherych, 1986: The necessity for a new parameterization of an empirical model for wind/ocean scatterometry. J. Geophys. Res., 91.

Determination of Boundary-Layer Fluxes With an Integrated Sounding System

W.F. DABBERDT[1], H. COLE[1], K. GAGE[2], W. ECKLUND[2] and W.L. SMITH[3]

(1) *National Center for Atmospheric Research*
Boulder, CO 80307 - U.S.A.

(2) *National Oceanic and Atmospheric Administration*
Earth Science Laboratories / Aeronomy Laboratory
Boulder, CO 80303 - U.S.A.

(3) *University of Wisconsin*
Madison, WI 5370 - U.S.A.

Abstract

An important atmospheric goal of TOGA COARE is to determine the exchange of momentum, and sensible and latent heat in the western Pacific over the time scales of convective storms, westerly bursts and lower frequency events. TOGA COARE will also require detailed moisture budget studies in support of improved understanding of sub-gridscale processes and the evaluation of model parameterization schemes. Present field-deployable measurement systems do not provide observations on the temporal and spatial scales necessary to properly address these and other issues. We present the concept of the so-called Boundary-Layer Integrated Sounding System (BLISS) as a means to provide these measurements. The BLISS consists of a suite of demonstrated in situ and remote sensing subsystems which together provide the measurements to sense directly or retrieve high-resolution profiles of winds, temperature and moisture and associated fluxes. Individual subsystems under consideration include: surface meteorological station; UHF Doppler wind profiling radar; radio acoustic sounder; infrared interferometer-spectrometer; microwave radiometer; and an Omega-VLF radiosonde system for in situ but low frequency profiles to ~20mb. Other features of the integral system include a central data acquisition and processing counter, real-time satellite telemetry link, and rugged, easily transported base station. We estimate the cost of to be sufficiently modest to enable deployment of a network of order 10-15 systems in support of TOGA COARE.

1. Background

The scientific requirements that have motivated the concept of a Boundary-Layer Integrated Sounding System (BLISS) are summarized in the early planning for the TOGA Coupled Ocean Atmosphere Response Experiment (e.g., see Lukas and Webster, 1988) as well as other major mesoscale and stormscale experiments such as the U.S. national Stormscale Operational and Research Meteorology program, STORM (NCAR, 1989). We summarize below some of the major objectives and scientific issues of TOGA COARE and the observational requirements provided by a network of integrated sounding systems.

ORSTOM
CENTRE DOCUMENTATION
Montpellier

*The National Center for Atmospheric Research is sponsored by the National Science Foundation.

F 30198

The warm waters of the Western Pacific play a major role in the dynamics of the coupled ocean-atmosphere El Niño/Southern Oscillation (ENSO) phenomena. ENSO forcing and response events are a major cause of low frequency atmospheric variability, especially in the tropics. A major objective of TOGA is to develop sufficient scientific understanding of ENSO phenomena to permit the eventual prediction of these events through the application of coupled ocean-atmosphere models. As recognized by TOGA scientists, the key to understanding the Southern Oscillation appears to lie in detailed knowledge of the physical processes that couple the tropical ocean and atmosphere.

It is widely recognized that the current observational effort of TOGA is insufficient to resolve certain key scientific issues that must be understood to make further progress. As identified by the 1987 Western Pacific Air-Sea Interaction Workshop (Lukas and Webster, 1988), and recently refined, these issues include the need to understand:

- Principal processes responsible for coupling of ocean and atmosphere in the Western Pacific warm pool system.
- Principal atmospheric processes that organize convection in the warm pool region.
- Tropical oceanic response to combined buoyancy and wind stress forcing in the Western Pacific.
- Multiple scale interactions that extend the oceanic and atmospheric influence of the Western Pacific warm pool region to other regions, including the role and significance of the westerly burst phenomenon.

One important and illustrative research goal of TOGA COARE will be to examine the dynamical interaction of the ocean and the atmosphere during westerly wind bursts. The occurrence of episodic westerly wind bursts over the Western Equatorial Pacific is thought to play an important role in the genesis of the El Niño. As discussed in Lukas (1988), the westerly wind bursts can provide the needed trigger to generate Kelvin waves in the Western Pacific Ocean. Furthermore, a series of westerly wind bursts could also provide the mechanism for moving the warm pool of water that normally resides in the Western Pacific eastward toward the dateline.

A complete understanding of the evolution of these bursts requires a better understanding of the dynamics of atmospheric circulation systems over the Western Pacific Ocean. The westerly wind bursts may be associated with surges of cold air originating from higher latitudes. Unfortunately, the Western Pacific Region is largely void of upper-air observations that are needed to answer some of the questions now being raised. For example, the vertical structure of the westerly wind bursts is largely unknown. Also, their relationship to convection and the recurring 30-60 day oscillation need to be explored.

Another important part of the TOGA COARE will be detailed moisture budget studies. Historically, budget studies have been done for the Atlantic as part of the GATE Experiment. The few budget studies that have been done for the tropical Pacific have shown a different heating profile. The heating profile is largely determined by latent heat release in convective storms. Climate models have been shown to be very sensitive to the detailed heating profile.

Rasmusson (1988) has recently pointed out that TOGA process studies aimed at addressing deficiencies in modelling the coupled ocean-atmosphere system must address both a proper

physical understanding of sub-gridscale processes and the "calibration" of simplified parameterization schemes. The latter goal can be achieved through careful budget studies.

Moisture budget studies require accurate high vertical resolution soundings of humidity and wind. The BLISS is designed to provide this information. The continuous lower troposphere wind profiling capability of the 915 MHz Doppler radar will be ideally suited for determining the perimeter vapor flux. Moisture profiling is also very important. The IR interferometer and microwave radiometer will provide this information together with periodic balloon soundings.

2. Boundary Layer Integrated Sounding System (BLISS)

2.1 Overview

The objective of the BLISS is to develop a sounding system that will provide the research community with a transportable facility which can satisfy the observational/scientific requirements of TOGA COARE and other programs by routinely measuring all important thermodynamic variables (and some radiative variables) through the lower troposphere. It is important that the BLISS function as an integrated system rather than as independent measurement systems. In this regard, an important aspect of the development is to mechanically engineer the facility within a common transportable housing, and to provide a central data acquisition, processing, display and communications capability.

The profiling requirements of the boundary-layer segment of the atmospheric science community were surveyed by Dabberdt *et al.* (1986). About 25 scientists participated in a survey and subsequent workshop to establish consensus priorities for the most important atmospheric variables and the performance specifications of the requisite profiling system(s). First-priority variables were identified to be: horizontal winds, temperature, and humidity; other variables and their relative priority (in parentheses) included: boundary-layer height (2), turbulence (3), cloud base height (3), aerosols (3), and trace gases (3) such as ozone, sulfur dioxide and nitrogen dioxide. Table 1 summarizes what the authors refer to as consensus requirements for profiling systems that will meet the needs of atmospheric scientists concerned with boundary-layer processes.

The performance of the UHF boundary-layer wind profiler reported by May *et al.* (1989) is virtually consistent with the needs summarized in Table 1. Significant progress has been made over the last few years in the measurement of temperature, another first-priority variable. The technology used to achieve this progress is the so-called radio acoustic sounding system, or RASS. The RASS approach measures the vertical profile of the speed of sound using a Doppler wind profiler to track the propagation of the refractive index gradient established by an acoustic wave. After corrections for humidity and atmospheric motion, the speed of sound is uniquely related to the square root of temperature. Whereas RASS is a straightforward extension of wind profiler technology, there presently is no comparable demonstrated application for humidity profiling. And even with RASS, there is a height limitation of a few kilometers. Although these heights meet the needs of the boundary-layer community, they do not satisfy the upper-level requirements of the mesoscale, synoptic and climate communities. As an attempt to achieve these requirements, we have proposed a suite of complementary active and passive remote and in situ sensors. Figure 1 is a conceptual illustration of the integrated sounding system. Candidate component sensors include: UHF wind profiler, RASS, navaid rawinsonde system, high resolution infrared interferometer-spectrometer (HIS), microwave radiometer, and surface meteorological system. The objective of

Table 1

Consensus Requirements for Boundary-Layer Profilers

Requirement	Variable														
	Horizontal Wind ($m\ s^{-1}$)					Temperature (K)					Specific Humidity ($g\ kg^{-1}$)				
	mean	s.d.	min	max	mode	mean	s.d.	min	max	mode	mean	s.d.	min	max	mode
Height coverage, km	3.4	1.1	1.5	5.0	3.0	3.7	1.4	1.0	6.0	5.0	3.6	1.4	1.0	6.0	3.0* 5.0*
Height resolution, km	82	53	10	200	100	58	39	10	100	100	72	34	10	100	100
Time resolution, min	15	14	1	60	15	15	15	1	60	1* 30*	16	16	1	60	30
Threshold	0.7	0.4	0.1	1.0	1.0	-	-	-	-	-	1.2	1.6	0.01	5.0	1.0
Accuracy	0.8	0.5	2.0	0.1	0.5	0.7	0.3	0.05	1.0	1.0* 0.5*	0.7	0.3	0.1	1.0	1.0
Precision	0.5	0.3	1.0	0.1	0.5	0.3	0.3	0.02	1.0	0.1* 0.2*	0.4	0.4	0.01	1.0	1.0

Source: Dabberdt *et al.* (1986)

* bi-modal response

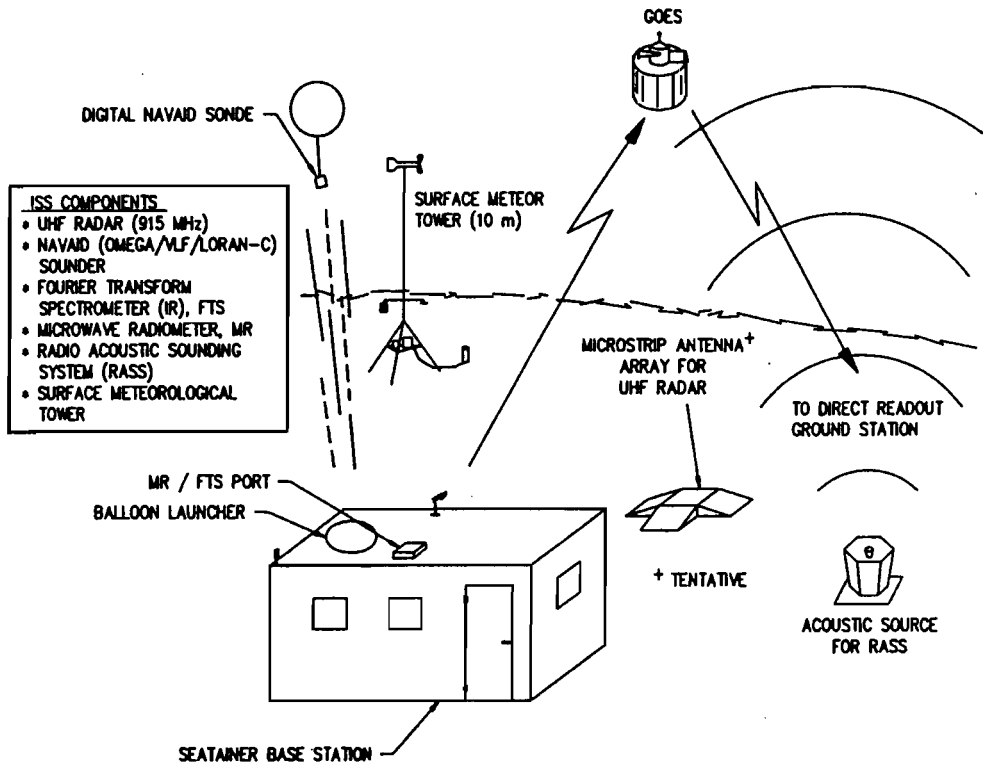

FIG.1. Conceptual design of the Boundary-Layer Integrated Sounding System.

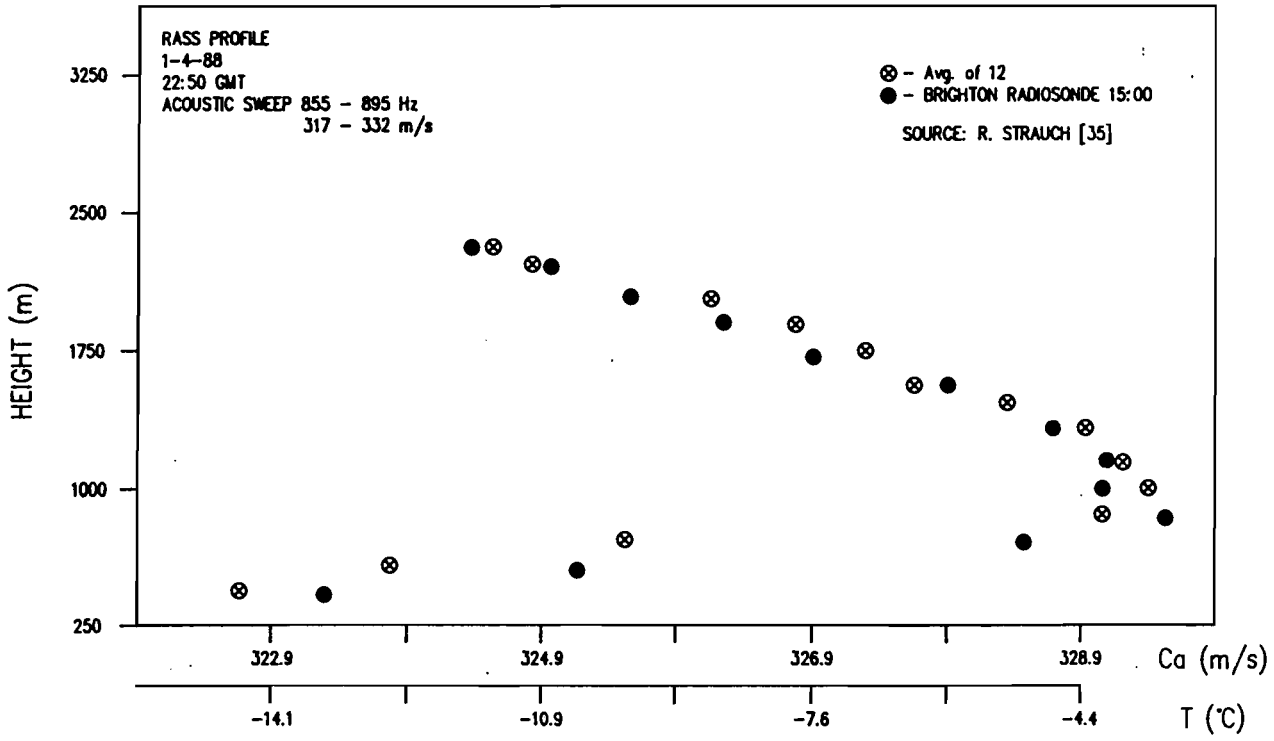

FIG.2. Comparison of near-coincident temperature profiles by RASS and radiosonde near Brighton, Colorado (USA).

the system is to provide comprehensive, continuous high-resolution thermodynamic profiling of the lower troposphere and lower resolution profiling of the upper troposphere and stratosphere. The integrated sounding system would be easily transported and deployed in coordinated networks for application in a wide range of research studies.

2.2 *Clear-Air UHF Radar*

Ecklund et al. (1988a) have developed a clear-air boundary layer radar using a microstrip antenna and a UHF frequency of 915 MHz to obtain three-component wind profiles with 150-m height resolution from a minimum height of 100m to a maximum height of several kilometers. In a recent test at Christmas Island with a 0.9 x 0.9m antenna area and an average transmitted power of only 1W, they were able to consistently obtain one-minute averaged profiles to a height of 1.8km. Using a larger antenna and a higher power output, we plan to incorporate a similar radar design into the BLISS that will yield maximum ranges (i.e. heights) of 3-4km; this should be possible with a tenfold increase in the radar sensitivity. The height resolution will be enhanced to 100m and possibly to 30m. Estimates of the measurement uncertainty of the current radar is estimated at about 1 m/s. Table 2 provides system specifications for the present NOAA prototype system as given by Ecklund et al. (1988b), as well as proposed specifications for the BLISS.

Table 2

BOUNDARY LAYER RADAR SPECIFICATIONS

	Present System	Proposed System
FREQUENCY (MHz)	915	915
WAVELENGTH (m)	0.33	0.33
ANTENNA AREA (m^2)	1 - 2	2 - 9
BEAMWIDTH (1 way, deg)	18 - 9	9 - 6
AVERAGE POWER (W)	1	10 - 30
RANGE RESOLUTION (m)	150	100
LOWEST HEIGHT (m)	150	100
AVERAGING TIME (s)	30 - 120	30 - 120
TYPICAL COVERAGE (km)	1 - 2 (clear air)	3+

2.3 *Radio Acoustic Sounding System*

Temperature profiles have been obtained by augmenting the clear-air wind profiling radar with an acoustic source that is swept across an acoustic band at approximately 1/2 the radar wavelength. The Bragg scattering condition is satisfied at the acoustic frequency where the maximum UHF backscattered return is obtained. By using the radar to measure the propagation of the acoustic wavefront, the profile of the speed of sound is obtained from which the temperature profile is derived by applying corrections for atmospheric humidity (obtained in the BLISS from the navaid sounding system or the passive sensors) and the wind speed (measured by the clear-air

radar). The RASS technique has successfully been tested by Currier et al. (1988) and Strauch (1988).

Strauch *et al.* (1989) evaluated three RASS systems using 50, 404 and 915 MHz wind profilers and 5, 5 and 50 W acoustic transmitters, respectively. The maximum altitudes achieved by the three systems were 5-9, 1.5-2.5, and 0.6-1.5 km, respectively. The lower maximum altitude at the higher frequencies is partially the result of the increased rate of acoustic absorption: 45 dB km^{-1} for a 2 kHz acoustic source and 915 MHz radar vs. 10 dB km^{-1} for a 900 Hz source and 404 MHz radar. Horizontal wind apparently has little effect on temperature retrieval for winds up to 10 ms^{-1}. The RMS difference between RASS temperatures (both 50 and 404 MHz systems) and co-located radiosonde measurements averaged 0.5K over a variety of weather conditions; Figure 2 is a comparison of RASS and radiosonde temperature profiles from some earlier work by Strauch (1988).

2.4 NAVAID Radiosonde System

The sounding component of the BLISS will follow the design of the TOGA sounding system now deployed on Kanton Island to support TOGA/ENSO studies. Many features of the system follow from earlier NCAR developments, such as the Automated Shipboard Aerological Program and the Cross-chain Loran Atmospheric Sounding System (CLASS). Figure 3 illustrates the Kanton Island System which consists of six components:

- A 3.7 x 3.7 m insulated plastic modular environmental shelter,
- A primary 1200-Watt solar panel/battery system and a secondary 1,000-Watt wind turbine/battery system,
- An Omega/VLF navaid upper-air sounding system,
- A nylon bag balloon launcher,
- A surface meteorological system, and
- A satellite communications system (GOES).

The upper-air sounding system in the Kanton Island station uses world-wide Omega navigation signals and the U.S. Navy VLF communications signals to compute upper-level winds. A commercial lightweight (200 gm) radiosonde contains an Omega/VLF receiver for receiving the navaid signals and a telemetry transmitter for retransmitting these signals to a ground receiving station (base station). The radiosonde also makes measurements of pressure, temperature and humidity (P,T,H) and telemeters this data to the base station. The radiosonde is transported vertically by a 200 gm balloon at an ascent rate of about 300 m/min; the state measurements (P,T,H) are obtained at a 1.2-s rate and smoothed over 20-s intervals (i.e. least squares fit), the Loran Time-Of-Arrival (TOA) measurements are made every 4-s and smoothed over a 30-s interval; the Omega/VLF Phase measurements are made every 10-s and smoothed over a 2-min interval. All data (P,T,H and winds) are output every 10-s. BLISS will have the capability to compute winds by using either the Omega/VLF navaid signals or by using multi-chain Loran-C signals. This added capability will provide improved wind accuracy and height resolution of the computed winds in areas where Loran-C coverage exists. We also will explore using the Global Positioning System for increased accuracy and better height resolution.

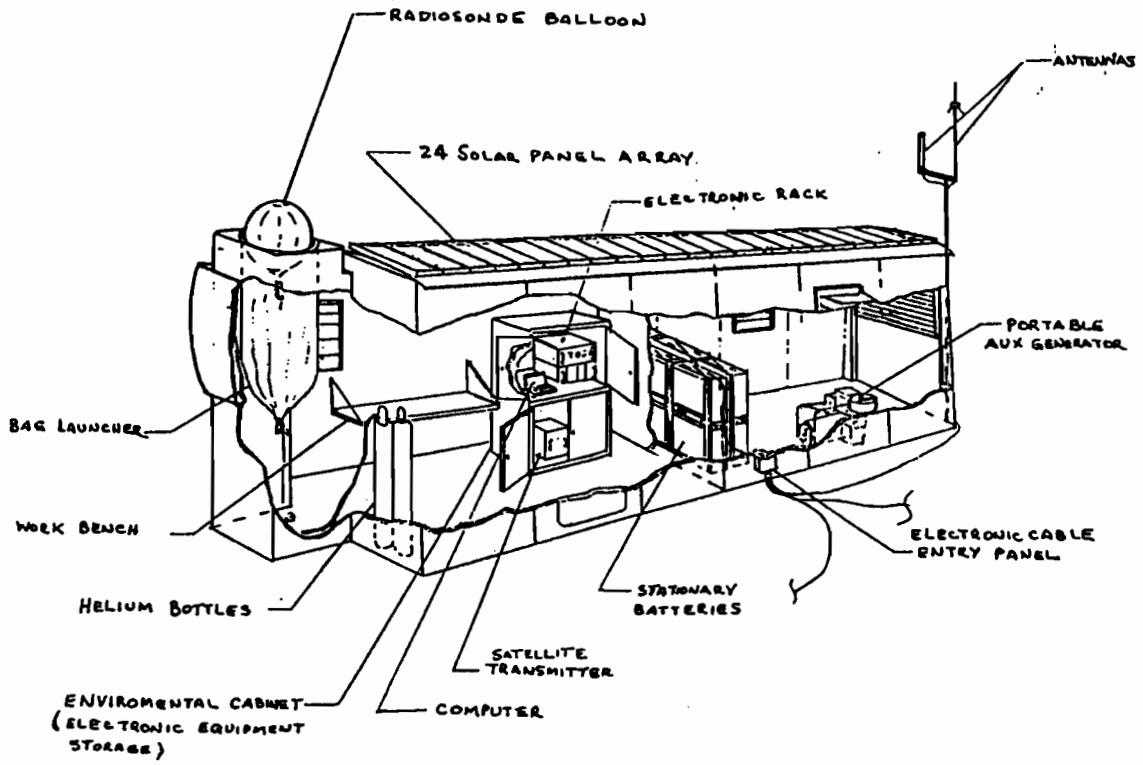

FIG.3. Layout of Kanton Island System.

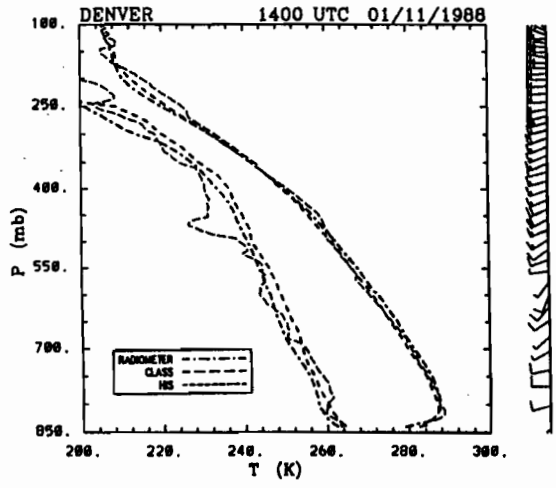

FIG.4. Coincident temperature and dewpoint profiles by radiosonde (CLASS), interferometer spectrometer, and microwave radiometer at Denver, Colorado - U.S.A. (source: Smith et al., 1989).

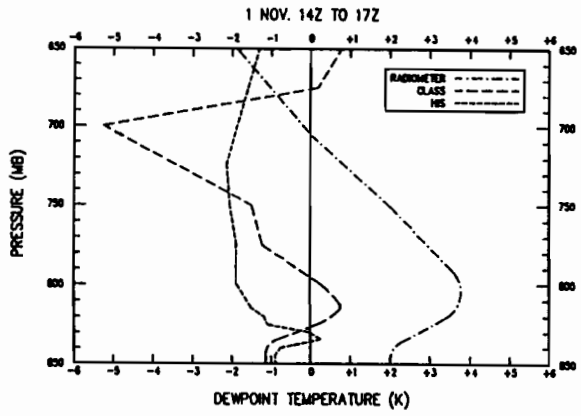

FIG.5. Three-hourly changes of dewpoint profiles obtained by radiosonde (CLASS), interferometer spectrometer, and microwave radiometer at Denver, Colorado - U.S.A. (source: Smith et al., 1989).

2.5 High Resolution Interferometer Spectrometer (HIS)

Fourier transform spectrometry (FTS) provides observations of high resolution continuous spectra of atmospheric emissions with relatively simple and inexpensive instrumentation. In the short and intermediate infrared region (3-20um), the $0.5cm^{-1}$ spectral resolution enables isolation of emission due to atmospheric H_2O, CO_2, N_2O, O_3, CH_4, and CO. A ground-based system looking upwards and observing downwelling radiation can be used to profile temperature and water vapor with high vertical resolution (≈200m near the surface, but diminishing with height); the other trace gases might also be profiled in a similar manner. The present high-resolution FTS system has successfully been used on high-altitude aircraft. Several lower spectral resolution FTS sounding systems have flown on earth-orbiting and planetary-mission satellites. A simplified ground-based system recently has been tested through comparisons with in situ tower-mounted sensors and radiosondes, and remote profiles obtained by radio acoustic sounding and microwave radiometers; these comparisons were made late in 1988 at Denver Stapleton Airport in conjunction with the NOAA/ERL/Wave Propagation Laboratory and NCAR.

Examples of temperature and dew-point profiles are given in Figure 4 from the recent Denver intercomparison experiment (Smith el al., 1989). The experiment compared coincident profile measurements obtained by HIS, microwave radiometer and the CLASS cross-chain LORAN radiosonde system, respectively. Data retrieval with the two passive sensors utilized seasonal climatology. Temperature profiles compare well up to 300 mb (surface pressure is about 840 mb) except for a smoothing of the inversion top around 815 mb and a failure to detect fine-scale structure in the upper levels (e.g. 575 and 450 mb). The remote moisture profiles are only representative in the broad sense, failing to sense significant features throughout most of the profile; e.g. note the dry layer between 450 and 500 mb. Another application is the detection of temporal changes in moisture. Figure 5 illustrates 3-h changes in the vertical profiles of dew point temperature corresponding to the period of the profiles of Figure 4. There is generally good agreement in the actual profiles of dew-point change resulting from CLASS and HIS, and very good agreement in a relative sense between CLASS and radiometer profiles. These early results suggest applications for hybrid systems that use periodic radiosonde profiles to obtain absolute measurements and continuous remotely sensed profiles to obtain temporal changes.

2.6 Microwave Radiometer

The microwave radiometer is a passive sensor that measures incident energy at various frequency bands; the candidate sensor for the BLISS operates at 21, 31, and 60 GHz to provide estimates of the vertical profiles of temperature and humidity, as well as the integrated precipitable water vapor and cloud liquid water content. The 21 GHz and 31 GHz channels are fixed frequency channels, whereas the 60 GHz channel is tunable over a 6 GHz bandwidth with measurements available at 11 frequencies. The humidity is determined by simultaneous measurements at two frequencies: the integrated precipitable water vapor is measured by the absorption at 22.2 GHz, and the cloud liquid water content is determined from absorption at 35 GHz. Temperature profiles are determined by measurements on oxygen absorption lines at 60 GHz, with corrections for cloud liquid water. Thermodynamic profile data from the navaid sounding system are used to initialize the profile inversion of the radiometric data, although climatological profiles can also be used (with lesser accuracy). Figures 4 and 5 illustrate the temperature and humidity profiles and temporal profile changes obtained with a similar radiometer in Denver, Colorado.

2.7. Meteorological Surface Station

The surface meteorological station will be patterned after the remote stations presently in use with the NCAR portable automated mesonet (PAM); see Brock et al. (1985). PAM remote stations measure pressure, temperature, humidity, winds, and liquid precipitation. So-called integrated sensors provide calibrated measurements in engineering units for pressure, temperature and humidity; an integrated wind sensor is nearing completion at present. Recent enhancements to the PAM remote station include a capability to measure the surface radiation budget through use of a radiation stand and a general purpose interface; this capability will be included in the BLISS.

3. Boundary-Layer Flux Estimates

3.1 Momentum Flux

The vertical flux of horizontal momentum is an important dynamical quantity that can be determined from measurements of the covariance of horizontal and vertical velocities. The technique of determining momentum flux from velocity measurements by a single Doppler radar using VAD analysis dates from early work by Lhermitte (1968) and Wilson (1970). The technique has been used by Kropfli (1986) to obtain measurements of turbulent fluxes in the planetary boundary layer. His measurements were confirmed using independent measurements of momentum flux obtained from the tower at the Boulder Atmospheric Observatory.

Momentum flux measurements have recently been made in the free atmosphere at several locations using wind profiling Doppler radar. The technique utilized is similar to the VAD analysis but typically involves velocity measurements in only a few (usually four) azimuthal directions. This adaptation was developed by Vincent and Reid (1983) for middle atmosphere research. In the middle atmosphere, momentum flux is primarily due to internal gravity waves but the principle of measurement remains the same.

According to the method (Vincent and Reid, 1986) momentum flux is measured by two radar beams symmetric with respect to the vertical direction. If beam 1 measures the radial component v_1

$$v_{R1} = -u_1 \sin\theta - w_1 \cos\theta \tag{1}$$

and beam 2 measures the radial component v_2

$$v_{R2} = +u_2 \sin\theta - w_2 \cos\theta \tag{2}$$

then with a few assumptions concerning horizontal homogeneity of the velocity field

$$\overline{u'w'} = (\overline{v_{R2}^2} - \overline{v_{R1}^2})/2 \sin 2\theta \tag{3}$$

where θ is the off-vertical beam angle.

Recent determinations of momentum flux utilizing wind-profiling Doppler radar and the technique of Vincent and Reid (1983) have been reported by Fukao *et al.* (1988), Fritts and Vincent (1987), Reid and Vincent (1987), and McAffee *et al.* (1989).

3.2 Scalar Fluxes

There are at least four methods of estimating vertical profiles of fluxes of scalar variables such as sensible and latent heat; these methods include eddy correlation; similarity theory; budget analyses; and conditional sampling. The authors are unaware at this time of any definitive tests and evaluations of any of the methods; with the very recent demonstration of the viability of RASS temperature profiling, we expect there will be significant research efforts in this area.

Eddy correlation is perhaps the candidate methodology that comes first into consideration, primarily because it is the only first-principle method of the group. The vertical flux of any scalar **c** is determined simply by the time average of the product of its fluctuation ($\mathbf{c}'$) with that of the vertical wind component ($\mathbf{w}'$), where flux = $\overline{c'w'}$. There are however several limitations in the sampling that may preclude rigorous application of eddy correlation. At lower levels the sampling rate is too slow (seconds) and the height resolution (30-50m, min.) too coarse. At higher levels these limitations may not be severe, but the low signal-to-noise ratio of the measurements may limit application in view of the (normally) smaller values of the fluxes aloft.

Similarity theory offers an alternative method. When the vertical profile of momentum flux and horizontal wind is known, the profile of the eddy diffusivity for momentum (K_u) is calculated from the ratio of the shear stress (or momentum flux) to the vertical gradient of the horizontal wind. Applying similarity implies that one can specify *a priori* the relationship between the eddy diffusivity for momentum and those for sensible heat and latent heat. In the simplest case, one may assume a ratio of unity; one also may estimate the profile of the ratio based on the profile of the gradient Richardson number (**Ri**). With independent estimates of the fluxes at the surface, the ratio can be calculated at the surface and assumed constant with height or the surface ratio used as an anchor point. Lacking definitive studies, one may assume a scaling approach based on a stability parameter such as **Ri** may offer the best chance for success.

The two methods above (and 'conditional sampling' discussed later) provide estimate from profile measurements at a single location; **budget analyses** provide line or area average estimates based on profile measurements at two or three or more locations, respectively. For the simple case of lateral homogeneity with respect to the flow, the vertical profile of the horizontal average (between sampling locations flux derives from knowledge of the flux at either the upper or lower boundary. The usual approach is to define the upper boundary of the budget domain as the first level where the vertical flux is assumed zero (typically where the scalar gradient goes to zero). The longitudinal fluxes are given by the average of the horizontal wind and the scalar, and the horizontal divergence of the longitudinal fluxes is balanced by a mean vertical flux. Although the authors are unaware of any budget analyses using remotely sensed profiles, there have been other similar applications. Johnson *et al.* (1971) and Ludwig and Dabberdt (1972) successfully applied the method using wind profiles from theodolites and carbon monoxide profiles obtained from an instrumented helicopter to estimate traffic emissions of CO from downtown San Jose and St. Louis.

Conditional sampling is a new concept recently introduced by Businger and Oncley (1989) that offers significant promise on the basis of preliminary evaluations using *in situ* measurements in both the surface layer and planetary boundary layer. The method is a simplification and

extension of the eddy accumulation technique (Desjardins, 1977), but seems to overcome some of the sampling constraints of the latter. The conditional sampling approach is based on the empirical relationship between the scalar flux and the difference between the mean upward (+) and downward (-) scalar concentration, where

$$\overline{w'c'} = b(\zeta)\sigma_w[\overline{c^+} - \overline{c^-}] \tag{4}$$

and $b(\zeta)$ is an empirical coefficient that is a slight function of stability, where $\zeta = z/L$ (z is height, and L the Monin-Obukhov length). Sensitivity tests by Businger and Oncley demonstrate that the method is relatively insensitive to stability, and vertical velocity threshold and bias. The insensitivity to w-threshold suggests the method may be applicable to the types of data available from disparate profiling systems (with similarly disparate sensitivities and sampling frequencies).

4. Concluding Comments

TOGA COARE and other mesoscale experiments require networks of sounding systems to estimate profiles of momentum and heat (sensible and latent) and their fluxes, as well as kinematic quantities. While no single technology can address all these requirements, an integrated sounding system consisting of active and passive profilers and in situ methods offers significant promise. Candidate sensing technologies have been reviewed, and a number of potentially applicable flux estimating methods described.

Acknowledgements

The authors gratefully acknowledge the word processing support provided by Ms. Mary Ann Pykkonen and Ms. Celia Darnell.

References

Brock, F.V., G.H. Saum and S.R. Semmer (1986): Portable automated mesonet II. J. Atm. Ocean. Tech., 3, 573-582.

Businger, J.A. and S.P. Oncley (1989): Flux measurement with conditional sampling, subm. to J. Atm. Ocean. Tech. (April).

Currier, P.E., W.L. Ecklund, D.A. Carter, J.M. Warnock, and B.B. Balsley (1988): Temperature profiling using a UHF wind profiler and an acoustic source. Proc. Symp. Lower Trop. Profiling, 31 May-3 June, 1988, Boulder, CO.

Dabberdt, W.F., J. Wyngaard, J. Businger, R.M. Hardesty, and S.F. Clifford (1986): Design study of a boundary-layer profiler. 1986 American Geophysical Union Spring Meeting, 19 May-23 May, Baltimore, MD.

Desjardins, R.L. (1977): Description and evaluation of a sensible heat flux detector. Boundary-Layer Meteor., 11, 147-154.

Ecklund, W.L., D.A. Carter, B.B. Balsley, and P.E. Currier, (1988a): A UHF Boundary Layer Wind Profiler. *Proc. Symp. Lower Trop. Profiling*, 31 May-3 June, 1988, Boulder, CO.

Ecklund, W.L., D.A. Carter, B.B. Balsley (1988b): A UHF wind profiler for the boundary layer: Brief description and initial results. *J. Atmos. Oceanic Tech.* 5(3), 432-441.

Fritts, D.C. and R. A. Vincent (1987): Mesospheric momentum flux studies at Adelaide, Australia: Observations and Gravity Wave/Tidal Interaction Model. *J. Atmos. Sci.*, **44**, 605-619.

Fukao, S., T. Sato, T. Tsuda, S. Kato, M. Inaba, and I. Kimura (1988): VHF Doppler radar determination of momentum flux in the upper troposphere and the lower stratosphere: Comparison of three- and four-beam methods. *J. Atm. Ocean. Tech.*, 5, 57-69.

Johnson, W.B., W.F. Dabberdt, F.L. Ludwig and R.J. Allen (1971): Field for initial evaluation of an urban diffusion model for carbon monoxide. SRI Project 8563, Stanford Research Institute, Menlo Park, CA 94025

Kropfli, R.A. (1986): Single Doppler radar measurements of turbulence profiles in the convective boundary layer. *J. Atm. Ocean. Tech.*, 3, 305-314.

Lhermitte, R.M. (1968): Turbulent air motion as observed by Doppler radar. *Proc. 13th Conf. on Radar Meteorology*, Montreal, AMS, 498-503.

Ludwig, F.L. and W.F. Dabberdt (1972): Evaluation of the APRAC-1A urban diffusion model for carbon monoxide. SRI Project 8563, Standard Research Institute, Menlo Park, CA.

Lukas, R. and Peter Webster (1988): Proceedings of the U.S. TOGA Western Pacific Air-Sea Interaction Workshop. U.S. TOGA Office, National Oceanic and Atmospheric Administration, USTOGA8.

Lukas, R., 1988: On the role of western Pacific air-sea interaction in the El Niño/southern oscillation phenomenon. U.S. TOGA Office, National Oceanic and Atmospheric Administration, USTOGA8.

McAffee, J.R., B.B. Balsley, and K.S. Gage (1989): Momentum flux over mountains: Problems associated with the symmetrical two-beam radar technique. *J. Atm. Ocean. Tech.* (in press).

May, P.T., R.G. Strauch, K.P. Moran and W.L. Ecklund (1989): Temperature sounding by RASS with wind profiler radars: a preliminary study. Submitted for publ. to *IEEE Trans. Geosc. Elect.*

National Center for Atmospheric Research (1989): STORM Program Plan, Second Draft - STORM Project Office, NCAR, Boulder, CO, January 31, 1989.

Reid, I.M. and R.A. Vincent: Measurements of mesospheric gravity wave momentum fluxes and mean flow accelerations at Adelaide, Australia. *J. Atmos. Terr. Phys.*, **49**, 443-460.

Smith, W.L., E. Westwater, R. Strauch, P. Moran and W. Dabberdt: GAPEX - a ground-based profiling experiment. Submitted to *Bull. Amer. Meteor. Soc.* (1989).

Strauch, R.G. (1988): Personal communication, NOAA ERL Wave Propagation Laboratory, Boulder, CO.

Strauch, R.G. (1988): Wind and temperature profiling in the lower troposphere. *Proc. Symp Lower Trop. Profiling*, 31 May-3 June, 1988, Boulder, CO.

Strauch, R.G., D.A. Merritt, K.P. Moran, P.T. May, B.L. Weber and D.A. Wuertz (1989): Doppler radar wind profilers in support of flight operations. Paper A1AA-89-0713, *27th Aerospace Sciences Meeting*, American Institute of Aeronautics and Astronautics, 9-12 January 1989, Reno, NV.

Vincent, R.A. and I.M. Reid (1983): HF Doppler measurements of mesospheric gravity wave momentum fluxes. *J. Atmos. Sci.*, **40**, 1321-1333.

Wilson, D.A. (1970): Doppler radar studies of boundary layer wind profiles and turbulence in snow conditions. *Proc., 14th Conf. on Radar Meteor.*, Tucson, AZ, AMS, 191-196.

MEETING COLLECTED PAPERS

WATER MASSES, SEA SURFACE TOPOGRAPHY, AND CIRCULATION

Some Thoughts about the West Pacific Warm Pool

Klaus WYRTKI

University of Hawaii, Honolulu
Hawaii, 96822 - U.S.A.

ABSTRACT

Large scale aspects of the West Pacific warm pool will be discussed on the basis of existing data and information. A definition of the warm pool in terms of an isothermal layer is simple and definitive in the vertical, but difficult with regard to its horizontal extent. Even if narrowly defined by the 28°C isotherm, the pool undergoes large annual variations in its horizontal extent. The region of overlap is only about one half of the size of the pool. The pool is persistent only between 10°N and 10°S with its center at 170°E. An inspection of the circulation of upper layer water indicates that the pool gains water from the two anticyclonic gyres, and discharges warm water by means of the countercurrent and the Indonesian throughflow. The residence time of water in the pool is only 1.3 years and makes the pool sensitive to interannual variations of heat advection and heat input. There seems to be little interhemispheric exchange of water through the pool.

The role of the countercurrent as a boundary current between the two gyres will be described, and its response to variations in the intensity of the two subtropical gyres. A strong South Pacific gyre will lead to a weak countercurrent and to an accumulation of warm water in the warm pool. This situation persists during the build-up phase before El Nino. In contrast, a strong North Pacific gyre will lead to a strong countercurrent and a drain of warm water from the warm pool as is occurring during El Nino. As a consequence, the variations of the volume of warm water in the warm pool and the occurrence of El Nino may well be linked to pulsations of the subtropical gyres in the two hemispheres.

1. Introduction.

The West Pacific Warm Pool has been the subject of much scientific interest in recent years because of its relation to the development of El Nino, and an entire large scientific experiment (TOGA COARE, 1988) devoted to it is in the final planning stages. It seems therefore appropriate to spend some time analyzing a few aspects of the warm pool based on existing data and information. In this brief study I would like to point out how difficult it is to generate a definition of the pool, discuss the circulation of water through the pool and its residence time, and to relate fluctuations of the water volume in the pool with fluctuations of the two subtropical gyres. Analysis of these fluctuations will result in some important insights into the role of the equatorial countercurrent in the dynamics of the warm pool.

2. Definition, size and depth of the warm pool.

The warm pool contains tropical surface water, which by definition is warm and of relatively low salinity due to excessive evaporation. Because of its low density it forms a lens of light water which floats on the denser waters below, which are of subtropical origin and therefore cooler and of higher salinity.

Such a warm pool exists in the eastern tropical Pacific off the coast of Central America. It is shallow, warm and of very low salinity, but most important it is contained by convergent movements of the two subtropical gyres. These horizontal flows form the

ORSTOM
CENTRE DOCUMENTATION
Montpellier

F.30199

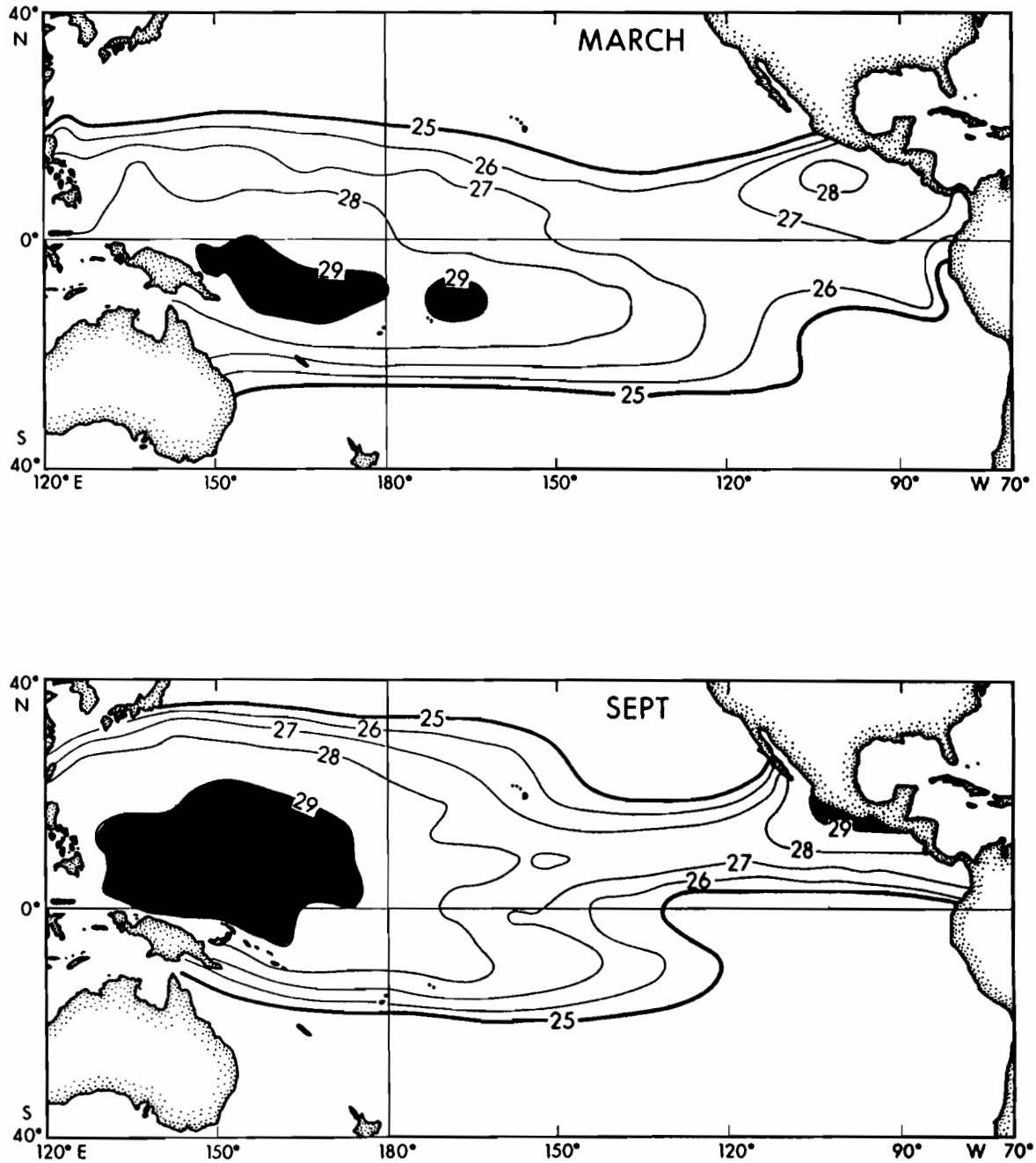

FIG.1. Average sea surface temperature in the tropical Pacific Ocean in March and September. Only isotherms warmer than 25°C are shown to define the warm pool.

Galapagos Front and the Cabo San Lucas Front and force the tropical surface water into a rather restricted area, from which it can escape only to the west, chiefly with the North Equatorial Current.

In the western tropical Pacific a similar pool is formed, but the warm layer is much deeper and can be stratified with respect to salinity as has recently been uncovered by Lukas and Lindstrom (1987). The water movements in the region are divergent and move water polewards into the western boundary currents. Therefore the pool is poorly defined horizontally.

A definition of the warm pool is relatively easy in the vertical through the use of a selected isothermal layer. In fact any isotherm above about 22°C would be useful, because the upper thermocline is very steep. A definition is much more difficult with regard to the pools horizontal extend. If one would use the 25°C isotherm, there would be only one large warm pool in the Pacific, and it would seasonally extend as far north as Japan and as far south as Brisbane, Australia (Fig. 1). Such a definition would clearly be undesirable. In contrast, the selection of the 29°C isotherm would define a pool that is too small and that might occasionally disappear. For these reasons the 28°C isotherm has been used by many scientists as a practical compromise for the definition of the west Pacific warm pool.

Accepting such a definition one is immediately confronted with large annual variations of the boundaries of the pool (Fig. 2). The extreme northerly position is reached in September, when the pool stretches far into the northern subtropical gyre. In March the pool barely reaches to 10°N. The annual fluctuations in the southern hemisphere are less pronounced, but the size of the pool doubles from September to March. The area covered permanently by the pool is relatively small, from about 10°N to 10°S and from Indonesia to 170°W, and represents only about half of the average area of the pool. The pool is slightly larger in the northern than in the southern summer. These large annual fluctuation of the boundaries of the pool make a definition of its size and volume rather difficult and somewhat uncertain. One also has to keep in mind that the annual heating and cooling cycles along the boundaries will add to or remove water from the pool.

The depth of the pool as given by the 28°C isotherm has been charted from XBT observations for each season, but only the maps for the July-August-September and the January-February-March periods are shown (Fig. 3). The maximum depth of the pool is just over 100 m, and the deepest area is near the equator and the date line, and not further west, where surface temperatures is warmest (Fig. 1). Where the pool is a permanent feature it is between 60 and 100 m deep. The distribution of depth changes little with the season, in contrast to its horizontal extend. Along the fringes, especially in the summer hemisphere, the pool is shallower and the boundary is not well defined.

In view of the poorly defined horizontal boundaries of the warm pool it is rather difficult to estimate its volume. Taking the average depth as 80 m and the area as 25×10^{12} m^2, the volume of the pool is about 20×10^{14} m^3. It should be noted that the area is about 15% larger in northern summer and 15% smaller in southern summer. The western boundary of the pool is arbitrarily assumed to be the line from the Philippines to New Guinea, not counting the warm water in the Indonesian Archipelago.

3. Circulation through the warm pool.

Waters of the subtropical gyres of the northern and southern hemisphere circulate through the warm pool and warm water leaves the pool in the North Equatorial Countercurrent and through the Indonesian Archipelago. It would be interesting to estimate the flows in and out of the pool in order to determine the pathways of water through the pool and to arrive at an estimate of the residence time of water in the warm

pool. This is not an easy undertaking because of the poorly defined boundaries of the pool, and estimates will off course be rather crude. Toole, Zou and Millard (1988) have tried to establish a mass budget for waters warmer than 12°C for a smaller area in the western Pacific, and they point to the difficulties inherent in such studies.

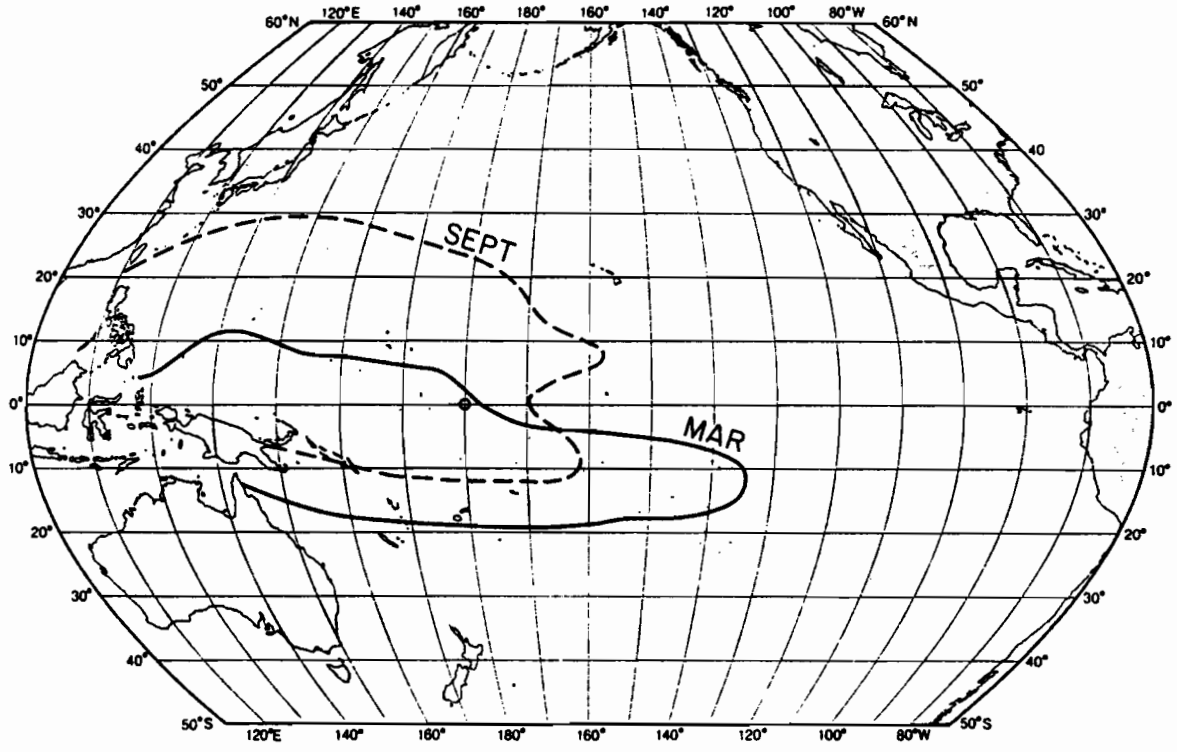

FIG.2. The warm pool in March and September as given by the 28°C isotherm. Note the small overlap.

All inflow into the warm pool occurs between Hawaii and Tahiti (Fig. 4). The Hawaii to Tahiti Shuttle Experiment has resulted in a rather solid determination of the geostrophic flows that enter and leave the warm pool in the east (Wyrtki and Kilonsky, 1984). Transports in the upper 400 m have been computed and they give 24 Sv (Sverdrup) for the North Equatorial Current, 20 Sv for the Countercurrent and 15 and 26 Sv for the two branches of the South Equatorial Current flowing north and south of the equator, respectively. Not all this water is warm enough to enter the warm pool, because these currents extend into the thermocline and even transport water below the thermocline. An inspection of the sections shown by Wyrtki and Kilonsky (1984) allows to estimate the flows of water in the mixed layer that enter or leave the warm pool between Hawaii and Tahiti.

The North Equatorial Current is deep reaching and only about half of its transport is in the mixed layer. As this water flows west the temperature of the surface water slowly increases to more than 28°C and it enters the warm pool, accounting for a contribution of about 12 Sv. The Countercurrent flow is much more concentrated in a shallow surface layer than the Northern Equatorial Current. Most of its water is warmer than 27°C and represents a loss of warm water from the pool. This flow can be estimated as about 15 Sv. The South Equatorial Current flows both north and south of the equator.

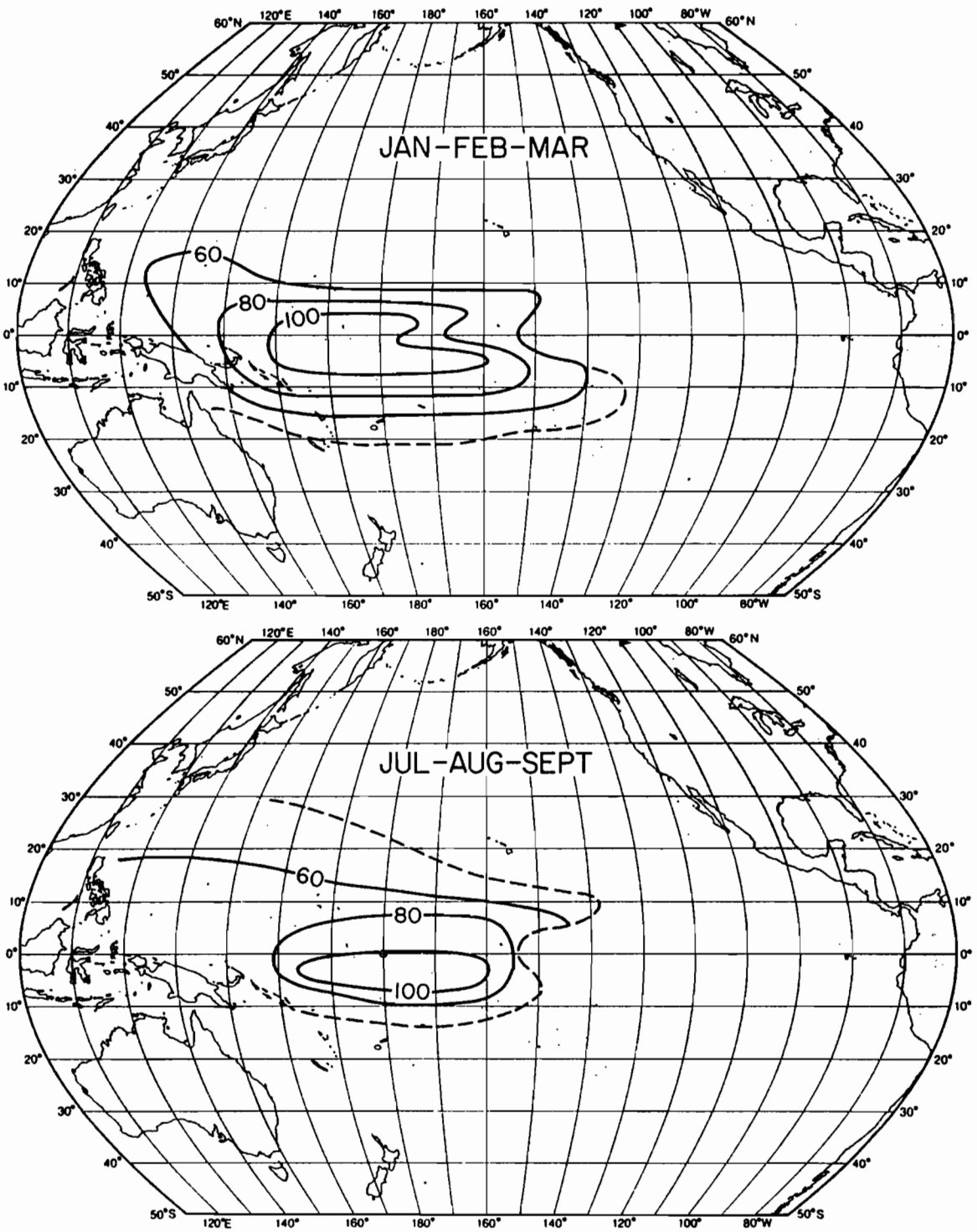

FIG.3. The average depth (in meters) of the 28°C isotherm as derived from XBT observations for the season January-February-March (top) and the season July-August-September (bottom).

Its northern part is very shallow and most of the flow consists of warm water. A reasonable estimate for this flow is 12 Sv. The southern part of the South Equatorial Current penetrates deeper into the thermocline and its westward flow of warm water may be estimated as 20 Sv between the equator and 8°S. South of this latitude flow is variable and weak, and westward flow is intertwined with the South Equatorial Countercurrent.

The warm pool looses water through the Indonesian Archipelago. Estimates of this throughflow vary between 5 and 14 Sv (Gordon, 1986), and some of the throughflow may involve water in and below the thermocline. Assuming a loss of warm water at a rate of 8 Sv appears reasonable.

So far we have estimated losses of water from the warm pool as 15 Sv in the Countercurrent and 8 Sv in the throughflow, and gains of 44 Sv in the North and South Equatorial Currents. The balance of 21 Sv must consequently leave the warm pool polewards with the western boundary currents. A schematic sketch of the pathways of warm water through the warm poll is given in Figure 4. It may be emphasized that most of the water entering the pool with the North Equatorial Current leaves again with the subtropical gyre circulation after only a short residence in the pool. The South Equatorial Current provides most of the water of the pool, which leaves as very warm water either with the Countercurrent or with the throughflow. About half of the water of the southern part of the South Equatorial Current participates in the circulation of the southern subtropical gyre. The pathways of water inside the gyre are off course speculative and simplified, but it seems rather clear that there is little interhemispheric exchange of water. The Indonesian throughflow is chiefly supplied from warm water of the southern hemisphere as assumed by Gordon (1986).

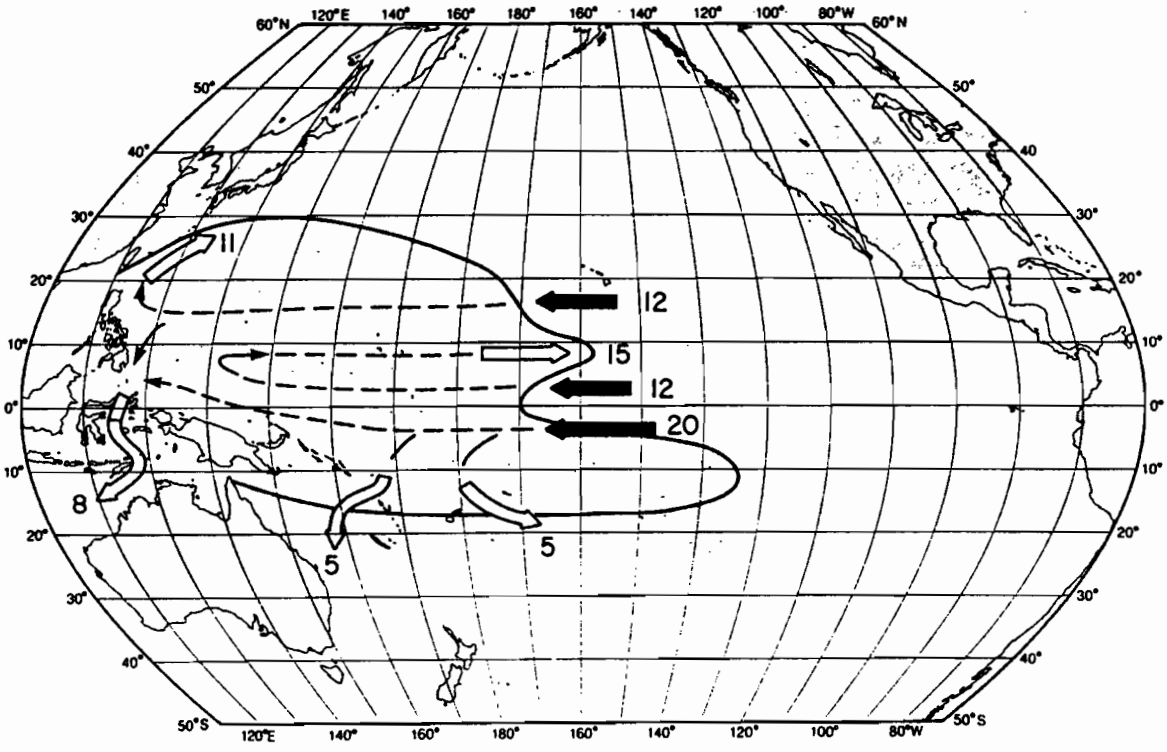

FIG.4. Estimates of water flowing into (solid arrows) and out of the warm pool (open arrows) in Sverdrups (10^6 m^3 s^{-1}).

Inside the warm pool water exchange between the various currents may be much more intense than sketched in this schematic diagram. The circulation to the north of New Guinea is subject to strong changes with the season, as shown by Schott (1939). Current measurements by Firing and Jiang (1989) have shown enormous fluctuations from year to year, and drifting buoy trajectories indicate strong water transfers between the various zonal currents (Hacker, Firing and Lukas, 1989).

Along the fringes of the pool, the water participating in the anticyclonic circulation of the subtropical gyres will be subject to the seasonal heating and cooling cycle. It will therefore become part of the pool when warmed, and disappear from the pool when cooled, an effect that results in the large annual variation of the poleward boundaries of the pool.

The above estimates of the water transports in and out of the warm pool allow to estimate the residence time of warm water in the pool. All inflow into the pool is from the east between Hawaii and Tahiti and it amounts to about 44×10^6 m^3 s^{-1}. The total volume of the pool is 20×10^{14} m^3. Dividing volume by circulation rate gives a residence time of only 1.3 years. This short residence time of warm water in the pool implies that the water in the pool is exchanged rather frequently and that the pool may be very sensitive to interannual variations of its volume. This residence time is short compared to the interval between El Nino events. It should also be noted that the warm pool gains its water from the two subtropical gyres and looses water with the Countercurrent and the Indonesian throughflow. The water lost with the Countercurrent will partially reach the warm pool in the eastern tropical Pacific and partially be re-circulated into the NEC, thus remaining in the tropical ocean. The water lost with the throughflow, on the other hand will be lost to the Pacific Ocean and represents an export of heat from the Pacific to the Indian Ocean.

The warm pool will also be very sensitive to interannual variations of its temperature and heat content. The average depth of the permanent, central portion of the pool is about 80 m. A slow change of its mean temperature by 1°C over a period of 2 years can certainly be detected by observations. Such a change can be produced by a small change of surface heat input of only 5 W m^{-2} , which is clearly below the threshold of detection.

4. The warm pool and the subtropical gyres.

Fluctuations of the volume of water in the warm pool are probably related to fluctuations of the circulation of the subtropical gyres. These gyres represent large masses of warm water that rotate in an anticyclonic direction. The warm upper layer of these gyres has a very characteristic shape, as shown by Shaw and Wyrtki (1972), especially when viewed as a two layer system. A schematic north-south section through the two subtropical gyres of the Pacific Ocean is shown in Figure 5. The mean depth of the upper layer in each gyre is given by the volume of warm water present in the gyre, which is probably very stationary because it is formed by the mean climatic conditions over a long period. The slope of the upper layer thickness from the center of each gyre toward the equator or toward the poles is a function of the strength of circulation in each gyre. A strong circulation will cause a larger slope than a weak circulation, and consequently a shallower position of the thermocline at the periphery and a deeper position in the center of the gyre, if the water volume remains constant. There is little doubt that changes in gyre circulation happen at much faster time scales than changes in their volume. The subtropical gyres are largely wind-driven, and consequently their circulation will vary with the wind forcing.

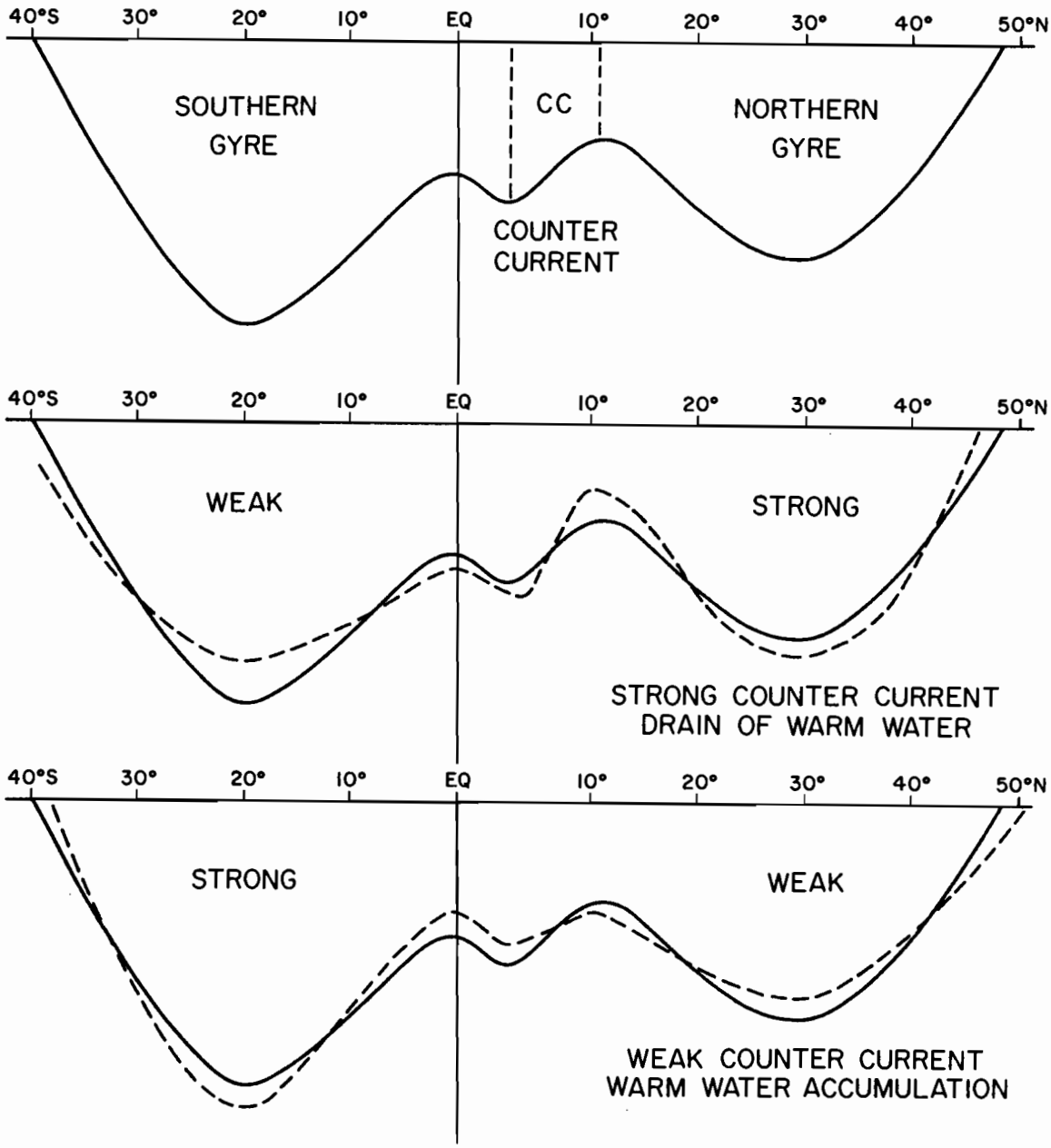

FIG.5. A schematic north-south profile of the shape of the thermocline across the two subtropical gyres in the Pacific (solid line) and possible patterns of oscillation (dashed lines) in relation to the strength of the countercurrent.

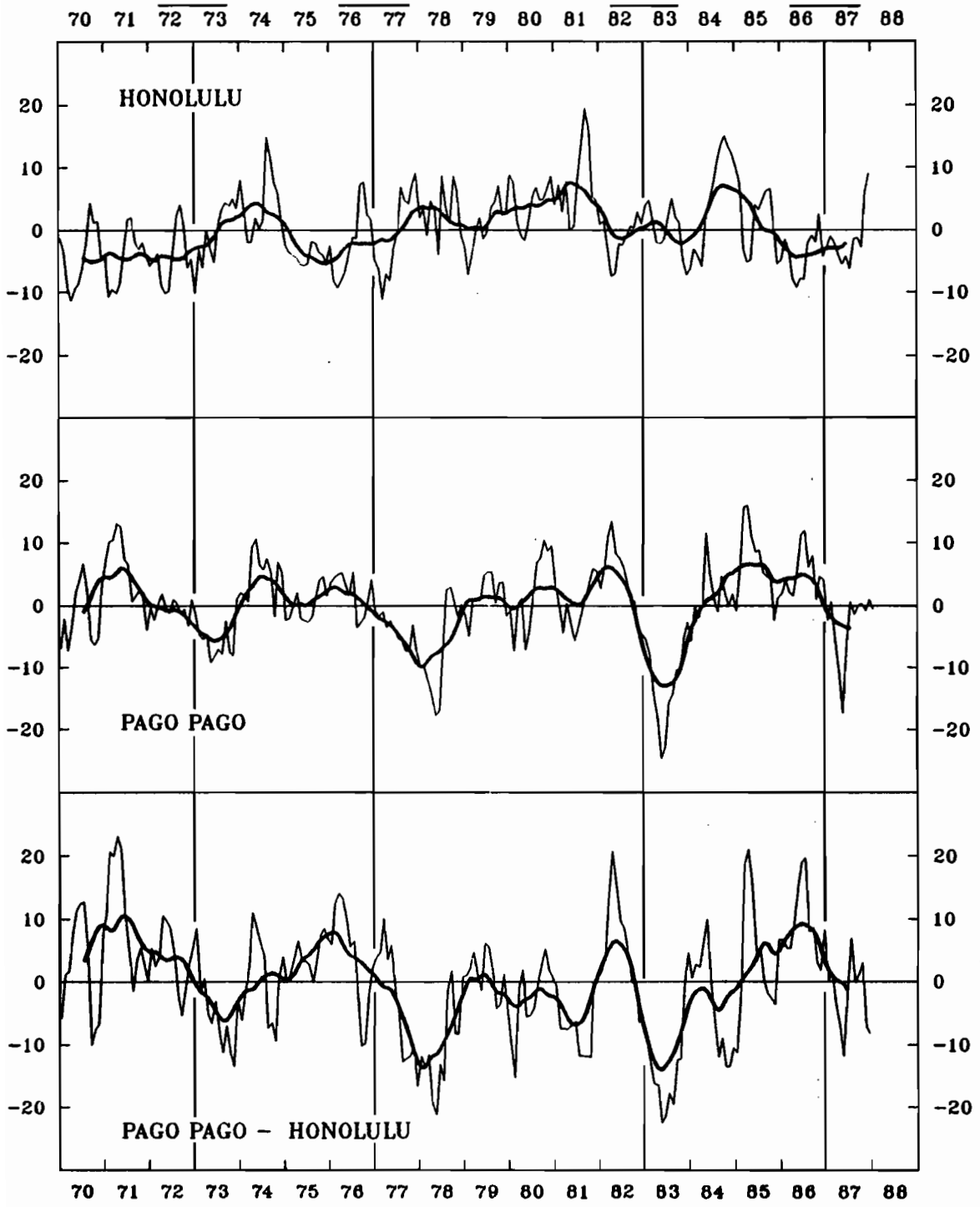

FIG.6. Monthly mean sea level at Honolulu and Pago Pago and their difference (in cm) from 1970 to 1988. The thick curves give the 12-month running means. The major El Nino events of 1972-73, 1976, 1982-83 and 1987 are marked by vertical lines.

Because the subtropical gyre of the southern hemisphere penetrates across the equator into the northern hemisphere, the slope of the thermocline reverses north of the equator. It is very unlikely that the volume of the two gyres and the intensity of their circulation match in such a way that the thermocline would have the same depth where the two gyres meet. In fact the thermocline of the northern gyre at its southern boundary is usually higher than the thermocline of the southern gyre at its northern boundary. This difference of thermocline depth causes a geostrophic current to develop between the two subtropical gyres, which is called the North Equatorial Countercurrent. It is therefore appropriate to consider the Countercurrent as a boundary current between the two subtropical gyres. Fluctuations in the intensity of circulation in the two gyres will cause fluctuations in the depth of the thermocline at their periphery and will change the slope of the thermocline across the Countercurrent. Consequently the Countercurrent will be subject to strong fluctuations caused by the fluctuations of the two gyres.

Fluctuations of the two subtropical gyres have been documented by Wyrtki and Wenzel (1984) by means of sea level observations. They have shown that the gyres oscillate out of phase with a period near 4 years, and that these oscillations are related to El Nino events. Fluctuations of the baroclinic structure of the subtropical gyre in the western North Pacific have been documented by White and Hasunuma (1980) and also show a periodicity related to El Nino events. It is useful to consider the reaction of the Countercurrent to oscillations of the gyres, and this is sketched schematically in Figure 5. If the northern gyre is strong, and the southern gyre weak, the difference of the thermocline across the Countercurrent will be large and the Countercurrent strong. This situation implies a strong drain of warm water from the warm pool, and is typical for El Nino conditions, when the warm pool looses mass. In contrast, when the southern gyre is strong, and the northern gyre is weak, the difference of the thermocline across the Countercurrent will be small, and the Countercurrent will be weak. This situation will lead to a small drain of water from the warm pool, but to a strong accumulation of warm water in the pool by an intensified South Equatorial Current. During this period the warm pool will grow, and that typically happens between El Nino events.

It remains now to relate the fluctuations of the subtropical gyres as observed by sea level at Honolulu and Pago Pago to the occurrence of El Nino. Wyrtki and Wenzel (1984) have used data from 1948 to 1982 to show that the sea level difference between Pago Pago and Honolulu increases between El Nino events, indicating an acceleration of the southern gyre. During these periods the South Equatorial Current is strong, adding warm water to the pool, and the Countercurrent is weak, draining less water from the pool. Both effects allow the warm pool to grow. During El Nino the sea level difference between Pago Pago and Honolulu decreases, the southern gyre becomes weaker, the Countercurrent stronger, and water is being drained from the warm pool. Six more years of sea level data have been added to the time series of Wyrtki and Wenzel (1984) covering the 1982-83 and the 1986-87 El Nino events (Fig. 6). During both events the same pattern is apparent: between El Nino events the sea level difference between the two gyres increases, and drops rapidly during these events. This confirms the contention that El Nino events involve an aperiodic discharge of warm water from the western equatorial Pacific as stated by Wyrtki (1985).

5. Conclusions.

The west Pacific warm pool gains water from the two subtropical gyres, but chiefly from the South Pacific gyre with the South Equatorial Current. The pool looses water with the Countercurrent, with the Indonesian throughflow and polewards with the subtropical gyres. Water in the pool has a short residence time and consequently the pool is sensitive to interannual variations of volume and heat content caused by fluctuations of advection

and surface heat flux. To understand fluctuations of the warm pool, the interactions with the two gyres must be taken into account. Fluctuations of the circulation in the two subtropical gyres are systematically linked to fluctuations of the Countercurrent and changes in the volume of the warm pool. The gyres are wind-driven and fluctuations of their circulation are due to fluctuations of the winds. Wind fluctuations in turn, in particular of the southeast trade winds in the Pacific, are linked to El Nino events, which only demonstrates how strongly fluctuations in the ocean and in the atmosphere are coupled.

It will be very difficult to measure the volume fluctuations of the warm pool and more difficult to measure the transports of the currents flowing in and out, so that a mass budget can be derived, and the contributions of the subtropical gyres to the pool can be determined. On the other hand there seems to be little doubt that the interaction of the two subtropical gyres is intimately involved in the fluctuations of the warm pool and in the creation of El Nino events. It may be a challenge to theoreticians to model these gyre-gyre oscillations.

Acknowledgements. Support for this research was provided by National Science Foundation, grant OCE8515404, with contributions from NASA, and National Oceanographic and Atmospheric Administration grant NA85ABH00032.

REFERENCES

Firing, E., and S. Jiang, 1989: Variable currents in the western Pacific measured during the USA-PRC bilateral TOGA project. Abstracts: Western Pacific International Meeting and Workshop on TOGA-COARE. ORSTOM. Centre de Nouméa, p. 19.

Gordon, A., 1986: Interocean exchange of thermocline water. *J. Geophys. Res.*, **91**, 5037-5046.

Hacker, P., E. Firing, R. Lukas, 1989: Observations of the low-latitude western boundary circulation in the Pacific during WEPOCS III. Abstracts: Western Pacific International Meeting and Workshop on TOGA-COARE. ORSTOM. Centre de Nouméa, p. 35.

Lukas, R., and E. Lindstrom, 1987: The mixed layer of the western equatorial Pacific Ocean. Proceedings of the 'Aha Huliko'a Hawaiian Winter Workshop on The Dynamics of the Oceanic Surface Mixed Layer. Honolulu, January 1987, P. Muller and D. Henderson, eds. 67-94.

Schott, G., 1939: Die aquatorialen Stromungen des westlichen Stillen Ozeans. *Annalen der Hydrographie und Maritimen Meteorologie*, **67**, 247-257.

Shaw, R., and K. Wyrtki, 1972: The shape of the warm surface layer in a subtropical gyre. In: Studies in Phys. Oceanogr. A. L. Gordon, ed., New York, p. 179-194.

TOGA COARE, 1988: A Coupled Ocean-Atmosphere Response Experiment for the Warm Pool Regions of the Western Pacific: Science Plan. U.S. TOGA COARE Science Working Group.

Toole, J. M., E. Zou, and R. C. Millard, 1988: On the circulation of the upper waters in the western equatorial Pacific Ocean. *Deep-Sea Res.*, **35**, 1451-1482.

White, W. B., and K. Hasunuma, 1980: Interannual variability in the baroclinic gyre. *J. Mar. Sci.*, **38**, 651-672.

Wyrtki, K., 1985: Water displacements in the Pacific and the genesis of El Nino cycles. *J. Geophys. Res.*, **90**, 7129-7132.

Wyrtki, K., and J. Wenzel, 1984: Possible gyre-gyre interaction in the Pacific Ocean. *Nature*, **309**, 538-540.

Wyrtki, K., and B. Kilonsky, 1984: Mean water and current structure during the Hawaii to Tahiti Shuttle Experiment. *J. Phys. Oceanogr.*, **14**, 242-254.

Comparison of the Results of two West Pacific Oceanographic Expeditions FOC (1971) and WEPOCS (1985-86)

Jean René DONGUY[1], Gary MEYERS[2] and Eric LINDSTROM[2]

[1] *Centre ORSTOM de Brest, IFREMER*
BP 70, 26263 Plouzane - France

[2] *CSIRO Division of Oceanography, GPO Box 1538*
Hobart, Tasmania 7001 - Australia

1. Introduction

After study of the 1982-83 ENSO, oceanographic research has focused on phenomena occurring in western equatorial Pacific. Consequently, the Western Equatorial Pacific ocean Circulation Study (WEPOCS) was launched in order to study problems located in this area such as the circulation, heat storage and water properties.

Two expeditions were conducted (June-August 1985, WEPOCS1; January-February 1986, WEPOCS2) by Australian and US scientists, in the region north and east of Papua New Guinea (PNG) (Fig. 1) (Lindstrom et al. 1987).

Fifteen years before, a similar series of cruises occurred in the same area (Fig. 1) and at the same season (January-February 1971, FOC1; June-July 1971, FOC2) conducted by French scientists from centre ORSTOM de Nouméa (Anonyme, 1980).

The methods of investigation present large differences as a result of technological advancements. During FOC cruises, hydrographic casts with Niskin bottles provided discrete measurements of temperature, salinity, oxygen and nutrient. Current measurements were obtained with HYTECH currentmeters used as profilers from the surface to 600 meters depth. Similar data were provided by WEPOCS cruises but using CTD stations (including discrete sampling for oxygen and nutrients) and a ship board Acoustic Doppler current Profiler (ADCP).

Both of these cruise series point out interesting results concerning the New Guinea Coastal Undercurrent (NGCU) the source of the Equatorial Undercurrent, the Pacific Equatorial Monsoon jet and upper ocean heat storage.

2. New Guinea Coastal Undercurrent

Northwest of Vitiaz strait, along the coast of Papua New-Guinea, a subsurface northwestward flow was found during the four cruises. The velocity maximum is usually centred at 200 meter depth. As the measurements of the four cruises stopped at 142°E, it is not certain now much of the transport of the undercurrent was caught by the eastward Equatorial Undercurrent and how much continues to the west.

The reverse of the monsoon has no effect on the direction of the NGCU : figure 2 shows during FOC2 (June-July 1971) at 142°30E a westward core of 40 $cm.s^{-1}$ and during WEPOCS2 (January-February 1986) at 143°E a westward core of 50 $cm.s^{-1}$. This velocity core is associated with a spreading of the 15°C-25°C isotherms against the shore. This spreading may be easily explained during WEPOCS2 when the NGCU is covered by a surface eastward current due to the N-W monsoon.

ORSTOM
CENTRE DOCUMENTATION
Montpellier

F 30200

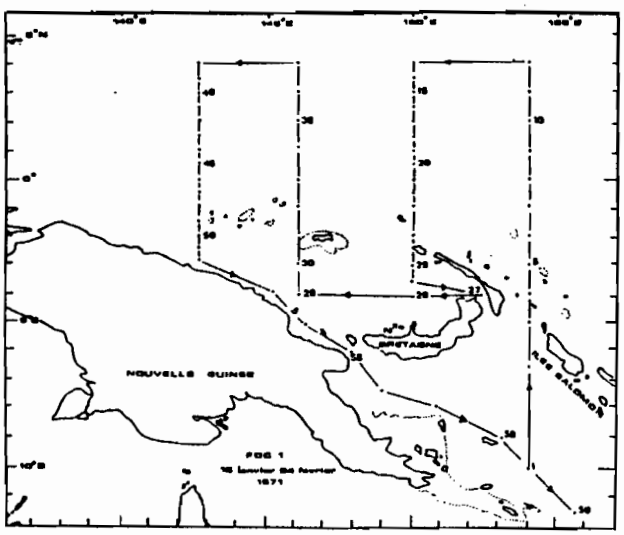

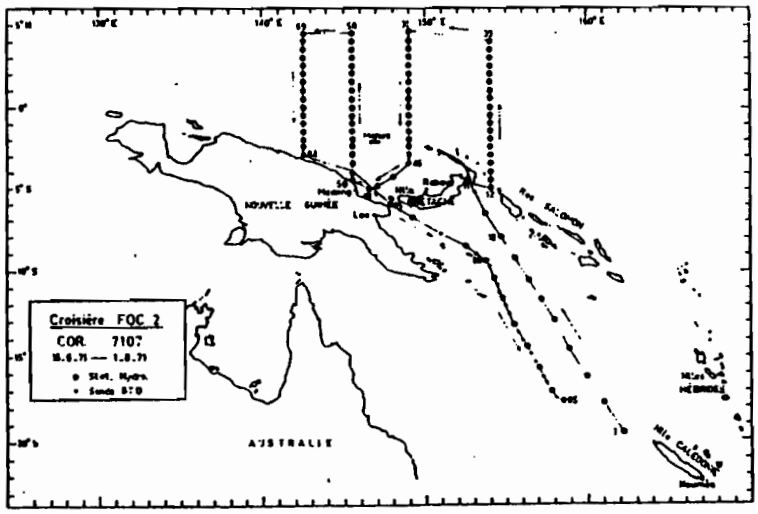

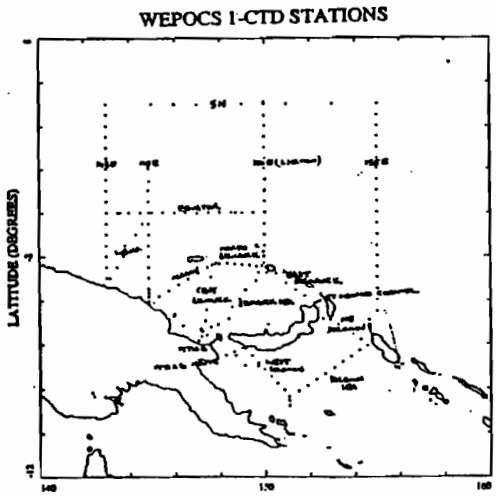

FIG.1. FOC1 (up), FOC2 (middle) and WEPOCS1 (down) cruises. Note that WEPOCS2 (not shown here) has the same design as WEPOCS1.

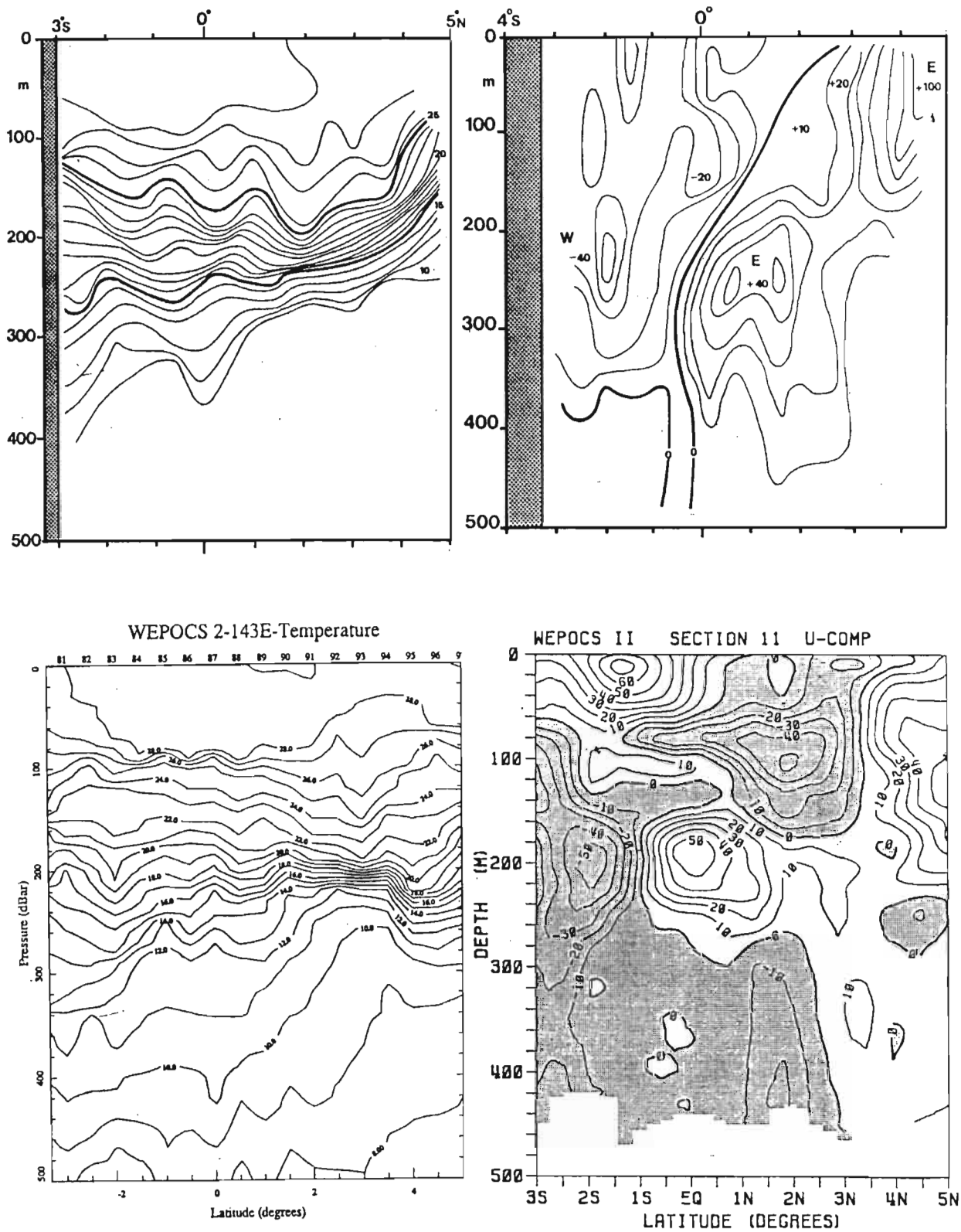

FIG.2. Sections of temperatrure and zonal velocity (cms^{-1}), in June-July 1971 at 142°.30E during FOC2 (upward panel) and in Jan.-Feb. 1986 at 143°E during WEPOCS2. Shaded areas and negative values indicate westward flows.

3. Source of the Equatorial Undercurrent

Isopycnal analysis for WEPOCS by Tsuchiya et al. (1989) provides interesting informations concerning the source of the Equatorial Undercurrent. A comparison with FOC cruises is added in this analysis.

At 300 cl/t (fig. 3), corresponding to 150-220 meter depth, salinities exceeding 35.6 extend to 146°E during the two series of cruises FOC and WEPOCS and have a westward extension. During the WEPOCS cruises, the high salinity tongue extends mainly through the Vitiaz Strait and along the coast of New Guinea, carried by the NGCU. A secondary source takes place north of New Ireland.

During the FOC cruises, the main source of the high salinity may occur north of New Ireland and the salinities exceeding 35.6 extends to 146°E during FOC1 and 143°E during FOC2, instead 150°E during WEPOCS. In the FOC data the secondary source is Vitiaz Strait (Colin et al., 1973), however the resolution of WEPOCS data in the Vitiaz Strait region is much greater.

At 200 cl/t, corresponding to 200-250 meters depth, there are two sources of water extending westward, one characterized by low oxygen content flowing north of New Ireland, other characterized by high oxygen content flowing through Vitiaz Strait along the coast of New Guinea (Fig. 4).

According to Tsuchiya (1968), low oxygen water is carried westward by the South Equatorial Current from the eastern Pacific. The values are increasing from the east to the west. High oxygen water comes from the Coral Sea and the values are decreasing westward away from the PNG coast. It seems that the convergence and the mixing of these two kinds of water lead to a water containing 3.4 ml/l of oxygen. This water is feeding the EUC in the vicinity of 140°E (Rougerie, 1969).

This feature is corroborated by oxygen content at 160 cl/t (220-300 meter depth) (Fig. 5). During the four cruises, high values are found from Coral Sea to the coast of New Guinea, whereas low values (less than 3.2) occur north of New Ireland reaching 145°E during WEPOCS cruises and only 153°E during FOC cruises.

4. Equatorial Monsoon Jet

During the N-W monsoon (January-February), westerlies are prevailing in the equatorial zone. At this time, the westward South Equatorial Current is replaced by an eastward current distinct from the Equatorial Undercurrent. Subsurface remanents of Westward flow are embedded between the surface eastward current and the eastward undercurrent. The surface eastward current is named Pacific Equatorial Monsoon Jet (Lindstrom et al., 1987).

This feature occurred in January-February during the cruises FOC1 and WEPOCS2. At 154°E and 155°E (Fig. 6), the Pacific Equatorial Monsoon Jet is exactly located on the equator, whereas at 142°30E and 143°E (fig. 7) it has shifted to the south.

Some occurrences of eastward flow at the surface are observed in the June-July cruises and may be the results of unseasonable transient wind forcing. The current system observed at 143°E and 155°E (Fig.9) in June-July 1985, is not noticeable at 165°E at the same period (Delcroix et al., 1987; Fig.4d). This observation is in favor of an explanation involving the transient influence of a wind change as already suggested by Hisard et al. (1970).

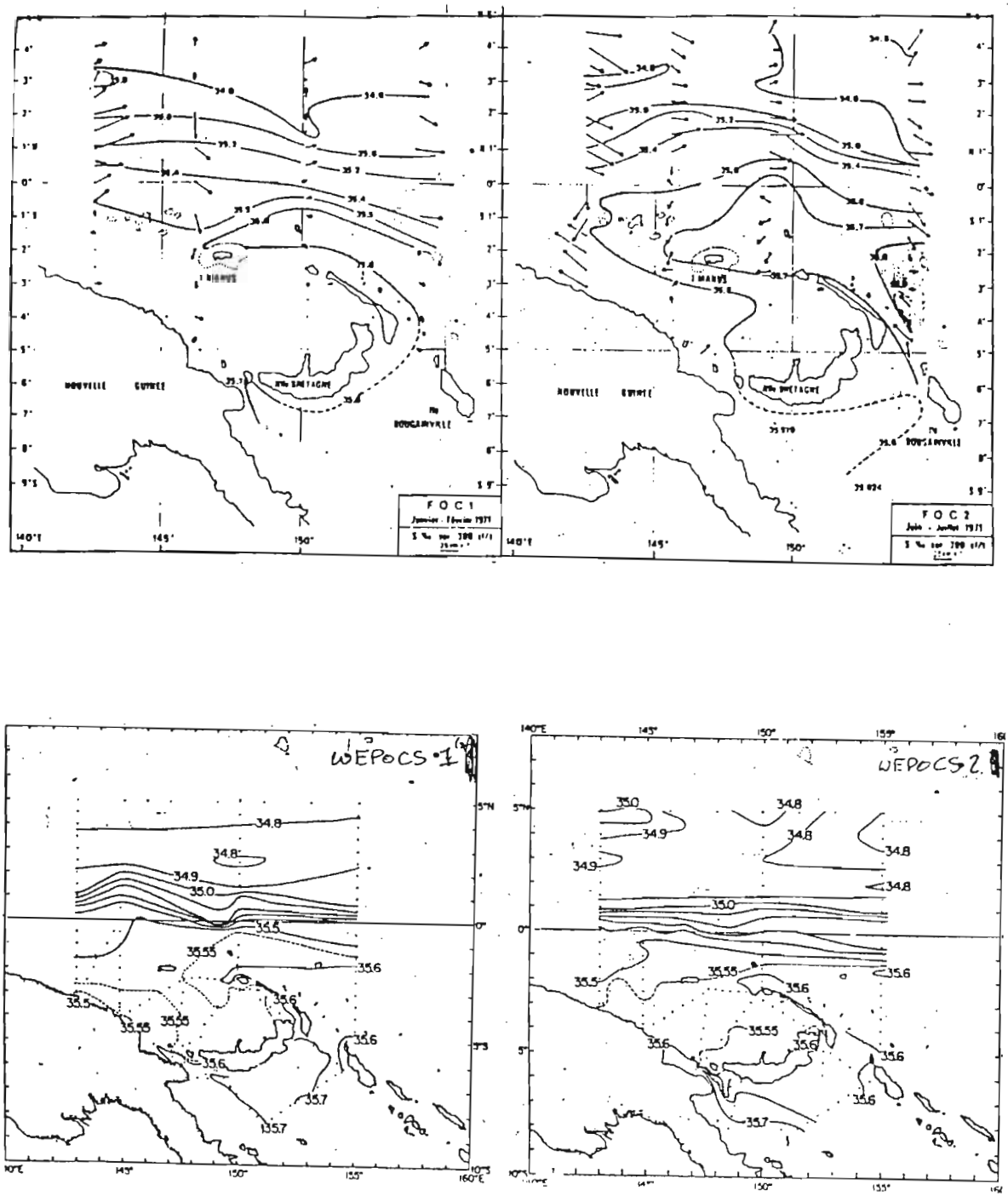

FIG.3. Salinity on surface 300 cl.t^{-1}, during FOC1 (upper left), FOC2 (upper right), WEPOCS1 (lower left) and WEPOCS2 (lower right).

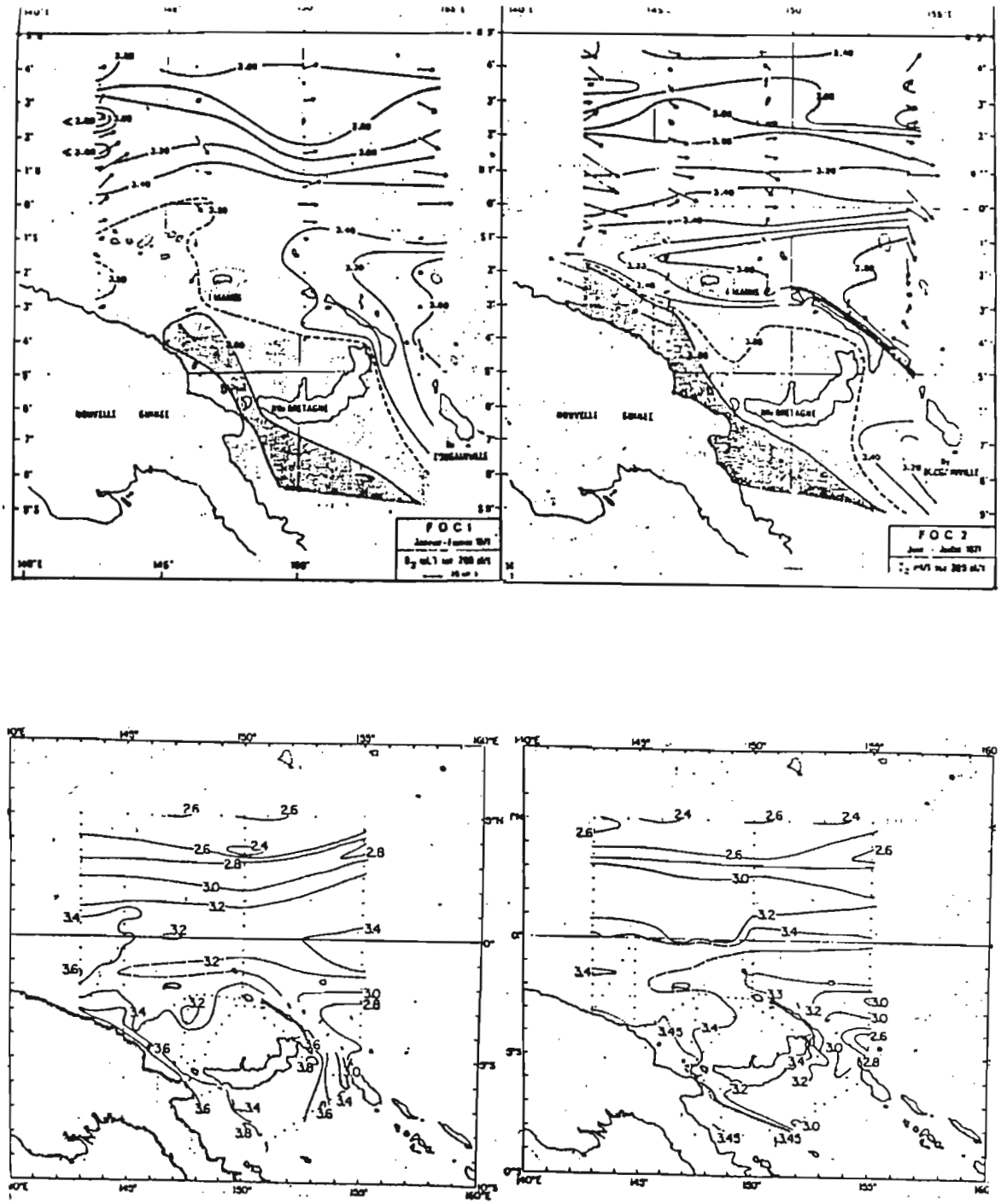

FIG.4. Oxygen (ml.l-1) on surface 200 cl.t-1, during FOC1 (upper left), FOC2 (upper right), WEPOCS1 (lower left) and WEPOCS2 (lower right).

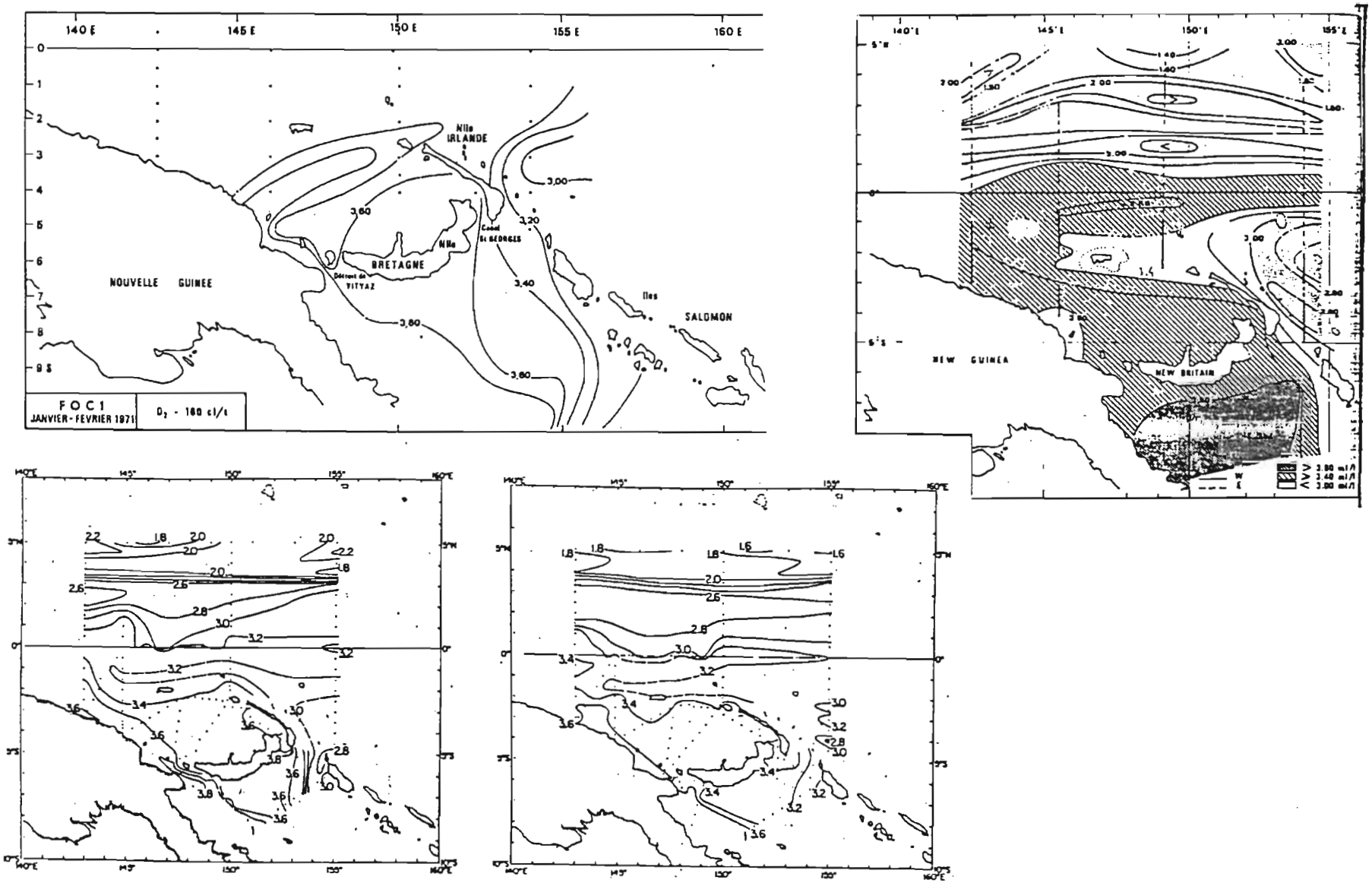

FIG.5. Oxygen (ml.l^{-1}) on surface 160 cl.t^{-1}, during FOC1 (upper left), FOC2 (upper right), WEPOCS1 (lower left) and WEPOCS2 (lower right).

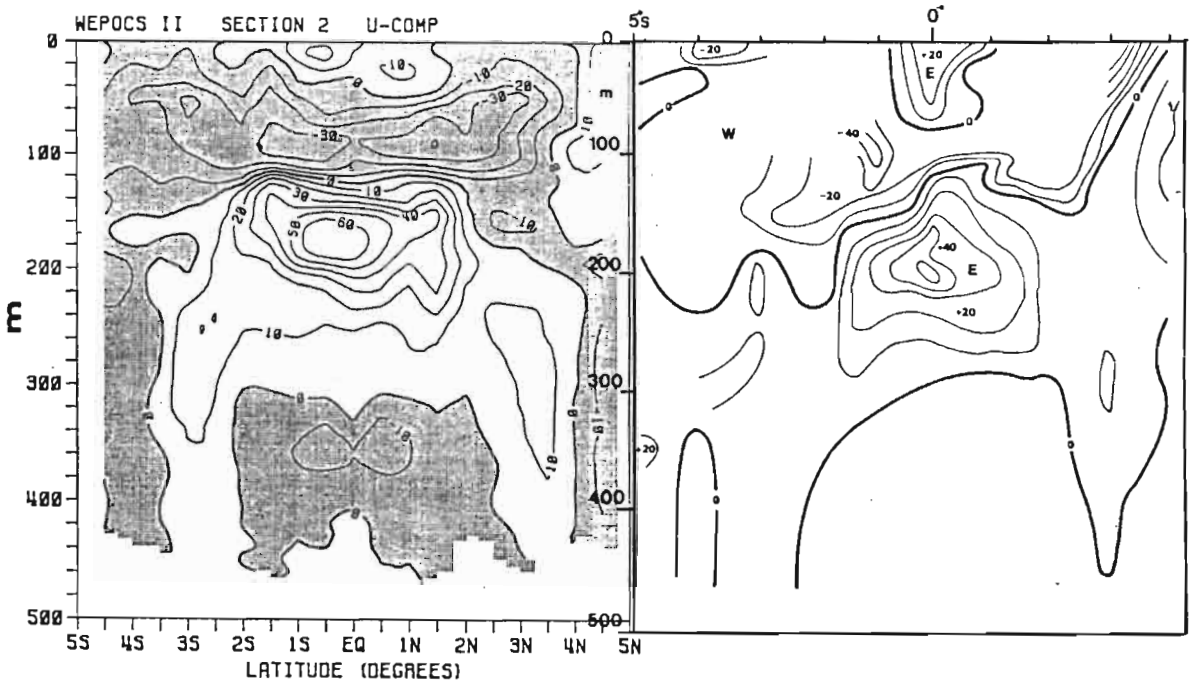

FIG.6. Section of zonal velocity (cm.s^{-1}) during FOC1 (right) at 154°E and WEPOCS2 (left) at 155°E. Shaded areas and negative values indicate westward flows.

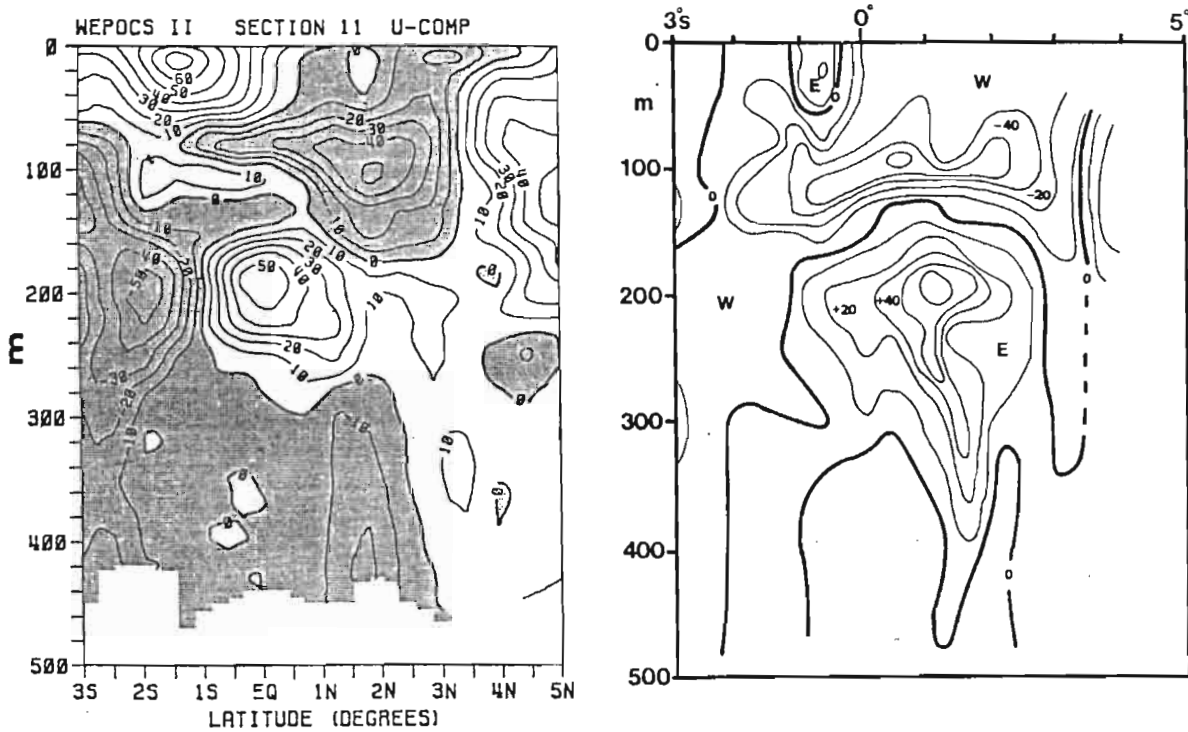

FIG.7. Section of zonal velocity (cm s^{-1}) during FOC1 (right) at 142°30E and WEPOCS2 (left) at 143°. Shaded areas and negative values indicate westward flows.

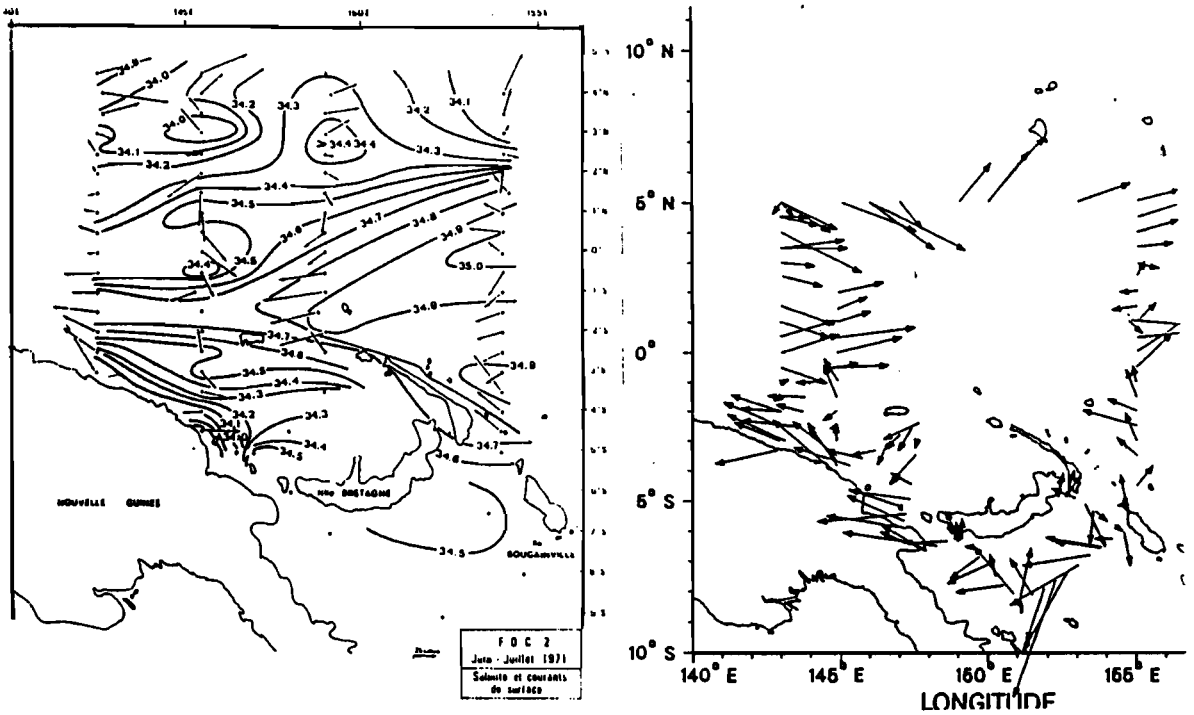

FIG.8. Surface circulation during FOC2 (left) and WEPOCS1 (right).

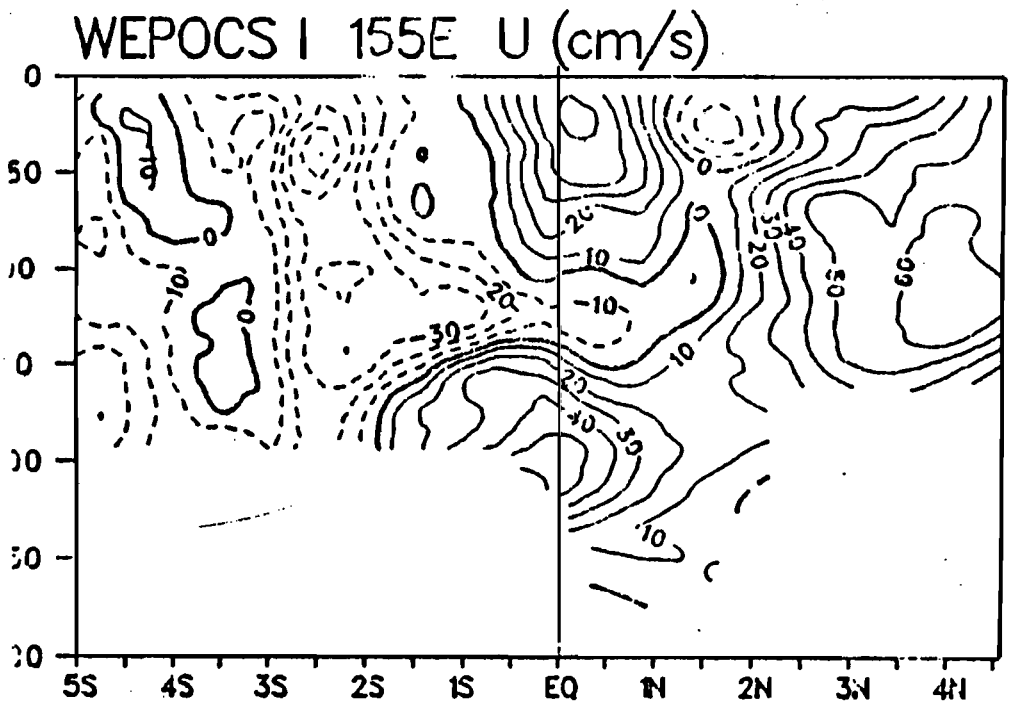

FIG.9. Section of zonal velocity (cm.s^{-1}) during WEPOCS1 (June-July 1985) at 155°E. Positive values indicate eastward flow.

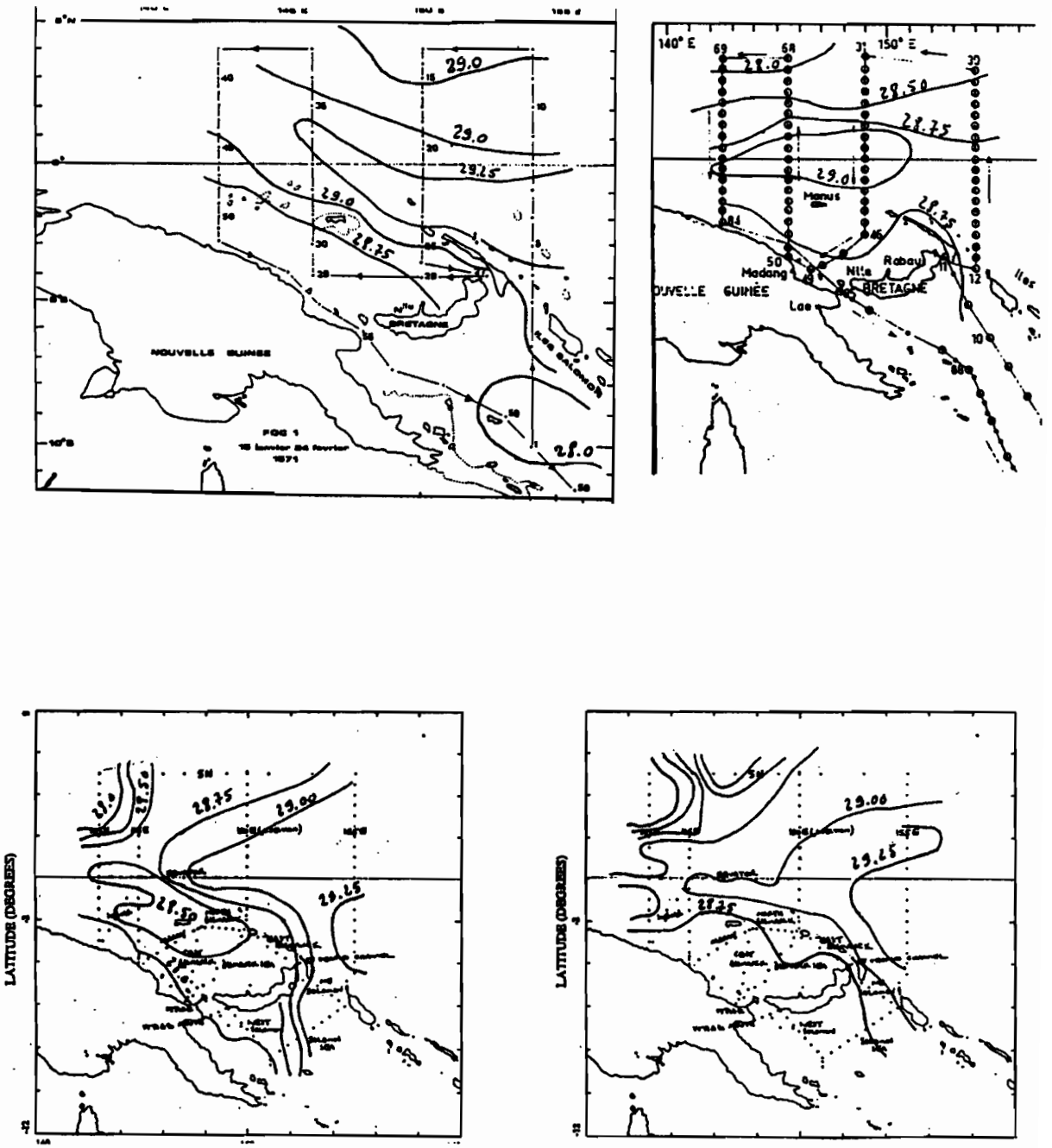

FIG.10. Mean temperature of the 0-100 meter-depth layer (°C). Up : FOC1 and FOC2 cruises. Down : WEPOCS2 and WEPOCS1 cruises.

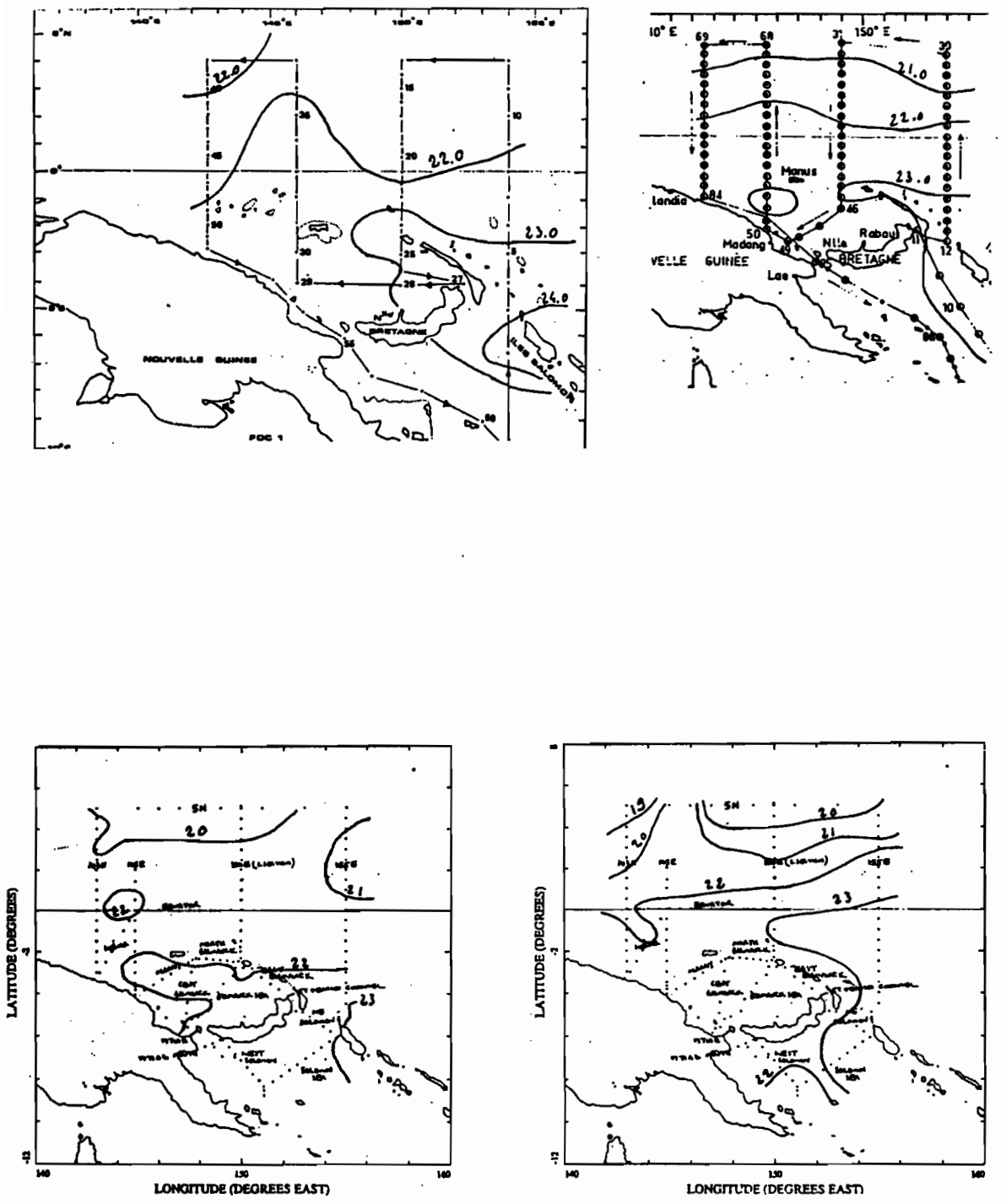

FIG.11. Mean temperature of the 0-300 meter-depth layer (°C). Up : FOC1 and FOC2 cruises : Down : WEPOCS2 and WEPOCS1 cruises.

5. Heat storage

Heat storage is considered during the FOC and WEPOCS cruises under the form of the mean temperature from the surface to 100 meters depth, and the mean temperature from the surface to 300 meters.

0-100 m mean temperature (Fig. 10) is very similar during the four cruises whatever the season : a maximum more than 29°C is located in the vicinity of the equator. West and north of this maximum, heat storage is decreasing.

O-300 m mean temperature (Fig. 11) is homogeneous for three cruises (FOC1, FOC2 and WEPOCS1) : a maximum more than 23°C is found south of the equator and heat storage is decreasing northward. The pattern is different during WEPOCS2 (January-February, 1986) : the mean temperature is 1° less than during the three other cruises. This low heat storage is connected to the appearance of the 1986-87 El Nino : it is likely that a part of the heat content stored in the equatorial western Pacific was already transported to the eastern Pacific through the North Equatorial Countercurrent (Meyers and Donguy, 1984).

6. Conclusion

These four cruises carried out at the same seasons but 15 years apart display very similar features. It seems that the patterns of the equatorial current system (eastward-westward-eastward and westward-eastward from the surface to 300 m depth), which has been observed are worthy of further investigation as to their relationship with the wind forcing. It would be interesting to ascertain how heat storage decrease in the western Pacific could be considered as a precursor of El Nino.

REFERENCES

Anonyme, 1980: Résultats des croisières équatoriales du centre ORSTOM de Nouméa (1971). *Rapports Scientifiques et Techniques*, **13**, Centre ORSTOM de Nouméa, New Caledonia.

Colin, C., J.R. Donguy, C. Hénin, C. Oudot, B. Wauthy, 1973: Upper waters north of New Guinea in 1971. *The KUROSHIO 3*. Proceeding of the third C.S.K. Symposium, Bangkok, Thailand.

Delcroix, T., G. Eldin, C. Hénin, 1987: Upper Ocean water masses and transports in the Western Tropical Pacific (165°E). *J. Phys. Oceanogr.*, **17**, 2248-2261.

Hisard, P., J. Merle, B. Voituriez, 1970: The equatorial Undercurrent at 170°E in March and April 1967. *J. Mar. Res.*, **28**, 281-303.

Lindstrom, E., R. Lukas, R. Fine, E. Firing, S. Godfrey, G. Meyers, M. Tsuchiya, 1987: The Western Equatorial Pacific ocean Circulation Study. *Nature*, **330**, 6148, 533-537.

Meyers, G., J.R. Donguy, 1984: The North Equatorial Countercurrent and heat storage in the western Pacific Ocean during 1982-83. *Nature*, **312**, 5991, 258-260.

Rougerie, F., 1969: Sur un noyau à forte teneur en oxygène dans la partie inférieure du courant de Cromwell. *Cah. ORSTOM, sér. Océanogr.*, **7**, n° 3, 21-28.

Tsuchiya, M., 1968: Upper water in the intertropical Pacific Ocean. *The John Hopkins oceanogr. studies*, **4**, 50 pp.

Tsuchiya, M., R. Lukas, E. Firing, R. Fine, E. Lindstrom - Source waters of the Equatorial Undercurrent, *Submitted to progress in Oceanography*.

The Western Boundary Current in the Far-Western Pacific Ocean

Dunxin HU and Maochang CUI

Institute of Oceanology, Academia Sinica
7 Nanhai Road, Qingdao,
People's Republic of China

1. Introduction

The Western Boundary Current (WBC) is well known, not only because of its being one of the strongest currents in the world ocean, but also its extremely important role in the global transport and redistribution of heat. The WBC in the North Atlantic (the Gulf Stream) is quite well understood by long period of various investigations. However, the WBC in the North Pacific (PWBC), especially east of the Philippines is relatively poorly understood, except the Kuroshio south of Japan, although much work has been done during CSK (Cooperative Study of the Kuroshio, 1965-1977). The PWBC is different from the WBC in the North Atlantic, where only exists a northward current in the Gulf Stream. Here, PWBC consists of two currents east of the Philippines : the Kuroshio a northward current, and the Mindanao Current towards the south. The latter is poorly understood.

From 1986 through 1988 about 70 CTD stations (Fig. 1) were occupied by R/V Science 1 of Academia Sinica Institute of Oceanology in each October. In the present paper some features of the PWBC are extracted from the CTD data by inversion manipulation.

2. Method

Since all the CTD casts did not reach the bottom, instead, just 1500 m, Wunsch's inverse method (1978) should be modified for calculation. In consideration of the fact that the velocity field should be of potential with f-plane approximation, we add one more equation

$$\int V \, X \, d s = 0$$

to

$$A \, b = - \Gamma$$

where V is the velocity vector, ds the tangential element vector, c the closed cruise track (loop). A is an m x n matrix, b a column vector consisting of n components, velocities at reference level, Γ a column vector of residual term, as described by Wunsch (1978). Then we have :

$$\Sigma \, \delta_j \, \rho r_j \, \Delta \chi_j \, b_j = 0$$

for reference level, say, 1500 m, where δ_j is +1 or -1 depending on whether the water flows into or out of the box, ρr_j the density at the reference level at the j-th station pair, $\Delta \chi_j$ the separation of the j-th station pair, and b_j the reference velocity at the j-th station pair at reference level.

As 1500 m is quite shallow and geostrophy is not quite valid in the upper layer, we divided the water column into two layers by σ_t = 27 or 27.5, which has been tested being the optimal, for every box, in which mass is conserved. Then some features are realized as follows.

ORSTOM
CENTRE DOCUMENTATION
Montpellier

F 30201

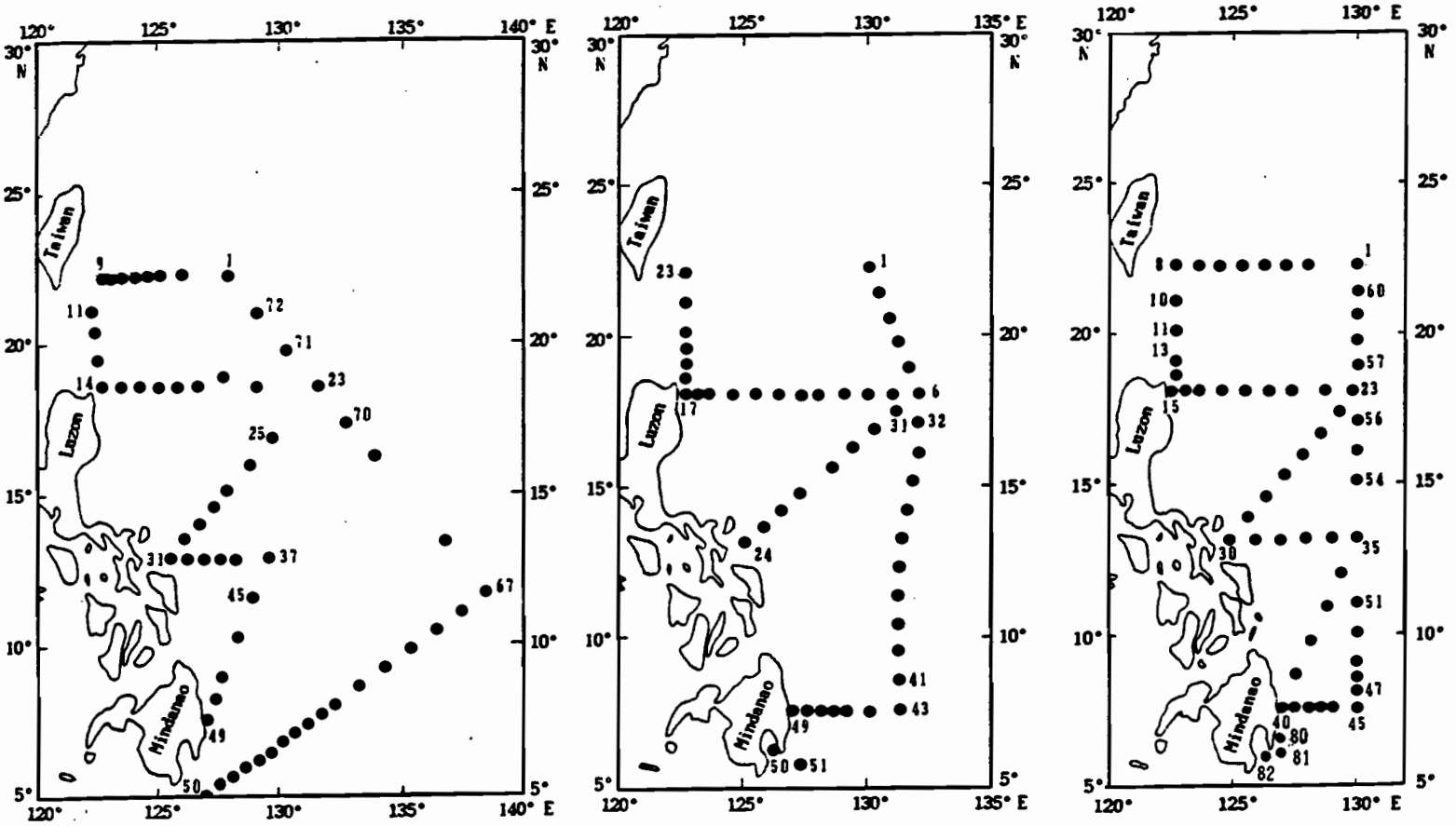

FIG.1. Cruise tracks in October 1986 (left), October 1987 (middle), and October 1988 (right).

3. Some Features of the PWBC

3.1. The Kuroshio at its origin

The Kuroshio is defined differently by different oceanographers (Kishindo, 1931; Sverdrup et al., 1942; Wyrtki, 1961; Nitani, 1972). Nitani (1972) stated that the current from just north of the place where the North Equatorial Current is separated into two branches offshore east of the Philippines to the east of Japan where the current veers away from land can be called the Kuroshio in a broad sense. At least, the beginning of the Kuroshio is in the region off the east coast of Luzon.

In order to detect the Kuroshio three sections east of northern Luzon and Taiwan were designed (Fig. 1). However, the latitude of the section east of the north end of Luzon for 1986 is half degree different (more) than 1987 and 1988. A summary can be made about the Kuroshio as follows from the inversion-calculated results.

a) Volume transport of the Kuroshio in its origin area

October 1986. The strength of the Kuroshio can be examined by westward volume transport through the meridional section east of Luzon Strait (approximately 122°20'E) and northward through the zonal sections (18°30'N and 22°10'N). It is seen from Fig. 2 that the main flows are concentrated in the upper 600m layer. A very narrow northward flow between st. 7 and 9 is more than 19.10^6 $m^3.s^{-1}$ in transport (Fig.2a). There are two westward flows between st. 9 and 11 (east of Taiwan) with 11.10^6 $m^3.s^{-1}$ in transport and between st. 12 and 14 (north of Luzon) with 19.10^6 $m^3.s^{-1}$ (Fig. 2b). A narrow eastward flow of $3.10^6 m^3.s^{-1}$ in transport gets through the meridional section (Fig. 2b). So if we use the northwestward flow from st. 7 and 14 to indicate the Kuroshio, the transport is about 46.10^6 $m^3.s^{-1}$ without the leakage in between st. 14 and Luzon coast (they are about 46 km apart. The velocity near st. 14 is more than 30 $cm.s^{-1}$. Suppose the average velocity in the upper 600 m is 18 $cm.s^{-1}$ southeast of st. 14, then the transport leaked is about $6.10^6 m^3.s^{-1}$. Therefore, the volume transport of the Kuroshio east of Luzon and Taiwan is about 52.10^6 $m^3.s^{-1}$ which is about 1.5 times of the normal transport (Hu, 1989). This can be circumstantially verified by the σ_t = 26 topography (Fig. 5a).

October 1987. Through 122°40'E section (Fig. 3a) gets a westward flow between st. 18 and 21 with a volume transport of 18.10^6 $m^3.s^{-1}$, and eastward flow with $18.7.10^6 m^3.s^{-1}$ in transport including a narrow eastward flow between st. 17 and 18 with $1.5 \times 10^6 m^3.s^{-1}$. Through 18°N section (Fig. 3b) take place a northward flow between st. 17 and 14 (transport is about 15.10^6 $m^3.s^{-1}$), and two bands of southward flow offshore with transport of 19.10^6 $m^3.s^{-}$ between st. 14 and 13 and 5.10^6 $m^3.s^{-1}$ between st. 9 and 8 in the upper layer. In consideration of the fact that st. 17 is about 50 km away from land, northwestward leakage between st.17 and Luzon might be about 5.10^6 $m^3.s^{-1}$. And then the transport of the Kuroshio is only about 20.10^6 $m^3.s^{-1}$, which is only half of the normal (Hu, 1989). Obviously, the Kuroshio is weaker during this time. A great deal of water getting through the section of 132°E (Fig. 3d-st. 5 to 1) turns right to the north in the place east of st. 1. This also can be verified by the σ_t = 26 topography (Fig. 5b).

October 1988. An obvious westward flow through the 122°40'E section (Fig. 4a) is between st. 10 and 15 mainly in the upper 600 m layer with a volume transport of about $30.10^6 m^3.s^{-1}$ and a return (eastward) flow in the upper 300 m layer exists between st. 8 and 10 with 7.10^6 $m^3.s^{-1}$ in transport. The section along 18°N (Fig. 4b) shows a strong $28.10^6 m^3.s^{-1}$ in transport and wide (about 300 km in width) northward flow, in the upper 600 m layer between st. 15 and 18 and a return flow, which is 300 km wide and with volume transport of 10.10^6 $m^3.s^{-1}$ in the upper 500 m layer in between st. 18 and 21. This year the volume transport of the Kuroshio here is about 33.10^6 $m^3.s^{-1}$ with the same estimate as above since the distance between st. 15 and Luzon is about 33 km. This tendency can be verified from figure 5c.

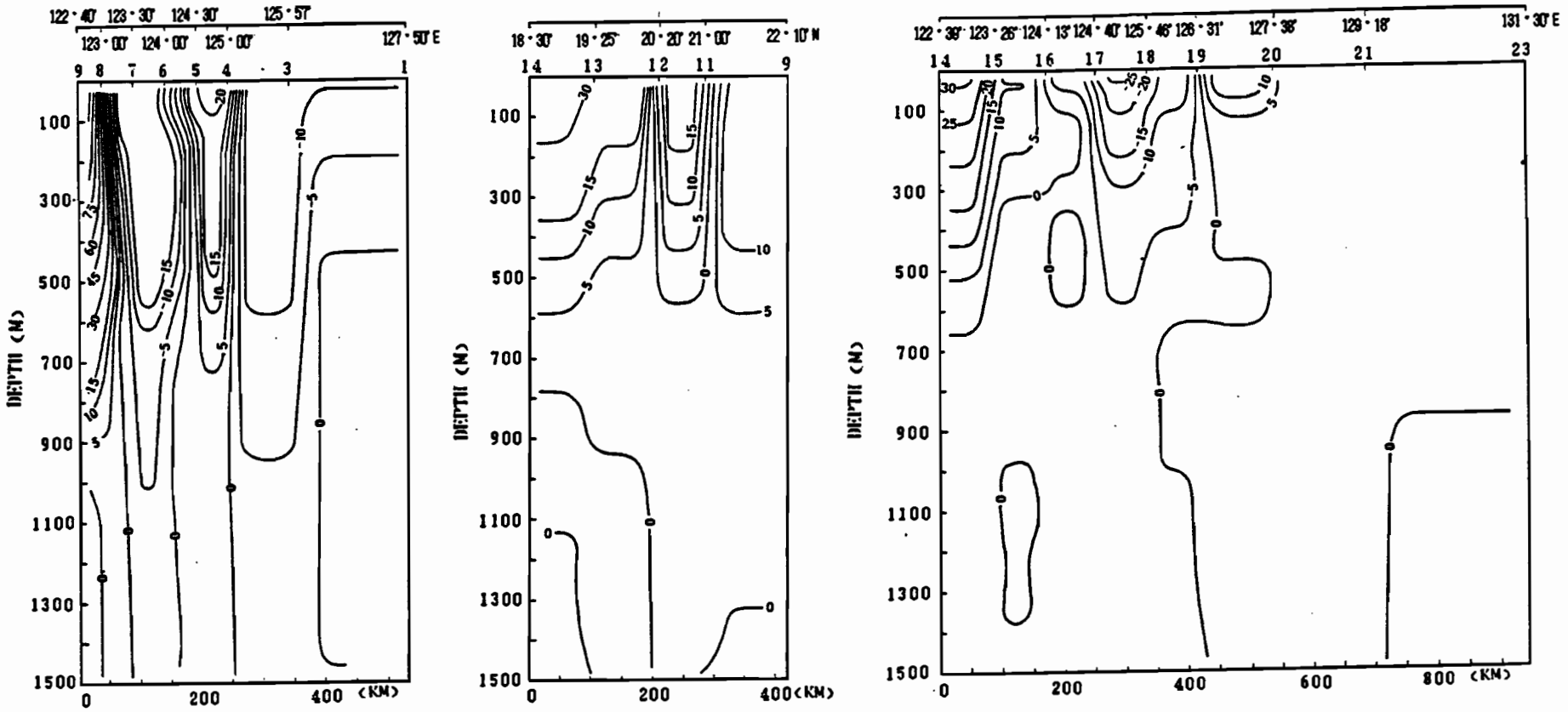

FIG.2. Velocity distribution in October 1986 along 22°10'N (left), 122°20'E (middle), and 18°30'N (right). Positive (negative) flow into (out of) the paper.

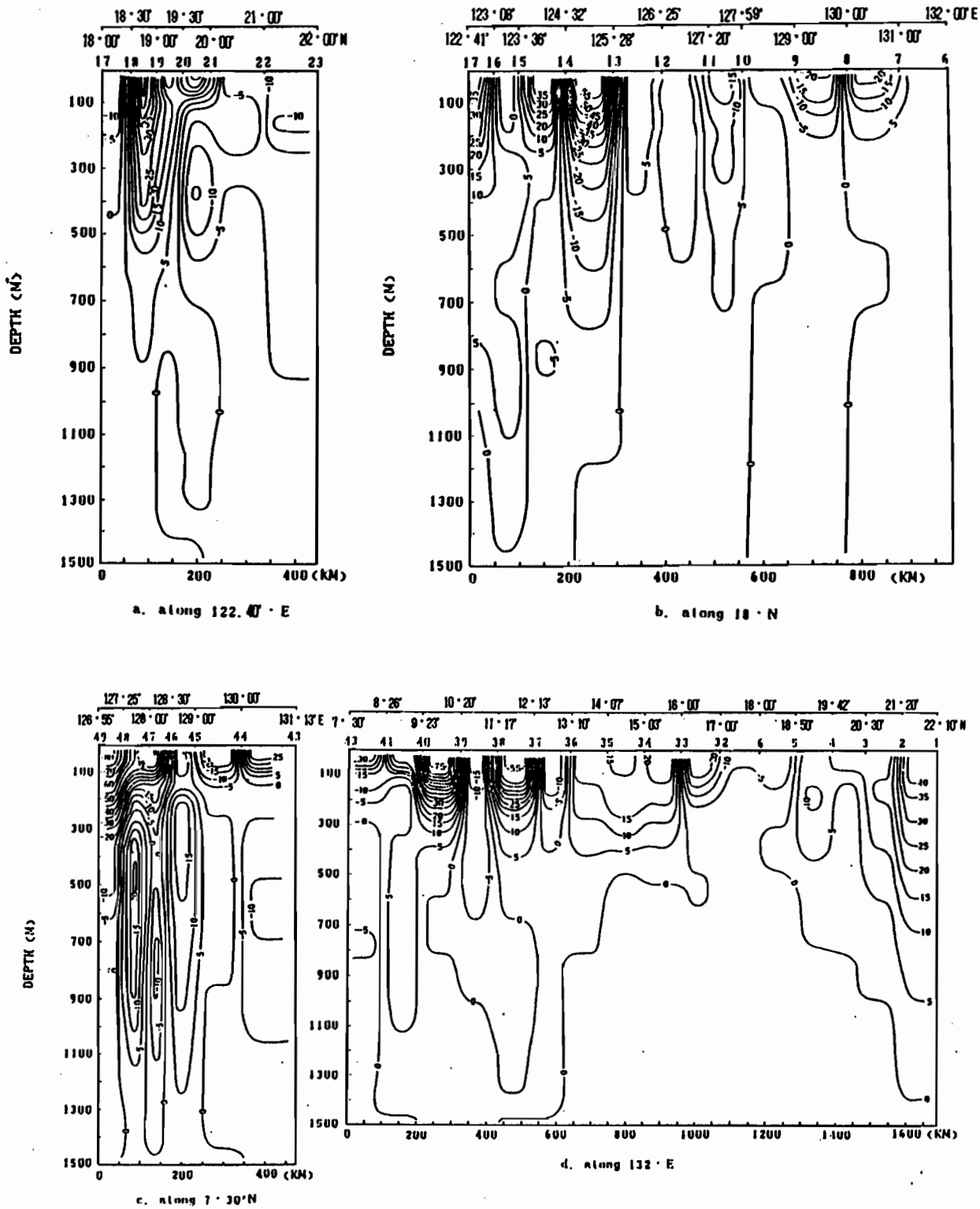

FIG.3. Velocity distribution in October 1987, determined by inverse method. Positive (negative) flow into (out of) the paper.

3. Some Features of the PWBC

3.1. The Kuroshio at its origin

The Kuroshio is defined differently by different oceanographers (Kishindo, 1931; Sverdrup et al., 1942; Wyrtki, 1961; Nitani, 1972). Nitani (1972) stated that the current from just north of the place where the North Equatorial Current is separated into two branches offshore east of the Philippines to the east of Japan where the current veers away from land can be called the Kuroshio in a broad sense. At least, the beginning of the Kuroshio is in the region off the east coast of Luzon.

In order to detect the Kuroshio three sections east of northern Luzon and Taiwan were designed (Fig. 1). However, the latitude of the section east of the north end of Luzon for 1986 is half degree different (more) than 1987 and 1988. A summary can be made about the Kuroshio as follows from the inversion-calculated results.

a. Volume transport of the Kuroshio in its origin area

October 1986. The strength of the Kuroshio can be examined by westward volume transport through the meridional section east of Luzon Strait (approximately 122°20'E) and northward through the zonal sections (18°30'N and 22°10'N). It is seen from Fig. 2 that the main flows are concentrated in the upper 600m layer. A very narrow northward flow between st. 7 and 9 is more than 19.10^6 $m^3.s^{-1}$ in transport (Fig.2a). There are two westward flows between st. 9 and 11 (east of Taiwan) with 11.10^6 $m^3.s^{-1}$ in transport and between st. 12 and 14 (north of Luzon) with 19.10^6 $m^3.s^{-1}$ (Fig. 2b). A narrow eastward flow of $3.10^6 m^3.s^{-1}$ in transport gets through the meridional section (Fig. 2b). So if we use the northwestward flow from st. 7 and 14 to indicate the Kuroshio, the transport is about 46.10^6 $m^3.s^{-1}$ without the leakage in between st. 14 and Luzon coast (they are about 46 km apart. The velocity near st. 14 is more than 30 $cm.s^{-1}$. Suppose the average velocity in the upper 600 m is 18 $cm.s^{-1}$ southeast of st. 14, then the transport leaked is about $6.10^6 m^3.s^{-1}$. Therefore, the volume transport of the Kuroshio east of Luzon and Taiwan is about 52.10^6 $m^3.s^{-1}$ which is about 1.5 times of the normal transport (Hu, 1989). This can be circumstantially verified by the σ_t = 26 topography (Fig. 5a).

October 1987. Through 122°40'E section (Fig. 3a) gets a westward flow between st. 18 and 21 with a volume transport of 18.10^6 $m^3.s^{-1}$, and eastward flow with $18.7.10^6 m^3.s^{-1}$ in transport including a narrow eastward flow between st. 17 and 18 with 1.5 X $10^6 m^3.s^{-1}$. Through 18°N section (Fig. 3b) take place a northward flow between st. 17 and 14 (transport is about 15.10^6 $m^3.s^{-1}$), and two bands of southward flow offshore with transport of 19.10^6 $m^3.s^-$ between st. 14 and 13 and 5.10^6 $m^3.s^{-1}$ between st. 9 and 8 in the upper layer. In consideration of the fact that st. 17 is about 50 km away from land, northwestward leakage between st.17 and Luzon might be about 5.10^6 $m^3.s^{-1}$. And then the transport of the Kuroshio is only about 20.10^6 $m^3.s^{-1}$, which is only half of the normal (Hu, 1989). Obviously, the Kuroshio is weaker during this time. A great deal of water getting through the section of 132°E (Fig. 3d-st. 5 to 1) turns right to the north in the place east of st. 1. This also can be verified by the σ_t = 26 topography (Fig. 5b).

October 1988. An obvious westward flow through the 122°40'E section (Fig. 4a) is between st. 10 and 15 mainly in the upper 600 m layer with a volume transport of about $30.10^6 m^3.s^{-1}$ and a return (eastward) flow in the upper 300 m layer exists between st. 8 and 10 with 7.10^6 $m^3.s^{-1}$ in transport. The section along 18°N (Fig. 4b) shows a strong $28.10^6 m^3.s^{-1}$ in transport and wide (about 300 km in width) northward flow, in the upper 600 m layer between st. 15 and 18 and a return flow, which is 300 km wide and with volume transport of 10.10^6 $m^3.s^{-1}$ in the upper 500 m layer in between st. 18 and 21. This year the volume transport of the Kuroshio here is about 33.10^6 $m^3.s^{-1}$ with the same estimate as above since the distance between st. 15 and Luzon is about 33 km. This tendency can be verified from figure 5c.

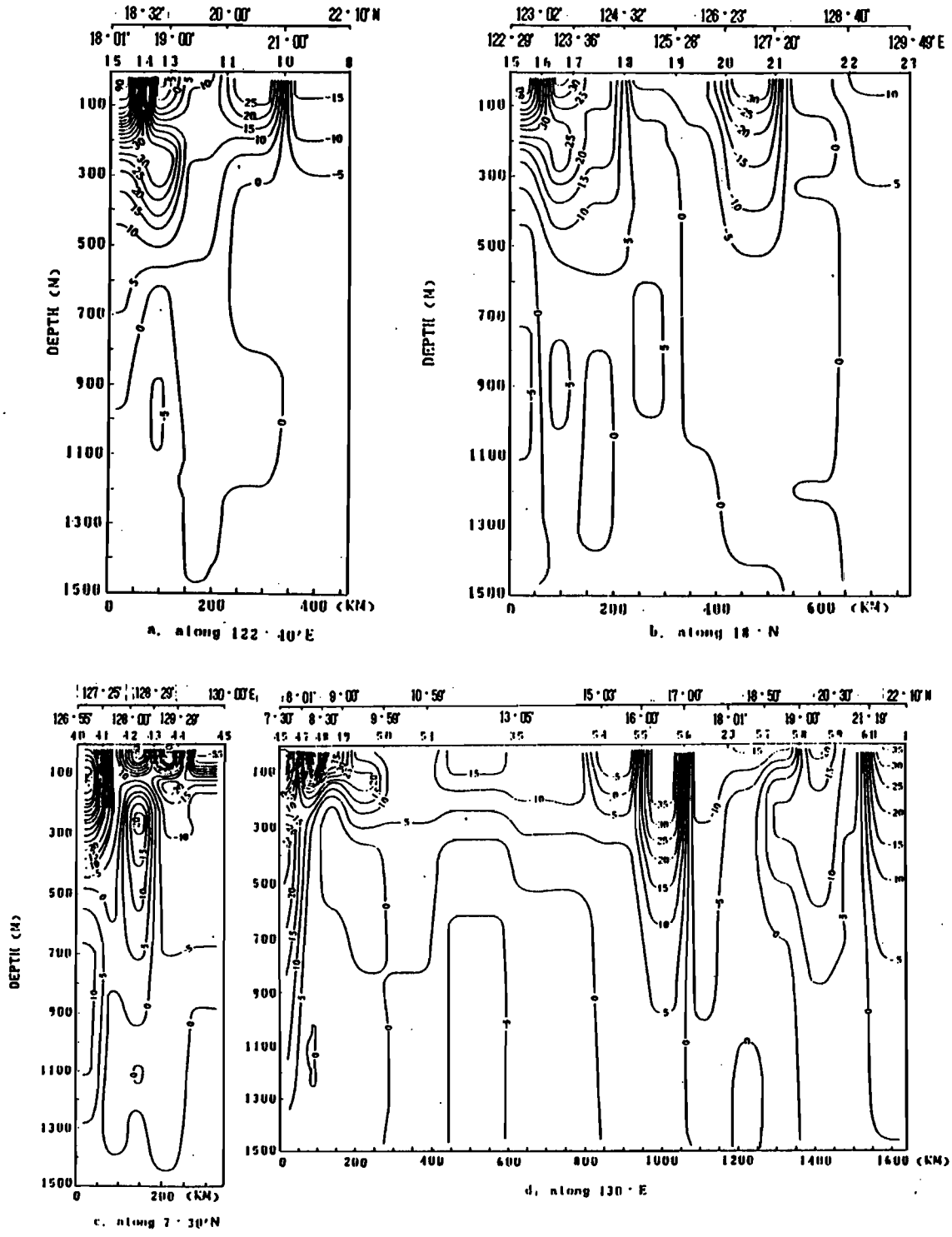

FIG.4. Velocity distribution in October 1988, detremined by inverse method. Positive (negative) flow into (out of) the paper.

In sum, the transport of the Kuroshio east of Luzon Strait is about 52, 20 and $33.10^6 m^3.s^{-1}$ for October of 1986, 1987 and 1988, respectively. Besides the difference in transport, there are still some differences from year to year. For 1986, more than half ($30.10^6 m^3.s^{-1}$) of the transport of the Kuroshio comes from offshore east of Taiwan directly and about 24.10^6 $m^3.s^{-1}$ from the northeast of Luzon. For 1987 the main feature is westward flow near Luzon and eastward flow near Taiwan and the net flux through the meridional section approaches to zero. For 1988, westward flow near Luzon is dominant through 122°40' section and a weak flow returns towards the east.

b. Velocities

1986. The maximum velocity occurs between st. 8 and 9 of about 107 $cm.s^{-1}$ (Fig. 2a). The maximum velocity near the north end of Luzon is about 37 $cm.s^{-1}$ between st. 13 and 14 (Fig. 2b). Flow with velocity greater than 5 $cm.s^{-1}$ appears in the upper 600 m layer on 122°40' section (Fig. 2b) and in the upper 900 m layer on the 22°10' section (Fig. 2a).

1987. The maximum velocity of 54 $cm.s^{-1}$ takes place between st. 19 and 18 north of Luzon (Fig. 3a). Velocity greater than 5 $cm.s^{-1}$ occurs mainly in the upper 800 m layer, which is deeper than 1986.

1988. Velocity takes its maximum of 96 $cm.s^{-1}$ is between st. 14 and 15 (Fig. 4a). Main (greater than 5 $cm.s^{-1}$) flow is concentrated in the upper 600 m layer. A striking feature different from 1986 and 1987 is the fact that there appears an undercurrent north of Luzon (Fig. 4a, b) below 500 m and centered at 900-1000 m with maximum velocity of 6-7 $cm.s^{-1}$ and transport of about 2.10^6 $m^3.s^{-1}$.

c. Eddies surrounding the Kuroshio

It is easily seen from various sections that a quite number of eddies (cyclonic and anticyclonic) take place, for instance, between st. 3 and 4, 5 and 6, 7 and 8, around st. 12, 11, 17, 19 for 1986 (Fig. 2); around st. 8, 11-12, 13, 14, 18, 20-21 for 1987 (Fig. 3); around st. 10, 18, 21 for 1988 (Fig. 4);

3.2. The Mindanao Current (MC) and the Mindanao Undercurrent (MUC)

a. The Mindanao Current

The Mindanao Current is a distinguished branch of the Western Boundary Current east of the Philippines. According to Nitani (1970) the MC east of Mindanao is stronger than the Kuroshio east of Luzon, and its volume transport is about 40.10^6 $m^3.s^{-1}$, while the Kuroshio is only 30.10^6 $m^3.s^{-1}$.

In the present study the MC is examined with a section along 7°30' from a station (126°55'E), which is about 37 km away from Mindanao coast, to a station (130°E) (Figs. 3c and 4c). This section was occupied in October of 1987 and 1988. In what follows, for convenience, it is described yearly first.

1987 (Fig. 3c). The MC is restricted within about 200 km from the coast of Mindanao in the upper 600 m layer (velocity greater than 5 $cm.s^{-1}$). There are two cores between st. 48 and 49 (maximum velocity-about 77 $cm.s^{-1}$) and between st. 44 and 45 (maximum velocity about 25 $cm.s^{-1}$). The calculated southward volume transport from st. 49 to 44 is about 28.10^6 $m^3.s^{-1}$. Suppose the leakage between st. 49 and land can be estimated with average southward velocity of 30 $cm.s^{-1}$, judging from Fig. 3c, in the upper 500 m layer, which accounts for about 6.10^6 $m^3.s^{-1}$. So the total volume transport of the MC in a broad sense should be abut 34.10^6 $m^3.s^{-1}$.

1988 (Fig. 4c). As Cui and Hu (1989) stated, the MC is mainly in the upper 600 m layer with three cores: (1) The strongest is near the coast in the upper 500 m layer with maximum velocity of about 80 $cm.s^{-1}$ located at 120 m. Its transport is approximately 15.10^6 $m^3 s^{-1}$. (2) Adjacent to the above is a shallow one in the upper 150 m with 4.10^6 $m^3.s^{-1}$ in transport and 50 $cm.s^{-1}$ in maximum velocity in between st. 41 and 43 (127°45'

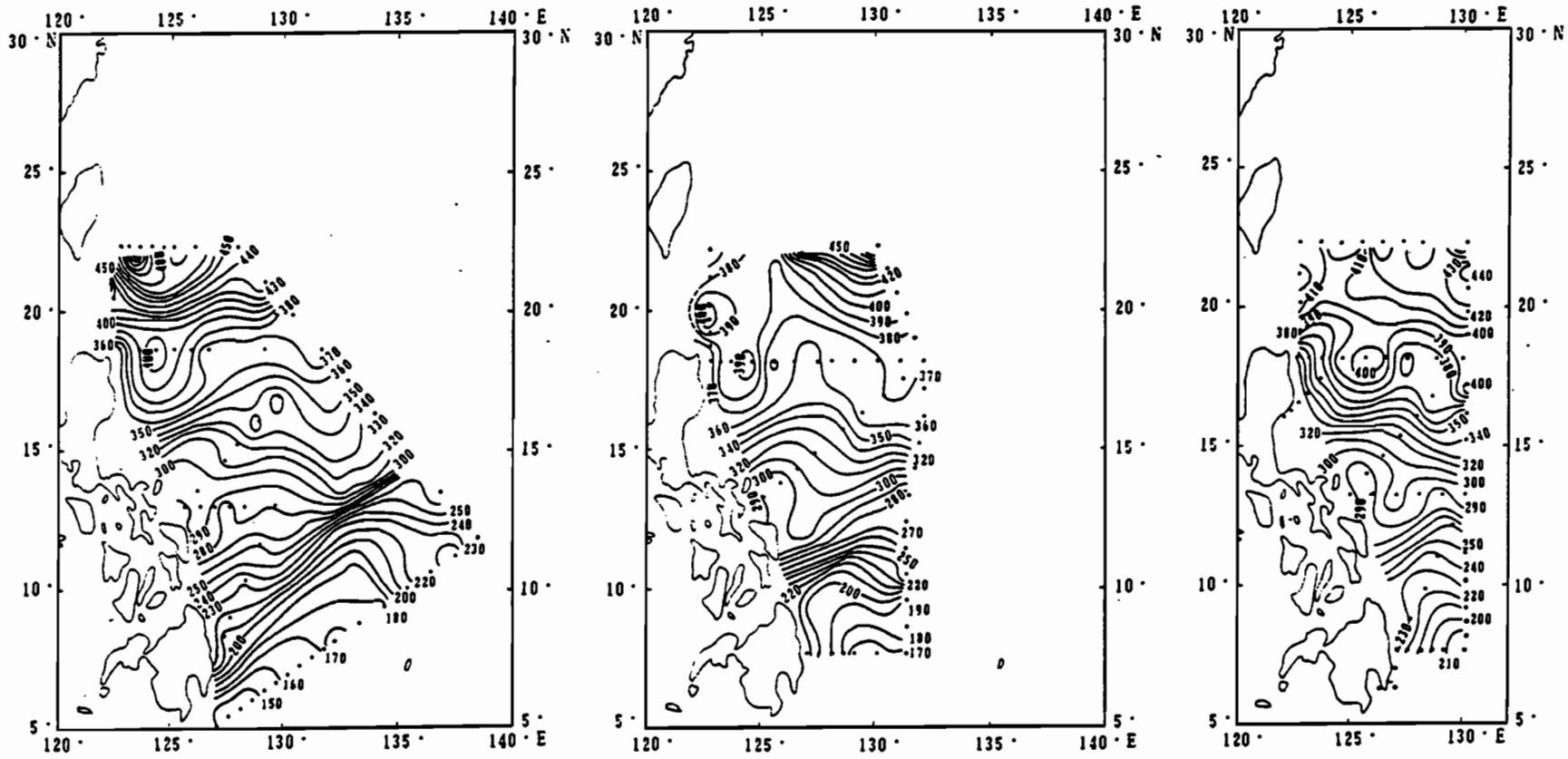

FIG.5. Sigma-t topography in October 1986 (left), October 1987 (middle), and October 1988 (right).

- 128°30'E). (3) Separated by a surface northward flow between st. 43 and 44 (128°30' - 129°E), is a thicker one reaching 1000 m in between st. 43 and 45 (128°30' - 130°E). Its transport is about 12.10^6 $m^3.s^{-1}$ with maximum velocity of about 56 $cm.s^{-1}$. We also calculated the leakage between st. 40 and land with a box consisting of st. 40, 80, 81 and 82, which should be about 5.10^6 $m^3.s^{-1}$. So the total MC volume transport is approximately 36.10^6 $m^3.s^{-1}$.

b. The Mindanao Undercurrent (MUC)

The MUC is definitely revealed on the section of 7°30'N (Figs. 3c and 4c). It seems multicore, penetrating into the MC, which should be considered as a wide flow spanning from the coast of Mindanao to about 130°E since generally the Mindanao eddy is centered at about 130°E.

1987 (Fig.3c). There are two northward quasi-subsurface flow cores, which are separated by an extremely narrow southward flow. The two subsurface flows look like twin with almost the same transport of 9.10^6 $m^3.s^{-1}$ extending from about 200 m to 1200 m with main core from 300 to 1000 m. However, the one closer to the coast is centered at about 500 m with 75 km in width mainly between 127°25' to 128°05'E and another is centered at about 350 m, occupying the whole column with main core from 200 to 900 m and 175 km wide. It seems that the northward flow between st. 43 and 44 (130°-131°E) and the southward flow between 129° and 130° E form an eddy and upwelling around st. 44 (130°E).

1988 (Fig. 4c). There are three northward cores. (1) A protruding northward subsurface current, about 85 km wide is in between 127°45' to 128°30'E with maximum velocity of 22 $cm.s^{-1}$ at 300 m level and thickness of about 650 m (150-800 m) and volume transport of about 5.10^6 $m^3.s^{-1}$. (2) Connected with the above is the nearshore subsurface northward flow below 500 m within less than 100 km from the coast of Mindanao. The core is located at 750 m with velocity of 12 $cm.s^{-1}$ and volume transport of approximately 3.10^6 $m^3.s^{-1}$. (3) A surface northward flow between st. 43 and 44 in the upper 100 m layer with maximum velocity of 39 $cm.s^{-1}$ and a little transport of $1.5.10^6$ $m^3.s^{-1}$.

It seems that the MUC in 1987 is different from and stronger than 1988. But it any case there are some things in common, for example, northward current (MUC) does exist and the three cores look like in somewhat connected.

3.3. The North Equatorial Current (NEC)

a. Volume transport

For 1986 dynamical method is used to estimate transport between st. 56 and 71, which is about 41.10^6 $m^3.s^{-1}$, and then plus 17.10^6 $m^3.s^{-1}$ from inversion for st. 1-72 (Fig. 1a), we have 58.10^6 $m^3.s^{-1}$ for NEC transport through around 130°E from 7°30' to 22°10'N. For 1987 the transport of the NEC, calculated from inversion, is 61.10^6 $m^3.s^{-1}$, and about half of which is transported to the north, west of st. 1 (Fig. 3d). For 1988, $45.10^6 m^3.s^{-1}$ is transported westward through section of 130° E from 7°30' to 22° 10'N (Fig. 4d) with almost no northward transport through section of 22° 10'N.

b. Flow pattern

Since there is no meridional section for 1986 around 130° E, comparison is meaningless. For 1987 there are three strong westward flows between st. 40 and 39, 38 and 37, 3 and 1, which constitute the main body of the NEC. And also there are a few bands of eastward flow (Fig.3d): (1) between st. 43 and 41 (7°30'-8°27'N) below 300 m; (2) 7.10^6 $m^3.s^{-1}$ mainly between st. 39 and 38 (10°20'-11°17'N) with maximum velocity 23 $cm.s^{-1}$; (3) 3.10^6 $m^3.s^{-1}$ between st 37 to 36 (12°13'-13°10'N) in the upper 400 m with maximum velocity 14 $cm.s^{-1}$; and (4) 16.10^6 $m^3.s^{-1}$ between st. 33 to 5 (16°-18°50'N) in the upper 500 m and between st. 36 to 3 (13°10'-20°30'N) below 500 m. It seems there

are three swift eastward flows near 11°, 12°30' and 16°30'N in the upper 400 m layer. In the lower layer below 600 m there exists wide sluggish eastward flow. In sum, in the upper layer (0-600 m) transport is $69.10^6 m^3.s^{-1}$ westward; in the lower layer (600-1500 m-) transport is $7.10^6 m^3.s^{-1}$ eastward.

For 1988, westward and eastward flows are alternate (Fig. 4d). There are two swift westward flows : one near 8°N with maximum velocity of about 122 cm/s and another near 16°30'N with maximum velocity of 37 $cm.s^{-1}$. Also there appear a few bands of eastward flow : one from 10° to 15°N in the lower layer (500-1500m) with transport of about $16.10^6 m^3.s^{-1}$, the second from 17° - 20°N from surface to 1500 m with volume transport of $15.10^6 m^3.s^{-1}$ and maximum velocity of about 16 $cm.s^{-1}$ at surface near 18°30'/N. As a whole, transport in the upper layer (0-600 m) is - $49.10^6 m^3.s^{-1}$ westward and in the lower layer (600x1500m) is - $5.10^6 m^3.s^{-1}$ eastward.

Summarizing, the NEC consists of a quite number of zonal flows, which are alternate and, as far as volume transport is concerned in the upper layer (0-600 m), it is westward and in the lower layer (600-1500 m) is eastward, which implies the undercurrents take place.

3.4. Dynamical aspects of the PWBC

a. Dynamical structure of the circulation in the far-western Pacific

As is know, the NEC is divided into two branches offshore east of the Philippines: the Kuroshio and the Mindanao Current. That is true for the surface layer. What happens for the lower layer?

From the velocity section along 7°30'N of 1987 and 1988 (figs. 3c and 4c) prominent northward undercurrent (MUC) takes place with considerable transport. Again, from the meridional section of 132°E (1987) or 130°E (1988), eastward flow in the lower layer is obvious.

Now, let us examine the situation off Luzon coast. First of all, from the section of 122°40'E of 1988 (Fig. 3a) an eastward subsurface flow can be seen near the coast centered at 1000 m with $2.10^6 m^3.s^{-1}$ in transport and 6 $cm.s^{-1}$ in maximum velocity. From the section of 18°N a southward subsurface flow can be found centered at 900 m with volume transport of $2.5.10^6 m^3.s^{-1}$ and a maximum velocity of 7 $cm.s^{-1}$.

Judging from the above, the dynamical structure of the circulation in the far-Pacific seems the following. In the surface layer, the NEC is divided into the Kuroshio and the Mindanao Current (MC) . In the lower layer, the Mindanao Undercurrent (MUC) flowing towards the north and the subsurface flow from the north to the south converge somewhere around 15°N east of Luzon and Samar causing eastward flow through 130°E section, which is consistent with the calculated transport through the section of 130°E or 132°E.

b. Possible role of the PWBC in climate

* The role of the Kuroshio in climate of southeast China.

The ocean plays a central role in the variability of global climate and appears to be as important as the atmosphere in the global transport and redistribution of heat. Poleward heat transport of the PWBC in a narrow band is the main channel of heat transport in the world ocean. On the other hand, the effect of the ocean on climate can be classified into two categories : remote effect and local effect. The first means that the ocean affects general atmospheric circulation, which furthermore makes effect upon climate in some area. The second means that the effect is more direct, for example, the area near coastal upwelling or cold currents will be colder than other places at the same latitudes. In terms of local response, East Asia, especially southeast China should be heavily influenced by the northward - flowing PWBC (Hu, 1989).

* Possible role of the Mindanao Current in formation and maintenance of the warm pool in the western Pacific

Surface warm water is driven by the trade wind to the west and piled up in the equatorial western Pacific. Since the western boundary near the equator, such as the Papua New Guinea and Indonesia coast is more zonal (of acute angle with the equator) rather than meridional, the following question will naturally turn out. How can the warm water stay near the equator of how can the warm pool be maintained? It is speculated that the Mindanao Current and continuous North Equatorial Countercurrent (NECC) play an important role as if they acted as solid boundary preventing the warm water to extend to the north. So MC and NECC are important for study of the warm pool.

Acknowledgment. This study is supported by the State Commission for Science and Technology of China, Academia Sinica and Natural Science Foundation of China. This support is gratefully acknowledged. Also we would like to thank all who worked on board of R/V Science 1 for gathering the CTD data. Finally, we are grateful to Shao-ying Bai, who worked very hard and carefully for the figures and to Ying Hu, who timely typed the manuscript.

REFERENCES

Cui, M. and D. Hu, 1989: Inversion calculation of the western boundary current in the Pacific during October 1988. *Submitted to Chin. J. Oceanol. Limnol.*

Hu, D., 1989: A thought on the role of western Pacific ocean circulation in climate change in southeast China. *J. Oceanol. Limnol.*, **7**, (1) : 93-94.

Kishindo, S., 1931: On the method of ocean current observation now used by the Hydrographical Department and some results obtained. Part 3 (in Japanese). *Hydr. Bull.*, **109**, 483-503.

Nitani, H., 1970: Oceanographic conditions in the sea east of the Philippines and Luzon Strait in summers of 1965 and 1966. In: *The Kuroshio* - A symposium on the Japan current (edited by J. C. Marr), East-West Center Press, Honolulu, 213-232.

Nitani, H., 1972: Beginning of the Kuroshio. In: *Kuroshio-its physical aspects. Tokyo Univ. Press*, 129-163.

Sverdrup, H.U., M.W., Johnson and R.H. Fleming, 1942: The Oceans - their physics, chemistry and general biology. Prentice-House, New-York, 1087 pp.

Wunsch, C., 1978: The north Atlantic circulation west of 50°W determined by inverse methods. *Space Phys.*, **16**, 582-620.

Wyrtki, K., 1961: Physical oceanography of the Southeast Asian Waters. Scientific results of marine investigations of the South China Sea and Gulf of Thailand, 1959-1961. *Naga report*, **2**, 195 pp.

Observations of the Low-latitude Western Boundary Circulation in the Pacific during WEPOCS III

Peter HACKER[1], Eric FIRING[2], Roger LUKAS[2],

Philipp L. RICHARDSON[3] and Curtis A. COLLINS[4]

[1] *Texas A&M University, College Station, Texas - U.S.A.*

[2] *University of Hawaii, Manoa, Honolulu, Hawaii -U.S.A.*

[3] *Woods Hole Oceanographic Institution, Woods Hole, Massachusetts - U.S.A.*

[4] *Naval Postgraduate School, Monterey, California - U.S.A.*

Introduction

In 1985, US and Australian investigators began a series of cruises to explore the hydrography and currents of the western equatorial Pacific Ocean. The first two sets of cruises in this Western Equatorial Pacific Ocean Circulation Study (WEPOCS) took place in July-August 1985 (WEPOCS I) and January-February 1986 (WEPOCS II; Lindstrom et al., 1987). They were designed to study the ocean response to the monsoon in the region from 143°E to 155°E, and to determine the source waters of the Equatorial Undercurrent (Tsuchiya et al., 1989). In the US part of the third WEPOCS cruise sequence (WEPOCS III), the focus of attention shifted further west, to the region from 124°E to 143°E, and north to the Mindanao Current and the North Equatorial Countercurrent (NECC). The South Equatorial Current (SEC) was also of interest as a source of water for the NECC.

The US WEPOCS III cruises, during June and July 1988, included the launch of satellite-tracked drifters, continuous acoustic Doppler current profiling (ADCP) along the entire cruise track, and CTD stations with water samples at close intervals along much of the cruise track. In this paper we will show the changing structure of the Mindanao Current as it flows south along the coast of the Philippines, the signature of the Mindanao Current in the salinity field, and the structure of the Halmahera Eddy and the beginning of the NECC (Figure 1). Currents along 141.5°E (and the characteristics of the ADCP data)

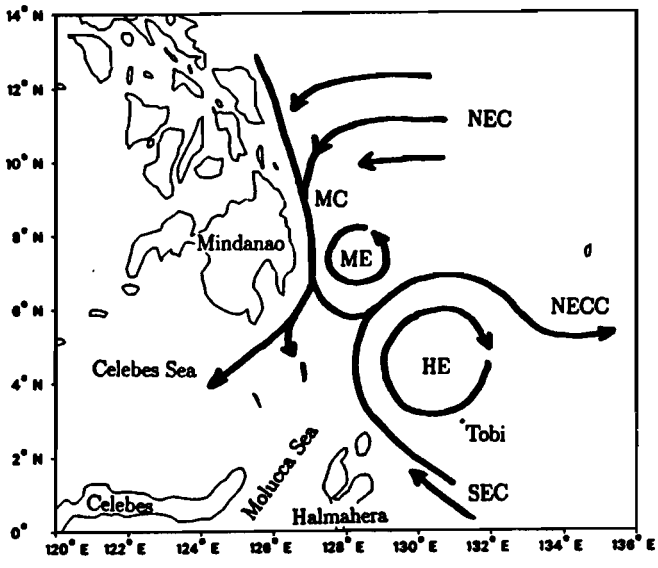

Figure 1: Currents of the low-latitude western boundary region during WEPOCS III: the North Equatorial Current (NEC), the Mindanao Current, the Mindanao Eddy (ME), the South Equatorial Current (SEC), the North Equatorial Countercurrent (NECC), and the Halmahera Eddy (HE).

ORSTOM
CENTRE DOCUMENTATION
Montpellier

F 30202

are discussed by Firing and Jiang (1989). Upper-ocean water properties and air-sea interaction during WEPOCS III are presented by Lukas (1989).

Drifter trajectories

Thirty-five satellite-tracked buoys drogued at 15 m were launched from the R/V Moana Wave during WEPOCS III. During the first three months (July–September) they provide for the first time a quasi-synoptic Lagrangian picture of the surface flow in the region (Figure 2). One group of drifters followed the SEC northwestward along the New Guinea coast, turned around the quasi-stationary (anticyclonic) Halmahera Eddy centered near 4°N 130°E, and proceeded eastward in the NECC. Four buoys made a complete circuit around the Halmahera Eddy. Buoys in the NECC meandered with meridional displacements of 300 km and wavelengths of 600–700 km. Of eleven buoys in the Mindanao Current, two continued through the Makassar Strait, five turned eastward into the NECC, joining those that had retroflected from the SEC, and the rest were grounded or stolen. Three buoys looped cyclonically around the Mindanao Eddy centered near 7.5°N 129°E.

Averaging all July-September drifter velocity measurements in 1° squares and lightly smoothing the gridded values (Figure 3), we find a remarkable similarity to the climatological mean ship drifts (Figure 4) averaged from May through November and smoothed in the same way. (Smoothing was done with the diffusion equation. An anomalous value was reduced by 83% relative to the background field, with 60% of the reduction going to the 8 nearest neighbors.) The Halmahera Eddy is not seen as a closed circulation in the climatology, as it is in the July 1988 drifter tracks, but it is indicated by a southward dip in the NECC at about 135°E. Note also the sharp northward bump in the NECC between 135°E and 140°E in both the drifter measurements (Figure 3) and the ship drifts (Figure 4). The similarity between the drifter tracks and climatology suggests that the WEPOCS III observations were not atypical, despite the cold event that was underway (Kousky, 1989).

The tangled appearance of the 3-month drifter trajectories, with a multitude of crossing paths (Figure 2), illustrates the temporal variability of the flow. For example, the 3 drifters launched in the region of the Mindanao Eddy initially travelled eastward. In early August they reversed course and during that month each made slightly more than one circuit around the eddy. During September their path was predominantly eastward. It appears that the eddy was present (at least in that location) only during August. Similarly, all the circuits around the Halmahera eddy occurred in July; in August, buoys in the NECC proceeded eastward with only a moderate southward dip near 132°E, which previously had been the east side of the eddy.

Currents as measured by the ADCP

The dominant features in the map of upper-ocean ADCP currents are the Mindanao Current and the Halmahera Eddy (Figure 5). The Mindanao Current appears to begin near the northern limit of the measurements, 13.5°N, and accelerates southward along the Philippine coast until it separates at the southern tip of Mindanao and extends as a jet into the Celebes Sea. There is a suggestion of an eddy just west of the separation point, but the cruise tracks there did not extend far enough from the coast to resolve this circulation. Along 130°E, between 12°N and 10°N, the North Equatorial Current (NEC) can be seen flowing west to supply the Mindanao Current. The southern limit of the NEC is not resolved by the WEPOCS III cruise track; it appears to have been between 10°N and 8°N during this cruise. The Mindanao Eddy, distinguished by closed loops in the drifter trajectories during August (Figure 2), is not evident in the ADCP measurements, which were made in July.

East-southeast of Mindanao and north-northeast of Halmahera is the Halmahera Eddy. There is little indication in this near-surface current field of eastward flow in the NECC. Instead, it appears that water enters the Halmahera Eddy north of Halmahera, circulates anticyclonically around the eddy, and exits southward near 133°E on the southeast side of the eddy. This picture is confirmed by the drifter trajectories during July. The partition of NECC source waters among three possible sources—the SEC, the Mindanao Current via the Celebes Sea, and the Molucca Strait (in which water may also come from the Mindanao Current via the Makassar Strait)—is not at all clear from the ADCP currents and the drifter tracks, and remains to be studied through isopycnal analysis.

In the mid-thermocline, 200-250m (Figure 5), the Mindanao Current looks much as it does near the surface apart from a reduction in speed by roughly a half. Elsewhere the mid-thermocline currents differ substantially from the near-surface currents. There is little westward flow in the thermocline that can be identified as the NEC, and little indication of anticyclonic circulation in the region of the Halmahera

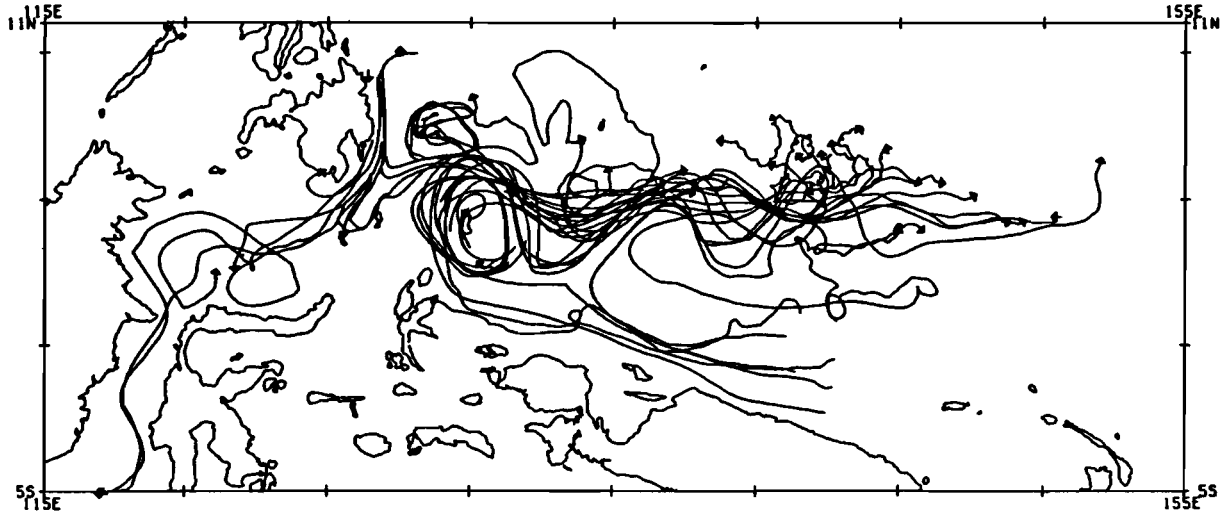

Figure 2: Trajectories of the WEPOCS III drifters, July–September.

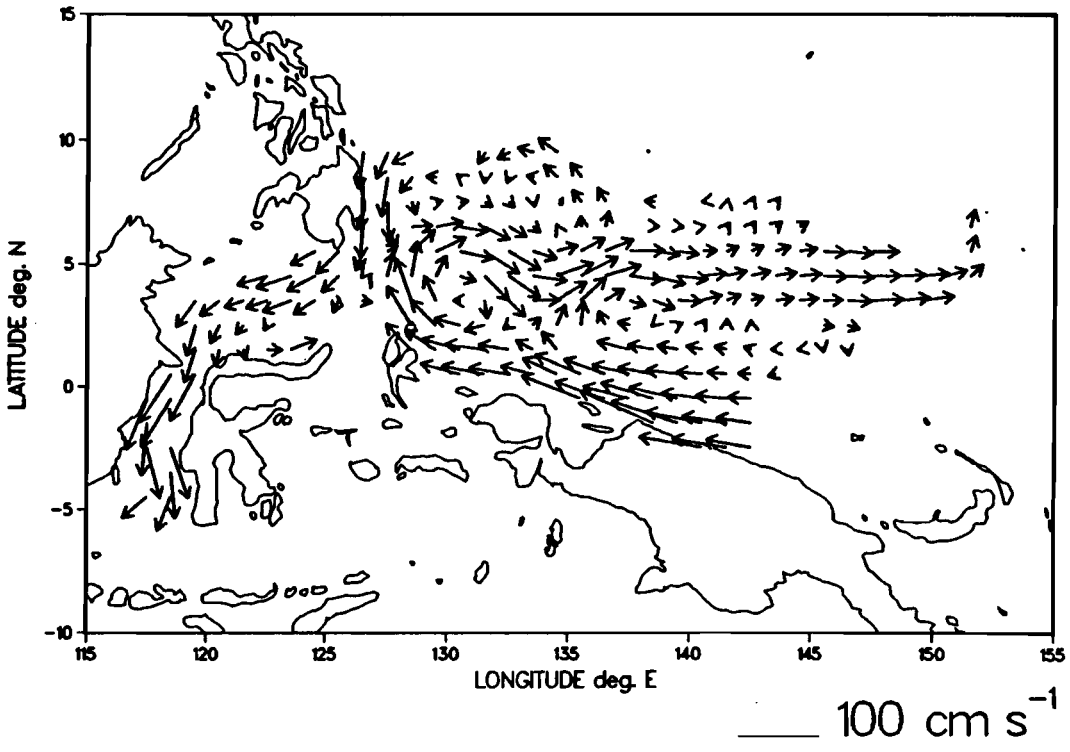

Figure 3: Drifter velocity vectors averaged by 1° squares, July–September 1988. Gridded data have been smoothed (see text).

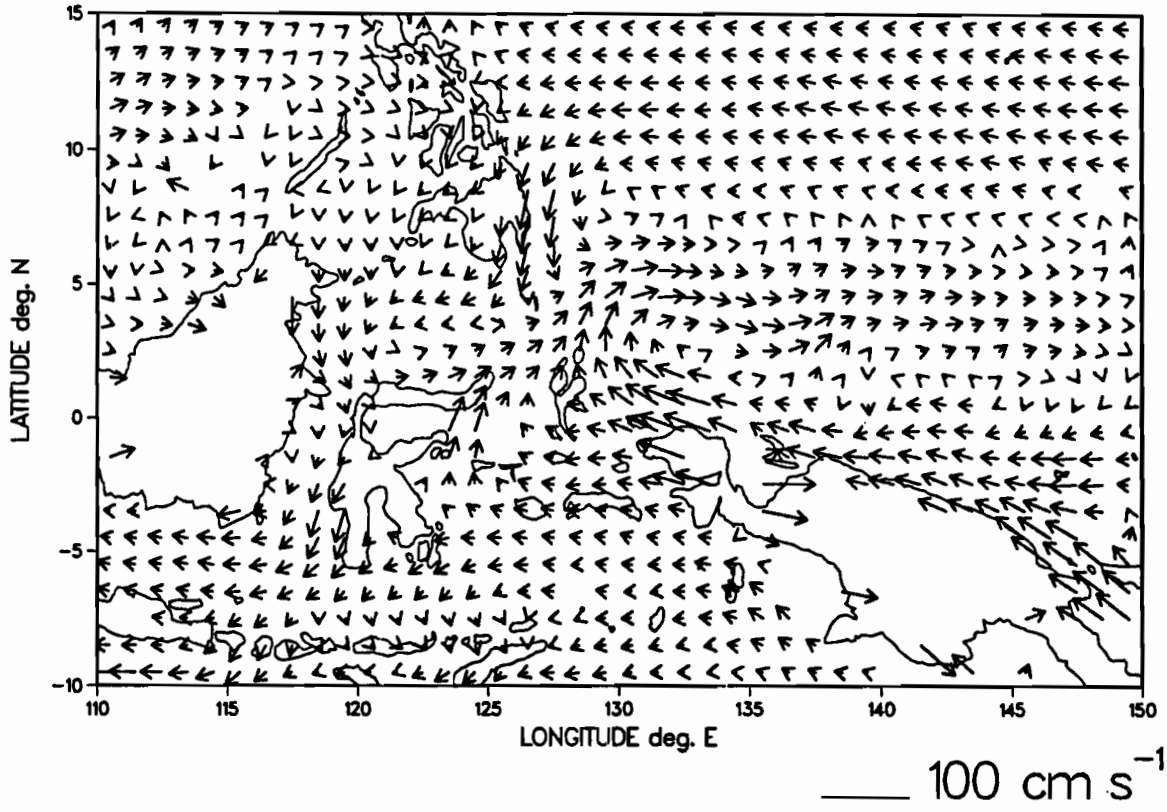

Figure 4: Historical monthly-mean ship-drift observations averaged from May through November in 1° squares and smoothed (see text).

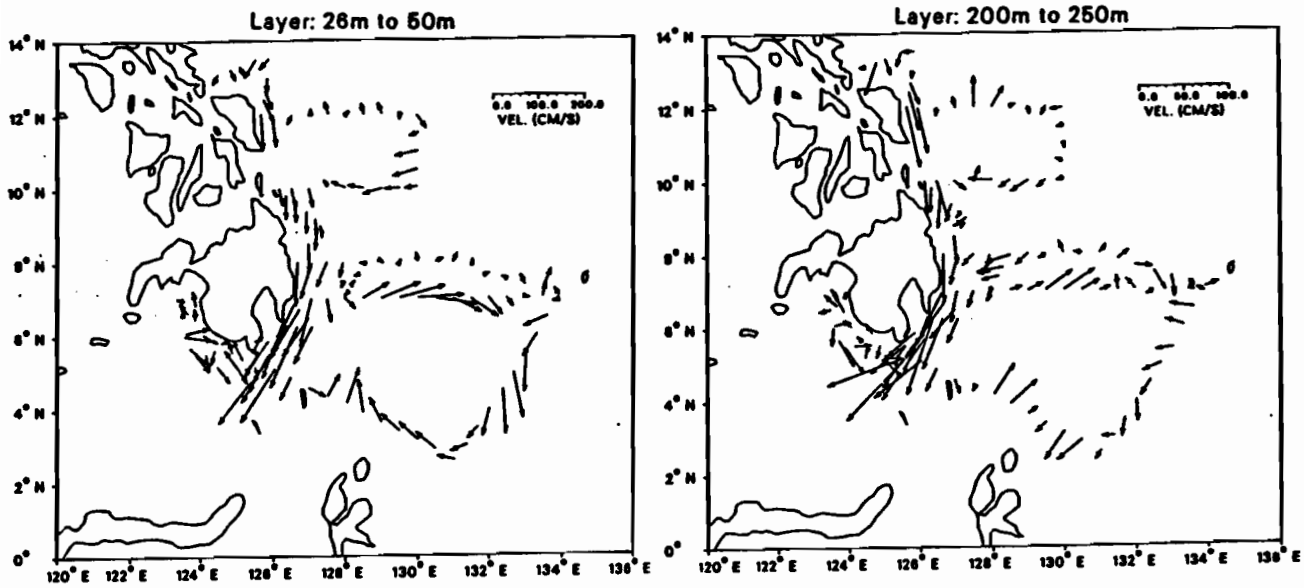

Figure 5: Currents measured by the ADCP, averaged from 25–50 m (left) and from 200–250 m (right). Note the change in velocity scale.

Eddy. The field of motion may include several unresolved eddies; if so, it appears that the surface eddies and the subsurface eddies are not coincident.

The downstream changes in the Mindanao Current can be seen more clearly in the sequence of zonal sections of meridional velocity component (Figure 6). All sections begin within 1 km of the Philippine coast. From 12°N to the southernmost section (Tobi–Mindanao), the vertical shear in the Mindanao Current tended to increase, and the current became increasingly intensified near the surface. The current was nearly uniform over the top 300 m at 12°N, where the maximum speed was about 80 cm/s; at the southernmost section the current increased from 30 cm/s at 300 m to 110 cm/s near the surface. In some of the sections, most notably at 7°N and 8°N, the maximum southward velocity component occurred in a subsurface core near 80 m. This shear reversal may have been caused by strong transient southwest winds retarding the surface current (Lukas, 1989). Offshore of the Mindanao Current, northward currents were found in all sections. The structure of the northward flow varied from section to section, but there appear to be two components: a near-surface current, and a deeper one, with its core near or below the maximum depth range of the ADCP (about 400 m). This subsurface northward current has been identified also in geostrophic sections by Hu and Cui (1989), who have named it the Mindanao Undercurrent.

Geostrophic currents and tracers

The geostrophic current section at 10°N (Figure 7) shows that the Mindanao Undercurrent there has a core depth of about 350 m, and a speed (relative to 1000 dbar) exceeding 20 cm/s, in agreement with the ADCP (absolute) velocity measurement. The undercurrent appears to extend over a large depth range; its full extent cannot be determined from these geostrophic calculations.

The geostrophic current section also agrees with the ADCP section in that both show a strong Mindanao Current, but otherwise the two estimates of current are surprisingly different. The geostrophic estimate of maximum southward component in the Mindanao Current is 165 cm/s, compared with only 60 cm/s from the ADCP. The northward surface current found above the Mindanao Undercurrent in the ADCP section is nearly absent in the geostrophic section. The geostrophic section shows two surface currents with speeds exceeding 40 cm/s—a southward current near 128°E and a northward current near 129°E—which have no obvious counterparts in the ADCP section. These differences between the geostrophic and ADCP current estimates appear to be real, not due to any deficiencies in the measurements, but they are not yet understood.

The salinity field at 10°N (Figure 7) shows two cores near the Mindanao coast that can be used to trace the Mindanao Current. A high-salinity core (>34.9 psu) at 390 cl/ton (about 100 m depth) next to the coast is separated by lower salinity from a second high-salinity core offshore. A low-salinity core (<34.4 psu) is found next to the coast at 150 cl/ton (about 300 m). Both of these cores can be traced along the Mindanao coast from 14°N to the southernmost section (Figure 8).

Transport

Estimates of Mindanao Current transport have ranged from 8 to 40 Sv (Table 1; Lukas, 1988), with the highest resulting from a calculation of Sverdrup transport (Kessler and Taft, 1987). Our estimates for 0–300 m from WEPOCS III, 10–24 Sv, are well within this historical range. Although ADCP and geostrophic transport estimates both increase downstream, the geostrophic estimates are systematically higher than the ADCP integrals on this cruise. The reasons for this difference, and whether it occurs in other observations such as those of the US/PRC Bilateral Air-Sea Interaction Program, remain to be investigated.

Conclusions

Although our analysis of the WEPOCS III data is at an early stage, we can draw some qualitative conclusions:

- Currents during the cruise, June–July 1988, appear to have been normal in spite of the ongoing cold event.
- A strong, narrow Mindanao Current flows southward very close to the coast as far as the southern tip of Mindanao, where it separates and continues as a jet into the Celebes Sea.
- Part of the Mindanao Current turns in the Celebes Sea to feed the NECC. A second major source of the NECC is the SEC, which curves around the Halmahera Eddy. There may also be a contribution from the Molucca Sea, which may in turn receive water from the Mindanao Current

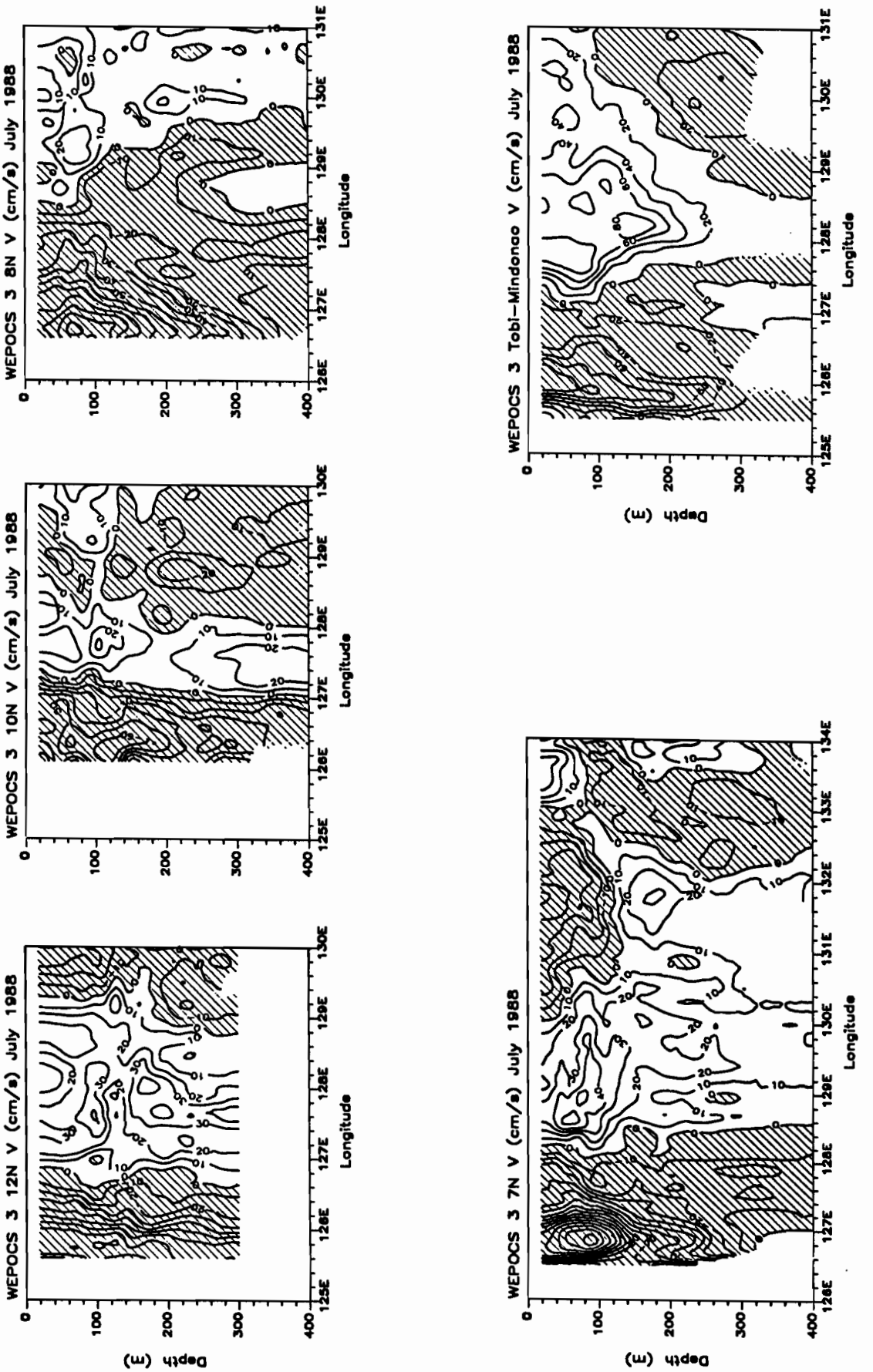

Figure 6: Meridional component of the Mindanao Current from 12°N to the southernmost section, which runs east-southeast from the southern tip of Mindanao at 5.5°N to the small island of Tobi at 2.5°N.

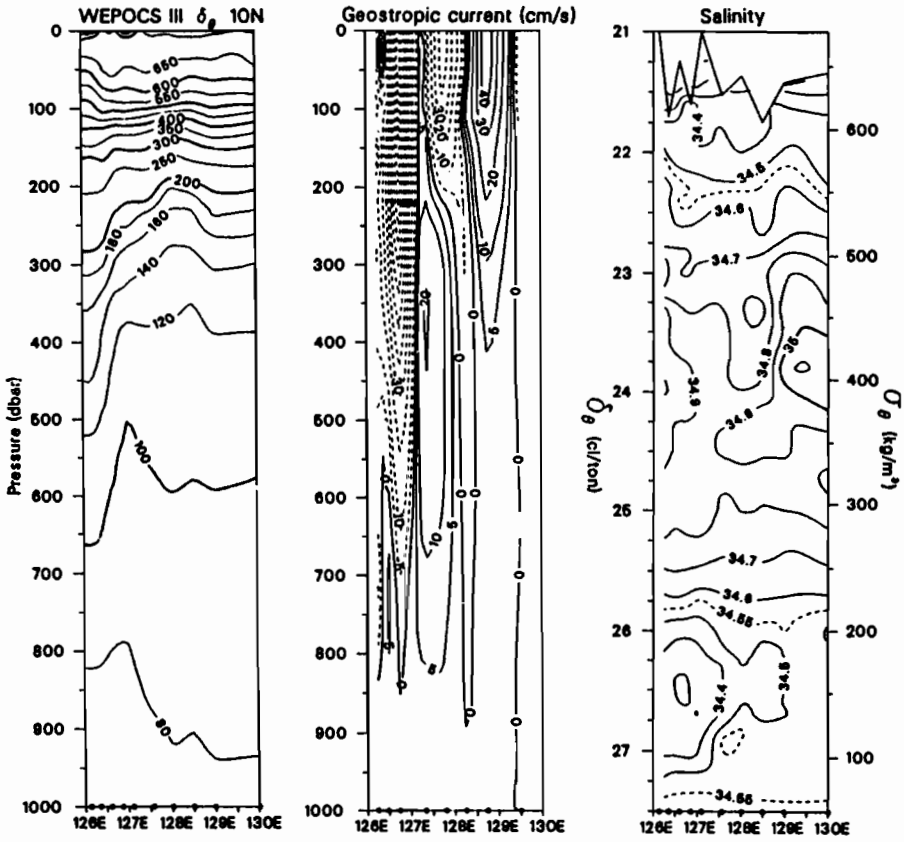

Figure 7: Isopycnals (left) and meridional component of geostrophic velocity (middle) as functions of depth along 10°N; and salinity (right) as a function of δ_θ. Note the high-salinity core next to the Mindanao Coast at 390 cl/ton, and the low-salinity core at 150 cl/ton.

Table 1: Mindanao Current Transport Estimates

Source	Transport	Notes
Wyrtki (1956, 1961)	8–12 Sv	upper 200 m only, friction included
Wyrtki (1961)	25 Sv	0–1000 dbar, relative to 1250, friction included
Masuzawa (1969)	13, 19, 26, 29 Sv	relative to 600 dbar
Kendall (1969)	24 Sv	historical data, geostrophy and mass balance
Cannon (1970)	18, 31 Sv	relative to 1000 dbar; rapid change in space/time
Nitani (1972)	24 Sv	relative to 1200 dbar; plus 15 Sv recirculating in Mindanao Eddy
Kessler and Taft (1987)	24–40 Sv	WBC transport needed to close Sverdrup circulation
Toole *et al.* (1988)	17–18 Sv	transport for T>12°C, relative to 1000 dbar
WEPOCS III	10 Sv at 10°N	ADCP, upper 300 m
	22 Sv at 5°N	
	18 Sv at 10°N	geostrophy, upper 300 m relative to 1000 dbar
	24 Sv at 7°N	

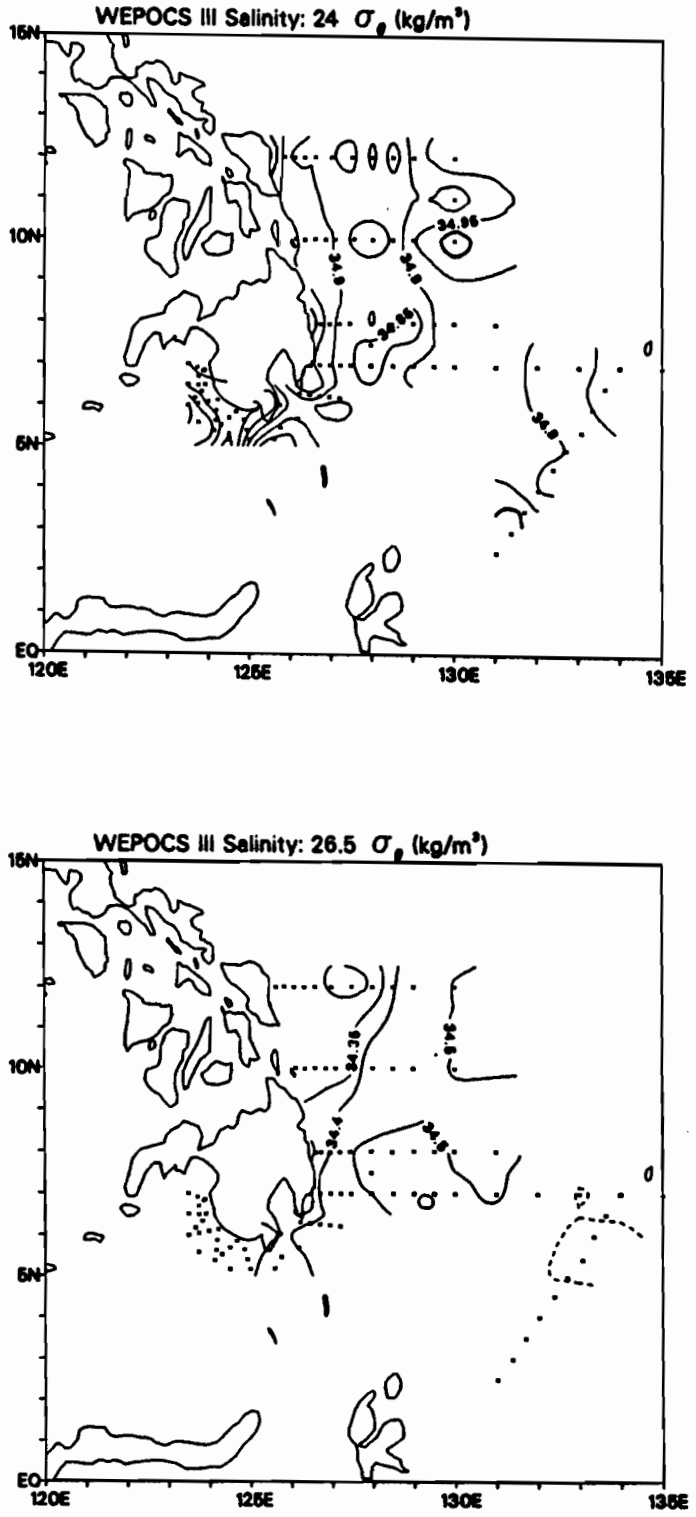

Figure 8: Salinity on the 24 (390 cl/ton; top) and 26.5 (150 cl/ton; bottom) σ_t surfaces. The Mindanao Current carries southward a high salinity core at 24 σ_t and a low salinity core at 26.5 σ_t.

via the Makassar Strait, but this is not resolved by the direct current measurements alone.

- The transport of the Mindanao Current increases rapidly downstream from 10°N to 6°N, as does the vertical shear in the upper 300 m.
- The Mindanao Current carries a high salinity core at 24 σ_t and a low salinity core at 26.5 σ_t.
- Geostrophic and ADCP current estimates in the Mindanao Current can differ by a factor of two.

More detailed analysis of the WEPOCS III data set is planned. In particular, we expect that the combination of isopycnal analysis with the direct current measurements and geostrophic calculations will clarify our picture of the circulation.

Acknowledgements

This work is supported by the National Science Foundation under grants OCE-8716509 and OCE-8716510.

References

Cannon, G. A., 1970: Characteristics of waters east of Mindanao, Philippine Islands, August 1965, in *The Kuroshio, A Symposium on the Japan Current*, edited by J. C. Marr, 205–211, East-West Center Press, Honolulu, Hawaii.

Firing, E. and S.-N. Jiang, 1989: Variable currents in the western Pacific, measured during the US/PRC Bilateral Air-Sea Interaction Program and WEPOCS, *Proceedings of the Western Pacific International Meeting and Workshop on TOGA-COARE*, ORSTOM, Noumea, New Caledonia (this volume).

Hu, D.-X. and M.-C. Cui, 1989: The western boundary current in the far-western Pacific Ocean, *Proceedings of the Western Pacific International Meeting and Workshop on TOGA-COARE*, ORSTOM, Noumea, New Caledonia (this volume).

Kendall, T. R., 1969: Net transports in the western equatorial Pacific Ocean. *J. Geophys. Res., 74*, 1388–1396.

Kessler, W. S. and B. A. Taft, 1987: Dynamic heights and zonal geostrophic transports in the central tropical Pacific during 1979–1984. *J. Phys. Oceanogr., 17*, 97–122.

Kousky, V. E., 1989: The global climate for September–November 1988: high Southern Oscillation Index and cold episode characteristics continued. *J. Climate, 2*, 173–192.

Lukas, R., 1988: Interannual fluctuations of the Mindanao Current inferred from sea level. *J. Geophys. Res., 93*, 6744–6748.

Lukas, R., 1989: Observations of air-sea interaction in the western Pacific warm pool during WEPOCS, *Proceedings of the Western Pacific International Meeting and Workshop on TOGA-COARE*, ORSTOM, Noumea, New Caledonia (this volume).

Masuzawa, J., 1969: The Mindanao Current. *Bull. Jpn. Soc. Fish. Oceanogr.*, spec. no. (Prof. Uda's Commem. Pap.), 99–104.

Nitani, H., 1972: Beginning of the Kuroshio, in *Kuroshio: Physical Aspects of the Japan Current*, edited by H. Stommel and K. Yoshida, 129–163, University of Washington Press, Seattle.

Toole, J. M., E. Zou, and R. C. Millard, 1988: On the circulation of the upper waters in the western equatorial Pacific Ocean, *Deep Sea Res., 35*, 1451–1482.

Wyrtki, K., 1956: The subtropical lower water between the Philippines and Irian (New Guinea), *Mar. Res. Indonesia, 1*, 21–52.

Wyrtki, K., 1961: Physical oceanography of the southeast Asian waters, *Naga Rep., 2*, 195 pp.

Comparison of Observations and Numerical Model Results in the Indonesian Throughflow Region

Stephen P. MURRAY[1], John KINDLE[2],
Dharma ARIEF[1] and Harley HURLBURT[2]

[1]*Coastal Studies Institute and Department of Geology and Geophysics, Louisiana State University, Baton Rouge, Louisiana 70803 - U.S.A.*
[2]*Naval Oceanographic Research and Development Activity, Code 323, Bay St. Louis, Mississippi 39529 - U.S.A.*

ABSTRACT

Observations of currents, transport, sea level, and sea level slope in Lombok Strait and west Flores Sea in 1985 and 1986 have been compared to a simulation of the NORDA global ocean model in the Indonesian throughflow region. Despite the relatively coarse grid scale of the model compared to topographic length scales in the region, the model appears to be realistically reproducing many of the observed features. The predicted transport through the Lombok Strait, for example, agrees with detailed observations of phase and magnitude, especially when corrected for grid size limitations. The sea surface fluctuations and sea surface slopes predicted by the model agree within less than a factor of 1.5 with sea level changes and slopes observed on tide gauges. There do appear to be several cases of phase difference of several months between model and observations that require further investigation.

1. Introduction

The importance of a net transport of mass, heat, and salt from the Pacific Ocean to the Indian Ocean through the Indonesian archipelago is now well recognized. Present estimates of the magnitude of the net transport (popularly referred to as the Indonesian throughflow) by various indirect methods vary greatly, from 1.5 to 20 Sv (1 Sv = 10^6 $m^3.s^{-1}$) (Cox, 1982; Fine, 1985; Fu, 1986; Godfrey, 1981; Piola, and Gordon, 1984; Wyrtki, 1961). For a general review, see Gordon and Golding (1986). It has been generally assumed that the throughflow is concentrated in the wide, deep passages bracketing Timor. The first direct observations of the throughflow, however, were taken in the Lombok Strait, presumably of secondary importance to the Timor passages on the basis of cross-sectional area. These observations (Murray and Dharma Arief, 1986) showed a net Indian Ocean-directed transport reaching 4 Sv in August 1985 with a 1985 annual average of 1.7 Sv. Extrapolating these results solely on the basis of cross-sectional area above the 200-m depth level suggests a total throughflow of 10-12 Sv. There could, however, be considerable differences between the pressure gradients driving the flows in the Lombok and Timor areas.

Recently Wyrtki (1987), using sea level data from Davao and Darwin and dynamic height data from the areas south of Mindanao and south of Java, showed that the strong pressure gradient between the Pacific and Indian oceans is concentrated in the upper 200 m. Interannual variations of the sea level differences agree well with the throughflow transport predicted by the NORDA wind-driven numerical model (Kindle et al., 1987).

The initial NORDA numerical model (Kindle et al., 1987) did not include the Lombok Strait, but the results in (Murray and Dharma Arief, 1986) instigated its inclusion in the updated version discussed here. The objective of this paper is a comparison and evaluation between current and sea-level observations made in the Lombok Strait and west Flores Sea in 1985-1986 and the model results.

ORSTOM
CENTRE DOCUMENTATION
Montpellier

F 30203

2. Observational program

In order to understand the processes controlling circulation in the Lombok Strait and adjacent sectors of the Java and Flores Seas (see Fig. 1), field work and data collection were conducted from January 1985 to March 1986. Seven current moorings were deployed, five in the Lombok Strait and two in the bathymetric trough (in the western Flores Sea) linking the Makassar Strait outflow to the Lombok Strait. More than 120 current meter months of data were collected. A total of 234 CTD casts were taken in the Lombok Strait, its Indian Ocean approaches, and the western Flores Sea extending as far north as the Makassar Strait and east into the Flores Sea to 119°E. Thirty-four meter months of sea level (pressure gauge) data were taken in the Strait and at the Makassar trough mooring site. Data on the regional sea level during our observations were collected from tide gauges in the Philippines and northwest Australia courtesy of Klaus Wyrtki, University of Hawaii, and the Flinders Tidal Observatory, Australia.

The annual cycle of current velocity in the Lombok Strait is best shown from the data obtained at the 35-m depth level at site 2 (Fig. 2). The period January 10 through February 15, 1985, was characterized by persistent strong southerly flows reaching 60 $cm.s^{-1}$ in late January. Large flow reversals to the north through most of February and again in late April appear closely controlled by tropical cyclone activity in the Timor Sea (Murray and Dharma Arief, 1986). Southward currents increase in magnitude from May through July, reaching peaks of 90 $cm.s^{-1}$ in August and September at the height of the Southeastern Monsoon. Late October through December 1985 is a period of weak flow with distinct northward flow reversals in early December 1985 and a strong reversal in January 1986. Monthly block average values from all the current meter data at sites 1 and 2 are used in reference (Murray and Dharma Arief, 1988) to compute the annual transport cycle discussed earlier.

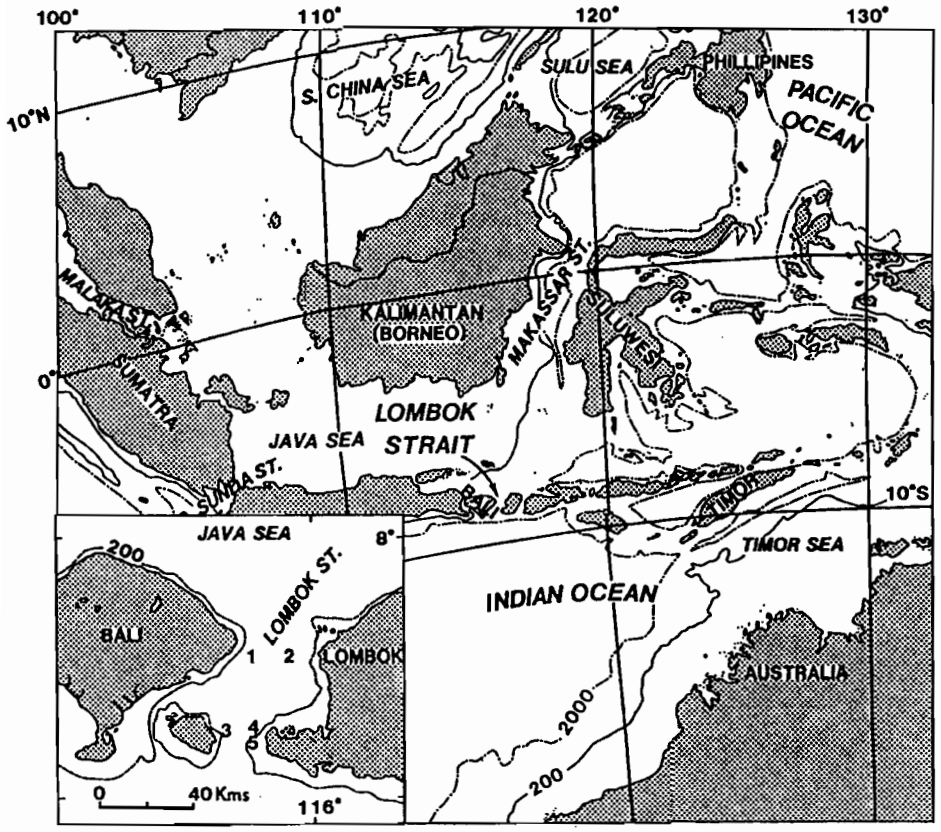

FIG.1. Map of the Indo-Pacific convergence zone with an inset showing mooring sites in the Lombok Strait

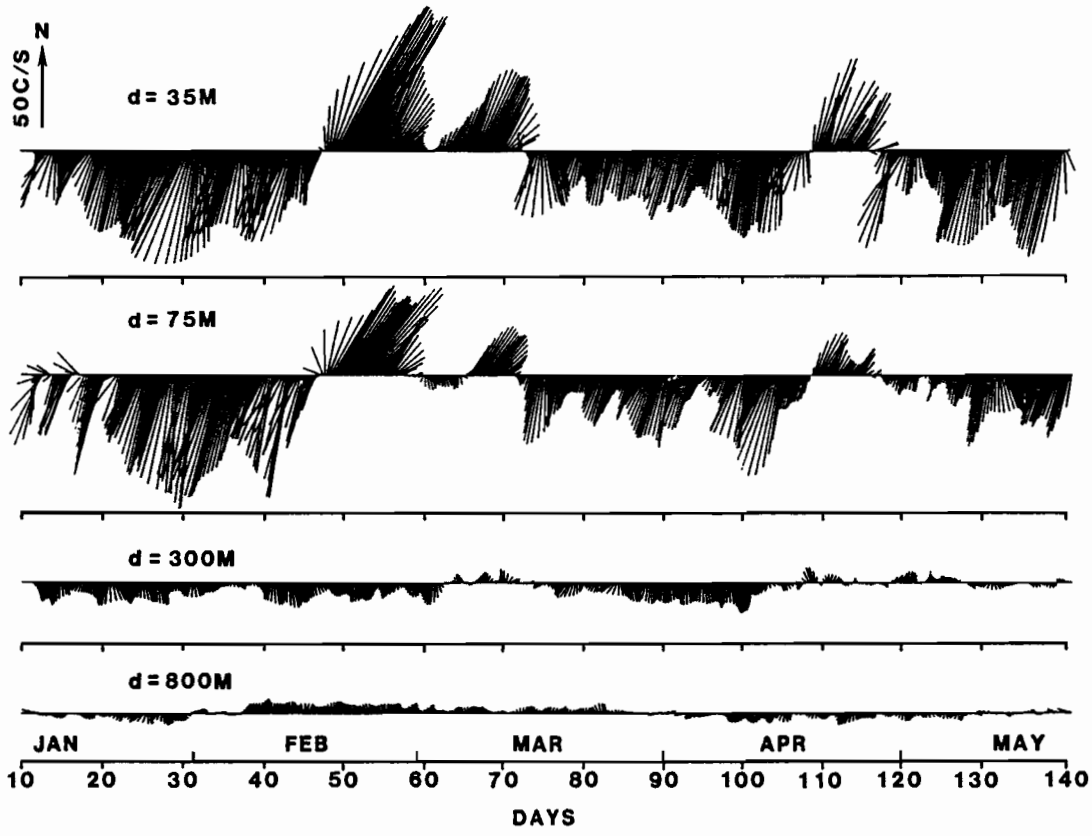

FIG.2. Fifteen-month time series of current vectors from the 35-m level at site 2, Lombok Strait.

3. The numerical model

To examine the mean, seasonal, and interannual variability of the Pacific to Indian Ocean throughflow and the forcing mechanisms responsible for the variability, we use the most recent version of the NORDA Global Model, forced by the European Center for Medium-Range Weather Forecasts (ECMWF) 1000 mb winds from 1980 through 1987.

The NORDA Global Model is a multi-layer, primitive equation formulation that incorporates a free surface, arbitrary coastline geometry, full-scale bottom topography in the lowest layer, and a semi-implicit time scheme. The numerical simulation utilizes a one-active-layer, reduced-gravity version of the model, which includes the effects of mixing and mean thermodynamics. Hence all transport is concentrated in the upper layer. The model grid resolution is 0.5° in latitude and 0.7° in longitude. For further details of the model, see accompanying papers by Kindle et al., and Hurlburt et al., in this volume.

a. Observations and Model Results

The annual mean wind stress in the western equatorial Pacific Ocean, especially these arising from the steady westerly directed trade winds, create a persistent elevated water surface south of the Philippines, clearly illustrated in both the model simulation (not shown) and the GDEM dynamic height climatology of the same area (O/1000 db), which shows a 21-24-cm drop in sea level from south of the Philippines to the Indian Ocean south of Java. A persistent southward flow down the Makassar Strait results throughout the year, as shown in both the ship drift observations and our model results. Figure 3 illustrates the model

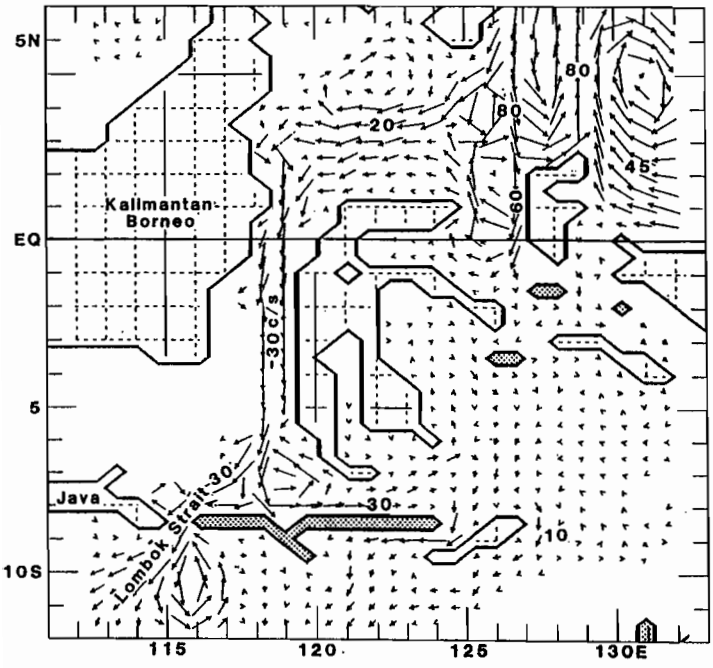

FIG.3. The model velocity field in the study area on May 28, 1985. Representative current speeds (cm/sec) are shown at a few locations.

results for the upper layer velocity field in the throughflow region on May 28, 1985. The strong southward flow in the Makassar Strait (30-60 cm.s^{-1}), fed from the Sulawesi Sea, bifurcates at the archipelago, one branch entering directly into the Indian Ocean through the Lombok Strait and the other branch flowing east through the Flores and Banda seas. The time series of transport predicted by the model for 1985-1986 is compared to our observations in Figure 4.

The computations of observed transport through the Lombok Strait presented in (Murray and Dharma Arief, 1988) are based on monthly block averages of current meter data, which allowed for temporal variation in the vertical current profile. In order to increase temporal resolution for a comparison to the model output, the carefully determined monthly average transports were regressed against monthly average velocity components from various current meters. A best-fit relation ($R^2 = 0.79$) determined over the range of the monthly averages ($5 \leq v \leq 55$ cm.s^{-1}):

$$T = 0.64\, e^{.032\, v}$$

where T is transport in Sv and v is the monthly average north-south component of current speed at the 35-m level (v_{35}) at the site 2 mooring, gave best results. Utilizing this relationship, the v time series from this current meter was passed through a 30-day low-pass filter (v (LP)) and used to compute transport. For the limited amount of data outside the range of the monthly averages where v (LP) < 5 cm.s^{-1}, we let $T \rightarrow 0$ linearly with v (LP). Correspondingly, when v (LP) > 55 cm.s^{-1}, an algorithm where v = constant = v_{35} in the upper 100 m and decreases parabolically to 0 at 200 m gave good results.

Figure 4 shows a comparison between transport through the Lombok Strait calculated from the observations in this manner and from the numerical model. In all figures, eastward- and northward-directed flows are positive; westward- and southward-directed flows are negative. Owing to restrictions on the model grid size, the Lombok opening in the model for the upper active layer is about 2.2 times the actual cross section of the strait above the 200-m depth level, where the net transport is calculated. Note a transport scale adjusted for this discrepancy on the figure. We note the general agreement in phase

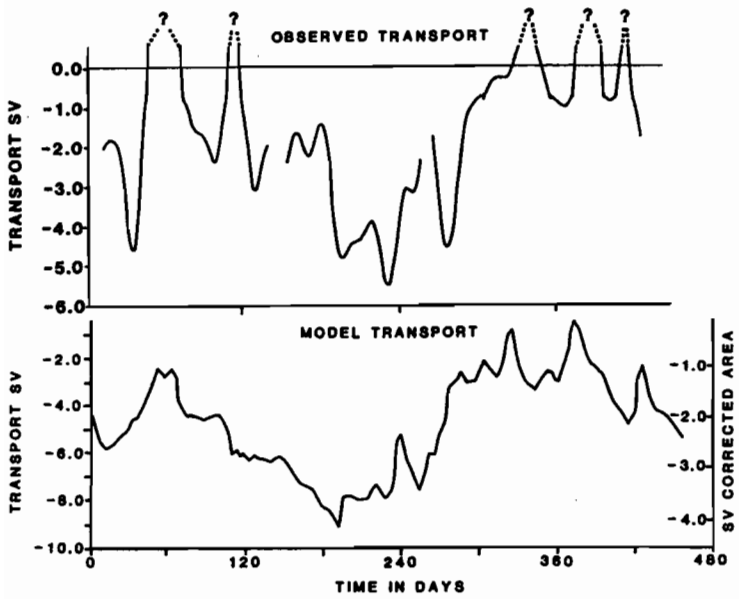

FIG.4. The transport through the Lombok Strait predicted by the model compared to the transport observed in the north strait. The right side of the lower panel is a scale corrected for excess cross-sectional area mandated by model limitations.

between the major pulse in southward transport and the good agreement in magnitude between the model adjusted transport and the observations. The distinct pulse of low southward transport in February because of intense cyclonic activity in the Timor Sea is present in both the observations and the model despite the fact that the model is driven by monthly averaged winds. The period of low transport in the observations from November 1985 to February 1986 appears to be well modeled also.

In Figure 5 the observed transport in Lombok is compared to the observed sea level difference between Davao and Darwin. While the period of largest southerly transport certainly occurs in the months of the northern summer, when the sea level difference is high, there does appear to be a 2-month lag of maximum Lombok transport with the greatest sea level difference. This suggests Darwin, with its location on the inside of the extremely wide Sahul shelf, is not the best index for the sea level in the Timor Sea. Despite this disagreement in phase, the long temporal drop in sea level slope from September 1985 to February 1986 is accompanied by decreasing transport.

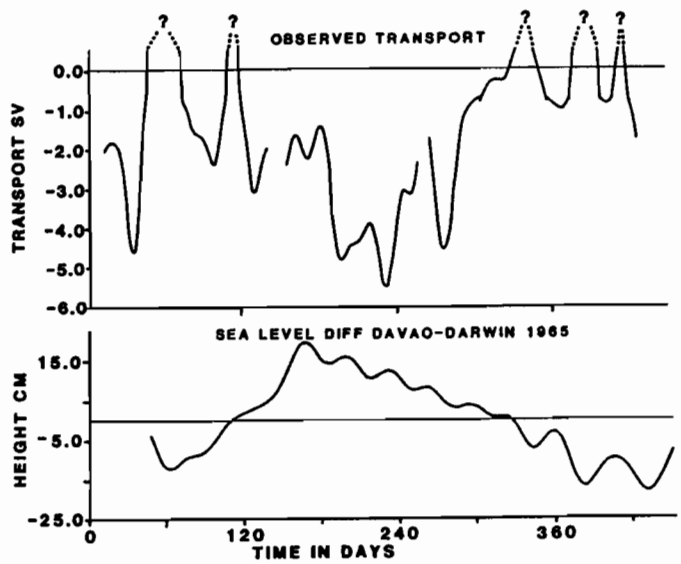

FIG.5. The observed transport in the strait compared to the Darwin minus Davao sea level difference, January 1985-March 1986.

The surface dynamic height field (0/500 db) determined during the first week of June 1985 is shown in Figure 6, and the model simulation of the free surface elevation is given in Figure 7. The general agreement in the overlap area, the west Flores Sea-Makassar Strait junction, is encouraging. A bulge of the sea surface south of Sulawesi and a drop in sea level of 8-10 cm from the Flores Sea south of Sulawesi to the Java shelf is present in both model and data.

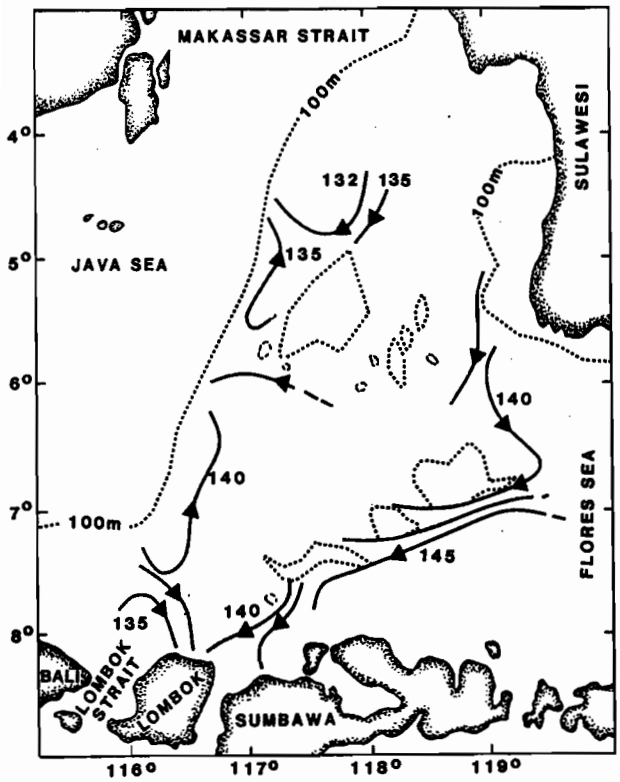

FIG.6. Dynamic height (dyn. cm) as observed on our cruise in the first week of June 1985.

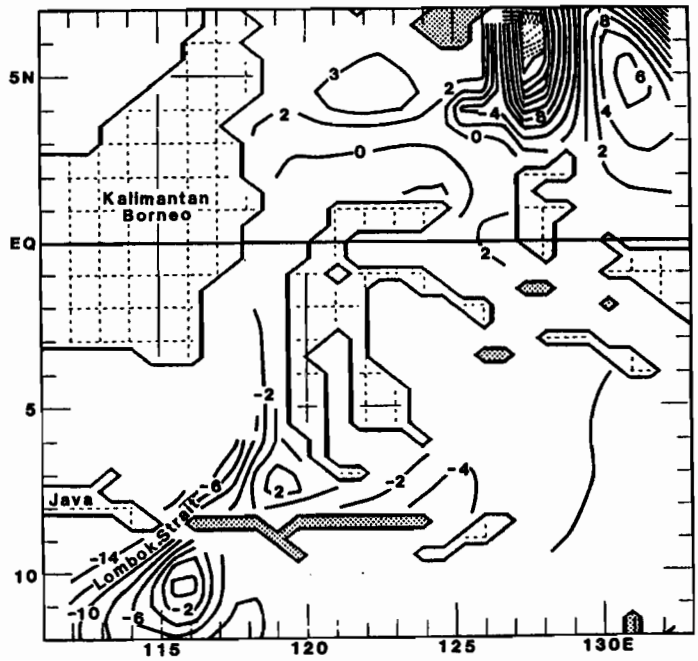

FIG.7. Deviation of the free surface predicted by the model for 28 May 1985. Compare the overlapping areas in Figures 6 and 7.

With a certain degree of confidence now established in the model, it is interesting at this point to investigate the model results relating the Lombok Strait transport to the total Indonesian throughflow. In Figure 8 the total throughflow (PACIO) computed across 114.75°E in the Indian ocean between Java and Australia reaches maximums of 17.5, 14, and 10 Sv in 1984, 1985, and 1986, respectively. Lombok (LBK) is predicted to carry roughly half the flow during maximum transport phases and the entire southward throughflow during low transport phases, there arising a back flow into the Banda Sea during these periods. The transport southward down the Makassar Strait predicted during these three years (Fig. 8, lower panel) suggests Makassar is carrying ~70% of the throughflow during peak periods. At certain times, however, as in the first quarter of 1986, the southward transport in the Makassar Strait exceeds the throughflow, indicating storage within the archipelago or a recirculation back into the Pacific through the passages between Irian Jaya and northeastern Sulawesi.

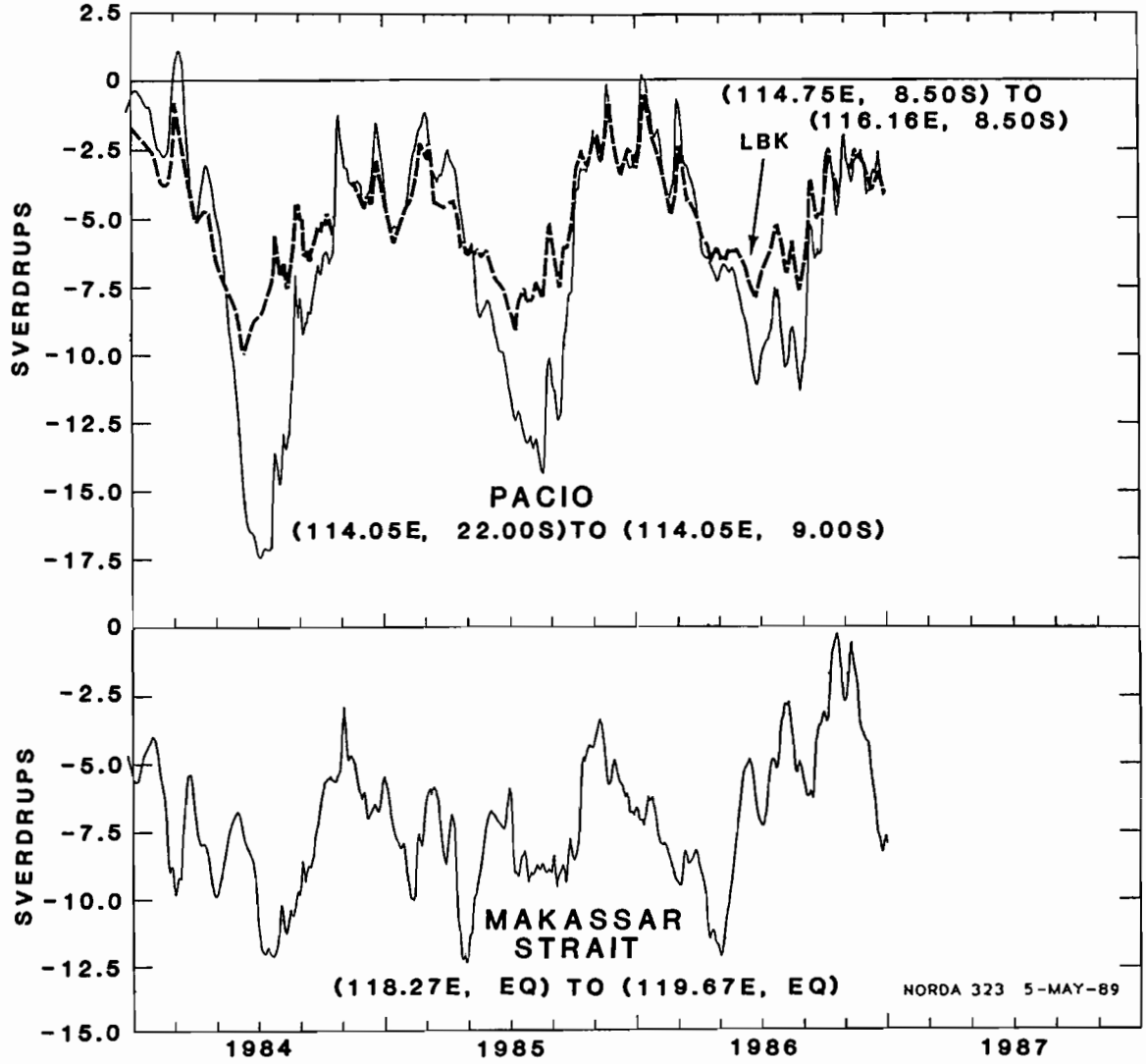

FIG.8. Transport through the Lombok Strait (LBK), the total Pacific-Indian throughflow (PACIO) across 114.75°E, and southward transport in the Makassar Strait across the equator, 1984-1987. Negative values of flow for Lombok and Makassar are southward directed, but westward for the PACIO flow.

b. Sea Level Differences

The observed Davao-Darwin sea-level difference and the observed zonal wind stress in the Indian Ocean south of the archipelago during our observation period are compared to the model transport through the Lombok Strait in Figure 9. The interrelationship between the three signals is clear. The westward zonal wind stress in the Indian Ocean appears to be a key factor in depressing the Timor Sea water level and in pulling water southward through the Lombok Strait.

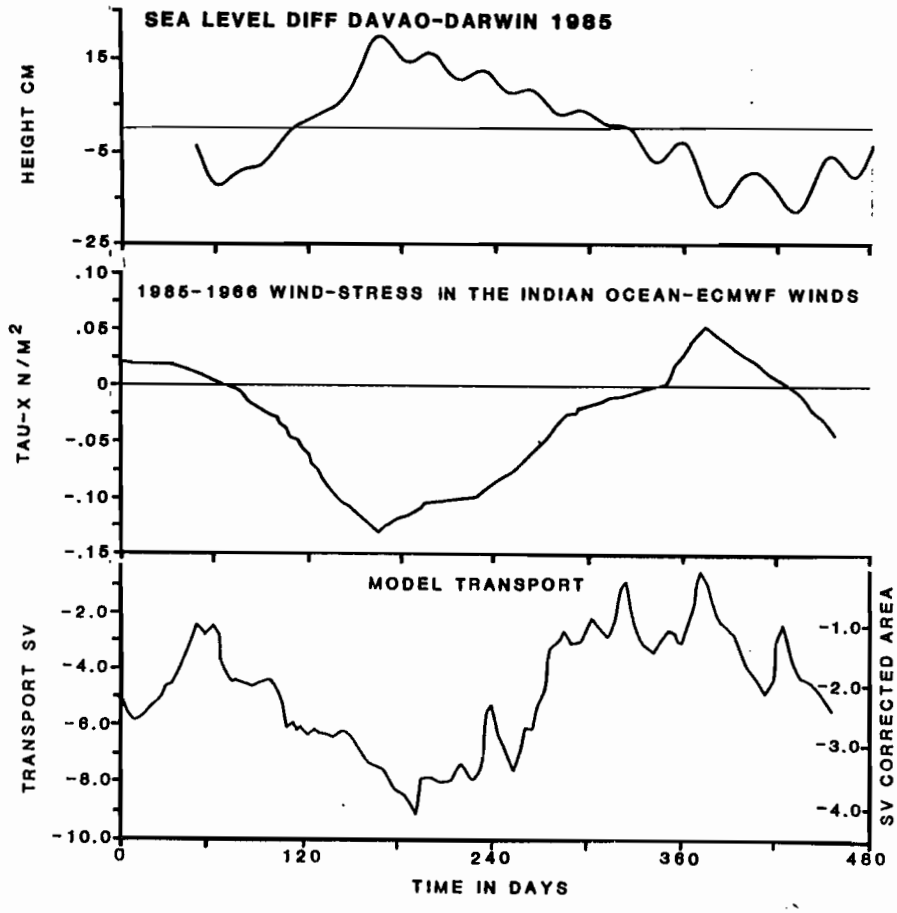

FIG.9. The model transport through the Lombok Strait compared to the average ECMWF wind stress in the Timor Sea and Davao-Darwin sea level difference for the period January 1985-April 1986.

The change in the free surface elevation in the model at 126°E, 6°N (off the Philippines) is compared to the observed Davao sea level in Figure 10. The 15-20 cm range in both signals and the sharp rise in the first 4-5 months of 1985, followed by a gradual 8-month drop, also in both signals, are all encouraging. The sea level difference between the Philippine grid point and the Lombok grid point compared to the observed Davao minus Darwin signal (Fig. 11) is considerably less satisfactory. We suspect Darwin is not a good representative point for sea level in the Timor Sea, a point that needs to be explored further.

The ranges of sea level differences at 20-30 cm and the occurrence of the maximum relative slope in mid-summer in both cases, however, supports the general validity of the model.

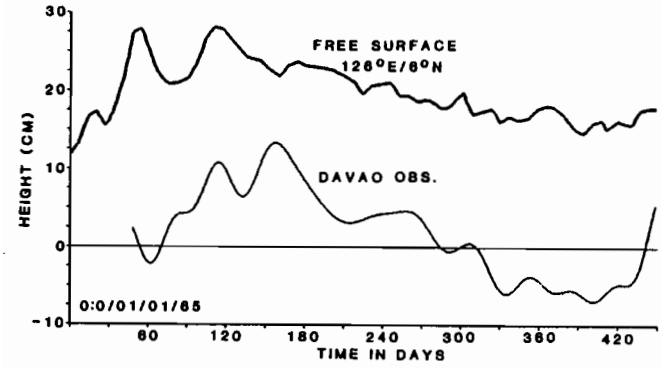

FIG.10. Observed sea level at Davao compared to sea level at the model grid point off the southern Philippines at 126°E, 6°N.

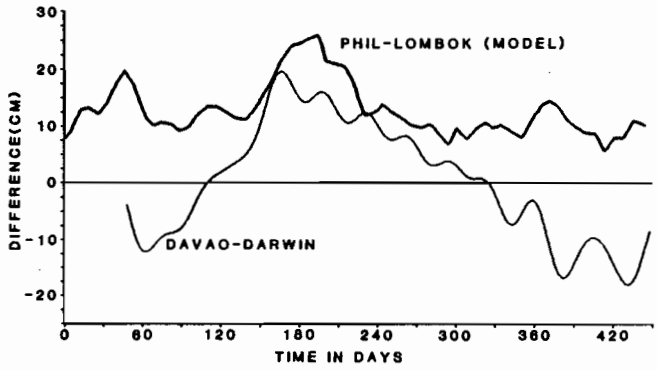

FIG.11. The Davao-Darwin sea level differences, January 1985-March 1986, compared to the sea level difference between the model grid points off the southern Philippines and the Lombok Strait.

4. Summary

Observations of currents, transport, sea level, and sea level slope in Lombok Strait and west Flores Sea in 1985 and 1986 have been compared to a simulation of the NORDA global ocean model in the Indonesian throughflow region. Despite the relatively coarse grid scale of the model compared to topographic length scales in the region, the model appears to be realistically reproducing many of the observed features. The predicted transport through the Lombok Strait, for example, agrees with detailed observations of phase and magnitude, especially when corrected for grid size limitations. The sea surface fluctuations and sea surface slopes predicted by the model agree within less than a factor of 1.5 with sea level changes and slopes observed on tide gauges. There do appear to be several cases of phase difference of several months between model and observations that require further investigation.

REFERENCES

Cox, M., 1982: Numerical Models of Ocean Circulation. National Academy of Science Press, Washington, D.C.

Fine, R. A., 1985: Direct evidence using tritium data for throughflow from the Pacific into the Indian Ocean, *Nature*, **315**, 478-480.

Fu, L., 1986: Mass, heat and freshwater fluxes in the south Indian Ocean, *J. Phys. Oceanogr.*, **16**, 1683-1693.

Godfrey, J. S., and T. J. Golding, 1981: The Sverdrup relation in the Indian Ocean, and the effect of Pacific-Indian Ocean through flow on Indian Ocean circulation and on the East Australian Current, *J. Phys. Oceanogr.*, **11**, 771-779.

Gordon, A. L., 1986: Interocean exchange of thermocline water, *J. Geophys. Res.*, **91**, 5037-5046.

Hurlburt, H. E., J. C. Kindle, and E. J. Metzger, Results from a global ocean model in the western tropical Pacific, 1989.

Kindle, J. C., G. Heburn, and R. Rhodes, 1987: An estimate of the Pacific to Indian Ocean throughflow from a global numerical model, Interannual variability of the Pacific to Indian throughflow, I : Further progress in equatorial oceanography (E. Katz and J. Witte, eds.), *Nova University*, In: Further progress in equatorial oceanography (E. Katz and J. Witte, eds.), *Nova University Press*, Ft. Lauderdale, FL, 317-321.

Kindle, J. C., H. E. Hurlburt, and E. J. Metzger, On the seasonal and interannual variability of the Pacific to Indian Ocean throughflow, 1989.

Murray, S. P., and Dharma Arief, 1986: Effect of Indian Ocean cyclones on net flow through the Lombok Strait, Indonesia (abs.), *EOS*, **67**, 1017, *AGU Fall Meeting*, December 1986.

Murray, S. P., and Dharma Arief, 1988: Throughflow into the Indian Ocean through the Lombok Strait, January 1985-January 1986, *Nature*, **333**, 444-447.

Piola, A. R., and A. L. Gordon, 1984: Pacific and Indian Ocean upper-layer salinity budget, *J. Phys. Oceanogr.*, **14**, 747-753.

Wyrtki, K., 1961: Physical oceanography of the Southeast Asian waters, Scientific Results of Maritime Investigations of the South China Sea and Gulf of Thailand 1959-1961, *NAGA Rep.*, **2**, 195 pp., Scripps Inst. Oceanogr., La Jolla, California, U.S.A.

Wyrtki, K., 1987: Indonesia throughflow and the associated pressure gradient, *J. Geophys. Res.*, **92**, 12941-12946.

Thermohaline Structure Variability along 165°E in the Western Tropical Pacific Ocean (January 1984 - January 1989)

Christian HENIN

Groupe SURTROPAC, Centre ORSTOM de Nouméa
Nouméa, New-Caledonia

ABSTRACT

Distribution of temperature, salinity and dynamic topography, using data from eleven SURTROPAC, three PROPPAC and three US/PRC cruises between January 1984 and January 1989, is examined. Long term changes of dynamic topography give a new view of oceanic variability in the western equatorial Pacific ocean:

a) After the 1982-83 El Nino event a drastic change occurs between 1984 and 1985 with a sudden accumulation of warm waters,

b) A steady and continuous loss of heat appears since 1985 with a shallowing of the thermocline culminating in 1987 with the associated El Nino episode.

Continuous temperature data from Atlas moorings confirm the slow tendency between 1985 and 1987 giving a new insight of the El Nino scenario in the Western Pacific. These cruises also give a more realistic temperature/salinity relationship along 165°E and have therefore made it possible to determine the accuracy of dynamic topography obtained by the Atlas temperature data set and Levitus T/S climatology.

In addition, the meridional surface dynamic topography distribution suggests a global seasonal displacement of the equatorial surface current system composed of North Equatorial Counter-Current (NECC), South Equatorial Current (SEC) and South Equatorial Counter-Current (SECC). Individual cruises show that the SECC related to the South Pacific Convergence Zone of the wind (SPCZ) which was neglected until now might sometimes in the austral summer displays a very strong eastward flow, which is compararable to the NECC flow and should be carefully considered in the COARE project as a major current in the western South Pacific Ocean.

1. Introduction.

In the framework of TOGA the SURTROPAC Group based at the ORSTOM Center in Nouméa has initiated (since January 1984) meridional transects along 165°E from 20°S to 10°N (Fig 1).

Two cruises per year permit a good description of hydrographic and current structures in the western equatorial Pacific ocean (Eldin, 1989). Other programmes have also carried out transects along the same meridian. They are issued from:

a) a close cooperation between the United States of America and the People Republic of China studying air-sea interactions in the western Pacific since January 1986, and

b) another ORSTOM programme, PROPPAC ("Production Pélagique dans le Pacifique"), since October 1987.

We have therefore a relatively large number of cruises (17) along the 165°E meridian, covering five years, including 1987 when an El Nino event occurred.

In addition, along 165°E monitoring of the temperature distribution of the 0-500m upper layer on a daily average has also been initiated by Pacific Marine Environmental Laboratory (PMEL) between 5°N and 5°S, in close cooperation with SURTROPAC Group since July 1985 (Hayes et al, 1988). Continuous temperature observation of the 0-500m layer at the equator has also been made since January 1986 by a current meter mooring deployed by US/PRC.

ORSTOM
CENTRE DOCUMENTATION
Montpellier

F 30204

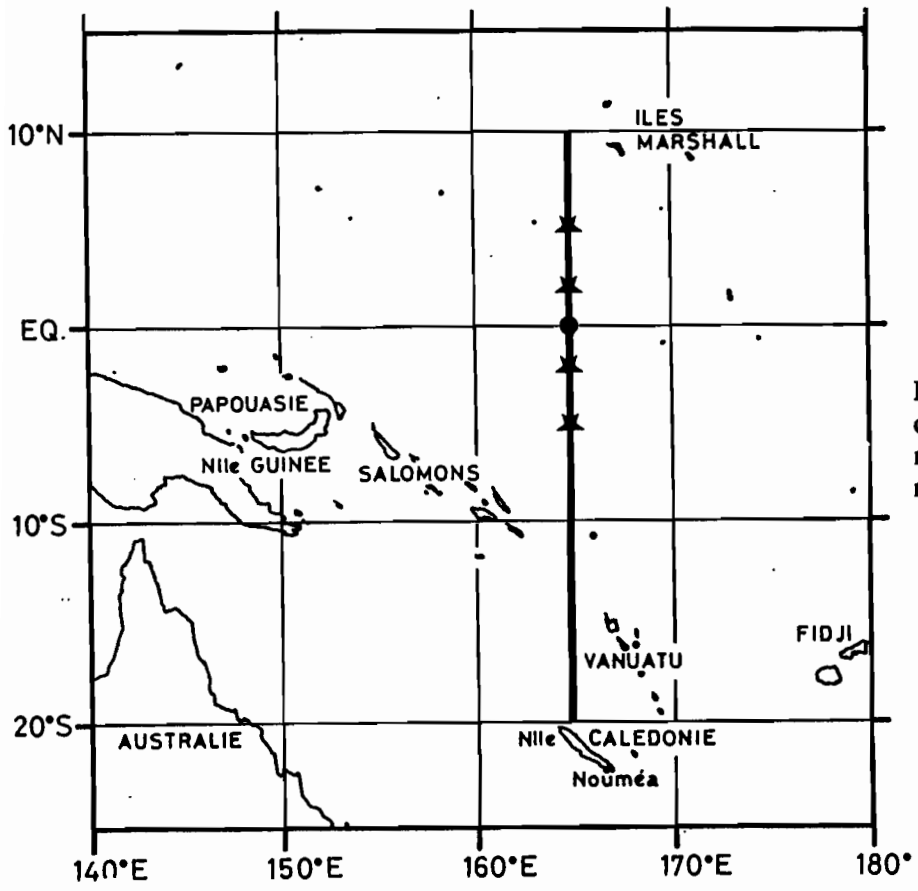

FIG.1. Location of oceanographic cruises and moorings along the 165°E meridian

This paper bring out the variability of dynamic topography, thermal and salinity structures using data sets from these cruises. Finally, a comparison of cruises and mooring data is made.

2. The 20°S-10°N transect.

The description of hydrologic stuctures using the first six Surtropac cruises between 1984 and 1986 has already been made in Delcroix et al. (1987), but the El Nino event in 1987 and the La Nina episode since 1988, bring out new elements of oceanic conditions in the western Pacific Ocean.

a. Thermal structure.

A typical temperature section made during Surtropac 11 cruise in January 1989 is presented Fig.2. An homogeneous upper layer is present on the equator from 5°S to 5°N. A well marked thermocline spreads on the equator at the location of the Equatorial Under-Current (EUC). The North and South Equatorial Counter-Currents (SECC and NECC) are characterised by a downward thermocline slope toward the equator. During this particular cruise the transport of SECC was of the same order of magnitude as the NECC (25 m^3s^{-1}). This suggests that this counter-current has to be considered in the volume budget of the western Equatorial Pacific.

The temperature distribution and in particular the thermocline depth governs its dynamic topography. Hence a large part of its variability came from the thermocline depth which varies in the range 50-200m near the equator during the period under consideration.

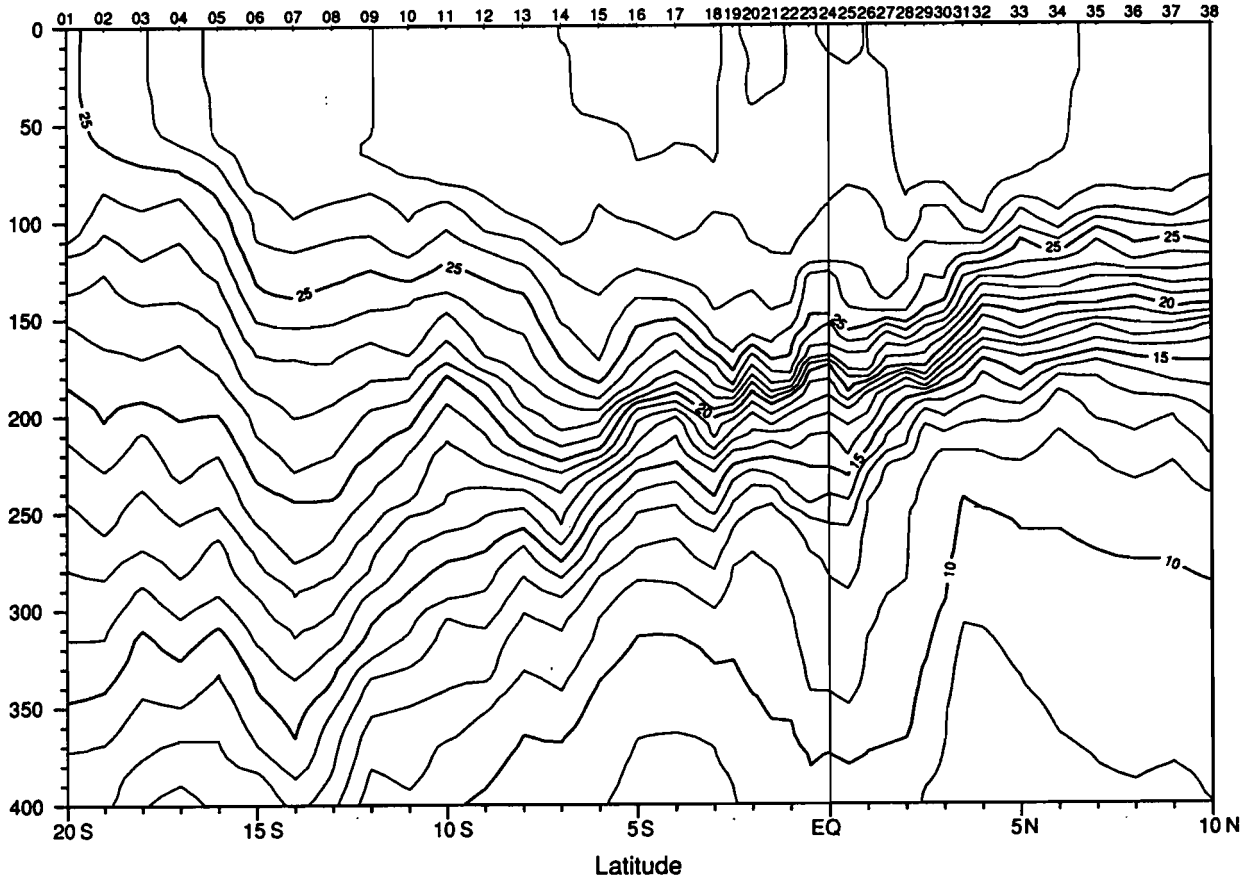

FIG.2. 0-400m temperature distribution along 165°E in January 1989.

b. Haline structure.

Salinity distribution along the transect (Fig.3) presents large gradients in both vertical and meridional directions:

a) vertical - Between surface low salinity waters in the NECC and SECC cores and the more salty water at the thermocline depth. The largest gradient lies between the waters of SECC with salinity smaller than 34.0, and the maximum of salinity greater than 36.0, which is the tropical water mass originating from French Polynesia in the southern hemisphere.

b) meridional - This tongue of high salinity waters reaches or crosses the equator and creates a meridional salinity gradient with low salinity northern hemisphere waters.

Although smaller than the effects of temperature on density, then on dynamic topography and on geostrophic circulation, the effect of salinity is quite marked particularly in the western equatorial Pacific, because of large variability of salinity values and haline gradients.

c. Dynamic topography.

To describe the dynamic topography variability in two contrasting seasons we have restricted Fig.4 to the SURTROPAC data set for January and June-July, since 1984.

The zonal equatorial current system is very well developed during January as indicated by upward dynamic height toward the equator in the two equatorial Counter-Currents (SECC between 10°S and 5°S and NECC between 9°N and 5°N). During austral summer, SECC is somewhat less pronounced while the two counter-currents seem to have shifted southward, the southern limit of NECC reaching 3°N.

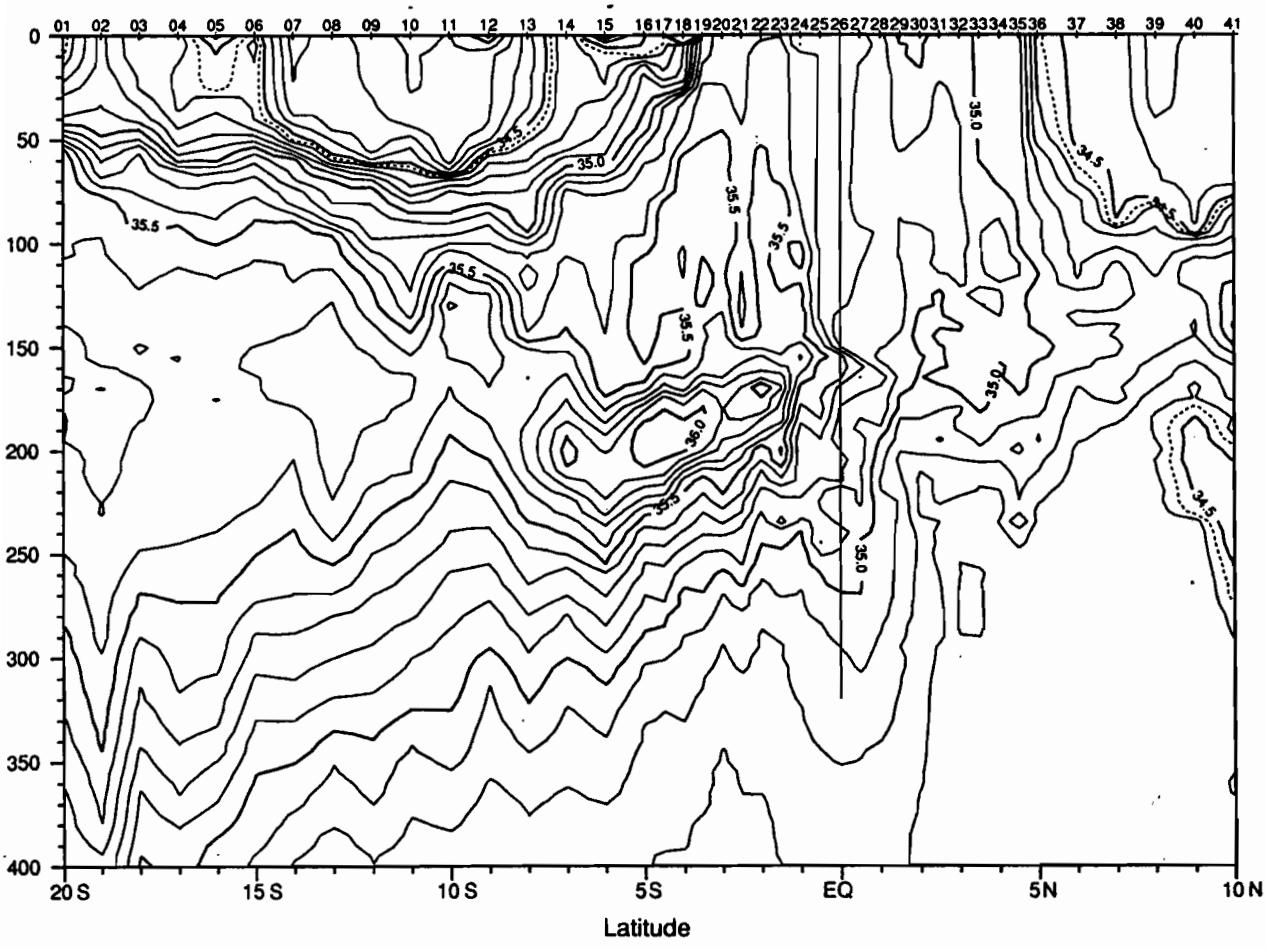

FIG.3. 0-400m salinity distribution along 165°E in January 1989.

The more striking feature is a very large interannual change (20-25 dyn.cm) between 1984 and 1987 occurring in the 5°N-5°S latitude band for January period and in the 0°-10°S latitude band for June-July. During 1984 surface dynamic height relative to 1000 db was low (185 dyn.cm), then a sudden change occurs in January 1985 with a maximum value of 205 dyn.cm, which was never noted before, then a slow decrease between 1985 and 1987. At this time the El Nino event was developing with low salinity waters and reduced upper layer.

d. Sea-Surface Salinity

Two typical distributions of surface salinity prevail during January and June-July (Fig 5):

a) In January the SECC usually carries low salinity waters with a minimum of 34.0. On the equator SSS is approximately 34.5 and the NECC is also characterized by low salinity surface waters (34.0 to 34.3).

b) In June-July the SECC is less pronounced and the SSS is somewhat saltier while the NECC being stronger carries lower salinity waters than in January (34.0). The change is much more developed in the equatorial band with a maximum of salinity of more than 35.0 related to upwelling associated with larger SEC.

Besides these typical distributions large anomalies occur such as the one observed during 1987 when the SECC disappeared in January eliminating the minimum observed generally near 10°S and in July when an eastward jet on the equator carried very low salinity waters

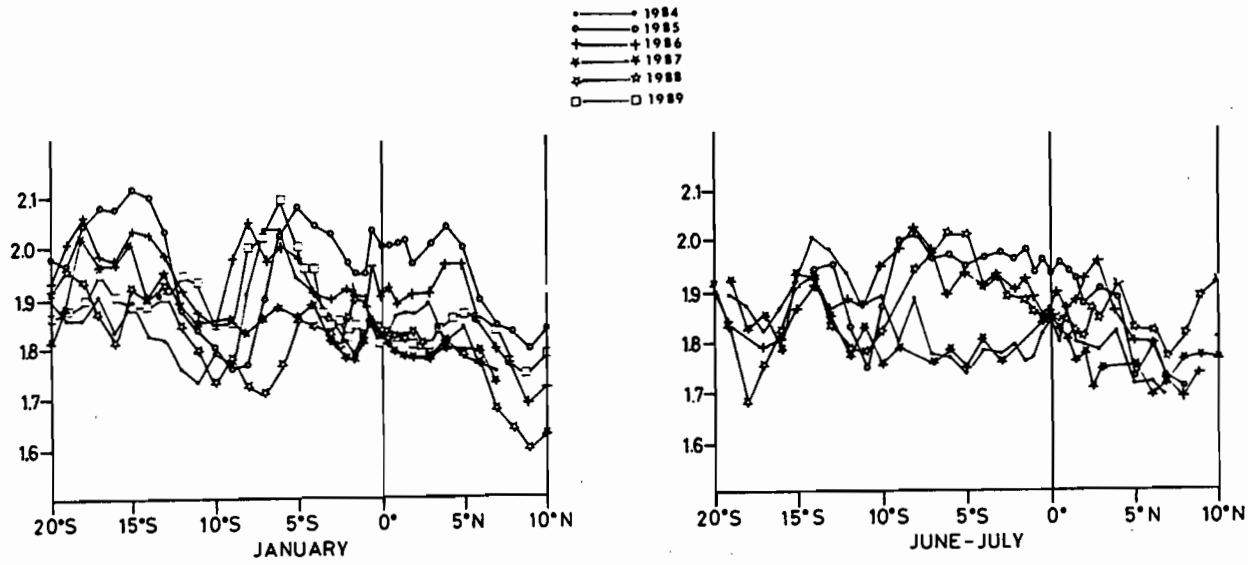

FIG.4. Surface dynamic height relative to 1000 db distribution along 165°E between January 1984 and January 1989. (left: January, right: June-July).

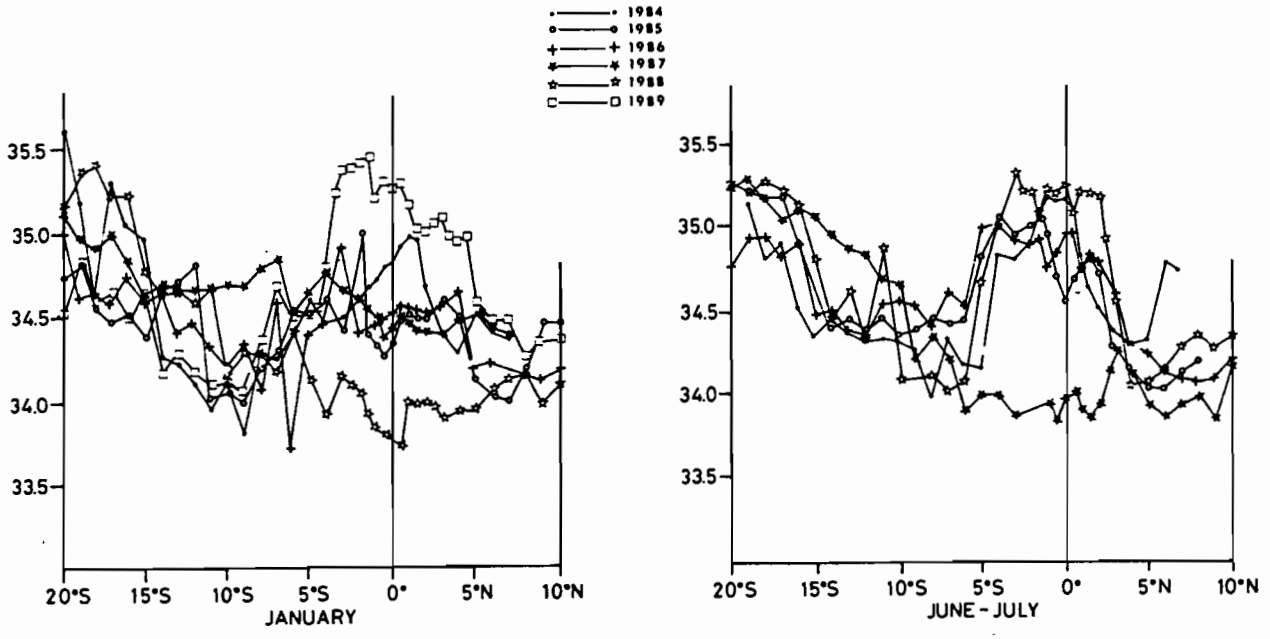

FIG.5. Sea surface salinity along 165°E between January 1984 and January 1989. (left: January, right: June-July).

(34.0 instead of 35.0). In January 1988 this low salinity remains on the equator before recovering normal values in July 1988. In fact, even in January 1989, the SSS was very high presenting a distribution generally observed in June-July. This may be explained by a very strong upwelling which started in April 1988 in the whole central and eastern Pacific reaching the 165°E meridian. At the same time, low rainfall contributed also to the presence of high salinity water on the equator for more than one year.

3. Equatorial band.

The equatorial band is of particular interest for the study of the variability of currents and thermal structure associated with waves which are developing in the equatorial wave guide (Moore and Philander, 1976).

At 165°E it is thermally monitored by Atlas thermistor chains at 5°S, 2°S, 2°N and 5°N by means of a joint PMEL-ORSTOM action and by US/PRC mooring on the equator (Fig 1). The SURTROPAC, PROPPAC and US/PRC cruises also gave information on the changes in time of SST, SSS and dynamic height on the equator.

a. Sea surface temperature (Fig 6).

The annual amplitude of the SST cycle is very small in the western Pacific where temperature is between 29.5 and 29.8°C for the 1984-87 period. January temperatures are generally higher than June-July temperatures by approximately 0.1-0.3°C. During the 1987 El Nino event SST was not different from that of previous years. However, a decrease of 1°C has been observed since April 1988 and remains till the last cruise in January 1989. As already mentioned the extension of La Nina toward the western Pacific has reached the 165°E meridian at that time.

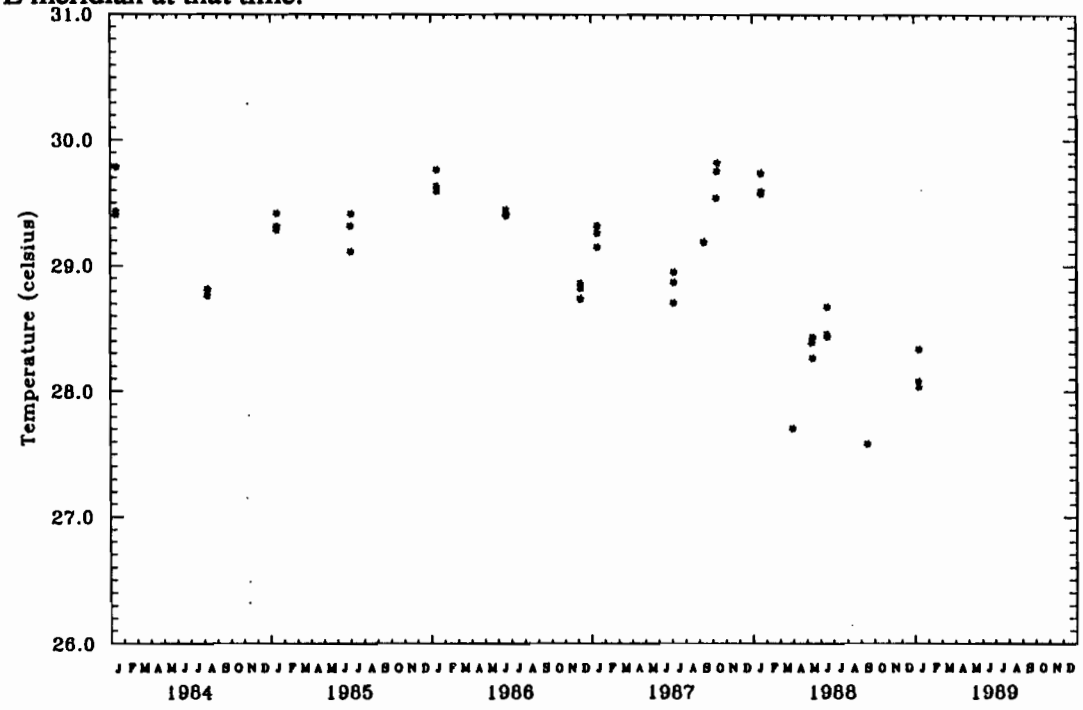

FIG.6. Sea surface temperature between 0°30 S and 0°30 N for the 1984-1989 period.

b. Sea surface salinity (Fig 7).

The annual amplitude of the SSS cycle is well marked during the first three years of observations (1984 to 1986). It will be noticed that SSS is larger in June-July than in January but the variation of SSS is confined to the 34.4-35.1 range. During the El Nino event, in 1987 SSS drops to a minimum of 33.6-34.0 due to low salinity waters from Western equatorial Pacific carried by eastward current. On the contrary, by April 1988, La Nina episode is marked by high SSS waters as already mentioned.

c. Dynamic height.

The surface dynamic height relative to 500 db versus time of the equatorial band 0.5°S-0.5°N from cruise data (Fig.8) shows a rapid increase between 1984 and 1985 and a

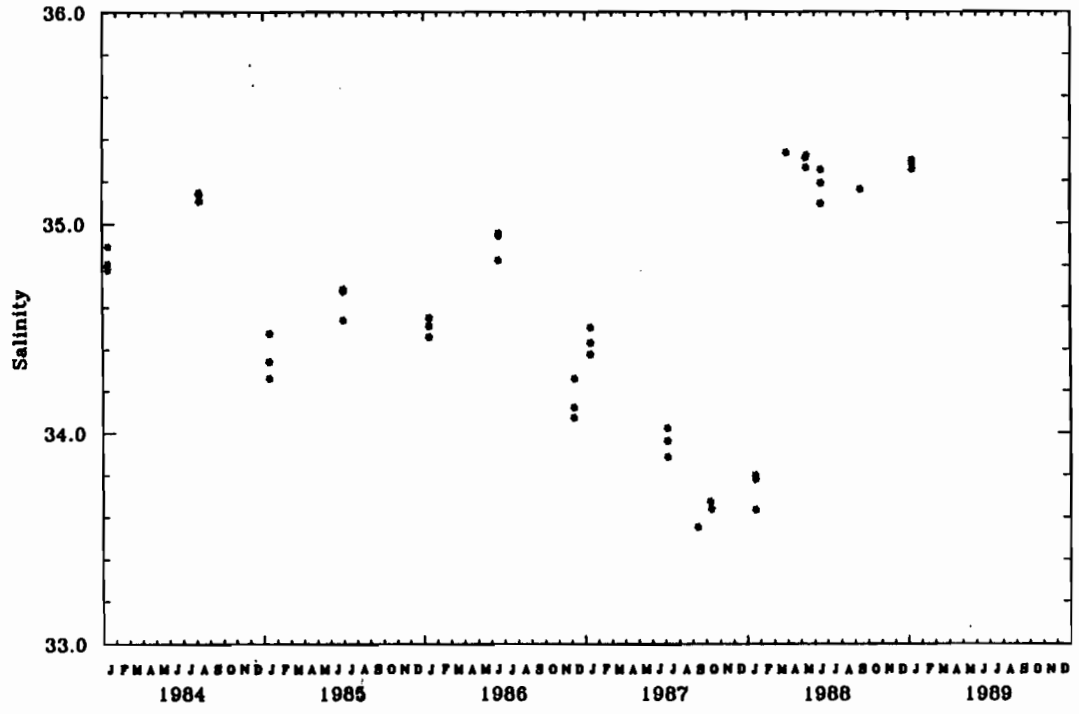

FIG.7. Sea surface salinity between 0°30 S and 0°30 N for the 1984-1989 period.

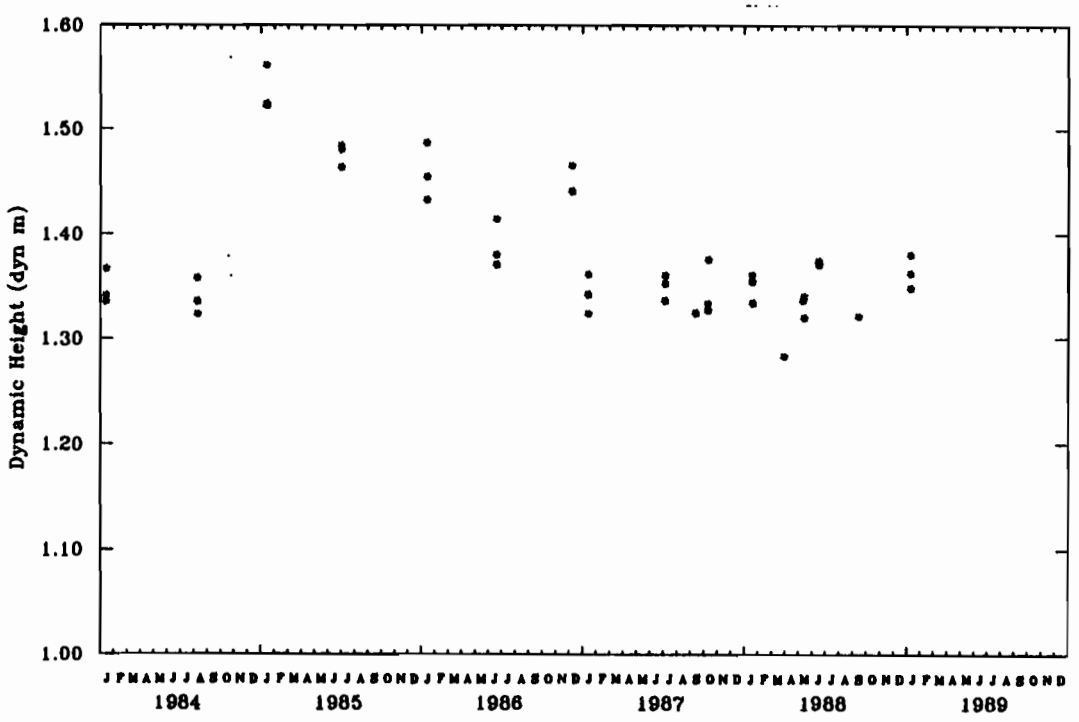

FIG.8. Surface dynamic height relative to 500 db between 0°30 S and 0°30 N for the 1984-1989 period.

slow decrease between 1985 and 1987. This diagram brings out the 20 dyn.cm variability

and shows that no change appears in dynamic height between the 1987 El Nino and the 1988 La Nina episodes.

4. Comparison between cruises and moorings.

A comparison of cruises data and daily averaged data from thermistor chain was possible at 2°S-165°E where the Atlas system provided the longest time serie of 0-500m temperature.

Temperature and heat content from the two data sets were quite comparable while dynamic height from cruises and from temperature given by moorings using mean Levitus (1982)'s T/S relationship presents noticeable differences. Figure 9 shows that errors made using mooring and T/S relationship may be of +10 or -10 dyn.cm during the period of simultaneous data (from June 1985 to July 1988). It shows also that the range of dynamic height estimated by mean T/S and temperature data is twice the range of dynamic height from CTD cruise data (40 cm.dyn versus 20 dyn.cm).

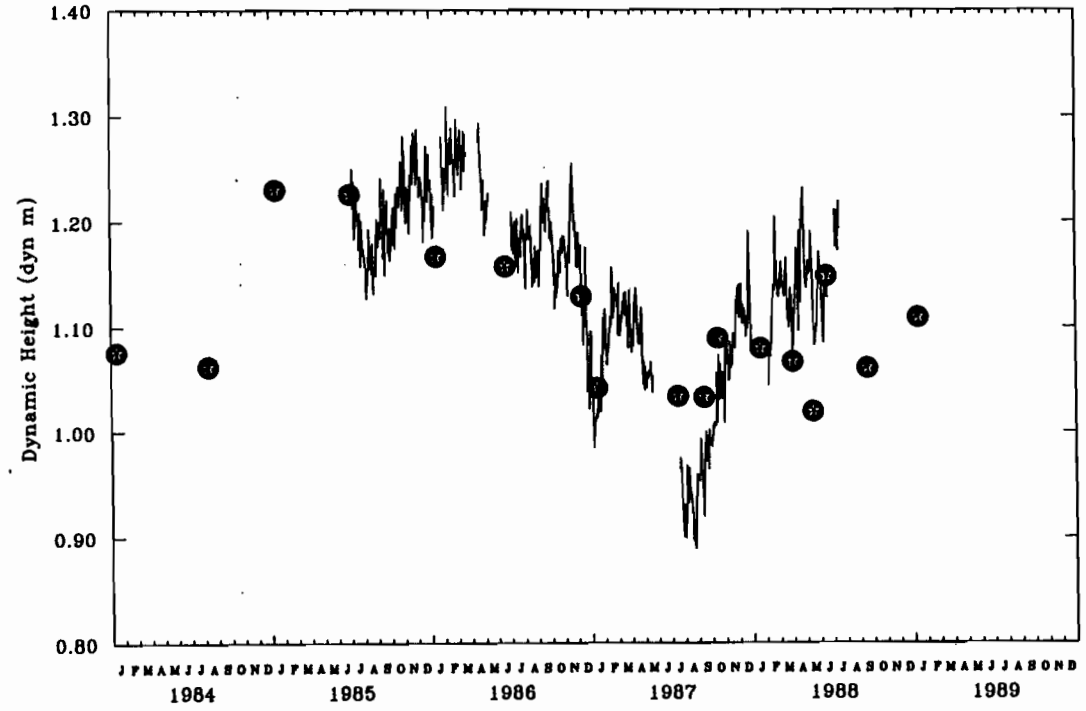

FIG.9. Surface dynamic height relative to 300 db at 2°S-165°E. Heavy lines : daily values from temperature distribution and mean Levitus T/S relationship; Dotted lines : dynamic height from individual cruises.

The reason for such differences lies in the T/S relationship change. Figure 10 reveals the very different T/S relationships at 2°S-165°E for each cruise. The dynamic height standard deviation has been estimated using the 17 available T/S relationships and the Atlas mooring temperature data set. It is of about 6 dyn.cm for the complete period of record. We may note also that the mean dynamic height using the cruise data set is very similar to the dynamic height obtained with mean Levitus T/S relationship.

5. Conclusion.

The results of the large monitoring effort in the western Pacific are encouraging. The need for monitoring is evident in this area of large changes in thermal and salinity distributions.

The effect of salinity on dynamic topography which was underestimated in the past has to be carefully examined in the western equatorial Pacific ocean.

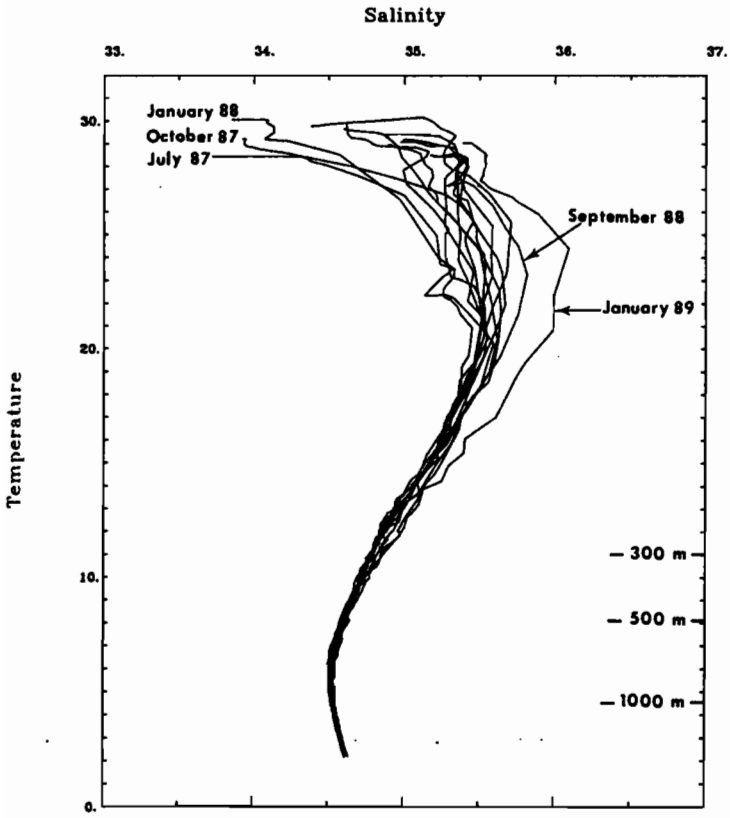

FIG.10. T/S curves for individual cruises at 2°S-165°E for the 1984/1989 period.

REFERENCES

Delcroix T., G. Eldin and C. Hénin, 1987: Upper ocean water masses and transports in the western tropical Pacific (165°E). *J. Phys. Oceanogr.*, **322**, 243-245.

Eldin G., 1989: Coupes verticales des structures océaniques physiques à 165°E observées au cours de dix campagnes SURTROPAC, 1984-1988. *Rapports Scientifiques et Techniques, Océanographie Physique*. Centre ORSTOM de Nouméa, New Caledonia, **1**, 130 pp.

Hayes S.P., L.J. Mangum, M.J. McPhaden, and J. Picaut, 1988. Thermal structure variability along 165°E. *Proc. of the Symposium on Western Pacific Air-Sea Interactions*, November 15-17, 1988, Beijing, PRC.

Moore D. and G. Philander, 1976: Modelling of the tropical oceanic circulation. In *The Sea*, **6**, Chapt. 8, Goldberg et al, eds, New-York, Interscience, 1048 pp.

Preliminary Results from Charles Darwin Cruise 34A in the Western Equatorial Pacific

David J. WEBB and Brian A. KING

Institute of Oceanographic Sciences, Wormley, Godalming, Surrey GU8 5UB - United Kingdom

ABSTRACT

In September 1988, the RRS Charles Darwin carried out a survey of the Western Equatorial Pacific between 127°E and 160°E and between 7°N and 3°S. The main instruments used were an undulating SeaSoar, carrying a CTD, which gave temperature and salinity sections down to 250 m, an acoustic doppler current profiler which gave velocities down to 300 m and the IOS MultiMet system measuring surface fluxes.

Data from the cruise is still being worked up. In this paper data from a long section made across the equator at 142°E between 7°N and 7°S is presented. The section is of interest because it shows up the importance of the salinity contrast between the more saline South Equatorial Current and the fresher North Equatorial Counter Current. This contrast shows up in both the almost isothermal near surface waters and in the thermally more complex region of the undercurrent.

1. Introduction.

In September of 1988, the United Kingdom research ship RRS Charles Darwin made a survey of the Western Equatorial Pacific between 127°E and 160°E and between 7°N and 3°S. The main instruments deployed were an undulating SeaSoar carrying a CTD, which gave temperature and salinity sections down to 250 m, an acoustic doppler current profiler (ADCP) which gave water velocities down to 300 m and the IOS MultiMet set of instruments measuring surface meteorological fluxes. Other instruments included a thermosalinograph, Transit and GPS satellite navigation, to give accurate position and absolute velocity of the ship, a precision echo sounder and a gravimeter.

The track of the ship during the survey is shown in Fig.1. The region covered is at the heart of the Western Pacific warm pool where sea surface temperatures can exceed 30°C. As a result atmospheric convection is very important (the region lies under the rising branch of the main Pacific Walker cell) and rainfall is high. Both the average winds in the region and the wave heights are very low, so surface mixing of the ocean by these two processes should be less than normal.

Interest in the region has increased in recent years because it may be responsible for triggering El Nino events. Simmons et al. (1983) also show that the region is involved in determining the position of atmospheric highs and lows in the northern hemisphere. The triggering of El Ninos may occur as a result of westerly wind bursts (Luther et al., 1983) an ocean temperature anomaly coupled to atmospheric convection (Gill, 1980) or the reflection of oceanic Rossby waves.

However because of its remoteness, the amount of good data available from the region has always been sparse and this has hindered the development of theoretical models of the coupling of the ocean and atmosphere in the region. For example one approximation that is often made when modeling the ocean near the equator, is that changes in salinity have only a small effect on ocean density and so can be ignored. In contrast, as we shall see, in the Western Equatorial Pacific the salinity often has an important effect.

Data from the cruise is still being worked up but in this paper we present preliminary

ORSTOM
CENTRE DOCUMENTATION
Montpellier
F 30205

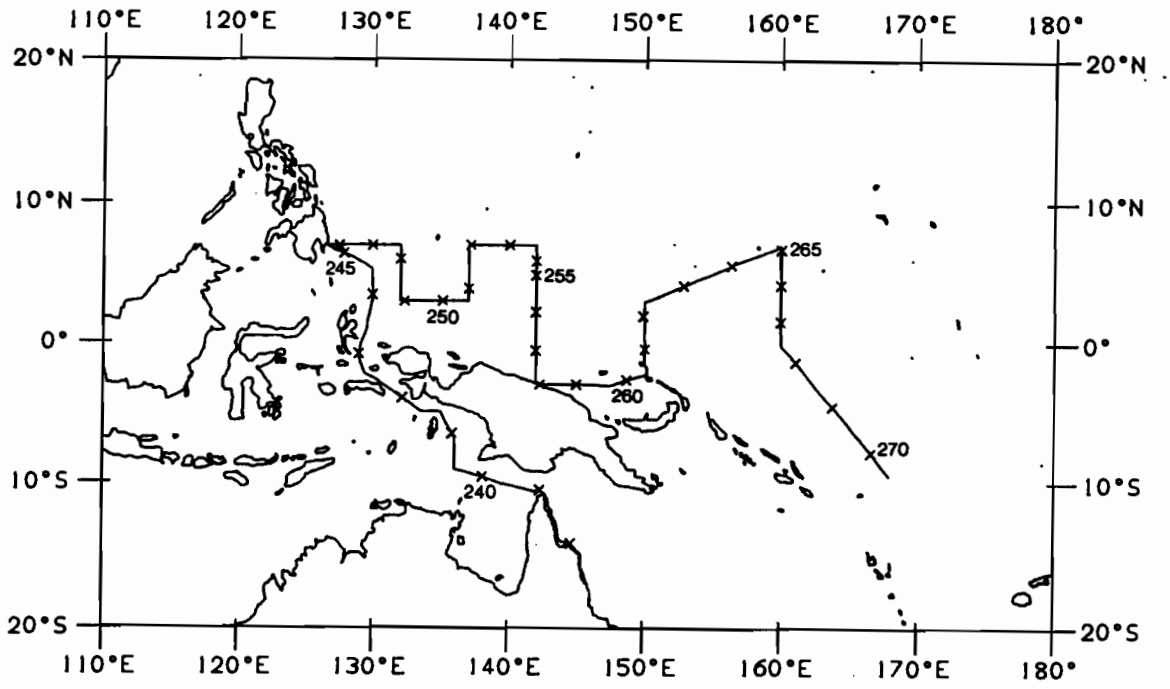

FIG.1. Tack of the RRS Charles Darwin during cruise 34A/1988. The crosses mark the ship's position at 000Z on the days indicated.

results from the long north-south section carried out on 142°E. Results are presented from the ADCP, showing the main current systems, and the SeaSoar, showing the structure of the temperature and salinity fields along the section.

2. The section on 142°E.

a. East-West Velocities

Currents were measured using a hull mounted R D Instruments ADCP. This was calibrated using the procedure described in Pollard and Read (1989). The instrument measures velocities relative to the ship averaged over 180 s intervals. Absolute velocities need the addition of the ship's speed and direction which is obtained from GPS, when available, and from Transit satellites. The latter fixes are carefully screened before use.

The east-west component of velocity obtained with this system is shown in Fig.2. Note that for plotting the data has been averaged into 12 km bins along the ship's track.

Near the surface the main core of the South Equatorial Current lies between 1°N and 1°S. Westward velocities in excess of 50 cm s^{-1} extend down to 100 m and the maximum velocity of 1 m s^{-1} is found near the southern boundary of the core region.

Further north the core of the North Equatorial Counter Current (NECC) is observed between 3°N and 5°N. The current also extends down to 100 m and has a maximum velocity in excess of 60 cm s^{-1}.

Below these lies the eastward flowing Equatorial Undercurrent. The outer limits extend from 1°S to 4°N, (the latter joining with the NECC), but the main current region lies between the equator and 3°N with a core at 2°N. Most of the current has speeds of over 30 cm s^{-1} and these rise to 70 cm s^{-1} in the core region.

Below the SEC, the undercurrent is limited in depth to a range between 150 m and 250 m but in its core region it has a much larger vertical extent, from 60 m to more than 300 m. Similar complex vertical structures has been observed by Eldin (1989).

Figure 2. East-west velocities on the section at 142E

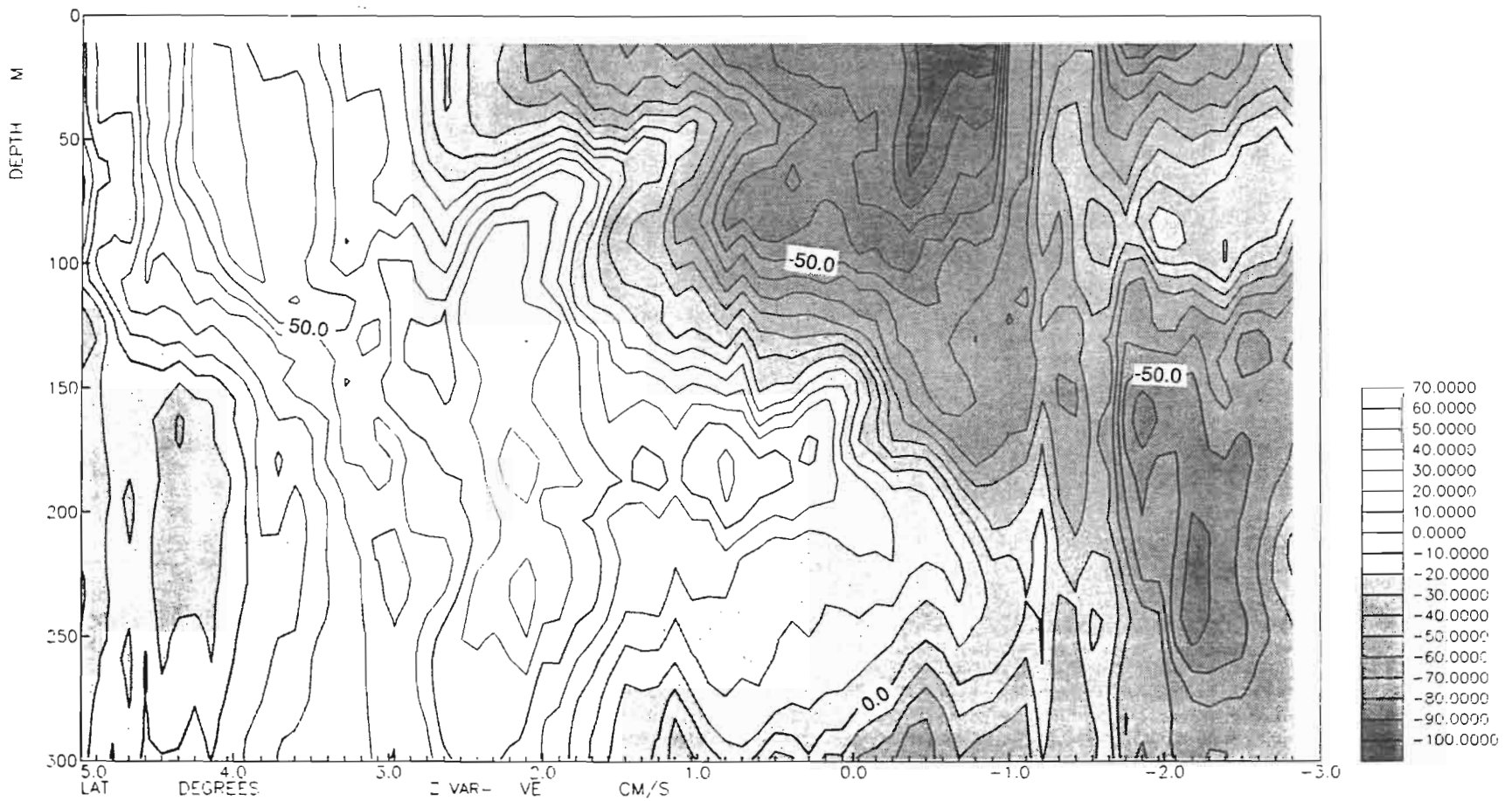

Near 3°S the New Guinea Coastal Undercurrent is observed between 100 and 300 m. It has a widths of about 100 kms and maximum velocities to the west of over 60 cm s^{-1}. At the surface, the flow is also westward, presumably this is another branch of the South Equatorial Current, but below this and extending from 60 m to 100 m is a region of weak easterly flows. The following section on 3°S shows this flow continuing to the east.

b. The temperature and salinity sections

Figs. 3 and 4 show the temperature and salinity fields measured by the CTD mounted in the SeaSoar. Calibration checks were made before and after the cruise and against water bottles during the cruise. Because of the possibility of fouling of the sensor, the salinity was checked at the top of each cycle against the ship mounted thermosalinograph. T/S profiles were also plotted during each cycle of the SeaSoar to check for jumps due to fouling but in the unproductive waters of the region such events were relatively rare. For plotting figures 3 and 4, data has been averaged into 4 km bins along the ships track.

The primary feature of the temperature record is the high and almost uniform near surface temperatures. The main thermocline lies below 100 m and the water above this appears reasonably well mixed in both the vertical and the horizontal.

The salinity on the section is shown in Fig 4. The main feature is a thick intrusion of high salinity South Pacific water, with salinities of over 34.8, which appears to be pushing northward into the less saline North Pacific waters.

However although the intrusion appears as a coherent feature, there is an important boundary at a depth of approximately 130 m between South Pacific waters advected westwards into the region by the surface South Equatorial current and by the deeper New Guinea Coastal Undercurrent.

In the lower layer, salinities of over 35.3 are found at a depth of 170 m extending from the New Guinea coast to 1°N. Slightly diluted the intrusion extends to 2°N where, with the upper layer, it meets the North Pacific water in a strong front right at the core of the Equatorial Undercurrent. Temperatures in the lower layer are generally less than 24°C.

The source of the upper layer appears to be the South Equatorial Current which brings South Pacific water into the region from the surface to 150 m with temperatures of over 28°C. This results in a sharp thermocline separating water from the two sources. Note also that despite their different origins, the two water masses combine to form a single intrusion into the North Pacific waters.

In the upper layer there is no high salinity core associated with the South Equatorial Current but there is continuity in water type between the water being advected westward by this current and the northward extension of the intrusion. Thus the change of salinity on an isopycnal between 0.5°S and 2°N is only 0.2 parts per thousand whereas the change in salinity across the front near 2.2°N is over 0.5 parts per thousand.

Between 0.5°S and 2°N the upper surface of the intrusion is marked by a strong halocline at a depth of 50 m. This halocline lies in a region of weak vertical temperature gradients. It has similarities to that reported by Lukas and Lindstrom (1987) but has a much larger salinity difference.

Another feature of this halocline is that it also marks the line of the upper extension of the equatorial undercurrent. Unfortunately the vertical resolution of the ADCP is not as good as that of the SeaSoar/CTD but the line of maximum westward flow follows the line of the main halocline in this region with more easterly flows in the North and South Pacific waters above and below.

The near surface halocline also extends, and affects the currents, right into the maximum current core of the South Equatorial Current at 0.5°S.

Between 1°S and 2°S the strong halocline disappears and in places the surface layer is mixed down to depths of 120 m and more. Similar deep mixed layers also show up in the surface North Pacific waters between 3°N to 4°N.

Figure 3. Temperature on the section at 142E

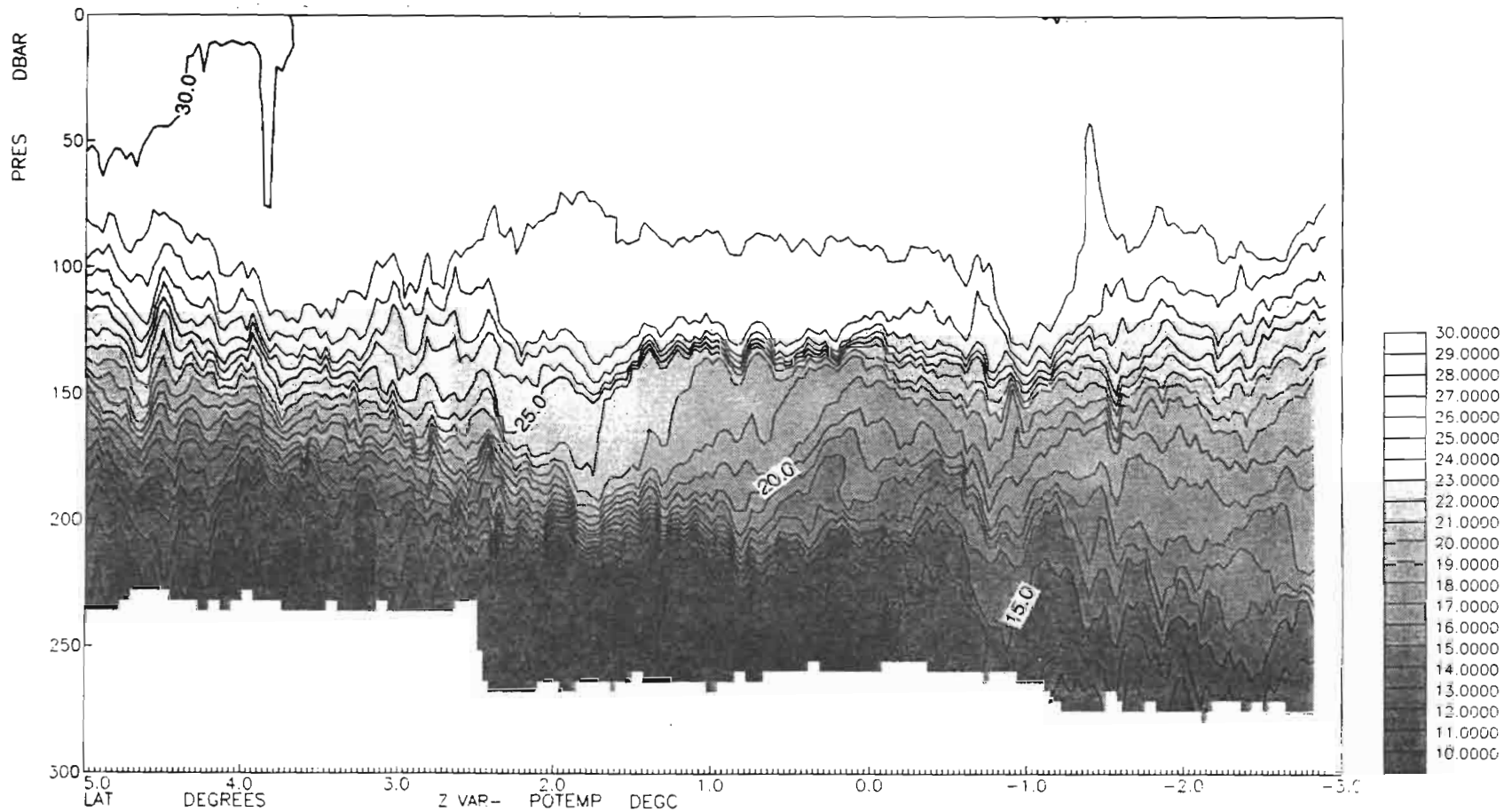

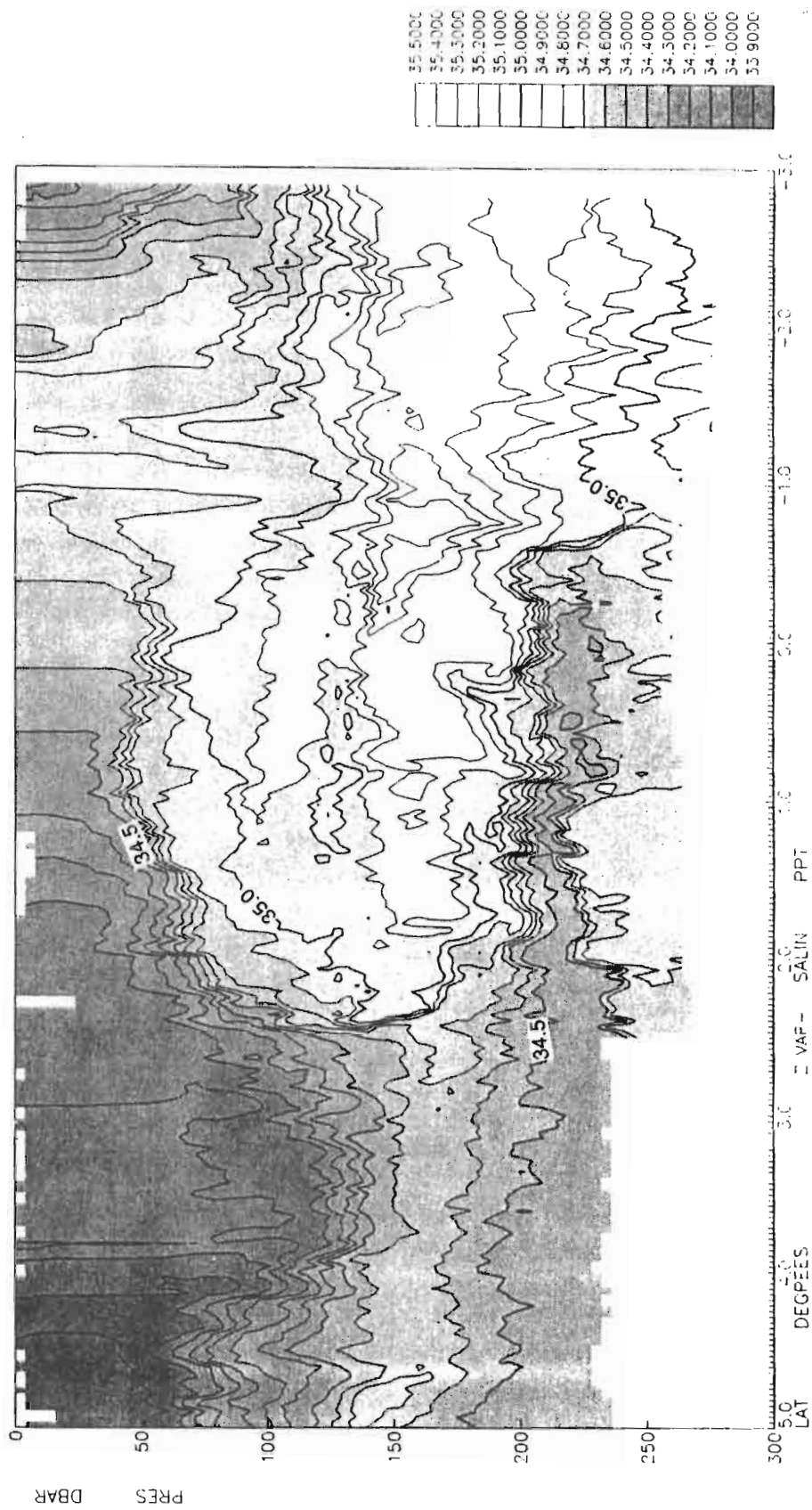

Figure 4. Salinity on the section at 142E

At the northern end of the section the North Pacific has a maximum salinity at a depth of 150 m. Above this salinities of below 34.0 are found in the surface layer. Similar low surface salinities are seen in the south at the New Guinea, probably the effect of river discharges.

At 220 m, below the main intrusion of South Pacific water, there is a further shallow intrusion of North Pacific water extending south to the equator and overlying another layer of South Pacific water at 250 m. The southern end of the intrusion at 220 m also corresponds to the southern edge of the Equatorial Undercurrent. Other small intrusions can be seen within the main South Pacific water mass, for example between the equator and 1°N at depths between 100 and 150 m.

3. Discussion.

The analysis of the data is still at an early stage but already a number of features are apparent. First the salinity contrast between the North and South Pacific water types is important with intrusions and strong fronts developing at the boundary of the two regions.

In the section along 142°E, the core of the Equatorial Undercurrent was found to be displaced north from the equator to 2°N. This may be connected to the observation that the core of the undercurrent coincides with the position of the northern limit of the main intrusion of South Pacific water or it may be coincidental. However at shallow depths the maximum eastward current follows the line of the halocline so the salinity front must be having some effect on the dynamics. Cooper (1988) also emphasizes the importance of salinity in tropical regions.

The strong halocline observed between the equator and 2°N at depths near 50 m between is very similar to that which has been observed using CTD casts in the region. The present results show that it can arise as a result of the saline South Pacific water intruding into the less saline North Pacific water.

The sharpness of the halocline at 50 m (and the one below the intrusion at 200m), is especially noticeable when compared to the more uniform north-south change in salinity in the top 50 m. Within the region surveyed, little turbulence is produced at the surface because of the low average winds and waves, so the observed fronts may be being sharpened up by turbulence caused by the strong vertical current shears present.

It is also noticeable that the strong near surface halocline has little effect on the ocean temperature structure in the top 100 m. The vertical flux of heat into the layers above and below the halocline must be small - at least compared to that due to advection or diffusion in from other areas unaffected by the halocline.

To conclude, data from RRS Charles Darwin cruise 34A is still being worked up by the results so far confirm that salinity is important in the Western Equatorial Pacific and that shear produced turbulence may also be important.

REFERENCES

Cooper, N., 1988: The effect of salinity on tropical ocean models. *J. Phys. Oceangr.*, 18, 697-707.

Eldin, G., 1989: Coupes verticales des structures océaniques physiques à 165°E observées au cours de dix campagnes SURTROPAC, 1094-1988. *Rapports Scientifiques et Techniques*, Sciences de la Mer, Océanographie Physique, N° 1 ORSTOM, Nouméa.

Gill, A.E., 1980: Some simple solutions for heat induced tropical circulations. *Quart. J. R. Meteorol. Soc.*, **106**, 447-462.

Lukas, R. and E. Lindstrom, 1987: The mixed layer of the western equatorial Pacific

Ocean.pp. 67 - 94 in, Dynamics of the oceanic suface mixed layer: proceedings 'Aha Huliko'a, 1987 (ed. P. Muller and D. Henderson). Hawaii institute of Geophysics, 310 pp.

Luther, D.S. D.E. Harrison, and R.A. Knox, 1989: Zonal winds in the central equatorial Pacific and El Nino. *Science,* 222, 327-330.

Pollard, R.T. and J.F Read, 1983: A method for calibrating shipmounted acoustic doppler profilers and the limitations of gyro compasses. *J. Atmos. Oceanic. Technol.*, (in press).

Simmons, A.J., J.M. Wallace, and G.W. Branstator, 1983: Barotropic wave propagation and instability, and atmospheric teleconnection patterns. *J. Atmos. Sci.*, **40**, 1363-1392.

Reflection of Annual Rossby Waves at The Maritime Western Boundary of the Tropical Pacific

Warren B. WHITE, Nicholas GRAHAM and Chang-Kou TAI

Scripps Institution of Oceanography
Mail Code A-030
University of California at San Diego
La Jolla, California 92093, U.S.A.

Baroclinic Rossby wave activity in the tropical Pacific was first observed by White (1977), who examined the annual cycle of subsurface thermal structure in the eastern region from 10°-20°N, finding westward propagating annual signals emanating from the eastern boundary, propagating eastward at baroclinic Rossby wave speeds to the longitude of the Hawaiian Archipelago. This work was followed by Meyers (1979), who observed westward propagation of the annual cycle in upper ocean thermal structure at baroclinic Rossby wave speeds near 6°N all across the Pacific. Subsequently, White (1983) examined interannual variability in the subsurface thermal structure in the western North Pacific, finding westward propagating signals traveling at baroclinic Rossby wave speeds from 6°-30°N. These interannual waves were associated with ENSO activity. Soon thereafter, interannual baroclinic Rossby wave activity in the latitude bands from 5°-15°N and from 5°-15°S was found to act as a precursor (e.g., White et al., 1985a; Pazan et al., 1986) to the onset of the 1982-1983 El Nino activity in the eastern equatorial Pacific; indirect evidence was found that the incidence of this baroclinic Rossby wave activity in these latitude bands was instigating baroclinic Kelvin wave activity in the equatorial wave-guide. Subsequently, White et al. (1987) used this information to demonstrate that both the observation and model simulation of baroclinic Rossby wave activity in the western tropical Pacific could be used to hindcast El Nino activity in the eastern equatorial Pacific for up to a year in advance over the 25-year period from 1962-1987.

The dynamical influence that baroclinic Rossby wave activity has upon in the maintenance of the quasi-cyclic behavior of ENSO (El Nino/Southern Oscillation) was discussed by Graham and White (1988). They established using a conceptual model that baroclinic Rossby wave activity influenced ocean/atmosphere coupling in the equatorial wave-guide by providing for a steady upwelling/downwelling (lasting from 3-9 months) through the excitation of upwelling/downwelling equatorial baroclinic Kelvin wave activity at the western boundary (via the Rossby wave reflection process). During the year prior to El Nino activity in the eastern equatorial Pacific, downwelling equatorial Kelvin wave activity was associated with a steady eastward advection of warm water from the western equatorial Pacific into the central and eastern equatorial ocean, advected by the associated zonal eastward current; this eastward displacement of warm SST's on the equator was hypothesized to instigate a coupled unstable wave in the ocean/atmospheric system along the equator, of the kind discussed by Schopf and Suarez (1988). Within this conceptual model, the reflection of baroclinic Rossby waves at the western boundary of the tropical Pacific also played an important role in turning the El Nino process off, leading to La Nina, as discussed in Graham and White (1988).

Sources of baroclinic Rossby wave activity in the tropical Pacific are fairly well known. White (1977) found evidence consistent with the idea that baroclinic Rossby waves were being generated at the eastern boundary through the action of the wind stress

ORSTOM
CENTRE DOCUMENTATION
Montpellier

F 30206

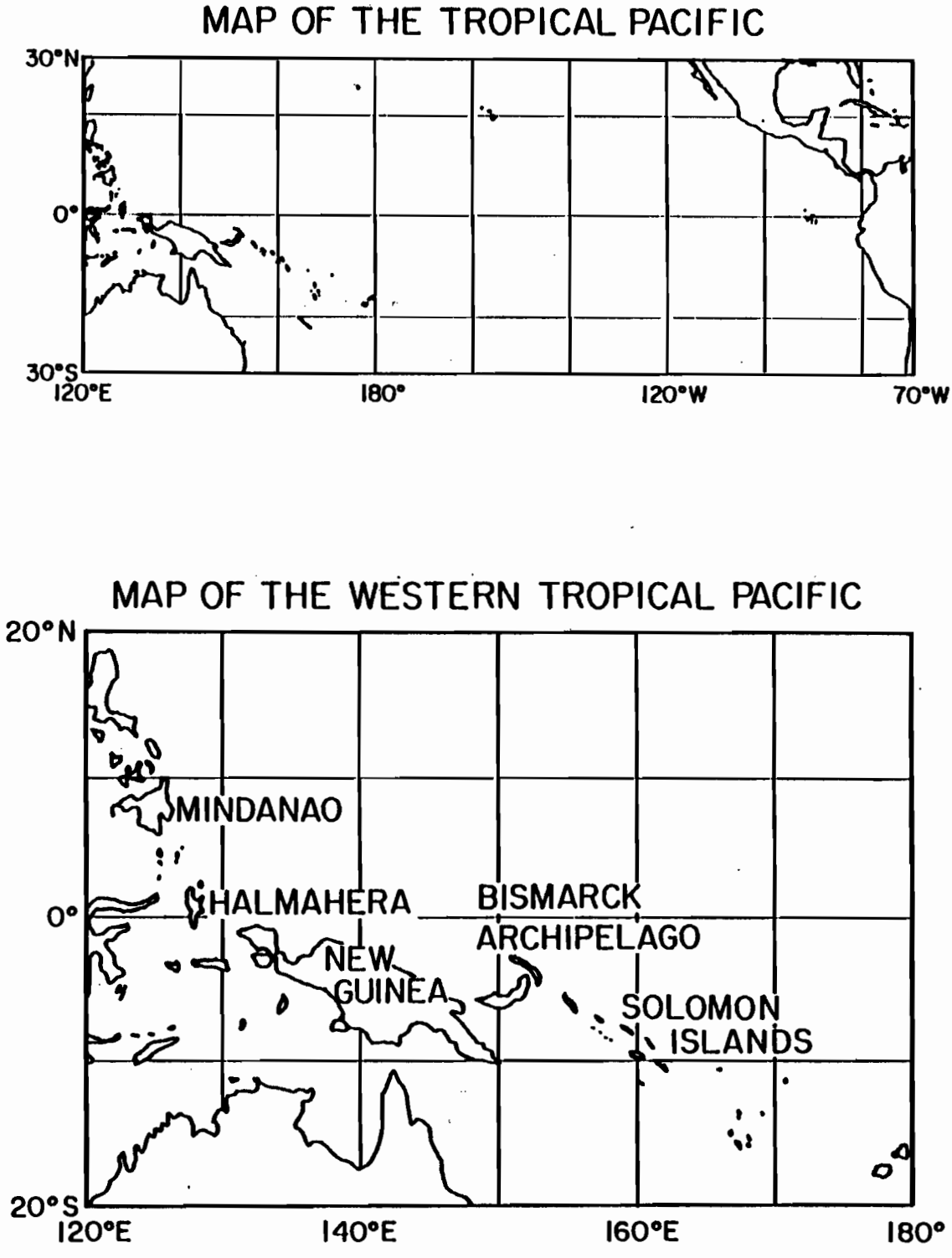

FIG.1. (Upper Panel): Map of the tropical Pacific from 30°N to 30°S where this study was conducted. (Lower Panel): Map of the western tropical Pacific, where the reflection of baroclinic Rossby waves by the maritime western boundary is emphasized.

curl. Meyers (1979) found baroclinic Rossby waves of annual period in the western and central tropical North Pacific to have been generated by the Ekman pumping in the Trade Wind field in the eastern tropical North Pacific. Later, White et al (1985b) demonstrated that the interannual baroclinic Rossby wave activity in the western North Pacific was wind-generated in response to Ekman pumping in the western and central tropical Pacific. Moreover, it was shown that baroclinic Rossby wave activity increased in amplitude toward the west in response to resonance with the wind stress curl forcing. Pazan and White (1987) computed a vorticity/volume budget for the western tropical Pacific from 4°-16°N, 160°E-160°W, finding the thermocline to have been pumped vertically in response both to the divergence of Ekman transport in the upper layer (i.e., indicative of Ekman pumping) and to the divergence of geostrophic transport in the region (i.e., indicative of Rossby wave propagation). More recently, White et al. (1989) demonstrated that it was possible to track interannual baroclinic Rossby wave activity all the way across the ocean from the eastern boundary to the western boundary in both observations and the models at approximately 12°N; regardless, Graham et al. (1989) found that most of the magnitude in this wave activity occurred in response to wind stress curl forcing in the central and western tropical Pacific, amplified by resonant forcing.

The reflection of baroclinic Rossby wave activity at the maritime western boundary of the tropical Pacific has been inferred from the statistical correlation between anomalous upper layer thickness in the off-equatorial western tropical Pacific (associated with baroclinic Rossby wave activity) and that in the central and eastern equatorial Pacific (associated with baroclinic Kelvin wave activity) in both models and observations (Pazan et al., 1986). Still, no direct observational evidence exists for the reflection of baroclinic Rossby wave activity at this western boundary and the subsequent generation of equatorial Kelvin wave activity emanating from it. A certain amount of skepticism surrounds the reflection process at the maritime western boundary (i.e., formed by the Philippines Archipelago in the northern hemisphere and possibly the Solomon Archipelago in the southern hemisphere, as shown in Fig. 1) because of the presence of gaps in the numerous archipelagoes that could conceivably constitute the maritime western boundary of the tropical Pacific. However, recently Clark (1989) and du Penhoat and Cane (1989) established that these particular archipelagoes were quite good reflectors of interannual Rossby wave activity, reflecting 70-80% of the incident baroclinic Rossby wave activity as baroclinic equatorial Kelvin waves.

In this study, the examination of GEOSAT altimetric sea level differences provides the first direct evidence of this reflection process operating at the maritime western boundary of the tropical Pacific in both the northern and southern hemisphere (see Fig.1). In an earlier study, Tai et al. (1989) analyzed altimetric sea level crossover differences from the first 17 months of the GEOSAT mission from November 1985-April 1987, finding statistically significant agreement with *in situ* measurements of sea level differences (i.e., island sea level and relative dynamic height). In that study the dominant time scale of variability that could be studied was the annual cycle; interannual variability could not be addressed because of the relatively short length of the record. So too in this study; only the wave reflection at the maritime western boundary of the tropical Pacific associated with the annual cycle is addressed.

In the earlier study of Tai et al. (1989), a time series of maps of altimetric sea level residuals in the tropical Pacific (17 months from April 23, 1985 to September 8, 1986, separated into thirty 17-day time steps) was generated. Verification of these maps was conducted by Tai et al., (1989) from the comparison of the maps of altimetric sea level residuals to similar maps of relative dynamic height (0/400 db) residuals, and time sequences of altimetric sea level residuals to similar time sequences of sea level residuals measured at island stations. Examples of these 17-day maps is given in Fig.2,

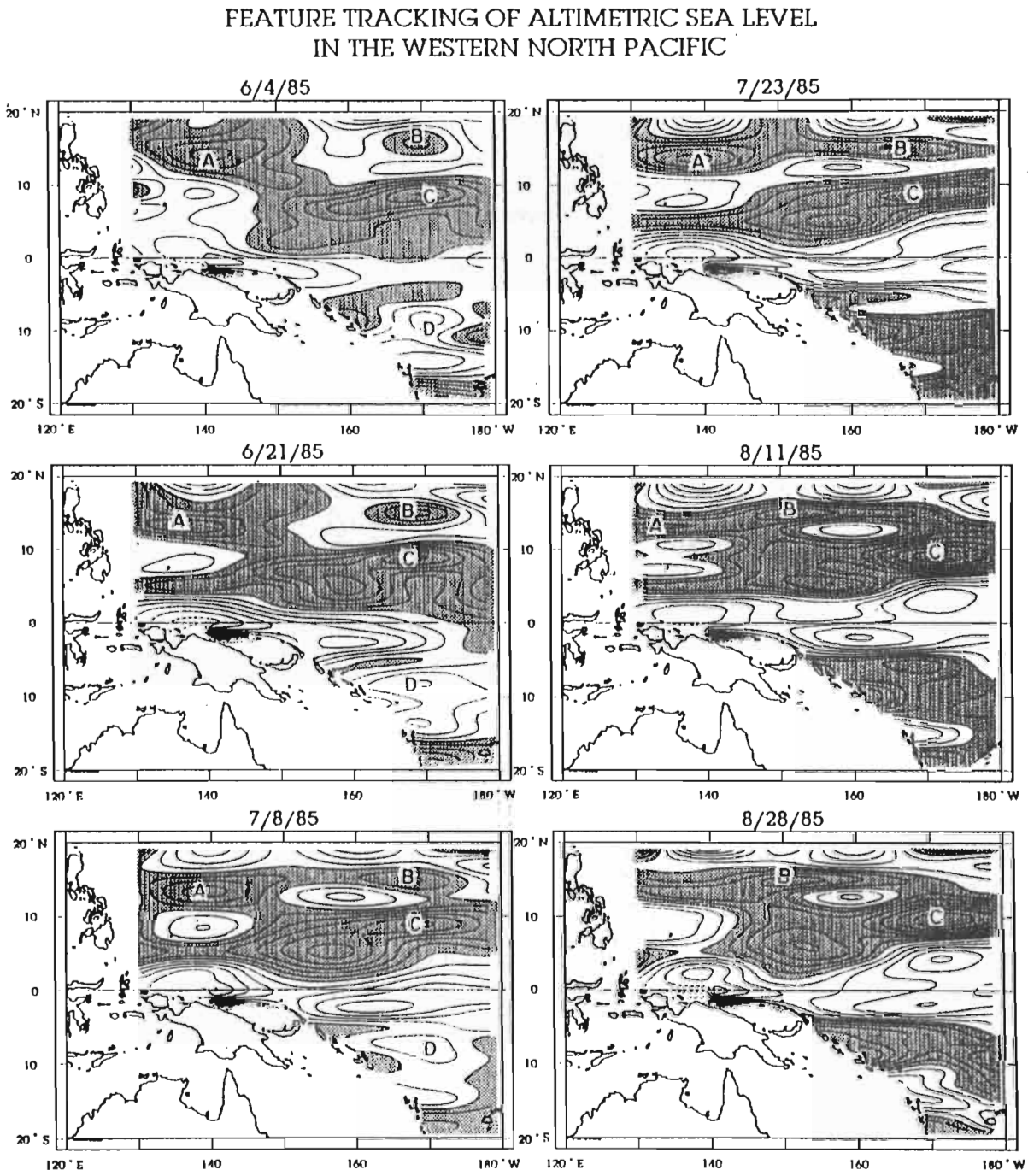

FIG.2. Altimetric sea level maps for June-August 1985. Features evolve smoothly and consistently through this series of maps (CI = 2cm, negative values are shaded).

concentrating on the western tropical Pacific, repeated from Tai et al. (1989). Notice that in the maps the Philippines Archipelago forms the maritime western boundary in the northern hemisphere from the equator to nearly 20°N, while the Solomon Archipelago/New Guinea complex forms the maritime western boundary in the southern hemisphere from the equator to approximately 10°S. Notice too that the sea level residual features labeled alphabetically in Fig.2 can be traced from map to map, often indicating (particularly A and B) westward propagation into the maritime western boundary of the tropical Pacific.

In order to extract the information that this time series of maps of altimetric sea level residuals has concerning the reflection of baroclinic Rossby waves from the maritime western boundary of the tropical Pacific, extended empirical orthogonal function (EEOF) analysis (Graham et al., 1987) was conducted upon the thirty-one 17-day maps of altimetric sea level differences about the mean for the 17-month period represented (i.e., from November, 1985-April, 1987). One EEOF analysis was conducted upon the entire field of altimetric sea level differences from South America to the maritime coast of Asia, allowing the evolution of the basin-scale redistribution of mass to be examined (Fig.4). Then, in order to focus on the reflection activity at the maritime western boundary of the tropical Pacific, the EEOF analysis was repeated upon the western tropical Pacific, from 20°S-20°N west of 160°W (Fig.5).

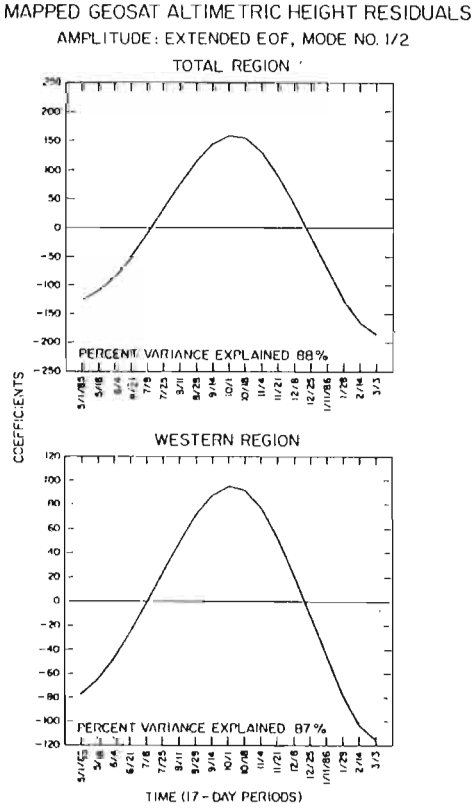

FIG.3. Time sequences for the fist extended empirical orthogonal functions of altimetric sea level residual computed for the tropical Pacific (Upper Panel) and the western tropical Pacific (Lower Panel),explaining 88% and 87% of the total variance in the 17-month time sequence. The evolutionary spatial patterns of these functions are given in Figs. 5 and 6.

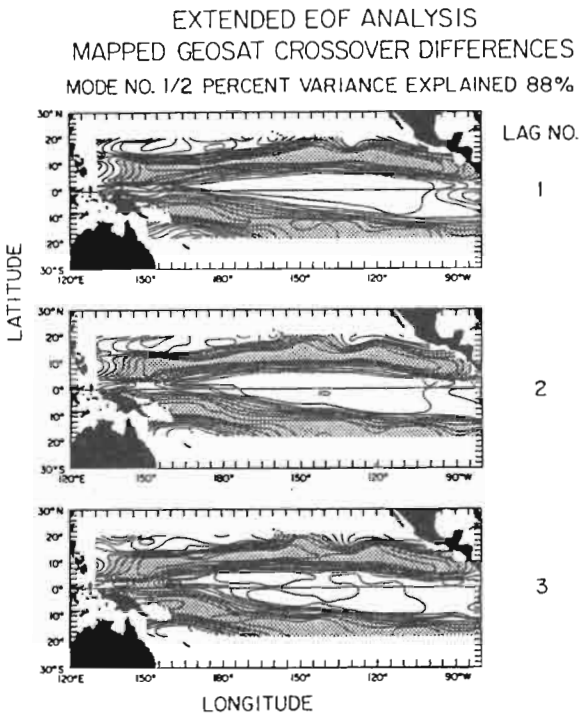

FIG.4.a Time sequence of the first three spatial patterns (1-3) of the first extended empirical orthogonal function for the tropical Pacific, the latter explaining 87% of the total variance in the 17-month time sequence. Shading indicates negative phase.

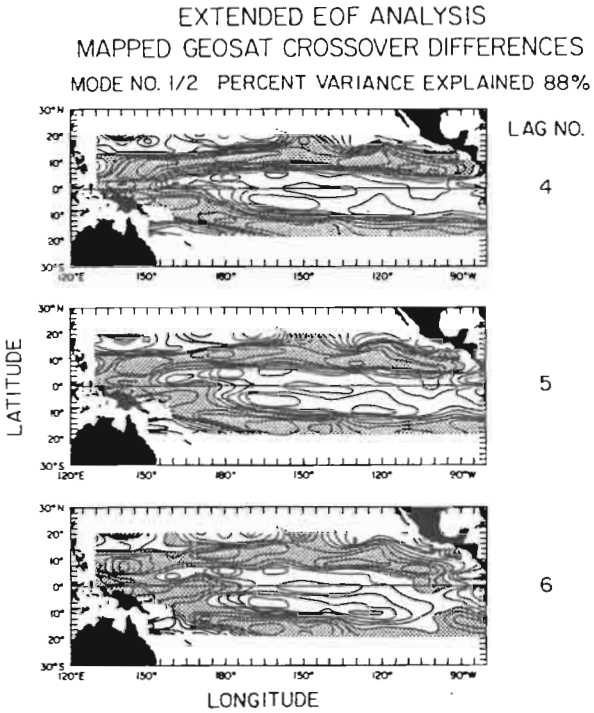

FIG. 4b. Time sequence of the second three spatial patterns (4-6) of the first extended empirical orthogonal function for the tropical Pacific, the latter explaining 87% of the total variance in the 17-month time sequence. Shading indicates negative phase.

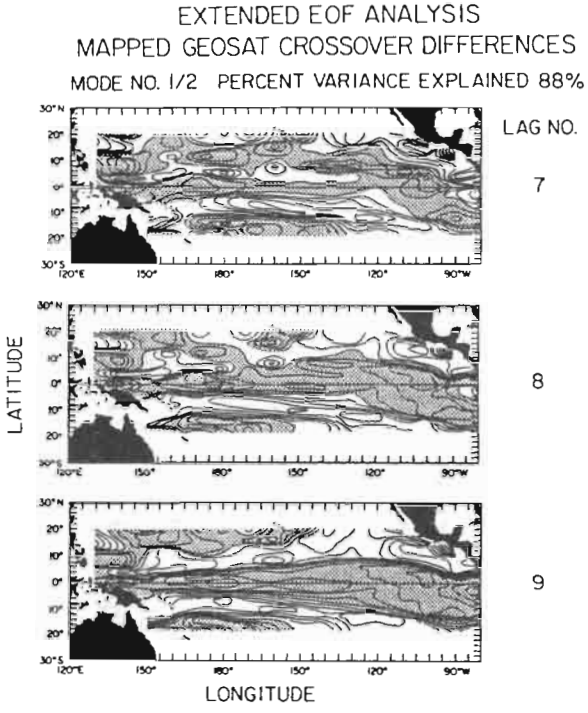

FIG. 4c. Time sequence of the third three spatial patterns (7-9) of the first extended empirical orthogonal function for the tropical Pacific, the latter explaining 87% of the total variance in the 17-month time sequence. Shading indicates negative phase.

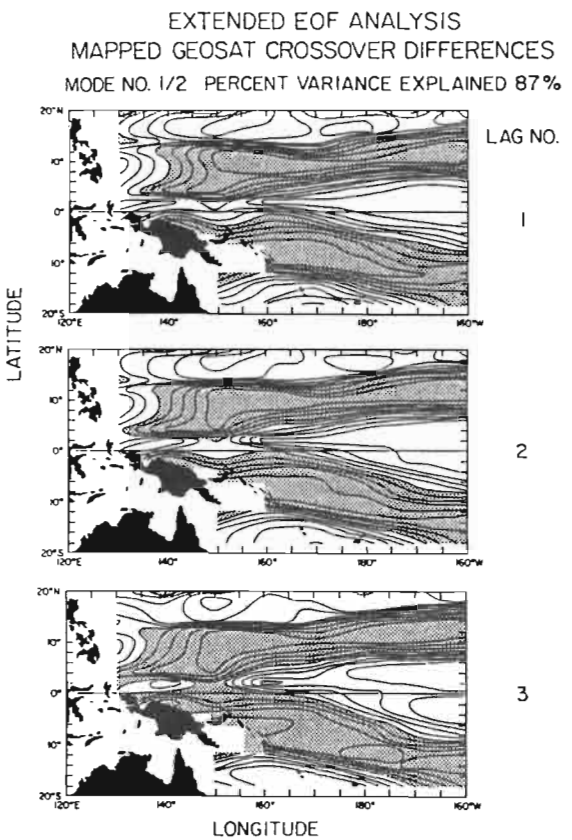

FIG. 5a. Time sequence of the three spatial patterns (1-3) of the first extended empirical orthogonal function for the western tropical Pacific, the latter explaining 88% of the total variance in the 17-month time sequence. Shading indicates negative phase.

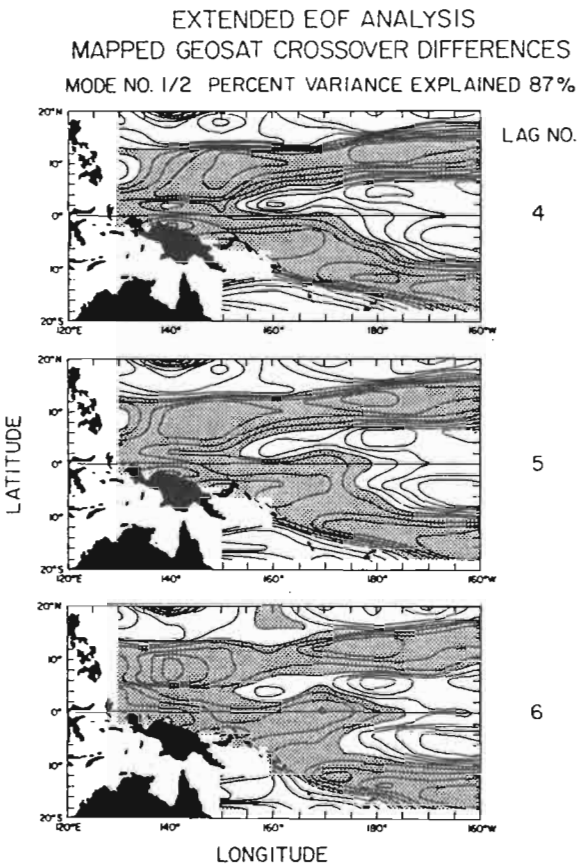

FIG. 5b. Time sequence of the second three spatial patterns (4-6) of the first extended empirical orthogonal function for the western tropical Pacific, the latter explaining 88% of the total variance in the 17-month time sequence. Shading indicates negative phase.

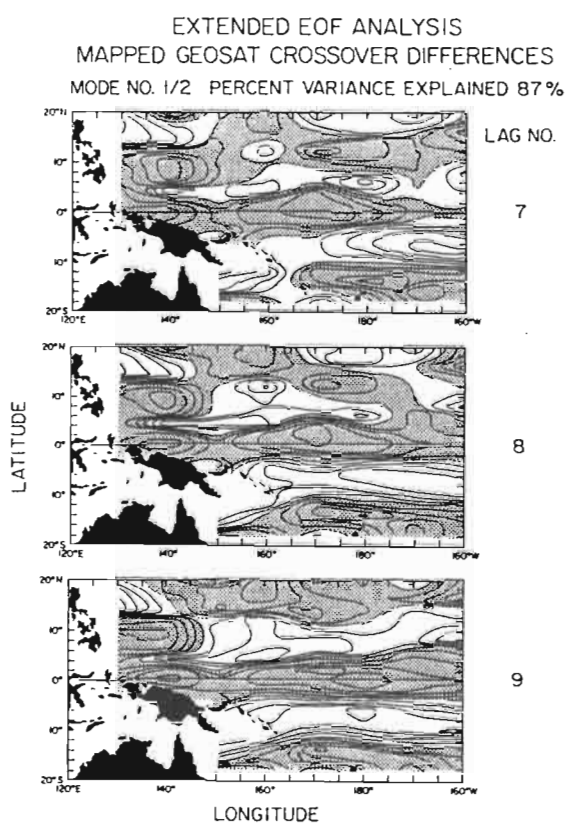

FIG. 5c. Time sequence of the third three spatial pattern (7-9) of the first extended empirical orthogonal function for the western tropical Pacific; the latter explaining 88% of the total variance in the 17-month time sequence. Shading indicates negative phase.

The time sequences of both of these EEOF's is given in Fig.3, with that for the entire tropical Pacific shown in the upper panel, and that for the western Pacific shown in the lower panel. Each are taken from the first two EEOF's, which together account for 88% and 87% of the total variance, respectively, in the tropical Pacific and the western tropical Pacific. The first two EEOF's tend to be redundant and, being orthogonal, give different phases of the same evolutionary behavior in the time sequence of maps (Graham et al., 1987). In this case, the time series of the two analyses are nearly identical, and strongly dominated by the annual cycle.

The EEOF on the basin scale maps is given in Fig. 4a, b, c, showing the evolution of the annual cycle through approximately half a cycle (i.e., 6 months), extending over nine 17-day time periods (i.e., 153 days). The time sequence of nine maps that constitutes the EEOF shows how the spatial pattern in Map 1 evolved into the opposite phase in Map 9 through the spring/autumn transition. In this series of maps, the latitude of approximately 8° marked a boundary where the phase of the annual cycle on the poleward side was opposite that on the equatorward side. This was also found to be true in the complex empirical orthogonal function (CFOF) analysis in Tai et al., (1989). In the present study, by following the evolution of the annual cycle through half a cycle with the aid of the EEOF analysis, from positive residual on the equator (i.e., Map 1) to negative residual on the equator (Map 9), this phase transition from winter to summer (and vice versa) can be understood.

In the first three maps of Fig.4a, the changes that took place in this phase transition are the following. In the off-equatorial region poleward of approximately 8° latitude, the negative residual propagated to the west, evident particularly in the western tropical Pacific. In the western equatorial Pacific, west of 160°E, the negative anomaly began to collapse onto the equator, more from the southern hemisphere north of the Solomon Archipelago/New Guinea complex than from the northern hemisphere. In the northern hemisphere, positive residuals along the coast of the Philippines Archipelago extended southward to the equator in Map 1 and Map 2, where they protruded eastward along the equator; this terminated in Map 3.

In the next three maps (i.e., Maps 4-6 in Fig. 4b), the transition in phase of the annual cycle found negative residuals on the equator in the western Pacific emanating from the Solomon Archipelago/New Guinea complex in the southern hemisphere. Moreover, these negative residuals began to extend eastward along the equator into the eastern equatorial Pacific forming a trough along the equator. In Map 4, this eastward extension of the trough along the equator seems to have originated from the southern hemisphere, but by Map 6 the trough seems to have originated from both hemispheres. At the eastern boundary, an interesting phenomenon began to occur in this sequence of three maps; apparent first-mode equatorial Rossby wave activity appears to have reflected from the eastern boundary (i.e., with local positive maxima at 4°N and 4°S) in response to incident Kelvin wave activity, associated with positive residuals extending northward along the coast of Central America. However, over these three maps (and, as we shall see, over the next three maps) this apparent first-mode equatorial Rossby wave activity did not propagate westward of the Galapagos Archipelago.

In the next three maps (i.e., Maps 7-9 in Fig. 4c), the autumn phase transition from positive to negative sea level residuals along the equator was completed. This occurred with the eastward propagation of negative sea level residuals, initially (Map 7) extending from the west along the equator and confined to the equatorial wave-guide, but later (Map 9) filling the entire region equatorward of approximately 8° latitude, apparently in response to wind stress forcing. In the northern hemisphere western Pacific, negative residuals can be seen to have propagated westward onto the Philippine Archipelago between 5°-15°N, extending equatorward along the maritime western boundary from 15°N to the equator, with negative residuals extending eastward along the

equator from the maritime western boundary of the tropical Pacific. This is indicative of the reflection of incident baroclinic Rossby wave activity and the excitation of baroclinic Kelvin wave activity. In the southern hemisphere western Pacific, positive residuals in the western Pacific began to be found along the Solomon Archipelago, nudging equatorward to begin the process of another phase transition (i.e., this time the spring transition) from the present negative equatorial state to a positive one on the equator.

The EEOF of the western tropical Pacific (i.e., 160°W to the maritime coast of Asia) is given in Fig. 5a, b, c, showing the evolution of the annual cycle through half a cycle (i.e., 6 months), extending over nine 17-day period (i.e. 170 days). It shows in detail the western boundary reflection of the annual baroclinic Rossby wave activity, associated with phase transition of the annual cycle over the entire tropical Pacific shown in Fig. 4a, b, c, and the subsequent Kelvin wave excitation in the equatorial wave-guide.

In the first three maps of Fig. 5a, the changes that took place in the western boundary, associated with the phase transition of the annual cycle from positive to negative residual on the equator, were able to be observed. In the off-equatorial region of the southern hemisphere (i.e., poleward of equatorial wave-guide, the latter extending to approximately 3° latitude), the negative residuals can be seen to have propagated to the west, clearly riding up onto the Solomon Archipelago/New Guinea complex from 160°-150°E, penetrating as far west as 130°E. Over this approximately 1 1/2 month period, the negative residuals also penetrated equatorward and intersected the equator in a relatively broad longitudinal band equatorward of the Solomon Archipelago and New Guinea. Poleward of the equator wave-guide in the northern hemisphere, positive residuals along the coast of the Philippines Archipelago (i.e. from 3°-14°N) extended southward to the equator, where they protruded eastward along the equator, indicative of the excitement of equatorial Kelvin wave activity by the coastal Kelvin-Munk wave activity (Godfrey, 1976). It is important to remember that each altimetric sea level datum along 130°E is a 10° longitude mean, so the information at the longitude extends from 125°-135°, representing information in sea level variability next to the Philippine coast at 123°-127°E, but smearing it with information eastward of there. East of the positive residuals adjacent to the Philippines Archipelago, negative residuals were observed to extend all across the tropical Pacific from 4°-12°N; in Fig. 5a these negative residual can be observed to have propagated to the west over the three maps shown penetrating over the two month period to the maritime western boundary from 2°-6°N and extending toward the equator north of New Guinea.

In the next three maps (i.e. Maps 4-6 in fig. 5b), the transition in annual phase finds the negative residual that had penetrated to the equator north of Solomon Archipelago/New Guinea complex in the western Pacific (over the previous 1 1/2 month) extending eastward along the equator, forming a trough from 130°E-160°W. In Map 4, the eastward extension of this trough along the equator originated from the southern hemisphere, but in Maps 5 and 6 the trough began to originate from both hemispheres, with the contributions from both hemispheres clearly visible. The earlier contribution from the southern hemisphere seemed to have occurred because the maritime western boundary in the southern hemisphere was located 20°-30° of longitude east of that in the northern hemisphere, coupled with the fact that the negative residuals in the off-equatorial region as a whole were relatively symmetric about the equator. The lag of the northern hemisphere behind the southern hemisphere was only 1-2 months. In the last map (i.e., Map 6) of this series of three in Fig. 5b, the off-equatorial negative residuals in the northern hemisphere penetrated to the maritime western boundary at approximately 10°N, with maximum values continuing equatorward along the boundary and extending east along the equator.

In the next three maps (i.e., Maps 7-9 in Fig. 5c) the autumn phase transition in the annual cycle from positive to negative residuals along the equator was completed, with the equatorial wave-guide filled with negative residuals emanating principally from the maritime western boundary in the northern hemisphere from 5-15°N. During these times, the southern hemisphere had positive residuals in the off-equatorial region from 5°-15°S, nudging equatorward to begin the reciprocal process of the spring phase transition from the present negative equatorial state to positive; not so in the northern hemisphere where an intense negative anomaly from 5°-15°N continued to supply off-equatorial influence to the equator via the maritime western boundary, helping to maintain the negative residuals in the equatorial wave-guide. In this maritime western boundary of the northern hemisphere, regional maxima in negative residuals were found directly east of Mindanao near 8°N and east of Halmera near 2°N; smaller values were found in between where a gap occurs in the maritime western boundary. Yet still, indications are that the negative residuals bridged this gap, particularly evident in Maps 6-9 in Fig. 5.

An interesting side-light of this examination of the baroclinic Rossby wave reflection occurring at the maritime western boundary of the tropical Pacific is the reflection (or, rather, the lack thereof) of the incident equatorial kelvin wave activity at the eastern boundary of the tropical Pacific (i.e., South America) that can be seen in Fig. 4a, b, c. The incident annual equatorial baroclinic Kelvin wave was observed to have generated coastal Kelvin wave activity (i.e., traveling poleward) and equatorially trapped Rossby wave activity (i.e., traveling westward). It is observed that the equatorially trapped Rossby wave activity, thus generated, did not propagate westward past the Galapagos Archipelago.

Acknowledgments. We thank Thomas Davis of the Navy Oceanographic Office, who kindly provided us with the GEOSAT crossover differences. Appreciation is given to Ted Walker and Paul Rasmusson who, as programmers, were instrumental in the analysis of these GEOSAT crossover differences. This study was supported principally by NSF Grant OCE86-07962. The research was also supported under NASA's TOPEX Altimetry Research in Ocean Circulation Mission, funded through the Jet Propulsion Laboratory. The computations was done partly on the San Diego Supercomputer Center's CRAY XMP-48.

REFERENCES

Clarke, A.J., 1989: On the reflection and transmission of low frequency energy at the irregular Pacific Ocean boundary - A preliminary report. In: *Western Pacific International Meeting and Workshop on TOGA-COARE. Noumea, New Caledonia.*

du Penhoat, Y., and M.A. Cane, 1989: Effect of low latitude western boundary gaps on the reflection of equatorial motions. In: *Western Pacific International Meeting and Workshop on TOGA-COARE. Noumea, New Caledonia.*

Godfrey, J.S., 1975: On ocean spindown I: A linear experiment. *J. Phys. Oceanogr.*, **5**, 399-459.

Graham, N., J. Michaelsen, and T.P. Barnett, 1987: An investigation of the El Nino Southern Oscillation cycle with statistical methods. 1. Predictor field characteristics. *J. Geophys. Res.*, **92**, 14, 251-14,270.

Graham, N., and W.B. White, 1988: The El Nino; a natural oscillator of the Pacific ocean/atmosphere system. *Science*, **240**, 1293-1302.

Graham, N., T.P. Barnett, V.G. Panchang, O.M. Smedsted, J.J. O'Brien, and R.M. Chervin, 1989: The response of a linear model of the tropical Pacific to surface wind from the NCAR general circulation model. *J. Phys. Oceanogr.*, **19**, 1222-1243

Meyers, G., 1979: On the annual Rossby wave in the tropical North Pacific Ocean. *J. Phys. Oceanogr.*, **9**, 663-674.

Pazan, S., and W.B. White, 1987: Short-term climatic variability in the volume budget of the western tropical Pacific during 1979-82. *J. Phys. Oceanogr.*, **17**, 440-454.

Pazan, S., W.B. White, M. Inoue, and J.J. O'Brien, 1986: Off-equatorial influence in dynamic height upon the equatorial Pacific during the 1982-83 ENSO event. *J. Geophys. Res.*, **91**, 8438-8449.

Schopf, P.S., and M.J. Suarez, 1988: Vacillations in a coupled ocean-atmosphere model. *J. Atmos. Sci.*, **45**, 549-566.

Tai, C.K., W.B. White and S.E. Pazan, 1989: GEOSAT crossover analysis in the tropical Pacific 2. Verification analysis of altimetric sea level maps with expendable bathythermograph and island sea level data. *J. Geophys. Res.*, **94**, 897-908.

White, W.B., 1977: Annual forcing of baroclinic long waves in the tropical North Pacific ocean. *J. Phys. Oceanogr.*, **7**, 50-61.

White, W.B., 1983: Westward propagation of short-term climate variability in the Western North Pacific Ocean from 1964-1974. *J. Mar. Res.*, **41**, 113-125.

White, W.B., G. Meyers, J.R. Donguy and S. Pazan, 1985a: Short-term climatic variability of the Pacific ocean during 1979-1982. *J. Phys. Oceanogr.*, **15**,, 917-935.

White, W.B., S. Pazan and B. Li, 1985b: Processes of short-term climatic variability in the baroclinic structure of the interior Western Tropical North Pacific. *J. Phys. Oceanogr.*, **15**, 386-402.

White, W.B., S. Pazan and M. Inoue, 1987: Hindcast/forecast of ENSO events based upon the redistribution of observed and model heat content in the Western Tropical Pacific. *J. Phys. Oceanogr.*, **17**, 264-280.

White, W.B., Y.H. He, and S.E. Pazan, 1989: Redistribution of subsurface thermal structure during the onset of the 1982-83 and 1986-87 ENSO events and the 1984-85 anti ENSO event. *J. Phys. Oceangr.*, (in press).

Observations of Long Rossby Waves in the Northern Tropical Pacific

William S. KESSLER

Joint Institute for the Study of the Atmosphere and Ocean
University of Washington
Seattle, WA 98115 - U.S.A.

ORSTOM
CENTRE DOCUMENTATION
Montpellier

1. Introduction

Long baroclinic Rossby waves are potentially important in the adjustment of the tropical (extra-equatorial) Pacific pycnocline to both annual and interannual wind stress curl fluctuations. The purpose of this paper is to document the occurrence of these waves from historical data and to show that much of the observed low-frequency pycnocline variability in the northern tropical Pacific may be represented by a simple model expressing the physical processes of Ekman pumping, the radiation of long (non-dispersive) Rossby waves due to such pumping in mid-basin, and the radiation of long Rossby waves from observed eastern boundary thermocline depth fluctuations. Evidence of long Rossby waves is found in bathythermograph (BT) observations of the depth of the 20°C isotherm, which is used as a proxy for pycnocline variability. The progenitor of the present study is Meyers' (1979a) investigation of the annual cycle of 14°C depth, which used a similar model of a low-frequency linear quasi-geostrophic two-layer ocean. Much of Meyers' (1979a) work was updated (and largely confirmed) in Kessler (1989a, b), with the addition of ten more years of both BT and wind observations.

In a series of papers, White and collaborators (White, 1977, 1983; White, et al., 1982, 1985; Inoue, et al., 1987; Pazan, et al., 1986; Pazan and White, 1987; Graham and White, 1988) have sought to interpret BT observations in the extra-equatorial north Pacific in terms of similar simple long Rossby wave dynamics, often using the linear reduced-gravity model developed by Busalacchi and O'Brien (1980). Some of their results are consistent with conclusions reported here, however the expendable BT (XBT) data available to these investigators are distributed primarily along a few shipping lines, with large gaps in some important areas, requiring relatively elaborate interpolation schemes between the ship tracks or the use of model output to fill data gaps. Because of this, their interpretation of observed interannual variability as evidence of zonal propagation has been controversial. An essential element of the present study is in the addition of a large set of mechanical BT (MBT) data taken by Japanese fishing vessels, which is concentrated in a previously data-poor region in the western tropical Pacific and makes possible the construction of long time series of thermocline depths in the western Pacific with a minimum of zonal interpolation.

Section 2 discusses the BT data sets, their processing and gridding. The simple model of low-frequency pycnocline variability is developed in Section 3, and the approximations made are discussed. Section 4 focuses on the role of long extra-equatorial Rossby waves in the evolution of El Niño, and the variability is discussed in terms of the simple dynamics outlined above, comparing the observations with hindcasts derived assuming either local Ekman pumping or including the radiation of low-frequency Rossby waves. Waves due to two principal forcing sources are identified: upwelling long Rossby waves generated in mid-basin by the large scale wind stress curl pattern associated with strong equatorial westerly wind anomalies; and downwelling long Rossby waves which radiate from the eastern boundary following the reflection of the deep equatorial thermocline anomaly which occurs during El Niños. The suggestion that long Rossby waves in the extra-equatorial tropics can be a trigger for subsequent El Niños, which has been debated in the recent literature, is evaluated from several time series which extend back to the 1950's, spanning seven major El Niño events.

A brief note on terminology is necessary: the word "tropical" is used in the sense of "extra-equatorial", to refer to the regions between about 5° and about 25° latitude. As discussed in Section 2, the observations are inadequate to study the rapid zonal propagation which occurs in the equatorial waveguide, so dynamical interpretation is confined to the extra-equatorial, "tropical" regions.

2. Data collection and processing.

a. Introduction

Several organizations hold large archives of historical BT observations, each of which densely samples particular regions; however none of these data sets individually has sufficient coverage to document zonally

F 30207

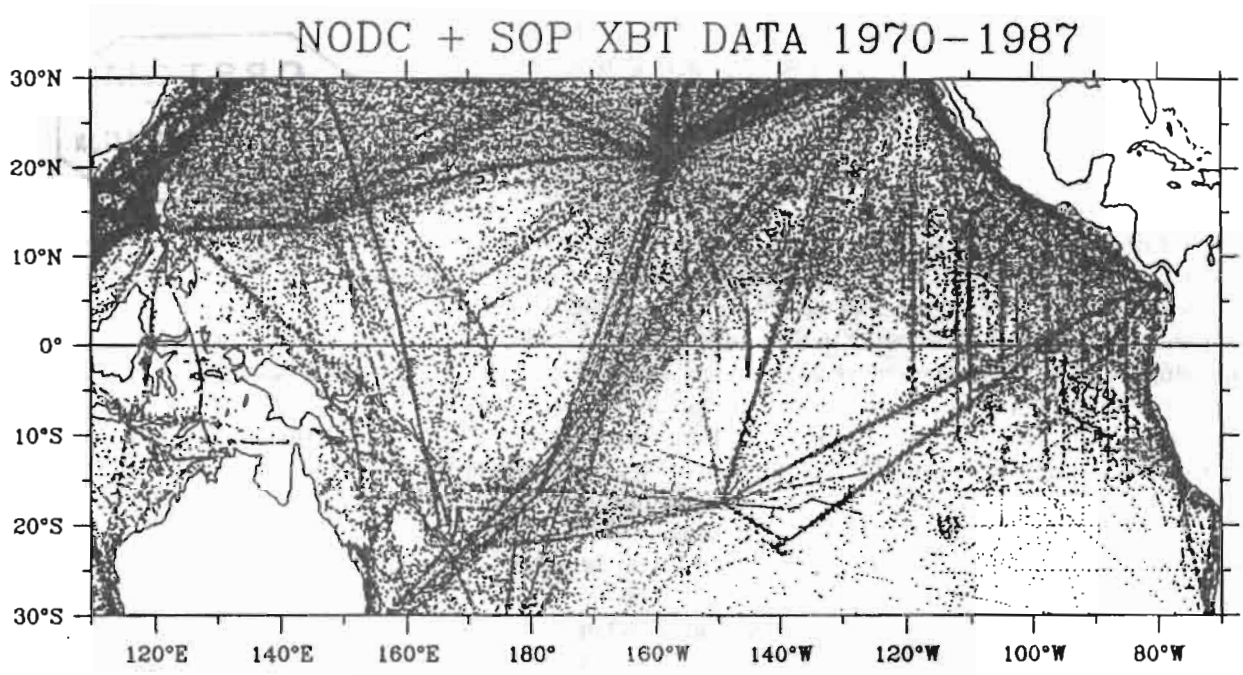

Figure 1a. Distribution of XBT observations during 1970 through 1987.

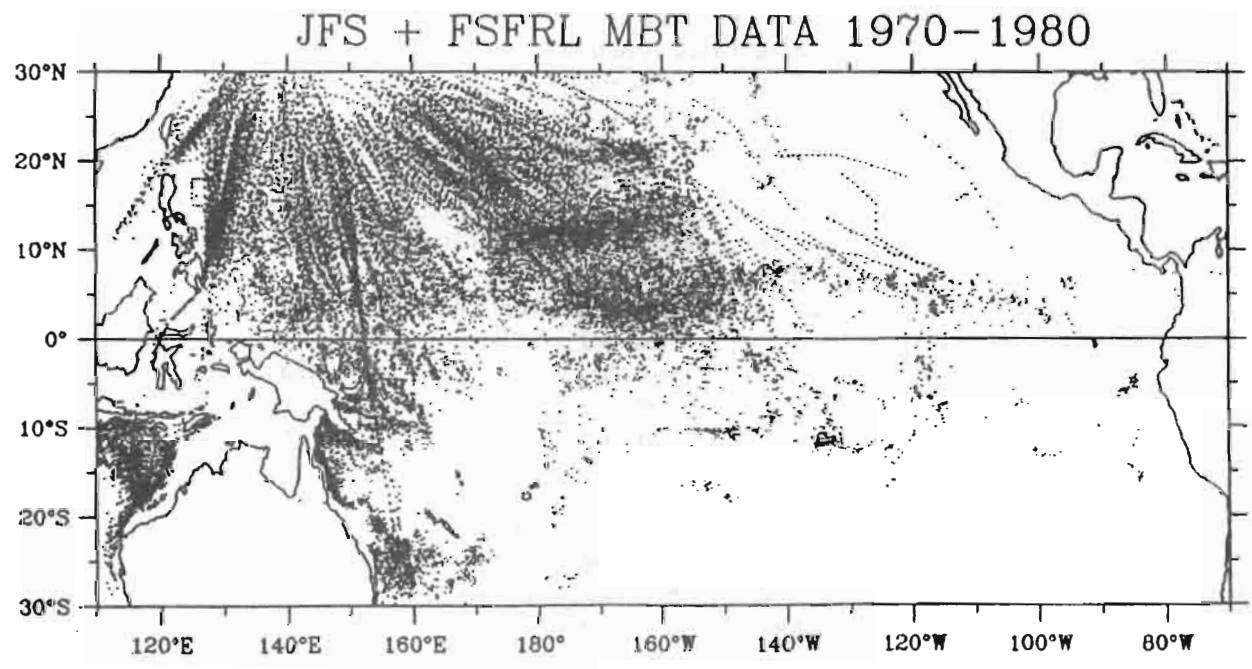

Figure 1b. Distribution of MBT observations during 1970 through 1980.

propagating events over the width of the tropical north Pacific. In particular, the XBT data sets which have formed the basis for many studies of tropical Pacific variability (e.g. Meyers and Donguy, 1980, 1984; Kessler, et al, 1985; Rebert, et al, 1985; White, et al, 1985; Pazan and White, 1987; Kessler and Taft, 1987; Graham and White, 1988; McPhaden, et al., 1988a,b) are derived principally from merchant and navy vessels, which densely sample a few specific shipping lanes, but poorly observe a large region of the western north Pacific southwest of Hawaii (Figure 1a). It has proven difficult to draw convincing evidence of zonal propagation from these data. On the other hand, many MBT profiles were made (mostly by Japanese fishing vessels) in the western tropical Pacific during the 1970's, which nicely complement the XBT data distribution (Figure 1b). Even the combined data are adequate to construct long time series only in the region between 5°N and 30°N, where the observations are densest and zonal propagation of long waves is relatively slow. Although it would be desirable to develop a historical time series of thermocline fluctuations in the equatorial waveguide, the data are insufficient to do so, particularly since time scales near the equator are so short. In most of the southern hemisphere east of 150°W the observations are so sparse that even the mean cannot be found with confidence. In this section the various data sets are described and the methodology and criteria for combining and gridding them are set forth. Although the BT sampling is highly irregular and the data are aliased by high-frequency phenomena, so gridding, interpolation and smoothing are necessary, every effort has been made to keep the processing of data to a minimum, in order to let the data "speak for itself". In particular, care was taken that interpolation in longitude was minimized to avoid the possibility that such interpolation would lead to a misleading interpretation as zonal propagation. Secondly, since the tropical Pacific is characterized by sharp zonally oriented ridge and trough features, interpolation in latitude might tend to smooth these structures; thus no interpolation in latitude was used.

b. Description of bathythermograph data sets

The largest single temperature profile data collection is in the archives of the National Oceanographic Data Center (NODC), consisting of 108632 XBT observations in the Pacific Ocean part of the region 30°S-30°N, 110°E-70°W, during 1967 through 1985. This data set provides much of the basis for the Levitus (1982) climatology. The NODC data comprise most of the XBT observations shown in Figure 1a, with the exception of the sharply defined route from New Caledonia (21°S, 166°E) to Japan and the routes emanating from Tahiti (17°S, 150°W), which are due to the French-U.S. ship of opportunity (SOP) program discussed below. About half the observations shown on the mid-basin routes from the southwest Pacific to Hawaii and North America were also made by SOP ships. The NODC data are densest on ship tracks traveled by United States Navy and merchant vessels, particularly between the U.S. mainland and Hawaii, Guam (13°N, 145°E), the Philippines, Japan and Australia (Figure 1a). However, south of the Hawaii-Guam-Philippines ship track and west of the Dateline the NODC data set has only sparse and sporadic sampling (Figure 1a). It is clearly an insufficient basis for study of time-dependant phenomena in the western tropical and equatorial Pacific.

The French-American SOP program began collecting surface observations (temperature, salinity and biological variables) in 1972 (Donguy and Dessier, 1983) and XBT profiles in 1979 (Meyers and Donguy, 1980) from volunteer merchant ships operating out of Noumea, New Caledonia. The ships traverse primarily three routes as mentioned in the previous paragraph (Figure 1a). A total of 26,373 XBT profiles were collected and made available under the SOP program during 1979 through 1987, only about one-quarter as many as in the NODC set, however the SOP data is much more concentrated in the tropics, with relatively dense sampling along the three tracks.

The combined XBT data shown in Figure 1a amounts to 135,005 total observations during 1967 through 1987. Almost all of the XBT profiles extend to 450 m depth, which is well below the thermocline in most of the tropical Pacific. Although this combined data set has been used to study zonal propagation of thermocline depth anomalies (e.g. White, et al, 1985), it is clear from Figure 1a that a very large region southwest of Hawaii was sampled principally on a single meridional section (crossing the equator near 160°E), which did not begin until 1979, so the XBT data alone is a poor antenna for zonally propagating variability in that important region, requiring relatively elaborate statistical interpolation schemes between the tracks (Pazan and White, 1987). Because of this interpolation, interpretation of observed variability as evidence of zonal propagation has been controversial. The present work avoids this problem by merging the XBT data with MBT data collected by Japanese fishing vessels, which fortuitously fills the large gap southwest of Hawaii (Figure 1b) and makes possible the construction of time series of thermocline depth across most of the northern tropical Pacific with a minimum of zonal interpolation.

The MBT data set studied here was compiled by the Japanese Far Seas Fisheries Research Laboratory (FSFRL), Shimizu, Japan, and was generously made available through a cooperative agreement with PMEL (K. Mizuno, personal communication). There is also a large collection of MBT observations taken before 1970 in the NODC archives, which were included in the Levitus (1982) climatology. These data are for the most part not used in the present study, since the data coverage in the tropical Pacific is not dense enough to grid on the relatively fine scales possible with the combined data after 1970. However, in a few regions (for example along the ship route from the U.S. West Coast to the Panama Canal) the NODC MBT data has been used to construct several long time series which are discussed in Section 4.

A total of 64,062 FSFRL MBT profiles were received, covering the period 1970 through 1980. The MBT observations extend only to 250 m depth, which is below the thermocline near the equator, but within the lower thermocline in the subtropical gyres. The 20°C isotherm is practically the deepest isotherm sampled over the entire tropical Pacific by MBTs. The MBT profiles studied here are taken principally in the course of fishing operations, in which many ships work for several months in a small region, and so have a different type of spatial distribution than the XBT data, which were generally sampled along underway ship routes (Figure 1b). Additionally, there is some seasonal variability in the MBT data distribution (Kessler, 1989a).

The interannual time distribution of the sampling was roughly constant during 1970 through 1980, when data from both the NODC and the FSFRL are available, with the highest sampling density during 1970 through 1975. The SOP data begins in 1979 while the FSFRL set ends in 1980, so the distribution in the large region between Hawaii and the Indonesian Archipelago changed at that time from the fishery MBT pattern (Figure 1b) to mostly meridional XBT tracks (Figure 1a). During the El Niño years of 1982-83 the observations available in this region were essentially just from the SOP program and have large gaps between the tracks. The total data set is thus most useful for studying zonally propagating events during the 1970's.

Kessler (1989a) compared the mean depth of several isotherms from the MBT and XBT data sets in regions where there was substantial overlap. He found an apparently systematic deep bias of MBT isotherm depths compared to the XBT, averaging 2 to 5 m for 20°C. However, in this paper it is principally anomalies of isotherm depth which are of interest, so this small instrument bias can be avoided by finding anomalies from the mean of the corresponding data set, rather than from the mean of the total. With this caveat, it is permissible to merge the MBT and XBT data sets, giving a total of 199,067 profiles of both types. After quality control, the cleaned data were gridded with a gridsize of 2° latitude, 5° longitude and 2 months. See Kessler (1989a, b) for a discussion of quality control and data gridding.

c. Wind data

In Section 2, a simple wind-forced model is developed to help explain observed pycnocline depth fluctuations. The winds which are used to force this model are produced by the Mesoscale Air-Sea Interaction Group at Florida State University under the direction of J. J. O'Brien and D. Legler, from ship winds subjectively analyzed onto a 2° latitude by 2° longitude grid (Legler, personal communication), and generously made available by them. This ship wind processing effort was begun at the University of Hawaii by G. Meyers and K. Wyrtki (Wyrtki and Meyers, 1975a, 1975b, 1976) and continued at Florida State University (Goldenberg and O'Brien, 1981). This wind data set has been used to force a variety of models of the tropical Pacific (e.g. Busalacchi and O'Brien, 1980; Busalacchi, et al., 1983; McPhaden, et al., 1988a,b; Harrison, et al., 1989). The pseudo-stress values provided were converted to stress using a value of 1.5×10^{-3} for the drag coefficient. Since the meridional scale of the wind stress is typically much smaller than the zonal scale, the wind stress curl was found by differencing τ^x over 2° latitude and τ^y over 4° longitude.

3. A simple model of low-frequency pycnocline depth variations.

a. Introduction

The field of 20°C isotherm depth was chosen as the clearest, simplest representation of the observed variability. Implicit in this choice is the idea that the tropical Pacific may be approximated as a two-layer system divided by a sharp pycnocline, for which the 20°C isotherm is a proxy. Meyers (1979a,b) used the depth of the 14°C isotherm in this way to study the annual cycle. Kessler and Taft (1987) showed that volume transports of the North Equatorial Current and Countercurrent derived from the two-layer assumption, using the vertical motion of the 20°C isotherm to represent interfacial movement, give a reasonably good estimate of zonal geostrophic volume transport variability. In the same spirit, many modelling studies have used a reduced

gravity, single-active-layer approximation (e.g. Busalacchi and O'Brien, 1980, and successors; see also McCreary, 1985). The principal advantage of this choice is that it simplifies the three-dimensional variability into a two-dimensional field which can be mapped and studied conveniently. For practical reasons, since the BT profiles extend to a variety of depths, a calculation needing a common reference level (such as dynamic height) poses problems and requires further assumptions necessary to extrapolate all profiles to the same depth (but see Kessler, et al., (1985) for a discussion of a scheme for dealing with this). As discussed in Section 2.b, the Japanese MBT data extends only to 250 m, so 20°C is effectively the deepest isotherm fully sampled over the entire tropical Pacific. The observations cannot be reasonably gridded with a time resolution of less than two months (and must be smoothed in time (see Section 2.c)), so the BT data set is suitable only for the study of low-frequency variability. Thus, the simple model was developed assuming that all variability can be described by low-frequency, large-scale (long wave limit) fluctuations of a sharp pycnocline.

b. The simple model

A simple quasi-geostrophic model of low-frequency pycnocline variability was employed by Meyers (1979a) to study annual fluctuations of the 14°C isotherm in the tropical (not equatorial) Pacific. The physical processes allowed by the model are Ekman pumping, the radiation of long (non-dispersive) Rossby waves due to such pumping in mid-basin, and the radiation of long Rossby waves from observed eastern boundary depth fluctuations. The ocean is assumed to consist of a rigid lid over a single active layer, separated by a sharp pycnocline from a deep motionless lower layer; both layers are homogeneous (the reduced gravity, $g' = g\Delta\rho/\rho$ describes the potential difference between them). The wind stress τ (see Section 1.c) is assumed to act as a body force in the upper layer. Since monthly average wind data is used, the forcing frequency is much slower than inertial ($\partial/\partial t << f$). The long wave approximation is made (see Kessler, 1989b, for discussion of this simplification). The momentum equations are linearized by assuming that the mean upper layer depth is spatially uniform. Then the low-frequency forced quasi-geostrophic vorticity equation as was used by Meyers (1979a) is:

$$h_t - (\beta c^2/f^2)h_x = -\,\mathrm{Curl}(\tau/\rho f), \qquad (3.1)$$

where $c^2 = g'H$ is the long baroclinic gravity wave speed squared. Balance (3.1) is the simplest relation obtainable describing time-dependant β-plane dynamics. The long wave, low frequency limit has been assumed by neglecting the local accelerations; this approximation makes wave solutions to (3.1) non-dispersive, so Rossby waves in the simple model propagate exactly westward. Thus, in this limit solutions at each latitude are independant. Furthermore, there is no need to assume that the forcing or solution have a sinusoidal form. There are no short Rossby waves in the model, so it is only valid where the zonal length scale of solutions is much greater than the local gravest internal Rossby radius, In addition, neglecting u_t excludes the equatorial Kelvin wave and is not valid within about 5° of the equator, so (3.1) is a mid-latitude approximation. Garzoli and Katz (1983) estimated the magnitude of the contribution of the acceleration terms which have been neglected to the balance (3.1), using BT data in the tropical Atlantic. They concluded that these terms did not contribute significantly to the thermocline displacement anywhere in the region which they studied (3° to 10°N).

Solutions h(x,t) to (3.1) are referred to as the "upper layer thickness anomalies" (ULT) (measured positive down, or thicker), continuing terminology used by Busalacchi and O'Brien (1980). These solutions were found according to the procedure given by Gill and Clarke (1974, section 7), integrating along characteristics (which are just latitude circles in the long wave limit) from the eastern boundary, where h(x=0,t) was taken to be the observed annual cycle of 20°C depth. Meyers (1979a) gives an equivalent procedure. If the wind stress τ is taken as given, then (3.1) can be straightforwardly solved if a value for the long Rossby wave speed $c_r = \beta c^2/f^2$ is known. As did Meyers (1979a), c_r was treated as an unknown and studied by integrating (3.1) at each latitude, trying all values of c_r from 1 cm/s to 1 m/s at 1 cm/s intervals, then correlating each solution h(x,t) with the observed 20°C depth variations, either at the annual period (Kessler, 1989a,b) or for interannual variability (Section 4), to find a best-fit value for c_r at each latitude. Since only the long gravity wave speed c is truly unknown, effectively the fitting process found an estimate of c which maximized the correlation between model and data over the width of the basin at each latitude.

Several limitations of the simple model (3.1) are evident: the assumption that all waves can be described by the long wave limit, the linearizing assumption in the derivation of the model that the mean pycnocline is flat and the strong zonal geostrophic currents of the tropical Pacific are absent, and the neglect of

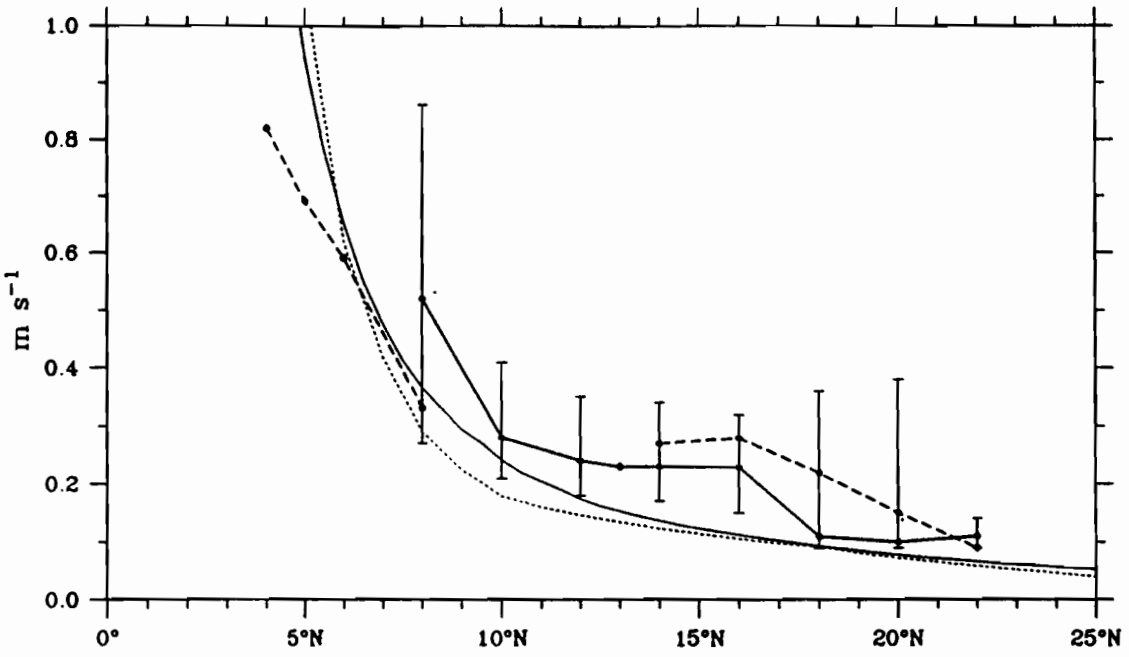

Figure 2. Best-fit estimates of the propagation speed of long Rossby waves. The two smooth curves represent the theoretical speeds $c_r = \beta c^2/f^2$; the thin solid line uses c found from a first baroclinic mode decomposition given in Emery, et al. (1984); the dotted line uses $c=\sqrt{g'H}$, where H is the depth of 20°C at 160°W. The two heavy lines represent best-fit estimates of c_r. The dashed line (discussed in Section 4.e) shows estimates for the annual cycle (no estimates were made at 10° or 12°N for annual cycle). The solid line shows best-fit estimates for interannual variability (discussed in Section 4.d). The "error bars" refer to these interannual estimates; the method used to calculate these is discussed in the text.

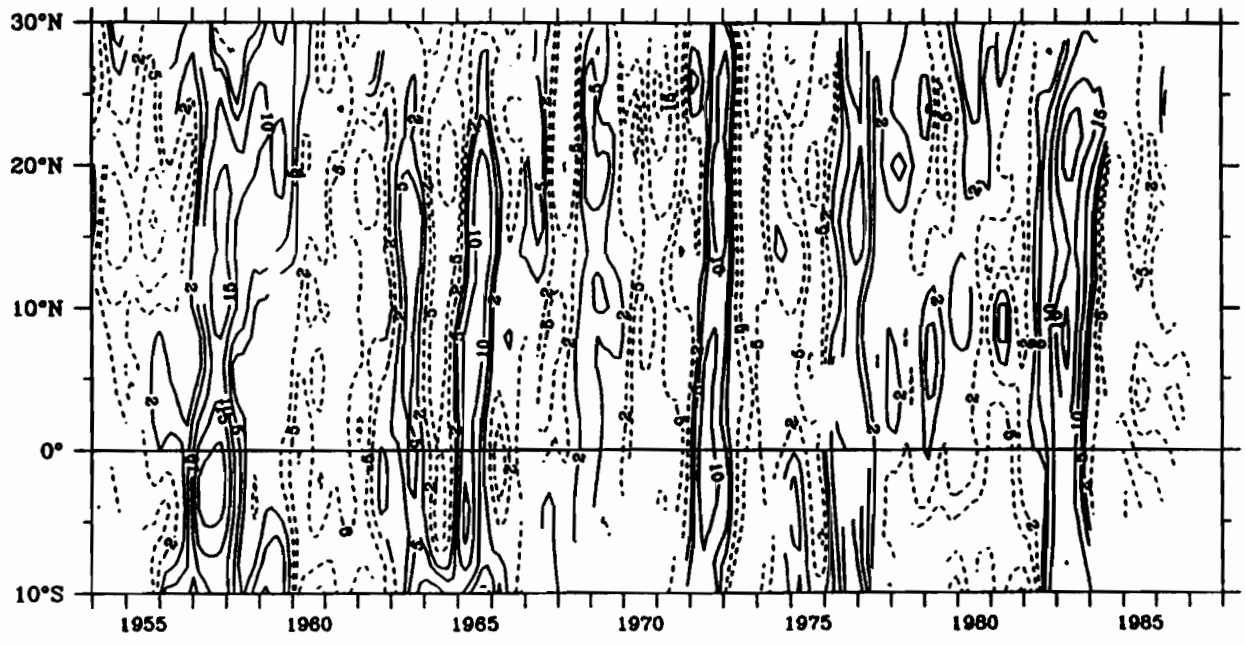

Figure 3. Interannual anomalies of 20°C depth (m) along the American coast. Contours are given at ±2, 5, 10, 15 and 20 m, with positive (deep) anomalies solid, negative (shallow) anomalies dashed.

the more complicated observed vertical structure in favor of simple single-active-layer dynamics. Kessler (1989a, b) discusses these limitations, concluding that for waves with periods greater than about one year in an ocean with a sharp pycnocline the long wave limit is appropriate, and that the zonal geostrophic currents do not modify wave propagation, due to the non-Doppler effect (see also Chang and Philander, 1989).

The observations are also compared with hindcasts derived asumming local Ekman pumping alone, that is, solutions $h_E(t)$ to:

$$\partial h_E / \partial t = - \text{Curl}(\tau/\rho f), \tag{3.2}$$

with the boundary condition that the mean h_E must be zero.

4. Interannual variability of 20°C depth

a. Introduction

Interannual variability was studied according to the same simple model as was annual variability, using the same vorticity equation (3.1). The reader is referred to Section 3 for discussion of the model and its limitations. The primary issue addressed in this section is the role of long extra-equatorial Rossby waves in the evolution of El Niño. In general, two types of long Rossby waves are thought likely to be produced in the tropics during El Niños. First, upwelling long Rossby waves may be generated in mid-basin by the large-scale wind stress curl pattern associated with equatorial westerly wind anomalies. Secondly, downwelling waves may occur following an El Niño, initiated by reflection off the eastern boundary of deep equatorial pycnocline anomalies. Although both waves occur in the tropical, extra-equatorial region, both originate from events in the equatorial waveguide. Such wave-induced variability has been noted in many model experiments. McCreary (1983) and McCreary and Anderson (1984) developed a simple model of coupled ocean-atmosphere interaction in which long Rossby waves were generated in the central tropical Pacific by idealized wind stress curl anomalies associated with changes of SST in the eastern equatorial Pacific. In this model, the travel time of these extra-equatorial waves set the oscillation period of El Niño events, and they played a crucial role in both triggering and turning off El Niños through reflection off the western boundary. Busalacchi, et al. (1983) used a linear reduced-gravity model forced by observed winds and showed that in this model shoaling of the western Pacific pycnocline observed in the latter stages of El Niño was due to the arrival of long Rossby waves. These waves were generated by the off-equatorial wind stress curl pattern associated with strong westerly wind anomalies near the equator at the height of the event. The physics of the Busalacchi, et al. (1983) model are similar to those expressed in the vorticity equation (3.1) for extra-equatorial regions, and one of the principal results of this section is that wave-induced fluctuations in the western Pacific like those seen in the model of Busalacchi, et al. (1983) can be observed in 20°C depth. More recently, Graham and White (1988) suggested that a mechanism similar in some important respects to that proposed by McCreary (1983) could be verified as triggering several observed El Niños. Results presented in this chapter suggest problems with the Graham and White (1988) scenario.

b. Interannual variability on the eastern boundary

As mentioned in Section 2, the NODC archives contain MBT data taken before 1970 which in a few regions of the Pacific is sufficient to construct long time series. One of these regions is along the shipping route between the U.S. West Coast and the Panama Canal, which hugs the coast of Mexico and Central America. A long time series of anomalous 20°C depth on the eastern boundary from 1954 through 1987 can be made by combining the early NODC MBT data with the later XBT data set. This time series shows El Niño events clearly as deep thermocline anomalies, which occurred in 1957, 1963, 1965, 1969, 1972, 1976, weakly in 1979, and in 1983 (Figure 3). The large El Niños (in 1957, 1965, 1972, 1976 and 1983) had amplitudes of 10-15 m at the equator on the eastern boundary, and the anomalies generally extend north to about 22°-25°N (which, possibly coincidently, is where the relatively smooth coast is broken by the Gulf of California). Thermocline deepening in these events typically lasted for 12-18 months (Figure 3). Kessler (1989a) discusses in detail how an idealized ocean would respond to such pulse-like forcing along the eastern boundary by radiating Rossby waves offshore; however, as will be shown later in this chapter, the signal of such offshore radiation was observed only far from the equator and did not appear to be a major contributor to the subsequent evolution of El Niños.

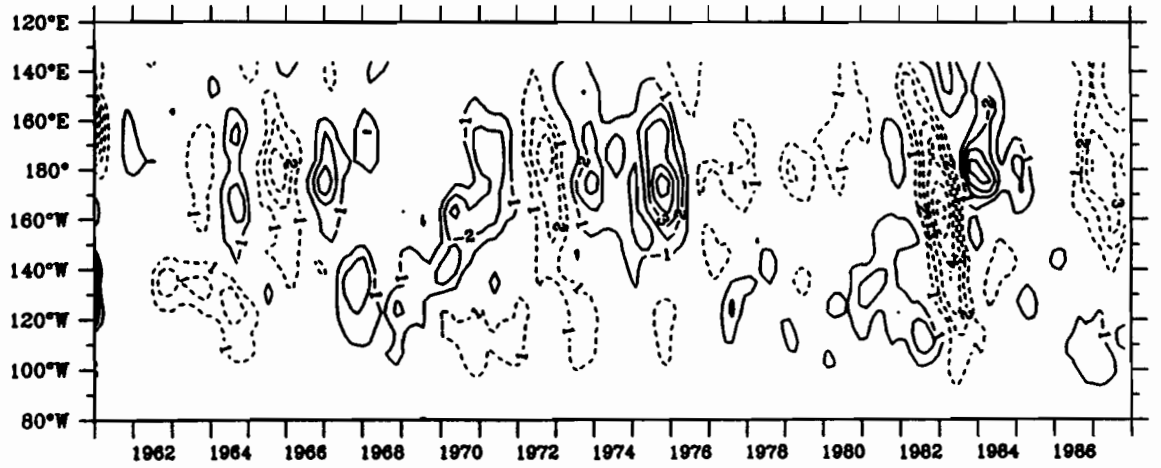

Figure 4. Anomalies from the average annual cycle of zonal wind stress (10^{-2} N m^{-2}) on the equator. Contours are given every 10^{-2} N m^{-2}, with positive (eastward) anomalies dashed and negative (westward) anomalies solid lines.

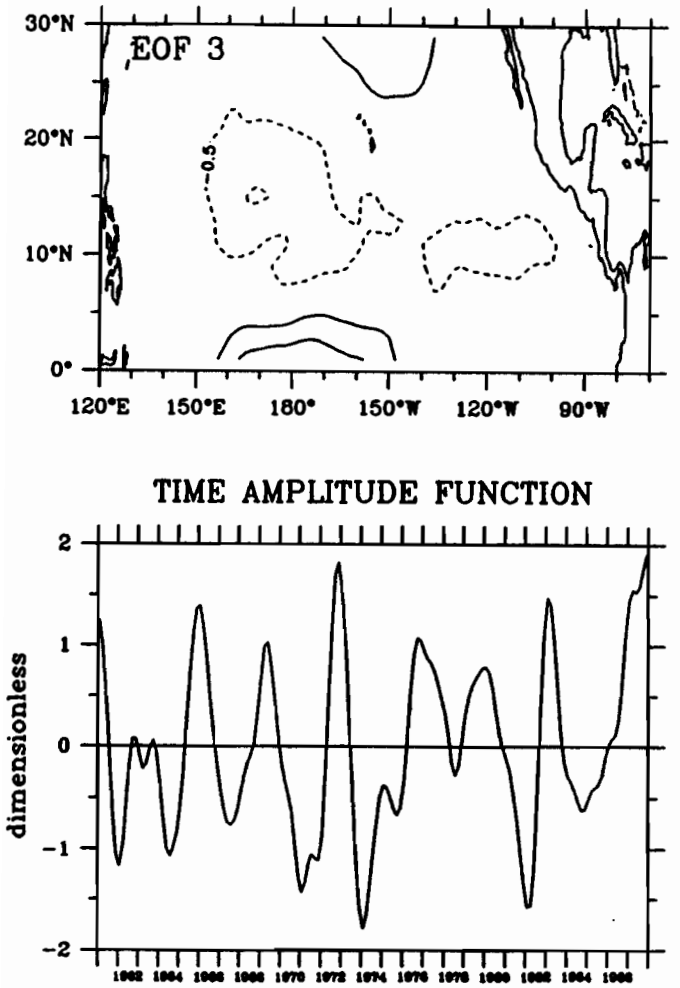

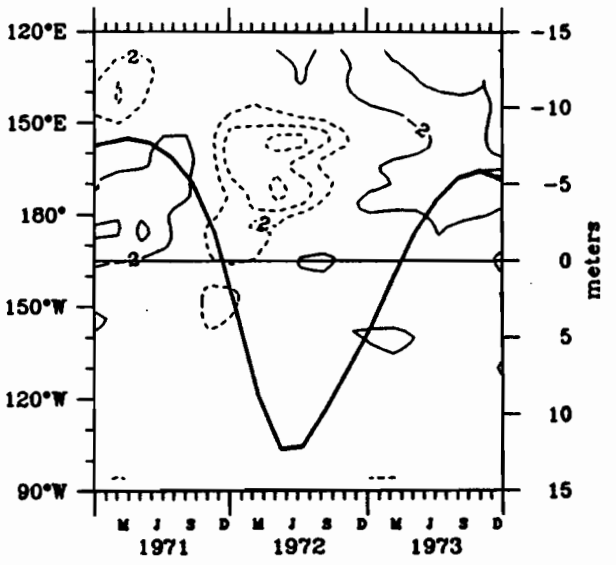

Figure 6. Contours of the curl of the wind stress (10^{-6} N m^{-3}) along 13°N (longitude scale on left axis) during 1971 through 1973. Dashed contours are positive curl (Ekman upwelling); solid contours are negative curl (Ekman downwelling). The heavy overlaid line is the time history of 20°C depth (m) on the equator at the eastern boundary, which is used as an index of the peak of El Niño of 1972. The scale for 20°C depths is on the right axis, with negative (shallow) 20°C depths shown upwards and positive (deep) anomalies shown downward.

Figure 5. Third empirical orthogonal function of zonal wind stress (1961-87), representing 12% of the total interannual variance in the northern tropical Pacific. The top panel is the eigenvector, in units of 10^{-2} N m^{-2}, while the bottom panel is the (dimensionless) time amplitude function. A positive product between the eigenvector and time amplitude function represents an eastward stress anomaly.

c. El Niño-related variability of the wind field

Although this paper does not focus on the wind field, it is appropriate to briefly discuss the type of wind fluctuations associated with El Niño which are important in generating extra-equatorial Rossby waves. The most prominent of these wind events is the occurrence of westerly anomalies in the equatorial waveguide at the height of El Niños, which leads to upwelling wind stress curl in the tropical regions. The time history of zonal wind stress on the equator (Figure 4) shows that during several strong El Niños (in 1965, 1972, 1982 and 1986, but not in 1976) major westerly wind anomalies (amplitudes typically 3×10^{-2} N m^{-2} or roughly 4-5 m/s) occurred near the Dateline. During the following year, easterly wind anomalies occurred in the same region with similar amplitude. The wind stress curl pattern associated with these equatorial anomalies is exemplified by the third Empirical Orthogonal Function (EOF) of the zonal wind stress τ^x in the northern hemisphere, representing 12% of the total interannual variance in this region (Figure 5). That this third EOF is characteristic of El Niño variability is shown by the high correlation (r=0.75) of the time amplitude function (bottom frame) with the time history of 20°C depth anomalies at the equator on the eastern boundary (the equatorial time series from Figure 3, discussed in 4.b above), which is a good index of El Niño events. The other EOF time amplitude functions had much lower correlations with this El Niño index (r<0.4) and are not shown. The third EOF (Figure 5) shows that the El Niño time history was associated with the westerly anomalies on the equator near the Dateline seen in Figure 4, and that these anomalies were confined south of about 5°-6°N, with easterly anomalies centered near 15°N. This pattern of wind stress anomalies implies that strong upwelling curl characteristically occurs in the tropical region between 5° and 15°N near the Dateline at the height of El Niños, and is often followed by a return of anomalously strong equatorial easterlies and hence by downwelling curl in the same region one to two years later.

This sequence of events is seen in a detail of the wind stress curl field at 13°N and eastern equatorial thermocline depth during the El Niño of 1972 (Figure 6). (13°N is approximately typical of latitudes between 5° and 15°N during this period, and is plotted to correspond to BT data at 13°N discussed below). 20°C depth at the South American coast peaked downward in May-June 1972, marking the height of the event. The wind stress curl field at 13°N indicates strong upwelling between about 170°W and 150°E slightly earlier than this, in March through July 1972. The following year, both fields had reversed sign, and the anomalies were smaller. A corresponding plot of the curl at 13°N during the El Niño of 1982-83 shows a similar phasing of curl variations relative to the eastern boundary peak, with the upwelling curl maximum occurring near the Dateline while the eastern boundary thermocline was falling, and a downwelling curl event about a year later. The effect of these curl fluctuations was to force an upwelling Rossby wave in the tropics near the Dateline during the height of El Niño, then a downwelling wave a year or so later.

d. Observed interannual 20°C depths and hindcasts from the simple model

The long Rossby speed $c_r = \beta c^2/f^2$ was treated as an unknown in the simple vorticity equation (3.1), and studied by solving (3.1) at each latitude using the interannual FSU winds, trying all values of c_r from 1 cm/s to 1 m/s, then correlating each solution h(x,t) with the observed interannual variations of 20°C depth. Significant peaks of correlation were found at all latitudes from 8°N through 22°N, with a summary of the results in Figure 2. An ad hoc estimate of the
uncertainty of fitting c_r was made by finding the range of c_r at each latitude such that the correlation of the solution h(x,t) with observed 20°C depth was within 10% of the best correlation; these uncertainties are shown as the "error bars" about the best-fit meridional profile in Figure 2. The uncertainties ranged from about ±3 cm/s at 22°N to about ±20-30 cm/s at 8°N, and were typically about ±10 cm/s in the region 10° to 18°N (Figure 2). The interannual best-fit long Rossby speeds were generally smaller than the annual speeds in the NEC region, but within the estimated uncertainty, except at 22°N. Despite the fact that evidence of an annual Rossby wave was found at 4° through 6°N (Kessler, 1989a,b), interannual propagation was not clearly detected by the present method at these latitudes.

Correlation of solutions to the long Rossby wave model (using the best-fit speeds c_r shown in Figure 2) with observed interannual 20°C depths was high in the west, with values above 0.7 west of the Dateline between 8° and 16°N, and also high east of the Dateline at 16° to 22°N (Figure 7, top). If we take the interannual autodecorrelation timescale to be roughly four years (as estimated by Kessler (1989a)), then with bimonthly data there are about 24 degrees of freedom, and a correlation of 0.4 is significant at the 95% level. Since the simple model took the observed 20°C depths at the American coast as a boundary condition, the correlations were exactly 1 at the coast; the fact that correlations fell off rapidly offshore south of about 14°N suggests that

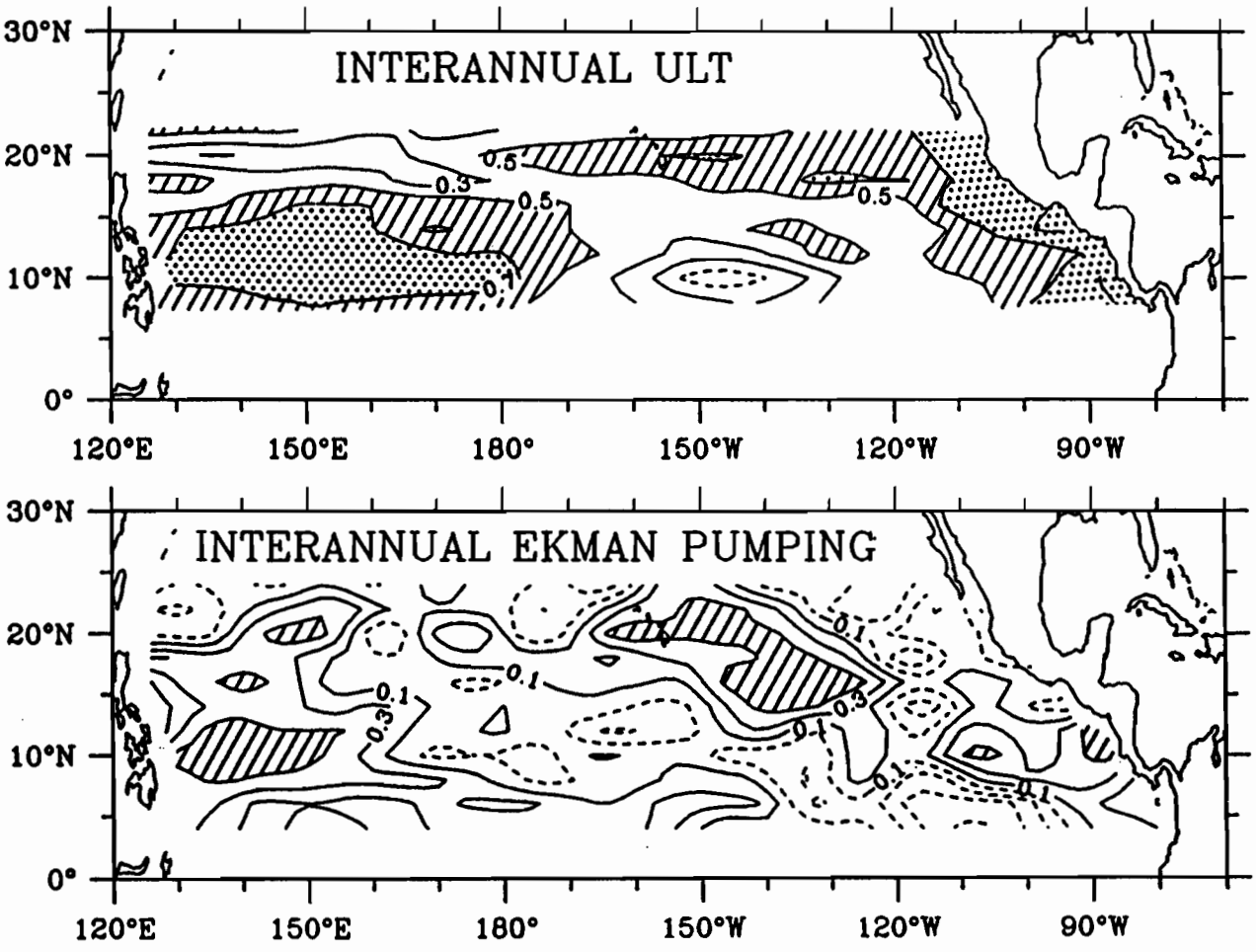

Figure 7. Top: correlation of observed interannual 20°C depth anomalies with the ULT hindcast made using the vorticity equation (3.1). Bottom: correlation of observed interannual 20°C depth anomalies with the hindcast made assuming Ekman pumping acting alone. In both, positive correlations are shown as solid contours, negative correlations as dashed contours. Dot shading is used to indicate correlations greater than 0.7, and hatching is used to indicate correlations greater than 0.5.

offshore radiation of boundary anomalies (which dominated the model variability in the region east of about 150°W) was probably not a major contributor to the variability in mid-basin equatorward of 14°N. Near 140°-150°W equatorward of about 12°N is a region of near-zero correlations. There is no obvious explanation for the poor model results in this area, which could be due to errors in the wind, aliasing or errors in the BT data (this is a relatively data-sparse area), or more complicated physical mechanisms at work than are expressed in the simple model (3.1) (an obvious possibility is the 20-30 day instability waves). In most other areas of the northern tropical Pacific, however, the simple model hindcasts were considerably more closely correlated with observed conditions than hindcasts made assumed Ekman pumping alone (equation (3.2); Figure 7, bottom). Over much of the central basin, the Ekman pumping hindcast was essentially uncorrelated with the data; only in small regions in the far west and near Hawaii does the Ekman pumping hindcast appear significantly correlated with the observations, and even in these regions the correlation was weaker than the simple model including long Rossby waves. In the region near 140°-150°W where the simple model hindcast was poorly correlated with the observations, the Ekman pumping hindcast was also uncorrelated. The poor interannual correlation with Ekman pumping contrasts with the results found in (Kessler, 1989a,b) for the annual cycle, in which at 10°-12°N Ekman pumping was found to be the dominant process at the annual period.

Interannual solutions of the vorticity equation (3.1) (referred to as the upper layer thickness anomaly, or ULT), are compared with observations and with pycnocline anomalies hindcast by Ekman pumping alone (the solution to (3.2)) in time-longitude plots at 13°N, Figures 8 and 9, for the periods 1970 through 1975 and 1980 through 1986. The comparison is made at 13°N because first, there is a greater density of data at that latitude than at any other, particularly in the west; second, because 13°N is sufficiently far from the equatorial waveguide that the variability there is clearly governed by the quasi-geostrophic dynamics expressed by (3.1); and third, because this latitude has been suggested as a likely region for long Rossby wave propagation which might be important in the evolution of El Niño (Graham and White, 1988). The observed variability of both the wind stress curl and the depth of 20°C at 13°N are relatively typical of latitudes from about 10° to 15°N (Kessler, 1989a). The periods 1970-75 and 1980-86 were chosen because they span the strong El Niños of 1972 and 1982-83. As noted in Section 1, the 1970-75 period was relatively well sampled due to the availability of data from both the Japanese fisheries and the NODC, with an average of one observation every 13 days in each 5° longitude box at 13°N during that six-year period. The 1980-86 period, which was observed only by XBTs, was much more sparsely sampled, with an average of one observation every 38 days in each box; gaps appear as "holes" in Figure 9. Note in particular the absence of observations between the Dateline and 160°E (Figure 9).

For interannual frequencies, Ekman pumping alone hindcasts unrealistically large amplitudes of variability within about 15° of the equator. At 13°N, the zonal average standard deviation of the Ekman pumping solution to (3.2) was about 25 m, whereas the standard deviation of the ULT solution to (3.1) was about 10 m and that of the observations of 20°C depth about 8 m (all three were higher in the west). The unrealistic magnitude of Ekman pumping is even more pronounced closer to the equator. This contrasts with the results reported in (Kessler, 1989a,b) for the average annual cycle where the amplitude of the Ekman pumping solution was found to be the same as that for the total ULT solution including Rossby waves. The difference is due to the fact that at the annual period there are at most six continuous months of one sign of pumping, while interannual wind stress curl variations frequently persist for several years, so the (integrated in time) interannual Ekman pumping solution can grow very large (bottom panels of Figures 8 and 9). If the dynamics includes Rossby waves, however, these anomalies radiate away before building up large amplitudes, thus the ULT (middle panels) had approximately the same amplitude as the observations (top panels).

Many overall aspects of the forcing were similar over much of the northern tropical Pacific during several El Niños. Upwelling wind stress curl is typically generated to at least 16°N in mid-basin by equatorial westerly wind stress anomalies during the peak of the event (see Section 4c). Along the eastern boundary, 5 to 15 m shallow thermocline anomalies were observed in the year preceding several events (Figure 3); these may also be a characteristic feature. This boundary signal is hindcast to radiate across the basin by the simple vorticity equation (3.1). However, equatorward of about 15°N, this boundary-induced shoaling was usually secondary in its effects on the mid-basin thermocline to that associated with the wind stress curl. In the final phase of the event, the deep equatorial pycnocline anomaly which is the primary signal of El Niño spread up the American coast (Figure 3), with an amplitude of 10-15 m; the ULT solution shows this signal radiating offshore. However, similarly to the shallow anomalies preceding the event, the boundary signal was in many cases a relatively small part of the thermocline deepening observed in the west, most of which was due to downwelling wind stress curl as the equatorial easterlies returned in force. In general, the simple model brings

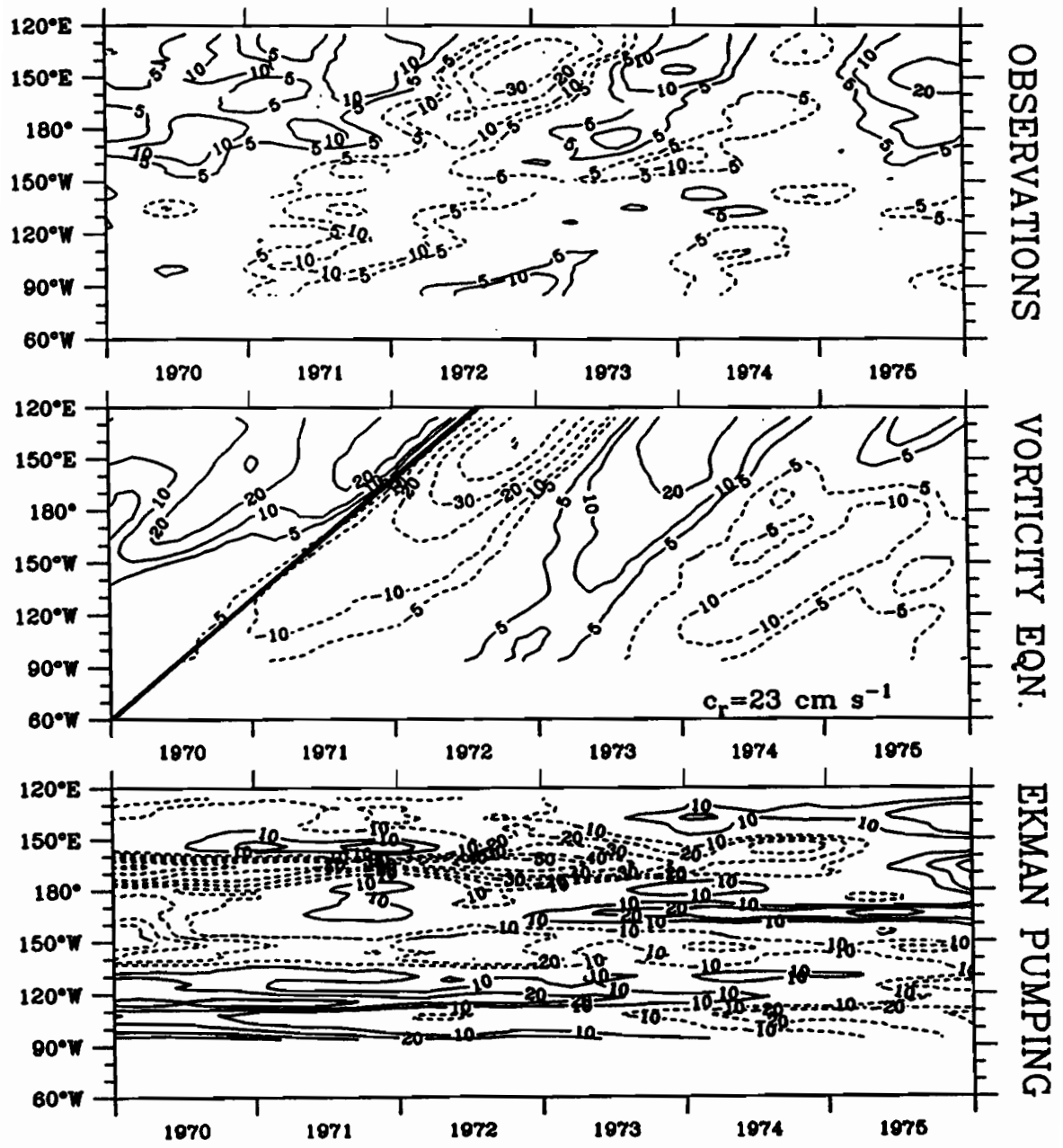

Figure 8. Top: interannual anomalies of 20°C depth (m) at 13°N during 1970 through 1975. Solid contours indicate deep anomalies, dashed contours shallow anomalies. Middle: hindcast of interannual upper layer thickness (ULT) anomalies (m) made using the vorticity equation (3.1) with best-fit speed c_r = 23 cm/s shown in lower right. The heavy line running up from the lower left corner shows this speed. Bottom: Hindcast of interannual pycnocline depth anomalies (m) made assuming Ekman pumping alone (equation 3.2).

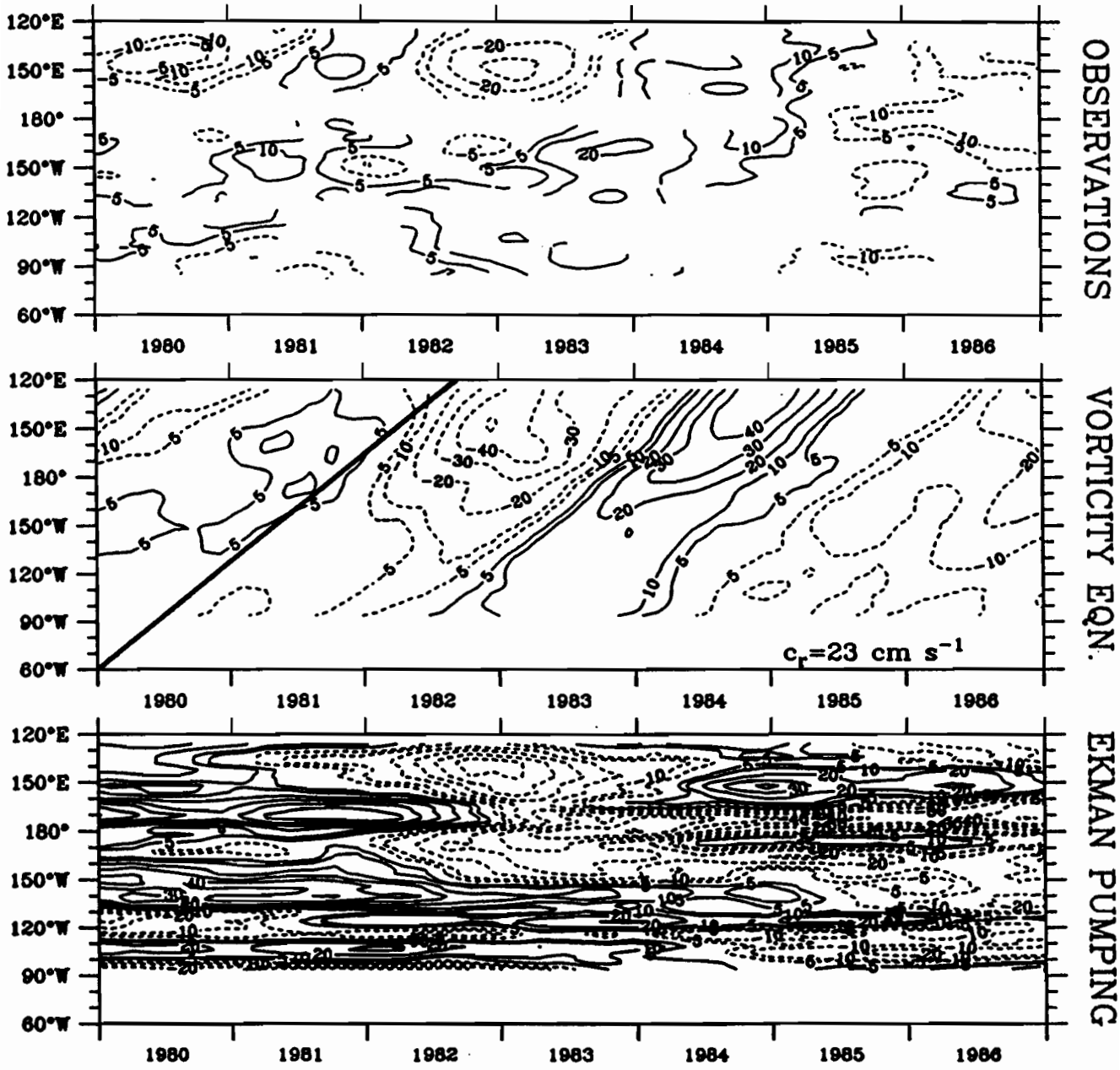

Figure 9. As Figure 8 but during 1980 through 1986.

out the fact that although the observations may appear as if a boundary reflection is propagating freely across the entire basin, this can be due to a coincidental occurrence of mid-basin curl-generated anomalies (Kessler, 1989a). It may be that the coincidence of timing has a deeper significance associated with the quasi-periodic nature of El Niño (which cannot be determined here), however the fact remains that at most locations in the western Pacific most of the amplitude of long Rossby waves generated by El Niños was produced in mid-basin by the wind stress curl. An exception is the region north of 15°N, where particular boundary forcing events can be traced for several years across much of the basin and accounted for significant fraction of the variability.

At 13°N during the 1970-75 period (Figure 8), the observations (top) show that in the two years leading up to the El Niño of 1972 the thermocline was deep west of 150°W but shallow in the east. The ULT (middle) has a roughly similar pattern; the deep anomalies in the west were forced in the model by wind stress curl in the final stage of the 1969 El Niño, while the shallow pycnocline in the east has emanated from the boundary. Note that in the east during this period the Ekman pumping solution (bottom) hindcasts anomalies of the opposite sign from those observed, indicating that boundary radiation and not wind stress curl probably accounted for the observed eastern shoaling. During the height of El Niño in mid-1972, the observed thermocline was anomalously shallow everywhere west of 90°W, while deep anomalies appeared in the east as the equatorial deepening arrived at the boundary and spread up the American coast. The simple model (middle) appears to show the shoaling event of 1972 as a continuous upwelling radiating from the eastern boundary and propagating across the basin. However, this boundary signal was quite weak and grew very slowly east of 150°W before amplifying in mid-basin due to the curl (to a much larger size than the original boundary fluctuation), so the western Pacific anomalies cannot be attributed primarily to the boundary reflection. Following the peak of El Niño, deep anomalies on the eastern boundary were observed in late 1972 and then were seen in early 1974 in the west, with some suggestion of propagation. The ULT (middle) makes clear that this is not the result of free propagation of the boundary anomalies, since the speed of free propagation means that waves radiating from the American coast in late 1972 would not have arrived in the west until late 1974; in fact the deep anomalies observed in the west were generated near the Dateline in mid-1973. There is little correlation between the Ekman pumping solution (bottom) and the observations (top); as noted, Ekman pumping hindcasts amplitudes more than twice as large as those observed.

The 1982-83 El Niño (Figure 9) had a somewhat similar sequence of events at 13°N, although observation is more difficult because of the sparser sampling and data gaps. The shallow western Pacific thermocline observed in 1980 (top), followed by a downward peak at the end of 1981, was due to wind stress curl fluctuations associated with the weak El Niño of 1979; these signals are accurately portrayed by the simple vorticity equation (middle). As in the El Niño of 1972, the 1982-83 event began with weak shallow anomalies on the eastern boundary which gained much larger amplitude in mid-basin; this sequence is seen both in the observations (top) and the simple model hindcast (middle). Unlike the El Niño of 1972, during 1982 strong upwelling curl covered the entire 13°N band west of about 150°W, and the Ekman pumping hindcast (Figure 9, bottom) also shows a shoaling event west of 150°W, so the observed shoaling cannot be attributed entirely to the radiation of long Rossby waves, but was locally forced over a wide region.

The eastern boundary deepening following the El Niño of 1982-83 was stronger and longer-lasting than the corresponding event in late 1972, with about a year of anomalies greater than 10 m and a peak of more than 15 m in mid-1983 (Figure 3). Both the observations (Figure 9, top) and the ULT (middle) show this signal apparently radiating across the entire basin at 13°N. However, the maximum deepening in the west at 13°N was observed at the end of 1984, only 18 months after the maximum on the eastern boundary, which is too fast for free propagation (this would imply a speed of about 35 cm/s). In fact, strong downwelling wind stress curl began in early 1983 near 150°E, which started the deepening in the west before the wave arrived from the eastern boundary. The combination of the two forcings produced a deep anomaly in the west which was about twice as large as the original eastern boundary signal (Figure 9, middle). Therefore, as in 1972, it would be an oversimplification to interpret this anomaly as due primarily to free radiation of an eastern boundary anomaly; both the boundary and mid-basin forcing played a strong role.

The above discussion, showing that long extra-equatorial Rossby waves of significant amplitude arrive at the western boundary (whether due to boundary reflection or mid-basin curl, raises the question of whether reflection of these waves from the *western* boundary as equatorial Kelvin waves could be a contributor to the subsequent evolution of El Niño. As noted in the introduction to this Chapter, such reflection has been suggested as a mechanism for triggering or turning off El Niño. In a recent paper, Graham and White (1988) proposed that downwelling long Rossby waves generated by wind stress curl anomalies near 12°N in mid-basin

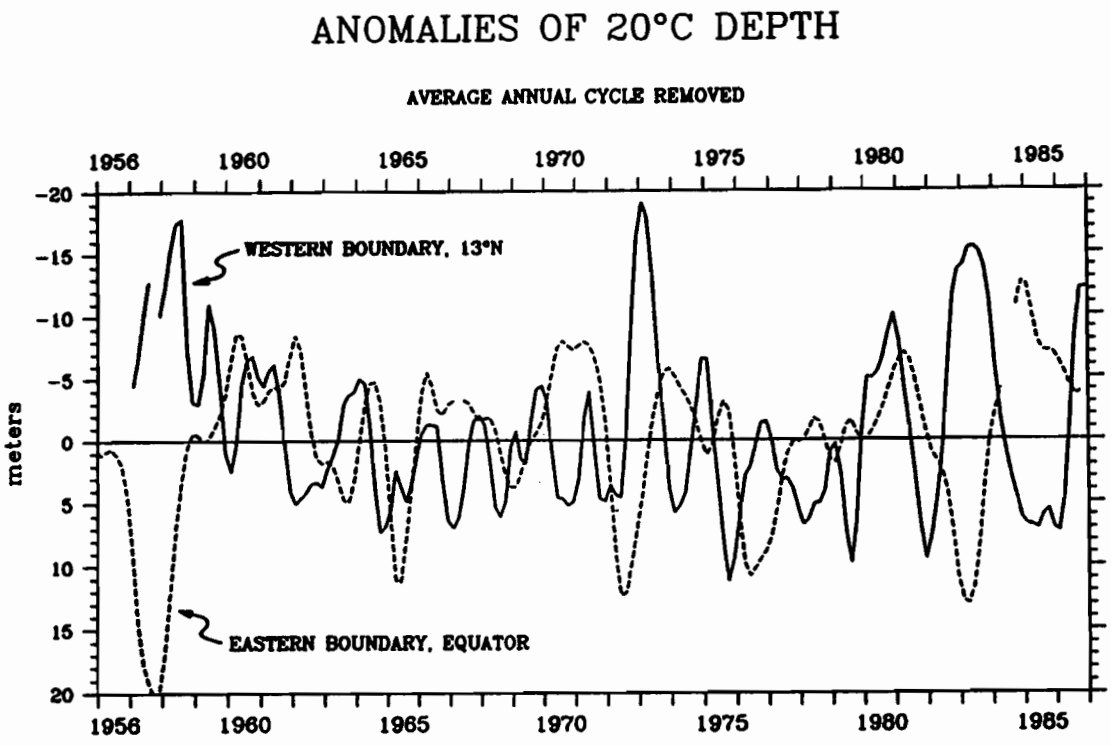

Figure 10. Time series of anomalous 20°C depth (m) at 13°N on the western boundary (solid line) and at the equator on the eastern boundary (dashed line) during 1956 through 1986. Deep anomalies are shown downwards and shallow anomalies upward.

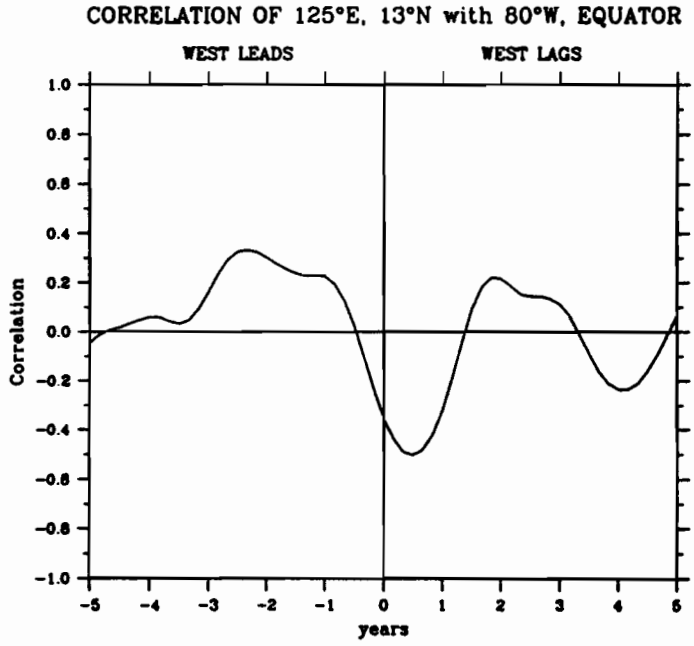

Figure 11. Lag correlation between anomalous 20°C depths at 13°N on the western boundary and at the equator on the eastern boundary (the two time series in Figure 10).

are reflected from the western boundary as downwelling equatorial Kelvin waves and act as triggers for El Niño. Aside from the questions of how efficient such a reflection could be given the irregular nature of the Philippine and Indonesian coastline, and the relatively high latitude, which are beyond the scope of this work (see Battisti, 1989), the data available here can be used to examine the lag relationship between off-equatorial Rossby pulses arriving at the western boundary and the subsequent occurrence of El Niños. To make this comparison long time series are desirable. In section 4.b a long time series of 20°C depth anomalies along the eastern boundary was shown to be a good index of El Niños (Figure 3); this time series can be summarized by the history at the equator along the eastern boundary. Along the western boundary it is not possible to construct a similarly long time series at most latitudes, however one location where data exist back to the 1950's is at 13°N, 125°E, which is where shipping headed for Manila from the east enters the Philippines Archipelago (San Bernardino Strait) (see Figure 1a). This location is almost exactly where Graham and White (1988) have proposed that the long Rossby waves in their scenario would arrive at the western boundary, and since Rossby events large enough to trigger El Niño should have a relatively broad meridional extent, this time series is thought to be representative of extra-equatorial large-scale western boundary variability. The two time series (now referred to as the eastern boundary, equator and the western boundary, 13°N) are overlaid in Figure 10, during 1956 through 1986, which includes eight El Niños (an El Niño is indicated by a deepening of the eastern boundary thermocline). Inspection of these time series shows that each El Niño is in fact preceded by a deep event in the west, as suggested by Graham and White (1988). However, there is not a consistent lag relation between the western and eastern deepening as would be expected if the connection between the two was a (nearly linear) oceanic wave process; the observed lag ranges from about three months to about fifteen months. Second, there were many more western boundary events than subsequent El Niños; during the thirty-one years shown in Figure 10 there were thirteen major western boundary downwellings but only eight El Niños. Given the inconsistency of the lags observed, it would be possible to find western boundary downwelling to precede almost any sequence of events. Third, there is no relation between the magnitude of the western deepening and that of the subsequent eastern event; for example a relatively large event in the west in 1978 was followed by a very weak El Niño in 1979, while a much weaker western downwelling in 1971 was followed by the strong El Niño of 1972. Lag correlation between the two time series (Figure 11) shows only a very weak anticipation of eastern events by those in the west, with correlations just above 0.2 for the west leading by one to one and one-half years, and about 0.3 for the west leading by two and one-half years (which seems much too long for a triggering mechanism). The only significant peak of correlation ($r = -0.5$) between the two time series occurs with the east leading the west by six months, with opposite sign (Figure 11). This represents the mechanism discussed in the main part of this section, in which upwelling long Rossby waves are generated in mid-basin near the height of El Niños (slightly earlier than when the eastern boundary thermocline peaks downward), so their arrival at the western boundary lags the eastern downward peak by about half a year. Such fluctuations can be seen in the two time series (Figure 10), for example in the 1972 El Niño, where the eastern boundary downward peak occurs in late 1972, while the western boundary shoaling peak at 13°N arrives in early 1973. In sum, while the observations presented here are inadequate to examine the reflection process in detail, the long time series suggest that the Graham and White (1988) scenario is unconvincing in its assertion that extra-equatorial long Rossby waves are the trigger for El Niños. A justifiable conclusion from the long time series is the more modest one that it is unlikely that an El Niño would occur at a time when the western tropical thermocline is anomalously shallow.

5. Summary and conclusions

A new set of BT data makes it possible to examine zonal propagation of thermocline fluctuations without extensive interpolation. The archives of the NODC contain several hundred thousand BT observations in the Pacific which have formed the basis for several previous studies; however these data are primarily distributed along particular shipping routes and leave large gaps, particularly in an important region of the western tropical Pacific. This has resulted in the necessity of relatively elaborate interpolation schemes in order to interpret thermocline variability in terms of zonal long-wave propagation, and has made such interpretation controversial. The new data set consists of MBT observations taken by Japanese fishing vessels during the 1970's; the sampling distribution complements the XBT data set in the western Pacific and allows the gridding of observations on a relatively fine 2° latitude by 5° longitude grid with a minimum of zonal interpolation. On this gridscale, the combined BT observations average one profile every 35 days in each gridbox during 1970

through 1987, with a higher density during the early 1970's. The sampling is concentrated in the northern hemisphere and in the southwest Pacific; the southeast Pacific is very poorly sampled. After extensive quality control, more than 185K profiles were available for analysis in the Pacific between 30°N and 30°S.

The field of 20°C isotherm depth was chosen as the clearest, simplest representation of the observed variability. The principal advantage of this choice is that it simplifies the three-dimensional thermal field into a two-dimensional variable which can be mapped and viewed conveniently. The assumption is made that the tropical Pacific may be approximated as a two-layer system divided by a sharp pycnocline, for which the depth of the 20°C isotherm is a proxy. This simplification has commonly been used in observational studies of the tropical Pacific, and in the same spirit many modelling experiments have used a reduced gravity, single-active-layer approximation.

A simple low-frequency long Rossby wave model (3.1) was used to study interannual pycnocline variability, with particular concentration on the El Niño of 1972 when the sampling was most dense. Ekman pumping alone hindcast unrealistically large amplitudes of interannual variability within about 15° latitude of the equator. This was due to the relative persistence of interannual wind stress curl anomalies, which commonly remain of the same sign for several years, so the (integrated in time) Ekman pumping solution can get very large. If the dynamics include Rossby waves, however, the anomalies radiate away before building up large amplitudes, so the simple model solution had approximately the same amplitude as the observations. The interannual hindcast assuming Ekman pumping alone was poorly correlated with the observations almost everywhere, while the Rossby wave solution had high correlations in the western Pacific; neither was significantly correlated in the east central Pacific (Figure 7), a region of poor data coverage (both wind and BT data). The simple model (3.1) was best-fit to the observations of interannual 20°C depth variability to find the phase speed which gave the highest correlations. The planetary wave character of the variability is shown by the meridional profile of these best-fit speeds (Figure 2), which falls roughly on the line $c_r = \beta c^2/f^2$, with the long gravity wave speed c chosen to be the zonal average of the first baroclinic mode long gravity speed found by Emery, et al. (1984).

A characteristic zonal wind stress anomaly pattern associated with El Niño is equatorial westerlies during the height of the event in the central Pacific, followed by a return of stronger than average equatorial easterlies the following year (Figure 4). Although the strongest wind *stress* anomalies are confined to the equatorial zone, the large scale wind stress *curl* pattern resulting from these anomalies is upwelling curl extending to about 15°N during the equatorial westerlies. In this tropical, extra-equatorial region, upwelling waves were generated during the height of the event which carried the upwelling signal to the western boundary, arriving about six months later (Figures 8 and 9). Thus although the anomalous wind stress curl forcing in the western extra-equatorial Pacific was relatively weak during several El Niños, large-scale shallow thermocline depth anomalies were observed there; these were forced in the central Pacific and radiated west. During the year following several El Niños, strong easterlies returned to the equatorial region, generating downwelling wind stress curl in the tropical central Pacific. The deep anomalies forced in this way in the central basin were also observed to propagate to the western boundary.

In addition to the mid-basin forcing, El Niños also generate boundary reflections of the deep equatorial thermocline anomalies which are the primary oceanic signal of the event. Along the American coast, deep anomalies of 20°C depth were observed to occur northward to at least 22°N, with typical amplitudes of 10-15 m (Figure 3). The speed of propagation along the coast was observed to be about 32 cm/s, which is slower than estimates of coastal Kelvin wave propagation found from long time series of sea level. The simple model radiates these anomalies offshore and predicts that they should form an dominant part of the variability in the eastern and central Pacific. However, equatorward of 15°N, the observations do not appear to be consistent with this hypothesis, which is largely why the simple model was found to be poorly correlated with the observations in this region (Figure 7). North of 15°N, however, reflections can be observed propagating across the entire basin over several years (Kessler 1989a,b).

It is clear from the observations reported here that long Rossby waves propagate across the tropical, extra-equatorial north Pacific, and that these waves can arrive at the western boundary with significant amplitude. It has been proposed that these waves reflect from the western boundary as equatorial Kelvin waves and contribute to the triggering of subsequent El Niños (Graham and White, 1988). This mechanism has also been suggested in theoretical and modelling studies which hypothesize that the approximate three to four year periodicity of these events is due to the relatively slow travel time of the long tropical Rossby waves. In a few locations in the Pacific, it is possible to construct long time series of 20°C depths going back to the 1950's, and

these time series, which span seven major El Niños, indicate problems with this idea. Figure 10 shows such long time series at 13°N on the Philippines coast (which gives a good index of waves arriving from the northern tropical Pacific, and is almost exactly where Graham and White have suggested that the triggering waves arrive at the boundary) and at the equator at the South American coast (which is a good index of El Niños). If a (nearly linear) oceanic wave mechanism connects these two locations, then there should be a significantly positively correlated lag relation between them, with the west leading the east. In fact the only significant correlation shows the east leading the west by about six months, with opposite sign. This represents the process discussed above whereby upwelling Rossby waves are generated in mid-basin by wind stress curl associated with equatorial westerly wind anomalies (occurring only slightly before the deep equatorial thermocline anomalies arriving in the east), which then take about six months to reach the western boundary. The proposed correlation with the west leading the east is a weak, broad peak with correlations about 0.2, which is probably not significantly different from zero. There is a suggestion in the time series (Figure 10) that many El Niños are preceded by a deep thermocline in the west, however there are almost twice as many deep events in the west as El Niños, and no apparent relation between the size of the western event and the subsequent eastern deepening, nor is the time lag at all regular, as would be expected if a nearly linear oceanic wave process were the primary mechanism. A more justifiable conclusion from these data is that it is apparently unlikely to have an El Niño occur following a period when the western Pacific thermocline is anomalously shallow. The data do not support the idea that there is a triggering of eastward propagation along the equator by long Rossby waves arriving at the tropical western boundary.

REFERENCES

Battisti, D.S., 1989: On the role of off-equatorial oceanic Rossby waves during ENSO. *J. Phys. Oceanogr.*, **19**, in press.

Busalacchi, A.J. and J.J. O'Brien, 1980: The seasonal variability in a model of the tropical Pacific. *J. Phys. Oceanogr.*, **10**, 1929-1951.

Busalacchi, A.J., K. Takeuchi and J.J. O'Brien, 1983: Interannual variability of the tropical Pacific – revisited. *J. Geophys. Res.*, **88**, 7551-7562.

Chang, P. and S.G.H. Philander, 1989: Rossby wave packets in baroclinic mean currents. *J. Mar. Res.*, in press.

Donguy, J-R. and A. Dessier, 1983: El Niño-like events observed in the tropical Pacific. *Mon. Wea. Rev.*, **111**, 2136-2139.

Emery, W.J., W.G. Lee and L. Magaard, 1984: Geographic and seasonal distributions of Brunt-Vaisala frequency and Rossby radii in the North Pacific and North Atlantic. *J. Phys. Oceanogr.*, **14**, 294-317.

Garzoli, S.L. and E.J. Katz, 1983: The forced annual reversal of the Atlantic North Equatorial Countercurrent. *J. Phys. Oceanogr.*, **13**, 2082-2090.

Gill, A.E. and A.J. Clarke, 1974: Wind-induced upwelling, coastal currents and sea-level changes. *Deep-Sea Res.*, **21**, 325-345.

Goldenberg, S.B. and J.J. O'Brien, 1981: Time and space variability of tropical Pacific wind stress. *Mon. Wea. Rev.*, **109**, 1190-1207.

Graham, N.E. and W.B. White, 1988: The El Niño cycle: A natural oscillator of the Pacific Ocean-atmosphere system. *Science*, **240**, 1293-1302.

Harrison, D.E., Kessler, W.S. and B.S. Giese, 1989: Ocean circulation model hindcasts of the 1982-83 El Niño: Thermal variability along the ship of opportunity tracks. *J. Phys. Oceanogr.*, in press.

Inoue, M., O'Brien, J.J., White, W.B. and S.E. Pazan, 1987: Interannual variability in the tropical Pacific for the period 1979-1982. *J. Geophys. Res.*, **92**, 11671-11679.

Kessler, W.S., B.A. Taft and M. McPhaden, 1985: An assessment of the XBT sampling network in the central Pacific. Univ. Corp. for Atmos. Res., US TOGA 4, 62 pp.

Kessler, W.S. and B.A. Taft, 1987: Dynamic heights and zonal geostrophic transports in the central tropical Pacific during 1979-84. *J. Phys. Oceanogr.*, **17**, 97-122.

Kessler, W.S., 1989a: Observations of long Rossby waves in the northern tropical Pacific. PMEL Technical Report. In press.

Kessler, W.S., 1989b: Observations of long Rossby waves in the northern tropical Pacific. *J. Geophys. Res.*. In press.

Levitus, S., 1982: Climatological atlas of the world ocean. NOAA professional paper 13, 173 pp.

Lukas, R., S.P. Hayes and K. Wyrtki, 1984: Equatorial sea level response during the 1982-1983 El Niño. *J. Geophys. Res.*, **89**, 10,425-10,430.

McCreary, J.P., 1983: A model of tropical ocean-atmosphere interaction. *Mon. Wea. Rev.*, **111**, 370-387.

McCreary, J.P. and D.L.T. Anderson, 1984: A simple model of El Niño and the southern oscillation. *Mon. Wea. Rev.*, **112**, 934-946.

McCreary, J.P., 1985: Modelling equatorial ocean circulation. *Ann. Rev. Fluid Mech.*, **17**, 359-409.

McPhaden, M.J., A.J. Busalacchi, J. Picaut and G. Raymond, 1988a: A model study of potential sampling errors due to data scatter around expendable bathythermograph transects in the tropical Pacific. *J. Geophys. Res.*, **93**, 8119-8130.

McPhaden, M.J., A.J. Busalacchi and J. Picaut, 1988b: Observations and wind-forced model simulations of the mean seasonal cycle in tropical Pacific sea surface topography. *J. Geophys. Res.*, **93**, 8131-8146.

Meyers, G., 1979a: On the annual Rossby wave in the tropical North Pacific Ocean. *J. Phys. Oceanogr.*, **9**, 663-674.

Meyers, G., 1979b: Annual variation in the slope of the 14°C isotherm along the equator in the Pacific Ocean. *J. Phys. Oceanogr.*, **9**, 885-891.

Meyers, G. and J.-R. Donguy, 1980: An XBT network with merchant ships. *Trop. Ocean-Atmos. Newslett.*, **2**, 6-7.

Meyers, G. and J.-R. Donguy, 1984: The North Equatorial Countercurrent and heat storage in the western Pacific Ocean during 1982-83. *Nature*, **312**, 258-260.

Pazan, S.E., W.B. White, M. Inoue and J.J. O'Brien, 1986: Off-equatorial influence on Pacific equatorial dynamic height variability during the 1982-83 ENSO. *J. Geophys. Res.*, **91**, 8437-8449.

Pazan, S.E. and W.B. White, 1987: Short-term climatic variability in the volume budget of the western tropical North Pacific Ocean during 1979-82. *J. Phys. Oceanogr.*, **17**, 440-454.

Rebert, J.P., J.-R. Donguy, G. Eldin and K. Wyrtki, 1985: Relations between sea level, thermocline depth, heat content and dynamic height in the tropical Pacific Ocean. *J. Geophys. Res.*, **90**, 11719-11725.

Taft, B.A. and W.S. Kessler, 1989: On the use of sea-level and XBT transects to measure geostrophic flow in the tropical Pacific Ocean. In preparation.

White, W.B., 1977: Annual forcing of baroclinic long waves in the tropical North Pacific Ocean. *J. Phys. Oceanogr.*, **7**, 50-61.

White, W.B., G. Meyers and K. Hasunuma, 1982: Space/time statistics of short-term climatic variability in the western North Pacific. *J. Geophys. Res.*, **87**, 1979-1989.

White, W.B., 1983: Westward propagation of short-term climatic anomalies in the western North Pacific from 1964-74. *J. Mar. Res.*, **41**, 113-125.

White, W.B., G. Meyers, J.-R. Donguy and S.E. Pazan, 1985: Short-term climatic variability in the thermal structure of the Pacific Ocean during 1979-82. *J. Phys. Oceanogr.*, **15**, 917-935.

Wyrtki, K. and G. Meyers, 1975a: The trade wind field over the Pacific Ocean. Part I. The mean field and the mean annual variation. Rep. HIG-75-1. Hawaii Inst. Geophys., Univ. of Hawaii, 26 pp.

Wyrtki, K. and G. Meyers, 1975b: The trade wind field over the Pacific Ocean. Part II. Bimonthly field of wind stress: 1950 to 1972. Rep. HIG-75-2. Hawaii Inst. Geophys., Univ. of Hawaii, 16 pp.

Wyrtki, K. and G. Meyers, 1976: The trade wind field over the Pacific Ocean. *J. Appl. Meteorol.*, **15**, 698-704.

Variable Currents in the Western Pacific Measured During the US/PRC Bilateral Air-Sea Interaction Program and WEPOCS

Eric FIRING[1] and Jiang SONGNIAN[2]

(1) *University of Hawaii, Manoa*
Honolulu, Hawaii - U.S.A.

(2) *National Oceanographic Data Center*
Tianjin, People's Republic of China

Abstract

As the ensemble of current profile sections in the western tropical Pacific increases, we begin to get a picture of the annual and interannual variability of circulation in the region. The data sets considered here—ADCP sections from two WEPOCS cruises and 4 US/PRC TOGA cruises—do not resolve the seasonal cycle, but they do span the 1986-87 El Niño event and show some of the current variability associated with it. The most striking result is the contrast between the ever-present New Guinea Coastal Undercurrent and equatorial undercurrent on 141°E, and the lack at 165°E of any persistent currents other than the Tsuchiya jets. The net transports across 165°E of water warmer than 26° were 77×10^6 m^3 s^{-1} to the east in December 1986, early in the El Niño event, and 50×10^6 m^3 s^{-1} to the west in May 1988, following the event. There was little net transport in October 1987.

1 Introduction

The US/PRC Bilateral Air-Sea Interaction Program (a contribution to TOGA: Tropical Ocean—Global Atmosphere) is a cooperative China-US meteorological and oceanographic study of the western tropical Pacific. Emphasis is on annual and interannual variability associated with El Niño and the Southern Oscillation. Five of the eight cruises planned have been completed, and a sixth is underway (as of mid-May, 1989). An acoustic Doppler current profiler (ADCP) was installed before the second of these cruises. Current measurements made with this instrument on cruises 2–4 and 6 show moderate variations in currents such as the Kuroshio, the Mindanao Current, and the New Guinea Coastal Undercurrent. In other areas the currents varied greatly in connection with the 1986-87 El Niño, which occurred during this series of cruises (McPhaden *et al.*, 1989). Cruise 2, November–December 1986, took place during the early stages of the event. Cruise 3, September–October 1987, was late in the El Niño. Cruise 4, April–May 1988, closely followed the end of the event.

The intersection between the equatorial waveguide and the western boundary, the north coast of New Guinea, is a particularly fascinating part of the western tropical Pacific. The growing ensemble of current surveys there includes ADCP measurements from three cruises of the Western Equatorial Pacific Ocean Circulation Study (WEPOCS; Lindstrom et al., 1987). Meridional sections from the second and third WEPOCS cruises (January–February 1986 and June–July 1988) are included here for comparison with the US/PRC sections.

2 Data

All data shown here were obtained with standard 150-kHz profilers made by RD Instruments. The profilers have been improved since the WEPOCS II, and areas of possible bias in the early cruises (WEPOCS II and US/PRC 2 and 3) have been identified (Chereskin et al., 1989). The magnitude of the bias cannot be predicted accurately enough to be removed, so regions where the bias may exceed about 10 cm/s have been edited out. This reduces the depth range of the earlier sections.

Navigation for the calculation of absolute velocities was provided by a single-channel Transit receiver (Magnavox 1105) on the PRC ships (Xiangyanghong #5 for cruise 2, Xiangyanghong #14 for the others), and by a dual channel Transit receiver (Magnavox

ORSTOM
CENTRE DOCUMENTATION
Montpellier

F 30208

1107 on WEPOCS II, Magnavox 1157 on WEPOCS III) combined with a GPS receiver (Trimble) on the Moana Wave. In WEPOCS III and in the US/PRC cruises starting with 4 the Transit fix quality was improved by using the ADCP as a speed log. The GPS receiver was also upgraded between WEPOCS II and WEPOCS III. The quality of the navigation is correspondingly highest on WEPOCS III and lowest on US/PRC 2.

Absolute velocities were calculated using a reference layer from about 50–170 m. (See Kosro, 1985, for a good explanation of the method of calculating absolute currents from ADCP measurements and position fixes.) For US/PRC 2–4 the absolute velocity of this reference layer averaged between Transit fixes was smoothed with a 12-hour Blackman filter. With the ship travelling at a maximum speed near 10 m/s, this causes wavelengths less than 200 km along the cruise track to be reduced in power by half or more. On sections with CTD stations the average speed of the ship was reduced to about 4 m/s, so the half-power wavelength was about 80 km. These limitations in horizontal resolution, imposed by the infrequency and inaccuracy of Transit fixes, cause the most serious distortions of our estimates of circulation in regions of large horizontal gradients, such as near the Philippines and Papua New Guinea. A narrower filter (typically 6 hours) was used to smooth the reference layer velocity on the cruises with better navigation, permitting finer horizontal resolution.

Various approaches have been used to calibrate the transducer orientation and amplitude factor for each of the cruises, depending on available navigation and other conditions (Pollard and Reed, 1989; Joyce, 1989). Calibration of the orientation averaged over several days appears to be good to something like 0.1° on the WEPOCS cruises, but could be uncertain to as much as 1.0° on US/PRC 2, the worst case. This would lead to a systematic 7-cm/s error in speed on the 165°E section, assuming an average ship speed of 4 m/s. The error in transport in a 100-m depth interval would then be 0.8×10^6 m^3 s^{-1} per degree latitude.

3 Maps of circulation

Maps of currents averaged from 30–75 m and 175–225 m show the general pattern of the circulation in the cruise region (Figure 1). Some points to note:

- The Mindanao current is consistently strong and deep, while the currents at comparable latitudes to the east are generally more variable and decay more rapidly with depth.
- Variability in the equatorial zone is much greater at the shallower level than near 200 m. For example, the shallow currents along the equator between 145°E and 157°E during May 1989 (US/PRC cruise 6) differ in direction by 90–180° from those one year earlier (US/PRC cruise 4).
- Currents are much more variable at 165°E than at 141.5°E at both levels shown here. At 141.5°E the NECC, the EUC, and the New Guinea Coastal Undercurrent (NGCUC) are present in all sections. There appears to be no major current common to all sections at 165°E.
- The region of high variability includes the NECC and the SECC, which are absent from 165°E in cruise 4 (May 1988).

The difficulty of distinguishing short-term temporal variations from spatial gradients is ever-present in the interpretation of data from cruise tracks at low latitudes. The US/PRC cruise tracks include three approximately meridional sections with equator-crossings between about 157°E and 165°E. The coherence of features among these sections on cruises 3 and 4 suggests that each map shows real spatial patterns, not just aliased temporal changes. For example, consider the 175–225-m layer during cruise 3. The zonal velocity component on the equator is eastward at 141°E (in the EUC), decreases toward the east to a null at about 157°E, and reverses to westward in the 165°E section. The null at 157°E is found both at the end of the section along the equator on October 7, and again on October 23 during the northwestward transit to Guam.

4 Meridional sections

The vector maps (Figure 1) show some current reversals near 141°E from one cruise to the next in the 30–75-m layer, but in the deeper layer the EUC and the NGCUC were always present. Looking at a series of meridional sections from January 1986 to May 1989 (Figure 2), we see that the strength of the NGCUC varied by about a factor of two, from just over 40 cm/s in early May 1988 to more than 80 cm/s in late June of the same year. The core depth was usually near 200 m. An exception is US/PRC 3, October 1987, when the NGCUC might be described as having "surfaced", and a core with 100 cm/s was found at 70 m.

The EUC near 141°E also varied in strength from one section to the next. The minimum in this series was about 40 cm/s in June 1988 and May 1989, and the maximum was 70 cm/s in October 1987. The

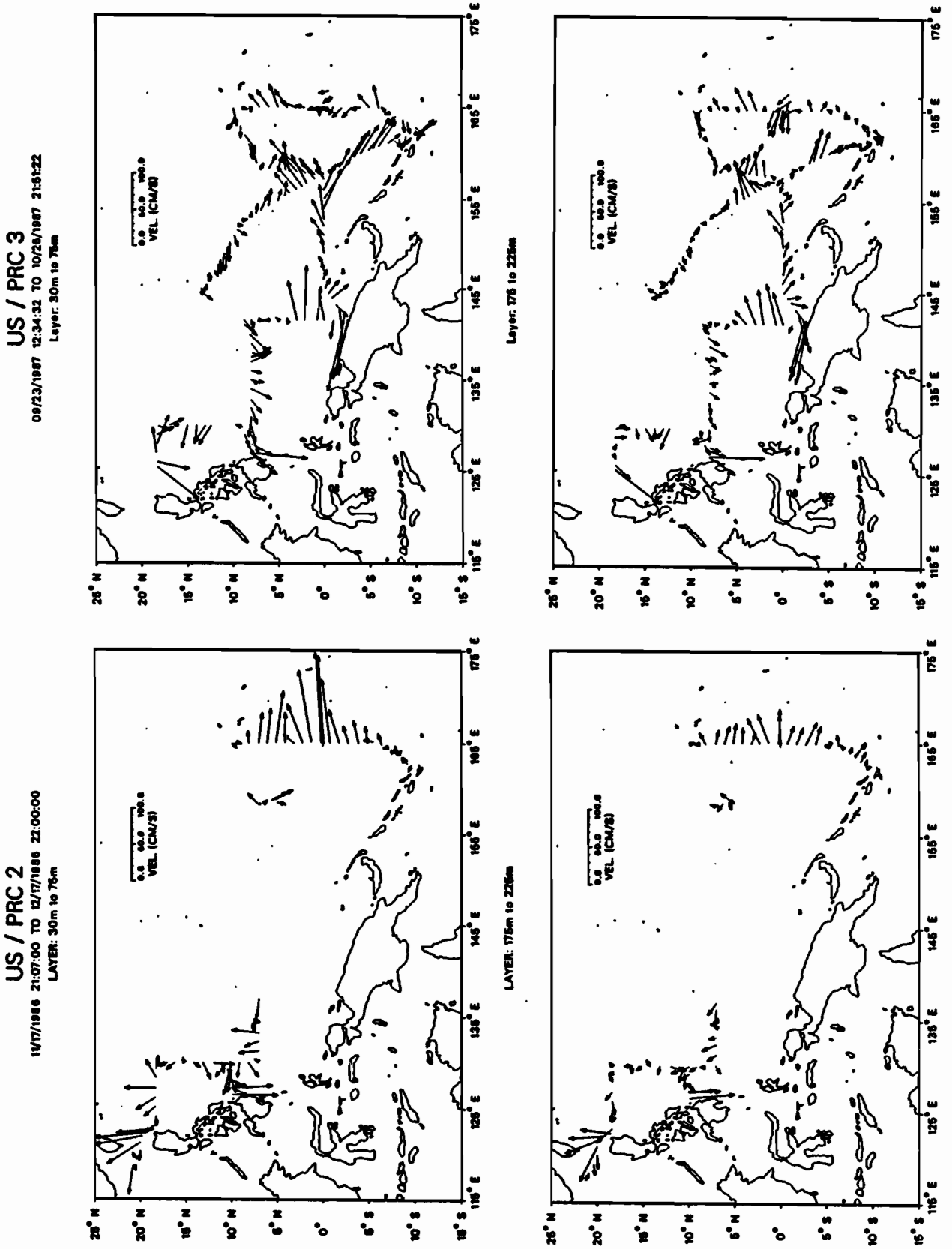

Figure 1: Currents averaged from 30–75 m (top) and 175–225 m (bottom) on the US/PRC cruises.

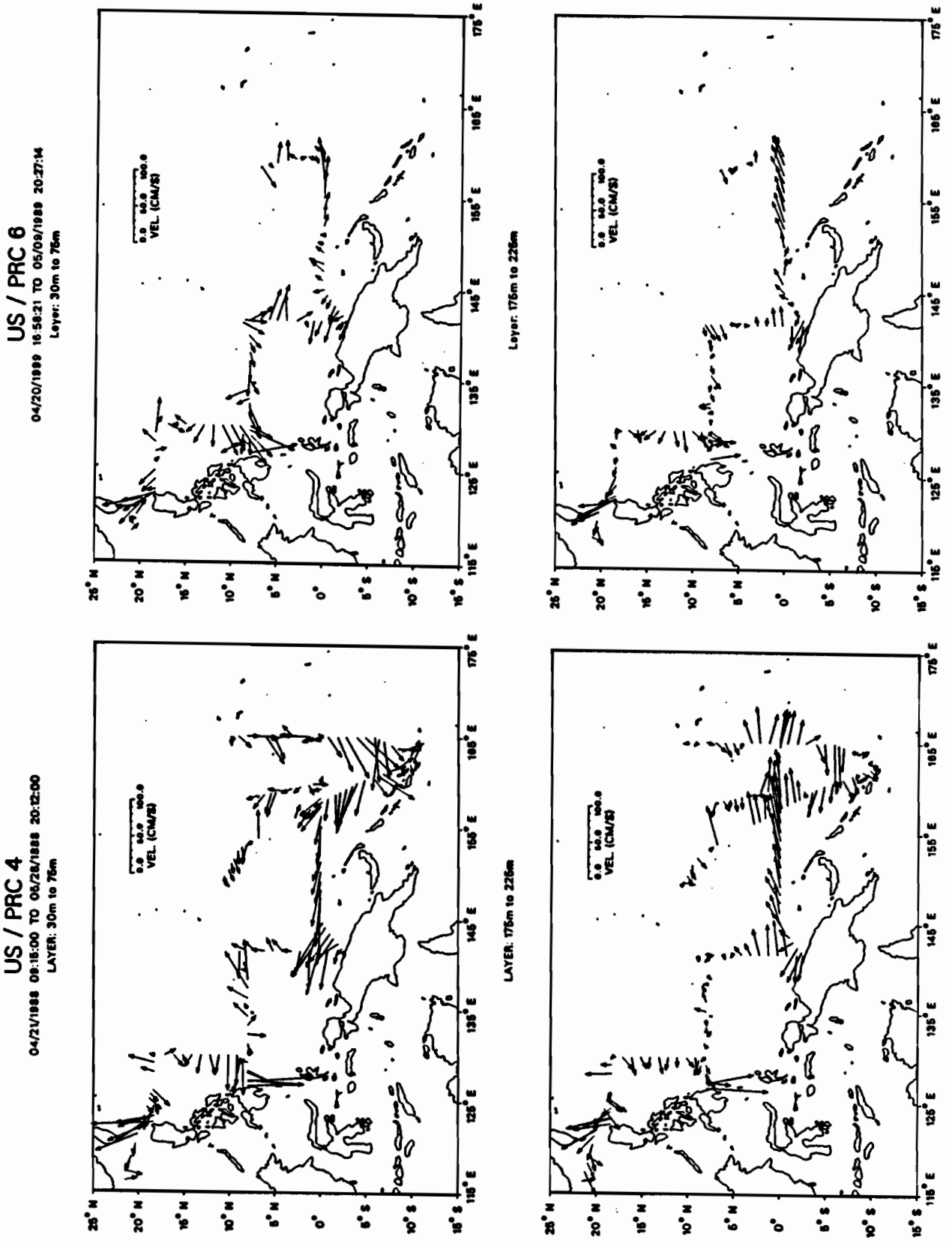

Figure 1, cont.

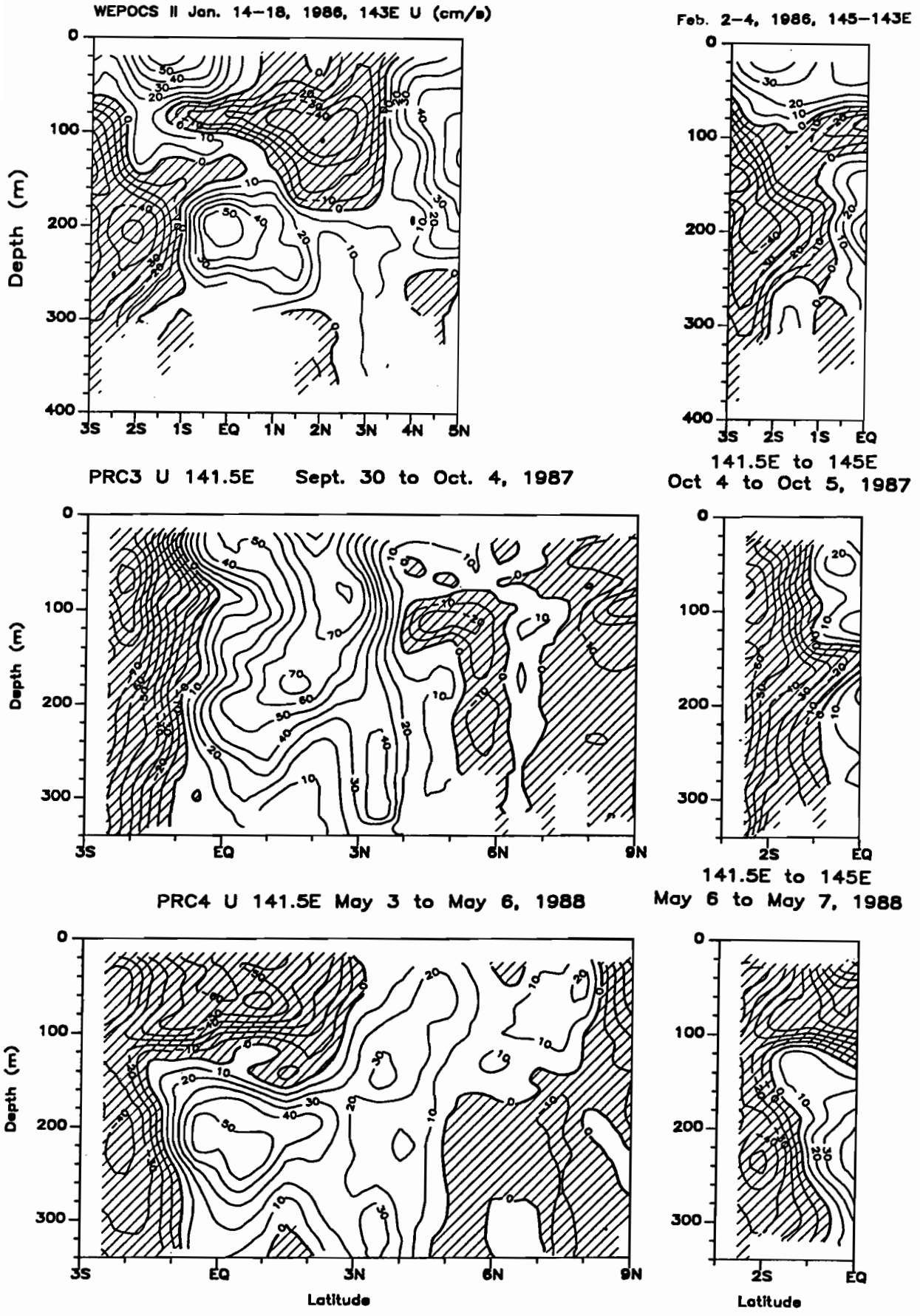

Figure 2: Zonal currents, 141°E to 143°E.

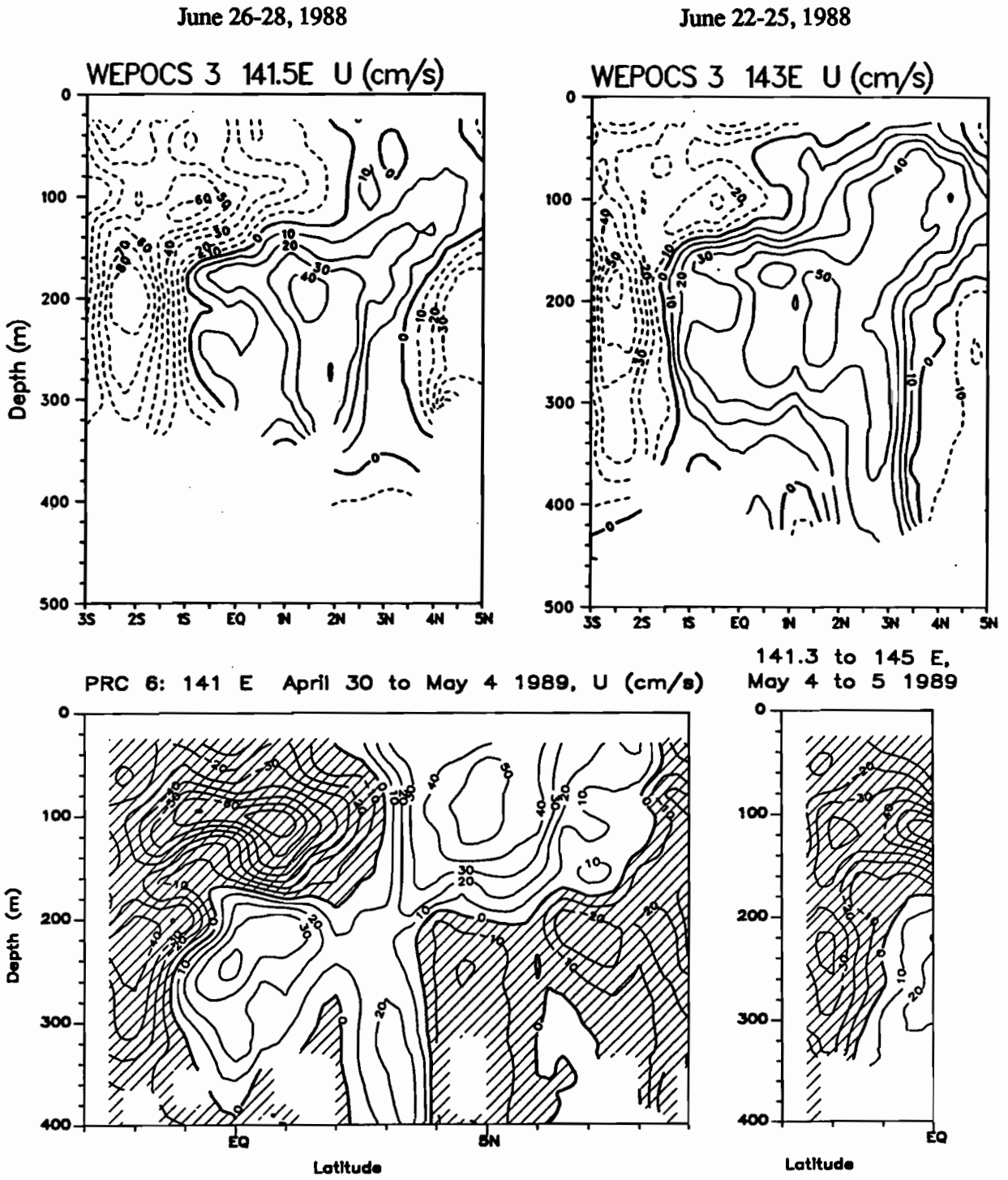

Figure 2, cont.

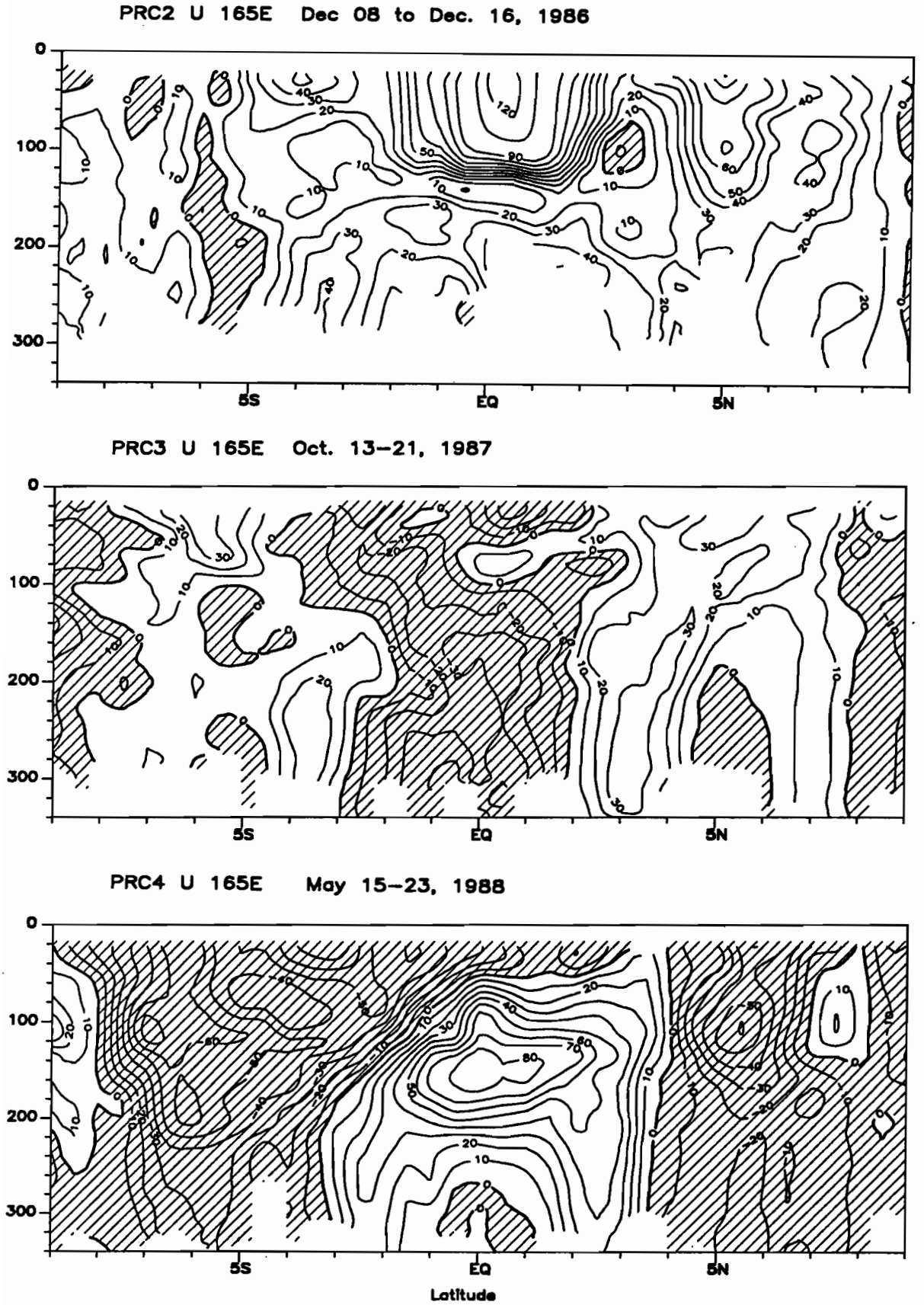

Figure 3: Zonal currents, 165°E.

core depth was usually near 200 m. The core was found on the equator in three of the sections, and at about 1.5°N in the other two (October 1987 and June 1988). These instances of large displacement from the equator suggest that a single equatorial mooring may give a poor index of EUC transport at this longitude. All sections near 141°E show the EUC connected by continuous eastward flow to the NECC and to the northern subsurface countercurrent (also known as a Tsuchiya jet; Tsuchiya, 1972, 1975).

On 165°E, the Tsuchiya jets are the only consistent features of the three sections shown (Figure 3). Otherwise these sections could hardly be more different. The outstanding features of US/PRC 2 in December 1986, early in the 1986-87 El Niño, are the preponderance of eastward flow throughout the section, and the intense eastward surface jet on the equator. The equatorial jet is very similar to one observed at 159°W in November 1982, early in the 1982-1983 El Niño. In October 1987 (cruise 3), late in the 1986-87 El Niño, currents were weak everywhere on this section, and westward almost everywhere within 3° of the equator. Following the El Niño, in May 1988 (cruise 4), the EUC was unusually strong for the western Pacific, and was embedded in an exceptionally strong and extensive westward flow with cores at 5–6° on either side of the equator.

5 Zonal transports at 165°E

Transports per unit width were calculated by integrating the velocity from the surface to 520 cl/t, from 520 to 450 cl/t, and from 450 to 300 cl/t. These isopycnals roughly correspond to the 26°, 23.5°, and 18° isotherms, respectively. The velocity was approximated as constant from the shallowest depth bin at about 20 m to the surface. Transports per unit width were then integrated trapezoidally in latitude to give a transport streamfunction (Figure 4).

Transports were weak in cruise 3, and eastward and westward transports were nearly in balance across the section. In cruises 2 and 4 the transports of warm water were predominantly of one sign; 77×10^6 m^3 s^{-1} to the east in cruise 2, and 50×10^6 m^3 s^{-1} to the west in cruise 4. Note that a sizeable fraction of the warm water transport, about 17×10^6 m^3 s^{-1}, was found north of the 4°N in cruise 2, and almost none was found south of 4°S. Most of the transport, 44×10^6 m^3 s^{-1}, was within 2° of the equator. In cruise 4 the distribution was different; most of the westward transport occurred south of the equator, and only about 10×10^6 m^3 s^{-1} occurred north of the equator.

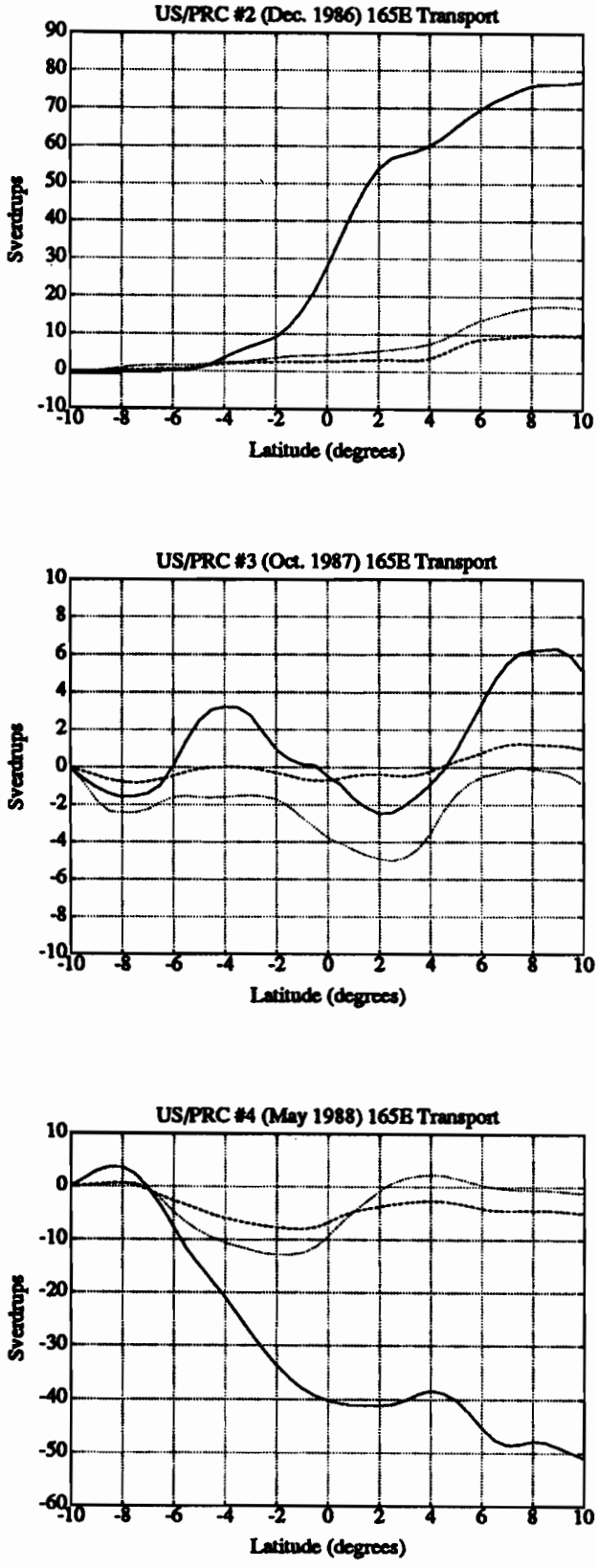

Figure 4: Transport streamfunction, 165°E.

Acknowledgements

This work is supported by the US TOGA Project Office of NOAA under cooperative agreement NA-85-ABH-00032, and by the National Science Foundation under grants OCE-8614965 and OCE-8716510. Joint Institute for Marine and Atmospheric Research Contribution Number 89-0178. Hawaii Institute of Geophysics Contribution Number 2157.

References

Chereskin, T., E. Firing, and J. Gast. 1989. On identifying and screening filter skew and noise bias in acoustic Doppler current profiler measurements. J. Atmos. Oceanic Technol., accepted.

Joyce, T. M. 1989. On in-situ "calibration" of shipboard ADCPs. J. Atmos. Oceanic Technol., 6, 169–172.

Lindstrom, E., R. Lukas, R. Fine, E. Firing, S. Godfrey, G. Meyers, and M. Tsuchiya. 1987. The Western Equatorial Pacific Ocean Circulation Study. Nature, 330, 533–537.

McPhaden, M. J., S. P. Hayes, L. J. Mangum, and J. M. Toole. 1989. Variability in the western equatorial Pacific Ocean during the 1986–87 El Niño/Southern Oscillation event. Submitted to J. Phys. Oceanogr.

Pollard, R., and J. Reed. 1989. A method for calibrating shipmounted acoustic Doppler profilers, and the limitations of gyro compasses. J. Atmos. Oceanic Technol., in press.

Tsuchiya, M. 1972. A subsurface north equatorial countercurrent in the eastern Pacific Ocean. J. Geophys. Res., 77, 5981–5986.

Tsuchiya, M. 1975. Subsurface countercurrents in the eastern equatorial Pacific Ocean. J. Mar. Res., 33 (Suppl.), 145–175.

Why are there Such Strong Steric Height Gradients off Western Australia ?

John S. GODFREY[1] and A. WEAVER[2]

[1]CSIRO Division of Oceanography, GPO Box 1538, Hobart, TAS 7001, Australia
[2]University of Washington, Seattle, Washington 98195 - U.S.A.

ABSTRACT

The Indonesian channel permits equatorial Pacific winds to maintain a bank of very warm (28°C) water along Australian's Northwest Shelf. This leads to net ocean cooling south of 20°S off Western Australia (compared to 40° or 50°S in the eastern Atlantic of Pacific). It is suggested that this convective cooling towards the latitude-dependent Haney equilibrium temperature in turn generates meridional pressure gradients and the onshore geostrophic flows that drive the Leeuwin Current; in this sense the equatorial Pacific winds drive the Leeuwin Current. Preliminary results from a numerical model support this hypothesis.

1. Annual mean flow patterns in the Leeuwin Current.

Steric height maps of the Western Australian region show a strong onshore geostrophic flow at the surface, that turns polewards near the coast. This polewards flow - the Leeuwin Current - moves directly into the prevailing equatorward wind, from 22°S to the southwest tip of Australia at 36°S (fig. 1a; from Godfrey and Ridgway, 1985). Below about 250m there is deep, slow equatorward flow along the coast feeding an offshore geostrophic flow - the Leeuwin Undercurrent. (Fig. 1b). Neither feature has any analogue in the Pacific or Atlantic.

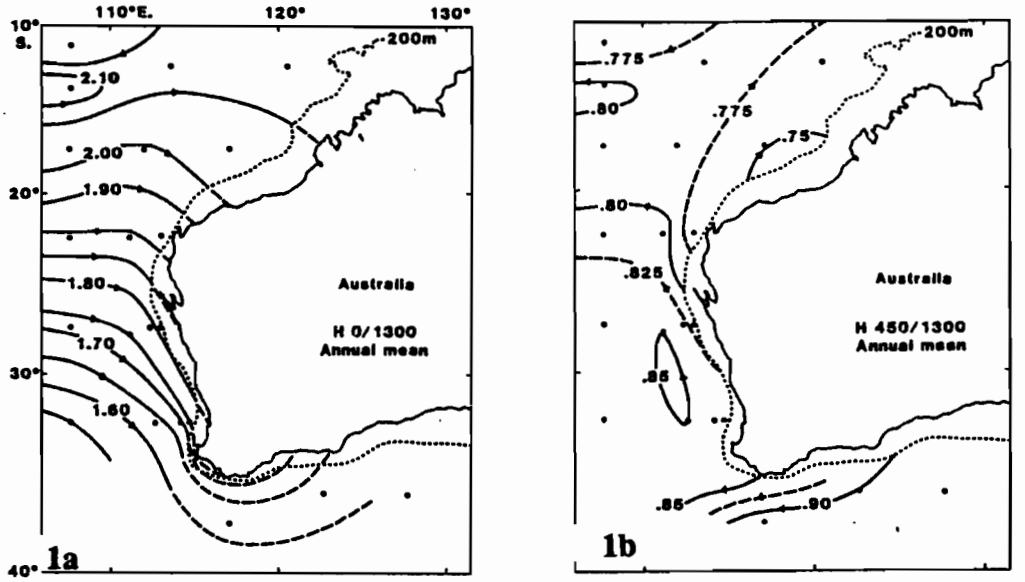

FIG.1. Annual mean steric sea level at (a) the surface and (b) 450 db, relative to 1300db, off Western Australia.

ORSTOM
CENTRE DOCUMENTATION
Montpellier

F 30209

2. Longshore steric height gradients in the Leeuwin Current.

The meridional gradients of steric height found offshore from Western Australia are much greater than those off other eastern boundaries and extend much deeper; and they reverse with depth. This is seen in Figure 2, which compares the annual mean steric height difference relative to 1500 db between 17.5°S and 32.5°S off Western Australia (open squares) with that off South America (diamonds). The data are 5°x5° averages from Levitus (1982). Recent modelling studies (McCreary et al., 1986; Weaver and Meddleton, 1989) have shown, that these large steric height gradients off Western Australia are responsible for driving the Leeuwin Current polewards, into the prevailing wind - and for the observed equatorwards undercurrent. However, why do these large, reversing gradients occur off Western Australia and not off any other subtropical eastern boundaries such as South America ?

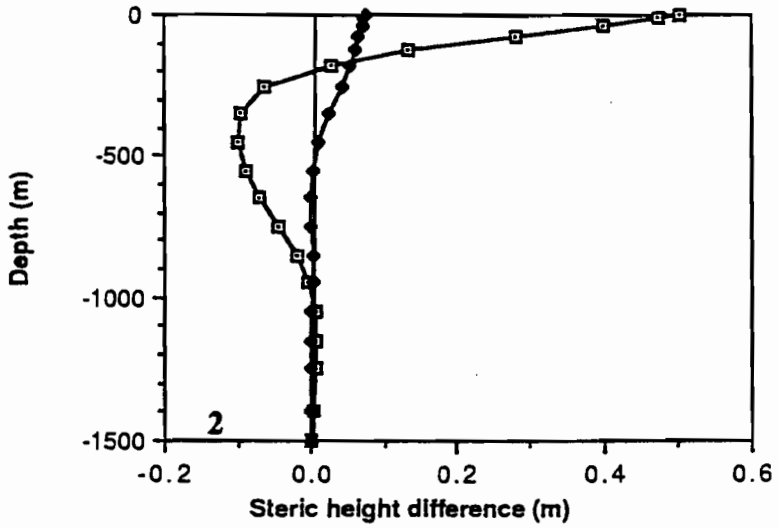

FIG.2. Differences in annual mean steric height relative to 1300 db, between 17.5°S and 32.5°S in 5°x5° squares along the coasts of Western Australian coast (open squares) and South America (diamonds).

3. Kelvin and Rossby wave propagation from the Pacific.

The large steric height differences of Fig.2 mostly reflect the fact that near-surface waters are much warmer off Northwestern Australia than off other eastern boundaries. We therefore begin by examining the reason for these warm northwest Australian temperatures. Below 100 m, the vertical profile of Specific Volume Anomaly (SVA) off northwestern Australia at 17.5°S (open diamonds in Fig.3a) is essentially identical to that in the western equatorial Pacific, just west of Irian Jaya (open squares). Both profiles are very different to those off other eastern boundaries such as South America (closed diamonds, squares with dots). It is suggested that internal Kelvin waves propagate with little dissipation or forcing from the western equatorial Pacific through the Indonesian archipelago along the northwestern Australasian shef edge, and that internal Rossby waves then propagate westwards, bringing SVA profiles off northwestern Australia close to that off Irian Jaya. As a result, annual mean water temperatures in the top 200 m are much warmer at 17.5°S off Western Australia than at the same latitude off South America (Fig. 3b).

4. Models forced by heat fluxes.

If the Kelvin and Rossby waves continued their poleward and westward propagation

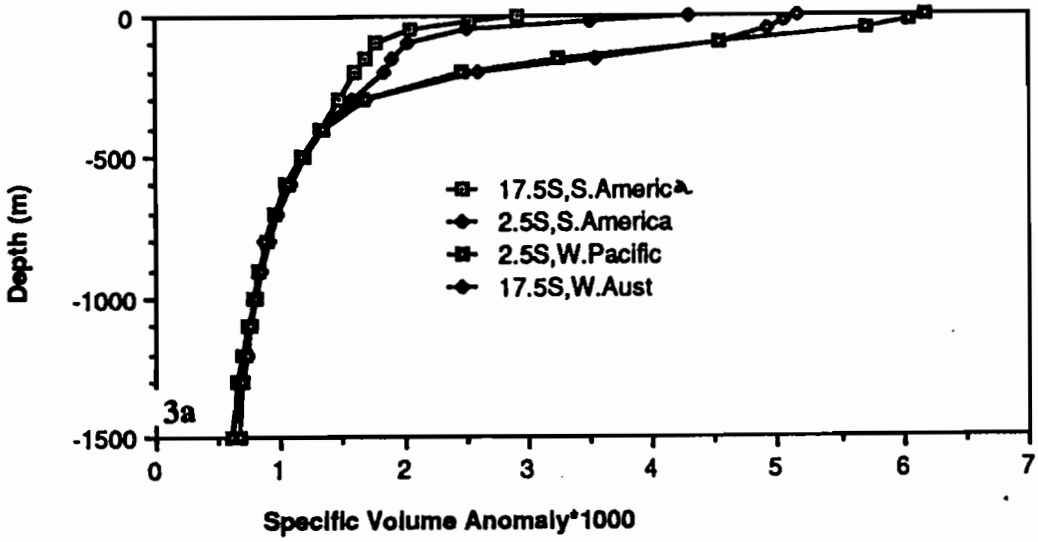

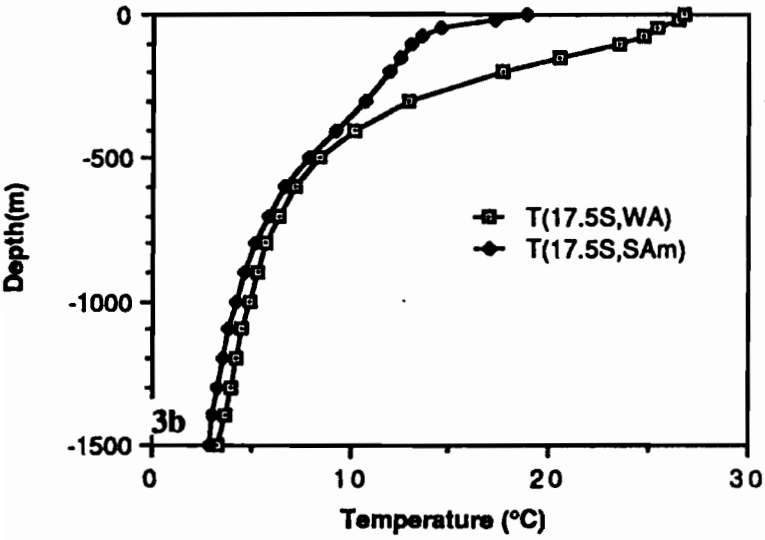

FIG.3. (a) Annual mean specific volume anomaly at various 5°x5° squares along the coasts of Western Australasia and South America. (b) Annual mean temperature profiles at 17.5°S off the two coasts.

without dissipation or forcing from 17.5°S to 32.5°S, the annual mean SVA profile off Western Australia at 32.5°S, would be like the SVA profiles of the equatorial west Pacific and at 17.5°S and 32.5°S seen in Fig. 3a; thus the large steric height differences between 17.5°S and 32.5°S seen in Fig.2 would not occur. Very strong forcing must occur off Western Australia between 17.5°S to 32.5°S to create the observed longshore gradients of Fig.2; much stronger than can be provided by the wind stress. The forcing between these latitudes is *not* primarily due to the wind - the Leeuwin Current flows into the wind.

McCreary, Shetye and Kundu (1986) introduced vertical heat diffusion into a linear model of the Leeuwin Current, and imposed a boundary condition that surface temperatures have the observed north-south gradient. Their vertical heat flux was unrealistically parameterized by $(\kappa T)_z$ rather than by κT_z, where K is the eddy diffusivity and T is the temperature at depth z; and away from the eastern boundary this heat flux was constant vertically from the surface through the ocean floor. Nevertheless they obtained a realistic-looking solution, both offshore and in the Leeuwin Current, as can be seen by comparing their steric height maps (Fig. 4a-b) with the observations of Fig.1. In particular they obtained both a poleward surface current and an equatorward subsurface undercurrent,

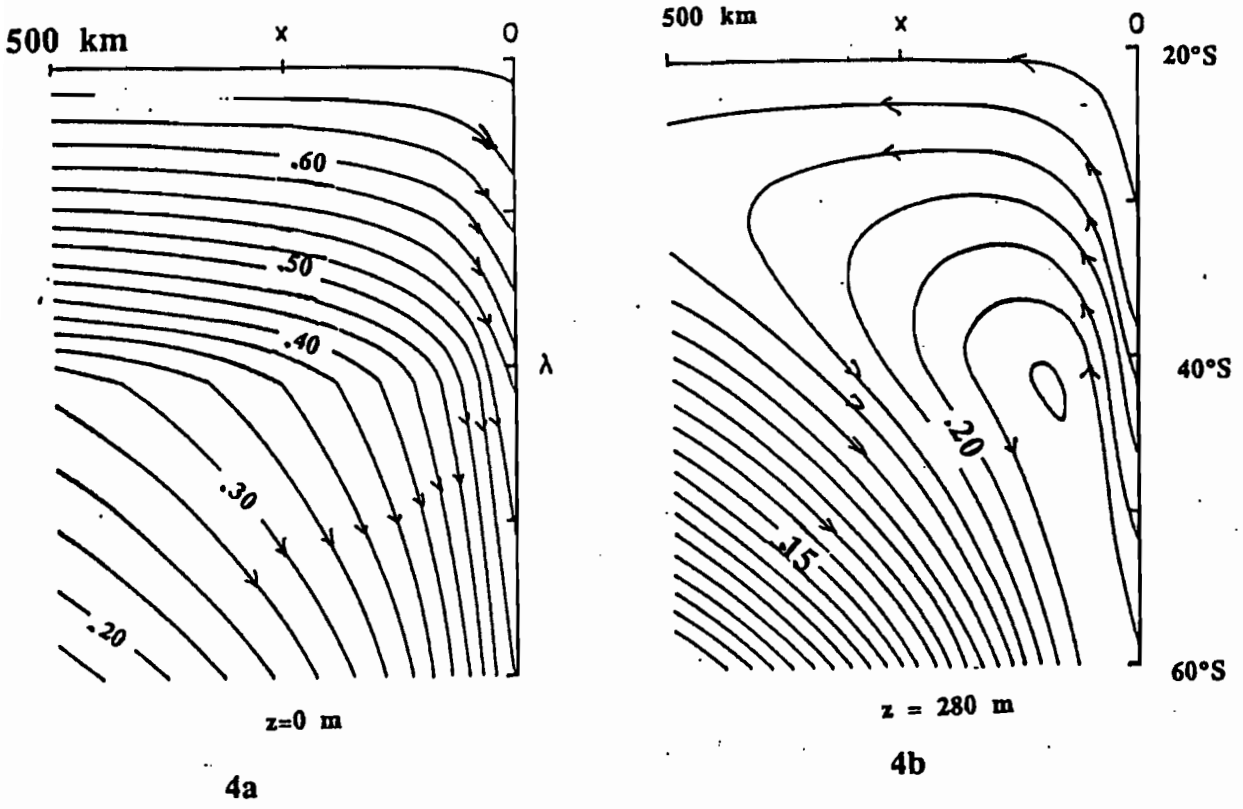

FIG.4. Predicted pressure pattern in the model of McCreary et al(1986) at the surface and 280m, for comparison with Fig.1.

at about the observed depths. This success suggests that the anomalous features of the Leeuwin Current relate to forcing by heat fluxes rather than by winds.

However, we can now restate the earlier question : Why should Western Australia be subject to heat flux effects so strong that they overwhelm the usual wind forcing, between 17.5°S and 32.5°S ? And why does this not occur off any other subtropical eastern boundary ?

5. Haney cooling.

Haney (1971) showed that annual mean heat fluxes into the ocean could be fairly well parameterized as $\lambda(T_e(y)-T)$, where T is annual mean sea surface temperature, $T_e(y)$ is and "equilibrium temperature" that is a function only of latitude and λ is a constant. Fig. 5a shows temperatures at various depths just offshore from the west Australasian continental shelf, compared to the Haney equilibrium temperature. Fig. 5b shows a similar comparison of South American temperatures with the Haney equilibrium temperature.

Annual mean temperatures in the top 50 m off Western Australia lie slightly above the Haney equilibrium temperature from about 15°S southwards: thus mean surface cooling and convective overturn can be expected. The temperatures of Fig. 5a appear to be constrained to follow the Haney equilibrium temperature, at least near the surface and possibly to as deep as 200m. By contrast, surface and subsurface temperatures are all well below the Haney equilibrium temperature off South America, to as far south as 40°S; and there is no apparent relation between the Haney temperature, and ocean temperatures there. The reason may be that when SST lies below the Haney temperature, the net heat flux is into the ocean, and the heat is trapped near the surface where it can be carried offshore by the Ekman flux.

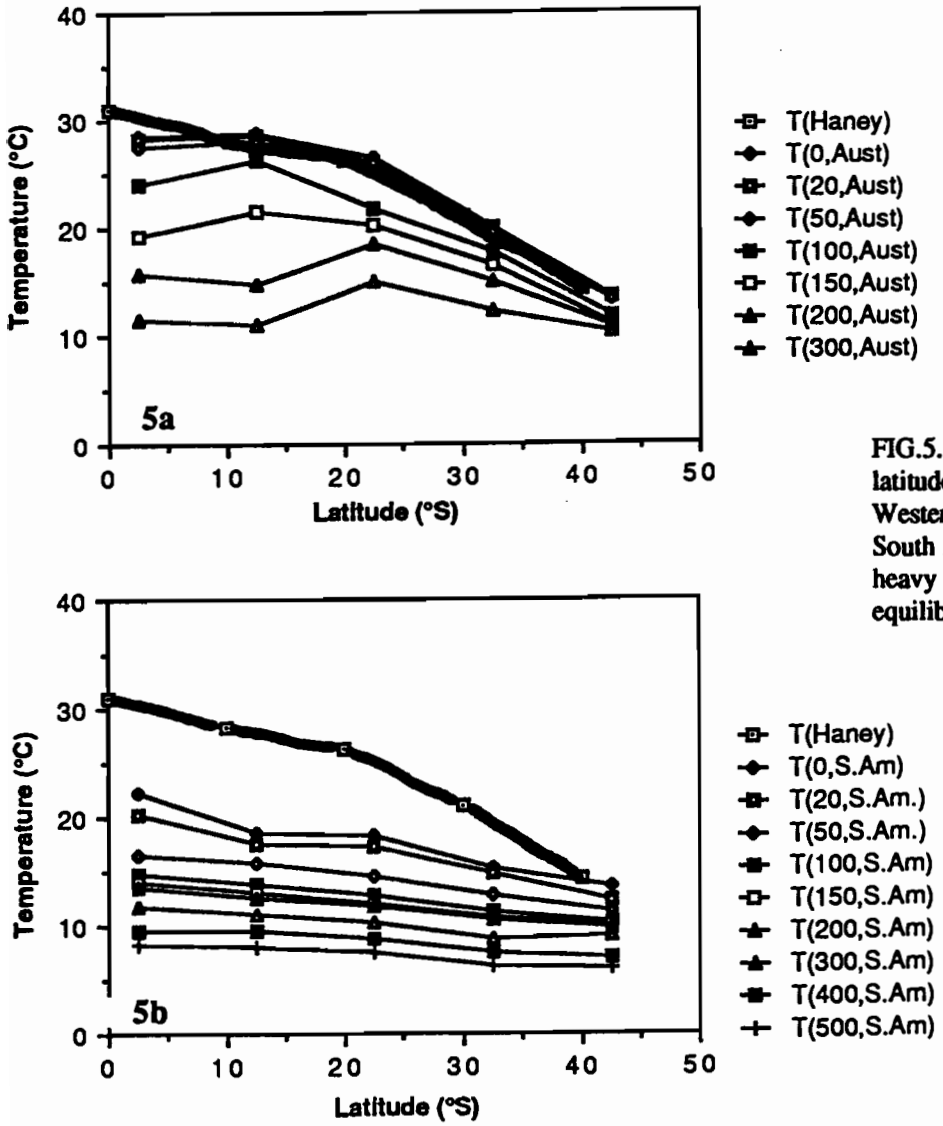

FIG.5. Temperature versus latitude at various depths, off Western Australasia (top) and South America (bottom). The heavy line shows Haney equilibrium temperature.

By contrast, when SST lies above the Haney temperature, convective overturn takes place: water will cool towards $T_e(y)$, no just at the surface but to substantial depths beneath. This in turn creates large meridional steric height gradients.

Looking at Fig.5 in a different way, the large meridional temperature gradients in the top 200 m of Western Australia (Fig. 5a) are also the reason for the strong onshore geostrophic flow there, and hence for the Leeuwin Current.

6. A Numerical experiment.

It is therefore thought that the near-equatorial temperatures off Western Australia are high enough so that poleward propagation of higher-mode Kelvin waves must induce convective overturn everywhere south of 20°S; by contrast, convective overturn will not occur till about 40°S for a South American equatorial SVA profile.

To test the idea that this convective overturn may help create the meridional SVA gradients that drive the Leuwin Current, some numerical experiments are being run with a Bryan and Cox model (which contains a good representation of convective overturn). Results are preliminary : one run only will be shown here. An idealized "Indian Ocean"

basin extends from the equator to 40°S, and is 30° wide: it is joined at its northeast corner to a "Pacific Ocean" which in our model serves simply as a reservoir of warm water for the Indian Ocean.

At the initial instant the SVA profile throughout the model domain is given by the western equatorial Pacific profile of Fig. 3a (open squares), with the corresponding temperature and salinity profiles: thus surface temperatures are 29°C everywhere. Cooling to the Haney equilibrium temperature is then started in the "Indian Ocean". A strong artificial forcing term brings temperature and salinity profiles in the "Pacific" back to the initial values with a 2.5-day time scale. A northward wind stress is applied between 22.5° and 32.5°S with a maximum strenght of 0.05 $N.m^{-2}$ (much like the observed winds off Western Australia).

7. Preliminary Results.

After 700 days of surface cooling, the Kelvin and Rossby wave adjustment is probably complete for a substantial distance from the eastern boundary; and convective cooling is nearly complete. Temperature at 20m has fallen below 16°C at 40°S (Fig. 6a). Temperature also shows a strong southward decrease at 60 and 110 m (not shown). Poleward advective effects can be seen along the eastern boundary, as observed off Western Australia, despite the imposed equatorward winds. A reversed meridional temperature gradient occurs at 295m throughout the ocean, but particularly along the eastern boundary (Fig. 6b), presumably as a results of downwelling where the induced zonal flows encounter the boundary. The surface steric height difference between 17.5°S and 32.5°S is about 25 cm - less than that observed (Fig.2), but of the right order of magnitude.

The corresponding flow patterns are seen in Figs. 6c-d. There is a vigorous surface flow into the "Indian" from the "Pacific" Ocean (Fig. 6c), connecting into a western boundary current that supplies the eastward geostrophic flow in the interior. Notice in Fig. 6c that the Ekman transport, which is greatest near 25°S, reduces the geostrophic flow to zero at this latitude; but at other latitudes the net flow is eastward - i.e. the convectively-induced flow overwhelms the Ekman drift. Flow is also onshore at 60 and 110 m (not shown), but at 295m (Fig.6d), the interior geostrophic flows are reversed. Note that these depths are well below the direct influence of surface convective overturn. Along the northern boundary, at 295m, the flow is *into* the Pacific, i.e. opposite to the surface flow: the net mass flux from the Pacific to the Indian Ocean is exactly zero in our model, but there is evidently a large net heat flux into the indian Ocean.

So far we do have a poleward Leeuwin Current, but it is much weaker than observed: Fig. 6c and d suggest that the geostrophic inflow sinks directly into the geostrophic outflow. Further numerical experimentation is planned to see if the reason for this can be found.

First results from coarser-grid runs with similar equatorward winds, but an equatorial SVA profile like that off South America (Fig.3) suggest that no significant convection-driven flows develop in this case: the familiar eastern-boundary upwelling occurs instead.

8. Connection with Pacific winds.

The model seems to demonstrate that continuity with the warm west Pacific causes convective cooling to the Haney (latitude-dependent) temperature, and hence leads to onshore geostrophic flow towards Western Australia. This flow in turn drives the path shown in Fig.7a, from the Hellerman and Rosenstein (1983) wind stresses; these are shown in Fig.7b (full line). Depth-integrated steric height is some 60-80 m^2 higher off Western Australia than in the east Pacific. Observed depth-integrated steric heiths relative to 1000

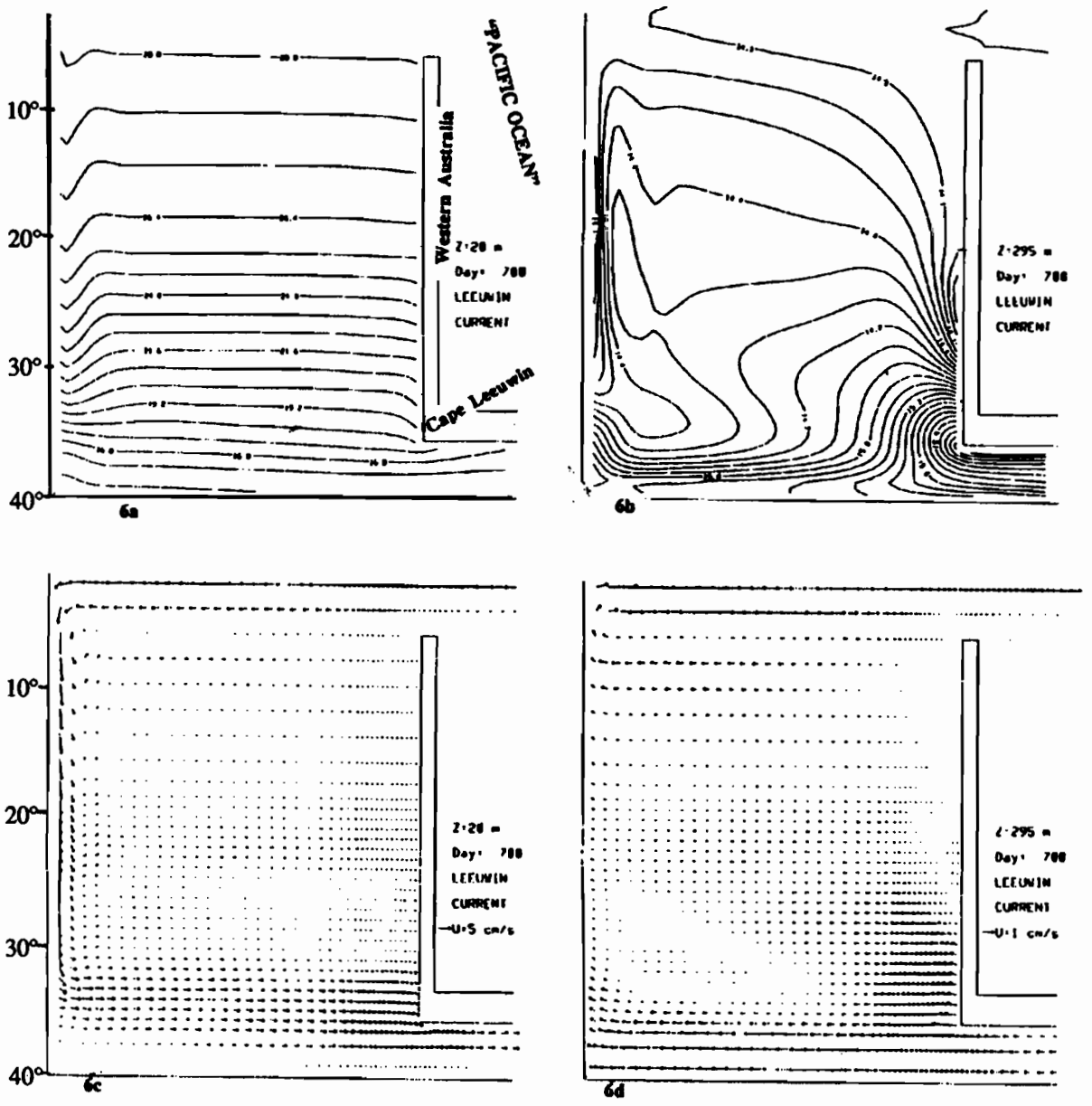

FIG.6. Temperature and velocity at 20m and 295m, in an idealized model of the Leeuwin Current, Western Australia.

db follow the Sverdrup prediction reasonably well, (squares in Fig. 8b), both along the equatorial Pacific and along the South American and Western Australian coasts (though with considerable noise along the latter two segments). The 60 m^2 difference in depth-integrated steric height (or double-depth-integrated SVA) across the Pacific is reflected in the difference between the east Pacific and the west Pacific-east Indian SVA profiles seen in Fig. 3.

In conclusion, the equatorial Pacific winds may be said to drive the Leeuwin Current, by maintaing the high near-equatorial temperatures that lead (throught convection) to the zonal geostrophic flows south of 20°S in the Indian Ocean.

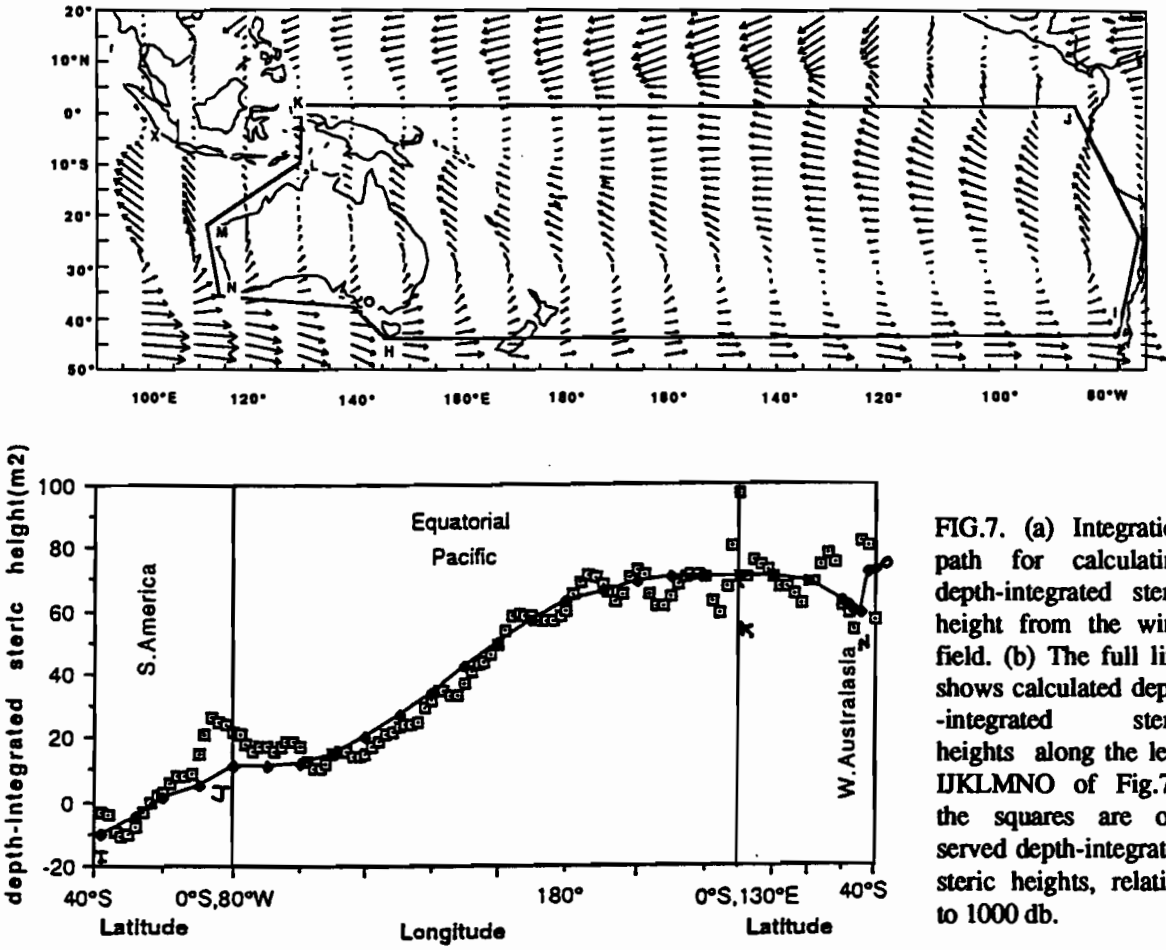

FIG.7. (a) Integration path for calculating depth-integrated steric height from the wind field. (b) The full line shows calculated depth -integrated steric heights along the legs IJKLMNO of Fig.7a; the squares are observed depth-integrated steric heights, relative to 1000 db.

REFERENCES

Godfrey, J.S. and K.R.R. Ridgway, 1985: The large-scale environment of the poleward-flowing Leeuwin Current, Western Australia: longshore steric height gradients, wind stresses and geostrophic flow. *J. Phys. Oceanogr.*, **15**, 481-495.

Haney, R.L., 1971: Surface thermal boundary condition for ocean circulation models. *J. Phys. Oceanogr.*, 1, 241-248.

Hellerman S. and M. Rosenstein, 1983: Normal monthly wind stress over the world ocean with error estimates. *J. Phys. Oceanogr.*, 13, 1093-1104.

Levitus, S., 1982: Climatological Atlas of the World Ocean. *NOAA Professional Paper*, 13.

McCreary, J.P., S.R. Shetye and P.K. Kundu, 1986: Thermohaline forcing of eastern boundary currents: with application to the circulation off the west coast of Australia. *J. Mar. Res.*, **44**, 71-92.

Weaver, A.J. and J.H. Middleton, 1989: Poleward boundary current off Western Australia. *J. Phys. Oceanogr.*, **19**, (in press).

Observations of the Pacific North Equatorial Current Bifurcation at the Philippine Coast

John M. TOOLE[1], R.C. MILLARD[1], Z. WANG[2] and S. PU[2]

[1]*Woods Hole Oceanographic Institution, Woods Hole, MA 02543 - U.S.A.*

[2] *First Institute of Oceanography, State Oceanic Admin., Qingdao - PRC.*

Hydrographic surveys were conducted off the Philippine coast in September 1987 and April 1988 as part of the United States/People's Republic of China cooperative research program. These cruises sampled the western Pacific Ocean where the North Equatorial Current (NEC) meets the western boundary and divides into the Kuroshio and Mindanao Currents. The requirement for mass conservation within a region enclosed by stations is utilized here to obtain absolute circulation fields for the two surveys. In both realizations, the surface flow of the NEC was observed to bifurcate near latitude 13°N; NEC flow poleward of this latitude turned north as the Kuroshio while flow to the south fed the Mindanao Current. Most striking was a twofold increase in the strength of the current system in spring 1988 as compared with fall 1987. The potential vorticity (Q) distributions of the surface waters were examined to explore the dynamics of the bifurcation. Within the NEC, Q was nearly constant (layer thickness change balanced meridional planetary vorticity variation.) Within the Kuroshio and Mindanao currents, near constant Q (with magnitude comparable to that in the NEC) was also found with a balance between relative vorticity variation and layer depth change as would be expected for inertial boundary currents.

Table 1. Mass transport observed on US/PRC Cruises 3 and 4 as determined by the inverse models. Units: 10^9 kg.s^{-1}

	Kuroshio	NEC	Mindanao
Cruise 3 Layer 1	12.3	32.5	14.0
Cruise 4 Layer 1	30.6	61.2	30.5
Toole et al. (1988)	15.7 (25)	43.6	17.9 (13)
Cruise 3 Total mass	21.4	13.7	-8.0
Cruise 4 Total mass	50.7	78.4	27.7

Note : Layer 1 was defined as all water above σ_θ = 26.25. Toole et al. (1988) estimated transport above the 12°C potential temperature surface relative to 1000 db. In the Philippine Basin, the σ_θ = 26.25 kg.m^{-3} and the θ = 12°C surfaces are within 20 m. Shown in parenthesis are their Kuroshio and Mindanao transports based on a 12°N NEC bifurcation.

ORSTOM
CENTRE DOCUMENTATION
Montpellier

F 30210

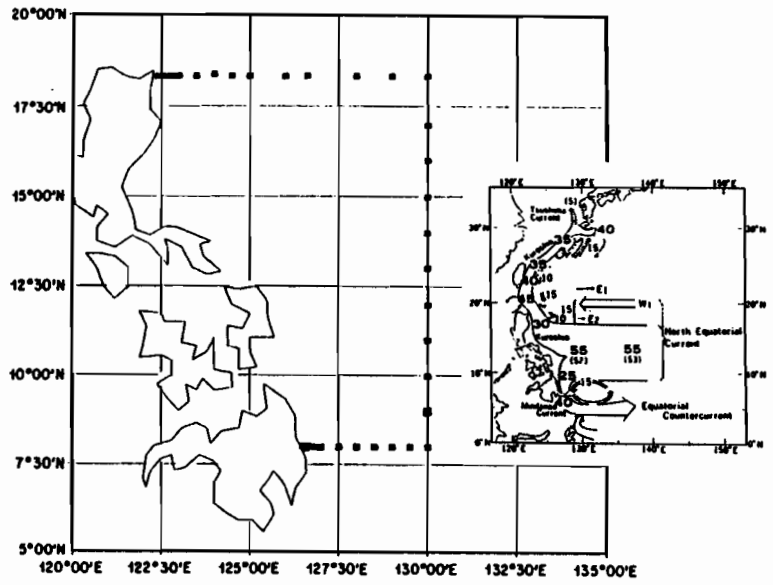

FIG.1. Station map for CTD/O_2 casts obtained by the US/PRC cooperative program in the Philippine Basin. The insert depicts a schematic of the upper ocean flow field in this region after Nitani (1972).

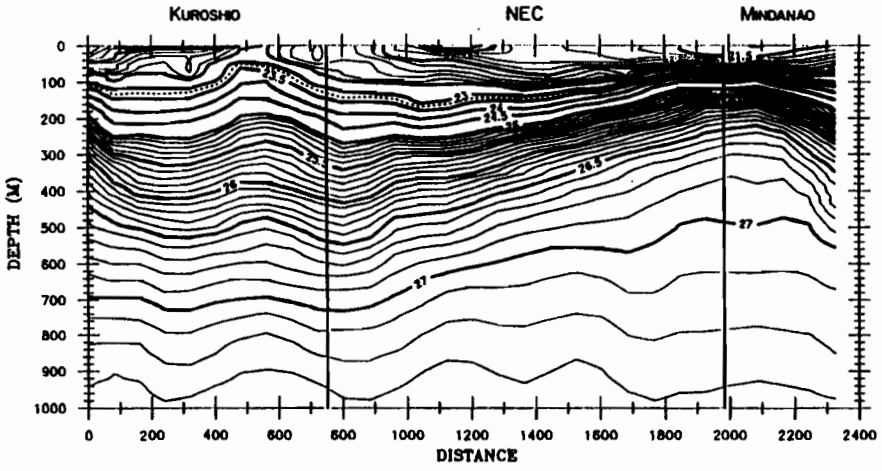

FIG.2. Section of potential density across the Kuroshio, NEC and Mindanao Currents obtained in spring 1988. The section runs clockwise around the stations shown in Fig.1. The distance axis begins at the coastal station on the 18°20'N section. The locations of the northeast and southeast corners of the station grid are marked.

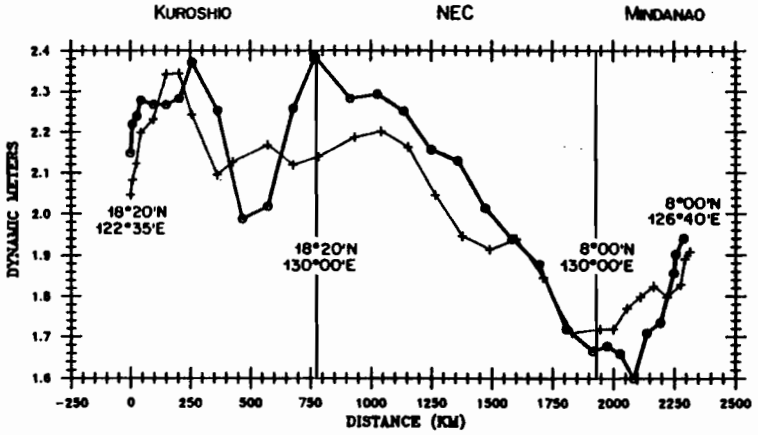

FIG.3. Dynamic height (0/1000db) observed on US/PRC Cruise 3 (thin line) and Cruise 4 (thick line). The plot runs clockwise around the grid of stations in figure 1 as discussed in the figure 2 caption.

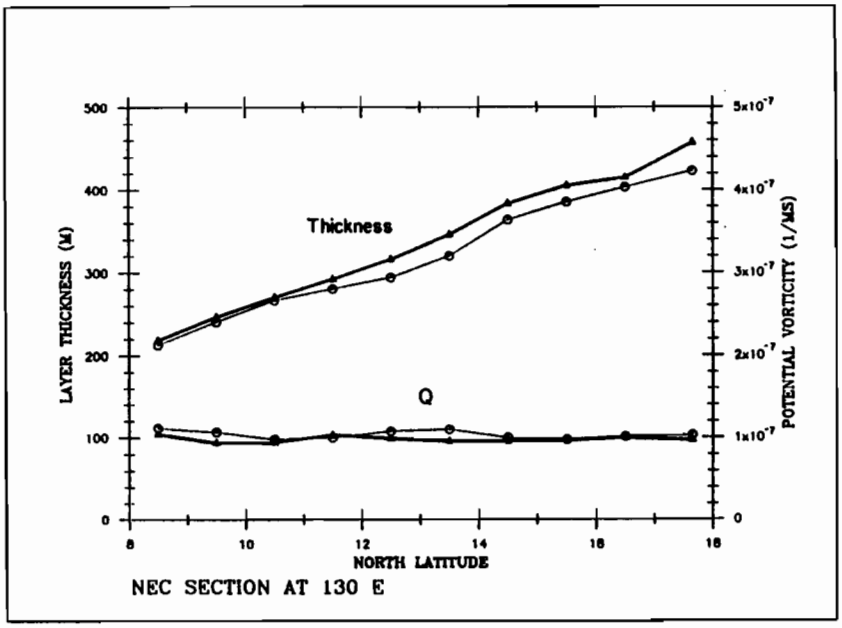

FIG.4. The latitudinal variation of layer 1 thickness and potential vorticity along the 130°E sections. The thin line is for the Cruise 3 data and the thick line is for Cruise 4.

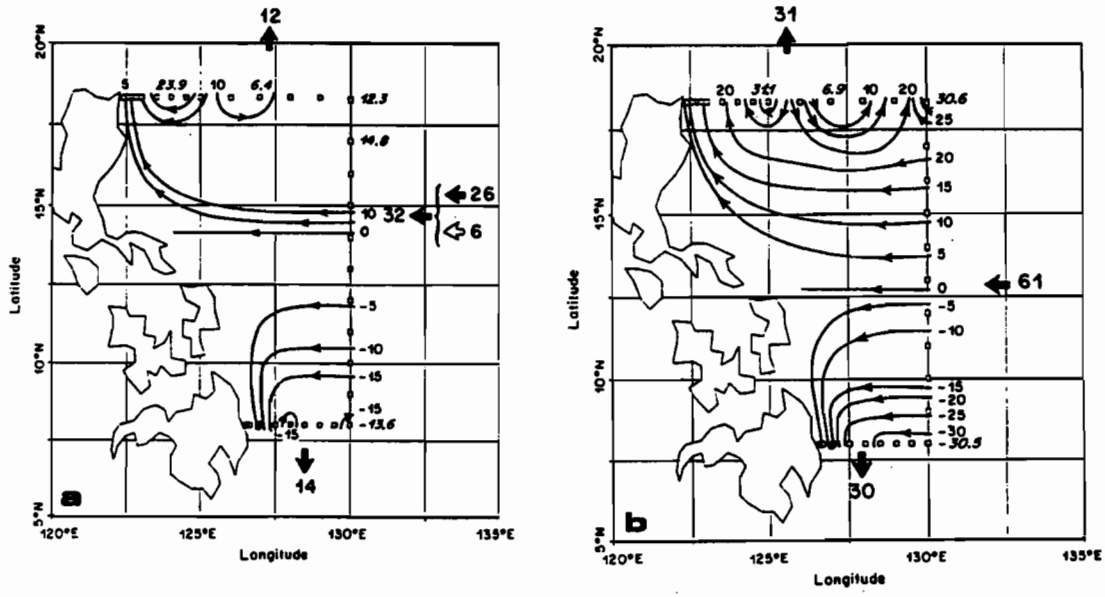

FIG.5. Maps of layer 1 mass transport streamfunction for Cruise 3 (panel a) and Cruise 4 (panel b). Between each contour is a transport of $5*10^9$ kg.s^{-1}. Solid arrows mark the section net transports. In panel a, the open arrow represents the convergent part of the layer 1 flow.

EL NINO / SOUTHERN OSCILLATION 1986-87

Air/Sea Interaction in the Western Tropical Pacific Ocean during 1982/83 and 1986/87

Gary MEYERS, Rick BAILEY, Eric LINDSTROM and Helen PHILLIPS

CSIRO Division of Oceanography
GPO Box 1538, Hobart Tasmania 7001, Australia

ABSTRACT

The Southern Oscillation Index (SOI), equatorial zonal wind, sea level anomalies at islands, sea surface temperature at Puerto Chicama Peru and mixed layer temperature and depth from the XBT ship-of-opportunity network are used to describe conditions during the past two ENSO episodes. Onset of sustained ENSO anomalies in the 1986/87 episode was in July 1986, one month later in the year than onset of the 1982/83 episode in June 1982. Both episodes of the 1980's developed later in the year than episodes of the 1970's. The XBT data show that during the episodes of the 1980's the usual surface temperature difference along the equator between 165°W and 160°E reversed and rapidly increased to 1°C in the other direction. ENSO warming of the central Pacific tends to be confined to the region 10°N-10°S whereas cooling of the western Pacific occurs in a broader region from 19°N-19°S, and extends westward into the eastern Indian Ocean. Evaluation of terms in the surface heat budget (for 1982/83 episode only) shows that the dominant mechanism of cooling surface temperature in the western Pacific is latent heat flux.

1. Introduction

The largest pool of warm (>28°C) surface water in the global ocean is located in the western Pacific and eastern Indian Oceans. The overlying air is also warm, giving it the capacity to hold a very large load of water vapour, relative to other tropical, marine air masses. Release of latent heat by deep atmospheric convection over the heat pool provides one of the main sources of energy for the global atmospheric circulation (Hénin and Donguy, 1980; Donguy, 1987). Air/sea interaction in this area has since the 1920's been recognised as an important factor in El Nino/Southern Oscillation (ENSO) (Berlage, 1966; Nicholls, 1989). The basic observation was an association between anomalous cooling in the area and the occurrence of drought, especially in Australia. It was suggested that, theoretically at least, cooling during ENSO could be caused by ocean currents, mixing of cool water from the thermocline into the surface layer, of heat fluxes at the sea surface; the dominant cause was not identified. A surface heat budget near the equator, at 160°E (Meyers et al., 1986) indicated that latent heat flux was an important factor in the cooling. In part the goal of this study is to expand earlier study into a wider area, drawing on results from Meyers et al. (1989a), and to extend the study in time to describe the 1986/87 ENSO episode.

The mature stage of this episode occurred in mid 1987 (Halpern, 1988) and it was characterized using definitions by Quinn et al. (1987) as weak-moderate in intensity (Quinn, personal communication, 1989). An aim of this study is to describe air/sea interaction associated with onset of the episode.

2. Data

Four standard indices of ENSO - a Southern Oscillation Index (Fig. 1), equatorial zonal wind (Fig. 2), Pacific sea level anomalies west of the dateline (Fig. 3) and sea surface temperature at Puerto Chicama, Peru (Fig. 4) - were assembled to determine the time of onset

ORSTOM
CENTRE DOCUMENTATION
Montpellier

F 30211

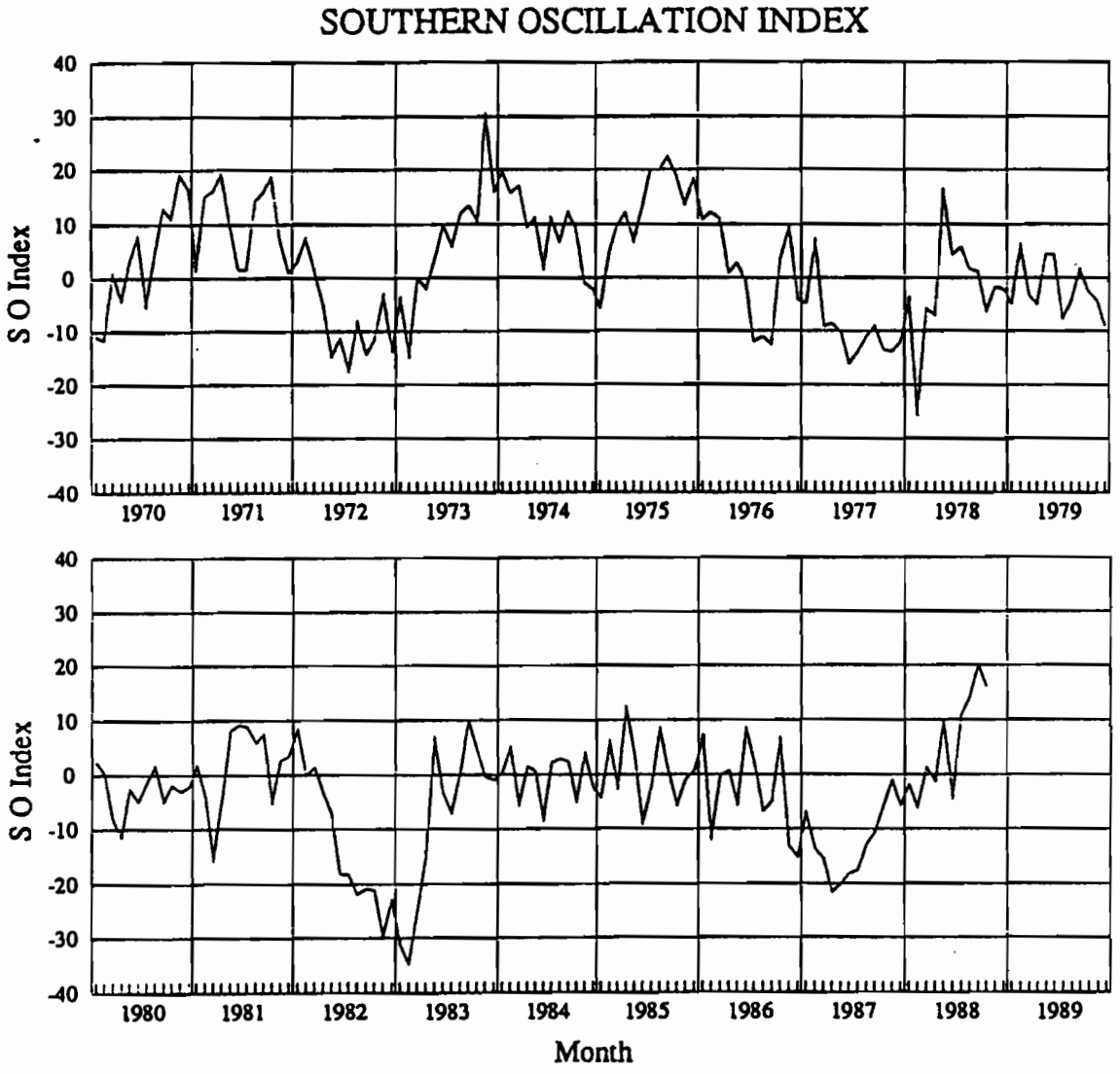

FIG.1. Southern Oscillation Index

for the last two episodes and to compare them to earlier episodes in the 1970's. The Southern Oscillation Index (SOI) is determined from barometric pressure at Tahiti and Darwin, seasonally adjusted with a 100 year record, and normalized to a standard deviation of 10. It is a very long time series, available since 1882, and the update is published monthly by the regional Bureau of Meteorology in the Darwin Tropical Diagnostic Statement (Halpern, 1988). The relationship of this index to the global field of barometric pressure has been discussed by Trenberth and Shea (1987). The sea level anomalies west of the dateline were averaged at 10-15 stations in the latitude band 15°N-15°S. The climatological monthly mean sea level used to evaluate anomalies was for the period 1975-1981. Maps of the anomaly are distributed monthly by K. Wyrtki and G. Mitchum of the University of Hawaii (Wyrtki et al., 1988). Sea surface temperature at Puerto Chicama was made available by electronic mail in near real time by D. Enfield of NOAA/AOML, in the form of monthly averages. It was compared to two climatologies for the periods 1925-1973 (A. Douglass, personal communication) and 1956-1982 (D. Enfield, personal communication). The use of Puerto Chicama SST as an index of El Nino and its relationship to the Southern oscillation has been

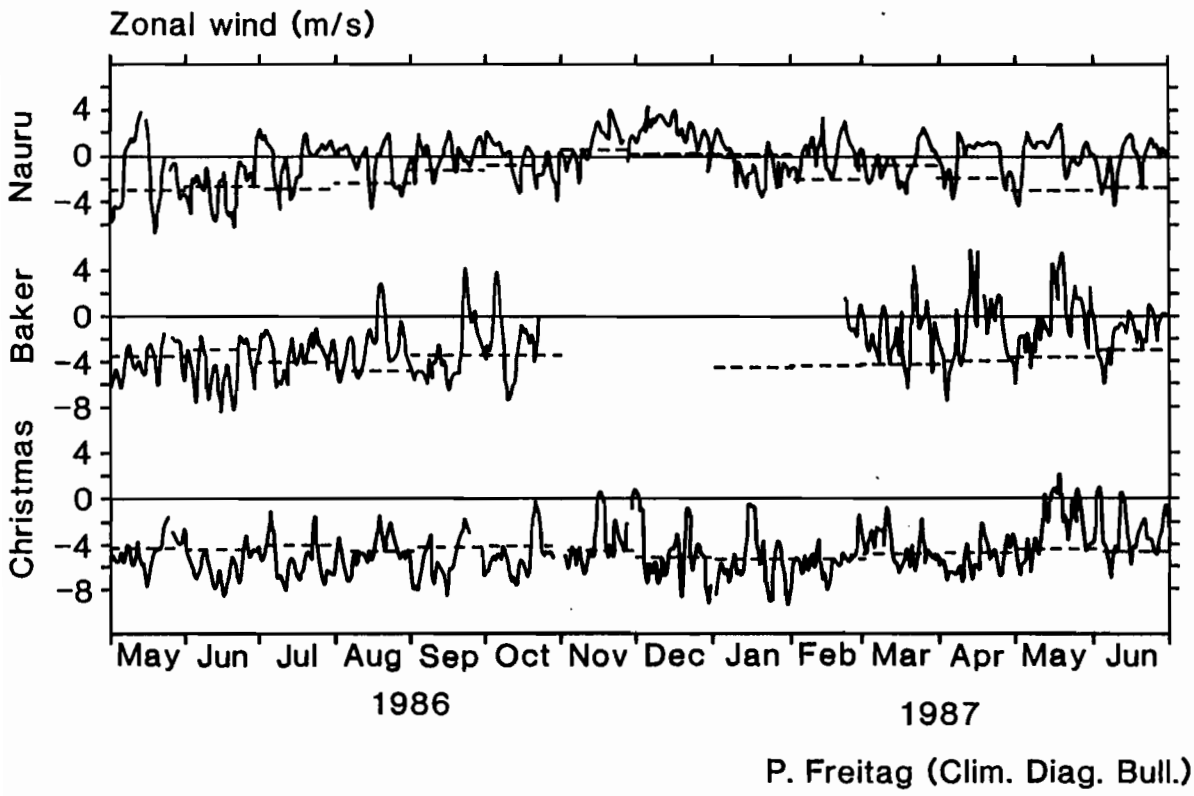

FIG.2. Equatorial zonal wind ($m.s^{-1}$) at Nauru, Baker and Christmas Islands.

discussed by Deser and Wallace (1987). The equatorial zonal wind index is based on daily values from island stations (McPhaden et al., 1988). The climatological values of Wyrtki and Meyers (1976) for the period 1900-1972 were used for comparison to normal monthly conditions. The wind indices were distributed in the US Climate Analysis Center's Climate Diagnostic Bulletin (Halpern, 1988).

Data from the TOGA expendable bathythermograph (XBT) ship-of-opportunity network (Donguy, 1987; Meyers et al., 1989a, b) were used to measure ocean thermal structure of the tropical Pacific and eastern Indian Oceans. The data permit a description of mixed layer temperature and depth and, using additional data on surface heat fluxes from Reed (1986), the dominant terms in the mixed layer heat budget are assessed.

3. Onset of the 1986/87 episode

Understanding the onset of ENSO is one way to improve models for its prediction. Past studies have suggested two scenarios of onset (see Lukas and Webster, 1988 for a review), depending on where the fundamental precursor is found, either in the ocean or the atmosphere. In one scenario, propagating oceanic signals carrying the seed of an ENSO episode are present throughout an entire ENSO cycle, and at a certain stage they amplify through an instability. The onset in this case might be associated with the oceanic signals just before they amplify. In the second scenario anomalous equatorial, westerly winds (possibly related to tropical-extra tropical atmospheric interaction) trigger an instability of the coupled ocean and atmosphere, which intensifies into a mature episode. The onset in this case would be determined by the time when sustained ENSO-type anomalies in the atmosphere first develop. The two scenarios are not necessarily mutually exclusive (Lukas, 1988) if the propagat-

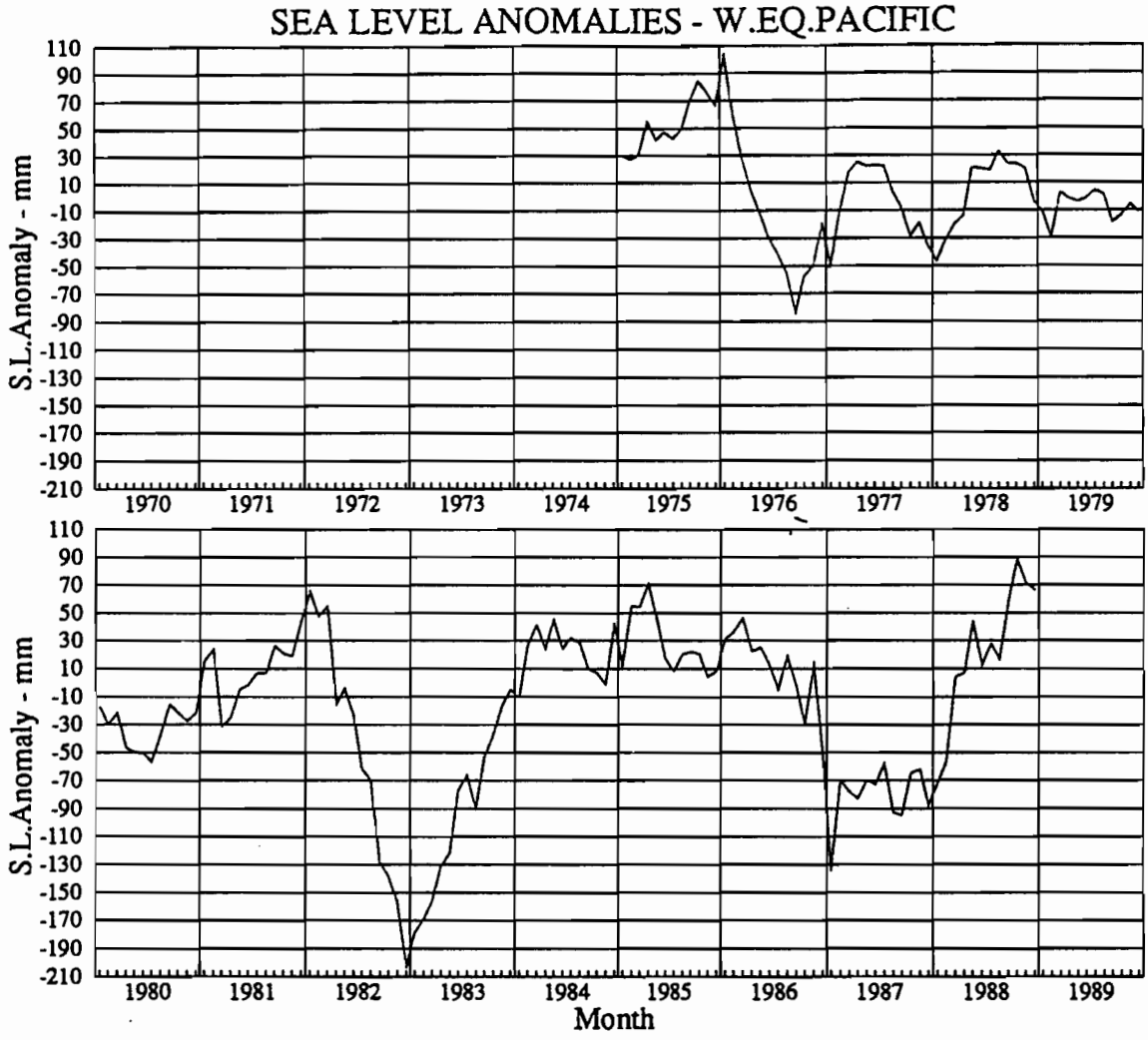

FIG.3. Average sea level anomaly (mm) western Pacific, 15°N-15°S, west of the dateline.

ing oceanic signals affect SST patterns, and through air-sea interaction, the wind field. We have looked for the 1986/87 onset in atmospheric parameter (Figs.1 and 2) and for the growing instability in oceanic parameters (Figs. 3 and 4). Whether or not the prediction issued in 1986 (Cane et al., 1986) successfully predicted the episode for the right reasons - that is, predicted it because the real episode in nature evolved with largely the same dynamics as in the model - can be partly decided in future studies by comparing models to the observed parameters.

Beginning with the SOI (Fig. 1) and equatorial zonal wind at Nauru (Fig.2) we see the onset of sustained ENSO-type anomalies in July 1986. A brief hiatus in October in both indices is followed by steady development to mature ENSO anomalies in March-June 1987 (Halpern, 1988), particularly evident in the zonal wind at Baker and Christmas Island. Changes in the wind field will produce dynamically consistent changes in the ocean. The development of the equatorial wind anomaly changes the structure of the field of trade winds in the western Pacific in a way that makes wind stress curl favourable for upward Ekman pumping of the thermocline (Pazan and Meyers, 1982; Donguy et al., 1982; Harrison et al., 1989). The rise in thermocline, and depletion of warm water in the upper layer should lead to a drop in sea level.

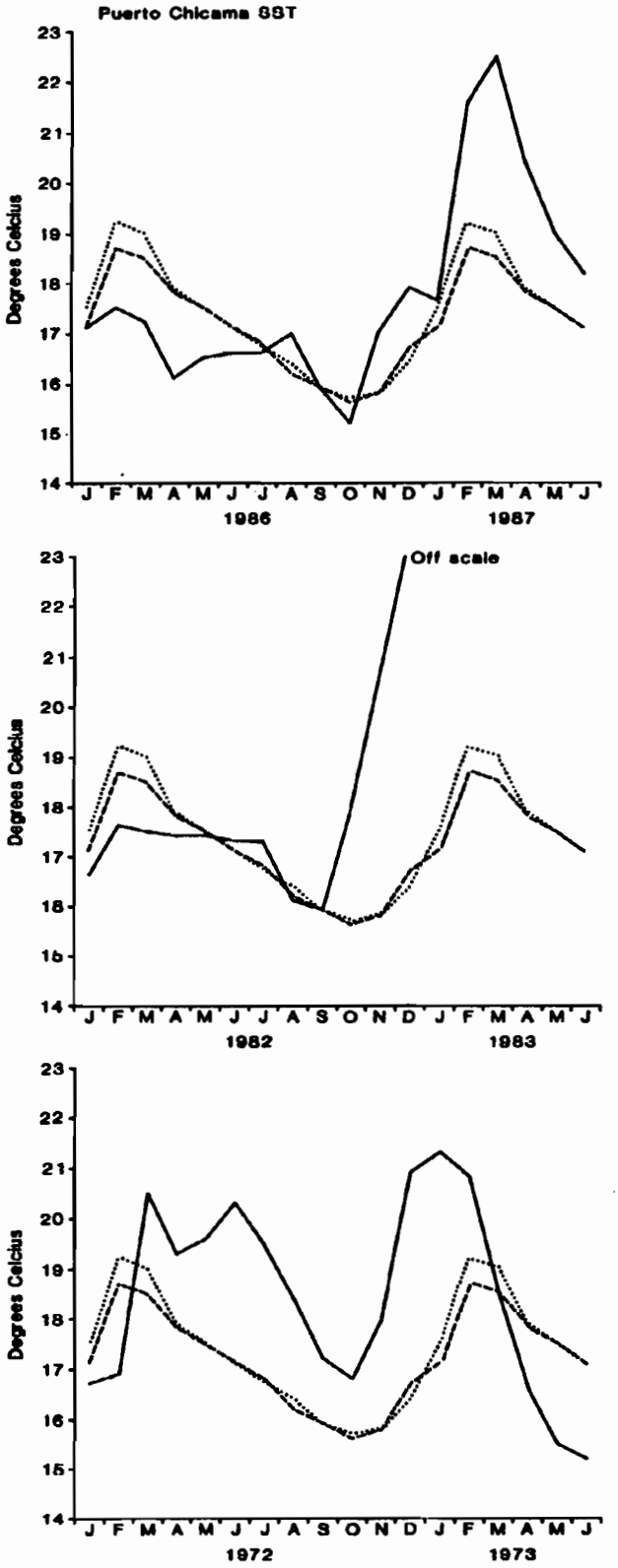

FIG.4. Sea surface temperature at Puerto Chicama, Peru during the ENSO episodes of 1986/87 (top), 1982/83 (middle) and 1972/73 (bottom), compared to the mean annual cycle, 1925-1973 (dotted line) and 1956-1982 (dashed line).

The westerly wind is also expected to generate anomalous eastward currents and downwelling which propagate to the eastern Pacific as Kelvin waves and affect the surface heat budget there (Harrison et al., 1989).

The sea level of the western Pacific (Fig. 3) and temperature at Puerto Chicama (Fig.4) show the corresponding development of anomalies. Sea level near the area of westerly wind developed sustained ENSO anomalies after August 1986, and except for a hiatus in November, rapidly reached levels of 7-11 cm below normal which were maintained throughout 1987. SST at Puerto Chicama rapidly increased after October 1986, reaching a peak in March 1987 with an anomaly in excess of 3°C, and it remained above normal at least until June 1987.

The atmospheric changes (Fig's 1 and 2) and expected response on either side of the ocean indicate in a dynamically consistent way that the onset of sustained ENSO type anomalies was in July 1987 (McPhaden et al., 1988).

Earlier in the year, bursts of equatorial, westerly wind were recorded near the dateline in January and May 1986 (McPhaden et al., 1988; Lander and Morrissey, 1988). The event in May generated an expected local response in the ocean; and a remote response carried by a Kelvin wavelike pulse (McPhaden et al., 1988), which arrived at 0°, 110°W in late June. The development of a slightly positive SST anomaly at Puerto Chicama (Fig. 4) and increasing temperature at other stations on the Peru Coast in late July (D. Enfield, F. Chavez, personal communications, 1986) may signal the passage of the Kelvin wave. The anomaly, however, did not persist, and normal seasonal cooling resumed at Puerto Chicama after August. Our indices (Fig's 1-4) agree with the conclusion of McPhaden et al., that the burst in May did not generate sustained ENSO type anomalies and the feedback between ocean and atmosphere necessary to generate ENSO did not occur. The onset is discussed further in analyzing temperature along the equator on TOGA XBT tracks.

4. Comparison to earlier episodes

The four ENSO episodes which have occurred since 1970 (1972/73,1976/77, 1982/83, 1986/87) were observed in each case with a quantum improvement in our capacity to document the ocean's dynamical role. In the case of 1972/73, the improvement was in understanding of the dynamics actually occurring in the ocean (Wyrtki, 1975). By 1976/77 the number of sea level stations had increased to the extent that sea level maps could be drawn on an oceanic scale (Wyrtki, 1985). By 1982/83 some of the outstanding improvements were an extensive network of XBT ships of opportunity to observe thermal structure to a depth of 400 m (Donguy, 1987), and longterm moorings established at a few sites along the equator for direct measurement of currents, (Halpern, 1987). The most important difference between 1986/87 and all the others was the relatively enormous resources to observe the ocean made available by the decade long (1985-1995) Tropical Ocean Global Atmosphere program (Halpern, 1988, for example) using in situ methods and remote sensing from satellites. Interpreting this great wealth of information will be one of the important activities of this conference. As a background to this task, we compare the 1986/87 episode to the earlier ones using the indices of Fig's 1, 3 and 4.

The SOI changes its nature somewhat over long time periods (Berlage, 1966) and the last two decades is not an exception. Before 1976 (Fig. 1) and extending back in time until 1950 (not presented) the SOI rose to levels above 10 for extended periods of several months. After 1976 the peaks did not develop for 12 years until 1988/89. Thus the 1986/87 episode was not preceded by the build-up of SOI associated with episodes of the 1950's, 60's and 70's, which are sometimes thought of as a cannonical-type of ENSO (Rasmusson and Carpenter, 1982). The time of onset also changed for episodes after 1976, as seen most clearly in Puerto Chicama temperature (Fig. 4). The warming event at this station began in 1972 with a faster than normal rise in temperature during January/February, in the middle of the

season of normal summer heating. It began in 1982 in September, just before the normal cooling season ended and in 1986 it began about one month later, early in the warming season. In assessing the importance and generality of the great wealth of observations on the most recent episode, we should keep in mind the differences between ENSO episodes.

5. Mixed layer temperature and depth

The distribution of SST along the equator in the Pacific and Indian oceans is one of the most important factors in variability of the Global climate system because it influences the release of latent heat (ie. formation of rainfall) in the tropical marine atmosphere, and thus affects the supply of energy to global general circulation. Using the SST pattern for climate prediction requires an accurate descriptive knowledge of the evolution of SST, as well as an understanding of the processes that control the changing SST pattern (Meyers et al., 1989a; England et al., 1989). The interactive mechanism of SST gradients and surface wind convergence may be a major influence on deep convection in the tropical atmosphere (see Halpern, 1988 for a summary of relevant studies), but large scale temperature measurements before the 1980's were not accurate enough to record the small changes in the gradients of the central and western Pacific.

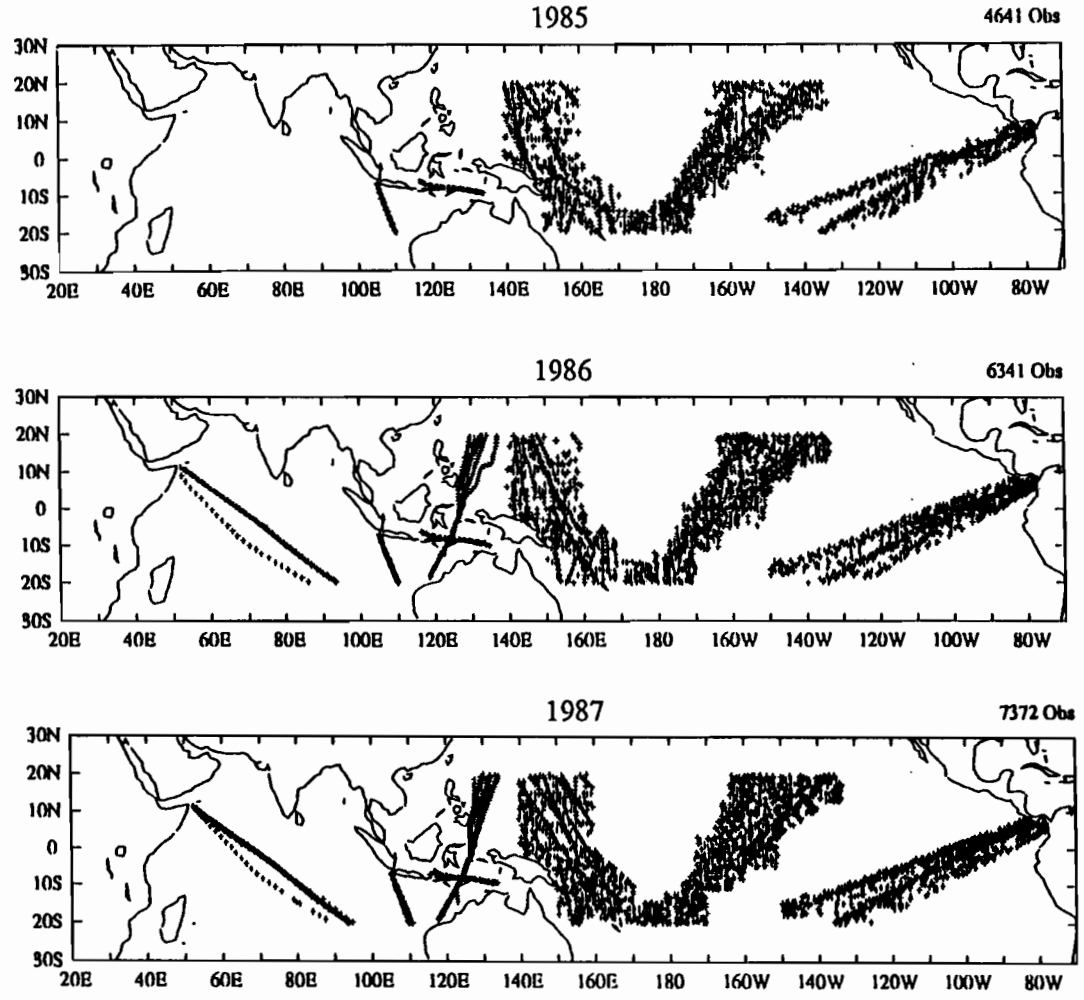

FIG.5. Expendable bathythermograph (XBT) stations used for their study.

The TOGA XBT network (Fig. 5) has provided a data set of high quality temperature soundings in the tropical Pacific and Indian Oceans which can be used to document the near surface thermal structure. For this study we used a subset of the total data set assembled at the TOGA Subsurface Data Center, Brest, France (J.P. Rébert, personal communication), selected to represent the areas where carefully controlled high quality (delayed-mode) data are regularly collected. The data were combined with data from a prototype of the network started in 1979 (Donguy, 1987) and used in earlier studies of the surface heat budget (Meyers et al., 1989a; England et al., 1989).

The mixed layer temperature along the equator in the Pacific was determined near 100°W (Eastern Pacific) 165°W, (Central Pacific) and 160°E (Western Pacific) for the period 1979-1988 to document variability of zonal MLT gradients. The MLT time series are monthly averages, smoothed by a (1/4, 1/2, 1/4) filter, for the latitude band 0°-6°N (Fig. 6) and 0°-6°S (Fig. 7). The 1982/83 ENSO episode stands out as a marked temperature change on both sides of the equator all across the Pacific. The temperature difference between the central and western tracks which usually increases about 1°C toward the west changed sign in July 1982 and rapidly increased to a 1°C anomalous gradient in the other direction. The reversal was preceeded by a large (>1°C) increase in central MLT starting in April 1982 and a small decrease in western MLT starting in March 1982 (Fig. 6). The eastern Pacific is usually 2°-5°C cooler than the central Pacific and has a dominant annual oscillation, which reached an ENSO peak in early 1983, when the zonal temperature gradient reversed all the way across the Pacific (Fig. 6).

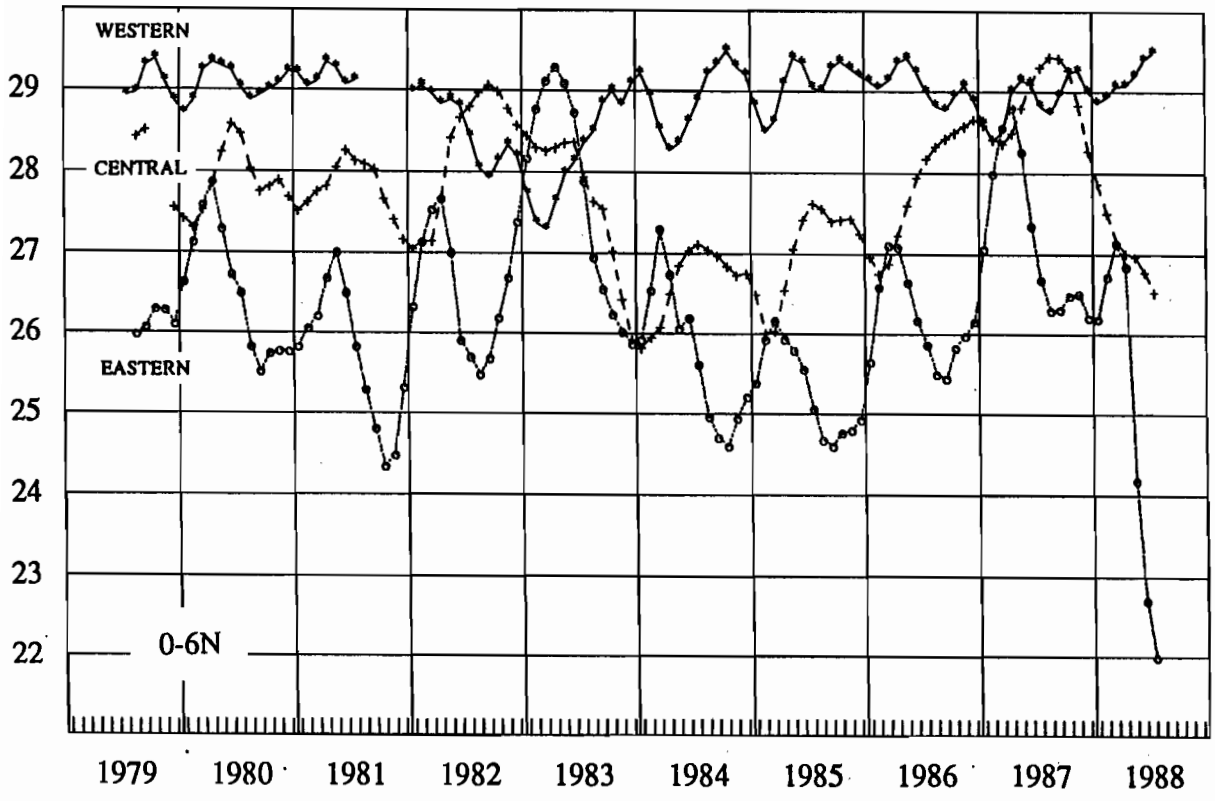

FIG.6. Mixed layer temperature (°C), 0°-6°N, on the western (≈160°W), central (≈165°W) and eastern (≈100°W) XBT tracks

In the 1986/87 ENSO reversal of the MLT gradient between 165°W and 160°E was observed again, primarily south of the equator (Fig. 7), beginning in December 1986. The western MLT dropped rapidly after May 1986, but the temperature at 165°W did not rise enough to make a reversal. Reversal north of the equator (Fig. 6) occurred briefly beginning in June 1987. The weaker intensity of this episode appears markedly in the eastern Pacific temperature. We cannot say on the basis of data in hand whether or not reversal of the MLT gradient along the equator was associated with the onset of 1986/87 ENSO. In the case of a weaker episode the initial reversal may be confined to a small distance along the equator, near the dateline on the eastern edge of the 28°C water pool. The measurements at 165°W may be too far eastward to see it. This highlights the need for more temperature observations in the area between the western and central Pacific XBT line.

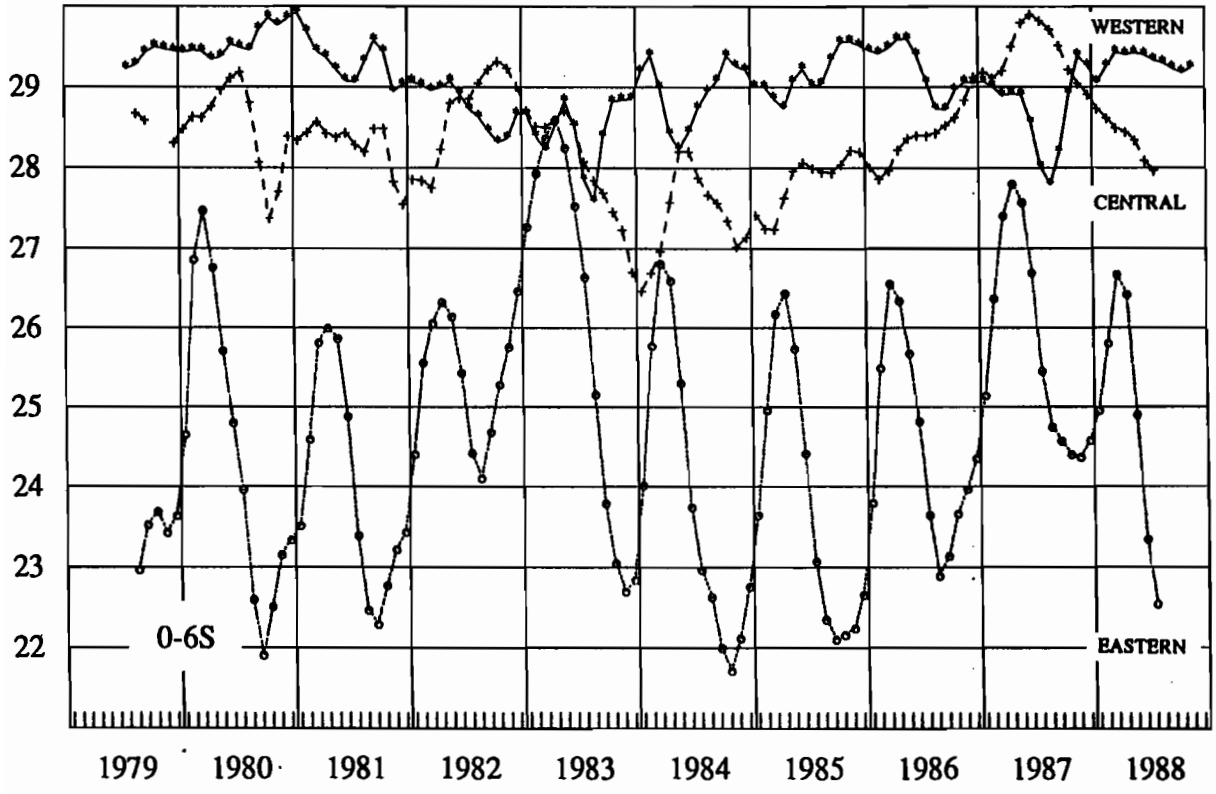

FIG.7. Mixed layer temperature (°C), 0°-6°S, as in figure 6.

Time series of mixed layer depth are presented in figures 8 and 9 in a format that facilitates comparison to MLT. The definition of MLD was the depth at which temperature is 1°C less than SST. It is compared to the result of other definitions of mixed layer depth and to depth of isotherms in the upper part of the thermocline in Meyers et al. (1989a). We have not found any simple direct relationship between MLD and MLT, probably because MLT at any given time is simultaneously influenced by surface fluxes, horizonal advection, and mixing. A data-based parameterization of mixing, in terms of MLD would first require removing the effect of other mechanisms.

MLT and MLD on the tracks west of the three main Pacific tracks suggest that western Pacific cooling during the 1986/87 ENSO extended at least as far westward as the Fremantle-Sunda Strait track (Fig. 10) as did the upward displacement of the thermocline (Fig. 11).

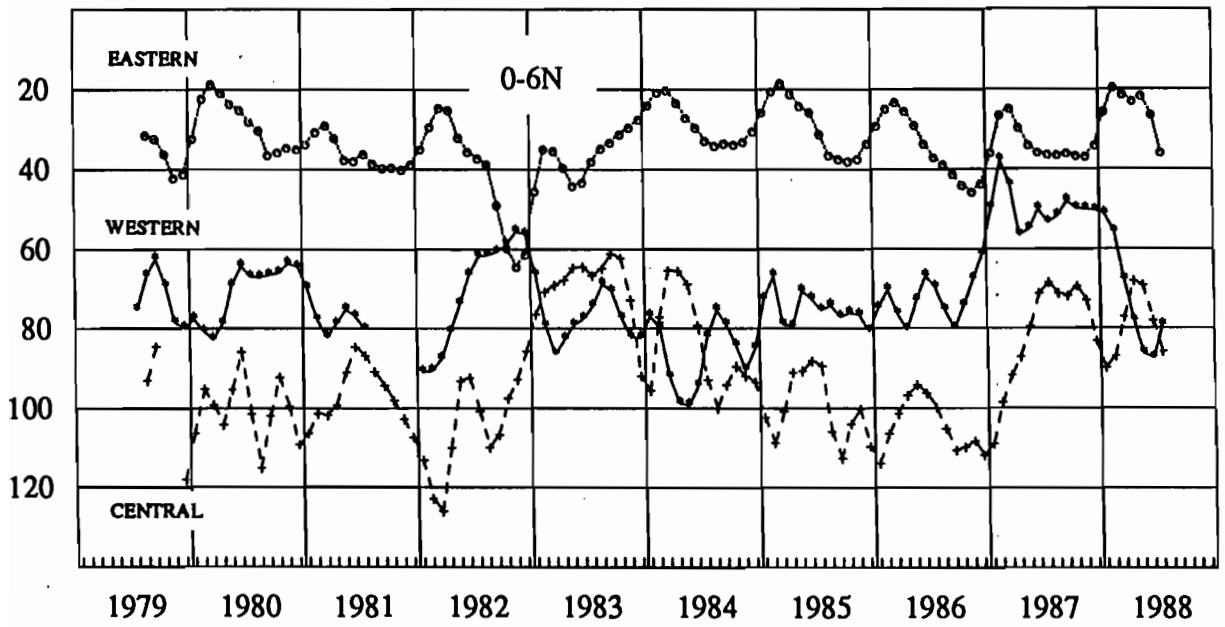

FIG.8. Mixed layer depth (m), as in figure 6.

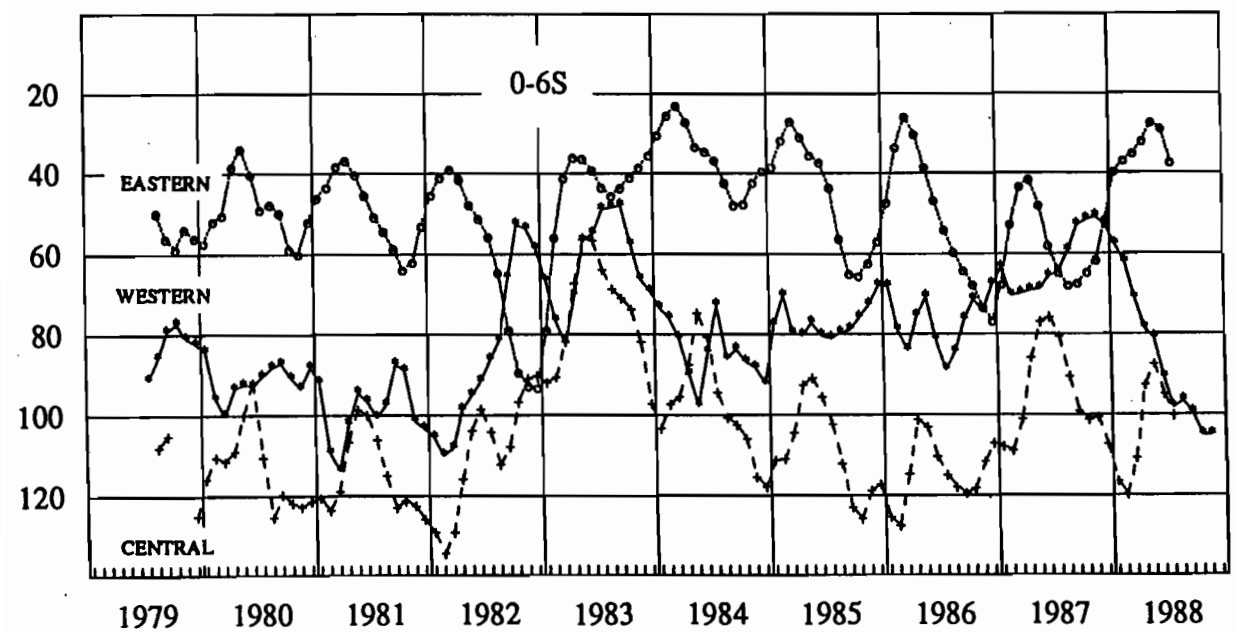

FIG.9. Mixed layer depth (m), as in figure 7.

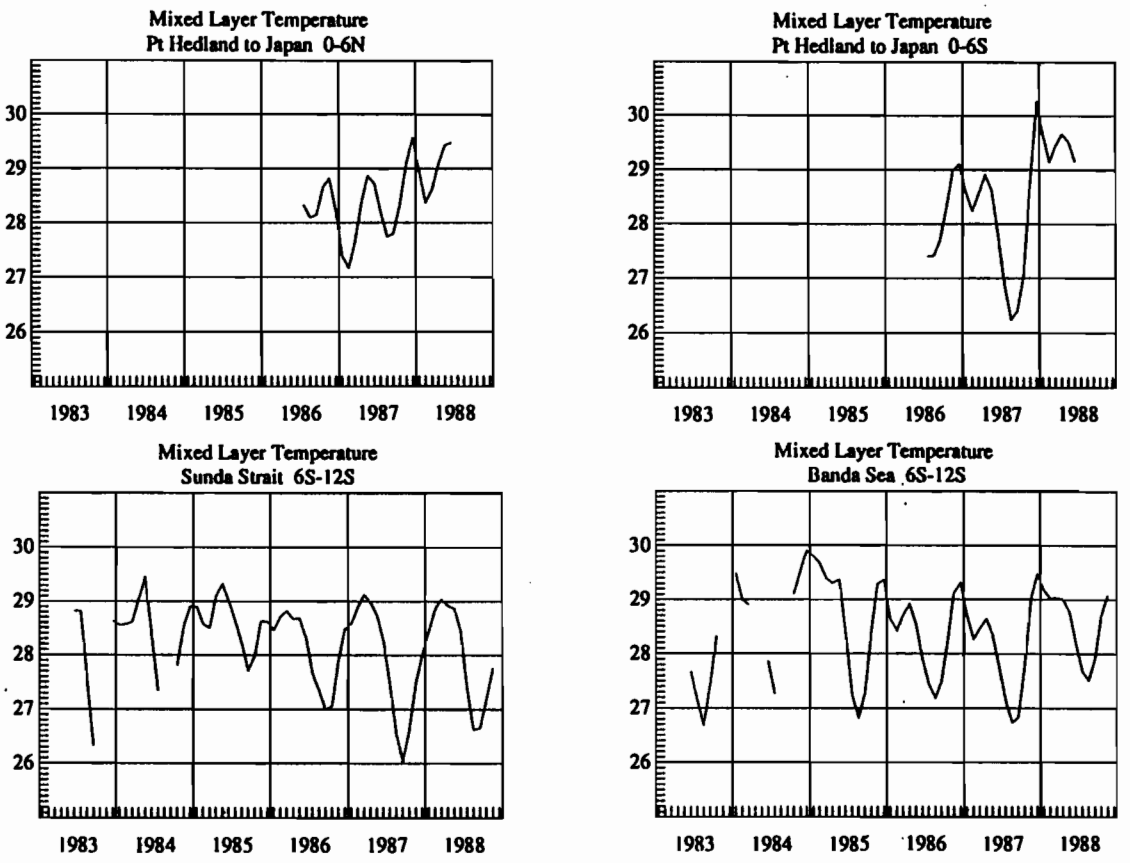

FIG.10. Mixed layer temperature (°C) on XBT tracks in the Indonesian Seas and Indian Ocean.

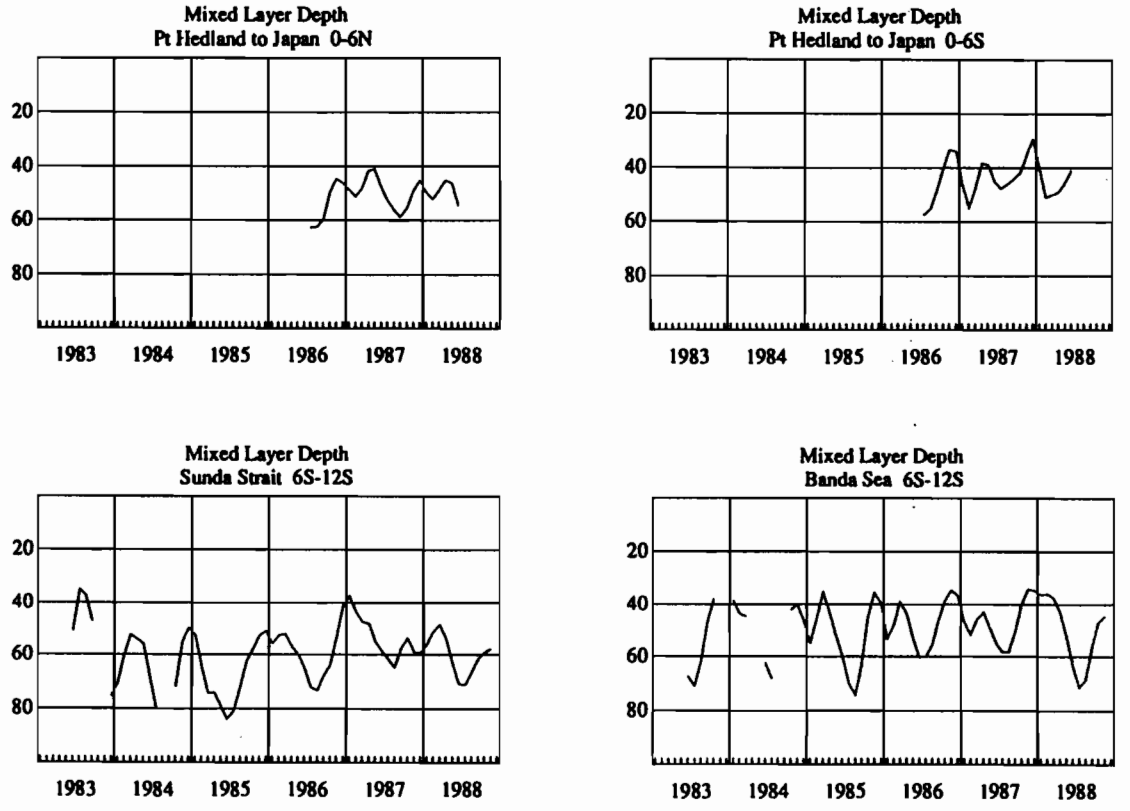

FIG.11. Mixed layer depth (m), as in figure 10.

6. Scales of mixed layer temperature variability

The scales of mixed layer temperature variability were analyzed by empirical orthogonal function (EOF) analysis in order to document differences in spatial scales for the central and western Pacific, and to guide the selection of a grid-size for a study of the surface heat budget. The following is a summary of work discussed in more detail by Meyers et al. (1989a).

The mean and standard deviation of MLT for the period 1979-1984 are presented in Figure 12 for the western, central and eastern tracks. The maximum temperature appears on the western track at 5°S and the central track at 9°S, where temperature exceeds 29°C. Minimum variability occurs at the temperature maximum. Minimum temperature and maximum variability occur in the equatorial cold tongue, on the eastern track near 1°S. The variability represented as standard deviation in Fig. 12 was decomposed into space and time signals using EOF analysis.

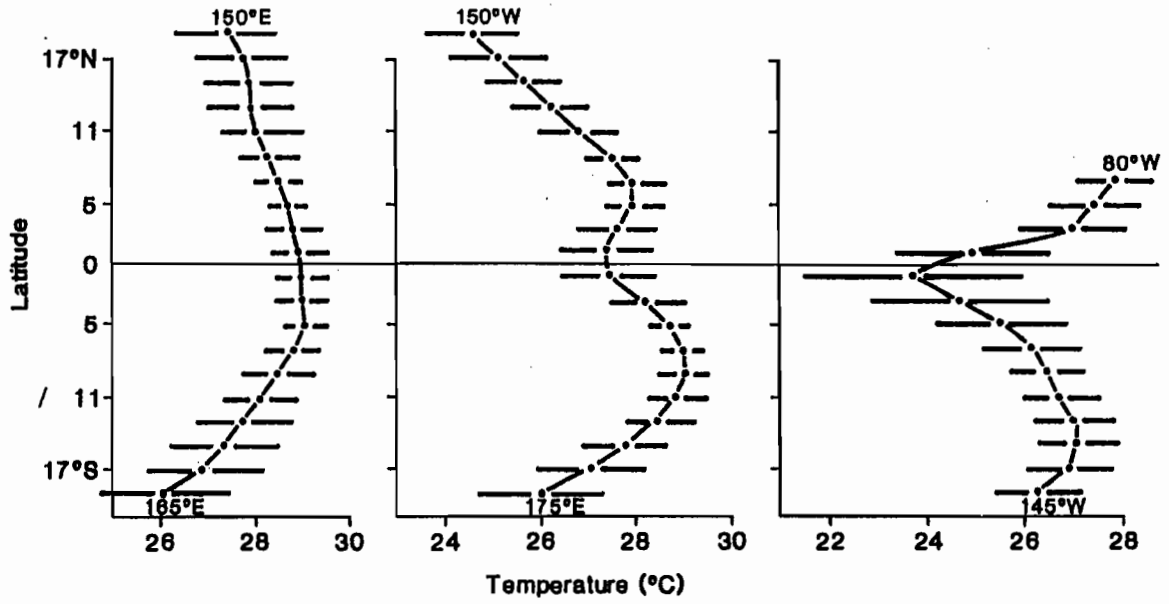

FIG.12. Mean (1979-1984) mixed layer temperature (°C) and ±1 standard deviation on the western (≈160°E), on central (≈165°W) and eastern (≈100°W) XBT tracks.

The method was applied to time series at each 2° latitude grid point after each series was normalized by standard deviation. The first three spatial (Fig. 13) and temporal (Fig. 14) EOF's represent 76% of the variance. All three EOF's are discussed in some detail by Meyers et al. (1989a). Here we highlight only the second EOF (20% of normalized variance) because the temporal function (Fig. 14) carries the signature of the 1982/83 ENSO. The spatial pattern (Fig. 13) shows a near equatorial signal on the central track confined to 10°N-10°S, indicating warming. A cooling signal appears on the western track in a larger area between 19°N and 19°S. The different spatial scales on the two tracks suggests that different processes may dominate the heat budget in the two regions. It is worth noting that the seasonal oscillation apparent in EOF2 (Fig. 14) during the first three years appears because the central Pacific annual cycle lags the eastern Pacific cycle, by 2-3 months. The annual cycle in the eastern equatorial Pacific and at extra equatorial latitudes was carried in EOF1.

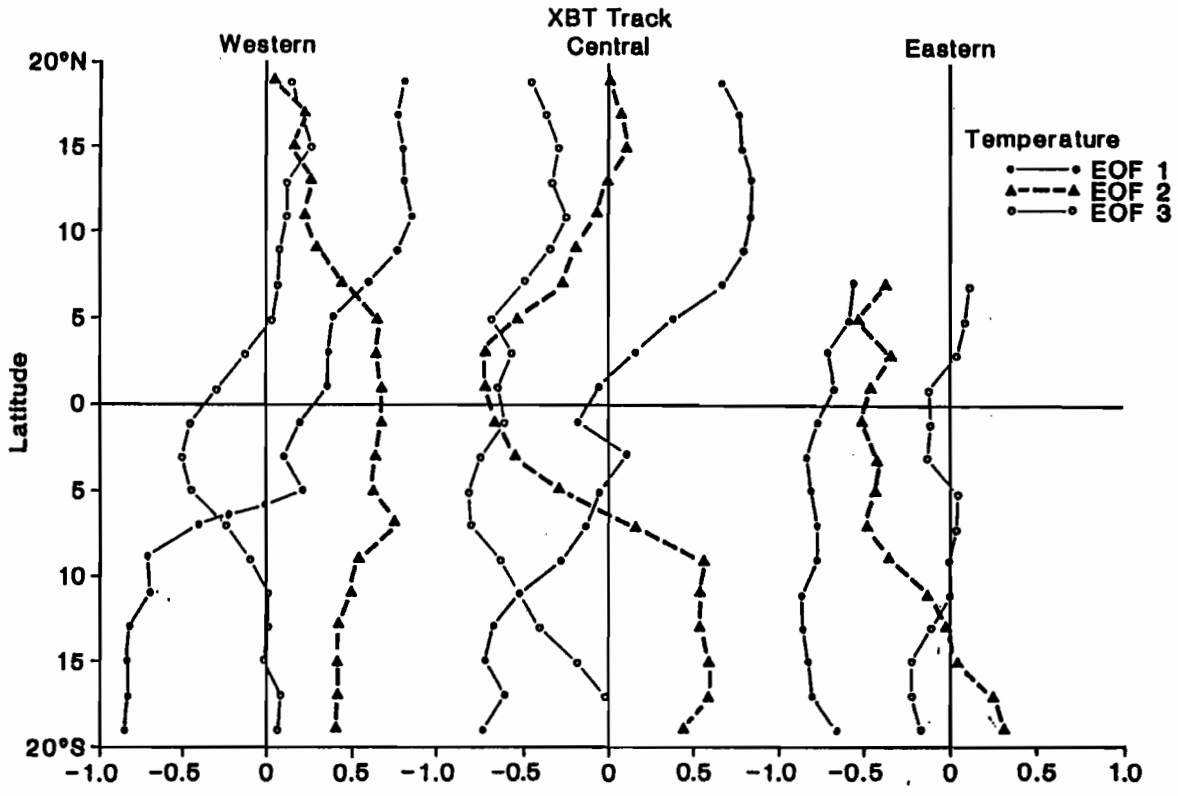

FIG.13. Spatial empirical orthogonal functions of mixed layer temperature.

7. Surface heat budget

The large spatial extent of western Pacific cooling extending from 19°N-19°S and spreading westward through the Indonesian seas into the Indian Ocean suggests an atmospheric origin (Meyers et al., 1986). A study of the influence of air/sea surface heat fluxes on the mixed layer heat budget through out the tropical Pacific is reported here. A study of the complete heat budget including fluxes, advection, mixing and other mechanisms was reported by England and Meyers (1989).

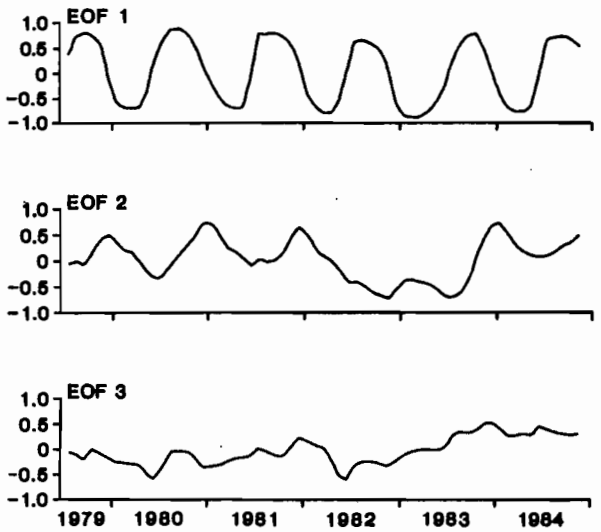

FIG.14. Temporal empirical orthogonal functions for spatial patterns in Fig.13.

	λ	H	σ_H	Q	σ_Q	$r_{H,Q}$	σ_{Q+E}	$r_{H, Q+E}$
12°N-18°N	160°E	-9	66	57	58	.85	62	.86
6°N-12°N	160°E	3	42	47	49	.62	50	.64
0° - 6°N	160°E	2	28	69	30	.49	31	.50
0° - 6°S	160°E	0	28	62	32	.35	33	.45
6°S-12°S	160°E	-5	39	57	54	.51	56	.55
12°S-18°S	160°E	0	60	20	82	.73	82	.75
12°N-18°N	150°W	-2	51	19	37	.69	38	.72
6°N-12°N	160°W	4	34	22	38	.40	38	.43
0° - 6°N	160°W	0	38	67	36	.26	37	.24
0° - 6°S	170°W	-2	51	74	26	.01	28	.04
6°S-12°S	170°W	3	32	54	28	.47	29	.51
12°S-18°S	180°W	0	54	26	65	.72	66	.73
0° - 6°N	100°W	0	31	62	41	.50	41	.52
0° - 6°S	110°W	4	61	125	39	.15	40	.20
6°S-12°S	120°W	-5	57	66	46	62	47	.64
12°S-18°S	140°W	-7	70	49	45	.77	48	.79

Table 1. Influence of surface fluxes on local heat storage measured in $W.m^{-2}$. Longitude (λ), mean and standard deviation during 1980-1983 of heat storage (H,σ_H), mean and standard deviation of net surface fluxes (Q,σ_Q), correlation between local storage and fluxes (r_{H+Q}), standard deviation of net fluxes plus entrainment (σ_{Q+E}), correlation of local storage and fluxes plus entrainment ($r_{H,Q+E}$).

The model of MLT variability tested in this study is a balance between total heat fluxes on the surface (Q) and the local rate of heat storage due to temperature change ($\rho C_p h T_t$) where T_t is the partial derivative of MLT with respect to time, h is MLD, ρ is density, and C_p is heat capacity of water. The model is thus;

$$Q = Q_{SW} - Q_{LW} - Q_S - Q_L \quad ; \qquad H = \rho C_p h T_t = Q$$

where H is the local heat storage rate measured by XBT and Q_{SW}, Q_{LW}, Q_S and Q_L are the shortwave, longwave, sensible and latent heat fluxes estimated by the bulk aerodynamic method from weather data.

Before testing the model by correlation analysis, values of Q and H from the 2° latitude grid were averaged over 6° latitude bands on the three main XBT tracks in the Pacific. The

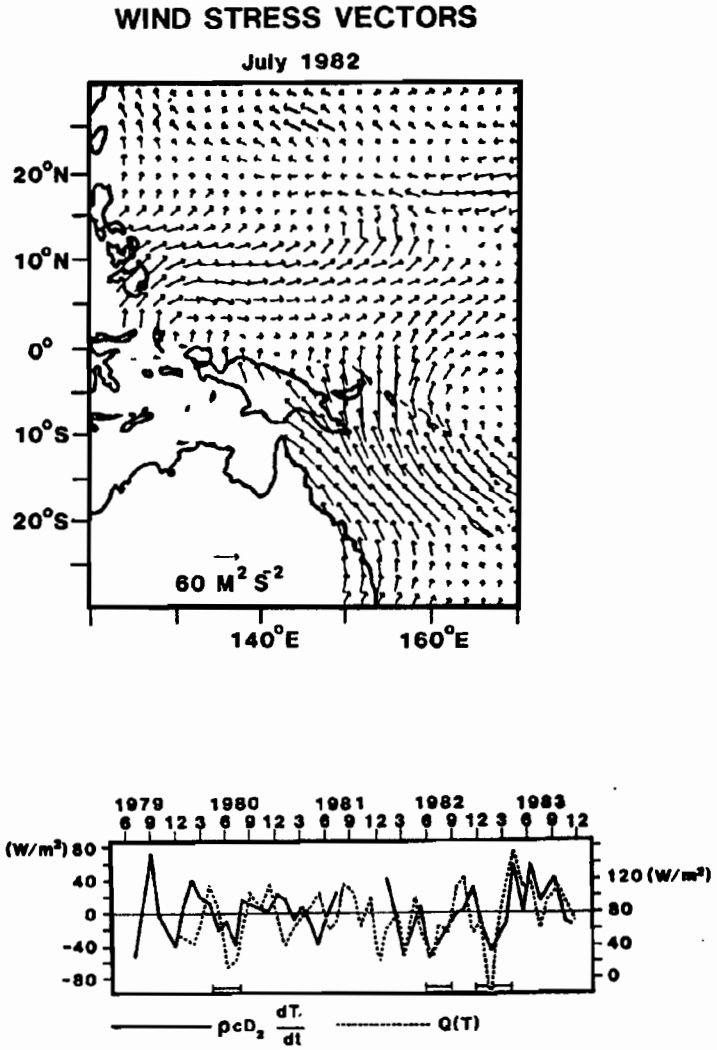

FIG.15. (TOP) Field of wind stress in July 1982. (BOTTOM) Local rate of heat storage measured by XBT (solid line) and total surface heat fluxes ($W.m^{-2}$) estimated by the bulk aerodynamic method using weather data (dashed line).

correlation coefficient (r_{HQ}) are presented in Table 1. (The other statistics in the Table are discussed in Meyers et al., 1989a, and for brevity is not repeated here). The highest values of r_{HQ} occur in the extra equatorial latitude bands because of strong, atmospherically driven seasonal oscillations in temperature. The seasonal oscillation also appears in Q and H in the eastern Pacific 0°-6°N. Focusing on near equatorial areas where the ENSO signal is most prominent, relatively high correlations extend across the equator in the western Pacific, while they drop to nearly zero in the central and eastern Pacific. The low correlation is consistent with the idea that MLT change during ENSO in the central and eastern Pacific is dominantly driven by anomalous eastward advection and downwelling (Harrison et al., 1989). The higher correlation coefficients in the western Pacific are consistent with the idea that an atmospheric process governs the whole latitude band grow 19°N-19°S. The errors of measurement in Q and H (see Meyers et al., 1989a for estimates) tend to reduce the magnitude of correlation coefficients below that for the values that would be obtained with error-free measurement. Thus the value of r_{HQ} do not indicate how much of the variance of heat storage is accounted for by the model.

A visual comparison of Q and H in the western Pacific (Fig. 15, bottom) helps us understand the cooling process. To a large extent the positive correlation is due to variations during the 1982/83 ENSO. Cooling during ENSO develops when anomalously strong winds blow from subtropical latitudes into the doldrum belt raising the latent heat flux by increas ing wind speed (Fig. 15, top). The shortwave and latent heat fluxes throughout the latitude band 19°N-19°S (Fig. 16) confirm that low values of total flux were associated with peaks of evaporation extending from the subtropics to the equator during the main cooling events, which came from the south during the southern winter and from the north during the northern winter.

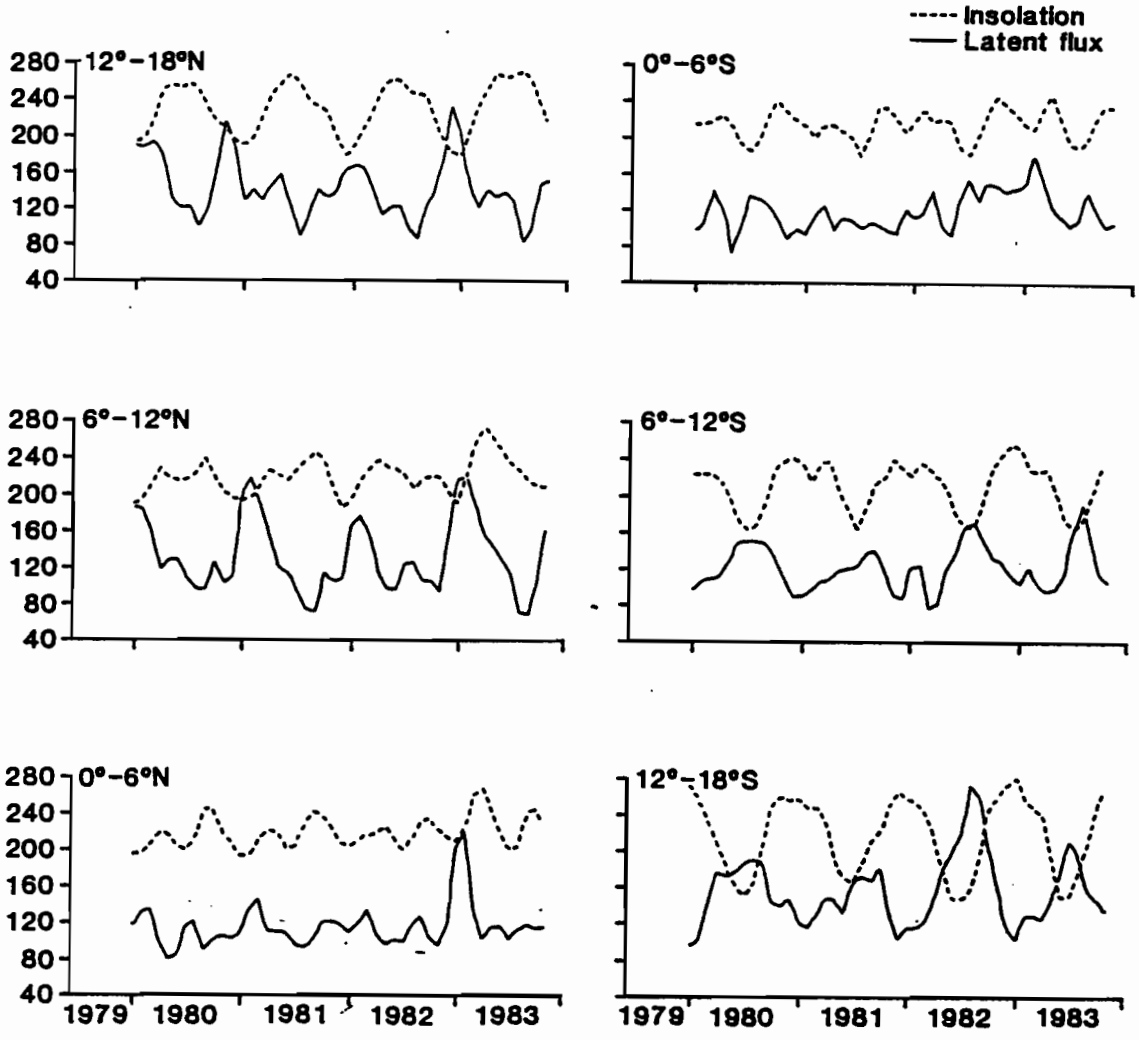

FIG.16. Incoming short wave radiation ($W.m^{-2}$) and outgoing latent heat flux ($W.m^{-2}$) near 160°E.

8. Summary and conclusion

The most important results of this study emerged from a study of the heat budget for the 1982/83 ENSO. Firstly a reversal of the temperature difference along the equator between 160°E and 165°W was observed at the onset of the episode, and may indicate that the dy-

namics of a direct thermal cell plays a roll in the onset and growth of ENSO (Lukas, 1988; Meyers et al., 1989a). Secondly, the influence of changes in surface heat fluxes in western Pacific cooling was documented, in contrast to the central Pacific where variability of surface fluxes has little to do with ENSO temperature changes, and anomalous eastward advection and downwelling are thought to be the dominant mechanism of temperature change.

The ENSO episode of 1986/87 had an onset and growth which was similar in some aspects to the 1982/83 episode, however a study of the heat budget for 1986/87 has not yet been completed because currently there is no readily accessible and reliable data base for the heat fluxes between the ocean and the atmosphere (Halpern, 1988).

REFERENCES

Berlage, H.P., 1966: The Southern Oscillation and World Weather. *K. Ned. Meteorol. Inst., Meded. Verb.*, **88**, 152 pp.

Cane, M.A., S.E. Zebiak and S.C. Dolan , 1986: Experimental forecasts of El Nino. *Nature*, **321**, 827-832.

Deser, C. and J.M. Wallace, 1987: El Nino events and their relation to the Southern Oscilla tion : 1925-1986. *J. Geophys. Res.*, **92**, 14189-14194.

Donguy, J.R., C. Hénin, A. Morliere and J.P. Rébert, 1982: Thermal changes in the western tropical Pacific in relation to the wind field. *Deep Sea Res.*, 869-882.

Donguy, J.R., 1987: Recent advances in the knowledge of the climatic variations in the tropical Pacific Ocean. *Prog. Oceanogr.*, **19**, 49-85.

England, M., and G. Meyers, 1989: The Southern Oscillation and heat storage in the equa torial Pacific Ocean, 1979-1984 : Part II: The influence of ocean dynamics. *J. Mar. Res.*, (submitted).

Halpern, D. , 1987: Observations of annual and El Nino thermal and flow variations at 0°, 110°W and 0°,95°W during 1980-1985. *J. Geophys. Res.*, **92**, 8197-8212.

Halpern, D., 1988: TOGA and Ocean Processes In : Contribution of Geophysics to Climate Change Studies. Proceedings of IUGG Symposium 15 , edited by A. Beiger, R. Dickinsen and J. Kindson, *AGU* Monography N° XX, *American Geophysical Union*, Washington DC.

Harrison, D.E., W. Kessler and B. Giese, 1989: Ocean circulation model hindcasts of the 1982-83 El Nino: Thermal variability along the ship-of-opportunity tracks. *J. Phys. Oceanogr.*, **19**, 397-418.

Hénin, C. and J.R. Donguy, 1980: Heat content changes within the mixed layer of the equa torial Pacific Ocean, *J. Mar. Res.*, **38**, 767-780.

Lander, M.A. and M.L. Morrissey, 1982: Genesis of twin typhoon associated with a west wind burst in the equatorial Pacific : a case study In: *Proceedings of the US TOGA Western Pacific Air-Sea Interaction Workshop*, USTOGA8, University Corporation for atmospheric Research, Boulder, 163-174.

Lukas, R., 1988: On the role of western Pacific air-sea interaction in the El Nino/Southern Oscillation Phenomenon In: *Proceedings of the USTOGA Western Pacific Air-Sea Interaction Workshop*, USTOGA8, University Corporation for Atmospheric Research, Boulder, 43-69.

Lukas, R. and P. Webster, 1988: *Proceedings of the US TOGA Western Pacific Air-Sea int eraction Workshop*, USTOGA8, University Corporation for Atmospheric Research, Boulder 207, pp.

McPhaden, M.J., H.P. Freitag, S.P. Hayes, B.A. Taft and Z. Chen, 1988: The response of the equatorial Pacific Ocean to a westerly wind burst on May 1986. *J. Geophys. Res.*, **93**, 10589-10603.

Meyers, G., J.R. Donguy and R.K. Reed, 1986: Evaporative cooling of the western equato rial Pacific Ocean by anomalous winds. *Nature*, **323**, 523-526.

Meyers, G., J.R. Donguy, M. England and R.K. Reed, 1988a: The Southern Oscillation and heat storage in the equatorial Pacific Ocean, 1979-1984. Part 1: Surface heat fluxes and local storage. *J. Mar. Res.*, (accepted).

Meyers, G., H. Phillips and J. Sprintall, 1989b: Space and time series for optimal interpola tion of temperature- Tropical Pacific Ocean. *J. Geophys. Res.*, (submitted).

Nicholls, N., 1989: Sea surface temperature and Australian Winter rainfall. *J. Clim.*, (in press).

Pazan, S. and G. Meyers, 1982: Interannual fluctuations of the tropical Pacific wind field and the Southern Oscillation. *Mon. Wea. Rev.*, **110**, 587-600.

Quinn, W. H., V.T. Neal and S.E. Antunez de Mayolo, 1987: El Nino Occurrences over the past four and a half centuries. *J. Geophys. Res.*, **92**, 14449-14461.

Rasmusson, E. and T. Carpenter, 1982: Variations in tropical sea surface temperature and surface wind fields associated with the Southern Oscillation El Nino. *Mon. Wea. Rev.*, **110**, 354-384.

Reed, R.K., 1986: Effects of surface heat flux during the 1972 and 1982 El Nino episodes, *Nature*, **322**, 449-450.

Trenberth, K.E. and D.J. Shea, 1987: On the evolution of the Southern Oscillation. *Mon. Wea. Rev.*, **115**, 3078-3096.

Wyrtki, K., 1975: El Nino - The dynamic response of the equatorial Ocean to atmospheric forcing. *J. Phys. Oceanogr.*, **5**, 572-584.

Wyrtki, K., 1985: Water displacements in the Pacific and genesis of El Nino cycles. *J. Geo phys. Res.*, **90**, 7129-7132.

Wyrtki, K. and G. Meyers, 1976: The trade wind field over the Pacific Ocean. *J. Appl. Met eorol.*, **15**, (7), 698-704.

Wyrtki, K., B.J. Kilonsky and S. Nakahara, 1988: The IGOSS Sea Level Pilot Project in the Pacific. JIMAR Contribution n° 88-0150 Data Report n° 003, University of Ha-waii, 59 pp.

GEOSAT Observations of Sea Level in the Tropical Pacific and Indian Oceans During the 1986-87 El Nino Event

Laury MILLER and Robert CHENEY

Charting and Geodetic Services
National Ocean Service, NOAA
Rockville, MD 20852 - U.S.A.

ABSTRACT

Using a combination of crossover and collinear techniques, we have derived times series of sea level anomalies throughout the tropical Pacific and Indian Oceans for the first 4 years of the GEOSAT mission (1985-88). This time interval is particularly valuable because it provides the first complete, multi-ocean picture of sea level variability during an El Nino event (1986-87). An analysis of sea level averaged over the entire tropical Pacific (20°N to 20°S) shows no evidence of an anomalous rise (increase in upper layer volume) prior to the warm phase of El Nino. However, sea level anomalies (relative to observations between April 1985 and March 1986) can be seen when averaging is performed over certain sub-regions. Beginning in April 1987, the region 8°N to 20°N gained 1.5 x 10^{14} m^3 of upper layer volume, while simultaneously the region 7°S to 7°N lost about the same amount. These anomalies persisted until early 1989, when both regions quickly returned to normal. In addition to these El Nino signals, large annual signals are evident over much of the tropical Pacific and Indian Oceans. In the Pacific, the annual signals are clearly organized in large zonal bands. The equatorial region (7°S to 7°N) is lowest in May and highest in November. Conversely, the north equatorial region (8°N to 20°N) is highest in May and lowest in November. The average annual amplitude in each region is approximately 10 cm. In the Indian Ocean, large scale annual signals occur predominately along the equator (where sea level is highest in June and lowest in January), and above 5°N (where sea level is highest in January and lowest in June). In addition to these basin-wide features, a strong (20 cm) southeast-northwest oriented positive anomaly appears in the southeastern Indian Ocean (20°S to 5°N) in September-October.

1. Introduction

Meridional transports of warm surface water into and out of the equatorial Pacific are thought to play an important role in regulating the El Nino-Southern Oscillation (ENSO) cycle. According to recent coupled model studies (Cane et al., 1986; Zebiak and Cane, 1987; Schopf and Suarez, 1988; Battisti, 1988; Graham and White, 1988), the ocean-atmosphere system oscillates between two states in the tropics: a cool (non-El Nino) phase and a warm (El Nino) phase. Although many different physical processes are involved in this coupled response, one key parameter appears to be the volume of upper layer water in the equatorial region. Prior to the onset of a warm event, there is a long, slow buildup of water volume in the central and western equatorial Pacific. At the onset of a warm event, the trade winds collapse, forcing a packet of Kelvin waves to propagate eastward along the equator and poleward along the eastern boundary, thereby initiating a rapid outflow of water to higher latitudes. Following a warm event, there is again a long interval during which water flows back into the equatorial region, setting the stage for the next warm event.

Wyrtki (1985) first suggested the idea of the ENSO cycle being regulated by the time required to recharge the equatorial Pacific with warm water. Using island tide gauge data from primarily the western Pacific and coastal stations along the eastern

ORSTOM
CENTRE DOCUMENTATION
Montpellier

F 30212

boundary, Wyrtki constructed sea level maps spanning the entire tropical ocean which he then integrated between 15°S and 15°N. The integrated sea level time series showed a gradual rise and then abrupt drop in conjunction with both the 1976-77 and 1982-83 warm events. Wyrtki argued that a warm event could not begin until there was a large enough surplus of water in the equatorial region, so that any significant weakening of the trade winds resulted in a massive shift of water eastward along the equator. Unfortunately, the number and distribution of island stations in the Pacific tide gauge network is inadequate to describe details of the large-scale movements of water that accompany El Nino. The ongoing program of XBT surveys by ships of opportunity (White et al., 1985) has come closest to providing a mapping capability, but the sheer size of the Pacific results in severe undersampling when any standard oceanographic technique is employed.

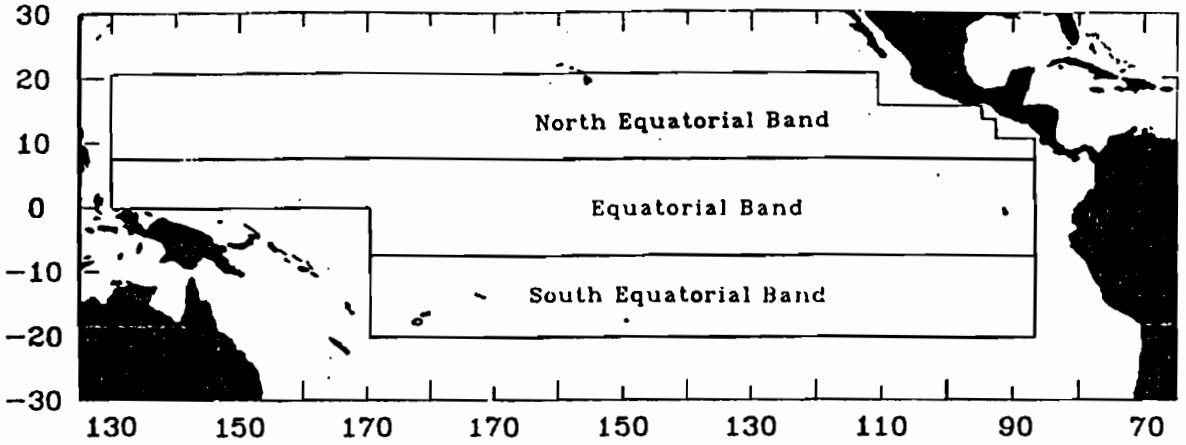

FIG.1. Boundaries of study area (20°S - 20°N, 130°E - 274°E) containing 2476 independent Geosat sea level time series for the 4-year period April 1985 - February 1989. Three latitude bands (20°S - 8°S, 7°S - 7°N, 8°N - 20°N) indicate areas described in Figures 5 and 6. Each band contains approximately 800 time series, each constructed using all altimeter data in 2x1 degree (longitude x latitude) cells.

To help overcome this sampling problem, we have used Geosat altimeter observations to produce a uniform, basin-wide grid of sea level records throughout the tropical Pacific (Fig.1). The U.S. Navy satellite Geosat has been in continuous operation since April 1985, and in its first four years generated a global data set consisting of approximately 600 million sea level observations (at the full 10/s resolution). As discussed by Cheney et al., (1986), crossover difference methods must be used to extract sea level time series from the initial, 18-month geodetic mission (GM), whereas either crossover or collinear differencing can be used for data collected during the ongoing exact repeat mission (ERM). Both methods produce comparable results for sea level variability and together enable construction of continuous records spanning the 1986-87 El Nino event. In this paper we present results showing large-scale sea level fluctuations and changes in upper layer volume in the tropical Pacific during the 4-year period April 1985 - February 1989. We also present results showing volume variations in the tropical Indian Ocean during this time interval.

2. Computation of sea level time series

A combination of crossover and collinear difference methods was used to construct continuous, 4-year sea level time series spanning both the GM and ERM. First, a 2.5-year crossover difference time series was computed from April 1985 to

November 1987. This record extends through the first year of the ERM. In such a solution the collinear ERM passes are analyzed together with the non-collinear GM passes strictly in terms of their crossings. Next, a collinear difference time series was computed at the same location using only ERM data from November 1986 to April 1989. The 1-year overlap between these two solutions is used to adjust the collinear solution relative to the crossover solution, resulting in a continuous record beginning in 1985. Details concerning each of these steps are given in Miller and Cheney (1990).

Sea level records computed from Geosat can be compared with in situ measurements to obtain a measure of their accuracy. Island tide gauges are one obvious source of surface data for such comparisons, as they are the only instruments capable of measuring sea level directly. Dynamic height computed from moored thermistor arrays are also valuable because they can provide surface truth in the open ocean where island data are not available. In a previous paper (Cheney et al., 1989) we compared Geosat geodetic mission time series with fourteen tide gauge records and two moorings in the tropical Pacific. Average agreement of Geosat with the surface measurements was 3.7 cm rms with a correlation of 0.68 for the 18-month period examined. Figure 2 shows results of a 4-year comparison the tide gauge at Christmas Island. In this figure both records have been adjusted to have zero mean over the their entire lengths. (However, unless otherwise stated, all of the time series which follow have been adjusted to have zero mean in the first 12 months, April 1985-86.) Based on monthly means, rms difference of the altimeter and tide gauge record at Christmas Island is 5.9 cm with 0.83 correlation. This example is typical of the altimeter/tide gauge agreement found throughout the tropical Pacific. At the same fourteen tide gauge sites used in Cheney et al., (1989), the 4-year comparisons yield an average of 5.3 rms difference with 0.86 correlation.

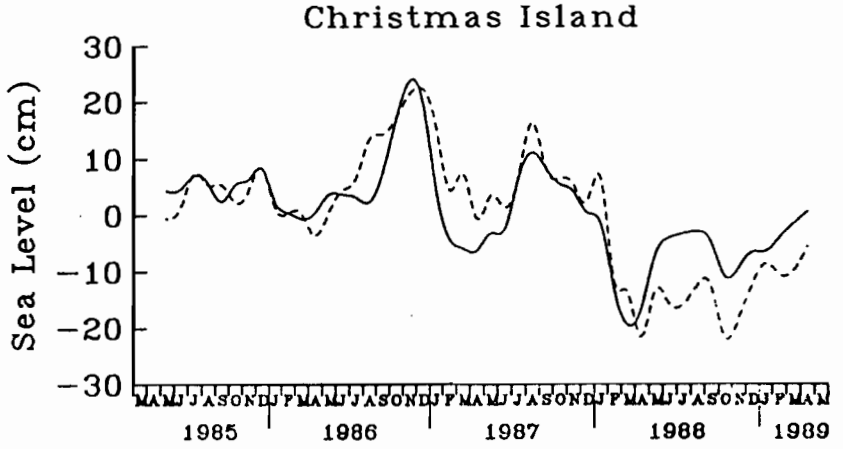

FIG.2. Comparison of Geosat time series (solid) for 2x1 degree region centered on 1°N, 157°E, with tide gauge data (dashed) from Christmas Island (1.9°N, 157.5°W). Both records have been adjusted to have zero mean over their entire lengths. Rms difference is 5.9 cm with correlation of 0.83. Statistics are based on monthly means. Tide gauge data were obtained from maps such as those in Wyrtki et al. (1988).

3. Pacific Ocean

a. Zonal averages of sea level.

Before attempting to compute averages over large areas of the tropical Pacific Ocean, it is useful to know something about the latitudinal structure of the sea level signals. Figure 3 presents the results of averaging all Geosat sea level time series in alternate 1 degree latitude bands extending across the full width of the study area. This

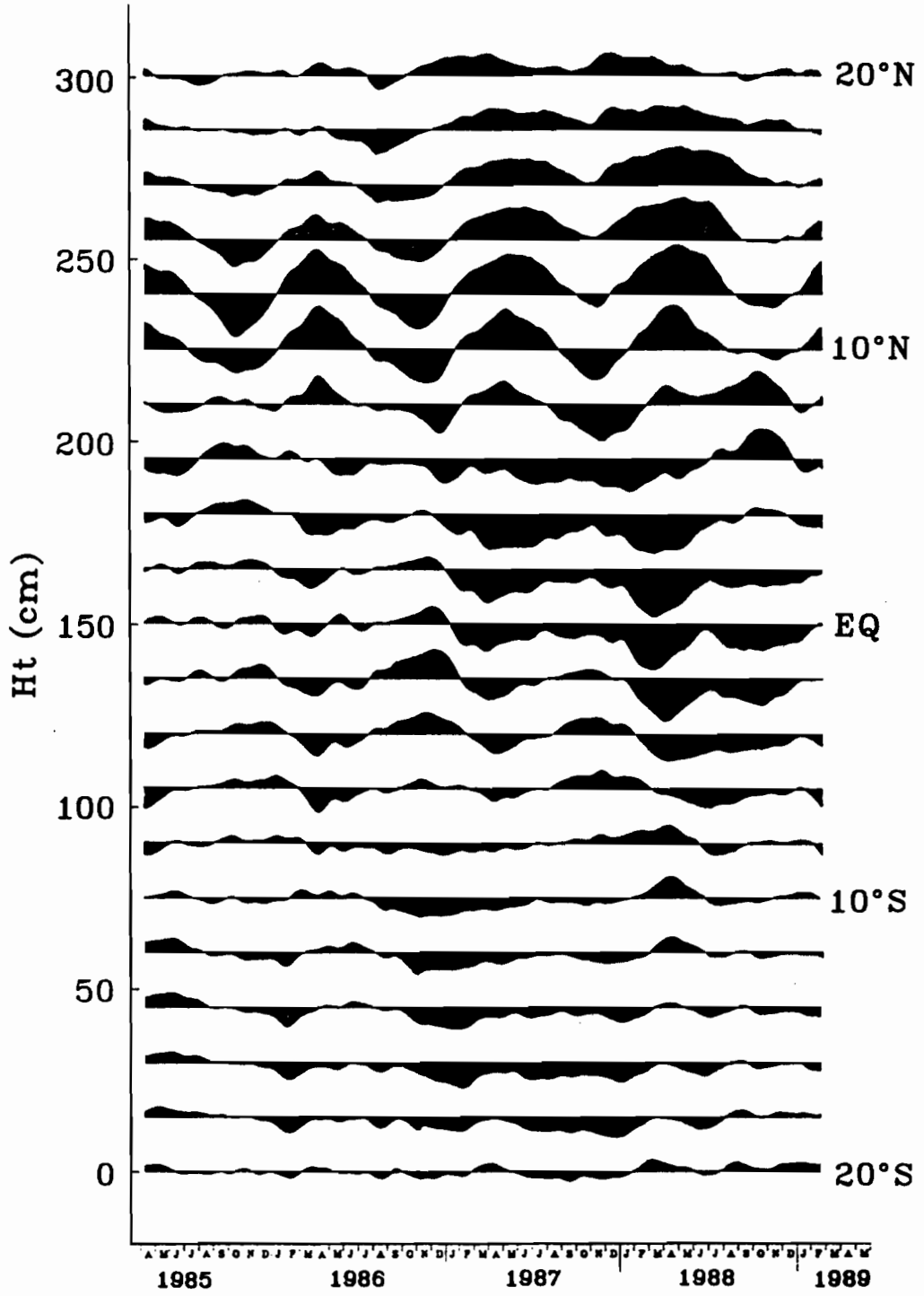

FIG.3. Zonally averaged sea level determined from all Geosat time series in alternate 1 degree latitude bands (20°S, 18°S, 16°S,...) extending across the entire Pacific. Vertical offset between series is 15 cm. Strongest signals are found in the northern hemisphere, principally the result of annual forcing by the wind. A distinct phase change exists between 6°N and 10°N during most years.

shows a clear separation of signals on the basis of latitude ranges. In general, the strongest annual and interannual signals are found north of the equator and the weakest south of the equator. The annual signals exhibit opposite phases above and below about 7°N. In the north equatorial (equatorial) region, sea level is generally high (low) in April-May and low (high) in November-December. The onset of the warm event is seen as a moderate intensification of the annual cycle in the equatorial region in November-December, 1986. Subsequently, this region exhibits negative sea levels throughout most of 1987 and 1988 while the north equatorial region exhibits positive anomalies.

b. Upper layer volume.

In order to determine to what extent these fluctuations represent net gains or losses of water to the entire study area, we have converted our sea level time series to variations of upper layer volume (defined as that portion of the water column above the 20°C isotherm), following the procedure outlined by Wyrtki (1985). Figure 4 (bottom) shows the upper layer volume variability calculated from all of the time series located inside the boundaries 20°S to 20°N, 130°E to 274°E. This record exhibits an annual oscillation with an amplitude of approximately 1.0 x 10^{14} m^3, and there is some evidence of longer period changes. (In terms of sea level, a change of 1.0 x 10^{14} m^3 in upper layer water volume is equivalent to 0.8 cm averaged over the entire region). The phase of the annual oscillation (high in April-May, low in November-December) is the same as that observed along both the northern and southern boundaries of the study area (see Figure 3), suggesting that some exchange of water is taking place across these boundaries on this time scale.

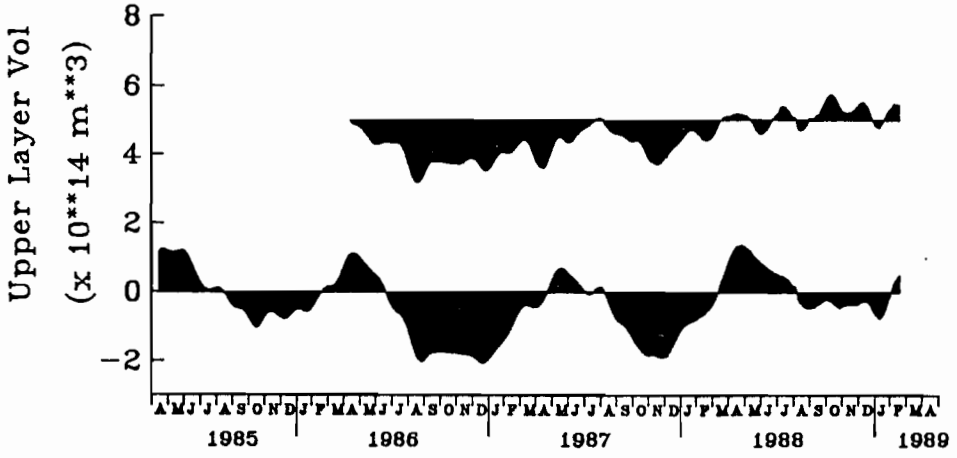

FIG.4. Upper layer volume determined from all Geosat time series located inside study area 20°S - 20°N, 130°E - 274°E. The upper layer is defined as water above the 20°C isotherm. (Bottom) Entire 4-year record referenced to zero mean for the first 12 months (April 1985-86). (Top) Anomalies with respect to the annual cycle observed during the first 12 months. (Offset 5 cm relative to the bottom curve.)

In the upper curve of Figure 4 we have subtracted the volume record over the first 12 months (April 1985-86) from each subsequent 12 month interval, hence the anomaly relative to one realization of the annual cycle. This curve shows that, relative to the 1985-86 annual cycle, upper layer volume dropped about 1.5 x 10^{14} m^3 in mid-1986 (prior to the onset of the El Nino), but then steadily increased over the next two years so that, by the middle of 1988, it had returned to 1985 levels. We would like to know which particular regions were responsible for these changes in water volume and also,

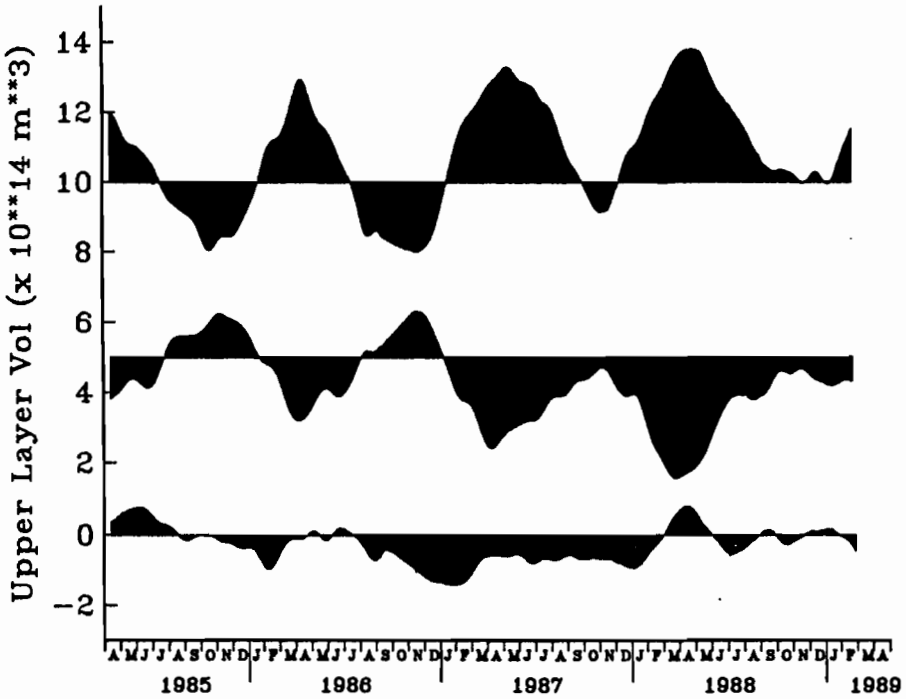

FIG.5. Upper layer volume determined from all Geosat time series in three latitude bands: 20°S to 8°S (bottom), 7°S to 7°N (middle), and 8°N to 20°N (top). The northern and equatorial bands have strong annual signals distinctly out of phase with each other. An annual signal is also apparent in the southern band but much smaller in amplitude.

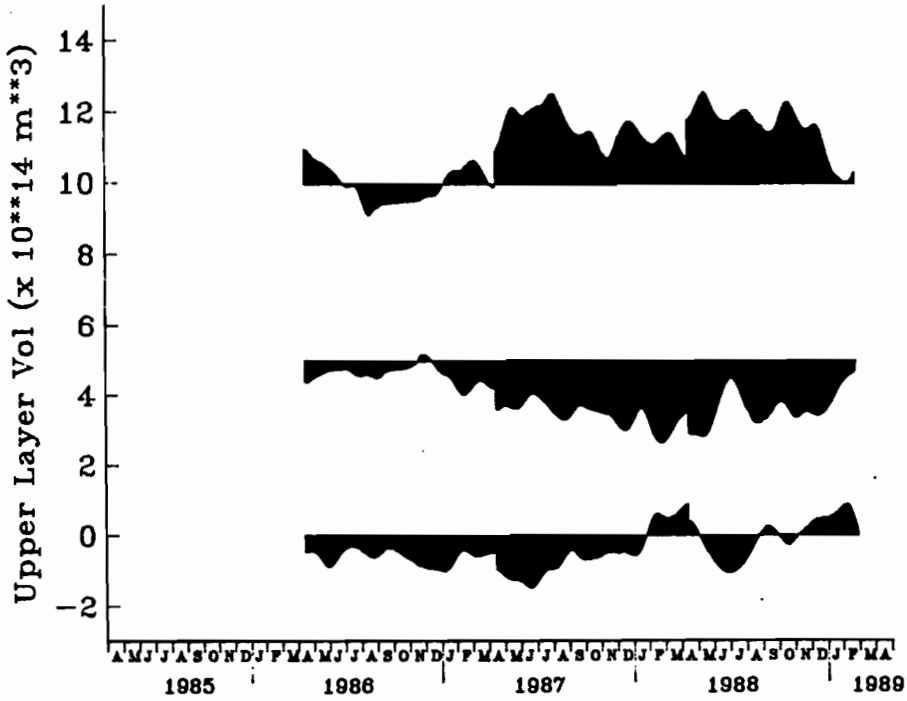

FIG.6. Same as previous figure, but expressed in terms of volume anomaly with respect to the April 1985-86 annual cycle. Long-term trends are now evident. The southern band displays negative anomalies beginning in mid-1986, whereas anomalies in the other bands do not develop until 1987. Relatively normal conditions return in the south in early 1988, whereas the equatorial and northern bands remain anomalous until early 1989.

how water is redistributed within the tropical Pacific during a warm event. Here we concentrate on meridional transport, as the low-frequency El Nino signal is often described as a displacement of water from the equatorial region to higher latitudes.

An examination of Figure 3 shows that both the annual and interannual signals are clearly organized in three latitude bands: south equatorial, equatorial, north equatorial. We have therefore computed the volume time series for these three bands separately, as defined in Figure 1 (20°S - 8°S, 7°S - 7°N, 8°N - 20°N). Figure 5 shows the volume variability in each region before removing the annual signal. The strongest annual signal (2.0×10^{14} m^3 amplitude) is found in the northern band. In the equatorial band the amplitude is about the same and out of phase with the northern band so that together these two regions tend to be balanced. The weakest annual signal is seen in the southern band. Phase in this region is similar to that in the northern band.

Of more significance to the ENSO problem is the fact that all three bands display long term trends. To enable examination of these trends uncontaminated by the energetic annual cycle, Figure 6 shows these records re-interpreted as volume anomalies relative to their respective April 1985-86 cycles. These curves may be compared to the upper curve in Figure 4, which is the volume anomaly for the entire study area. Although the onset of the warm (El Nino) event took place during the middle of the second year (April 1986-87), only the southern band shows significant anomalies during this time interval. It is apparent that although the southern band has the smallest annual signal, it is largely responsible for the loss of water seen in Figure 4 (upper) during the second year. Because of the timing of this signal (beginning in mid-1986) and its relatively small amplitude, it is not clear whether it is directly related to El Nino. All three bands exhibit large anomalies during the third year (April 1987-88) with larger than normal volume in the northern band, a corresponding deficit in the equatorial region, and continued low volume in the south. These anomalies persisted in the two northern bands until the end of the fourth year (early 1989), when the volume in both bands finally returned to first-year levels. In the southern band a return to more normal values occurred one year before (early 1988).

c. Comparison with a wind-driven model.

Existence in the Geosat records of low-frequency sea level signals with periods of 2 years or more is consistent with the El Nino phenomenon, but because of their relatively small amplitude (only a few centimeters in terms of mean sea level in any one band) it is reasonable to ask whether these trends could be caused by other factors. Uncertainty in the water vapor field could have a low frequency component, for example, particularly during El Nino when large scale changes in meteorological patterns are known to occur. The ionosphere correction is also a potential problem, ranging as it has from near-zero in 1985 to more than 10 cm in 1989 as we approach the solar maximum. Accuracy of the Geosat orbits has also varied during the Geosat mission, and tide model error can alias into lower frequencies. Until improvements are made in these and other correction fields for the Geosat data, comparison with independent determinations of sea level continues to be our best means of verification.

We have found good agreement between the altimeter records and island tide gauge data, but this calibrates the data in only a few places. Only numerical models are capable of providing large scale fields comparable to those provided by the altimeter. We have made comparisons with the ocean general circulation model (GCM) of Philander and Seigel (1985) which has been used by A. Leetmaa and M. Ji (personal communication) to determine the structure of the tropical Pacific Ocean during 1985-89. The model was forced with observed monthly average surface wind stress and also included any available XBT and surface thermal information. Dynamic height was computed relative to the bottom, and anomalies were expressed with respect to the same

annual mean used in the GEOSAT maps. Model sea level was converted to volume using the same relationship applied to the altimeter data. Here we examine this model in terms of upper layer volume in the same three regions of the Pacific defined in Figure 1.

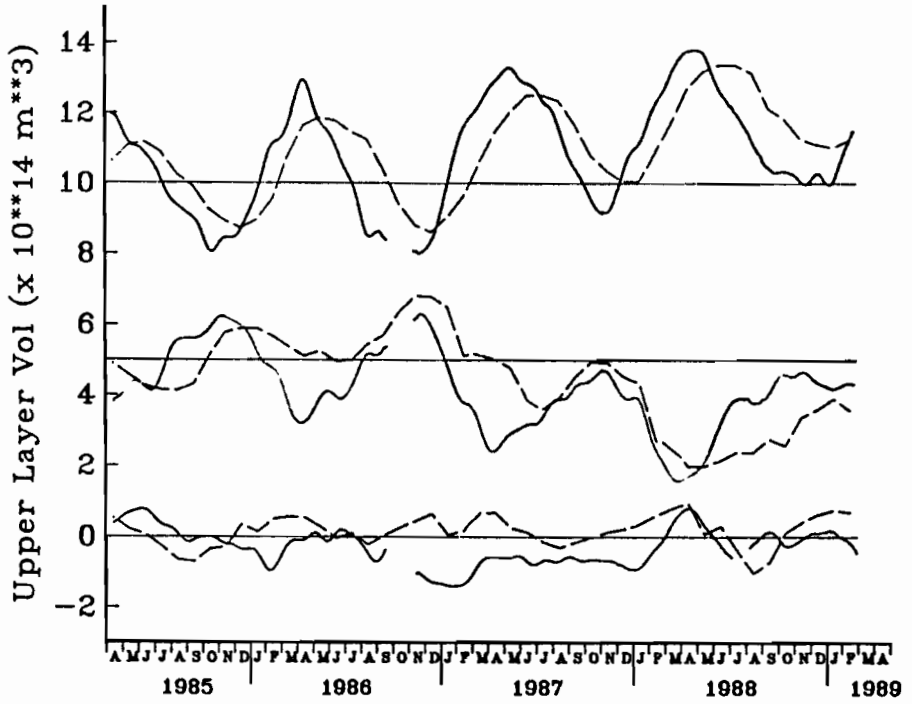

FIG.7. Comparison between model (dashed) and Geosat (solid) upper level volume in the three bands: 20°S to 8°S (bottom), 7°S to 7°N (middle), and 8°N to 20°N (top). Model sea level results were produced with an ocean GCM, using observed winds, sea surface temperatures, and ship-of-opportunity XBTs as inputs. (Leetmaa and Ji, personal communication). Both show variations with similar amplitudes and long-term trends, although phase differences of the annual signal are evident.

The comparison in Figure 7 shows that in each band the character of these two independent records is quite similar. Amplitudes of the annual signals in the northern and equatorial bands are in close agreement although, curiously, the altimeter signal leads the model in phase by 1-2 months. This phase shift may be the result of systematic discrepancies in signal amplitude in certain subregions which modify the overall phases of the zonal bands. Agreement in the southern band is similar to the other two regions, but the altimeter and model records appear less correlated because of the relatively small signal. In particular, the model does not reproduce the negative volume seen by the altimeter from late 1986 to early 1988. This southern region is rather poorly sampled in terms of surface winds, so it is difficult to draw any conclusions about which record is more accurate here.

The most significant result of the model/altimeter comparison is the excellent agreement of the low-frequency trends in the northern and equatorial bands where the largest volume changes were observed. It demonstrates that the altimeter results are reasonable (at least to the extent that the GCM output can be believed) not just over periods of weeks and months, but also for interannual time scales. The picture that evolves from both the altimeter and the model is one in which water is transferred from the equatorial band to the northern band during this particular El Nino. Volume changes in the southern band are smaller by comparison and have a completely different phase, raising the question of what role, if any, this area plays in the El Nino sequence.

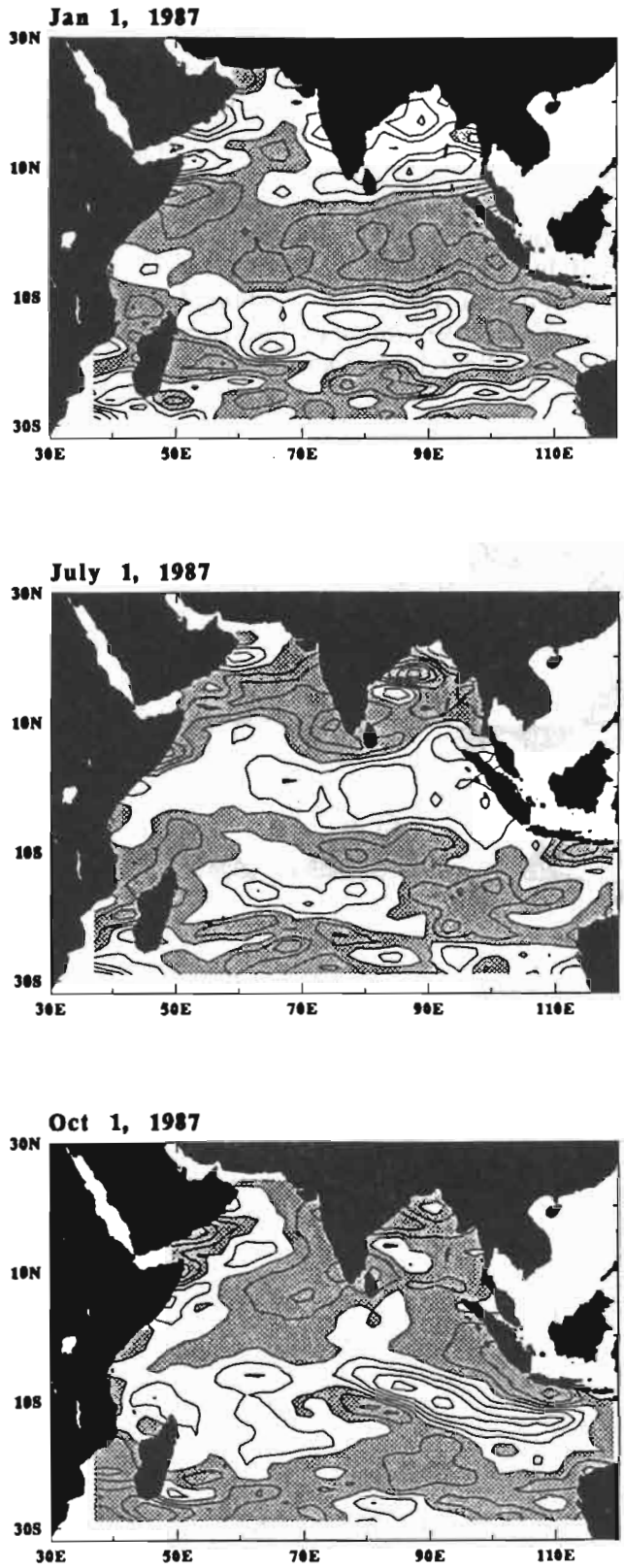

FIG.8. Maps of Indian Ocean sea level anomaly for the months of January, July and October, 1987.

4. Indian Ocean

In addition to examining inter-annual variability in the Pacific Ocean, we have also used Geosat data to look for evidence of El Nino-related signals in the tropical Indian Ocean. As shown in Figure 8, large scale annual signals in the Indian Ocean occur predominately along the equator (where sea level is highest in June and lowest in January), and above 5°N (where sea level is highest in January and lowest in June). These changes are caused by shifts in the monsoonal winds, between the southwest phase (boreal summer) and the northeast phase (boreal winter). In addition to these basin-wide features, a strong (20 cm) southeast-northwest oriented anomaly appears in the southeastern Indian Ocean in September-October.

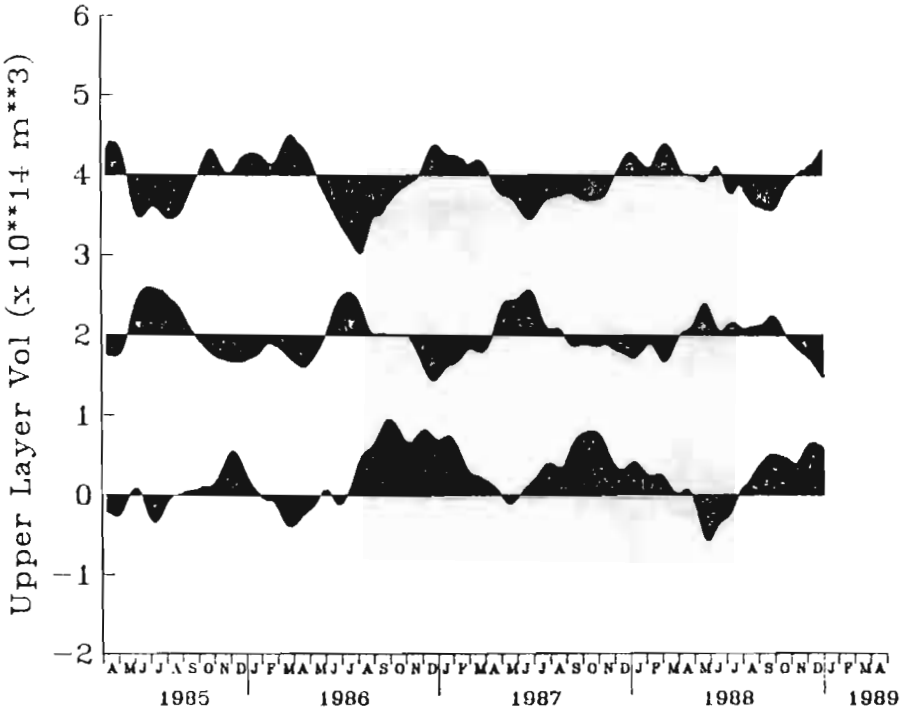

FIG.9. Upper layer volume determined from all Indian Ocean Geosat time series in three latitude bands: 20°S to 5°S (bottom), 4°S to 4°N (middle), and 5°N to 20°N (top).

Figure 9 presents the upper layer volume variability for three latitudinal bands: 20°S - 5°S (bottom), 4°S - 4°N (middle), 5°N - 20°N (top). This shows (as in the Pacific) an annual exchange of water taking place between the equatorial and north equatorial bands, but very little evidence of inter-annual variability. In contrast, note that the south equatorial band shows large positive anomalies in September-December of both 1986 and 1987. Presumably, these reflect the movement of water into the study area from further south.

5. Conclusions

By integrating Geosat derived sea level time series over the entire width of the tropical Pacific, we have been able to determine the net meridional exchange of warm surface water between different latitude bands during the 1986-87 ENSO cycle. Following the onset of the warm event in late 1986, the equatorial region in the Pacific lost about 1.5 x 10^{14} m^3 of water, while the north equatorial region gained a similar

amount. These volume anomalies persisted for nearly two years, during which time the warm event gave way to an unusually severe cold event (Nino3 SST index of -2.0°C). Finally, in early 1989, the volume anomalies in both regions quickly returned to normal, as did the SST anomalies along the equator in the east.

REFERENCES

Battisti, D.S., 1988: The dynamics and thermodynamics of a warm event in a coupled ocean-atmosphere model, *J. Atmos. Sci.*, **42**, 615-629.

Cane, M.A., S.E. Zebiak, and S.C. Dolan, 1986: Experimental forecasts of El Nino, *Nature*, **321**, 827-832.

Cheney, R.E. and L. Miller, 1990: Recovery of the sea level signal in the western tropical Pacific with Geosat data, *J. Geophys. Res.*, submitted to issue on Geosat.

Cheney, R.E., B.C. Douglas, and L. Miller, 1989: Evaluation of Geosat altimeter data with application to tropical Pacific sea level variability, *J. Geophys. Res.*, **94**, (C4), 4737-4747.

Cheney, R.E., B.C. Douglas, R.W. Agreen, L. Miller, D. Milbert, and D. Porter, 1986: The GEOSAT altimeter mission: A milestone in satellite oceanography, *EOS Trans. AGU*, **67 (48)**, 1354-1355.

Graham, N.E., and W.B. White, 1988: The El Nino oscillator of the Pacific ocean-atmosphere system, *Science*, **240**, 1293-1302.

Miller, L., and R.E. Cheney, 1990: Large scale volume changes in the tropical Pacific Ocean during the 1986-87 El Nino from Geosat, *J. Geophys. Res.*, submitted to issue on Geosat.

Miller, L., R.E. Cheney, and B.C. Douglas, 1988: Geosat altimeter observations of Kelvin waves and the 1986-87 El Nino, *Science*, **239**, 52-54.

Schopf, P.S., and M.J. Suarez, 1988: Vacillations in a coupled ocean atmosphere model, *J. Atmos. Sci.*, **45**, 3283-3287.

White, W.B., G. Meyers, J.R. Donguy, and S.E. Pazan, 1985: Short-term climatic variability in the thermal structure of the Pacific Ocean during 1979-82. *J. Phys. Oceanogr.*, **15**, 917-935.

Wyrtki, K., 1985: Water displacements in the Pacific and the genesis of El Nino cycles, *J. Geophys. Res.*, **90 (C4)**, 7129-7132.

Zebiak, S.E., and M.A. Cane, 1987: A model El Nino/Southern Oscillation, *Mon. Wea. Rev.*, **115**, 2262-2278.

GEOSAT Sea Level Anomalies in the Western Equatorial Pacific during the 1986-87 El Nino, Elucidated as Equatorial Kelvin and Rossby Waves

Thierry DELCROIX, Gérard ELDIN and Joël PICAUT

Groupe SURTROPAC, ORSTOM BP A5,
Nouméa - New Caledonia

ABSTRACT

Thanks to the GEOSAT altimeter data set, information on sea level changes during the 1986-87 El Nino is presented. Special emphasis is placed on the warm pool area, with an evaluation, a detailed description and tentative explanation of the observed Sea Level Anomaly (SLA) changes.

Near the 165°E longitude, the onset of the 1986-87 El Nino is characterized by a rapid development of a positive (>14 cm) equatorial SLA in November/December 1986. This feature occurs in response to an eastward wind anomaly appearing between 140°E-170°W along the equator. The wind induces a downwelling equatorial Kelvin wave with phase speed of about 2.3 $m.s^{-1}$. Thereafter, equatorial SLA remains quite constant from January to April/May 1987. In June 1987, equatorial SLA decreases to a minimum value, just after an abrupt change of the zonal wind stress anomaly, west of 165°E. Such anomaly seems to force an upwelling equatorial Kelvin wave propagating at about 2.3 $m.s^{-1}$. Two patches of negative SLAs then appear in September 1987 at 4°N and 4°S, symmetrical about the equator. These are the signature of a first baroclinic upwelling equatorial Rossby wave (n=l=1) arising from the eastern boundary, at c = 0.9 $m.s^{-1}$ phase speed. These calculations suggest that first baroclinic mode Kelvin waves and Rossby wave were the dominant sources of sea level changes in the equatorial band, over the November 1986-November 1987 El Nino period.

1. Introduction.

Before 1985, large scale monitoring of the tropical Pacific Ocean relied on island sea level and/or XBT networks. Both monitoring approaches were quite successful in describing and understanding the main tropical Pacific Ocean variability (e.g., Wyrtki, 1985; White et al., 1985). However, these observations were respectively limited by the poor spatial coverage of the islands, especially in the eastern Pacific, and the poor temporal resolution of XBT measurements which were also restricted to commercial shipping routes.

The U.S. Navy GEOSAT (GEOdetic SATellite) was launched in March 1985, which coincided with the beginning of the international TOGA programme. Hence, the 1986-87 El Nino phenomenon was the first to be captured by a satellite altimeter, providing unprecedented spatial and temporal resolutions of the tropical Pacific ocean surface variability.

Previous works (Cheney and Miller, 1988; Miller et al., 1988; Tai et al., 1989) have already demonstrated the usefulness of GEOSAT in monitoring the whole tropical Pacific ocean. As a complement, the goal of this note is to specifically focus upon the Sea Level Anomalies (SLAs) measured in the tropical Pacific warm pool during the 1986-87 El Nino. To this end, we first briefly present the GEOSAT data and data processing, then give a description of the SLAs observed in the "center" of the warm pool (165°E longitude), and finally try to understand the origin of the altimeter-derived SLAs.

ORSTOM
CENTRE DOCUMENTATION
Montpellier

F 30213

2. Data

a. Data processing.

Detailed information about the GEOSAT mission may be found in a review released by the Applied Physics Laboratory of the Johns Hopkins University (APL, 1987). It is worth reiterating here that the GEOSAT spacecraft was originally launched into a non repeat orbit (March 12, 1985), and then put into a 17-day repeat/collinear orbit configuration (November 18, 1987), for oceanographic applications. Only part of that phase of the mission, referred to as the Exact Repeat Mission (ERM), will be considered here.

The GEOSAT data we have analysed were kindly provided by C. Koblinsky (NASA, Greenbelt). All environmental corrections, e.g. water vapour derived from the Fleet Numerical Oceanographic Center's 12-hour model, were already included. The Sea Level Anomalies (SLAs) data we received, stem from the first year of the ERM; SLAs are thus relative to the mean of the November 1986-November 1987 period. The data consist of 22 grids of SLAs, and figure 1 shows the ground tracks of such a grid over the tropical Pacific ocean. Tracks are separated from each other by about 1.5° at the equator, and there is a measurement every about 7 km along each track.

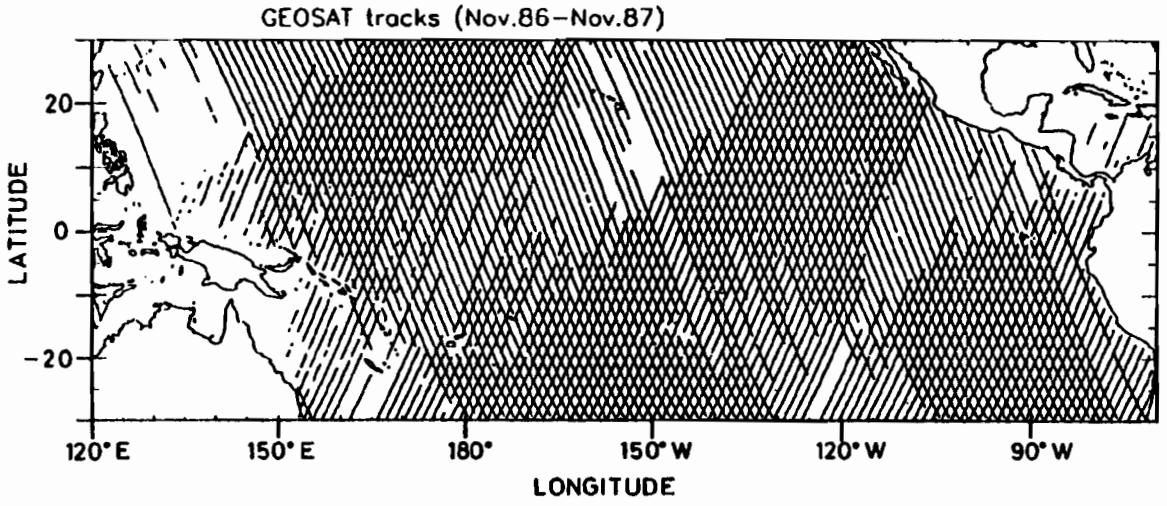

FIG.1. Ground tracks of the GEOSAT 17-day collinear orbit over the tropical Pacific ocean.

Our own data processing was made in three steps. Firstly, along track SLAs were smoothed using 300 km width non-linear median and linear Hanning filters. An example of such processing is given in figure 2. Secondly, by combining several tracks (6-7) in the zonal direction, time series of SLAs were generated in 0.5°x10° latitude-longitude boxes. Finally, smoothed records were produced by low-pass filtering in time and latitude using a 31-day and 3°-latitude Hanning filters. No smoothing in longitude was performed.

b. Evaluation

Comparisons between GEOSAT sea level and data from tide gauges, inverted echo sounders, and thermistor chains at various locations throughout the Pacific have suggested that altimeter time series have an RMS accuracy of about 3 cm (Cheney et al., 1988). As an example of our intercomparison figure 3 shows a GEOSAT SLA time series obtained in the warm pool (2°S-165°E), together with the 0/300db dynamic height anomaly derived from the ATLAS thermistor chain mooring at 2°S-165°E, and the 0/500db dynamic height anomaly obtained from CTD stations made during seven cruises. Although the data may differ by as much as 5 to 12 cm, they generally agree within a few centimeters. Notable

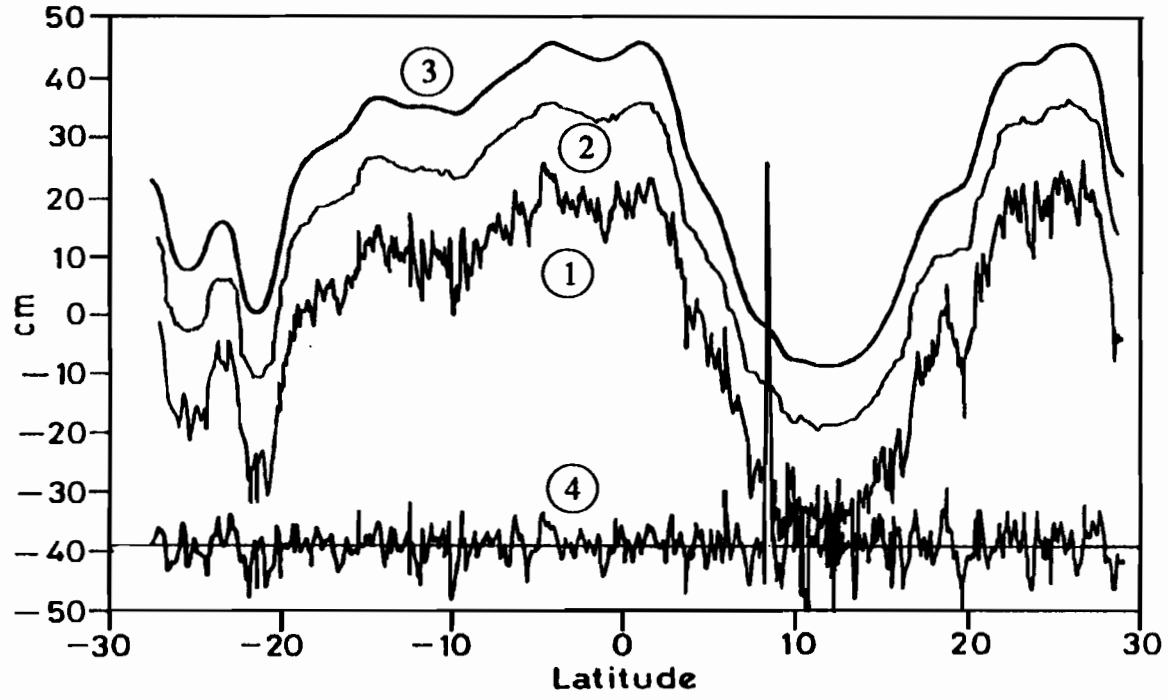

FIG.2. Along track processing of meridional sea level anomalies. Curve 1 denotes the raw sea level anomaly (cm) from 30°S to 30°N. Curve 2 is curve 1 shifted by +10 cm and despiked with a 3°-latitude non-linear median filter. Curve 3 is curve 2 shifted by +10 cm and smoothed with a 3°-latitude Hanning filter. Curve 4 is curve 1 minus curve 3.

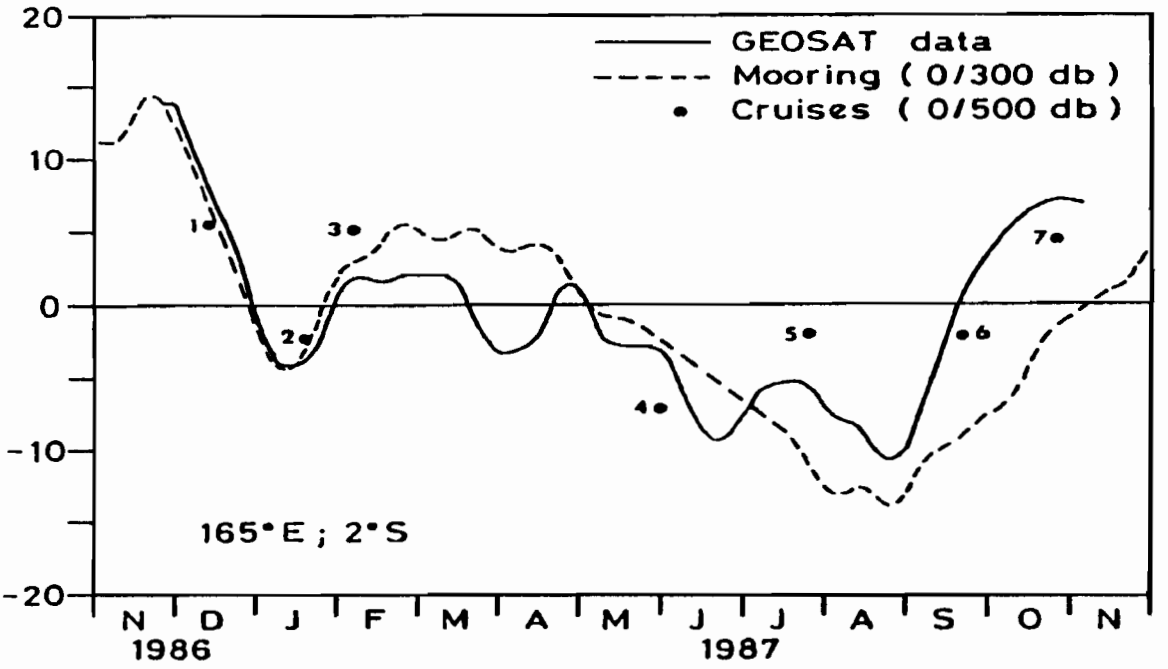

FIG.3. Comparison between Geosat SLA time series (full line), 0/300db dynamic height anomaly time series obtained from ATLAS thermistor chain moorings (broken line), and spot 0/500db dynamic height anomaly measurements derived from CTD stations from seven different cruises. Note that the 0/300 db data were linearly interpolated from May 20 to July 21, 1987. Cruise numbers are (1) US/PRC-2, (2) SURTROPAC-7, (3) JENEX-1, (4) SAGA-2, (5) SURTROPAC-8, (6) PROPPAC-1, and (7) US/PRC-3. The vertical scale denotes either cm (GEOSAT data) or dyn.cm (mooring and cruises).

differences between time series may be due to incomplete correction of environmental errors and/or they may reflect the idiosyncrasies of each type of observations (e.g., the dynamic height time series do not include the variability below 300 db as well as the salinity effects upon dynamic height computation; the CTD stations represent only spot measurements, etc...). The RMS scatter about the fitted line between the altimeter SLAs and the 0/300 db dynamic height anomaly is 4 cm. Thus, based on previous evaluations and on this last comparison, we conclude that GEOSAT altimeter data seems adequate for monitoring sea level variations in the tropics with an RMS accuracy of 4 cm. As a consequence, only SLAs above ± 8 cm, corresponding to a signal/noise = 2, will be further considered.

3. Results

Figure 4 represents the SLAs along the 165°E longitude, as a function of time and latitude. Four patches of SLA above ± 8 cm appear in the equatorial band. Our purpose is to sequentially analyse the mechanisms that generated these patches. In support of this analysis, we will refer to figures 5a-b presenting the zonal wind stress anomaly and SLA along the equator, both as a function of time, from the western to the eastern Pacific.

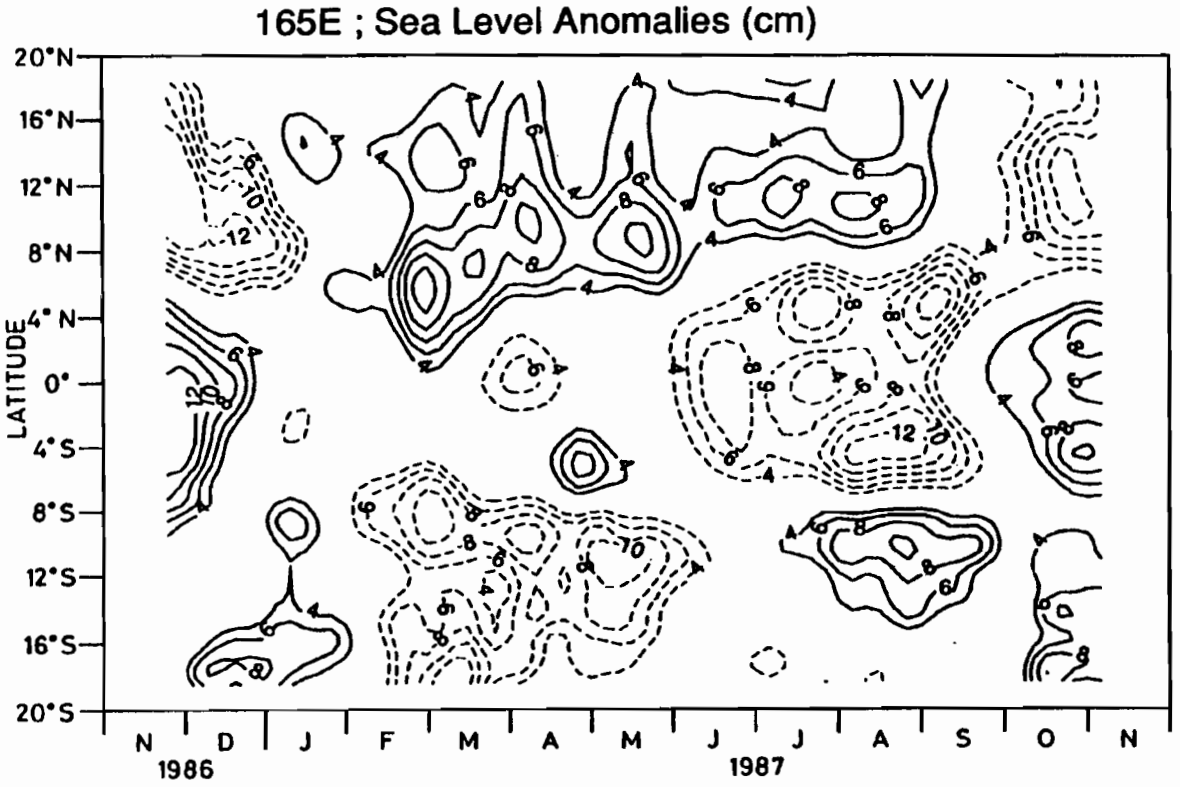

FIG.4. Geosat sea level anomalies (cm) as a function of time and latitude, along the 165°E longitude.

The first significant patch of SLA appears in November/December 986 (Fig.5b). It occurs in response to eastward wind anomaly located west of about 170°W (Fig.5a). The wind induces a downwelling equatorial Kelvin wave which propagates across the entire basin at about the first baroclinic phase speed c^k_1= 2.3 m.s^{-1} (Eriksen, 1982), as already documented by Miller et al. (1988). A Gaussian fit of the meridional SLA structure, east of the forcing area, is clearly in excellent agreement with the data, within ± 5° of the equator using c^k_1 = 2.3 m.s^{-1} (Fig.6).

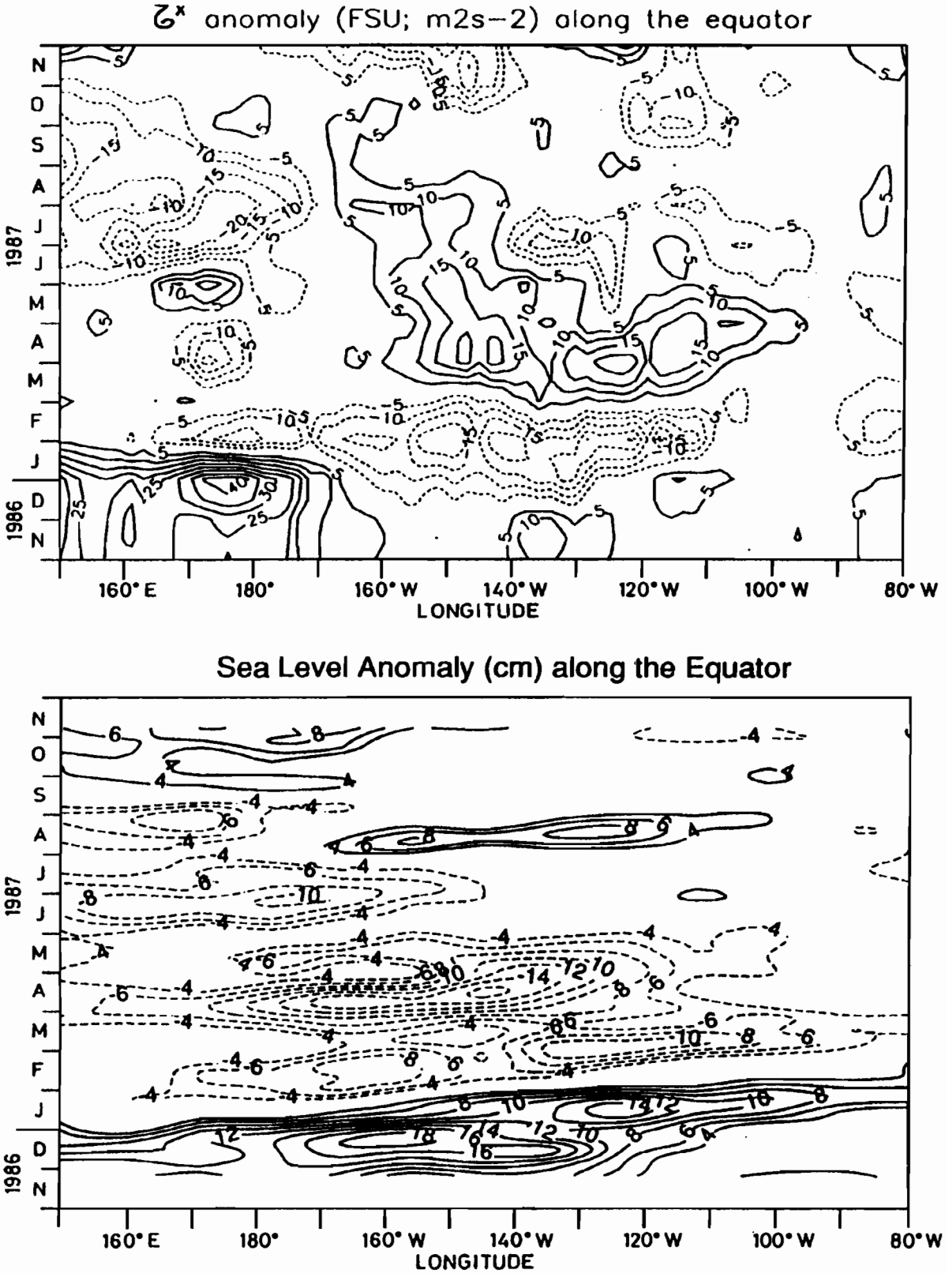

FIG.5. Top (a): Zonal wind stress anomaly ($m^2.s^{-2}$) along the equator as a function of time and longitude; Bottom (b): Sea level anomaly (cm) along the equator as a function of time and longitude.

The second significant sea level signal emerges in June 1987 (Fig.5b), just after a rapid zonal wind stress change near the 165°E longitude (Fig.5a). The wind seems to generate an upwelling Kelvin wave (Fig.5b) that propagates at least to the middle of the basin, where the Kelvin wave meets a downwelling-favorable wind stress. Figure 7 shows that a Gaussian fit of the meridional SLA structure, east of the forcing area, corresponds quite well to the data, within ± 5° of the equator, using c^k_1=2.3 m.s^{-1}.

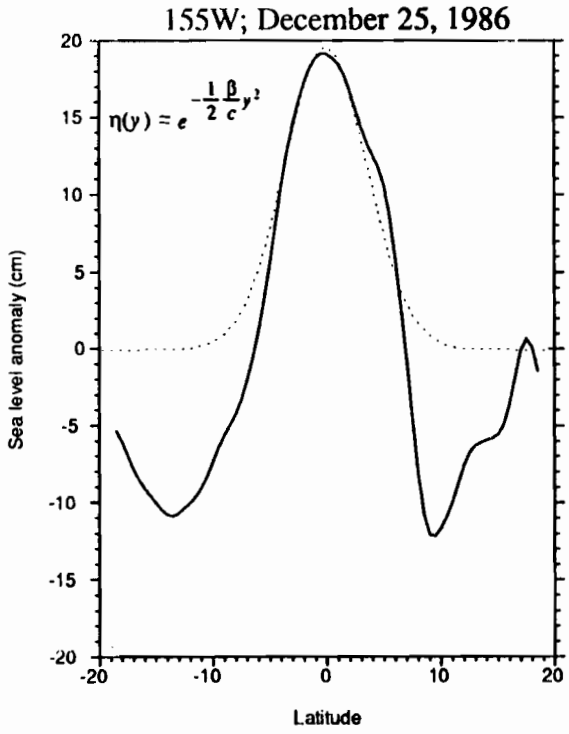

FIG.6. Gaussian fit (broken line) of the meridional (20°S-20°N) sea level anomaly structure (full line) at 155°W longitude, on December 25, 1986.

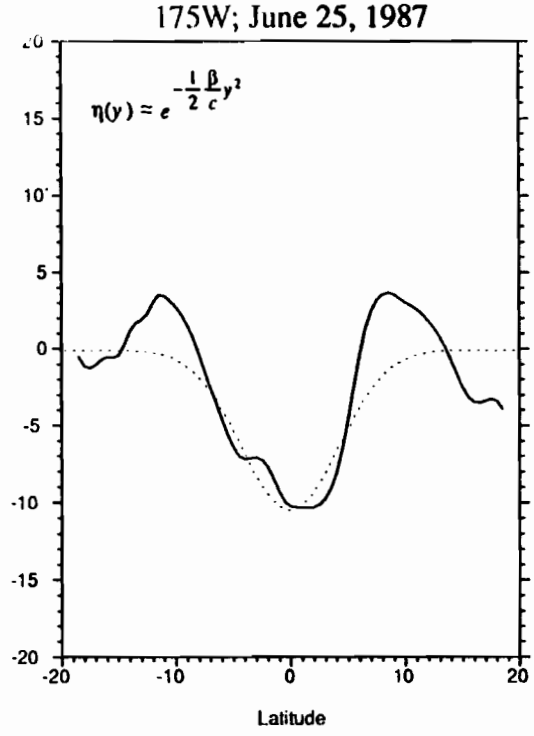

FIG.7. Gaussian fit (broken line) of the meridional (20°S-20°N) sea level anomaly structure (full line) at 175°W longitude, on June 25, 1987.

Two patches of SLAs in excess of ± 8 cm then arise in August-September 1987, at 165°E, symmetrical about the equator at about 4°N and 4°S (Fig.4). They result from the westward propagation of a first baroclinic (n=1) first horizontal (l=1) Rossby wave, as shown in Figure 8. The Rossby wave propagates at about c^R_1=0.9 m.s^{-1}, i.e. about one third (2l+1=3) of the aforementionned Kelvin wave phase speed. Figure 10 shows the good agreement between the meridional SLA structure and the theoretical shape of the Rossby wave (n=l=1), involving Gaussian and Hermite functions.

The upwelling Rossby wave portrayed in Figure 8 may result from two different mechanisms. First, due to the excellent timing agreement, we suggest that it might be the reflection of the upwelling equatorial Kelvin wave generated by the fast zonal wind stress change occuring east of 165°E , by the end of January 1987 (Fig.5a). This upwelling equatorial Kelvin wave, evidenced in figure 5b, hits the eastern coast by the end of March 1987, and then might reflect as an equatorial upwelling Rossby wave (Fig.8). Second, it should be noted that the upwelling Rossby wave may also be amplified or eventually generated by local forcing, as exemplified in figure 9 which shows a positive Ekman pumping anomaly beginning in early March 1987, between about 100°W and 160°W.

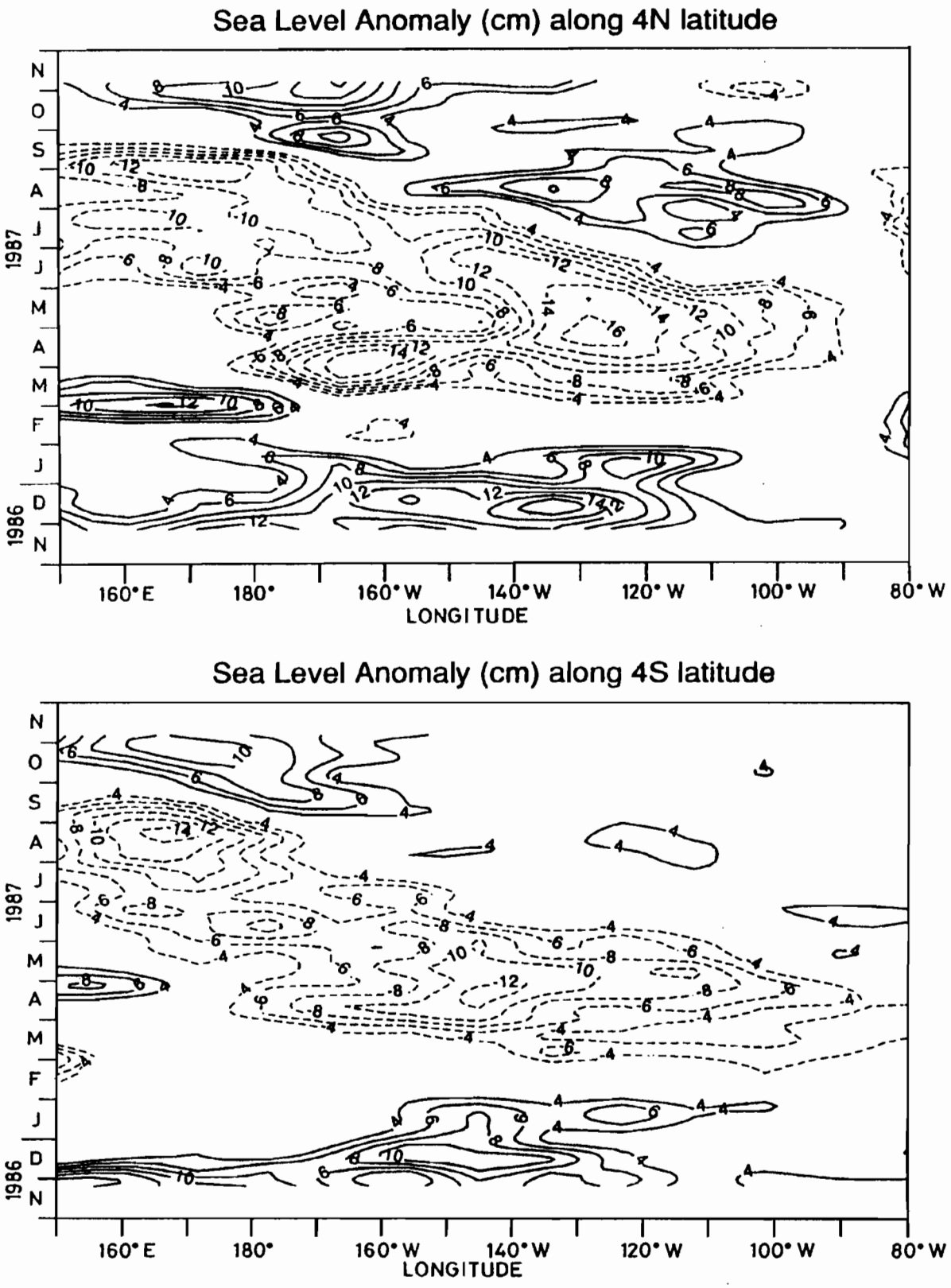

FIG.8. Sea level anomaly (cm) along the 4°N (top panel) and 4°S (bottom panel) latitudes, as a function of time and longitude.

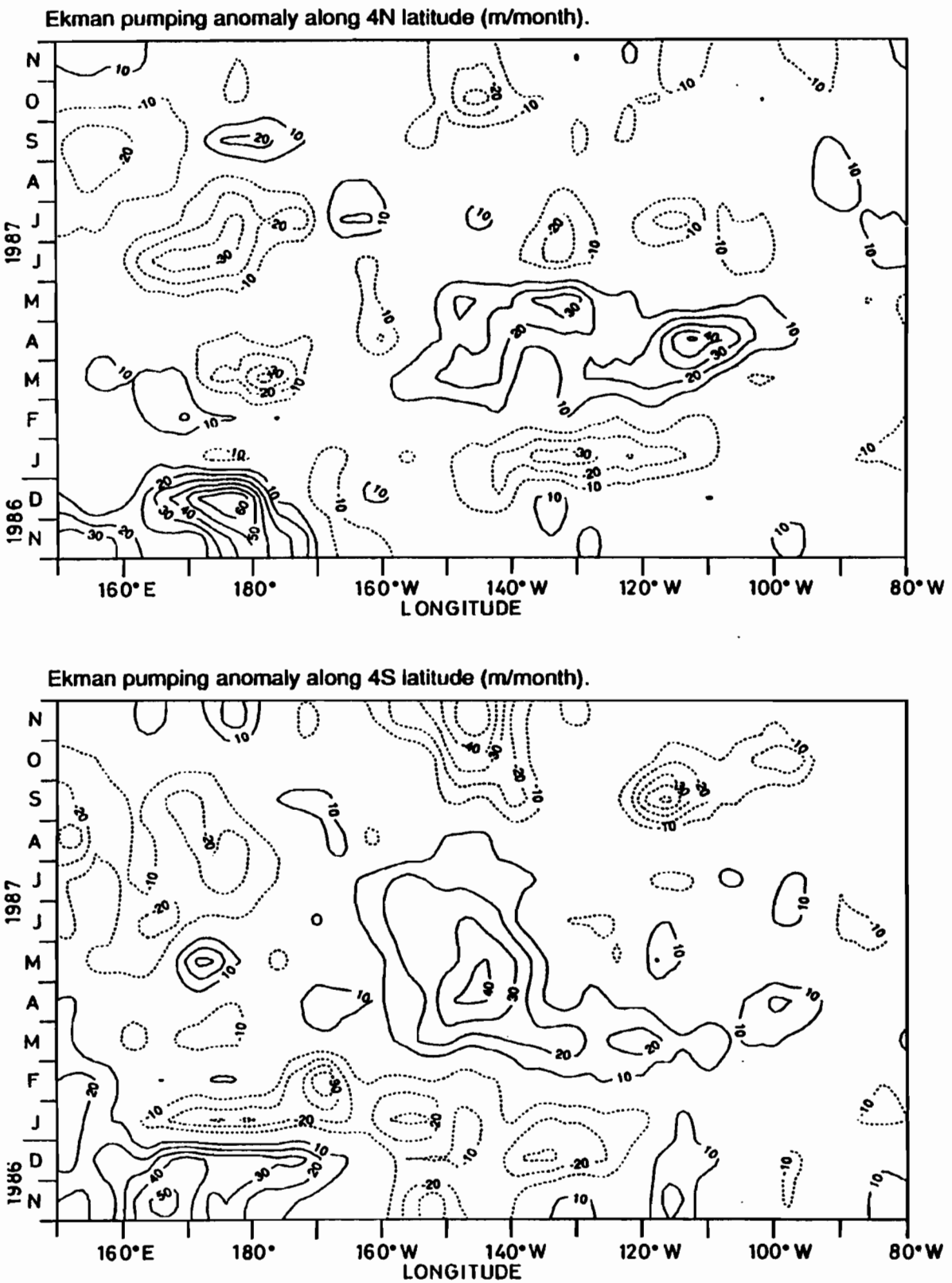

FIG.9. Ekman pumping anomaly (m.month^{-1}) along the 4°N (top panel) and 4°S (bottom panel) latitudes, as a function of time and longitude. Positive value is upward motion.

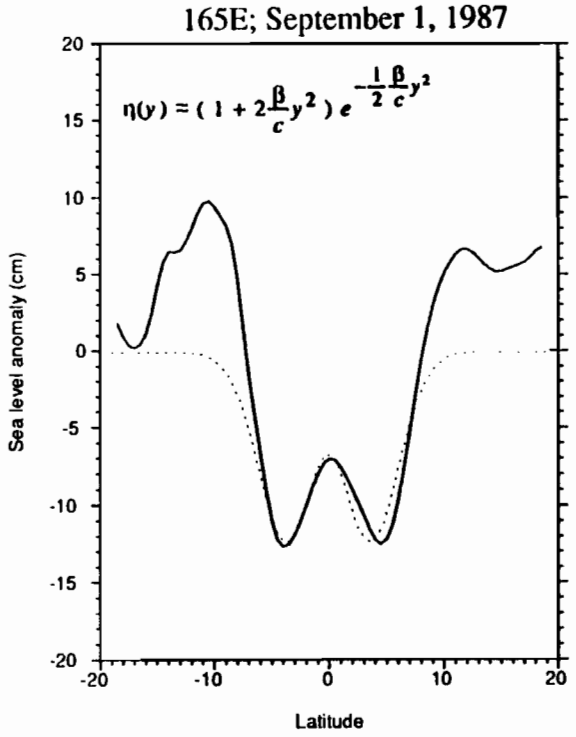

FIG.10. Least square fit (broken line) of the meridional (20°S-20°N) sea level anomaly structure (full line) at 165°E longitude, on September 1, 1987.

The relative importance of both mechanisms is now part of an ongoing study involving linear numerical model results.

In conclusion, we believe that first baroclinic Kelvin waves and (n=l=1) Rossby wave are the dominant sources of sea level changes in the equatorial band, during the 1986-87 El Nino.

Acknowledgements. Fruitful discussions with Yves du Penhoat have been much appreciated. This work could not have been conducted without the GEOSAT data provided by Chet Koblinsky and the programming support of François Masia. Support for this work, as part of the TOPEX/POSEIDON Science Working Team, was provided by the "Programme Télédetection Spatiale", trough AIP 59.88.46 and 9.88.25.

REFERENCES

APL, 1987: The Navy GEOSAT mission, Johns Hopkins Applied Physics Laboratory, technical digest, vol. 8, No 2, 290 pages. (Johns Hopkins Road, Laurel, MD 20707, USA).

Cheney R. and L. Miller, 1988: Mapping the 1986-1987 El Nino with GEOSAT data. *EOS*, 69, 754-755.

Cheney R., B. Douglas and L. Miller, 1988: Evaluation of GEOSAT altimeter data with application to tropical Pacific sea level variability. *J. Geophys. Res.*, **95**, 4737-4749.

Eriksen C., 1982: Equatorial wave vertical modes observed in a western Pacific island array. *J. Phys. Oceanogr.*, **12**, 1206-1227.

Miller L., R. Cheney and B. Douglas, 1988: GEOSAT altimeter observations of Kelvin waves and the 1986-87 El Nino. *Science*, **239**, 52-54.

Tai C.K, W. White and S. Pazan, 1989: Geosat crossover analysis in the tropical Pacific. 2. Verification of altimetric sea level maps with XBT and island sea level data. *J. Geophys. Res.*, **94,** 897-908.

White W., G. Meyers, J.R. Donguy and S. Pazan, 1985: Short term variability in the thermal structure of the Pacific ocean during 1979-82. *J. Phys. Oceanogr.*, **15,** 917-935.

Wyrtki, 1985: Water displacements in the Pacific and the genesis of El Nino cycles. *J. Geophys. Res.*, **90,** 7129-7132.

Vertical Thermal Structure Variability along 165°E During the 1986-87 ENSO Event.

Gérard ELDIN and Thierry DELCROIX

Groupe SURTROPAC, ORSTOM, BP A5, Nouméa, New Caledonia.

ABSTRACT

Modifications of the intertropical thermal structure along the 165°E meridian linked to the 1986-87 ENSO are described and analyzed from results of a series of cruises carried out by ORSTOM from Nouméa, and additional data from the US-PRC Western Pacific program cruises.

During the evolution of the ENSO event, changes in the vertical distribution of temperature are found to be restricted mostly to the upper 400m. Therefore, temperature anomalies and vertical displacements of isotherms can be computed in relation to a climatology deduced from XBT data available in the region.

Warming and deepening of surface layers are apparent before the onset of the ENSO event, more important in the southern hemisphere warm pool ; then, a cooling of thermocline layers appears close to the equator at the beginning of 1987. The corresponding equatorial shoaling of isotherms extends progressively poleward in both hemispheres to 10° of latitude, while reaching sub-thermocline layers. This anomalous temperature pattern persists until the first half of 1988. In June 1988 temperature anomalies have lowered or changed sign, returning to a configuration close to that observed prior to the onset of ENSO.

Dynamic height and heat content anomalies are shown to be correlated to large scale sea level anomalies from GEOSAT altimeter data. Differences emphasize the smoothing of structures by satellite measurements. Mechanisms for large scale evolutions away from the equator are searched for in the effects of local wind stress forcing.

1. Introduction.

In the western tropical Pacific, a large part of the oceanic variability associated to ENSO events is generated through heat accumulation and release, and forcing of equatorial trapped waves (Wyrtki, 1985, Busalacchi and O'Brien, 1981). Because of high surface temperatures, strong ocean-atmosphere energy transfers occur there, particularly in the region of SST > 28°C known as the Warm Pool. Effects of atmospheric forcing are most important in the surface layer, by affecting surface mixing, sea level and thermocline depth, while variability is weaker below the thermocline. In this surface layer, above 400m, availability of XBT temperature measurements for a long time permits us to compare between ENSO and non-ENSO periods.

To better understand the variability of the zonal circulation system and thermohaline structure of the western tropical Pacific, a series of semi-annual cruises has been undertaken since 1984 along 165°E (ORSTOM's SURTROPAC program). Other research programs have since begun and are still carried out in the region, mainly the US-PRC cooperative program. A general description of the hydrology from historical cruises and for the 1984-86 period has been done previously (Delcroix *et al*, 1987, Toole *et al*, 1988).

The purpose of this paper is to use results from these cruises carried out from 1986 to mid-1988 to study how the occurrence of the 1986-87 ENSO event affected thermal structure and heat storage.

From November 1986-November 1987 are also available sea-level anomaly data from the GEOSAT Exact Repeat Mission (ERM), which are directly related to 'real' sea level and dynamic heights. We will then examine how much of the thermal variability observed during these cruises is reflected in satellite altimeter data.

ORSTOM
CENTRE DOCUMENTATION
Montpellier

F 30214

From monthly wind stress data produced by the Florida State University (FSU) analysis, local contributions of wind forcing to the variability will be estimated.

2. Data.

Data gathered during 11 cruises are available to us at this time; Table 1 gives characteristics of these cruises. 10 are carried out along the 165°E meridian, but the Saga 02 cruise follows a different path, from 160°E to 170°E. Its results can still be used because of weak longitudinal variability. Best common coverage is obtained from 10°N-10°S, and emphasis will be put on this region.

Sections collected, 1986-88.

Cruise	Origin	Time	Section track
Surtropac 5	ORSTOM	10-26 January 1986	20°S-10°N.
Surtropac 6	ORSTOM	17-27 June 1986	20°S-10°N.
US-PRC 2	WHOI-SOA	8-16 December 1986	10°N-6°S at 165°E, then to 10°S at 160°E.
Surtropac 7	ORSTOM	10-27 January 1987	20°S-10°N.
Saga 2	SIO-IAG	23 May-6 June 1987	20°N-5°S at 160°E, then 10°S-19°S at 170°E.
Surtropac 8	ORSTOM	2-21 July 1987	20°S-10°N.
Proppac 1	ORSTOM	9-20 September 1987	20°S-6°N.
US-PRC 3	WHOI-SOA	13-22 October 1987	Same as for US-PRC 2.
Surtropac 9	ORSTOM	16-28 January 1988	20°S-10°N.
Proppac 2	ORSTOM	28 March-8 April 1988	20°S-6°N.
Surtropac 10	ORSTOM	14-27 June 1988	20°S-10°N.

TABLE 1. Detail of cruise tracks and dates. ORSTOM = Institut Français de Recherche Scientifique pour le Développement en Coopération, Nouméa, New Caledonia. WHOI = Woods Hole Oceanographic Institution, Woods Hole, MA, USA. SOA = State Oceanic Administration, Qingdao and Guangzhou, PRC. SIO = Scripps Institution of Oceanography, La Jolla, CA, USA. IAG = Institute of Applied Geophysics, Moscow, USSR.

All cruises have stations every degree of latitude, and every 1/2 degree close to the equator, excepted the Saga 02 cruise, where sampling is coarser. However, time sampling is very irregular; periods between cruises range from 1 to 6 months; fortunately, denser sampling is found at the peak and relaxation phases of the event, during the second half of 1987 and the beginning of 1988. Because of dense meridional sampling and coarse time sampling, it would be misleading to try to study these cruise results as time series at given latitudes, because time between cruises is often longer than time coherence of meridional structures.

Satellite sea-level anomaly data are filtered in time and space to remove noise and bad satellite tracks (Delcroix *et al*, this volume). This technique eliminates variability below 15 days and 1.5 degree of latitude. Only anomalies > |4cm (above rms accuracy) are kept as significant.

3. Climatology.

Anomalies of thermal structure are computed for each cruise from a monthly climatology obtained from XBT data for 1979-81 + 1984-85, in the 155°E-175°E region. Previous works (Hanawa and Yorikata, 1987, Hénin, personnal communication) have shown that differences in temperature data from XBT and CTD measurements are negligible; however, a difference of about 5% in depth measurements can be found. At the depth of the thermocline, this leads to an overestimation of isotherm depths of less than 10m in XBT data, which is small compared to observed displacements of the thermocline.

Figure 1 presents the climatological thermal structure seasonally averaged for December-February and June-August. Prominent features of this climatology are summarized below:

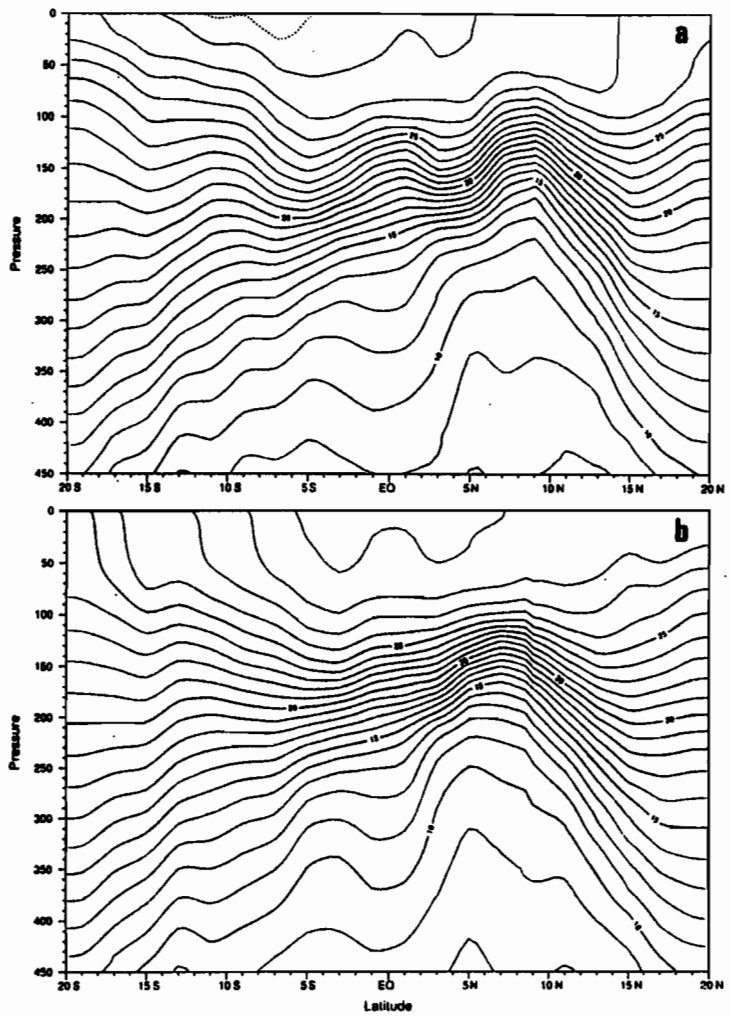

FIG. 1. Seasonal averages of temperature 0-400m, a) December-February (DJF) and b) June-August (JJA), from a monthly climatology obtained from XBT data 1979-81, 1984-85, in the 155°E-175°E region.

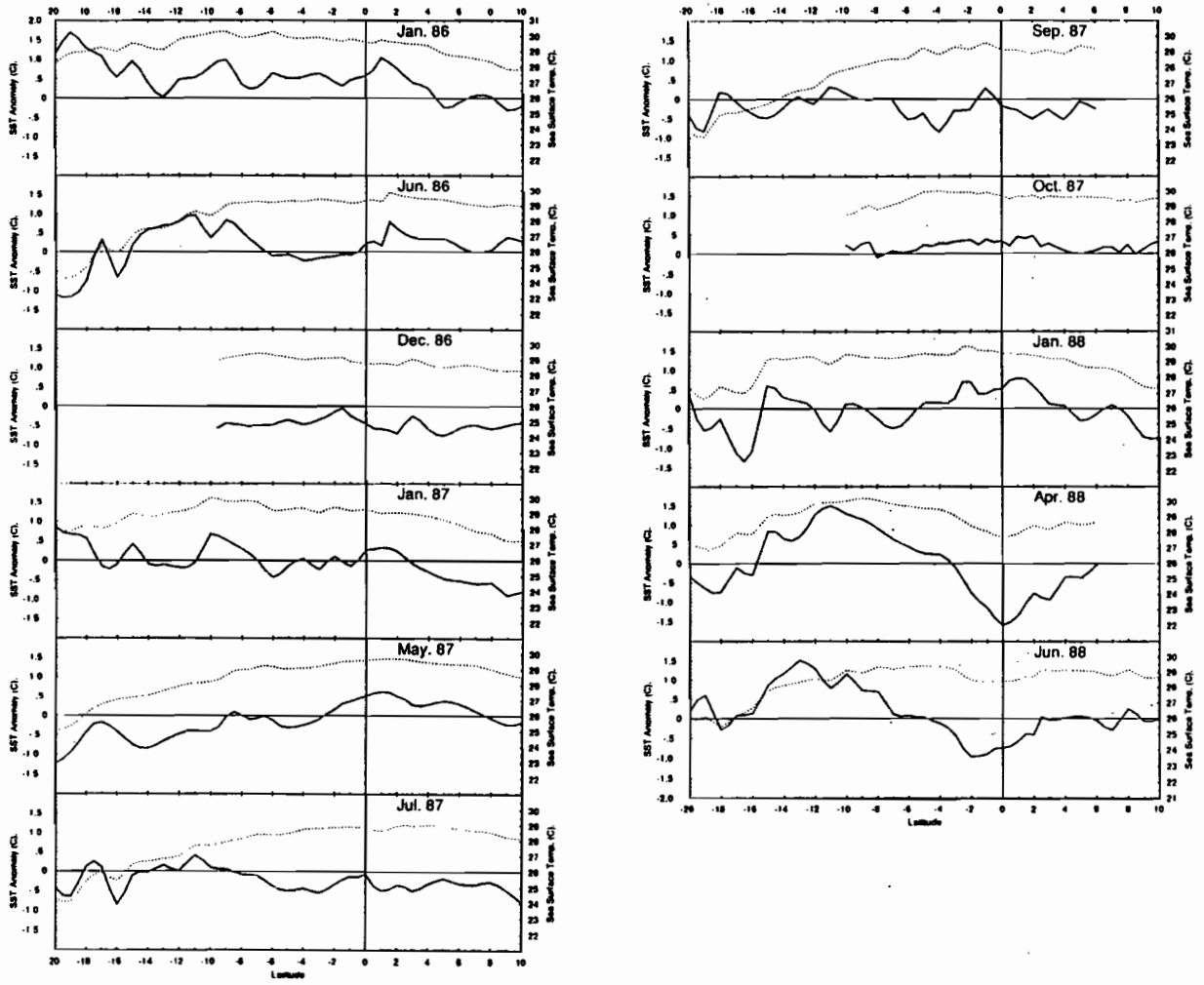

FIG. 2. SST and its anomaly for each of the 11 cruises as a function of latitude. SST: dotted lines, values on rightaxis. SST anomaly: solid lines, left axis.

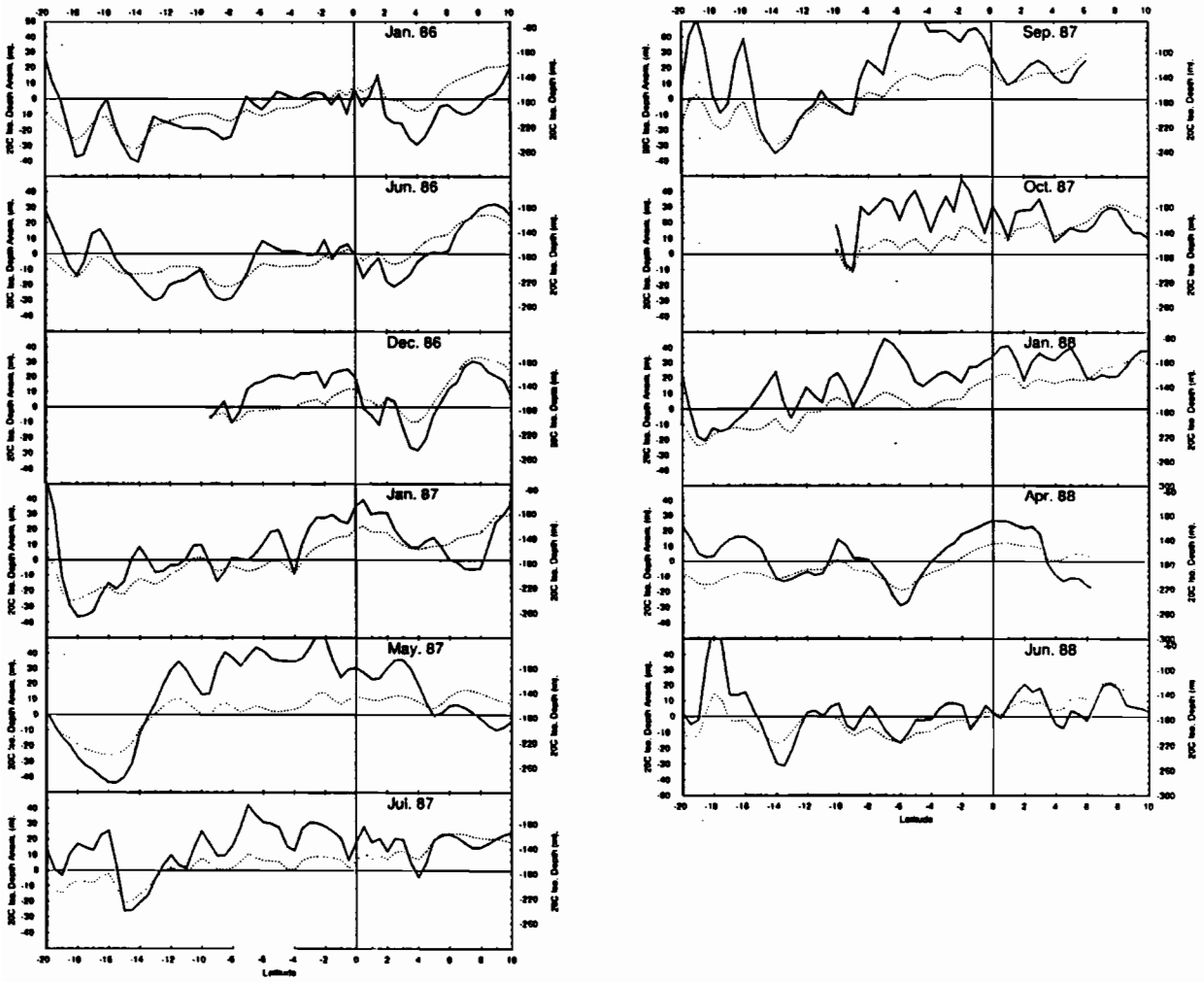

FIG. 3. Depth of the 20°C isotherm and its anomaly for each cruise. Isotherm depth: dotted line, right axis. Isotherm depth anomaly: solid line, left axis.

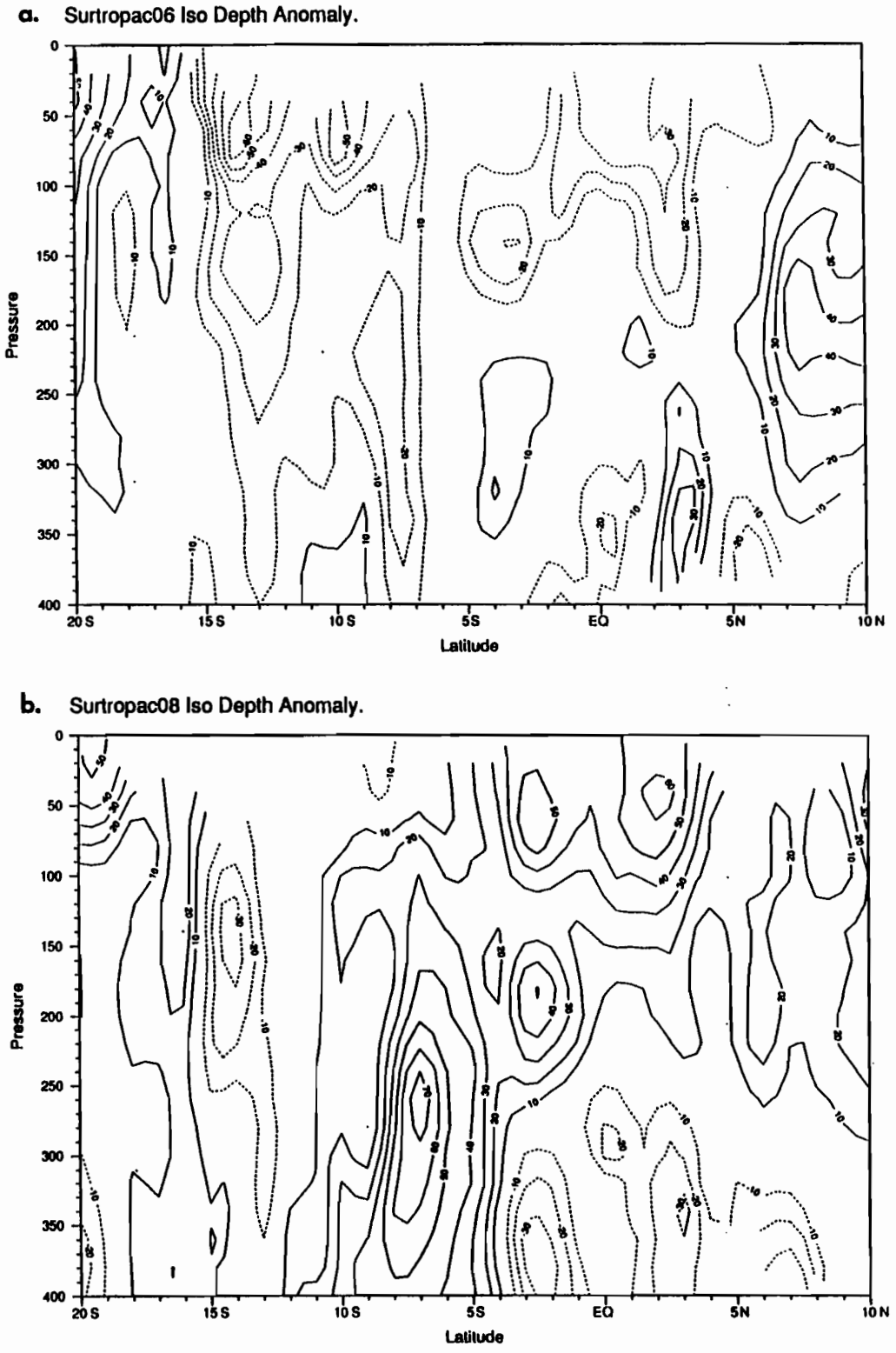

FIG. 4. Isotherm depths anomalies during a) the build-up and b) the peak phases of the 1986-87 ENSO. Anomalies at a given depth represent deviations of the corresponding isotherm depth from its monthly climatological value. Upward deviations positive, solid lines; downward deviations, dotted lines. Contouring interval is 10m.

-Weak seasonal variability of SST from 5°S-5°N, where SST stays above 29°C.
-Seasonal displacements of the warm pool, defined as the region where SST is above 28°C, which moves from 18°S-15°N to 10°S-20°N, following the summer hemisphere.
-Presence of a strong thermocline, centered around 20°C, with the ridges and troughs associated to geostrophic circulation in the 10°S-15°N band
-Weak seasonal variations below the 13°C isotherm.

4. Thermal structure evolution.

In the frame of this report, it is not possible to examine the complete 0-400 m structure for each cruise. Instead, three parameters are selected, as representatives of the upper water column:
-SST, which variability is weak, but which plays an important role in heat and moisture exchange.
-Depth of the 20°C isotherm, which is linked to the depth of the thermocline as shown by climatology.
-Heat content above 300m (HCo, given as 0-300m averaged temperature), which shows effects of combined local heating and advection.

a. SST.
Figure 2 presents the evolution of SST from January 1986-June 1988: SST anomalies stay weak, especially in the 10°S-10°N region, almost never exceeding 1°C. This explains that short term variability may hide evolutions from cruise to cruise. Noticeable are high temperatures found in January 1986 from 20°S-5°N; afterwards, the general trend is toward negative anomalies, reaching -1°C, especially north of the Equator during 1987, with exception of the Saga 02 cruise. After January 1988, SSTs climb, but this is obscured from 5°S-5°N by an unusual equatorial upwelling in April and June 1988.

b. Depth of 20°C Isotherm.
The evolution of the 20°C isotherm depth is presented on Figure 3: the three 1986 cruises show anomalous deepening (20-30m) of the thermocline from 15°S-8°S and 3N°-6°N, while the equatorial region stays close to normal. Also, an important increase in slope from 6°N-10°N corresponds to the increase in North Equatorial Countercurrent (NECC) transport already noted (Toole *et al*, 1988); this strong slope persists at the end of 1986, but the equatorial thermocline is now shoaled by 20m; in anomalies, this shoaling is enhanced because against seasonal variations. Shoaling increases again in 1987 to 30-40m and extends poleward in both hemispheres, as the NECC slope disappears. Anomalously high thermocline persists from 10°S-10°N, until at least January 1988. In June 1988, on the 20°S-10°N average the thermocline has returned to normal, after the upwelling episode of April 1988.
This evolution of the thermal structure is illustrated in Figure 4, which presents isotherm depths anomalies for all isotherms on the 0-400m depth range, at the beginning and during the peak phase of the ENSO event: in June 1986, the thermocline isotherms are deepened from 15°S-5°N, while they tend to shoal northward of 5°N. A year later, these isotherms are all displaced upward by more than 20m from 10°S to at least 10°N.

c. Heat Content.
Variations of heat content (not shown) are in agreement with thermocline displacements: heat accumulates at the beginning of 1986, and then is released, from June 1986 on, first around the equator, and extending poleward to 10°S-10°N. During 1987, average temperature from 10°S-10°N is more than 1°C below normal. Again this situation inverses rapidly in the first half of 1988, while going through the upwelling event.

These three parameters lead to the conclusion that the 1986-87 ENSO is characterized by a slow cooling of the warm pool, beginning at the equator in June 1986, extending to 10°S-10°N in mid-1987. Thermocline stays 30-40m shallower than normal, and average 0-300m temperature 1°C below normal, until sometime between January and April 1988: during that period a strong upwelling further cools the equatorial region, while heating poleward of 5° of latitude takes the thermal structure back to normal.

5. Comparison with GEOSAT Sea Level Anomalies.

It has been shown that results from cruise stations reflect long term variations associated with the ENSO event, but partly hidden by short scale variability. For part of the period of interest GEOSAT Sea-Level Anomaly data (GSLA) is available to complement cruise results. Several studies (Wyrtki, 1987, Miller *et al*, 1988, Tai *et al*, 1989) have shown that GSLA are good approximations of island sea level and dynamic height anomalies on scales larger than 1 month and a few hundredths of kilometers. Our purpose is to assess how much of the thermal variability captured by discrete cruises is also reflected in GSLA.

During the November 1986-November 1987 ERM period, six cruises are carried out, of which results can be used for comparisons. GSLAs are expected to better reflect vertically integrated parameters, like dynamic height (DH) and heat content (HCo, defined as above). To allow comparison , anomalies of DH and HCo are computed relative to the ERM period (11/86 - 11/87). At each latitude, we use an average of data from the 6 cruises, gridded on a 15 days, half-degree of latitude grid. To obtain a spatial smoothing comparable to what was used for GSLA, cruise data are smoothed alongtrack by a Hanning filter of 300km length.

Figure 5 shows scatter plots for DH and HCo vs GSLA. Correlation coefficients are 0.71 (DH) and 0.65 (HCo), but points are not independent and multiple smoothings do not allow for precise significance of these correlations. Rms difference about the fitted line for DH is about 4cm. Correlations are slightly better when limited to 10°S-10°N, which is in agreement with the fact that SL, DH and HCo are better correlated in this band because of the presence of a steeper pycnocline (Rébert *et al*, 1985).

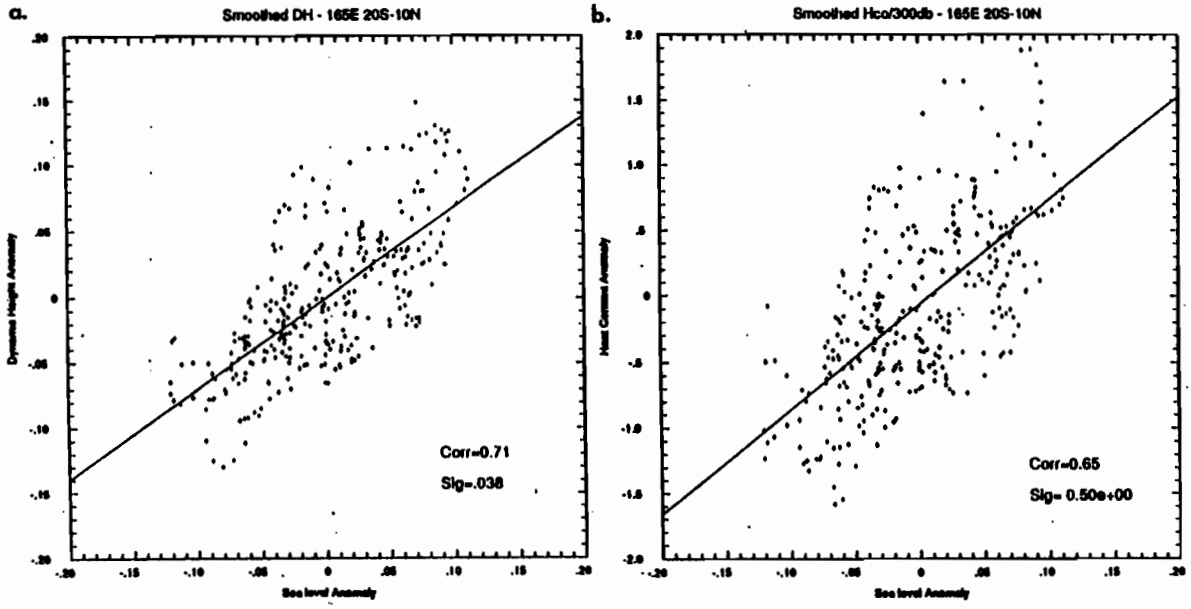

FIG. 5. Scatter plots of a) dynamic height anomalies and b) heat content anomalies versus GEOSAT sea level anomalies. Dynamic height and heat content values are obtained by interpolation to every 1/2 degree of latitude of 6 cruises stations to match GEOSAT 1/2 degree sampling. Solid line shows least squares linear regression fit.

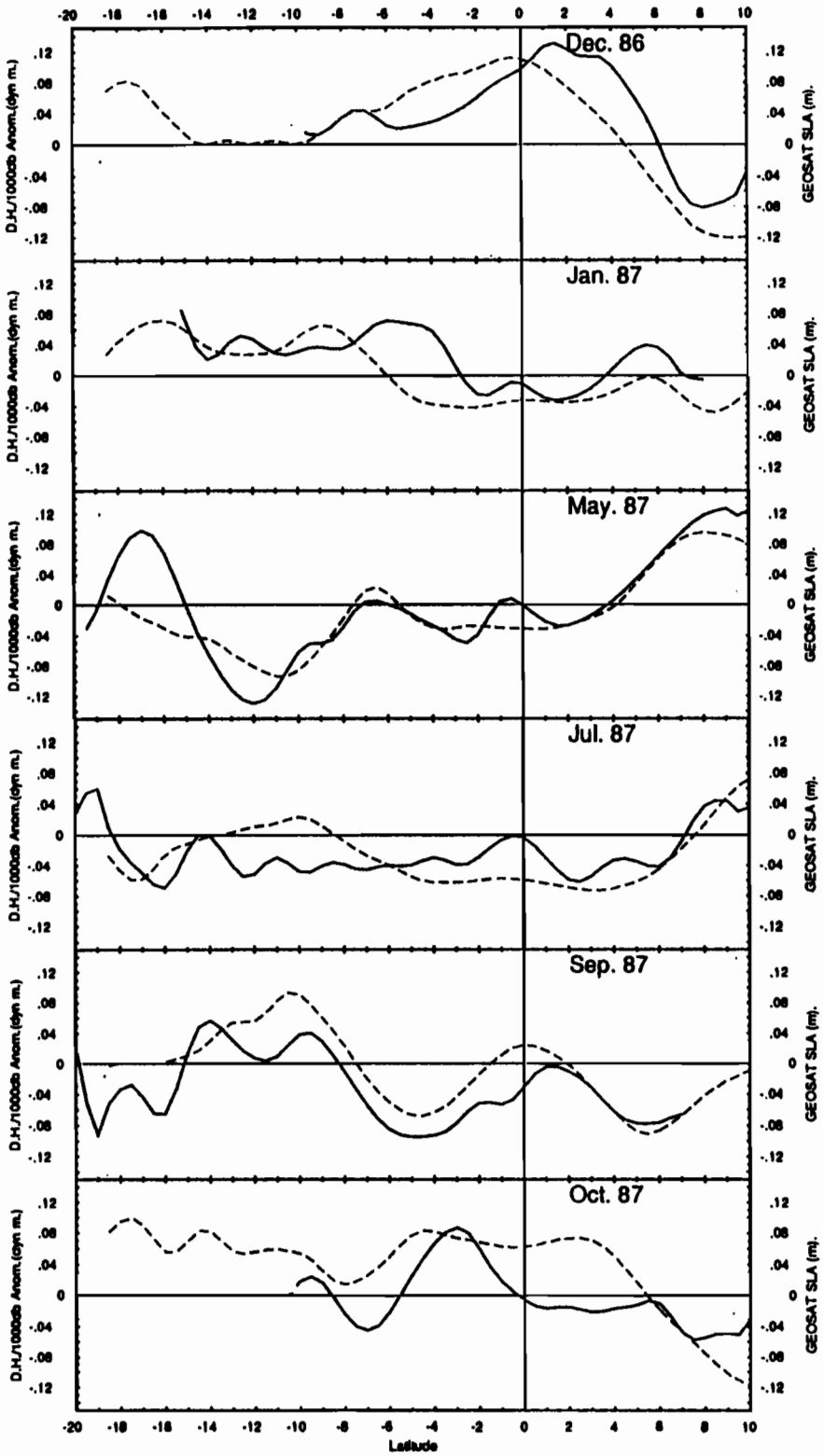

FIG. 6. Dynamic height (DHA) and GEOSAT sea level anomalies (GSLA) for each of the 6 cruises as a function of latitude. DHA: solid lines . GSLA: dashed lines.

More insight on relations between DH and GSLA can be obtained by comparing these two data sets for each cruise (Figure 6). The December 1986 cruise crosses a patch of high GSLA centered on the equator, which has been shown (Miller *et al*, 1988, Delcroix *et al*, this volume) to be associated to a downwelling Kelvin wave excited west of our zone. This high sea level is also reflected in DH, but displaced to the North by 2 degrees of latitude. In January 1987 this pulse has already disappeared, in GSLA and DH. The relatively high DH around 5°S is not reflected in GSLA; it must be noted that, from 5°S-5°N GSLA are close to the noise level (below 4cm). Best agreement is found in May 1987 for the Saga 02 cruise, excepted south of 14°S. There , cruise path is in the wake of Vanuatu islands, and sampling coarse. This is also a place of poor satellite coverage. North of 12°S good agreement may be explained in part by a lack of short scale variability for this particular cruise. In July 1987 DH is flat, excepted north of 5°N: agreement is good only along this northward slope. For the last 2 cruises DH are generally below GSLA, but difference does not exceed the 4cm rms difference.

Comparisons between HCo anomalies and GSLA (not shown) reveal the same indications as dynamic height, which shows that variability of sea level is mostly related to vertically integrated temperature variations.

It is noteworthy that, because of the generally low sea level state over which GSLA are computed, positive deviations are enhanced compared to what is referenced to a climatology: the most striking example is the positive pulse of GSLA at the beginning of 1987, which hardly appears in climatological anomalies, although it is a signature of important dynamics.

6. Indications from local wind forcing.

Anomalies of wind stress and wind stress curl along 165°E can provide some hints on the importance of local forcing in the observed variability of the temperature structure: from pseudo wind stress values from the FSU analysis, anomalies are computed relative to the 1979-81 + 1984-85 reference period, to allow comparison with thermal anomalies (Fig. 7).

The first half of 1986 is characterized by a weak north-west monsoon south of the equator, and stronger trades, i.e. easterly anomalies. Beginning in October 1986 strong westerly anomalies appear corresponding to a strong monsoon, and also strong trades in the extreme north and south of the zone. Through 1987 generally westerly anomalies continue, peaking with the return of the seasonal monsoon, still abnormally strong. February-June 1988 is characterized by a return of the trades, strong in the north, and weak in the southern hemisphere.

Close to the equator the consequences of local forcing are generally indiscernible. However, in April-June 1988, the return of trades across the equator can explain the unusually strong upwelling reaching deep in the thermocline.

Away from the equator, poleward of 4-5 degrees, Ekman pumping can play a role (Fig. 8): caused mainly by the strong meridional gradients of the zonal wind stress component, Ekman pumping shows a tendency to lift up the thermocline from the end of 1986 to the end of 1987. This may qualitatively explain the poleward extension of anomalously high thermocline which develops after January 1987, and particularly in May 1987 south of 10°S, after the strongest anomalies. In the first half of 1988, effects of Ekman pumping reverse, consistently with the deepening of the thermocline observed poleward of 4 degrees in April and June 1988.

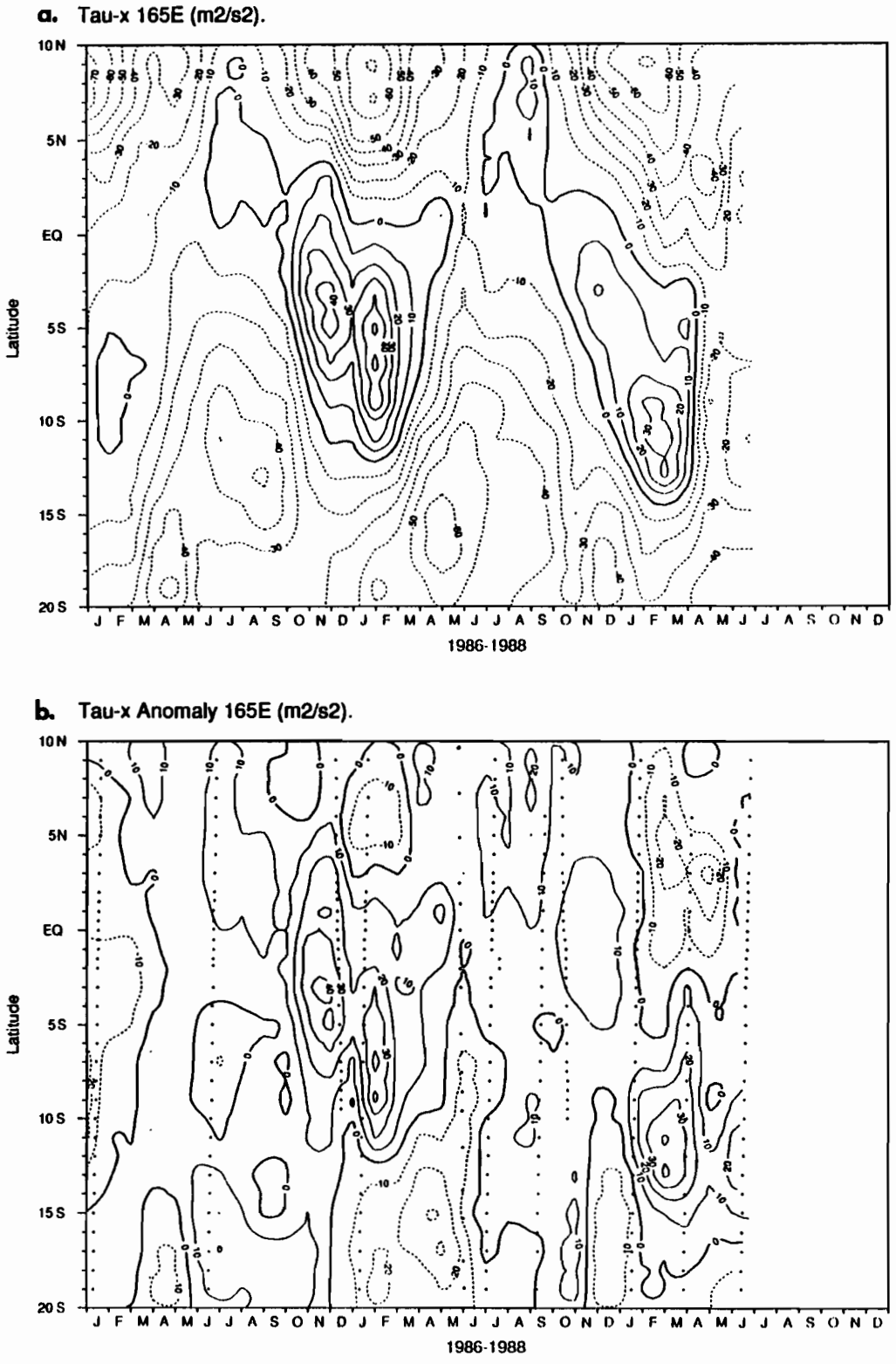

FIG . 7. Zonal component of pseudo wind stress (a) and its monthly anomaly (b) for 1986-88, from Florida State University Analysis. Positive values eastward, solid contours. Negative values westward, dashed contours. Contouring interval is 10 m^2s^{-2}.

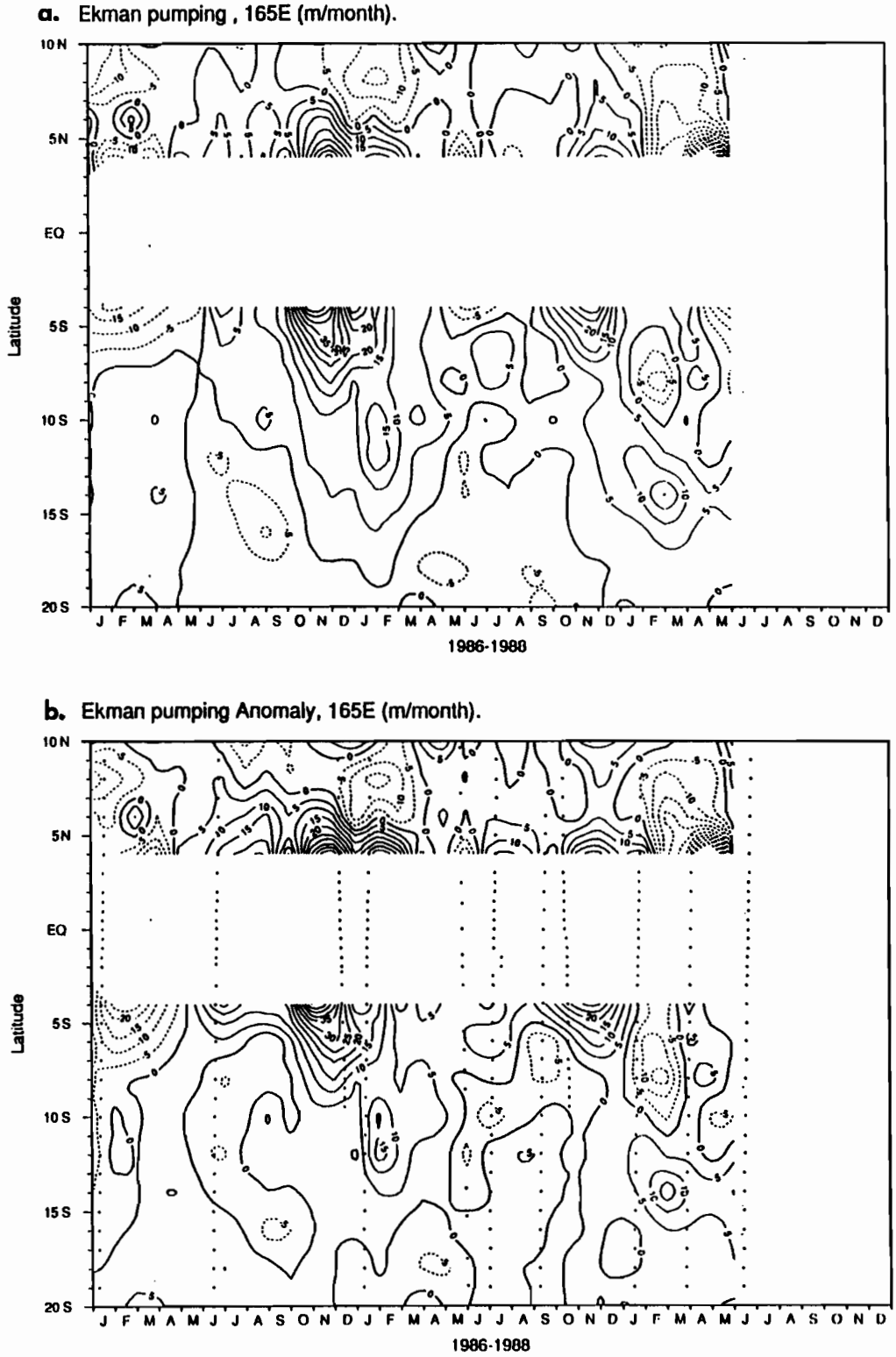

FIG. 8. Ekman pumping (a) and monthly anomaly (b), poleward of 4° of latitude, for 1986-88. Upward pumping positive, solid contours. Downward pumping, dashed contours. Contouring interval is 5 m.month^{-1}.

7. Conclusion.

Temperature data from 11 cruises carried out in the Western Pacific in 1986-88 have been used to study the variability of the vertical thermal structure during the 1986-87 ENSO event.

The 1986-87 ENSO along 165°E is characterized by a small increase of SST (0.5°C) in the 10°S-10°N band at the beginning of 1986, associated to a deepening of the thermocline of 20-30m. Then, SST decreases by about 1°C, and thermocline shoals by about 40m, beginning at the equator in January 1987, and extending poleward to 10°N-10°S. Average temperature above 300m is lowered of about 1°C.

GEOSAT Sea Level Anomalies are fairly correlated to cruise results for dynamic height and heat content, showing the same large scale patterns.

This anomalous thermal structure is maintained in part by equatorial wave dynamics, but also by Ekman pumping caused by anomalously westerly winds. This situation is rapidly reversed sometime between January and April 1988, where thermocline is deepened poleward of 5 degrees of latitude, and strong trades cause a return of equatorial upwelling.

Acknowledgments. We gratefully thank J. Toole from WHOI for having provided the US-PRC cruises data, and L. Talley, SOI, who made the Saga 2 cruise data available. We are indebted to C. Koblinsky from NASA/Goddard Space Flight Center for pre-processing and timely distribution of the GEOSAT altimeter data.

REFERENCES

Busalacchi A.J., and J.J. O'Brien, 1981: Interannual Variability of the Equatorial Pacific in the 1960's. *J. Geophy. Res.*, **86-C**, 901-907.

Delcroix T., G. Eldin and C. Hénin, 1987: Upper Ocean Water Masses and Transports in the Western Tropical Pacific (165°E). *J. Phys. Oceanogr.*, **17**, 2248-2262.

Hanawa K., H. Yorikata, 1987: Detection of Systematic Errors in XBT Data and their Cor rection. *J. Ocean. Soc. Japan*, **43**, 68-76.

Miller L., R.E. Cheney and B.C. Douglas, 1988: GEOSAT Altimeter Observations of Kel vin Waves and the 1986-87 El Nino. *Science*, **239**, 52.

Rébert J.-P., J.-R. Donguy, G. Eldin, K. Wyrtki, 1985: Relations Between Sea Level, Ther mocline Depth, Heat Content, and Dynamic Height in the Tropical Pacific Ocean. *J. Geophy. Res.*, **90-C**, 11719-11725.

Tai C.K., W.B. White, S.E. Pazan, 1989: GEOSAT Crossover Analysis in the Tropical Pa cific. 2: Verification Analysis of Altimetric Sea Level Maps with XBT and Island Sea Level Data. *J. Geophy. Res.*, **94-C**, 897-908.

Toole J.M., E. Zou and R.C. Millard, 1988: On the Circulation of the Upper Waters in the Western Equatorial Pacific Ocean. *Deep Sea Res.*, **35**, 1451-1482.

Wyrtki K., 1985: Water Displacements in the Pacific, and the Genesis of El-Nino Cycles. *J. Geophys. Res.*, **90-C**, 129-132.

Wyrtki K., 1987: Comparing GEOSAT Altimetry and Sea Level. *Eos AGU Trans.*, **68**, 731.

On the Relationship between Winds and Upper Ocean Temperature Variability in the Western Equatorial Pacific

Michael J. McPHADEN

Pacific Marine Environmental Laboratory
National Oceanic and Atmospheric Administration
7600 Sand Point Way NE
Seattle, WA 98115/0070 - U.S.A.

ABSTRACT

In this study we examine the relationship between winds and upper ocean temperature variability using data from an equatorial mooring at 0°, 165°E. The analysis focuses primarily daily to monthly time scale variations during 1986 and 1987 at the height of the 1986-87 El Niño/Southern Oscillation event. The period is one of high mean sea surface temperatures (≥29°C) and frequent outbreaks of westerly winds. We infer that in general wind-driven vertical advection and entrainment from the thermocline are not likely to be important processes affecting surface temperatures in the western equatorial Pacific. Conversely, we conclude that variations in evaporative cooling may account for a significant percentage of the observed surface layer temperature variance during the study period.

1. Introduction

Mean sea surface temperatures ≥29°C in the western equatorial Pacific are among the warmest in the world ocean. Thus, this region is characterized by vigorous air-sea interaction because turbulent heat exchange between the ocean and the atmosphere is a highly nonlinear function of sea surface temperature (SST). In extreme cases, air-sea interactions in the western Pacific may lead to El Niño/Southern Oscillation (ENSO) events which are coupled ocean-atmosphere phenomena occurring every 4–7 years [*Rasmusson and Wallace,* 1983]. ENSO has global climatic impacts, some of which can be traced to western Pacific SST anomalies of ≤1°C (e.g. *Nicholls,* 1985; *Palmer and Mansfield,* 1984). These impacts may be predictable months to years in advance provided the processes involved in SST change can be understood and reliably modeled.

While it is generally conceded that understanding SST variability is important for understanding and predicting ENSO, little is known quantitatively about the atmospheric and oceanic processes that control this variability. The purpose of this study therefore is to examine the relationship between wind forcing, SST and surface layer heat content using data from an equatorial current meter mooring at 0°, 165°E. The analysis is based on data collected during 1986 and 1987 and focuses mainly on time scales of days to months. This period coincides with the 1986–87 ENSO during which pronounced interannual variations occurred throughout the tropical Pacific (*Kousky and Leetmaa,* 1989; *McPhaden et al.,* 1990).

The paper is outlined as follows. Section 2 briefly describes the data used in this study. This is followed in Section 3 by discussion of how wind variations may be related to turbulent fluxes across the air-sea interface, vertical advection and entrainment from the thermocline. Major results and conclusions are summarized in Section 4.

ORSTOM
CENTRE DOCUMENTATION
Montpellier

F 30215

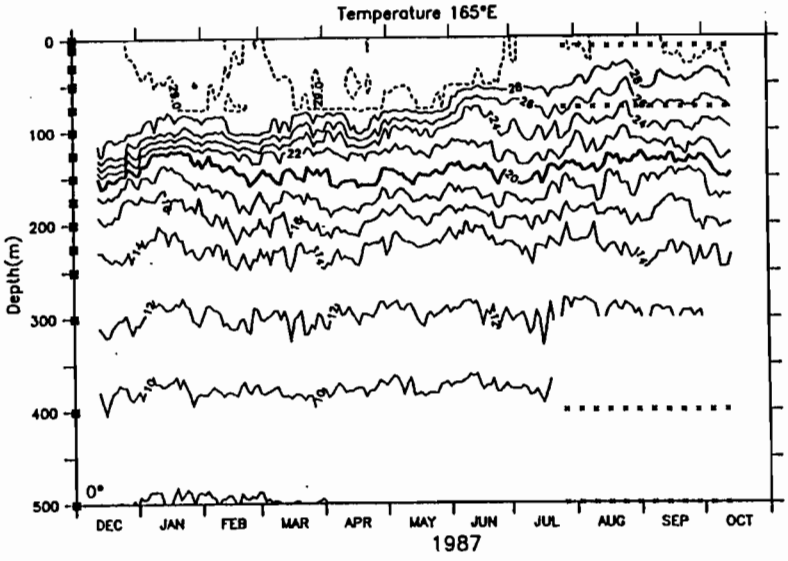

Figure 1. Contours of daily averaged temperatures at 0°, 165°E for 13 December 1986 to 14 October 1987. Contour interval is 2°C, except that the 29°C contour is shown as a dashed line. Sensor depths are indicated on the left axis; 7 days of missing data is indicated by an x.

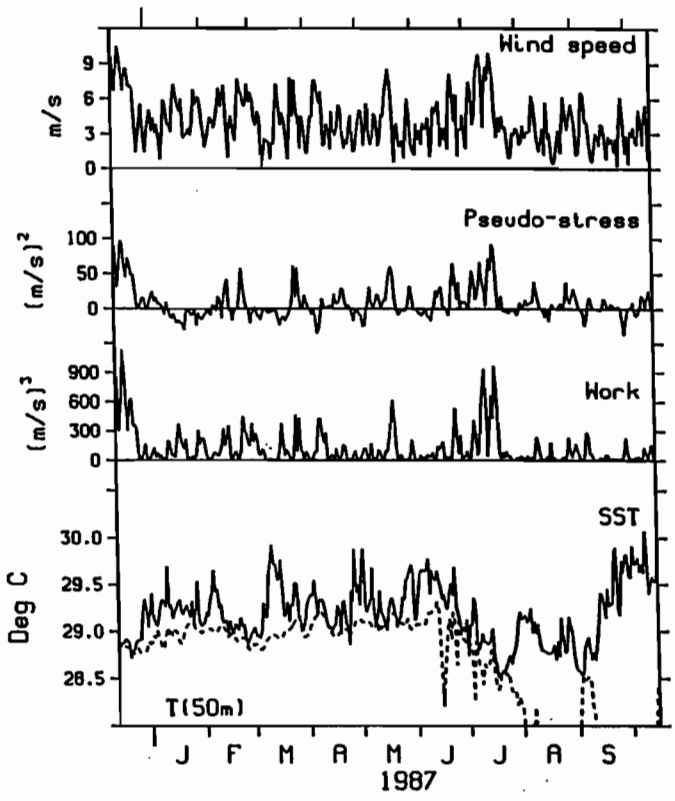

Figure 2. Time series of daily averaged wind speed ($|\vec{U}|$), zonal wind pseudostress ($|\vec{U}|U^{(x)}$), wind pseudowork ($|\vec{U}|^3$), SST and temperature at 50 m (dashed line) from the current meter mooring at 0°, 165°E for the period 13 December 1986 to 14 October 1987.

2. Data

The data used in this study were collected from a surface mooring located at 0°, 165°E in the western Pacific warm pool. Winds were measured at 4 m height above mean sea level from a wind recorder mounted on the surface toroid. Temperatures were measured at 15 depths with the shallowest measurement at 1 m (nominally termed SST) and the deepest at 500 m (Figure 1). Details concerning instrumental accuracies, sampling characteristics and data processing can be found in *Freitag et al.* [1987] and *McPhaden et al.* [1990].

3. Surface turbulent fluxes, vertical advection and entrainment

Figure 2 shows daily time series of wind speed ($|\vec{U}|$), zonal wind pseudostress ($|\vec{U}|U^{(x)}$) and pseudowork ($|\vec{U}|^3$) from the mooring at 0°, 165°E for December 1986 to October 1987. Ignoring the weak wind speed dependence of surface turbulent exchange coefficients for the range of speeds shown in Figure 2, turbulent air-sea heat exchange will be proportional to $|\vec{U}|$, Ekman pumping proportional to $|\vec{U}|U^{(x)}$, and wind work proportional to $|\vec{U}|^3$. Also shown in Figure 2 is SST and 50 m temperature from the mooring.

Table 1 summarizes the means and standard deviations of the time series in Figure 2. The mean wind speed is only 4.0 m s^{-1} and the mean zonal pseudostress is westward at 8.2 m^2 s^{-2} (for a constant drag coefficient of 1.2×10^{-3}, this pseudostress translates into a mean zonal stress of 0.01 N m^{-2}). Standard deviations in both of these variables are also small: 2.1 m s^{-1} for $|\vec{U}|$ and 22 m^2 s^{-2} for $|\vec{U}|U^{(x)}$ (equivalent to 0.03 N m^{-2}). SST is high on average (29.2°C) with a standard deviation of 0.31°C. Temperature at 50 m is 29.0°C on average with a standard deviation of only 0.11°C.

Table 1. Summary of means and standard deviations for wind speed ($|\vec{U}|$), zonal wind pseudostress ($|\vec{U}|U^{(x)}$), pseudowork ($|\vec{U}|^3$), SST and temperature at 50 m depth from the current meter mooring at 0°, 165°E. All statistics are calculated for the period 13 December 1986–14 October 1987, except T(50 m), which is for 13 December 1986–31 May 1987 (i.e. when the 50 m level was always found in the surface layer above the thermocline).

	Wind Speed ($m\ s^{-1}$)	Zonal Pseudostress ($m^2\ s^{-2}$)	Pseudowork ($m^3\ s^{-3}$)	SST (°C)	T(50 m) (°C)
Mean	4.0	8.2	127	29.2	29.0
Standard Deviation	2.1	22.3	188	0.31	0.11

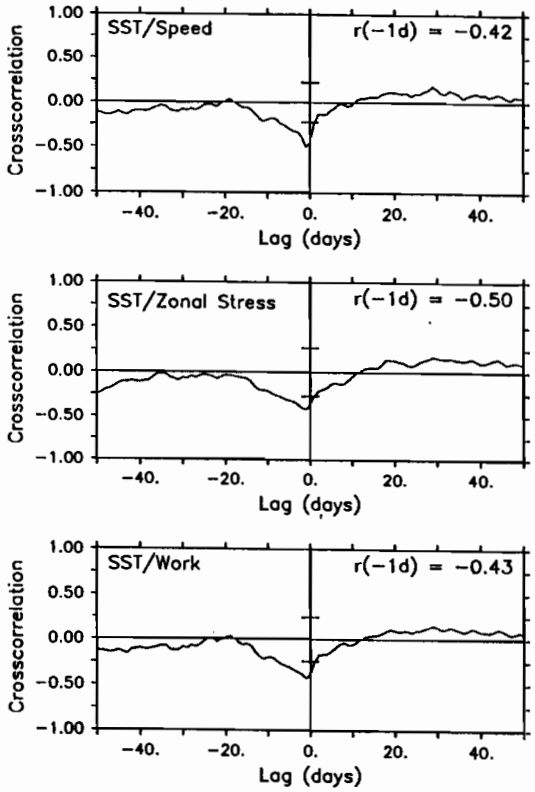

Figure 3. Crosscorrelations between SST and wind speed, zonal wind pseudostress, and wind pseudowork. Crosscorrelation extrema (r) and the lag (in days) at which they occur are shown. In each case, the lag indicates that cold SST follows high winds by one day. 95% confidence limits for the null hypothesis of uncorrelated variability are indicated by horizontal bars on the abscissa.

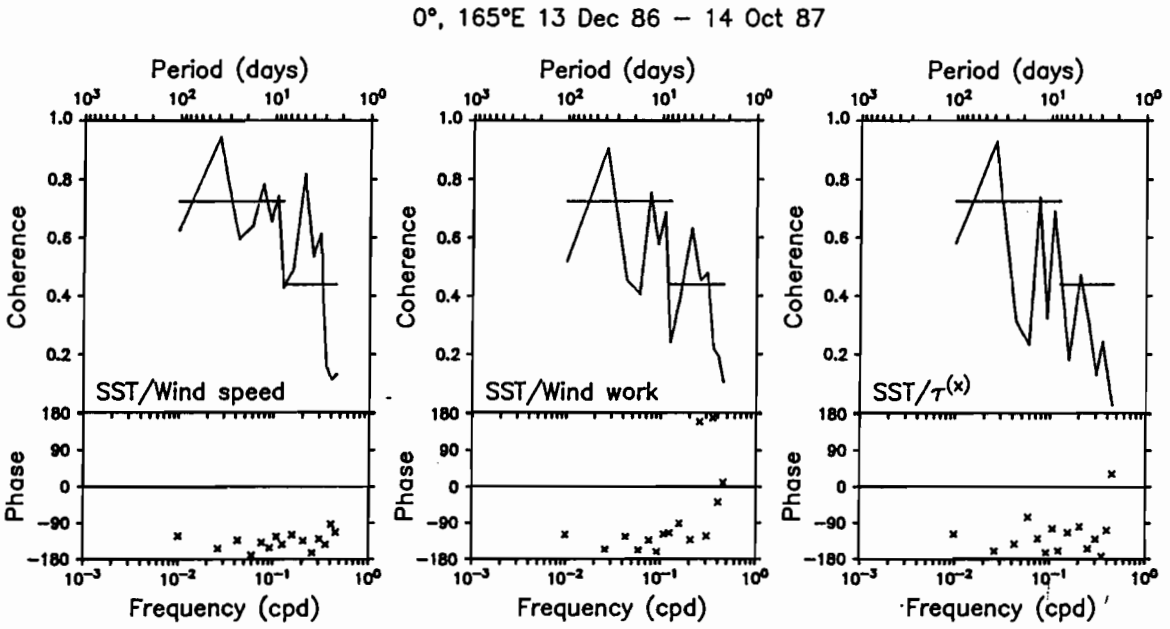

Figure 4. Coherence and phase spectra for SST and wind speed, zonal wind pseudostress, and wind pseudowork at 0°, 165°E for the period 13 December 1986 to 14 October 1987. Positive phase indicates that high winds lead high SST. Observed negative phases imply that high winds lead low SST.

Figure 3 indicates that crosscorrelations of the three wind constructs with SST are significantly nonzero at the 95% level of confidence and range between –0.42 (for zonal pseudostress) and –0.50 (for wind speed). The negative correlation indicates that high wind speed, high wind work and westerly wind stress (relative to the mean) are associated with cool SST; and that low wind speed, wind work and easterly wind stress (relative to the mean) are associated with warm SST. In each case the maximum crosscorrelation occurs with SST lagging the winds by 1 day, consistent with the atmosphere forcing the ocean on these time scales. Although not presented, the magnitude of the crosscorrelation between meridional wind pseudostress and SST is generally ≤ 0.2 over the range of lags shown in Figure 3.

Another way to view these relationships is in the frequency domain. Figure 4 shows the coherence and phase as a function of frequency between the 3 wind constructs and SST. Two bands of high and statistically significant coherence are evident. These are at periods between approximately 3–8 days and 30–60 days; to a lesser extent, variations at 10–20 days are also coherent. Consistent with the crosscorrelation statistics, the phase in most frequency bands is between –90° and –180° implying that maxima in the winds are followed by cold SST and minima by warm SST. Coherence at periods shorter than 20 days may be related to westerly wind burst activity. Coherence at periods of 30–60 days could be related to atmospheric fluctuations associated with *Madden and Julian* [1972] waves.

Note that although there are differences among the coherence and phase diagrams in Figure 4 and the crosscorrelation analyses summarized in Figure 3, the statistical relationships of the 3 wind constructs with SST share many similarities; indeed, wind speed, zonal wind pseudostress and wind work are highly correlated among themselves (0.61–0.90). Based on these statistics alone, one cannot unambiguously identify which of the processes related to the wind field are most important in affecting SST. Hence, we now examine the coherence structure as a function of depth for temperature and the 3 wind constructs in Figure 2.

Figure 5 shows coherence amplitude as a function of depth in the 3–8 day period band. The coherence profiles in other period bands, e.g. for the 30–60 day band, are similar to those shown in Figure 5. Also shown in Figure 5 is the mean temperature profile for December 1986-October 1987. Wind speed, wind stress and wind work are all significantly coherent with temperature variations between 1–10 m. Coherence drops rapidly below these depths however, and is statistically insignificant at the 95% level in the lower part of the surface layer between 50–75 m. In the thermocline, wind speed and wind work are generally incoherent with temperature fluctuations; on the other hand, zonal pseudostress shows a clear pattern of coherence between 125–300 m. Figure 6 shows that the phase of zonal pseudostress coherence is such that warm thermocline temperatures lag relative westerly winds by 90° and cold thermocline temperatures lag relative easterly winds by the same amount. This is consistent with an Ekman pumping hypothesis for thermocline variations. However, phase changes by 180° across the base of the surface layer, indicating the temperature variations are of opposite sign in the surface layer and thermocline. Vertical advection from the thermocline is therefore not likely to be the principal mechanism controlling SST on these time scales. Similarly, the rapid decrease in coherence with depth below 10 m in Figure 5 suggests that entrainment from the thermocline is not important in controlling SST. One would expect coherence between temperature and $|\vec{U}|^3$ to be much higher at 50–75 m if the thermocline were the source of cold water for the surface layer. This leaves turbulent surface fluxes proportional to $|\vec{U}|$ as the most likely candidate for affecting SST and surface layer heat content.

Further evidence to support the role of wind related surface turbulent heat flux variations can be found in an examination of upper ocean heat content, defined as $H = \rho C_p h T$. We calculated $\partial H/\partial t$ over 2 depth ranges: 0–10 m (where coherence with the wind speed is highest) and 0–75 m (the average depth of the surface layer). Heat content standard deviations are 34 W m^{-2} in the 0–10 m layer and 102 W m^{-2} in the 0–75 m layer. As expected from our earlier

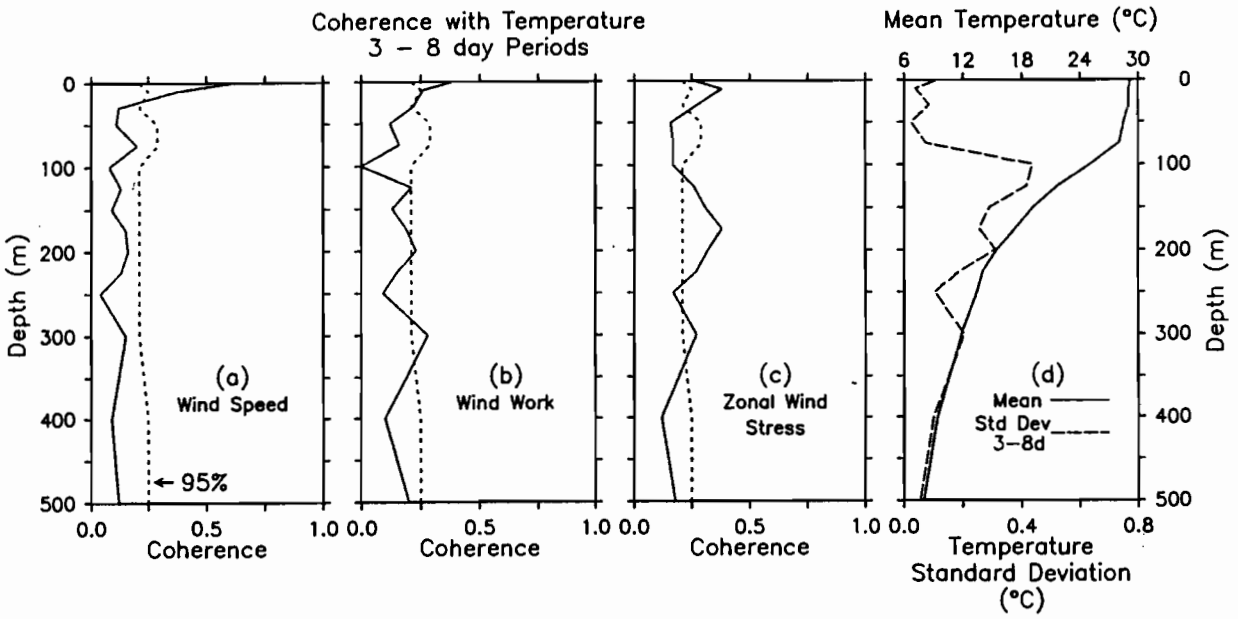

Figure 5. Coherence amplitude as a function of depth averaged over periods of approximately 3–8 days (i.e. 36–65 frequency bands depending on depth) for temperature and wind speed, zonal wind pseudostress, and wind pseudowork at 0°, 165°E. 95% confidence limits for the null hypothesis of incoherent variability are indicated by the dashed lines. Note that the temperature record lengths for this analysis were chosen such that the statistics were stationary; e.g. the period June-October 1987 was excluded at 50 m and 75 m. Shown on the right are the mean temperature profile (solid curve) and the standard deviation of temperature variations at periods of approximately 3–8 days (dashed curve) for 13 December 1986 to 14 October 1987.

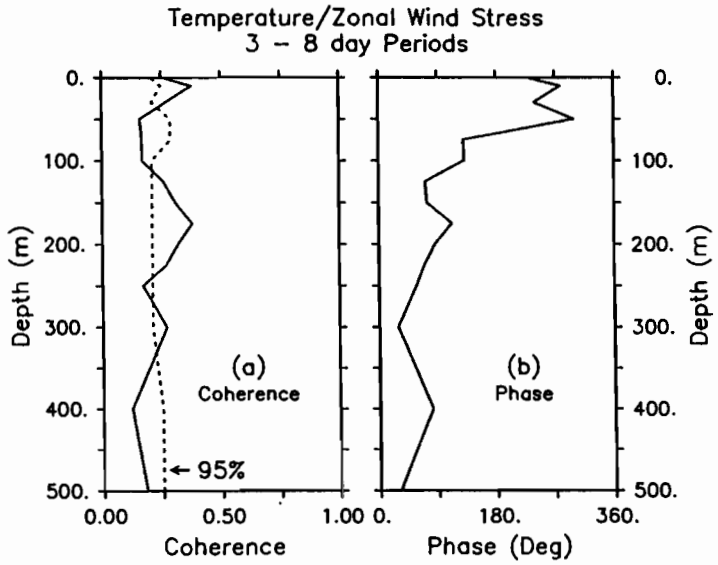

Figure 6. Coherence amplitude and phase as a function of depth averaged over periods of approximately 3–8 days (i.e. 36–65 frequency bands depending on depth) for temperature and zonal wind pseudostress at 0°, 165°E. 95% confidence limits for the null hypothesis of incoherent variability are indicated by the dashed lines.

results, the crosscorrelation with $|\vec{U}|$ is negative, and higher over the shallower layer (–0.38) than over the deeper layer (–0.29). When multiplied together, these standard deviations and crosscorrelation statistics imply that $|\vec{U}|$ accounts for 13 W m^{-2} in the layer 0–10 m and 30 W m^{-2} in the layer 0–75 m. The 0–75 m estimate is comparable to what would be expected for latent heat flux variations (Q_L) and typical observed parameter values. Specifically, $Q_L \approx 35$ W m^{-2} for wind speed variations of 2.1 m s^{-1} (Table 1), an exchange coefficient of 1.2×10^{-3} [*Large and Pond,* 1982] and a typical air-sea specific humidity difference of 5 g kg^{-1} [*Reed,* 1985; *Liu,* 1988].

These calculations, and Figure 5, indicate that surface cooling associated with Q_L converges nonlinearly in the upper 75 m. The upper 10 m (13% of the surface layer depth) takes up 13 W m^{-2} (43% of the latent heat flux forcing). The remaining 17 W m^{-2} (57% of the forcing) is absorbed over 10–75 m, which represents 87% of the surface layer depth. Using an integral time scale (t_i) for wind speed and temperature variations of 3–4 days (based on the crosscorrelation analysis in Figure 3) and a $\frac{\partial H}{\partial t}$ of 13 W m^{-2} (0-10 m) and 17 W m^{-2} (10-75 m), we find the expected magnitude of temperature variations associated with latent heat flux variations in each of these depth ranges to be 0.1°C and 0.02°C, respectively. The latter number is close to the instrumental accuracy of our temperature sensors (e.g. *McPhaden et al.,* 1990) and probably accounts for the insignificant temperature and wind coherences on a pointwise basis for depths greater than 10 m in the surface layer.

4. Conclusions

We have inferred that wind-related latent heat flux variations of about 30 W m^{-2} lead to temperature changes in the upper 75 m of 0.02°–0.1°C. The largest of these variations occur in the upper 10 m, perhaps because of the existence of surface layer salinity stratification as discussed in *Lukas and Lindstrom* [1987] and *Godfrey and Lindstrom* [1989]. Salinity stratification would act to isolate the near surface from the thermocline, trapping surface heat fluxes while at the same time reducing the effect of vertical advection and entrainment on SST. These results are consistent with those of *Meyers et al.* [1986], who found that evaporative fluxes led to significant surface cooling in the western Pacific during the 1982-83 ENSO, whereas entrainment from the thermocline was relatively unimportant. This would also explain why surface layer temperature variations at 50 m are less than those for SST as noted in Table 1.

It is however clear that evaporative cooling accounts for only a fraction of SST and surface layer heat content changes. Other processes, e.g. lateral advection and radiative heating and cooling, must also be important. A complete analysis of the upper ocean heat budget in the western equatorial Pacific thus requires information on the velocity field and on the surface radiation balance.

5. References

Freitag, H. P., M. J. McPhaden and A. J. Shepherd, Equatorial current and temperature data: 108°W to 110°W; October 1979 to November 1983, *NOAA Data Report, ERL PMEL–17,* 99 pp., 1987.

Godfrey, J. S. and E. J. Lindstrom, The heat budget of the equatorial western Pacific surface mixed layer, *J. Geophys. Res., 94,* 8007–8017, 1989.

Kousky, V. E. and A. Leetmaa, The 1986–87 Pacific warm episode: Evolution of oceanic and atmospheric anomaly fields, *J. Climate, 2*, 254–267, 1989.

Liu, W. T., Moisture and latent heat flux variabilities in the tropical Pacific derived from satellite data, *J. Geophys. Res., 93*, 6749–6760, 1988.

Lukas, R. and E. Lindstrom, The mixed layer of the western equatorial Pacific Ocean, Proc. 'Oha Huliko'a Hawaiian Winter Workshop on the Dynamics of the Ocean Surface Mixes Layer, University of Hawaii, Honolulu, January 1987, 67-94.

Madden, R. A. and P. Julian, Description of global scale circulation cells in the tropics with a 40–50 day period, *J. Atmos. Sci., 29*, 1109–1123, 1972.

McPhaden, M. J., S. P. Hayes, L. J. Mangum and J. Toole, Variability in the western equatorial Pacific during the 1986–87 El Niño/Southern Oscillation event, *J. Phys. Oceanogr.*, 1990.

Meyers, G., J.-R. Donguy and R.K. Reed, Evaporative cooling in the western equatorial Pacific Ocean by anomalous winds, *Nature, 323*, 523-526, 1986.

Nicholls, N., Impact of the Southern Oscillation on Australian crops, *J. Climatology, 5*, 553–560, 1985.

Palmer, T. N. and D. A. Mansfield, Response of two atmospheric general circulation models to sea-surface temperature anomalies in the tropical east and west Pacific, *Nature, 310*, 483–488, 1984.

Rasmusson, E. M. and J. M. Wallace, Meteorological aspects of the El Niño/Southern Oscillation, *Science, 222*, 1195–2002, 1983.

Reed, R. K., An estimate of the climatological heat fluxes over the tropical Pacific Ocean, *J. Climate Appl. Met., 24*, 833–840, 1985.

Sea Level and Thermal Response to the 1986-87 ENSO Event in the Far Western Pacific

John S. GODFREY, K. RIDGWAY, Gary MEYERS and Rick BAILEY

CSIRO Division of Oceanography, GPO Box 1538, Hobart, Tas. 7001, Australia

ABSTRACT

Sea levels at the Papua New-Guinea (PNG) coast responded to the 1986-87 ENSO event much as would be expected for points on the inshore edge of a western boundary current, driven by remote sea level disturbances. The first EOF of sea level in the region accounts for 60% of the variance, and shows a clear western boundary current signal. Sea level estimates from tide gauges and adjacent XBT's are in good agreement, so XBT data are used to supplement sea level results; specifically, we obtain an estimate of the western boundary current as a function of depth. The anomalous transport varied by about 15 Sverdrups during the event. The boundary current followed the Tobriand Island ridge, rather than the main PNG coastline, and appears to bifurcate along southern New Britain. A maximum response to the ENSO occurred south of New Ireland, where steric sea level appeared to vary about 45 cm due to the ENSO event.

1. Introduction.

This report is a preliminary version of a comprehensive paper (Ridgway et al., in prep.). The 1986/87 ENSO event was the most completely monitored yet to have occurred. It is the first such event to occur in the TOGA decade and hence many new observing systems were in place. One such system (Fig.1) was a network of seven tide gauges installed around Papua New Guinea (PNG), which started operation in September 1984, enhancing the existing Pacific network (Wyrtki, 1979). The density of the stations is greater than for elsewhere in the Pacific network, because it was anticipated that, along with observations of the large scale response to climatic variations, they might measure a western boundary current adjacent to the PNG mainland. During 1986-87, a weak ENSO event occurred (Miller et al., 1988). This provided the first opportunity to detect the presence or absence of these anomalous boundary currents and, if they were present in the sea level data, to obtain a picture of their behavior. It was hoped that the new network would provide answers to questions such as whether the western boundary current follows the PNG mainland coast (through Vitiaz Strait) or whether some or all of the anomalous transport follows along the coasts of New Britain and New Ireland.

2. Methods.

A full description of the instrumentation and procedures associated with the PNG sea level network is given in Ridgway (1989), hence only a brief discussion of the salient points will be included here. At each of the seven sites marked with solid squares in Fig.1, float-well gauges have been installed which incorporate Stevens analogue to digital recorders (ADR). The sea level data are recorded every 15 minutes on punched paper tape. A local observer collects the tape at the end of every month and sends the results to Hobart for processing.

XBT data covering the same time as the sea level data, for an area surrounding the expected western boundary currents, (outlined in Fig.1) were obtained from the TOGA Sub-surface Temperature Data Centre in Brest.

ORSTOM
CENTRE DOCUMENTATION
Montpellier

F 30216

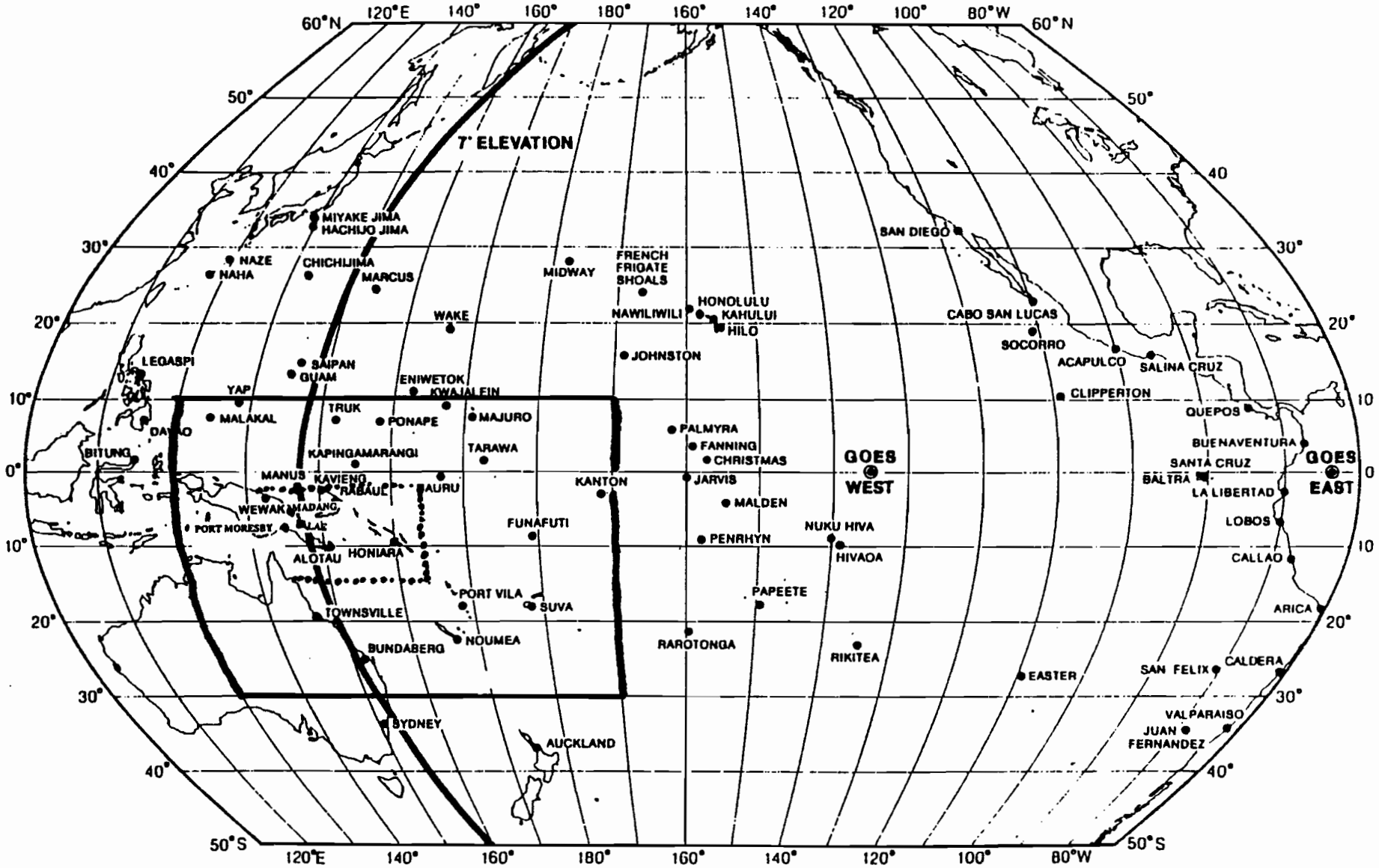

FIG.1. Monthly mean sea levels from within the full square (10°N-30°S, 130°E-170°W) have been used to obtain a picture of anomalous response in the tropical southwest Pacific. XBT steric heights have been calculated within the dotted region, for closer study of the western boundary current.

3. Data Processing.

The sea level data are processed in several stages in moving from the raw fifteen minute observations to a series of standard data products. Quality control procedures are used to remove any reference level and phase changes, and to fill small breaks in the data series. The observed series is then converted to hourly data using a simple binomial filter and a further Lanczos cosine filter is applied (Thompson, 1983) and the data are decimated to produce 12 hourly values. This removes the diurnal and semi-diurnal tidal frequencies but retains longer period signals, including those of tidal origin. In fact it was found that the fortnightly tides, Mf and Msf, were large enough to cause problems and so they were also removed. Plots of the time series of this 12 hourly data for all PNG stations are presented in Ridgway (1989).

Monthly mean sea levels were produced from simple averages of the hourly data. The annual cycle of sea level at each station was determined by procedures previously adopted by Wyrtki and Leslie (1980), in which a 2 harmonic curve was fitted to the data for the period September 1984 to December 1987. Monthly sea level anomalies were therefore obtained by subtracing the 1984-87 mean seasonal cycle of sea level from the monthly means. This procedure was also applied to the monthly mean data from other western Pacific stations (as published in the ISLPP maps (Wyrtki et al., 1988).

Annual mean temperature-salinity relationships were obtained from the Levitus (1982) data set in 2°x2° squares, and used with the XBT's to obtain steric heights at the surface, and at 50, 100, 150, 200 and 300 db relative to 450 db. Individual steric height measurements were grouped into 2°x2° bins within the area show, in Fig. 1; 5 pairs of bins were combined, where data were thought to be inadequate in the individual bins.

4. Results.

a. Sea level

Fig.2 shows the monthly mean anomalies of sea level at the PNG gauges and several of the other western Pacific gauges. Most of the records show a drop in sea level towards the end of 1986, persisting for nearly 12 months; the magnitude and sharpness of the drop varies from station to station. The largest and sharpest drop occurs at Honiara where from December 1986 to April 1987 there was a 25 cm reduction in sea level. However, not all stations show this pattern; for example, there is no corresponding large negative anomaly in the sea level at Port Moresby, and anomalies in the monthly mean sea level there are restricted to about 5 cm over periods of 2 to 3 months.

An empirical Orthogonal Function (EOF) analysis was performed on the data from the 25 stations in the region for the period 1984 to 1987. This technique allow the most significant "standing wave" contributions to the variance to be extracted from each data record in the form of a set of orthogonal functions. Not surprisingly, the time amplitude of the first EOF (Fig. 3a) shows a drop at the end of 1986, as seen in many individual records in Fig.2; though for some reason the sharpness of this drop is greater than in most of the individual records. Nevertheless, this mode evidently captures the variance associated with the 1986-87 ENSO. The first mode accounts for 60% of the variance in sea level (the next mode only accounts for 16%). The corresponding spatial structure of the first EOF is show, in Fig. 4.

The large region of depressed sea level centred at Honiara seen in Fig. 4, within a generally zonal band between the equator and 15°S, is similar to behavior seen in earlier ENSO events (e.g. Wyrtki, 1985). The low sea level region is bounded by sharp gradients, implying strong westward and eastward geostrophic flow in the south and north respectively. A new feature, revealed by the PNG gauges, is that the westward flow is turned equatorward once having reached the PNG coast thus forming an anomalous western boundary current. Contours are hand drawn in Fig.4 , and it has been assumed that sea level

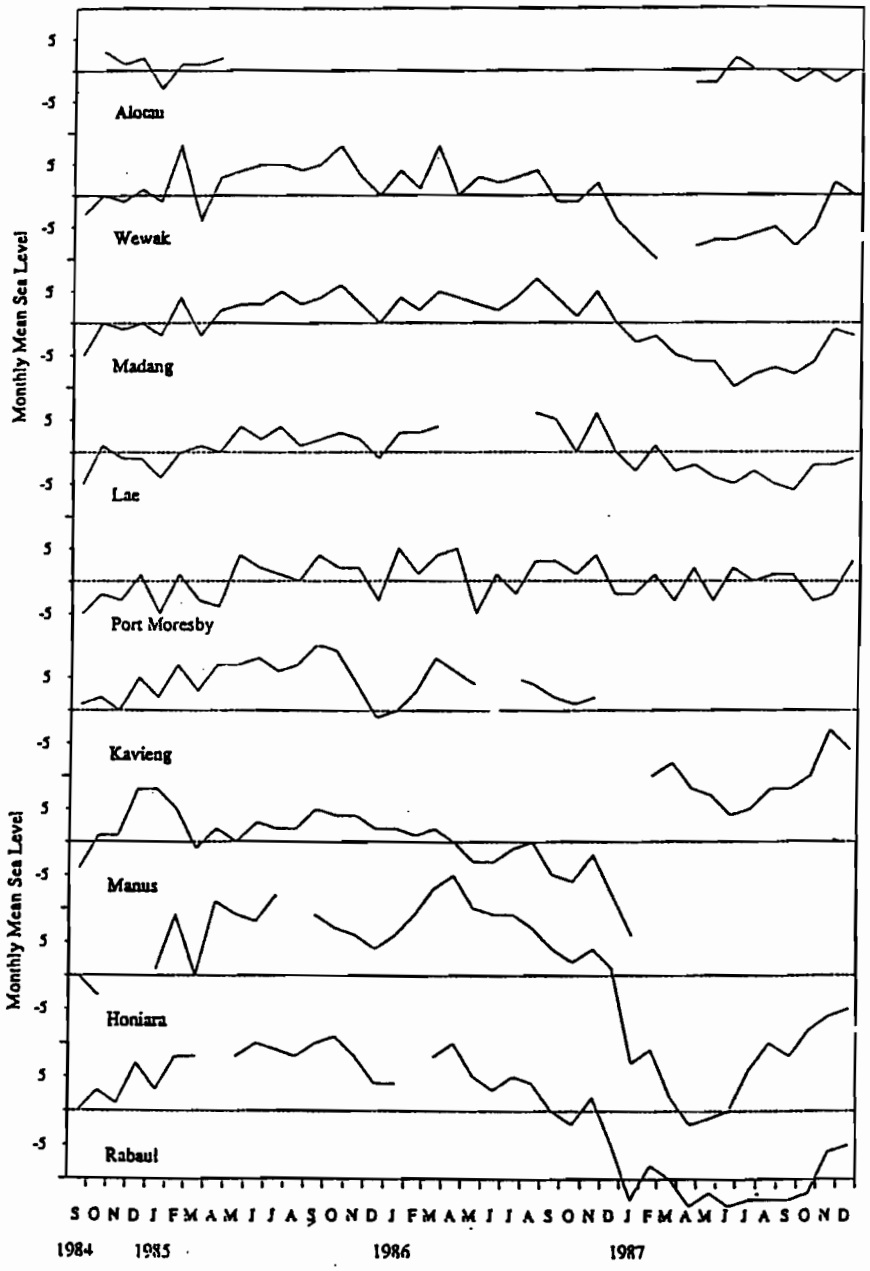

FIG.2. Monthly mean sea level anomalies at selected stations from Fig.1. Units along each ordinate are in cm.

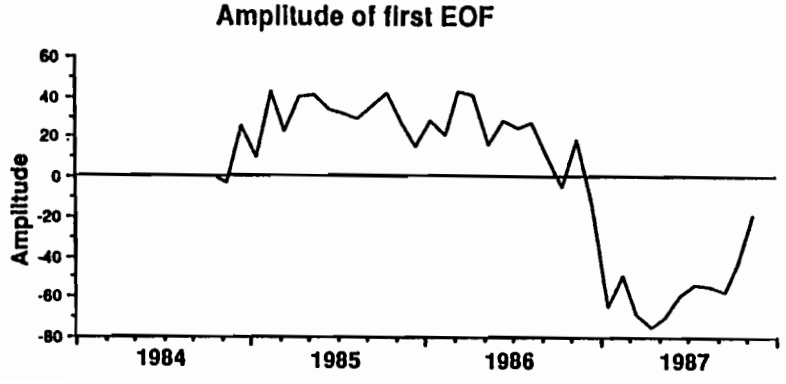

FIG.3. Time amplitude of the first empirical orthogonal eigenfunction of the sea level anomaly, for the 25 stations inside the large square of Fig.1.

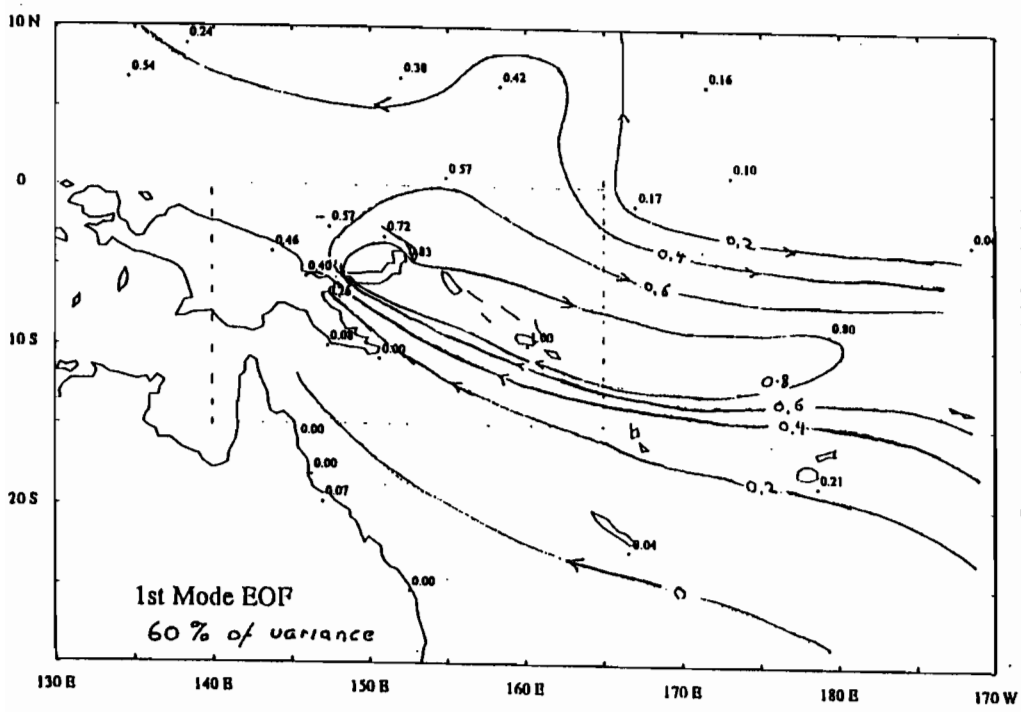

FIG.4. Spatial patterns of sea level anomaly in the first EOF of Fig.3. Contours have been hand-rawn, assuming that sea level is constant along the New Britain coast.

gradients along the New Britain coast are zero. Other choices, consistent with the observations, have non-zero gradients along the New Britain coast and less intense geostrophic currents through Vitiaz Strait; but a strong western boundary current remains.

It would be useful if some areas of ambiguity in this contour map of the sea level data could be removed. A sea level gauge at the western end of New Britain would be very useful for this purpose. Unfortunately data is not available on the western end of New Britain for the whole period; we do have, however, a limited data set spanning the 7-month period of the WEPOCS experiment (Lindstrom et al., 1987) for the stations Pililo, Long Island, Rabaul, Lae and Madang which encircle Vitiaz Strait. Plots of the band-pass filtered (tides and periods longer than 30 days removed) sea level have been prepared for each of these sites. As we are interested in the geostrophic current along the PNG coast we have used the Madang - Pililo and the Port Moresby - Honiara differences as representatives of this current. There is significant correlation for periods below 30 days and above the amplitude is at least of the same order; but the record is too short to resolve the contouring ambiguity in Fig.4.

b. Steric sea level.

A second approach is to augment the sea level data with results from XBT-derived steric heights. Before attempting this, it is useful first to compare XBT steric height observations taken within (say) 100 km of a tide gauge with the record of sea level from that gauge. Fig. 5 compares 12-hourly mean sea levels from tide gauges with simultaneous steric heights, from XBT's dropped within about 100 km of the gauge, for four representative stations. The difference between the two sets of observations has a standard deviation of less than ±5cm, even in the case of Lae where neither set of observations shows much variability. (Note that the seasonal signal has been retained in all the sets of observations in Fig. 5). These results confirm the general conclusion that XBT steric sea levels are a useful proxy for actual mean sea levels at islands (e.g. Rébert et al., 1985). In addition - rather surprisingly - Fig.5

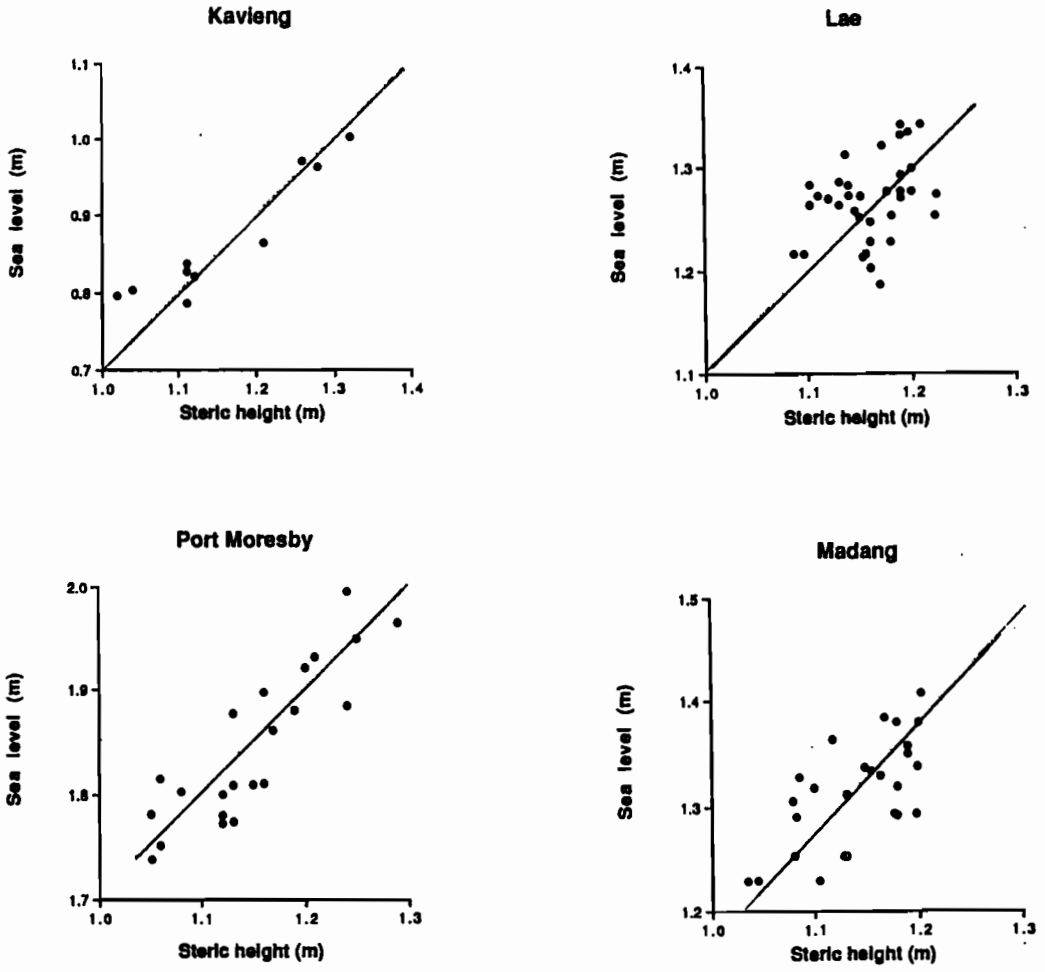

FIG.5. 12-hourly mean sea level at some coastal and island stations, compared to the simultaneous values of steric sea level within 100 km of the station (a) Kavieng, (b) Port Moresby, (c) Lae, (d) Madang.

suggests that this is true even for those of our gauges (Madang, Port Moresby, Lae) lying inshore from coastal boundary currents. This may simply reflect the fact that the continental shelf is narrow and the Coriolis parameter small for our gauge locations, so that geostrophic sea level differences between the tide gauge location and the shelf edge (where most of the XBT's are dropped) is likely to be small.

We have divided the region up into 2°x2° squares for further analysis, as illustrated in Fig.1. Fig.6 shows the time series of steric sea levels from a line of bins with centres along 153°E; the least-squares fit to these data by the first EOF amplitude of Fig.3 has been superimposed on each curve. Note that the amplitude of this curve (which is simply the regression coefficient of the time series of steric sea levels on the amplitude of the EOF) decreases suddenly between 7° and 9°S, and stays small at all points south of 9°S. Note also the very large amplitude of the best-fit curve at 7°S: this may be spurious, since no data are available in mid-1987 when the EOF amplitude of Fig.3 is very negative. Fig.7 shows the regression coefficients on the first EOF of Fig.3 from all 2°x2° squares, and from all sea level stations. Note that some 2°x2° squares have been combined, due to inadequate amounts of data in individual bins.

There are some substantial differences between Fig.7 and the original hand-contoured version of Fig.4, which was based on tide gauge data only. As already noted, the high

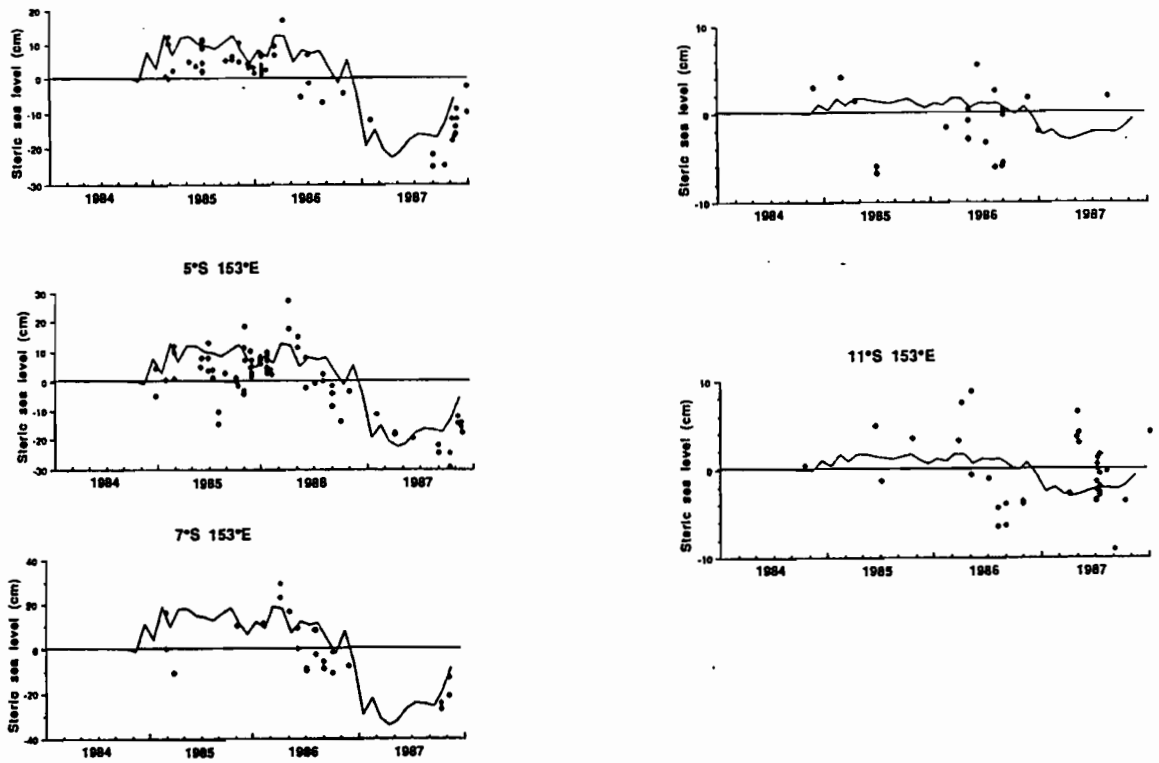

FIG.6. Time series of steric sea levels in 2°x2° bins, between 2° and 12°S, centred on 153°E. The time series of Fig.3, multiplied by its regression coefficient with the steric height data, is also shown. N.B. Seasonal cycle of steric height is still present in figure 6, but has been removed in preparing Fig.7. Note also the different vertical scales.

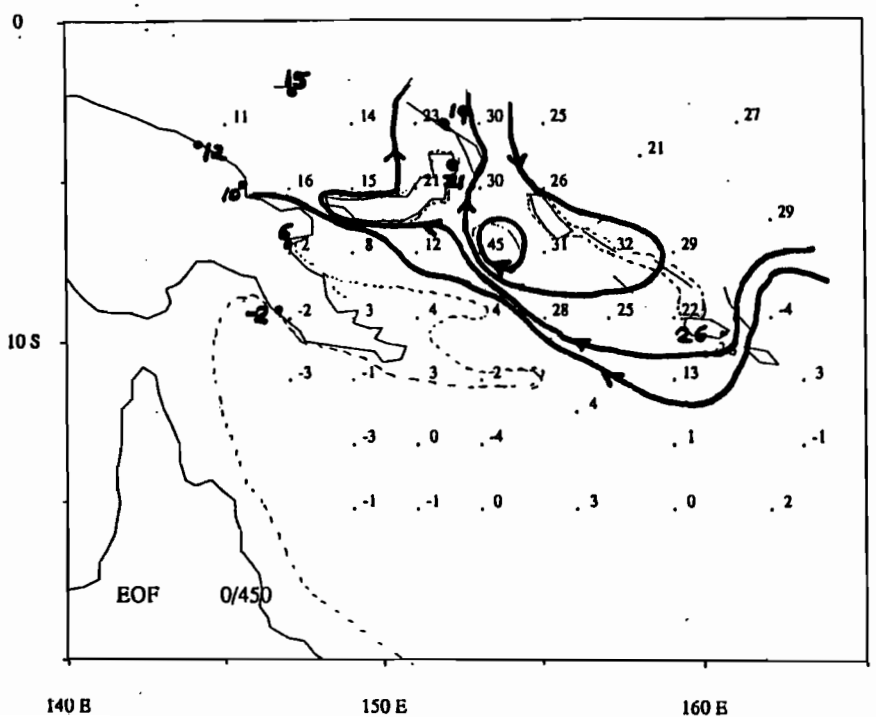

Fig.7. Contour plot of regression coefficients of steric height anomalies with the amplitude of Fig.3.

amplitude (45 cm) at (7°S, 153°E) may be due to a lack of data when the EOF was at a minimum, in this square. However, other differences between the two versions are probably real. In particular, there is a broad area off New Ireland and the northern Solomon islands where the regression coefficients are higher than found at any of the sea level gauges. It should be noted that the Solomons and Bougainville present a solid western boundary to the Pacific from 10°S to 5°S, below 200m, but there is a deep gap between northern Bougainville and New Ireland. Thus the higher values of ENSO response east of the Honiara and Rabaul gauges may reflect the Solomon island western boundary current.

Between 8° and 10°S, the PNG current is centred at 155°E in Fig.7. This result, though at first sight surprising, can be understood from PNG topography in these latitudes; the 200m contour extends to 153.5°E at 9°S (Budibudi Island). However, no such explanation can be offered for the fact that Fig.7 does *not* appear to show a western boundary current along the PNG coast between 6° and 8°S: the main geostrophic current appears to be some 400 km from the coast, i.e. near 153°E, and the water between 153°E and the PNG mainland is deep and unobstructed.

A strong "spike" is seen in several of the time series of steric heights, around April-May 1986 (e.g. Fig.6). This is partly due to the fact that Fig.6 shows full steric sea level values, rather than anomalies, but the spikes are present in the anomaly records as well. The spikes are mainly seen in the steric height records with large amplitudes in Fig.7, and is not seen in sea level records; it may influence the regression coefficients of fig.7. However - although we have not yet attempted to obtain an objective measure of the errors in the regression coefficients of Fig.7 - we do not believe the errors are large enough to account for all of the 30 cm difference in steric sea level between 151° and 153°E along 7°S, seen in Fig.7. If one accepts this feature as real, one possible explanation is that the eddy at (7°S, 153°E) may represent an inertial overshoot of the Solomon-Bougainville western boundary current, as it passes through the Bougainville - New Ireland gap.

This places some uncertainty on the interpretation of the flows along the PNG coast as western boundary currents: nevertheless, our best interpretation is that about half the current flows along the southern New Ireland coast, and another half through Vitiaz Strait; the small sea level difference between Rabaul and Kavieng suggests that little flow passes through St. George's Channel. It is interesting that the captain of the "Nimos" (the vessel that drops many of the XBT's in the PNG region) reports (pers. comm.) that they frequently encounter westward currents along the western half of the south New Britain coast and eastward currents along the eastern half of that coast. This agrees qualitatively with the interpretation of Fig. 7.

It may be noted that, perhaps due to the large number of islands through this region, the GEOSAT altimeter product of Miller et al., (1988) does not yet cover the region. Thus our data remains, for the present, the only source of information on the western boundary current anomalies in the Papua New Guinea region.

c. Geostrophic mass transports.

Maps such as Fig.7 have been prepared for the 50, 100, 150, 200 and 300 m levels from the XBT data. Briefly, each map is qualitatively similar to Fig.7 , and shows the expected weakening with depth. The anomalous currents seem to have an e-folding depth of about 150 m (if our choice of a 450 db reference level is justified). Fig.8 shows the anomalous transports as a function of time, estimated from the sea level differences between Port Moresby and Honiara (10°S) and between Madang and Rabaul (5°S). The anomalous transport changes by about $15.10^6 m^3 s^{-1}$ between mid-1986 and early 1987. Fig.7 suggests that these estimates may be too small, because they are based on sea level differences from tide gauges: thus they do not take into account the large changes in steric sea level just to the east of the Solomons and New Ireland.

Acknowledgments. We are indebted to Prof . K. Wyrtki and Dr. R. Lukas for tide and pressure gauge data; also to the PNG tide gauge operators and the officers and crew of M/V

"Nimos" for obtaining much of the data in this paper.

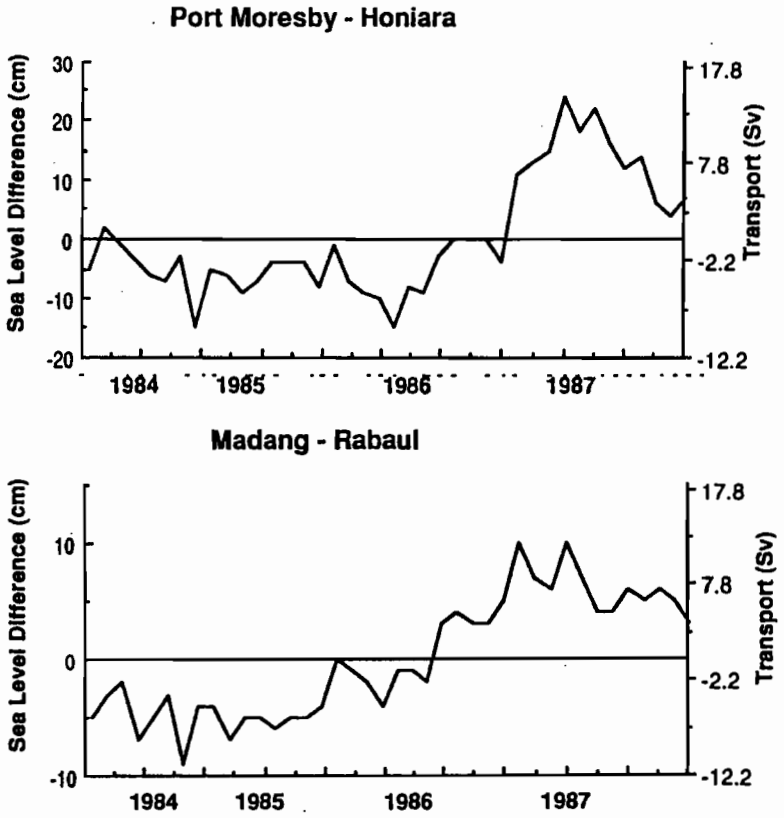

FIG.8. Amplitude of the geostrophic western boundary flow, estimated as the sea level differences g(Port Moresby-Honiara) x150m / f(10°S); and as (Madan-Rabaul) x 150m / f(5°S).

REFERENCES

Levitus, S., 1982: Climatological Atlas of the World Ocean. NOAA Professional Paper 13.

Lindstrom, E., R. Lukas, R. Fine, E. Firing, J.S. Godfrey, G. Meyers, G., and M. Tsuchiya, 1987: The Western Equatorial Pacific Ocean Study. *Nature*, **330**, 533-537.

Miller, L., R.E., Cheney and B.C., Douglas, 1988: GEOSAT altimeter observations of Kelvin waves and the 1986-87 El Nino. *Science*, **239**, 52-54.

Rébert, J.D., J.R. Donguy, G. Eldin and K. Wyrtki, 1985: Relations between sea level, thermocline depth, heat content and dynamic height in the tropical Pacific Ocean. *J. Geophys. Res.*, **90**, 11, 719-11, 725.

Ridgway, K.R. 1989: Sea level variations around Papua New Guinea; 1984-1987. CSIRO Marine Laboratories Report N° 73 pp.

Thompson, R.O. R.Y., 1983: Low pass filters to suppress inertial and tidal frequencies. *J. Phys. Oceanogr.*, **13**, 1077-1083.

Wyrtki, K., 1979: Sea level variations; Monitoring the breath of the Pacific. *Trans. Amer. Geophys. Union*, **60**, 25-27.

Wyrtki, K., 1985: Sea level fluctuations in the Pacific during the 1982-83 El-Nino. *Geophys. Res. Lett.*, **12**, 125-128.

Wyrtki K. and W. Leslie, 1980: The mean annual variations of sea level in the Pacific Ocean. University of Hawai, HIG 80-5, 159 pages.

Wyrtki, K., B. Kilonsky and S. Nakahara, 1988: The IGOSS Sea Level Pilot Project in the Pacific. JIMAR Contribution N° 88-°0150. Data Report N° 003.

Surface Equatorial Flow Anomalies in the Pacific Ocean During the 1986-87 ENSO Using GEOSAT Altimeter Data

Joël PICAUT[1], Bruno CAMUSAT[1], Thierry DELCROIX[1],
Michael J. McPHADEN[2] and Antonio J. BUSALACCHI[3]

(1) *Groupe SURTROPAC, ORSTOM*
Noumea, New Caledonia

(2) *Pacific Marine Environmental Laboratory/NOAA*
Seattle, WA 98115 - U.S.A.

(3) *Laboratory for Oceans*
NASA/GSFC, Greenbelt, MD 20771 - U.S.A.

ABSTRACT

Estimates of surface geostrophic zonal flow in the equatorial Pacific are deduced from the 17-day exact repeat orbit GEOSAT measurements for the period November 1986-November 1987. This period coincides with the height of the 1986-87 ENSO. Along-track altimeter height anomalies are first smoothed using a combination of linear and nonlinear filters. By combining several tracks in the zonal direction and filtering in time, we are able to obtain low frequency sea surface height at any point of the tropical Pacific. Currents are calculated from the differentiated form of the meridional momentum equation at the equator and from the classical first derivative of the meridional pressure field away from the equator. Comparisons of low frequency near-surface zonal current directly measured from equatorial moorings at 165°E, 140°W and 110°W yield a correlation of 0.83, 0.84 and 0.50 respectively with a mean rms difference of 0.23 $m.s^{-1}$. Sea level and zonal velocity solutions from a tropical Pacific numerical model are used as proxy data sets in order to quantify errors induced to quantify the geostrophic calculation by the GEOSAT space-time sampling.

In December 1986, a downwelling equatorial Kelvin wave is generated in the western Pacific and shows up, near the forcing area, as an intense local 1 $m.s^{-1}$ eastward equatorial surface flow anomaly. This Kelvin wave propagates into the eastern equatorial Pacific with a phase speed of about 2.5 $m.s^{-1}$ and is associated with eastward equatorial current anomalies of 0.3-0.5 $m.s^{-1}$. In February 1987, an upwelling equatorial Kelvin wave is excited near the date line and propagates eastward. This wave, characterized by a westward flow anomaly of 0.3-0.8 $m.s^{-1}$, reaches the eastern Pacific boundary in March 1987 where it forces apparently an upwelling first meridional mode equatorial Rossby wave. This Rossby wave propagates westward in the ocean interior at about 0.8 $m.s^{-1}$ as a patch of equatorially trapped eastward flow (0.6-0.8 $m.s^{-1}$ maximum) flanked, in both hemispheres, by 0.2-0.4 $m.s^{-1}$ westward flow anomalies which decreased the South Equatorial Current and the North and South Equatorial Countercurrents. The equatorial Rossby wave propagation could be traced sequentially through the eastern, central and western Pacific from April to September 1987. Thus GEOSAT altimeter data indicate that equatorial Kelvin waves and possible eastern reflection as equatorial Rossby waves are an important component of basin scale surface current variability during the 1986-87 ENSO.

1. Introduction

One of the principal advantages of satellite oceanography is the potential for global monitoring of geostrophic ocean circulation and its variability. In the tropics, detection of current variability is complicated by stringent observational accuracies for

ORSTOM
CENTRE DOCUMENTATION
Montpellier

F 30217

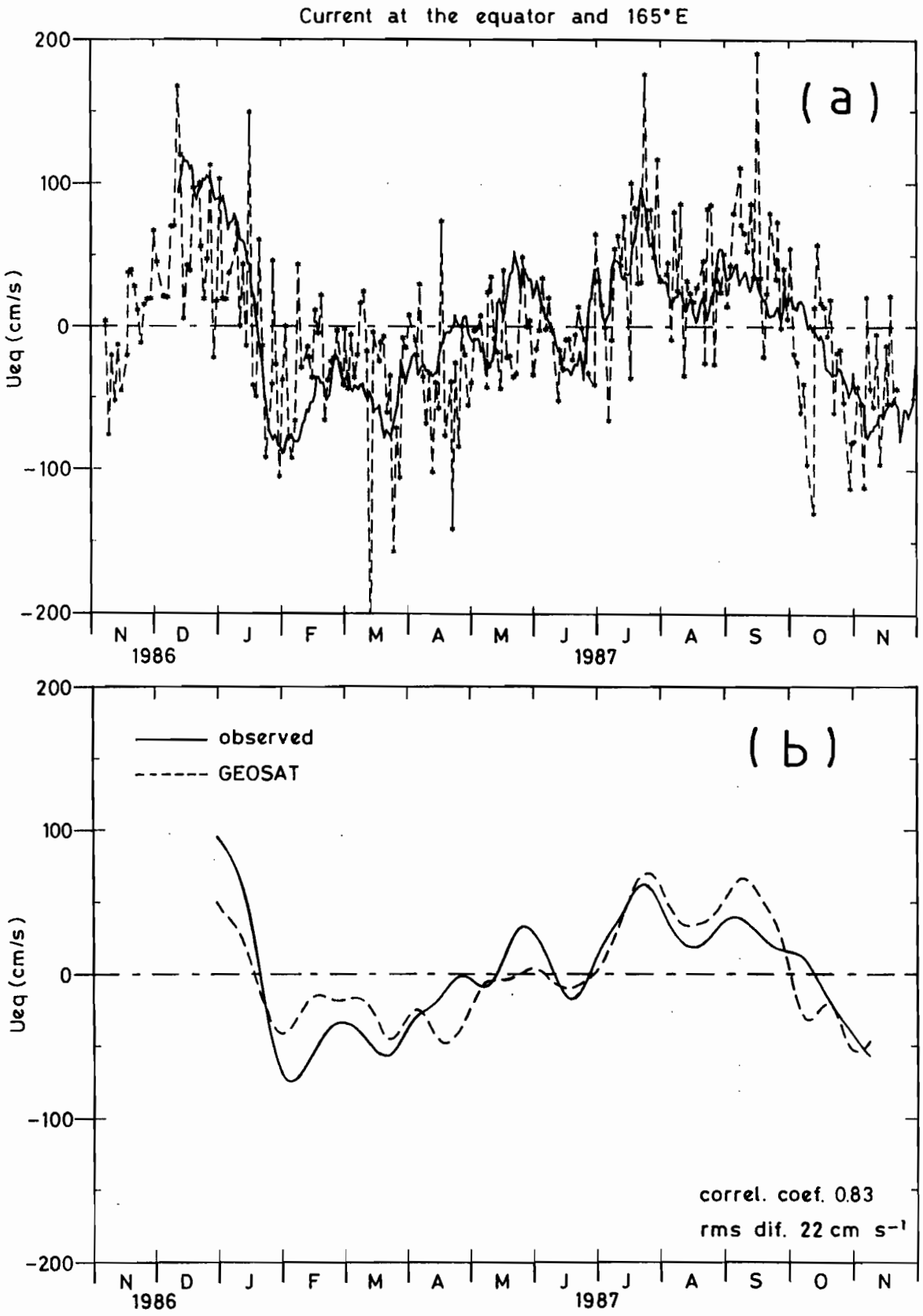

FIG.1. Geostrophic zonal flow estimated from GEOSAT altimeter data (dashed line) and daily averaged near surface zonal flow measured directly from an equatorial mooring at 165°E (solid line). a) daily mooring time series and 1.5 day GEOSAT time series, b) time series low pass filtered with a 31-day Hanning filter.

estimating geostrophic currents because the horizontal component of the Coriolis force tends to zero. In a recent paper, Picaut et al. (1989) were the first to show that, based on comparisons with in situ data and a specific processing of GEOSAT sea surface heights, it is possible to obtain relatively good estimates of low frequency geostrophic zonal velocity at the equator from altimeter measurements. In this note, we summarize this paper and extend the geostrophic current technique calculation to the entire tropical Pacific. The present work is an useful complement of the GEOSAT sea level anomaly study of Delcroix et al. (1989; this volume, hereafter defined as DEP) since it mainly shows that, over the November 1986-November 1987 ENSO period, Kelvin waves and probably reflected Rossby wave are a dominant source of variability of the major surface equatorial currents.

2. Data processing and current intercomparisons

The GEOSAT data (Cheney et al., 1987) and its additional processing is succinctly presented in DEP and is detailed in Picaut et al. (1989). In the present study, the data correspond to the first 22 cycles of the 17-day Exact Repeat Mission (ERM) covering the period November 8, 1986 to November 18, 1987. At first, instrumental and oceanic small scale noise are filtered from along-track sea surface heights, using a combination of nonlinear and linear filters. Then all the ascending and descending tracks within 10° longitude band are combined together in order to reduce the original GEOSAT 17-day time step (down to 1.5 day right at the equator). Finally, high frequency temporal variability is suppressed from the resulting sea surface height time series with a 31-day Hanning filter. This processing results in a 3-dimensional GEOSAT sea level anomaly (GSLA) grid (0.5°latitude X 10°longitude X 5 days) over the tropical Pacific for the November 1986-November 1987 period.

The geostrophic zonal currents are then calculated from the sea level anomaly η and finite derivative schemes, outside the equator using the classical geostrophic equation:

$$f.u = -g.\eta_y \qquad (1)$$

and right at the equator using its meridional derivative on a β plane (Jerlov, 1953)

$$\beta.u = -g.\eta_{yy} \qquad (2)$$

For the specific current intercomparisons study of Picaut et al.(1989), the sequence for applying the second derivative equation is different from the previous one, since it is done immediately after the along track filtering. The results are very similar since the remaining processing (finite derivative, data grouping within 10° band and temporal filtering) are mainly linear. In that study, comparison of low frequency calculated and observed zonal currents, from equatorial moorings at 165°E, 140°W and 110°W, yields correlations of 0.83, 0.85 and 0.51, respectively with a mean rms difference of 0.23 $m.s^{-1}$. Figure 1 illustrates such intercomparisons at 165°E between non-filtered and filtered zonal currents. At 110°W, the inconclusive correlation is due to the lack of descending tracks around the mooring site (Cf. Fig. 1 in DEP). Finally, in the intercomparisons study, a discussion of errors existing in the geostrophic calculation at the equator is presented using sea level and zonal velocity solutions from a tropical Pacific numerical model as proxy data sets.

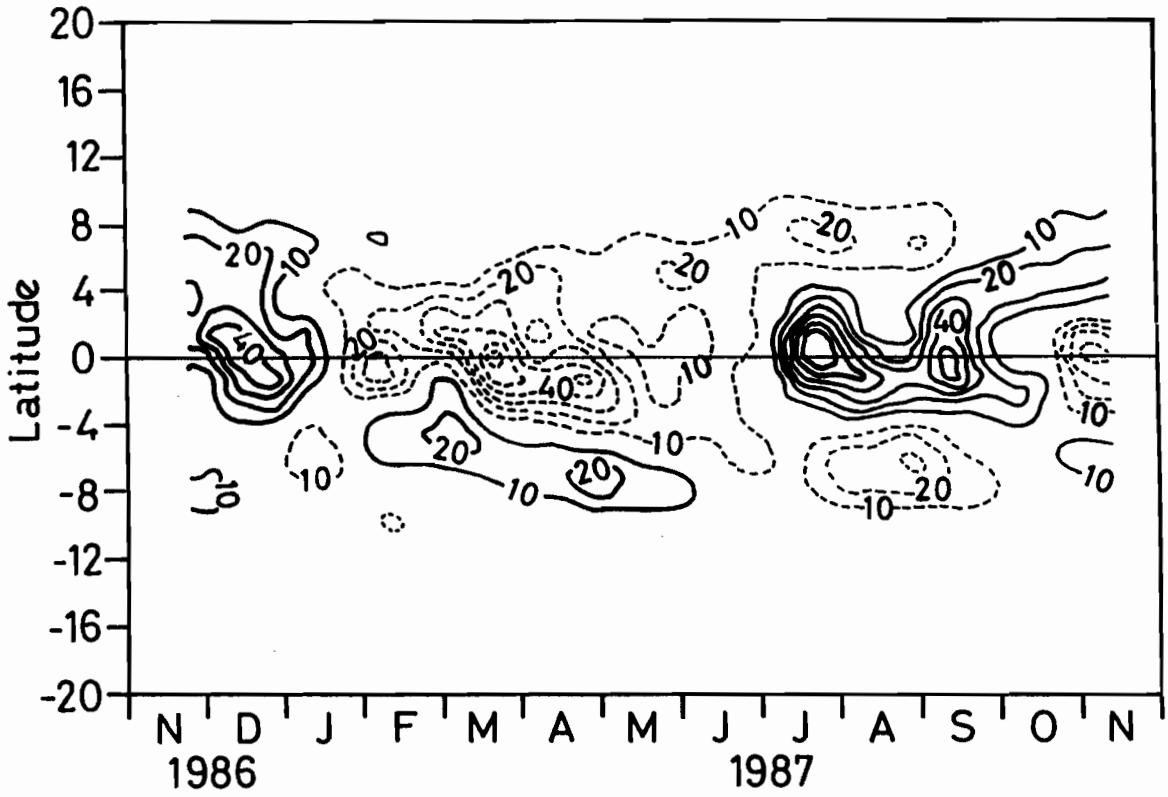

FIG.2. GEOSAT zonal current anomalies (cm.s^{-1}) as a function of time and latitude, along the 165°E longitude.

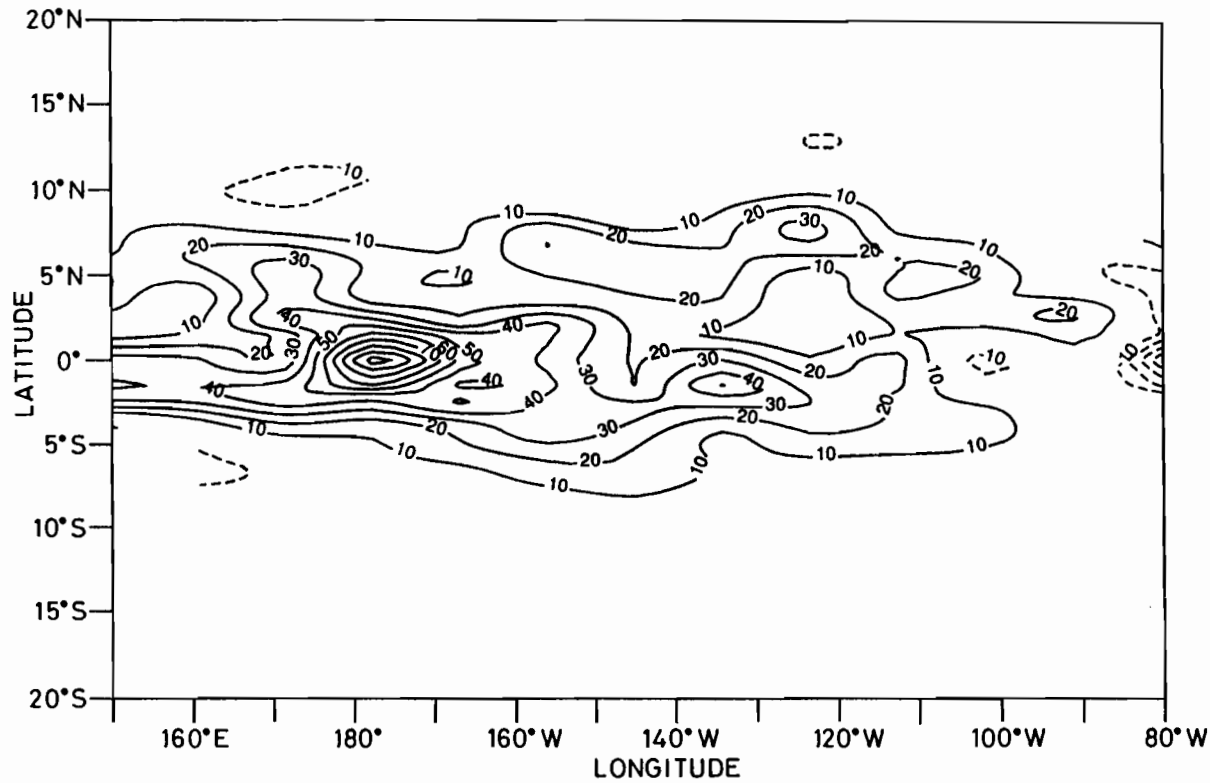

FIG.3. GEOSAT zonal current anomaly (cm.s^{-1}) signature of the downwelling Kelvin wave on January 5, 1987.

3. Surface current variations in the tropical Pacific

DEP have focused on the major GEOSAT sea level anomaly (GSLA) equatorial patches along 165°E and have shown that most of them could be interpreted as equatorial Kelvin and Rossby waves. Similarly, we now present the corresponding GEOSAT zonal current anomalies (GZCA). Similar to the GSLA study, one must keep in mind that the GZCA are relative to their mean over the November 1986-November 1987 period. A discussion of a directly measured currents at 0°, 165°E, and their relation to local wind forcing during the 1986-87 ENSO, is presented in McPhaden et al. (1989).

Figure 2 represents GZCA along the 165°E longitude, as a function of time and latitude. This figure shows that surface current anomalies are unimportant poleward of 10° and are mostly trapped to the equator. The strongest zonal current variations appear at the equator and are very similar to the observed variations depicted in figure 1. From this latter figure, we note that the rms difference between the observed and calculated current is 0.22 $m.s^{-1}$ which implies that, at the equator, GZCA are questionable when smaller than this value. Outside the equator, and due to the 1/f ratio in Eq. (1), the zonal current uncertainty is smaller than at the equator. This ratio 1/f is also the reason why the currents are generally trapped to the equator. This is clearly evident on figure 3 which represents the current structure associated with the downwelling Kelvin wave, generated in November-December 1986 in the western Pacific (Miller et al., 1988). Near the wind forcing area (Cf. Fig.5 in DEP), the eastward equatorial current goes up to 1 $m\ s^{-1}$. Then the equatorially trapped current structure (0.3-0.5 $m.s^{-1}$ maxima) propagates into the eastern equatorial Pacific at a phase speed of about 2.5 $m.s^{-1}$ (Fig.4). This figure also shows evidence, in the surface current from February to March 1987, for the generation and propagation of the equatorial upwelling Kelvin wave as noted in DEP. Referring back to figure 2, we note that the last notable current structure anomaly occurs in July-September 1987, along the 165°E longitude. This structure appears as a large equatorial eastward flow anomaly up to 0.6 $m.s^{-1}$ associated on the northern and southern sides by two westward flow anomalies down to -0.2 $m.s^{-1}$. According to DEP, the corresponding GSLA patch has the meridional structure of a first vertical first meridional equatorial Rossby wave.

In contrast to an equatorial Kelvin wave, the theoretical profile of zonal currents associated with an equatorial Rossby wave is far different from its sea level representation (e.g. Fig.9 in DEP). As noted above, it appears as a strong equatorially trapped current flanked in both hemispheres by two opposite currents of smaller amplitude. Such equatorial Rossby current structure is more evident in the eastern and central Pacific than in the western Pacific. Figure 5 illustrates such observed meridional current structure at 145°W and its least square fit to the theoretical first meridional Rossby wave function:

$$U(y) = U_0\, 2^{-3/2}\, \pi^{-1/4}\, (-3/2 + \beta y^2/c)\, \exp(-\beta y^2 / 2c)$$

The associated Kelvin wave speed c corresponds to 2.7 $m.s^{-1}$, i.e. the first vertical mode. Theoretically the first meridional equatorial Rossby wave propagates westward at a phase speed equal to c/3. Figure 6 represent the time/space sequence when the Rossby wave is most evident in the current structure. The equatorially trapped current anomaly (0.5 to 0.8 $m.s^{-1}$ maximum), accompanied by the northern and southern westward current anomalies (-0.2 to -0.4 $m.s^{-1}$ maxima), propagates between April 15 to June 1 from the eastern to the central tropical Pacific at a mean phase speed of 0.8 $m\ s^{-1}$. This propagating current structure is no longer evident between 150°W and the date line but

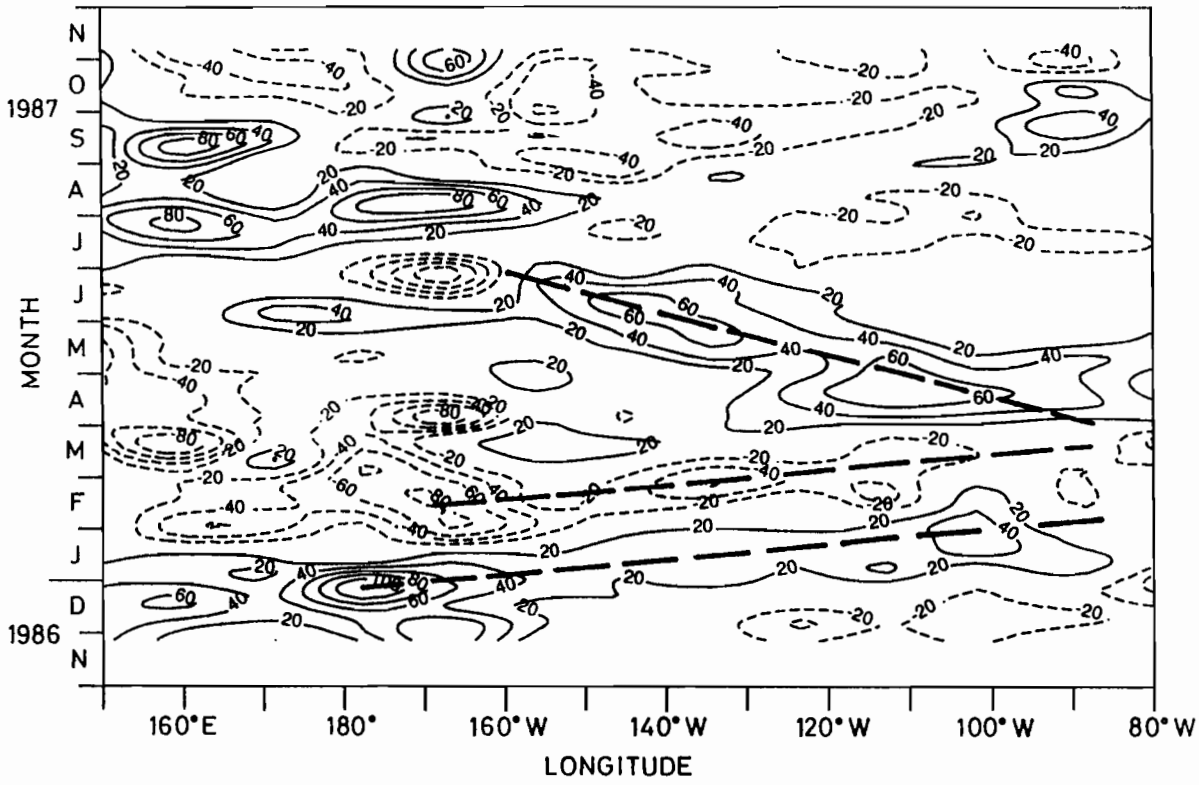

FIG.4. GEOSAT zonal current anomalies (cm.s^{-1}) along the equator as a function of time and longitude. Heavy broken lines indicate the propagation of equatorial Kelvin and Rossby waves.

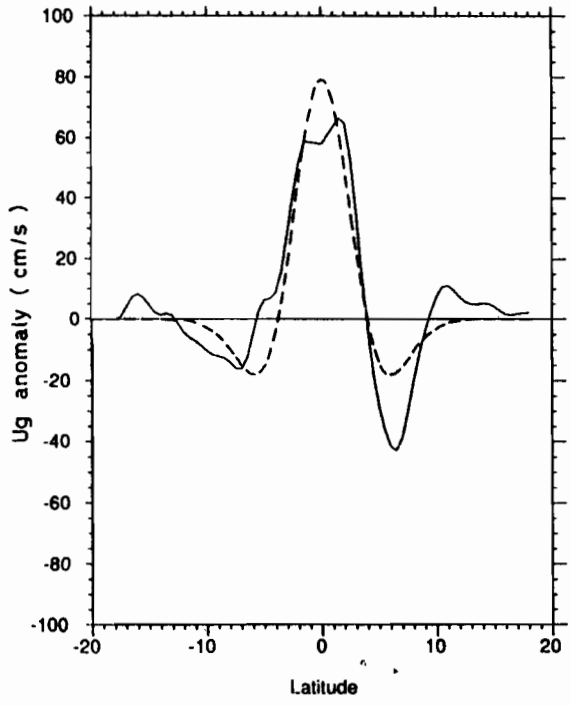

FIG.5. Meridional GEOSAT zonal current profile along 145°W in June 1, 1987 (solid line). The dotted line corresponds to the least square fit of the theoretical zonal current associated with the first meridional equatorial Rossby wave.

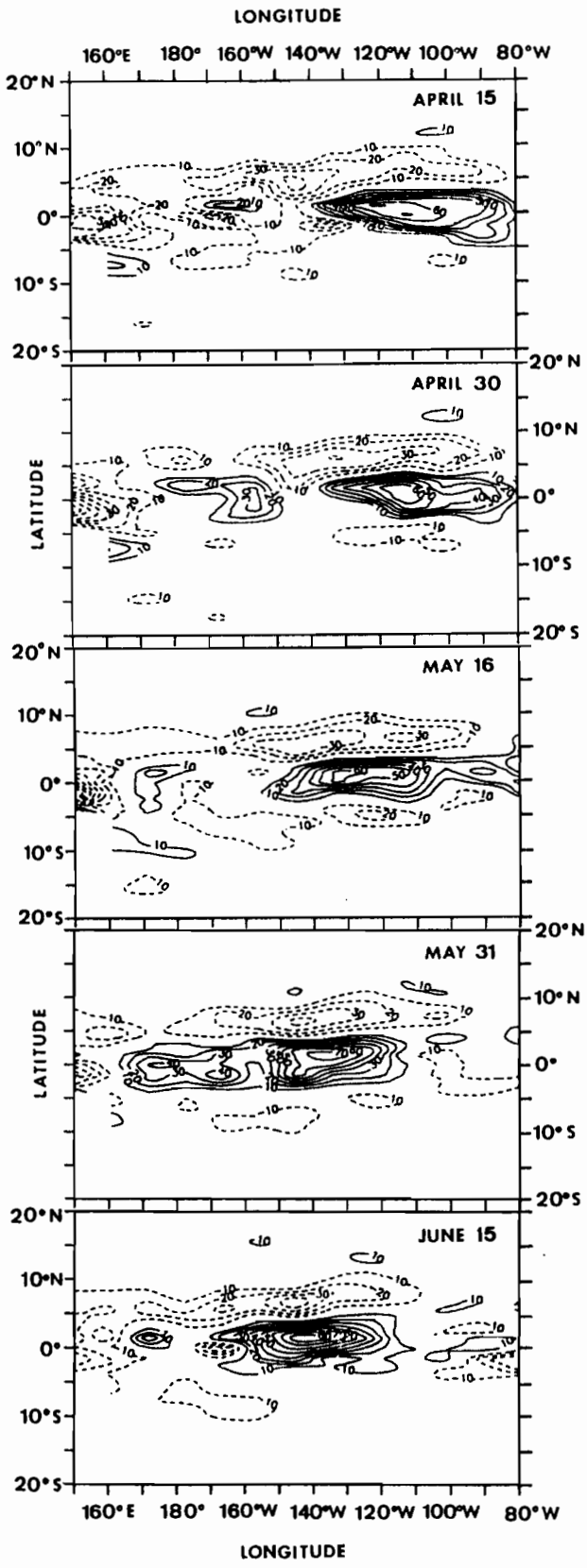

FIG.6. Time/space representation of the GEOSAT zonal surface current (cm.s^{-1}) from April 15 to June 15, 1987. It evidences the westward propagation of the equatorial upwelling Rossby wave from the eastern to the central tropical Pacific.

reappears around 165°E (Figs.2 and 4). Between the gap the equatorial Rossby wave GZCA is probably blurred by other equatorial phenomena or imprecise GEOSAT data (Cf. Fig.1 in DEP).

4. Discussion and conclusion

In this note we first summarize the study of Picaut et al. (1989) who have shown that, based on comparisons with in situ current data at three sites in the Pacific Ocean, it is possible to make physically meaningful estimates of surface geostrophic zonal velocity variations at the equator using GEOSAT data. The high correlations and relatively small rms at 165°E and 140°W is surprising when one considers that a 1 cm error in sea level, if uncorrelated over 1° latitude on which the present geostrophic flow is computed, would lead to errors of 0.7 $m.s^{-1}$. The success of such a computation is due to the accumulation of several factors such as the efficiency of the filtering technique, a current decorrelation scale in the meridional direction that is probably much greater than our grid size, and a zonal decorrelation scale of low frequency zonal current variations large enough to justify the combination of all ascending and descending tracks within each 10° longitude band. Since the computation of geostrophic zonal current is more sensitive to noise contamination at the equator than at higher latitude it has been possible to extend the geostrophic calculation with GEOSAT data to the entire tropical Pacific ocean.

Over the November 1986-November 1987 period of available GEOSAT measurements, we have shown that zonal surface current variability in the tropical Pacific are substantially influenced by two types of surface current structures. The first one corresponds to a downwelling (or upwelling) equatorial first vertical mode Kelvin waves which is characterized by an eastward (or westward) equatorially trapped zonal flow anomalies. These anomalies can reach 1 $m.s^{-1}$ near the forcing area and decrease to less than 0.5 $m.s^{-1}$ further east. The second current structure corresponds to a first meridional, first vertical, equatorial upwelling Rossby wave. It is composed of an equatorial eastward flow of 0.5-0.8 $m.s^{-1}$, flanked on the northern and southern sides by two westward flows of 0.2-0.4 $m.s^{-1}$. From the first panel of figure 6 it seems that this Rossby wave emanates from the eastern boundary of the tropical Pacific and figure 4 indicates that it could be due to the reflection of the upwelling equatorial Kelvin generated near the date line in February 1987. Because of their amplitude and propagating nature, these equatorial Kelvin and Rossby wave current structures strongly influence the variability of the South Equatorial Current and the North and South Equatorial Countercurrents over most of the tropical Pacific. The GEOSAT ERM data used in the present study does not precede or extend beyond the 1986-87 ENSO period. Therefore it is not possible yet to determine if the equatorial wave current structures we observed are prevalent in a normal years as well.

Acknowledgments. The authors are deeply indebted to Chet Koblinsky of NASA/GSFC for providing the pre-processed GEOSAT sea surface height data. Programming assistance by François Masia is appreciated. Support for this work as part of the TOPEX/POSEIDON Science Working team was provided by Programme Télédétection Spatiale trough AIP 59.88.46 and 9.88.25 (JP, BC, TD) and NASA RTOP 671-161-20-31 (AJB). Financial support for the equatorial mooring measurements was provided under the auspices of NOAA's EPOCS Program and the US/PRC Bilateral Air-Sea Interaction Program (MJM).

REFERENCES

Cheney, R.E., B.C. Douglas, R.W. Agreen, L. Miller and D.L. Porter, 1987: GEOSAT altimeter geophysical data record user handbook, NOAA Technical Memorandum NOS NGS-46, Rockville, Md, 29pp.

Delcroix T., G. Eldin and J. Picaut, 1989: GEOSAT sea level anomalies in the western equatorial Pacific during the 1986-87 El Nino, elucidated as equatorial Kelvin and Rossby waves. In: J. Picaut, R.Lukas and T.Delcroix (Editors), *Proceeding of the Western Pacific International Meeting and Workshop on TOGA-COARE, Nouméa; May 24-30, 1989.*

Jerlov, N.G., 1953: Studies of the equatorial currents in the Pacific. *Tellus*, **5**, 308-314.

McPhaden, M.J., S.P. Hayes, L.J. Mangum and J.M. Toole, 1989: Variability in the western equatorial Pacific Ocean during the 1986-87 El Nino/Southern Oscillation event. *J. Phys. Oceanogr.*, in press.

Miller, L., R.E. Cheney and B.C. Douglas, 1988: GEOSAT altimeter observations of Kelvin waves and the 1986-87 El Nino. *Science*, **239**, 52-54.

Picaut J., A.J. Busalacchi, M.J. McPhaden and B. Camusat, 1989: Validation of the geostrophic method for estimating zonal currents at the equator from GEOSAT data. *J. Geophys. Res.*, special GEOSAT issue, in press.

THEORETICAL AND MODELING STUDIES OF ENSO AND RELATED PROCESSES

An Overview of Coupled Ocean-Atmosphere Models of El Nino and the Southern Oscillation

Julian P. McCREARY, Jr.

Oceanographic Center, Nova University,
8000 North Ocean Drive, Dania, FL 33004 - U.S.A.

1. Introduction

The phenomenon of El Nino and the Southern Oscillation (ENSO) exhibits a time scale of 2-9 years. An intriguing hypothesis, for which there is an increasing body of supportive evidence, is that ENSO is the result of strong coupling between the ocean and the atmosphere in the tropics. A number of coupled models have been developed in the past few years to explore this idea. Specifically, the models address the question: How can the ocean and the atmosphere interact to produce oscillations with the long ENSO time scale?

In this overview, as much as is possible the coupled models discussed are arranged in a hierarchy of increasing dynamical complexity. Useful categories for this purpose are: conceptual models, simple models, intermediate models, and coupled general circulation models (GCM's). **Conceptual models** drastically reduce the spatial structure of the atmosphere and ocean, consisting typically of a few variables and coupled equations that depend only on time, whereas **simple models** represent the ocean and/or atmosphere with simplified, but familiar, sets of partial differential equations. Conceptual and simple models are useful because they illustrate possible fundamental processes of air-sea interaction; they are limited, however, in that it is generally difficult or impossible to compare their solutions closely with observations, and hence many of them are untestable. **Intermediate models** are defined here to be the set of coupled systems that utilize reduced-gravity oceanic and atmospheric models with realistic ocean thermodynamics. They are sophisticated enough to produce realistic solutions and so are testable, and yet they are also simple enough to be relatively easy to diagnose. **Coupled GCM's** can, and should, be closely compared to observations, but the important processes at work in them are not always easy to determine.

2. Conceptual and Simple Models

a. *Oceanic Rossby waves*

McCreary (1983) constructed a simple model which showed how oceanic Rossby waves might be involved in generating the low-frequency oscillations associated with ENSO (Fig. 1). The ocean was a reduced-gravity model [equations (4a)], and sea surface temperature (SST) in the eastern Pacific was specified to be either cold or warm depending on whether the thickness of the upper layer h_e there was less than or greater than a specified thickness h_{cr} (Fig. 1a). The model atmosphere consisted of two patches of zonal wind stress, τ_w and τ_H, that were assumed to interact with the ocean in a way first suggested by Bjerknes (1966, 1969): when the eastern ocean is cool ($h_e < h_{cr}$) the equatorial easterlies τ_w strengthen in the central ocean, thereby simulating Bjerknes' Walker circulation; when the eastern ocean is warm ($h_e > h_{cr}$) the extra-equatorial easterlies τ_H strengthen, thereby simulating an enhanced Hadley circulation. Wind curl associated with τ_H deepens the model interface to form ridge A (panel 1 of Fig. 1b). This ridge subsequently propagates slowly westward as a Rossby wave, and reflects from the western boundary as an equatorially trapped Kelvin wave that gradually deepens h_e (panels 2 and 3). Eventually h_e deepens beyond h_{cr}, SST

ORSTOM
CENTRE DOCUMENTATION
Montpellier

F 30218

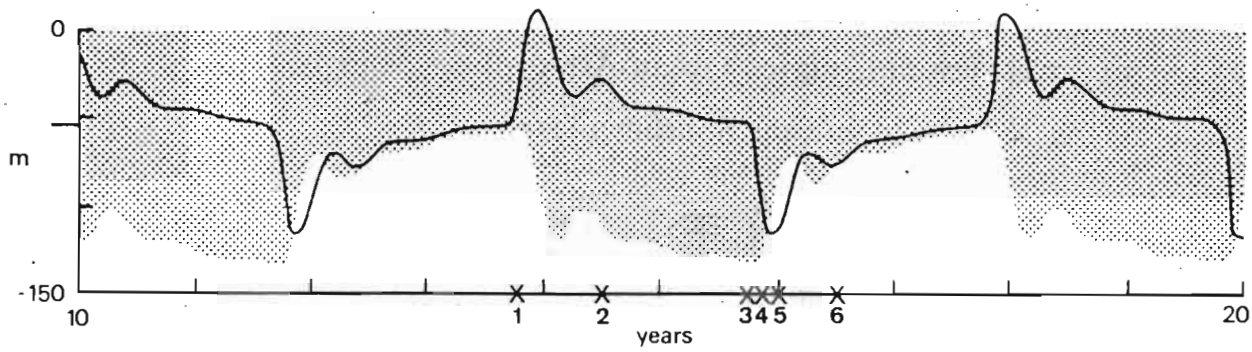

FIG.1a. The thickness of the model interface in the eastern equatorial ocean h_e (solid curve) and in the western equatorial ocean (bottom edge of the shaded area). The straight line indicates the value of h_{cr} = 53.5 m. The x's indicate times of the plots in Figure 1b. Transitions from one wind state to another are marked by El Nino or anti-El Nino events in the eastern ocean. (From McCreary, 1983.)

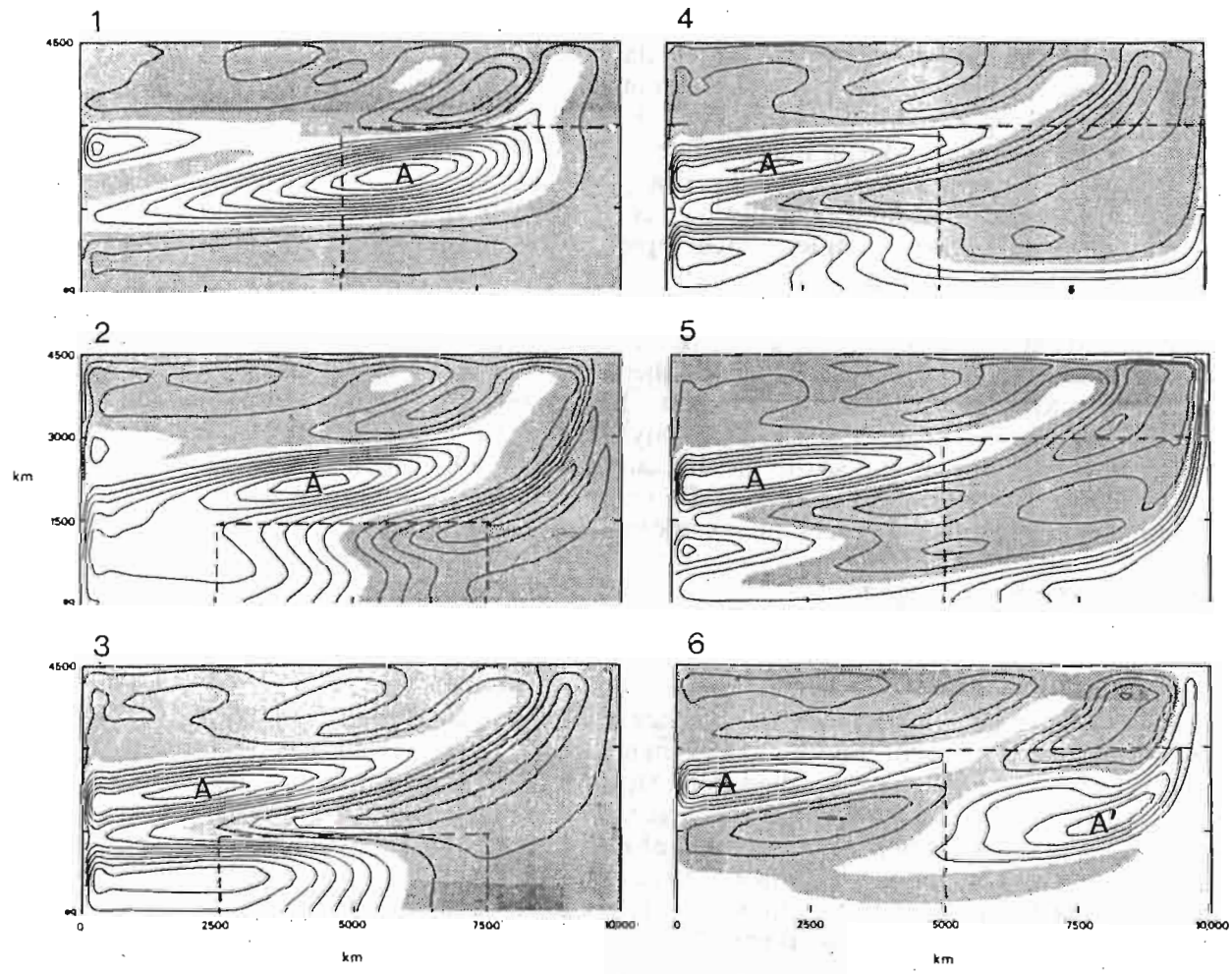

FIG.1b. Plots of upper-layer thickness anomaly for the 6 times indicated in Figure 1a. The contour interval is 10 m, there is no zero contour, and the shaded regions indicate negative anomalies (where h is less than 100 m). The dashed rectangles indicate the location of the wind patches τ_H and τ w. The slow propagation time of ridge A across the ocean basin sets the time scale of the model ENSO. (From McCreary and Anderson, 1984.)

warms in the eastern ocean, and an ENSO event is triggered (panels 4 and 5). It is the long propagation time of ridge A across the ocean basin that sets the period of the oscillation. A new ridge A' begins to spin up that will eventually trigger the next model ENSO at year 20 (panel 6).

Graham and White (1988) presented a conceptual model involving four variables: η_e and T_e representing the anomalies of upper-layer thickness and SST in the eastern Pacific, η_c being the upper-layer thickness anomaly in the off-equatorial central Pacific, and τ denoting the strength of the equatorial zonal wind stress anomaly. The four equations relating these variables are

$$\eta_e(t) = a\, T_e(t) + \eta_c(t-\delta)\,; \qquad \eta_c = -c\tau,$$
$$\dot{\tau} = -\tau + \alpha\,(ab)^{-1}\, T_e; \qquad Te = b\,\eta_e, \tag{1a}$$

where ε is a stochastic forcing, δ is a time lag, and the dot indicates a time derivative. The relationships in these equations all have sensible physical interpretations. For example, η_e is determined in part by $\eta_c(t-\delta)$, the lag simulating the delayed effect of Rossby waves that reflect from the western ocean boundary (like ridge A in Figure 1b); τ is linearly related to T_e, this relationship modeling Bjerknes' idea that the equatorial winds are determined by SST in the eastern Pacific. Solving for a single equation in τ yields

$$\dot{\tau} = (\alpha-1)\,\tau - c\,\tau\,(t-\delta) + \varepsilon\, d/\alpha \tag{1b}$$

Graham and White (1988) took $\alpha < 1$, so that (1b) is the equation for a damped oscillator. Without external forcing ε, then, the system has no oscillations, but rather adjusts to the state $\tau = 0$. With external forcing but without time-delayed feedback, solutions oscillate at the time scales of ε ; when time delayed feedback is included, they oscillate with a dominant period of the order of δ .

b. *Two equilibrium states*

A limitation of the McCreary (1983) model is that it involves τ_H, a wind component not clearly present in the observations. McCreary and Anderson (1984) modified the earlier model to eliminate τ_H. Parameters of the new system were adjusted so that in the absence of seasonal or random forcing solutions would adjust to one or the other of two equilibrium states: an ENSO state with τ_w switched off, and a "normal" state with τ_w switched on. When a seasonably varying wind stress τ_s is included, solutions can jump from being near one equilibrium state to being near the other (Fig. 2). Note in Figure 2 that after τ_w switches on (for example, after point A) h_e first overshoots and then gradually relaxes back toward its equilibrium depth, a relaxation that is due to Rossby waves reflected from the western boundary. This relaxation must be sufficiently complete before the seasonal cycle can trigger an ENSO event; thus, reflected Rossby waves also play an important role in generating the oscillations in this system. Note also that the onset of the model ENSO is phase located to the warm phase of the annual cycle (h_e deep), consistent with many observed events. With proper adjustment of the critical thickness h_{cr} the solution remains in a normal state longer than an ENSO state (lower panel of Fig. 2).

Schopf (1986) and Suarez and Schopf (1987) discussed solutions to the equation

$$\dot{X}(t) = X(t) - X^3(t) - cX(t-\delta) \tag{2}$$

suggesting that this conceptual model explained the oscillatory behavior of their coupled, numerical model of ENSO (see below). Schopf (1986) also pointed out similarities of this conceptual system to the McCreary and Anderson (1984) model just discussed. Note the

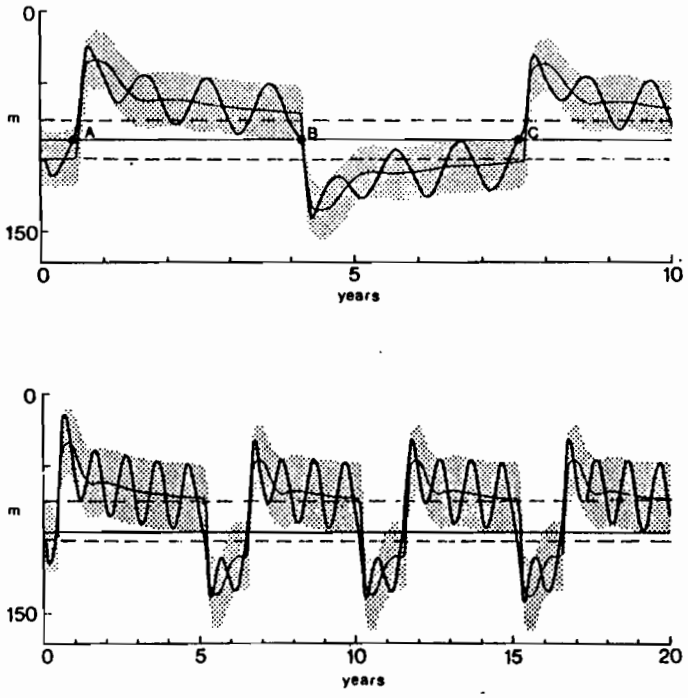

FIG.2. The time development of h_e (solid curves) when h_{cr} = 86.5 m (upper panel) and when h_{cr} = 95.3 m (lower panel). The solid straight lines indicate the values of h_{cr}, and the dashed lines indicate the two equilibrium values of h_e (74 m and 100 m) that are possible when there is no seasonal forcing τ S. In the lower panel, the model remains longer in a "normal" state, and ENSO events last only for 1 - 1 1/2 years. (From McCreary and Anderson, 1984.)

similarity to Graham and White's system (1c), in particular the presence of a time-delayed feedback term. In contrast to (1c), equation (2) has a strong positive feedback term X with a nonlinear negative feedback term $-X^3$ included to limit the growth of unstable perturbations. As a result, without time-delayed feedback the system adjusts to either of the two equilibrium states $X = \pm 1$ (the third equilibrium state $X = 0$ being unstable). With time-delayed feedback, the system develops oscillations at periods greater than 2δ ; indeed, oscillations still occur even if the reflection coefficient c is as small as 0.15.

Vallis (1988) considered a variety of conceptual models. One of them consisted of a one-dimensional equatorial ocean, defined in the domain $0 < x < L$. The system involves three variables: anomalous SST along the equator T(x), an x-independent anomalous zonal wind τ , and an x-independent equatorial zonal current u. The three equations relating these variables are

$$\begin{aligned} T_t + uT_x &= -AT \\ u_t &= \tau + c(u^*-u) + \varepsilon \\ \tau &= B\,[T(L) - T(0)] \end{aligned} \qquad (3)$$

where u^* represents a surface current due to the background trades, and ε is a random forcing. Boundary conditions for the T-equation are: $T(0) = 0$ if $u > 0$ and $T(L) = 0$ if $u < 0$, ensuring that the ocean advects water into the domain that is neither anomalously warm or cold. Again the physical processes described by (3) are sensible; for example, the last of equations (3) expresses Bjerknes' idea that the equatorial wind τ is determined by the SST difference between the eastern and western Pacific Ocean. Without stochastic forcing, the system adjusts to either a normal state with $u < 0$ and a cool eastern ocean, or an El Nino state with $u > 0$ and a warm eastern ocean. Figure 3 shows time series that result for various choices of model parameters. For sufficiently strong stochastic forcing and with $u^* < 0$, the system usually remains near the normal state, but occasionally jumps to being near the El Nino State (panel d of Fig. 3). It is not clear just what sets the time scale for ENSO events in panel d; the system lacks time-delayed feedback, and so the time scale is probably due to the particular nature of the stochastic forcing.

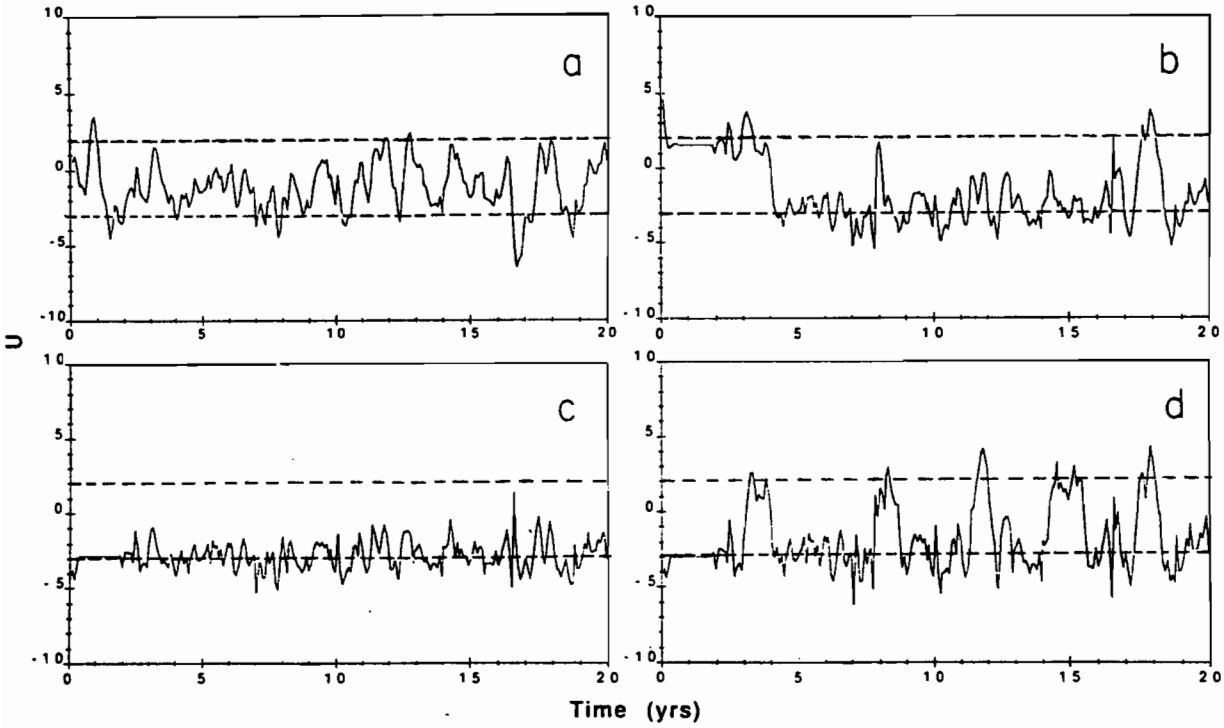

FIG.3. Time series of zonal current u, showing effects of variations of parameters. The dashed lines show the two equilibrium states to which the model will adjust in the absence of random forcing ε. Panel (a): B = 0, so that there is no temperature feedback. Panel (b): As for panel (a), but with $B \neq 0$. Panel (c): As for panel (b), but ε has a shorter correlation time scale. Panel (d): As for panel (c), except that ε has a larger amplitude. (From Vallis, 1988.)

c. *Unstable coupled modes*

Coupled models that study unstable modes nearly all utilize linear, reduced-gravity models of both the ocean and the atmosphere. Equations of motion for the model ocean are

$$u_t - fv + g' \eta_x = -\upsilon u + \tau^x/d,$$

$$v_t + fu + g'\eta_y = -\upsilon v + \tau^y/d, \qquad (4a)$$

$$\eta_t + d\,(u_x + \upsilon_y) = 0,$$

where d is the undisturbed thickness of the upper layer, and a simple equation like

$$T = \sigma \eta \qquad (4b)$$

describes ocean thermodynamics. Equation (4b) states that the anomalous temperature of the upper layer is directly proportional to the anomalous thickness of the upper layer, a relation that models the effect of equatorial upwelling on SST; Hirst (1985, 1986) has also modified (4b) to include a term representing the zonal advection of SST (see below). Equations for the model atmosphere are:

$$U_t - fV + g'' H_x = -AU$$

$$V_t + fU + g'' H_y = - AV \qquad (4c)$$
$$H_t + D (U_x + V_y) = - BH + Q.$$

Typically, the time derivative terms are ignored in (4c), a valid assumption because the atmosphere rapidly adjusts to equilibrium with the slowly varying forcing Q; an exception occurs when equations (4c) include effects of moisture convergence (see the discussion at the end of this section). Coupling between the two systems is provided by

$$\tau^x/d = \gamma U; \quad \tau^y/d = \gamma V; \quad Q = - \alpha T/\sigma \qquad (4d)$$

Solutions to equations (4) are found either numerically or by looking for mode solutions proportional to exp(ikx - iω t), in which case the operators ∂_x and ∂_t are replaced by the imaginary numbers ik and -iω , respectively.

Lau (1981) considered a simpler version of system (4) in order to understand the coupling that might exist between oceanic and atmospheric Kelvin waves. Essentially, he dropped f, v, V and τ^y from (4) and neglected y-derivatives. Mode solutions to this system satisfy the quadratic dispersion relation

$$(\omega^2 - c^2_a k^2) (\omega^2 - c^2_0 k^2) = \omega^2_c \; k^2 c^2_o \qquad (5a)$$

where $c_a = (g'D)^{1/2}$ and $c_o = (g'd)^{1/2}$ are the phase speeds of atmospheric and oceanic Kelvin waves, respectively, and $\omega_c = \alpha\gamma$ is a parameter measuring the strength of the coupling between the two fluids. Because $c_a >> c_o$, the two solutions to (5a) are approximately

$$c_1 = c_a; \qquad c_2 = c_o (1 - \omega_c^2/k^2c^2_a)^{1/2} \qquad (5b)$$

According to (5b), the phase speed of the atmospheric Kelvin wave c_1 is not much affected by the coupling ω_c, but the speed of the oceanic Kelvin wave c_2 is. As $\omega_c^2/(k^2c_a^2) \cong \phi$ increases to 1, c_2 decreases to zero, and for larger values it is imaginary; thus, for $\phi > 1$ this coupled mode is unstable.

The unstable solution in (5b) describes a fundamental process of air-sea interaction that appears to occur in most of the more complex models of ENSO. Figure 4 illustrates that process schematically. Suppose initially that the interface deepens by an amount η . This deepening causes an increase in T [equation (4b)], an increase in Q [equation (4d)], a convergent wind field U [the third of equations (4c)], and convergent ocean currents u [equations (4a)]; the convergent u-field leads to a further increase in η, and so on.

Hirst (1985, 1986) and Yamagata (1985) looked for mode solutions to the full system (4), and their resulting dispersion relations are shown in Figure 5. In each case there is a root with $\omega_i > 0$, a growing instability. This solution also propagates eastward with a phase speed (ω_r/k) similar to, but slower than, the oceanic Kelvin wave speed. Indeed for weaker coupling this root reduces to that of an ordinary oceanic Kelvin wave, leading both Hirst and Yamagata to refer to this unstable root as a "coupled Kelvin wave"; in order to differentiate more clearly this root from its uncoupled counterpart, I will subsequently refer to it as the "Kelvin mode". The process causing the instability is essentially that shown schematically in Figure 4. The upper panel of Figure 8b shows the horizontal structure of Hirst's Kelvin mode; note its similarity along the equator to the diagram in Figure 4, the primary difference being that the region of convergent winds and currents is shifted somewhat east of the maximum of η .

Figure 5 also has dispersion curves of several decaying Rossby modes. Hirst considered an alternate form of ocean thermodynamics in which (4b) was replaced by:
$T_t + u \langle T_x \rangle = 0$, where $\langle T_x \rangle$ is an assumed background temperature gradient. With this

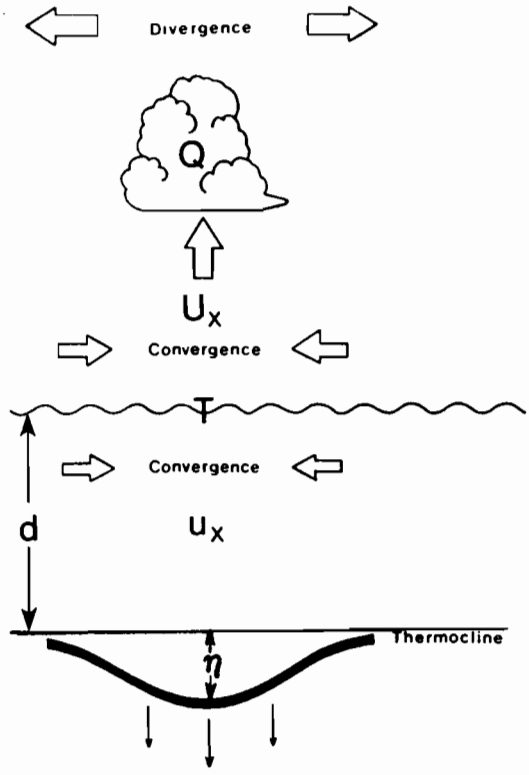

FIG.4. A schematic picture illustrating an important mechanism of unstable air-sea interaction in the tropics. An anomalous increase in the thickness of the upper layer η leads to a positive SST anomaly T, strenghtened atmospheric heating Q, a convergent wind field U_X, and a convergent oceanic flow u_X, which can further increase η. (From Yamagata, 1985.)

ocean thermodynamics, the system has growing Rossby modes and decaying Kelvin modes. It is not clear whether growing Rossby modes play an important role in more complex models, although Philander et al. (1989) suggest that they might exist in their coupled model (see section 4).

Philander et al. (1984) solved equations (4) numerically without using the normal-mode approach. Figure 6 shows the response of their model to an initial increase of interface depth. A growing disturbance develops that propagates eastward at a speed of about 43 $cm.s^{-1}$ considerably slower than that of an uncoupled oceanic Kelvin wave. Hirst (1986) concluded that the instability in Figure 6 was due to the presence of unstable Kelvin modes (upper panel of Fig. 8b).

A problem with all the preceding models of unstable modes is that their solutions continue to grow indefinitely. Anderson and McCreary (1985a) considered a coupled system similar to equations (4), in which the ocean thermodynamics was improved to ensure that T had a realistic upper bound. Consequently, the heating of the atmosphere Q was also bounded, and unstable modes were limited in amplitude. Figure 7 shows the equatorial T field that results when both the ocean and atmosphere are assumed to be cyclic with a wavelength of 15,000 km. After a spin-up period of about 1 year an instability appears that rapidly grows to attain an equilibrium amplitude. It has a period of 2000 days and a very slow eastward propagation speed of 15,000/2,000 $km.day^{-1}$ = 8.7 $cm.s^{-1}$. Anderson and McCreary argued that the mechanism generating this instability is the same as that illustrated in Figure 4. Thus, the instability appears to be a very slowly propagating Kelvin mode, its slow propagation speed probably being due to the fact that the mode is no longer growing in amplitude.

Hirst (1988) extended his earlier mode calculations to include ocean boundaries. Figure 8a shows the SST anomaly that develops when the atmosphere is cyclic with a wavelength of 30,000 km but the ocean is bounded with a width of 15,000 km. Anomalies appear in the western ocean, propagate eastward with a speed of 32 $cm.s^{-1}$, and intensify. When they

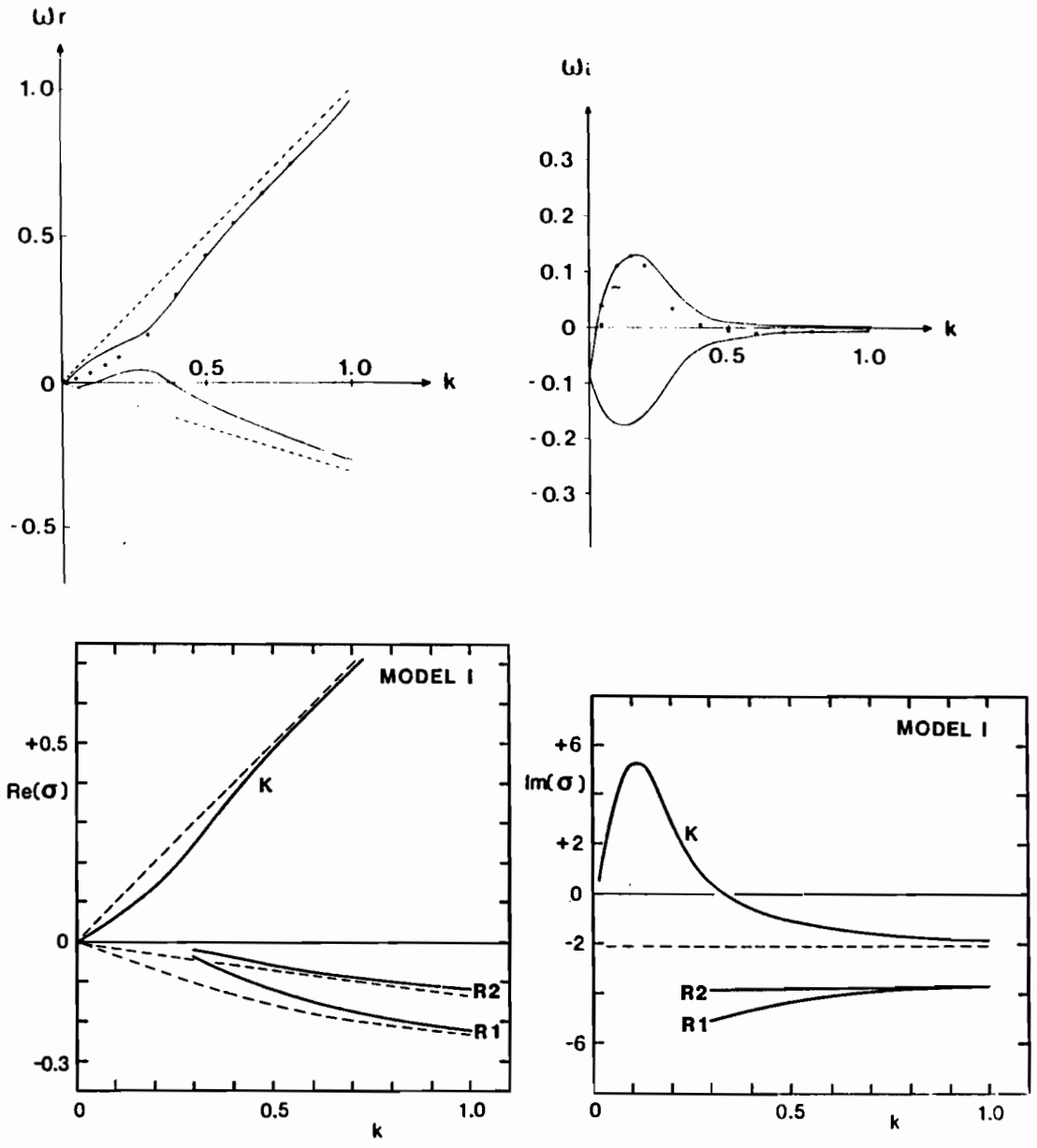

FIG.5. Dispersion curves for the coupled-mode solutions to equations (4) from Yamagata (1985) and Hirst (1986), in the upper and lower panels, respectively. The ω and k axes are normalized using the usual equatorial ocean length and times scales, and both the real and imaginary parts of ω are plotted. Dashed lines in the left panels are the dispersion curves of oceanic Kelvin and Rossby waves in the absence of coupling.

reach the eastern boundary they weaken, and eventually vanish. Figure 8b contrasts the solutions in the bounded ocean (lower panel) with the Kelvin-mode instability in an unbounded ocean (upper panel). The striking property is the similarity in the structure and propagation speed of the two solutions. Hirst concluded that the Kelvin-mode instability was crucial to the dynamics of the oscillation in the bounded, as well as unbounded, ocean.

Finally, it is worth noting that Lau and Shen (1988) and Hirst and Lau (1989) found mode solutions to the coupled system (4) when the atmospheric Kelvin-wave speed c_a was greatly reduced from its dry value by including a term in (4c) parameterizating low-level

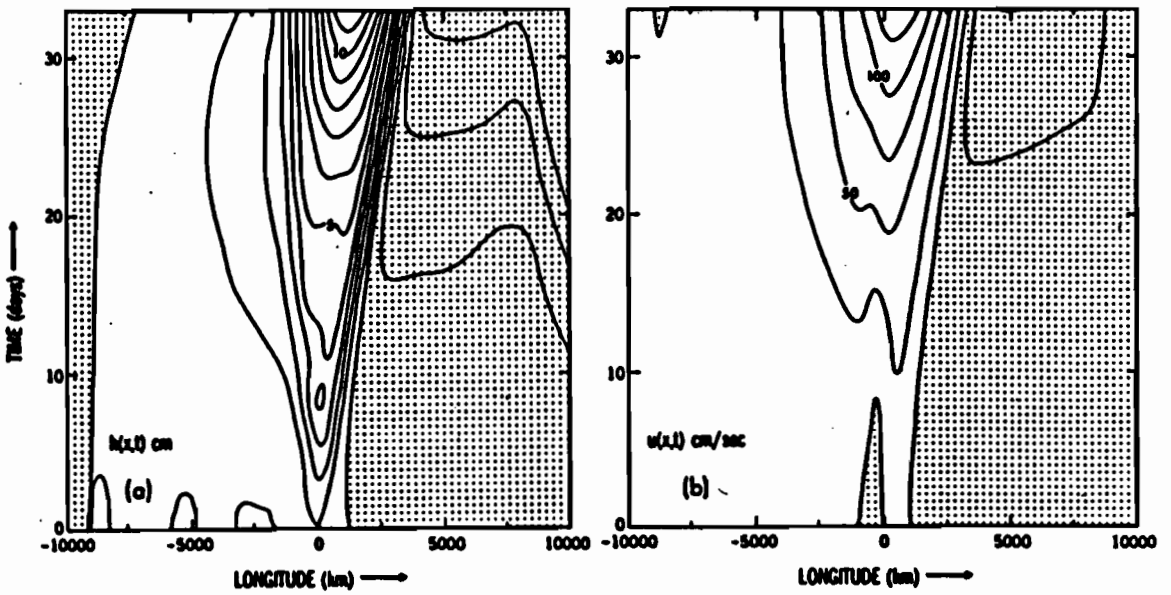

FIG.6. Upper-layer thickness anomaly (left panel) and zonal oceanic current (right panel) in a numerical solution of equations (4), in which an initial positive anomaly of upper-layer thickness is imposed. An instability develops that propagates eastward with a speed of about 43 cm.s^{-1}, considerably slower than that of an uncoupled oceanic Kelvin wave. Compare this instability with the unstable Kelvin mode in the upper panel of Figure 8b. (From Philander et al., 1984.)

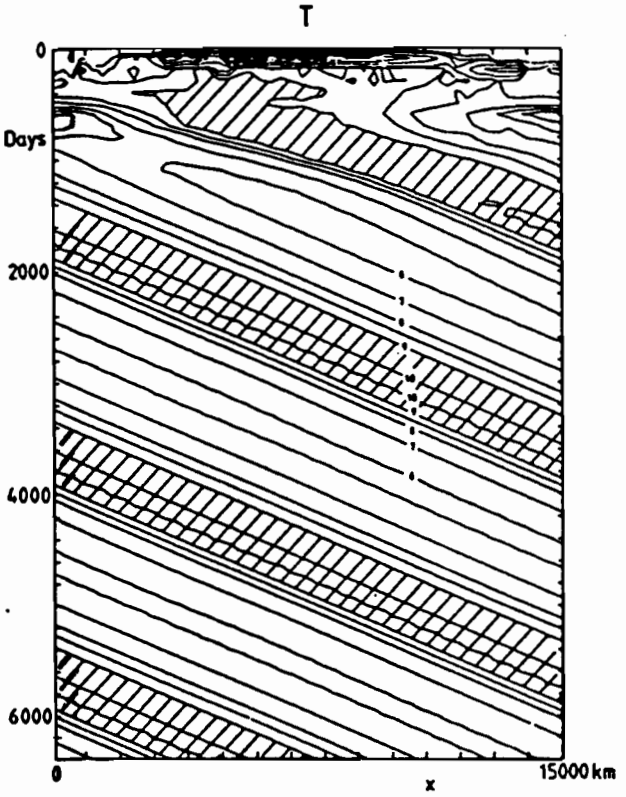

FIG.7. A longitude-time plot of equatorial temperature in a coupled model with cyclic boundary conditions and more realistic ocean thermodynamics. SST relative to a deep ocean temperature of 20^{o}C is shown. After an initial spin-up period, a coupled instability develops that propagates very slowly eastward with a speed of only 8.7 cm.s^{-1}. The improved ocean thermodynamics prevents SST from increasing much beyond 30^{o}C, and so the instability reaches an equilibrium amplitude. (From Anderson and McCreary, 1985.)

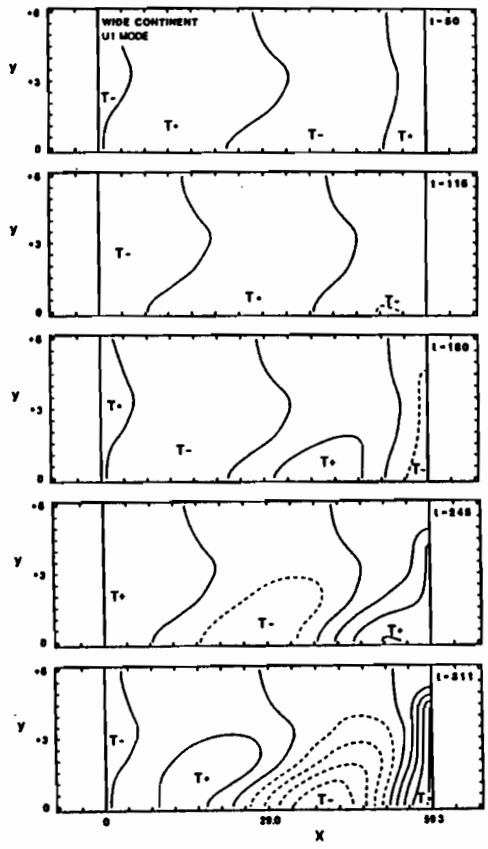

FIG.8a. Plots of SST anomaly for an unstable mode calculation in a bounded ocean basin. Values of x,y and t are in non-dimension units with one unit of space being 2.3° and of time being 2.1 days; thus, the width of the basin is 15,000 km, and the period of the oscillation is 548 days. (From Hirst, 1988.)

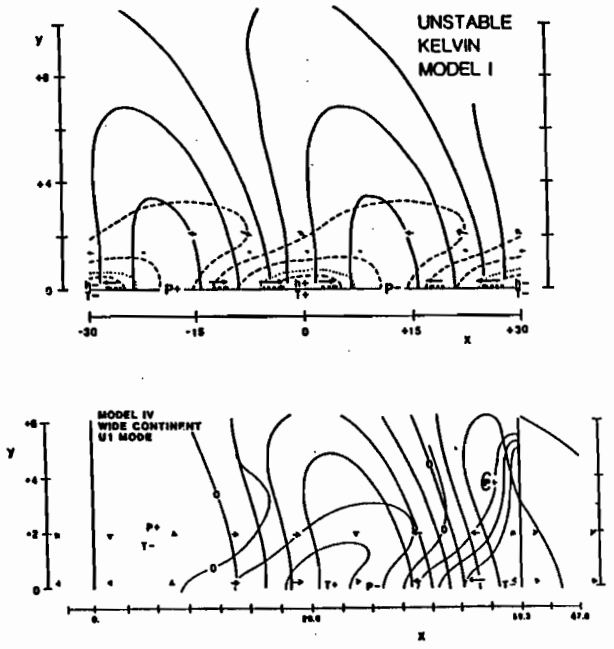

FIG.8b. As in Figure 8a, except showing plots of SST anomaly T (dashed lines or thin solid lines), atmospheric pressure P (thick solid lines), and wind (arrows) for an unstable mode calculation when the ocean is unbounded (upper panel) and bounded (lower panel). The similarity in structure and propagation speed of the two solutions identifies the unstable mode in the lower panel (and in Fig. 8a) as being the unstable Kelvin mode. (From Hirst, 1986, 1988.)

moisture convergence. In this case, the atmosphere no longer adjusts rapidly with respect to the ocean, and so it is necessary to retain the time-derivative terms in equations (4c). Low-frequency unstable waves, similar to those in Figure 5, still exist. In addition, when $c_a \sim c_o$ there is a new set of high-frequency waves with periods of 30-70 days that are essentially coupled oceanic and atmospheric Kelvin waves. The authors hypothesized that the presence of these high-frequency modes help to trigger ENSO events.

3. Intermediate models

Anderson and McCreary (1985a, 1985b) also reported several solutions when the atmosphere was cyclic with a wavelength of 30,000 km but the ocean was bounded. Figure 9a shows the resulting equatorial T when the ocean basin is confined to the region $15{,}000 < x < 30{,}000$ km and there is an external, atmospheric heating function Q_1 imposed over land to the west of the ocean representing the heating associated with convection over Indonesia. The system develops an oscillation with a period of about 4.5 years. Similar to the mode solution in Figure 8a, instabilities appear in the western or central ocean, propagate slowly eastward with a speed of roughly 15,000/1,600 km.day^{-1} = 11 cm.s^{-1}, and eventually dissipate near the eastern boundary. The dissipation is clearly associated with the growth of

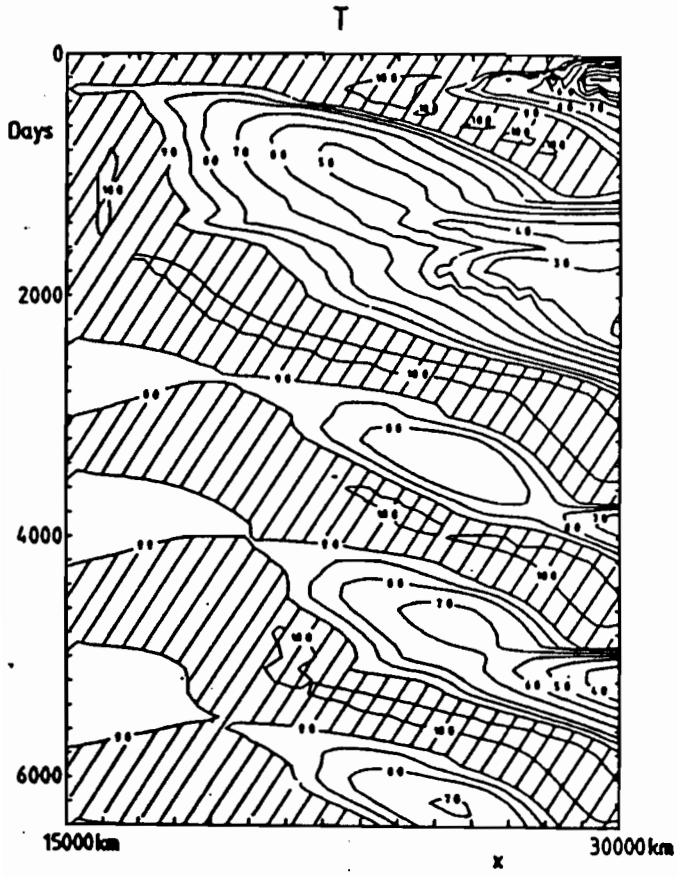

FIG.9a. As in Figure 7, except in a bounded ocean basin. The system develops an oscillation with a period of about 4.5 years. (From McCreary and Anderson, 1985a).

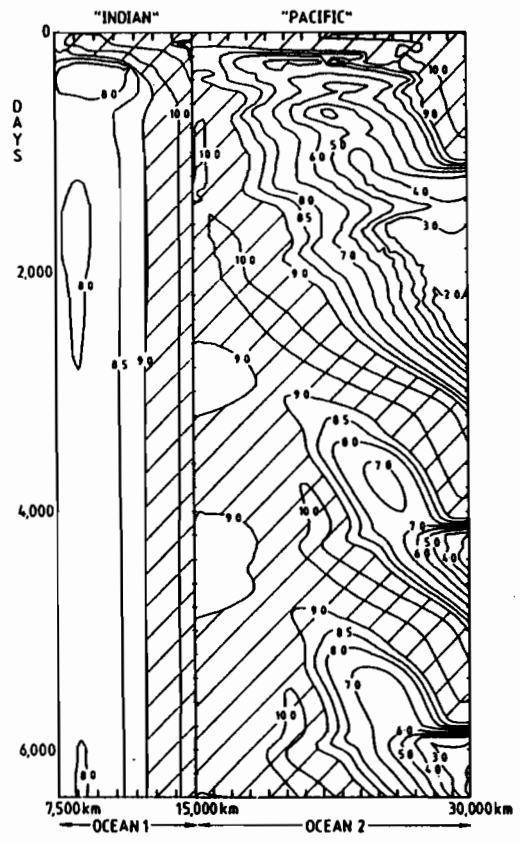

FIG.9b. As in Fig. 9a, except that an "Indian Ocean" is included. The "Indian Ocean" adjusts to an equilibrium state with warmest water in the east, whereas the "Pacific Ocean" undergoes low-frequency oscillations very similar to those in Figure 9a. (From McCreary and Anderson, 1985b.)

another disturbance in the west. Anderson and McCreary, noting the similarity between Figures 7 and 9a, concluded that an important part of the dynamics of the oscillation was the generation of a Kelvin-mode type of instability; they did not comment on whether reflected Rossby waves might also be involved. Hirst (1986) also remarked that a Kelvin-mode instability must account for the oscillation in Figure 9a, suggesting that its slow propagation speed was due to the use of large coupling coefficients. As noted earlier, the slow speed may also be due to the fact that the solution in Figure 9a is not a growing mode, but rather is adjusted to an equilibrium amplitude.

As might be expected, the strength of Q_1 in the preceding model strongly influences the response: with $Q_1 = 0$, an equilibrium state is reached with SST warmest in the eastern ocean (ENSO state), whereas with Q_1 sufficiently large the system adjusts to an equilibrium state with cool eastern SST (a normal state). Budin and Davey (1989) report similar sensitivities to the strength of land convection in their coupled model.

Figure 9b shows a solution to the Anderson and McCreary model when there is a second ocean confined to the region $7500 < x < 15{,}000$ km separated from the first by a thin

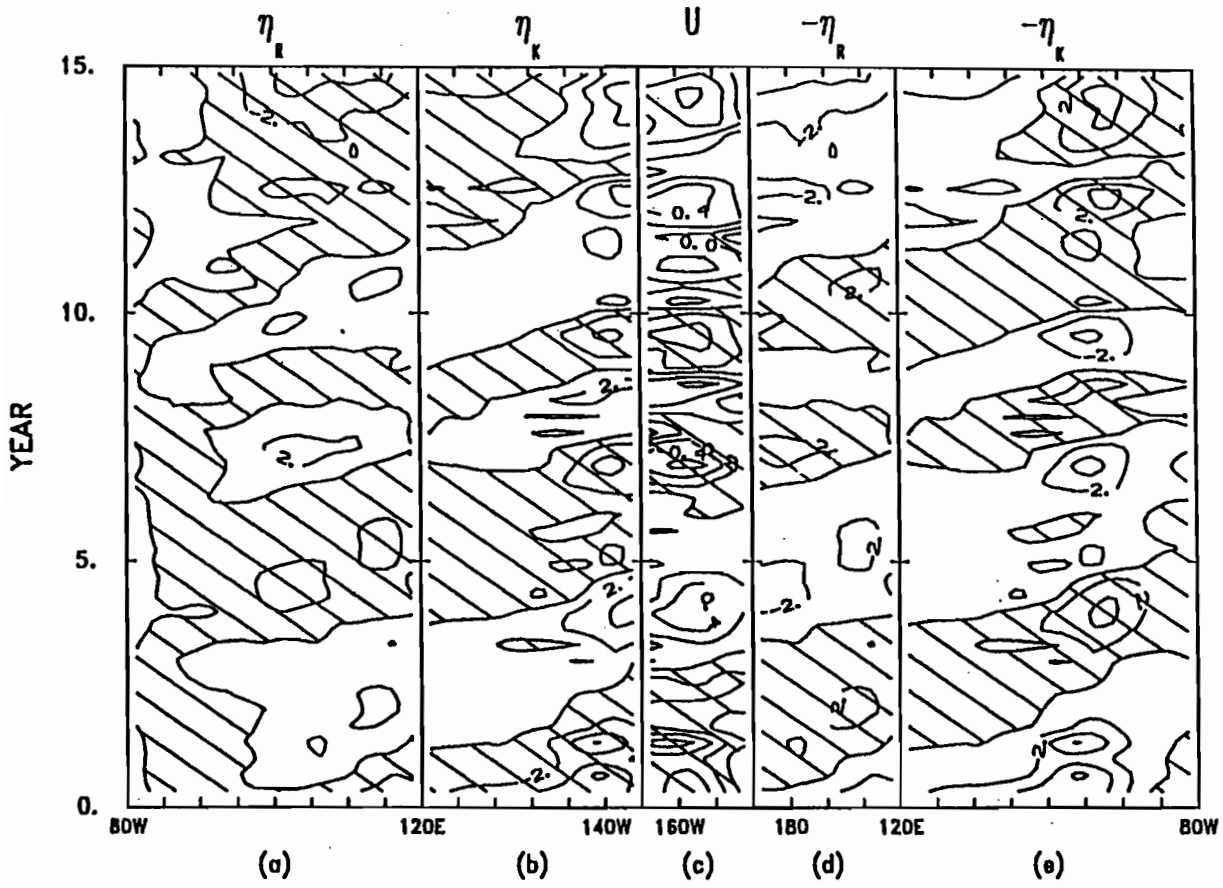

FIG.10. Longitude-time plots of upper-layer-thickness anomalies on the equator η_K and off the equator η_R (averaged from 5°N to 7°N) and of zonal wind U. To illustrate more clearly the importance of westward-propagating Rossby waves, η_R is plotted in reverse from east to west; in addition, in panels (a) - (c) positive anomalies are hatched, whereas in panels (d) and (e) negative anomalies are hatched. The presence of bands sloping upward from left to right suggests the importance of Rossby waves in both the onset and termination of ENSO events.

barrier, and there is no externally imposed forcing Q_1. The smaller "Indian Ocean" quickly adjusts to a stable state with warmest water and strongest atmospheric convection located in the eastern Indian Ocean. The larger "Pacific Ocean" exhibits low-frequency, eastward propagating oscillations, very similar to those in Figure 9a. The similarity of the two solutions in Figure 9 indicates that the model response over the Indian Ocean is dynamically equivalent to specifying Q_1 there.

Schopf and Suarez (1988) developed a coupled ocean-atmosphere model using a 2 1/2 -layer ocean model (a 3-layer model with an inert lower layer) and a 2-layer atmospheric GCM. Figure 10 is a plot showing upper-layer thickness anomaly off the equator (averaged from 5°N to 7°N) η_R and along the equator η_K, and also the zonal wind speed anomaly in the central Pacific U. The solution has an irregular oscillation at ENSO time scales. The irregularity is traceable to the generation of atmospheric variability by nonlinearities associated with the GCM; in a solution utilizing a linearized version of the GCM, the oscillations were perfectly periodic. In Figure 10, η_R is plotted in reverse (from east to west) in order to illustrate the important effect of the propagation of Rossby waves. About year 2, for example, a positive anomaly in η_R appears in the western Pacific and propagates westward as a Rossby wave; the Rossby wave reflects from the western boundary and

increases η_K; this increase triggers the development of a Kelvin-mode instability that increases U (weakens the equatorial wind), and causes an ENSO event about year 4. The positive wind anomaly at this time also acts to raise η R in the western ocean, generating a negative-anomaly Rossby wave that eventually triggers the end of the ENSO event. Interestingly, this sequence of events is very similar to that in the simple model of Figure 1, with the atmospheric switch from τ w to τ_H in the simpler model being replaced here by the development of a Kelvin-mode instability.

The Zebiak and Cane (1987) model is a coupled system similar to (4) except for the following differences: the ocean model has an embedded mixed layer and realistic ocean thermodynamics, climatological winds are included as an external forcing in order to maintain a realistic background ocean circulation, and a parameterization of moisture convergence is added to the specification of Q. Solutions oscillate at ENSO time scales, and are somewhat irregular due to the moisture-convergence term. Battisti (1988) used their model, and diagnosed its response for the presence of Rossby waves and Kelvin waves (modes). He concluded that the dynamics of the oscillations were much the same as in the Schopf and Suarez (1988) model. In particular, reflected Rossby waves were involved in both the onset and decay of ENSO; indeed, in a run in which the reflection of Rossby waves was suppressed, the coupled system adjusted to a permanent ENSO state.

4. Coupled GCM's

At the present, time there are only a few ENSO models that use both oceanic and atmospheric GCM's (a deficiency that no doubt will soon be alleviated). The development of coupled GCM's that can accurately simulate ENSO events is likely to be difficult. Gordon (1989), for example, reports that his solutions tend to adjust toward a permanent ENSO state, and that they are sensitive to the specification of the heat fluxes across the air-sea interface.

The coupled model of Philander et al. (1989) generates low-frequency oscillations. Figure 11a shows time series of eastern Pacific SST anomalies for two cases: when the oceanic GCM has a coarse resolution (4.5° of latitude) and when its resolution is fine (1/3° of latitude near the equator). The low-frequency oscillations in the coarse-resolution model (solid line) propagate westward, and so do not at all resemble ENSO signals; the authors attribute this failure to the fact that the coarse grid cannot resolve the Kelvin-mode instability, and suggest that the westward-propagating disturbances might be related to Hirst's unstable Rossby modes. In contrast, ENSO events in the fine-resolution model develop more realistically via eastward-propagating instabilities. Note in Figure 11b that the weak ENSO event in year 8 appears to be triggered by the reflection of equatorial Rossby waves from the western boundary; compare this time sequence with that of the much simpler model in Figure 1b. On the other hand, there is no obvious reflection of Rossby waves preceding the strong event in year 13. The authors suggest that the onset of ENSO events in their model may be triggered in several different ways.

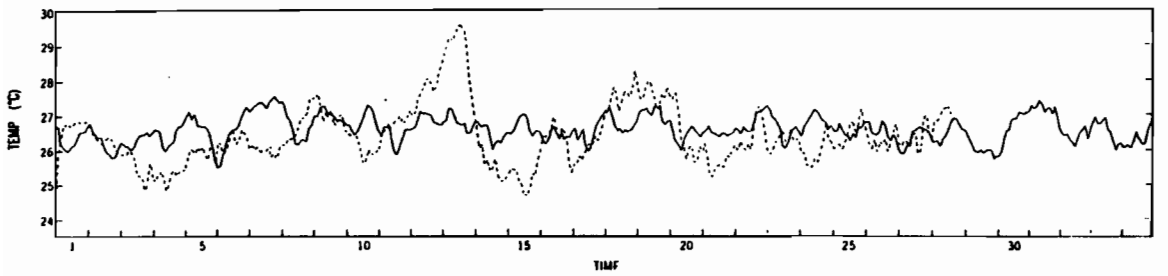

FIG.11a. SST anomalies in the eastern equatorial Pacific Ocean when the coupled model utilizes a coarse-resolution oceanic GCM (solid line) and a fine-resolution oceanic GCM model (dashed line). (From Philander et al. 1989.)

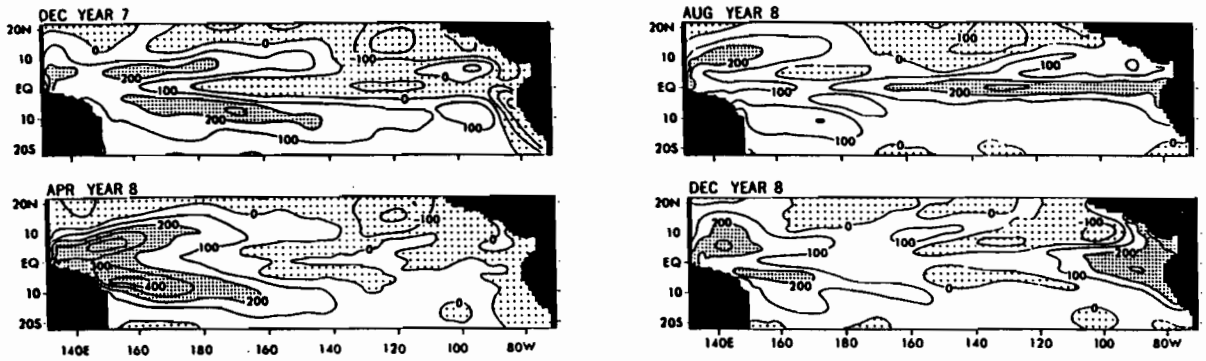

FIG.11b. Vertically integrated temperature from the surface to 300 m in the high-resolution case, effectively showing changes in the depth of the thermocline. The contour interval is 100 cal.cm^{-2}. Lightly stippled regions indicate where the thermocline is elevated, and heavily stippled areas indicate where the thermocline deepening is greater than 200 cal.cm^{-2}. Compare this sequence of panels with those in Figure 1b. (From Philander et al. 1989)

5. Summary and Discussion

Conceptual and simple models illustrate three types of possible ocean-atmosphere interactions that may be involved in ENSO dynamics. In the first type, it is the slow propagation speed of *oceanic Rossby waves* across the basin that sets the oscillation period for ENSO events. In the second, the coupled system has *two equilibrium states* for the same values of model parameters, and a "trigger" causes the system to jump from being near one equilibrium state to being near the other. In the third, slowly propagating *coupled instabilities* develop.

In all of the more complex models, the presence of coupled instabilities, particularly the Kelvin mode, is crucial. In most of them, Rossby waves reflected from the western ocean boundary are involved in both the onset and decay of ENSO; exceptions are the solutions of Philander et al. (1989), and possibly of Anderson and McCreary (1985a, 1985b) who did not discuss the role of Rossby waves in their oscillatory solutions. None of the complex models have been demonstrated to have two equilibrium states, although Suarez and Schopf regard the idea as being useful for discussing the behavior of their system [equation (2)].

Solutions are sensitive to nonlinearities in the model atmosphere: with linearized atmospheres oscillations are exactly periodic, whereas with nonlinear atmospheres they are irregular. They are also sensitive to the specification of convection over Indonesia and the Indian Ocean, and to the parameterization of heat fluxes through the air-sea interface. Clearly, these processes must be properly represented in order to improve models of ENSO.

REFERENCES

Anderson, D.L.T. and J.P. McCreary, 1985a: Slowly propagating disturbances in a coupled ocean-atmosphere model. *J. Atmos. Sci.*, **42**, 615-629.

Anderson, D.L.T. and J.P. McCreary, 1985b: On the role of the Indian Ocean in a coupled ocean-atmosphere model of El Nino and the Southern Oscillation, *J. Atmos. Sci.*, **42**, 2439-2442.

Battisti, D.S., 1988: The dynamics and thermodynamics of a warming event in a coupled tropical atmosphere/ocean model, *J. Atmos. Sci.*, **45**, 2889-2919.

Bjerknes, J., 1966: A possible response of the atmospheric Hadley circulation to equatorial anomalies of ocean temperature. *Tellus*, **18**, 820-829.

Bjerknes, J., 1969: Atmospheric teleconnections from the equatorial Pacific. *Mon. Wea. Rev.*, 163-172.

Budin, G.R. and M.K. Davey, 1989: Land effects in a simple model of the tropical coupled ocean-atmosphere. *Tropical ocean-atmosphere newsletter*, **50**. (Unpublished manuscript.)

Gordon, C., Tropical ocean-atmosphere interactions in a coupled model. (Unpublished manuscript.)

Graham, N.E. and W.B. White, 1988: The El Nino cycle : A natural oscillator of the Pacific ocean-atmosphere. *Science*, **240**, 1293-1302.

Hirst, A.C. 1985: Free equatorial instabilities in simple coupled atmosphere-ocean models. In: *Coupled Ocean-Atmosphere Models*, J.C.J. Nihoul, ed., Elsevier: Amsterdam, 153-165.

Hirst, A.C., 1986: Unstable and damped equatorial modes in simple coupled ocean-atmosphere models. *J. Atmos. Sci.*, **43**, 606-630.

Hirst, A.C., 1988: Slow instabilities in tropical ocean basin-global atmosphere models. *J. Atmos. Sci.*, **45**, 830-852.

Hirst, A.C. and K.-M. Lau, 1989: Intraseasonal and intra-annual oscillations in coupled ocean-atmosphere models. *J. Atmos. Sci.* (In press.)

Lau, K.-M., 1981: Oscillations in a simple equatorial climate system. *J. Atmos. Sci.*, **38**, 248-261.

Lau, K.-M. and Shen, 1988: On the dynamics of intraseasonal oscillations and ENSO. *J. Atmos. Sci.*, **45**, 1781-1797.

McCreary, J.P., 1983: A model of tropical ocean-atmosphere interaction. *Mon. Wea. Rev.*, **111**, 370-387.

McCreary, J.P. and D.L.T. Anderson, 1984: A simple model of El Nino and the Southern Oscillation. *Mon. Wea. Rev.*, **112**, 934-946.

Philander, S.G.H., T. Yamagata and R.C. Pacanowski, 1984: Unstable air-sea interactions in the topics. *J. Atmos. Sci.*, **41**, 604-613.

Philander, S.G.H., N.C. Lau, R.C. Pacanowski, and M.J. Nath, 1989: Two different simulations of the Southern Oscillation and El Nino with coupled ocean-atmosphere general circulation models, *Phil. Trans. Roy. Soc.* (Submitted.)

Schopf, P.S., 1986: Coupled dynamics of the tropical ocean-atmosphere system. In: *Further Progress in Equatorial Oceanography*, E.J. Katz and J. Witte, eds., Nova University Press: Ft. Lauderdale, 279-286.

Schopf, P.S. and M.J. Suarez, 1988: Vacillations in a couple ocean-atmosphere model. *J. Atmos. Sci.*, **45**, 549-566.

Suarez, M.J. and P.S. Schopf, 1988: A delayed action oscillator for ENSO. *J. Atmos. Sci.*, **45**, 3283-3287.

Vallis, G.K., 1988. Conceptual models of El Nino and the Southern Oscillation. *J. Geophys. Res.*, **93**, 13,979-13,991.

Yamagata, T., 1985: Stability of a simple air-sea coupled model in the tropics. In: *Coupled Ocean-Atmosphere Models*, J.C.J. Nihoul, ed., Elsevier: Amsterdam, 637-658.

Zebiak, S.E. and M.A. Cane, 1987: A model El Nino-Southern Oscillation. *Mon. Wea. Rev.*, **115**, 2262-2278.

On Warm Rossby Waves and their Relations to ENSO Events

Kensuke TAKEUCHI

Department of Geophysics
Hokkaido University
Sapporo, 060 Japan

ABSTRACT

The hypothesis suggested by several simple air-sea coupled models is examined with an ocean numerical model driven by FSU wind stress for the period from 1963 to 1987. The examined hypothesis is that warm Rossby waves generated by stronger trades associating with cold events following warm episodes are responsible for triggering the next warm events. As results, followings are found.

1) Warm Rossby waves are always found approaching the western boundary of the tropical Pacific in the preceding winters of the warm events.
2) However, some winters are not followed by warm episodes even though warm Rossby waves are found near the western boundary.
3) The warm Rossby waves are mostly generated in the central and western tropical Pacific in the preceding years and no clear relations have been found between the previous warm events.

1. Introduction

Is ENSO cyclic or random ? This is the most fundamental question about ENSO. If ENSO is cyclic, the previous warm event is the causes of the next cold event which in turn gives rise to the next warm event. On the other hand, if ENSO is essentially random, the trigger of an event has no relation to the previous events.

Recently, several simple atmosphere-ocean coupled models succeeded to reproduce ENSO-like vacillations (Cane and Zebiak, 1985; Schopf and Suarez, 1987; Xie, 1988). One notable common feature of their results is that warm events are triggered by warm Kelvin waves which are generated by reflection of warm Rossby waves at the western boundary. The warm Rossby waves are forced by stronger than usual Trades in the cold events following the previous warm events. So, these results suggest ENSO is cyclic.

It has been already pointed out by several authors that the warm water pile-ups in the western tropical Pacific are nearly always found in the previous northern winter of the beginning of warm events (White et al., 1985; Matsumoto and Takeuchi, 1988). However, relations between these pile-ups and the previous events are still not clear. Observational data are not enough to examine them.

Therefore, in the present study, a numerical model is used to examine the formation process of the warm water pile-ups in the western tropical Pacific, for the period from 1969 to 1984.

2. MODEL

The model simulates the tropical Pacific Ocean between 30°S and 30°N. The model ocean has realistic coastline at western and eastern sides of the model, but no bottom topography. The numerical procedure for the integration is similar to that described in Bryan (1969). The model specifications are:

ORSTOM
CENTRE DOCUMENTATION
Montpellier

F 30219

Coordinate :	Cartesian delta-plane
Horizontal resolution :	2/3° in both direction
Vertical resolution :	15 levels, 25 m in upper 250 m
Horizontal mixing :	Bi-harmonic
Vertical mixing :	Richardson number dependent mixing coefficient, similar to Pacanowski and Philander (1981)
Salinity :	Not included
Sea surface heat flux :	Haney (1971)'s type
Wind stress :	FSU (Goldenberg and O'Brien 1981)

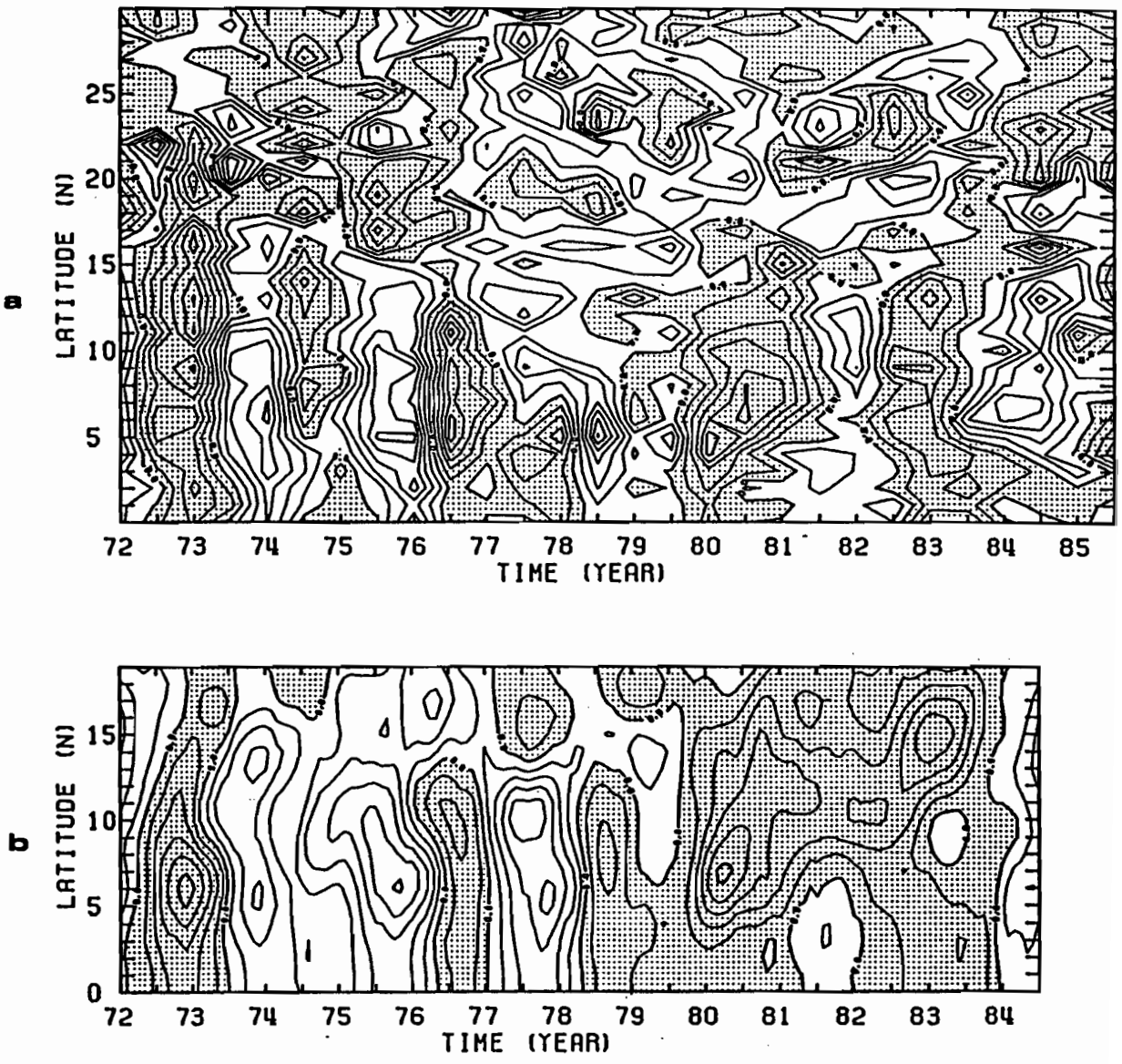

FIG.1. Surface dynamic height anomaly (re. 400db) along 137°E, as derived from (a) observed data taken by Japan Meteorological Agency, and (b) the model.

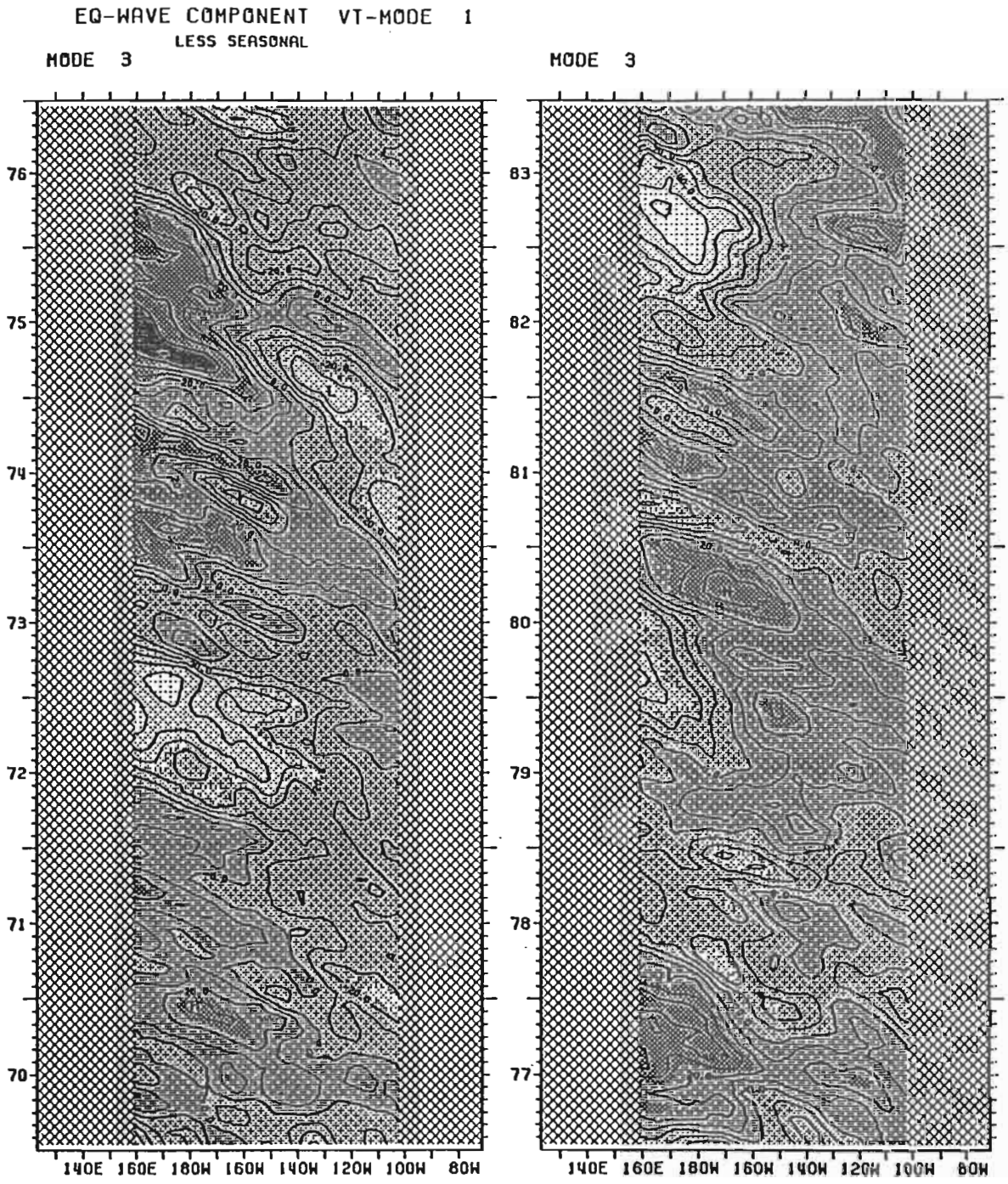

FIG.2. Time versus longitude diagram showing the amplitude of the 3rd meridional first vertical mode Rossby wave. Big tip-marks on the vertical axis are boundaries between years. Darker shade indicate warm Rossby wave.

At the northern and southern boundaries, the meridional volume transport is calculated assuming Sverdrup relation. Otherwise, there is no derivative in north and south direction. Newtonian dumping is applied for temperature near the boundaries to the climatology.

Initially, the ocean is at rest and uniformly stratified. First, the model is driven by annual mean wind for more than ten years, using one degree resolution model, then three years using 2/3 degree resolution model. The integration is continued for three years using climatological seasonal wind, and then interannual run take over the integration.

3. Warm water pile-up in the model and the real ocean

Analyses of the model results are meaningless unless the model simulates the real ocean well enough. As the purpose of the present study is to examine the pile up processes of warm water in the western tropical Pacific, comparison between model and observation is made for dynamic height anomaly along the 137°E (Fig. 1). Observed dynamic height is calculated from data taken by Japanese Meteorology Agency in cruises carried out routinely twice a year.

Quasi-biannual variations can be seen in both figures in lower latitudes in the 70's. Positive anomalies at the beginning of 1972 and 1976 are followed by warm events. For the 1982-1983 event, preceding positive anomalies are not strong, but are still visible. Therefore, as far as these periods are concerned, all warm events are preceded by positive anomaly in dynamic height, which is a consequence of the warm water pile up. However, the contrary is not true. For example, strong positive anomaly found at the beginning of 1974 is not followed by a warm event.

Two conclusions can be derived. First, warm water pile up is a necessary precondition for a warm event, but not a sufficient condition. Second, the model simulate the warm water pile up well enough to suggest that analyses of the model is meaningful.

4. Equatorial wave analysis

The piling up process can be either dynamical or thermal. However, the thermal process is suggested to be not essential as the positive dynamic height anomalies are also reproduced in 1.5 layer model which doesnot include any thermal process at all (Takeuchi, 1987).

If the process is dynamical, and if non-linear effects are not too strong, the process may be understood in terms of wave dynamics. From the wave dynamic point of view, the warm water piling up process can be seen as formation process of warm Rossby wave, thus generation and propagation can better be seen.

For the purpose, each equatorial wave component is isolated. First, the mean density field is calculated, and vertical mode functions are computed at every location using the mean density distribution. Next, pressure anomaly distribution is decomposed onto vertical modes. Finally, each meridional mode is isolated using hyperbolic cylindrical functions.

Fig. 2 shows time versus longitude distribution of the third Rossby wave component of the first vertical mode. In this figure, we can see warm Rossby waves are approaching the western boundary in the periods when positive dynamic height anomalies are found in Fig. 1. Other lower mode Rossby wave show similar behavior. It indicates that the warm water pile up is not formed locally. Then the problem is where and when the warm Rossby waves are generated. The figure shows that the formation area is the central Pacific, say, between the date line and 150°W. They are generated in the previous years of the beginning of warm events.

Also very notable is the similarity between the one to tow year periods preceding the major warm events, 1972-1973 and 1982-1983. Three warm Rossby packets are propagating from central Pacific to the western boundary in each period. The first packets are strongest but tend to die out before reaching the western boundary. The second ones are responsible for the positive anomaly appeared in Fig. 1. The similarity also can be seen to some extent for the 1976 minor warm event.

Another common feature is that each warm event is followed by positive dynamic height anomaly in the western tropical Pacific, as seen in Fig. 1. Warm Rossby waves are also found in Fig. 2. However, in the period analyzed in the present study, no warm event follow the warm water piling up.

5. Discussion and conclusion

Through the present study, the followings are found.

1) Piling up of warm water in the western tropical Pacific is a necessary precondition for a warm event to develop, but not an efficient condition.
2) The piling up of warm water is formed in the central Pacific in the previous year of the beginning of each warm event and propagates to the west as warm Rossby wave.
3) The longitude versus time distribution of Rossby wave component shows similar pattern in each 1 to 2 year period previous to the beginning of warm event.
4) In the following years of warm events, formation of warm Rossby waves are always found, but not followed by the next warm event.

These results suggest that ENSO cycle is not as simple as simple coupled models indicate, even if it is a cycle. After a warm event terminates, a cold phase appears and stronger than usual trade winds generate warm Rossby waves in the central Pacific which propagate westward resulting in an anomalous warm water piling up in the western Tropical Pacific. However, at least in the period examined in the present study, no warm event developed in such a situation.

On the other hand, generation of warm Rossby waves in the previous year of each warm event seems to have no apparent relation with the previous warm event. We still have missing rings to be found. The similarity of the behavior of central to western tropical Pacific in the previous year of 1972-73 and 1982-83 events seems to be very suggestive.

REFERENCES

Bryan, K., 1969: A Numerical Method for the Study of the Circulation of the World Ocean. *J. Compt. Phys.*, **4**, 347-376

Cane, M.A. and S.E. Zebiak, 1985: A theory for El Nino and the Southern Oscillation. *Science*, **228**, 1085-1087

Goldenberg, R.L. and J.J. O'Brien, 1981: Time and space variability of tropical Pacific wind stress. *Mon. Wea. Rev.*, **109**, 1190-1207

Haney, R.L., 1971: Surface Thermal Boundary Condition for Ocean Circulation Models. *J. Phys. Oceanogr.*, **1**, 241-248

Matsumaoto, Y. and K. Takeuchi, 1988: Interannual Variation in the Western Tropical Pacific Ocean and Its Relation to ENSO, seen in the Japan Meteorological Agency 137°E Line Observations. *Geophys. Bul. Hokkaido Univ.*, **51**, 63-75

Pakanowski, R. and S.G.H. Philander, 1981: Parameterization of vertical Mixing in Numerical Models of Tropical Oceans. *Geophys. Res. Lett.*, **11**, 802-804

Pazan, S.E., W.B. White, M. Inoue and J.J. O'Brien, 1986: Off-equatorial Influence upon pacific Equatorial Dynamic Height Variability during the 1982-1983 El Nino/Southern Oscillation Event. *J. Phys. Oceanogr.*, **91**, 8437-8449

Schopf, P.S. and M.J. Suarez, 1987: Vacillations in a coupled ocean-atmosphere model. *J. Atmos. Sci.*, **45**, 549-566

Takeuchi, K., 1987: Forerunners of El Nino/Southern Oscillation Appearing in the FSU Model, *Geophys. Bul. Hokkaido Univ.* **49**, 381-386.

Effect of Low Latitude Western Boundary Gaps on the Reflection of Equatorial Motions

Yves du PENHOAT[1] and Mark A. CANE[2]

[1]*Groupe SURTROPAC, ORSTOM BP A5, Nouméa - New Caledonia*
[2]*Lamont Doherty Geological Observatory, Palisades, NY 10964 - U.S.A.*

ABSTRACT

The western tropical Pacific is thought to be an important zone for generating El Nino : reflections at the boundary make it a potential source region of equatorial Kelvin waves. Calculations of the effect of a gappy western boundary on the reflection process are carried out in the framework of the low frequency limit of the shallow water equations and are highly idealized. The method is also applied to a schematic version of the flow through the Indonesian seas from the western Pacific to the Indian oceans.

The results indicate some strong sensitivities to the location of the gap and to the structure of the incoming flows. In addition, the results can be quite different depending on whether the zonal extent of the gap is assumed to be infinite or finite. (More precisely, the latter means that the extent of the gap is short compared with the zonal wavelength of the relevant free waves at that frequency.)

Due to the complexity of the results for even such a simplified model, it will be very difficult to be confident of any modeling study of the Indonesian throughflow short of a highly resolved numerical calculation with a detailed representation of the geometry and bathymetry. Nonetheless, we offer tentative conclusions concerning the efficiency of the western Pacific boundary as a reflector. Our results suggest that the realistic boundary will not greatly alter expectations on a simple solid boundary if the reflections important for El Nino are primarily in motion represented by low order Rossby modes. This is also consistent with observational evidence which tends to support that there is no anomalous throughflow during El Nino events.

1. Introduction

Recent studies have recognized that ocean dynamics have an important role in development of the phenomena known as El Nino and the Southern Oscillation (ENSO). In theory as well as in observations, the influence of equatorial Kelvin waves has been established. For example, White et al (1985), studying the increase of heat content, claimed that extra-equatorial Rossby waves generated by anomalous wind curl, after impinging on western coasts, could generate an equatorial Kelvin wave which in turn would trigger an El Nino event. However Battisti (1988, 1989) tempers their conclusions and finds that off-equatorial waves (poleward of 6° from equator) Rossby waves could not be invoked as a triggering mechanism in his model, although he also points out the importance of western boundary reflections for event terminations. Zebiak (1989), in the context of a linear dynamical model, discusses the role of Rossby waves and western boundary reflections : some of the equatorial transport near the western boundary originates at higher latitude in the interior basin due to the structure of Rossby wave induced circulation, but the zonal convergence/divergence at the western boundary determines the nature of the Kelvin wave signal.

Wether of not extra-tropical influences are important depend on how well the western boundary can reflect disturbances into equatorial Kelvin waves. In oceanic models and coupled models as well, reflection of Rossby waves at the western boundary

ORSTOM
CENTRE DOCUMENTATION
Montpellier

F 30220

is the basic mechanism to overcome the feedback tending to raise sea level. In numerical models (with the exception of the NORDA model; Kindle et al, 1989), the western Pacific boundary is a nice smooth wall, but in reality, it consists of irregular island chains. Therefore, it could be a poor wave reflector, allowing Rossby waves to pass through its many passages.

Our motivation for the work was to know how efficient the Pacific western boundary is at generating equatorial Kelvin waves by reflection of mean flux incident at the boundary. How efficient is the "gappy" western boundary of the Pacific Ocean at generating equatorial Kelvin waves by reflections of incident mass flux ? Does the irregular, "porous", western boundary support the simple planetary wave reflections which occur in numerical models (with a full boundary) ?

We focus this investigation on the effects of leaky boundaries on basin wide adjustment processes rather than on details of boundary layers in the vicinity of coasts or gaps. Our approach uses extensively techniques and results of Cane and Sarachick (1977, 1981) and is an extension of Cane and du Penhoat (1982) and du Penhoat, Cane and Patton (1983). Calculations are carried out in the framework of the linear shallow water equations that we solve for the asymptotic flow which results when a source is switched on at $t=0$ and remains steady thereafter. The results of this the problem are easily generalized to all low frequency flows.

2. The basic problem

At $t=0$, a flow comprised of Rossby waves impinges on a western boundary at $x=0$. The flow has a $H(t)$ form, a step function in time. The coast is oriented north-South, thus presenting a gaps of width $d=a-b$. We are interested in low frequency motion for which frequency is small compared to the equatorial scaling frequency. We seek the asymptotic response as $t \to +\infty$. Cane and Sarachick (1976) have shown that for large t, the asymptotic motions are of three kinds (all variables have been scaled by the usual equatorial scaling) :

(i) Long eastward propagating Kelvin waves, with zonal velocity u and height h proportional to ψ_0 , the zeroth order Hermite function :

$$(u, v, h) \sim \left[\psi_0(y), 0, \psi_0(y)\right] \quad \text{with} \quad \psi_0(y) = \pi^{\frac{-1}{4}} e^{-\frac{y^2}{2}}$$

(ii) Long Rossby waves, propagating energy westward. Both the equatorial Kelvin wave and the long Rossby waves satisfy the meridional geostrophic relation.

The equatorial Kelvin wave has meridional velocity $v = 0$ and long Rossby waves have $v \approx 0$. For these two kinds of asymptotic motions, the large t response is steady and independant of x.

(iii) Short Rossby waves (included the mixed Rossby-gravity wave). Sum of such modes is an ever thinning boundary layer trapped to $x=0$ (see Cane and Sarachick, 1979), thus forming a western boundary current.

In this work, we exploit the fact that at low frequency there is a streamfunction for the sum of eastward propagating short Rossby waves and that the only part of the reflection that propagates away from the boundary is the equatorial Kelvin wave.

Let $(\hat{u}, \hat{h})$ be the low frequency incoming Rossby waves. The flow statisfies the geostrophic relation and is orthogonal to the Kelvin wave.

Two conditions have to be satisfied at $x=0$, the longitude of the coast :

1) $u=0$ at the coast, i.e., for $y>a$ and $y<b$

2) u and h are continuous across the gap, i.e, at $b<y<a$

When the incoming wave hits the coast, part is transmitted into the gap and part is reflected into an equatorial Kelvin wave of amplitude T^k.

The continuity condition at the gap longitude and the geostrophic balance east and west of the gap imply that there is no short Rossby waves in the gap. It also implies that discontinuities in h are thus possible at $y=a$ and $y=b$. Since west of the boundary u and h are in geostrophic balance, we must allow for an infinite zonal velocity at $y=a$ $(y=b)$ to balance the jump in h, i.e.

$$u = A\,\delta(y-a) + B\,\delta(y-b) \text{ at } y=a,b$$

Integration of the continuity equation leads to :

$$A = \int_a^{+\infty} \hat{u}\, dy + T^k \int_a^{+\infty} \psi_0(y)\, dy \text{ and } B = \int_{-\infty}^{b} \hat{u}\, dy + T^k \int_{-\infty}^{b} \psi_0(y)\, dy$$

and the boundary currents at the tips of the gap are simply fed the boundary currents along the North-South coast. The amplitude of the reflected Kelvin wave is then obtained by using the completness and orthogonality properties of the eigenfunctions of the shallow water equations (cf. Cane and Sarachick, 1977, 1981) :

$$T^k = -\frac{\int_a^b (\hat{u}(y)+\hat{h}(y))\psi_0(y)dy + \psi_0(a)\int_a^{+\infty} \hat{u}(y)dy + \psi_0(b)\int_{-\infty}^{b} \hat{u}(y)dy}{2\int_b^a \psi_0^2(y)dy + \psi_0(a)\int_a^{+\infty} \psi_0(y)dy + \psi_0(b)\int_{-\infty}^{b} \psi_0(y)dy}$$

Therefore, T^k, A and B determine the complete solution.

3. Results

All results are presented in nondimensional units. Distances are scaled by the standard equatorial radius of deformation (see values in Table I).

Results differ if the zonal extent of the gap is infinite (as supposed in calculations of section 1) or finite. More precisely, the latter means that the zonal extent of the gap is short compared with the zonal wavelength of the relevant free waves at that frequency. (It can also be treated equivalently as infinitesimally thin width; cf. Cane and du Penhoat, 1982). At low frequencies, it corresponds to the case of islands while the former case is relevant to a semi-enclosed sea.

On Fig. 1 are plotted the amplitude of the reflected Kelvin wave for different incoming Rossby waves. The results are sensitive to the location and width of the gap and to the meridional structure of the incoming flow.

For example, for the $n=1$ incoming Rossby wave, the reflected Kelvin wave is minimum if the gap is centered at the equator. However, the amplitude of the reflected Kelvin wave is not negligible. (On Fig. 1, the amplitude T^k has been normalized by the value of the Kelvin wave amplitude if the boundary were a full boundary). As the gap width decreases, wherever the gap is centered, the amplitude of the reflected Kelvin wave is over 0.9 : all the incoming mass flux is reflected back into the Kelvin wave and is equivalent to the full boundary case.

Plots for $n=2$ and $n=3$ incoming Rossby waves (Figs. 1b and 1c) show more structure, since as n increases, waves are less equatorially trapped and have a more complex oscillating structure. For $n=2$ incoming Rossby waves, which have an antisymmetric meridional structure, there is a weak reflected Kelvin wave as far as the gap is not centered on the equator. (For a full boundary, there is no reflected Kelvin wave; Cane and Sarachick, 1977; the amplitude of the reflected Kelvin wave is not normalized on Fig. 1b).

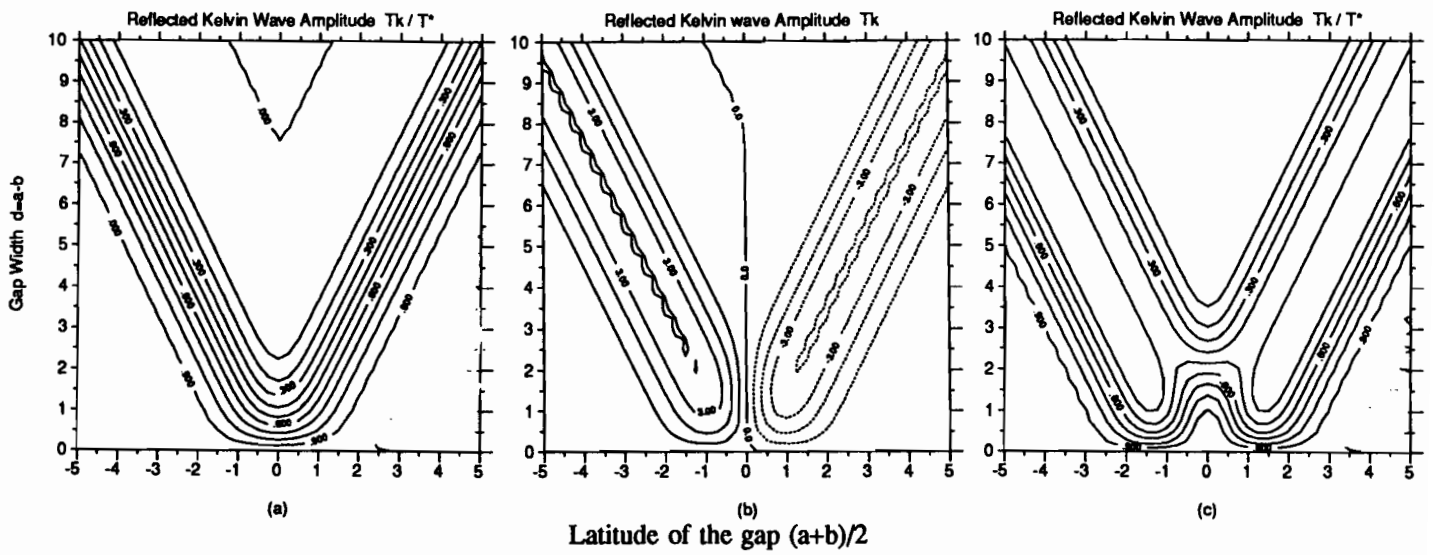

FIG. 1. Reflected Kelvin wave amplitude for a gap of infinite zonal length a)For $n=1$ incoming Rossby wave. Amplitude has been normalized by the reflected Kelvin wave amplitude for a full boundary. b) For $n=2$ Rossby wave, c) For $n=3$ incoming Rossby wave, normalized by the reflected Kelvin wave amplitude for a full boundary.

Results for a gap of finite zonal length are presented in Fig. 2. The methods used in section 1 apply. The solution differs as, in the downstream region west of the gap, the boundary condition $u=0$ at $y>a$ and $y<b$, together with the geostrophic relation leads to $h=D_a$ at $y>a$ and $h=D_b$ at $y<b$. D_a and D_b are constant. In this case, some mass flux must escape to set up a constant sea level on the western side of the gap. D_a and D_b are determined by projecting the Kelvin wave onto the solution west of the gap :

$$D_a=\hat{h}(a)-aA+T^k\psi_0(a) \quad \text{and} \quad D_b=\hat{h}(b)+bB+T^k\psi_0(b)$$

A and B have the same expression as in the former case. The amplitude of the reflected Kelvin wave is then :

$$T^k=-\frac{\int_a^b(\hat{u}+\hat{h})\psi_0dy+\psi_0(a)\int_a^{+\infty}\hat{u}dy+\psi_0(b)\int_{-\infty}^b\hat{u}dy+\hat{h}(a)\int_a^{+\infty}\psi_0dy+\hat{h}(b)\int_{-\infty}^b\psi_0dy-a\int_a^{+\infty}\hat{u}dy\int_a^{+\infty}\psi_0dy+b\int_{-\infty}^b\hat{u}dy\int_{-\infty}^b\psi_0dy}{2\int_b^a\psi_0^2(y)dy+2\psi_0(a)\int_a^{+\infty}\psi_0(y)dy+2\psi_0(b)\int_{-\infty}^b\psi_0(y)dy+b(\int_{-\infty}^b\psi_0(y)dy)^2-a(\int_a^{+\infty}\psi_0(y)dy)^2}$$

Figs. 2 show the amplitude of the Kelvin wave for $n=1,2,3$ incoming Rossby waves. Though in some respects they present the same kind of pattern as in the former case, striking differences exist. First, this case is less efficient in reflecting waves. For example, for a gap centered at the equator and for $n=1$ Rossby wave, the amplitude of the reflected Kelvin wave is still minimum compared to an off-equatorial gap, but the amplitude of the reflected Kelvin wave is much smaller than in the infinite case : with $d=1$ and a gap centered at $y=1$, $T^k=0.3$ for the finite case and $T^k=0.7$ for the infinite case. With $d=1$ and a gap centered at the equator, $T^k=-0.1$ for the finite case and $T^k=0.45$ for the infinite case.

When the gap width gets infinitesimally small, we might expect the same answer as previously, namely all the mass is returned in the reflected Kelvin wave. In fact for the $n=1$ Rossby wave, the amplitude gets surprisingly small : all the mass flux is in the boundary currents and is used to set up the sea level on the other side of the gap. This effect depends on the latitudinal structure of the incoming flow as shown in Figs. 2.

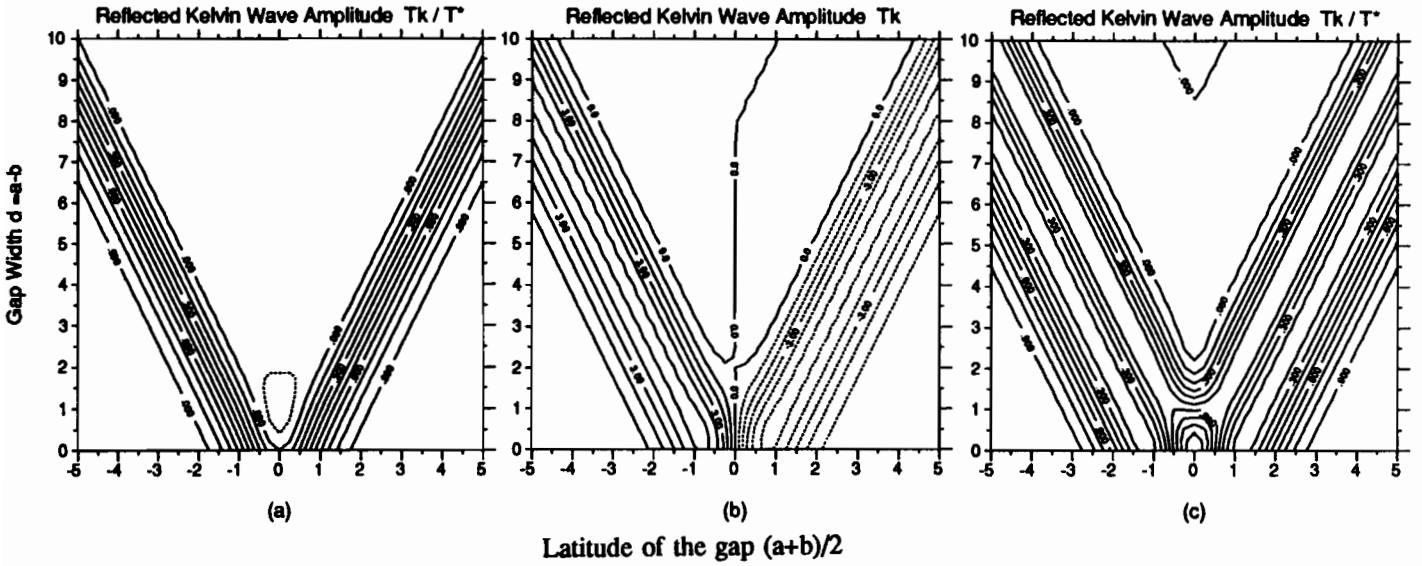

FIG. 2. As in Fig. 1 but for a gap of finite zonal length a) For $n=1$ incoming Rossby wave, b) For $n=2$ incoming Rossby wave, c) For $n=3$ incoming Rossby wave.

4. Application to the western Pacific boundary

The western Pacific boundary consists of an irregular chain of islands. We now apply the method developed in previous sections to know how good it is as a reflector. We know from mass conservation that the mass flux through the Indonesian seas is just the difference between the incident flow (Rossby waves) and the reflected Kelvin wave flow. The partition between transmitted and reflected mass flux is determined by the way the pressure gradient adjusts to the geometry, i.e. to the pattern of the height field h.

We first must simplify the very complex geometry of this region. The assumptions made in our theory are certainly questionnable, but once they are made, certain topological invariances are obtained. Then the flow through the complex region is the same as that through an equivalent simple geometry.

Cane and Gent (1984) presented a theory for calculating the effect of a solid sloping western boundary on low frequency wave reflections : as the frequency becomes sufficiently small, the effect of the sloping coast disappears. Throughout our calculations, we have made the assumption that the frequency is low enough so that phase differences with longitudes may be ignored. Thus the sloping coast may be replaced by a zig-zagging coastline in the manner so familiar in numerical models, and finally by a straight coast. Only the gaps matter.

Similarly, while the latitude of the gap is important, the longitude is not : the offset between islands has no effect for long low frequency waves and as far as we are concerned with the interior flow. We finally end up with a simplified geometry shown in Fig. 3, roughly deduced from the 1000m isobath. The coast north of a is representing the Mindanao coastline and b stands for the New Guinea, Halmahera and Celebes islands, assuming that there is no significant flow through Molucca Strait. The connection to the Indian ocean is through the Strait of Makassar. We also assume that there is no flow through the Arafura Strait. The latitude of the Indonesian islands is determined by d (see table I). An alternative representation is given by Clarke, 1989. Using results of previous sections, we are able to compute the different pieces which make up the solution but we need one more condition. This is obtained from the relation for h, which constrains the

possible pressure gradient to drive the flow through. We also assume that there is no Kelvin wave incoming from the Indian ocean, i.e. west of g. Then we get for T_6 , the amplitude of the reflected Kelvin wave in the Pacific ocean :

$$T_6 = -\frac{\hat{h}(b) + b\int_{-\infty}^{b} \hat{u}(y)dy + \left(\int_{-\infty}^{+\infty} \hat{u}(y)dy\right)\left(\psi_0(g) - g\int_{g}^{+\infty} \psi_0(y)dy\right)\left(\int_{-\infty}^{+\infty} \psi_0(y)dy\right)^{-1}}{\psi_0(g) - g\int_{g}^{b} \psi_0 dy + \psi_0(b) + b\int_{-\infty}^{b} \psi_0(y)dy}$$

This relation simply indicates that the resulting amplitude of the reflected Kelvin wave in the Pacific Ocean part depends only on the latitude of the Indian and Pacific Ocean entrances, i.e. g and b. This is consistent with conservation of mass and with our simplifying rules.

For our schematization of the western Pacific boundary (Fig. 3), we choose b=3 $\mathcal{N}$ (representing Halmahera and Morotai islands) and g=8.5 $\mathcal{S}$ standing for the latitude of the Lombok and Timor straits. Table I gives the computed amplitude of the reflected Kelvin wave in the Pacific Ocean for the first three baroclinic modes and for different incoming Rossby waves.

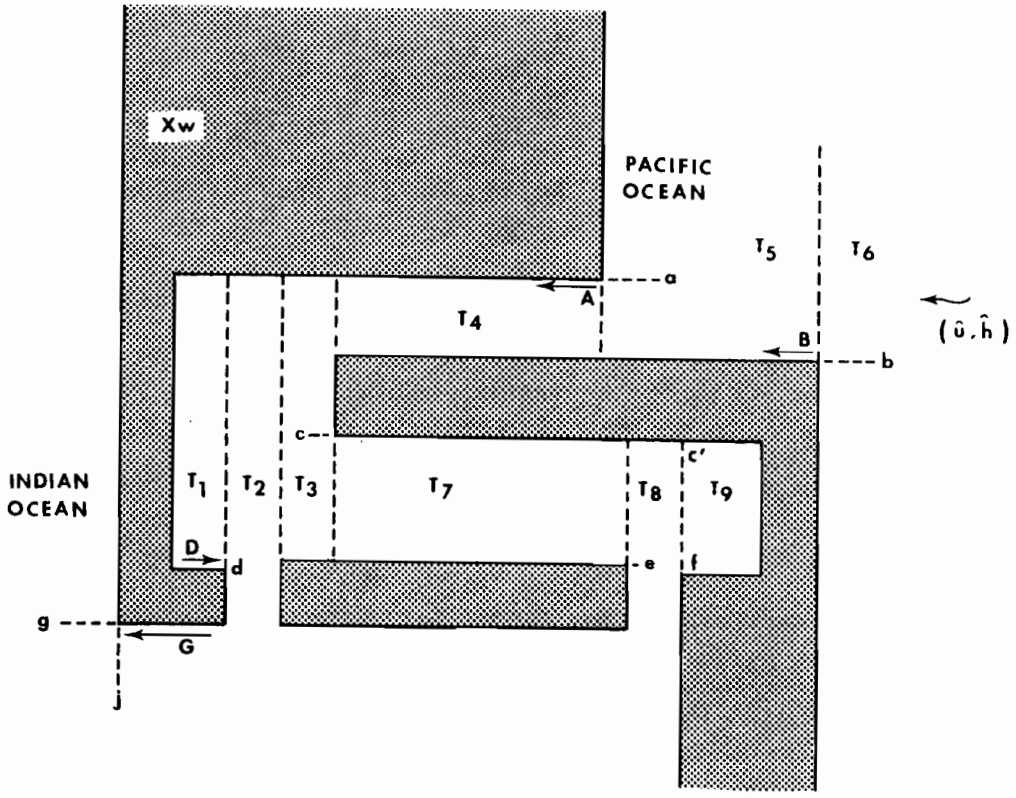

FIG. 3. Schematic geometry of the Western Pacific Boundary and of the Indonesian seas.

For the first Rossby mode, the amplitude of the reflected Kelvin wave is 85% of the amplitude if the boundary were a full boundary. It is over 90% for higher baroclinic modes which are more equatorially trapped. For antisymmetric (n even) Rossby modes, the presence of a gap allows a reflected Kelvin wave to exist whereas a full boundary would not. Therefore as far as this theory is concerned, the western Pacific boundary acts as a substantial reflector.

Table I : Results for a schematic Pacific western boundary as in Fig.3

Latitude : b = 3 N g = 8.5 S

$t \rightarrow \infty$

Baroclinic mode #	l = 1			l = 2			l = 3		
Radius of deformation	356.9 km			278.8 km			222.6 km		
	Rossby #			Rossby #			Rossby #		
	1	2	3	1	2	3	1	2	3
T^k	0.15	-0.016	0.026	0.16	-0.011	0.027	0.168	-0.007	0.0287
$\frac{T^k}{T^\infty}$	0.85	-	0.74	0.91	-	0.76	0.95	-	0.79

5. Conclusion

The analytical techniques used in this note are an extension of those used by Cane and du Penhoat (1982) to study the effect of low latitude islands. The results show that the amplitude of the reflected equatorial Kelvin wave is sensitive to the location of the gap and the structure of the incoming flow. In addition, the results can be quite different depending on whether the zonal extent of the gap is assumed to be infinite or finite. (More precisely, the latter means that the extent of the gap is short compared with the zonal wavelength of the relevant free waves). A coastline with a finite zonal length gap is a less efficient wave reflector than an infinite zonal length gap. In particular, the difference is non-negligible close enough to the equator for $n=1$ Rossby wave.

In carrying out a calculation as idealized as the one here, one hopes the results will be robust enough so that their possible application to the real world is obvious. We are not concerned with the details of the boundary flows, but did hope to deduce some general rules about the strength of the interior flow, i.e., the amplitude of the reflected Kelvin wave. The complexities of even such a simplified model convinces us that it will be very difficult to be confident of any modeling study of the Indonesian flowthrough short of a highly resolved numerical calculation with a detailed representation of the geometry and bathymetry. Nonetheless, we offer a few tentative conclusions concerning the efficacy of the western equatorial Pacific "boundary" as a reflector. As the greatest sensitivity in our results concerns the region very near the equator and since the western Pacific is effectively blocked within one or two radius of deformation off the equator, low n Rossby modes will be largely reflected. Thus, if as proposed by Zebiak (1989) and Battisti (1989) among others, the reflections important for El Nino are primarily in motions well represented by the low n Rossby modes, then this result suggests that the realistic boundary will not greatly alter the expectations based on a simple solid boundary.

REFERENCES

Battisti, D. S., 1988 : The dynamics and thermodynamics of a warm event in coupled atmosphere/ocean model. *J. Atmos. Sci.*, **45**, 2889-2919.

Battisti, D.S., 1989 : On the role of off-equatorial oceanic Rossby waves during ENSO. *J. Phys. Oceanogr.*, **19**, 551-559.

Cane, M.A., and P.R. Gent, 1984 : Reflection of low frequency equatorial waves at arbitrary western boundaries. *J. Mar. Res.*, **42,** 487-502.

Cane, M.A., and Y. du Penhoat, 1982 : The effect of islands on low frequency equatorial motions. *J. Mar. Res.*, **40,** 937-962.

Cane, M.A., and E. S. Sarachik, 1977 : Forced baroclinic ocean motions. II The linear equatorial bounded case. *J. Mar. Res.*, **35,** 395-432.

Cane, M.A., and E.S. Sarachik, 1979 : Forced baroclinic ocean motions. III The linear equatorial basin case. *J. Mar. Res.*, **37,** 355-398.

Cane, M.A., and E. S. Sarachik, 1981 : The response of a linear baroclinic ocean to periodic forcing. *J. Mar. Res.*, **39,** 651-693.

Clarke, A. J., 1989 : On the reflection and transmission of low frequency energy at the irregular western Pacific Ocean boundary. *This volume.*

du Penhoat, Y., M.A. Cane and R.J. Patton, 1983 : Reflections of low frequency equatorial waves on partial boundaries. *Hydrodynamics of the Equatorial Ocean,* J.C.J. Nihoul, Ed., Elsevier, 237-258.

Kindle, J. C., H. E. Hurlburt and E. J. Metzger, 1989 : On the seasonal and interannual variability of the Pacific to Indian Ocean throughflow. *This volume.*

White, W.B., G. Meyers, J.R. Donguy, and S. Pazan, 1985 : Short-term climatic variability in the thermal structure of the Pacific Ocean during 1979-1982. *J. Phys. Oceanogr.*, **15,** 917-935.

Zebiak, S.E., 1989 : Oceanic heat Content variability and El Nino cycles. *J. Phys. Oceanogr.*, **19,** 475-486.

Results from a Global Ocean Model in the Western Tropical Pacific

Harley HURLBURT[1], John KINDLE[1], E. Joseph METZGER[1] and Alan WALLCRAFT[2]

[1] *JAYCOR;* [2] *NORDA*
Stennis Space Center, MS 39529 - U.S.A.

1. Introduction.

The circulation of the western equatorial Pacific is examined using two NORDA ocean models, a global model on a .5 x .7 degree grid (lat,long) and a North Pacific model (N. of 20°S) on a .25 x .35 degree grid. This is the resolution for each dependent variable. The models use detailed coastline geometry including the islands resolved by the grid. The models are reduced gravity with the lowest layer infinitely deep and at rest and they include thermodynamics and mixing. The models have been forced by the Hellerman-Rosenstein (1983) (HR) wind climatology and by winds from the European Centre for Medium-range Weather Forecasting (ECMWF) (1980-1987). The discussion will focus on the Pacific west of the dateline and ± 20 degrees latitude, including the Indonesian archipelago. The models simulate detailed aspects of the circulation in the region.

2. Mean flow and sea surface height.

Figure 1a,b shows the sea surface height (SSH) from the global model driven to statistical equilibrium by the HR monthly wind stress climatology. Between the subtropical and subpolar gyres, it shows the bifurcation of the Kuroshio/Oyashio Current system into subarctic and subtropical fronts. The frontal positions are in good agreement with those given by Roden and Robinson (1988). The simulated North Equatorial Current (NEC) is centered at 12°-13°N and the North Equatorial Countercurrent (NECC) at about 5°N similar to the U.S. Navy's GDEM climatology (Teague et al, 1989) (Fig 1c). The Mindanao eddy is simulated east of the south Philippines coast.

Figure 1b shows the annual mean SSH from the same global simulation for the western tropical Pacific. Figure 1d shows the same field from the .25° Pacific model. Both experiments have one active layer, hereafter referred to as 1.5 layers. The NEC splits at the Philippine coast into the Mindanao current and the beginning of the Kuroshio current. The location of the split shows a seasonal variation of only about 1° in the models. In the Pacific model (Fig. 1d) the mean location is in close agreement with Wyrtki (1961) and the GDEM climatology (Fig. 1c). However, the global model (Fig. 1b) has the split 1.5° further north.

A comparison of two global experiments with the south Sulu Sea open and closed shows that this occurs because the south Sulu Sea is open in the Pacific model experiment and closed in the global one. With the south Sulu Sea open there is a net cyclonic flow around the Philippines which weakens the Mindanao Current and strengthens the Kuroshio Current east of Luzon. Hence, more of the SSH contours associated with the NEC must go north when the south Sulu Sea is open and the split point must be further south. Flow through the south Sulu strait has little effect on the transports south of the Celebes Sea, east of 130°E, and north of the Luzon Strait. The mean transports for the Mindanao Current at 8°N (coast to 134.4°E) and the Kuroshio

ORSTOM
CENTRE DOCUMENTATION
Montpellier

F30221

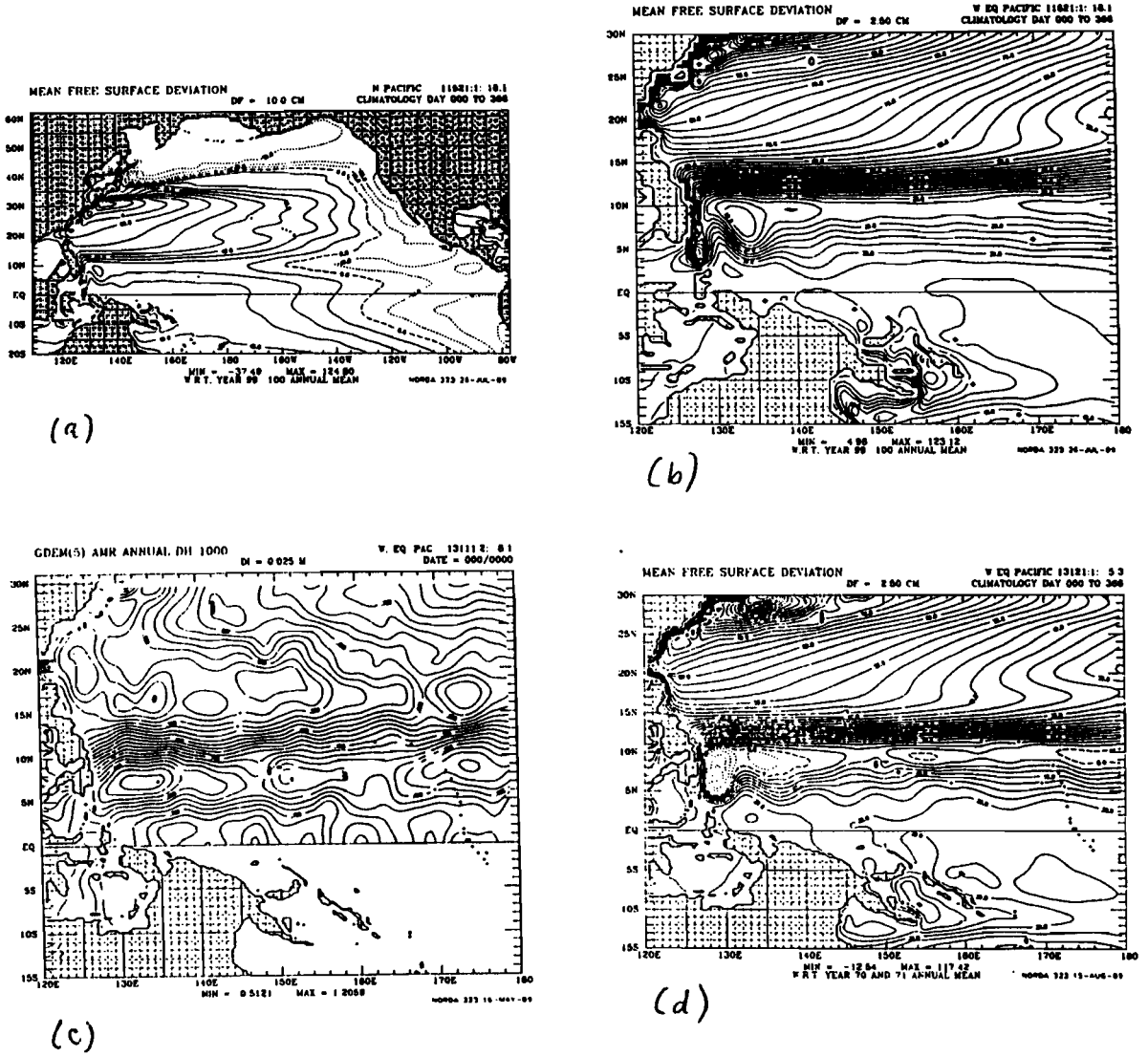

Fig. 1. (a) Mean SSH from the .5° 1.5 layer global model driven by the Hellerman-Rosenstein (HR) wind stress climatology. (b) Mean SSH for the western tropical Pacific from the same numerical experiment. (c) Annual mean surface dynamic height relative to 1000 m from the U.S. Navy's .5° GDEM climatology (Teague et al, 1989) smoothed with 5 passes of a 9-point real smoother for a spherical grid. The global areal mean from the Levitus (1982) climatology has been subtracted. (d) Same as (b) from the .25° 1.5 layer Pacific model. The model land-sea boundary is the 200 m isobath.

Current at 18°N (coast to 124.6°E) are 27 Sv, 22 Sv for the 1.5 layer Pacific model (S. Sulu open), 34 Sv, 12 Sv for the 1.5 layer global model (S. Sulu closed) and 24 Sv, 17 Sv for a 3.5 layer global experiment (S. Sulu closed).

Focusing on the global model, the Mindanao current splits near the south end of the Philippines. Some flow recirculates in the eddies. The strongest branch heads southward before joining the NECC. Wyrtki (1961) notes this branch passing between Sangihe and Talaud Islands which form a channel between 125.8°E and 126.8°E at 4°N. The configuration of the island geometry and the bottom topography (parallel ridges bounding the current) suggest that they might influence the path of the current. However, they are not included in the .5 degree global model which shows the mean current centered at 126.7°E. The Pacific model which includes the islands shows the current centered at 127.3°E and not extending as far south. The lack of Pacific-Indian Ocean throughflow and the net cyclonic flow around the Philippines with the south Sulu Sea open are likely factors in this.

In the global model another branch of the Mindanao Current proceeds westward through the Celebes Sea where some flow returns eastward north of Suluwesi Island, and some proceeds southward through the Macassar Strait. The flow through Macassar again divides into Pacific-Indian Ocean throughflow (see Kindle et al, Murray et al, this volume) and flow that returns northward east of Suluwesi and Halmahera Islands where it joins the NECC. For the latter flow, the standard deviation is larger than the mean and the mean is <1 Sv. In the model little or none of the Mindanao Current flows around the south side of Halmahera Island before joining the NECC.

In the annual mean there is a westward coastal current along the New Guinea coast in the 1.5 layer model, Fig. 2a, but in the 3.5 layer model the westward coastal current is an undercurrent with only weak mean westward flow at the surface (Fig. 2c, d). Another prominent difference between the 1.5 and 3.5 layer models occurs in the equatorial waveguide. In the 1.5 layer model the equator is roughly the southern edge of the NECC in the annual mean. In the 3.5 layer model a westward equatorial surface current and an eastward equatorial undercurrent are found. Thermodynamics was not included in the 3.5 layer simulation, but vertical mixing of mass and momentum were. The vertical mixing and at least two active layers are required for these currents to exist in the annual mean.

Figure 2b shows the effect of the Pacific-Indian Ocean throughflow on the u-component of velocity in the 1.5 layer global model. This was obtained by subtracting a solution with the Pacific-Indian Ocean throughflow closed from one with the throughflow open. In the western equatorial Pacific the throughflow influence is confined mainly to an increased westward component along the New Guinea coast and into the Celebes Sea. It also slightly weakens the Mindanao eddy and shifts the cyclonic eddy to the east of it (Fig. 1b) slightly further to the east.

The region also exhibits several prominent eddies in the annual mean SSH field (Fig. 1b, d). However the strength, location, and even existence of these is quite variable. The most notable is the cyclonic Mindanao eddy centered at 5°N, 127.5°E in the global model (Fig. 1b) and 6°N, 128.5°E in the Pacific model (Fig. 1d). A second cyclonic eddy is found to the east in both models centered at 8°N, 133°E and 9°N, 134.5°E, respectively. Additional cyclonic centers are found to the east along the SSH trough at 9°N. The longitudinal structure is in good agreement with the GDEM climatology (Fig. 1c). Both GDEM and the Pacific model show a center between 150°-155°E. A test of the Pacific model with and without the Gilbert Islands did not show any notable differences. An anticyclonic eddy is found near 3°N, 132°E, ENE of Halmahera.

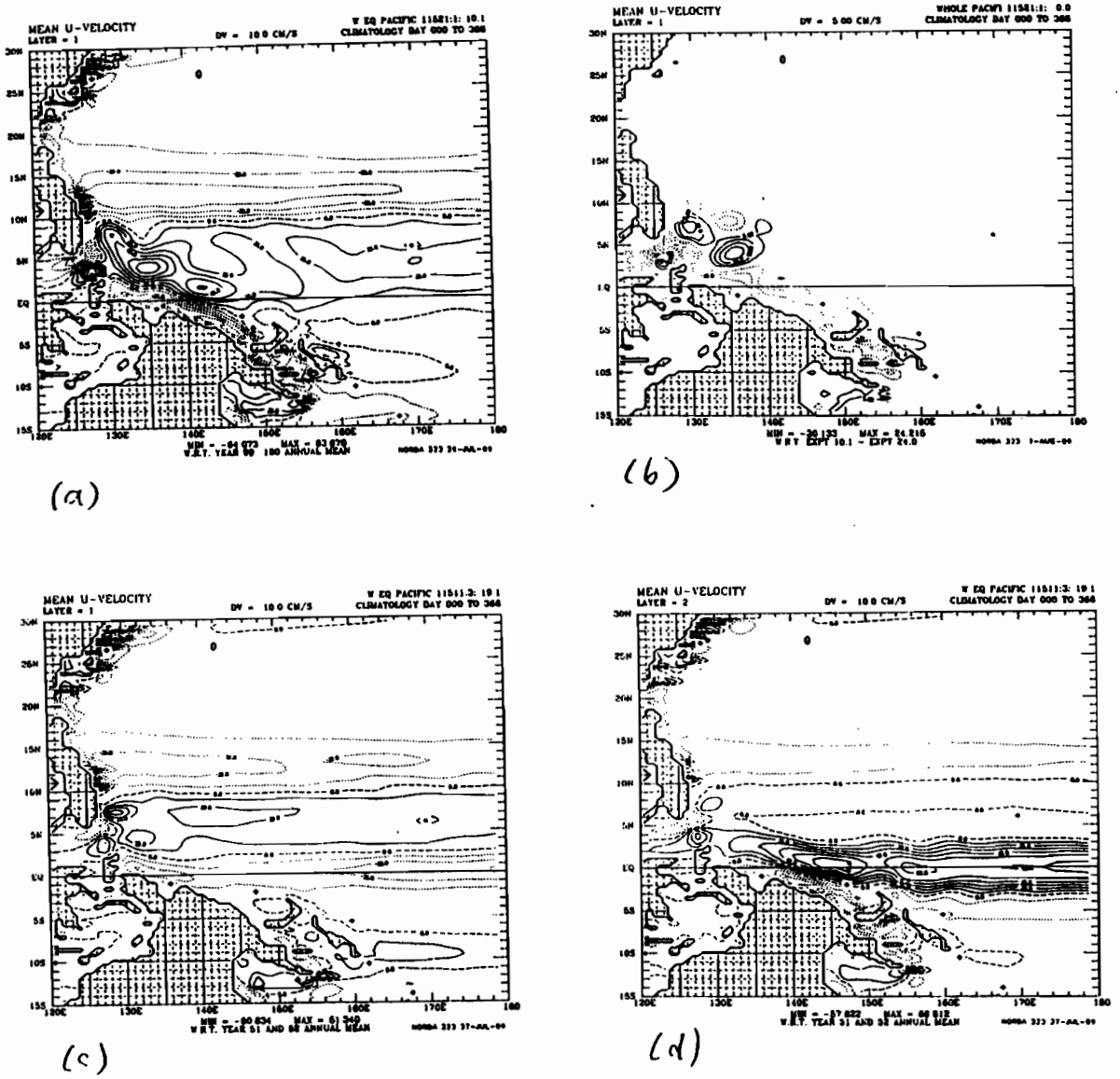

Fig. 2. Mean u-component of velocity for (a) the 1.5 layer global model, (b) the difference between two 1.5 layer global experiments, Pacific-Indian Ocean throughflow open minus Pacific-Indian Ocean throughflow via Indonesia closed, (c) layer 1 of the 3.5 layer global model, and (d) layer 2 of the 3.5 layer global model. Dashed contours are westward. HR monthly mean wind stress forcing.

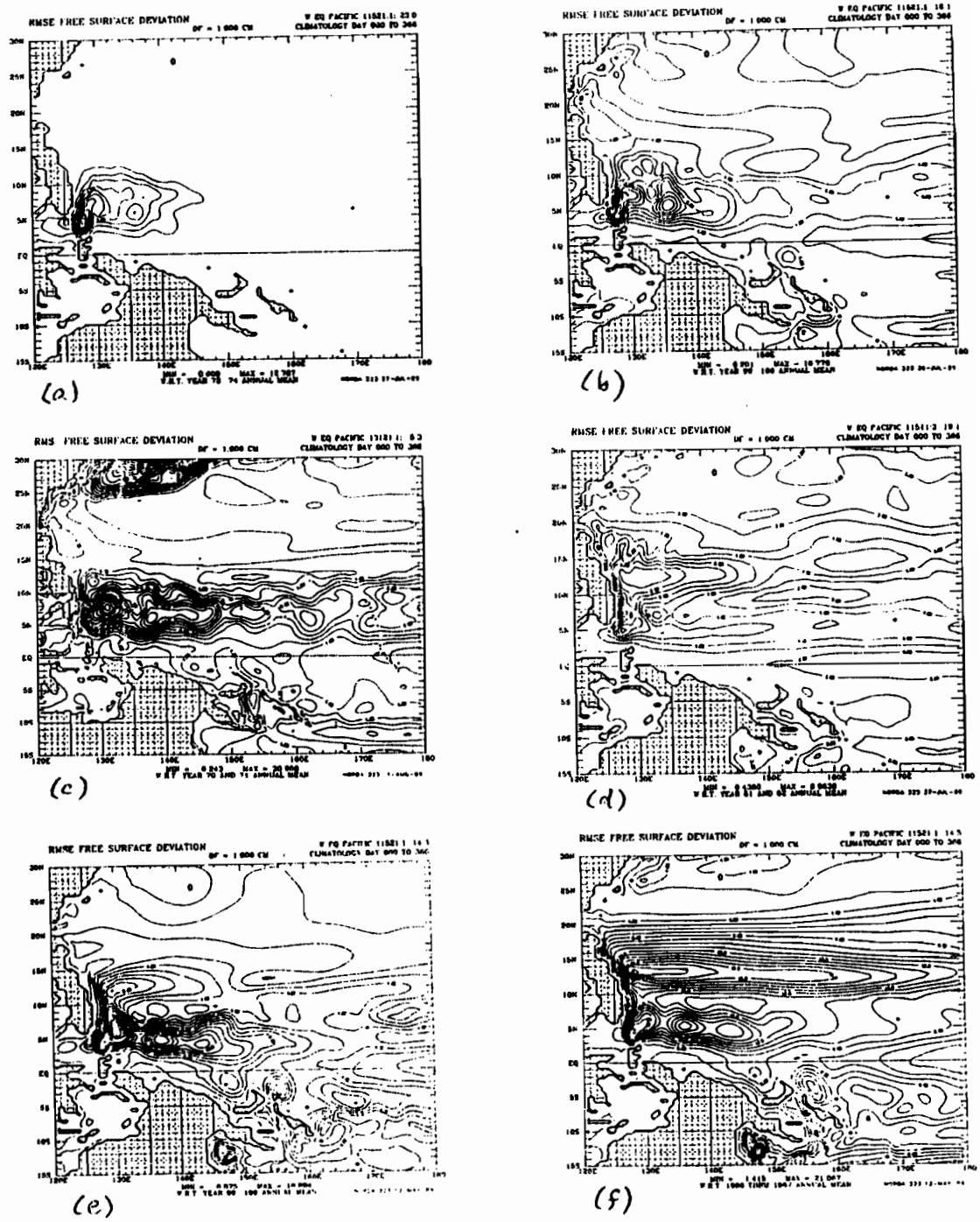

Fig. 3. RMS SSH variability from model experiments listed in Table 1. (a) .5° 1.5 layer global model driven by annual mean HR wind stress, (b) same driven by the monthly HR climatology, (c) .25° 1.5 layer Pacific model driven by the HR monthly climatology (d) .5° 3.5 layer global model driven by the HR monthly climatology, (e) the .5° 1.5 layer global model driven by a monthly 1000 mb ECMWF wind climatology based on 1980-1987 winds, and (f) .5° 1.5 layer global model driven by monthly mean 1000 mb winds for individual years from ECMWF, 1980-1987.

In the southern hemisphere cyclonic eddies are found in the Bismarck Sea and east of New Ireland. In the 3.5 layer model these eddies occur in the undercurrent layer, but unlike the 1.5 layer model, they are not found in the surface layer in the annual mean. Cyclonic eddies are also found in the Coral Sea and the Solomon Sea. Many more transient eddies are present.

3. Variability.

The RMS variability of the SSH in the western equatorial Pacific has been calculated for several different numerical experiments shown in Figure 3. The forcing and model for the experiments are listed in Table 1.

TABLE 1 - Model Experiments shown in Figure 3

Figure	Wind forcing	Model
3a	annual mean HR climatology	.5° , 1.5 layer global
3b	monthly HR climatology	.5° , 1.5 layer global
3c	monthly HR climatology	.25° , 1.5 layer Pacific
3e	monthly ECMWF climatology	.5° , 1.5 layer global
3d	monthly HR climatology	.5° , 3.5 layer global
3f	ECMWF monthly means for individual years, 1980-1987	.5° , 1.5 layer global

The ECMWF climatology is a monthly mean of 1000 mb winds 1980-1987 on a 2.5° grid. The 1000 mb winds were multiplied by a constant to produce surface winds. All of the experiments include thermodynamics except for the 3.5 layer global. Global experiments a,b use an eddy viscosity of A = 2000 m^2 s^{-1} and d-f use A = 1500 m^2 s^{-1}. The Pacific model uses A = 500 m^2 s^{-1}.

The experiments shown in Figure 3 are designed to help sort out variability due to flow instabilities, seasonal variations in winds from different wind sets and interannual variability. In Figure 3a the RMS variability is due only to flow instabilities. With only one vertical mode, baroclinic instability is excluded from all but Figure 3d. Figure 3f is the only one to include interannual variability, but some of the interannual variability may be fictitious due to changes in the ECMWF wind product over the 8-year period.

In Figure 3a, driven by annual mean winds, flow instabilities occur within 12° of the equator west of 150°E. Strongest instabilities are associated with the Mindanao eddy and the NECC. The tongue of variability into the Celebes Sea is associated with eddy shedding from the Mindanao eddy. Usually pieces of the eddy break off, but occasionally the whole eddy propagates into the Celebes Sea. The eddy shedding is irregular but occurs at roughly 40-80 day intervals. At 141°E spectral peaks in the transport 2°-5°N occur at 50-60 and 73 days in a 2-year time series. Between the New Guinea coast (2.5°S) and the equator additional peaks are found at 25 and 40 days. The Mindanao eddy itself is not one eddy, but a series of eddies that propagate in from the east and strengthen there, either merging with or replacing the Mindanao eddy. This occurs less frequently than the eddy shedding.

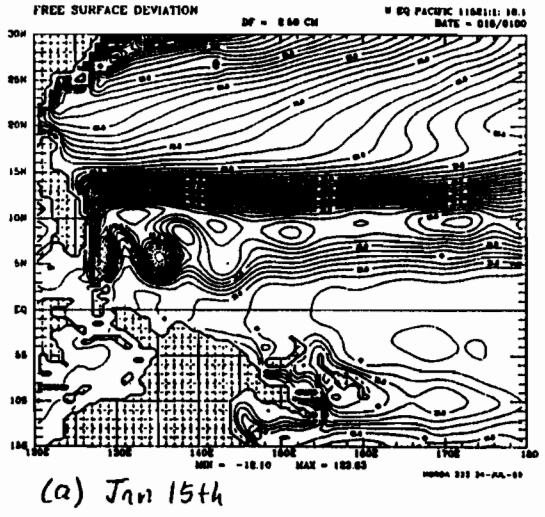

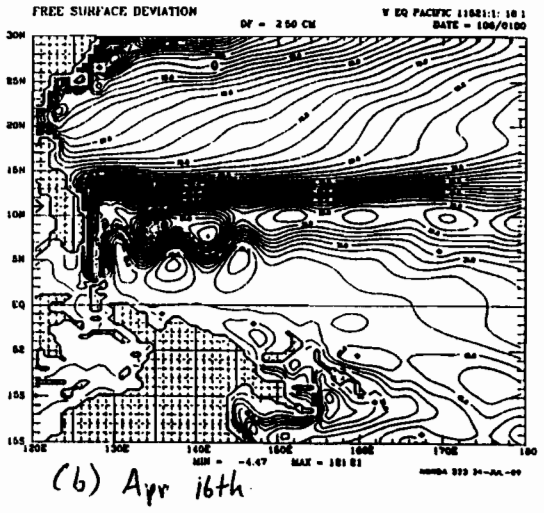

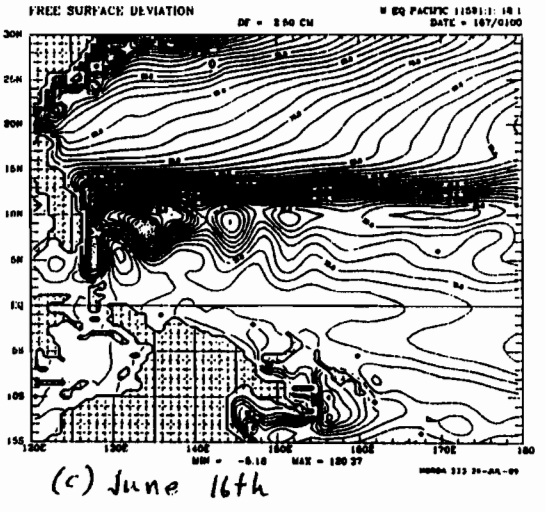

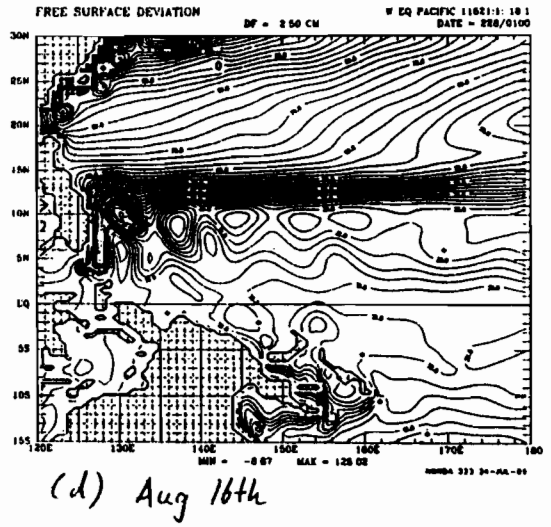

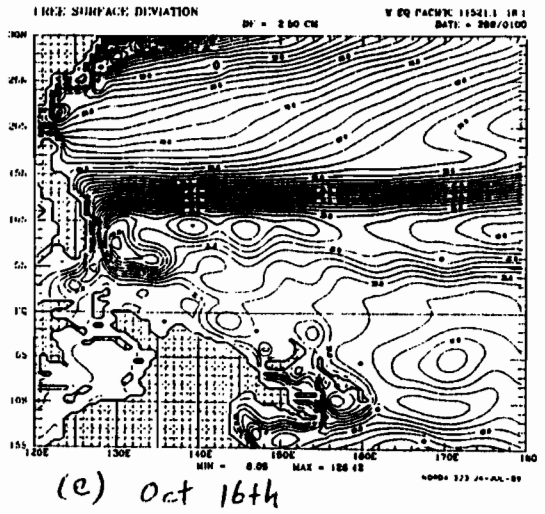

Fig. 4. Instantaneous SSH from the .5° 1.5 layer global model driven by the HR monthly wind stress climatology for (a) Jan. 15th, (b) Apr 16th, (c) June 16th, (d) Aug 16th, and (e) Oct. 16th.

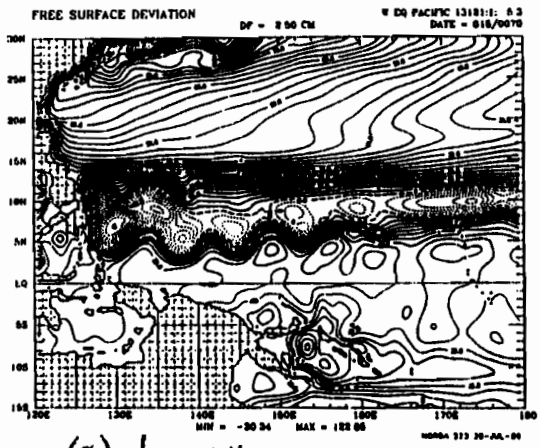

(a) Jan 15th

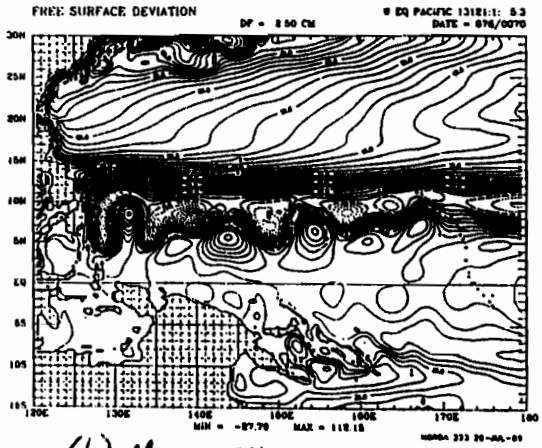

(b) Mar 17th

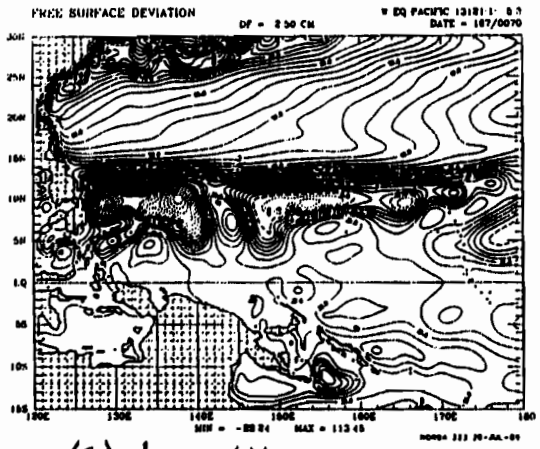

(c) June 16th

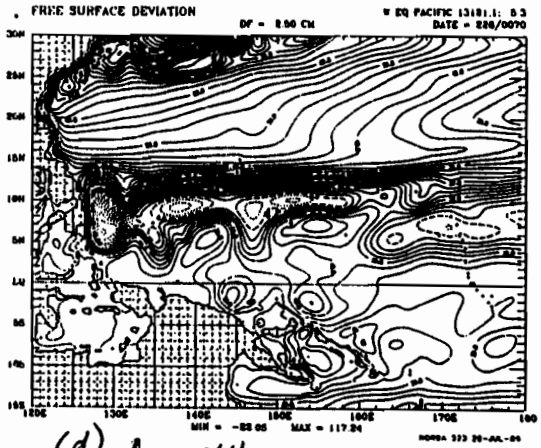

(d) Aug 16th

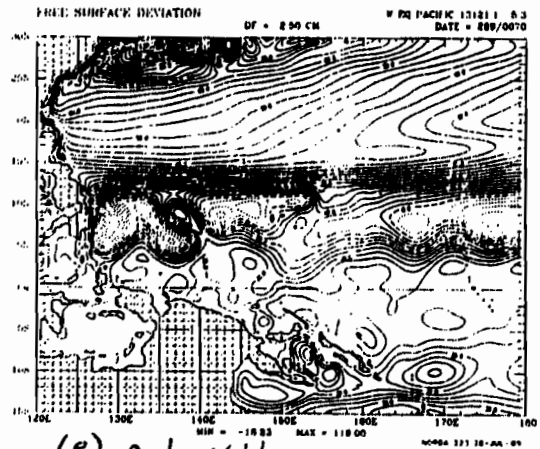

(e) Oct 16th

Fig. 5. Instantaneous SSH from the .25° 1.5 layer Pacific model driven by the HR monthly wind stress climatology for (a) Jan 15th, (b) Mar. 17th, (c) June 16th, (d) Aug 16th, and (e) Oct 16th.

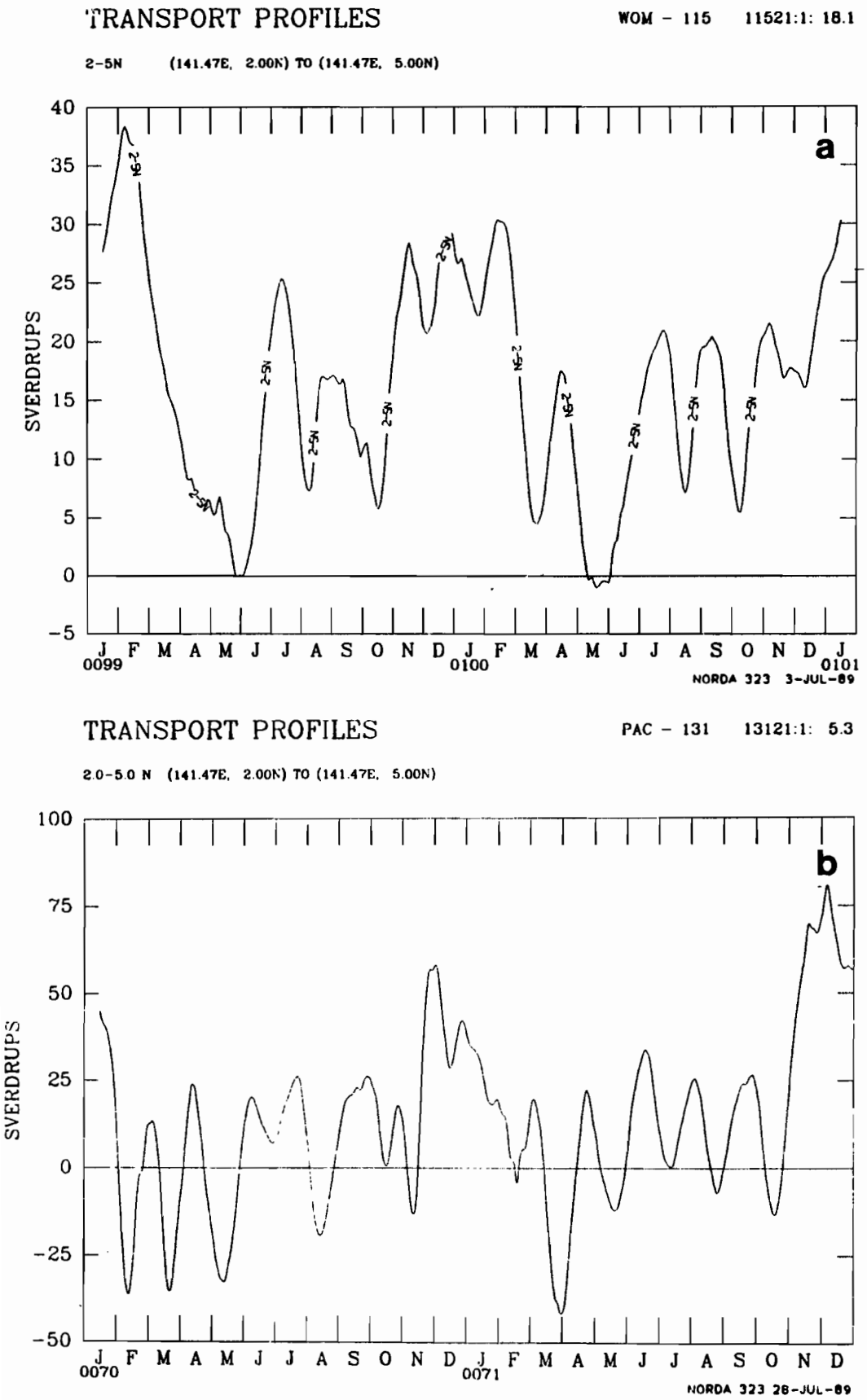

Fig. 6. Two-year transport time series from (a) the 1.5 layer global model and (b) the 1.5 layer Pacific model at 141.5°E, 2-5°N driven by the HR monthly climatology. The time series begin on Jan. 15th and ticks mark 1 month intervals.

Similar flow instabilities are found north of the equator in the western Atlantic Ocean and just south of the equator in the western Indian Ocean. The latter are discussed by Kindle and Thompson (1989) who reported similar periodicities.

Figures 3b-e driven by monthly wind climatologies all show patterns of RMS SSH variability with maxima in bands N and S of the equator. We anticipate that the minimum along the equator would disappear in maps of eddy kinetic energy (which we have not calculated yet). The longitudinal location of the variability maxima are very similar in Figures 3b, 3c, and 3e whether driven by Hellerman-Rosenstein or ECMWF winds, suggesting a standing wave. Such maxima are not clearly evident in the 3.5 layer model (Fig. 3d).

In all cases there are tongues of high variability into the Celebes Sea. Although eddy fragments break off the Mindanao eddy year round and propagate into the Celebes Sea, occasionally the whole Mindanao eddy propagates into the Celebes Sea sometime during May through October.

SSH variability maxima in the Bismarck Sea and east of New Ireland are also consistent features except in the 3.5 layer model. The eddies in the Bismarck Sea form north of the Vitiaz Strait and propagate northwestward. Similarly, eddies form east of the strait between New Ireland and the Solomon Islands from July through October. As noted earlier (Fig. 2) the mean upper layer flow is westward along the northern New Guinea coast in the 1.5 layer model, but only weakly so in the 3.5 layer model. In the 3.5 layer model there is a westward coastal undercurrent and the eddies in the Bismarck Sea and east of the New Ireland are also present only below the surface layer in the mean.

The Coral Sea is a region of high variability with the ECMWF winds, but not with the HR. Figures 3c,e,f also show variability in parts of the Solomon Sea.

The western NEC is another region of slightly to markedly elevated variability in Figures 3b-f. A striking difference between the .25° Pacific model and the .5° global model is seen north of 25°N where the .25° model shows strong flow instabilities in the Kuroshio and the .5° model does not.

The interannual variability (Fig. 3f) is larger in amplitude and more wide spread. It shows the features of the seasonal variability with elevated amplitude, but the maximum variability is associated with shifts in the latitude of the NEC. Two-year means of SSH 1980-81, 1982-83, etc. suggest that some of the interannual variability is due to changes in the ECMWF 1000 mb wind product over the years. The two-year means become distinctly more realistic with time.

4. Seasonal Cycle.

Figures 4 and 5 show the seasonal cycle of the SSH from the .5° 1.5 layer global model (Fig. 4) and the .25° 1.5 layer Pacific model (Fig. 5). Both show a similar seasonal cycle, but with more eddy activity in the Pacific model. Because of the flow instabilities, substantial interannual variation occurs in both models even though they were driven by the Hellerman-Rosenstein wind climatology, especially west of 160°E, within 10° of the equator. Jan. 15th shows the SSH gradient associated with the NECC at a lower latitude in the western part of region. By March the latitude has increased in the western part and we see the onset of strong anticyclonic eddies on the south side. These show up as 50-60 day oscillations in the transport time series at 141.5°E, 2°-5°N (Fig. 6). In summer a new trough appears at a lower latitude in the east (June 16th and Aug 16th). By Oct. 16th it has increased in latitude. This rise appears to follow the rise in latitude of the wind curl pattern. There is no obvious propagation of an annual Rossby wave associated with the increase in latitude.

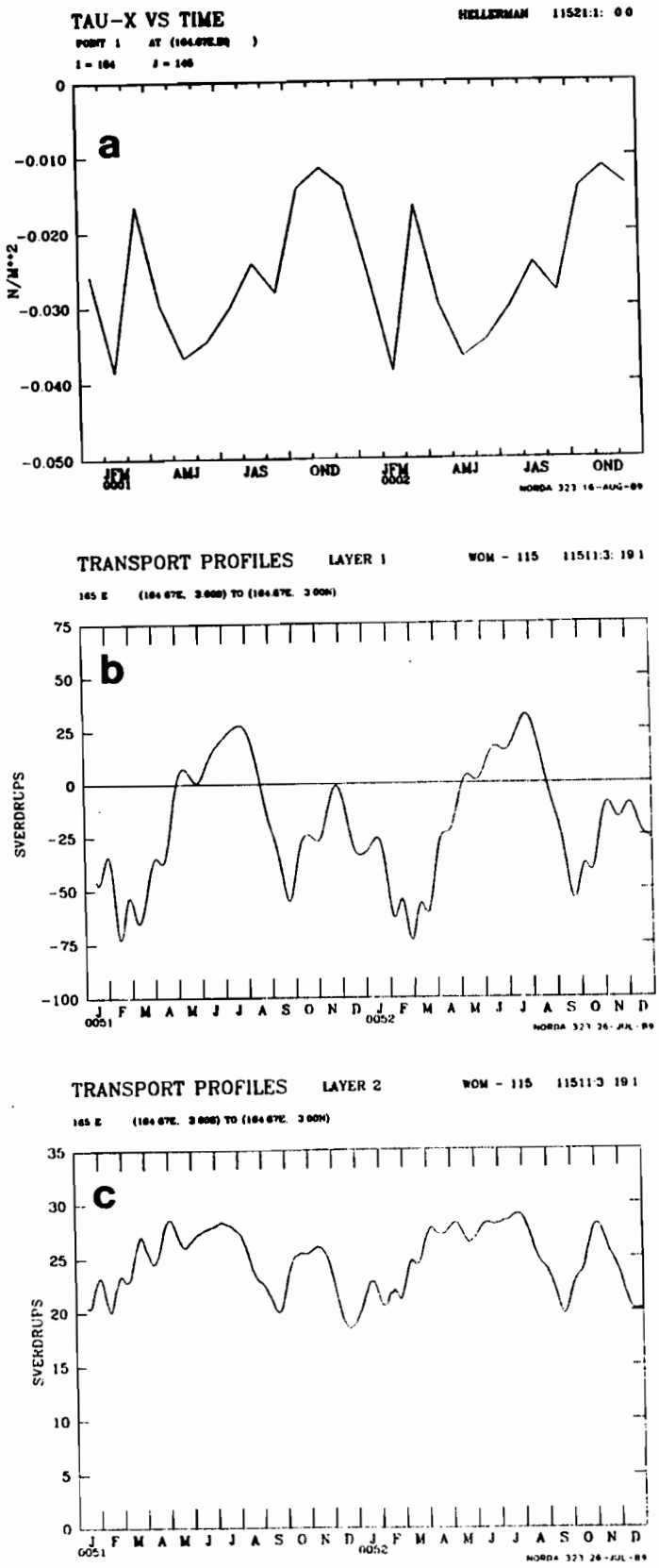

Fig. 7. Two-year time series of (a) the equatorial component of the HR wind stress climatology at 165°E, (b,c) transports of the equatorial (b) surface current in layer 1 and (c) undercurrent in layer 2 from the 3.5 layer global model. For the wind stress component the monthly average is placed midway between the ticks. The 15th of the month falls midway between the ticks in the transport time series.

Other features of the variability are also evident such as the eddy shedding into the Celebes Sea. Eddy plumes are seen north of New Britian Island. The eddy activity east of New Ireland is most pronounced in the latter part of the year. Eddy activity in the Coral and Soloman Seas is also evident. In the .25° Pacific model eddy activity (north of 25N°) is associated with the Kuroshio.

Figure 7 shows time series of the equatorial surface current and undercurrent from the 3.5 layer global model at 165°E. For comparison the equatorial u-component of the HR wind stress for 165°E is also shown.

Strong 30-day oscillations are evident with onset in winter and late summer. The oscillations are nearly in phase in the two layers. Although the surface current and undercurrent tend to be opposite in direction, their transport tends to accelerate in the same direction.

Acknowledgements. The authors would like to thank Pat Hogan, Bill Teague, Amy Summers and Greg Vega for their assistance on this project. The computations were performed on the CYBER 205 at Fleet Numerical Oceanography Center in Monterey, CA. We would like to thank Dana Thompson, George Heburn and Robert Woodyard for their contributions to the developmental work. The manuscript was typed by Debbie Black. Approved for public release; distribution is unlimited. NORDA Contribution #PR-89:059:323.

REFERENCES

Hellerman, S., and M. Rosenstein, 1983: Normal monthly wind stress over the world ocean with error estimates. *J. Phys. Oceanogr.*, **13**, 1093-1104.

Kindle, J.C., H.E. Hurlburt, and E.J. Metzger, 1989: On the seasonal and interannual variability of the Pacific to Indian Ocean throughflow. (this volume).

Kindle, J.C., and J.D. Thompson, 1989: The 26 and 50-day oscillations in the western Indian Ocean: Model Results. *J. Geophys. Res.*, **94**, 4721-4736.

Levitus, S., 1982: Climatological atlas of the world ocean. NOAA Professional Paper 13, 173 pp.

Murray, S.P., J.C. Kindle, D. Arief, and H.E. Hurlburt, 1989: Comparison of observations and numerical model results in the Indonesian throughflow region. (this volume).

Roden, G.I., and A.R. Robinson, 1988: Subarctic frontal zone in the northeastern Pacific: mesoscale structure and synoptic description. Reports in Meteorology and Oceanography #31, Harvard University.

Teague, W.J., M.J. Carron, and P. Hogan, 1989: A comparison between the GDEM and Levitus climatologies. (Submitted to JGR-Oceans).

Wyrtki, K., 1961: Physical Oceanography of the southeast Asian waters. NAGA Report #2, Scripps Inst. Oceanogr., 195pp.

On the Seasonal and Interannual Variability of the Pacific to Indian Ocean Throughflow

John C. KINDLE, Harley E. HURLBURT and E. Joseph METZGER
NORDA, Code 323
Stennis Space Center, MS 39529 - U.S.A.

1. Introduction.

The Pacific to Indian Ocean transport through the Indonesian Archipelago may play an important role in a variety of ocean circulation regimes. Gordon (1986) suggested that the Indonesian throughflow is a crucial component of the global thermohaline circulation associated with the formation of the North Atlantic Deep Water. Additionally, the extent to which the throughflow modifies the regional circulation may be an important factor in the maintenance and variability of the heat content within the warm pool of the western Pacific and the interannual variability of the coupled ocean-atmosphere system in that region. Furthermore, determination of accurate mass and heat budgets for Pacific and Indian Oceans requires an adequate assessment of the magnitude and variability of the throughflow.

There are no long term direct measurements of the net Indonesian throughflow. Estimates of the mean value and seasonal variability of the transport have been determined from a variety of in-situ and indirect observations as well as from modelling studies. Gordon (1986) presents a summary of the estimated values. The magnitudes of the mean throughflow inferred from observations generally range from 5-15 Sv (10 m s^{-1}). The only year long direct measurement of a portion of the throughflow was provided by Murray and Arief (1988) who observed a mean transport through the Lombok Strait of about 1.7 Sv for 1985.

Results from modelling studies yield a similar scatter for the values of the throughflow. Multi-level global simulations forced by the Hellerman and Rosenstein (1983) wind stress climatology yield a mean value of approximately 15 Sv (Semtner and Chervin, 1988). A global Sverdrup model by Godfrey (1989) predict a mean Pacific to Indian Ocean throughflow of 16 $\pm$ 4 Sv. The one-layer reduced gravity global model described in Kindle et al. (1987) utilized the Fleet Numerical Oceanographic Center (FNOC) surface winds from 1977 to 1984 and yielded a mean value for the Indonesian throughflow of approximately 8 Sv with a seasonal variation (maximum in August and minimum in January) of about 4 Sv.

Wyrtki (1987) discussed the pressure gradient between the western Pacific and the eastern Indian Oceans as a mechanism which drives the mean and seasonal variation of the Indonesian throughflow. His examination of sea level and dynamic height in this region supports the hypothesis that the mean pressure gradient between the two basins drives the mean transport and that the dynamic height difference between Davao, Phillipines and Darwin, Australia (~16 dynamic centimeters) is an adequate measure of the inter-basin pressure gradient. In addition, Wyrtki (1987) found that the seasonal variation of the sea level difference between Darwin and Davao exhibited a similar phase to the seasonal variation of the throughflow from a NORDA 1-layer reduced-gravity model simulation provided by Kindle. The model used in the calculations was identical to the one described in Kindle et al.(1987) except for a longer spin-up and the inclusion of the Macassar Strait. Wyrtki hypothesized that the low-frequency variations of the interbasin pressure gradient (as denoted by the Davao-Darwin sea level difference) could be used to monitor the variability of the Pacific to Indian Ocean throughflow.

ORSTOM
CENTRE DOCUMENTATION
Montpellier

F 30222

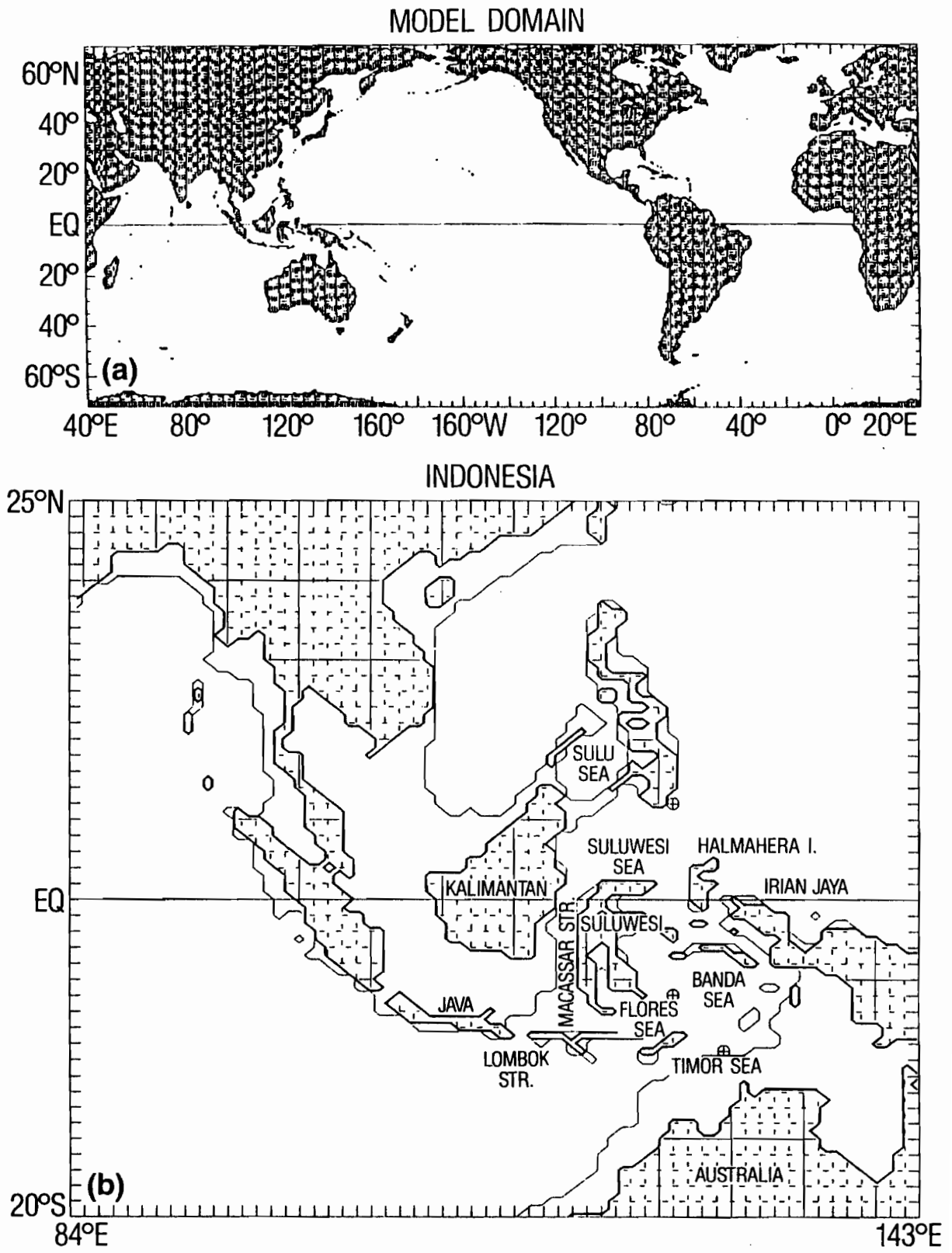

FIG.1. Model Domain a) Coastline geometry for global model. b) Enlargement of western Pacific-east Indian Ocean region. Thin line denotes 200 m isobath; ocean areas with depths shallower than 200 m are treated as land by the model.

In the present study, we use the most recent version of the NORDA Global model forced by the Hellerman and Rosenstein (1983) thereafter, (HR) wind stress climatology and the European Center for Medium-Range Weather Forecasts (ECMWF) 1000 mb winds from 1980 through 1987 to examine the mean, seasonal and interannual variability of the Pacific to Indian Ocean throughflow and the forcing mechanisms responsible for the variability.

The NORDA global model is a multi-layer, primitive equation formulation which incorporates a free surface, arbitary coastline geometry, full scale bottom topography in the lowest layer and a semi-implicit time scheme. A more detailed description of the model can be found in Wallcraft (1989). The model equations are formulated in spherical geometry over a latitudinal extent ranging from 71°N to 72°S. The model global geometry and an enlargement of the Indonesian Archipelago are shown in Figure 1. Lateral boundaries are located at the 200-m contour using bathymetric data from the SYNBAPS (Van Wyckhouse, 1979) data base. The walls are rigid and the no-slip condition is prescribed on the tangential flow.

The simulations described in this paper use a one active layer reduced gravity version of the model which includes the effects of mixing and mean thermodynamics. Density gradients within the upper layer are permitted and are modified by horizontal advection, entrainment, eddy diffusion and relaxation to a mean density climatology based on Levitus (1982). The model formulation permits the specification of surface heat fluxes, but that option was not utilized in these simulations. The model grid resolution for the experiments described in this report is .5 degree in latitude and .7 degree in longitude. A full list of model parameters is given in Table 1.

TABLE 1

PARAMETER	DESCRIPTION	VALUE
A(m)	Horizontal eddy viscosity (Momentum)	1500 m^2 s^{-1}
A(d)	Horizontal eddy viscosity (density)	5000 m^2 s^{-1}
g	Gravity	9.8 m s^{-2}
dx	Grid spacing in longitude	.7 deg
dy	Grid spacing in latitude	.5 deg
dt	Time step	60 min.
H	Initial layer depth	250 m
hm	Maximum layer thickness for which mixing is initiated	60 m

This section examines the results of two experiments: the climatology case forced by the HR wind stress data set (Exp 18.0) and the ECMWF case forced by the ECMWF 1000 mb winds from 1980 to 1987 (Exp 14.5). Prior to integrating the model with ECMWF product, the 12-hourly 1000 mb winds are averaged to form a mean for each month from 1980 to 1987 and reduced in strength by 20 percent. A constant drag coefficient of .0015 is applied to form a wind stress. No directional changes are made in reducing the winds from the 1000 mb level. It is recognized that such winds may provide only a coarse approximation to the actual 10 meter winds. However, in the absence of a better alternative, it was judged worthwhile to examine the interannual variability of a global ocean circulation model driven by such a product. As a check, the winds will be compared in the near future to the recently available ECMWF/TOGA 10 meter winds for the period 1985 to 1988.

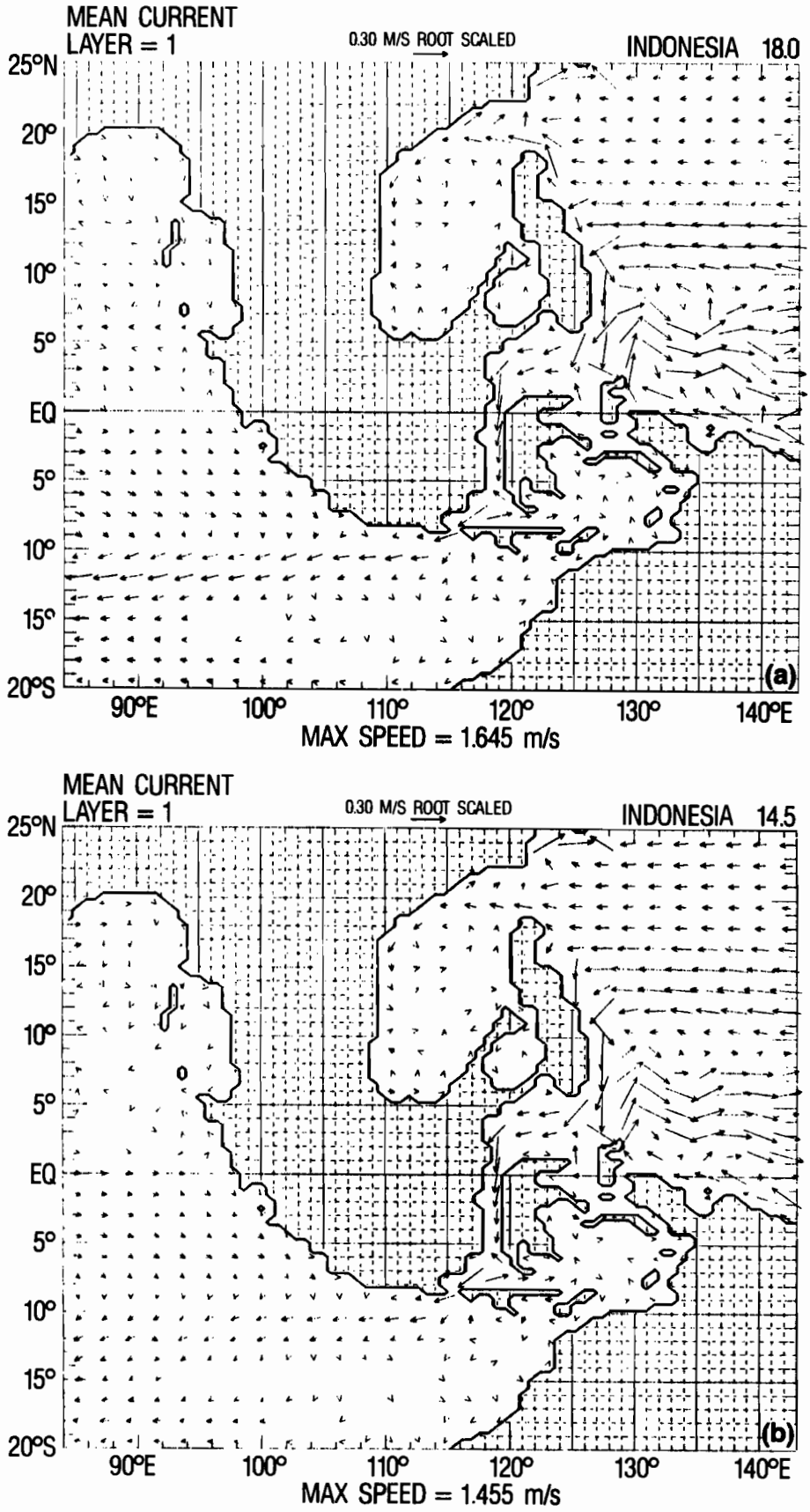

FIG.2. Current vectors for mean model velocity fields of a) Experiment 18.0 and b) Experiment 14.5 for PAC-IO region.

The mean model current fields in the Western Pacific-East Indian Ocean (PAC-IO) region for experiments 18.0 and 14.5 are shown in Figure 2. Note that qualitatively, the means from the two experiments are quite similar. The path of the model Pacific to Indian Ocean throughflow begins as a southwestward branch of the Mindanao Current and is directed through the Suluwesi Sea and the Macassar Strait. In both cases, most of the Indonesian throughflow enters the Indian Ocean through the Lombok Strait; this behavior is discussed in more detail below. The excess of Macassar Strait over Lombok Strait transport passes east through the Flores Sea and, upon entering the Banda Sea, branches north and south. The north branch returns to the Pacific Ocean through the Halmahera and Molucca Seas and adds to the North Equatorial Countercurrent. The branch that turns south from the Banda Sea enters the Indian Ocean both north and south of Timor.

It is recognized that the Lombok Strait transport is larger than observed values (approximately 1.7 Sv) as given by Murray and Arief (1988). The large model values are due to the fact that the minimum model width of an east-west port is .7 degree whereas the actual Lombok Strait is significantly smaller. In terms of studying the net throughflow, this deficiency of the model is not a serious one, because even if the Lombok Strait is blocked, most of the transport which would have exited through Lombok enters the Indian Ocean through the Timor Passages. This aspect is discussed further in Murray et al. (1989) in which the model Lombok Strait transport from Exp. 14.5 is compared to observations for the period January, 1985 to March 1986. Future experiments will address the problem by using finer grid resolution and/or increased friction at the port.

Table 2 lists the mean model transport values through the major passages listed above for Exp. 18.0 and 14.5. The mean throughflow transport for the HR case (Exp. 18.0) is 7.5 Sv versus a value of 4.5 Sv for the ECMWF case (Exp. 14.5). Given that the patterns of the circulation in the throughflow region is very similar for both cases, the different magnitudes may be the result of a calibration problem in reducing the winds from 1000 mb to 10 meters.

TABLE 2

MEAN TRANSPORT VALUES (IN SVERDRUPS)

	EXPERIMENT #	
	18.0 (HR)	14.5 (ECMWF)
SECTION		
Net Indonesian Throughflow	7.5	4.5
Lombok Strait	5.5	4
Macassar Strait	8.5	5.5
Suluwesi-Irian Jaya	1	1
Timor	2	.5

One distinct difference between the circulation patterns of Experiments 18.0 and 14.5 is that the bifurcation of the North Equatorial Current (NEC) at the Phillipines coast occurs at 15°-16°N in Exp. 18.0 and at 17°-18°N in Exp. 14.5. Observations (Wyrtki, 1961; Levitus, 1982) show the NEC splitting at 13°-14°N. Hence, the ECMWF case (Exp. 14.5) results in a particularly unrealistic north-south extension of the Countercurrent trough. The degree to which this property of the model solution modifies the height field in the western Pacific and the mean throughflow is not clear. It will be of interest to note whether future simulations using the ECMWF/TOGA 10m winds also display this characteristic.

Figure 3 shows the model mean seasonal variability of the low pass filtered net Indone-

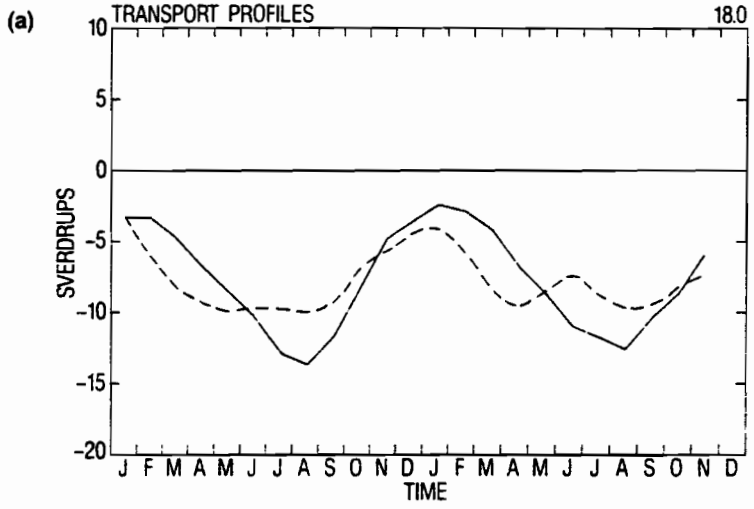

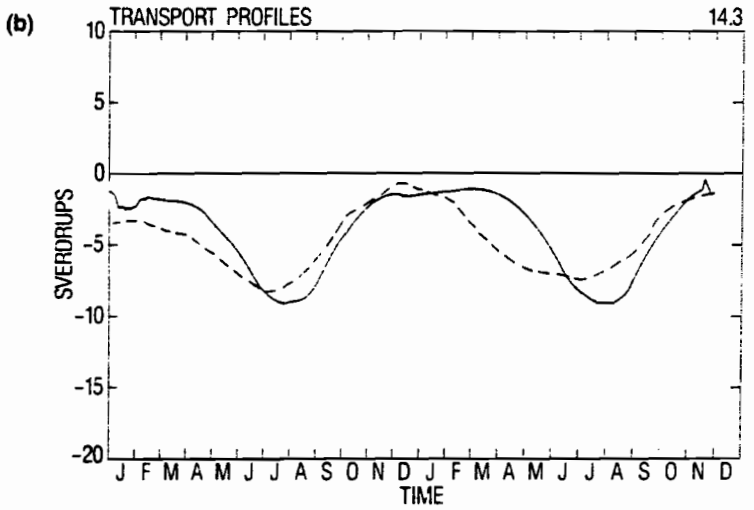

FIG.3. Transports (3-month running mean) vs. time of Pacific to Indian Ocean throughflow for a) Exp. 18.0 and b) for Exp. 14.5. Solid line denotes Indian Ocean section while dashed line represents equatorial section as defined in text.

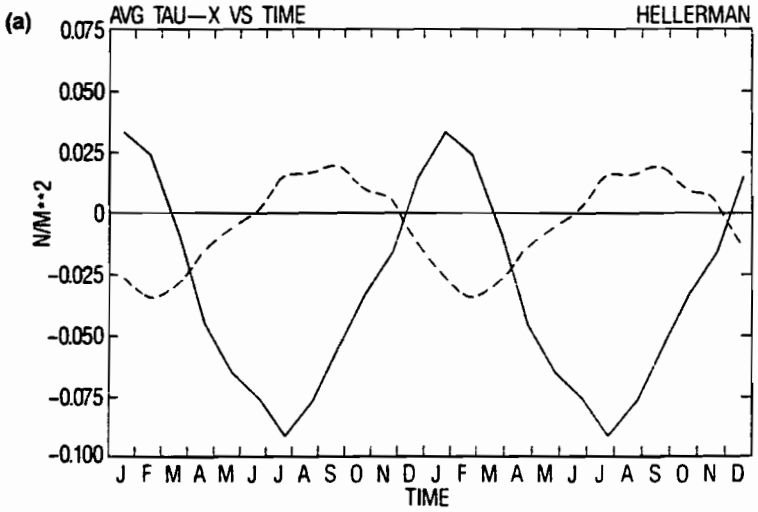

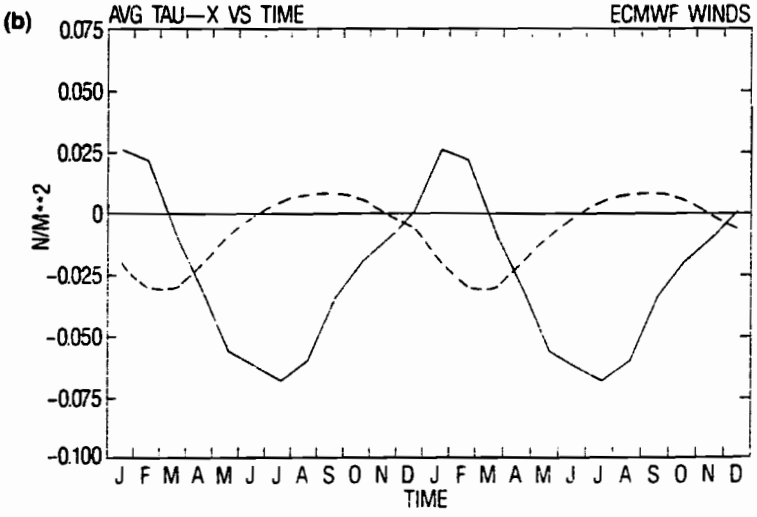

FIG.4. Area average of zonal wind stress component vs time for a) Hellerman and Rosenstein Climatology and b) ECMWF 1000 mb winds. Solid line represents average over an area bounded by 9°S and 19°S extending from 105°E to 120°E; dashed line is for an area bounded by the equator and 10°N extending from 125°E to 140°E.

sian throughflow from Exp. 18.0 and 14.5. Two sections are shown for each experiment: 1) the net throughflow extending from south Java to Australia at 114°E and 2) the net Pacific to Indian Ocean transport across an equatorial section extending from Kalimantan to Irian Jaya. Note that in each experiment, mass convergence occurs in the region bounded by the two sections during the north monsoon while divergence is present during the south monsoon. This is in agreement with Wyrtki (1961, 1987) who described downwelling in the Banda Sea during the north monsoon and upwelling during the period May to September.

The phases of the seasonal variation of the model free surface elevation for two points which are nearest the location of Davao and Darwin do not agree with the observations of Wyrtki (1987) who discovered a 180 degree phase change between the annual sea level variations at Davao and Darwin. The model free surface difference between Davao and the east Timor Sea (nearest model point to Darwin) displays a weak annual signal. The exclusion of the shelf circulation on the north coast of Australia and the resolution of the intense sea level gradients near Davao are factors contributing to the discrepancies. However, the lack of a strong seasonal cycle in the model sea level differences between Davao and Timor suggests that the seasonal variability of the Pacific to Indian Ocean throughflow is not regulated by the seasonal variation of the inter-basin pressure gradients or that Davao-Darwin in the model is not a good measure of this.

An examination of the seasonal variability of the wind-stress forcing, though, provides some insight into the seasonal variability of the throughflow. We form a mean value of the x-component of the wind stress for two regions: 1) an east Indian Ocean area bounded by the latitudes 9°S to 19°S extending from 105°E to 120°E and 2) a west Pacific region bounded meridionally by the equator and 10°N extending from 125°E to 140°E. The temporal variability of these means for both the HR and ECMWF winds are plotted in Figure 4. Note that both data sets display a maximum westward wind stress in the Indian Ocean region in July and the Pacific region in February.

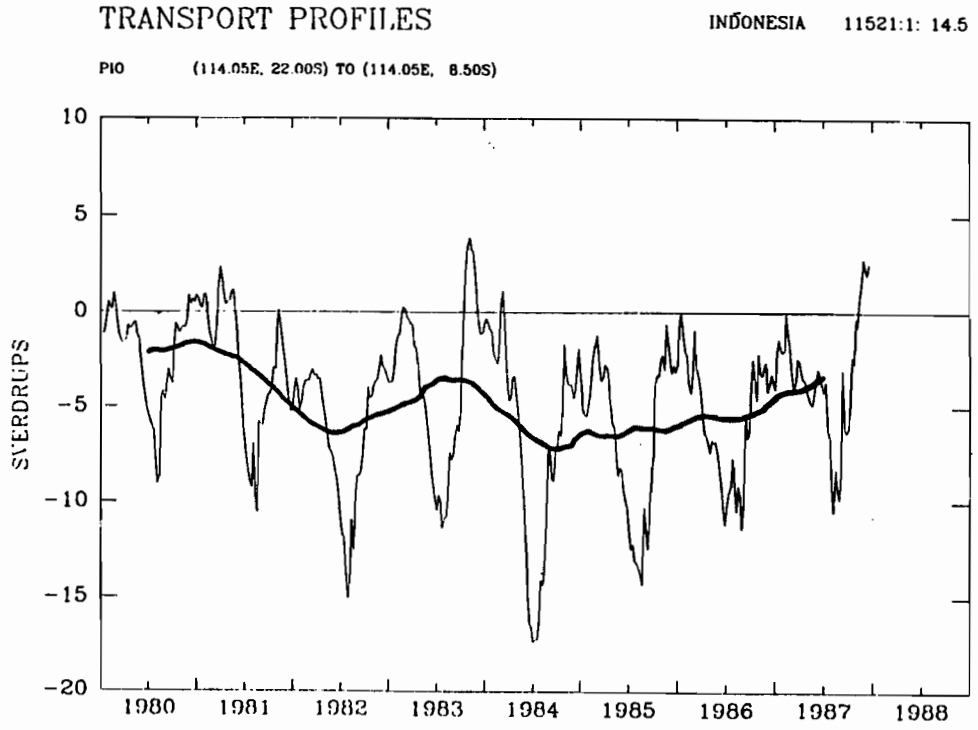

FIG.5. Pacific to Indian Ocean transport across a section from Java to Australia at 114°E for the years 1980 to 1987 (Experiment 14.5). Solid line is 12-month running mean.

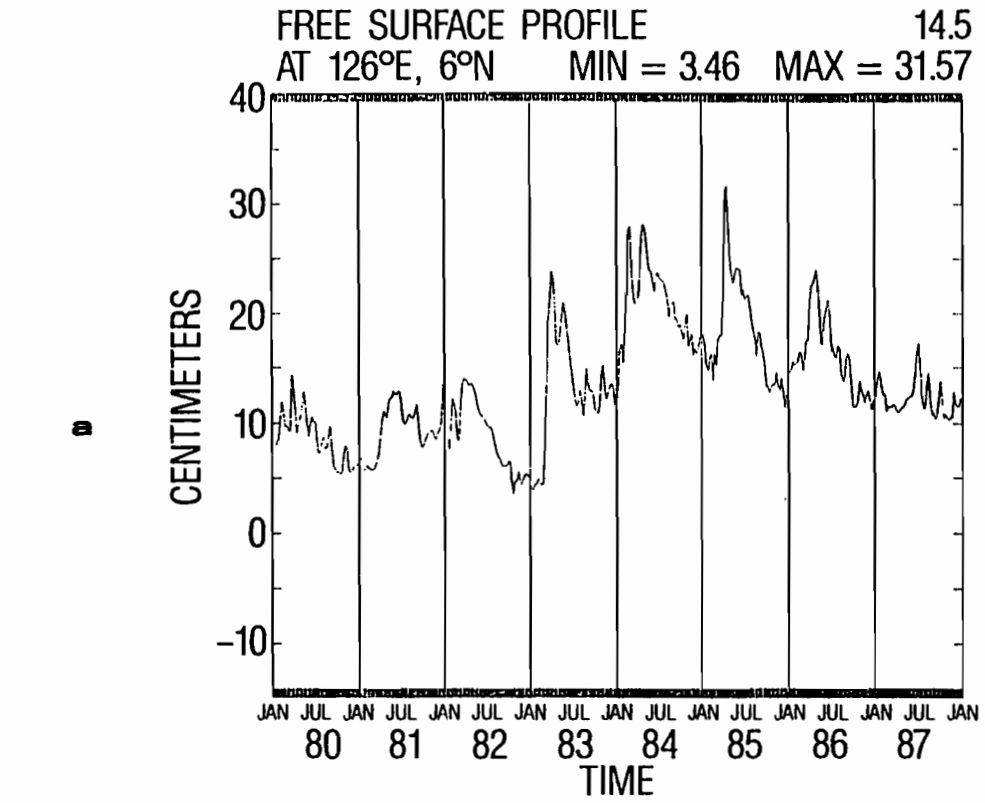

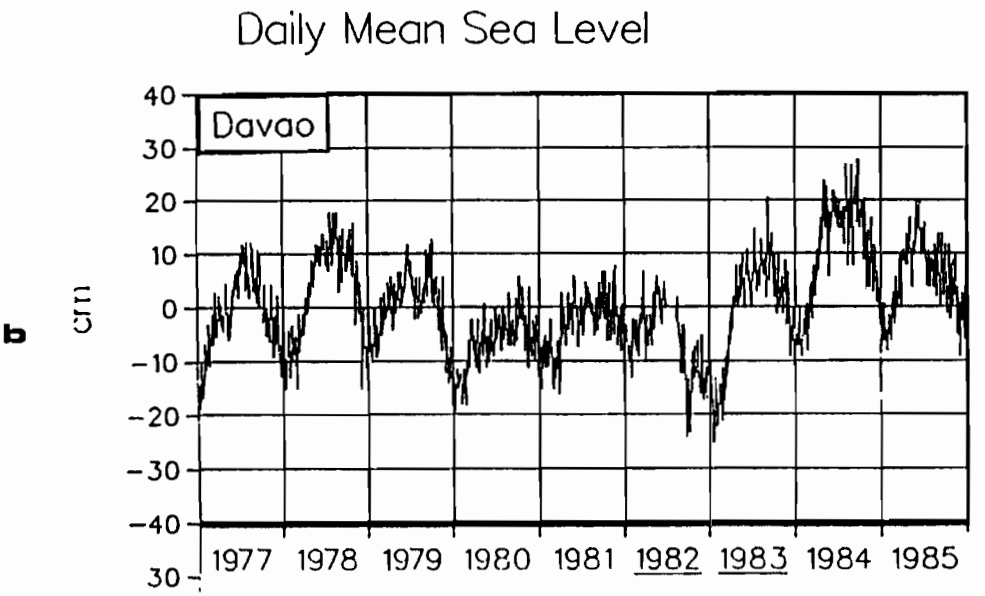

FIG.6. a) Model free surface deviation versus time at 126°E, 6°N for the period 1980 to 1987 from Exp. 14.5. b) Observed daily mean sea level at Davao from 1977 to 1985 (from Lukas, 1988).

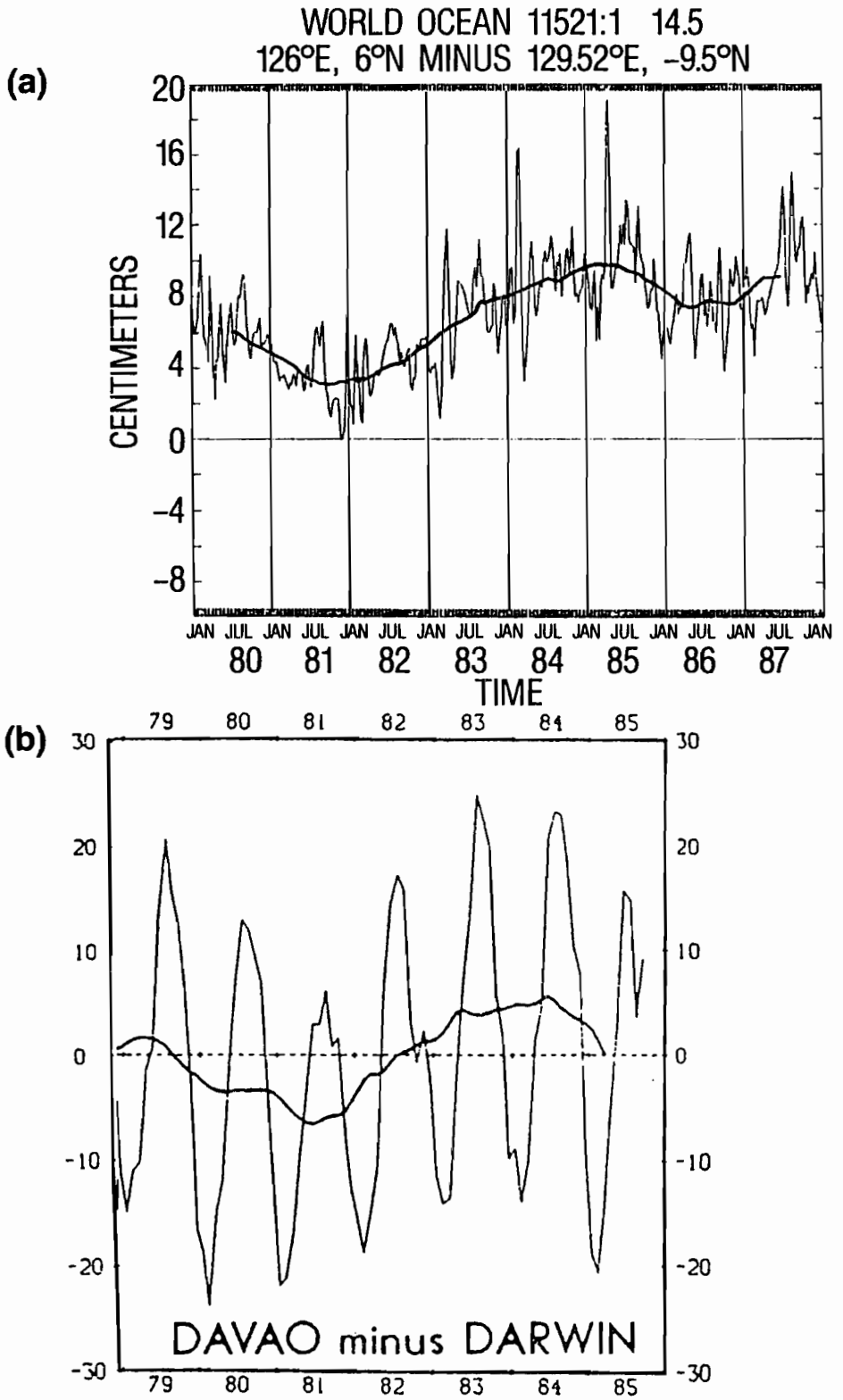

FIG.7. a) Model free surface difference between (126°E, 6°N) and (129°E, 9.5°S) for the years 1980 to 1987 from Exp. 14.5. These points represent the model locations of Davao and Darwin. b) Observed sea level difference between Davao and Darwin from 1980 to 1985 (from Wyrtki, 1987). Dark line in both curves is 12-month running mean.

A comparison of Figures 3 and 4 suggests that the seasonal variation of the zonal winds in the east Indian Ocean dominates the seasonal signal of the net throughflow. However, the convergence/divergence cycle of the winds over the entire region is large enough to produce a mass convergence/divergence within the throughflow domain. Additional analysis of model sea level, wind stress and wind stress curl using EOF and Principal Pattern Analysis (PEP) will be described in a future report.

The net model Indonesian throughflow between Java and Australia is plotted in Fig. 5 for the period 1980 to 1987 as given by Exp. 14.5. As stated previously, the mean is 4.5 Sv with an annual variation of 4 Sv. The July maximum of the Pacific to Indian Ocean transport ranges from 9 Sv in 1980 to 17 Sv in 1984. With the exception of 1983, the maximum transport increases monotonically from 1980 to 1984 and decreases from 1984 to 1987. The low pass filtered values of the throughflow show a similar variation although not as pronounced. The 12-month running mean average of the throughflow varies from a low of 2 Sv in 1980 to 7.5 Sv in 1984. Also note anomalous seasonal changes such as 1983-84 when the model transport increased by nearly 20 Sv from December, 1983 to July, 1984.

In order to examine whether the interannual variability of the model inter-basin pressure gradient is an adequate measure of the throughflow, the model sea level variability of the points representing Davao and Darwin are analyzed. Fig. 6 is a comparison of the model sea level for Davao and the observed sea level as presented by Lukas (1988). The model is able to represent the interannual variability of the observed Davao sea level quite accurately, such as the relatively weak variability from 1980 to mid-1982, the large drop in sea level associated with the 1982 ENSO and the subsequent rise to a peak in 1984 followed by a fall which in the model continues into 1987. Although the amplitude of the variability is less than observed values, the relative scale of the variability is reproduced. The interannual sea level variations at Darwin are also represented quite well by the model (not shown).

The difference in free surface elevation between the model Davao and Darwin points for the period 1980 to 1987 is plotted in Fig. 7 along with the observed sea level values from Wyrtki (1987) for the period 1979 to 1985. Except for a slight (relative to the time scale of the interannual variability) phase shift, the model and observations show a similar interannual variation given by a decrease from 1980 to 1981-82 followed by a rise to a peak in 1984-85 and a subsequent decrease during 1985. The amplitude of the model variations are approximately 60% of observed values. The close correspondence between the model results and observations of the Davao-Darwin sea level difference on interannual time scales is intriguing in view of the significant discrepancy for the annual signal.

The increase in sea level difference between Davao and Darwin during the period 1982-84 and the subsequent decrease suggest a rough correspondence to a similar variation in the Pacific to Indian Ocean transport (Fig. 5). Noteable exceptions are the years 1980-81 and 1983. There are other measures of the inter-basin pressure gradient that agree more closely with the interannual variability of the Indonesian throughflow. For example, the north Sulawesi Sea - Darwin difference exhibits a monotonic increase from 1980 to late 1984 followed by significant decrease (not shown). This suggests that an appropriate measure of the inter-basin pressure gradient may be used to monitor the interannual variability on longer time scales, but that variations from one year to the next may not be well represented by such sea level differences. A more detailed analysis of the relationship between model sea level, wind forcing and the Indonesian throughflow on interannual time scales will be reported in a future study.

Finally, we note that future investigations will examine the influence of the throughflow on the circulation of the Indian Ocean (including the Leeuwin Current) and the variability of the path of the throughflow from the western Pacific Ocean. In addition models with finer resolution, multiple layers and bottom topography will be utilized to investigate the roles of the New Guinea Coastal Undercurrent, the intermediate and deep Indonesia throughflow and the effects of bottom topography on the circulation.

Acknowledgements. The work was sponsored by the Office of Naval Research. We are grateful to Alan Wallcraft, Dana Thompson, George Heburn for contribution to the development of the numerical model and comments during the course of the research. We would also like to thank Pat Hogan, Bill Teague, Wes Youtsey, Robert Woodyard, Amy Summers and Greg Vega. The graphics software was in part provided by the National Center for Atmospheric Research (Sponsored by the National Science Foundation).

REFERENCES

Godfrey, A.L., 1989: A Sverdrup model of the depth-integrated flow for the world ocean allowing for island circulations. *Geophys. Astrophys. Fluid Dynamics*, 45, 89-112.

Gordon, A.L. 1986. Interocean exchange of thermocline water. *J. Geophys. Res.*, **91**, 5037-5046.

Hellerman, S., and M. Rosenstein, 1983: Normal monthly wind stress over the world ocean with error estimates. *J. Phys. Oceanogr.*, **13**, 1093-1104.

Kindle, J., G. Heburn and R. Rhodes 1987: An estimate of the Pacific to Indian Ocean throughflow from a global numerical model. *Further progress in Equatorial Oceanography*, (eds Katz, E.J. & Witte, J.M.) Nova, University Press, Ft. Lauderdale, FL, 317-321.

Levitus, S., 1982: Climatological Atlas of the World Ocean, NOAA Professional Paper 13, 173 pp.

Lukas, R., 1988: Interannual fluctuations of the Mindanao Current inferred from sea level, *J. Geophys. Res.*, **6**, 6744-6749.

Murray, Stephen P. and Dharma Arief, 1988: Throughflow into the Indian Ocean through the Lombok Strait, January 1985 - January 1986. *Nature*, **333**, 444-447.

Murray, Stephen, John Kindle, Dharma Arief and Harley Hurlburt, 1989: Throughflow between the Western Pacific and the Indian Ocean: Comparison between model and observations. In : *Proceedings from Western Pacific International Meeting and Workshop on TOGA-COARE*. In Press.

Semtner, Albert J., and Robert M. Chervin, 1988. A simulation of the global ocean circulation with resolved eddies. *J. Geophys. Res.*, **93**, 15, 502-15, 522.

VanWyckhouse, R.J., 1979: SYNBAPS, vol. 1, Data sources and data preparation, NORDA Tech. Note 35, Naval Ocean Research and Development Activity, Stennis Space Center, MS. Wallcraft, A. J., 1989: The NORDA layered ocean model user's guide. Naval Ocean Research and Development Activity Report. (In preparation)

Wyrtki, K., 1961: Physical oceanography of the southeast Asian waters. Naga Rep. 2, Scripps Inst. Oceanogr.: 1-195.

Wyrtki, K., 1987: Indonesian Throughflow and the Associated Pressure Gradient. *J. Geophys. Res.*, **92**, 12941-12946.

Uncertainties in Tropical Pacific Ocean Simulations : The Seasonal and Interannual Sea Level Response to Three Analyses of the Surface Wind Field

Antonio J. BUSALACCHI[1], Michael J. McPHADEN[2], Joël PICAUT[3] and Scott SPRINGER[4]

[1] *Laboratory for Oceans, NASA / Goddard Space Flight Center*
Greenbelt, Maryland - U.S.A.

[2] *NOAA / Pacific Marine Environmental Laboratory*
Seattle, Washington - U.S.A.

[3] *Groupe SURTROPAC, ORSTOM*
Nouméa - New Caledonia.

[4] *School of Oceanography, University of Washington*
Seattle, Washington - U.S.A.

ABSTRACT

The purpose of this study is to characterize differences in the time/space structure present among conventional descriptions of the tropical Pacific surface wind field, and in turn, to quantify the impact of these differences on our ability to model the dominant wind-forced variability of the tropical Pacific Ocean on seasonal and interannual time scales. A linear, multiple vertical mode ocean model is used as a transfer function to determine the influence of three distinct surface wind stress products for the period 1979-1983. This five-year period was chosen for study because it encompasses three years of a fairly regular seasonal cycle leading up to the 1982-83 El Niño for which there are several coincident oceanic and surface wind data sets. The three different wind analyses used are the Florida State University subjective analysis, the University of Hawaii subjective analysis, and the Fleet Numerical Oceanography Center objective analysis. We examine first the three mean seasonal cycle solutions prior to El Niño which then serve as self-consistent bases for analyzing the significant anomalies about the mean in 1982-83.

The impact of uncertainties in the forcing functions is discussed relative to the dominant seasonal and interannual scales of variability for the wind-driven oceanic response. On seasonal time scales, critical differences in the wind stress products, of order 0.2-0.4 dynes cm^{-2}, were in wind regimes of surface convergence and significant gradients such as the ITCZ and SPCZ. These uncertainties in the wind fields were manifested in model sea level solutions as 6-12 cm discrepancies near the NECC Trough and east of New Guinea. On interannual time scales, the influence of greater sampling along the major ship tracks was evident. Away from the major shipping lanes rms differences in the wind stress anomalies (1979-1983) about the mean seasonal cycle (1979-1981) reached up to 0.5 dynes cm^{-2}. The combined effect of these differences in the wind products resulted in 8-20 cm rms differences in the model sea level simulations. The largest of these discrepancies tended to exist at the terminus of equatorial wave characteristics, e.g. in the east along the equator and in the west off the equator.

ORSTOM
CENTRE DOCUMENTATION
Montpellier

F 30223

1. Introduction

Tropical ocean variability on time scales from months to years is considered to be principally deterministic (WCRP, 1985). In this regard the dynamic response of the tropical ocean is governed by the temporal and spatial structure of the surface wind stress. It follows that our ability to model accurately the upper tropical ocean circulation is intimately tied to our ability to describe accurately the surface wind field. Unfortunately, as a result of the logistical problems in monitoring the surface wind field over tropical oceans it is difficult to assess the accuracy of gridded fields of surface wind stress generated from sparse ship, buoy, island, or cloud motion observations or operational center analyses. Little is known even of the similarities or differences, on both seasonal and interannual time scales, among the various wind products presently available. The implications of possible and likely discrepancies and uncertainties in surface wind stress prescriptions for tropical ocean simulations is then also unknown.

The most straightforward way of assessing the dynamic, wind-driven response of the tropical ocean circulation is via vertically integrated variables, such as sea level, dynamic height, and heat content, which tend to average out nonlinear, nonadiabatic effects. Previous tropical Pacific model sea level studies have demonstrated that the quality of interannual hindcasts is higher along the equator and eastern boundary where the response is an integral function of the equatorial zonal wind stress to the west (Busalacchi and Cane, 1985). The quality of sea level hindcasts is degraded away from the equator where the solution is determined, in part, by a derivative of the forcing, i.e., the wind stress curl. Random errors present in wind stress data would tend to have a greater influence off the equator where they would be differentiated as opposed to on the equator where their effect would be integrated.

Recently, a series of numerical experiments have been performed in order to assess the impact of wind stress uncertainties on the dynamic response of wind-driven tropical Pacific Ocean simulations. McPhaden et al. (1988a) examined simulations of the mean seasonal cycle using a multiple vertical mode linear model forced with three different surface wind stress products averaged over the period 1979-1981. Simulated mean seasonal cycles in dynamic height and sea level were then compared with observed variations based on expendable bathythermograph (XBT) and island tide gauge data averaged over the same 1979-1981 period. Landsteiner et al. (1989) examined the Sverdrup responses to the three-year mean (1979-1981) wind stresses and compared those responses to XBT-derived pressures and transports for the same period. Busalacchi et al. (1989) extended these studies to consider the interannual variability for the five years 1979-1983 including the anomalies associated with the 1982-83 El Niño. This allowed the similarities and discrepancies between the three wind products on seasonal time scales to be quantified and intercompared with those on interannual time scales. The impact of the differences in the wind field was assessed by a similar treatment of the model sea level solutions. Related studies were also performed in which the model solutions were used to address array design and sampling questions pertaining to the XBT (McPhaden et al., 1988b) and sea level (Springer et al., 1989) observations. The purpose of the present note is to summarize succinctly the differences in the time/space structure present among conventional descriptions of the tropical Pacific surface wind field, and in turn, to quantify the impact of these discrepancies on our ability to model the dominant wind-forced variability of the tropical Pacific Ocean on seasonal and interannual time scales.

2. Wind Stress Products and Ocean Model

The period of interest, 1979-1983, was chosen because it provided an interesting contrast between a fairly regular mean seasonal cycle for 1979-1981 and the extreme El

Niño event that followed in 1982-83. More importantly, it was also a time for which there are three different wind stress products available, each resulting from a consistent analysis scheme over the full five years. Two of these data sets are derived from subjective analyses, and the third is derived from an operational objective analysis. One of the subjective analyses is the Florida State University (FSU) analysis of ship-board observations provided by J. J. O'Brien. The analysis procedure of transforming individual ship wind observations into monthly mean wind stress fields on a 2° x 2° grid is described by Goldenberg and O'Brien (1981). The second subjective analysis is a combination of satellite-observed, low-level cloud motion vectors, ship wind observations, island wind observations, and buoy wind observations performed by J. Sadler at the University of Hawaii. The production of monthly mean surface wind and wind stress data sets on a 2.5° x 2.5° grid is described by Sadler and Kilonsky (1985) and Sadler et al. (1987). The third data set is an objectively analyzed operational product from the Global Band Analyses of the U. S. Navy's Fleet Numerical Oceanography Center (FNOC). An objective analysis based on Cressman (1959) is used on all reports (ship, island, buoy, etc.) in an operational data base for 6-hour intervals on a 2.5° x 2.5° grid. Six-hourly stresses are computed and averaged to form monthly means. A constant drag coefficient of 1.5×10^{-3} is used to convert from wind to wind stress for each of the three wind data sets.

A linear, numerical treatment of the shallow water wave equations is used as a transfer function to analyze the wind-driven dynamic response of a model tropical Pacific Ocean to different representations of the surface wind stress. The model basin extends from 20°N to 20°S and 126°E to 70°W. For the purposes here, sea level is the variable of interest. In response to the monthly mean forcing from January 1979 to December 1983 model height field solutions are generated for the first four baroclinic modes. A final sea level solution is found by summing the individual contributions to sea level from each of the four vertical modes. We consider both the mean seasonal cycle of sea level during the pre-El Niño period 1979-1981 and the anomalies for 1979-1983 about the 1979-1981 mean seasonal cycle.

3. Results

In this note we will only focus on the zonal wind stress since it is the dominant component of the trade winds and the most important for driving the tropical ocean circulation. Root mean square (RMS) differences between all three wind stress products for both the seasonal cycle and interannual anomalies are used as a measure of the discrepancies and uncertainties among the three data sets. Similarly, rms differences between the three model sea level solutions are used to depict how the differences in the total wind stress forcing become manifest in the forced integrated response of sea level. Busalacchi et al. (1989) provide a more in depth treatment of the signal and uncertainty in the annual mean, seasonal variability, and interannual variability of the zonal wind stress, meridional wind stress, wind stress curl, and resultant model sea level response.

On seasonal time scales, as defined by the mean seasonal cycle for 1979-1981, the largest fluctuations for the zonal wind stress (standard deviations of 0.4-0.7 dynes cm^{-2}) are similar in all three wind products and are associated with the broad-band seasonal excursions of the Intertropical Convergence Zone (ITCZ) in the Northern Hemisphere and the monsoon circulation of both hemispheres in the far western portion of the basin. With this seasonal signal as background, the largest rms differences in the seasonal zonal wind stress, as shown in Figure 1, are of order 0.2-0.4 dynes cm^{-2} along 8°-10°N and in the Southern Hemisphere where there are few wind observations. The maximum rms differences usually coincide with the largest seasonal fluctuations, i.e., the error is largest where the signal is largest. Of the three rms product combinations, the FSU and Sadler zonal wind stress appear to be the most similar to each other and conversely the largest

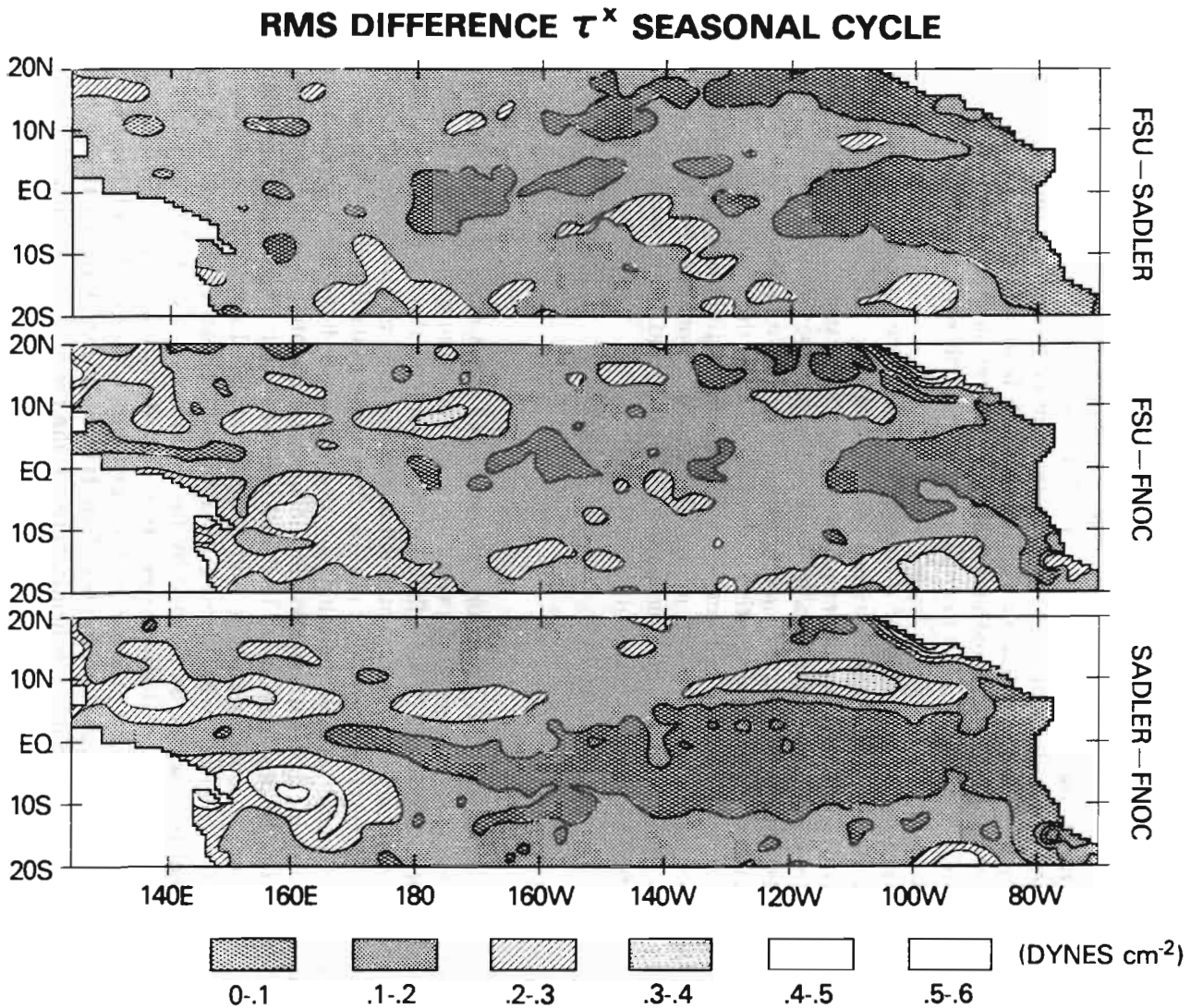

Figure 1. Root mean square difference between the seasonal cycles (1979-1981) of the zonal wind stress for a) FSU - Sadler b) FSU - FNOC c) Sadler - FNOC

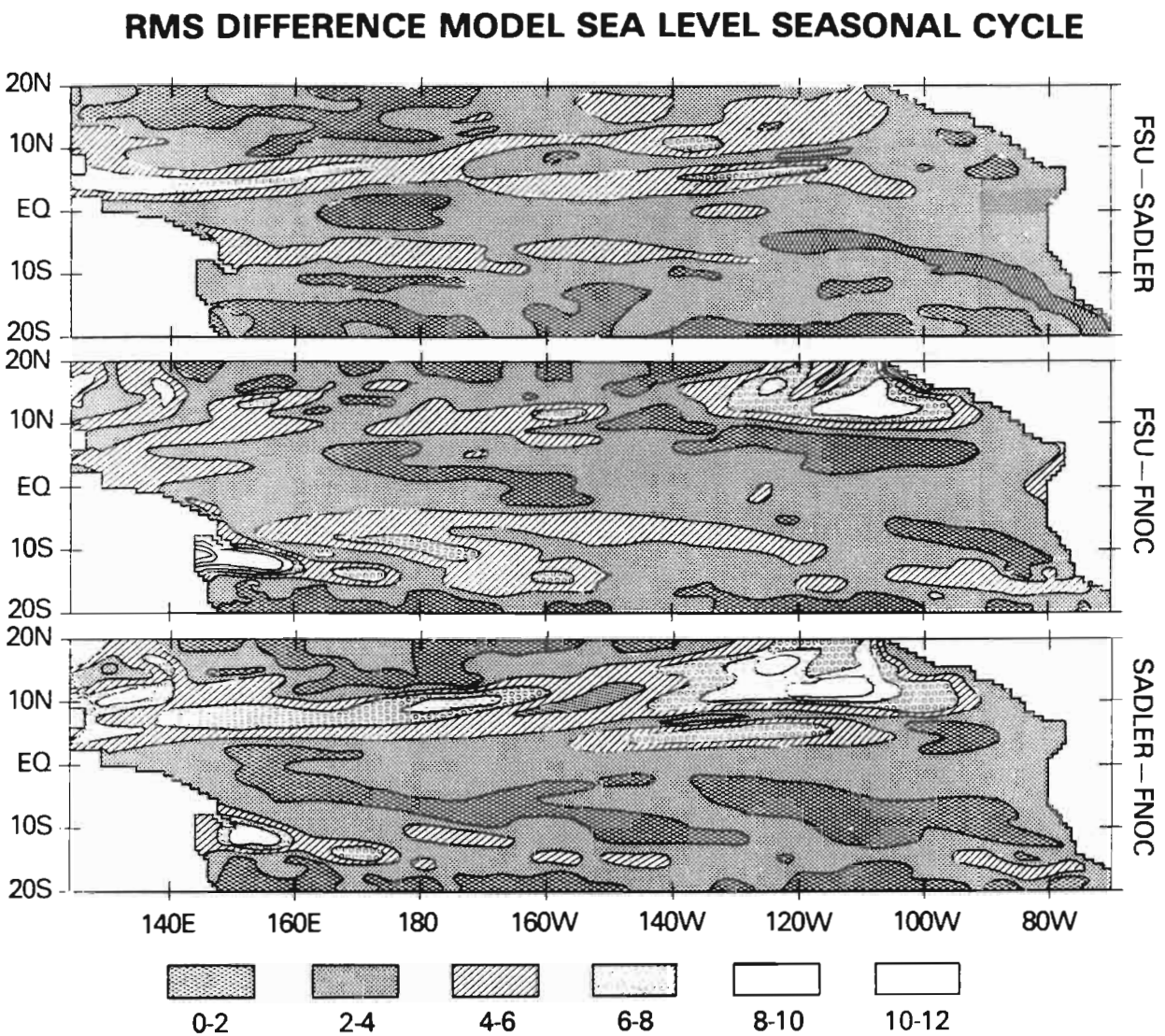

Figure 2. Root mean square difference between the seasonal cycles (1979-1981) of the wind-driven model sea level for a) FSU - Sadler b) FSU - FNOC c) Sadler - FNOC

rms differences are with the FNOC data. In general, the rms differences are less than the standard deviation of the seasonal cycle when viewed on the basin scale. If the discrepancies that the rms differences represent are taken to be a measure of the uncertainty or noise within the forcing data and the seasonal standard deviations as signal, then a crude signal/noise measure of approximately 1.5 is obtained for the seasonal zonal wind stress. A similar measure is also found for the seasonal meridional wind stress.

Whereas the basin-scale structure of the seasonal variability for the three zonal wind stress products was similar, the sea level responses to the total wind stress forcing are dissimilar. The only aspect of the seasonal response common to all three solutions is a region of maximum variability of 6-9 cm in the northeast corner of the basin. The rms differences between the three seasonal sea level solutions are shown in Figure 2. The largest differences, of order 6-9 cm, are in the vicinity of the North Equatorial Countercurrent (NECC) Trough beneath the ITCZ and are of similar amplitude to the maximum of the seasonal sea level response. The location of these differences signifies major inconsistencies in the seasonal variability and structure for the NECC and North Equatorial Current across the entire basin in the three solutions. The most significant of these differences is found to occur between the Sadler and FNOC forced solutions. Other notable differences, from 4-12 cm, are found beneath the South Pacific Convergence Zone (SPCZ) in the southwestern tropical Pacific. As a result of equatorial wave radiation away from regions of significant forcing, uncertainties in the wind stress can propagate to points far beyond the region of forcing. Thus, the signal to noise ratio of 1.5 that characterized the zonal and meridional wind stress components does not hold for the integrated response of the model sea level. The rms differences in sea level across the basin are nearly equivalent to the mean seasonal sea level signal implying a signal to noise ratio of 1.

The interannual variability is addressed by considering the anomalies for 1979-1983 about the mean seasonal cycle for the pre-El Niño years of 1979-1981. In terms of the zonal wind stress, the largest anomalous variations are in the central equatorial Pacific between 140°W and 160°W of 0.4-0.5 dynes cm^{-2} for both the FSU and Sadler products. The maximum anomalies for FNOC are smaller and further to the east. Inspection of individual monthly anomaly maps indicates this region of maximum interannual variability is the result of equatorial westerly anomalies during the onset of the 1982-83 El Niño. The basin-wide mean for this interannual signal is approximately 0.25 dynes cm^{-2} for all three products. The largest rms differences in the anomalies of the zonal wind stress, between 0.25-0.5 dynes cm^{-2}, are also located in the central equatorial Pacific (Fig. 3). A second area of large rms differences is in the Northern Hemisphere between 160°E and 170°W. Bordering these regions we are able to see the influence of denser sampling along the major shipping lanes. From Fiji to the Philippines/Japan and Fiji to Hawaii/North America the rms differences are often between 0.1-0.2 dynes cm^{-2}. For these specific regions of enhanced observations the signal/noise is greater than 1. Away from these ship tracks the rms differences in the wind stress anomalies may reach up to 0.5 dynes cm^{-2} and hence the signal to noise is considerably less than 1.

In response to the five years of anomalous zonal and meridional wind stress forcing, the largest interannual sea level variability in the FSU and Sadler solutions is in the southwestern Pacific of 12-15 cm. Another region of large variability is a symmetric equatorial response found in the east of 9-12 cm. As in the wind stress forcing the most significant sea level anomalies occur during the 1982-83 El Niño. The FSU and Sadler sea level solutions are clearly the most similar (Fig. 4). Root mean square differences range between 4 and 12 cm and imply a basin-wide signal to noise ratio greater than 1. The rms differences involving the FNOC forced sea level solutions are considerably larger and exhibit broad regions of sea level discrepancies greater than 12 cm. The signal to noise ratio for the two product combination involving FNOC are

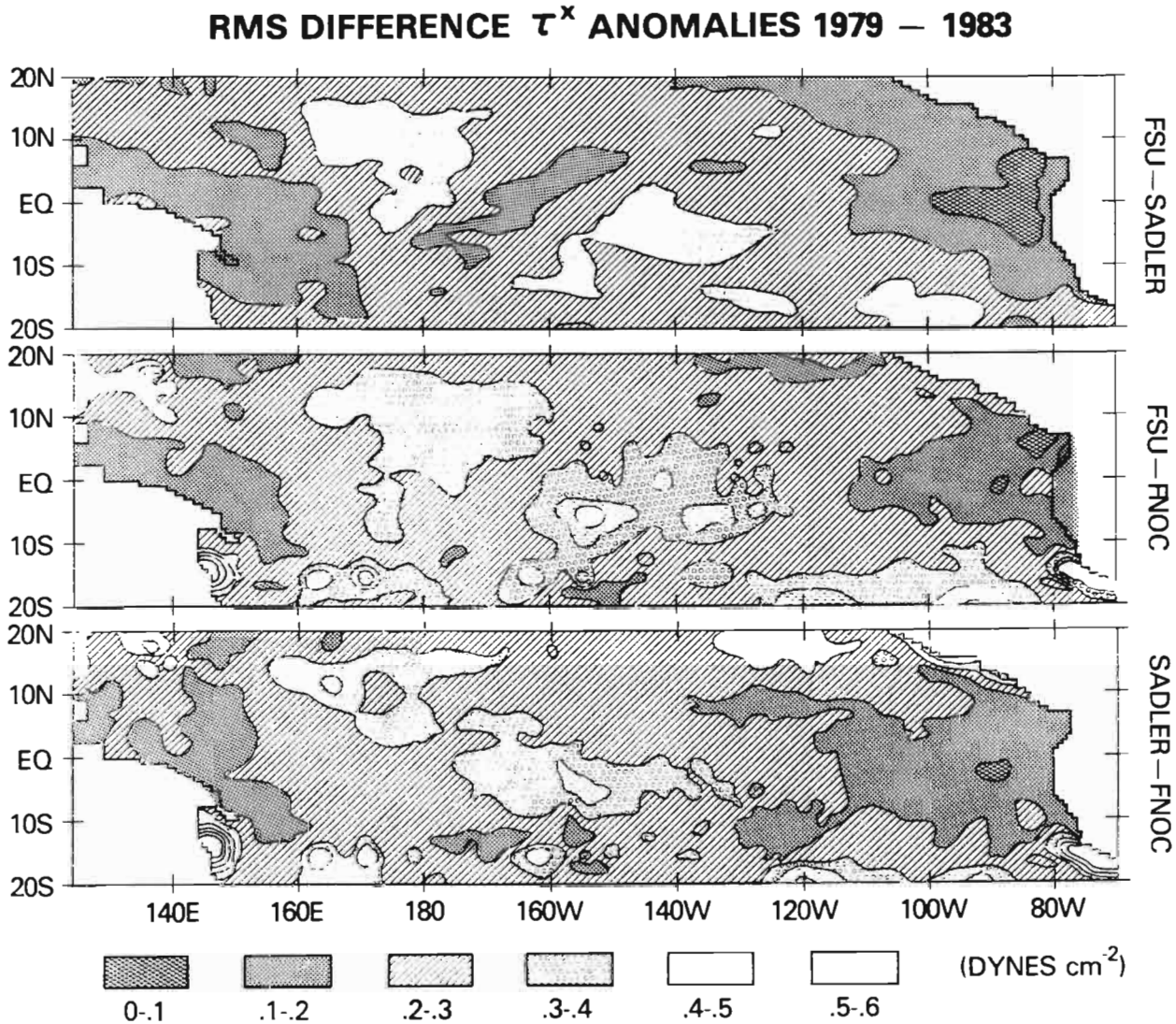

Figure 3. Root mean square difference between the anomalies (1979-1983) about the mean seasonal cycle (1979-1981) of the zonal wind stress for
a) FSU - Sadler b) FSU - FNOC c) Sadler - FNOC

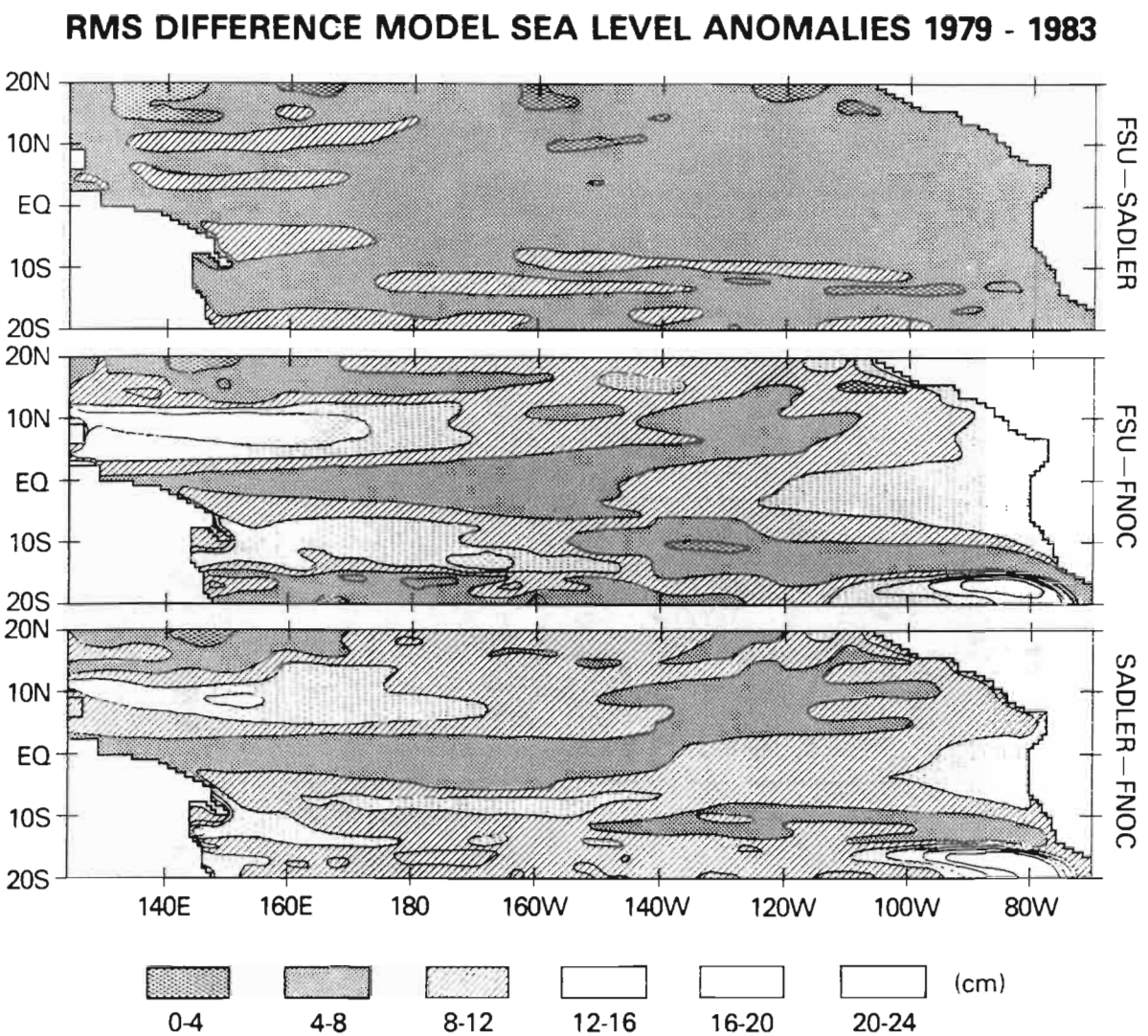

Figure 4. Root mean square difference between the anomalies (1979-1983) about the mean seasonal cycle (1979-1981) of the wind-driven model sea level for
a) FSU - Sadler b) FSU - FNOC c) Sadler - FNOC

significantly less than 1. Characteristic of all three rms difference pairs is an increase in the direction of equatorial wave propagation, i.e., from west to east along the equator and from east to west off the equator.

4. Discussion and Conclusions

The principal objective of this activity was to acquire, analyze, and intercompare "conventional" wind stress products for the tropical Pacific Ocean on seasonal and interannual time scales. Subsequently, these data were used to drive a linear, multi-mode numerical ocean model wherein the model served as a transfer function for the integrated response to the various wind forcings. On seasonal time scales, some of the greatest differences among the FSU, Sadler, and FNOC wind stress products, of order 0.2-0.4 dynes cm^{-2}, were in wind regimes of surface convergence and significant gradients such as the ITCZ and SPCZ. These uncertainties in the wind fields were manifested in model sea level solutions as 6-12 cm discrepancies near the NECC Trough and east of New Guinea. On interannual time scales, the influence of greater sampling along the major ship tracks was evident. Away from the major shipping lanes rms differences in the anomalies (1979-1983) about the mean seasonal cycle (1979-1981) reached up to 0.5 dynes cm^{-2}. The combined effect of these differences in the wind products resulted in 8-20 cm rms differences in the model sea level simulations. The largest of these discrepancies tended to exist at the terminus of equatorial wave characteristics, e.g. in the east along the equator and in the west off the equator.

The results presented here indicate that of the three wind stress products, the FSU and Sadler data were the most consistent on both seasonal and interannual time scales. The same held true for the sea level solutions forced by these data sets. The largest discrepancies were found to occur with the FNOC zonal wind stress and FNOC driven sea level solution. The signal/noise ratios, or more correctly the signal/uncertainty ratios, that were used to characterize these wind data and wind-forced solutions tend to support previous intercomparisons of the model sea level with XBT-derived dynamic heights and tide gauge observations. McPhaden et al. (1988a) found coherence estimates of 0.5-0.7 between the three model simulations and the observations for the 1 cycle per year harmonic, which dominates the seasonal cycle over most of the tropical Pacific. However, no wind stress product was capable of being judged to be clearly superior to the others based on the comparisons of the model sea level and dynamic height solutions with the in-situ observations. Although the signal to noise ratio for the seasonal cycle of the zonal wind stress was greater than one, this measure yields little information regarding how well gradients in the wind stress are being described, e.g. $\partial\tau^x/\partial y$. When the seasonal variability is considered in terms of the wind stress curl, which is the most appropriate representation of the wind stress when considering the off-equatorial oceanic response, the signal to noise is reduced to one. This is consistent with the signal to noise estimated for the seasonal model sea level response.

For the interannual variability, Busalacchi et al. (1989) correlated the time series of sea level anomalies from the model solutions with those observed at 36 island and coastal stations. The correlations were based on typically four to five years of data spanning 1979-1983. The overall quality of the FSU forced and Sadler forced sea level solutions was virtually indistinguishable. Cross correlations between the FSU forced solutions with the observed sea level ranged between -0.01 to 0.93 with an ensemble mean correlation coefficient of 0.58. Cross correlations between the Sadler forced solutions with the observed sea level ranged between -0.45 to 0.98 and also had a mean correlation coefficient of 0.58. The skill of the hindcast driven by FNOC winds was significantly less. Correlation coefficients ranged between -0.74 to 0.74 with an ensemble mean correlation of only 0.17. Consistent with these intercomparisons are the

signal/noise ratios for the anomalous sea level solutions that are greater than 1 between FSU and Sadler but less than 1 when involving FNOC.

Only the FSU, Sadler, and FNOC wind stress data sets were considered to be permissible for our analyses of the seasonal and interannual variability as these were the only products available for which there was a consistent analysis scheme in place for the entire five year period. Periodic improvements and changes to the analysis schemes at other operational centers such as ECMWF and NMC precluded the use of these products. Nonetheless, an internally consistent analysis scheme is essential to any research investigation of interannual variability. The importance of the El Niño phenomenon brings this issue to the forefront. By restricting their focus to only the 1982-1983 El Niño, Harrison et al. (1989) were recently able to consider the response of an ocean general circulation model to the three wind sets considered here as well as the operational wind fields from NMC and ECMWF. Comparison of dynamic heights from the primitive equation model solutions with those derived from ship-of-opportunity XBT data also indicated better hindcast skill for the solutions forced by the subjective analyses than the operational center analyses. The problems encountered in these types of modelling studies clearly demonstrate the need, sometime during the TOGA decade, for a reanalysis of atmospheric model based data, such that a multiyear record of surface winds is produced with an internally consistent analysis. The subsequent use and scrutiny of these winds in ocean simulation studies will prove very useful in evaluating the reanalyzed atmospheric data.

References

Busalacchi, A. J., and M. A. Cane, Hindcasts of sea level variations during the 1982-83 El Niño, *J. Phys. Oceanogr.*, *15*, 213-221, 1985.

Busalacchi, A. J., M. J. McPhaden, J. Picaut, and S. Springer, Sensitivity of wind-driven tropical Pacific ocean simulations on seasonal and interannual time scales, to appear in Coupled Ocean-Atmosphere Models: Proceedings of the 21st International Liege Colloquium on Ocean Hydrodynamics, J.C.J. Nihoul, Ed., Elsevier, 1989.

Cressman, G. P., An operational objective analysis system, *Mon. Weather Rev.*, *87*, 367-374, 1959.

Goldenberg, S. B., and J. J. O'Brien, Time and space variability of tropical Pacific wind stress, *Mon. Wea. Rev.*, *109*, 1190-1207, 1981.

Harrison, D. E., W. S. Kessler, and B. S. Giese, Ocean circulation model hindcasts of the 1982-83 El Niño: Thermal variability along the ship-of-opportunity tracks, *J. Phys. Oceanogr.*, *19*, 397-418, 1989.

Landsteiner, M. C., M. J. McPhaden, and J. Picaut, On the sensitivity of Sverdrup transport estimates to the specification of wind stress forcing in the tropical Pacific, J. Geophys. Res., (in press), 1989.

McPhaden, M. J., A. J. Busalacchi, J. Picaut, and G. Raymond, A model study of potential sampling errors due to data scatter around expendable bathythermograph transects in the tropical Pacific, *J. Geophys. Res.*, *93*, 8119-8130, 1988a.

McPhaden, M. J., A. J. Busalacchi, and J. Picaut, Observations and wind-forced model simulations of the mean seasonal cycle in tropical Pacific Sea Surface Topography, *J. Geophys. Res.*, *93*, 8131-8146, 1988b.

Sadler, J. C., and B. J. Kilonsky, Deriving surface winds from satellite observations of low-level cloud motions, *J. Clim. Appl. Meteorol.*, *24*, 758-769, 1985.

Sadler, J. C., M. A. Lander, A. M. Hori, and L. K. Oda, Tropical marine climatic atlas, II, Pacific Ocean, *Tech. Rep. UHMET 87-02*, Dep. of Meteorol., Univ. of Hawaii, Honolulu, 1987.

Springer, S., M. McPhaden, and A. J. Busalacchi, Oceanic heat content variability during the 1982-83 El Niño, (manuscript in preparation), 1989.

World Climate Research Program, Scientific Plan for the Tropical Ocean and Global Atmosphere Programme, 146pp., WCRP Publications Series No. 3, 1985.

Intraseasonal Variability - A Critical Component of ENSO ?

Stephen E. ZEBIAK

Lamont-Doherty Geological Observatory
Palisades, NY 10964 - U.S.A.

ABSTRACT

The impact of intraseasonal variability on ENSO is studied in the context of the Zebiak and Cane (1987) coupled atmosphere-ocean model, and an idealized representation intraseasonal forcing. The effects of the parameterized forcing are examined in both simulation and forecast experiments, with similar results: the intraseasonal variability generally plays a minor role in altering the model behavior. Despite the uncertainties inherent in both the coupled model and the specified forcing, the results clearly suggest that intraseasonal variability is not an essential component of ENSO. At the same time, they present evidence of occasional sensitive periods or states of the coupled system in which intraseasonal forcing (and possibly other forcings) can indeed disrupt the future course of events.

1. Introduction

Since the pioneering work of Madden and Julian (1971,1972), the so-called 40-50 day oscillation (also known as the 30-60 day oscillation, or Madden-Julian oscillation) has been the subject of intense study. It is a prominent mode of variability on intraseasonal timescales throughout most of the tropics, with clear signatures in upper and lower level tropospheric zonal wind, and convective activity (Madden and Julian 1971,1972; Lau and Chan 1985,1986a; Knutson and Weickmann 1987; Chen and Murakami 1988). Its significance is further heightened by suggested relationships with a number of other phenomena; among them, fluctuations of the Indian monsoon (Krishnamurti and Subrahmanyan 1982; Murakami et al. 1984,1986; Cadet and Greco 1987), fluctuations of the Southeast Asian monsoon (Chen et al. 1988), westerly wind bursts in the western Pacific (Lau et al. 1988), and the onset of El Niño (Lau and Chan 1986b,1988). The latter two are related inasmuch as westerly wind episodes typically characterize the early stages of El Niño events (Luther et al. 1983). The proposed relationship between 30-60 day activity (hereafter referred to as intraseasonal variability or ISV) and El Niño is the subject of this study. Specifically, we will assess the impact of ISV on the Zebiak and Cane (1987) coupled model in both simulation mode and forecast mode.

One can easily imagine, following the authors cited above, that the energetic ISV forcing, if not an essential element of ENSO, is often influential in the timing of events. On the other hand, the theory emerging from simple coupled models points to an essentially deterministic interannual cycle. If one accepts this theory, then the role of ISV would seem to be secondary; or more correctly, the role of that component of ISV not controlled by the slower, ENSO-mode variability would seem secondary. Whereas one perspective treats El Niño occurrences as individual events, dependent on some triggering mechanism(s), the other views warm (and cold) events as the inevitable consequence of a systematic preconditioning process, and part of an ongoing, self-sustaining cycle. Of course, there is the possibility that both viewpoints are partially correct. A

ORSTOM
CENTRE DOCUMENTATION
Montpellier

F 30224

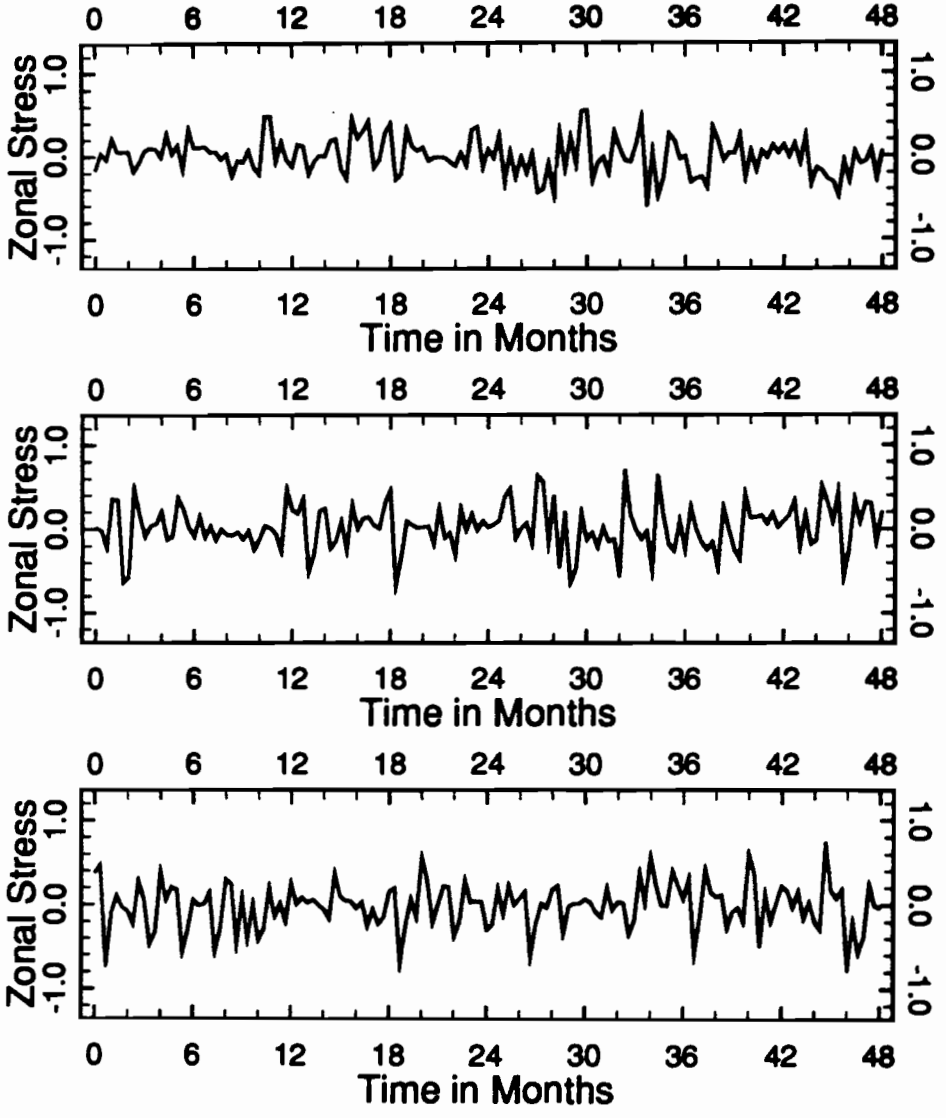

Fig. 1. Three 48-month realizations of the stochastic ISV model defined by Eq. (1).

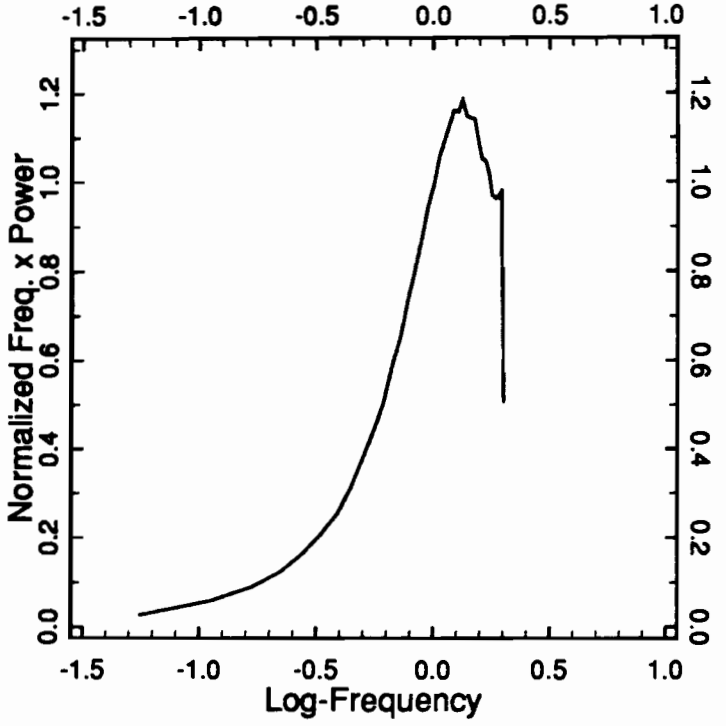

Fig. 2. Spectrum of model ISV. Abscissa has been scaled so that zero represents a 40-day period (logarithms are in base 10).

deterministic, but chaotic, ENSO cycle likely would be characterized by periods of lesser and greater susceptibility to various external forcing factors, including ISV. Even if this forcing were not usually sufficient to disrupt the cycle, at particular times or in extreme instances it might well do so. It is the purpose of this paper to determine which of these scenarios obtains in the context of the ZC model.

2. A Model of Intraseasonal Forcing

Intraseasonal variability appears naturally in atmospheric models with time-dependent dynamics, and reasonable representations of convective heating (e.g., Lau and Lau,1986; Chang and Lim,1988; Hendon,1988; Sui and Lau,1989). It does not occur in the simpler, steady-state models such as that of ZC. Thus, for the present purposes it is necessary to specify the intraseasonal variability in some fashion. To do this, several observational results are utilized: (i) the low-level wind signal is dominantly zonal in the equatorial region, (ii) the 30-60 day period band contains most of the power, and (iii) the disturbances are energetic in the west Pacific, but weaker (at the surface) in the eastern Pacific. In the model to be constructed here the spatial structure of the imposed anomalies is fixed in time, and positioned in the western Pacific at the equator. The eastward propagation aspect is not included as it is considered relatively unimportant in terms of the ocean response (especially the remote response to the east of the forcing region). Specifically, the following form is chosen for fluctuations in zonal wind stress:

$$\tau^{(x)}(t) = A\Big[R(t) + 2R(t-\Delta t) + R(t-2\Delta t)\Big]\ \cos(\omega_0 t + t_0)\ \exp\left[\frac{y}{10^\circ}\right]^2 \exp\left[\frac{x-x_0}{30^\circ}\right]^2, \qquad (1)$$

where R is a normal random variable with zero mean and unit variance, and t_0 represents a uniform random variable on $(0,2\pi)$. This forcing is evaluated at time intervals of Δt, which for the ZC model is 10 days. The parameters ω_0 and x_0 were taken to be $2\pi/40 days$ and $146^\circ E$, respectively, and the amplitude A was set at $.015\ N/m^2$.

Fig. 1 shows three 48-month realizations of this forcing function. Anomalies as large as the climatological mean stress (about $.05\ N/m^2$) occur frequently; the model forcing is at least as strong, and probably stronger, than what is observed (Madden, personal communication). A spectrum of the forcing (Fig. 2) shows that, like the real ISV, most of the total power resides in the 20-60 day band. Subsequent coupled model runs incorporate this forcing with one exception: the amplitude A is reduced during simulated warm episodes. We reduce A in proportion to $(\text{NINO3})^{1/2}$ for NINO3 >1, where NINO3 is the area averaged SST anomalies for the region $(90^\circ W - 150^\circ W, 5^\circ S - 5^\circ N)$. The rationale behind this is that convective activity is generally observed to decrease in the west Pacific during El Niño events. The reduction in model forcing is modest (always less than a factor of two), so that the simulated ISV is still energetic by observed standards.

3. Model Simulations/Forecasts with Imposed ISV

Two 1000-year simulations were done, one with and one without ISV forcing, for the standard physics case as described in ZC. Such a lengthy simulation reveals a wide range of behavior in the unperturbed coupled model (Fig. 3), including periods of large, regular warm events, periods of more irregular cycles, and even periods of almost no variability. How much can a powerful ISV forcing alter this pattern? Given this range of behavior in the basic model, it is perhaps not surprising to find that there is little effect (Fig. 4). The favored 4 year period, and transitions between regimes of larger and smaller amplitude variability all occur analogously. A more quantitative comparison is shown in Fig. 5. The two time series were divided into segments of 24 years duration, Fourier analyzed (with a Welch window applied to minimize aliasing effects), and then averaged to form a mean spectrum. The two spectra are nearly identical; only

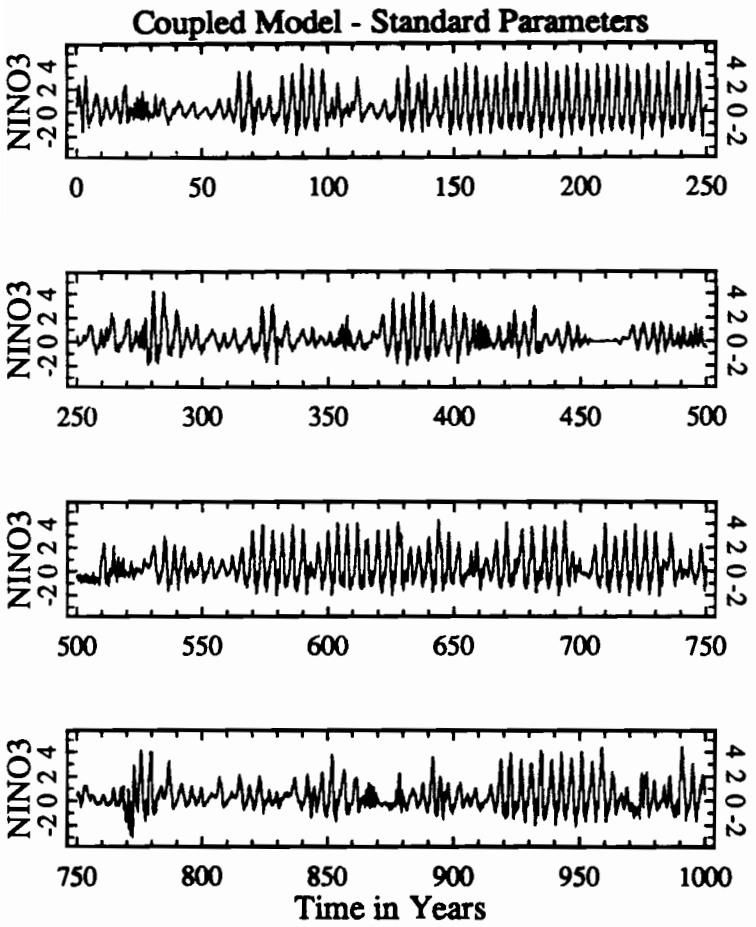

Fig. 3. NINO3 index from a 1000-year run of the coupled model with no ISV forcing.

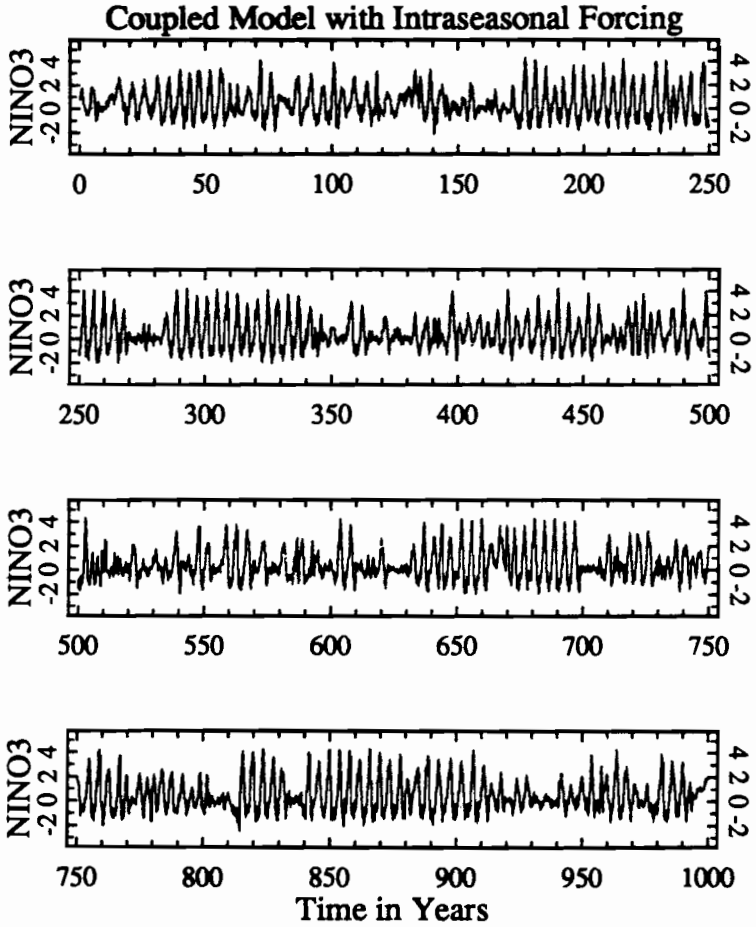

Fig. 4. As Fig. 3, except with added ISV forcing.

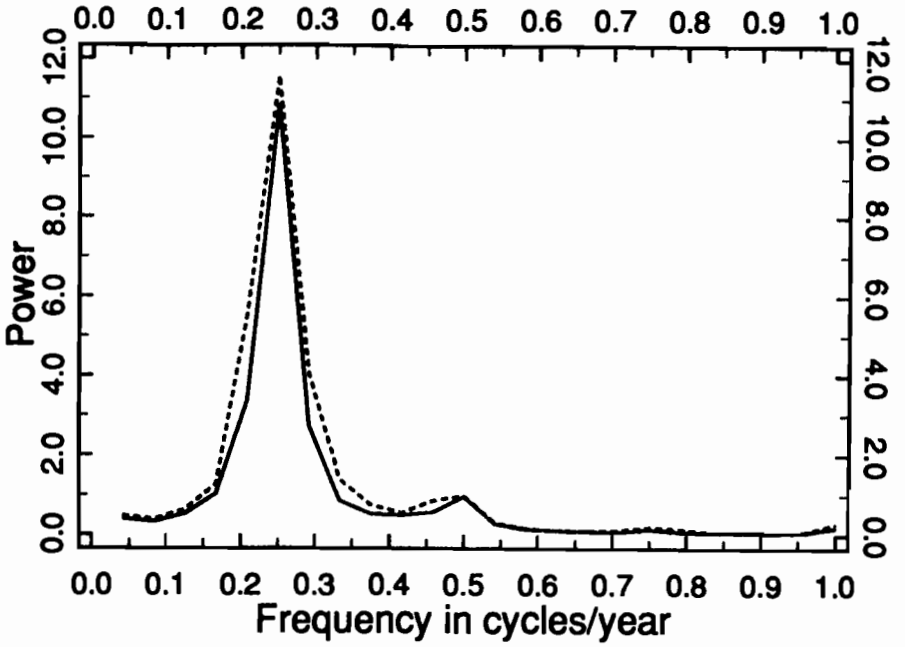

Fig. 5. Spectra of the time series in Figs. 3 and 4, for the period range 1-24 years.

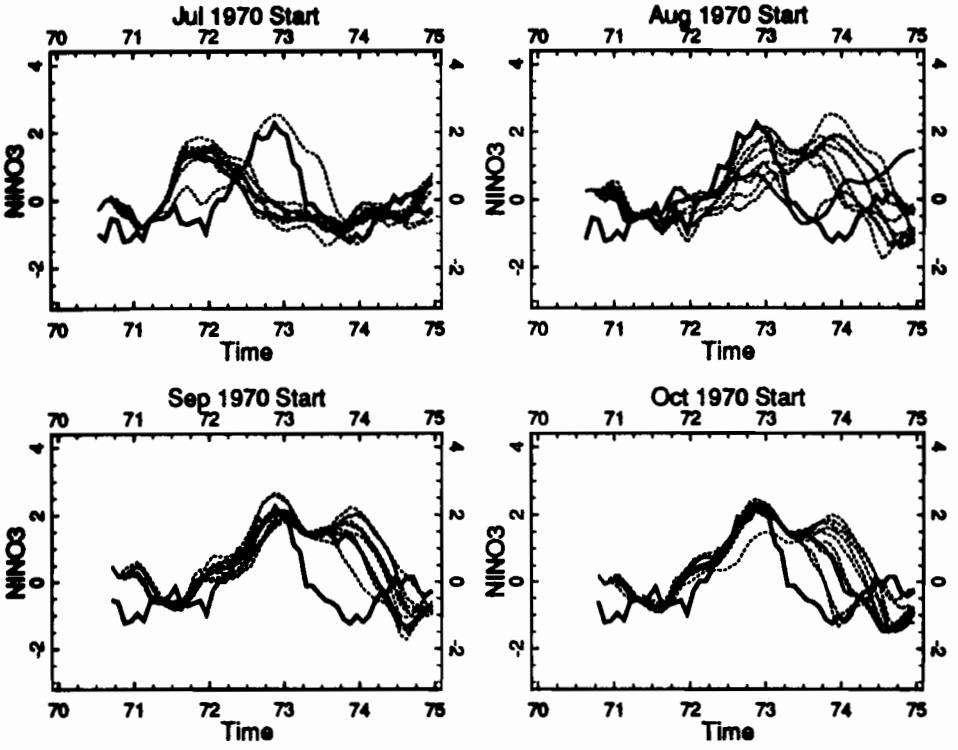

Fig. 6. Observed NINO3 (heavy solid line), and forecasts of NINO3 made with the coupled model alone (light solid line) and with added ISV forcing (dashed lines), starting from July 1970 through October 1970.

a minute spreading about the central period of four years is detectable in the ISV-forced case.

Previously, we have used the ZC model to make predictions of tropical Pacific SST during the period 1970 to 1988. (The experimental forecast procedure is described in detail in Cane et al., 1986.) Forecasts were made starting from each month of the period, with the initial conditions determined as follows: a detrended and smoothed version of the FSU pseudo-stress fields (Goldenberg and O'Brien, 1981) was used as a forcing for the ocean component of the coupled model. The result is a sequence of simulated ocean states for the entire period (mid-1960's to the present). The SST from this simulation was then used as a forcing for the atmospheric component, resulting in a corresponding sequence of simulated atmospheric states for the same period consistent with the coupled model physics.

The fact that ISV has little effect on the overall statistics of the coupled model does not guarantee that it is unimportant for prediction purposes. Indeed, some have speculated that ISV is a major factor in the onset or termination of warm events. To test this, all of the previous forecasts were rerun with 9 separate realizations of ISV forcing. A small but representative sample of the results is shown in Figs. 6-9. The NINO3 index from the original forecasts (no ISV), from each of the perturbed forecasts, and from observations is presented for sequences originating in four consecutive months.

The July-October 1970 sequence (Fig. 6) represents a transitional time between incorrect and correct predictions of the 1971-1972 period in the unperturbed forecasts. All but one of the perturbed forecasts from July follow the original in producing a warming in 1971, and moreover all from August follow the original in producing no warming in that year, despite rapid spreading thereafter. Another period showing large month-to-month differences in the original forecasts is September-December 1975 (Fig. 7). Once again, it is evident that the entire envelope of ISV forecasts is tending to follow the unperturbed ones, with apparently greater spreading at times when the month-to-month stability of unperturbed forecasts is small. In contrast to other times, the 1977-1978 period is remarkable in that almost none of the original forecasts produced any warm events over a three year period. The addition of ISV for February-May 1978 (Fig. 8) hardly alters this pattern at all, resulting in only a weak warming in the third year or beyond in about 10% of the cases. If anything, the periods just prior to or during warm events are even more stable with respect to ISV forcing. A typical example is September-December 1986 (Fig. 9), where the envelopes tightly bracket the original forecasts throughout the extended warm episode, and subsequent cooling in 1988.

The picture emerging from these results is that ISV forcing can be important at particular times, but that on average, it does little to alter the evolution as predetermined by the initial conditions. In fact, the sensitivity to consecutive monthly changes in initial conditions appears greater than that associated with ISV. This can be quantified by a calculation in the spirit of predictability studies.

The usual predictability experiment consists of a series of model integrations with small changes in initial conditions. A measure of predictability is obtained from calculating the spread among individual "predictions", compared with the expected differences among randomly chosen states of the model or observed variables. While the theoretical limit of predictability is a function of the governing physics alone, an analogous predictability can be defined on the basis of any method of perturbing the system, whether it be in the initial conditions, or some external forcing. In this case, the rate at which the envelope spreads is a function not only of the model physics, but also the form and size of perturbations. The rate of spreading provides a means for evaluating the dynamical significance of a particular type of initial condition perturbation or external forcing. For example, if perturbations to which the system is very insensitive are introduced, the rate of spreading will approach the theoretical one - only model physics matter. On the other hand, if sizeable or otherwise dynamically significant perturbations are introduced, the rate of spreading

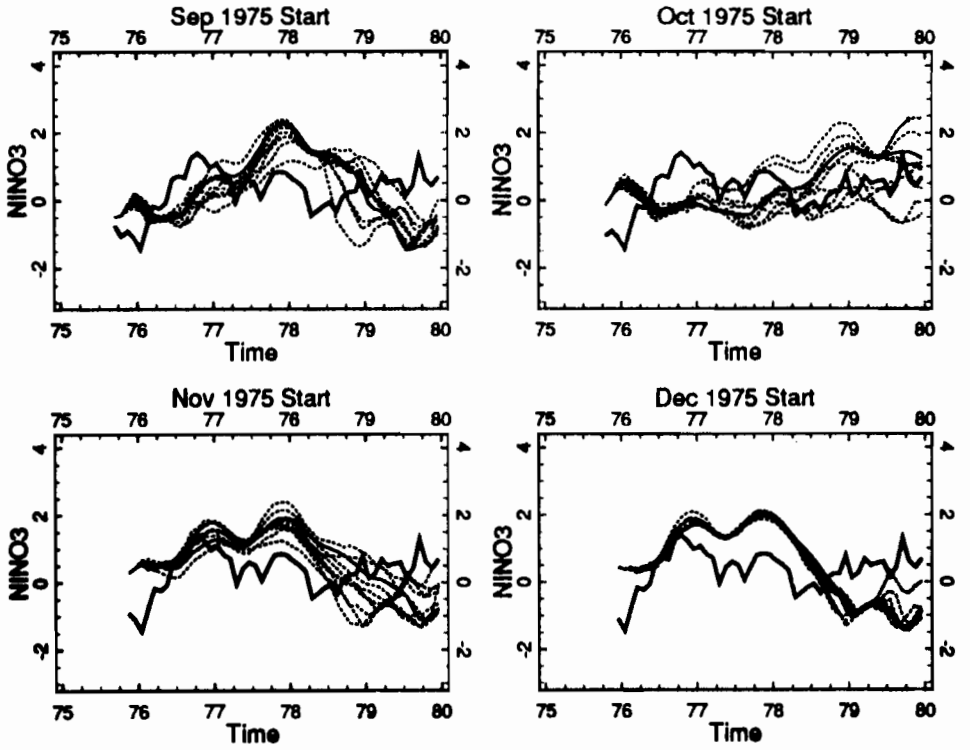

Fig. 7. As Fig. 6, except for September 1975 through December 1975.

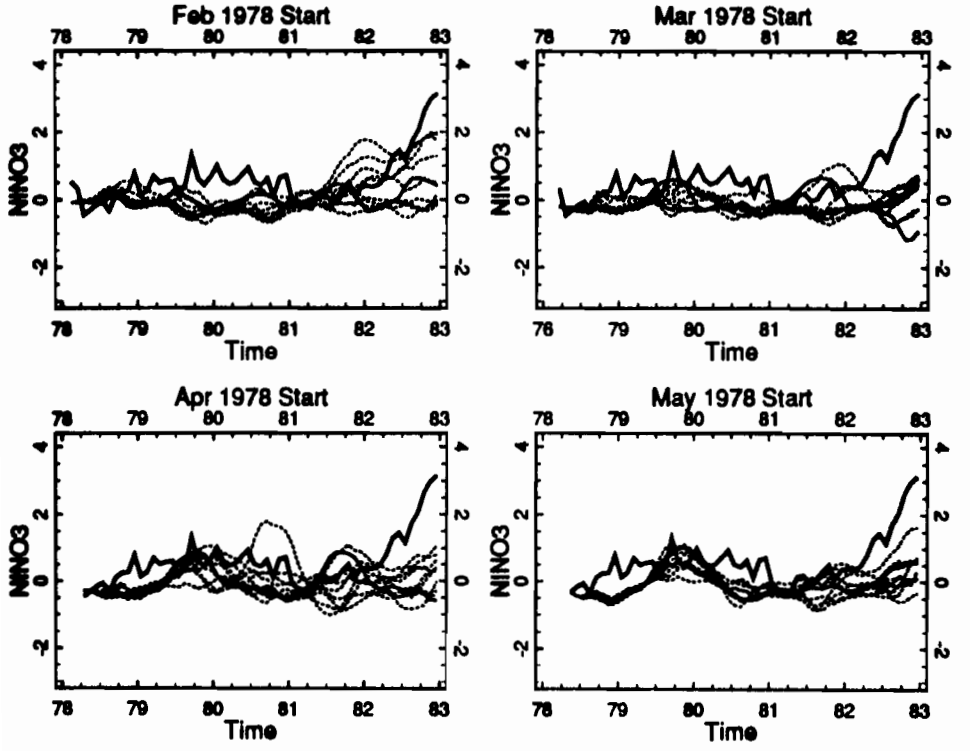

Fig. 8. As Fig. 6, except for February 1978 through May 1978.

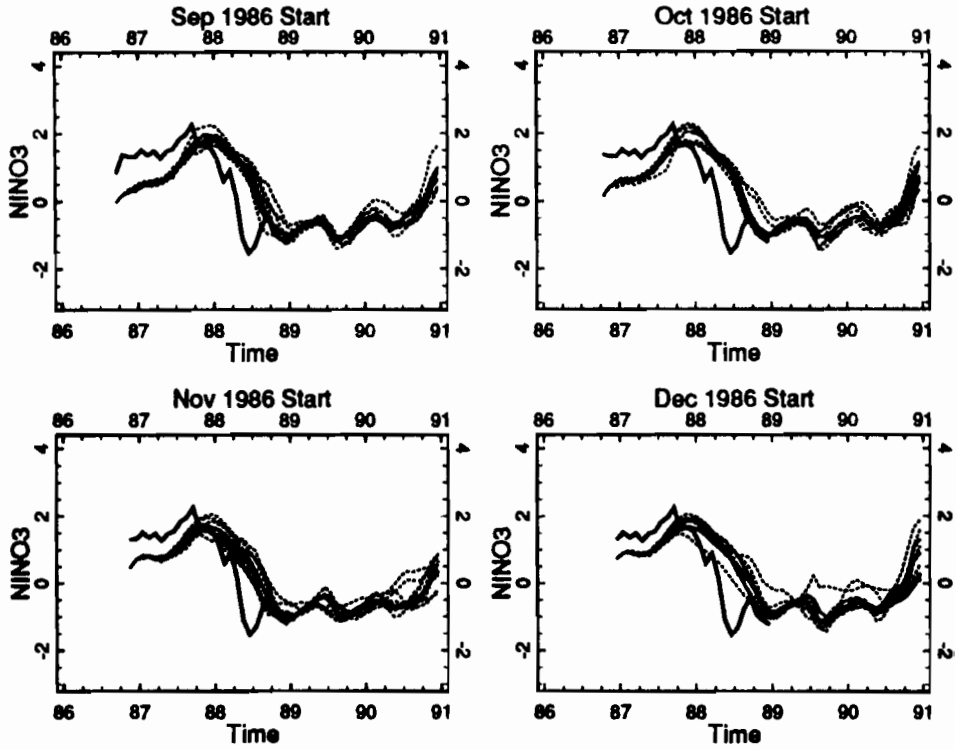

Fig. 9. As Fig. 6, except for September 1986 through December 1986.

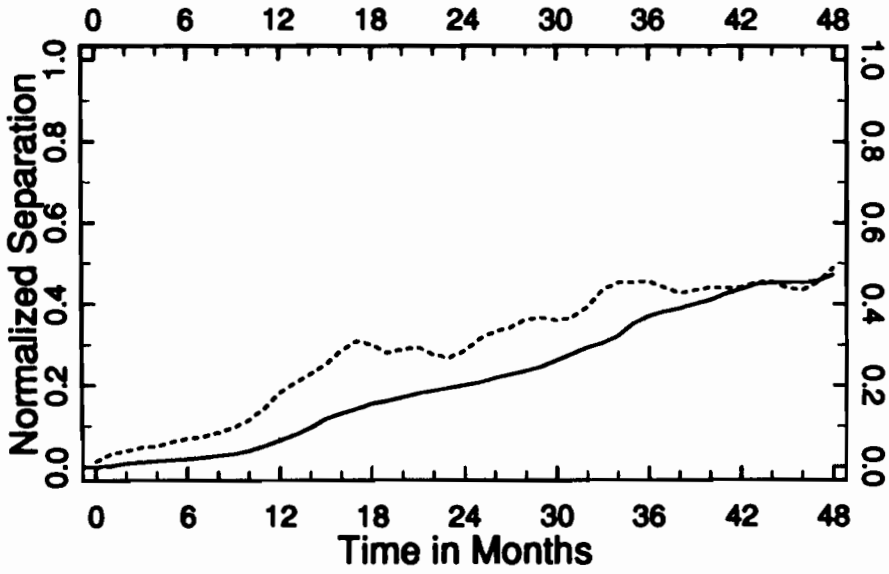

Fig. 10. Root mean square separation among all pairs of forecasts starting from the same initial conditions, but with different realizations of ISV (dashed line), compared with the same quantity computed from pairs of forecasts without ISV beginning one month apart (solid line).

will be much larger, and the predictability limit will be reached sooner.

For the present purposes we wish to compare the spreading rates associated with ISV forcing and one-month differences in start time. The former is determined by computing the mean square difference among all pairs of forecasts starting from the same initial conditions, but with different realizations of intraseasonal forcing. Similarly, the latter is determined from the mean square difference between forecasts starting one month apart, and with no ISV (only the overlapping time period enters for this calculation). Both are shown in Fig. 10. The results confirm what was suggested in the sets of individual forecasts: the ISV forcing has less overall effect on the forecasts than does moving the start time by one month.

4. Discussion

The question of intraseasonal variability and its impact on ENSO has been addressed in the context of the Zebiak and Cane (1987) coupled model and an idealized representation of ISV. From several different analyses, the results are unambiguous: ISV has only a marginal effect on ENSO. Lengthy integrations of the model with and without ISV yield nearly identical statistics. The majority of individual forecast experiments show little spreading over a two year period as a result of this forcing. Predictability calculations show that, even relative to the differences among forecasts starting one month apart, the ISV influence is small. (The comparison with forecasts starting two months or more apart is more dramatic.)

It is worth noting that the initial conditions in our forecast experiments are generated with a filtered (and detrended) version of the FSU pseudo-stress fields. This involves a temporal 1-2-1 smoothing of monthly averages, and therefore has nearly all intraseasonal variability removed. Thus the changes in initial conditions from month to month in the forecasts do not simply reflect ISV, but rather reflect somewhat lower frequency wind changes at varying preceeding times depending on position. The results show that the sensitivity to these lower frequency components of the wind field (whether real or spurious) supersedes the effects of ISV.

Despite the consistency of the results, conclusions should be considered tentative for two reasons. Our ISV model, though motivated by observations, is highly idealized in many respects and may not represent the real phenomenon faithfully. Also, the ZC model has systematic biases, and quite possibly is overly insensitive to the imposed west Pacific forcing. Both of these potential problems in principle can be reduced with better or more complete models. Awaiting such further studies, the present results can be regarded as suggestive of a secondary role for ISV in relation to ENSO.

Finally, it is interesting to consider the relatively infrequent periods where the imposed intraseasonal forcing *did* have an important effect on forecasts. This leads to question: what characteristics of the coupled system determine whether or not the future is well determined? Is there some feature symptomatic of an uncertain future evolution, beyond our imperfect knowledge of the state of the system at any given time? In general, can we know when predictability is more and less limited? It seems certain that a careful study of these issues will give new insight into the model dynamics, but may also contribute to a better understanding of the real climate system.

ACKNOWLEDGMENTS

This work was supported by the National Science Foundation under grant ATM-8612570, and by NOAA under grant NA-84-AA-D-00031. Computations were carried out at the John Von Neumann National Supercomputer Center under award NAC 401.

REFERENCES

Cadet, D. L., and S. Greco, 1987: Water vapor transport over the Indian Ocean during the 1979 summer monsoon. Part I: Water vapor fluxes. *Mon. Wea. Rev.*, **115**, 653-663

Cane, M.,A., S. E. Zebiak, and S. C. Dolan, 1986: Experimental forecasts of El Niño. *Nature*, **321**, 827-832

Chang, C. P., and H. Lim, 1988: Kelvin wave-CISK: a possible mechanism for the 30-50 day oscillations. *J. Atmos. Sci.*, **45**, 1709-1720

Chen, T.-C., and M. Murakami, 1988: The 30-50 day variation of convective activity over the western Pacific Ocean. *Mon. Wea. Rev.*, **116**, 892-906

Chen, T.-C., M.-C. Yen and M. Murakami, 1988: Water vapor transport associated with the 30-50 day oscillation over the Asian monsoon regions during 1979 summer. *Mon. Wea. Rev.*, **116**, 1983-2002

Goldenberg, S. B., and J. J. O'Brien, 1981: Time and space variability of tropical Pacific wind stress. *Mon. Wea. Rev.*, **109**, 1190-1207

Hendon, H. H., 1988: A simple model of the 40-50 day oscillation. *J. Atmos. Sci.*, **45**, 569-584

Knutson, T. R., and K. M. Weickmann, 1987: 30-60 day atmospheric oscillations: composite life cycles of convection and circulation anomalies. *Mon. Wea. Rev.*, **115**, 1407-1436

Krishnamurti, T. N., and D. Subrahmanyam, 1982: The 30-50 day mode at 850 mb during MONEX. *J. Atmos. Sci.*, **39**, 2088-2095

Lau, K. M., and P. H. Chan, 1985: Elements of a stochastic dynamical theory of the long-term variability of the El Niño/Southern Oscillation. *J. Atmos. Sci.*, **42**, 1552-1558

Lau, K. M., and P. H. Chan, 1986a: Aspects of the 40-50 day oscillation during the northern summer as inferred from outgoing longwave radiation. *Mon. Wea. Rev.*, **114**, 1354-1367

Lau, K. M., and P. H. Chan, 1986b: The 40-50 day oscillation and ENSO: a new perspective. *Bull. Amer. Meteor. Soc.*, **67**, 533-534

Lau, K. M., and P. H. Chan, 1988: Interannual and intraseasonal variations of tropical convection: a possible link between the 40-day mode and ENSO? *J. Atmos. Sci.*, **45**, 506-521

Lau, K. M., L. Peng, C. H. Sui, and T. Nakazawa, 1989: Dynamics of super cloud clusters, westerly wind bursts, 30-60 day oscillations and ENSO: an unified view. *Japan Meteor. Soc.*

Lau, N. C., and K. M. Lau, 1986: Structure and propagation of intraseasonal oscillations appearing in a GFDL GCM. *J. Atmos. Sci.*, **43**, 2023-2047

Luther, D. S., D. E. Harrison, and R. A. Knox, 1983: Zonal winds in the central equatorial Pacific and El Niño. *Science*, **222**, 327-330

Madden, R. A., and P. R. Julian, 1971: Detection of a 40-50 day oscillation in the tropics. *J. Atmos. Sci.*, **28**, 702-708

Madden, R. A., and P. R. Julian, 1972: Description of global-scale circulation cells in the tropics with a 40-50 day period. *J. Atmos. Sci.*, **29**, 1109-1123

Murakami, M., T. Nakazawa, and J. He, 1984: On the 40-50 day oscillation during the 1979 Northern Hemisphere summer. Part II: heat and moisture budget. *Japan Meteor. Soc.*, **62**, 469-484

Murakami, M., L.-X. Chen, and A. Xie, 1986: Relationship among seasonal cycles, low-frequency oscillation, and transient disturbances as revealed from outgoing longwave radiation data. *Mon. Wea. Rev.*, **114**, 1450-1465

Sui, C.-H., and K. M. Lau, 1989: Origin of low-frequency (intraseasonal) oscillations in the tropical atmosphere. Part II: effect of an improved treatment of moist processes. *J. Atmos. Sci.*

Zebiak, S. E., and M. A. Cane, 1987: A Model El Niño/Southern Oscillation. *Mon. Wea. Rev.* **115**, 2262-2278

Behavior of Convective Activity over the "Jovian-type" Aqua-Planet Experiments

Akimasa SUMI

University of Tokyo
Geophysical Institute, Faculty of Sciences,
Bunkyo, Tokyo 113 - Japan

1. Introduction

Condensation heat released in the cumulonimbus over the tropics is one of the major driving force for the atmospheric general circulation. As the ocean circulation is also driven by the wind field, its role is very important for climate dynamics. Then, it becomes necessary to understand how convection will distribute under the given boundary condition.

However, there are so many factors to determine the convective activities over the tropics, such as Sea Surface Temperature (SST), stability, land surface condition and land-ocean contrast. Then, it is very difficult to clarify the mechanism by conducting usual numerical experiments (so called twin experiments). Therefore, we are planning to conduct a series of numerical experiments where a simplified boundary condition is used to investigate the distributions of convective activity corresponding to the given boundary conditions (see Table 1).

Table 1: A series of numerical experiments.

	No-int.	Int.	
Aqua-Planet type	x	?	a free mode type response
Desert-Planet type	planning	planning	
Monsoon type	x	on-going	a forced mode type response

There are two type of mechanism to determine the distribution of convection: a free mode type mechanism and a forced mode type mechanism. A free mode type mechanism is the way where the distribution of convection is determined by the internal dynamics of moist atmosphere. On the contrary, a forced type mechanism is the way where it is determined by the physics related to the boundary forcing.

An example of a free mode type response is the Aqua-Planet type experiments as conducted by Hayashi and Sumi (1986). Its purpose is to understand the characteristics of free mode of convection activity distribution. An example of a forced mode type mechanism is the Monsoon type experiment conducted by Sumi (1987). He showed that it exists a specific distribution associated with desert-like land and ocean contrast.

Even for the distribution of convective activities over the Aqua-Planet experiments there may be possible several patterns. Sumi (1989) showed the possible patterns corresponding to the SST distribution (see, Fig. 1). As numerical experiments in the extreme case where there exists the north-south SST gradient (denoted as "Earth-type" Aqua-Planet) has been

ORSTOM
CENTRE DOCUMENTATION
Montpellier

F 30225

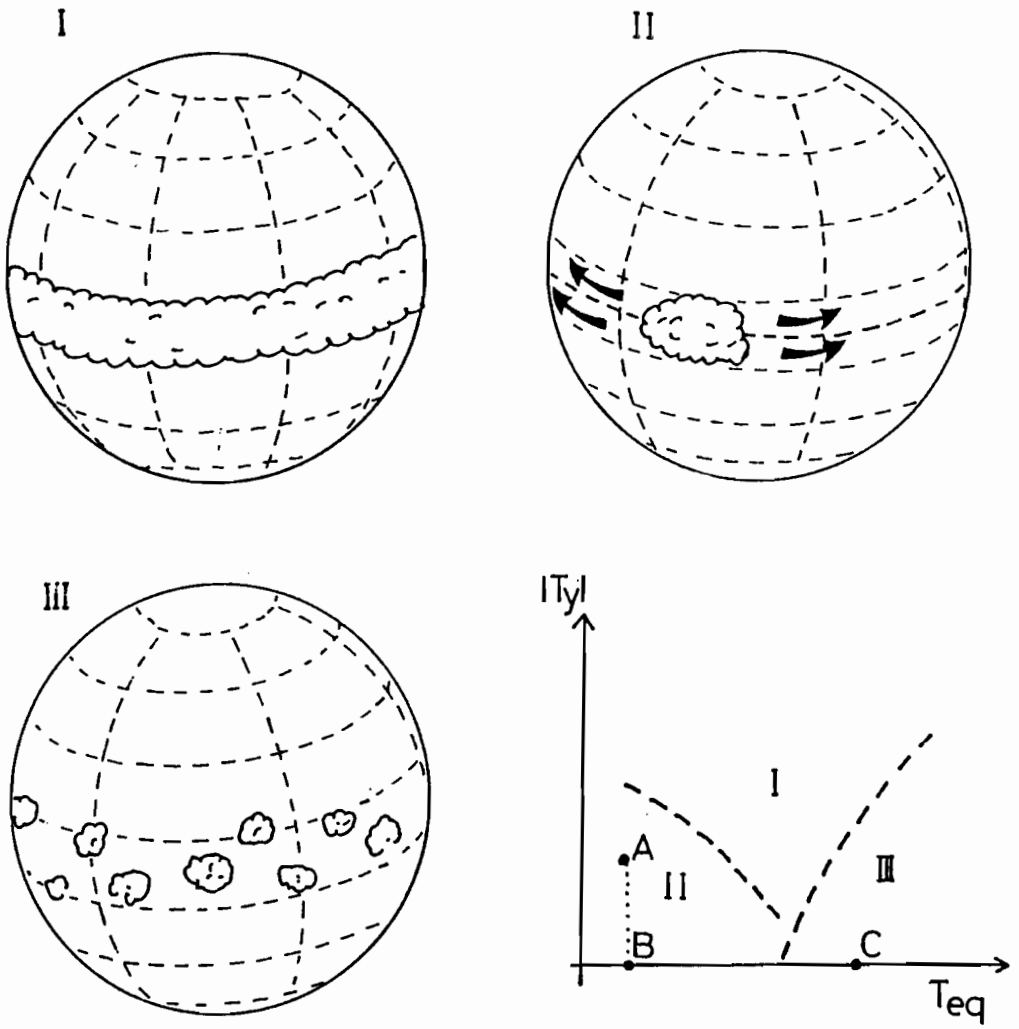

FIG.1. Schematic diagram of various pattern of convection over the "Aqua-Planet". Ordinate is the meridional gradient of SST, and abscissa denotes the magnitude of SST at the equator. A represents the condition of Hayashi and Sumi (1986), and B and C is corresponding to the case described in this paper. Case I represents the zonal distribution of convection over the warmest SST. Case II represents the case where there exists some organization and each cell is propagation eastward or westward. Case III represents the case where convection distributes randomly.

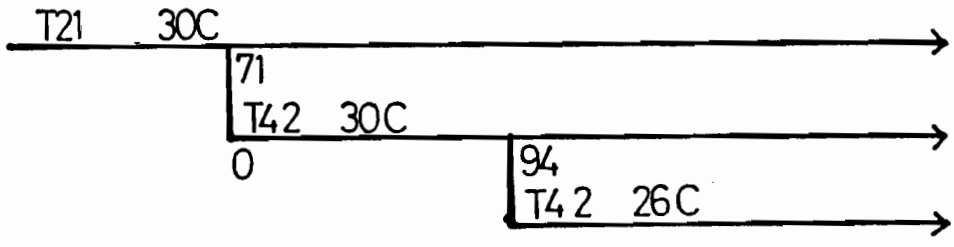

FIG.2. Experimental procedure.

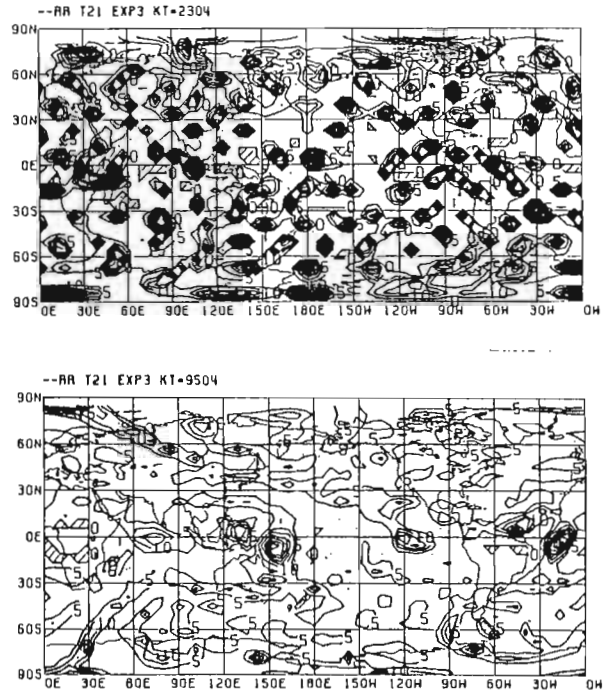

FIG.3. Daily precipitation due to the T21-model. Top is day 25 and bottom is day 325. Unit is mm.(2days)$^{-1}$.

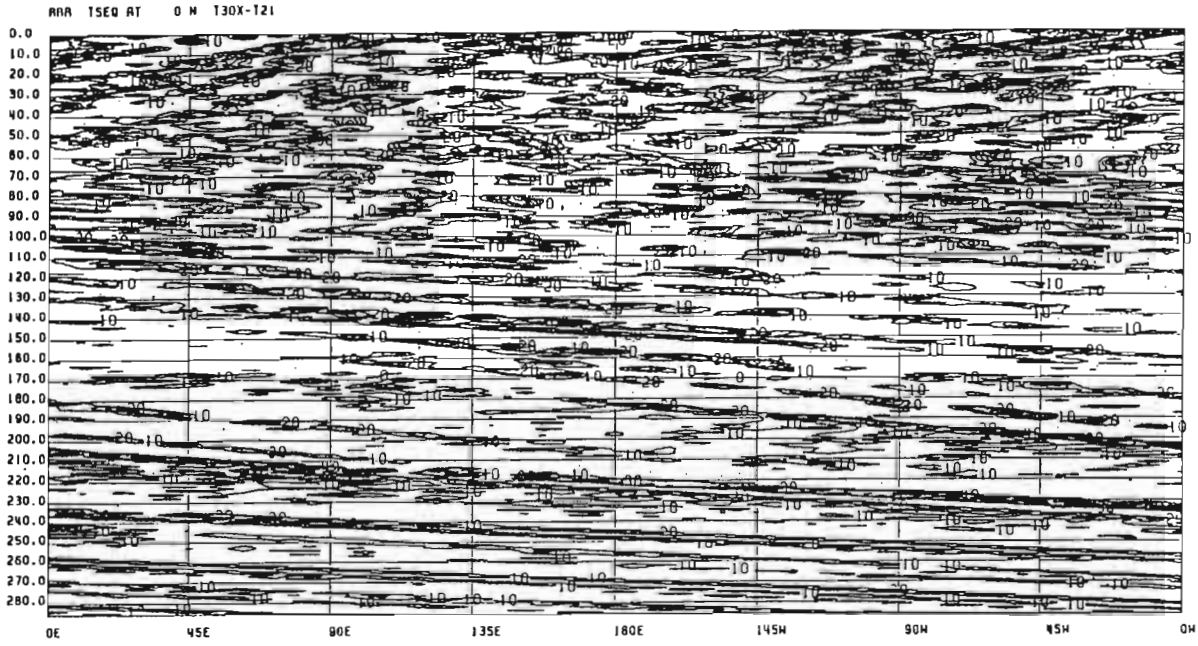

FIG.4. Zonal-time cross-section of daily precipitation on the equator (2.5°N - 2.5°S).

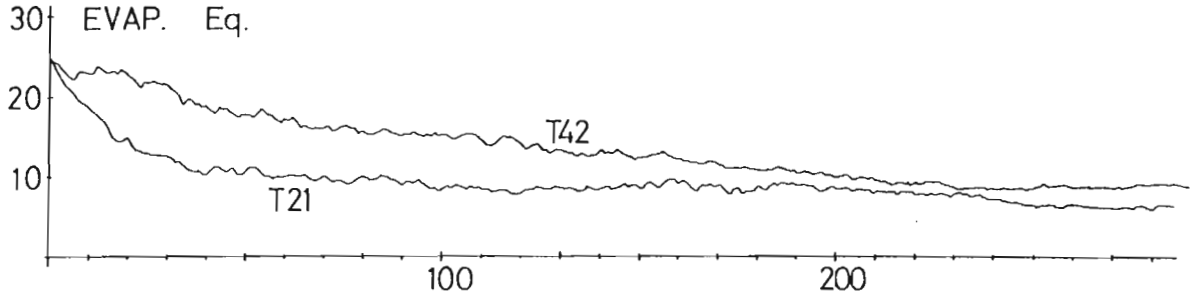

FIG.5. Zonally averaged evaporation for T21-case and T42-case. Unit is 10 W.m^{-2}.

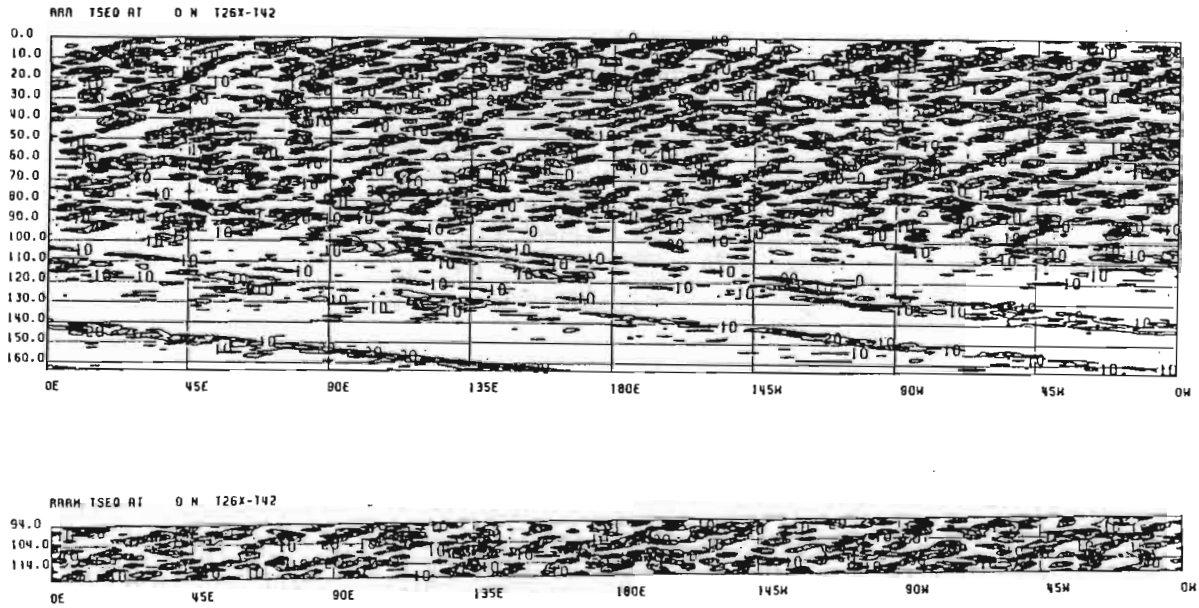

FIG.6. (Top) Same as Fig.4, except for the condition where SST was suddenly decreased from 30°C to 26°C at day 94. (Bottom) Same as above, except that drag coefficients are 10 times multiplied.

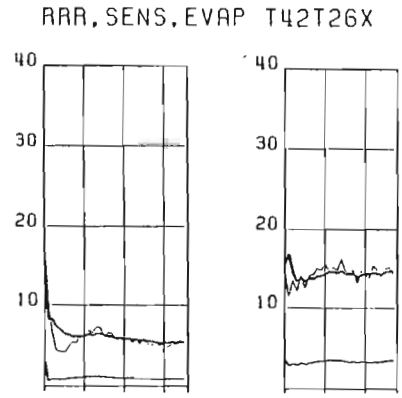

FIG.7. Zonally averaged evaporation rate (thick line). Unit is 10 W.m^{-2}. LEFT is corresponding to the case of 26°C, and RIGHT is corresponding to the case where drag coefficient is multiplied 10 times.

conducted by Hayashi and Sumi (1986), results corresponding to the other extreme where there is no north-south SST gradient (denoted as "Jovian-Type" Aqua-Planet) will be presented in this paper.

2. Experimental Procedure

The experimental procedure is the following:

1) Model is Community Climate Model (Global spectral model) of the University of Tokyo, where the low resolution version (T21) and the high-resolution version (T42) are used.

2) Vertical resolution is 12 levels.

3) Radiational process is simplified. Uniform cooling is assumed to compensate the globally averaged heating at each level. That is, global averaged vertical temperature profile is assumed to be constant.

4) SST is assumed to be 30°C. Later, 26°C experiment has been conducted.

5) Initial state is the zonally and north-south averaged state of analysis of a certain day, and 400 day time integration was conducted by using T21-model. To eliminate the influence of the initial state, day 71 is designated as day 0. T42-model was integrated from day 0 and 26°C experiment was done from day 94 by using T42-model (see, Fig.2). It should be noted that the integration was started from almost April condition.

6) Other physical processes except for radiational process are the same as those in the previous experiments (Hayashi and Sumi, 1986; Sumi, 1987).

3. Results

Results are presented in this section. In Fig. 3, daily rainfall simulated by T21-model at day 25 (top) and day 325 (bottom) are displayed. Apparently, it is clear that the randomly distributed convective activity at the early stage of time integration has been organized to be a few localized convective activities. This change is also noted in the zonal-time cross-section of the daily rainfall on the equator (fig. 4). At the early stage, each convective cell is short-lived, tends to move westward or eastward, and is not well organized. In the later stage, each localized convective cell tends to live longer and finally it starts to propagate eastward; In the last, a few convective cells are selected and they are moving consistently eastward along the equator.

This feature is also noted in the results of the T42-model. However, in this case it took more time to realize this state. In order to investigate this reason, the zonally averaged evaporation rate was checked (see Fig. 5). It was found that evaporation rate had almost the same value for both cases when organization happened (about day 120 for T21 and day 220 for T42). Then, the reason of this may be considered as follows.

1) As long as sufficient moisture is supplied, many convective cells are possible and distributed randomly.

2) However, once moisture supply is below a certain level, a few convective cell is selected. Then, as environmental condition is consistent with movement of a convective cell, it starts to propagate further and further.

In order to confirm the results described above, additional experiments have been conducted, where SST was suddenly changed from 30°C to 26°C at day 94. Results are shown in Fig.6 (top). Immediately after SST decreased, convective cells have been filtered and two cells have started to propagate eastward. In this case phase speed is approximately 8 $m.s^{-1}$. Apparently evaporation has been decreased (see, Fig. 7 (left)).

To maintain the same evaporation rate of 30°C under 26°C condition, another experiment is carried out with drag coefficients multiplied by ten. The results are shown in Fig. 6 (below). In this case almost similar amount of evaporation rate is realized.

Another interesting aspect is the meridional band structure of rainfall. In Fig.7, the zonal

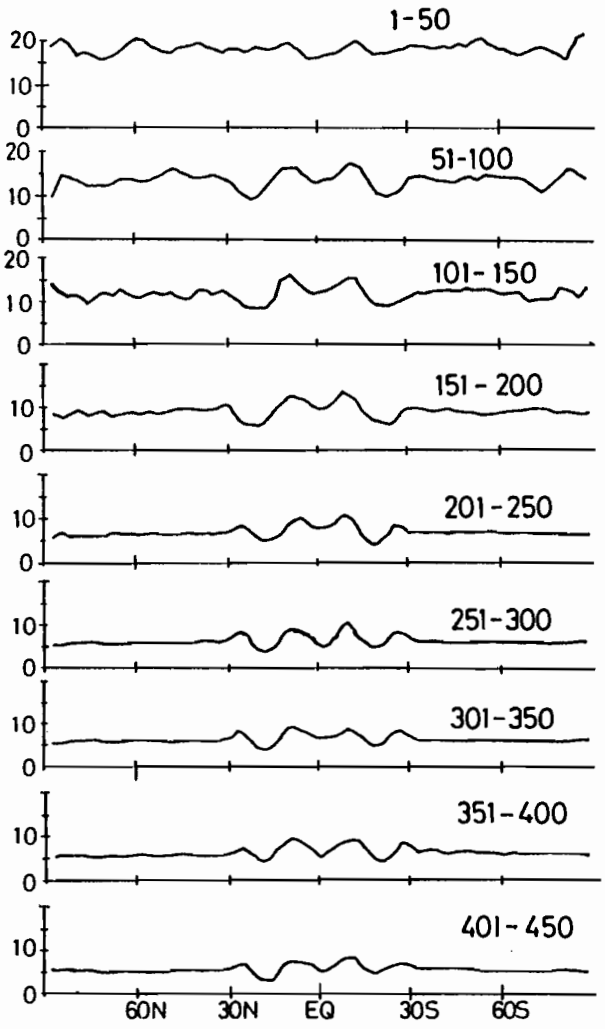

FIG.8. Zonally averaged rainfall in the T42-model.

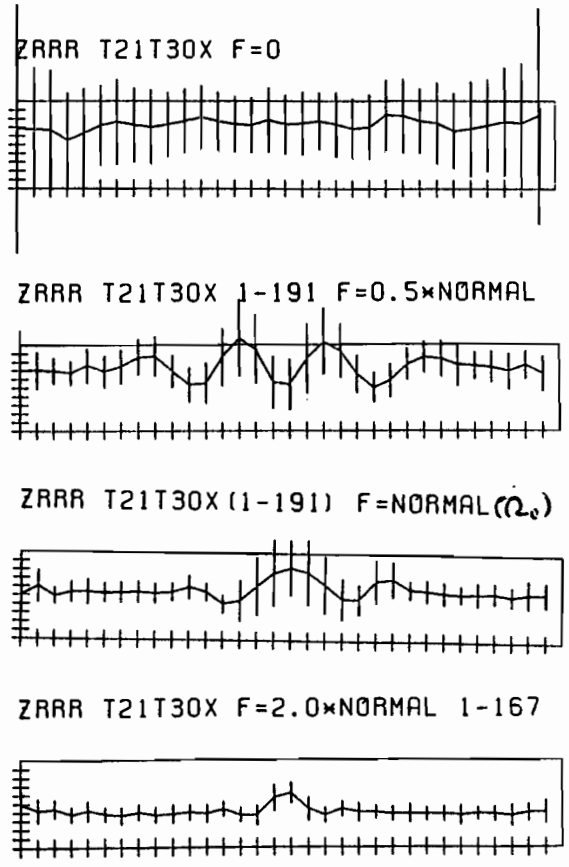

FIG.9. Zonally averaged rainfall corresponding the various Earth rotation rate (Ω_0) is the present Earth rotation rate.

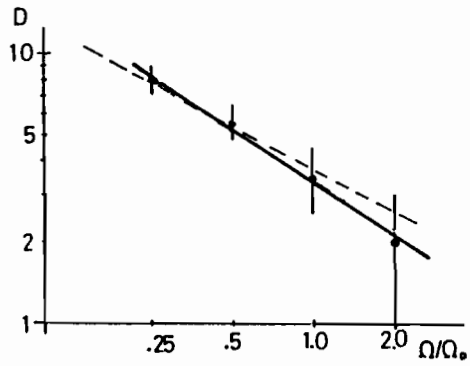

FIG.10. Relation between the location of rainfall minimum and the Earth rotation rate.

averaged rainfall distribution due to T42-model integration is displayed. Maximum symmetric about the equator are noted. However, a single maximum is noted in the T21-model. The reason for this difference is considered as follows:

1) There is a specific pattern of response due to heating in the tropics. However, if meridional resolution is not sufficient, the response in the subtropics cannot be resolved. If sufficient meridional resolution exists, we can resolve this response.

2) However, this does not mean the double ITCZ-like feature is permanent to this condition. It depends on the relative strength between the heating in the subtropics and the heating in the tropics. It is also dependent on the stability of atmosphere and amount of vapour in the atmosphere.

This band structure is supposed to be related to the Earth rotation effect. To investigate this aspect, we have conducted similar experiments where the Earth rotation rate is changed. The zonally averaged and time averaged daily rainfalls are shown in Fig. 9. It is worth noting that as the Earth rotation rate decreases the maximum of rainfall propagates poleward. The relation between the position of rainfall minimum and the rotation rate is supposed to be consistent with the relation as is expected from the formulation of radius deformation in the tropics (see, Fig. 10).

4. Conclusion

The characteristics of distribution of convective activity over the "Aqua-Planet" with the globally uniform SST has been investigated using numerical experiments.

The following conclusions were obtained;

1) As moisture supply decreases below a certain level, convective activity is selected. This filtering occurs only over the tropical area.

2) Convective activity is organized in the zonal-band structure, where its latitude may be related to the Earth rotation effect.

Further experiments will be necessary to obtain a conclusion of the pattern formation of convective activity.

REFERENCE

Hayashi, Y.Y. and A. Sumi, 1986: The 30-40 day oscillations simulated in an "Aqua-Planet" model, *J. Meteor. Soc. Japan*, **64**, 451-467.

Sumi, A., 1987: Characteristics of simulated convective activity over a tropical ocean with zonally uniform SST surrounded by the dry continents, *J. Meteor. Soc. Japan*, **65**, 113-124.

Sumi, A., 1989: Pattern formation of convective activity over the Aqua-Planet with globally uniform Sea Surface Temperature. To be submitted.

Dynamics of Multi-Scale Interactions Relevant to ENSO

Ka-Ming LAU

Laboratory for Atmospheres, NASA/Goddard Space Flight Center
Greenbelt, MD 20771 - U.S.A.

1. Introduction.

This study is an extension of the work of Lau and Peng (1987, hereafter referred to as LP) on the origin of intraseasonal oscillations (ISO, also known as the 30-60 day oscillation) in the tropical atmosphere. In this note we present some preliminary results of numerical experiments focusing on the mechanism of multi-scale interaction, in particular those related to origin of ISO, supercloud cluster (SCC), westerly wind burst (WWB) in the western Pacific region (cf. Nakazawa, 1988; Keen, 1987; Nitta and Motoki, 1988; Lau and Chan, 1988). The relationship between SCC and ISO has been identified previously in Hayashi and Sumi (1986) and LP. Here it will be shown that WWB can be linked to the same family of multi-scale processes that govern SCC and ISO and ENSO over the western Pacific.

2. Model description.

The model used in this study is similar to that used LP - 5 vertical level spectral model with rhomboidal truncation to 15 wavenumbers. A semi-implicit time differencing scheme with Robert-Asselin type averaging is used in the integration. This provides strong damping of gravity waves in the model. The present version includes nonlinearity in the advective terms which are computed on a Gaussian grid at a resolution of approximately 7.5 degree by 4.5 degree. The vertical heating profile used has maximum heating between 500 and 700 mb (see Sui and Lau ,1989, for further details). The atmosphere has no mean motion and the horizontal mean temperatures are given by the observed equatorial zonal mean temperatures, with fixed specific humidity.

3. Mobile wave-CISK modes and SCC.

It is clear from LP and Sui and Lau (1989) that the propagation speed and vertical structure of the 30-60 day oscillation is sensitive to the level of maximum heating in the troposphere. The vertical zonal wind distribution of the mobile wave-CISK mode for different vertical heating distributions is examined in the section. Three cases are considered with a similar heating profile except having.

I Maximum heating near 300 mb,
II Maximum heating between 500 and 700 mb, and
III Heating profile as in Case II and evaporation and sensible heating proportional to the 900 mb wind according to a bulk aerodynamic formulation. All the sensible heating is assumed to be realized in the lowest model layer (1000-900 mb; see Sui and Lau, 1988, for details).

When the heating is concentrated in the upper troposphere (case I, Fig. 1a), the vertical scale of the disturbance is large, the westward tilt with height extend throughout the troposphere. The westerly wind is maximum in the upper troposphere and to the east of the heat source. At the surface, the westerly (Rossby) is slightly stronger than the easterly (Kelvin) inflow towards the heat source. The eastward propagation speed for

ORSTOM
CENTRE DOCUMENTATION
Montpellier

F 30226

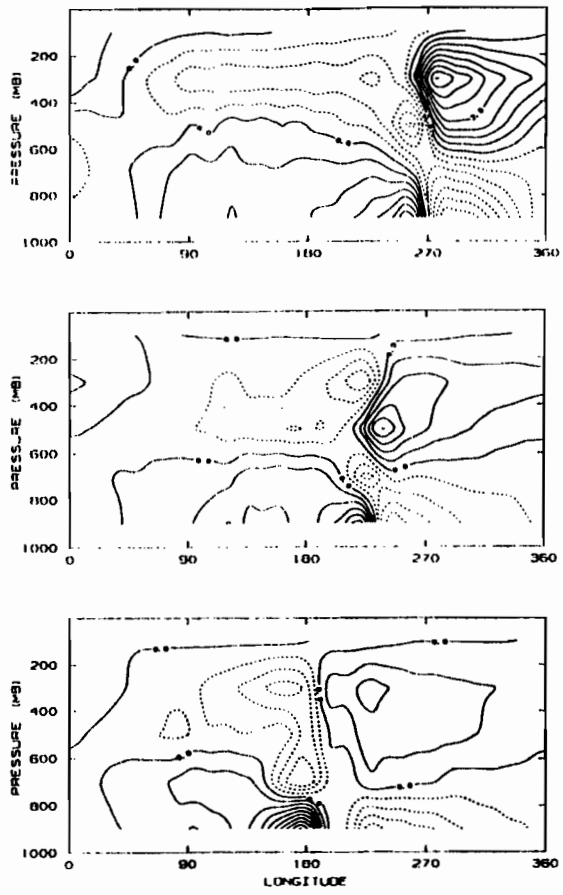

FIG.1. Vertical cross-section of zonal wind mobile wave-CISK mode for different heating profiles. a) maximum heating near 300 mb. b) maximum heating between 500 and 700 mb and c) same as in b) but include surface heating.

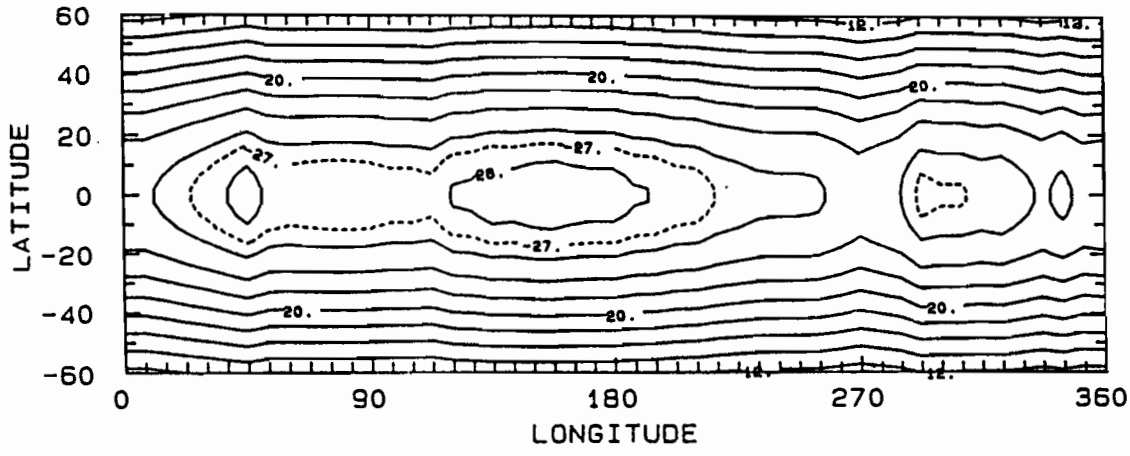

FIG.2. Spatial variation of SST used for the westerly wind burst experiment.

this mode is about 23 ms^{-1} (20 day oscillation). When the heating maximum is between 700 and 500 mb (case II, Fig. 1b,) the vertical scale is reduced and the westward tilt with height is limited to the lower troposphere. At the surface, the westerlies flow is stronger than the easterlies, suggesting the increasing importance of Rossby waves. This mode propagates with an eastward phase speed of about 9 ms^{-1} (50 day oscillation). When latent and sensible heat flux is included, the vertical distribution of the SCC changes drastically (case III, Fig. 1c). First, the vertical phase tilt is reduced and the zonal wind maximum is further away from the convective center. Second, the east-west asymmetry of the surface zonal winds become very pronounced. Strong surface westerlies are found in a shallow layer to the west of the convective center and the easterlies are considerably weaker. The eastward propagation speed is about 13 ms^{-1} (36 day oscillation). Evaporation provided additional source of moisture for deep convection through wave-CISK. More importantly, it appears that sensible heating is responsible for the presence of the shallow layer of westerlies in the wake of the eastward propagating SCC. Thus, low tropospheric heating and in particular, surface heating may be important in leading to an asymmetric low level westerly wind in the model. This may have important implication on the connection between SCC and the westerly wind burst phenomenon in reality.

4. Westerly wind burst experiment

The effect of asymmetric SST and surface heating on the structure and propagation of mobile wave-CISK modes have been examined in detail in Sui and Lau (1988). The following is a discussion of an experiment focusing on the surface wind fluctuation in the model which we tentatively identify with WWB. In the experiment, a bogus low level convergence center is imposed on the equator initially. An eastward propagating precipitation and circulation complex resembling SCC is formed as a result of mobile-wave CISK. The equilibrium SCC structure shown in figure 1c is allowed to propagate through a zonally varying SST distribution as shown in figure 2 which mimics the climatological SST distribution along the equator. Here, the effect of the varying SST is to produce a varying amount moisture available for moist convection through evaporation as well as to provide different amount of surface heating as a function of the air-sea temperature difference and wind. The detailed evolution of the SCC vertical structure and phase speed as a function of the longitude is similar to that shown in Sui and Lau (1988) and will not be repeated here. Only features deemed to be related to SCC and WWB are highlithed in the following.

Figure 3a shows the longitude-time section of precipitation for the first 96 days of the integration. As the SCC (maximum precipitation region) propagates over the warm water, it undergoes vigorous dynamical adjustment because of the changing moisture and stability in the overlying atmosphere. This is manifested in the eastward organization of the SCC by Kelvin waves and the westward propagation of convective elements associated with Rossby waves. The SCC disappears over the eastern Pacific, due to the inhibition of deep convection over the cold water. It revives somewhat over the warm and moist Amazon region, before disappearing over the Atlantic and finally recovered over the Indian Ocean/Western Pacific region. The cycle appears to be repeated indefinitely about every 36 days. Although the SCC appears to turn on and off at different longitudes, it appears to follow more or less the same longitude-time path indicating a somewhat constant underlying phase speed. This is because the large scale zonal winds in the lower troposphere maintained both by convection and surface heating are basically continuous over the entire journey around the equator (Fig. 3b). The wavy appearance of the surface westerlies behind and the relatively steady easterlies ahead of the mobile heat source is quite apparent. It is also noticed that this east-west asymmetry is most pronounced over the warm part of the ocean between 90° and 180° longitude.

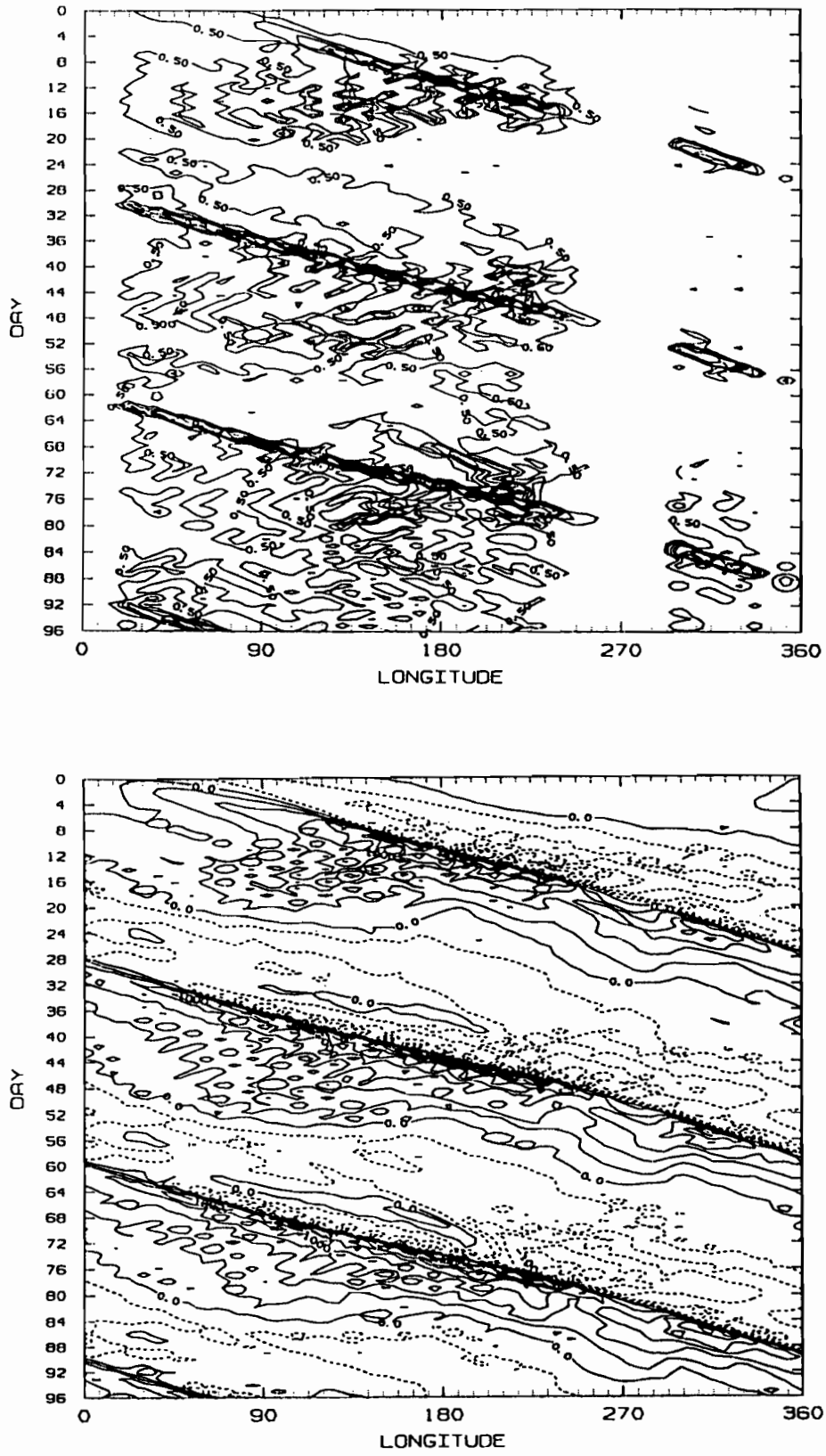

FIG.3. Time-longitude section of (a:top) precipitation (mm.day^{-1}) and (b:bottom) 900 mb wind (ms^{-1}) associated with the model SCC.

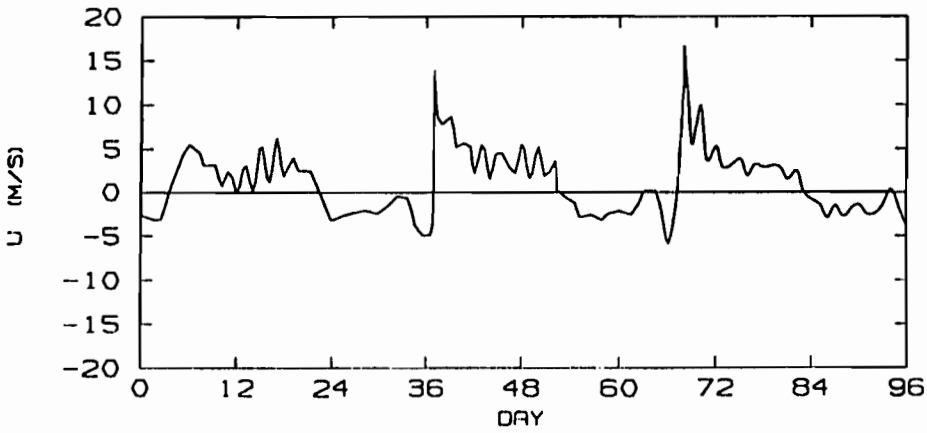

FIG.4. Time series of 900 mb zonal wind at 160°E showing the strong asymmetry between the westerly and the easterly phase of the model 30-60 day oscillation.

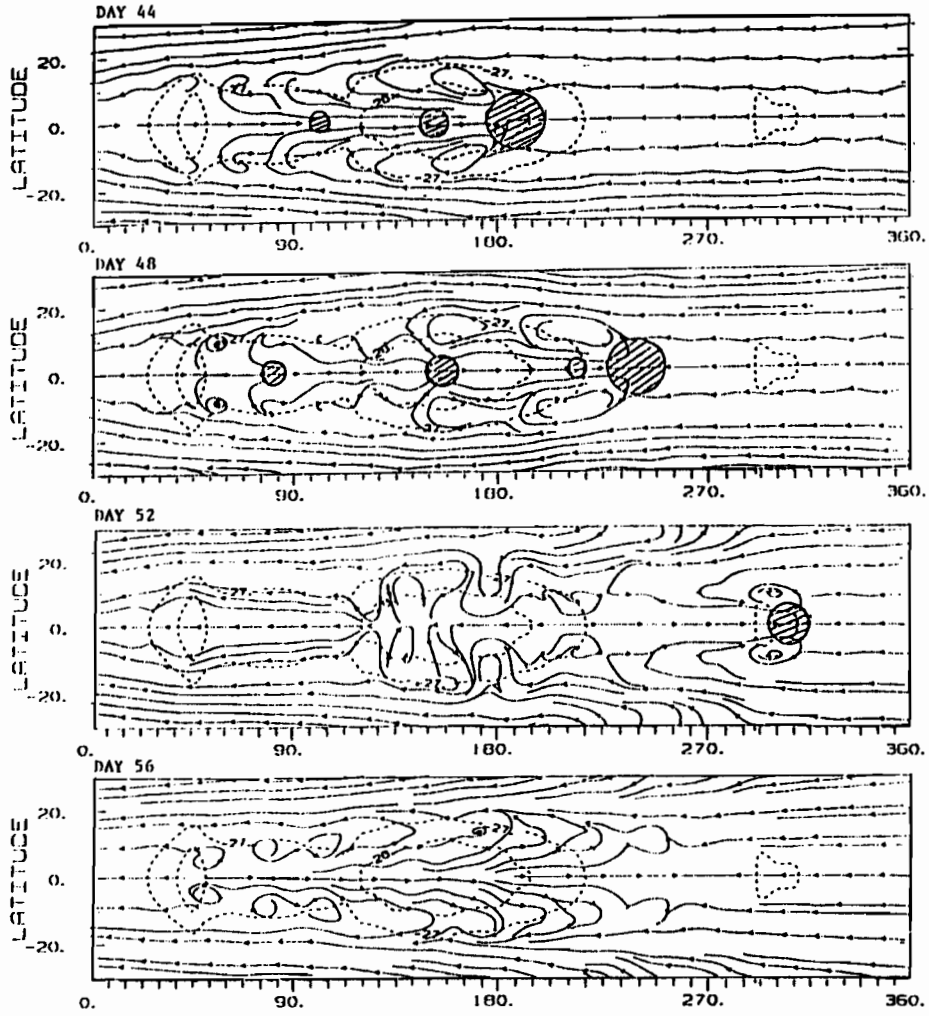

FIG.5. Horizontal distribution of streamline in relation to SCC precipitation centers (hatched circles), and the warm water region (SST >27°C, dotted contour), at selected dates.

Figure 4 shows the time series of 900 mb zonal wind at a fixed point around 160°E. The strong asymmetry and the front-like reversal between the westerly and the easterly component of the zonal wind is clearly seen. The easterly component is quite steady but the westerly component is very spiky and contains many high frequency fluctuations. This is related to the strong east-west asymmetry of the intrinsic structure of the SCC noted in figure 1c and the global picture described in figures 3a and 3b. As the SCC propagates eastward, an observer over the warm ocean will first experience the steady surface easterlies due to Kelvin waves. The passage of the convective center marks the abrupts shift from easterlies to westerlies. This is followed by high frequency zonal wind fluctuation in the westerly phase due to Rossby waves shedded off the main heat source as it propagates further to the east. The above situation is repeated in 36-day cycles in the model. For each cycle, the westerly phase of the oscillation lasts about 20-25 days and the easterly phase about 10-15 days. The spatial distribution of 900 mb wind in relation to the location of SCC and large scale SST is shown in figure 5. While the main SCC center propagates eastward, secondary centers move westward. Each of the centers is associated with a Rossby wave couplet or double cyclone as they propagate away from the warm water pool. As a result, the westerlies expand zonally with the major convection confined to the eastern terminus of the region of westerlies. There is a remarkable contrast between their steady easterly wind east of the SCC and the wavy circulation patern in the region of the westerlies over the warm pool.

5. Dynamical origin of westerly wind burst

Based on the above results, it may be concluded that the sudden occurrence of westerly wind over the open warm water region (equatorial western and central Pacific) associated with WWB may be due to:

(a) a direct response of the lower tropospheric wind to the passage of the eastward propagating main SCC heat source associated with the 30-60 day oscillation and/or
(b) zonal wind fluctuations on the equatorial side of the twin cyclonic vortices emanating from the main heat source.
(c) The eastward propagating SCC which is at the eastern extreme of the region of westerlies is directly related to strong convection while those associated with Rossby waves may or may not be accompanied by strong convection. This may be the reason why the most intense precipitation is often found near the eastern terminus of the westerlies and that some westerlies outbursts are not related *locally* to convection (Keen, 1987).
(d) The rapid expansion of the region of surface westerly is the result of the SCC complex extending both eastward (by Kelvin waves) and westward (by Rossby waves) as the large scale circulation and the latent heating fields undergo mutual adjustment.

A summary of the above features in illustrated schematically in figure 6.

6. Relevance to ENSO

A recent study by Lau and Shen (1988) suggests that a new set of unstable coupled ocean-atmosphere modes arises as a result of including the physics of the 30-60 day oscillation in the atmospheric model. Figures 7a and 7b show the dispersion relationship of an unstable coupled mode as a function of the mean SST. This unstable mode is due to the interaction of zonal SST advection and atmospheric zonal wind fluctuations such as the multi-scale processes described in the preceding sections. As SST increases, the atmospheric disturbances move slower as indicated by the decreasing

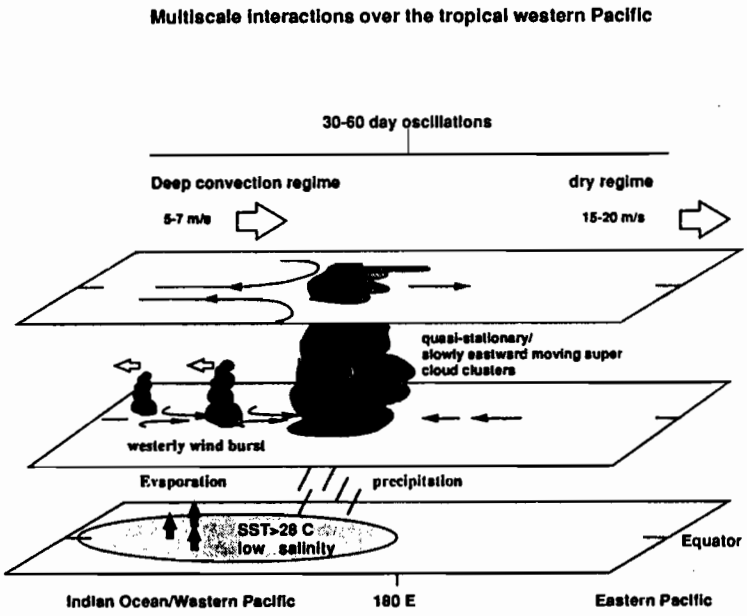

FIG.6. Schematic showing the hierarchical structure of intraseasonal oscillation, westerly wind burst and super cloud cluster over the tropical Pacific as inferred from observations and model simulations.

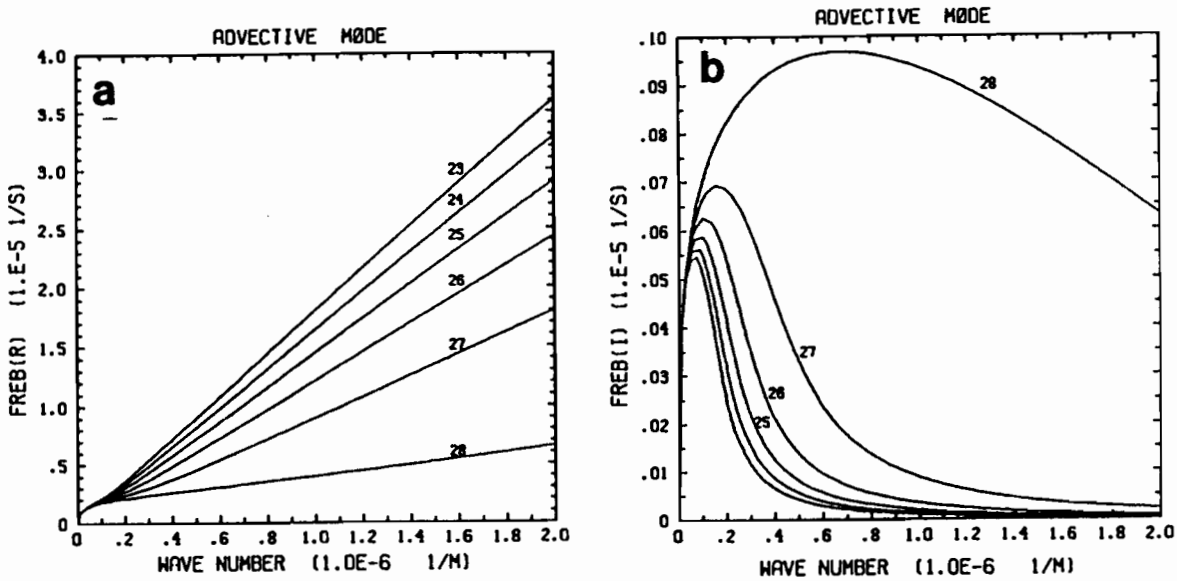

FIG.7. Dispersion relationship for unstable coupled moist ocean-atmosphere modes as a function of SST for (a) real part and (b) imaginary part of the frequency. The atmospheric model contains explicit moist physics. Only zonal SST advection is included in the ocean model (adapted from Lau and Shen, 1988).

slope of the dispersion curves (Fig.7a). More importantly, as the mean SST increases, the coupled instability increases drastically between 27° to 28° C as indicated by the large increase in the imaginary frequency between these two SSTs (Fig.7b). This critical range of SST is a function of the unstable or marginally stable stratification of the tropical western Pacific and the nonlinearity in the Clausius-Claperyron relationship governing saturated moisture and temperature (see Lau and Shen ,1988, for details). The strong dependence of the stability on SST alone may be an over-simplification of the model. But the possibility that the entire hierarchy of motions depicted in figure 6 may be dynamically unstable when coupled to the ocean is a crucial factor that need to be taken into account in our understanding of the onset mechanisms for ENSO.

The results presented here is consistent with the view that the ISO, WWB may be instrumental in triggering the onset of ENSO (Lau, 1985; Lau and Chan, 1988). It is important to note that ISO, WWB, double vortices or even typhoon that have been invoked as causes for ENSO onset should not be regarded as separate or single phenomenon that by itself will cause ENSO. The key to the triggering is the strengthening of the equatorial surface westerly wind. Features like double vortices may occur as necessary accompaniments to the increase in surface westerly wind. Typhoons may be further development of these vortices away from the equator. At best, they serve as signals of strong westerly wind that are occurring in the equatorial region but are themselves not germane to the ENSO triggering process. An important consideration from the present study is that the surface westerlies during ENSO onset occur episodically and with a high degree of variability. Interactions among the intermediate to high frequency components such as ISO, SCC and WWB may play key roles in the onset of ENSO.

REFERENCES

Hayashi, Y., and A. Sumi, 1986: The 30-40 day oscillations simulated in an "aqua-planet" model. *J. Meteor. Soc. Japan,* **64**, 451-467.

Keen, R.A., 1982: The role of cross-equatorial tropical cyclone pair in the southern oscillation. *Mon. Wea. Rev.*, **110**, 1405-1416.

Keen, R.A., 1987: Equatorial westerlies and the Southern Oscillation. Proceedings of the US TOGA western Pacific air-sea interaction workshop. September 16-18, Honolulu, Hawaii.

Lau, K.M., 1985: Elements of a stochastic dynamical theory of the long-term variability of the El Nino/Southern Oscillation. *J. Atmos. Sci.*, **42**, 1552-1558.

Lau, K.M., and P.H. Chan, 1988: Interannual and intraseasonal variations of tropical convection: a possible link between the 40 day mode and ENSO? *J. Atmos. Sci.*, **45**, 506-521.

Lau, K.M., and L. Peng, 1987: Origin of low-frequency (intraseasonal) oscillations in the tropical atmosphere. Part I: basic theory. *J. Atmos. Sci.*, **44**, 950-972.

Lau, K.M., and S. Shen, 1988: On the dynamics of intraseasonal oscillation and ENSO. *J. Atmos. Sci.*, **45**, 1781-1797.

Lau, K.M., L. Peng, C.H. Sui and T. Nakazawa, 1989: Dynamics of westerly wind burst, super cloud cluster, 30-60 day oscillation and ENSO: an unified view. *J. Meteor. Soc. Japan.* **67**, (in press).

Lukas, R., 1988: On the role of western Pacific air-sea interaction in the El Nino/Southern Oscillation phenomenon. Proceeding of US TOGA Western Pacific Air-Sea interaction Workshop, September, 16-18, 1987, Honolulu, Hawaii.

Luther, D.S., D.E. Harrison and R.A. Knox , 1983: Zonal winds in the central equatorial Pacific and El Nino. *Science,* **222**, 327-330.

Nakazawa, T., 1988: Tropical super clusters within intraseasonal variations over the western Pacific. *J. Meteo. Soc. Japan*, **66**, 823-839.

Nitta, T., and T. Motoki, 1987: Abrupt enhancement of convective activity and low level westerly wind burst during the onset phase of 1986-87 El Nino. *J. Meteor. Soc. Japan*, **65**, 497-506.

Sui, C.H., and K.M. Lau, 1988: Origin of low-frequency (intraseasonal) oscillations in the tropical atmosphere. part II: effect of an improved treatment of moist processes. *J. Atmos. Sci.*, **46** 37-56.

Hydrological Effects on the Air-Ocean Coupled System

Pecheng C. CHU and Roland W. GARWOOD, Jr

Department of Oceanography, Naval Postgraduate School
Monterey, CA 93943 - U.S.A.

ABSTRACT

The ocean and atmosphere are driven by the fluxes of momentum, heat, and water mass. The importance of the fluxes of momentum and heat is well recognized by both meteorologists and oceanographers. The hydrological cycle is, however, only given considerable attention in atmospheric models since the latent heat release is an important source of the atmospheric general circulation. The hydrological cycle is given less attention in ocean models although it is realized that evaporation and precipitation are contributors to the surface buoyancy flux which determines the depth of mixing and drives the thermohaline circulation.

The cloud and the ocean mixed layer are highly coupled by both the heat and moisture fluxes across the air-ocean interface. Two time scales are found in this paper: a sea surface temperature (SST) time scale, τ_T, that is virtually controlled by the oceanic planetary boundary layer (OPBL), and a cloud-SST coupling time scale, $\tau_{n,T}$. These two time scales depend on the stability of the marine atmospheric boundary layer (MABL).

An air-ocean model is developed in this paper for the coupled system of an unstable atmosphere overlying a stable ocean. The model results demonstrate that the exchanges of heat and water fluxes across the sea surface leads to both growing and decaying modes of oscillation on 3-6 day and 20-30 day time scales. These oscillatory solutions are entirely thermodynamic and do not require wave dynamics for their existence.

1. Introduction

Since 1970 significant progress has been made both in our ability to carry out air-sea interaction field work and in our understanding of many of the processes found on both sides of the air-sea interface. Many studies, both observational and theoretical, have shown that the surface wind and the SST are two important elements in the air-sea coupled system (Chu, 1989). Since clouds have significant effects on the large-scale atmospheric circulation through the transfer of heat and moisture, and on the OPBL through the attenuation of the solar radiation at the ocean surface, there may be strong feedback between the clouds and the OPBL. Fig.1 shows the main physical processes (heat, mass, and momentum fluxes) at the two adjacent boundary layers: the OPBL and the marine atmospheric boundary layer (MABL). Fig.2 illustrates the feedback pathways between the clouds and the ocean mixed layer.

ORSTOM
CENTRE DOCUMENTATION
Montpellier

F.30227

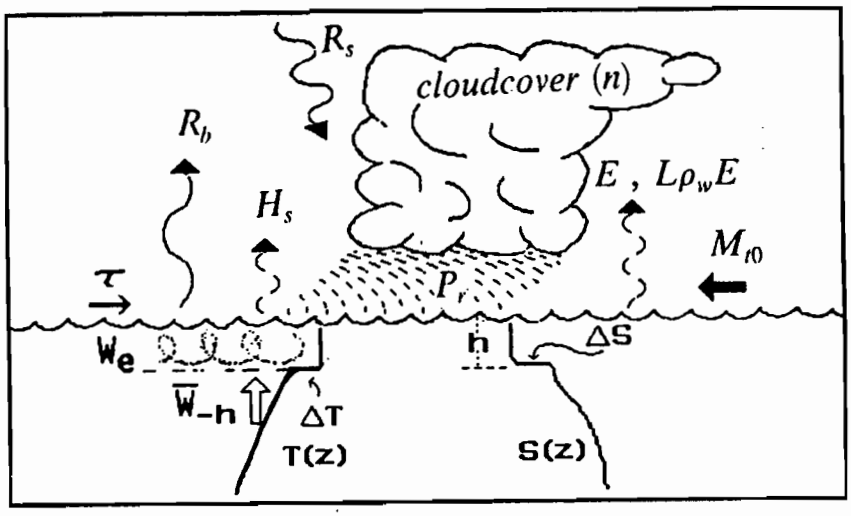

Fig.1 Main physical processes at the two adjacent boundary layers.

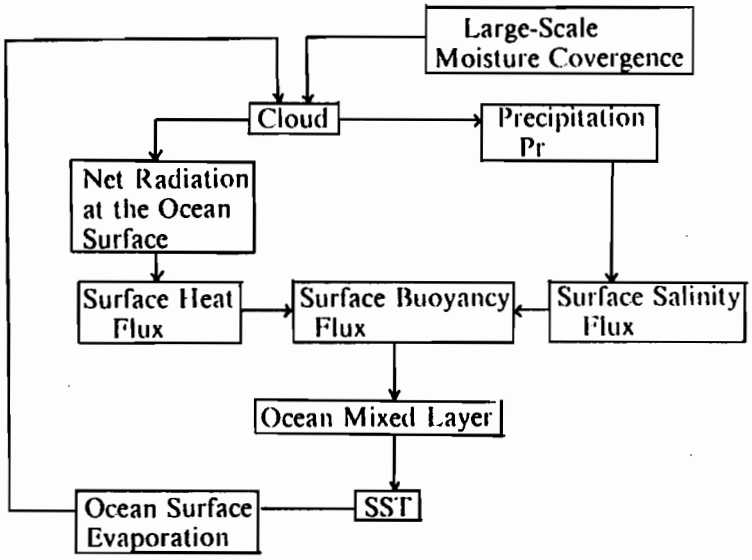

Fig.2 Feedback paths between OPBL and clouds.

The feedback mechanism between clouds and ocean mixed layer in the buoyant forcing regime (upward buoyancy flux at the ocean surface) was illustrated by Chu and Garwood (1989). However, the TOGA (Tropical Ocean Global Atmosphere Program) observations have shown the warm pool regions of the western Pacific to be in the buoyant damping regime (downward buoyancy flux) for the OPBL due to fresh water influx caused by an excess of precipitation over evaporation. The OPBL is usually stable, and the MABL is generally unstable. Therefore, the feedback mechanism in this coupled system (unstable MABL - stable OPBL) should have different form from the buoyant forcing case.

Although our coupled model is one-dimensional, we are aware of the importance of the horizontal advection and the limitation of one-dimensional models. However, the intent of this work is to develop a formalism to examine thermodynamic feedback between the two fluids. Because we wish to concentrate on the thermodynamic interaction, horizontal advection is ignored initially.

2. Similarity Functions in the MABL

According to the similarity theory it is assumed that if a variable (wind, temperature, or moisture, etc.) is appropriately scaled, then its profile follows a universal function whose form, in general, is determined empirically. For the barotropic atmosphere the appropriate scales for wind and height are

$$U = U_g, \quad h_a = \frac{\alpha u_{a^*}}{|f|} \tag{1}$$

where U_g is the geostrophic wind speed, which is assumed here to be $10 m/s$, u_{a^*} is the atmospheric friction velocity. The geostrophic drag coefficient C_g is defined by Yamada (1976) as

$$C_g = \frac{u_{a^*}}{|U_g|} = \kappa\{[\ln(\frac{h_a}{z_0}) - A]^2 + B^2\}^{-1/2} \tag{2}$$

where κ is the von Karman constant, 0.4. The roughness parameter, z_0, is approximately $1.5 \times 10^{-4} m$. The ratio h_a/z_0 is 0.6×10^7 for an MABL height, $h_a = 1 km$. The heat and moisture transfer coefficients are determined by

$$C_H = -\frac{\overline{w'_a \theta'}|_0}{u_{a^*}[\hat{\theta} - \theta(z_0)]}, \quad C_E = -\frac{\overline{w'_a q'}|_0}{u_{a^*}[\hat{q} - q(z_0)]} \tag{3}$$

where w, θ, q are the vertical velocity, potential temperature, and specific humidity, respectively. The superscript " ' " means the disturbance, and " $\wedge$ " indicates the values being taken at the top of the MABL. The heat transfer coefficient is further computed by Yamada (1976) as

$$C_H = = \frac{\kappa}{Pr_0}[\ln(\frac{h}{z_0}) - C]^{-1} \tag{4}$$

where Pr_0 is the turbulent Prandtl number for neutral stability, having a value of 0.74 according to Businger et al. (1971). Based on the Wangara data, the similarity functions A, B, C are experimentally determined by Yamada (1976) for the stable atmosphere:

$$A = 1.855 - 0.38 h_a/L_a \quad (0 \le h_a/L_a \le 35),$$

$$A = -2.94(h_a/L_a - 19.94)^{1/2} \quad (35 < h_a/L_a);$$

$$B = 3.02 + 0.3 h_a/L_a \quad (0 \le h_a/L_a \le 35),$$

$$B = 2.85(h_a/L_a - 12.47)^{1/2} \quad (35 < h_a/L_a);$$

$$C = 3.665 - 0.829 h_a/L_a \quad (0 \le h_a/L_a \le 18),$$

$$C = -4.23(h_a/L_a - 11.21)^{1/2} \quad (18 < h_a/L_a) \tag{5a}$$

and for the unstable atmosphere ($h_a/L_a < 0$)

$$A = 10.0 - 8.145(1 - 0.008376 h_a/L_a)^{-1/3},$$

$$B = 3.02(1 - 3.29 h_a/L_a)^{-1/3},$$

$$C = 12.0 - 8.335(1 - 0.03106h_a/L_a)^{-1/3} \tag{5b}$$

where L_a is the atmospheric Obukhov length scale. The computation for the moisture transfer coefficient is not very clear yet. In this paper we assume that

$$C_E = C_H \tag{6}$$

Substitution of (5 a,b) into (2) and (4) leads to the apparently strong dependence of C_g, C_H, C_E on the atmospheric stability parameter h_a/L_a, as shown in Fig.3. These parameters have much larger values for the unstable than for the stable atmosphere, i.e.,

$$C_g \sim 0.0316, \quad C_H, C_E \sim 0.063 \quad (h_a/L_a < 0)$$

$$C_g \sim 0.003, \quad C_H, C_E \sim 0.004 \quad (h_a/L_a > 0) \tag{7}$$

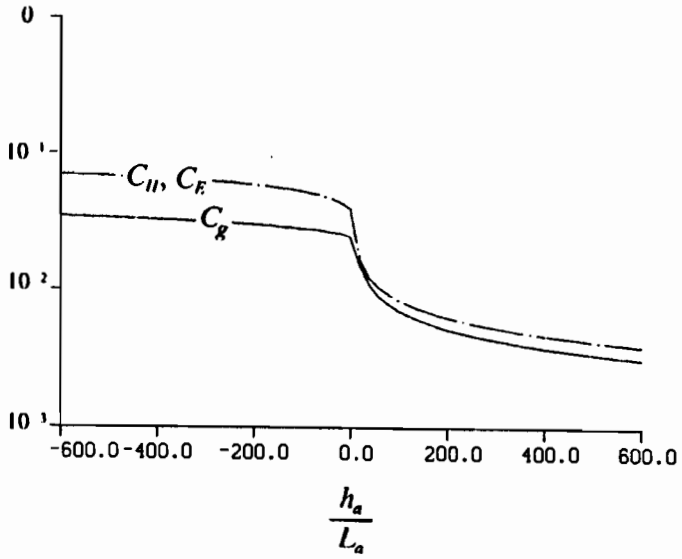

Fig.3 Dependence of C_g, C_H, C_E on the atmospheric stability parameter (h_a/L_a).

3. Time Rate of Change of the Cloud Cover

The time rate of change of cloud cover is assumed to be proportional to the moisture supply divided by the amount of water vapor necessary to produce the model cloud. The main processes causing the cloud dissolution are precipitation and mixing with the environmental air. The cloud evaporation due to mixing with ambient air is a complicated problem, and is neglected for the sake of simplicity here. Thus the equation for cloud cover is

$$\frac{\partial n}{\partial t} = \frac{(M_{t0} + E - P_r)}{h_c} \tag{8}$$

where h_c is the total amount of water vapor needed to create the cloud over a unit area. From mean distributions of temperature and mixing ratio in the environmental air outside the cloud and inside a deep cumulus cloud (Kuo, 1965), we estimate that $h_c \sim 5$ *cm*. The large-scale horizontal moisture convergence in the column of atmosphere per unit area is denoted M_{t0}.

4. Relationship between Precipitation Rate and Cloud Cover

By linear regression of hourly rain amounts and satellite IR brightness data obtained during Phases I, II, and III of GATE, Albright et al. (1985) presented a linear relationship between average precipitation rate P_r in boxes 1.5° (168 km) on a side and cloud cover n of the boxes by clouds with tops colder than −36° C:

$$P_r(ms^{-1}) = (0.472 + 8.333\, n) \times 10^{-7} \tag{9}$$

This result confirms Arkin's (1979) earlier analysis for the GATE B-scale array.

5. Ocean Mixed Layer

Much of the one-dimensional theory for the OPBL or mixed layer is dependent upon the validity of two crucial hypotheses. The first of these is that vertical mixing within the turbulent boundary layer and entraiment mixing at its base occur in response to the local atmospheric forcing - the surface wind stress and the buoyancy flux at the sea surface. The second hypothesis is that the mechanical energy budget is the key to the understanding and prediction of mixed layer dynamics (Garwood, 1977, 1979).

The buoyancy flux is attributable to heat flux, evaporation, and precipitation. The shear production of turbulence is attributable to surface wind stress. In the western Pacific warm pool regions, the excess precipitation effect prevails over the buoyancy effect of heat lost at the ocean surface, causing the net buoyant flux to be downward. The mixed layer depth equals the Obukhov length scale:

$$h_w = L_w = \frac{2u_{w*}^3}{B} \tag{10}$$

where L_w is the oceanic Obukhov length scale. The oceanic friction velocity is

$$u_{w*} = \left(\frac{\rho_a}{\rho_w}\right)^{1/2} u_{a*}$$

and B is the downward surface buoyancy flux

$$B \equiv \beta g S(P_r - E) - \frac{\alpha g F}{\rho_w c_{pw}} \tag{11}$$

where ρ_a, ρ_w are the air and sea water densities, α is the sea water thermal expansion coefficient, and β is the salinity contraction coefficient. Because the OPBL is in the buoyant damping regime, the mixed layer heat and salinity budgets include no entrainment:

$$\frac{\partial T_w}{\partial t} = -\frac{F}{\rho_w c_p^{(w)} h_w} - A_T \tag{12}$$

$$\frac{\partial S}{\partial t} = +\frac{(E - P_r)S}{h_w} - A_S \tag{13}$$

where $c_p^{(w)}$ is the specific heat under constant pressure. The parameters A_T and A_S are the horizontal advection for temperature and salinity, respectively.

The effects of clouds on the buoyancy flux at the ocean surface are two-fold: (1) decreasing B_0 through the increase in the net heat loss at the ocean surface, F, by reducing the incoming solar radiation, and (2) increasing B_0 due to precipitation. The net heat loss from the ocean surface is given by

$$F = R_b - R_s + \rho_a c_{pa} C_g U_G C_H [T_w - \hat{\theta}] + L\rho_a C_g U_G C_E [q_s(T_w) - \hat{q}] \qquad (14)$$

where q_s(T) is the saturated mixing ratio. The incoming solar radiation absorbed by the ocean surface is R_s, and R_b is the net energy loss from the ocean surface by longwave radiation, L is the latent heat of vaporization of water, and H_s is the sensible heat flux to the air. The standard bulk formulae are used to calculate the surface evaporation:

$$E = \rho_a C_g U_g C_E [q_s(T_w) - \hat{q}]/\rho_w \qquad (15)$$

6. Cloud Effects on the Net Radiation at the Ocean Surface

Clouds reduce the solar radiation incident at the ocean surface by scattering and absorption, which is computed by Budyko's (1978) formula

$$R_s = [1 - \alpha_{sn} n - \alpha_{s0}(1 - n)]R_{s0} \qquad (16)$$

Here R_{s0} (340 W m^{-2}) is the solar radiation absorbed by the ocean surface layer under a clear sky. The parameters α_{sn} and α_{s0} represent albedos of the earth-atmosphere system with complete cloud cover and a cloudless sky, respectively, and have the following values:

$$\alpha_{sn} = 0.46, \qquad \alpha_{s0} = 0.2$$

The ocean surface emits longwave radiation to the atmosphere and to space. However, clouds, as well as dry air, partially absorb the radiation and re-emit longwave radiation back to the ocean surface. Thus the net upward energy loss by longwave radiation at the ocean surface, R_b, is corrected for the downward radiation by the clouds and the air. From longwave radiation data, Budyko (1978) derived a semi-emprical formula:

$$R_b = a + bT - (a_1 + b_1)n \qquad (17)$$

The dimensional coefficients a, b, a_1, and b_1 are

$$a = -377.6\ Wm^{-2},\ b = 2.2\ Wm^{-2}K^{-1},$$

$$a_1 = -389.8\ Wm^{-2}, b_1 = 1.6\ Wm^{-2}K^{-1}$$

7. Basic Equations for Perturbations

When the coupled system is perturbed from its equilibrium state, the thermodynamic feedback mechanism between the cumulus clouds and the oceanic mixed layer makes the perturbation either grow (positive feedback) or dampen (negative feedback). The principal purpose here is to study thermodynamic feedback mechanisms between clouds and the oceanic mixed layer. Hence the energy exchange at the air-ocean interface is a primary focal point. Therefore, we shall neglect initially the perturbations of those variables which are not di-

rectly related to the exchange at the air-ocean interface. From the basic equations of the coupled system (8), (10), (12), and (13), the perturbations satisfy the following equations:

$$\frac{\partial n'}{\partial t} = \frac{1}{\bar{h}_c}\left(\frac{\partial E}{\partial T_w} T'_w - \frac{\partial \bar{P}_r}{\partial n} n'\right) \tag{18}$$

$$h'_w = -\frac{\bar{h}_w}{\bar{B}} B' = \frac{\bar{h}_w}{\bar{B}}\left[\left(\frac{\alpha g}{\rho_w c_{pw}} \frac{\partial \bar{F}}{\partial T_w} + \beta g \bar{S} \frac{\partial \bar{E}}{\partial T_w}\right) T'_w\right.$$

$$\left. - \beta g \bar{S}(\bar{P}_r - \bar{E}) S' + \left(\frac{\alpha g}{\rho_w c_{pw}} \frac{\partial \bar{F}}{\partial n} - \beta g \bar{S} \frac{\partial \bar{P}_r}{\partial n}\right) n'\right] \tag{19}$$

$$\frac{\partial T'_w}{\partial t} = -\frac{1}{\rho_w c_p^{(w)} \bar{h}_w}\left(\frac{\partial \bar{F}}{\partial n} n' + \frac{\partial \bar{F}}{\partial T_w} T'_w + \frac{\bar{F} h'_w}{\bar{h}_w}\right) \tag{20}$$

$$\frac{\partial S'}{\partial t} = \frac{(\bar{E} - \bar{P}_r)}{\bar{h}_w} S' + \frac{\bar{S}}{\bar{h}_w}(E' - P'_r) + \frac{(\bar{P}_r - \bar{E})\bar{S}}{\bar{h}_w^2} h'_w \tag{21}$$

8. Three Basic Time Scales

Three time scales are found from (18)-(21):

Cloud time scale

$$\tau_n^{-1} = \frac{1}{h_c} \frac{\partial \bar{P}_r}{\partial n} \tag{22}$$

Using (9) and taking $h_c = 5cm$, we have

$$\tau_n \sim 0.6 \ day \tag{23}$$

SST variation time scale

$$\tau_T^{-1} \equiv \frac{1}{\rho_w c_{pw} \bar{h}_w} \frac{\partial \bar{F}}{\partial T_w} \tag{24}$$

The net heat loss from the ocean surface is computed by (14). Assuming that $\hat{\theta}$ and $\hat{q}$ are determined by the large-scale atmospheric motion, we have

$$\frac{\partial \bar{F}}{\partial T_w} = \rho_a c_{pa} U_g \left(1 + \frac{L^2 q_s}{c_{pa} R_v T_w^2} \frac{C_E}{C_H}\right) C_g C_H$$

therefore

$$\tau_T^{-1} = \frac{\rho_a c_{pa} U_g}{\rho_w c_{pw} \bar{h}_w}\left(1 + \frac{L^2 q_s}{c_{pa} R_v T_w^2} \frac{C_E}{C_H}\right) C_g C_H \tag{25}$$

Cloud and SST coupling time scale

$$\tau_{n,T}^{-1} \equiv \frac{1}{\rho_w c_{pw} \bar{h}_w} \frac{\partial \bar{F}}{\partial n} \frac{\partial \bar{E}}{\partial T_w} / \frac{\partial \bar{P}_r}{\partial n} \tag{26}$$

Substitution of (22) into (26) leads to

$$\tau_{n,T}^{-1} = [\frac{\tau_n U_G L q_s \frac{\partial F}{\partial n}}{\rho_w c_{pw} h_w h_c R_v T_w^2}] C_g C_E \tag{27}$$

Using (16) and (17) we have

$$\frac{\partial F}{\partial n} = \frac{\partial (R_b - R_s)}{\partial n} \sim 15 Wm^{-2}$$

Among these three time scales, τ_n is the shortest. The other two, τ_T and $\tau_{n,T}$, largely depend on the parameters C_g, C_H, and C_E, which are functions of the atmospheric stability. Fig.4 shows the dependence of τ_T and $\tau_{n,T}$ on the atmospheric stability. For the unstable atmosphere ($h_a/L_a < 0$), $\tau_{n,T} \sim 3 - 6$ days, and $\tau_T \sim 20 - 30$ days. For the stable atmosphere ($h_a/L_a > 0$), $\tau_{n,T} \sim 0.3 - 1$ years, and $\tau_T \sim 1 - 3$ years.

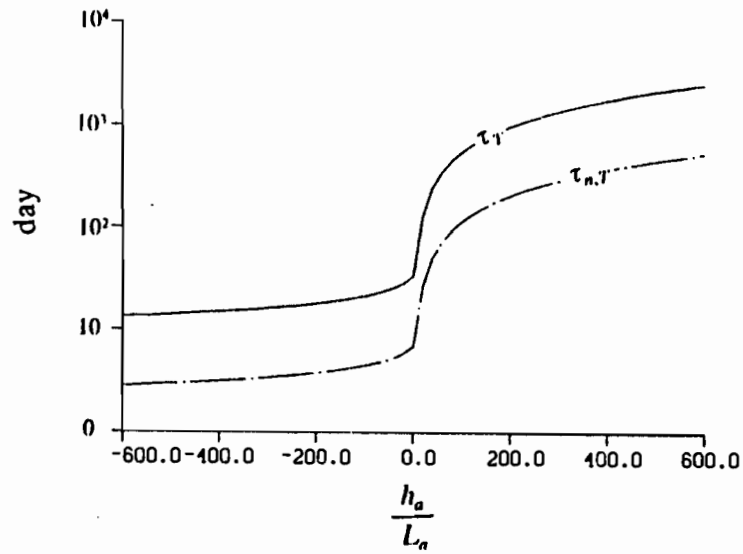

Fig.4 Dependence of τ_T and $\tau_{n,T}$ on the atmospheric stability parameter h_a/L_a).

9. Solutions

Since the time scale for cloud feedback is so much shorter than that for SST feedback, i.e., $\tau_n \ll \tau_T$, the cloud cover perturbation, n', almost instantaneously follows the SST for the temperature feedback:

$$n' = \frac{\partial \bar{E}/\partial T_w}{\partial \bar{P}_r/\partial n} T'_w \tag{28}$$

Eq.(9) shows that

$$\frac{\partial \bar{P}_r}{\partial n} \sim 8.33 \times 10^{-7} ms^{-1},$$

and for $\overline{T}_w = 25°C$, $u_{a*} = 0.1 m/s$,

$$\frac{\partial \overline{E}}{\partial T_w} = C_E u_{a*} \frac{dq_s(z_0)}{dT_w} \sim 4.63 \times 10^{-7} ms^{-1} K^{-1}.$$

Therefore, a $1°C$ change in SST implies a 0.56 change in cloud cover.

Neglecting the small terms in the prognostic equations for T'_w and S' and eliminating three among the four variables n', T'_w, S', and h'_w from (19), (20), (21), (28), we obtain the second order differential equation,

$$\frac{\partial^2 \psi}{\partial t^2} - \frac{2\mu - \gamma}{\gamma - \mu}(\tau_{n,T}^{-1} + \tau_T^{-1}) \frac{\partial \psi}{\partial t} + \frac{\mu\gamma^2}{(\gamma - \mu)^2}(\tau_{n,T}^{-1} + \tau_T^{-1})^2 \psi = 0 \tag{29}$$

where ψ represents n', T'_w, S', and h'_w. There are two nondimensional parameters,

$$\mu = \frac{4\alpha g \overline{F}/\rho_w c_{pw}}{\beta g \overline{h}_w \overline{S}(\tau_{n,T}^{-1} + \tau_T^{-1})}, \quad \gamma = \frac{4\beta g(\overline{P}_r - \overline{E})\overline{S}}{\beta g \overline{h}_w \overline{S}(\tau_{n,T}^{-1} + \tau_T^{-1})} \tag{30}$$

that indicate the relative importance of mean heat and mean salinity fluxes in the mean surface buoyancy flux (11). The general solutions of (29) have the form:

$$\psi = C_1 \exp(\sigma_1 t) + C_2 \exp(\sigma_2 t) \tag{31}$$

where C_1 and C_2 are integral constants, and σ_1 and σ_2 are the eigenvalues which are the roots of the second-order algebraic equation

$$\sigma^2 - \frac{2\mu - \gamma}{\gamma - \mu}(\tau_{n,T}^{-1} + \tau_T^{-1})\sigma + \frac{\mu\gamma^2}{(\gamma - \mu)^2}(\tau_{n,T}^{-1} + \tau_T^{-1})^2 = 0 \tag{32}$$

10. Instability and Oscillation Criteria

The instability criteria for the thermodynamically coupled air-ocean system are

$$Re(\overline{\sigma}) \begin{cases} < 0 & \textit{decaying} \\ = 0 & \textit{neutral,} \\ > 0 & \textit{growing} \end{cases} \tag{33}$$

where $\overline{\sigma}$ is σ_1 or σ_2, the root of the second-order equation (32). The oscillatia criterion for the coupled system are

$$Im(\overline{\sigma}) \begin{cases} = 0 & \textit{nonoscillatory} \\ \neq 0 & \textit{oscillatory} \end{cases} \tag{34}$$

The roots σ_1 and σ_2 are

$$\sigma_{1,2} = \frac{(2\mu - \gamma)}{2(\overline{\gamma} - \mu)}(\tau_{n,T}^{-1} + \tau_T^{-1})[1 \pm \sqrt{(1 - \mu\gamma^2/(2\mu - \gamma)^2} \tag{35}$$

The condition for the generation of growing/decaying modes, which can be deduced from (38), is:

$$\frac{2\mu-\gamma}{\gamma-\mu} \quad \begin{cases} <0 & \textit{decaying} \\ =0 & \textit{neutral,} \\ >0 & \textit{growing} \end{cases} \tag{36}$$

and the condition for oscillatory/nonoscillatory modes is:

$$(1-\frac{2\mu}{\gamma})^2 \quad \begin{cases} >\mu & \textit{nonoscillatory} \\ <\mu & \textit{oscillatory} \end{cases} \tag{37}$$

Separation of different modes in the $\gamma-\mu$ plane is shown in Fig.5. For the buoyant damping regime ($\overline{B}>0$, i.e., $\gamma>\mu>0$) which corresponds to the western Pacific warm pool regime, the relative importance of the mean surface heat and salinity fluxes in the mean buoyancy flux $\overline{B}$ is a key factor controling the modes of the coupled air-ocean system. The mean surface salinity flux, measured by γ, makes the upper ocean more buoyant (stabilizing factor), however, the mean upward heat flux, measured by μ, makes the upper ocean less buoyant (destabilizing factor). The larger the parameter γ (μ), the stronger the negative (positive) feedback mechanism. Combining (36) and (37) leads to the same results:

$$\gamma>\frac{2\mu}{1-\sqrt{\mu}} \qquad \Rightarrow \textit{Nonoscillatory Damping}$$

$$\frac{2\mu}{1-\sqrt{\mu}}>\gamma>2\mu \qquad \Rightarrow \textit{Oscillatory Damping}$$

$$2\mu>\gamma>\frac{2\mu}{1+\sqrt{\mu}} \qquad \Rightarrow \textit{Oscillatory Growing}$$

$$\frac{2\mu}{1+\sqrt{\mu}}>\gamma>\mu \qquad \Rightarrow \textit{Nonoscillatory Growing} \tag{38}$$

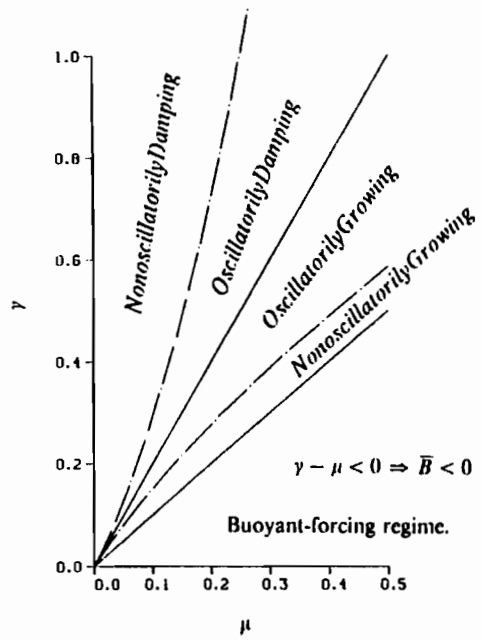

Fig.5 Separation of different modes in the (γ, μ) plane.

11. Conclusion

The feedback between the cloud and OPBL in the coupled MABL and stable OPBL system is investigated by a coupled model. The time scales largely depend on the stability of the MABL. For the stable atmosphere, the two time scales are quite long: $\tau_T \sim$ 100-300 days, and $\tau_{n,T} \sim$ 1-3 yr. For the unstable atmosphere, however, the two time scales are much shorter: $\tau_T \sim$ 3-6 days, and $\tau_{n,T} \sim$ 20-30 days. In the western Pacific warm pool regions, the MABL is usually unstable. Therefore, this theory may provide some explanation of the two time scales (3-6 and 20-30 days) of intense convection in the western Pacific.

In the coupled system, the fresh water influx at the ocean surface due to the excess precipitation over evaporation is a damping factor (negative feedback). However, the surface cooling is a forcing factor (positive feedback). The relative strengths of these two surface fluxes determine the mode type: decaying or growing, oscillatory or nonoscillatory.

Acknowledgements.

This research was supported by the National Science Foundation, the Office of Naval Research, and the U.S. Naval Postgraduate School.

REFERENCES

Albright, M.D., E.E. Recker, R.J. Reed, and R.Q. Dang, 1985: The diurnal variation of deep convection and inferred precipitation in the central tropical Pacific during January-February 1979. Mon. Wea. Rev., **113,** 1663-1680.

Arkin, P.A., 1979: The relationship between fractional coverage of high cloud and rainfall accumulations during GATE over the B-scale array. Mon. Wea. Rev., **107,** 1382-1387.

Budyko, M.I., 1978: The heat balance of the earth. Climatic Change (ed. J. Gribbin), Cambgidge Univ. Press, 85-113.

Chu, P.C., 1989: Relationship between thermally forced surface wind and sea surface temperature gradient. Pure & Appl. Geophys., **130,** 31-45.

Chu, P.C., and R.W. Garwood, Jr., 1988: Comment on "A coupled dynamic-thermodynamic model of an ice-ocean in the marginal ice zone" by Sirpa Hakkinen. J. Geophys. Res., **93,** 5155-5156.

Chu, P.C., and R.W. Garwood, Jr., 1989: Cloud - ocean mixed layer feedback. AMS Symposium on the Role of Clouds in Atmospheric Chemistry and Global Climate, 39-44.

Garwood, R.W. Jr., 1977: An oceanic mixed layer capable of simulating cyclic states. J. Phys. Oceanogr., **7,** 455-468.

Garwood, R.W. Jr., 1979: Air-sea interaction and dynamics of the surface mixed layer. Rev. Geophys. Space Phys., **17,** 1507-1524.

Kuo, H.L., 1965: On formation and intensification of tropical cyclones through latent heat release by cumulus convection. J. Atmos. Sci., **22,** 40-63.

Yamada, T., 1976: On the similarity functions A, B, and C of the planetary boundary layer. J. Atmos. Sci., **33,** 781-793.

A one Dimensional Coupled Air-Sea Model for Diagnostic Studies during TOGA-COARE

Sam F. IACOBELLIS and Richard C.J. SOMERVILLE

SCRIPPS Institution of Oceanography
University of California, San Diego
La Jolla, California 92093 - U.S.A.

ABSTRACT

A process-oriented diagnostic model has been developed, which couples an atmospheric column model to an upper ocean model. In vertical structure and representation of physical processes, the atmospheric model resembles a single horizontal grid point of a general circulation model. It includes vertical transports by convection and turbulent mixing, radiative transfer with interactive clouds, and a complete hydrologic cycle. The ocean model is a simple mixed layer, synchronously coupled to the atmosphere through a surface energy budget computation.

Time-dependent observational analyses of horizontal atmospheric transports of momentum, heat and moisture are used to force the coupled model. The model then produces such fields as temperature, humidity, cloudiness and diabetic heating rate components, all as functions of height and time. Sample integrations of the model for test cases in the 1979 Indian summer monsoon onset are presented and verified against observations. These diagnostic analyses suggest that this type of model may be useful in TOGA COARE for applications such as interpretation of results from multidimensional models, validation of surface flux data, and estimation of sensitivity to alternative physical processes. It may also be used to aid in designing the intensive field phase of TOGA COARE by means of numerical observing system simulation experiments.

1. Introduction

A one-dimensional diagnostic model of an atmospheric column coupled to and upper ocean has been developed. The essential time-dependent input to the model is the large-scale wind field, together with observed horizontal gradients of temperature and moisture. From these data, the model then computes the time evolution of variables such as precipitation, surface fluxes and the vertical profiles of temperature, humidity, cloudiness and diabatic heating rate components. These results may be verified against detailed local measurements.

The atmospheric component of the model is a generalization of a typical radiative-convective model, which has been supplemented by additional parameterizations of diabatic processes and subgrid transports. This portion of the model thus closely resembles a single column of a modern atmospheric general circulation model. The physical parameterizations in our model include shallow convection (Tiedtke et al., 1988), deep moist convection (Kuo, 1974; Anthes, 1977), solar radiative transfer (Lacis and Hansen, 1974), terrestrial radiative transfer (Morcrette, 1984), distribution of surface fluxes (Krishnamurti et al., 1987), prognostic clouds (Slingo, 1987), and vertical diffusive mixing. At present, the atmospheric model is coupled to a very simplistic ocean mixed-layer model (Niiler and Kraus, 1977).

The principal role of such a process-oriented model is not as a predictive tool, but as a test environment for parameterization development and as a mean of gaining physical insight. This diagnostic model can also be a valuable aid in explaining the behavior of multidimensional forecasting models. The restriction to one space dimension makes the model computationally efficient and relatively easy to interpret. At each atmospheric level, the model produces budgets of heat, moisture and momentum which are consistent with the

ORSTOM
CENTRE DOCUMENTATION
Montpellier

F 30228

observationally derived estimates of horizontal advection. In TOGA COARE, potential applications of this model include assessments of the role of cloud-radiation interactions, validation of model surface flux data, estimating sensitivity of multidimensional models to alternative physical parameterizations, and performing observing system simulation experiments to aid in the design of the intensive field phase. As an example of the capabilities of the model, we now present results from applying it to a particular case study: the onset of the Indian summer monsoon in 1979.

The model examines an area four degrees in latitude by four degrees longitude which extends from the surface to the top of the atmosphere (0.50 mb). The time period of the model run is four weeks, extending from May 27 to June 23, 1979 (in this year the monsoon onset occurred on approximately June 17). The model atmosphere is divided into 15 layers in addition to the underlying ocean mixed layer. The model uses a timestep of one hour, a surface albedo of 0.05 (typical of ocean surfaces) and a solar constant of 1360.0 $W.m^{-2}$. The model has been applied at two locations in the Arabian sea. Area 1 extends from 66°E to 70°E and from 12°N to 16°N while area 2 covers 68°E to 72°E and 6°N to 10°N.

2. Model results

The vertical profiles of both temperature and specific humidity from both areas correspond well when compared to observational data supplied from the FGGE III-b data set and TOVS satellite data. Some minor discrepancies in the model temperatures include a slight underestimation of the temperature at higher altitudes (above 500 mb) and a sharp drop in the 500 mb temperature at the time of the monsoon onset which has been determined to depend sensitively on the timing of the occurrence of deep convection in the model.

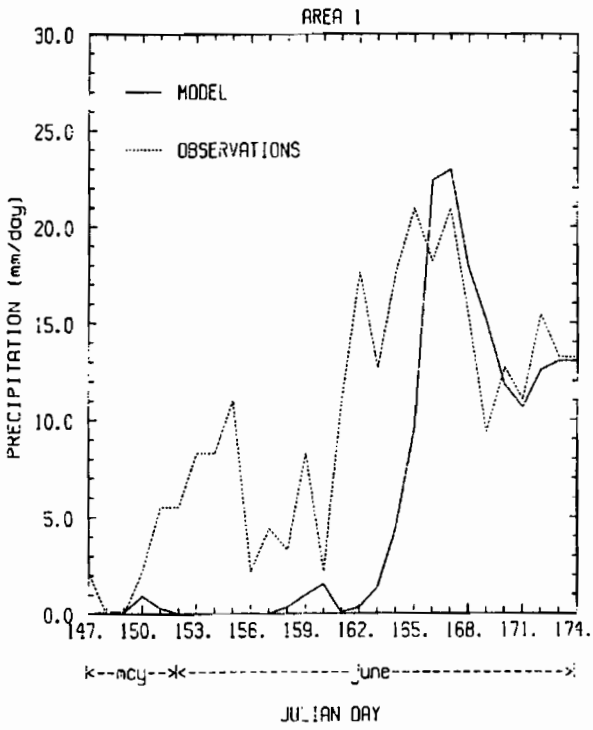

FIG.1a. Area 1 precipitation vs. time. Solid line denotesdata from model and dashed line is observational data

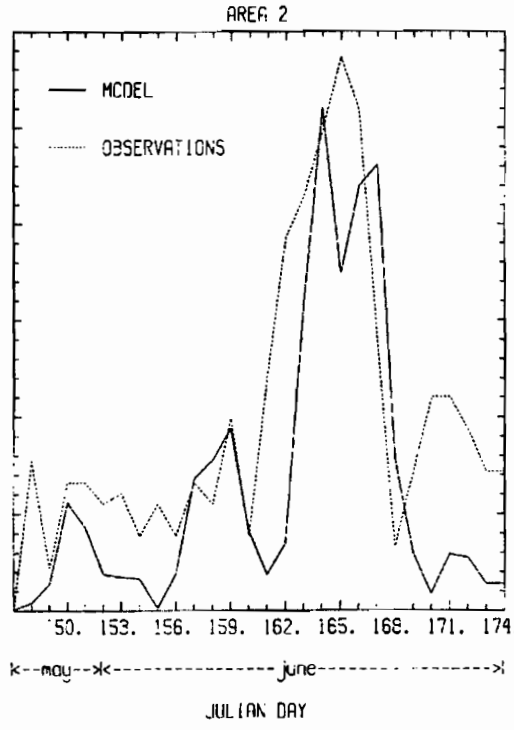

FIG.1b. Same as figure 1a, except for area 2.

Figure 1a shows a comparison between the model precipitation in area 1 and observational rainfall data taken from Cadet and Greco (1987). Figure 1b shows the same comparison for area 2. In both areas the model data compares well with the observational data, especially at the time of the monsoon onset where the precipitation reaches a maximum. During the pre-onset phase the observational data may be overestimating the precipitation as the method employed by Cadet and Greco does not account for any moistening of the atmosphere. Figures 2a and 2b show a comparison between the model values and satellite derived values (Gautier, 1986) of the average daily net short-wave at the surface (NSW). Throughout the integration period there is very good agreement between the model data and the satellite data including the large drop of NSW at the time of the monsoon onset. There are three instances where the model is underestimating the NSW when compared to the satellite data, at approximately day 150 and day 160 in area 1 and at day 151 in area 2. These three brief underestimations of the NSW can be seen to directly correspond with three episodes of minor rainfall. It appears that the cloud parameterization is producing too much cloudiness, hence lowering NSW at the surface, during episodes of low convective rainfall. During periods of large rainfall amounts such as those associated with the monsoon onset, the NSW corresponds very well with the satellite data thus implying that the amount of cloudiness produced by the model during these conditions is representative of the actual cloudiness. This simple analysis indicates that the cloud parameterization used in this model may need some refining for low convective rainfall amounts. This analysis also illustrates how this type of simple yet physically realistic model may be used to evaluate parameterization schemes.

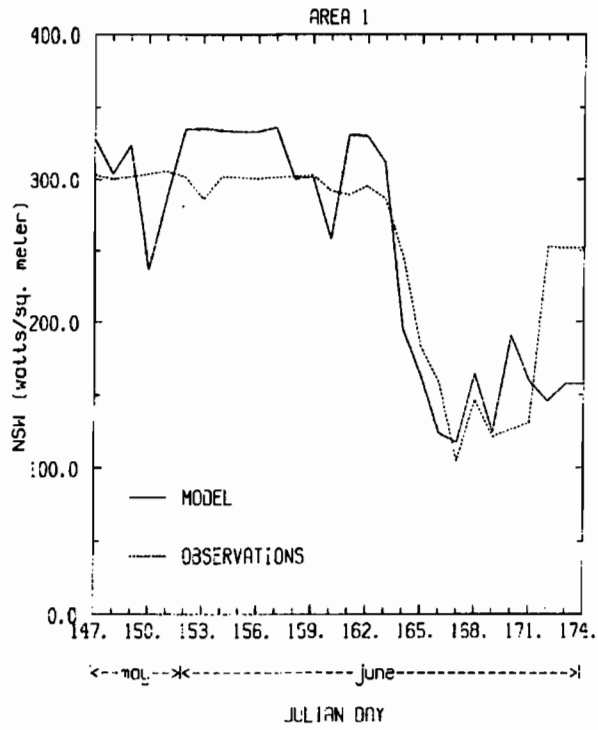

JULIAN DAY

FIG.2a. Area 1 netshort-wave radiation (NSW) at surface vs. time. Solid line denotes data from model and dashed line is satellite observations.

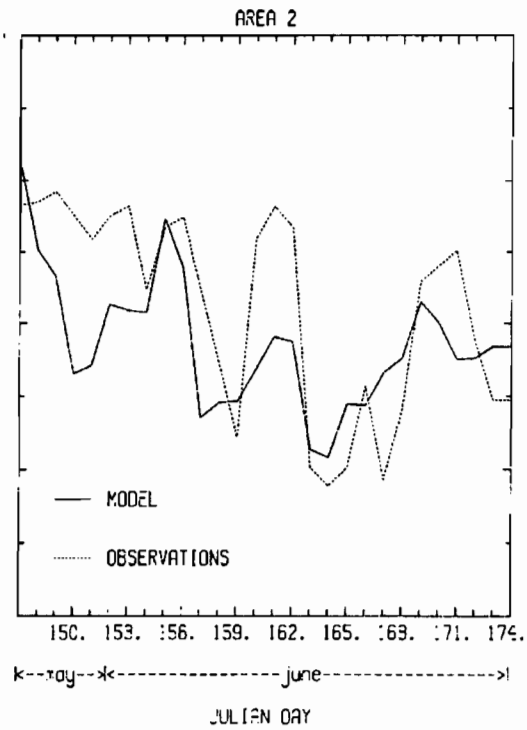

JULIAN DAY

FIG.2b. Same as figure 2a, except for area 2.

Acknowledgments. Our research has been supported in part by the University of California Institutional collaborative Research Program, the National Science Foundation (Grant N° ATM86-12815), the National Aeronautics and Space Administration (Grant Nos. NAG5-236 and NAGW-981), the National Oceanographic and Atmospheric Administration (Grant N° NA86-AA-D-CP104), and the California Space Institute (Grant N° CS-89-88). We are grateful to Dr. Jean Jacques Morcrette for making his radiative transfer scheme available.

REFERENCES

Anthes, R.A., 1977: A cumulus parameterization scheme utilizing a one dimensional cloud model. *Mon. Wea. Rev.,* **105**, 270-286.

Cadet, D.L. and S. Greco, 1987: Water vapor transport over the Indian Ocean during the 1979 summer monsoon. Part I: Water vapor budgets. *Mon. Wea. Rev.,* **115**, 2358-2366.

Gautier, C., 1986: Evolution of the net surface short-wave radiation over the Indian Ocean during summer MONEX (1979). *Mon. Wea. Rev.,* **114**, 525-533.

Krishnamurti, T.N., S. Low-Nam, A. Kumar, J. Sheng and M. Sugi, 1987/ Numerical Weather Prediction of Monsoons. *Monsoon Meteorology,* C.P. Chang, Ed., Oxford University, (501-544).

Kuo, H.L., 1974: Further studies of the parameterization of the influence of cumulus convection on large scale flow. *J. Atmos. Sci.,* **31**, 1232-1240.

Lacis, A.A. and J.E. Hansen, 1974: A parameterization for the absorption of solar radiation in the earth's atmosphere. *J. Atmos. Sci.,* **31**, 118-133.

Morcrette, J.J., 1984: *On the parameterization of radiation in atmospheric general circulation models*. State doctoral thesis, University of Science and Technology, Villeneuve d'Ascq, Lille, France.

Niiler, P.P. and E.B. Kraus, 1977: One-Dimensional Models of the Upper Ocean. *Modeling and Prediction of the Upper Layers of the Ocean*, E.B. Kraus, Ed., Pergamon Press, (143-172).

Slingo, J.M., 1987: The development and verification of a cloud prediction scheme for the ECMWF model. *Quart. J. Roy. Meteor. Soc.,* **113**, 899-927.

Tiedtke, M., W.A. Heckley and J. Slingo, 1988: Tropical forecasting at ECMWF: the influence of physical parameterization of the mean structure of forecasts and analyses. *Quart. J. Roy. Meteor. Soc.,* **114**, 639-664.

On the reflection and Transmission of Low Frequency Energy at the Irregular Western Pacific Ocean Boundary - a Preliminary Report

Allan J. CLARKE

Department of Oceanography
and Geophysical Fluid Dynamics Institute
Florida State University
Tallahassee, Florida 32306 - U.S.A.

ABSTRACT

The western boundary of the tropical Pacific is not continuous and leakage of low frequency energy from the Pacific to the Indian Ocean is possible. At low frequencies equatorial Kelvin and Rossby waves have very large east-west scales compared with the east-west scale of the land masses in the region. Consequently, these land masses may be treated as islands that are infinitesimally thin in the east-west direction. By generalizing previous theory for a single island, the leakage of low frequency energy through the seven major 'islands" forming the boundary of the western Pacific can be studied. The major results are as follows.

(1) When a mode 1 low frequency Rossby wave is reflected at the discontinuous western Pacific boundary, the eastward reflected Kelvin wave energy flux is about one third of the incoming energy flux or about two thirds of that expected for a solid meridional wall.
(2) In phase interannual sea levels should occur along Australia's western coast. The latter prediction is in agreement with observation.
(3) Negligible low frequency Kelvin wave energy from the Indian Ocean is transmitted into the Pacific.
(4) Strong narrow currents are predicted to occur westward of some island tips.

ORSTOM
CENTRE DOCUMENTATION
Montpellier

F 30229

1. Introduction

The western 'boundary' of the tropical Pacific is discontinuous. The reflection of low frequency energy from this western boundary may be crucial to interannual coupled ocean-atmosphere dynamics (Battisti, 1988). But present models assume that the boundary is a solid wall when it clearly is not. Just how well does the gappy western Pacific reflect low frequency energy compared to a solid wall?

In order to answer this question, it is important to realize that because low frequency westward propagating energy has such a large east-west scale, land masses forming the western tropical Pacific boundary can dynamically be treated as being infinitesimally thin east-west. The single 'island' results of Cane and du Penhoat (1982) then apply. These results can be generalized to the several island case and the multiple reflection and transmission of low frequency energy in the western tropical Pacific can be analyzed.

Theory for low frequency flow near a single irregularly shaped island is discussed in the next section and this is generalized in section 3 to the several island case. Section 4 presents some results for the west Pacific.

2. Theory for a Single Island

I will suppose that the large-scale, low-frequency flow is linear. The linear equations for perturbations to a continuously stratified constant depth ocean at rest can be separated into vertical modes (e.g., Gill and Clarke, 1974; Moore and Philander, 1977) and in the following I will consider a single baroclinic mode. The horizontal equations for each vertical mode are nondimensionalized in standard equatorial fashion, viz., $(c/\beta)^{1/2}$ for length and $(c\beta)^{-1/2}$ for time. (In these expressions β is the northward gradient of the Coriolis parameter and c is the Kelvin wave speed for the vertical mode). The coordinates x and y will represent non dimensional distance eastward from the origin and northward from the equator.

At the very low frequencies of interest here, large scale waves carrying energy westward are Rossby waves while those carrying energy eastward are equatorial Kelvin waves. At low frequencies these waves have very large east-west scales and the motion can be assumed to be independent of x. By geostrophy,

$$v(\text{large scale}) = p_{x/y} = 0 \tag{2.1}$$

Consider now an irregularly shaped island with a well defined single eastern and a single western boundary. The island's northern most and southern most points are defined by y=a and y=b respectively. Analysis to be reported elsewhere shows that the boundary conditions for that island,

together with (2.1) and p and u independent of x imply that the irregular island is dynamically equivalent to an island which extends from y=b to y=a and is infinitesimally thin from east to west. Specifically, the infinitesimally thin island results of Cane and du Penhoat (1982) are valid for an irregular island provided

$$\varepsilon\omega << 1 \quad \text{and} \quad k\,\Delta x << 1 \tag{2.2}$$

where ε, Δx and k are, respectively, the nondimensional width of the boundary layer east of the island, half of the east-west extent of the island and the largest wave number of all large scale motion of significant amplitude near the island.

The Cane and du Penhoat (1982) results for an incident unit amplitude equatorial Kelvin wave striking a north south island are shown in Figure 1. The transmitted Kelvin wave has amplitude α and so by continuity the p and u fields west of the island for $y > a$ and $y < b$ have the form

$$p_W = \alpha\psi_0 \tag{2.3a}$$

$$u_W = \alpha\psi_0 \tag{2.3b}$$

where ψ_0 is the zeroth order Hermite function. West of the island and in its latitude range $b < y < a$, the boundary condition at the island and u and p independent of x imply

$$u_W = 0 \tag{2.4a}$$

$$p_W = D = \text{constant} \tag{2.4b}$$

As pointed out by Cane and du Penhoat, (2.4b) and (2.3a) cannot simultaneously hold without there being a discontinuity in pressure at y=a or y=b or both. By geostrophy, this leads to a δ function behaviour for u and so (2.3b) can be written as

$$u_W = \begin{cases} \alpha\psi_0 + A\delta(y-a) & \text{for } y \geq a \\ \alpha\psi_0 + B\delta(y-b) & \text{for } y \leq b \end{cases} \tag{2.5}$$

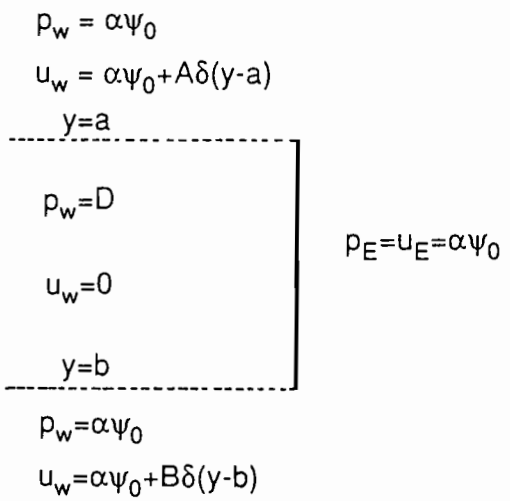

Figure 1

p and u fields for a low frequency equatorial Kelvin wave striking an island extending from y=b to y=a. The incoming Kelvin wave has $u=p=\psi_0$. P_E and u_E are given for the large-scale field outside the narrow western boundary layer east of the island. δ is the Dirac delta function.

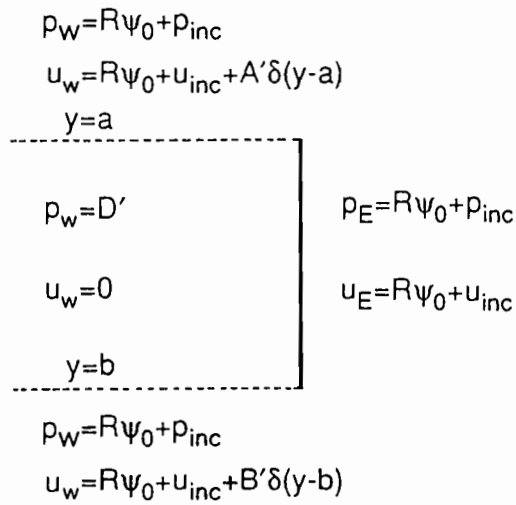

Figure 2

p and u fields for a low frequency Rossby wave striking an island extending from y=b to y=a. The incoming Rossby wave has $u=u_{inc}$ and $p=p_{inc}$. P_E and u_E are given for the large-scale field outside of the narrow boundary layer east of the island.

The transports A and B supply the western boundary current on the eastern side of the island. This boundary current redistributes mass to allow the transmitted Kelvin wave with amplitude α to leave the island. Cane and du Penhoat provide formulae for α, A, B and D.

A similar analysis can be carried out for the case of a Rossby wave striking a north-south island (see Fig. 2). Formulae for the amplitude R of the reflected Kelvin wave and A', B' and D' are provided by Cane and du Penhoat.

3. Several Island Theory

To examine the reflection and transmission at the western Pacific 'boundary', theory must be developed for the interaction of low frequency fields with several islands. Proceeding westward from the easternmost island, number the islands i = 1, 2, ... The western Pacific Ocean boundary appears to consist of seven major islands (see Figs. 3 and 4).

Consider low frequency transmission and reflection occurring at island i (see Fig. 5). Define T_i to be the amplitude of the Kelvin wave transmitted past island i due to the Kelvin wave coming into the island from the west and R_i as the amplitude of the Kelvin wave reflected from island i due to an incoming Rossby wave field from the east. Represent this Rossby wave field as

$$u = u^R_{i-1} , \qquad p = p^R_{i-1} \tag{3.1}$$

If α_i is the transmission coefficient for island i, then since $(R_{i+1}+T_{i+1})$ is the amplitude of the incoming Kelvin wave it follows that

$$T_i = \alpha_i \, (R_{i+1} + T_{i+1}) \tag{3.2}$$

where, from Cane and du Penhoat's single island results

$$\frac{1}{\alpha_i} = \frac{2(a_i-b_i)(1-I_i) + 2J_i[a_i\Psi_0(b_i) - b_i\Psi_0(a_i)] - [\Psi_0(a_i) - \Psi_0(b_i)]^2 - a_i b_i (J_i)^2}{2(a_i-b_i)} \tag{3.3}$$

In (3.3)

$$I_i = \int_{b_i}^{a_i} \Psi_0^2 \, dy \tag{3.4}$$

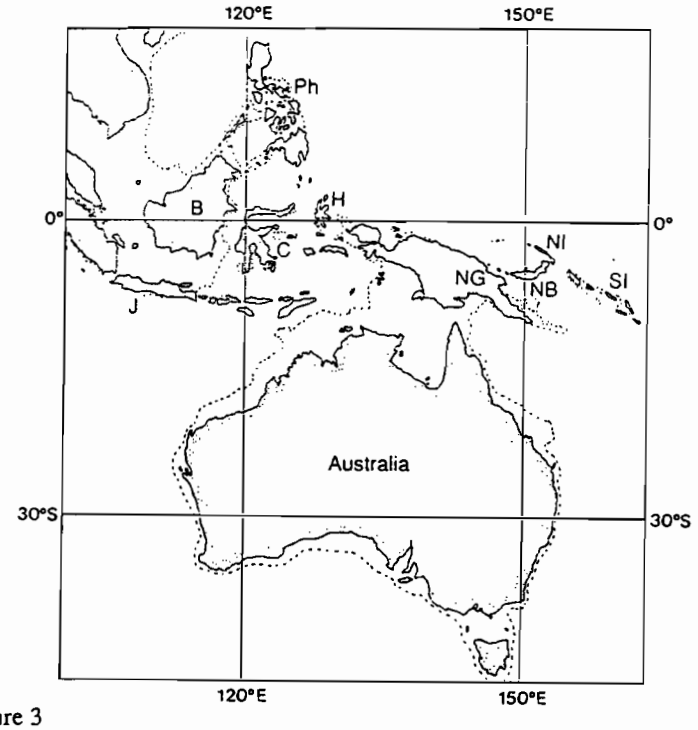

Figure 3

The western Pacific region under study. The dashed line is the 200 m isobath. SI=Solomon Islands, NB=New Britain, NI=New Ireland, NG=New Guinea, H=Halmahera, C=Celebes, Ph=Philippines, B=Borneo and J=Java.

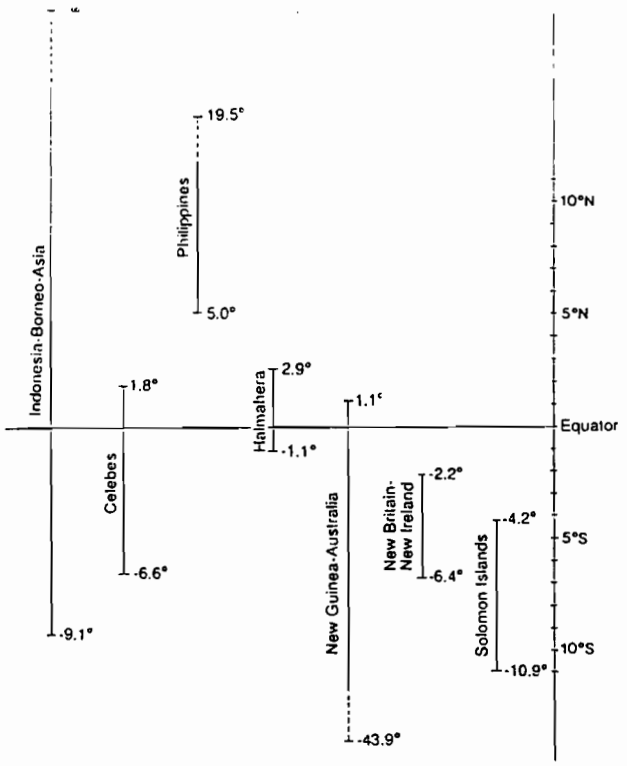

Figure 4

Thin island approximation to the western Pacific boundary. The northern and southern latitudes were based on the northern and southern limits of the 200 m isobath for each island.

and

$$J_i = \int_{b_i}^{a_i} \Psi_0 \, dy \tag{3.5}$$

Define A_i and B_i to be transport around the northern and southern tips of island i due to the incoming Kelvin wave and A_i' and B_i' to be similar transports for the incoming Rossby wave. The pressure D_i west of island i is associated with the incoming Kelvin wave and the pressure D_i' with the incoming Rossby wave. Then from the single island results of Cane and du Penhoat,

$$A_i = \lambda_i T_i \tag{3.6}$$

$$B_i = \mu_i T_i \tag{3.7}$$

$$D_i = \nu_i T_i \tag{3.8}$$

$$R_i \Psi_0(a_i) - D_i' + a_i A_i' + P_{i-1}^R(a_i) = 0 \tag{3.9}$$

$$-R_i \Psi_0(b_i) + D_i' + b_i B_i' - P_{i-1}^R(b_i) = 0 \tag{3.10}$$

$$2R_i[1-I_i] + D_i' J_i + A_i' \Psi_0(a_i) + B_i' \Psi_0(b_i) - K_i = 0 \tag{3.11}$$

$$-R_i J_i + A_i' + B_i' - U_i = 0 \tag{3.12}$$

where

$$\lambda_i = -\frac{1}{a_i - b_i} \left| \Psi_0(a_i) - \Psi_0(b_i) + b_i J_i \right| \tag{3.13}$$

$$\mu_i = \frac{1}{a_i - b_i} \left| \Psi_0(a_i) - \Psi_0(b_i) + a_i J_i \right| \tag{3.14}$$

$$\nu_i = a_i \lambda_i + \Psi_0(a_i) \tag{3.15}$$

and the K_i and U_i are known in terms of P^R_{i-1} and u^R_{i-1} as

$$K_i = \int_{b_i}^{a_i} \left(u^R_{i-1} + p^R_{i-1}\right) \Psi_0 \, dy \tag{3.16}$$

$$U_i = \int_{b_i}^{a_i} u^R_{i-1} \, dy \tag{3.17}$$

Fig. 5 shows the p and u fields east and west of island i.

To solve the problem posed by (3.2) and (3.6)-(3.12) for the unknowns A_i, B_i, D_i, T_i, R_i, A_i', B_i' and D_i' (i=1,2,...,7), I must find expressions for the Rossby wave fields u^R_{i-1} and p^R_{i-1} so that the K_i and U_i can be evaluated. The p and u fields west of island i consist of the required long Rossby wave field and the incoming Kelvin wave field with amplitude $T_{i+1}+R_{i+1}$. Thus we can obtain p^R_i and u^R_i by subtracting off the Kelvin wave field. From Figure 5 and Eqs. (3.2) and (3.6)-(3.12), the Rossby wave field west of island i is given by

$$p^R_i = \left[T_i\left(1-\frac{1}{\alpha_i}\right) + R_i\right] \Psi_0 + p^R_{i-1} \qquad y \geq a_i \tag{3.18a}$$

$$u^R_i = \left[T_i\left(1-\frac{1}{\alpha_i}\right) + R_i\right] \Psi_0 + u^R_{i-1} + (A_i' + \lambda_i T_i)\delta(y-a_i) \tag{3.18b}$$

$$p^R_i = \nu_i T_i + D_i' - T_i \Psi_0/\alpha_i \qquad b_i < y < a_i \tag{3.18c}$$

$$u^R_i = -T_i \Psi_0/\alpha_i \tag{3.18d}$$

$$p^R_i = \left[T_i\left(1-\frac{1}{\alpha_i}\right) + R_i\right] \Psi_0 + p^R_{i-1} \qquad y \leq b_i \tag{3.18e}$$

$$u^R_i = \left[T_i\left(1-\frac{1}{\alpha_i}\right) + R_i\right] \Psi_0 + u^R_{i-1} + (B_i' + \mu_i T_i)\delta(y-b_i) \tag{3.18f}$$

In (3.18) p^R_{i-1} and u^R_{i-1} can be similarly written in terms of T_{i-1}, R_{i-1}, D_{i-1}, A'_{i-1}, B'_{i-1}, p^R_{i-2} and u^R_{i-2}. This process can be repeated until i=1 when p^R_0 and u^R_0 are known incoming Rossby wave fields from the Pacific interior. Thus equations (3. 9)-(3.12) and (3.2) are all linear equations in terms of the 35 variables T_i, R_i, D_i', A_i' and B_i' (i=1,...,7). The form of the equations will differ depending on the relative positions of the islands. Note that since there is no eighth island, $(R_8 + T_8)$ is the given amplitude of the incoming Kelvin wave from the Indian Ocean.

The 35 linear equations can be written in terms of the 35 unknowns as a matrix problem

$$Ex = q \tag{3.19}$$

where x is the column vector consisting of elements T_1, R_1, D_1', A_1', B_1', ... A_7', B_7', q is a known vector with elements derived from T_8 and the incoming known Rossby p and u fields and E is the appropriate 35x35 matrix associated with the linear equations. E consists mainly of zeros and its structure is influenced by the relative positions of the islands. Equations (3.9)-(3.12) for i=1 indicate that A_1', D_1', A_1' and B_1' can be found separately but for structural convenience I kept the problem in the 35x35 form and solved it by standard techniques.

4. Application of the Theory to the Western Pacific

4.1 Validity of the theory

To apply the theory to the western Pacific, the criteria in (2.2) must first be checked. For $\beta = 2.29\text{x}10^{-11}\text{m}^{-1}\text{s}^{-1}$, $c = 2.74\text{ms}^{-1}$, an ENSO frequency of $2\pi/3$ years, k corresponding to a Kelvin wave or first mode Rossby wave and Δx corresponding to 2900km (half of total east-west distance occupied by the 7 island 'boundary'), the maximum magnitude of $k\Delta x$ and $\omega\epsilon$ is 0.2. Thus the requirement that this maximum magnitude be small compared with unity is marginally satisfied.

A further theoretical restriction is that the motion be linear and inviscid. While this is reasonable for the large scale Kelvin and westward propagating Rossby wave fields, it will break down for the strong currents at the island tips and east of the island. As noted by Cane and du Penhoat, friction and nonlinear effects will broaden these strong currents. The large scale balances on which the theory is based will be neglegibly affected, however.

4.2 Results

I briefly discuss some of the major results below. A more detailed discussion will be given in a future report.

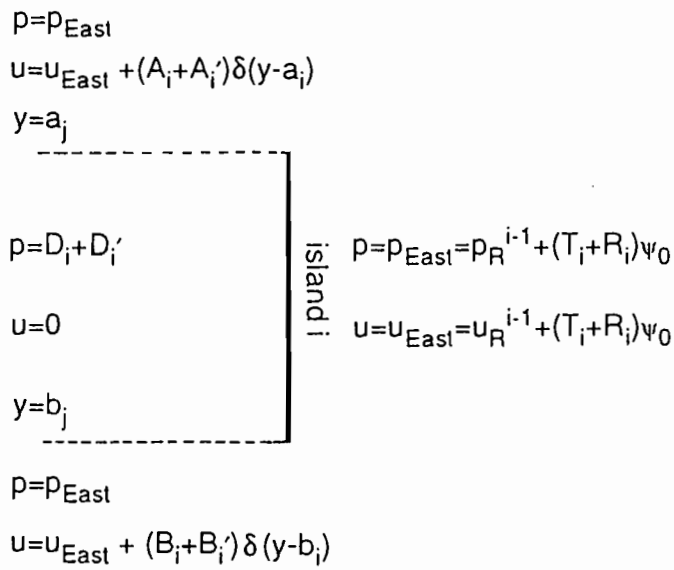

Figure 5

The u and p fields for reflection and transmission at island *i* due to an incident Rossby wave from island *i*-1 and an incident equatorial Kelvin wave from island *i*+1.

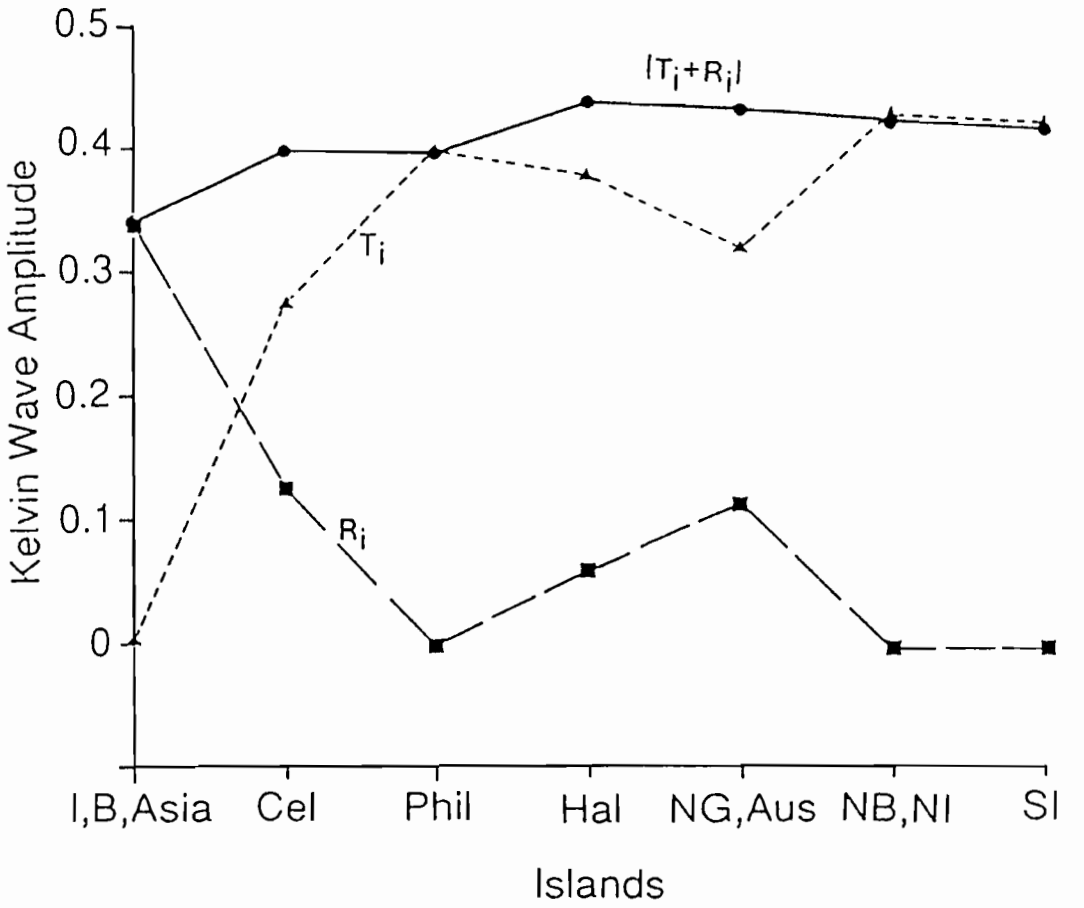

FIG.6. Kelvin wave amplitudes R_i, T_i and R_i+T_i for the seven islands forming the west Pacific boundary. I, B, Asia=indonesia, Borneo, Asia; Cel=Celebes, Phil=Philippines, Hal=Halmahera, NG=New Guinea, Aus=Australia, NB=New Britain, NI=New Ireland, SI=Solomon Islands.

a. Reflection and transmission of a model Rossby wave

Figure 6 shows the transmitted and reflection Kelvin wave amplitudes plotted for each island. The large value of R_7 compared to the other R_i indicates that the mode 1 Rossby wave energy is mainly reflected at the western most island (Indonesia/Borneo/Asia). The total Kelvin wave amplitude does not vary much from island to island because all islands are good to excellent transmitters of the Kelvin wave reflected at Indonesia/Borneo/Asia.

If the western Pacific boundary were a solid north-south wall then the magnitude of the Kelvin wave energy flux reflected back into the Pacific compared to the incident mode 1 Rossby wave energy flux would be 0.5 (Clarke, 1983). The ratio for the 7 island model is 0.34, i.e., about two-thirds of that expected for a solid wall.

The solution also indicates that $D_3 + D_3'$ is substantial and that therefore interannual sea level fluctuations should be observed along Australia's western coast. These sea level fluctuations should be in phase and of constant amplitude. This is in good agreement with observation (Pariwono et al, 1986).

Strong jets occurring westward of some island tips are suggested by the model. These have been observed in numerical models (Luther, personal communication) and recent observations near the Philippines suggest a westward jet from the southern tip [Lukas (1988), Hacker and Firing (1988)]. For the model incoming mode 1 Rossby wave the strongest jet is predicted at the southern end of the Philippines. If this mode were to have a sea level amplitude of 7 cm at the equator, then the upper layer transport in a 1½ layer model with upper layer depth of 100 m would be about 6 Sverdrups at the southern end of the Philippines.

b. Reflection and transmission of an Indian Ocean equatorial Kelvin wave

The western most island (Indonesia/Borneo/Asia) prevents transmission of almost all of an incoming Indian Ocean Equatorial Kelvin wave. Only small transmission is expected because this island extends further north and south than the north-south scale of the incoming Kelvin wave. A Kelvin wave eventually reaches the Pacific by proceeding past the other islands, but its energy flux is less than 5% of the original energy flux.

Acknowledgements

I am very thankful to Steve VanGorder, Paula Tamaddoni-Jahromi and Pat Klein. Steve efficiently obtained all the numerical results and patiently checked my mathematics while Paula and Pat expertly typed the manuscript and drafted the figures. This work was supported by NSF Grant OCE-8723157.

References

Battisti, D.S., 1988: Dynamics and thermodynamics of interannual variability in the tropical atmosphere/ocean system. Ph.D. Thesis, University of Washington, 152 pp.

Cane, M.A., and Y. du Penhoat, 1982: The effect of islands on low frequency equatorial motions. ***J. Mar. Res.*, 40,** 937-962.

Clarke, A.J., 1983: The reflection of equatorial waves from oceanic boundaries. ***J. Phys. Oceanogr.*, 13,** 1193-1207.

Gill, A.E. and A.J. Clarke, 1974: Wind-induced upwelling, coastal currents and sea level changes. ***Deep-Sea Res.*, 21,** 325-345.

Hacker, P., and E. Firing, 1988: Acoustic doppler current observation of the Mindanao current during WEPOCS III. ***Trans. Am. Geophys. Union*, 69,** 1227.

Lukas, R., 1988: Hydrographic observations of the Mindenao current during WEPOCS III, ***Trans. Am. Geophys. Union*, 69,** 1227.

Moore, D.W., and S.G.H. Philander, 1977: Modeling of the tropical oceanic circulation. ***The Sea*, Vol. 6,** E.D. Goldberg, I.N. McCave, J.J. O'Brien and J.H. Steele, Eds., Wiley, 319-362.

Pariwono, J.I., J.A.T. Bye and G.W. Lennon, 1986: Long-period variations of sea level in Australasia. ***Geophys. J. R. Astr. Soc.*, 87,** 43-54.

Equatorial Entrainment Zone : the Diurnal Cycle

Roland W. GARWOOD, Jr[1], P.C. CHU[1], Peter MULLER[2] and Niklas SCHNEIDER[2]

[1] *Department of Oceanography, Naval Postgraduate School*
Monterey, CA 93943 - U.S.A.

[2] *Department of Oceanography, University of Hawaii at Manoa*
Honolulu, HI 96822 - U.S.A.

Abstract. A model for the entrainment zone of the equatorial turbulent boundary layer is used to compute the turbulent fluxes of buoyancy and momentum and the dissipation of turbulent kinetic energy in the pycnocline well below a relatively shallow (order 20 m) quasi-homogeneous surface layer. In the presence of a steady westward wind stress, diurnal variation of the surface buoyancy flux triggers dynamic instabilities that "ripple" downward (order 100 m) during the night into the pycnocline above the undercurrent core, causing a strong diurnal cycle in dissipation and in the depth of penetration of the turbulent fluxes into the upper 100-150 meters of the water column.

1. Introduction

It may seem that observations of the rate of dissipation of turbulent kinetic energy, $\varepsilon(z)$, in the equatorial oceans have raised as many new questions as have been resolved. New investigations have been stimulated concerning the importance of the undercurrent shear (Crawford and Osborn, 1981), sampling biases and the relative importance of spacial (meridional) and temporal (diurnal) structures to the dissipation field (Moum *et al.*, 1986), the relationship between dissipation and eddy mixing coefficients (Peters *et al.*, 1988), and the computation of Reynolds stress with dissipation-method techniques accepted in non-equatorial domains (Dillon *et al.*, 1989).

Although an overall understanding of the dynamics of equatorial turbulence has not yet emerged, consistent descriptions of the diurnal cycle of dissipation on the equator have been documented (Paka and Fedorov, 1982; Peters *et al.*, 1988; and Moum *et al.*, 1989). However, none of the mixed layer model applications at the equator to date (including Hughes, 1980; Schopf and Cane, 1983; and Garwood *et al.*, 1985) appear to have adequate physics to explain the deep diurnal penetration of dissipation below the well-mixed surface layer. Although Garwood *et al.* (1985) showed that the northward component of planetary rotation may act with the Reynolds stress to increase the depth of the well-mixed layer, this mechanism cannot explain the diurnal increase of dissipation in the pycnocline well below the surface layer.

The scientific objective of a collaborative equatorial mixed layer study by the Departments of Oceanography at the Naval Postgraduate School and the University of Hawaii is to understand and construct models for the dynamics and thermodynamics of the equatorial and tropical mixed layer system. Here we report model results that offer an explanation for how turbulence that is locally generated by surface forcing can "penetrate" rapidly and deeply into the not-so-well-mixed zone between the surface well-mixed layer and the undercurrent core. The Naval Postgraduate School mixed layer model (Garwood, 1977) is augmented to include a finite-thickness entrainment zone that was postulated for possible general application

ORSTOM
CENTRE DOCUMENTATION
Montpellier

F 30230

at all latitudes (Garwood, 1987), but has been neglected at the equator. The equatorial mixed layer system appears to be an ideal location to verify this phenomenon because of the strong vertical shear, the lack of rotation and the nearly steady surface wind.

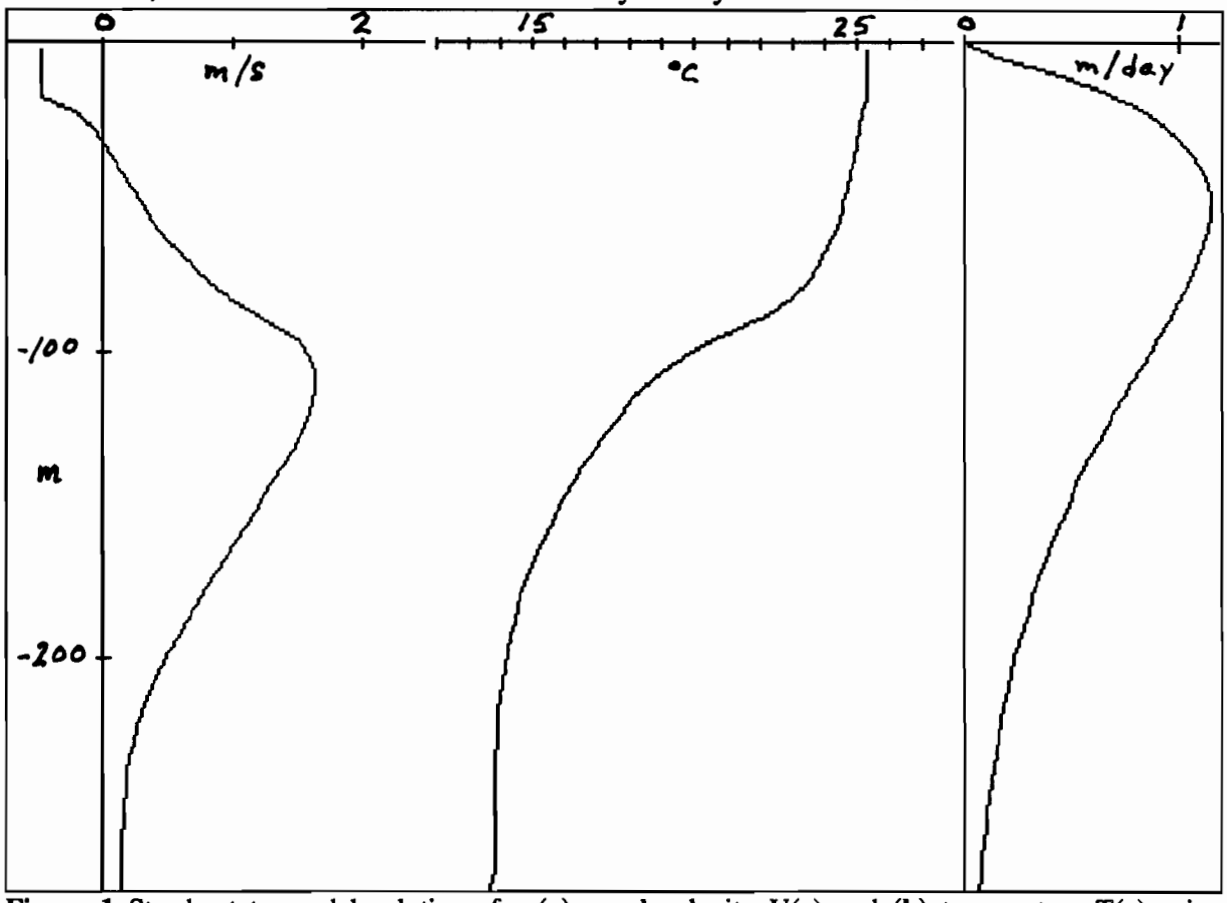

Figure 1 Steady-state model solutions for (**a**) zonal velocity U(z) and (**b**) temperature T(z) using prescribed (**c**) vertical velocity W(z), and constant surface wind stress and constant heating.

2. Steady-State Finite-Thickness Entrainment Zone With Upwelling

The mixing model for the entrainment zone is based upon two hypotheses. Firstly, there will be no significant turbulent fluxes of mass, momentum or buoyancy unless the gradient Richardson number is less or equal to a critical value, $Ri \leq Ri_{CR} \sim \frac{1}{4}$. Secondly, if a dynamic instability is initiated, the mixing ratios of momentum and buoyancy will be equal and just sufficient to achieve dynamic stability. This method has been established by Adamec *et al.* (1981), but has not been applied previously to flows at the equator. The value of Ri_{CR} that is appropriate for the entrainment zone at the equator appears to be about ¼ or somewhat larger (Gregg *et al.*, 1985 and Peters *et al.*, 1988). Possibly, Ri_{CR} should not even be constant in time. If internal wave energy is propagated vertically (Muller, 1976) in the entrainment zone, it is possible that the vertical convergence of pressure transport of turbulent kinetic energy contributes significantly to the turbulent kinetic energy budget in the entrainment zone (Dillon *et al.*, 1989). This extra source of energy would cause the value of Ri_{CR} to be greater than the commonly assumed value of ¼. A range of values up to ½ have been tested, but the results shown here were all derived with the traditional value of $Ri_{CR} = \frac{1}{4}$.

Implicit in the application of this entrainment model is the assumption that the entrainment zone is marginally dynamically stable. A slight decrease in the downward buoyancy flux at the top of the entrainment zone will trigger a dynamic instability that may "ripple" down a considerable distance until it reaches a part of the water column that is sufficiently stable to stop the vertical propagation of the event.

Figures 1 (a) and (b) show profiles of the mean zonal velocity and the temperature that are generated by spinning up the mixed layer-entrainment model to an approximate steady state under the conditions of a time-invariant wind stress, a diurnally varying surface buoyancy (heat) flux, a prescribed vertical velocity (Figure 1 c) and a prescribed zonal pressure gradient (not shown) that decays exponentially in depth (Dillon *et al.*, 1989) with a zonal surface slope, η_x=-0.5x10^{-7}. For this case the net downward surface heat flux is taken to be Q_0 = 100 watts/m^2. The wind stress is westward, τ_x = -10^{-4} Nm^{-2} and τ_y = 0.

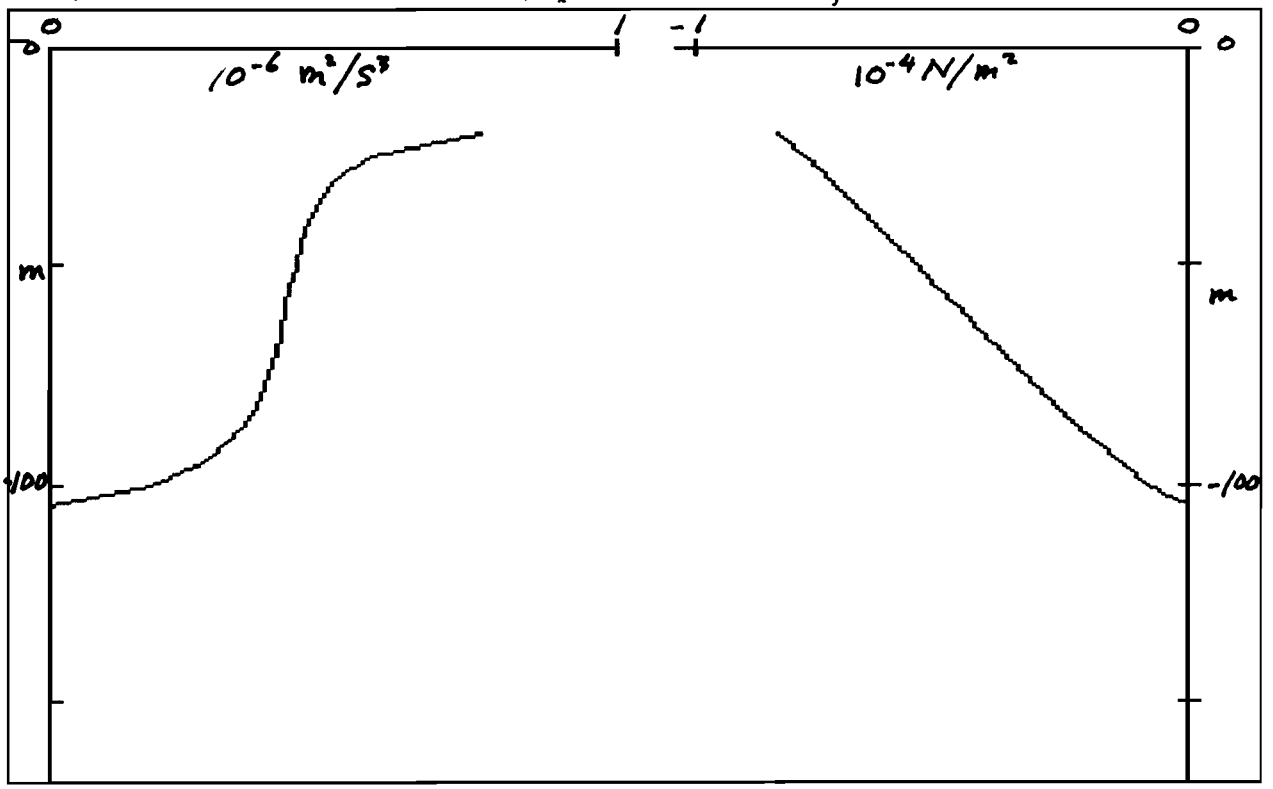

Figure 2 (a) Dissipation and (b) Reynolds' stress profiles for constant surface forcing case.

With no surface buoyancy flux, at mid latitudes planetary rotation would limit the depth of penetration of momentum and kinetic energy from the wind to Rossby and Montgomery's (1935) neutral planetary boundary layer scale ~u$_*$/f, where u$_*$ is the surface friction velocity and f is the Coriolis parameter. This also appears to be the scale size of the potential maximum thickness of the "entrainment zone" below a shallowing mixed layer that is surface-heated and wind-stirred (Garwood, 1987). Under the influence of a net downward surface buoyancy flux B_0>0, the thickness of the surface well-mixed layer above the entrainment zone is expected (Muller *et al.*, 1984) to be proportional to be equal to one half the Obukhov length scale, h=L/2≈u$_*^3$B$_0^{-1}$ (Obukhov, 1946), and the underlying entrainment zone reaches a maximum thickness of approximately 0.2u$_*$/f. At higher latitudes, the entrainment zone has typically been approximated as a discontinuity. As f→0, the entrainment zone would thicken indefinitely were it not for advection. At the equator, in the absence of rotation, a mean upwelling velocity

W>0 enables a steady state in the entrainment zone of thickness δ~100 m beneath the well-mixed surface layer of depth h~20 m. Figure 2 shows that the dissipation and the Reynolds stress terminate at a depth of about 110 m, well below the well-mixed layer.

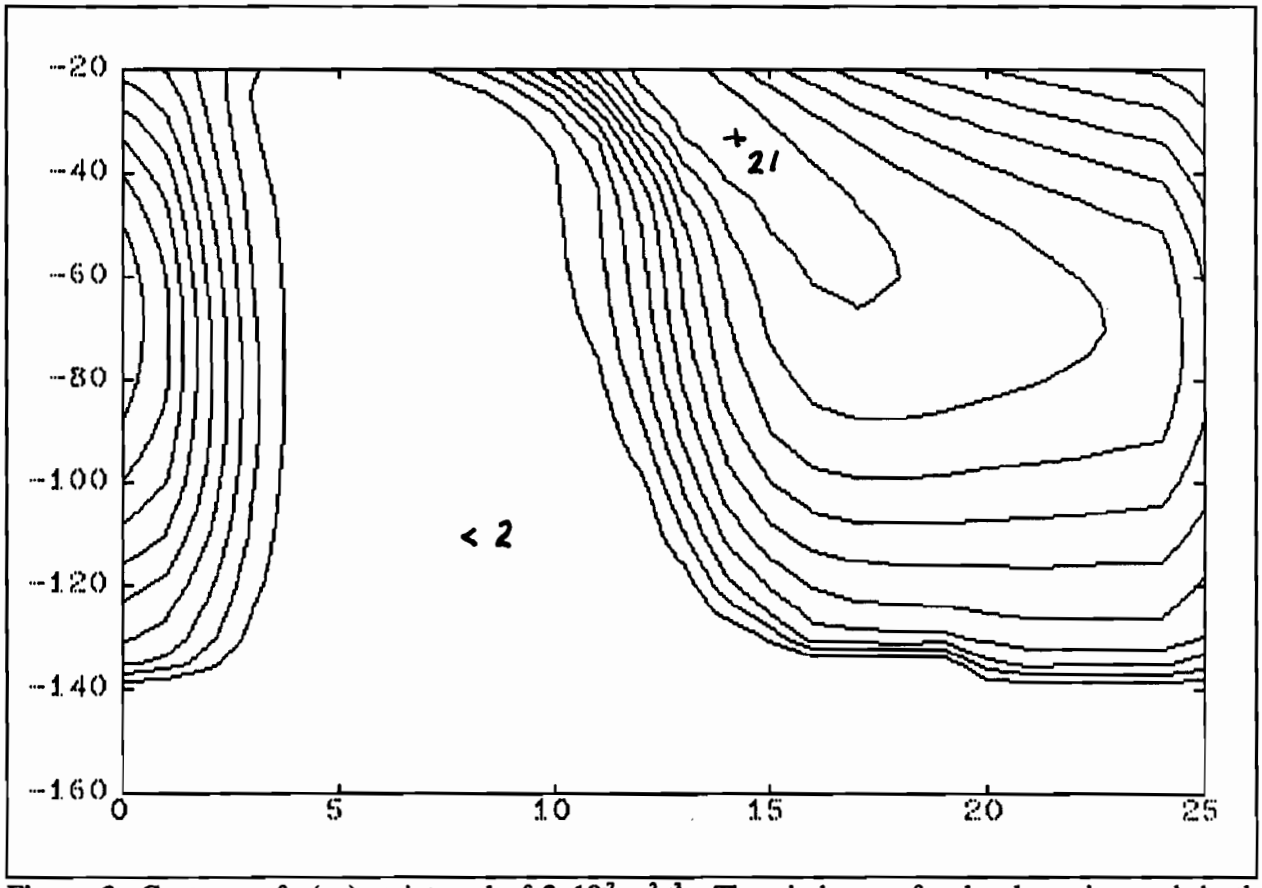

Figure 3 Contours of $\varepsilon(t,z)$ at interval of 2×10^{-7} m^2s^{-3}. Time is hours after local sunrise, and depth is meters below surface.

3. Response to Diurnal Surface Buoyancy Flux and Constant Wind Stress

After the model has come to an approximate steady-state condition, with the profiles of velocity, temperature, dissipation and stress shown in Figures 1 and 2, the surface heat flux is changed to include an incident solar radiation having a maximum value of 800 watts/m^2 at noon. The total heat flux plus radiation is adjusted so that the daily-average net heat input at the surface is still 100 watts/m^2.

Although the values of the surface fluxes, averaged over one day, are unchanged, the modeled mixed layer-entrainment zone system requires a few days to again achieve a near equilibrium state. Four days after initiating the diurnally-varying surface heat flux, a cyclical steady state is achieved approximately. The diurnal response of the dissipation (Figure 3) shows that the dissipation of turbulent kinetic energy below the mixed layer falls to near zero from about 3 hours after sunrise until almost sunset. At the top of the entrainment zone, z=-20 m, the maximum dissipation rate of 2.1×10^{-7} m^2s^{-3} occurs at about hour 13 (7 p.m. local time). The time of maximum dissipation is depth dependent. The time of maximum

dissipation occurs later and later with depth. The peak dissipation at z=-120 m does not occur until just before sunrise.

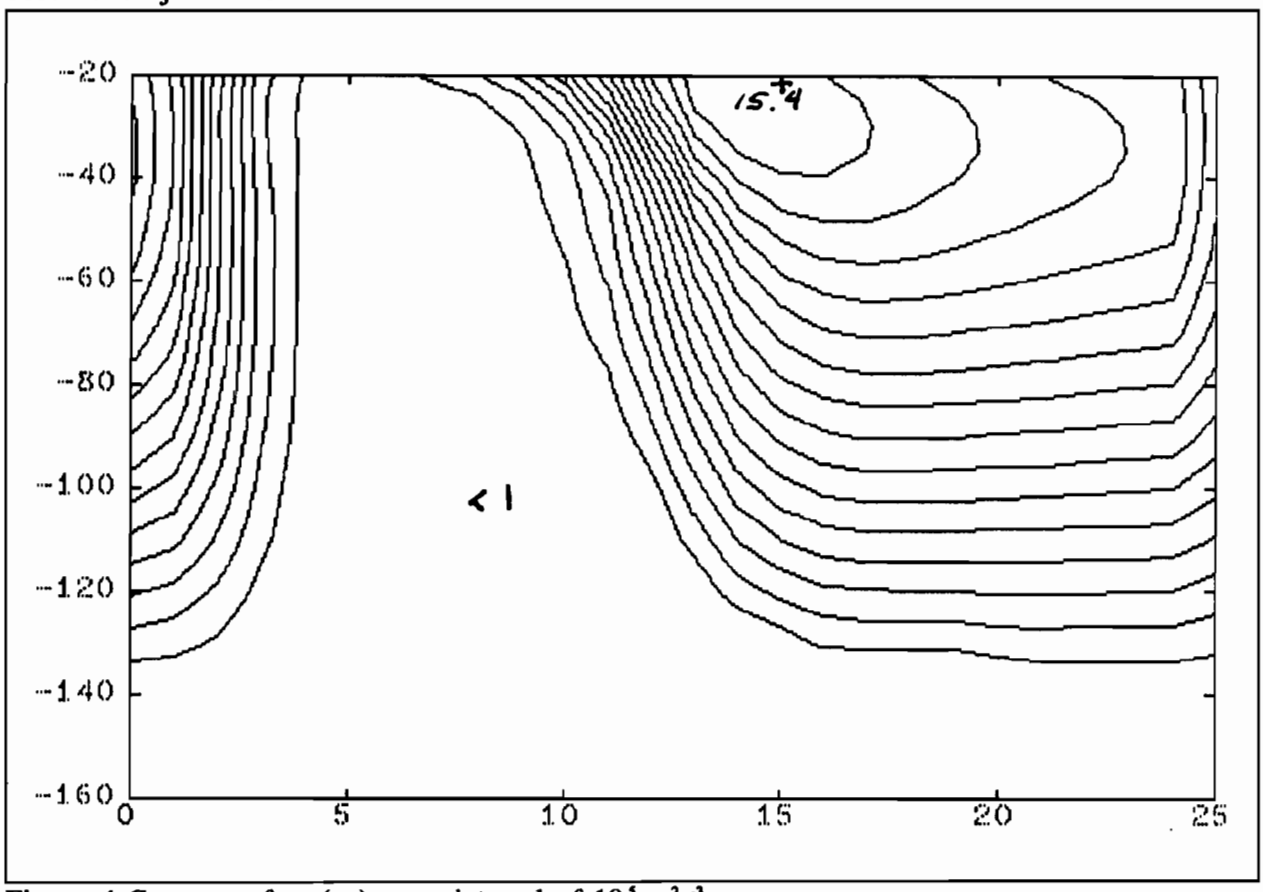

Figure 4 Contours of uw(t,z) at an interval of 10^{-5} m^2s^{-3}.

The structures of the vertical fluxes of momentum (Figure 4) and heat (Figure 7) also have a strongly diurnal behavior. With the diurnal variation in the prescribed net heat flux, the diurnal dependence for the turbulent heat flux is not surprising. However, the maximum downward heat flux (exceeding 400 watts/m^2) at z=-100 m doesn't occur until about 14 hours after local noon (hour 20). The vertical dependence of the zonal stress also has a strong diurnal dependence, even though the surface stress is held constant at 10^{-4} Nm^{-2}. It is noteworthy, also, that the maximum stress near the top of the entrainment zone at z≈-30 m exceeds the surface stress by more than 50%. This phenomenon is explained by the daytime storage of momentum in the overlying well-mixed layer. This momentum is released to the re-activated entrainment zone by the dynamic instability that starts in the late afternoon and continues throughout the night.

In spite of the large diurnal variation in the fluxes, the value of the gradient Richardson number changes only slightly in the region between z=-30 m and z=-120 m (Figure 5). In the turbulently inactive region, Ri increases because of net effects of vertical advection and the baroclinic component of the horizontal pressure gradient. If it weren't for advection and the horizontal pressure gradient, the value of Ri would be identically equal to the critical value for this model solution.

The results of these solutions here suggest that the intensity of turbulence and mixing in the entrainment zone does not depend upon the gradient Richardson number, to a first order. To demonstrate this point, the effective vertical eddy viscosity, $K_M = -uw(\partial U/\partial z)^{-1}$, was

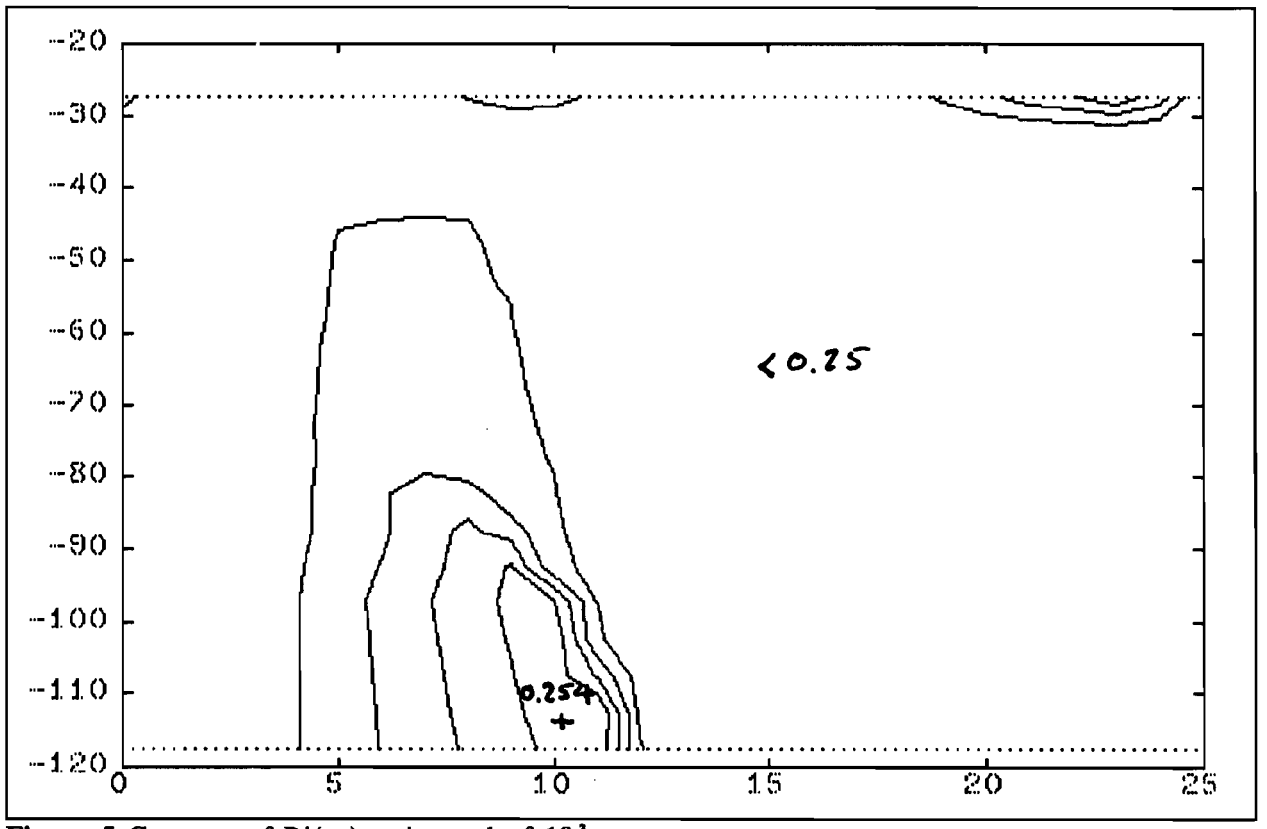

Figure 5 Contours of Ri(z,t) at interval of 10^{-3}.

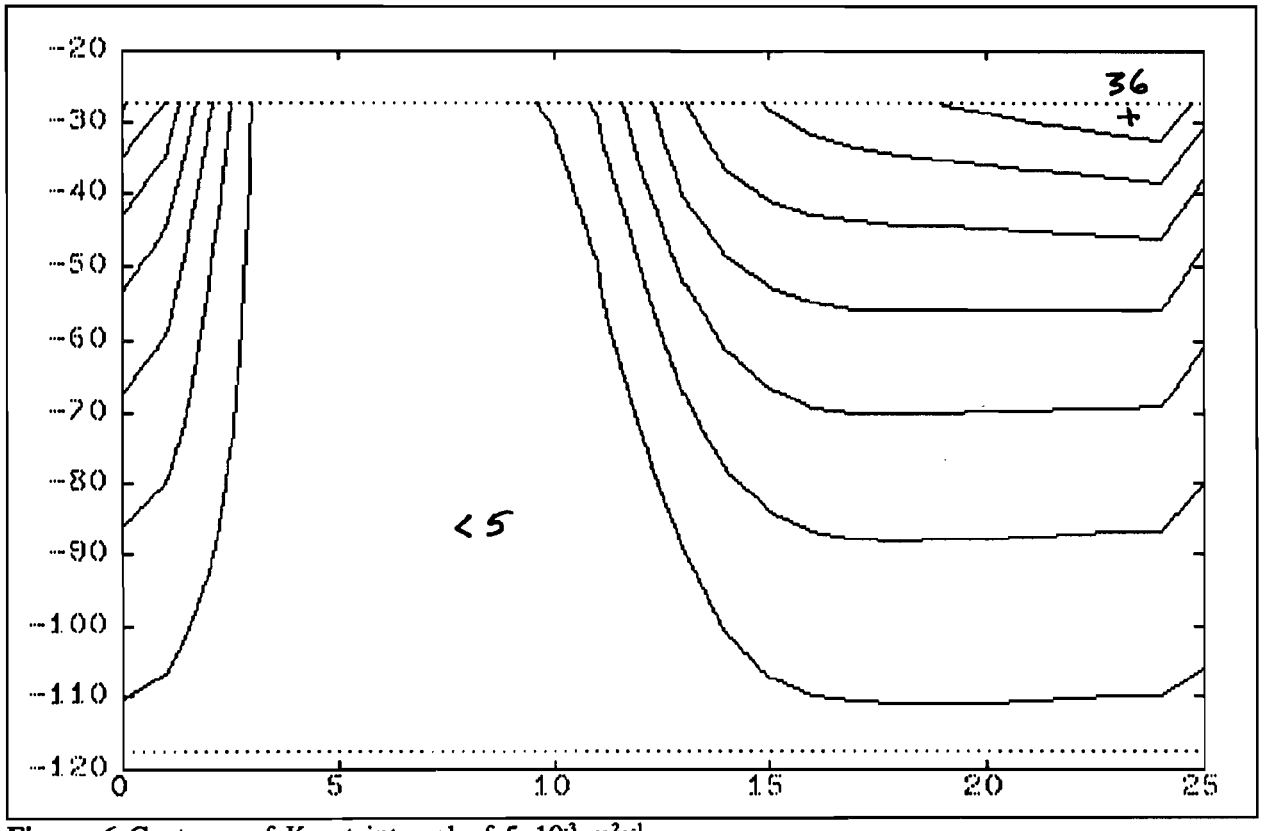

Figure 6 Contours of K_M at interval of $5x10^{-3}$ m^2s^{-1}.

computed (Figure 6). As can be seen K_M varies between 0 and more than $30x10^{-3}$ m^2s^{-1}, while Ri is nearly constant. This result supports the conclusion of Peters *et al.* (1988) that earlier models for KM(Ri) are inadequate for application at the equator.

4. Conclusions

Although the equatorial momentum budget is still not well understood, realistic vertical profiles for the zonal velocity and the temperature are predicted by application of typical values of local surface forcing, the pressure field, and the vertical velocity, together with the proposed mixed layer-entrainment model. Vertical mixing adjusts on a several-day time scale to cause a near equilibrium balance between advection and vertical mixing.

Entrainment mixing is modulated strongly at depths well below the relatively shallow well-mixed surface layer by the diurnal cycle in the surface buoyancy flux. Instabilities initiated just below the surface layer ripple down into the water column and reach the deepest extent only after many hours. This causes a considerable phase delay in dissipation and in the turbulent fluxes, relative to the phase of the surface buoyancy flux.

This study needs to be widened to address several questions:

i) What is the appropriate value for the critical Richardson number at the equator, and is this really a universal constant for all oceanic entrainment zones?

ii) What is the effect of transient wind events, with changes in both speed and direction? To address this second question, the prognostic model needs to be made fully three-dimensional, with model-computed advection instead of prescribing the non-local terms of the momentum budget, as done for this initial simulation.

iii) Does this dynamic instability process influence the region below the undercurrent, also a high-shear zone? Numerical experimentation indicates that this region may become dynamically unstable, depending upon the vertical velocity field and the baroclinicity of the flow. Turbulence beneath the undercurrent does not appear to be as strong in this region, however, as it is above the undercurrent core.

iv) What is the role of asymmetry about the equator in the surface forcing? Meridional fluxes may be significant, and even transient meridional velocity events they may have an important role in determining the equilibrium state at the equator.

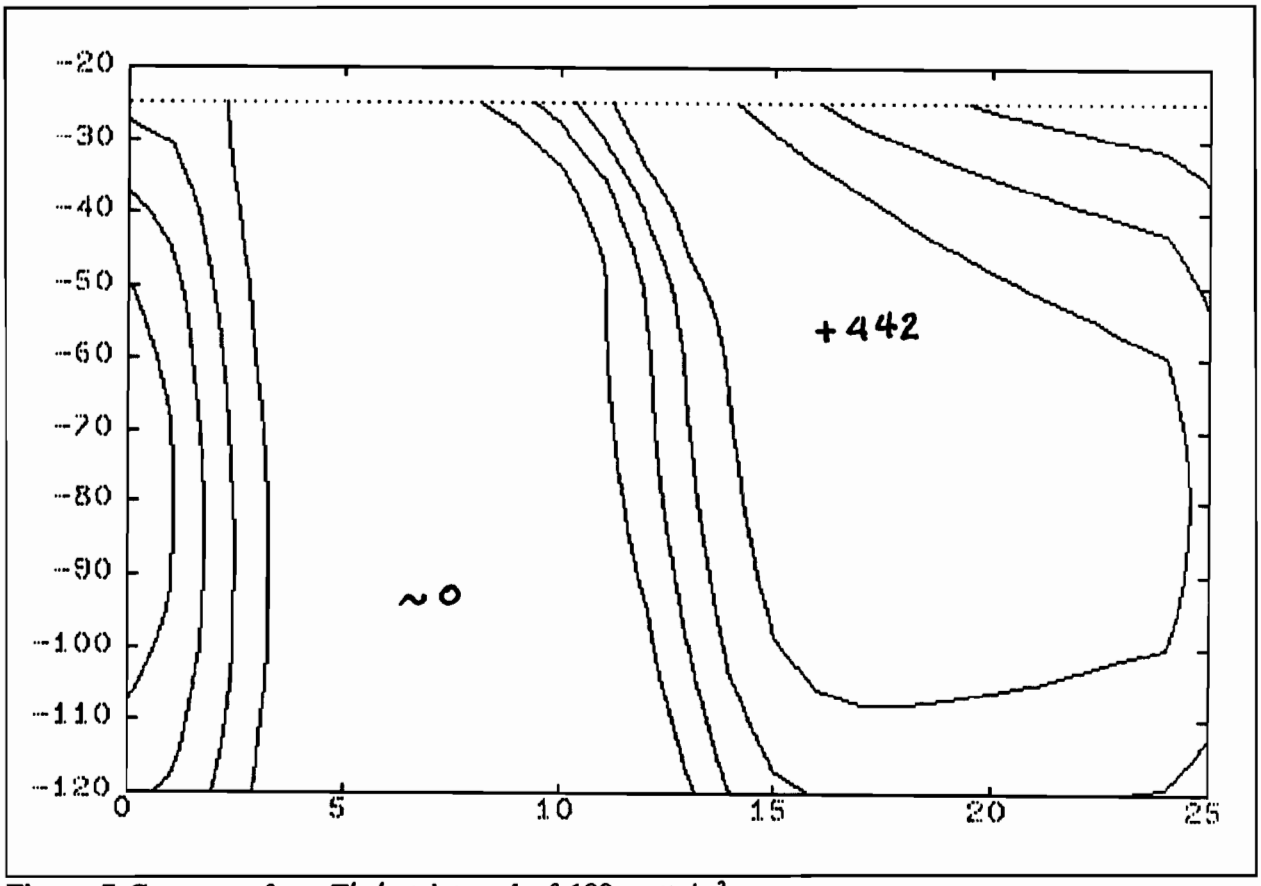

Figure 7 Contours of $-\rho c_p \overline{T'w'}$ at interval of 100 watts/m^2.

References

Adamec, D. D., R. L. Elsberry, R. W. Garwood, Jr., and R. L. Haney, 1981: An embedded mixed layer ocean circulation model. *Dyn. Atmos. Oceans*, **6**, 69-96.

Bryden, H. L., and E. C. Brady, 1985: Diagnostic model of the three-dimensional circulation in the upper equatorial Pacific Ocean. *J. Phys. Oceanogr.*, **15**, 1255-1273.

Crawford, W. R., and T. R. Osborn, 1981: Control of equatorial ocean currents by turbulent dissipation. *Science*, **212**, 439-540.

Dillon, T. M., J. N. Moum, T. K. Chereskin, and D. R. Caldwell, 1989: Zonal momentum balance at the equator. *J. Phys. Oceanogr.*, **19**, 561- 570.

Garwood, R. W., Jr., 1977: An oceanic mixed layer model capable of simulating cyclic states. *J. Phys. Oceanogr.*, **7**, 455-468.

Garwood, R. W., Jr., 1987: Unsteady shallowing mixed layer. *Proceedings 'Aha Huliko'a*, Hawaiian Winter Workshop, January 1987, Hawaii Inst. of Geophys. Special Publication, P. Muller and D. Henderson, Eds., 119-129.

Garwood, R. W., Jr., P. Muller, and P. C. Gallacher, 1985: Wind direction and equilibrium mixed layer depth in the tropical Pacific Ocean. *J. Phys. Oceanogr.*, **15**, 1332-1338.

Gregg, M. C., H. Peters, J. C. Wesson, N. S. Oakey, and T. J. Shay, 1985: Intensive measurements of turbulence and shear in the equatorial undercurrent. *Nature*, **318**, 140-144.

Moum, J. N., and D. R. Caldwell, 1989: Mixing in the equatorial surface layer. *J. Geophys. Res.*, **94**, 2005-2021.

Moum, J. N., D. R. Caldwell, C. A. Paulson, T. K. Chereskin, and L. A. Regier, 1986: Does ocean turbulence peak at the equator? *J. Phys. Oceanogr.*, **16**, 1991-1994.

Muller, P., 1976: On the diffusion of momentum and mass by internal gravity waves. *J. Fluid Mech.*, **77**, 789-823.

Muller, P., and R. W. Garwood, Jr., 1988: Mixed layer dynamics: Progress and new directions. *EOS*, **69**, 2-12.

Muller, P., R. W. Garwood, Jr., and J. P. Garner, 1984: Effect of vertical advection on the dynamics of the oceanic surface mixed layer. *Annales Geophys.*, **2**, 387-398.

Obukhov, A. M., 1946: Turbulence in an atmosphere with a nonuniform temperature. *Trudy Inst. Teoret. Geofiz. AN SSSR*, **1**; translated and reprinted in *Bound.-Layer Meteor.*, **2**, 1971.

Hughes, R. L., 1980: On the equatorial mixed layer. *Deep-Sea Res.*, **27A**, 1067-1078.

Paka, V. T., and K. N. Fedorov, 1982: Influence of the thermal structure of the upper ocean layer on the development of turbulence. Izvest., *Atmos. Ocean Phys.*, **18**, 134-138.

Peters, H., M. C. Gregg, and J. M. Toole, 1988: On the parameterization of equatorial turbulence. *J. Geophys. Res.*, **93**, 1199-1218.

Rossby, C. G., and R. B. Montgomery, 1935: The layer of frictional influence in wind and ocean currents. *Pap. Phys. Oceanogr. Meteor.*, **3**, 101 pp.

Schopf, P. S., and M. A. Cane, 1983: On equatorial dynamics, mixed layer physics and sea surface temperature. *J. Phys. Oceanogr.*, **13**, 917-935.

Weare, B. C., P. T. Strub, and M. D. Samuel, 1981: Annual mean surface heat fluxes in the tropical Pacific Ocean. *J. Phys. Oceanogr.*, **11**, 705-717.

Wyrtki, K., 1981: An estimate of equatorial upwelling in the Pacific. *J. Phys. Oceanogr.*, **11**, 1205-1214.

Wyrtki, K., and G. Meyers, 1976: The trade wind field over the Pacific Ocean. *J. Appl. Meteor.*, **15**, 694-704.

A New Ocean GCM for Tropical Ocean and ENSO Studies

Peter R. GENT

NCAR, P.O. Box 3000,
Boulder, CO 80307 - U.S.A.

ABSTRACT

A new reduced gravity, primitive equation model of the upper equatorial ocean has been developed by Gent and Cane (1989). It has been configured to simulate the annual cycle in the tropical Pacific Ocean. It is forced by the monthly winds from Rasmusson and Carpenter (1982) and a new heat flux formulation from Seager et al. (1988). The coefficients of vertical eddy viscosity and conductivity depend upon the Richardson number of the flow. With this mixing a deep warm pool forms in the Western Pacific, increasing the west-east gradient of the thermocline and equatorial undercurrent. The model has been diagnosed as to what factors maintain this deep warm pool.

1. Heat flux parameterization.

Heat Flux = Incoming Solar - Latent - (Sensible + Longwave)

* Incoming Solar Flux = $(1 - A)\,(1 - 0.62\,C + 0.0019\,\theta)\,Q_0$
  A is albedo, C is % cloud cover, θ is solar altitude, Q_0 is clear sky flux

* Latent Heat Flux = $\rho_a\, C_E\, L\, |\mathbf{u}|\, (1-\delta)\, q_s(SST)$
  $|\mathbf{u}|$ is wind speed with minimum of 4 m s^{-1}, $q_s(SST)$ is saturation humidity, and humidity factor δ is related to relative humidity, δ_{rh},

$$\delta\, q_s(SST) = \delta_{rh}\, q_s(T_a)$$

* Sensible + Longwave Flux = α (SST - T*)

[$A = 0.06$, $\delta = 0.78$, $\alpha = 1.8$ m s^{-1}, $T^* = 2.8°C$]

2. Vertical mixing coefficients.

* Diffusivity: $\nu = 10^3\,(1+10R_i)^{-2} + \nu_B$ $\qquad cm^{-2}\ s^{-1}$

* Conductivity: $K = 10^3\,(1+10R_i)^{-3} + K_B$ $\qquad 0 < R_i < 3$

$\nu_B\,(z)$ varies between 1 and 2 $cm^2\ s^{-1}$
$K_B\,(z)$ varies between 1/2 and 1 $cm^2\ s^{-1}$

In the COARE volume, R_i is nearly always > 3, so that the vertical mixing is done solely by the background values ν_B and K_B.

Sections of average temperature and zonal velocity in January along the equator down to 400 m and along 160° E down to 500 m are shown in Figures 1-4.

ORSTOM
CENTRE DOCUMENTATION
Montpellier

F 30231

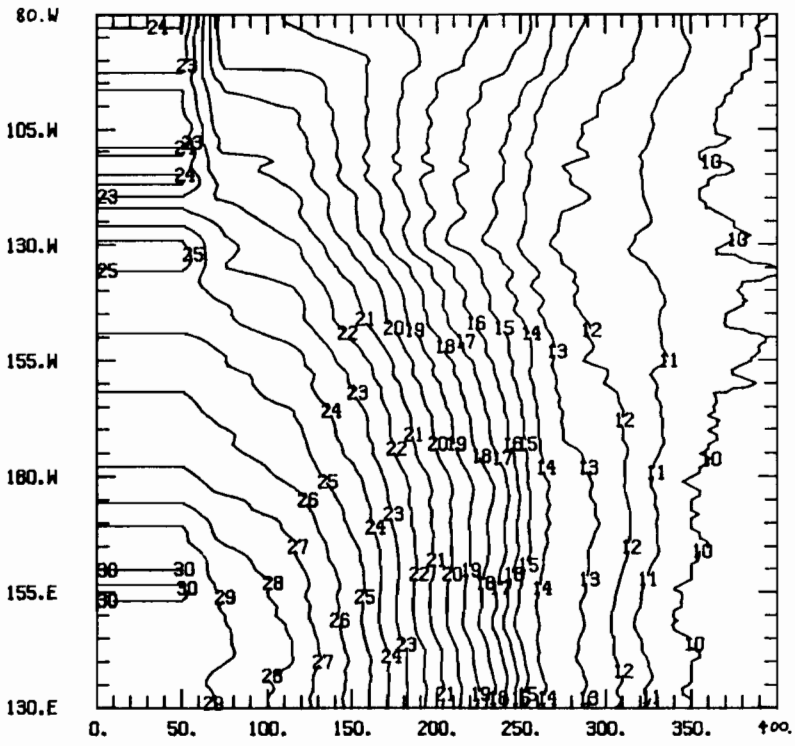

FIG.1. Average January Temperature (°C) along Equator.

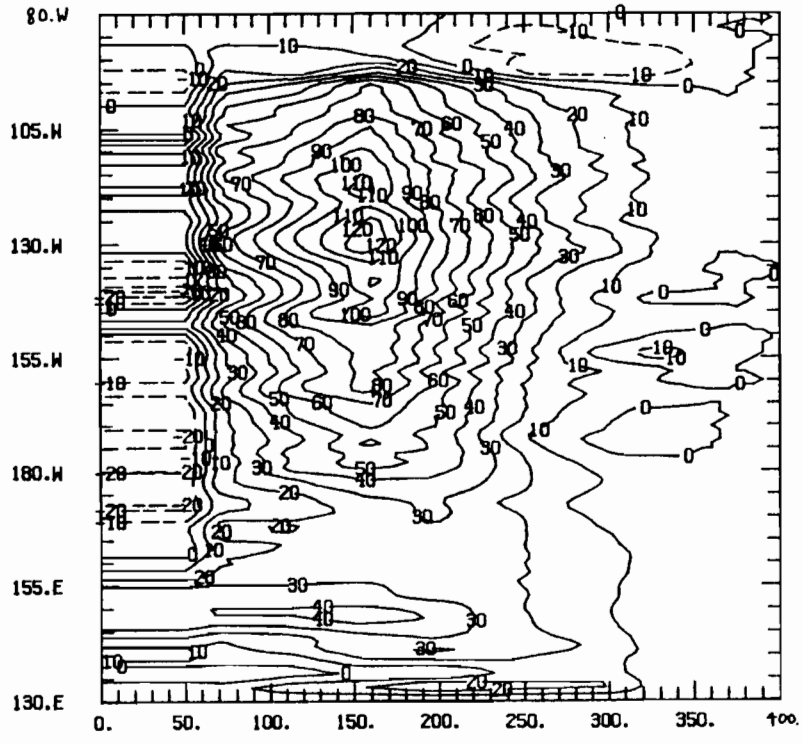

FIG.2. Average January Zonal velocity ($cm.s^{-1}$) along Equator.

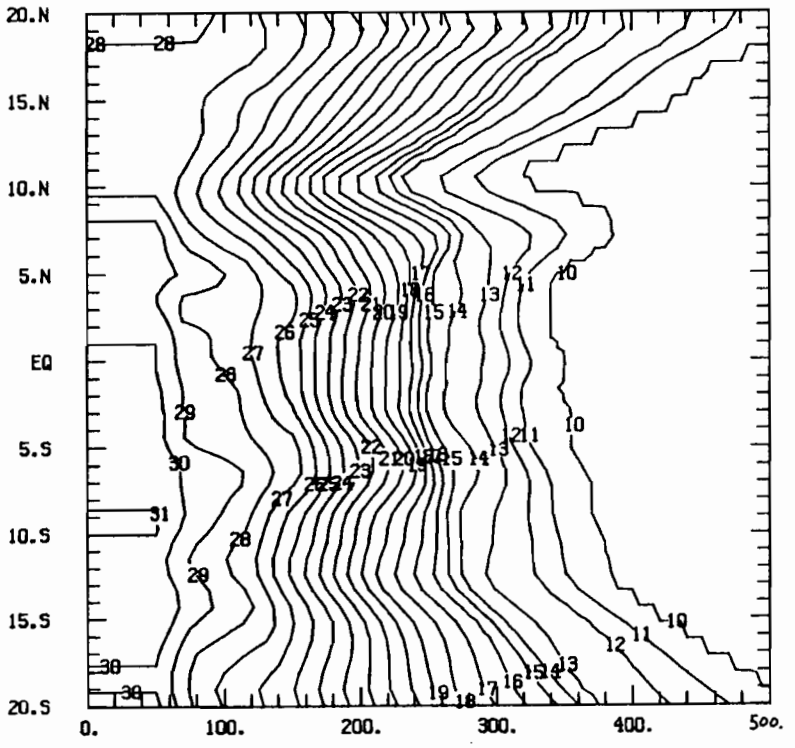

FIG.3. Average January Temperature (°C) along 160°E.

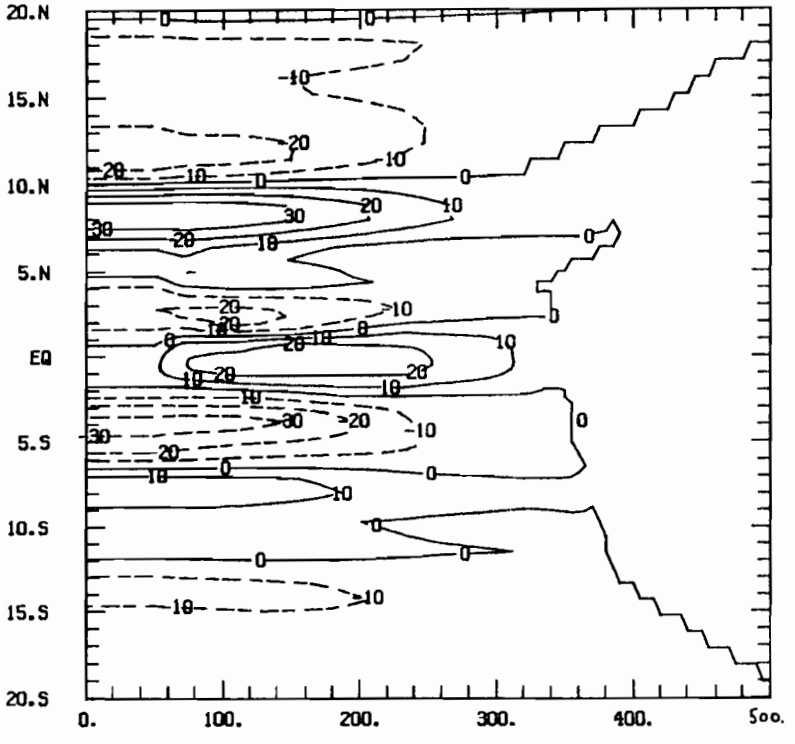

FIG.4. Average January Zonal Velocity (cm.s^{-1}) along 160°E.

3. Heat balance over the TOGA-COARE domain.

140°E-180°E; 10°S-10°N; 0-150 m (average)

Advection and temperature gradients in the domain are small, and the advection tends to be parallel to the isotherms, so that the 3-D heat advection in the domain is small. Thus, if the vertical heat diffusion is small, then the heat flux must also be small. This is confirmed in the model, where over the COARE domain Ri mixing and horizontal diffusion are negligible. Thus, over a year

$\partial/\partial t(hT) =$	-3-D Advection	+ Heat Flux	- Vertical diffusion
$0 \approx$	-3.9	+ 13.5	- 9.4 W m^{-2}

The model SST for January and the SST such that $Q \approx O$ (Figures 5 and 6) show that, over the COARE area, SST is set by $Q(SST) \approx 0$.

Heat Flux =	Incoming Solar	- Latent	- (Sensible + Longwave)
13,5 =	189,8	- 117,6	- 58,7 W m^{-2}

$\nabla.(huT)$	= $\partial/\partial x(huT)$	+ $\partial/\partial y(hvT)$	+ $\partial/\partial s(wT)$	
3.9	= -246.3	+ 202.1	+ 48.1	W m^{-2}

Thus the 3-D heat advection is a small residual of large component terms and, therefore, will be very difficult to measure. Alternatively, a small error in the very small angle between velocity and isotherms will cause a large error in the 3-D advective heat flux estimate. Quantitatively

$$| \nabla.(huT) | / \{ \Sigma[\partial/\partial x_i(hu_iT)]^2 \}^{1/2} = 0.012$$

4. What sets the SST and depth of the warm pool?

The hypothesis that $0 < Q(SST) < 20$ W m^{-2} was confirmed by setting the minimum value of $|u|$ to 3 m s^{-1} (not 4) in the latent flux. This increases the temperature, such that $Q = O$, from about 29.5 → 30°C (min = 4) to about 33 → 33.5°C (min = 3) on the equator between 130°E and 150°E. The actual model SST in this region increases from about 29.5°C (min = 4) to about 32°C (min = 3). When the minimum is set to 3 $m.s^{-1}$, the outgoing latent flux is reduced by 1/4 in the region, or about 30 W m^{-2}. Thus, the sensitivity of SST in this region to errors in the heat flux is

$$\textit{Sensitivity} \equiv dT/dQ = 2.5/30 = 1/12 \text{ °C W}^{-1} \text{ m}^{-2}$$

Thus, an error of 16 W m^{-2} in Q will lead to an error of 1°C in SST in this region of the model. With $|u|$ min = 3 m s^{-1}, the heat balance over a year is

$$0 \approx -5.5 (3 - D A) + 17.7 (H F) - 10.5 (V D) \text{ W m}^{-2}$$

This similar to the min = 4m s^{-1} case, but is not so close to equilibrium.

The depth of the warm pool in this model is set by K_B. In a run where K_B and ν_B were increased by factors of 2 and 10, with no R_i mixing, the depth of the warm pool (water>27°C) was reduced by about 50m. Thus the run with smaller K_B, which can sustain a sharper thermocline, has a deeper warm pool. With a larger K_B, there is more vertical diffusion of heat, so that the COARE region SST is reduced by close to 1°C to produce a larger heat flux. With increased ν_B and K_B, the heat balance over a year is

$$0 \approx 3.2 (3 - D A) + 25.0 (H F) - 21.3 (V D) \text{ W m}^{-2}.$$

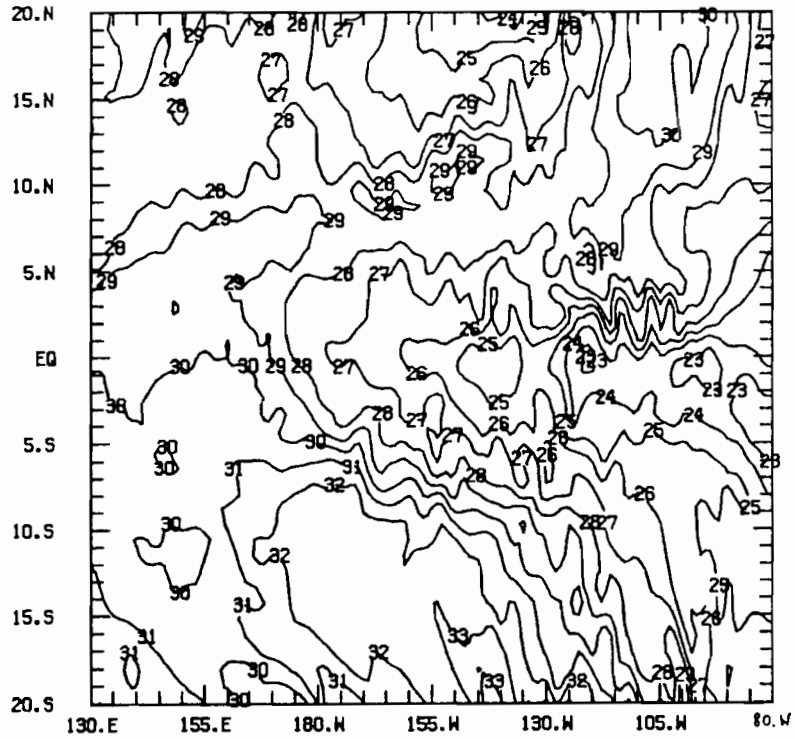

FIG.5. Average January Sea Surface Temperature (°C).

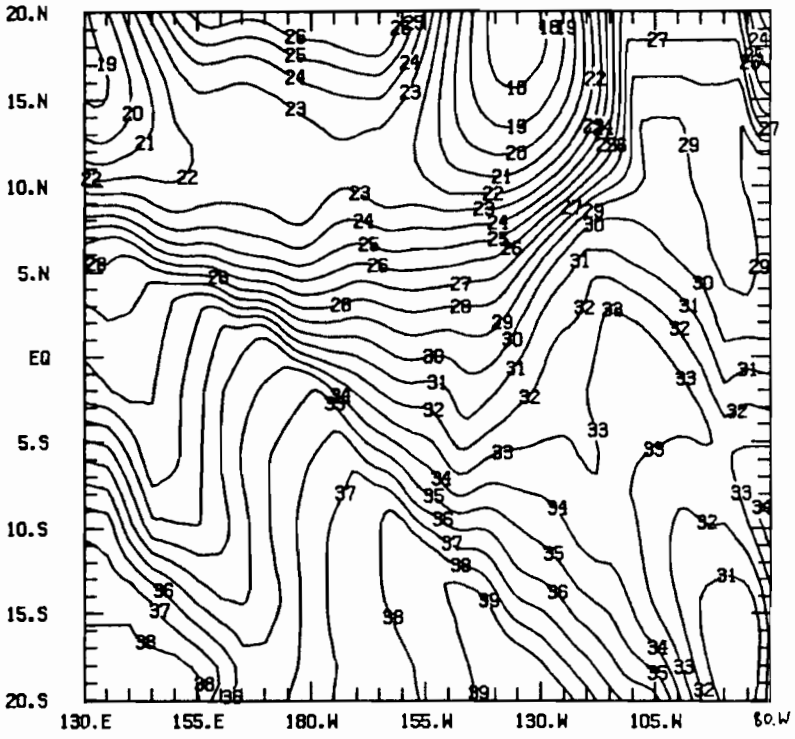

FIG.6. Average January Temperature (°C) such that Q = 0.

REFERENCES

Gent, P.R. and M.A. Cane, 1989: A reduced gravity, primitive equation model of the upper equatorial ocean. *J. Comp. Phys.*, **81**, 444-480.

Rasmusson, E.M. and T.H. Carpenter, 1982: Variations in tropical sea surface temperature and surface wind fields associated with the Southern oscillation/El Nino. *Mon. Wea. Rev.*, **110**, 354-384.

Seager, R., S.E. Zebiak and M.A. Cane, 1988: A model of the tropical Pacific sea surface temperature climatology. *J. Geophys. Res.*, **93**, 1265-1280.

The Steady State Response of Indonesian Sea to a Steady Wind Field

Wasito HADI and NURAINI

Meteorological and Geophysical Agency
Jakarta, Indonesia

ABSTRACT

A barotropic fluid model based on the vertically integrated equations of motion was used for studying the steady-state response of Indonesian sea to a steady wind field. Using climatological wind field in Indonesia, the model results yield reasonable direction of water transport due to wind. It was also found that direction of water transport vary according to the direction of the wind.

1. Introduction.

Information about sea water transport in Indonesia is important. Sea water transport may be caused by wind, tidal forces, fresh water discharges, etc.

This study aims to determine the steady state response of Indonesian sea to steady wind field. For this purpose, Indonesian sea was assumed to be barotropic.

2. Theoretical background.

The circulation of a confined body of water is governed by a set of hydrodynamic equations derived from Newton's Law of motion and the mass conservation principle. The basic hydrodynamic equations are presented in their primitive form. Using the right-handed rectangular coordinate system in which x is eastward, y is northward, and z is the vertical coordinate positive upward, and the term definitions display in Table 1, the equations are :

$$u_t + uu_x + vu_y + wu_z - fv = \rho^{-1} (-p_x + \tau^x{}_z) \quad (1)$$

$$v_t + uv_x + vv_y + wv_z - fu = \rho^{-1} (-p_y + \tau^y{}_z) \quad (2)$$

$$w_t + uw_x + vw_y + ww_z = -\rho^{-1} p_z - g \quad (3)$$

$$u_x + v_y + w_z = 0 \quad (4)$$

where, for example, u_x is $\partial u/\partial x$.

Invoking the barotropic assumption, it is possible to define horizontal component of water transport,

$$U = \int^{\xi}_{-h} u \, dz \qquad \text{and} \qquad V = \int^{\xi}_{-h} v \, dz \quad (5)$$

If the Coriolis force is negligible, Jorge De Las Alas and Marzan (1982), simplified the equation, and the steady-state solution for horizontal component are :

$$gh \, \xi_x = \rho^{-1} (\tau^x{}_w - \tau^x{}_b) \quad (6)$$

ORSTOM
CENTRE DOCUMENTATION
Montpellier

F 30232

$$gh\,\xi_y = \rho^{-1}\,(\tau^y{}_w - \tau^y{}_b) \tag{7}$$

$$u_x + v_y = 0 \tag{8}$$

with,

$$\tau^x{}_w = \rho_a\, C_d\, |u_a|\, u_a \quad \text{,and} \quad \tau^y{}_w = \rho_a\, C_d\, |v_a|\, v_a \tag{9}$$

$$\rho^{-1}\,\tau^x{}_b = DU \quad \text{,and} \quad \rho^{-1}\,\tau^y{}_b = DV \tag{10}$$

Using (9) and (10), equation (6) and (7) become :

$$gh\,\xi_x = \rho_a\, C_d\, |u_a|\, u_a - DU \tag{11}$$

$$gh\,\xi_y = \rho_a\, C_d\, |v_a|\, v_a - DV \tag{12}$$

From equation (8) assumed

$$U = -\,\psi_y \quad \text{,and} \quad V = -\,\psi_x \tag{13}$$

and equations (6) and (7) can be simplified as:

$$\Delta\psi - h^{-1} h_x\, \psi_x - h^{-1} h_y\, \psi_y = G(x,y) \tag{14}$$

with

$$G(x,y) = \rho_a \rho^{-1}\, C_d\, D^{-1}\, [\, (|v_a|\, v_a)_x - (|u_a|\, u_a)_y - h^{-1}(|u_a|\, u_a\, h_x - |v_a|\, v_a\, h_y)\,]$$

---

x = eastward coordinate axis
y = northward coordinate axis
z = vertical coordinate axis
u = fluid velocity component along x axis
v = fluid velocity component along y axis
w = fluid velocity component along z axis
f = coriolis parameter ($2\omega \sin\phi$)
ω = angular velocity of the earth
ϕ = latitude
ρ = density of fluid
ρ_a = density of air
p = hydrostatic pressure
$\tau^x{}_b$, $\tau^y{}_b$ = stress components along x and y axis
u_a = wind velocity component along x axis
v_a = wind velocity component along y axis
ξ = height of the free water surface above undisturbed level
h = undisturb depth of water
$\tau^x{}_w$, $\tau^y{}_w$ = stress components due to the wind
C_d = drag coefficient
U = water transport along x component
V = water transport along y component
Δ = Laplacian operator

Table 1. Definition of terms used in the paper.

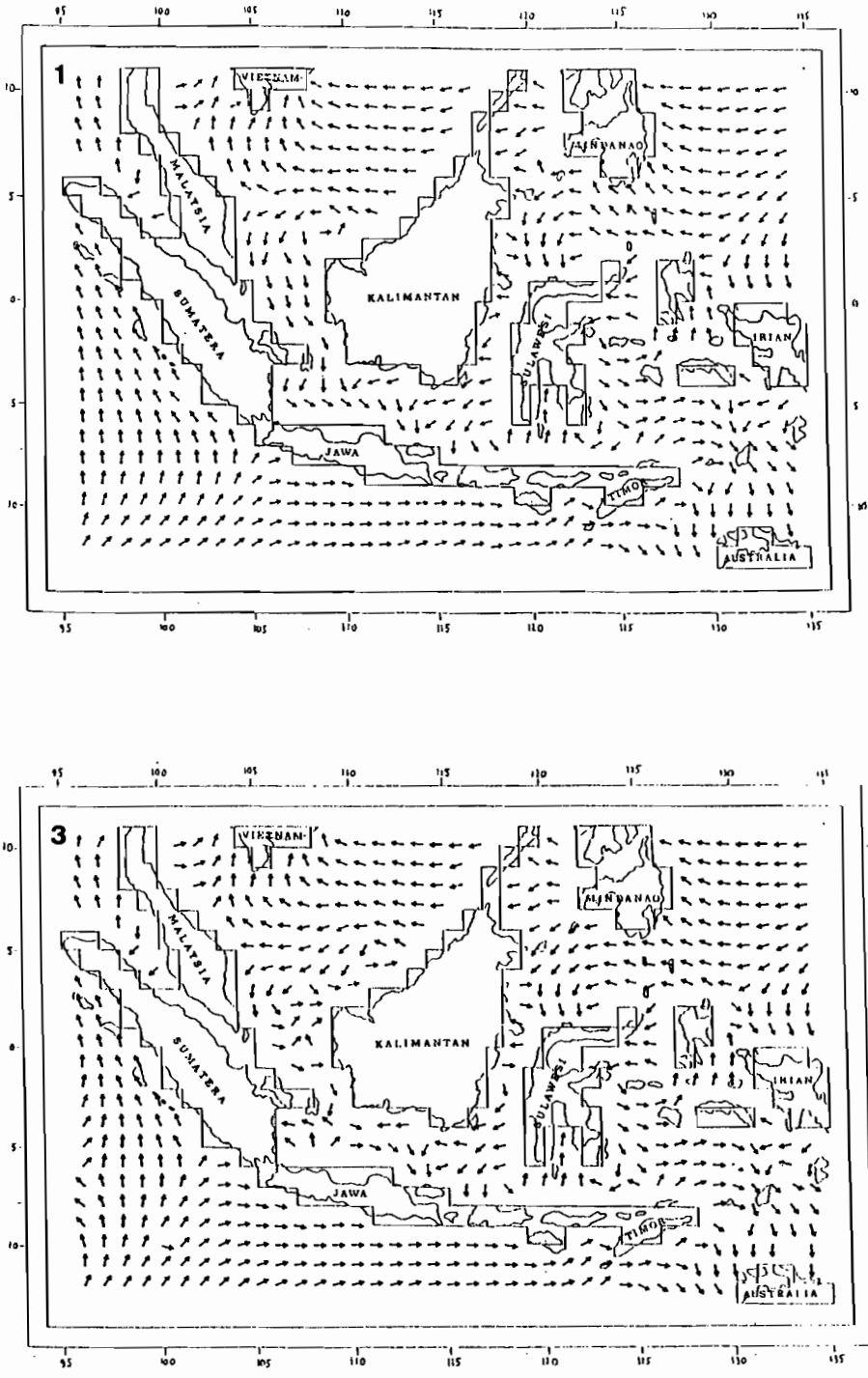

FIG.1. Direction of water transport (#1 is January, #3 is March, *etc*...)

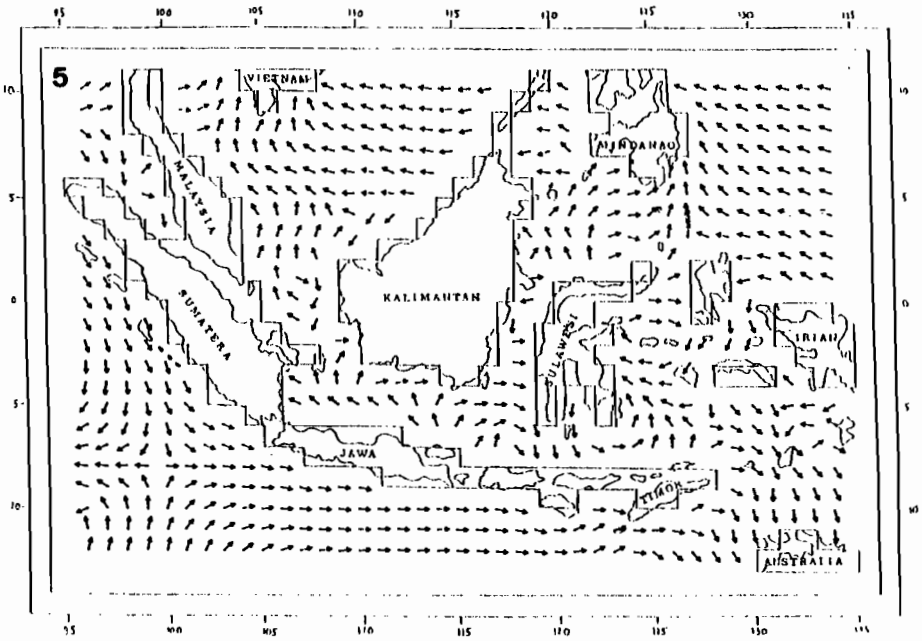

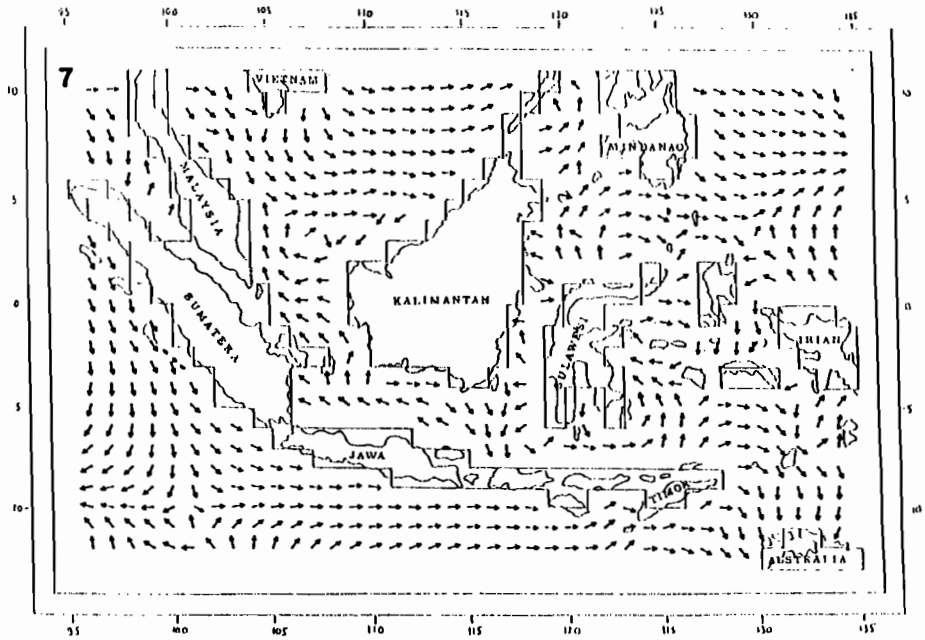

FIG.1. (Continue)

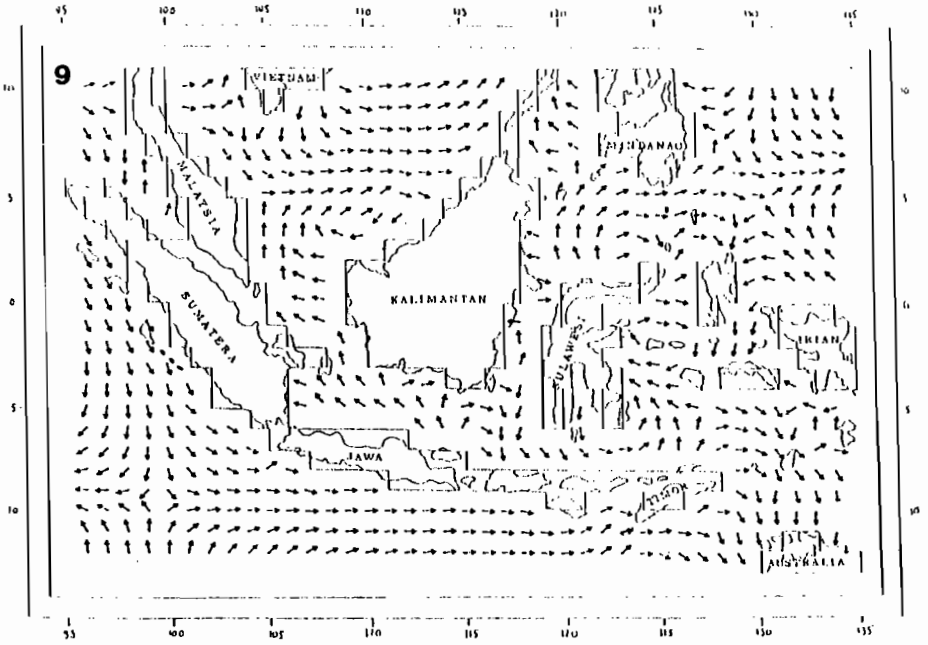

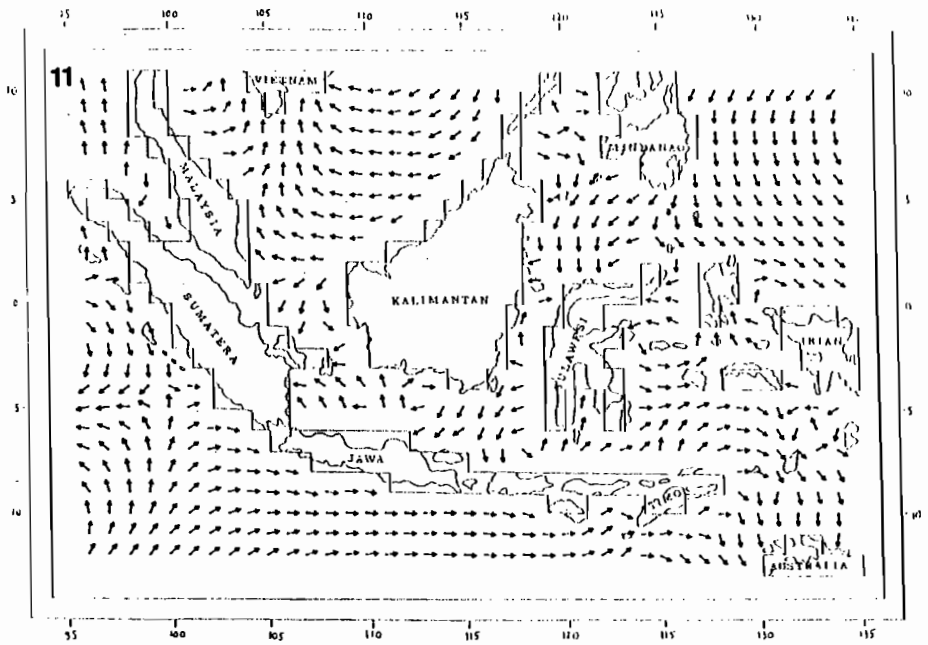

FIG.1. (Continue)

2. Numerical solution.

Equation (14) is Poisson type partial differential equation which can be solved by relaxation method. For lateral boundary condition, ψ along the coast line was set to zero. A grid network consist of square grid elements which are 1°latitude by 1°longitude.

3. Results.

Using monthly wind field in Indonesia, the direction of sea water transport due to wind are presented in Fig. 1. The results clearly evidence water movement from Pacific Ocean to Indian Ocean and vice versa. The direction of water transports of Indonesian sea vary according to the direction of the wind.

From the barotropic assumption, it is possible to define the vertically averaged horizontal velocity component of the current. The results of the model yield reasonable current speed.

REFERENCES

De La Alas, Jorge and M. Marzan, 1982: Modeling the Circulation Of Laguna Lake. *Natural and Applied Science Bulletin.* **4,** College of Science, University of the Philippines.

Haltiner, G.J. and R.T. William, 1980: Numerical Prediction and Dynamics Meteorology. In: *John Willey and Son.* New York.

Welander, P., 1961: Numerical Prediction and Storm Surges. In: *Advances Geophysics,* **8,** Academic Press.

Instability Conditions and Energetics in the Equatorial Pacific

Pedro RIPA

CICESE, Espinoza 843,
22800 Ensenada, BC - Mexico

ABSTRACT

Instability conditions applicable to zonal flows in the equatorial oceans are presented. A multi-layer model, with either rigid bottom (including the effects of topography) or "reduced gravity" lower boundary, is employed. Preliminary use of these theoretical results is illustrated with the zonal geostrophic velocity profiles calculated from the Hawaii-Tahiti Shuttle Data (Wyrtki and Kilonsky, 1984). Sufficient stability conditions - or necessary instability ones - come in two different sets : the second one is related to the sign of the energy of growing perturbations.

1. Introduction

In a 11/2-layer model, if there exists a value α such that

$$[U(y)-\alpha]\,(dQ/dy) < 0 \qquad (1a)$$

and,

$$g'H(y) > [U(y)-\alpha]^2 \qquad (2a)$$

for all y, then the zonal flow (u, v, h)≡(U, 0, H) is stable (Ripa 1983)[1]. There are sufficient stability conditions; necessary instability conditions are, therefore, that for any value of α, either (1a) or (2a) or both must be violated.

In a model with two layers (Ripa, 1987, 1989a-b; McPhaden and Ripa, 1990), stability condition (1a) is simply replaced by

$$[U_1 -\alpha]\,(dQ_1/dy) < 0 \quad \text{and} \quad [U_2 -\alpha]\,(dQ_2/dy) < 0, \qquad (1b\text{-}c)$$

whereas the second condition, (2a), changes into

$$g' > [U_1 - \alpha]^2/H_1 + [U_2 - \alpha]^2/H_2 \qquad (2b)$$

if the system has a rigid bottom (which might include topography), or into

$$g'_2{}^2 < [g'_1+g'_2 - (U_1 - \alpha)^2/H_1]\,[g'_2 - (U_2-\alpha)^2/H_2] \qquad (2c)$$

in the "reduced gravity" case (i.e., when the lower boundary is the interface with a third, motionless layer); these last two systems are called the "2-layer" and "21/2-layer" model, respectively.

Two peculiarities of the stability conditions might call the attention :

Firstly, an arbitrary constant α may be subtracted from the fields $U_j(y)$: the variations of U is what matters. Thus uniform flow, U_j = constant is stable to finite amplitude perturbations. In particular, there is no "baroclinic instability" in a 11/2-layer

1. The notation is standard, e.g., g' is the reduced gravity and Q = (f - dU/dy)/H, denotes potential vorticity. The basic flow is in geostrophic balance : fU +g'dH/dy = 0.

ORSTOM
CENTRE DOCUMENTATION
Montpellier

F 30233

model. This powerful property follows from zonal homogeneity of the system equations and boundary conditions (e.g., -plane or the sphere, with topography function only of latitude, and with coasts along parallels), as well as of the basic flow under consideration.

Secondly, there are two different stability conditions, or two sets of them. Even though this is by no means novel, it is because of the absence of the second condition in the quasi-geostrophic models (not applicable to the equatorial zone) that some readers find it difficult to accept. The method used to find the stability conditions, and the relationship of the second one with the sign of perturbation energy is discussed next.

2. Stability conditions and integrals of motion.

The procedure devised by Arnol'd (1965, 1966) consists in finding conditions such that if satisfied by a particular basic flow, [u,h] = [U,H], then a certain integral of motion, S[u,h], has an extreme at the basic solution, i.e.,

$$S[u,h] = \text{constant},$$

for any initial condition, and

$$\delta S = S[U+u', H+h'] - S[U,H] > 0,$$

for all finite perturbations, [u',h'], which are different from zero and sufficiently small. Now, δS is an exact, finite-amplitude, constant of motion (N.B., S[U,H] = constant, because the basic flow is steady) which, to lowest order, is quadratic in the perturbation. This lowest order is composed of two parts : the first one involves the square of the perturbation potential vorticity, and the second one is the perturbation energy[2]. The latter is *not* necessarily positive, because there might exist perturbations that diminish the total kinetic energy more than they increase the total potential energy, by means of anti-correlated changes of velocity and layer thickness. The two stability conditions, e.g. (1a, b, or c) and (2a, b, or c), are precisely those that guarantee that both quadratic parts of δS are positive definite.

Since δS is constant, in the case of an unstable basic flow a small perturbation must have a *vanishing* net value of the quadratic part of δS (Just think of an infinitesimal wave whose amplitude grows exponentially with time.) If the first condition is not violated (for instance, when the basic flow has uniform potential vorticity), then the perturbation energy must be negative (e.g., Marinone and Ripa, 1982) or zero (e.g., Hayashi and Young, 1987).

Non-positive wave energy is present in a well-known phenomenon, namely, Kelvin-Helmholtz instability (e.g., see Miles 1980). However this seems to be ignored by many researchers, particularly those with prejudices formed in the realm of the quasi-geostrophic models, for which the energy of a growing perturbation is always positive (that is why, incidentally, only the first condition is needed in the quasi-geostrophic case). In Kelvin-Helmholtz instability theory, there are no gradients of potential vorticity involved and the energy of a growing perturbation must be exactly zero, whereas the energy of a neutral wave can have either sign.

---

2. More precisely, "energy - α (zonal momentum)", but I call it "energy", for short.

3. Stability conditions for the N-layer model.

Consider a general N-layer model. A value of N = n1/2-layers with integer n, actually means a (n+1) - layer model in which the deepest layer is at rest; it is, then, a n-layer, system with a "soft" bottom. On the other hand, in a regular N-layer model, i.e. with integer N, the deepest layer has a rigid bottom, which may include topography. I am working with the primitive equations, and making use of the hydrostatic, Boussinesq and "rigid lid" approximations; one can easily deal without the last two, but that only complicates the algebra without much gain in physical insight. The model is completely specified by the total volume of each layer (or the mean thickness, in the case of an unbounded horizonal domain) and the buoyancy jumps across the interfaces, g'_j. The dynamical variables are the thickness, h_j , and horizonal current in each layer u_j; the latter is independent of the vertical coordinate.

The stability of a general basic zonal flow, ($U_j = U_j(y)$, $V_j \equiv 0$, $H_j = H_j(y)$ is guaranteed if there exists a value α such that[3]:

$$[U_j - \alpha]\,(dQ_j/dy) < 0 \qquad (1d)$$

and

$$\mu_j > [U_j - \alpha]^2/H_j \qquad (2d)$$

where the fields μ_j are defined in the following paragraph. These sufficient stability conditions are the generalization of (1a) and (2a) for the multi-layer case. Necessary instability conditions are that, *for any* α, either (1d) or (2d) or both must be violated.

First define $\gamma_j \equiv (U_j-\alpha)^2 / H_j$. For the *reduced gravity* case, n1/2-layer model, first make $\mu_n \equiv g'_n$ and then $\mu_{j-1} \equiv g'_{j-1} - \mu_j\gamma_j / (\mu_j-\gamma_j)$ for j decreasing from n-2 down to 2. For the *rigid bottom* case, n-layer model one starts from $\mu_{n-1} \equiv g'_{n-1} - \gamma_n$ and then one does a similar thing, decreasing j from n-3 down to 2. As a check, notice that one goes from N = n+1 to N = n1/2 by making $H_{n+1} \to \infty$, which implies $\gamma_{n+1} \to 0$. Similarly, one formally goes from N = n1/2 to N = n by making $g'_n \to \infty$; I say "formally" because the n-layer model might have topography, and therefore is not truly derivable from the n1/2-layer one.

Let us review the second condition, for systems with few layers. Perturbation energy must be positive definite if

N = 1: always

N = 1 1/2: $g' > \gamma$

N = 2: $g' > \gamma_1 + \gamma_2$

N = 2 1/2: $g'^2_2 < (g'_1 + g'_2 - \gamma_1)\,(g'_2 - \gamma_2)$

N = 3: $(g'_2 - \gamma_3)^2 < (g'_1 + g'_2 - \gamma_3 - \gamma_1)\,(g'_2 - \gamma_3 - \gamma_2)$

N = 3 1/2: $\mu^2 < [g'_1+\mu-\gamma_1]\,[\mu-\gamma_2]$ $\qquad \mu=g'_2-\gamma_3 g'_3/(g'_3-\gamma_3)$

where $\gamma_j \equiv [U_j-\alpha]^2/H_j$.

3. In all three cases, the first condition, (1d), must be satisfied in every layer (j = 1, ..., n), whereas the second one, (2d), must be fulfilled for (j = 1, ..., n) in the reduced gravity case or (j = 1, ..., n-1) in the rigid bottom case.

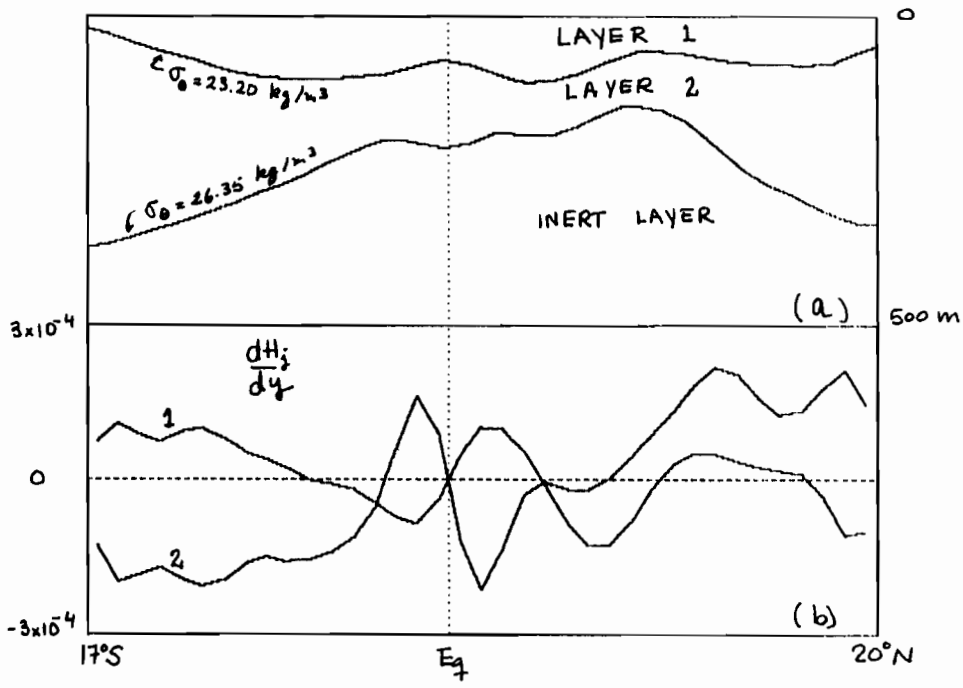

FIG.1. (a) 2 1/2-layer model of the equatorial Pacific, defined by the surface and the σ_θ=23.20 kg.m^{-3} and σ_θ=26.35 kg.m^{-3} isopycnals (the third layer is assumed infinitely deep and motionless). The isopycnals mean depths were calculated from the data of Wyrtki and Kilonsky (1984). (b) Meridional derivatives of the layer thicknesses.

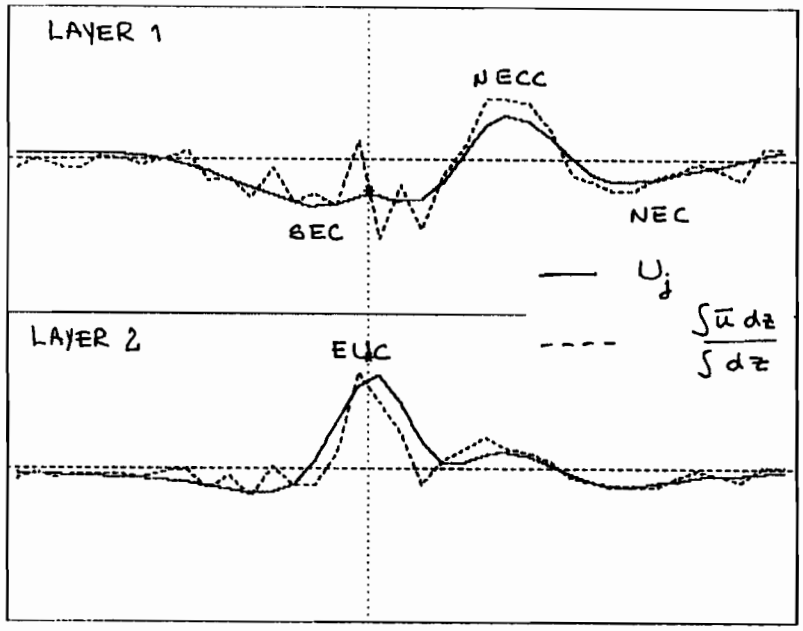

FIG.2. Geostrophic currents in each layer (solid lines) and average velocities calculated from Wyrtki and Kilonsky (1984) continuous field (dashed lines).

4. From one to infinity : the ultraviolet problem.

The second condition (perturbation energy positive definite) is more restrictive on the shear of the basic flow as the number of layers is increased. Moreover, assume that one builds successive approximations to a continuously stratified medium by N-layer models, with increasing N: As the layer thicknesses are diminished, say $H \rightarrow \varepsilon H$, with $\varepsilon < 1$, so are the buoyancy jumps, $g' \rightarrow \varepsilon g'$, but the fields γ are increased, $\gamma \rightarrow \gamma/\varepsilon$, and thus the second condition is harder to satisfy, by a factor of $1/\varepsilon^2$. The inevitable conclusion is that there are no conditions on the basic flow that make the energy of an arbitrary perturbation positive definite : one has to resort to conditions that also involve properties of the disturbance.

For instance, following Holm and Long (1988), one can use as the "second condition" in a continum system.

$$N^2/m^2 > (U-\alpha)^2, \qquad (3)$$

where N is the Brunt-Vaisala frequency (N^2 is the vertical gradient of the basic buoyancy profile) and m is a local vertical wavenumber of the perturbation[4]. Unlike conditions (2a-d), which only involve the basic flow, (3) also bounds the vertical scale of the perturbations : short enough disturbances will violate it (as happenes with the horizontal scale in the case of Kelvin-Helmholtz instability). Therefore, (3) is indeed a condition for linear stability : in a fully nonlinear problem, there is no way to assure that m^2 will be bounded at all times, even if it so initially.

5. Preliminary results of an application to the equatorial Pacific

A model of equatorial currents with some pretense of realism must, at least, have two layers. Prof. Klaus Wyrtki has been kind enough to provide me with the mean annual data shown in the Wyrtki and Kilonsky (1984) paper; figure 1a shows a 21/2-layer model (i.e., the third one is assumed infinitely deep and motionless) with interfaces defined as the σ_θ=23.20 kg.m^{-3} and σ_θ=26.35 kg.m^{-3} isopycnals, respectively. The meridional derivatives of the layer thicknesses, figure 1b, vanish right at the equator, which is a necessary condition for geostrophic balance.

Geostrophic currents in each layer (solid lines in figure 2) show, not surprisingly, good agreement with the average velocities (dashed lines) calculated from Wyrtki and Kilonsky "continuous " field, using buoyancy jumps equal to g'_1 = 27 mm.s^{-2} and g'_2 = 15 mm.s^{-2}. The south equatorial current (SEC), north equatorial countercurrent (NECC) and current (NEC) are clearly seen in the first layer. The equatorial undercurrent (EUC) is observed in the second layer, along with the SEC, NECC (or the subsurface one), and NEC.

The meridional gradient of potential vorticity is always positive everywhere in the first layer and only south of 10°N in the second layer. The first stability condition is violated at the site of NECC, in the first layer, and of the EUC, in the second one, if a value $\alpha = 0$ is used. However, with α = 60 cm.s^{-1}, the first condition is not violated in those regions, but rather, north of 10°N in the second layer. The second stability condition is found to be satisfied for both values of α.

In summary, the second condition is satisfied (i.e., the vertical resolution is not rich enough to allow for negative energy perturbations) but the first one is violated; the place where this occurs depends on the value of α. A normal mode calculation is

4. The generalization of the "first condition" to the continuum case is straightforward.

underway. I expect to find the flow to be unstable, much like in the work of Philander (1976, 1978), and it will be interesting to compare the localization of a growing perturbation and the regions where (1c) is violated, depending on the value of α.

6. Finale

Laplace tidal equations are probably the archetype of ocean dynamical models. When they are linearized in the deviation from a resting ocean, *two* types of waves are found : Poincaré and Rossby ones (these become gravity waves and vertical modes, respectively, in the absence of Coriolis effects). Two is also the number of conditions that guarantee the stability of the steady solutions of those equations, as discussed here and elsewhere.

It is my conjecture that growing perturbations from an unstable flow that violates (1) but satisfies (2) are Rossby-like. Conversely, an unstable steady solution that fulfills (1) but not (2), is presumed to have growing perturbations which are Poincaré-like. Marinone and Ripa (1982) studied unstable easterly equatorial jets in a 1 1/2-layer model, finding that the narrower jet violated (1a) but not (2a); the opposite was true for one with a width equal to the deformation radius. The structure of the perturbations in each case was like as described above (Rossby and Poincaré-like, respectively). Of course, I expect my conjecture to hold true not only for the 1 1/2-layer model, but also for cases with richer vertical resolution, for which the second condition is harder to satisfy.

In the strictly two-dimensional (non-divergent) case as well as in the quasi-geostrophic models, there is only one type of linear waves (i.e., Rossby ones), and also there is only one stability condition, namely that corresponding to (1), in accordance with that expressed above. For all other cases two sets of stability conditions are found. The second condition is associated to the possibility of perturbations with negative or vanishing energy. It is important to examine this concept further, particularly in the equatorial region, where Poincaré waves cannot be avoided in any truly non-linear model.

REFERENCES

Arnol'd, V.I., 1965: Condition for nonlinear stationary plane curvilinear flows of an ideal fluid, *Dokl. Akad. Nauk. USSR*, **162**, 965-978; (English transl: *Soviet Math.*, **6** : 773-777, 1965).

Arnol'd, V.I., 1966: On an a priori estimate in the theory of hydrodynamical stability, *Izv. Vyssh. Uchebn, Zaved. Matematika.*, **54**, 3-5; (English transl. *Amer. Math. Soc. Transl., Series* **2**, 79, 267-269, 1969).

Hayashi, Y.Y., and W.R. Young, 1987. Stable and unstable shear modes of rotating parallel flows in shallow water. *J. Fluid Mech.*, **184**: 477-504.

Holm, D.D., and B. Long, 1988: Lyapunov stability of ideal stratified fluid equilibria in hydrostatic balance., *Nonlinearity*. In press.

Marinone, S.G. and P. Ripa, 1982: Energetics of the instability of a depth-independent equatorial jet, *Geophys. Astrophys. Fluid Dyn.*, **30**, 105-130.

McPhaden, M.J. and P. Ripa, 1990: Wave-mean flow interactions in equatorial oceans, Ann. *Rev. Fluid Mech.* In press.

Miles, J.W., 1980: On Kelvin-Helmholtz instability, *Phys. Fluids*, **23**, 1915-1916.

Philander, S.G.H., 1976: Instabilities of Zonal Equatorial Currents. *J. Geophys. Res.*, **81**, 3725-3735.

Philander, S.G.H., 1978. Instabilities of Zonal Equatorial currents, 2. *J. Geophys. Res.*, **83**, 3679-3682.

Ripa, P., 1983: General stability conditions for zonal flows in a one-layer model on the beta-plane or the sphere, *J. Fluid Mech.*, **126**: 463-487.

Ripa, P., 1987: Flow stability in equatorial oceans. In *Further Progress in Equatorial Oceanography: A report of the U.S. TOGA Workshop on the Dynamics of the equatorial Oceans, E.* Katz & J. White, Eds. Honolulu, Hawaii, 1986. Nova Univ. Press, Ft. Lauderdale, Florida. pp. 351-356.

Ripa, P., 1989a: On the stability of ocean vortices. In *Mesoscale/synoptic coherent structures in geophysical turbulence.* J.J. Nihoul and B.M. Jamart Eds., Elsevier Oceanographic series, Amsdertam, 167-179.

Ripa. P., 1989b: General stability conditions for a multi-layer model. *J. Fluid Mech.*, submitted.

Wyrtki, K. and B. Kilonsky, 1984: Mean water and current structure during the Hawaii-to-Tahiti Shuttle Experiment. *J. Phys. Oceanogr.*, **14**, 242-254.

Mixed Layer Modelling in the Western Equatorial Pacific Ocean

Lewis M. ROTHSTEIN

School of Oceanography, WB-10
University of Washington
Seattle, WA 98195 -U.S.A.

1. Introduction

Designing a numerical model for the mixed layer of the Western Equatorial Pacific presents difficult issues for representing the various processes associated with the regional maintenance of the SST. One clearly has to include the effects of buoyancy forcing (due to the strong evaporation-precipitation contrasts) on the equatorial mixed layer property budgets as well as the vigorous 3-dimensional circulation. Some studies have also suggested that the heretofore neglected effect of the earth's horizontal component of rotation (i.e., the traditional approximation) should also be included (Garwood et al., 1985). The unique nature of the mixed layer in this region demands that the model be able to distinguish the following: the interface between the South Equatorial Current and the Equatorial Undercurrent, the interface between the turbulent mixed layer and the thermocline, and the interface between a fossil isothermal layer and a fresh water cap that appears to be embedded in the layer above the thermocline. The model must be able to incorporate the property exchanges that take place amongst these very different physical regimes. The choice of turbulent mixing parameterization (i.e., how the model numerically "couples" these distinct regions) thus becomes the central issue. A successful model would be required to explain why the surface waters of the region hover around 28°-30°C with little variability and why the region is a "pool", i.e., lacking large horizontal variability (Figure 1). Equally as important is the vertical structure and the explanation of the isohaline-isothermal subsystem (Figure 2) and its effects on entrainment of cold subthermocline waters.

This paper briefly reviews the issues mentioned above, as well as the added complexity of the short time scale wind forcing and the western boundary currents, that one must contend with in designing a mixed layer model of the region. I will argue that although the problem seems to require a "kitchen sink" GCM, it would be dangerous to rely on only such a modelling effort. We have to define testable hypotheses that are more amenable to a process oriented modelling approach. In fact we already have a hypothesis of the maintenance of the fresh water cap in an isothermal layer that provides a test for the model. This is the idea of Lukas and Lindstrom (1987) that will be mentioned later. There is also a need for very simple kinematical models that address fundamental issues like how much of the pressure head is representable in terms of only the evaporation-precipitation flux. Models that simply advect temperature and salinity as passive tracers are also quite useful and could be quickly developed. Finally, one-dimensional mixed layer models would be useful in helping to sort out the complex vertical structure of salinity and temperature.

2. Modelling Considerations

There are a number of considerations in designing the mixed layer model that are unique to the warm pool domain. In this section I briefly outline what I consider to be the most important of these.

ORSTOM
CENTRE DOCUMENTATION
Montpellier

F 30234

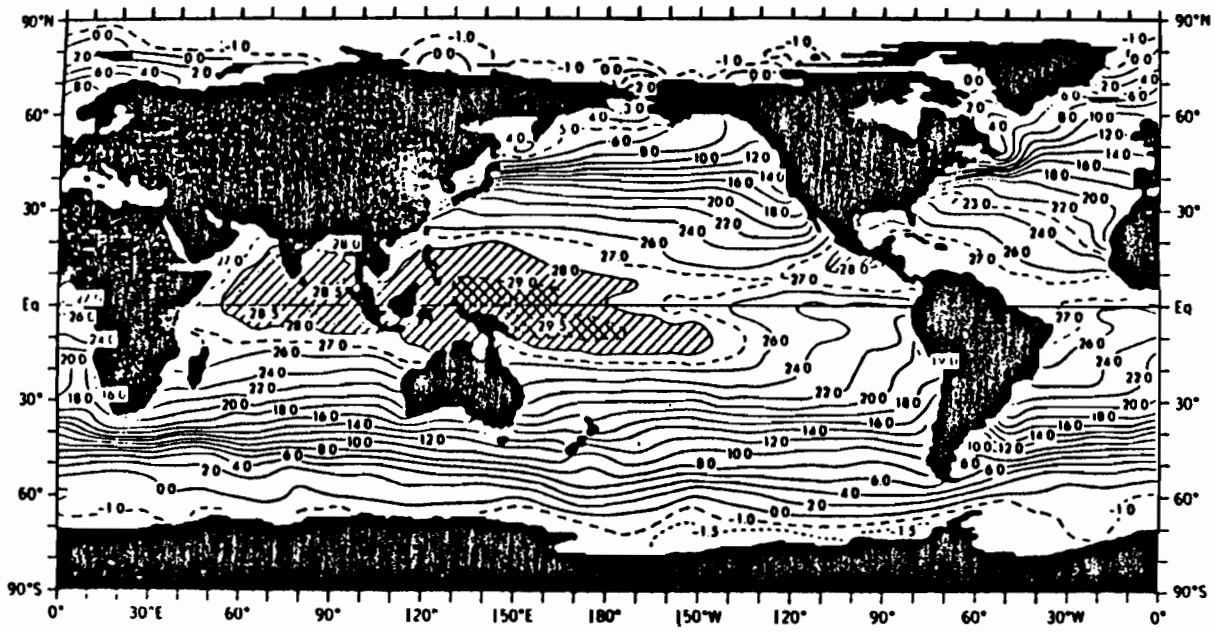

Fig. 1 The 28°C surface isotherm approximately bounds the warm water pool of the western Pacific and eastern Indian oceans. The warmest part, temperatures greater than 29°C, lies between 140°E and 170°E, north of New Guinea. Adapted from Levitus, 1982.

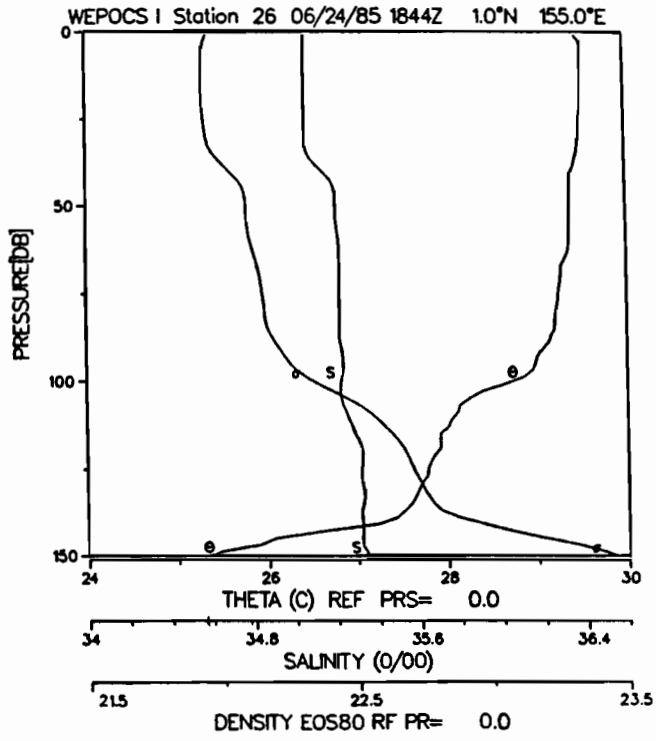

FIG.2. Profiles of temperature (θ, °C), salinity (S, %.) and density at 1°S-155°E from the WEPOCS experiment. The temperature and salinity are plotted on scales such that equal abscissa variations will result in similar variations of density. The upper ocean is clearly not mixed and shows an overlaying structure of stable layers resulting from varitions in the salinity and temperature structure. 80% of the WEPOCS stations in the western Pacific possessed similar structural complexity. (Lukas, personal communication).

2.1 Salinity Effects

Salinity effects have traditionally been "turned off" or at most used as passive tracers in most numerical experiments of the equatorial circulation. If resolving the fresh water cap and determiniing its influence on the SST is an important goal of the Coupled Ocean-Atmosphere Response Experiment (COARE), then one must include a dynamically active salinity component in the modelling effort.

It appears that salinity effects are most important in influencing the entrainment of cold water from below the thermocline and not in directly forcing currents. From scaling the relative importance of wind and buoyancy forcing, one finds that the buoyantly forced currents are an order of magnitude smaller than the wind forced currents (Rothstein, 1984). However, salinity is hypothesized to play an important role in DIRECTLY determining the regional SST (Lukas and Lindstrom, 1987). In a one-dimensional model, Miller (1976) found that the vertical salinity profile is crucial in the evolution of the mixed layer depth, determining whether the mixed layer warms or cools under a given surface forcing. This can be understood as follows. The mixed layer efficiently cools through entrainment of thermocline water into the upper layer. The fresh water cap can provide a "barrier" between surface forcing and entrainment cooling (Figure 2), effectively insulating the waters of the thermocline from wind effects. With the additional stability provided by the barrier layer, a given wind would find it more difficult to entrain cold thermocline waters than in the absence of the barrier layer. Entrainment cooling, therefore, is only effective when the winds are strong enough to erode the barrier layer. Turbulent mixing parameterizations unique to the Western Equatorial Pacific are required.

2.2 Wind Forcing

We've just finished arguing for the relative unimportance of entrainment cooling except for strong wind forcing. The COARE region, of course, happens to be a region of strong wind forcing, albeit on relatively short time scales. Although southeast trades prevail over the warm pool, sudden bursts of westerly winds exert more stress. The trades are light and are interrupted by the westerly bursts between November and May. These wind events usually last only a few days; however, some have been observed to persist for a few weeks with amplitudes sometimes reaching 15 m/sec (Figure 3). These are "downwelling" winds which can precondition the isothermal layer for the "upwelling" trades. Since the location of the cold water source is important for SST prediction, how a model handles detrainment due to these wind bursts appears to be a crucial issue.

2.3 Detrainment

For large heating rates or downwelling, the mixed layer depth becomes large and surface layer turbulence cannot be sustained over the entire layer depth. The interface between turbulent and non-turbulent fluid retreats, leaving behind a fossil turbulent layer ABOVE the main thermocline. This fossil (detrained) mixed layer water needs to be accounted for in the model and there are a number of possibilities. Mixing the detrained water back into the (isohaline) mixed layer would correspond to a view of the ENTIRE layer above the thermocline (isohaline and isothermal layers) as the mixed layer, clearly at odds with COARE hypotheses. Mixing the fossil layer into thermocline waters would be more consistent with the view of the isohaline layer as the mixed layer but this choice would eliminate the possibility of resolving the isohaline-isothermal substructure. It seems appropriate that this fossil layer should retain its own character, i.e., it should not be mixed into the isohaline layer nor should it be mixed down into thermocline water.

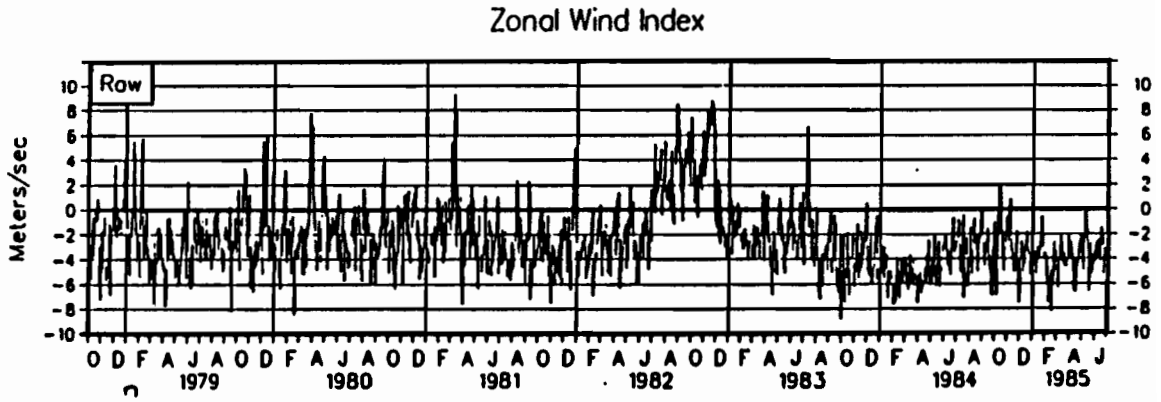

Fig. 3 Composite zonal winds measured on islands near 170°E (kindly supplied by R. Lukas). At the eastern end of the warm pool, the dominant winds are easterly trades. Nevertheless, a very strong, sustained westerly burst in late 1982 was associated with the intense 1982-1983 El Niño.

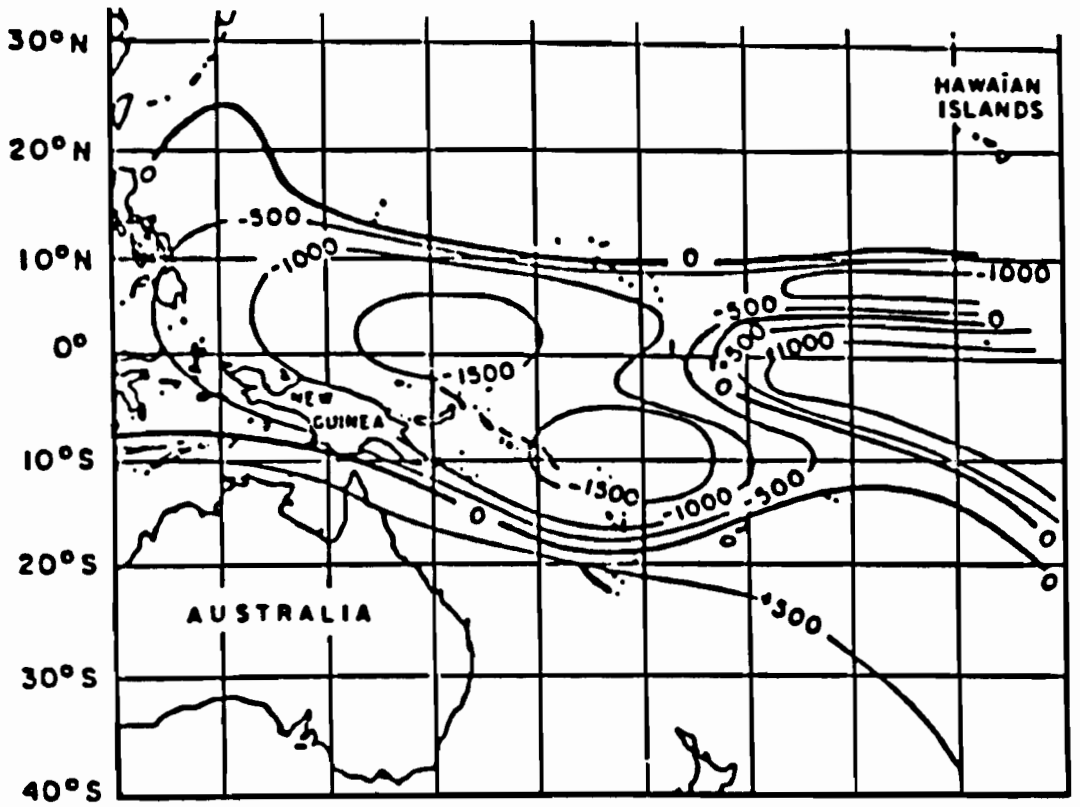

Fig. 4 Evaporation-Precipitation balance expressed in millimetres per year in the Western Pacific. (from WEARE et al, 1981a)

We conclude that a successful mixed layer model must be able to account for these short time scale wind events and accurately represent the (NON?)mixing that goes with detrainment. We again see that issues related to turbulent mixing are the central ones in these models.

2.4 Mixing Parameterizations

Entraiment and detrainment are critical processes for the model to develop realistic SST gradients. In fact, THE essential physics of SST evolution and mixed layer modelling in the western equatorial Pacific could arguably be the influence of the fresh water cap on entrainment cooling. In the central Pacific, the TROPIC HEAT experiment has shown us that the mixed layer is about 40-50 meters deep, with a pronounced diurnal cycle of mixing due to surface nighttime cooling and convective overturning (Gregg et al., 1985). However, in the COARE region, the stratification is almost always stable due to the excess precipitation (Figure 4). How, then, does one parameterize the mixing? This is perhaps the crucial question for all of oceanography these days. The laws that ultimately govern the coupling between the various layers of a mixed layer model are poorly known. We can proceed on an ad hoc basis, trying different schemes (simple switches for entrainment-detrainment, Richardson number mixing, explicit Kraus-Turner turbulent mixing schemes, etc.), but this phase of the modelling will have to be closely linked with the microstructure observational component of COARE. I feel this is one of the central issues for the experiment.

2.5 Other Considerations

There are a number of other items that one must contend with in the proper design of a model to treat the mixed layer of the COARE region. In this section I briefly review these issues.

2.5.1 Surface buoyancy forcing

In an active thermodynamic model like the one that is being designed for COARE, one has to be able to locate a realistic surface buoyancy forcing. This takes the form of both heat and fresh water flux at the surface. The algorithms presently used in calculating the various contributions to the total surface heat flux should be checked against COARE observations. In the early stages of the modelling effort, it would be useful to force the model with various idealizations of the real forcing. For example, it would be interesting to look for the response to a mean E-P pattern (Figure 4) in a decoupled experiment, i.e., don't allow for the readjustment of heat and salinity by the dynamics (a passive tracer experiment). After gaining confidence in the physics of the model (testing the various paremeterization schemes), attempts can be made to activate salt and heat and force the model more realistically, ultimately atttempting a coupling to a moist atmospheric mixed layer model. The atmospheric model must be able to obtain intense, small scale convection such as the model of Lau and Peng (1987).

2.5.2 Western boundary effects

The "boundary" of the western equatorial Pacific is not well defined, yet theoretical and modelling studies have recently placed particular emphasis on the reflection of equatorially trapped Kelvin waves as the mechanism by which a growing, coupled air-sea instability in the central and eastern equatorial Pacific is shut down (Schopp & Suarez, 1988). In fact, a COARE hypothesis is that the upwelling Kelvin wave necessary to shut off the growing coupled air-sea instability is primarily influenced (generated?) by air-sea

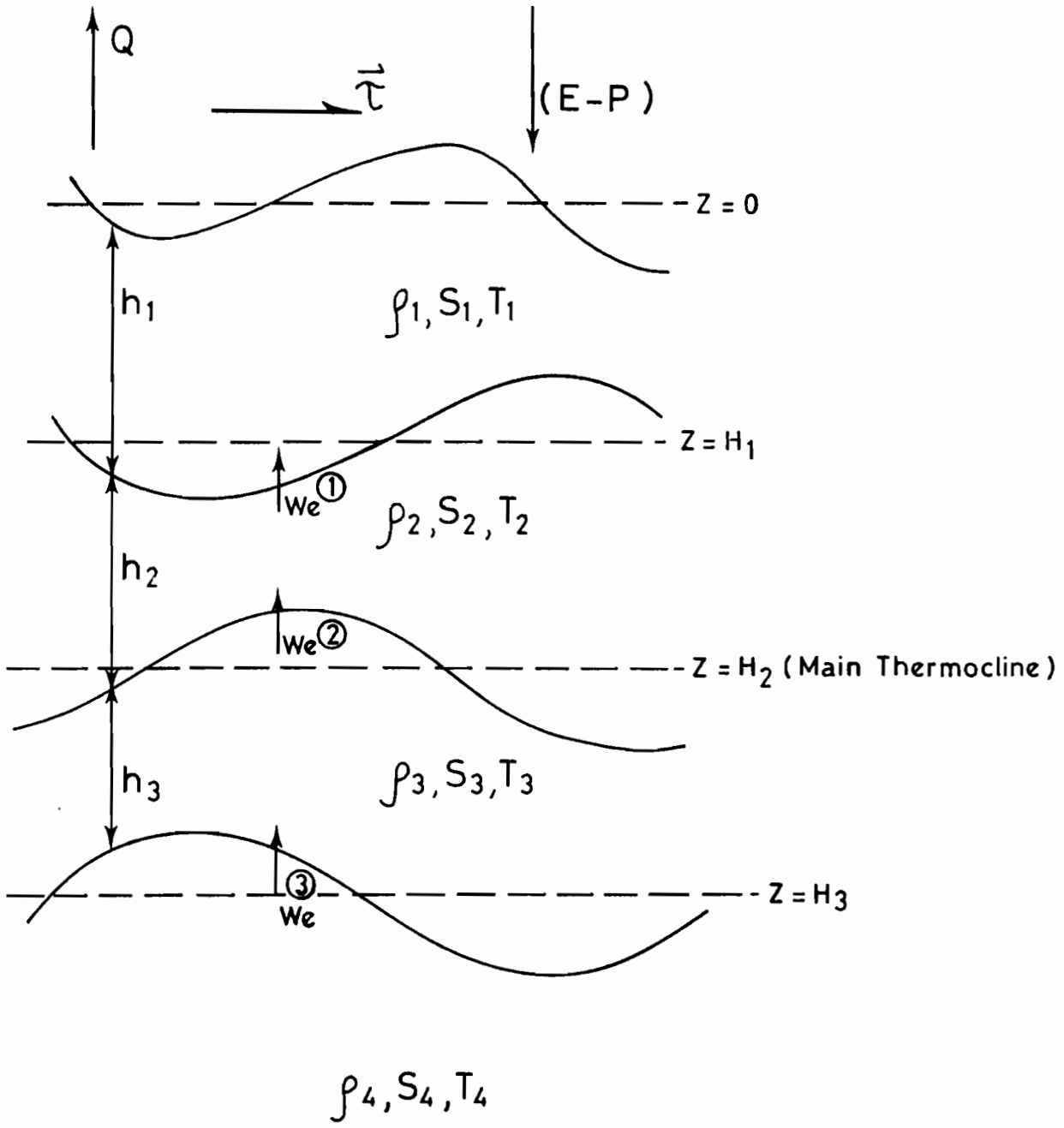

Fig. 5 Schematic of the 3-1/2 layer model.

interactions in the warm pool region (wind burst forcing of Kelvin waves). It becomes important to sort out the relative role played by all potential sources of Kelvin waves. Furthermore, the western boundary acts as a conduit of information from higher latitudes, i.e., the circulation associated with the western boundary can also play an important role in the maintenance of the warm pool. All these issues need to be resolved properly in a mixed layer model. Due to the geometrical complexity of the Indonesian archipelago, realistic simulations must await finely resolved GCMs. However, simpler models with closed sloping boundaries and artificial dampers would prove useful.

2.5.3 The traditional approximation

Garwood et al. (1985) argue for the importance of the "traditionally" neglected horizontal component of the earth's rotation vector in affecting the depth of the mixed layer on the equator. The interaction between the planetary rotation and zonal wind stress increases the turbulent kinetic energy and is hypothesized to be the reason for the deep isothermal mixed layer of the western equatorial Pacific. Their model does not include a salt budget. These are interesting questions and the inclusion of these additional terms in the model does not seem to require a tremendous amount of numerical effort, i.e., no new time scales are introduced into the system.

3. The Subduction Hypothesis: Model Testing

As a first stringent test of any model that includes salinity, I would think that the recreation of the isothermal-isohaline substructure would be an essential requirement. There is a testable hypothesis for maintaining this structure; the subduction hypothesis of Lukas and Lindstrom (1987). Put simply, the maintenance of the isothermal (and saltier) layer below the fresh water cap is thought to be due to zonal advection from the east in the Souh Equatorial Current. Due to excess evaporation in the central equatorial Pacific, the water advected in this way is denser than the warm pool waters and upon encounter with the warm pool the possibility exists that the denser waters would subduct. The meridional circulation may also play a role. The elements of the model that I am building include all of the physics that can adequately test this hypothesis. The proposed model follows.

4. The Model

To design a model short of a GCM we must make decisions to cut corners somewhere. I propose to limit the number of degrees of freedom in the vertical to three active layers overlying a motionless abyss. This is just sufficient to resolve the distinct regimes reviewed in the introduction. The model is designed with the hypothesis that horizontal advection is important. Again the important parametrizations appear as coupling between the layers (the entrainment-detrainment process) and must be chosen with care. Figure 5 is a schematic representation of the 3.5 layer model forced by a wind stress and surface heat and fresh water fluxes. The equations governing the dynamics and thermodynamics in each active layer are:

Layer 1

$$(h_1\bar{v}_1)_t + \nabla \cdot (\bar{v}_1 h_1 \bar{v}_1) + \beta y \bar{k} x h_1 \bar{v}_1 + h_1 \overline{\nabla p_1} = \bar{\tau} + We^1 \bar{V}_2 + \nu_h \nabla^2 (h_1 \bar{v}_1) - {}_m h_1 \bar{v}_1 - {}_z h_1 \bar{v}_1$$

$$(h_1)_t + \nabla \cdot (h_1 \bar{v}_1) = We^1 + K_h \nabla^2 h_1 - {}_z(h_1 - H_1)$$

$$(T_1)_t + \bar{V}_1 \cdot \nabla T_1 = Q/h_1 - We^1(T_1-T_2)/h_1 + K_h\nabla^2 T_1$$

$$(S_1)_t + \bar{V}_1 \cdot \nabla S_1 = (E-P)/h_1 - We^1(S_1-S_2)/h_1 + K_s\nabla^2 S_1$$

Layer 2

$$(h_2\bar{v}_2)_t + \nabla \cdot (\bar{v}_2 h_2 \bar{v}_2) + \beta y \bar{k} x h_2 \bar{v}_2 + h_2 \overline{\nabla p_2} = We^2 \bar{V}_3 - We^1 V_2 + \nu_h \nabla^2 (h_2 \bar{v}_2) - {}_m h_2 \bar{v}_2 - {}_z h_2 \bar{v}_2$$

$$(h_2)_t + \nabla \cdot (h_2 \bar{v}_2) = We^2 - We^1 + K_h \nabla^2 h_2 - {}_z(h_2 - H_2)$$

$$(T_2)_t + \bar{V}_2 \cdot \nabla T_2 = Qd/h_2 + We^1(T_1-T_2)/h_1 - We^2(T_2-T_3)/h_2 + K_h\nabla^2 T_2$$

$$(S_2)_t + \bar{V}_2 \cdot \nabla S_2 = Sd/h_2 + We^1(S_1-S_2)/h_1 - We^2(S_2-S_3)/h_2 + K_h\nabla^2 S_2$$

Layer 3

$$(h_3\bar{v}_3)_t + \nabla \cdot (\bar{v}_3 h_3 \bar{v}_3) + \beta y \bar{k} x h_3 \bar{v}_3 + h_3 \overline{\nabla p_3} = -We^2 \bar{V}_3 + \nu_h \nabla^2 (h_3 \bar{v}_3) - {}_m h_3 \bar{v}_3 - {}_z h_3 \bar{v}_3$$

$$(h_3)_t + \nabla \cdot (h_3 \bar{v}_3) = -We^2 + K_h \nabla^2 h_3 - {}_z(h_3 - H_3)$$

$$(T_3)_t + \bar{V}_3 \cdot \nabla T_3 = Qd/h_3 + We^2(T_2-T_3)/h_2 - We^3(T_3-T_4)/h_3 + K_h\nabla^2 T_3$$

$$(S_3)_t + \bar{V}_3 \cdot \nabla S_3 = Sd/h_3 + We^2(S_2-S_3)/h_2 - We^3(S_3-S_4)/h_3 + K_h\nabla^2 S_3$$

where

$$\overline{\nabla p_1} = g\alpha\nabla \{h_1 (T_1-T_4) + h_2 (T_2-T_4) + h_3 (T_3-T_4)\} - g\alpha \frac{h_1}{2} \nabla T_1$$

$$+ gB\nabla \{h_1 (S_1-S_4) + h_2 (S_2-S_4) + h_3 (S_3-S_4)\} - gB \frac{h_1}{2} \nabla S_1$$

$$\overline{\nabla p_2} = g\alpha (T_2-T_3-T_4) \nabla (h_1+h_2+h_3) + g\alpha \frac{h_2}{2} \nabla (T_2-T_3-T_4)$$

$$+ gB (S_2-S_3-S_4) \nabla (h_1+h_2+h_3) + gB \frac{h_2}{2} \nabla (S_2-S_3-S_4)$$

Surface heat flux (Haney, 1971):

$$Q = (H_1/t_h)\,(T_0-T_1)$$

B.C.

$\overline{V}_1 = \overline{V}_2 = \overline{V}_3 = 0$ (No slip); $T_{1n} = 0$(No flux); $h_{1n} = h_{2n} = h_{3n} = 0$ (mass conserved) and Qd and Sd represent diabatic exchanges of heat and salt.

The model will be tested this fall and results reported shortly thereafter.

5. Conclusions

I have briefly presented the important issues and proposed a model for studying the mixed layer physics of the COARE region. Space has not allowed me to discuss simpler, one-dimensional models which I feel are necessary in the modelling hierarchy. At this time I do not feel that GCMs have much to contribute simply because they are not efficiently designed for hypothesis testing. The parameter space that must be explored for this problem is simply too large for efficient use of a GCM.

An important numerical issue which I have not mentioned is the treatment of surfacing layers. Clearly the isohaline layer is not a feature of the entire equatorial basin and would seemingly surface to the east. Historically the surfacing of layers has been dealt with in several ways. In most two-layer models the interface is kept from surfacing by positioning it far below the sea surface. O'Brien et al. (1977), however, uses turbulent entrainment of water to keep the interface submerged. Bleck and Boudra (1981) propose a quasi-isopycnic vertical coordinate. These various methods will be investigated for specific application to the COARE mixed layer model.

REFERENCES

Bleck, R. and D.B. Boudra, 1981: Initial testing of a numerical ocean circulation model using a hybrid (quasi-isopycnic) vertical coordinate. *J. Phys. Oceanogr., 11*, 755-770.

Garwood, R.W., P. Miller and P.C. Gallacher, 1985: Wind direction and equilibrium mixed layer depth in the tropical Pacific Ocean. *J. Phys. Oceanogr., 15*, 1332-1338.

Gregg, M.C., H. Peters, J.C. Wesson, N.J. Oakey and T.J. Shay, 1985: Intensive measurements of turbulence and shear in the equatorial undercurrent. *Nature, 318*, 140-144.

Haney, R.L., 1971: Surface thermal boundary conditions for ocean circulation models. *J. Phys. Oceanogr., 1*, 241-248.

Lau, K.M. and L. Peng, 1987: Origin of low-frequency (intraseasonal) oscillations in the tropical atmosphere, part I: Basic theory. *J. Atmos. Sci., 44*, 950-972.

Lukas, R. and E. Lindstrom, 1987: The mixed layer of the western equatorial Pacific Ocean. *Proceedings of the 'Aha Huluko'a Hawaiian Winter Workshop on the Dynamics of the Ocean Surface Mixed Layer*, Honolulu, January 1987, P. Miller and D. Henderson, ed., 67-94.

Miller, J., 1976: The salinity effect in a mixed layer ocean model. *J. Phys. Oceanogr., 6*, 29-35.

O'Brien, J.J., R.M. Clancy, A.J. Clarke, M. Crepon, R. Elsberry, T. Gammelsrod, M. McVean, L.P. Roed and J.D. Thompson, 1977: Upwelling in the ocean: two- and three-dimensional models of upper ocean dynamics and variability. *Modeling and Prediction of the Upper Layers of the Ocean*, E.B. Kraus, ed., Pergamon Press, 178-228.

Rothstein, L.M., 1984: A model of the equatorial sea surface temperature field and associated circulation dynamics. *J. Phys. Oceanogr., 14*, 1875-1892.

Schopf, P.J. and M.J. Suarez, 1988: Vaccillations in a coupled atmosphere-ocean model. *J. Atmos. Sci., 45*, 549-566.

An Oceanic Subsurface Thermal Analysis Scheme with Objective Quality Control

Neville R. SMITH

Bureau of Meteorology Research Center
Melbourne, Vic. 3001 - Australia.

1. Introduction

In view of the strong impact of interannual climate variability in the Australian region in the form of droughts and other extreme weather events, and of the strategic proximity of Australia to climatically sensitive regions of the tropical oceans, the Bureau of Meteorology Research Centre and CSIRO Division of Oceanography have jointly initiated a project to provide an oceanic analysis system for the tropical Indian and Pacific Oceans. The primary function of the project is to provide timely local analyses with scope for extra attention to the Indonesian Archipelago and Western Pacific regions. This paper will concentrate on the objective quality control procedures that have been implemented with the scheme, using the 1986-87 period to illustrate their operational function. Details of the methodology and implementation are given elsewhere [Blomley et al. 1989]. We hope to provide to tropical ocean analysis the variety of approach that has proved invaluable in the meteorological community.

2. The analysis scheme

Statistical (or optimal) interpolation (SI) is used to analyze data from an irregularly spaced observation network onto a regular grid. Such methods have previously been used to analyze short-term climatic variability in the Pacific Ocean [e.g. White et al. 1985]. The SI scheme used here is a univariate adaption of the ECMWF scheme [Lorenc 1981], incorporating elaborate techniques for data checking and validation, and introduces novel methods for data selection and analysis sector merging. Analyses are provided for sea surface temperature, mixed-layer depth, depth-averaged temperature to 150m and 400m, depth of the 15°, 20° and 25° isotherms, and at 15 standard NODC levels to 500m.

SI utilises prior knowledge of the statistical structure of first-guess and observation errors (deviations from the true field) to transport information from the observation points to some regular grid. Let O, F and A be the observed, first-guess (e.g. a model forecast) and analyzed fields, and E^o and E^f be the estimated errors in the observed and guessed fields. Now define normalised observation and analyzed fields,

$$q_i = (O_i - G_i)/E^f \quad (1)$$

$$r_k = (A_k - G_k)/E^f \quad (2)$$

for i=1,N observations and k=1,K grid points. Each observation deviation q_i is weighted according to its

ORSTOM
CENTRE DOCUMENTATION
Montpellier

F30235

worth as an estimator for the true deviation r_k at grid point k,

$$r_k = \underline{W}_k q_i \tag{3}$$

where $\underline{W}_k$ is an N x K matrix. The weight matrix is determined by the statistical structure through the relationship

$$\underline{W}_k = \underline{M}^{-1}_{ij} h_{jk} , \tag{4}$$

where $\underline{M}_{ij}$ is the correlation matrix and $\underline{M}^{-1}$ is its inverse. h_{jk} is the correlation vector for observations i at grid point k (refer to Blomley et al. 1989 for further detail). The analysis error is given by

$$(e^a_k)^2 = 1 - h_{ik}\underline{M}^{-1}_{ij} h_{jk} . \tag{5}$$

The data for real-time analyses are drawn from the Melbourne node of the GTS in the form of BATHY and TESAC messages. The data base for research quality analyses is supplemented by data supplied by NODC and the TOGA Subsurface Data Centre (TSDC). Observations are checked for reasonableness and exact- and near-duplicates eliminated from the data base.

3. Quality control and data selection

Fig. 1 is a schematic of an idealised data distribution and first-guess estimate in a one-dimensional domain. One of the unique features of the scheme is that it brings to oceanography the powerful methods of data checking routinely used in meteorology, thus eliminating labour-intensive manual checking of data.

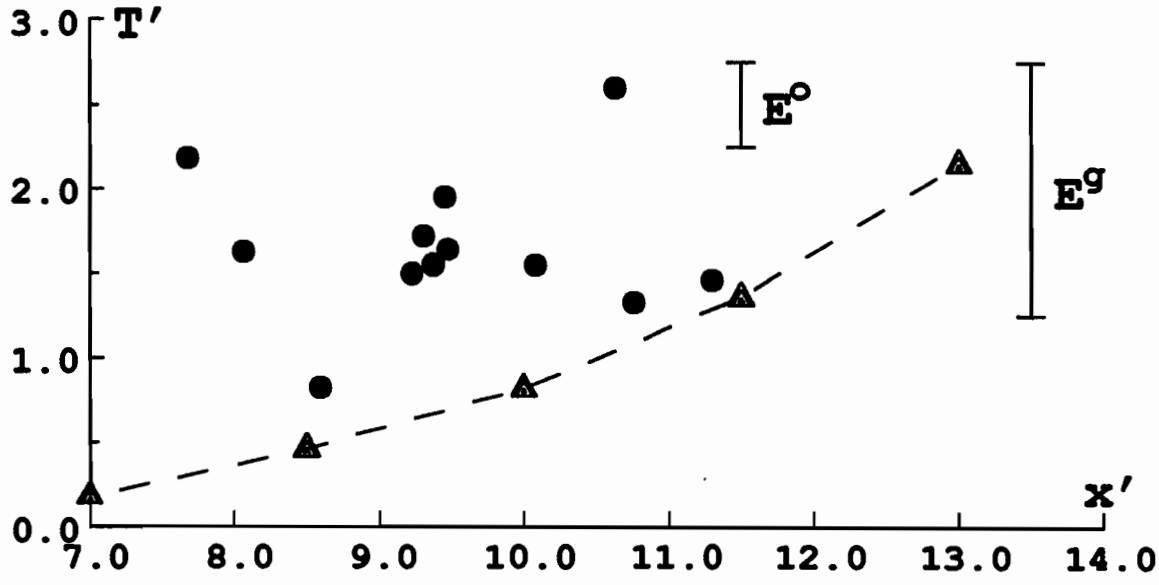

FIG. 1. The distribution of the original observations [●] and the first-guess (dashed curve) for some arbitrary field T'. The decorrelation scale is 1.5 in the arbitrary space units of x'.

Observations are stored internally as normalised deviations from a first-guess field, usually derived from climatology [e.g. Levitus 1984]. In this case the estimated error of the first-guess E^g is simply the standard deviation of the true field. E^o is the standard deviation of the observations about the true field (i.e. the instrumental and geophysical noise). Observations are pre-checked within the analysis using a

3-sigma test against the first-guess (Fig. 2), each suspect observation being flagged and temporarily omitted.

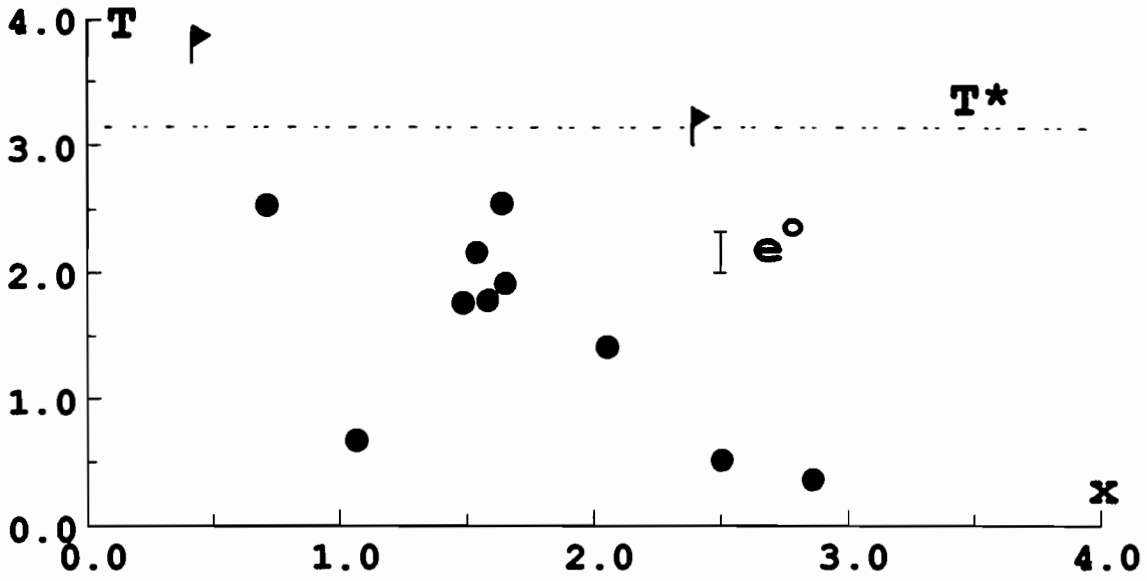

FIG. 2. A map of the observations in the normalised domain. The tolerance T' is a function of the noise-to-signal ratio e' and the rejection criteria R'. Suspect observations are flagged [▶].

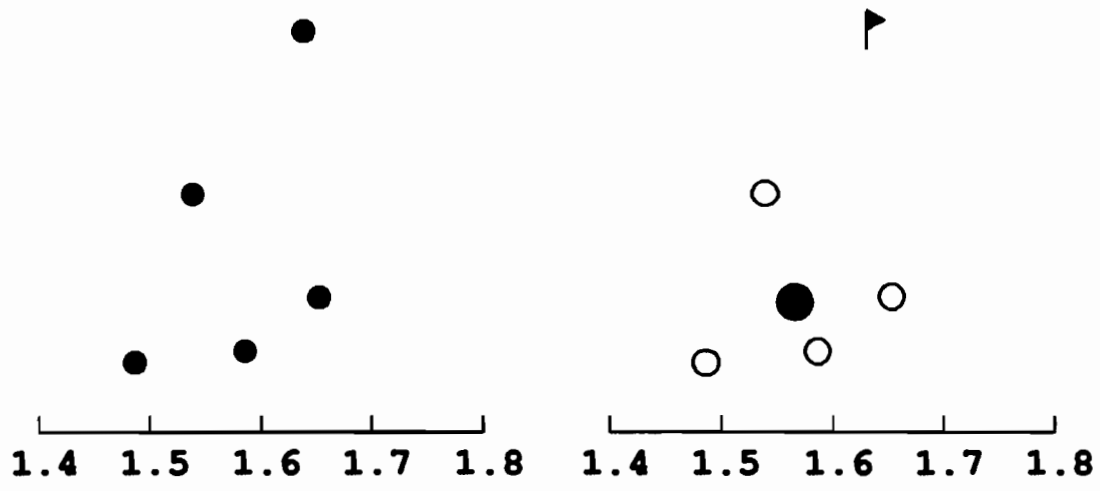

FIG. 3. Schematic of super-observation formation. A group of close observations [●] (left panel) are checked and suspect data are flagged (right panel). A new observation [◉] is formed from the redundant data [○].

Next, close groups of data - here "close" means the data are statistically indistinguishable - are considered for combination into super-observations (Fig 3). Modified SI equations are used to inter-calibrate the individual observations against the expected super-observation value. Redundant data are cancelled and suspect data temporarily flagged. Super-observations are henceforth considered to be of superior accuracy (smaller error) compared to their constituent data. Both the cross-validation and final

analysis are instituted through an arrangement of inter-meshed analysis sectors (Fig. 4). The number of observations will usually exceed the numerical capability for matrix inversion and the domain must be subdivided into manageable analysis sectors. This arrangement ensures all observations are selected at least once. The inter-meshing may be adjusted to eliminate the overlap altogether or to encourage multiple-selection of all observations. The weighting between interpolations from different sectors is decided by the estimated error of the individual analyses.

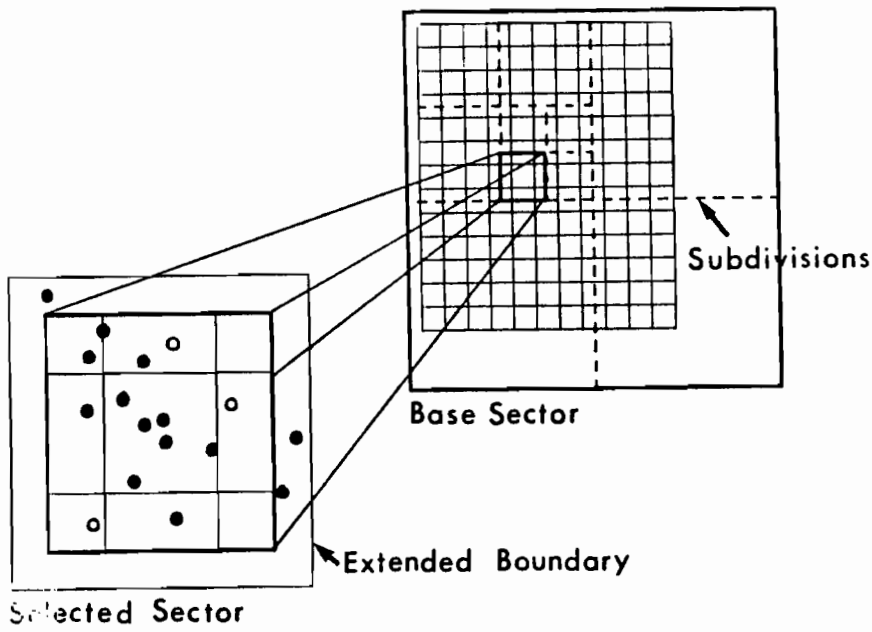

FIG. 4. A schematic of data selection. The analysis grid (upper right) is subdivided until the number of data selected for the sector is optimum (lower left). The inner sector is extended to facilitate sector overlap (outer box).

Remaining single observations and super-observations are cross-validated against the projected grid analysis (Fig. 5) with data incurring two or more flags being permanently deleted. Temporarily flagged data are rechecked and flags made permanent or lifted (Fig. 6). The cross-validation process should not be viewed solely as a mechanism for detecting rogue observations but also as an integral part of analysis "smoothing"; observations which are not consistent with the imposed statistical model may be eliminated.

Finally the analysis is performed over all sectors using the remaining single and super-observations (Fig. 6). In addition to the analyzed increments r_k the analysis error ϵ^a is also estimated. The analysis error is a measure of the relative confidence in the individual estimates and is used to control the merging of interpolations from adjacent sectors as well as to form the analysis error field for the final analysis. The final analysis (Fig. 7) will favour the observations in data rich regions and the error will be small (e.g. near x^*=9.3). In data sparse areas the analysis is near the first-guess and the error approaches the first-guess error (e.g. at x^*=13). If there is only a single observation within a radius of the decorrelation scale, the estimated error will be just less than the observation error.

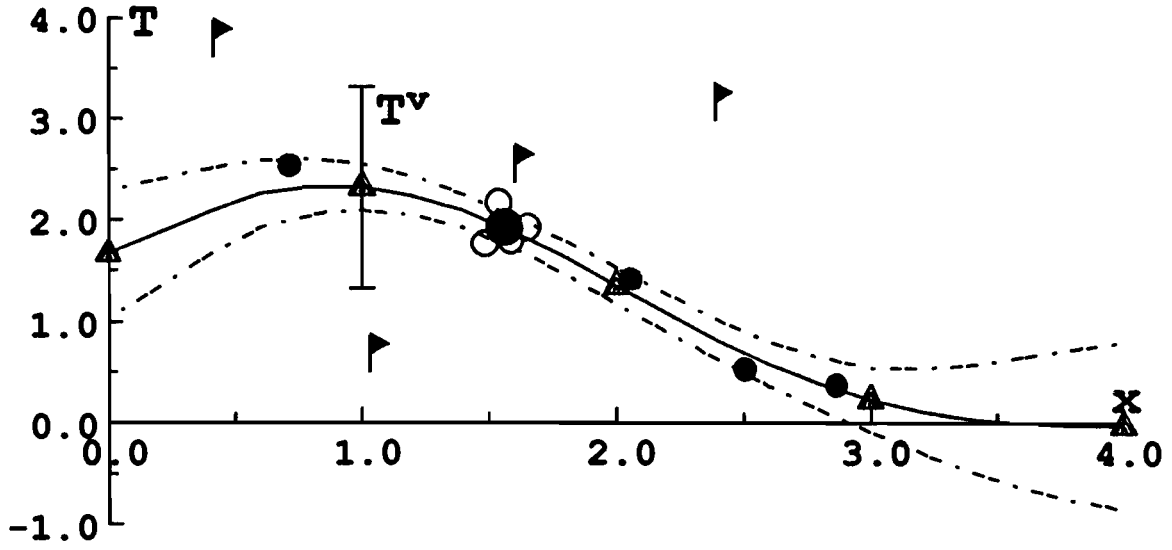

FIG. 5. Observations are checked by cross-validation against an independent analysis [-▲-]. The tolerance T^V is based on the estimated error e^* (dashed) and a rejection criteria R^V. Suspect data (e.g. near x=1) are flagged.

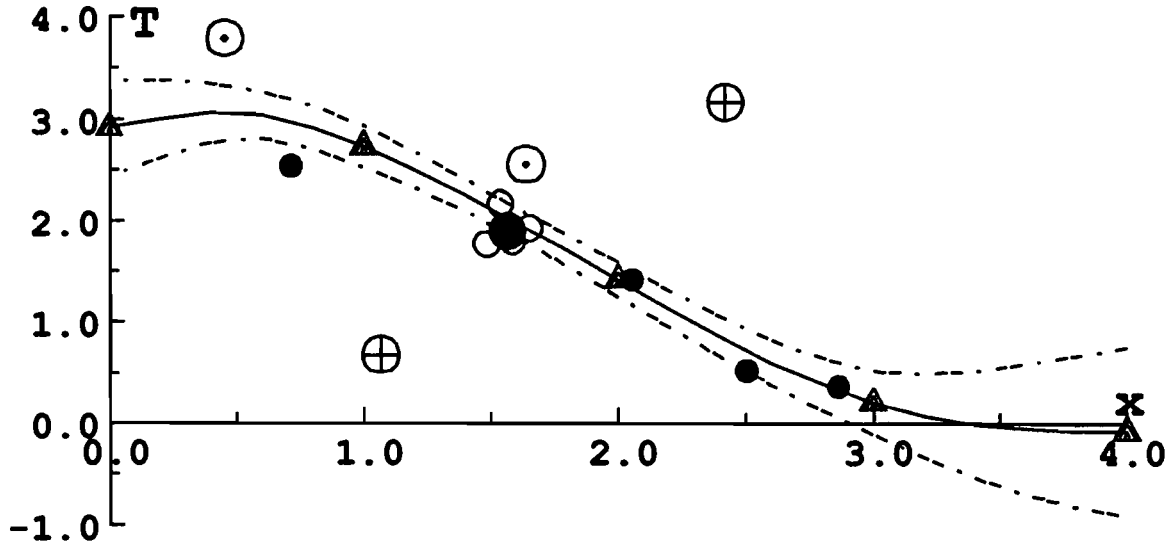

FIG. 6. Flagged data are rechecked against the analysis [▲]. Some data are readmitted [⊙] while failures are deleted [⊕]. The solid and dashed curves are the final normalised analysis and estimated error.

4. Quality control procedures in operation

The operational implementation of quality control procedures is complicated by the non-isotropic, spatially varying nature of the auto-correlation functions for the tropical oceans. Currently the decorrelation scales are 1500 km x 300 km in the equatorial region, varying smoothly to 500 km x 500 km in midlatitudes and 100 km in coastal regions [Meyers et al. 1989]. Particular care must be taken to avoid indeterminate calculations for the analysed field and its associated error. Even then, observations may occasionally be unjustly excluded, usually in regions of dense data coverage or in coastal regions

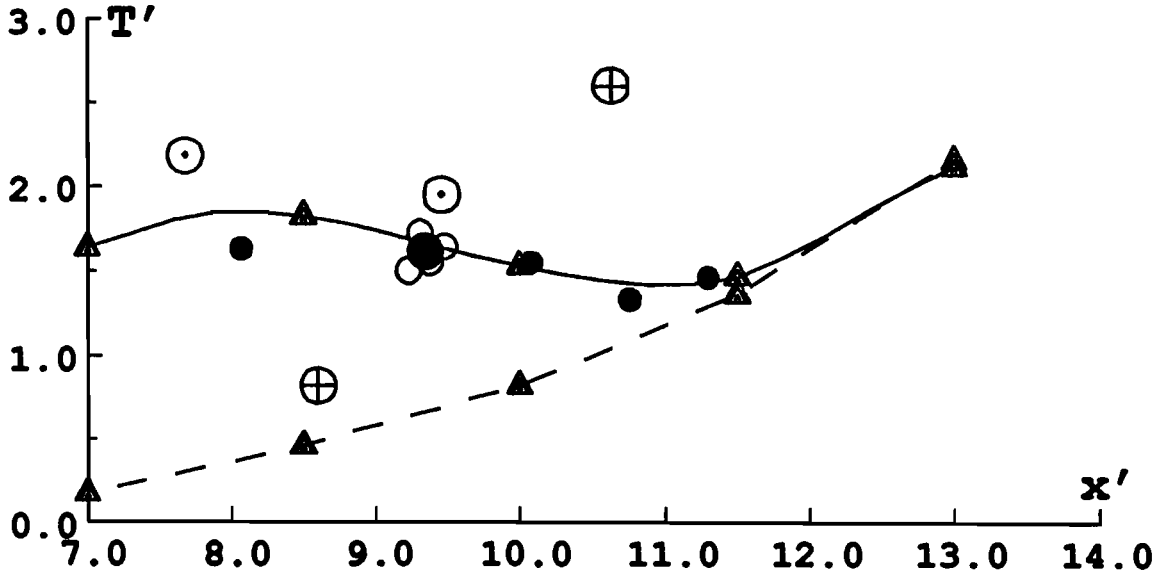

FIG. 7. Final analysis with observations mapped to the original unnormalised domain. [●], [○] and [◉] are single, redundant and super-observations respectively. [⊕] and [⊙] are deleted and validated suspect data.

where the imposed statistical structure varies rapidly. Given sufficient information on which to make an objective assessment, the scheme has proved more than satisfactory as an arbiter of poor measurements, . For the real-time analyses the path from the GTS BATHY/TESAC message data base to the grid point analysis fields is entirely objective, thus avoiding the labour intensive, subjective interventions.

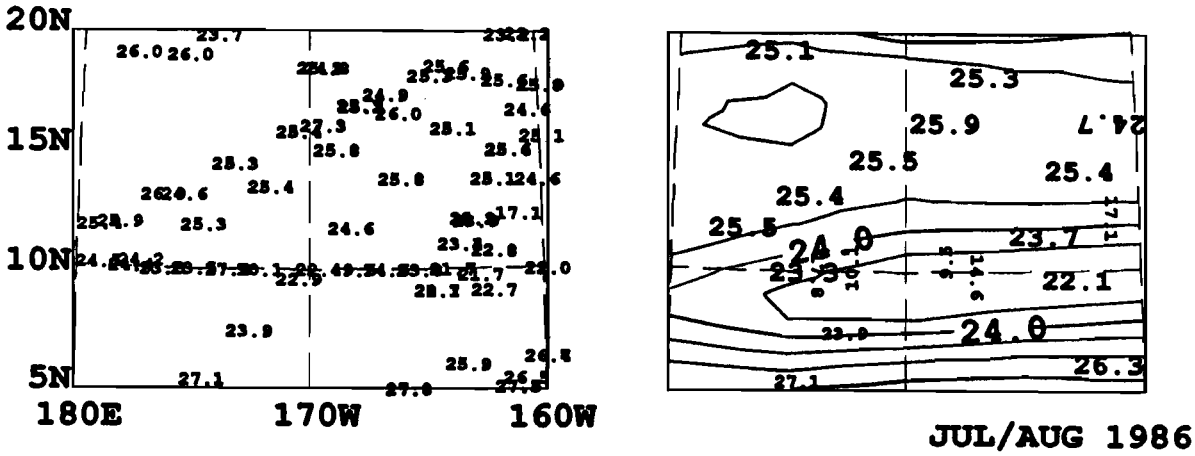

FIG. 8. An expanded view of the T_{150} analysis. The left panel shows the original data while the right panel shows the ultimate distribution together with analysis.

As an illustration of the operational action of the scheme, figure 8 presents details of an analysis over a restricted region of the Pacific for the 150 m depth-averaged temperature (c.f. the schematic examples of Figs 1 through 7). Single and super observations are written horizontally, with super-

observations being shown slightly larger. Deleted observations are rotated through 90°, while suspect (but cleared) data are upside-down. The original data have been duly screened by pre-checking and cross-validation for inconsistent and suspect data. Excessive redundancy has been removed by combining groups of close observations into super-observations. This example clearly demonstrates the degree to which data are payed by the analysis. For ordinary, single observations this is determined by the imposed noise-to-signal ratio. For super-observations, the observational error assigned to the new datum truly reflects the information content - if the constituents were evenly spread in time and space (as determined by the decorrelation scales) then the new datum is considered to be more accurate than its components. Conversely, if the constituents are very close in both space and time (for example, many measurements at a single station) then the newly formed datum will be of similar accuracy to its components. Clearly the efficacy of the quality control procedures depends on the quality of the first-guess field (climatology is by no means ideal), on the imposed statistical structure, and on the many internal parameters of the SI scheme. These dependencies have yet to be examined in detail but experience with the near real-time system, and with analyses of NODC and TSDC data, suggest the present configuration is satisfactory.

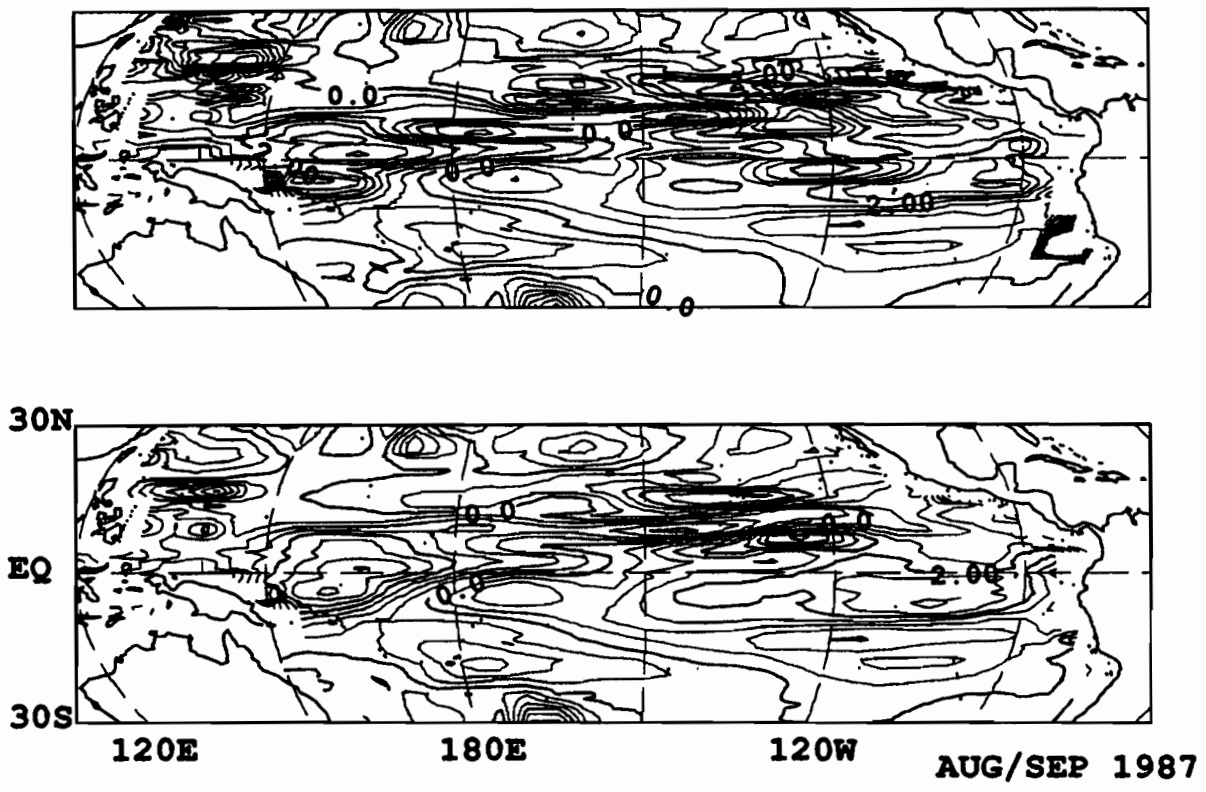

FIG. 9. A comparison between an analysis with no quality control (upper panel) and an analysis with full quality control (lower panel) over the equatorial Pacific. The field is the 150m depth-averaged T_{150} increment.

As a further illustration of objective quality control, figure 9 compares the increments from an analysis with regular controls with an analysis where all controls have been turned off. The data in this case are derived from the BATHY message data base. A marked deterioration in the analysis is evident, particularly east of the dateline in the North Pacific. Some of the changes can be traced to spurious

observations, while others appear to be related to subtleties of the SI scheme. For example, the depression near 18°N, 170°W can be directly attributed to the retention of a bad observation. Combination of doubtful data into super-observations, and changes in the data selection sequence, have led to less substantial changes elsewhere. The positive impact of data validation procedures is undeniable and forms the cornerstone of the analysis project.

5. An analysis sequence: T_{150} for the 1986-87 El Niño

Figure 10 presents bimonthly analyses for the 150m depth-averaged temperature for the equatorial Pacific for the period 1986-87 which includes an El Niño event. The data are drawn from the TSDC files and analyzed on a 5° x 1° grid using Levitus' (1982) climatology as the first-guess field. TSDC have eliminated most of the poor data so the principal role of quality control here is to ensure the mapping is consistent with the imposed statistical structure. The event begins to take shape between the July/August and September/October 1986 bimonths. An unusual cold anomaly is located near 150°W on the equator. By the end of 1986 most of the central and eastern equatorial Pacific is anomalously warm. The cooler water just north of the NECC trough is probably an artifact of the excessive smoothing used in the climatology [Blomley et al. 1989]. The event matures by mid-1987 with eastern Pacific anomalies occasionally in excess of 4°C. The axis between the warm eastern Pacific and the cool western Pacific is coherent through most of 1987 being located near 165°W. Western Pacific cooling is of the same order as the eastern Pacific warming. By late 1987 cool water from the west can be seen penetrating toward the east along the equator signalling the decay of the event.

This example embodies the rationale for developing objective interpolation methods for the analysis of oceanographic data. Large data sets, spread unevenly in both space and time, can be efficiently mapped onto regular grids to facilitate better interpretation and utilisation of the data. There is however a clear need for a more refined treatment of statistical structure and for an improved first-guess field, either through the use of a ocean general circulation model (in a manner analogous to meteorology) or through stochastic methods (e.g. use of a persistence/regression model). These improvements are currently being examined.

6. References

Blomley, J.E, N.R. Smith, and G. Meyers, 1989. An oceanic subsurface thermal analysis scheme. Research Report, Bureau of Meteorology Research Centre .

Levitus, S., 1982. *Climatological Atlas of the World Ocean.* NOAA Prof. Paper 13, 173 pp., 17 microfiche, U.S. Govt. Printing Office, Washington, DC.

Lorenc, A., 1981. A global three-dimensional multivariate statistical interpolation scheme. *Mon. Wea. Rev.*, **109**, 701-721.

Meyers, G., J. Sprintall, H. Phillips and J. Peterson, 1989. Design of an ocean temperature observing network in the seas north of Australia. Part 1: Tropical Pacific ocean statistics. CSIRO Tech. Report.

White, W.B., G. Meyers, J.R. Donguy and S.E. Pazan, 1985. Short-term climatic variability in the thermal structure of the Pacific Ocean during 1979-82. *J. Phys. Oceanogr.*, **15**, 917-935.

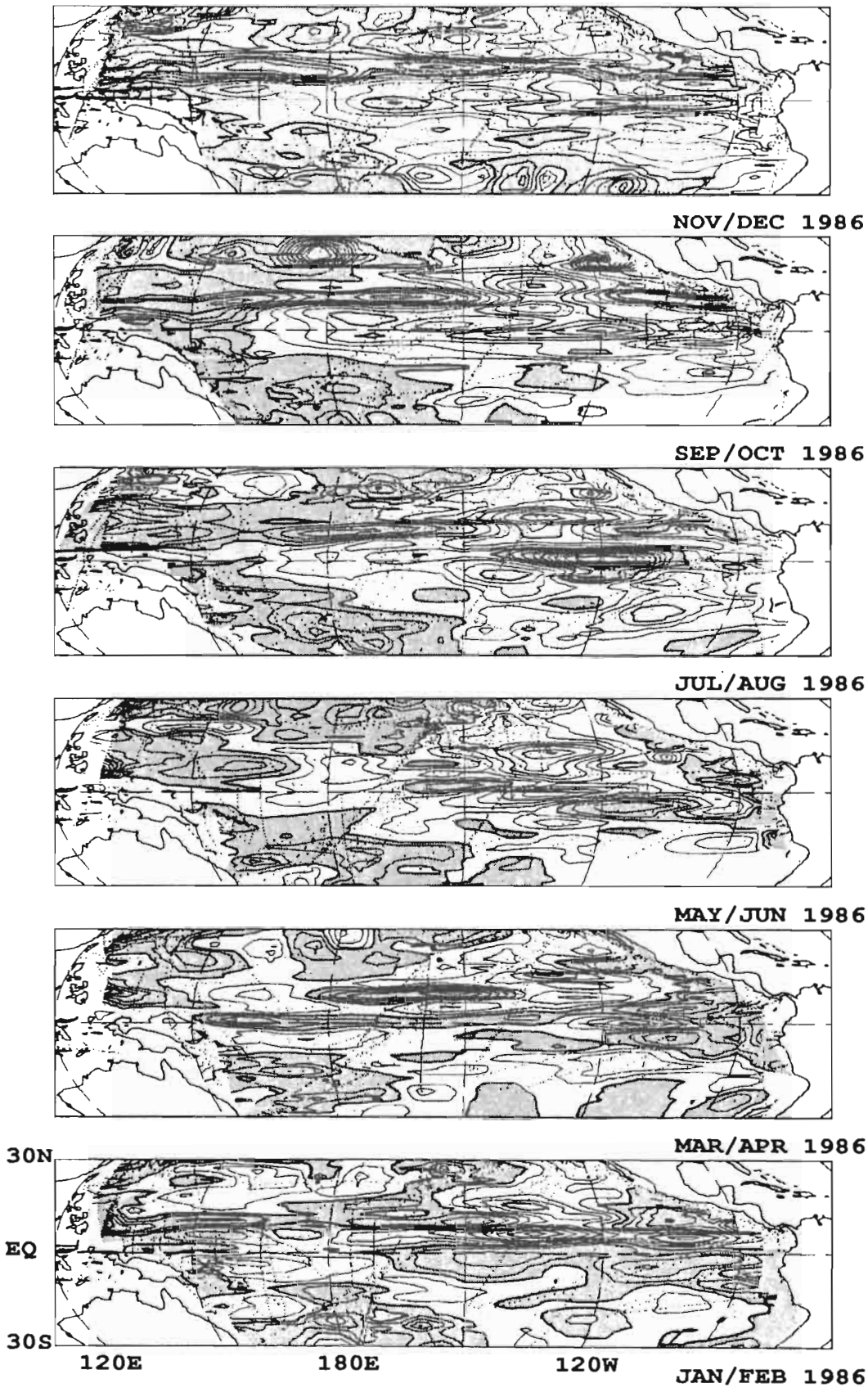

FIG. 10a. Bimonthly maps of the anomalous T_{130} field for 1986. Negative anomalies are shaded. The location dots mark the position of effective single and super-observations. The contour interval is 0.5°C with emphasised contours every 2°C.

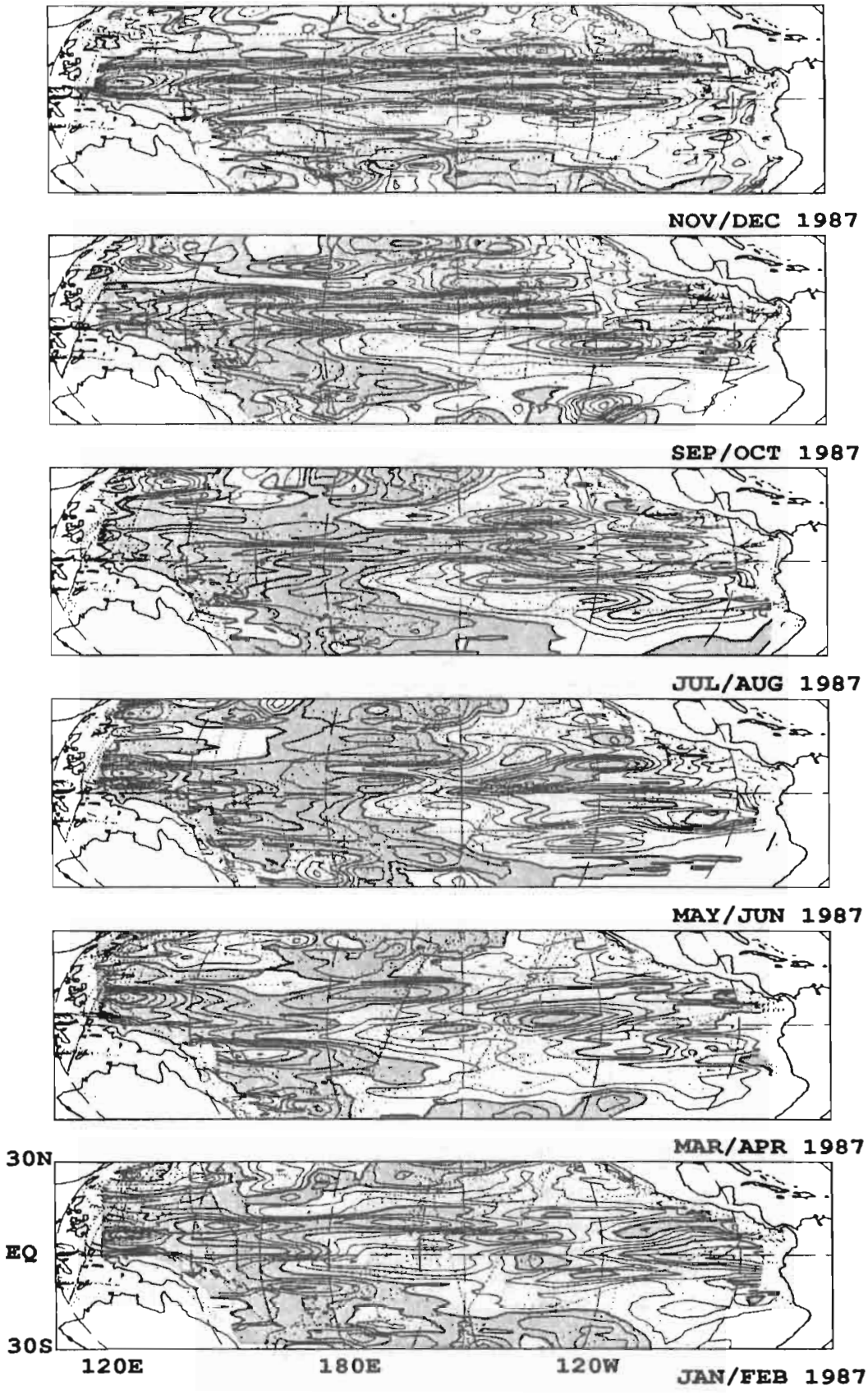

FIG. 10b. As Fig. 10a but for 1987.

The hydrological Cycle of the Intraseasonal Oscillation

Duane E. STEVENS, Qi HU, Graeme STEPHENS and David RANDALL

Department of Atmospheric Science,
Colorado State University
Fort Collins, CO 80523 - U.S.A.

1. INTRODUCTION

Since better understanding of 30-60 day oscillation can lead to improvements in medium and long range weather prediction, this phenomenon has attracted considerable attention. The 30-60 day oscillation was identified by Madden and Julian (1971, 1972) as the eastward propagation of a wavenumber 1 disturbance in tropical, tropospheric zonal wind and surface pressure fields. The range of the period of this disturbance corresponds to a zonal phase speed of 10 to 15 ms^{-1}. Other observational studies have documented disturbances with a similar period of 30 to 60 days in other physical fields. These findings include the oscillations in atmospheric angular momentum (Anderson and Rosen, 1983, and Risbey and Stone, 1988), convective activities and cloudiness (Yasunari, 1980), outgoing long wave radiation over the Indian-Western Pacific Oceans (Murakami *et al.*, 1986, among others) and perturbations in precipitation amount over the same area (Hartmann and Gross, 1988). In addition to atmospheric phenomena, 30-60 day fluctuations of sea level height (Enfield, 1987, and Mitchum and Lukas, 1987) and sea surface temperature (SST) (Enfield, 1987) have also been found. From these studies it is obvious that the 30-60 day oscillation is a complex process involving disturbances in both the tropical atmosphere and ocean.

Despite the multitude of observational studies, a satisfactory theoretical explanation of the 30-60 day oscillation has yet to be agreed upon. Since Gill's (1982) finding, that the phase speed of the tropical waves can be significantly reduced due to reduction of the static stability (hence the equivalent depth) of the atmosphere by latent heat release, the linear tropical wave theory (Matsuno, 1966) after being refined by the diabatic heating parameterization, has been widely applied in explanation of the 30-60 day oscillation. For example, Lau and Peng (1987) proposed the 'mobile wave CISK' mechanism and Chang and Lim (1988) developed the 'Kelvin wave CISK' theory. Although the selected or the newly generated waves in these theories were indeed amplifying as propagating eastward the phase speed of these waves was crucially dependent on the diabatic heating profile used in these models. In order to have a phase speed close to the observed one the heating profile has to have a peak in the lower troposphere. This heating profile, however, is more representative of situations for the mid-latitude than of the tropics (Reihl and Malkus, 1958).

Attempts were also made to find new modes which could be responsible for the observed 30-60 day oscillation. Anderson and Stevens (1987), for example, specified several slow poleward propagating unstable modes in their 2-D eigenvalue model which included an equatorial symmetric Hadley circulation.

Studies in which the intraseasonal oscillation was regarded as an atmospheric response to a sporadic external heating with a 30-60 day period is another category in the approach. By postulating an oscillatory heating as the forcing, many experiments with different atmospheric models were able to produce the expected low frequency oscillatory features (Yamagada and Hayashi, 1984, and Salby and Gacia, 1987). The lack of an explicit instability mechanism in this category of explanation remains questionable, however, if one views the 30-60 day oscillation as purely an intrinsic atmospheric oscillation.

The sporadic 'external' forcing may turn into an 'internal' one when the ocean and atmosphere are considered as one system. Krishnamurti *et al.* (1988) has found the observational evidence of the air-sea interaction on the time scale of 30-60 days. Emanuel (1987) and Neeling *et al.* (1987) looked at the evaporation-wind feedback effect in an ocean-atmosphere system. They showed that the low frequency oscillation can be amplified by drawing energy from the warm ocean surface through this feedback. Although the existence of the oscillation does not depend on the evaporation-wind feedback (Neeling *et al.*, 1987) their studies certainly provided a different perspective for understanding this problem.

In this study, we propose a new theory explaining the origin of low frequency oscillations in the tropics. In our models both the lower atmosphere and upper ocean layers are included and are treated as a fully coupled system. Based on the model results, we suggest that the observed 30-60 day oscillations in the tropical troposphere and in the ocean are the manifestation of the cloud-radiation, atmosphere-ocean feedback processes, and that their realization depends on the hydrologic cycle in this system.

In the next section, the basic physical mechanism for the 30-60 day oscillation in terms of the hydrologic cycle is presented. Sections 3, 4 and 5 describe three different models and their results. Our conclusions are summarized in Section 6.

2. MECHANISM

The tropical atmosphere above the warm ocean surface is heated through the energy exchanges with the ocean. Meanwhile evaporation from the ocean moistens the lower part of

ORSTOM
CENTRE DOCUMENTATION
Montpellier

F 30236

the tropical troposphere. The warmer the ocean mixed layer, the more heat and more moisture are added into this part of the atmosphere.

The removal of the accumulated 'extra' heat and moisture from the tropical atmosphere occurs through deep cumulus convection (Riehl and Malkus, 1958). This convection is crucial in the hydrologic cycle of the tropical atmosphere-ocean system. When explaining the conditional instability in the tropical atmosphere, Ooyama (1969) showed that the vertical temperature and moisture structures in the tropics possess a conditionally unstable character before the onset of convection. However, this instability is realized only when the lower troposphere is sufficiently moistened, through surface evaporation and/or large-scale convergence. This characteristic of the tropical atmosphere is important as it highlights the key role played by the moisture in the occurrence of tropical convection. In our conceptual models, presented in the next two sections, we will set a critical moisture value as the 'model atmospheric moisture tolerance' to represent this thermodynamic feature of the tropical atmosphere. This treatment principally follows the philosophy in parameterizing cumulus convection (Kuo, 1975, and Stevens and Lindzen, 1978) and is based on empirical evidence such as the observed moisture changes in synoptic scales wave disturbances (Reed and Recker, 1971).

When the conditional instability is being released, the convection not only diminishes the extra moisture in the atmosphere through precipitation but, through cloud-radiation interaction, also reduces the sea surface temperature by attenuating the solar radiation energy available at the ocean surface. The result of this is to return the extra water substance in the atmosphere back to the ocean and to reduce the sea surface temperature to its 'climatological' value.

In short, a natural cycle represented by the hydrologic process in the atmosphere-ocean system is spontaneously carried on in the tropics. Our model shows that, simply restricted by the 'moisture tolerance', such a cycle possesses an intraseasonal time scale.

3. A SIMPLE MODEL WITH FIXED SST

a) The Model

In this section we demonstrate the existence of the hydrologic cycle in a simple atmosphere-ocean system with *fixed* ocean parameters. The schematic structure of this model is given in Fig. 1. As shown in Fig. 1 only thermodynamic process are considered in this model. Our attention is to describe the accumulation of the extra water content in the atmospheric mixed layer through evaporation and the removal of this content by precipitation; horizontal convergence and divergence are neglected.

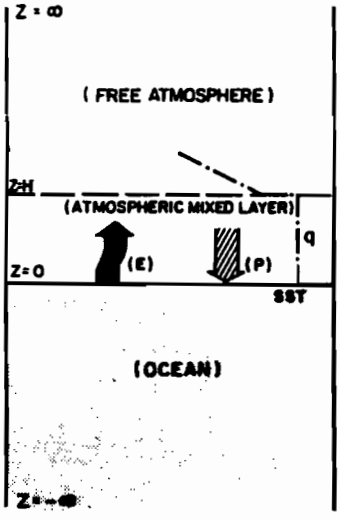

Fig. 1: Schematic structure of the model (MD1) with a fixed sea surface temperature (SST).

The temperature of the atmospheric mixed layer is characterized by a near-surface atmospheric temperature $T_a = T_s - \Delta T(^\circ C)$. Precipitation is assumed to take place when the 'atmospheric moisture tolerance' is achieved. As an initial approach we specify this critical condition as that when the mixing ratio of the atmospheric mixed layer reaches 90% of the saturation value at its temperature, T_a.

The amount of moisture evaporated in each time interval, Δt, is calculated by

$$\Delta E = \int_{\Delta t} E(t)dt\,, \tag{1}$$

where,

$$E(t) = \rho_a C_D |u_s||q_{sat}(T_s) - q_{atm}(t)| \tag{2}$$

(Neeling *et al.* 1987). In (2), ρ_a is the mean density of the atmospheric mixed layer, C_D is the surface drag coefficient and is treated as a constant of 0.001. The parameter u_s is the low level wind at 10 meters above the sea surface, $q_{sat}(T_s)$ is the saturation mixing ratio of the atmosphere at temperature T_s and $q_{atm}(t)$ is the actual mixing ratio of atmospheric mixed layer at time t. The value of q_{atm} is updated at time step $t + \Delta t$ by an increment Δq given by

$$\Delta q = \frac{1}{(\rho_a H)} \int_{\Delta t} (E(t) - P)dt\,. \tag{3}$$

Here P represents the precipitation rate and is assumed as a constant, $2.5mm/day$ (Wang, 1988) during the model's rainy period and H is the mixed layer depth.

By using a mean atmospheric moist state and the precipitation rate, the model is integrated with a one hour time interval for 1000 days.

b) Model Result and Sensitivity

Fig. 2 shows the results of two model integrations. Model parameters used in these integrations are listed in the figure caption. The displayed field, extra water content, indicates the column moisture amount above an assumed background state, which corresponds to a mixing ratio (q_{atm}) of $15g/kg$ in the atmospheric mixed layer.

An *ad hoc* parameterization of the low-level wind, intended to represent the higher winds and associated transfers between atmosphere and ocean during convection,

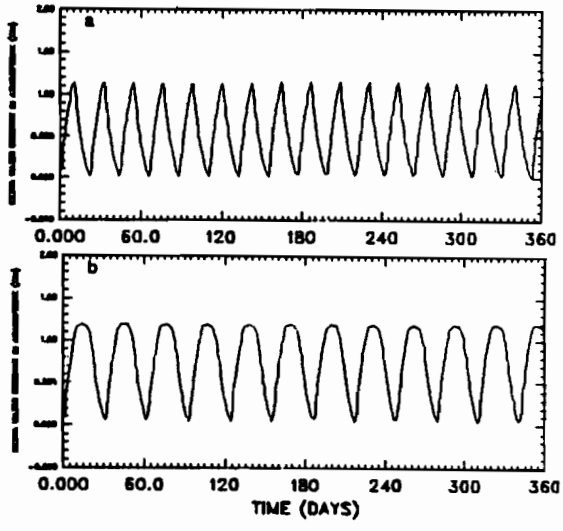

Fig. 2: Predicted hydrologic circulation in the model atmosphere-ocean system. The model low level wind, u_s, used in (a) is a constant of 2.0 m/s, and in (b) is that given in Eq. (4), with $u_b = 2\,m/s, u_m = 12\,m/s$, and $\Delta t_d = 13days$. Other model parameter values are $T_s = 28.5^\circ$C, $T_a = 28.0^\circ$C, $H_{atm} = 1500m$ and $P = 2.5mm/day$.

$$u_s(t) = \begin{cases} u_b & t \le t_c \\ u_m & t_c \le t \le t_c + \Delta t_m \\ u_m - \frac{u_m - u_b}{\Delta t_d}[t - (t_c + \Delta t_m)], & t_c + \Delta t_m \le t \le t_c + \Delta t_m + \Delta t_d, \end{cases} \quad (4)$$

is used in getting the result in Fig. 2b. In this expression u_b is the mean background wind speed and t_c is the time when the atmospheric moisture tolerance is achieved. The maximum wind speed, u_m is assumed to occur during the prescribed time interval Δt_m when deep cumulus convection is present. This time increment is prescribed to be 2 days,

From the results shown in Fig. 2 the existence of the hydrologic cycle operating in this simple atmosphere-ocean system is clearly evident. Through the processes of evaporation and precipitation, which are constrained by the moisture tolerance and its implied conditional instability, the hydrologic cycle is naturally introduced in this system. Furthermore, through a comparison of these two results, we see that the presence of this cycle is independent of the detailed structure of the low level wind. This independence suggests that the oscillation in the low level wind field may be considered a consequence of the hydrologic cycle. Since the time evolution of the heating profile in the tropical troposphere is directly related to the different phases of the hydrologic cycle, this cycle provides an external heat/energy source for the atmosphere. This source disturbs the energy state of the tropical atmosphere to which the wind and mass fields of the atmosphere then adjust. Thus this hydrologic cycle is a plausible mechanism for initiating oscillations of similar frequency in wind and mass fields in the tropical atmosphere. The influence of the varying low level wind field on the frequency of the hydrologic cycle is also noticeable in Fig. 2, although it is does not determine the existence of the cycle *per se*.

Results of model integrations with different model parameters are presented in Fig. 3. These results were obtained with the same low level winds as used to produce Fig. 2b. A significant characteristic shown in this figure, is that the period of the resultant hydrologic cycle in this system increases with increasing model SST. This result is consistent with the observation that low frequency oscillations are preferred in regions of warmest SSTs (Webster, 1987).

The model sensitivities to different low level wind speeds and values of precipitation rate are also illustrated in Fig 3.

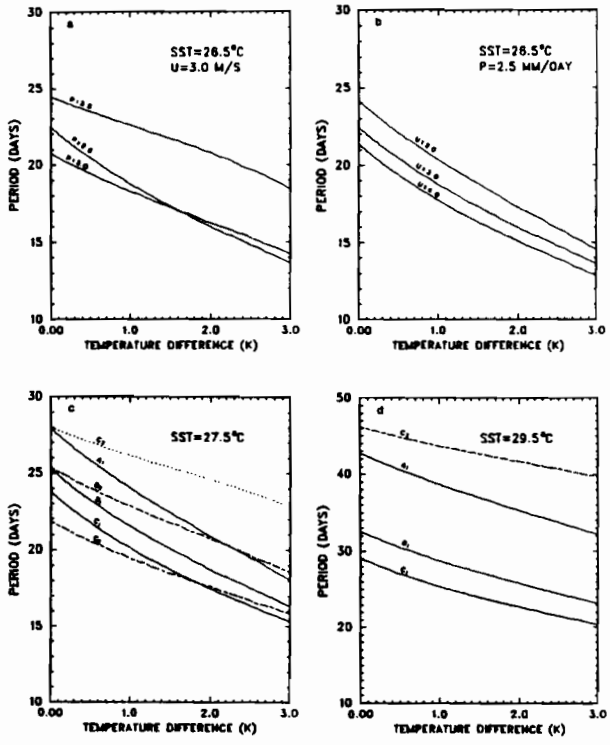

Fig. 3: Predicted period of hydrologic circulation with different model conditions. The abscissa shows the temperature difference between the ocean and the atmosphere. (a) and (b) show the model sensitivities to the changes in precipitation rate P [unit: mm/day] and the model low level wind u_s [unit: m/s], respectively. In (c) and (d), the 3 groups of results, e.g. A_i, B_i and C_i are for 3 different P's used in the model, i.e. 2.5, 3.0 and 3.5 mm/day. The subscript i, from 1 to 3, stands for different low level wind conditions of 2.0, 3.0 and 4.0 m/s. Lines are not plotted in (c) and (d) when a balance between E and P is the case and therefore no oscillation occurs.

4. COUPLED INTERACTIVE ATMOSPHERE-OCEAN MIXED LAYER MODEL

The existence of the hydrologic cycle and its relationship to the low frequency oscillation in the tropical troposphere have been shown by the one-way interaction model (hereafter MD1) of Section 3. Since a fixed SST was applied in MD1, the question of how this cycle as well as its time scale is influenced by a time varying SST still remains. In this section we address some aspects of this issue.

a) The Model

The model structure and the major physical processes are schematically illustrated in Fig. 4. As in MD1, we focus on the thermodynamics of this atmosphere-ocean system and ignore any detailed dynamics. The model's ocean mixed layer process follows that in Kraus and Turner (1967), and Denman (1973)

In this model to incorporate in the model SSTs which vary in time, a detailed energy budget in the ocean mixed layer is required. As the only energy source in this budget, the input solar energy at the ocean surface needs to be included. This input further varies with presence or absence of cumulus convections through cloud-solar radiation interaction. On the other hand, the energy losses through infrared radiation (IR) from ocean surface, and sensible and latent heat exchanges with the atmosphere are also considered. Since explicit prediction of key processes, such as cloud generation and interaction of clouds with solar radiation, is beyond the scope of this mechanistic study, we parameterize their effects. To express the cloud influence on the solar radiation, for example, we assume different values of the solar irradiance at the surface under varying convective cloud cover conditions. These values are obtained from observations and theoretical studies. A similar method is also applied to represent the IR cooling process. The main reason for neglecting the detailed treatment of these processes is to avoid the uncertainties associated with complex processes involving multiple scales, some of which are poorly understood, and therefore to concentrate more on the basic physical mechanisms.

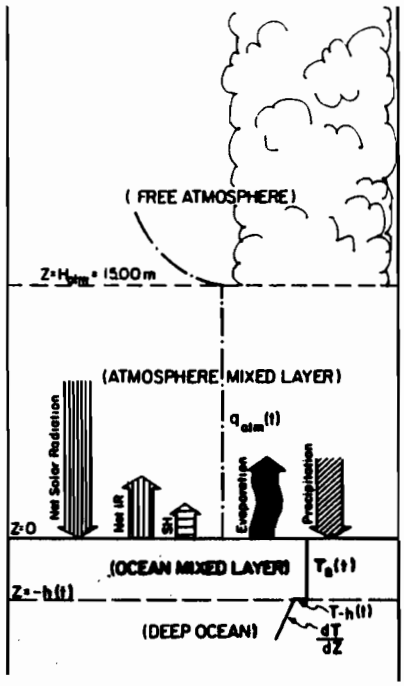

Fig. 4: Schematic structure of the fully coupled atmosphere-ocean mixed layer model (MD2).

In the model atmosphere, the process is similar to MD1. The moisture amount transferred into the model atmospheric mixed layer is calculated again using the bulk aerodynamic formula

$$E(t) = \rho_a C_D |u_s(t)| (q_{sat}|T_s(t)| - q_{atm}(t)) . \qquad (5)$$

Here, $q_{sat}|T_s(t)|$ is time dependent as SST varies with time in this model. A Bowen ratio of 0.2 is used to obtain the value of the sensible heat flux required as an input to the ocean model.

The solar irradiance at the ocean surface are specified by the step function

$$R_{sw} = \begin{cases} R^n_{sw}, & \text{non-convective;} \\ R^c_{sw}, & \text{convective.} \end{cases} \qquad (6)$$

The values in (6) are based upon the satellite and observational data analyses by Gautier and Katsaros (1984), Gautier (1986) and Gautier (1988). With these values, the bulk features of the influence of deep cumulus convection on the solar radiation transfer in the atmosphere have been included. Likewise the step function for IR change is

$$R_{IR} = \begin{cases} R^n_{IR}, & \text{non-convective;} \\ R^c_{IR}, & \text{convective,} \end{cases} \qquad (7)$$

where the values for R^n_{IR} and R^c_{IR} are based on a study by Stephens *et al.* (1981).

b) Model Results

Table 1 lists some of the model experiments we conducted. The physical parameters, their values, and the model predicted quantities are included in this table.

Since only thermodynamic and turbulent mixing processes in the two mixed layers are considered, only a few of these experiments reach a steady or an equilibrium state through the period of integration. Fig. 5 shows the result from one of the experiments (experiment 1 in Table 1) in which an equilibrium state has been reached. From this figure we see that the oscillation of the extra water content in the atmospheric mixed layer still experienced when the model has varying SST. This oscillation, through the coupling and feedback with the solar radiation and hence the surface energy process, influences the processes in the ocean mixed layer (Figs. 5b,c and d). The time scale of these oscillations predicted by the model is 33 days.

As we have discussed in Section 2, in the process of the hydrologic circulation a pulsating energy disturbance is released in the convection phase. This disturbance then causes dynamic perturbations in the atmospheric momentum and mass fields (Salby and Garcia, 1987). The observed oscillation in the atmospheric relative angular momentum (Anderson and Rosen, 1983) may also be related with this pulsating energy disturbance. On the other hand, this energy disturbance, in addition to the change in the solar energy input, affects the energy budget of the ocean mixed layer. As a consequence of the hydrologic circulation in the atmosphere-ocean system, the 30-60 day oscillations therefore appear in both the tropical atmosphere and ocean.

Because the thermodynamic processes depend on SST in a highly nonlinear fashion, the results illustrated in Table 1 differ from those obtained from MD1. In Fig. 3, a higher SST in the one-way model causes a dramatic increase in the period of the model's hydrologic circulation. Results from the fully coupled model, however, are not as simple. Using $29°C$ as the initial SST, the hydrologic cycle reaches a steady period of 35 days (experiment 2 in Table 1). This period is quite close to that predicted in experiment 1 where the initial SST is $28°C$. However when a colder SST is used to start the model run, the predicted result are distinctly different (Fig. 6).

Results presented in Table 1 also show the model sensitivity to other model parameters.

5. ONE-DIMENSIONAL GCM AND RESULTS

To test our hypothesis in a more complete manner different experiments have also been conducted with the one-dimensional version of the UCLA/CSU GCM (Randall and Dazlich, 1989). This 1-D model includes the full radiation and moist physics parameterization of the GCM, and is coupled to a slab of ocean of fixed depth. The slab ocean does not exchange energy with deeper ocean layers; its temperature is controlled entirely by the surface energy flux.

At this stage some very preliminary results from experiments with this 1-D GCM model have been obtained and are shown in Figs. 7 and 8. These results support the major findings from our previous conceptual models. When run with a ocean slab depth of $60m$, the model produces obvious oscillation of sea surface temperature, with amplitude $0.4°C$ and a period of 60 days (Figs. 7a and 8a). This oscillation is accompanied by 60-day fluctuations of the surface energy flux, precipitation rate and cloudiness (Figs. 7b, 7c and 8b). The changes in the surface energy flux are due to changes in the absorbed solar radiation, which are controlled by the cloudiness fluctuations or model convections.

During the warming phase of the oscillation, the sea surface temperature and the convective precipitation rate gradually increase. Eventually the cloudiness increases to the point that the solar radiation absorbed by the ocean is reduced, allowing the ocean to begin cooling. This cooling is followed by a reduction in the model convective activity, which leads to a reduction in the cloudiness. The absorbed solar radiation then increases, and the model hydrologic cycle is re-initiated.

Table 1: Model Experiments and Results – Among the output quantities, r is the predicted period of the model hydrological circulation. Σq is the maximum extra water amount accumulated in the model atmosphere before convection starts. ΔT and Δh are respectively the amplitudes of changes in the SST and depth of ocean mixed layer in a hydrological circulation. When a steady state is not reached in a model run, these quantities are given from a nominal cycle in model integration.

Physical Parameter	Experimental Value					
	1	2	3	4	5	6
$R^n_{SW}\,(W/m^2)$	250	250	250	250	250	260*
$R^c_{SW}\,(W/m^2)$	120	120	120	120	120	105*
$R^n_{IR}\,(W/m^2)$	40	40	40	40	40	40
$R^c_{IR}\,(W/m^2)$	40	40	40	40	40	40
u_s : $(u_b, u_m, \Delta t_d)$	(2, 12, 13.0)	(2, 12, 13.0)	(2, 12, 13.0)	(2, 12,11.5*)	(2, 12, 15.0*)	(2, 12, 13.0)
$P\,(mm/day)$	2.5	3.0*	2.5	2.5	2.5	2.5
$T_s(t=0)(°C)$	28.0	29.0*	26.0*	28.0	28.0	28.0
$T_{-h}(t=0)(°C)$	25.0	26.0*	23.0*	25.0	25.0	25.0
Output Quantity	Model Predicted Result					
r (days)	33	35	the 5th: 23 the 9th: 15	the 5th: 33 the 20th: 37	the 5th: 33 the 20th: 26	31
$\Sigma q\,(cm/m^2)$	1.49	1.51	the 9th: 0.35	the 20th: 1.70	the 20th: 0.80	1.40
$\Delta T_s(°C)$	1.68	1.63	the 9th: 0.83	the 20th: 1.67	the 20th: 1.41	1.83
$\Delta h(m)$	21.85	21.39	the 9th: 13.51	the 20th: 21.48	the 20th: 19.50	24.93

*: Parameter value different from that in the controlled experiment (experiment 1).

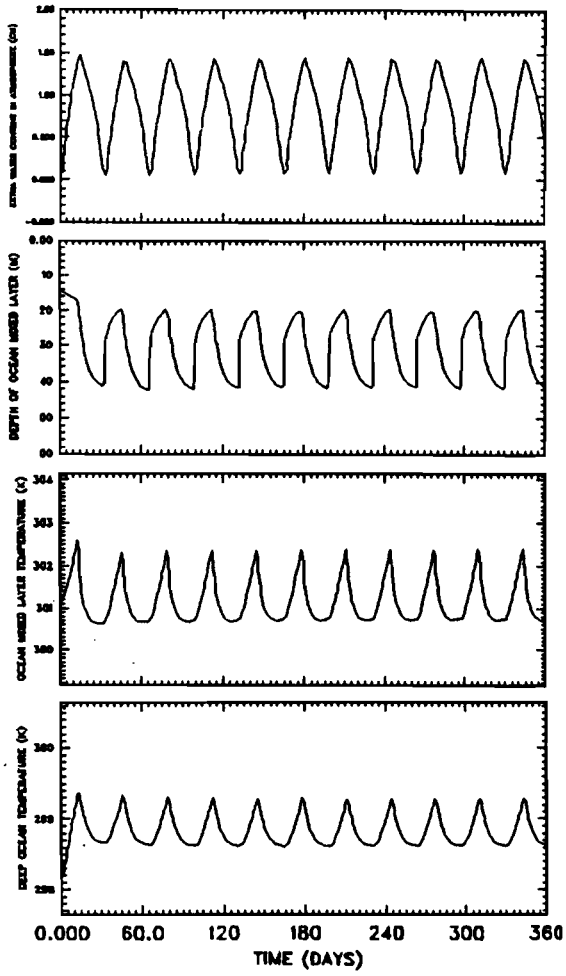

Fig. 5: Model results from experiment 1 in Table 1.

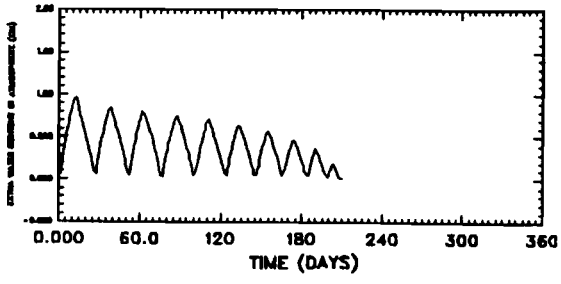

Fig. 6: Temporal variation of the extra water content in the model atmosphere from experiment 3 in Table 1.

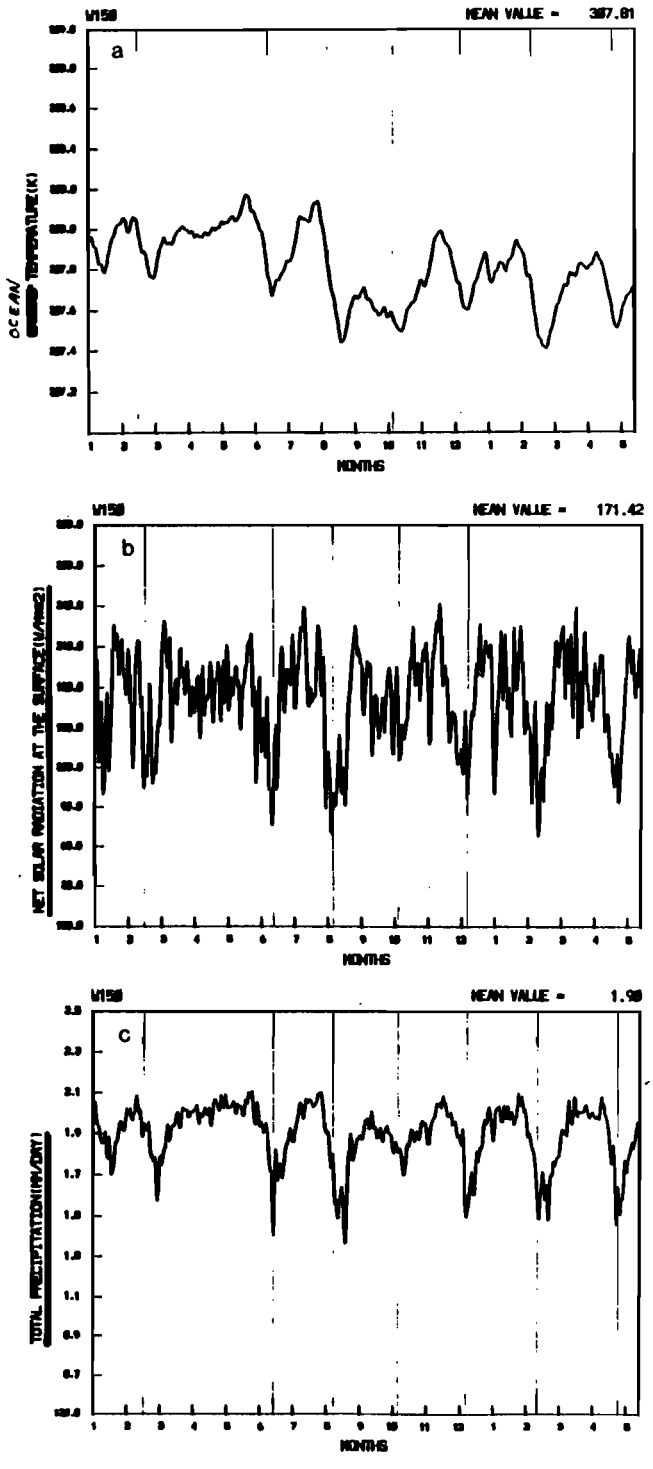

Fig. 7: Temporal variations of (a) SST, (b) solar radiation absorbed at the ocean surface, and (c) daily precipitation from the 1-D GCM.

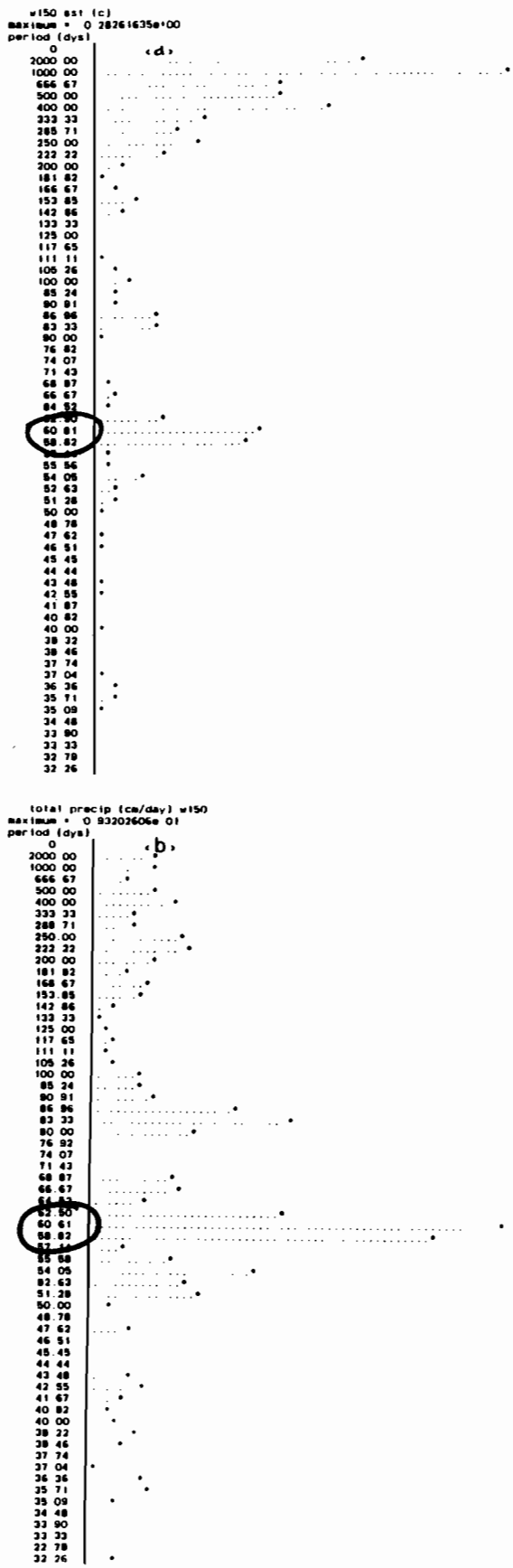

Fig. 8: Square of the amplitudes of the Fourier harmonics of (a) model SST, and (b) model precipitation. Peaks at about 60 days are outstanding.

6. CONCLUDING REMARKS

In this study we have shown that the 30-60 day oscillations in the tropical atmosphere and ocean can result from the hydrologic circulation in a coupled atmosphere-ocean system. This circulation is intrinsic to this system and is a consequence of the energy exchange and energy balance in this system.

The time scale of this circulation can be determined in a simple coupled atmosphere-ocean model when the role of moisture played in the atmosphere is incorporated in the model. By parameterizing this role in terms of the 'model atmospheric moisture tolerance' in our conceptual models we showed that the hydrologic cycle is spontaneously carried on in the tropical atmosphere-ocean system. Its existence was basically independent of the variations of the low level wind.

Our hypothesized relationship between the hydrologic circulation and the intraseasonal oscillation in the tropical atmosphere and ocean was also examined in a 1-D GCM. The model results were positive in supporting this relationship. Meanwhile, the analysis of the thermodynamic process in the 1-D GCM illustrated the mechanism we proposed.

Based on our results we conclude that the hydrologic cycle in the tropical atmosphere-ocean system is fundamental to the observed intraseasonal oscillations in the tropics. The physical restriction of the accumulation of latent heat in the lower tropical troposphere and the reduction of the source supply of energy to the tropical atmosphere-ocean system, through cloud-solar radiation interaction, are crucially important to the presence and time scale of this hydrologic cycle.

7. ACKNOWLEDGMENTS

We would like to thank Ms. Gail Cordova for preparing this manuscript and Ms. Judy Sorbie for drafting the schematic figures. This research has been supported by the National Science Foundation under grant ATM-8609731 to Colorado State University. Computations were carried out on the computers at the National Center for Atmospheric Research, which is also sponsored by the National Science Foundation.

8. REFERENCES

Anderson, J.R., and R.D. Rosen, 1983: The latitude–height structure of 40– 50 day variations in atmospheric angular momentum. *J. Atmos. Sci.*, **40**, 1584–1591.

Anderson, J.R. and D.E. Stevens, 1987: The presence of linear wavelike modes in a zonally symmetric model of the tropical atmosphere. *J. Atmos. Sci.*, **44**, 2115–2127.

Anderson, J.R. and D.E. Stevens, 1987: The response of the tropical atmosphere to low–frequency thermal forcing. *J. Atmos. Sci.*, **44**, 676–686.

Chang, C.-P., and H. Lim, 1988: Kelvin Wave–CISK: A possible mechanism for the 30–50 day oscillations. *J. Atmos. Sci.*, **45**, 1709–1720.

Denman, K.L., 1973: A time–dependent model of the upper ocean. *J. Phys. Oceanogr.*, **3**, 173–184.

Emanuel, K.A., 1987: An air–sea interaction model of intraseasonal oscillations in the tropics. *J. Atmos. Sci.*, **44**, 2324–2340.

Enfield, D.B., 1987: The intraseasonal oscillation in eastern Pacific sea levels: How is it forced? *J. Phys. Oceanogr.*, **17** 1860-1876.

Gautier, C., 1986: Evolution of the net surface short wave radiation over the Indian ocean during summer MONEX (1979): A satellite description. *Mon. Wea. Rev.*, **114**, 525-533.

Gautier, C. and K. Katsaros, 1984: Insoluation during STREX. Part I: Comparisons between surface measurements and satellite estimates. *J. Geophys. Res.*, **89**, 11779-11788.

Gautier, C., 1988: Surface solar radiance in the central Pacific during Tropic Heat: Comparisons between *in situ* measurements and satellite estimates. *J. Climate*, **1**, 600-608.

Gill, A.E., 1982: Studies of moisture effects in simple atmospheric models: the stable case. *Geophys. Astrophys. Fluid Dynamics*, **19**, 119-152.

Hartmann, D.L., and J.R. Gross, 1988: Seasonal variability of the 40-50 day oscillation in wind and rainfall in the tropics. *J. Atmos. Sci.*, **45**, 2680-2702.

Kraus, E.B., and J.S. Turner, 1967: A one-dimensional model of the seasonal thermocline II: The general theory and its consequences. *Tellus*, **19**, 98-106.

Krishnamurti, T.N., D.K. Oosterhof, and A.V. Mehta, 1988: Air-sea interaction on the time scale of 30-50 days. *J. Atmos. Sci.*, **45**, 1304-1322.

Kuo, H.-L., 1975: Instability theory of large-scale disturbances in the tropics. *J. Atmos. Sci.*, **32**, 2229-2245.

Lau, K.M., and L. Peng, 1987: Origin of low-frequency (intraseasonal) oscillations in the tropical atmosphere. Part I: Basic theory. *J. Atmos. Sci.*, **44**, 950-972.

Madden, R., and P.R. Julian, 1971: Detection of a 40-50 day oscillation in the zonal wind in the tropical Pacific. *J. Atmos. Sci.*, **28**, 702-708.

Madden, R., and P.R. Julian, 1972: Description of global-scale circulation cells in the tropics with a 40-50 day period. *J. Atmos. Sci.*, **29**, 1109-1123.

Matsuno, T., 1966: Quasi-geostrophic motions in the equatorial area. *J. Meteor. Soc. Japan*, **44**, 25-42.

Mitchum, G.T., and R. Lukas, 1987: The latitude-frequency structure of Pacific sea level variance. *J. Phys. Oceanogr.*, **17**, 2362-2365.

Murakami, T., L. Chen and A. Xie, 1986: Relationship among seasonal cycles, low-frequency oscillations, and transient disturbances as revealed from outgoing longwave radiation data. *Mon. Wea. Rev.*, **114**, 1456-1465.

Neeling, J.D., I.M. Held and K.H. Cook, 1987: Evaporation-wind feedback and low-frequency variability in the tropical atmosphere. *J. Atmos. Sci.*, **44**, 2341- 2348.

Ooyama, K., 1969: Numerical simulation of the life cycle of tropical cyclones. *J. Atmos. Sci.*, **26**, 3-40.

Randall, D. A. and D. Dazlich, 1989: The *CSU* general circulation model: *A user's guide*. informal manuscript.

Reed, R.J. and E.E. Recker, 1971: Structure and properties of synoptic-scale wave disturbances in the equatorial western Pacific. *J. Atmos. Sci.*, **28**, 1117-1133.

Riehl, H., and J.S. Malkus, 1958: On the heat balance in the equatorial trough zone. *Geophysica*, **6**, 3-4.

Risby, J.S., and P.H. Stone, 1988: Observations of the 30-60 day oscillation in zonal mean atmospheric angular momentum and high cloud cover. *J. Atmos. Sci.*, **45**, 2026-2038.

Salby, M.L., and R.R. Garcia, 1987: Variations induced by interference of stationary and traveling planetary waves. *J. Atmos. Sci.*, **44**, 2679-2711.

Stephens, G.L., G.G. Campbell and T.H. Vonder Haar, 1981: Earth radiation budgets. *J. Geophys. Res.*, **86**, C10, 9739-9760.

Stevens, D.E. and R.S. Lindzen, 1978: Tropical wave CISK with a moisture budget and cumulus friction. *J. Atmos. Sci.*, **35**, 940-961.

Wang, B., 1988: Dynamics of tropical low-frequency waves: An analysis of the moist Kelvin wave. *J. Atmos. Sci.*, **45**, 2051-2065.

Webster, P.J., 1987: The role of hydrological processes in ocean-atmosphere interaction. USTOGA 8, 71-100.

Yamagada, T., and and Y. Hayashi, 1984: A simple diagnostic model for the 30-50 day oscillation in the tropics. *J. Meteor. Soc. Japan*, **62**, 709-717.

Yasunari, T., 1980; A quasi-stationary appearance of 30-50 day period in the cloudiness fluctuations during the summer monsoon over India. *J. Meteor. Soc. Japan*, **58**, 225-229.

Transmission Characteristics of the Dynamic Response to Episodic Forcing in the Warm Pool Regions of the Tropical Oceans

Peter J. WEBSTER, Hai-Ru CHANG and Chidong ZHANG

Department of Meteorology
The Pennsylvania State University
University Park, PA, 16802 - U.S.A.

ABSTRACT

In the warm pool region of the Pacific Ocean, the strongest and most intense convective heating in the global atmosphere occurs. The form of the heating is episodic, lasting for periods of days with scales of order 2-3000 km generating a spectrum of waves. The modes that are excited range from the mixed Rossby-gravity wave to the equatorially trapped Rossby and Kelvin waves. However, these transient modes are produced in a complex basic state which includes both horizontal and vertical shear and horizontal stretching deformation. To determine how they extend their influence from the warm pool region to other, more remote areas of the globe, we are required to reconsider the basic theory of equatorial waves in basic states of different signs, latitudinal shear and longitudinal stretching deformation. It is shown that the waves are extremely sensitive to each of these factors. Depending on the sign of the basic state, the waves "swell" poleward differentially. In particular, the turning latitudes of modes in the equatorial westerlies is about twice that for the equatorial easterlies; 15° compared to 30°-40° for observed values of the basic flow. The longitudinal stretching deformation causes regions of energy accumulation within the equatorial westerlies. Modes reach the accumulation zone in different directions depending on their scale. The short-scale end of the excited wave packet, which has initial weak easterly group speeds and stronger eastward Doppler-shifted group speeds, approaches the westerlies from the west. Through the modifications that the wave must undergo from conservation principals, the Doppler-shifted group speed approaches zero in the region of negative stretching deformation. The long-wave end of the packet, with westward group speeds, approaches the westerlies from the east where, for the same conservation reasons, the Doppler-shifted group speed also approaches zero. In the equatorial westerlies, the accumulated wave energy "swell" to higher latitudes as the turning latitudes of the modes modify in the westerly wind regime. In this manner, corridors through which energy passes from the convective regions of the tropics to higher latitudes are created.

1. Introduction

The warm pool regions of the tropical oceans contain the most vigorous convection on the globe. The largest warm pool exists between the western Pacific Ocean and the eastern Indian Ocean, spanning the Indonesian Archipelago. If sea surface temperatures greater than 28°C are used as a criterion, the West Pacific-East Indian Ocean warm pool covers about one eighth of the surface area of the globe. Within the heart of the warm pool, annual precipitation exceeds 4 m. The convection associated with the precipitation appears to be highly organized with space and time scales of greater than 2-3000 km and of the order of a week or greater, respectively (Nakazawa, 1988, Lau et al, 1988). Observations and models suggest that the intense and impulsive convection may promote the excitation of transient modes. Other studies (e.g., Lau and Chan, 1985) suggest that these transients exert considerable influence on the extratropics and that the midlatitude response is often phase locked irrespective of the phase of the equatorial forcing.

ORSTOM
CENTRE DOCUMENTATION
Montpellier

F 30237

Despite the evidence of the existence of strong forcing in the warm pool regions and the observations of energy radiating away from the energy source both along the equator and into the mid latitudes, there exists a relative ignorance of how the influence is transmitted globally. Part of the problem is that the forcing takes place in an extremely complicated basic or background state. The basic flow, forced by the slowly varying heating associated with the sea surface temperature (SST) field contains both horizontal and vertical shear and horizontal stretching deformation (Webster and Chang, 1988). Figure 1a provides a schematic diagram of the near-equatorial background flow in the longitude-height plane at extremes of the Southern Oscillation (Webster, 1987). Figure 1b shows the character of the boreal winter upper tropospheric flow. Elementary theory of equatorial modes is not applicable to such complicated basic states. Thus, to understand wave transmission in complicated basic states, it is necessary to examine existing theory.

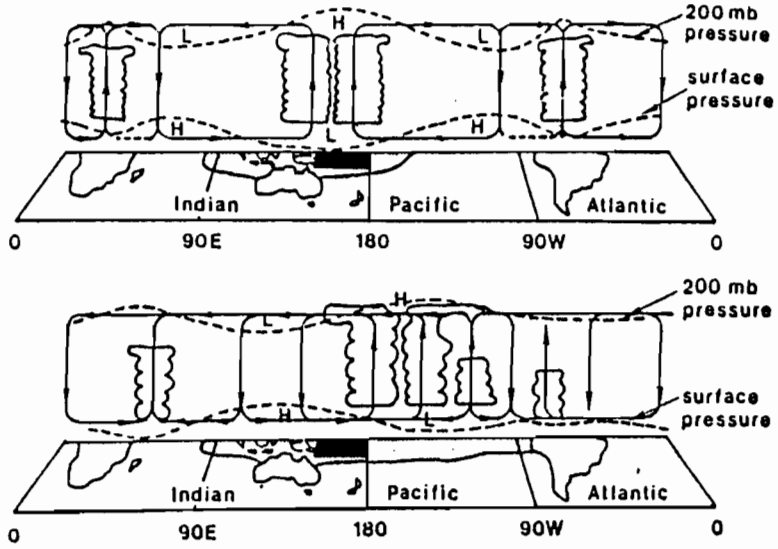

FIG.1. Schematic diagram of the zonal circulations along the equator for La Nina (upper panel) and El Nino (lower panel). Clouds represent regions of maximum mean convection. Stippled regions indicate sea surface temperatures warmer than 28°C. Waves represent genesis regions of equatorial transients. (after Webster, 1983)

Equatorial dynamics has a relatively short history in the atmospheric sciences. It was not until the late 1960's that a series of observational and theoretical studies provided a new basis for understanding the elementary physics of the large-scale tropical atmospheric circulation. Foremost in these studies was Matsuno (1966) which provided new and enlightening perspectives. It showed that classes of very large-scale modes existed which possessed a mix of divergent and rotational characteristics that were trapped about the equator. Matsuno's study, which used a β plane formulation in a quiescent fluid, showed that there were a number of mode families that were equatorially trapped. These were the Rossby wave, the eastward and westward propagating mixed Rossby-gravity and gravity modes and the Kelvin mode. Later, Longuet-Higgins (1968) was able to show that Matsuno's solutions were asymptotics of general spherical modes as the parameter $(4\Omega^2a^2/gh)$ becomes large. The dispersion curves for modes with h=300 m are shown in Fig. 2.

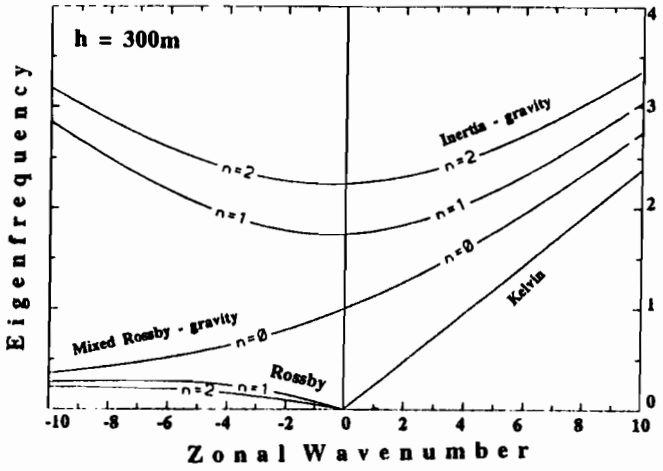

FIG.2.Dispersion curves of equatorially trapped modes for an h=300 m fluid. (Zhang and Webster, 1989).

A number of studies considered the properties of equatorial modes in simple non-zero basic states. As the complexity of the states increased so did the applicability of the theory to the solution of practical physical problems. Using zonally symmetric basic states (i.e., U=U(y)), Webster (1972, 1973) and Gill (1980) suggested that the mean structure of the tropics could be thought of as the response of equatorially trapped modes to stationary forcing produced by the latent heat release associated with the mode itself and the sea-surface temperature distribution. Opsteegh and Van den Dool (1980), Hoskins and Karoly (1981), Webster (1981, 1982), among others, have speculated that anomalous forcing along the equator within simple U(y) flows produce propagating wave trains. Thence, the theory continues, the global climate is perturbed during periods of anomalous forcing such as El Nino. Figure 3 shows the boreal winter and summer anomalous atmospheric responses relative to anomalous equatorial heating akin to the difference between latent heating during warm events and more normal times in the Pacific Ocean.

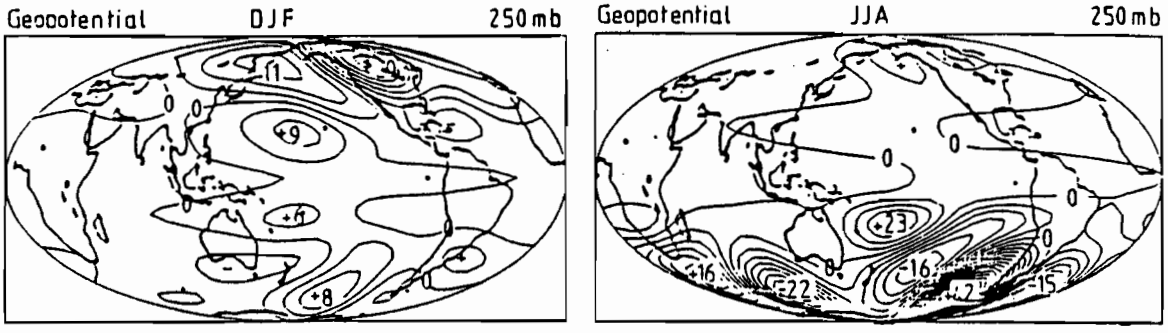

FIG.3. The 250 mb geopotential response of a zonally symmetric boreal winter (right panel) and summer (left panel) zonal wind distribution to a steady heat source placed in the central Pacific Ocean. (Webster, 1982).

Whereas the steady state models predict many features of the observed anomalous behavior, including maximum perturbation of the winter hemisphere, it has become apparent that the physical basis of the system is too simplistic. In other words, the steady state theory suffers from a number of problems. First, if the forcing moves in location, the pattern must also move. Observations show that warm events differ markedly in form and intensity. Both observations and numerical modeling show that the

global influence pattern is more robust and is relatively invariant in its' position to the shape and magnitude of the forcing function. Also, a steady state model ignores the transient nature of the atmosphere. The mean annual heating is comprised of a series of strong impulsive events. Thus, unless the state model can somehow mimic the aggregate of these transients, one can expect differences between the steady state solutions and the mean atmospheric response. Finally, the excitation of the Rossby wave train from within the easterlies, which the steady state models predict, requires either that the forcing extends to the westerlies or that nonlinear effects are important (Sardeshmukh and Hoskins, 1988).

Besides impacting the circulation of the higher latitudes, equatorial forcing also produces a considerable perturbation to the mean flow at low latitudes, at least in its' aggregate effect. The combination of forced equatorially trapped Rossby and Kelvin modes produces regions of perturbation easterlies and westerlies along the equator. The perturbations are sufficiently strong to produce regions of net westerlies in the tropical upper troposphere which are apparent for most of the year over the eastern Pacific and Atlantic Oceans. Thus, in reality, the basic flow, at least as far as the transients are concerned, has a strong three-dimensionality such that U=U(x,y,z).

2. Magnitude, scale and duration of episodic convective heating in the tropical regions: the case for strong episodic forcing.

Outgoing longwave radiation (OLR) has been used as a surrogate for precipitation for a number of years (Arkin and Meisner, 1987). Figures 4a and b show the boreal summer (upper panel) and winter (lower) OLR distributions in the equatorial strip. Concentrating on values of OLR < 240 $W.m^{-2}$, we note that there are three major minima: over equatorial Africa and the central Americas and, the largest, over the eastern Indian Ocean and western Pacific Ocean which spans Indonesia. All three centers show an annual cycle with a migration towards the summer hemisphere. At all times of the year, a large minima remains in the western Pacific Ocean. By extension (Arkin and Meisner, 1987), we can infer that intensive precipitation occurs at all times of the year. Heating functions derived from such precipitation distributions have been used to drive steady state circulation models in an attempt to model the mean tropical circulation (e.g., Webster, 1972[1], 1981, 1982, Opsteegh and van den Dool, 1980, Hoskins and Karoly, 1981). To a large degree, these models were able to simulate and explain the strong three-dimensional character of the mean tropical flow such as that shown in Figs. 1 and 3.

Assessing the magnitude of the western Pacific Ocean precipitation with accuracy is rather difficult. Figure 5 provides an estimate of the Pacific Ocean annual precipitation using island data (Taylor, 1972). The analysis shows a broad region of precipitation in the western Pacific Ocean of order of 4-5 m and an elongated maximum north of the equator. The first feature appears to be associated with the warm pool region of the western Pacific Ocean (i.e., surface temperature > 28°C) and the second with the ITCZ. Whereas it is very difficult to determine absolutely if the magnitudes of Taylor's analysis is representative away from the islands, the satellite estimates of Motell and Weare (1987) indicate that, at least, the patterns of precipitation are reasonable. The task is to determine the heating associated with this precipitation, with the transient

1. Actually, in Webster (1972) brightness data was used to infer convective cloudiness and, thence, precipitation and latent heating. Visible brightness data alone, however, provides an ambiguous estimate of precipitation as both stratus layers and desert areas are also bright. Thus, a certain degree of subjectivness was used.

components of the mean heating and the scale of the divergence associated with them. Measures of the associated divergence are necessary as these are used to drive the free surface barotropic model.

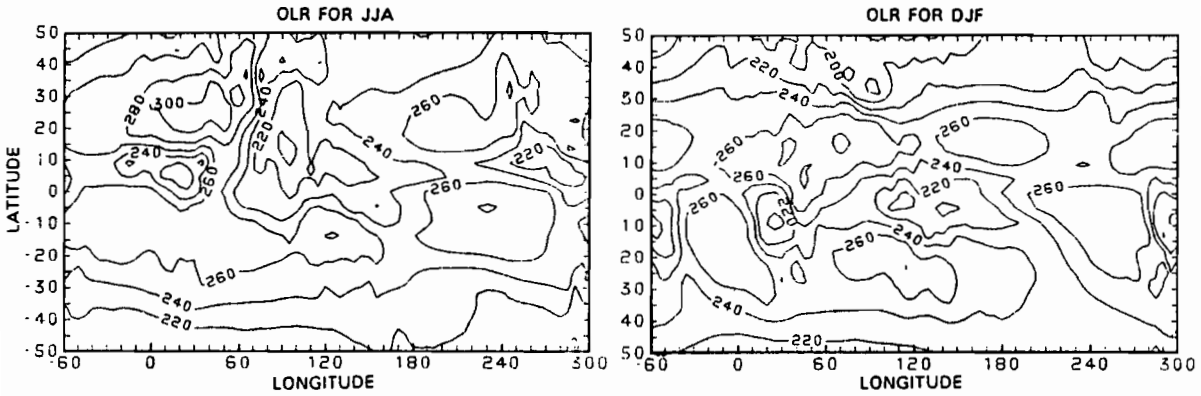

FIG.4. The mean outgoing longwave radiation observed from satellite for (a), the boreal summer and (b), the boreal winter. Units $W.m^{-2}$.

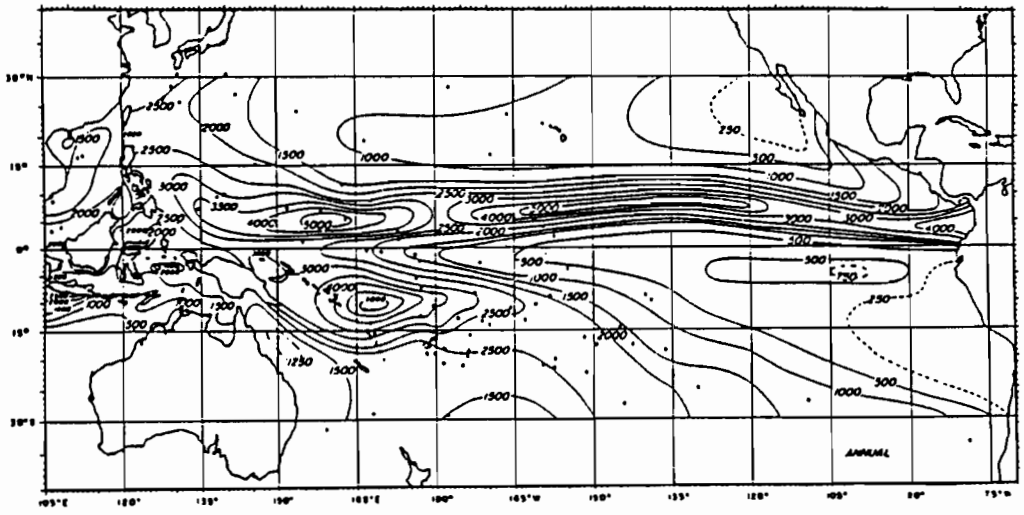

FIG.5. Estimate of the mean annual precipitation in the Pacific Ocean using ocean island rainfall data. (Taylor, 1972).

a. Mean heating rates in the warm pool regions.

Using an estimate of 3.5 m as the annual precipitation over the western Pacific Ocean from Fig. 5, the equivalent heating rate per unit mass of air can be calculated to be about 2°C day^{-1}. An estimate of the average divergence associated with the heating can be calculated by assuming a rough balance between diabatic heating and the ensuing adiabatic ascent (e.g. Webster, 1983). For a simple vertical structure extending through the entire tropical troposphere with a maximum in the middle troposphere, the resulting low level convergence associated with the 2°C day^{-1}; heating is 0.6×10^{-6} s^{-1}.

We can check this estimate with divergences obtained from the European Centre for Medium Range Weather Forecasting/World Meteorological Organization (ECMWF/WMO) Global Analysis Data Sets. The data sets consist of six physical variables at seven standard pressure levels listed twice per day (12 and 00 Z) on a 2.5 x 2.5° latitude-longitude grid. Figure 6 shows the annual average (upper panel) and a series of 2-month averages (lower panels) of the horizontal divergence at 850 mb (left column)

and 200 mb (right column), respectively, along the equator between 90°E and 150°W for 1980. At 850 mb, the region between 140°E and 180°E shows persistent convergence (shaded) of magnitudes of -1 to -2 x 10^{-6} s^{-1}. The region of convergence spans the maritime continent of Indonesia and the western Pacific Ocean warm pool. During the boreal summer, substantial convergence exists in the Indian Ocean. Very strong upper level divergence (shaded) is apparent over the Indonesian West Pacific region at all times of the year. Clearly, from Figure 6, it is obvious that there is strong heating in the mean between about 140°E and 180°E. However, it does not show the spatial and temporal scales of the higher frequency organized divergence which aggregates to provide the mean divergence fields.

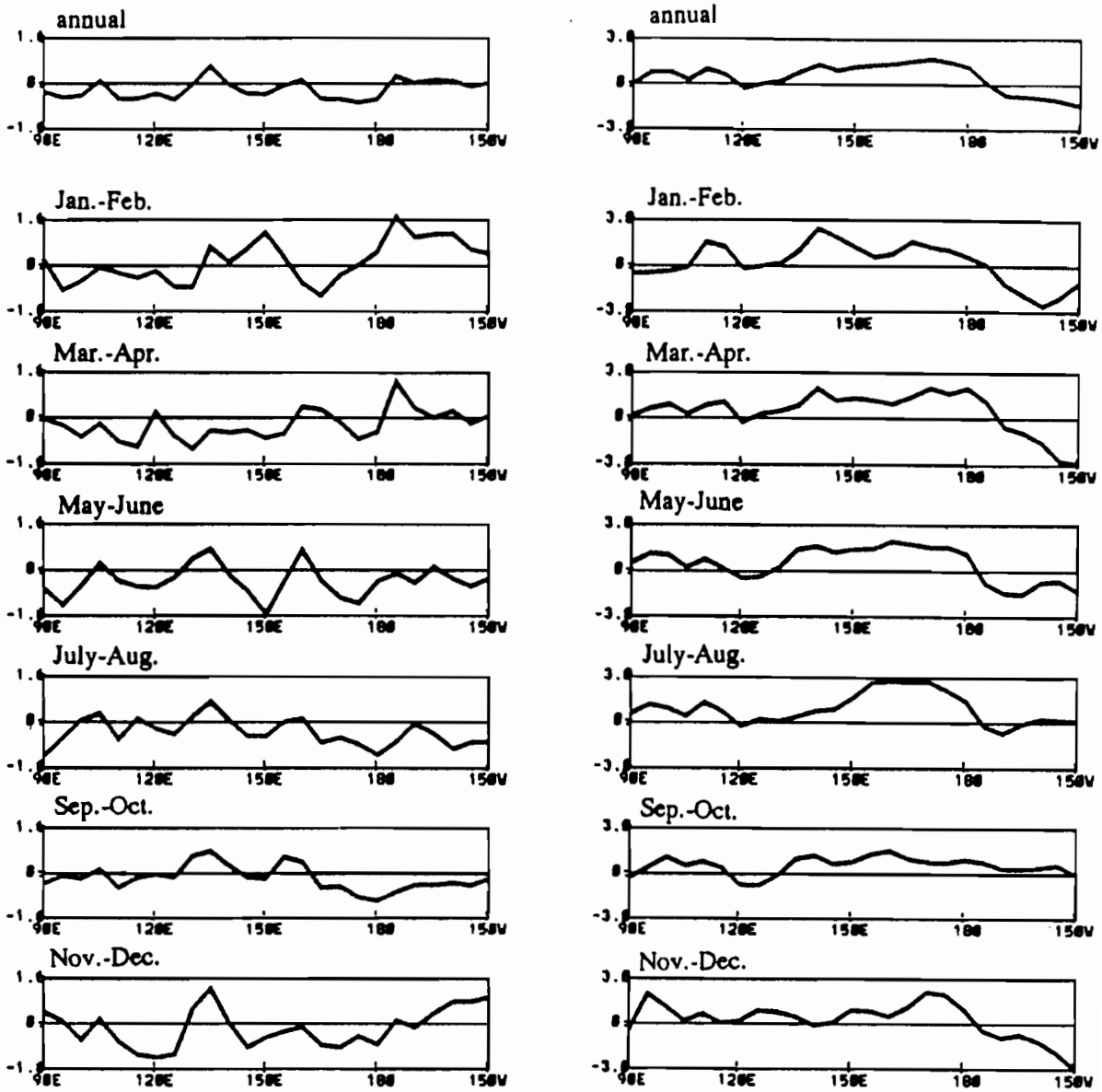

FIG.6. The horizontal divergence at 850 mb (left column) and 200 mb (right column). The annual average is shown in the two top panels. Bi-monthly averages are shown in the lower panels. Units 10^{-6} s^{-1}.(Chang and Webster, 1989).

b. Low frequency variations in the heating rates in the warm pool regions.

Figures 7a-d show longitude time sections along the equator of divergence (units 10^{-6} s^{-1} between 90°E and 150°W. Each panel shows two month segments. Regions of convergence are shaded. By comparing these sections with Figure 6, we can see that the moderate values of net convergence are replaced with large, low frequency periods of divergence. Indeed, values often exceed -5 x 10^{-6} s^{-1} for periods of days and scales of order 3-5000 km. That is, the annual divergence pattern over the warm pool regions is comprised of a series of strong episodic events. Such events have been referred to as "super clusters" by Nakazawa (1988) and Lau et al. (1989). We show here that the "super clusters" are associated with convergence on an order of magnitude greater than the annual mean. Thus, the heating rates associated with the episodic events range from 10° to 20°C.day^{-1} and have typical periods of days and longitude scales of 3-5000 km.

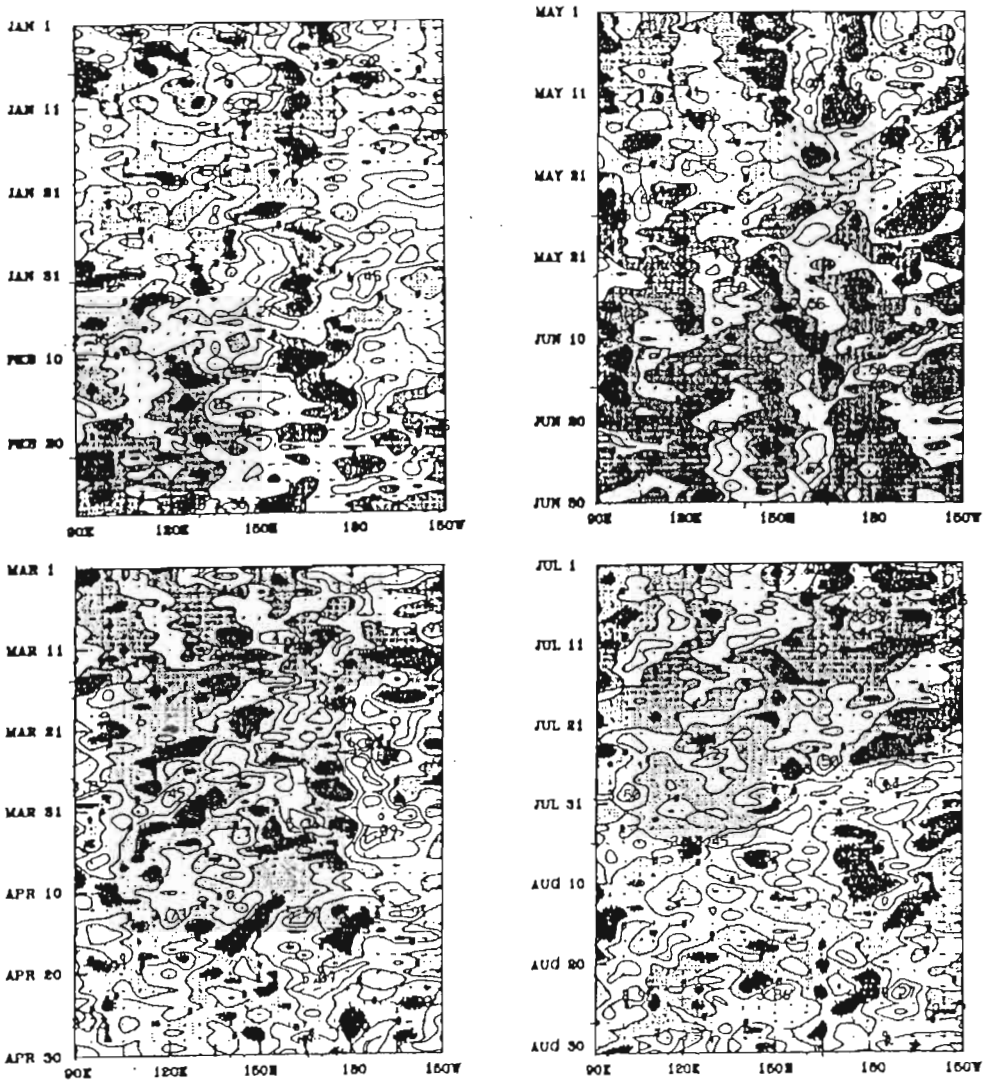

FIG.7. Time-longitude sections of the 850 mb divergence fields plotted between 90°E and 150°W. The sections show the substructure of the first four mean bi-monthly lower tropospheric divergence fields shown in the left column of Fig. 3. Shaded areas denote convergence. Heavier shading indicates convergence > 2 x 10^{-1} s^{-1} and the heaviest shading > 4 x 10^{-1} s^{-1}. Note the prolonged periods of convergence occurring along broad regions along the equator.

c. Formulation of a realistic transient tropical heating function.

If a free surface barotropic model (see Webster and Chang, 1988) is used to model the tropical atmosphere, a divergence function acts as a mass source-sink function. This is equivalent to heating in a baroclinic model. With the divergence fields displayed in Fig. 7 in mind, we define an appropriate transient forcing function as:

$$m(x,y,t) = E\, J(x,y)\, \tau(t) \qquad (1)$$

where E is the mass source sink amplitude function J and τ are the spatial and temporal functions

$$J(x,y) = \exp(-|x-x_0| / 2) \,.\, \exp(-|y-y_0|^2 / 4) \qquad (2)$$

and

$$\tau(t) = (t^3 / 2\delta^3) \exp(-t/\delta) \qquad (3)$$

Figure 8a shows the variation of the amplitude function with respect to time (i.e). The right hand scale shows the equivalent divergence and heating rates associated with the episodic forcing. Figure 8b plots the horizontal distribution function J(x,y). With an appropriate equivalent heating function defined, we are ready to study the basic modes in more realistic basic flows.

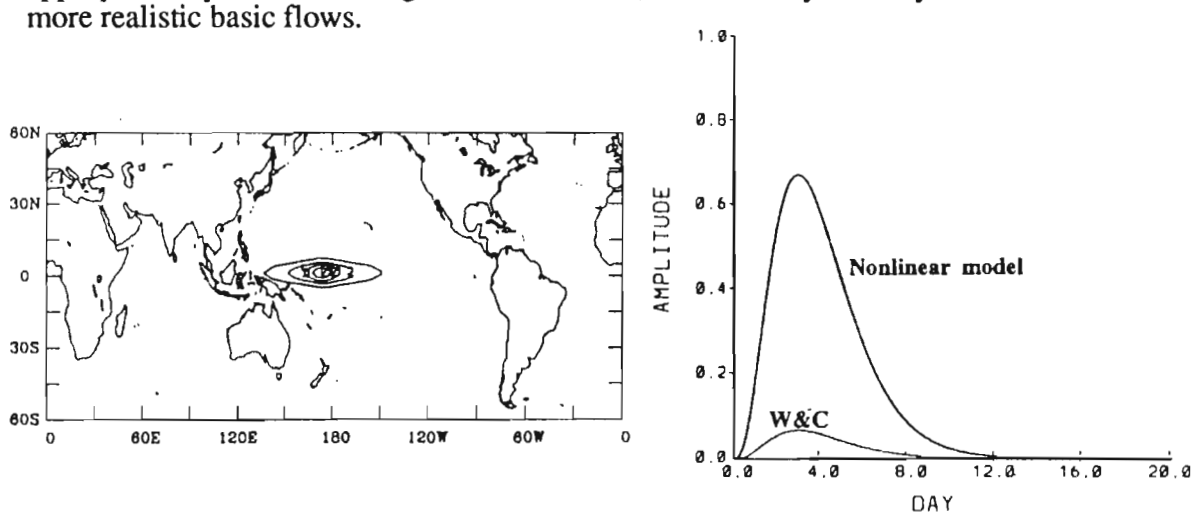

FIG.8. (a) The time evolution of the forcing function defined in (1). Units: 10^{-1} s^{-1}. (b) The spatial distribution of the forcing is normalized to a value of 5.

3. New concepts of equatorial waves: consideration of more realistic basic flows.

a. Influence of the sign of the basic state and latitudinal shear on the structure of equatorial transients.

On a rotating sphere, the longitudinal phase and group speed of a rotational wave are determined by the scale of the mode, the rate of rotation, and the basic state within which the mode resides. That is, the distribution of the mode is determined by the local ambient potential vorticity gradient (Zhang and Webster, 1989: Z&W) inherent in the basic state. In the tropics, the result is a longitudinal cell (often referred to as the Walker Circulation) which produces variations of the zonal velocity along the equator (Webster, 1983). These regional westerlies may then be further enhanced by the equatorward transport of westerly momentum through the "westerly duct" by extratropical eddies (Webster and Holton, 1982).

Figure 9 shows the observed 200 mb zonal velocity component for the boreal winter. Note that along the equator, distinct regions of easterly and westerly winds exist, ranging roughly from -15 m.s^{-1} to 20 m.s^{-1}. The eastern hemisphere is characterized by very strong latitudinal shear and easterlies along the equator. The western hemisphere, on the other hand, possesses much weaker shear and, in general, also produces westerlies along the equator. For the boreal summer, easterlies extend around most of the equator. However, the longitudinal structure of the first derivative of the zonal wind component (U_x) remains much the same.

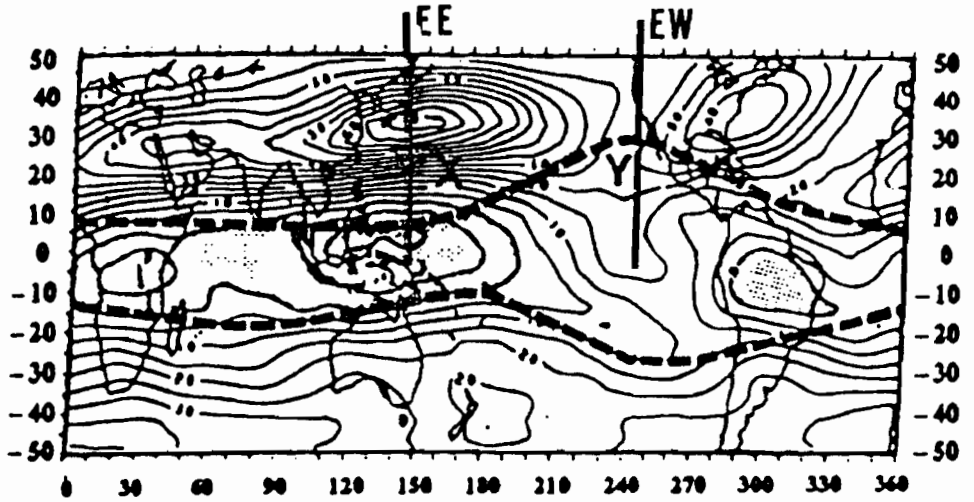

FIG.9. The mean 200 mb zonal wind field. Shaded areas denote easterlies. The lines EE and WE show typical shears through the eastern and western hemispheres. The dashed line refers to the turning latitude of a k=3, n=1 Rossby wave. (Zhang and Webster, 1989).

Figure 10 shows the perturbation zonal velocity component of the n=2, k=3 equatorial Rossby wave on an equatorial β plane for constant basic states of U=+10, 0 and -10 m.s^{-1} (Z&W). Note that in the westerly regime, the mode extends considerably more poleward. Z&W show that the impact of the variation of the basic state increases with increasing k and n. Figure 11 depicts contours of the turning latitudes of the modes as functions of k and n for U=+10 and -10 m.s^{-1}. Clearly, when the basic flow is westerly, the equatorial trapped mode encroaches extensively into higher latitudes as k and n increase. In Section 3(e), we will see that this encroachment or swelling property of the equatorially trapped mode is rather important, especially in regions where the stretching deformation is substantial. There, the scale of the transients must change.

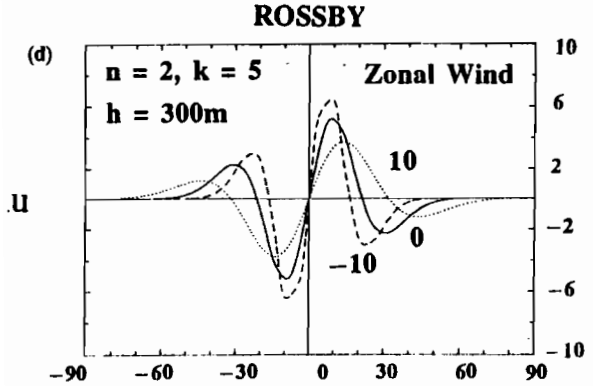

FIG.10. The latitudinal structure of the perturbation zonal velocity of the n=2, k=3 Rossby mode for background basic states of U= -10, 0, and 10 m.s^{-1}.

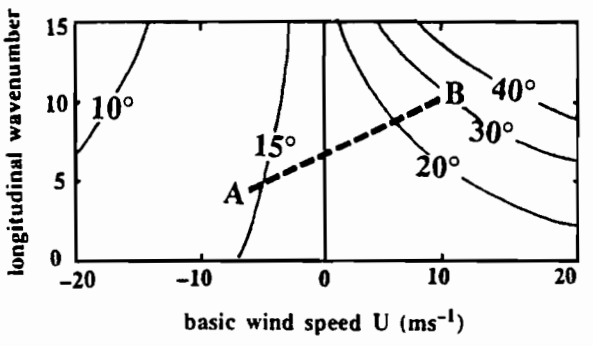

FIG.11. Contours of the turning latitude of the Rossby modes as a function of U as a function of k for n=1.

Figure 12 shows the zonal velocity structure of the equatorial Rossby wave in the shear flows EE (shear flow with equatorial easterlies) and EW (equatorial westerlies) from Fig. 8. Very little difference exists between the two cases and each is less equatorially trapped than in a basic state at rest. Z&W use potential vorticity arguments to show that the structure variation in different basic states is consistent with the variation restoring force associated with the ambient potential vorticity latitudinal gradient.

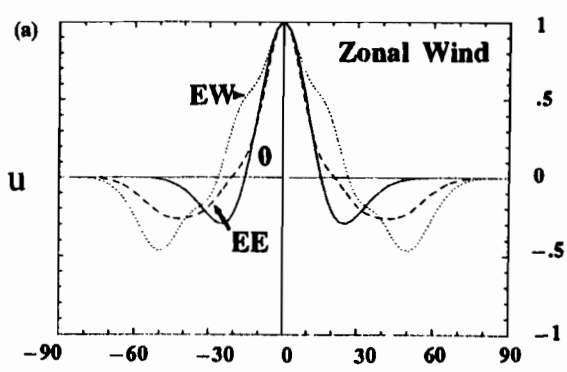

FIG.12. The perturbation zonal velocity component of the equatorial Rossby wave in shear flows EE and EW of Fig. 9. From Zhang and Webster (1989).

b. Extratropical influences on the tropics.

Most studies have concentrated on the horizontal variation of the low frequency basic flow, i.e., U=U(x,y). Using a barotropic model, Karoly (1983) showed that the ray paths of equatorial modes were greatly affected by the horizontal variability of the basic state. However, being a barotropic model, Karoly could not consider equatorially trapped modes as such modes do not exist in a barotropic fluid (see Webster and Chang, 1989: W&C). With a free surface barotropic model, and, thus, a divergent system, Webster and Holton (1982) were able to show that regions of westerlies, which they termed the "westerly duct", acted as wave guides or conduits across the equator between the westerlies of the extratropics of each hemisphere. Thus, in general, the equatorial regions may be thought of as being much more "porous"; to extratropical influence than initially thought, for example, by Charney (1969) and Mak (1969). In addition, Webster and Holton found evidence that the extratropical forcing also produced trapped modes about the equator, although they could not explain the result. Figure 13 shows the response of the Webster-Holton model to forcing located at different longitudes in the extratropics.

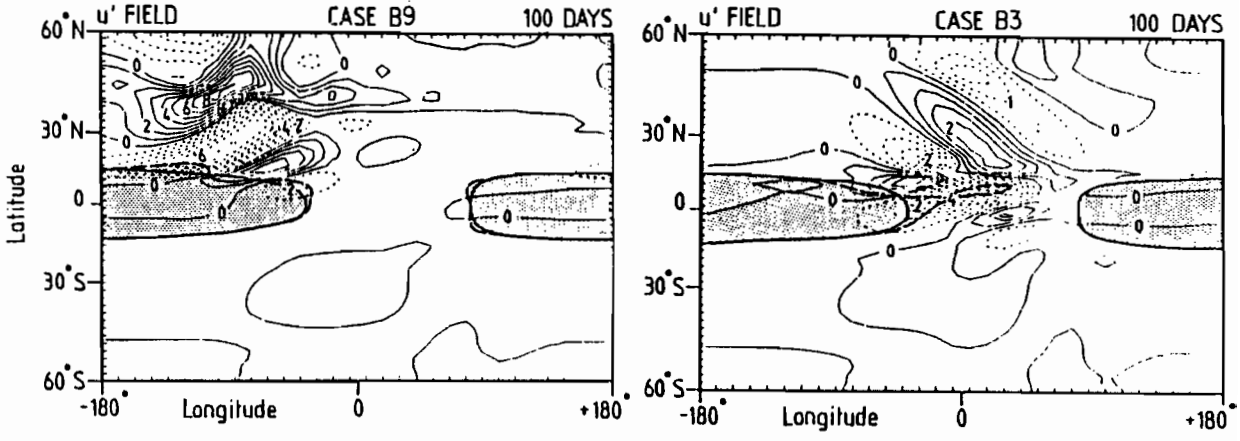

FIG.13. Responses of a U(x,y) basic state to forcing located at different regions in the extratropics. Shaded region denotes easterlies. From Webster and Holton (1982).

c. Equatorial transient wave energy accumulation:

The low frequency standing waves along the equator which produce the three dimensional basic state provide a very complicated flow through which equatorially trapped transients must propagate. Indeed, the study of free and forced modes within a more realistic basic state has revealed a much richer structure than was previously thought to exist.

In a series of recent studies (Frederiksen and Webster, 1987; Webster and Chang, 1988; W&C; and Zhang and Webster, 1989), the importance of the slowly evolving background flow (or at least the horizontal part of it, U(x,y)) of the tropical atmosphere on transient tropical structurers, has been studied at length. W&C showed that an equatorially trapped Rossby mode propagating along the equator is severly modified by the longitudinal variation of the basic flow. Specifically, they showed that regions where $U_x < 0$ (note the regions to the east of the equatorial westerlies in Fig. 9), were regions of energy accumulation. Basically, transient equatorially trapped modes would tend to accumulate in this region for a number of fundamental reasons. A major deduction of the W&C study was that, irrespective of where excitation occurred along the equator, ultimately, forced modes would become trapped in the regions of negative stretching deformation.

The physical basis for the arguments of W&C are rather simple. The combination of the strength of the basic flow and the stretching deformation and the group speeds of equatorially trapped modes allow for the possibility of the Doppler-shifted group speed C_{gd} to approach zero. Figure 14 shows the variation of the group and phase speeds as a function of the equivalent depth. For small k, the velocities are generally easterly. The shaded region denotes the regime within which group and phase speeds are equal and opposite the observed westerly winds shown in Figure 9. That is, zero Doppler-shifted group speeds are possible. Note that for larger values of k, the group speeds are westerly. Thus, it would seem that for these smaller scale modes, Doppler-shifted group zeros are not possible. However, it will be shown (see d below) that the equatorial westerlies provide a wave attractor region such that in the observed parameter range, produce Doppler-shifted group speed zeros for all scales.

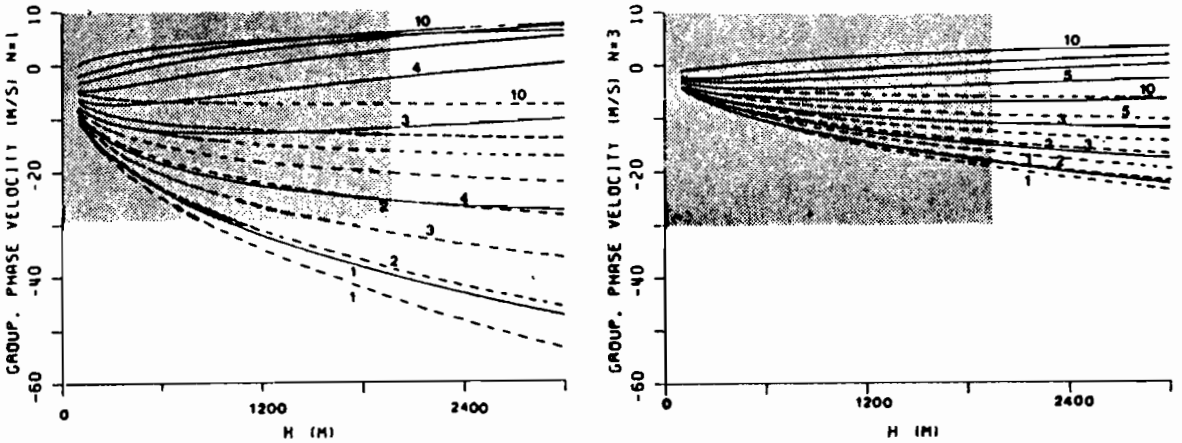

FIG.14. Variation of the group (solid lines) and phase (dashed) speeds for various k. Shaded region denotes the observed parameter range of the westerly winds and the vertical scale. From Webster and Chang (1988).

It turns out, however, that the situation is far more complicated than would seem by merely considering the Doppler-shifted characteristics of a mode in a variable basic state. W&C show that along a ray within a flow where U=U(x), the horizontal wave

number must change in order to conserve the Doppler-shifted frequency $\omega_d = (\omega - kU)$ if the basic flow is time invariant. For a trapped Rossby mode, the rate of change of k along a ray is given by:

$$dk/dt = \partial k/\partial t + (U + \partial\omega/\partial k) \partial k/\partial x = -k\, dU/dx \qquad (4)$$

Thus, if $U_x < 0$, a propagating mode must increase its' scale (k larger) and, conversely, if $U_x > 0$, the mode must increase its' scale (k smaller). Consistent arguments relating to the wave action flux show that:

$$\partial\varepsilon/\partial t + C_{gd}\, \partial\varepsilon/\partial x = -\varepsilon\, dU/dx \qquad (5)$$

where ε is the wave energy density. Thus, where $U_x < 0$, there is a convergence of wave energy and vice versa. W&C conclude that, for the observed parameter range suggested in Figure 9, there should be considerable modification of the equatorial wave characteristics by the longitudinal variation of the basic flow.

W&C did note that if the scale of the initial westward propagating transient was sufficiently large, it would be possible for the mode to pass through the negative stretching deformation "trap". Although the mode would suffer under distribution during its' passage through the zonally varying flow, it could, nevertheless, be free to continue its' westward propagation. However, they concluded that, in the real atmosphere, the strength of the basic flow is sufficiently strong to trap all but the gravest transient mode. Chang and Webster (1989) were able to show that the accumulation process was sufficiently robust to transcend linearity into the non-linear regime.

With the W&C hypothesis of accumulation and Z&W mode sensitivities to the form of the basic state in mind, it is possible to anticipate the total impact on a mode propagating through a basic state which possesses substantial stretching deformation along a ray.

d. The concept of the "westerly attractor".

W&C concentrated on the long wave end of the spectrum where waves possess westward group and phase speeds. They showed that these long waves, presumably forced in the convective regions of the eastern Indian and western Pacific oceans (where U(200 mb) << 0), would propagate into regions where $U_x < 0$. If the frequency of these modes is greater than that of the variation of the basic state, then (1) and (2) indicate that the mode must *decrease* its' longitudinal scale during westward propagation. Figure 15 shows how the Doppler shifted frequency approaches zero in the $U_x < 0$ region for such modes. Clearly, as k increases with westward propagation into the $U_x < 0$ region, C_g decreases negatively. Somewhere near where $U_x < 0$ is a maximum. W&C show that $C_{gd} \rightarrow 0$.

W&C, at the time, did not consider the excitation of smaller scale modes which would initially possess positive group velocities so that $C_{gd} > 0$. Such modes would propagate eastwards into regions of increasing westerlies and where $U_x > 0$! Thus, from (1), k must decrease as it moves eastward and C_g must increase negatively so that C_{gd} also goes to zero for these modes. The approach to zero of the Doppler-shifted group speed for the small scale case is also shown in Figure 9.

Figure 16 (Chang and Webster, 1989) shows a time-longitude plot along the equator of the perturbation zonal velocity component for the linear and nonlinear cases using a numerical model with an U(x,y) basic state for the linear and nonlinear basic states. The bottom panel shows the difference fields. Note the similarity of the linear and nonlinear results. Figure 17 shows a sequence of the longitude-latitude plots of the divergence field. The Rossby waves are denoted as R_i and the Kelvin wave as K. The

latter mode propagates rapidly eastward with the basic state having little impact on its' characteristics. Two Rossby wave packets (R_1 and R_2 emerge from the region of excitation but in different directions. Both packets accumulate in the region of the westerlies. Respectively, they represent the backward and forward accumulation of the short- and long-wave Rossby packets.

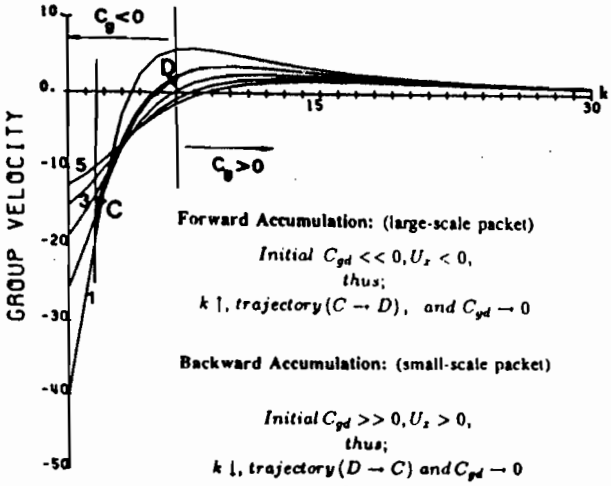

FIG.15. Plot of the group speed as a function of k for various n. As the scale changes subject to the laws (4) and (5), the group speed changes so that the Doppler group speed approaches a zero in the negative stretching deformation region. For the parameter range given by the low latitude basic state at low latitudes, all modes will accumulate at some point along the equator.

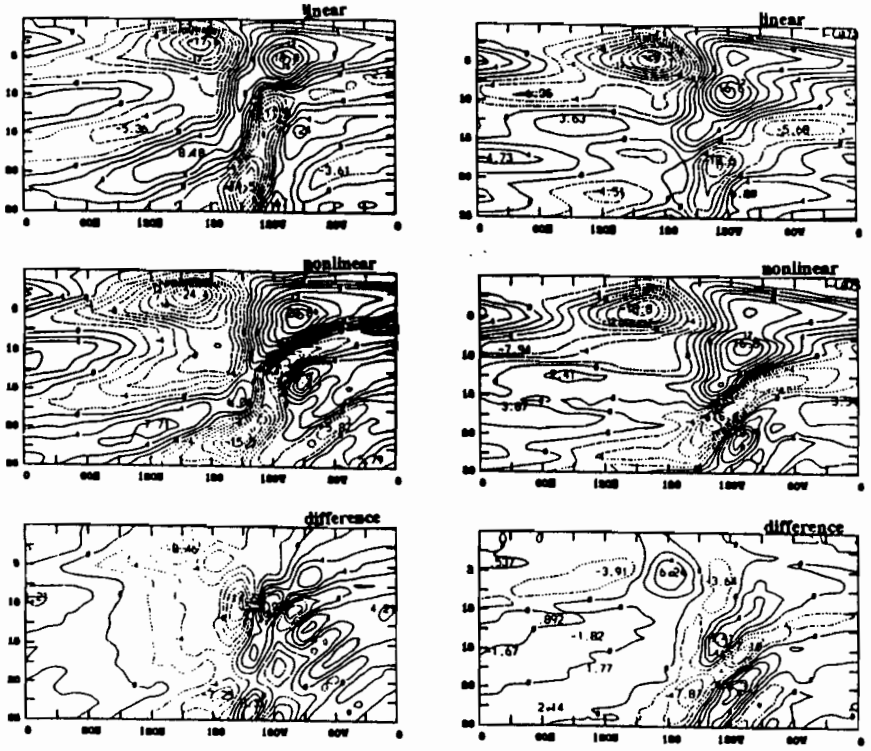

FIG.16. Time-longitude plots of the zonal velocity component around the equator of the linear (upper panels), nonlinear (middle) and the difference fields (bottom) for fluids of equivalent depths of 2000 m (left column) and 500 m (right column).

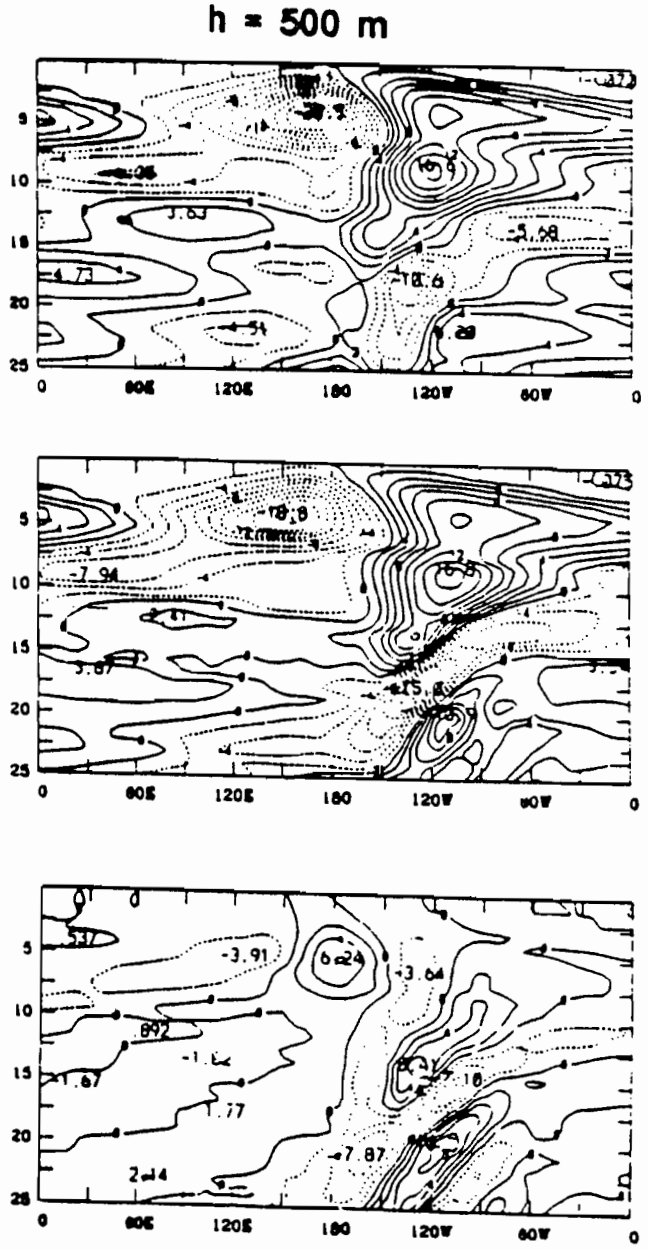

FIG.17. Time evolution of the divergence field for a 500 m fluid forced at location B in Fig. 6. Plots are shown at two day intervals for the first 23 days of integration. Lines indicate the characteristics of Rossby waves (R_1, R_2 and R_3) and the Kelvin wave (K). Distinctions between the modes are made in the text.

In summary, for all equatorial Rossby modes, irrespective of their longitudinal scale, the equatorial westerlies act as a "wave attractor"; or as a general energy accumulation region. For reference, we refer to those modes that move westward to the accumulation region as "forward accumulation". The reverse, the eastward propagation and modification, we refer to as "backward accumulation". It turns out that it is very important to understand the difference in the form of the accumulation, especially when vertical propagation of the equatorial modes is considered.

e. Extensions (swelling) of equatorially trapped modes into the extratropics: An interpretation of the influence of tropical transients on higher latitudes:

In their numerical experiments, W&C noticed that, from the region of accumulation along the equator, and to the east of the equatorial westerlies (see Fig. 9), disturbances appear to emanate to higher latitudes. Similar results have been obtained from experiments using considerably more sophisticated models (Frederiksen and

Webster, 1987, and, Gelaro, personal communication). Although it appears that the accumulation region is acting as a Rossby wave-train source in the form of Hoskins and Karoly (1981), it does not appear as a likely explanation simply because the emanation exists in the linear model results as well as in the nonlinear calculations. Thus, if nonlinear interactions are not possible, there must be another explanation.

An explanation arises quite simply out of the W&C and Z&W results. Rather than a propagating mode being produced, it appears more likely that the influence at higher latitudes is being caused by the increase in the turning latitude of the equatorially trapped modes as they propagate into the equatorial westerlies. As a mode moves along the equator from regional easterlies to westerlies, the turning latitude will change with the change as shown in Figure 11. At the same time, at least for the westward propagating mode, the longitudinal scale will decrease due to the impact of the stretching deformation. The turning latitude-wavenumber trajectory as the mode moves to the west from easterlies to westerlies can be seen as the dashed line A-B in Figure 5. A schematic representation for both forward and backward modes is shown in Figure 18.

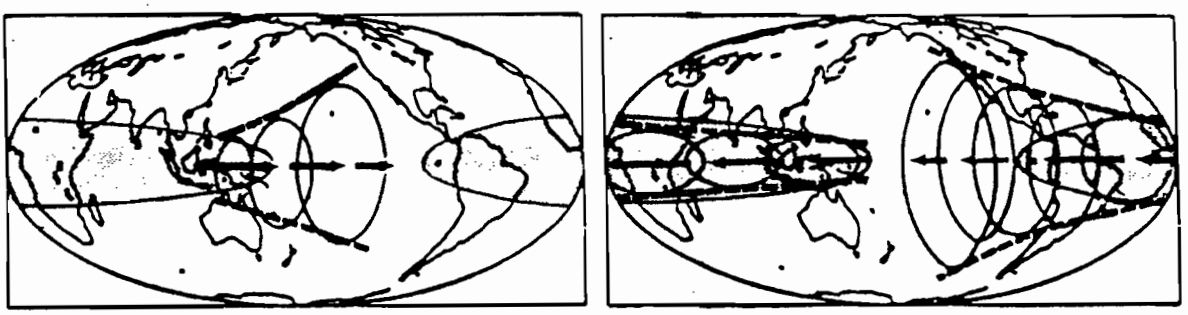

FIG.18. Schematic representation of "backward" (left panel) and "forward" (right panel) accumulation along the equator. Note, despite the direction of the initial propagation, the modes accumulate in the westerlies and "swell" to higher latitudes. The swelling is due to the increase of the turning latitude of the Rossby mode as it moves from the background easterlies to the westerlies.

f. Extratropical influences on the tropics:

The extensions of the equatorial modes to higher latitudes in the regions of the upper tropospheric equatorial westerlies has considerable impact on the interaction of extratropical transients on the tropics. The equatorial westerlies, of course, correspond to Webster and Holton's "westerly duct". Rather than extratropical modes merely propagating through the duct from one hemisphere to the other, as proposed by Webster and Holton, it is possible for extratropical forcing to produce a *trapped* equatorial response. There are two factors which determine the equatorial response to forcing. The longitudinal location of the forcing determines the proximity of the mode to the duct (see Webster and Holton). Given that the forcing is meridionally aligned with the duct, the latitudinal position relative to the turning latitude of an equatorially trapped mode is important. If the forcing is within the turning latitude (location Y poleward of the dashed line in Fig. 9), the forcing can project onto the trapped mode and an equatorially trapped response will be invoked. If the forcing is poleward of the turning latitude (location X, Fig. 9), a propagating mode (untrapped) will ensue. Figure 13 shows easterly and westerly basic flows forced by extratropical forcing. With the westerly turning latitudes that extend well poleward, an odd equatorial trapped mode is produced. In the easterly, where the turning latitudes are constrained near the equator, there is no equatorially trapped response.

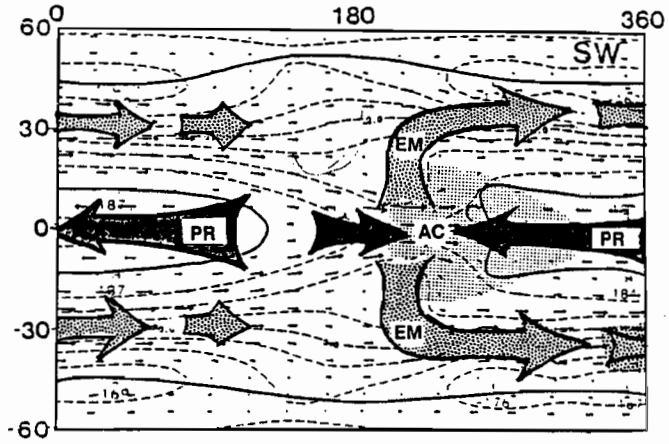

FIG.19. Schematic diagram showing the corridors of transmission of energy from the convective regions of the tropical warm pools to higher latitudes.

4. Conclusions.

It is clear that the basic flow invokes an extremely strong control on the form of the response to forcing from either tropical or extratropical sources. The control of the basic flow extends from the *in situ* response to the remote response and determines, to a great degree, how influence is manifested, in both directions, between the tropics and higher latitudes. In other words, to understand the interaction of the basic flow and the transients, it is necessary to take into account both the longitudinal and latitudinal variation of the basic flow and its' divergent characteristics. Finally, it would appear that much of the interaction can be understood in terms of the structure of equatorially trapped modes within varying basic flows and still be within the confines of equatorially trapped modes.

Within the framework of the theory outlined above, we can summarize the hypothesis of how transient waves, originating in the convectively active warm pools, transmit their influence to other regions of the tropics and the higher latitudes. Figure 19 provides a summary of the hypothesis. Waves propagate away from the source region in both directions along the equator. The large scale end of the wave packet propagates westward while the short scale end propagates eastward. Both trains accumulate in the negative stretching deformation region where they assume a greater latitudinal extent due to the scale modifications occurring in the westerly flow. In this manner, corridors through which energy passes from the convective zones to higher latitudes are created.

There are still a number of questions that remain unanswered. For example, the vertical propagation of the modes moving away from the convective source regions needs to be addressed. Also, we have not explicitly taken into account in our discussion the characteristics of the mixed Rossby-gravity mode. At larger scales, the mode possesses a relatively high frequency but asymptotes the lower Rossby wave frequency range at smaller scales. Zhang and Webster (1989) have shown that the mode is only moderately affected by the basic state. Thus, it presents the possibility of extending directly poleward from the point of excitation. Clearly, the role of the mixed Rossby-gravity mode deserves investigation.

REFERENCE

Chang, H-. R. and P. J. Webster, 1989: Energy accumulation and emanation at low latitudes. Part II: Nonlinear response to strong episodic forcing. Submitted to *J. Atmos. Sci.*

Charney, J. G., 1969: A further note on the large scale motions in the tropics. *J. Atm. Sci.*, **34**, 901-910.

Gill, A., 1980: Some simple solutions for heat induced tropical circulations. *Quart. J. Roy. Met. Soc.*, **106**, 447-462.

Hoskins, B. J. and D. Karoly, 1981: The steady state response of a spherical atmosphere to thermal and orographic forcing, *J. Atmos. Sci.*, **38**, 1179-1196.

Karoly, D., 1983: Rossby wave propagation in a barotropic atmosphere, *Dyn. Atmos. Oceans.*, **7**, 111-125.

Longuet-Higgins, M. S., The eigenfunctions of Laplaces tidal equations, *Phil. Trans. R. Soc.*, **A262**, 511-607.

Mak, M-. K.: Laterally driven stochastic motions in the tropics. *J. Atmos. Sci.*, **26**, 41-64.

Matsuno, T, 1966: Quasi-geostrophic motions in the equatorial area, *J. Meteor. Soc. Japan*, **44**, 25-42.

Nakazawa, T., 1988: Tropical super-clusters under intraseasonal variation, Japan-U.S. Workshop on the ENSO Phenomena, University of Tokyo, Nov. 3-7, 1987, Meteoroloical Research Report, #88-1, Department of Meteorology, Geophysical Institute, 76-78.

Opsteegh, J. D., and H. M. Van den Dool, 1980: Seasonal differences in the stationary response of a linearized primitive equation model: Prospects for long-range forecasting? *J. Atmos. Sci.*, **37**, 2169-2185.

Sardeshmukh, P. D. and B. J. Hoskins, 1988: The generation of global rotational flow by idealized tropical divergence. *J. Atmos. Sci.*, **45**, 1228-1251.

Webster, P. J., 1971: Response of the tropical atmosphere to local steady forcing. *Mon. Wea. Rev.*, **100**, 518-540.

Webster, P. J., 1973: Temporal variation of low latitude zonal circulations, *Mon. Wea. Rev.*, **101**, 803-816.

Webster, P. J., 1981: Mechanisms determining the atmospheric response to sea surface temperature anomalies. *J. Atmos. Sci.*, **38**, 554-571.>

Webster, P. J., 1982: Seasonality in the local and remote response to sea surface temperature anomalies, *J. Atmos. Sci.*, **39**, 41-42.

Webster, P. J., 1983: Large scale structure of the tropical atmosphere. *Large-scale Dynamical Processes in the Atmosphere*, B. J. Hoskins and R. P. Pearce, Eds, Academic press, 392 pp.

Webster P. J., and H-. R. Chang, 1988: Equatorial energy accumulation and emanation regions: Impacts of a zonally varying basic state, *J. Atmos. Sci.*, **45**, 803-829.

Webster, P. J., and J. R. Holton, 1982: Cross equatorial response to mid-latitude forcing in a zonally varying basic state. *J. Atmos. Sci.*, **39**, 722-733.

Zhang, C. and P. J. Webster, 1989: Effects of zonal flows on the equatorially trapped waves, to appear in *J. Atmos. Sci.*

MOMENTUM, HEAT, AND MOISTURE FLUXES BETWEEN ATMOSPHERE AND OCEAN

An Overview of Bulk Parametrization and Remote Sensing of Latent Heat Flux in the Tropical Ocean

W. Timothy LIU

M.S. 300-323
Jet Propulsion Laboratory
California Institute of Technology
Pasadena, CA 91109 - U.S.A.

ORSTOM
CENTRE DOCUMENTATION
Montpellier

1. INTRODUCTION

The only practical way of determining large-scale air-sea exchanges in momentum, heat and moisture is through the bulk formulae which link the microscale turbulent transfer to macroscale parameters measured routinely. The coefficients used in these formulae were derived and verified with observations taken in moderate wind conditions (4-15 m/s) under near neutral condition. Over large areas in the tropical Pacific, the mean wind is weak (< 3 m/s) and the sea-air humidity difference reaches above 7 g/kg (e.g., Hsiung 1986). The moisture induced buoyancy destabilizes the atmosphere and increases evaporation. The characteristics of the coefficients under these conditions will be discussed

Except near coastal area and in major shipping lanes, meteorological reports are sparse in the tropical ocean. *In situ* measurements are not adequate to delineate the temporal and spatial variabilities of the fluxes. Spaceborne sensors provide repeated and uniform coverage. A method of computing the moisture flux using spaceborne sensors will be described and examples of scientific application will be presented.

2. FORCED CONVECTION

The bulk parameterization formulae are

$$\tau = \rho C_D U^2 \tag{1a}$$

$$H = \rho c C_H U (T_s - T) \tag{1b}$$

$$E = \rho C_E U (Q_s - Q) \tag{1c}$$

where τ is the wind stress, H is the sensible heat flux, E is the moisture flux, ρ is surface air density, c is the isobaric specific heat. The latent heat flux (LE) is the product of E and the latent heat of vaporization. The measurements required are the sea surface temperature (T_s), the wind speed (U), the temperature (T), and the specific humidity (Q) measured on board ships. The specific humidity at the air-sea interface (Q_s) is generally taken to be the saturation value at T_s and Q can be derived from the dew-point temperature measured. The transfer coefficients (C_D, C_H and C_E) used are generally assumed to be constant and determined by regression of spot measurements (10 min to 1 hr time averages at a fixed location). The coefficients, in theory, depends on the reference height, the stability and surface roughness. Liu et al. (1979) developed a model to account for these variabilites.

F 30238

In the model of Liu et al. (1979), which is a physical approach to bulk parameterization, the three non-dimensional profiles based on similarity theory are solved simultaneously. The similarity relations are,

$$U/U_* = 2.5(z/z_0 - \psi_U) = C_D^{-1/2}, \tag{2a}$$

$$(T - T_S)/T_* = 2.2(z/z_T - \psi_T) = C_D^{1/2}C_H^{-1}, \tag{2b}$$

$$(Q - Q_S)/Q_* = 2.2(z/z_Q - \psi_Q) = C_D^{1/2}C_E^{-1}. \tag{2c}$$

By definition, $U*$, $T*$, $Q*$ are function of τ, H, and E. The ψ_U, ψ_T, and ψ_Q are function of the stability parameter (ζ) and can be expressed in terms of the three fluxes. The lower boundary parameters z_o, z_T, and z_Q are functions of τ and fluid properties. The three unknowns τ, H, and E can be determined by solving the three implicit equations. This method is similar to that used by Deardorff (1968) to account for the effects of stability on the values of the transfer coefficients and is equivalent to using (1) with variable coefficients.

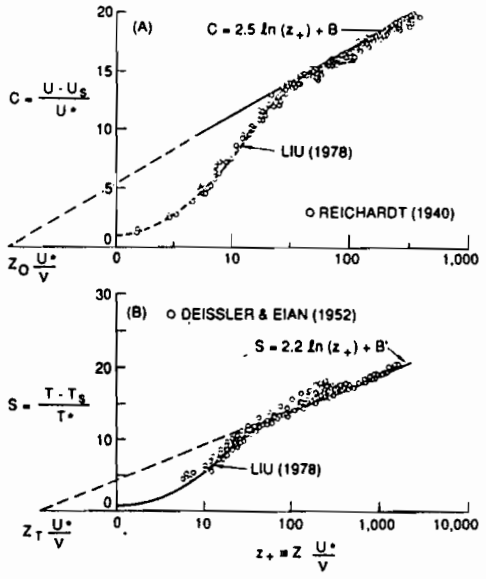

Fig.1 Laboratory measurements of the vertical profiles of (A) velocity and (B) temperature, (from Liu, 1978).

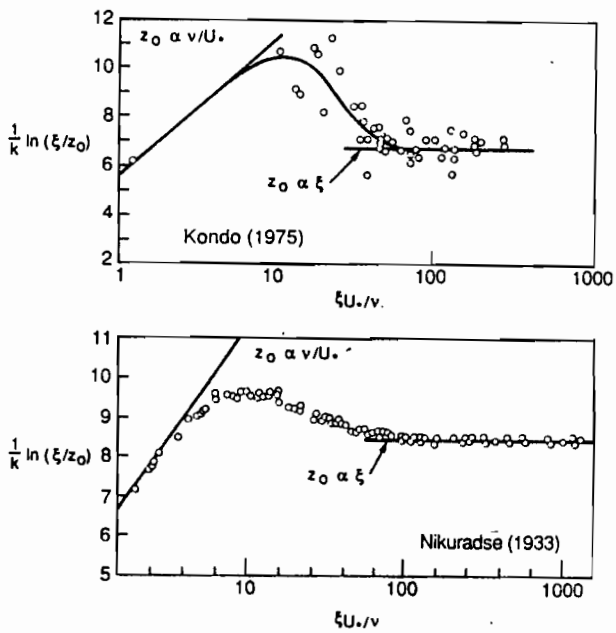

Fig.2 Variation of the roughness parameter in pipe flow (A) and at the sea-air interface (B), (from Liu, 1978).

Under neutral stability ($\psi_U=\psi_T=\psi_Q=0$), the variabilities of the coefficients are governed by the variabilities of z_o, z_T, and z_Q. The three parameters reflect the transport processes near the surface. The velocity and and temperature distributions measured in smooth channels by Reichardt (1940) and Deissler & Eian (1952) are shown in Fig. 1. Away from the surface, the flow is turbulent and the measurements follow a logarithmic law. Near the surface, viscosity and conductivity become important and the profiles agree with the postulation based on a surface renewal model by Liu et al.(1979). The imagery height at which the $U-U_s=0$ along the extrapolaiton of the logarithmic profile is z_o. The interpretation of z_T and z_Q are the same except for temperature and specific humidity. Schlichting (1968) suggested that a surface is aerodynamically rough when the roughness elements penetrate the viscous sublayer and it is smooth if the sublayer covers the roughness elements. The scaling depth of the sublayer is $\nu/U*$, where ν is the kinematic viscosity. Alternatively, rough flow can be viewed as the state when the local velocity scale and the characteristic scale of the roughness elements, ξ, combined to form a roughness Reynolds Number ($\xi U*/\nu$) that exceed a critical value. The velocity measurements in pipe flow by Nikuradse (1933) are shown in Fig. 2A. ξ is the actual mean diameter of the the sand-grains used as roughness elements. The measurements of Kondo (1975) at an air-sea interface are shown in Fig. 2B and ξ is the square root of the integral of the one dimensional wave spectrum between two selected frequencies. In smooth flow, $\xi << \nu/U*$, momentum is mainly transported by viscosity, z_o is proportional to $\nu/U*$, and, therefore, C_D increases with decreasing $U*$. In rough flow, $\xi>>\nu/U*$, momentum is mainly transported by pressure force on the roughness element and the flow is independent of ν, and z_o is proportional to ξ. In the case of a rough sea surface, ξ increases with wind and, therefore, C_D increases with wind. Charnock (1955) postulated that z_o is proportional to $U*^2/g$ where g is the acceleration due to gravity.

When the interface is smooth, momentum, heat and water vapor are all transported by molecular processes near the interface and the variations of C_D, C_H, and C_E should share the same characteristics, i.e., increases with decreasing winds. When the roughness of the surface increases, turbulent transport is facilitated and the transfer coefficients increase with wind speed. While momentum can be transported by pressure forces on the roughness elements independent of viscosity, the slow molecular diffusion is the only process which transport heat and mass at the interface. Increase in roughness increases the sheltering effect and the fluid stays longer in contact with the surface before turbulence carries it away. The opposing effects on the C_E is shown in Fig. 3. The thick curve represents C_E at neutral stability from the model of Liu et al. (1979). At low wind speed, it decreases with increasing wind speed, having the characteristics of smooth flow described above. The behavior of C_E at low winds was recently supported by the measurements of Bradley et al. (1989) in the Brismack Sea. As the wind speed increases and the surface becomes rough, the opposing effects of increase stirring and sheltering balance out and the C_E remains rather constant at 1.3×10^{-3} in good agreement the empirical values (shown as dashed lines) by Anderson and Smith (1981) (A&S) and Large and Pond (L&P). The value given by Bunker (1976) (B), however, increases with wind speed, following the characteristics of C_D.

In (2), ψ_U, ψ_T, and ψ_Q are functions of the stability parameter ($\zeta \equiv z/L$), where z is the height and L is the Monin-Obukhov length. The parameter is the ratio of turbulence production by buoyancy to those by shear. Assuming $C_D=C_H=C_Q=C$, it can be approximated (Deardorff, 1968) by

$$\zeta \equiv \frac{kgz\,(\Delta T + 0.619\Delta Q)}{\sqrt{C}\,\theta\,U^2} \qquad (3a)$$

where k is the von Karman's constant, $\Delta T \equiv T_s - T$, $\Delta Q \equiv Q_s - Q$, and θ is the average absolute temperature. As the flux-profile relations, initially developed over land, are extended over water, the effects of humidity fluctuation on buoyancy is often overlooked. Bunker (1976), for example, tabulated the values of the transfer coefficients according to classes of U and ΔT but not ΔQ. In the extratropical oceans, the effects of humidity fluctuations may be small compared with the effects of temperature fluctuations. But in the tropical oceans, due to the rapid increase of saturation humidity at high temperature (Clausius-Clapeyron Equation), humidity fluctuations can have significant effects on atmospheric stability and the variability of the transfer coefficient. Fig 4 shows the ratio of ζ / ζ_*, where

$$\zeta_* \equiv \frac{kgz\,\Delta T}{\sqrt{C}\,\theta\,U^2} \qquad (3b)$$

at various T_s and two values of ΔT, assuming C=1.3 $x10^{-3}$, U=7 m/s and a relative humidity of 80%. It is obvious that the error for omitting ΔQ can be larger than 50% over warm water (>25°C). In the western tropical Pacific and eastern Indian Ocean, with a typical wind speed of 4 m/s, and a typical sea-air humidity difference of 6 g/kg (Hsiung, 1986), the coefficient is approximately $1.8x10^{-3}$ as shown in Fig. 3. This will give a latent heat flux approximately 40% higher than the value given by a neutral coefficient of $1.3x10^{-3}$. The typical ΔT may be small and the temperature induced buoyancy alone cannot adequately account for the stability effect on C_E.

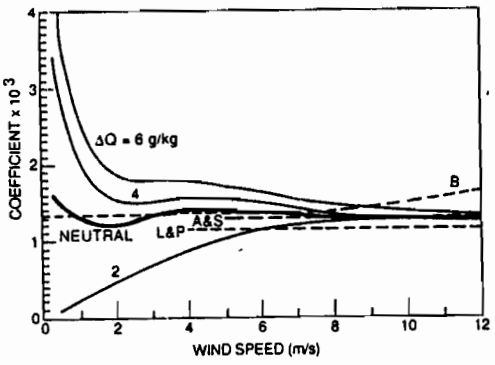

Fig.3 Variation of the moisture transfer coefficient with wind and sea-air humidity difference computed with model of Liu et al. (1989), with the thick line representing values at neutral stability.

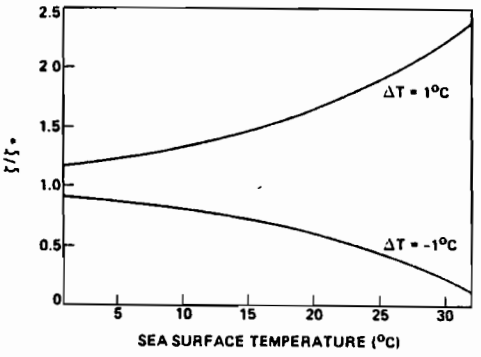

Fig 4. The ratio of the stability parameter including humidity effects to the stability parameter excluding humidity effects as a function of temperature for two cases of sea-air temperature differences (ΔT).

3. FREE CONVECTION

The bulk formula (1) imply that there is no heat and moisture transfer at zero wind speed which, of course, is not true. Convection caused by buoyancy force as a result of heating or concentration gradient will transport heat and moisture. The similarity profiles (2) are not valid under free convection when buoyancy dominates over shear in turbulence production. In open oceans, free convection is rare and is not well studied. However, there are many studies of free convection of homogeneous fluids, particularly in laboratory Liu (1984) gave a detailed review. Krishnamurti (1973) showed that the circulation in a fluid goes from laminar to fully turbulent as the Raleigh number for temperature ($Ra_T \equiv \alpha g \Delta T d^3/(\kappa_T \nu)$) increases. In the definition of Ra_T, α is the coefficient of thermal expansion and κ_T is the thermal conductivity. When the flow is fully turbulent, theoretical and empirical studies suggest that the heat transport is governed by

$$Nu = A\, Ra_T^{1/3} \qquad (4)$$

where $Nu \equiv Hd/(\rho c \kappa_T \Delta T)$ is the Nusselt number, and A depends on the Prandtl Number $Pr = \nu/\kappa_T$. Fig. 5, from Liu (1974), shows the results of an experiment with a deep well-insulated tank of water under an evaporating free surface Surface heat flux is equated to water heat loss derived from calorimetry. Water surface temperature was measured both by an Barnes PRT-5 radiometer mounted above the tank and by moving a 25 micron diameter resistant film probe across the surface. The bulk temperature was measured by a thermometer. The 110 pairs of data have a correlation coefficients of 0.997 and the linear fit corresponds to a relation $Nu = 0.156 Ra_T$. Eqn (4) can be reduced to

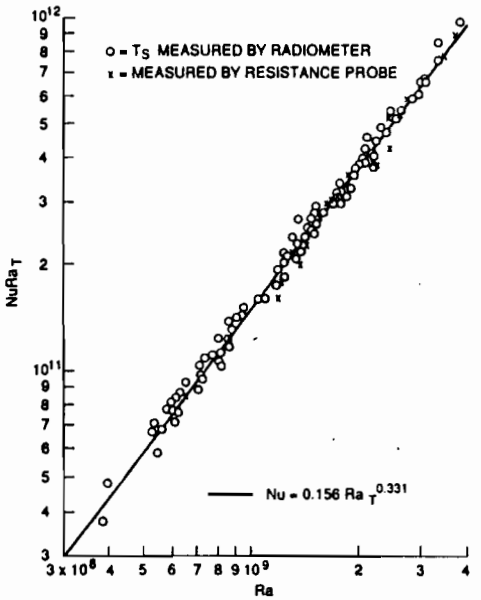

Fig 5 The relation between Nusselt (Nu) and Raleigh Number for temperature (Ra_T) for natural convection under a free surface (from Liu, 1974)

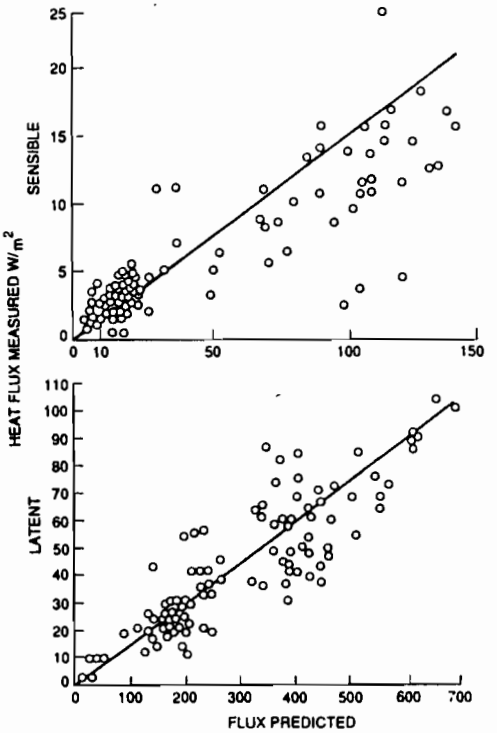

Fig 6 Comparison of field measurements of heat flux under free convection and values predicted by (6) (from Golitsyn and Grachov, 1988).

$$H = A\rho c \left(\frac{\alpha g \kappa_T^2}{\nu} \right)^{1/3} \Delta T^{4/3} \tag{5}$$

The relation between Q and ΔT is independent of the depth of fluid. For a inhomogeneous fluid like the atmosphere over ocean, (4) can be generalized to include moisture transport,

$$Nu = A\left[Ra_T + Ra_Q \left(\frac{Pr}{Sc} \right)^{3/2} \right]^{1/3} \tag{6a}$$

$$Sh = A\left[Ra_Q + Ra_T \left(\frac{Sc}{Pr} \right)^{3/2} \right]^{1/3} \tag{6b}$$

where $Sh \equiv Ed/(\rho \kappa_Q \Delta Q)$ is the Sherwood number, $Sc = \nu/\kappa_Q$ is the Schmidt number, κ_Q is the diffusivity of water vapor, $Ra_Q \equiv \beta g \Delta Q d^3/\kappa_Q \nu$ is the Raleigh number for humidity, and β is the expansion coefficient due to water vapor. The heat and moisture fluxes can be reduced to functions of ΔT and ΔQ. Fig. 6, from Golitsyn and Garchov (1986), compared field measurements of heat and moisture fluxes to those predicted by (6).

Wyngaard et al. (1971) recognized that the similarity theory breaks down when there is no mean wind and introduce a free convection scale for the atmospheric mixed layer with depth d

$$U_f = \left(\frac{\alpha g d H}{c\rho} \right)^{1/3} \tag{7}$$

and Businger (1973) postulated that convection will induce local surface friction velocity, $U*$ and $U*/U_f$ is a decreasing function of d/z_o. Assuming

$$\frac{U^*}{U_f} \propto \left(\frac{d}{z_o} \right)^{-1/3} \tag{8}$$

and that the resident time scale of the fluid at the surface is equal to the Kolmogorov time scale, Liu et al. (1979) derived (4) from (8). Schuman (1988) suggested that (4) is applicable only to smooth flow. In rough flow, he suggested

$$Nu = A\, Ra_T^{1/2} \tag{10}$$

Under free convection conditions, the flow is always smooth over the ocean. The independence of heat flux from any depth scale,as in (6), remains to be vigorously tested.

4. LATENT HEAT FLUX FROM SATELLITE DATA

Of the three parameters required to compute LE, spaceborne sensors can measure T_s and U, but cannot measure Q. It was found that at the monthly time scale, atmospheric water has a single dominant mode of variability and Q can be derived from the columnar

water vapor (W) measured by microwave radiometers. A statistical Q-W relation was established using 17 years of radiosonde reports from mid-ocean meteorological stations (Liu, 1986). This relation was found to be adequate in describing the seasonal and interannual variations over global oceans except in high latitudes during summer, with accuracy estimated to be 0.4-0.8 g/kg. With this relation, monthly fields of LE from 1980 to 1983 in the tropical Pacific were computed using data from Nimbus/SMMR. In comparison with monthly data from equatorial moorings and atolls, the scatters were found to be 0.6 m/s in U, 0.8°C in T_s and 0.4 g/kg in Q. The random error in LE is estimated to be 26 W/m^2 (Liu, 1988). The errors for T_s and LE were likely to be overestimated since a 200x200 km satellite average was compared with a spot measurement in an area of very large meridional gradient.

Fig. 7 shows the time-longitude distribution of T_s, U, W, and LE centered on the equator between 90°W and the date-line. The 1982-83 ENSO episode is envisioned as an apparent eastward migration of the warm water pool marked by the 28°C isotherm starting in June 1982. This results in a reverse of zonal T_s gradient near the date-line. The organized deep convection marked by high W also moves east from the date-line starting June 1982, leaving dry air behind. The seasonal cycle of U is disrupted by the eastward migration of low wind center representing surface convergence associated with the organized convection at the eastern terminal of anomalous westerlies. During April 1983, zonal belts of high T_s, high W and low U stretch across the entire equatorial Pacific. Detailed evolution of these three parameters during the episode is described in Liu (1989a). Despite the warm water, LE is below normal due mainly to the low U near the convergence center. The annual October high does not reach the expected level.

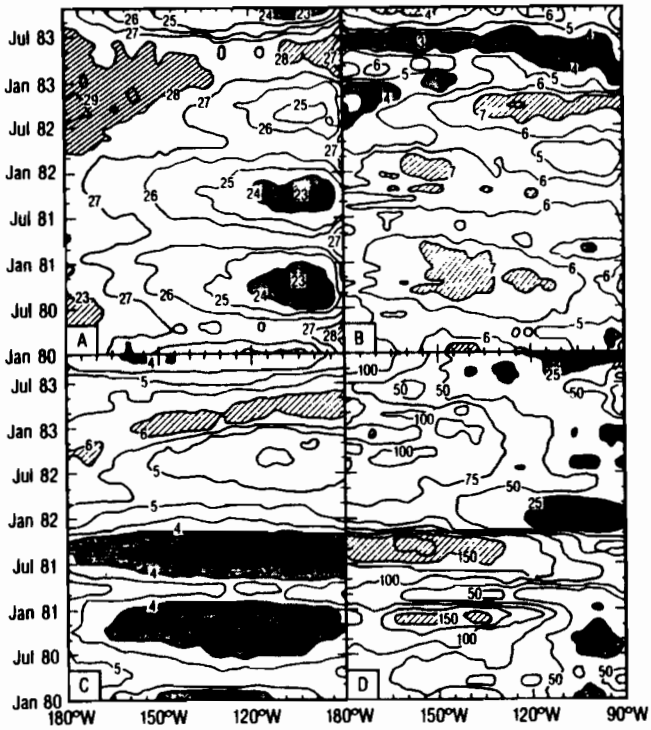

Fig.7 Time-longitude variation, centered on the equator, of (A) sea surface temperature, (B) surface wind speed, (C) columnar water vapor, and (D) latent heat flux. The intervals between isolines are 1°C, 1m/s, 0.5 g/cm^2, and 25 W/m^2 respectively.

The change of heat storage in the upper ocean is governed by the balance of heat gain from the surface and the loss through ocean dynamics. Fig. 8A shows the distribution of the contemporary correlation coefficient, at 2° latitude by 2° longitude grids, between LE and the time rate of change of sea surface temperature ($\partial T_s/\partial t$) for the period between February 1980 and September 1983, including an intense El Nino and Southern Oscillation episode. The gradient of the linear regression for three consecutive months of T_s is used to represent $\partial T_s/\partial t$. The 44 months of LE and $\partial T_s/\partial t$ fields were reconstructed from the first three empirical orthogonal functions accounting for 60% and 83% of the variance respectively. The low correlation in the near equatorial regions (left) is due the cloud and insolation variabilities in areas of organized convection and surface convergence (e.g., ITCZ) and due to ocean upwelling (along the equator). Off phase moisture variation is likely to be cause of low correlation at 20°N. Outside of these regions, the correlations are significant, indicating dominant influence of surface latent heat flux in upper ocean heat balance. By adding the surface shortwave radiation derived from observations from the VISSR (Visible Infrared Spin Scan Radiometer) (Liu and Gautier, 1989) to the latent heat flux, the area of low correlation is concentrated in a narrow belt around the equator (Fig. 8B) showing that in this equatorial wave guide, ocean dynamics plays a dominant role.

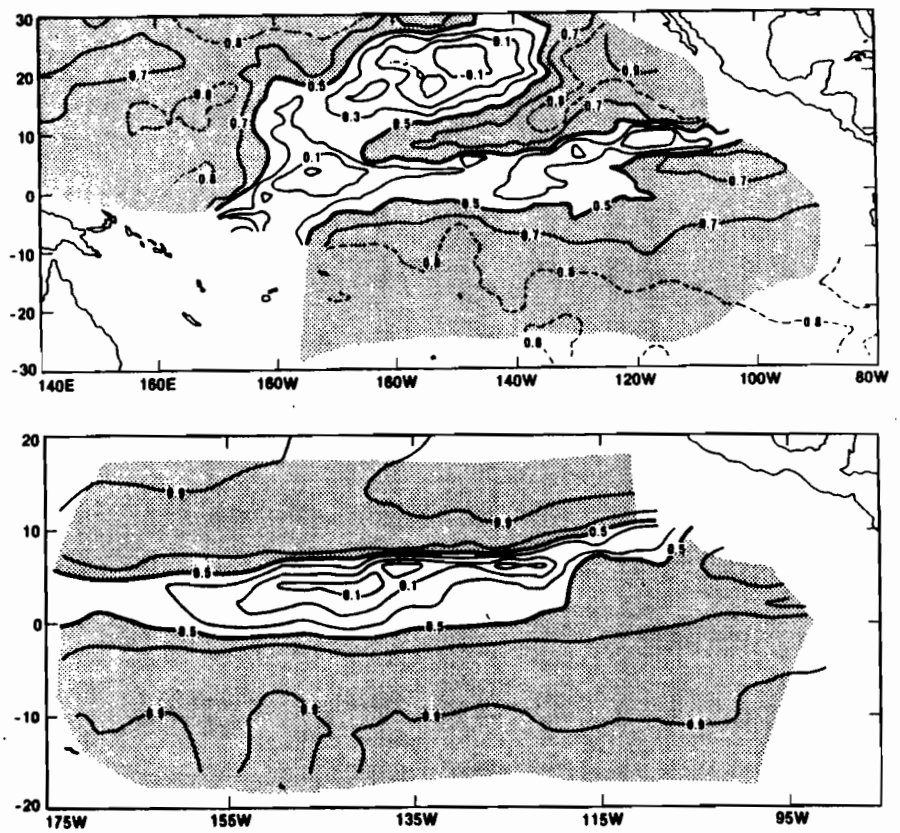

Fig. 8 Contemporary correlation coefficient between time rate of change of sea surface temperature and (A) latent heat flux (top), and (B) net heat flux (bottom). Solid isolines have 0.2 intervals.

5. CONCLUSION

C_E is constant only as a crude approximation. Most values used in the past led to underestimation of E in the western tropical Pacific (where winds are very light) because they do not account for the smooth flow characteristic of increasing values with decreasing winds and they neglect the moisture-induced instability. A scheme for parameterization under free convection is also described which still needs further validation. Inhomogeneous and non-stationary conditions, related to thermal plumes or convection, are not addressed and required more studies and scrutiny.

A method of estimating E with observations from spaceborne microwave is described. Application has been confined to monthly means but extension of the technique to higher temporal frequencies is being explored (Liu, 1989b). Combination of LE with surface shortwave radiation demonstrated the ocean's response to surface thermal forcing.

ACKNOWLEGMENTS

This study was performed at the Jet Propulsion Laboratory, California Institute of Technology, under contract with the National Aeronautic and Space administration. The computation of net heat flux is part of the TOGA Heat Exchange Project, an interagency supported research program.

References

Anderson, R.J. and S.D. Smith, 1981: Evaporation coefficient for the sea surface from eddy flux measurements, *J. Geophys. Res., 86*, 449-459.

Bradley, E.F., P.A. Coppin, and J.S. Godfrey, 1989: Measurements of heat and moisture fluxes from the western tropical Pacific Ocean. This Proceeding.

Businger, J.A., 1973: A note on free convection. *Boundary Layer Meteor., 4*, 323-326.

Bunker, A.F., 1976: Computations of surface energy flux and annual air-sea interaction cycles of the North Atlantic Ocean, *Mon. Wea. Rev., 104*, 1122-1140.

Charnock, H., 1955: Wind stress on a water surface. *Quart. J. Roy. Meteor. Soc., 81*, 639-640.

Deardorff, J.W., 1968: Dependence of air-sea transfer coefficients on bulk stability. *J. Geophys. Res., 73*, 2549-2557.

Deissler, R.G., and C.S. Eian, 1952: Analytical and experimental investigation of fully developed turbulent flow of air in a smooth tube with heat transfer with variable fluid properties. *NACA Tech. Note 2629*.

Golitsyn, G.S., and A.A. Grachov, 1986: Free convection of multi-component media and parameterization of air-sea interaction at light winds. *Ocean-Air Interactions, 1*, 57-78.

Hsiung, J., 1986: Mean surface energy fluxes over the global ocean. *J. Geophys. Res., 91*, 10585-10606.

Kondo, J., Y. Fujinawa, and G. Naito, 1973: High frequency component of ocean waves and their relation to aerodynamic roughness. *J. Phys. Oceanogr., 3*, 197-202.

Krishnamurti, R., 1973: Further studies on transition to turbulent convection. *J. Fluid Mech., 60*, 285-303.

Large, R.G. and S. Pond, 1982: Sensible and latent heat flux measurements over the ocean, *J. Phys. Oceanogr., 12*, 464-482.

Liu, W.T., 1974: *Thermal Structure and Heat Transport in the Molecular Boundary Layer under an Evaporating Surface of a Deep Tank of Water*. Master Thesis, University of Washington.

Liu, W.T., 1978: *The Molecular Effects on Air-sea Exchanges*. Ph.D. dissertation, University of Washington.

Liu, W.T., 1986: Statistical relation between monthly precipitable water and surface-level humidity over global oceans. *Mon. Wea. Rev., 114*, 1591-1602.

Liu, W.T., 1988: Moisture and latent heat flux variabilities in the tropical Pacific derived from satellite data. *J. Geophys. Res., 93*, 6749-6760, 6965-6968.

Liu, W.T., 1989a: The annual and interannual variabilities of precipitable water, surface wind speed, and sea surface temperature, over the tropical Pacific. *Ocean Air Interaction*, in press.

Liu, W.T., 1989b: Remote sensing of surface turbulence heat flux. *Surface Waves and Fluxes: Current Theory and Remote Sensing*, Chapter 16, G. Geerneart (ed.), Reidel Publishing Co.

Liu, W.T., C. Gautier., 1989: Remote sensing of the thermal forcing on the tropical Pacific. *Proc. of IGARSS 89*, to appear.

Liu, W.T., K.B. Katsaros, and J.A. Businger, 1979: Bulk parameterization of air-sea exchanges of heat and water vapor including the molecular constraints at the surface, *J. Atmos. Sci., 36*, 1722-1735.

Nikuradse, J., 1933: Stromungsgesetze in Raubven Rohren. *V.D.I. Forschungsheft 361*.

Reichartdt, H., 1940: Die Warmeubertragung in turbulenten Reibungsschichten Z. *Angew. Math. Mech., 20*, 297-328.

Schlichting, H., 1968: *Boundary Layer Theory*, McGraw Hill, New York.

Schumann, U., 1988: Minimum friction velocity and heat transfer in the rough surface layer of a convective boundary layer. *Bound. Layer Meteor., 44*, 311-326.

Wyngaard, J.C., Cote, O.R., and Izumi, Y., 1971: Local free convection, similarity and budgets of shear stress and heat flux. *J. Atmos. Sci., 28*, 1171-1182.

Measurements of Heat and Moisture Fluxes from the Western Tropical Pacific Ocean

E.F. BRADLEY[1], P.A. COPPIN[1] and J.S. GODFREY[2]

[1] *CSIRO Centre for Environ. Mechanics, GPO Box 821, Canberra, ACT 2601 - Australia*

[2] *CSIRO Division of Oceanography, GPO Box 1538, Hobart, Tas. 7001 - Australia*

ABSTRACT

Micrometeorological measurements, including direct eddy-correlation heat and moisture fluxes, have been made under light wind conditions in the western equatorial Pacific. The sea surface "cool skin" of about 0.5°C was observed; air-sea temperature differences were 1-1.5°C larger than longterm averages from merchant-ship data. Bulk transfer coefficients for both fluxes increased markedly as wind speed fell below 4 m/s, in excellent agreement with the predictions of Liu et al. (1979). Dissipation estimates of the fluxes are about half the covariance measurements below 4 m/s. Observations of the individual components of radiation suggest that commonly used empirical formulations overestimate both long- and shortwave in this region by 15-20 W/m^2. application of all possible corrections would reduce Reed's (1985) estimate of net heat flux into the ocean by some 80 W/m^2 to around only 20 W/m^2 in this region of the Pacific.

1. INTRODUCTION

Thermodynamic interactions between atmosphere and ocean in the equatorial western Pacific play a dominant role in determining global weather patterns including, as an extreme example, the well-documented El Nino - Southern Oscillation (ENSO) phenomenon. One well-known precursor of ENSO is the sea surface temperature (SST) anomaly in the tropical Pacific, and eastward displacement of the so-called "warm pool" normally situated just northeast of New Guinea. Clearly, such changes to SST must result from variations in some or all of various components of the near-surface heat balance of the ocean; i.e. advective or diffusive transport within the ocean body itself and ocean-atmosphere coupling.

A much better understanding of the physics and dynamics of these transport processes is required if SST is to be properly simulated in models of the coupled ocean-atmosphere system. Several authors (e.g. Ramage 1984, Schlesinger and Mitchell 1987) agree that, in the context of climate change research, an additional energy input of only 10 W/m^2 to the ocean and troposphere would be very significant. Yet, as Godfrey and Lindstrom (1989) point out, uncertainty of the order of 80 W/m^2 is apparent in current climatological estimates of the heat budget of the surface mixed layer of this region. They estimated that only 5-10 W/m^2 could be mixed downwards through the surface isothermal layer; other authors (Enfield 1986, Niiler and Stevenson 1982) found that horizontal advection in this region is also only 5-10 W/m^2. This leads to an estimated net capacity for the ocean to carry heat away from the surface of 10-20 W/m^2. This is smaller than four recent estimates of the long-term mean heat flux into this region (Weare et al. 1981, Esbensen and Kushnir 1981, Reed 1985, Hsiung 1985), which range between 25 and 80 W/m^2.

Either there are horizontal transport processes unaccounted for by earlier authors, such as the eddies seen in the eastern Pacific (Legeckis et al. 1983); or some unknown and quite large source of turbulent kinetic energy must exist to mix this heat flux downwards; or the heat flux estimates must all be too large.

The exchange of energy between the ocean and the atmosphere is given by the heat budget:

$$N = S - L - H - E \tag{1}$$

where the net heat input to the ocean, N, results from the absorption of solar radiation, S, less amounts lost to the atmosphere through net longwave radiative transfer, L, sensible heat flux, H, and latent heat flux, E. Annual values of the quantities on the right-hand side of the equation have been calculated for the tropical Pacific region by the authors mentioned above using ship-of-opportunity observations. S is dominated by cloud cover; L by sea surface temperature, atmospheric water vapour content and cloudiness; and H and E by turbulent transfer processes which depend on wind speed, sea state and air-sea temperature differences. Sensible and latent heat fluxes are usually estimated from bulk transfer relationships:

$$H = \rho C_p \bar{U} C_H (T_s - T_a) \tag{2}$$

ORSTOM
CENTRE DOCUMENTATION
Montpellier

F30239

$$E = \rho L_E \overline{U} C_E (q_s - q_a) \quad (3)$$

where ρ and C_p are the density and specific heat of air, L_E is latent heat of vaporisation, $\overline{U}$ the mean wind speed and T and q the temperature and specific humidity in air at some specified level and at the water surface according to the subscripts. C_H and C_E are empirically defined bulk transfer coefficients.

Individual estimates of the fluxes at a particular location vary considerably, partly a result of the different formulations used to convert the data; S, for example, over the range 160–225 W/m^2, L from 60–120 W/m^2 . Blanc (1985) reviews ten variations on equations (2) and (3), illustrating particularly the wide range of transfer coefficients C_H and C_E in common use. There are also, we believe, systematic biases resulting from the rather special weather conditions prevailing in the western equatorial Pacific which may preclude the use of parameters determined for other parts of the globe. Frequent convective storms, localised and with high cumulus towers, make any objective, regional specification of cloud cover almost impossible. Frequent rainstorms provide a source of energy transfer not accounted for in the above heat budget. A further measure of uncertainty arises from the high humidity levels and light winds which are a feature of the region.

Between April 23 and May 25 1988, oceanographic measurements were made from R/V "Franklin", along the track shown in Figure 1, in the western equatorial Pacific. The primary purpose of the cruise was to make hydrographic and ocean turbulence measurements as a continuation of the WEPOCS cruises (Lindstrom et al. 1987). However, a secondary purpose was to examine some aspects of the above heat budget discrepancy; there were four main objectives:

* to attempt direct eddy-correlation measurements of heat and moisture fluxes. This is not usually possible because of ship motion, so that indirect methods of flux measurement are used (bulk, profile, dissipation), all of which are believed to fail in light winds;
* to define bulk transfer coefficients for these very low wind conditions. Models predict a significant increase with approach to the free convection regime, but this has never been tested by experiment;
* to make accurate measurements of the sea–air temperature gradients and look for the "cool skin" effect, i.e. evaporative cooling of the actual water interface relative to the bulk temperature;
* to measure all the terms in the radiation budget.

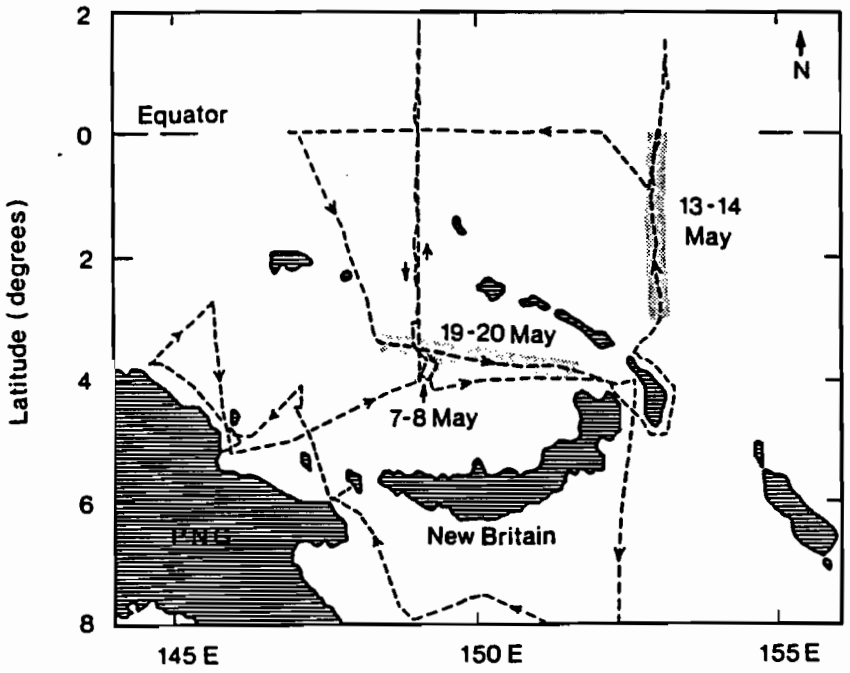

Figure 1. Cruise track of R/V "Franklin". Hatched sections show meteorological observation periods.

2. INSTRUMENTATION

The general layout of the vessel and instruments is shown in Figure 2. R/V "Franklin" is a Voluntary Observing Ship for WMO and makes the usual routine meteorological observations: wind speed and direction, engineroom thermograph temperature and wet and dry bulb air temperature at 6 h intervals. The engineroom intake is about 2 m below the surface and 13 m aft of the bow; temperature is measured about 1 s after water enters the ship. The air thermometers are located in a Stevenson screen above the bridge, and the anemometer atop the main mast.

Other meteorological equipment was mounted at the end of a retractable boom, 10 m forward of the bow to minimise disturbance to the air by the ship. The boom carried a vertical section, as shown in Figure 2, extending from about 3 m to 10 m above the sea surface. Cup anemometers and aspirated psychrometers were mounted at upper, middle (6 m) amd lower levels to obtain gradients. A 3-dimensional sonic anemometer (Coppin and Taylor 1983) and a Lyman-α humidiometer were also mounted at the 6 m level. Three orthogonal accelerometers were mounted on the boom about 1 m aft of the sonic anemometer, and pitch and roll sensors located near the ship's centre of gravity.

Three radiometers were installed: an Eppley pyranometer and a pyrgeometer at the top of the main mast and a net radiometer at the end of the boom. In addition, an infrared radiometer (kindly provided by Dr. Ian Barton) was mounted above the bridge and aimed at the sea surface, clear of the ship's wake. This radiometer has a bandpass of 1 micron centred on the 11 micron band similar to channel 4 of the AVHRR instrument.

Signals from the fast-response instruments (the sonic, Lyman-α and accelerometers) were recorded at 20 Hz sampling rate on digital computer tape. Time series were recorded continuously to fill a tape (about 5 h) and subsequently broken up into a sequence of 15 min runs. The other 'slow' sensors were sampled at 5 s intervals, and 15 min averages recorded on a data logger.

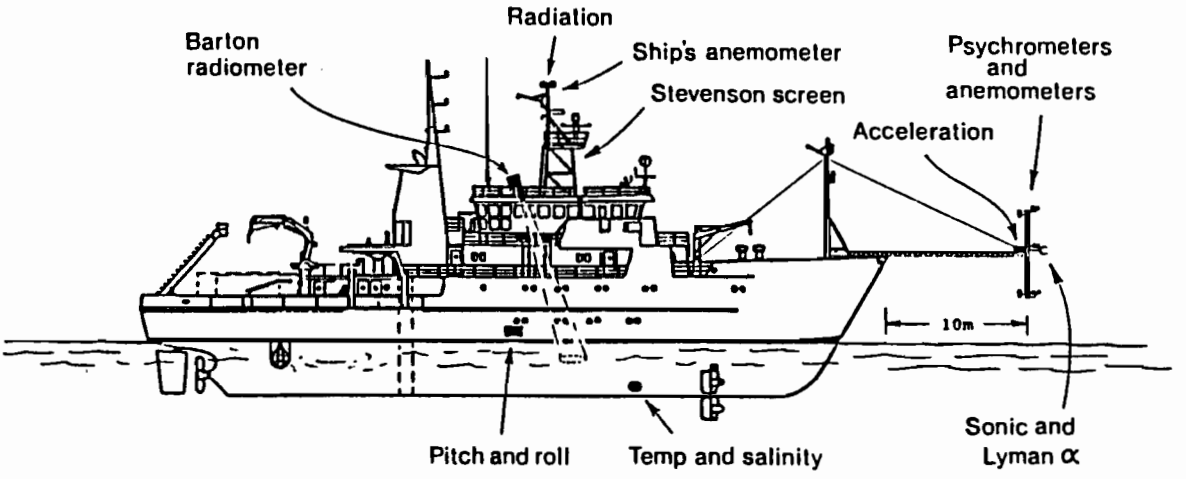

Figure 2. R/V "Franklin", (55 m 1200 t) and instrument locations.

3. OBSERVATION CONDITIONS

Data from the radiometers, cup anemometers and psychrometers were recorded continuously whenever possible throughout the cruise. During infrequent occasions of strong winds or heavy swell, when the bottom of the vertical boom section was in danger of dipping into the water, the boom was retracted to a position about 3 m forward of the bow. The sonic, Lyman-α and Barton radiometer were mounted only when conditions were favourable for eddy-flux measurement i.e. light wind, smooth sea and no rain. This occurred principally during three 24 h periods; two of these were in the Bismarck Sea with the ship's track determined by us; the third was during a northerly run from New Ireland to the equator. They are shown hatched in Figure 1.

The motion sensors were installed to enable ship motion to be removed from the wind signal. In the event, the pitch and roll sensors were inadequate so that correlations between fluctuating wind components, needed for stress and drag coefficient measurements, have not been possible. However, the scalar correlations are much less sensitive so that, with the almost imperceptible ship motion which occurred during our three observation periods (less than 1° pitch and 2° roll), covariance heat and moisture flux measurements were successful. Examples of spectra measured with a swell running, Figure 3, illustrates the ship's 10 s roll as a prominant peak in the vertical velocity spectrum. The humidity spectrum is clean, excepting for high frequency noise caused by the ship's engine vibration, and the cospectrum contains a notch at the roll frequency equivalent, however, to only 8% loss of moisture flux. In contrast, Figure 4 shows typical spectra from periods in which ship motion is imperceptible.

Because of the quiet sea conditions, also, the usual salt contamination problems created by spray were not encountered.

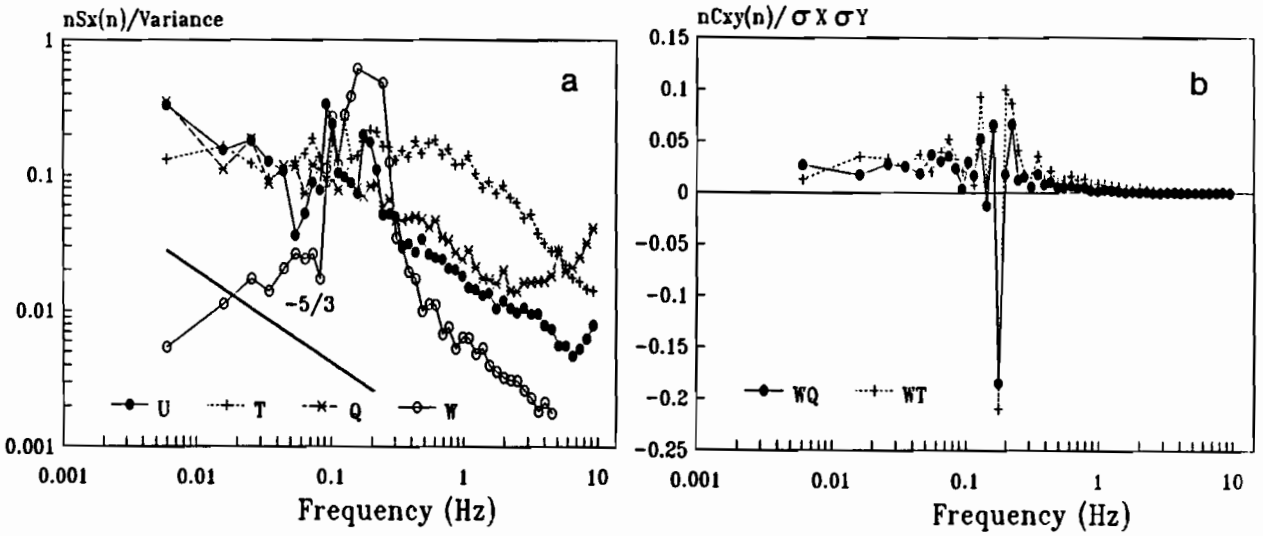

Fig 3. Normalized spectra (a) and Co-spectra (b) for a period of high ship motion.

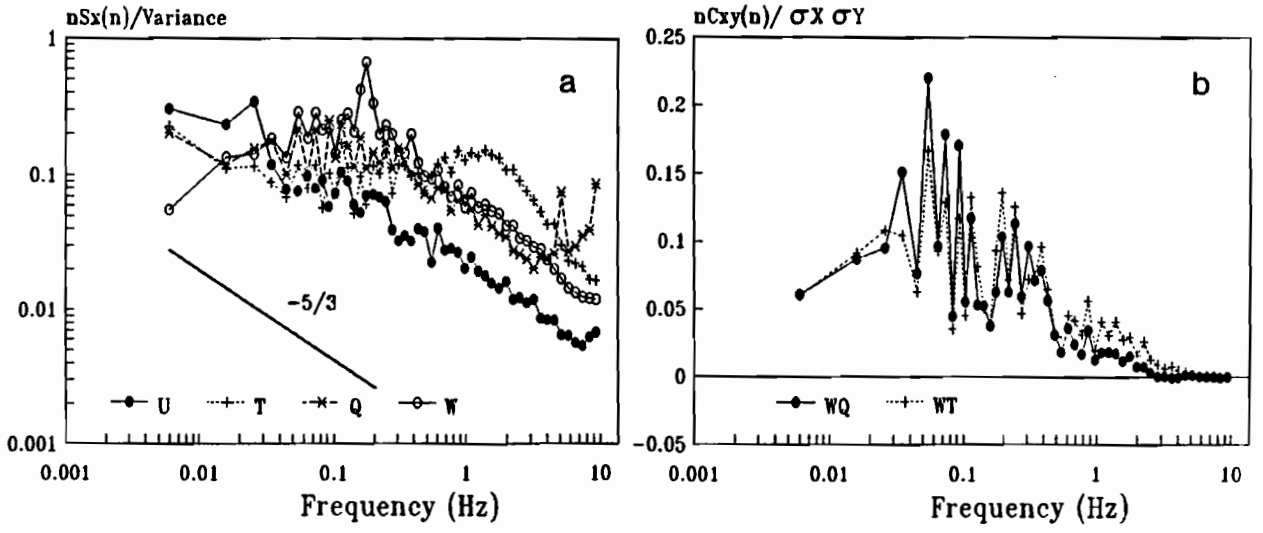

Fig 4. Normalized spectra (a) and Co-spectra (b) for a typical period with low ship motion.

4. RESULTS

4.1 Temperature, humidity and wind measurements

The behaviour of these parameters is illustrated by time sequences during the third observation period, 19–20 May. Figure 5a shows temperatures measured by the psychrometers, the Barton radiometer and the ship's thermosalinograph. There are several notable features. The temperature gradient in the air between 3 and 10 m is extremely small and consistent at 0.2–0.3°C. The difference between these air temperatures and sea temperature at about 2 m below the surface (the 'bulk' temperature) is considerably larger – typically 1–2°C during fine conditions. The sharp decrease in air temperature at 0800 was the outflow from a nearby rainstorm. During the cruise it was not uncommon for the air temperature to fall to as low as 26°C during such storms and the air–sea difference to remain between 2° and 3°C for several hours. These observations are compatible with those from moored buoys in the western equatorial Pacific (McPhaden and Hayes, Lindstrom, personal communication) but at variance with the long-term mean temperature differences obtained from marine climatic data by Esbensen and Kushnir (1981) or by Weare et al. (1981), which are only about 0.5°C in this region.

To examine this further, we have compared four days of air temperature measurements from "Franklin's" routine 2-hourly meteorological observations with those from the 10 m psychrometer on the boom. Agreement was 0.1°±0.6°C for the dry bulb and 0.1°±0.4°C for the wet bulb with the ship's measurement higher in each case. During this period $(T_s - T_a)$, with thermosalinograph temperatures for T_s and the ship's observations for T_a, averaged 1.35°C. So the discepancy remains unexplained. The implications of such large systematic errors for climatological estimates of latent and sensible heat fluxes are discussed below.

The Barton infrared radiometer measures the surface skin temperature of the sea, which is more directly related to the thermodynamic processes which determine sea–air energy exchange rates than is the bulk temperature. With moderate winds and a well-mixed surface layer the difference may well be insignificant; under the conditions we encountered, the skin temperature was typically 0.5°C lower than the thermosalinograph reading and, as in the example shown, can be as much as 0.9°C when the wind speed (Figure 5b) drops completely just before dawn. The surface steadily warmed by 1.5°C through the morning; the thermosalinograph remained steady until 1000 when heating suddenly appeared at this depth. Simple calculation, using reasonable extinction coefficients for the fairly clear water, indicates that sufficient energy penetrates 2–3 m to support the rate of temperature rise shown. The way in which the temperature signal follows the radiation (Figure 5d) and the persistence of the skin temperature depression suggests very little convective mixing in the surface layer. Wind stress is very small until the arrival of a storm at 1600.

The 'cool skin' effect is a possible source of error in the calculation of sensible and latent heat fluxes using bulk transfer equations (2) and (3). Figure 5c shows that use of the infrared temperature to determine vapour pressure at the ocean surface (the saturation value with a 0.98 salinity correction) gives values up to 2 mb lower than those obtained by using the thermosalinograph temperature. The effect of using the bulk temperature is to overestimate both fluxes, partially counteracting the apparent systematic *underestimation* of sea–air temperature difference noted above. Figure 5c also shows vapour pressure at the three boom levels. Some difficulty was experienced with drying out of the psychrometer wet bulbs, and data from the 6 m instrument is missing for most of this day (also, instrument positions were interchanged from time to time; in this case at about 1400). It is clear that the humidity gradient between 3 and 10 m in the air, usually less than 0.5 mb, is very small compared with the air–sea difference of 10–12 mb.

Such small temperature and humidity gradients are extremely demanding of instrumental technique, and effectively rule out the prospect of accurate flux determination using profile methods. Similarly, the wind speed gradients over the 3–10 m height interval were so small as to be almost unmeasurable.

4.2 Latent and sensible heat fluxes and bulk transfer coefficients

Figure 6 shows the eddy-correlation measurements of sensible and latent heat fluxes during the third observation day. Both follow the wind speed (Figure 5b) quite closely as it varied around 1 m/s for most of the day and increased to 4 m/s in late afternoon. Sensible heat flux is small, but always positive, while latent heat flux is an order of magnitude greater.

Altogether 64 h of flux data were recorded during the three observation days. It has been combined with the corresponding measurements of air–sea temperature and humidity difference to calculate bulk transfer coefficients from equations (2) and (3). For most of the time, the sea surface temperatures measured by the infrared radiometer have been used; otherwise those measured by the thermosalinograph. The 6 m psychrometer measurements have been used although, as we have seen, height of measurement in the air is not critical. Total wind speed is the sonic anemometer measurement corrected for the ship speed.

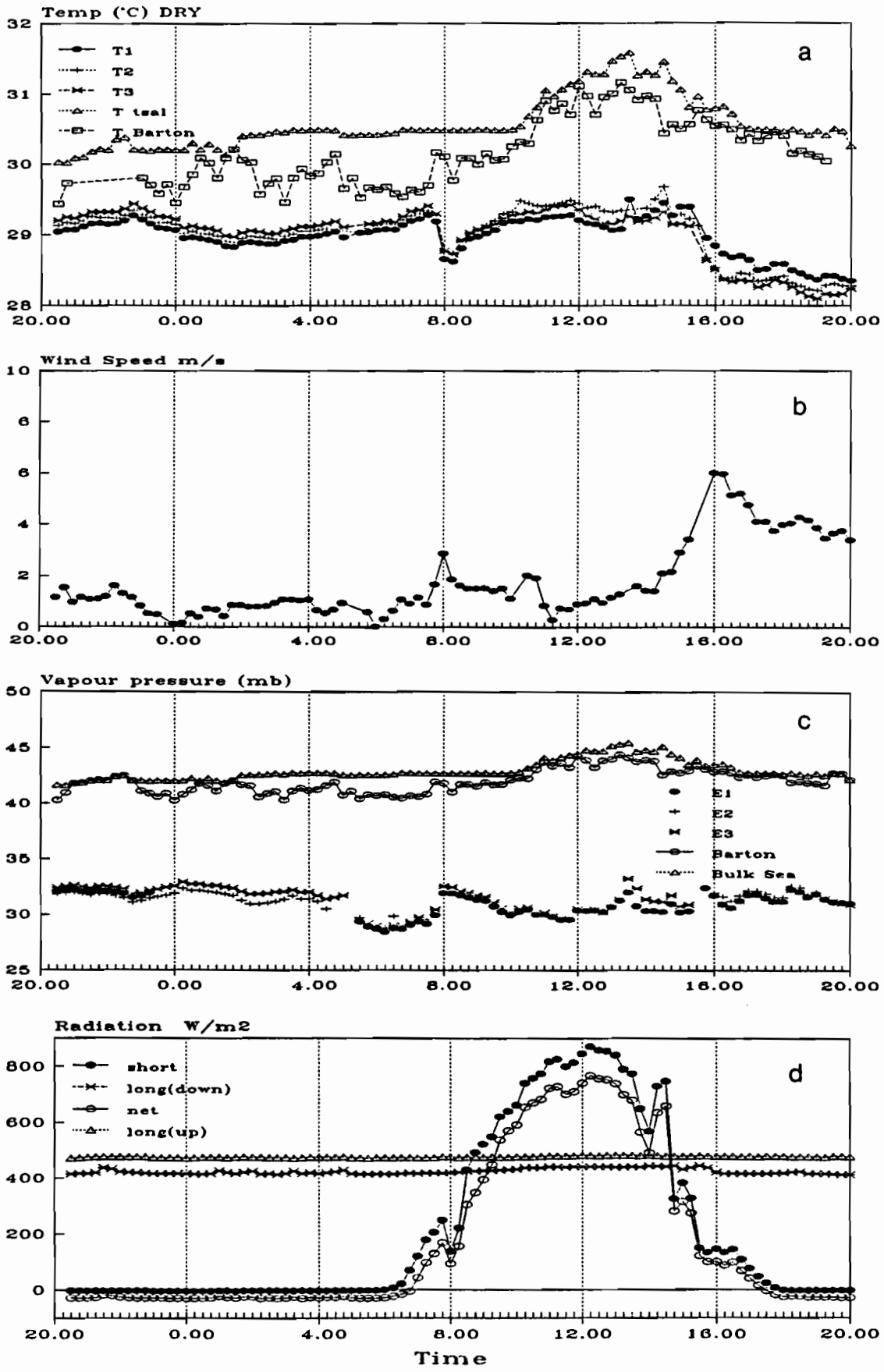

Figure 5. Time sequences of various quantities during third observation period 19–20 May.

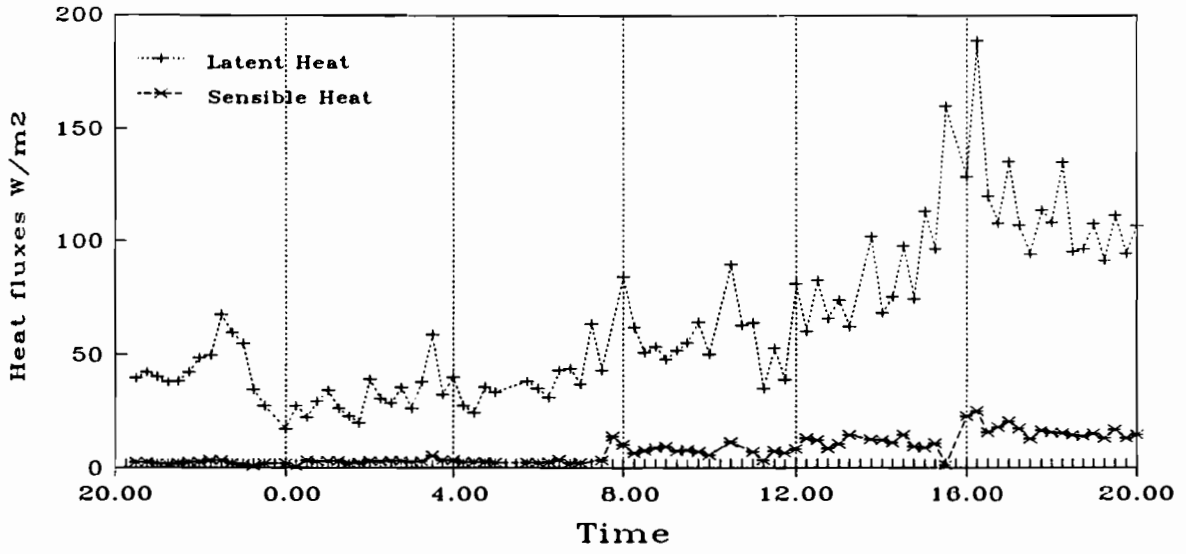

Figure 6. Eddy-correlation measurements of latent and sensible heat during the third observation period 19-20 May.

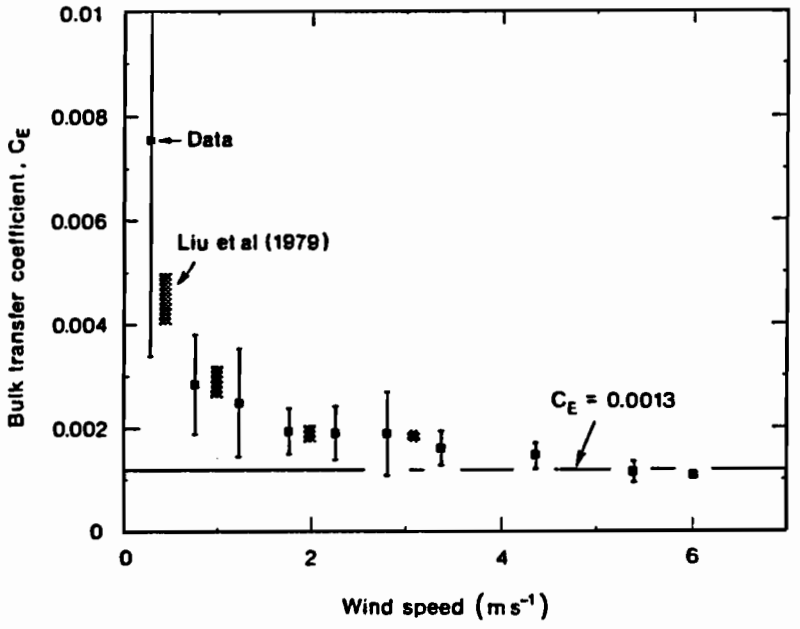

Figure 7. Measured and predicted bulk transfer coefficients for latent heat-flux.

Figure 7 shows the resulting transfer coefficient for water vapour as a function of wind speed. For clarity 15-min measurements have been grouped into 0.5 or 1 m/s wind speed classes and plotted as the mean and standard deviation for each class. The dashed, straight line represents the commonly used value of 0.0013 (e.g. Reed 1985). (A comparison between ten schemes for the parameterisation of C_E is illustrated in Figure 3 of Blanc (1985) and, for these modest wind speeds, C_E ranges from 0.001 to 0.0016.) The hatched areas in Figure 7 give the range of values of bulk transfer coefficients obtained by Liu et al. (1979) for the observed range of sea and air temperatures; their model of the coefficients considers the nature of molecular and sublayer dynamics on either side of the air-sea interface. They predict the rise at low wind speeds, in excellent agreement with the observations. The bulk transfer coefficients for sensible heat are not illustrated here, but behave in a precisely similar fashion. Clearly, in a region where low wind speeds predominate, climate predictions based on conventional transfer coefficients may be significantly in error, as discussed below.

4.3 Dissipation calculations

The inertial dissipation method is being increasingly used to estimate the turbulent fluxes from ships at sea. It is based on the assumption that the spectra of horizontal velocity, $S_u(f)$ and scalars, e.g. $S_q(f)$, (where f is the measured frequency), can be related to the turbulent fluxes of momentum and water vapour through the dissipation rates of turbulent kinetic energy and scalar variance (e.g. Fairall and Larsen 1986). The measurements need only be well behaved, e.g. free from ship motion contamination, in the inertial subrange where the spectra follow the $f^{-5/3}$ relationship. Although much work has been done using this technique, it remains to be shown that the method is applicable under the very unstable, light wind conditions encountered on this cruise. We have calculated the fluxes of momentum and humidity from the relations

$$u_* = [4\alpha_u S_u(f) f^{5/3}]^{1/2} [2\pi/\bar{U}]^{4/3} [kz]^{1/3} [\phi_\epsilon(\xi)]^{-1/3} \tag{4}$$

$$E = \rho L_E [2\pi k z/\bar{U}]^{2/3} f^{5/3} [S_u(f) S_q(f)] [\alpha_u \alpha_q \phi_q(\xi) \phi_\epsilon(\xi)^{1/3}]^{1/2} \tag{5}$$

where k is the von Karman constant, $\alpha_u = 0.55$ and $\alpha_q = 0.8$ are the Kolmogorov constants and $\xi = z/\Lambda$, with the Monin-Obukov Length

$$\Lambda = -u_*^3 T/[gk(\overline{w\theta} + 0.61 T \overline{wq})] \tag{6}$$

where T is absolute temperature, g gravitational acceleration and the unstable dimensionless profile functions, ϕ_ϵ and ϕ_q are given by

$$\phi_\epsilon(\xi) = (1 + 0.5|\xi|^{2/3})^{3/2} \qquad \xi < 0 \tag{7a}$$

$$\phi_q(\xi) = (1 - 14\xi)^{-1/2} \qquad \xi < 0 \tag{7b}$$

The frequency chosen for the spectral estimates was 1 Hz and, as can be seen from Figure 3a, this is in the -5/3 region and clear of either the ship motion at lower frequencies or the vibration problems in q at higher frequencies. The stability corrections, ϕ_ϵ and ϕ_q, were calculated by iteration starting with the neutral dissipation estimates, but with measured $\overline{w\theta}$. The contribution to Λ from $\overline{wq}$ was often comparable to that from $\overline{w\theta}$.

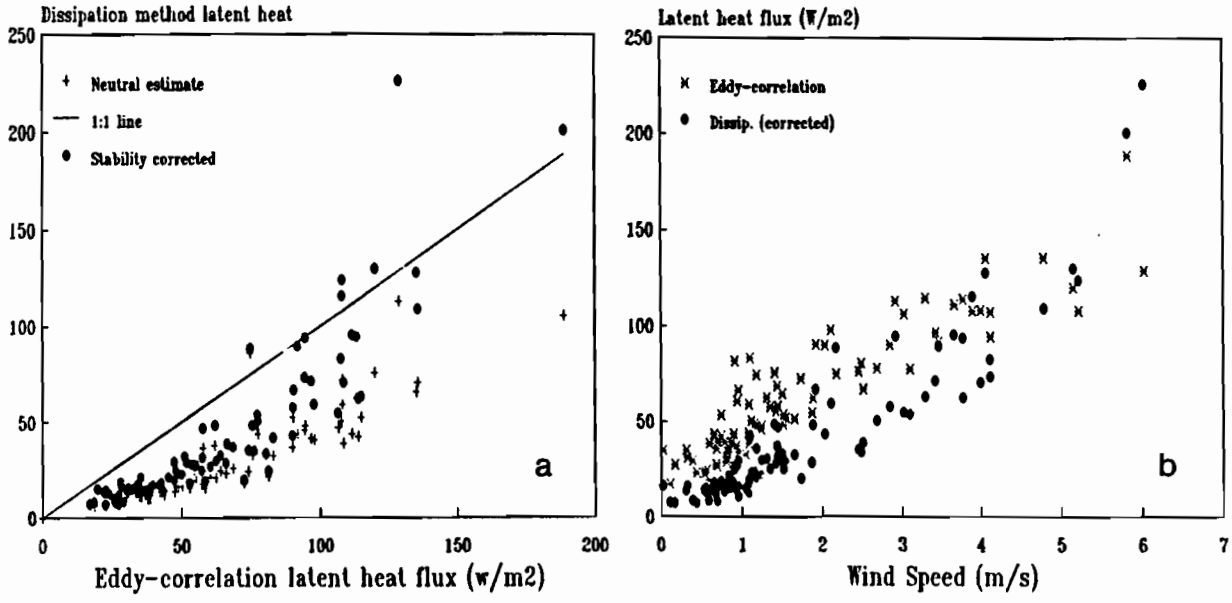

Figure 8. Comparisons of latent heat fluxes derived from eddy-correlation and inertial dissipation methods.

Figure 8a shows the comparison between the covariance and inertial dissipation methods for determining latent heat fluxes. The dissipation method generally underestimates the actual flux but with an improvement

towards higher values of E. In absolute terms the difference is reasonably constant with wind speed (Figure 8b). Some of the assumptions inherent in the inertial dissipation method have questionable validity and the values of some of the constants used have large uncertainty at these low wind speeds and high instabilities (z/Λ approaches -3 and the stability correction approaches a factor of 2): thus the disagreement is not unexpected (Fairall and Larsen 1986, Geernaert et al. 1988).

4.4 Radiation

Radiation measurements through our third observation period appear in Figure 5d. The sky was quite clear during the night, with some light cloud during the day, and became heavily overcast around 1600 with the onset of a storm. Incoming short- and longwave components are directly measured by the pyranometer and pyrgeometer respectively, and outgoing longwave calculated from Stefan's law assuming an emissivity of 0.97 for sea water. The almost constant sea temperature and atmospheric water vapour content lead to a very small diurnal variation in the net longwave balance of 40–60 W/m^2. Assuming an average albedo of 0.08 to account for outgoing shortwave, two estimates of net radiation are available: one from the separate components and the other directly from the net radiometer. A comparison has been made on the basis of 2-hourly averages over the 13-day period 8–20 May, as shown in Figure 9. There appears to be a systematic discrepancy of around 20 W/m^2 in the middle range, which could be explained by poor cosine response of the net radiometer during morning and evening, but overall the agreement is within the accuracy normally accorded such radiation instruments.

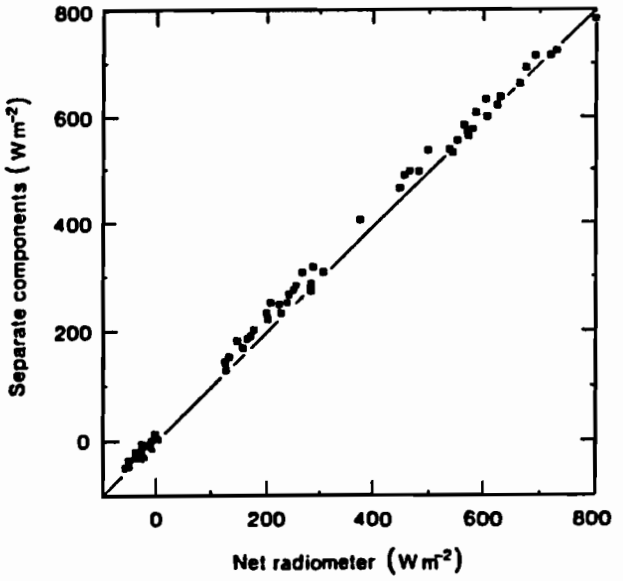

Figure 9. Comparison of net radiation measured in two ways.

5. THE HEAT BUDGET

By analysing ship-of-opportunity meteorological data, Reed (1985) found annual mean values of N into the Pacific near (0°S,150°E) to be between 80 and 100 W/m^2. The results presented above have sufficient resolution (~10 W/m^2) to test the contention by Godfrey and Lindstrom (1989) that long-term heat flux into the region is, in fact, close to zero. Using "Franklin's" routine meteorological observations, we examine the terms on the RHS of Equation (1) over the period 8–20 May. Average daily values of both incoming shortwave and net longwave radiation were very close to the longterm climatology (Esbensen and Kushnir 1981, Reed 1985), indicating that this period, although necessarily short, was sufficiently representative for our purpose. The formulations specified in Reed (1983,Appendix) provide the basis for discussion.

The formula used to predict incoming shortwave radiation is based on solar altitude and mean daily cloud cover. In this region, cloudiness follows a typical diurnal pattern of stormy days and clear nights. Reed (personal communication) accounted for this by including only daytime cloud observations. We have adopted a daytime-weighted modification of the formula which, for the conditions during our 13-day period, reduces the estimate of S by some 25 W/m^2. Our pyranometer measurements for the period average 17 W/m^2 less than the unmodified formula; i.e. the original formula seems to overestimate S, because of the particular cloud conditions by around 20 W/m^2.

The net longwave radiation depends primarily on sea temperature and atmospheric water vapour content as well as cloud cover. Reed's formulation leads to estimates of L which are about **15** W/m^2 less than our measurements (Figure 10), whereas the more complicated version due to Brunt and Berliand (see Budyko 1963) gives much closer agreement.

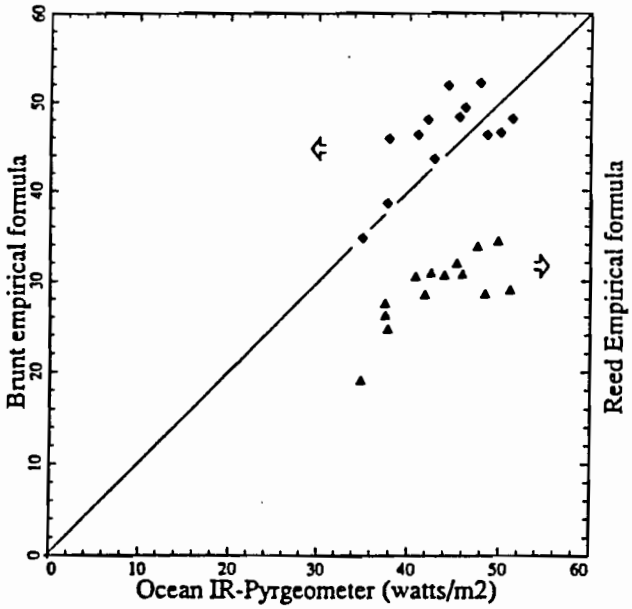

Figure 10. Comparison of two empirical formulae for net longwave radiation, with measurements.

As our measurements show, estimation of sensible and latent heat components of the energy budget using bulk formulae can incur a number of important errors in this particular region. We have shown that the difference ($T_s - T_a$) may be overestimated by perhaps 0.3–0.5°C in the long term due to the 'cool skin', but that there also seems to be a serious discrepancy between merchant ship reports of sea–air temperature difference and our own. Our work suggests that the climatology underestimates sea–air temperature difference by perhaps 0.7–1.0°C, but whether in the measurement of air or sea temperature is difficult to say. If the former, it is probable that the wet bulb and hence q_a are similarly affected; if the latter, the effect ripples through the formulations for q_s, L etc. Sensitivity tests, on the basis of 1°C errors, suggest an overall decrease in N of between **11** and **34** W/m^2.

For the turbulent heat fluxes, it seems more appropriate to use the bulk transfer coefficients of Liu et al. (1979) than the constant value of 0.0013 used by Reed; the difference amounted to **27** W/m^2 for our observation period. The distribution of wind speeds during this time was typical of those in climate atlases, so this value is assumed to represent the longterm effect.

All of the above possible corrections to commonly–used empirical flux formulae operate in the same direction – to reduce estimates of N: in the unlikely event that **all** are valid simultaneously, by between **70** and **100** W/m^2.

Tentative support for small values of net heat flux come from ocean surface layer observations. During May 8–9 "Franklin" deployed a profiling drifter buoy near (4°S,150°E); she returned to the same region on May 20, having followed the track shown in Figure 1. XBT temperature profiles showed that the top 25 m of the sea had warmed by about 0.33°C during the 13 days, which would require a mean heat flux of 30 W/m^2 if it were to be accomplished by local heating. By comparison, our estimates of the net heat flux along "Franklin's" track over the period averaged 38 W/m^2. Such a comparison must obviously be treated with caution; the period was short, the ship travelled into other water bodies and the measurements were interrupted by the port call at Rabaul. However, weather conditions were very consistent day to day over the period, and it seems reasonable to conclude that a substantial fraction of the net heat input of about 40 W/m^2 between May 8 and May 20 was used to heat the surface layer.

6. ACKNOWLEDGEMENTS

None of the above would have been possible without the enthusiastic involvement of Ian Helmond who, among other things, designed the boom. Manuel Nunez and Ian Barton kindly loaned us their radiometers. We are particularly grateful for the support of our cruise leader, Eric Lindstrom, and for the cooperation of Capt. Neil Cheshire and the crew of the "Franklin".

7. REFERENCES

Blanc T.V. (1985) J. Phys. Oceanogr., **15**, 650–669.
Budyko M.I. (1963) Atlas of the Heat Balance of the Earth (in Russian), Kartfabrika Gosgeoltehiyda, 41 pp.
Coppin P.A., and K.J. Taylor (1983) Boundary-layer Meteorol., **27**, 27–42.
Enfield D.B. (1986) J. Phys. Oceanogr., **16**, 1038–1054.
Esbensen S.K., and Y.Kushnir (1981) Climatic Res. Inst. Rep. No. 29, Oregon State University, Corvallis.
Fairall C.W., and S.E. Larsen (1986) Boundary-Layer Meteorol., **34**, 287–301.
Geernaert G.L., K.L. Davidson, S.E. Larsen and T. Mickkelsen (1988) J. Geophys. Research, **93**, 13913–13923.
Godfrey J.S., and E.J. Lindstrom (1989) J. Geophys. Res. (in press)
Hsiung J. (1985) J. Phys. Oceanogr., **15**, 1405–1413.
Legeckis R., W. Pichel and G. Nesterczuk (1983) Boundary-Layer Meteorol., **34**, 287–301.
Lindstrom E., R. Lukas, R. Fine, E. Firing, S. Godfrey, G. Meyers and M. Tsuchiya (1987) Nature, **330**, 533–537.
Liu W.T., K. Katsaros and J.A. Businger (1979) J. Atmos. Sci., **36**, 1722–1735.
Niiler P., and J. Stevenson (1982) J. Mar. Res., **40** Suppl., 465–480.
Ramage C.S. (1984) J. Clim. App. Meteorol., **23**, 187–193.
Reed R.K. (1983) J. Geophys. Res., **88**, 9627–9638.
Reed R.K. (1985) J. Clim. App. Meteorol., **24**, 833–840.
Schlesinger M.E., and J.F.B. Mitchell (1987) Rev. Geophys., **25**, 760–798.
Weare B.C., P.T. Strub and M.D. Samuel (1981) J. Phys. Oceanogr., **11**, 705–717.

CORRIGENDUM

In this paper, some of the radiation estimates are incorrect. Estimates of solar input from Reed's (1983) formula are too small by typically 15 watts/m2, due to use of radians rather than degrees for noon solar angle. In estimating the net outgoing longwave radiation from pyrgeometer readings, the pyrgeometer reading was not multiplied by the emissivity; allowance for this increases the net outgoing longwave radiation by about 13 watts/m2, to 56 watts/m2. Broad conclusions of the paper are not changed. A corrected version will be submitted to J. Geophys. Res.

Evaluation of NMC's Operational Surface Fluxes in the Tropical Pacific

Richard W. REYNOLDS and Ants LEETMAA

Climate Analysis Center
NMC/NWS/NOAA
Washington, DC 20233, U.S.A.

A major part of our effort at the Climate Analysis center (CAC) consists of the evalutation of surface fields from the data assimilation/forecast cycle of the NMC medium range forecast (MRF) model. This is done using direct comparison of the NMC fields with independent data and by comparing the response of the CAC tropical ocean model to different forcing fields. Here, we evaluate the accuracy of the NMC surface winds and surface heat flux fields. Because sea surface temperature (SST) is an important parameter in the coupling of atmospheric and oceanic models, a high resolution SST product is also presented.

To determine the accuracy of different surface wind analyses in the tropical Pacific, we have compared the NMC MRF surface winds analyses with independent wind observations from Pacific Marine Environmental Laboratory (PMEL) meteorological buoys. In an initial study, Reynolds et al., (1989) evaluated the NMC analysis for a six-month period (February 1 through July 31, 1987). The study reported here is a continuation of the comparison. The starting date of this comparison was selected to be September 1, 1987, because NMC implemented a higher resolution forecast model in August 1987.

Preliminary results of this new comparison have been completed for daily winds for a one year period (September 1, 1987 to August 31, 1988) using eight PMEL buoys located within five degrees of the equator. The long-term mean winds for the period are shown in Figure 1. The results show that the zonal NMC and PMEL wind components agree to within 1.1 $m.s^{-1}$ except at 5°N, 110°W. However, the agreement in the meridional component is generally worse especially at 5°N, 110°W. These results are similar to the results from the 6-month comparison.

Cross-correlation statistics were computed between pairs of the daily wind time series at the same locations. The correlations (not shown) varied from 0.15 to almost 0.7. At all locations the zonal correlations are superior to the meridional correlations. The correlations were all significantly different from zero except the meridional correlation at 5°S, 110°W.

Figure 2 shows the time series of the PMEL and NMC meridional wind components for the one year period (366 days) at 5°N, 110°W. This is the location and wind component with the worst agreement in the long term mean. (Both time series have been smoothed by a five-point binomial filter for visual clarity). The two time series are similar during the first 30 days. After this period, a strong bias (over 5 $m.s^{-1}$) develops which persists until approximately day 120. This bias corresponds to the seasonal shift of the Intertropical Convergence Zone (ITCZ). This bias corresponds to the seasonal shift of the Intertropical Convergence Zone (ITCZ). During the period of high bias, the ITCZ shifted close to the position of the buoy. This suggests that the NMC analysis may tend to underestimate tropical divergent and convergent areas. (Missing buoy winds are due to instrument problems.)

ORSTOM
CENTRE DOCUMENTATION
Montpellier

F 30240

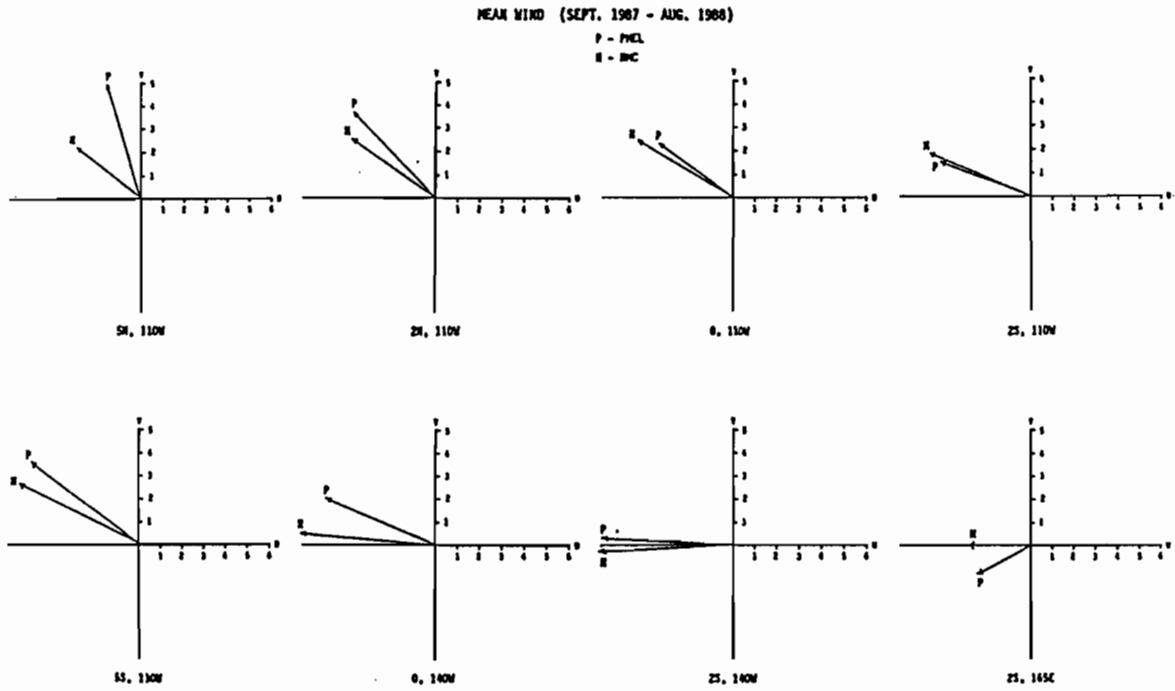

FIG.1. The long-term mean (September 1, 1987 - August 31, 1988) surface wind vectors at the 8 buoy locations in the tropical Pacific. The vectors were from PMEL buoys (labeled P) and the NMC operational analysis (labeled N).

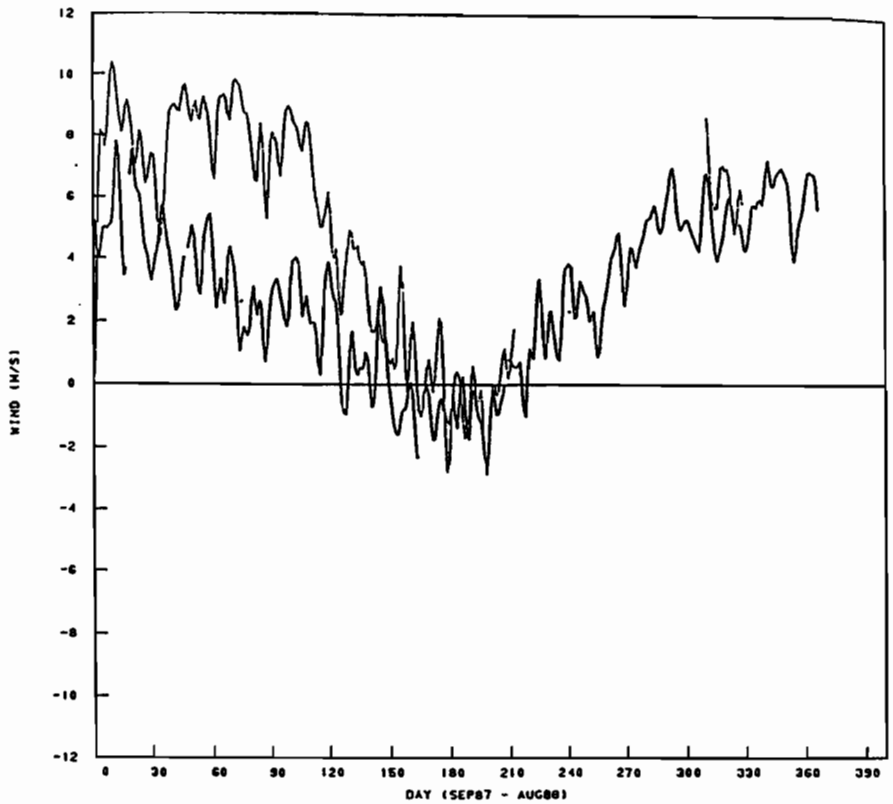

FIG.2. Daily time series (see text) of the meridional wind components of PMEL (light line) and NMC (heavy line) at 5°N, 110°W. The time series have been smoothed by a five-point binomial filter.

To help quantify these results with the other products, the monthly pseudo stress fields produced at Florida State University (henceforth, FSU) (see Goldenberg and O'Brien, 1981) for details, and the monthly wind stress climatology of Hellerman and Rosenstein (1973) (henceforth, H&R) were used. To avoid the non-linearity in converting between monthly averaged winds and monthly averaged wind stress, the daily averaged winds from the buoys and NMC were converted to daily pseudo stresses and averaged. The H&R climatological wind stress were converted to constant pseudo stress by approximating the H&R drag coefficient as a constant of 1.4×10^{-3}. Monthly differences between the buoys and the NMC, FSU and H&R pseudo stresses were computed if there were at least 25 days of buoy data per month. Table 1 shows the RMS errors of the three analyses relative to the buoys. At each buoy location the RMS errors are usually the worst for the FSU analysis. The H&R climatology and the NMC analysis alternate in having the lowest RMS error. Although climatology does as well as NMC, this result may not apply to other periods, especially El Nino periods.

	ZONAL			MERIDIONAL		
BUOY	H&R	NMC	FSU	H&R	NMC	FSU
5°N/110°W	3.9	7.5	9.7	21.1	36.1	32.5
2°N/110°W	10.2	6.6	10.2	5.4	10.6	11.2
0° /110°W	7.5	10.3	10.1	10.3	4.5	7.6
2°S/110°W	7.3	7.3	10.0	11.5	4.0	10.2
5°S/110°W	7.2	7.1	10.0	10.2	9.9	10.3
0° /140°W	12.5	13.0	16.5	4.9	10.3	8.6
2°S/140°W	9.6	4.8	15.1	12.5	4.1	10.1
2°S/165°E	13.9	6.5	12.2	4.9	8.4	10.2

Table 1. The monthly RMS error (in $m^2.s^{-2}$) between the buoy wind pseudo stress and the pseudo stress from the H&R climatology and the NMC and FSU surface wind analyses for the period : September 1987 - August 1988.

These surface wind comparisons will be continued. They will be of special interest during the next year when more PMEL buoys become operational and when the PMEL data are made available on the GTS. Because of the present deficiency of low-level wind observations in the tropical Pacific, the addition of the PMEL wind data to the GTS should significantly improve the quality of the assimilated surface wind analyses. This assumption will be tested as soon as possible.

Surface heat and momentum fluxes are computed at NMC in the boundary layer of the MRF model. These fluxes became available during last December 1989, and a daily archive was begun at CAC to save these fields. Comparisons of monthly averages of the sensible and latent heat fluxes and the net short wave and long wave radiation with the climatology of Oberhuber (1988) show that the MRF fields show some important features, e.g. the ITCZ, correctly but can have biases. In particular, each month (e.g. see fig.3) showed a large positive net heat flux into the ocean. This would result in a larger global warming than is observed in the changes in monthly SSTs. Much of the error is due to inadequate cloud cover in the MRF which results in large net incoming radiative fluxes. We plan to continue these evaluations.

The present TOGA sea surface temperature (SST) analysis is a monthly product which is designed to use both *in situ* (ship and buoy) and satellite data. This product "blends" the two types of observations by using an *in situ* analysis to define "ground

truth" temperature values in regions of frequent *in situ* observations and a satellite analysis to define the shape of SST field in regions with little or no *in situ* data. This technique permits the automatic adjustment of possible satellite biases for each analysis period. The automatic adjustment of satellite biases is the major advantage of the blended technique. To provide accurate *in situ* "ground truth", the *in situ* analysis is spatially smoothed by a median filter which degrades the resolution to approximately 6 degrees. This affects the resolution of the blended product. The degradation of spatial resolution is the major disadvantage of the blended technique. Complete details of the analysis techniques can be found in Reynolds (1988).

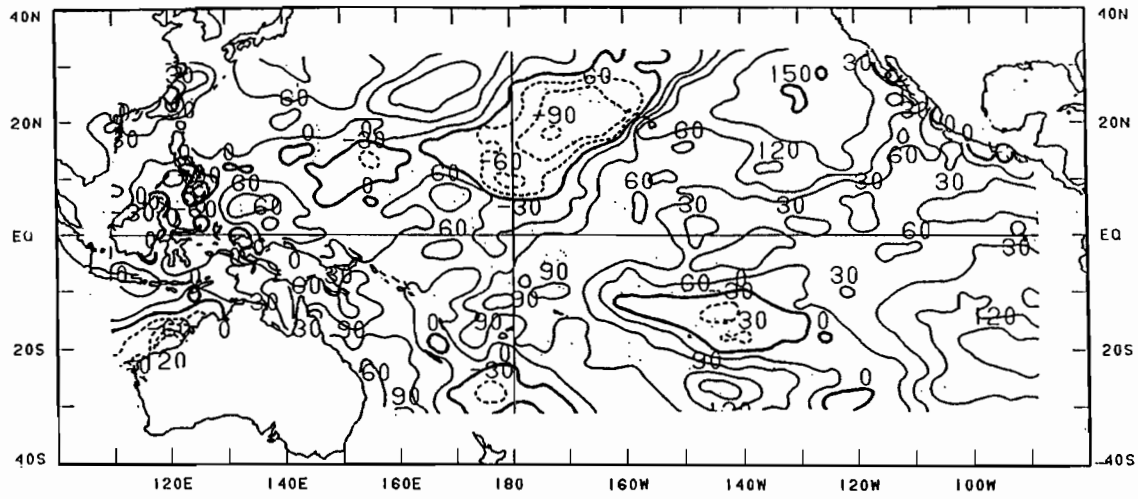

FIG.3. The NMC net heat flux anomaly for March 1989. The anomaly is computed relative to the climatology of Oberhuber (1988). The contour interval is 30 $W.m^{-2}$. Negative contours are dashed.

To improve the spatial and temporal resolution of the SST analysis, a weekly higher resolution analysis was designed. The analysis is done on the grid of the CAC tropical Pacific ocean model (Philander and Seigel, 1985) which has a zonal grid spacing of 1° and meridional spacing of 1/3° within 10° of the equator. The model provides a dynamically consistent first guess SST for an optimum interpolation (OI) analysis (Gandin, 1963) which uses expendable bathythermograph (XBTs) as well as the ship, buoy and satellite data used by the blended analysis. Because the improved resolution results in fewer observations per grid interval, careful quality control of the data is required. The quality control was provided by a regional data base management system which permits evaluation and comparison of the various data sets and analyses.

The weekly SST analysis is of sufficient resolution to define the tropical instability waves and the eastern boundary and eastern equatorial upwelling regions. Figure 4 shows the blended and the OI analyses for April 1989. The monthly OI field is formed by averaging four weekly analyses made during the month. Although the four week averaging process smooths any instability waves, the upwelling regions are better represented by the OI analysis. The difference between the two analyses (lower panel of fig.4) shows that the differences between the two analyses are small in other regions.

The data base for the OI separates daytime and nighttime satellite retrievals. The retrievals are done using the Advanced Very High Resolution (AVHRR) instrument. Because the satellite observations measure a "skin temperature" (i.e. the temperature of a surface layer on the order of millimeters) while the *in situ* observations measure a "bulk

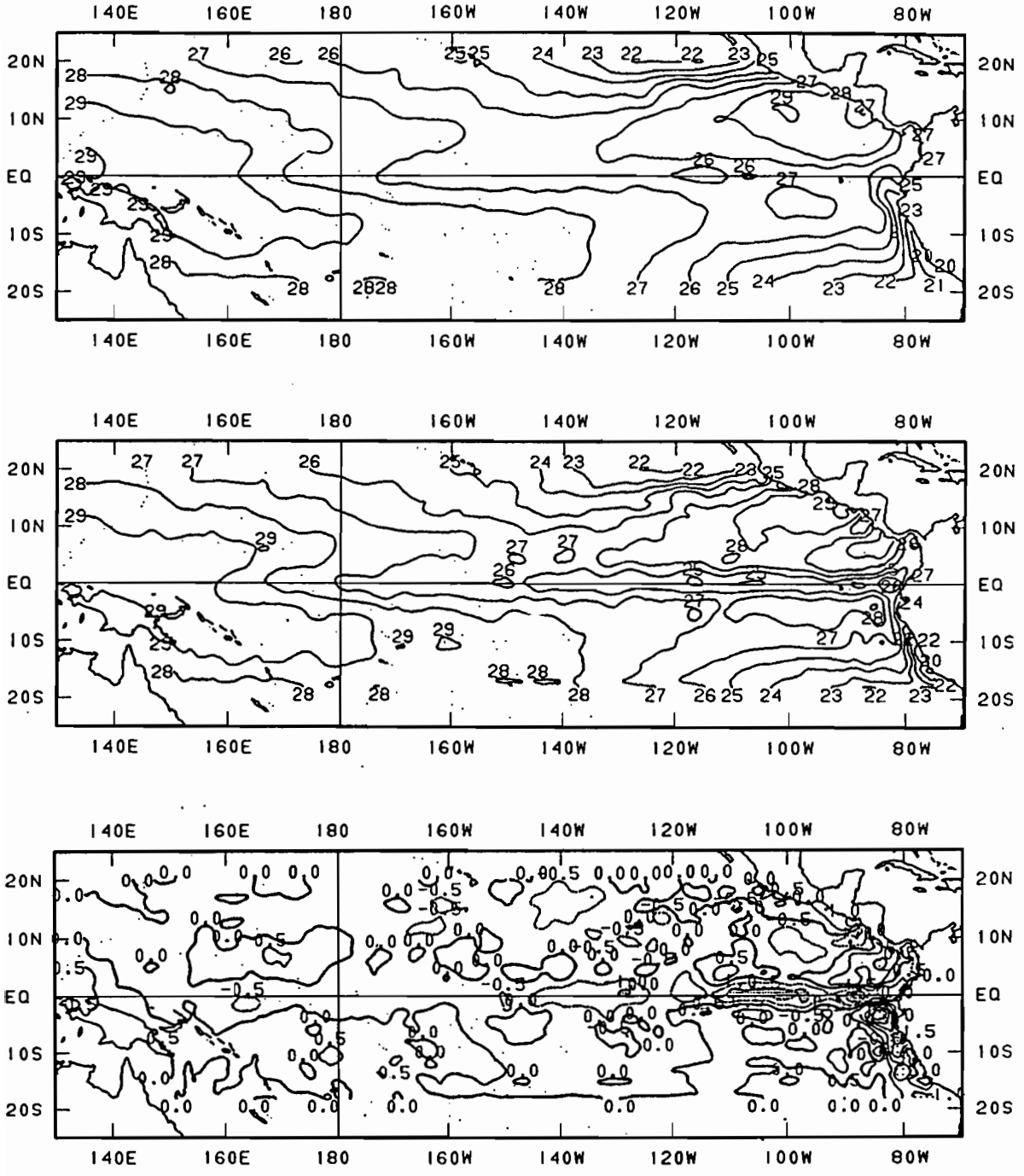

FIG.4. The blended SST analysis (upper panel) and OI analysis (middle panel) for April 1989. The difference between the OI and the blend (lower panel). The contour interval is 1°C (upper and middle panels); the contour interval is 0.5°C (lower panel). The 0°C contour is a heavy line; negative contours are dashed.

temperature" (i.e. the temperature of a surface layer on the order of meters), the satellite algorithms were adjusted to produce a "bulk" value by regression against drifting buoys (see McClain et al., 1985).

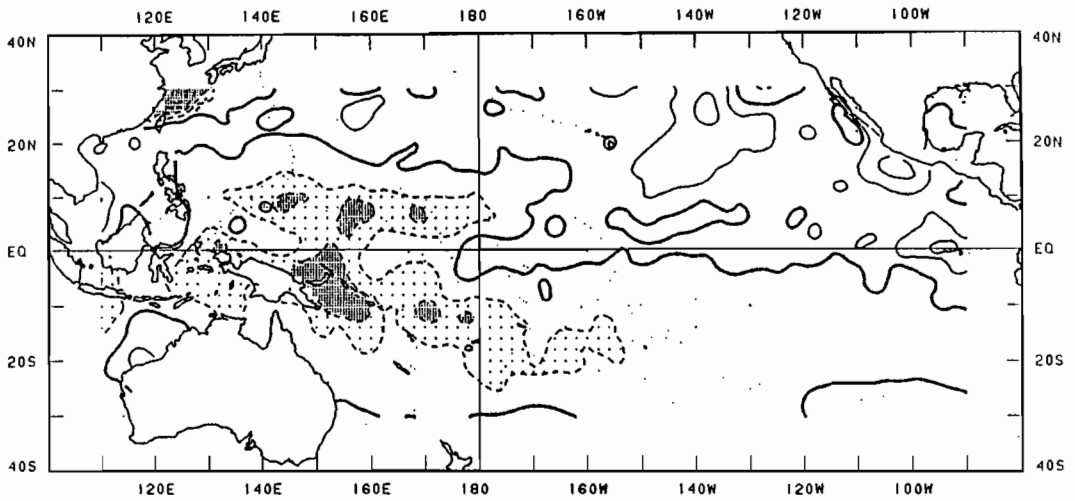

FIG.5. The difference between the daytime and nighttime satellite analysis for the tropical Pacific for April 1989. The contour interval is 0.5° C. The 0°C contour is a heavy line; negative contours are dashed. Dotted regions indicate differences between -0.5° C and -1°C. Stippled regions indicate differences less than -1°C.

Because the OI cannot correct satellite biases, it is necessary to eliminate or correct biased satellite data. To illustrate that biases occur in the satellite data, the April 1989 monthly difference between the daytime and nighttime satellite retrievals is shown in figure 5 for the tropical Pacific. In the western tropical Pacific there is a large region where the daytime temperatures are more than 0.5°C colder than the nighttime temperatures. This pattern has persisted since NOAA 11 became operational in November 1988. Comparison with buoy SST data from the data base showed that the daytime satellite data were biased cold in the western Pacific. To avoid this bias only nighttime satellite data was used in the OI analysis. Although, both daytime and nighttime data were used in the blended analysis, the automatic adjustment technique corrected much of the satellite bias. This is illustrated by the small difference between the OI and the blend in the western Pacific.

To examine the biases with time, figure 6 shows the monthly anomaly time series for the blended analysis and analyses using only *in situ* (ship and buoy) and only satellite data for all ocean areas between 20°S and 20°N. The anomalies from the *in situ* analysis (dotted) and blended anomalies (heavy line) are almost identical to each other. However, the satellite analysis (light line) shows a strong warming trend over the period. In these results, there is little evidence of any important trends in either the *in situ* or the blended anomaly time series.

The satellite retrieval algorithm was affected by the aerosols injected into the stratosphere by the April 1982 eruptions of the El Chichon volcano. This resulted in a negative bias in satellite SST retrievals from April 1982 through the end of 1983 which has a major effect on the satellite trends. During our period of interest, two El Nino/Southern Oscillation event (1982-83 and 1986-87) caused anomalous SST warming of the tropical oceans, primarily in the Pacific. Figure 6 shows both these warmings in the *in situ* and blended analyses. Because of the effect of the El Chichon aerosols, the satellite analysis does not show the warming associated with the 1982-83 event.

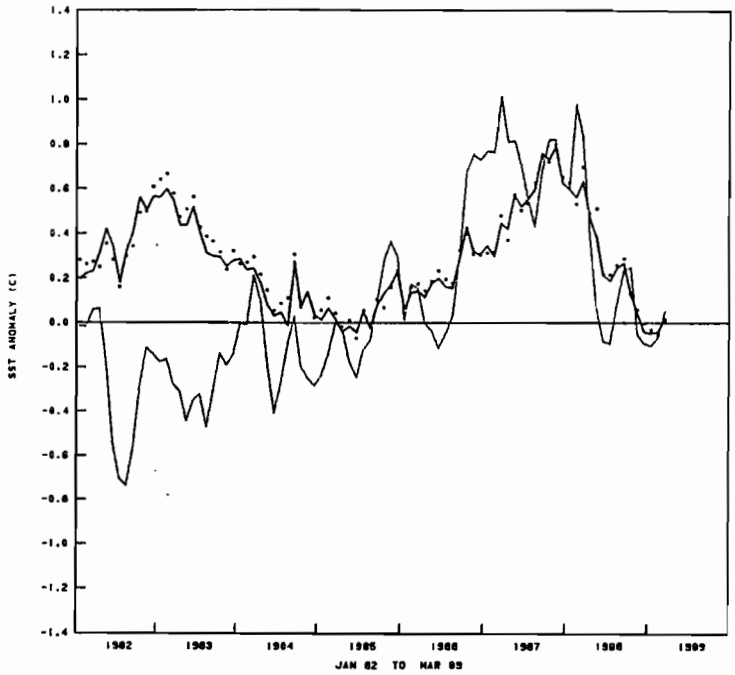

FIG.6. Time series of the SST anomalies for all ocean regions between 20°S and 20°N. The satellite anomaly is indicated by a light line; the blended anomaly is indicated by a heavy line; the *in situ* anomaly is dotted.

The OI technique shows great promise. During the next year we will be implementing a global ocean model and will be extending the OI method to the global domain. However, careful adjustment of the satellite data will be required before they are assimilated into the analysis. We are now testing and developing these methods.

REFERENCES

Goldenberg, S.B., and J.J. O'Brien, 1981 : Time and space variability of tropical Pacific wind stress. *Mon. Wea. Rev.*, **109**, 1190-1207.

Hellerman, S., and M. Rosenstein, 1983: Normal monthly wind stress over the world ocean with error estimates *J. Phys. Oceanogr.*, **13**, 1093-1104.

Gandin, L.S., 1963: Objective analysis of meteorological fields. (Translated from Russian by the Israeli Program for Scientific Translations, 1965) 242 pp.

McClain, E.P., W.G. Pichel and C.C. Walton, 1985: Comparative performance of AVHRR-based multichannel sea surface temperature. *J. Geophys. Res.*, **90**, 11587-11601.

Oberhuber, Josef M., 1988: An atlas based on the "COADS" data set: the budgets of heat, buoyancy and turbulent kinetic energy at the surface of the global ocean. *Max-Planck-Institut für Meteorologie*, Report N° **15**, 196 p.

Philander, S.G.H., and A.D. Seigel, 1985: Simulation of El Nino 1982-83. *Coupled ocean-atmosphere models*, J.C.J. Nihoul, Ed., Elsevier Science Pub., Amsterdam, 517-541.

Reynolds, R.W., K. Arpe, C. Gordon, S.P. Hayes, A. Leetmaa, and M. McPhaden, 1989: A comparison of tropical Pacific surface wind analyses, *J. Climate*, **2**, 105-111.

Reynolds, R.W., 1988: A real-time global sea surface temperature analysis. *J. Climate*, **1**, 75-86.

The Influence of Sea-Surface Temperature on Surface Wind in the Equatorial Pacific Ocean

Stanley P. HAYES[1], Michael J. McPHADEN[1], John M. WALLACE[2] and Joël PICAUT[3]

(1) *Pacific Marine Environmental Laboratory*
National Oceanic and Atmospheric Administration
7600 Sand Point Way NE
Seattle, WA 98115, U.S.A.

(2) *Department of Atmospheric Sciences*
University of Washington
Seattle, WA 98195, U.S.A.

(3) *Groupe SURTROPAC*
ORSTOM, B.P. A5
Nouméa, New Caledonia

Recent studies suggest that sea surface temperature gradients in the tropics can directly modify surface winds by perturbing the atmospheric sea level pressure field (Lindzen and Nigam, 1987) or by modifying the boundary layer shear profile (Wallace et al., 1989). The latter reference used historical ship data to analyze the seasonal and interannual variability in the eastern Pacific. In this region strong seasonal changes occur and SST gradients are large. During the cold season (July through November) the equatorial cold tongue is well developed and SST cooler than 25°C extends westward to 130°W. Temperature changes of 3°-4°C occur across the equatorial front at the northern edge of the cold tongue. During the warm season (March through June) surface temperatures colder than 25°C are confined to the coast of South America and the equatorial front is weak or non-existent. During El Nino years, SST in the cold tongue is elevated throughout the year; the equatorial front nearly disappears.

Surface winds vary in concert with the changes in the SST distribution in the eastern Pacific. The mean southeasterly winds are strongest during the cold season. As this southerly flow crosses the equatorial front it accelerates, leading to a pronounced horizontal divergence. During the cold season of the colder (i.e. non El Nino) years, when the equatorial cold tongue and the oceanic front are most developed, the southerly surface wind on the equator is anomalously weak, but northerly wind near 5°N is anomalously strong. Hence, the divergence over the equatorial front is enhanced relative to the climatological mean.

Wallace et al., (1989) interpret these correlations in the eastern Pacific as evidence that at least two processes are important in the dynamics of the surface wind field near the equator. The seasonal and interannual variability of the surface wind field is due, in part, to hydrostatic sea-level pressure changes induced by changes in the strength of the associated cold tongue. Such a direct coupling between SST and sea-level pressure anomalies was discussed by Lindzen and Nigam (1987). However, Wallace et al., 1989) note that the sea-level pressure and the surface wind speed are not linearly related to each other or to the underlying SST gradient. They suggest that atmospheric boundary layer dynamics contribute to this discrepancy. As boundary layer flow passes from the cold tongue to the warmer water north of the equatorial front, the

ORSTOM
CENTRE DOCUMENTATION
Montpellier

F 30241

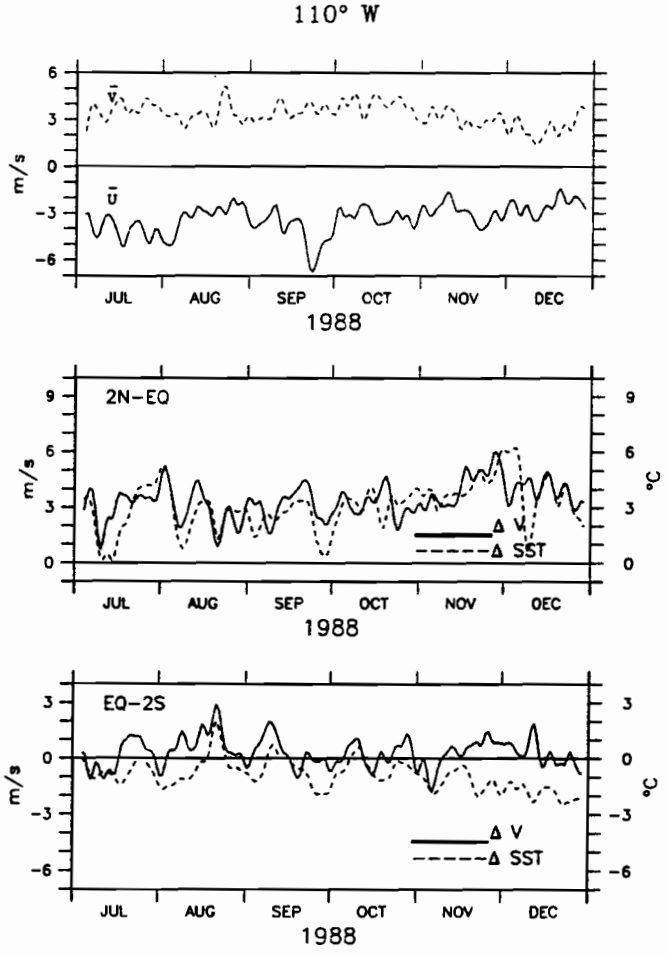

FIG.1. Low-pass filtered near equatorial wind and SST time series along 110°W during the period July through December 1988. Top panel: spatially averaged wind components (U and V) estimated from the measurements at 2°N, 0°, and 2°S. Middle panel: the difference in meridional wind (solid) and SST (dashed) between 2°N and the equator. Bottom panel: the difference in meridional wind (solid) and SST (dashed) between the equator and 2°S.

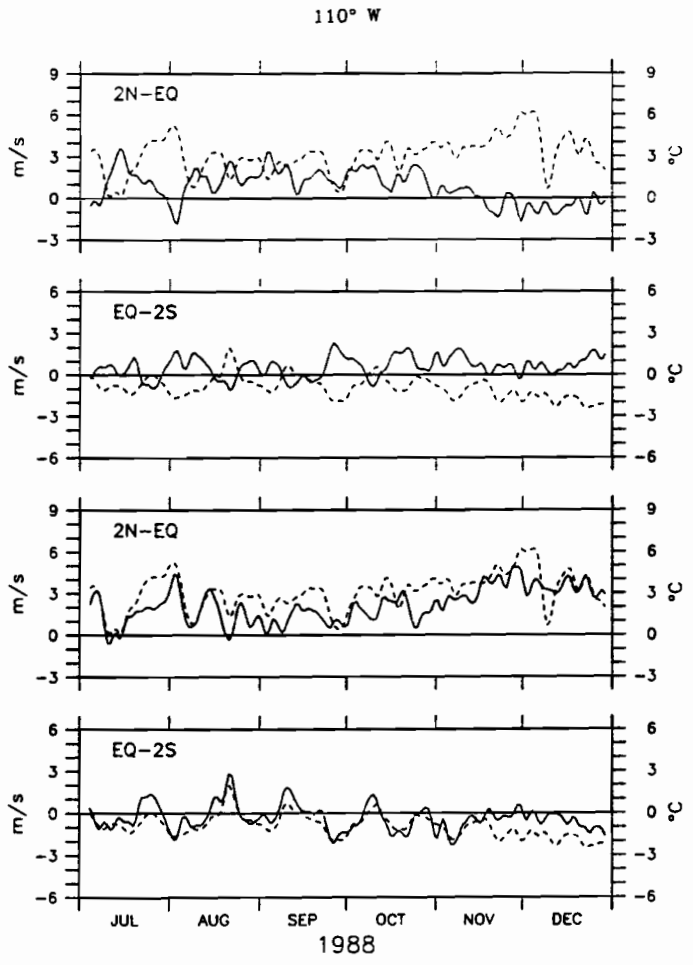

FIG.2. Low-pass filtered near equatorial wind and SST time series along 110°W during the period July through December 1988. Top two panels are the differences in zonal wind (solid) and SST (dashed) between 2°N and the equator and between the equator and 2°S; bottom two panels are the differences in scalar wind speed (solid) and SST (dashed) over the same latitudes.

vertical stratification decreases. Wind shear near the surface is reduced and hence, surface wind speeds increase. This increase is associated with the turbulent transfer of momentum from a low level jet to the surface during unstable boundary layer conditions.

The correlations of SST and surface wind observed in the seasonal and interannual changes can also be seen in the weekly to monthly variability using buoy measurements (Hayes et al., 1989). Figure 1 shows the average wind from buoy measurements along 110°W at 2°N, 0° and 2°S for the cold season of 1988 (July through December). During this season the southeast trades were persistent; equatorial SST was anomalously cold, and the equatorial front was well developed. Tropical instability waves, caused by instabilities of the zonal currents near the equator, were pronounced in the SST field. These waves have periods of about 20 days and contribute much of the SST variability in the week to month time period. Their properties are reviewed by Legeckis (1986) and Halpern et al., (1988). Since these waves are a feature of the ocean dynamics and are not directly wind forced, they are a convenient probe for examining the influence of the ocean on the atmosphere. Evidence of the instability waves can be seen in the differences of SST between 2°N and the equator and between the equator and 2°S (figure 1). North of the equator this difference is about 3°C on average and varies from 0° to 6°C. South of the equator the mean SST gradient is near zero but differences of more than 2°C are observed. These fluctuations of SST gradient are clearly correlated with changes in the meridional wind gradient shown by the solid lines in figure 1. Wind gradients rather than the wind itself are used in this analysis as a means of isolating the smaller spatial scale features of the wind field. Both north and south of the equator the meridional wind and SST gradients are significantly correlated (R = 0.6) at the 95% confidence level. Zonal wind gradients were also correlated with SST gradients during this period (fig.2, upper panels). In this case correlations were negative (R = -0.66 from 2°N to the equator and R = -0.73 from the equator to 2°S). The sign of the correlations indicates that the southeast tradewinds at the surface are stronger over the warm water. Indeed, the best correlations observed were between meridional gradients of wind speed and SST (fig.2, lower panels). The correlation coefficients are 0.75 north and 0.83 south of the equator. Fluctuations of the wind speed associated with the passage of instability waves were 1-2 m s^{-1}.

The high correlation between wind speed and SST gradient suggests that boundary layer stability is a key factor in causing the fluctuations in surface wind. If so, then one expects that the surface wind speed will correlate with the difference between air and sea surface temperature. In order to investigate this correlation the wind records at each buoy were demeaned by removing the spatially averaged wind between 2°N and 2°S. This subtraction again tended to remove the large scale wind variability and focused on the small scale changes. Figure 3 shows the demeaned wind speed at 2°S plotted as a function of air-sea temperature difference. The correlation is significant (R = 0.7) and the highest wind speeds are associated with SST warmer than air temperature. These results support the hypothesis that modification of the boundary layer stratification plays a key role in determining surface winds in the eastern Pacific.

The clear correlation between SST and surface wind gradients may only be a feature of the eastern equatorial Pacific where the southerly winds are strong and blow across the strong SST front. In the central Pacific surface winds are more nearly zonal and the strength of the equatorial front is reduced. West of the dateline surface winds are more variable and SST gradients are very weak. Correlations in these regimes were briefly examined using buoy measurements at 140°W and 165°E. At the former location significant correlation between surface wind speed and SST gradients were again observed (fig.4); however correlations between wind speed and air-sea temperature

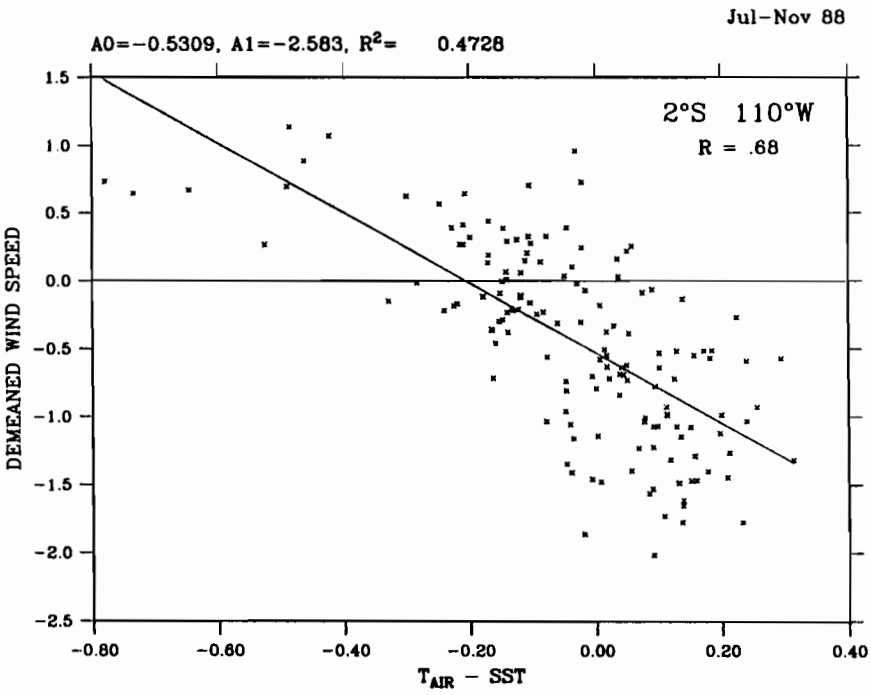

FIG.3. Scatter plot of demeaned wind speed versus air-sea temperature difference for 2°S, 110°W. Period of the observations is the same as figure 2. Regression line is least squares fit to the observations.

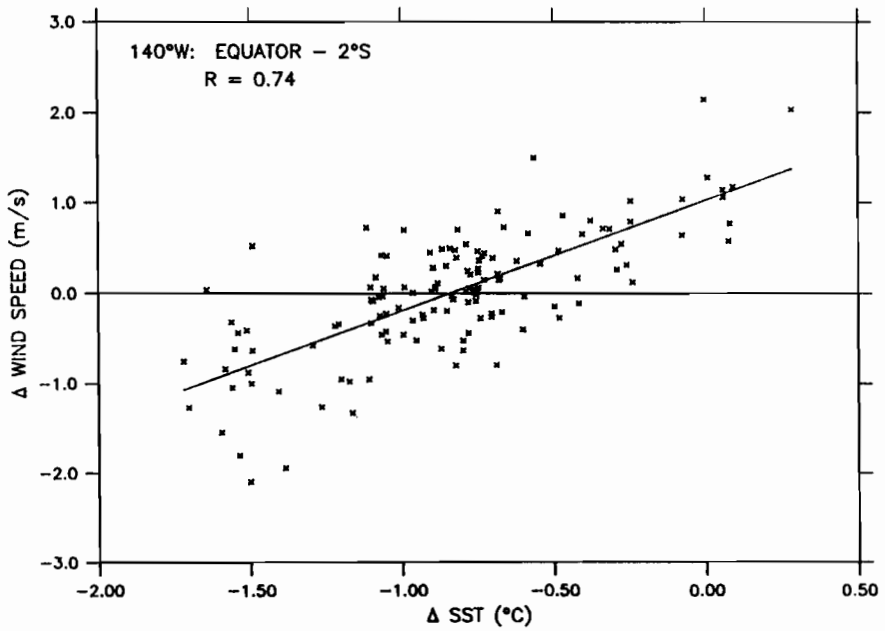

FIG.4. Scatter plot of change in wind speed between the equator and 2°S versus the change in SST between these latitudes at 140°W for the period September 1987 to February 1988. Regression line is least squares fit to the observations.

difference were lower than at 110°W. In the western Pacific, measurements at 165°E failed to show significant correlations between surface wind speed and SST gradients for any of the periods considered.

The structure of the boundary layer winds in the eastern Pacific need to be more fully examined before the processes responsible for the observed correlations can be clearly defined. However, based on the limited data available, it appears that the existence of a low level southeasterly jet and the strong SST gradients over which this boundary layer passes are crucial parameters in determining the surface wind field. Further investigations using shipboard profiling as well as the surface measurements are needed to understand the dynamics involved.

Contribution No. 1142 from NOAA/Pacific Marine Environmental Laboratory.

REFERENCES

Halpern, D., R.A. Knox, and D.S. Luther, 1988: Observations of 20-day period meridional current oscillations in the upper ocean along the Pacific equator. *J. Phys. Oceanogr.*, **18**, 1514-1534.

Hayes, S.P., M.J. McPhaden and J.M. Wallace, 1989: The influence of sea surface temperature on surface wind in the eastern Pacific: weekly to monthly variability. *J. Climate* (in press).

Legeckis, R., 1986: A satellite time series of sea surface temperatures in the eastern equatorial Pacific Ocean. *J. Geophys. Res.*, **91**, 12,879-12,886.

Lindzen, R.S., and S. Nigam, 1987: On the role of sea-surface temperature gradients in forcing low-level winds and convergence in the tropics. *J. Atmos. Sci.*, **44**, 2440-2458.

Wallace, J.M., T.P. Mitchell, and C. Deser, 1989: The influence of sea surface temperature on surface wind in the eastern equatorial Pacific: seasonal and interannual variability. *J. Climate* (in press).

A Preliminary Morphology of Precipitation Systems In Tropical Northern Australia

T. KEENAN(*) and R. E. CARBONE(#)

(*)*BMRC PO Box 1289K GPO*
Melbourne, Australia 3001

(#)*NCAR*[1] *PO Box 3000*
Boulder CO 80307.3000-U.S.A

1. Introduction.

An observing station has been established in Darwin, north Australia (12°S-131°E) to provide monsoon rainfall data required for the Tropical Rainfall Measuring Mission (TRMM) of the National Aeronautics and Space Administration (NASA) and the Tropical Oceans and Global Atmosphere (TOGA) project.

The Darwin station consists of the National Oceanic and Atmospheric Administration (NOAA)/TOGA Doppler radar, rawinsondes every 12h, wind soundings every 6h, a mesoscale network of 26 tipping bucket raingauges and surface observing network. Details of the Darwin area, the network and observational procedures are given by Keenan et al (1988).

The aim of this paper is to present a preliminary morphology of the precipitation systems that were observed during the 1987-88 summer monsoon period. Climatological characteristics of Darwin are presented together with examples of precipitation systems observed during monsoon and drier transition and break periods. Precipitation systems are also discussed in the general context of the Bulk Richardson number parameter i.e. convective available potential energy (CAPE) and vertical shear of the lower tropospheric winds.

Herein, radar "reflectivity" Z is defined as the sixth moment of the raindrop size distribution. In accordance with standard practice, $dBZ=10\log_{10}Z$ and is expressed in units of $mm^6\ m^{-3}$. For quasi-equilibrium drop-size distributions:

$23dBZ=1\ mmh^{-1}$
$55dBZ=100\ mmh^{-1}$ (Marshall and Palmer, 1948)

2. Climatological characteristics of the summer monsoon.

Darwin is situated in the maritime continent region and experiences pronounced wet and dry seasons. The wet season extends from December through March and is characterized by low level equatorial westerly flow with so-called "transition" and "break" periods when there is a low- to mid-level easterly flow. As shown in Fig.1, the 1987-88 break and transition easterly flow had a relatively uniform layer of shear extending to the easterly maximum near 700 mb. While westerly flow is normally encountered in the 400-150 mb level during the break and transition periods, the 1987-88 wet season mean shows weak easterly flow in this layer. During the monsoon westerly

1. NCAR is sponsored by the National Science Foundation

ORSTOM
CENTRE DOCUMENTATION
Montpellier

F 30242

flow, the low level shear is reversed and the surface shear layer is very shallow. Maximum westerly winds occur at 900 mb but extend to 400 mb in a deep layer of westward shear. Easterly flow was apparent above 400mb during the monsoon westerly flow.

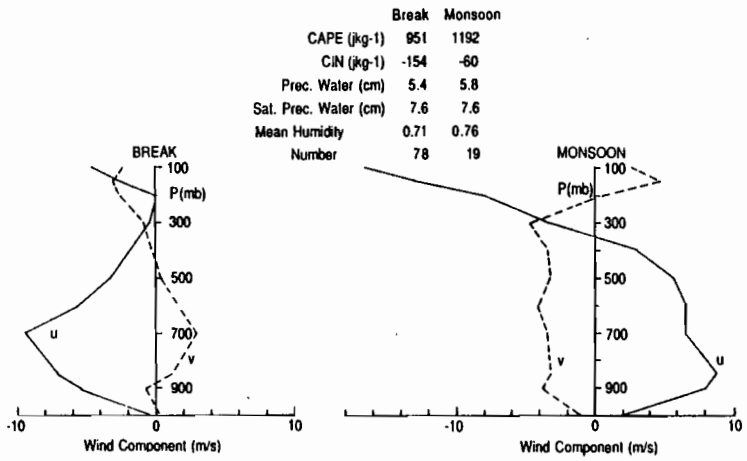

FIG.1. Mean vertical structure of 1987-88 break and monsoon period flow at Darwin.

The CAPE (Moncrieff and Green, 1972) is comparable during both the break and monsoon periods although the Convective Inhibition (CIN), as defined by Colby (1983) is slightly larger for the former. The mean precipitable water content for the two regimes are large and typical of tropical situations. In comparison, they are at least twice the size of values found in the Oklahoma data of Bluestein and Parks (1983).

The preceding climatological data gives the mean characteristics of the monsoon and break season flow. The aim will now be to present some examples of convective systems and to relate the occurrence of the systems to specific dynamic regimes. The examples have been selected to highlight the population of systems encountered at Darwin and to elucidate some features relevant to convective structure and propagation mechanisms.

3. Monsoon flow systems.

Figure 2 illustrates a typical monsoon condition with widespread coastal and oceanic precipitation containing relatively disorganized and weak convection. The RHI in the direction of 270° reveals echo tops between 10 and 14 km with very weak horizontal reflectivity and vertical shear of the horizontal wind above the 0°C melting level near 5 km. The most vigorous convection appears to be within 10 km of the radar where low-level reflectivity gradients are strongest and echo tops are highest. Radial velocities confirm westerly flow below 5 km and easterly flow above. Patches of westerly momentum above 5 km are likely the result of convective momentum transport. CAPE of 450 J kg^{-1} is relatively small and low-level shear[2] of 1.9×10^{-3} s^{-1} is weak. The region of precipitation is quasi-stationary throughout the event.

Figure 3 depicts another monsoon situation showing embedded convection organized in patches and short line-segments. The reflectivity exceeds 50 dBZ in the more intense convective cores. The echoes are quasi-stationary but there is some

2. Unless otherwise stated the shear has been taken over the lowest 3km in this paper.

tendency for slow southward movement with a gradual trend toward more linear organization in the convective areas. Soundings reveal CAPE of 1700 Jkg^{-1} and low-level shear is $3.3x10^{-3}$ s^{-1}.

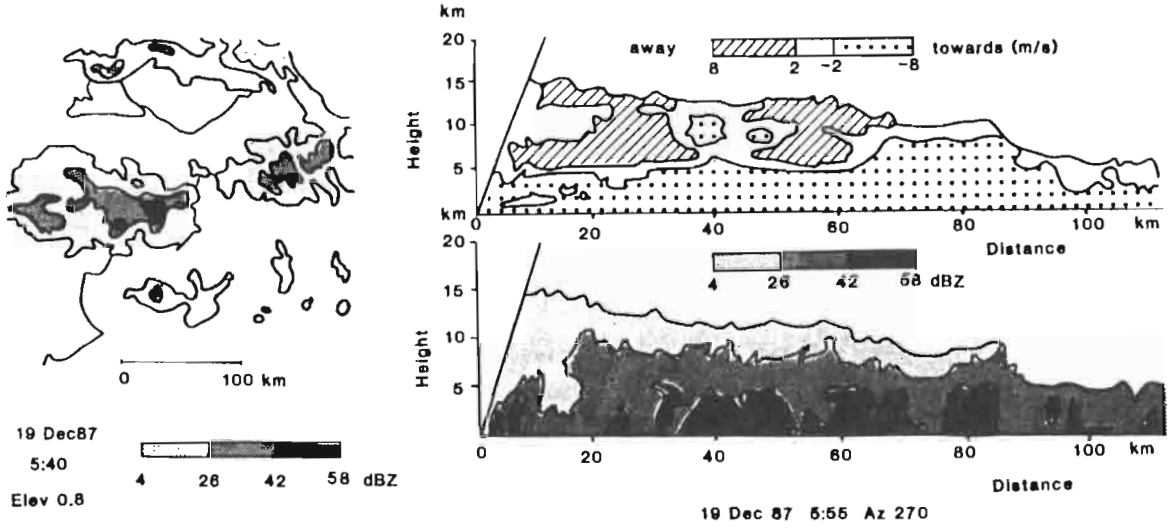

FIG.2. Radar reflectivity of a monsoon band observed at Darwin. PPI structure (a) and RHI reflectivity and radial velocity (b). RHI reflectivity (c).

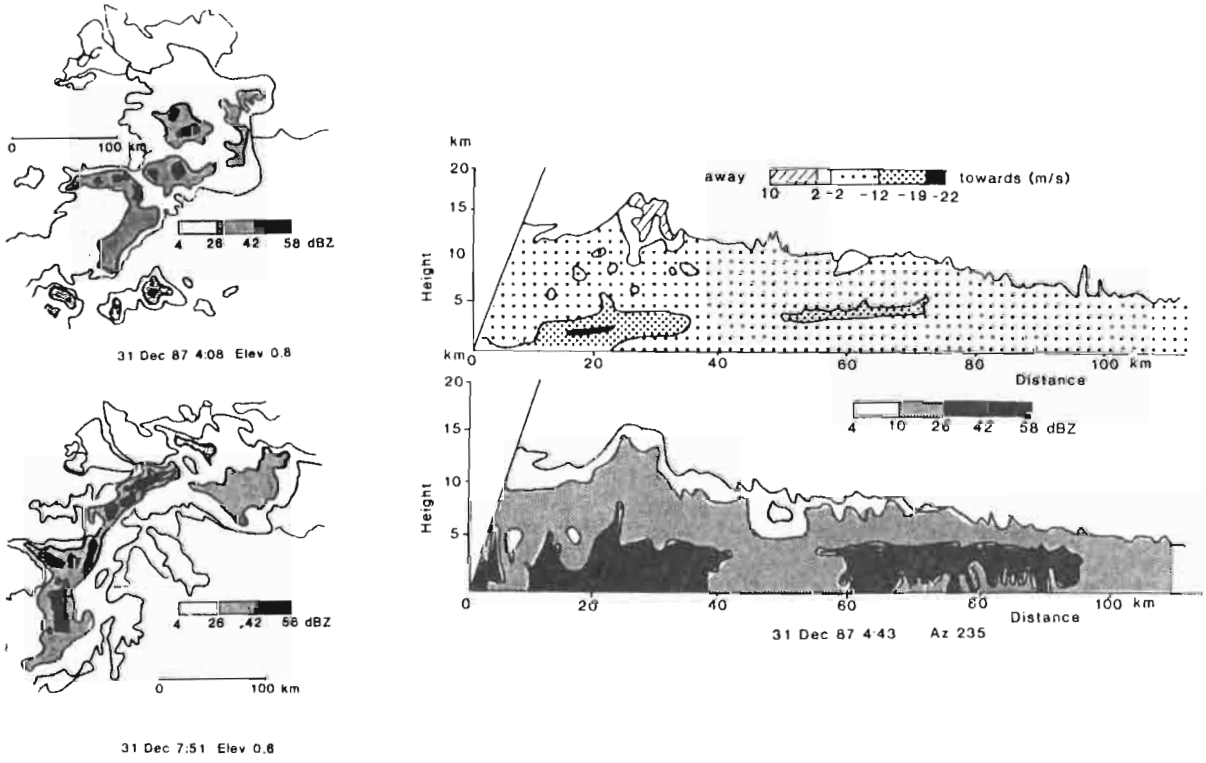

FIG.3 Evolution of the horizontal reflectivity structure of a monsoonal band (a) and (c) and RHI cross-section of reflectivity and radial velocity (b).

The entire system is embedded in westerly flow throughout the 10 km depth of precipitation echo as evidenced in Fig.3b which is an RHI along 235° azimuth. The scan plane passes through two major convective line segments and trailing stratiform precipitation. The melting level is evident from increased reflectivity near 5 km and the depth of convection is seen to range from 10 to 15 km in the near and far bands, respectively. Doppler velocity structure reveals downward transport of southwesterly momentum descending from the 4 km level at 70 km range to less than 2 km at 12 km range underneath the convective bands. This low-level westerly jet structure is part of the strong confluence field at the base of deep convection. By inference from reflectivity and velocity structures, we conclude that updrafts are tilted 30° to 40° (from zenith) toward the southwest in a downshear direction (above 3 km). This organization is reminiscent of classical tropical squall lines as depicted by Houze (1977).

Figure 3c illustrates a much higher degree of organization at 0750 LST where a major convective line is evident. The precipitation region has reversed motion to a northerly direction such that the major band is now located off-shore. Lower amplitude, periodic transverse structure is also evident with 20-50 km spacing. This degree of convective organization is often not evident in monsoon situations.

4. Break and transition season systems.

a. Continental Convection.

Continental convection, is observed regularly during the afternoon and evening periods of the break and transition season. The characteristic evolution consists of scattered isolated cells later aggregating and often forming weak squall lines. Such structure is depicted in Fig.4. Typically, as shown in Fig. 4b the cells are vertically erect and deep with tops above 15 km. Continental cells form under a wide range of conditions. For this example, the CAPE was 920 J kg^{-1} and the low level shear was $2.9x10^{-3}$ s^{-1}.

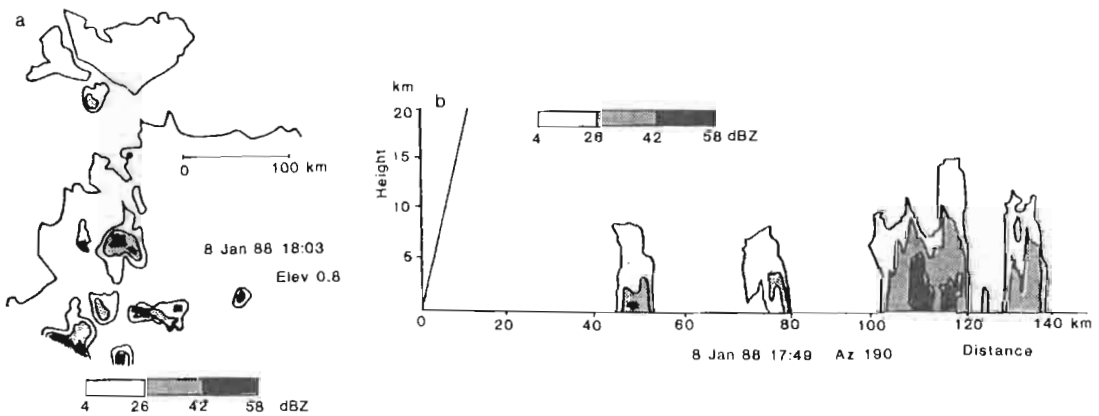

FIG.4. PPI (a) and RHI (b) of continental convection observed with the Darwin radar.

b. Maritime Continent Thunderstorms.

Thunderstorms characteristic of the maritime continent are observed on 65% of days over the islands to the north of Darwin during the transition and break seasons. These storms can exhibit a variety of forms including both single and multiple cell storm. A multicellular type is shown in Fig.5. As shown in the RHI of Fig 5b, the major cells are vertically erect reaching up to 17-18km with a simple low level convergent and upper level divergent structure. CAPE and low level shear values representative of the

pre-storm environment in Fig.5 are 1620 J kg^{-1} and $1.6x10^{-3}$ s^{-1} respectively. The Island Thunderstorm Experiment, described by Keenan et al (1989) was undertaken during November and December 1988 to obtain experimental data on these systems. The tilted column of receding Doppler velocity reveals the upward transport of boundary layer momentum in the main updraft. The updraft is tilted 40° from zenith.

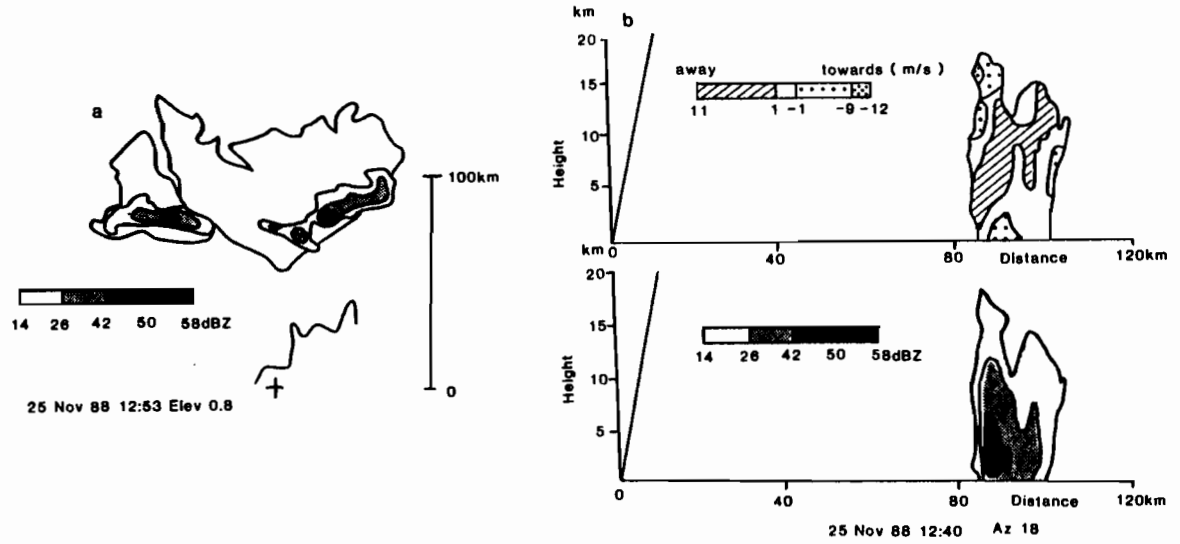

FIG.5. PPI (a) and RHI (b) of reflectivity and radial velocity of an island thunderstorm observed with the Darwin radar.

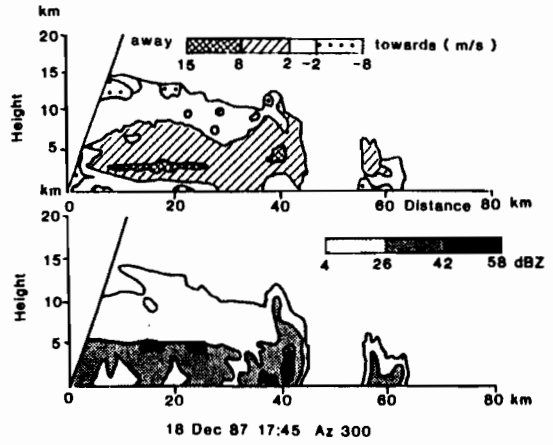

FIG.6. Darwin radar RHI of reflectivity and Doppler derived radial velocity through a "classical" tropical squall line.

c. Squall lines.

Figure 6 is an RHI perpendicular to a classical tropical squall line very similar to those reported from the Global Atmosphere Research Program Atlantic Tropical Experiment (GATE) by Houze (1977), Zipser and LeMone(1980), Barnes and Sieckman (1984) among others. Such squall lines are noted for continual development of new cells along the leading edge of the convective line; a rear-to-front, descending mid-level inflow jet; and pronounced trailing stratiform precipitation. Often there is a precipitation "trough" between the rear flank of the convective line and the stratiform area. In Fig. 6, these features are evident in the reflectivity and Doppler velocity fields. CAPE is 920 J kg^{-1} and low-level shear is $1.1x10^{-3}$ s^{-1}. These conditions are very similar to those

experienced in GATE (Barnes and Sieckman, 1984). Of special interest is the wave-like pattern in Doppler velocity behind the convective line. The pattern is suggestive of a 20-30 km gravity wave where the first depression (at 28 km) is coincident with the rear flank "trough". Increased vertical shear and vertical mixing is also suggested by the echo top pattern at 15 km range and 10 km height. The rear (easterly) inflow jet is located at 3 km height and has a magnitude of 10 m s^{-1}. The undisturbed environmental flow at 3 km was 5 m s^{-1}, the same speed as the squall line movement.

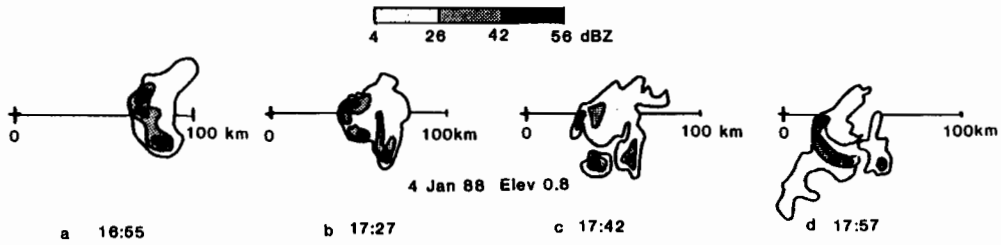

FIG.7. Darwin radar reflectivity time sequence for a squall line exhibiting discontinuous propagation.

Figures 7 show a time sequence of squall line evolutions on 4 January 1988. We distinguish this situation from that shown in Fig.6 because propagation is clearly discontinuous. Close examination of Figs 7a-d reveals a succession of three small convective lines which initiate 10-30 km ahead of the previous line. While direct thermodynamic evidence is not available, Doppler velocities at low levels behind each convective line suggest that a rapidly forward-spreading cold pool is responsible in each instance. While each individual convective line translates from 7-10 m s^{-1}, the aggregate convective system propagates at 16.5 m s^{-1} eastward. This rate of propagation exceeds the environmental easterly winds at any level (12 m s^{-1} maximum). Only a shallow planetary boundary layer cold pool transports mass at a rate which equals or exceeds the aggregate propagation rate. Conditions in this case have CAPE=618 J kg^{-1} and low-level shear of 3.9×10^{-3} s^{-1}.

Figures 8 show the squall line of 13 January which exhibits characteristics similar to mid-latitude systems. The plan view of reflectivity (a) shows slight bowing in the shape of a vigorous convective line together with a weak trailing precipitation region. Reflectivity and velocity RHI's, along azimuth 68°, reveal a well-developed leading anvil and an updraft which is tilted rearward ~55° from zenith. This is a consequence of unusually deep and strong easterlies aloft which exceed the squall line translation speed by roughly 5 m s^{-1}. Convective cells develop continually at the leading edge as predicted by the theory of Rotunno et al (1988). An advancing surface cold pool is implied by very strong approaching Doppler velocities near the surface in the heavy precipitation cores. Intense vertical shear of the horizontal wind is evident at 43 km range, between 1.5 and 2 km, where shear exceeds 2×10^{-2} s^{-1}. CAPE is quite large, at 2050 J kg^{-1}, a value comparable to that found in mid-latitudes. Environmental low-level shear is moderate at 4.2×10^{-3} s^{-1}. Convective line movement is toward the west at 12.5ms^{-1}. This speed is faster than low to mid-tropospheric easterlies and slower than easterly momentum generated by the hypothesized spreading cold pool.

Figure 9. shows an RHI of a squall system with a relatively large CAPE of 2100 J kg^{-1} and low-level shear of 3.2×10^{-3} s^{-1}. The RHI is at 68° azimuth and shows a stratiform region ahead of the westward-moving squall line. The stratiform region is, in fact, the product of a preceding squall line with the new convective line overtaking it from the rear. Note the elevated reflectivity maximum between 5 and 9 km height, the rear flank weak echo vault between 9 and 14 km height and the strong, mid-tropospheric convergence several kilometres below. The depth of convection extends to nearly 20 km.

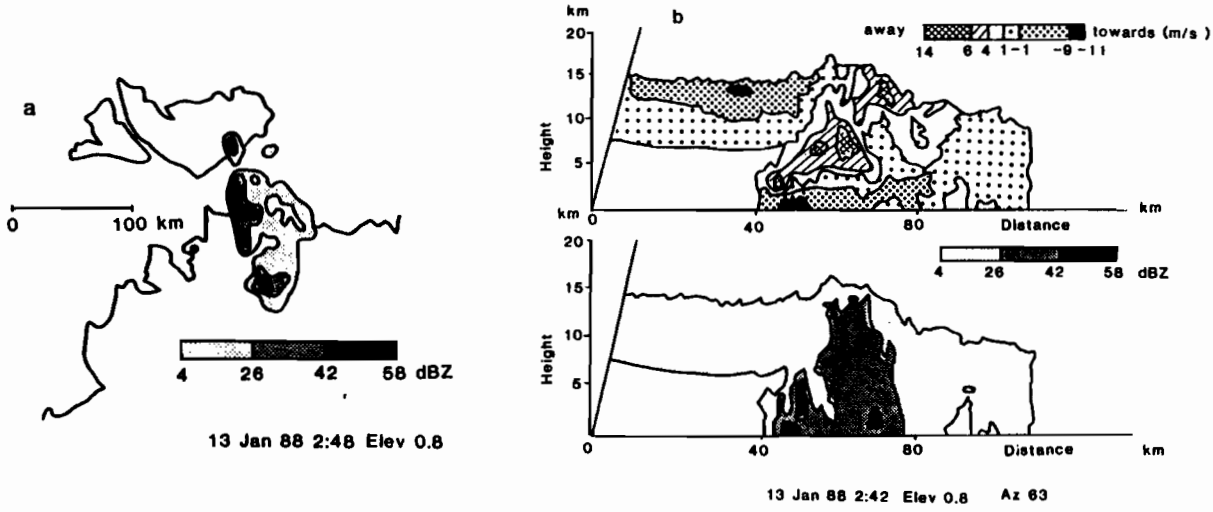

FIG.8. Darwin PPI (a) and RHI (b) observed reflectivity and radial velocity for a squall line exhibiting the characteristics of a mid-latitude system.

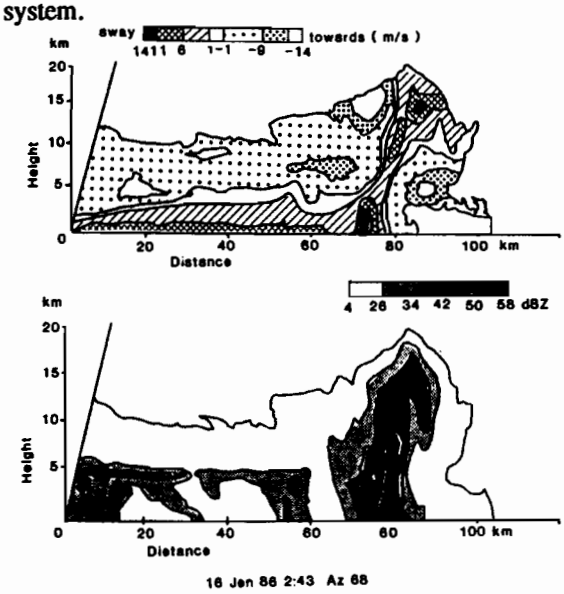

FIG.9. RHI of reflectivity and radial velocity for a very intense tropical squall observed at Darwin.

Clearly there are a diversity of squall line structures in the Darwin area which sometimes differ markedly from tropical squall organizations observed in the GATE area and in Africa.

5. Convective organization and mesoscale environment.

The aim of this section is to consolidate some ideas by examining the relationship of convective organizations observed near Darwin with the variety of convective systems observed elsewhere. In addition, some concepts relevant to squall line motion will be discussed.

a. Bulk Richardson number depiction.

A convenient method of classifying the spectrum of convective systems is through the CAPE and kinetic energy associated with the vertical shear of the flow e.g. Moncrieff and Miller (1976), Weisman and Klemp (1982) and Rasmussen and

Wilhelmson (1983), Carbone et al. (1989), Ray (1989). Such a classification provides a basis for incorporating the roles played by buoyant energy of the storm and that of the environmental kinetic energy with which the storm interacts.

A depiction of storm types based on the above principle is summarized in Fig. 10 using low level shear and CAPE in the manner of Rasmussen and Wilhelmson (1983). In the context of this paper, low level shear is taken to be representative of the depth of the naturally occurring shear layer. Thus various levels have been used to calculate the low level shear but all range over the lowest 20-35% of the depth of convection. e.g. for hurricane and cold frontal rainband data we employ shear layers 1-2km deep; for Darwin, we use the 0-3km shear; data taken from Rasmussen and Wilhelmson (1983) use the 0-4 km. Shear magnitude is calculated for the component perpendicular to linear convective lines where applicable.

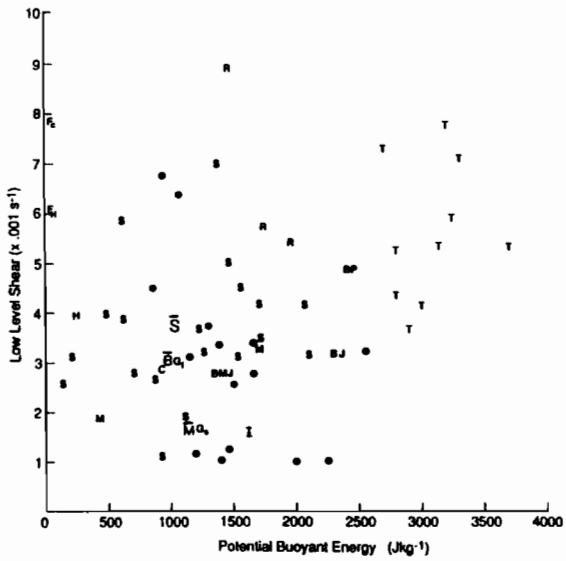

FIG.10. Storm occurrence as a function of buoyant energy and low level shear. See text for a description.

The data presented in Fig.10 are based on the following:

1. Tornadic storms (T), non-tornadic storms with a mesocyclone (R), and various other North American storms (•) as given by Rasmussen and Wilhelmson (1983);
2. Darwin systems-Squall lines (S), Monsoon systems (M), the example of Continental convection (C), the example of an island thunderstorms (I), the mean of the squall systems (S) and as per Fig.1 the Monsoon Mean (M "bar") and the Break Mean (B "bar");
3. GATE fast (G_f) and Slow (G_S) moving squalls as given by Barnes and Sieckman (1984);
4. Mean values representative of hurricane rainbands using values given by Barnes et al (1983), Barnes and Stossmeister (1986);
5. Frontal rainbands as presented by Carbone (1982), Hobbs and Persson (1982)
6. Non-severe squall lines (BMJ) of Bluestein et al (1987), severe squall lines (BJ) of Bluestein and Jain (1985), and isolated super cell storms (BP) of Bluestein and Parks (1983).

The most significant feature evident in Fig.10 is the considerable range of buoyant energy and wind shear over which Darwin storms extend. They range from the expected tropical range of relatively low shear and buoyant energy to that expected from

midlatitude severe storms. The centroid of the Darwin squall cluster is somewhat less than the mean representative of the environment of North American plains type non-severe squall lines of Bluestein et al (1987). The dynamic range of the spectrum of systems encompasses that of the Oklahoma severe squall lines presented by Bluestein and Jain (1985). This edge of the tropical convective activity includes the likelihood of systems exhibiting mesoscale cyclonic rotation and possibly even tornadic storms. That such phenomena could occur or be postulated to occur from such a small sample of cases is surprising but is supported from Bureau of Meteorology reports of tornadic damage on occasions in the Darwin area.

The so-called "typical" tropical squall line i.e. the line most similar to that discussed by Houze (1977) appears somewhat dissimilar to many of the examples presented herein. The location of this storm in Fig.10 is toward the low shear extreme of Darwin conditions at 9201.1×10^{-3}.

As Darwin is affected by tropical cyclones, it would be expected that that low buoyant energy/average shear range of hurricane rainbands shown in Fig.10 would also be experienced in Darwin. Only the very high shear/low buoyancy regions of frontal rainbands and high shear extreme buoyancy regimes are not represented in the Darwin cases examined.

The monsoon systems also demonstrate a significant range of possible modes. The data presented here show that monsoon systems appear to be best characterized by differences in CAPE values. The case in Fig.3 had a CAPE of 1700 J kg^{-1} and represents a departure from the almost moist-adiabatic profile expected for monsoon conditions. It also contained various convective line structures both in the early and late stages of its lifetime. During these periods, the planetary boundary layer shear was as strong as 5×10^{-3} s^{-1}.

The relationship of Darwin data to those of the much examined GATE systems raises questions about representing the tropics. The GATE fast movers of Barnes and Sieckman (1984) are on the lower buoyancy and lower shear side of the tropical squall spectrum. The GATE slow movers appear to occur in conditions similar to the Darwin monsoon systems. That differences exist between mean GATE population and those observed herein has important implications in the use of GATE derived vertical convective heating profiles. The observed differences in the dynamical characteristics of the convective systems implies both larger amplitude heating and higher heating in the troposphere than in the GATE region. Recent results from the Australian Monsoon Experiment of Frank and McBride (1989) offer support that the vertical profile of convective heating in the Australian region is indeed different from GATE. Conversely many similarities may be noted to West African tropical squall systems as examined by Roux (1988).

b. Propagation.

Some lines of the Darwin squalls translate at or near the speed of the environmental winds and others move faster. The latter indicate some form of convective system propagation. The kinematic evidence suggests that cold pool spreading is a common mechanism, but this hypothesis requires confirmation from thermodynamic data. Such a convective-scale mass transportive process seems to be very important. The rate of spreading of the cold domes appears to be prevalent in these examples, given strong rear-to-front flow near the surface immediately behind the convective line.

Continuous propagation is observed in most of the squall systems including the mid-latitude analogy of Fig.8. The convective lines of cells moved faster than the environmental wind at any level although cell motions were less than the rate of expansion of the cold pool. Discontinuous propagation was also evident where the

aggregate system propagated faster than the individual line motion and faster than any environmental flow. Individual convective lines moved slower than the maximum low level environmental winds.

6. Relationship to the TOGA COARE western Pacific warm pool.

The relationship of mesoscale precipitation systems near Darwin to those which occur over the TOGA COARE Western Pacific Warm Pool (WPWP) is unclear. As this study has demonstrated, a large variety of modes of convection can exist within one area. In addition, as the worldwide comparison with GATE has indicated a convective regime in one area may not be representative of that found elsewhere. As a result, major differences can exist in the vertical profile of heating as found by Frank and McBride (1989) for the GATE, Western Pacific and AMEX regions.

Darwin observations are subject to jet-like easterly flow during break and transition season flow. This is in contrast to weaker, deep easterly flow anticipated over WPWP. However, westerly bursts over the the equatorial warm pool are likely to be shallow if they are related to Boreal winter synoptic disturbances. The combination of shallow, westerly bursts with overlying easterlies could provide a low-level shear similar to that experienced in Darwin during break periods. The WPWP region also experiences a period of monsoonal westerly type flow over the southern hemisphere during the northern winter (Atkinson, 1971). The possibility of a similarity with Darwin monsoon type systems therefore exists at that time. If so, then Darwin data may be a good proxy dataset for the mesoscale structure of convective systems within WPWP.

Bulk Richardson number considerations alone, however, are insufficient to establish the relationship between the propagation of mesoscale convective systems (MCS) and the WPWP. Near Darwin, evidence exists for spreading cold pools being the dominant planetary boundary layer (PBL) mechanism for MCS maintenance and propagation. This mechanism is very dependent both on the PBL hydrodynamic stability and the overlying relative humidity structure where evaporation and melting of hydrometeors generate the spreading cold pool. Conditions over TOGA COARE may not be favourable for cold pool production and maintenance, thus invalidating this propagation and maintenance mechanism. The underlying oceanic surface may act to destroy the cold pool more quickly than over continental regions. Stability in the oceanic PBL may be more conducive to the excitation of trapped gravity waves as the dominant propagation mechanism.

Such potential differences have far-reaching consequences to the phase relationship between the WPWP and the location of mature MCS's. Furthermore, these differences markedly alter the surface wind stress experienced at the interface surface since cold pools are mass-transportive whereas gravity waves are essentially energy-transportive. As a consequence of such uncertainties, it is not possible to project whether convective lines will lead or lag eastward-migration of the warm pool.

The foregoing indicates a need to gather a comprehensive microscale and mesoscale data set on storms within the WPWP region. An intensive wind profiler and thermodynamic sounding network together with Doppler radar and research aircraft observations could assist to resolve the many uncertainties.

7. Summary.

Using a limited sample of convective storms observed during the summer monsoon at Darwin during 1987-88 it has become apparent that a surprisingly wide range of convective modes can exist in a tropical environment. The applicability of these

modes of convective activity to the mesoscale structure of the TOGA COARE region is largely unknown and requires investigation before fundamental questions on the relationship between the convection and the TOGA COARE warm pool is understood.

Acknowledgments. The authors wish to thank Dr Joanne Simpson, NASA Goddard Space Flight Center, Dr. J. Michael Hall of NOAA, Office of Climate and Atmospheric Research and Dr M. Manton of the BMRC, Australia for their continued support of this project.

REFERENCES

Atkinson, G.D., 1971: Forecasters guide to tropical meteorology. *Tech. Rept. 240 Air Weather Service (MAC) US AirForce*, 360 p.

Barnes, G.M., E.J. Zipser, D.P. Jorgensen and F.D. Marks, 1983: Mesoscale and Convective Scale Structure of a Hurricane Rainband. *J. Atmos. Sci,* **40**, 2125-2137.

Barnes, G.M., and K.Sieckman, 1984: The Environment of Fast-and- Slow-Moving Tropical Mesoscale Convective Cloud Lines. *Mon. Wea. Rev.*, **112**, 1782-1794.

Barnes, G.J., and G.J. Stossmeister, 1986: The Structure and Decay of a Rainband in Hurricane Irene (1981). *Mon. Wea. Rev.*, **114**, 2590-2601.

Bluestein, H.B., and C.R. Parks, 1983: A Synoptic and Photographic Climatology of Low-Precipitation Severe Thunderstorms in the Southern Plains. *Mon. Wea. Rev.*, **111**, 2034-2046.

Bluestein, H.B., and M.H. Jain, 1985: Formation of Mesoscale Lines of Precipitation: Severe Squall Lines in Oklahoma during the Spring. *J. Atmos. Sci.*, **42**, 1711-1732.

Bluestein, H.B., G.T. Marx and M.H.Jain, 1987: Formation of Mesoscale Lines of Precipitation: Nonsevere Squall Lines in Oklahoma during the Spring. *Mon. Wea. Rev.*, **115**, 2719-2727.

Carbone, R.E., 1982: A Severe Frontal Rainband Part I: Stormwide Hydrodynamic Structure. *J. Atmos. Sci.*, **39**, 258-279.

Carbone, R., B. Foote, M. Moncrieff, T. Gal-Chen, W. Cotton, M. Hjelfelt, F. Roux, G. Heymsfield, E. Brandes, 1989: *Radar in Meteorology*, Chapter 26b, Panel Report on Convective Dynamics, Amer. Meteor. Soc., Boston, Mass., Ed. D.Atlas (In press)

Colby, F.P. Jr., 1983: Convective inhibition as a predictor of the outbreak convection in AVE-SESAME II. *Preprints, 13th Conf. on Severe Local Storms*, Tulsa, Amer. Meteor. Soc., 324-327.

Frank, W.M. and J.L.McBride, 1989: Vertical Profiles of the Convective Heat Source in AMEX: A Comparison with GATE. Submitted to *Mon. Wea. Rev.*

Hobbs, P.V., and P.Ola G. Persson, 1982: The Mesoscale and Microscale Structure and Organization of Clouds and Precipitation in Midlatitude Cyclones. Part V: The Substructure of Narrow Cold- Frontal Rainbands. *J. Atmos. Sci.*, **39**, 280-295.

Houze, R.A., Jr., 1977: Structure and Dynamics of a Tropical Squall-line System. *Mon. Wea. Rev.*, **105**, 1540-1567.

Keenan, T.D., G.J. Holland, M.J.Manton and J.Simpson, 1988: TRMM Ground Truth in a Monsoon Environment: Darwin, Australia. *Aust. Meteor. Mag.*, **36**, 91-90.

Keenan, T.D., B.R. Morton, M.J. Manton and G.J. Holland, 1989: The Island Thunderstorm Experiment (ITEX)-A Study of Tropical Thunderstorms in the Maritime Continent. *Bull. Amer. Meteor. Soc.*, **70**, 152-159.

Marshall, J.S. and W.M. Palmer, 1948: The distribution of raindrops with size. *J. Meteor.*, **5**, 165-166.

Moncrieff, M.W. and J.S.A. Green, 1972: The propagation and transfer properties of steady convective overturning in shear. *Quart. J. Roy. Meteor. Soc.*, **98**, 336-352.

Moncrieff, M.W., and M.J Miller, 1976: The dynamics and simulation of tropical cumulonimbus and squall lines. *Quart. J. Roy. Meteor. Soc.*, **102**, 373-394.

Rasmussen, E.N. and R.B. Wilhelmson, 1983: Relationships between Storm Characteristics and 1200 GMT Hodograph, Low Level Shear and Stability. Preprints, *13th Conference on Severe Local Storms*, Tulsa, Ok, Amer. Meteor. soc., Boston, 55-58.

Ray, P.S. 1989: *Radar in Meteorology*, Chapt. 26a, Convective Dynamics, Amer. Meteor. Soc., MA, Ed. D.Atlas (In press).

Roux F., 1988: The West African Squall Line Observed on 23 June 1981 during COPT 81: Kinematics and Thermodynamics of the Convective Region. *J. Atmos. Sci.*, **45**, 406-426.

Weisman, M.L., and J.B. Klemp. 1982: The Dependence of Numerically Simulated Convective Storms on Vertical Wind Shear and Buoyancy. *Mon. Wea. Rev.*, **110**, 504-520.

Weisman, M.L., and J.B, Klemp. 1986: Characteristics of Isolated Convective Storms, Chapt. 15, *Mesoscale Meteorology and Forecasting*, Amer. Meteor. Soc., Ed. P.Ray, 793 p.

Zipser, E.J., and M.A. LeMone, 1980: Cumulonimbus Vertical Velocity Events in GATE. Part II: Synthesis and Model Core Structure. *J. Atmos. Sci.*, **37**, 2458-2469.

Estimation of Large-Scale Oceanic Rainfall for TOGA

Phillip A. ARKIN

Climate Analysis Center NMS/NWS/NOAA
5200 Auth Road Washington, DC 20233 - U.S.A.

1. Introduction

The Global Precipitation Climatology Project (GPCP) of the World Climate Research Programme (WCRP) is responsible for producing global analyses of large-scale monthly rainfall through the use of a mix of satellite and conventional data. Over the tropical oceans, the primary information source is rainfall estimates derived from geostationary IR digital data using a simple thresholding algorithm, supplemented by polar-orbiting IR and microwave observations. Estimates using IR data are now available for the tropics for 5-day periods beginning in January 1986 using data from GOES East and West, Meteosat, GMS and NOAA-9, 10 and 11. In this paper we will describe the GPCP and the interannual variability in tropical oceanic precipitation during 1986-1988 depicted by its analyses.

2. The global precipitation climatology project

The need for analyses of large-scale areally-averaged precipitation for periods of 5 days to monthly covering at least the tropics to satisfy the requirements of the WCRP became clear in early 1985, as the Tropical Ocean-Global Atmosphere (TOGA) Programme was beginning. A workshop on Global Large-scale Precipitation Data Sets for the WCRP was held in Camp Springs, MD, USA in July 1985, and recommended (WCRP, 1986) that a GPCP be instituted to use available algorithms and data to produce these analyses. Its objectives include :

a. the production of estimates of tropical precipitation from areas of 2.5° latitude x 2.5° longitude for periods of 5 days using geostationary satellite data;
b. the derivation of rainfall estimates for similar spatial scales and for months from passive microwave radiometric data;
c. the use of these data together with conventional rainfall data to produce analyses of monthly rainfall on a near-global scale; and
d. the development of a capability to validate and calibrate the various satellite estimates.

The organization of the GPCP is shown in Fig.1. The production of estimates from geostationary data requires the routine production of statistics, including histograms, means and spatial variances, of IR brightness temperatures for 5-day periods from each of the available satellites. This activity is carried out at the several Geostationary Satellite Data Processing Centers (GSDPCs). The integration of these data into rainfall estimates for the global tropics is done by the Geostationary Satellite Precipitation Data Centre (GSPDC). Data from the SSM/I (Special Sensor Microwave/Imager) instrument on the U.S. Defense Meteorological Satellite Program polar-orbiting satellite is processed at the Polar Satellite Data Processing Centre (PSDPC) and sent to the Polar Satellite Precipitation Data Centre (PSDPC), where it is used to obtain estimates of monthly oceanic precipitation. Both of the Precipitation Data Centres use calibration and validation information provided by the Surface Reference Data Centre (SRDC), where developmental work on new methods of measuring rainfall over the oceans is also coordinated. The Global Precipitation

ORSTOM
CENTRE DOCUMENTATION
Montpellier

F 30243

Climatology Centre (GPCC) receives the various satellite estimates and, by combining them with conventional rainfall measurements, produces monthly analyses of near-global rainfall.

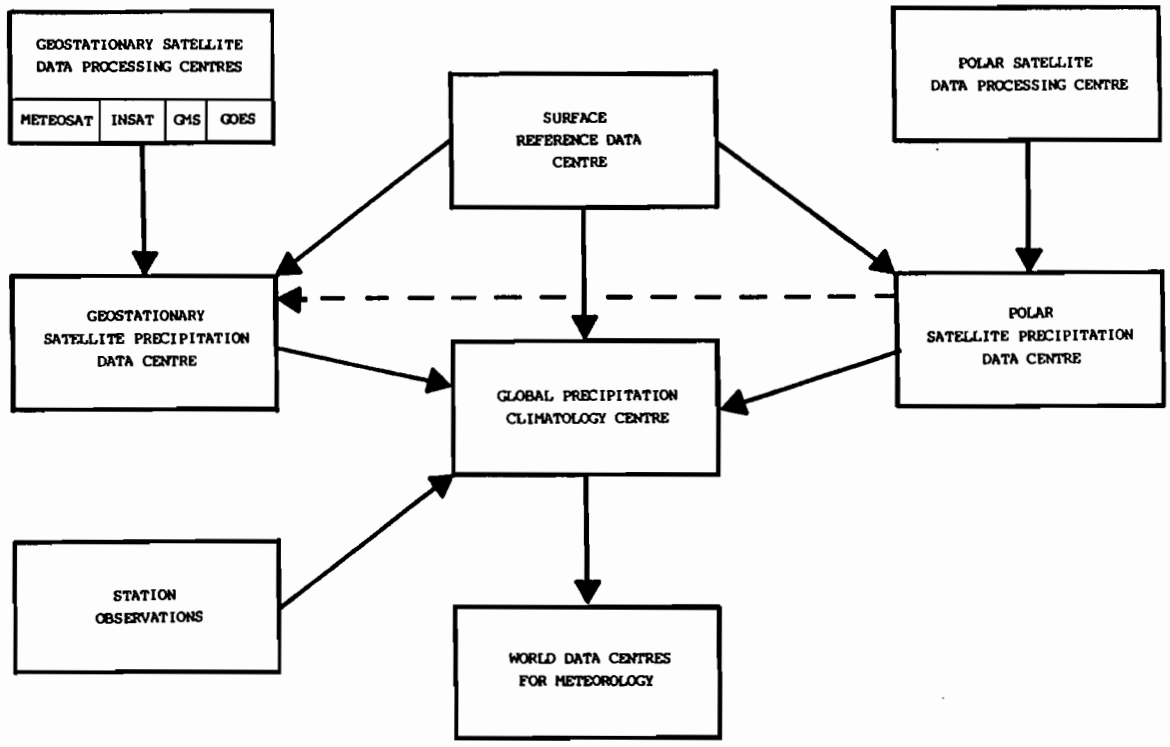

FIG.1. Organization and data flow of the Global Precipitation Climatology Project.

The GSDPCs for each of the geostationary satellites are currently producing the statistics required by the GPCP and, with the exception of that for INSAT, are regularly deliverying data. Figure 2 shows the status of geostationary data for the GPCP as of May 1989. The GSDPC for GOES is colocated with the GSPDC and has been producing data routinely for both satellites since July 1987. The GSDPCs for Meteosat and GMS, operated by the European Space Agency (ESA) (under contract from Eumetsat) and the Japan Meteorological Agency (JMA), respectively, have been delivering data since late 1987. Both JMA and ESA have completed post-processing and delivery of older data. While, India has not yet agreed to participate in the GPCP, the functional duties of an INSAT GSDPC have been carried out since June 1, 1986, by the India Meteorological Department as a result of a collaborative effort under a joint Indo-U.S. research program.

The GSPDC has developed preliminary merging and quality control algorithms, and analyses have been obtained for all pentads from January 1986 through December 1988. Rainfall estimates are computed from each satellite for each 5-day period, and then merged into an analysis covering the global tropics. Data from the NOAA polar-orbiting satellites are used to fill spatial and temporal gaps. The experience gained by the Global Processing Center of the International Satellite Cloud Climatology Project has proven very useful. Figure 3 shows an example of estimated tropical rainfall for a 30-day period during June 1988 in which data from GOES West, GOES East, Meteosat, GMS, NOAA-9 and NOAA-10 were used.

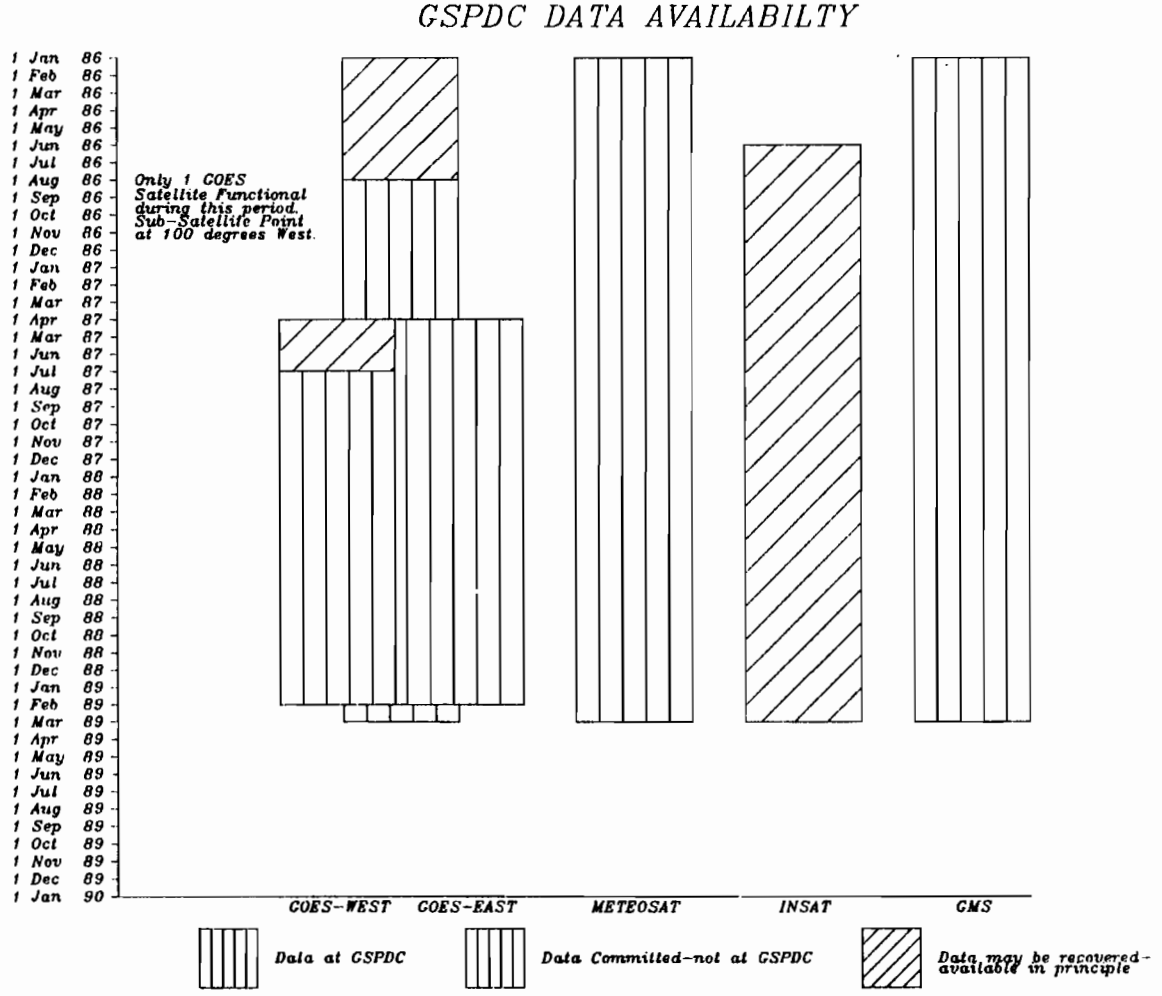

FIG.2. Availability of geostationary satellite Data at the Geostationary Satellite Precipitation Data Center as of May 1989.

Estimates of rainfall based on passive microwave observations from the SSM/I instrument on a polar-orbiting satellite of the Defense Meteorological Satellite Program offer considerable potential for supplementing and improving the geostationary estimates. The satellite was launched on June 19, 1987, and data began to be produced near the end of that month. No formal commitments for either the PSDPC or the PSPDC have been received, although initial data processing, as well as development and testing of estimation algorithms, is under way.

SSM/I data will be archived at NOAA/NESDIS, and the possibility that the Satellite Data Services Division of NESDIS could provide the PSDPC is being explored. In the interim, data are being supplied by a NASA/NESDIS contractor to a group headed by T. Wilheit and A. Chang at NASA/Goddard Space Flight Center. This group has agreed to furnish the PSPDC provided a satisfactory arrangement for supply of the data can be made. They have presently applied their preliminary estimation algorithm to data for the period from July 1987 to May 1988 (see example, Fig. 4). This algorithm, which uses 18 GHz data and a physically-based model of the absorption due to raindrops, appears to give plausible patterns over the tropical oceans, but with amounts which are systematically less than those

estimated from IR data. Other microwave algorithms are being developed in a number of locations.

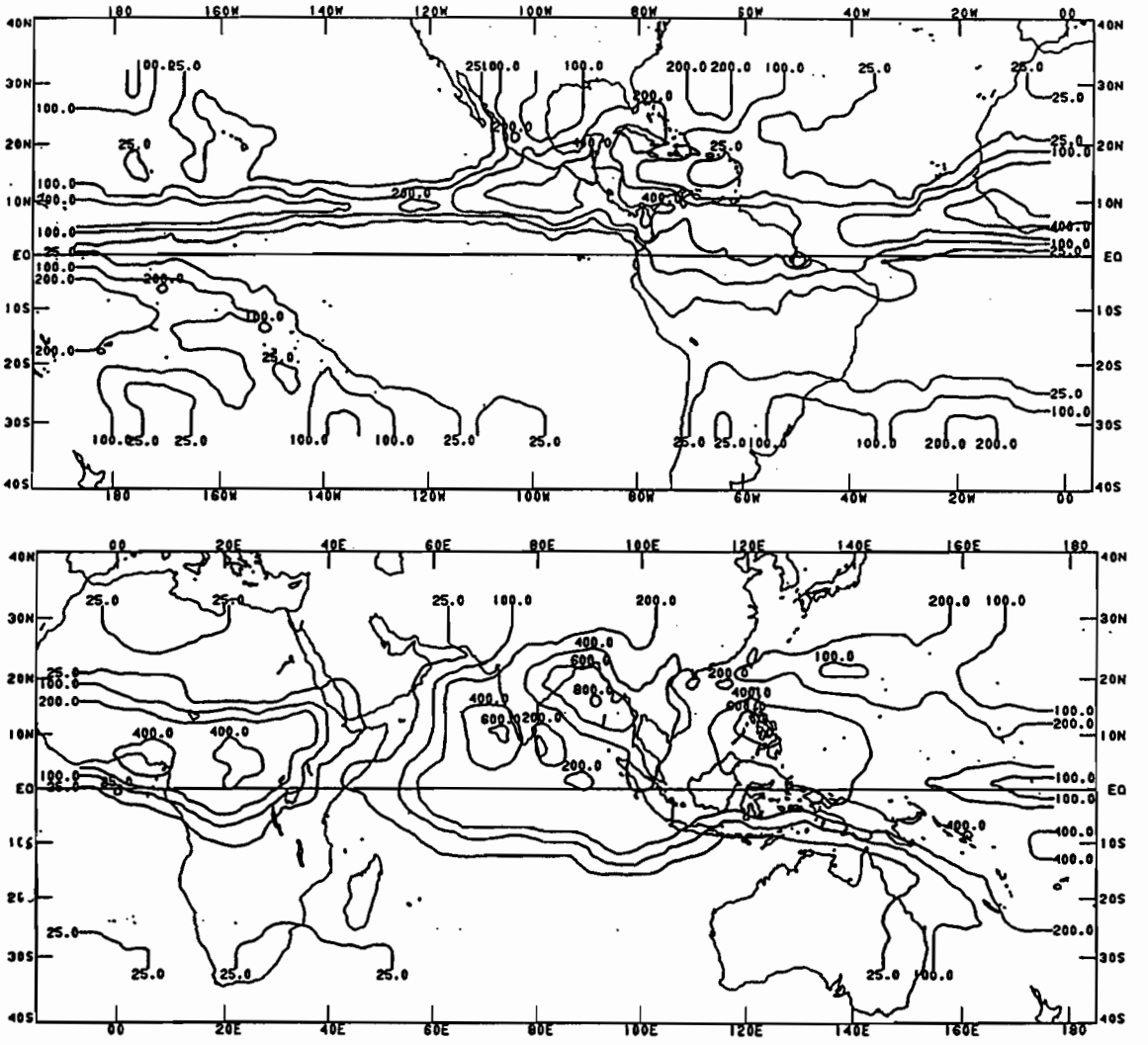

FIG.3. Merged IR-based estimates for May 31-June 29, 1988 using data from GOES-E, GOES-W, GMS, Meteosat, NOAA-9 and NOAA-10. Contours at 200 mm intervals beginning from 200 mm and at 25 and 100 mm.

The use of indirect estimates of rainfall (such as those based on observations of clouds or ice particles) requires calibration and validation in order to be used with confidence (WCRP, 1988). The Calibration/Validation (Cal/Val) Program of the GPCP consists of three principles efforts: the acquisition and organization of surface observations of rainfall from areas representing different climatic regimes; sponsorship and coordination of efforts to develop new methods of observing rainfall over the oceans; and the execution of an Algorithm Intercomparison Program which will use detailed, relatively short-term rainfall analyses and satellite observations to refine existing algorithms and develop new ones.

The first algorithm intercomparison project will be conducted during June-August 1989 in an area of the northwest Pacific Ocean encompassing the main islands of Japan (Fig. 5). It will use GMS visible and IR data with SSM/I observations, and will compare estimates with a composite rainfall analysis constructed by JMA from automated raingauge

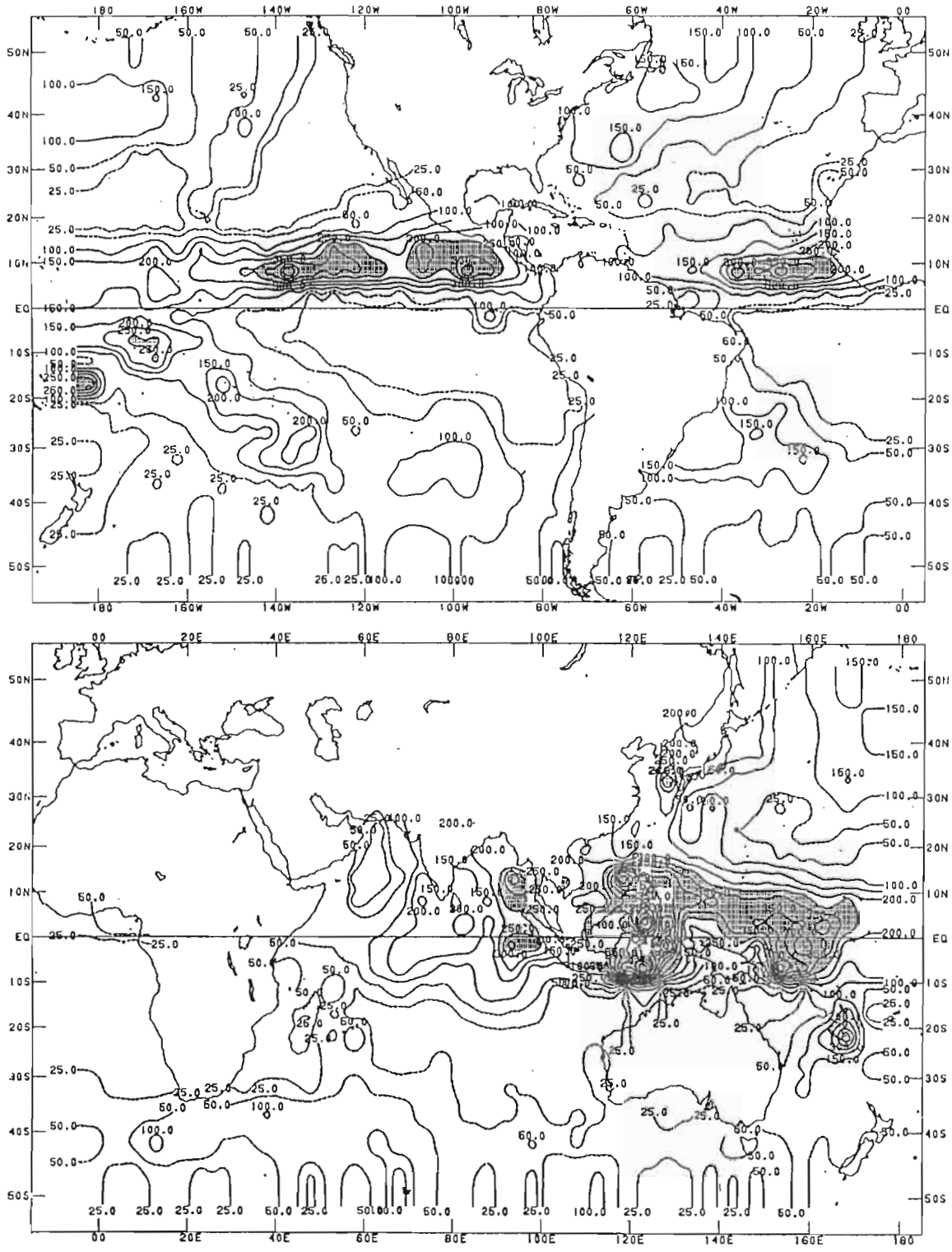

FIG.4. Estimated rainfall for August 1988 using 19 GHz data from SSM/I and an absorption algorithm (see text).

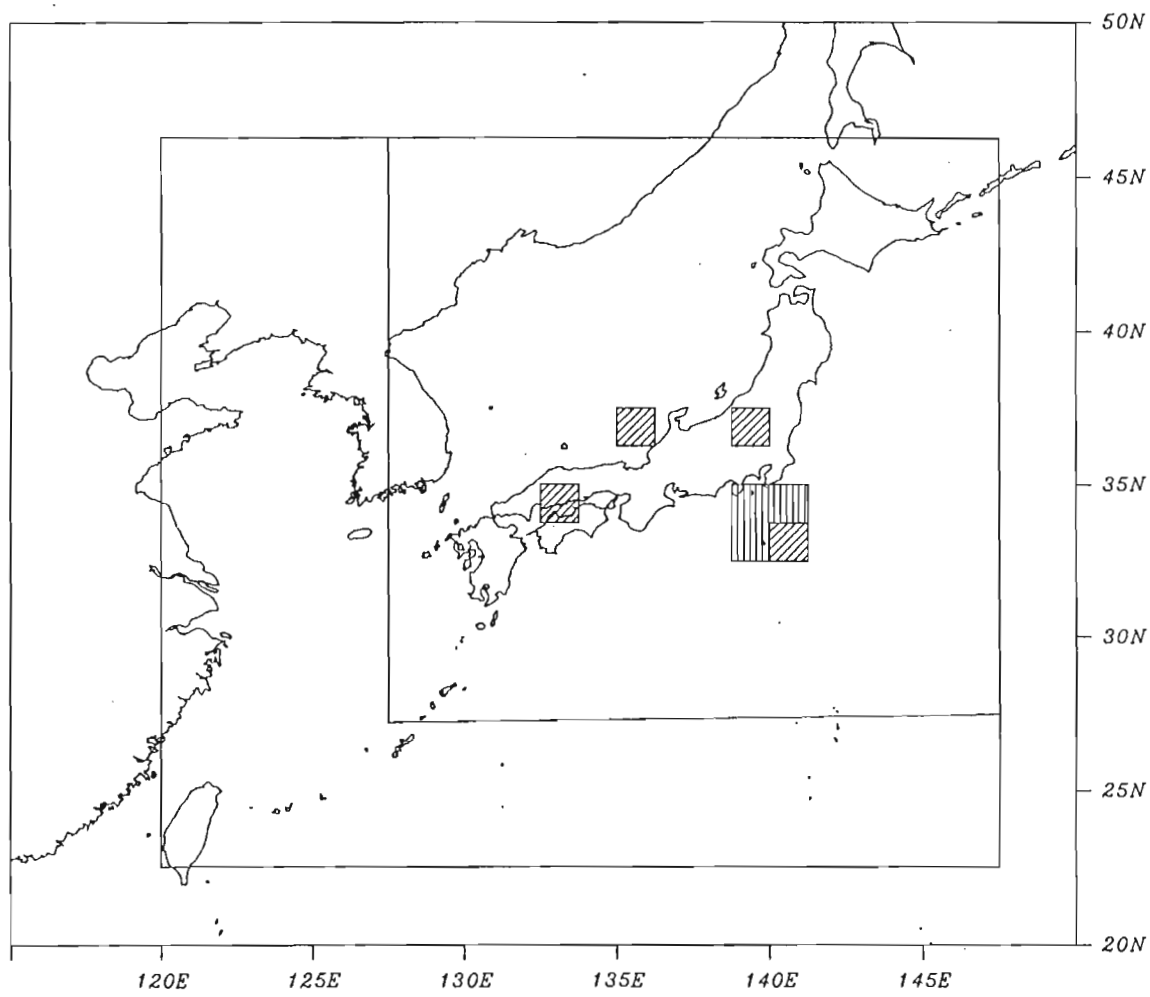

FIG.5. Area of the first project of the Algorithm Intercomparison Programme. Large open boxes represent areas for which satellite data are to be available; hatched boxes are regions where detailed comparisons between radar and satellite estimates are to be made.

observations over Japan and digital radar data for the nearby ocean regions. The proposed TOGA Coupled Ocean-Atmosphere Response Experiment (COARE) is expected to provide the data for an algorithm intercomparison in the western Pacific.

3. Oceanic precipitation during 1986-88

During late 1986, a warm episode of the El Nino/Southern Oscillation (ENSO) began. The warmest surface water in the equatorial Pacific shifted eastward to near the date line, and the maximum in convective activity moved eastward, as well. Near the beginning of 1988, the warm episode ended. Warmer than normal sea surface temperatures (SSTs) disappeared from the central and eastern equatorial Pacific and were, within a few months, replaced by below normal SSTs. This cold episode was characterized by less than normal convective activity in the central Pacific, with a pronounced westward extension of the equatorial dry zone.

The interannual change in SST can be seen in Fig. 6, where seasonal SST has been taken from the blended analysis of Reynolds (1988). Note the change in the eastward extent of the 29° isotherm in the central and western equatorial Pacific. The estimated precipitation for the December-February (DJF) and June-August (JJA) seasons during this period (Fig. 7 and 8) clearly shows the large decrease in rainfall near the intersection of the equator and the

dateline from the warm episode to the cold episode.

Estimated seasonal totals of more than 1 meter during the warm episode are replaced by totals than 25 mm during DJF 1988-89.

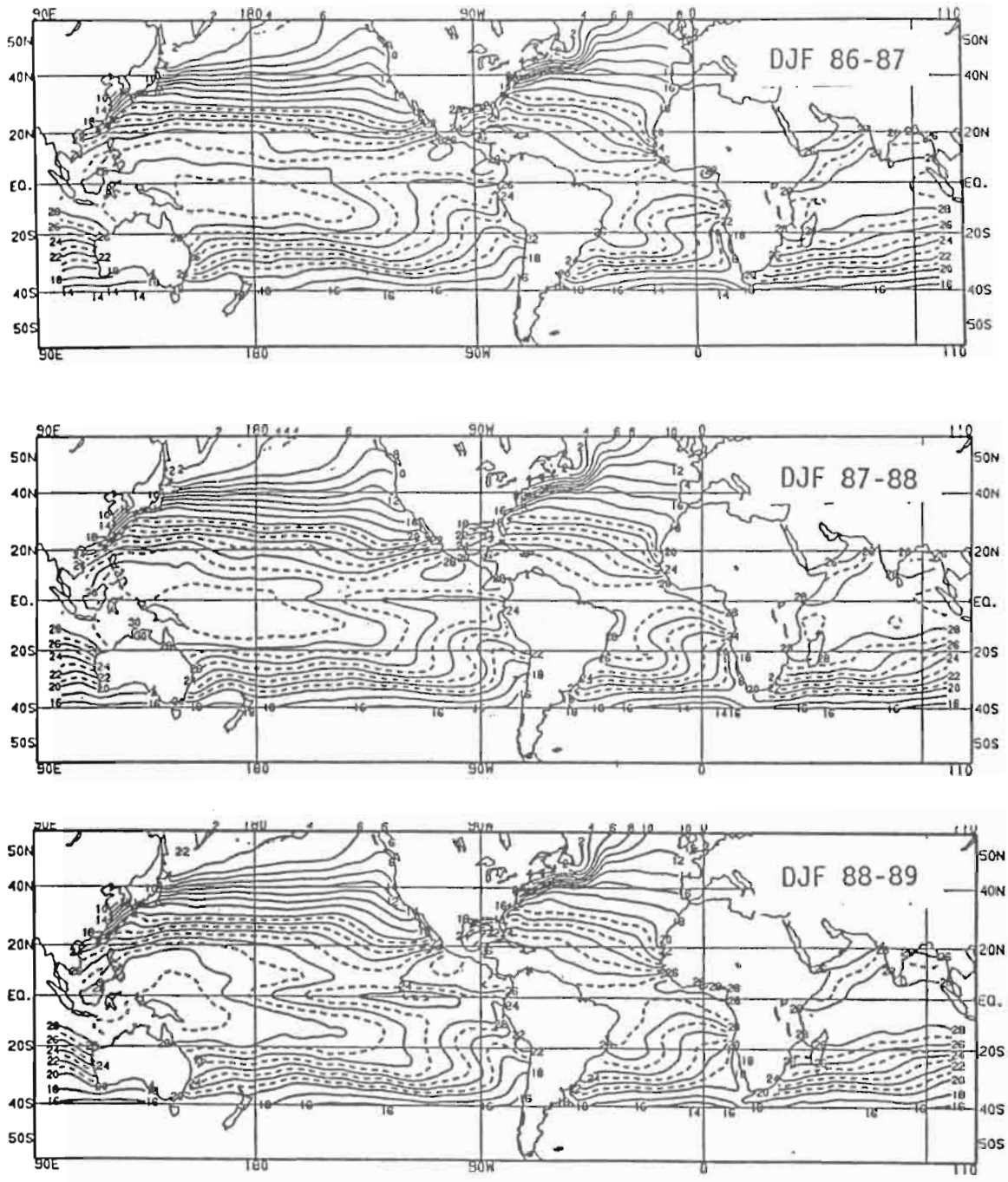

FIG..6. Mean sea surface temperatures for the indicated seasons from the blended analysis of Reynolds (1988).

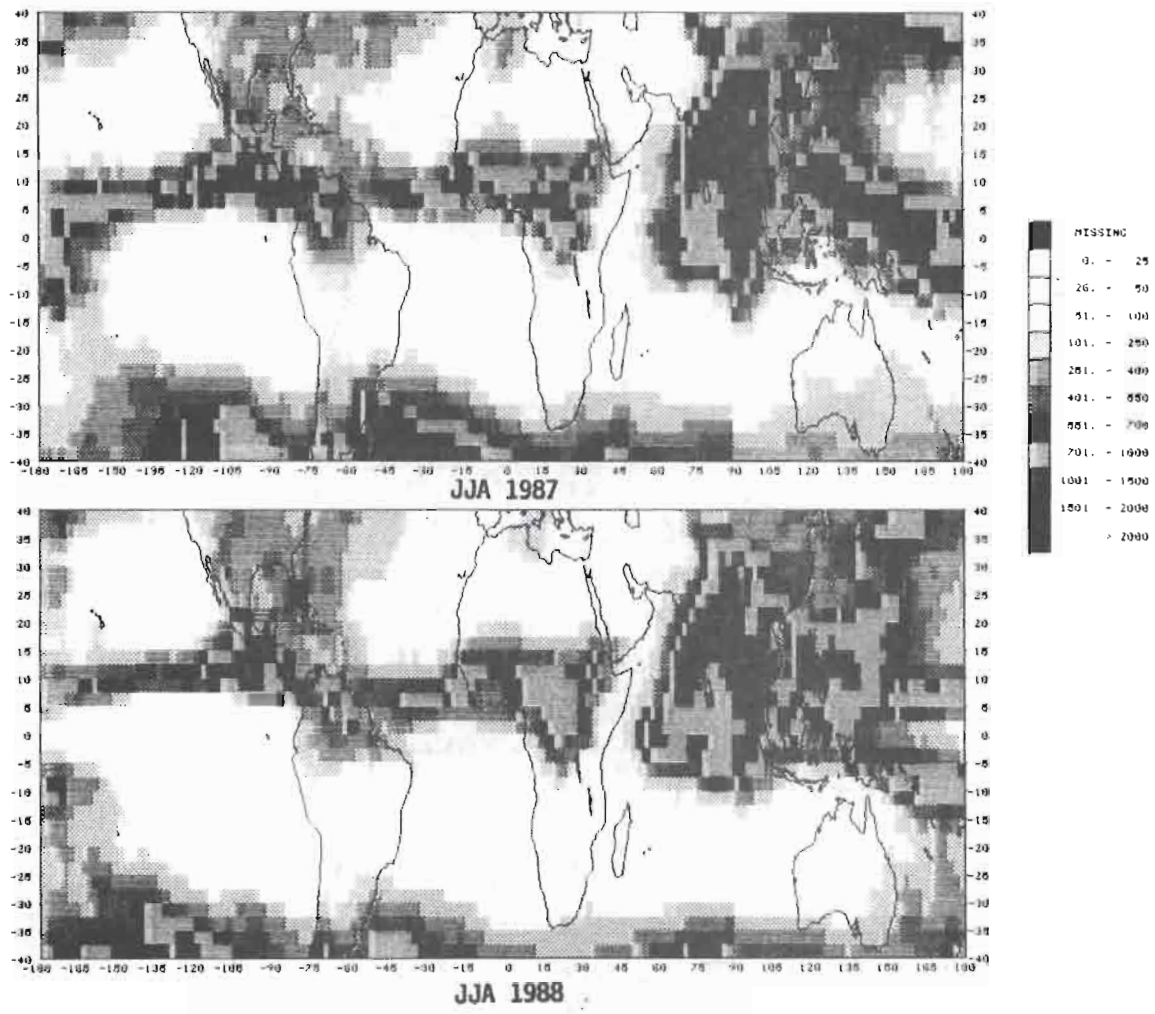

FIG.8. As in Figure 7, except for JJA (top) and JJA 1988 (bottom).

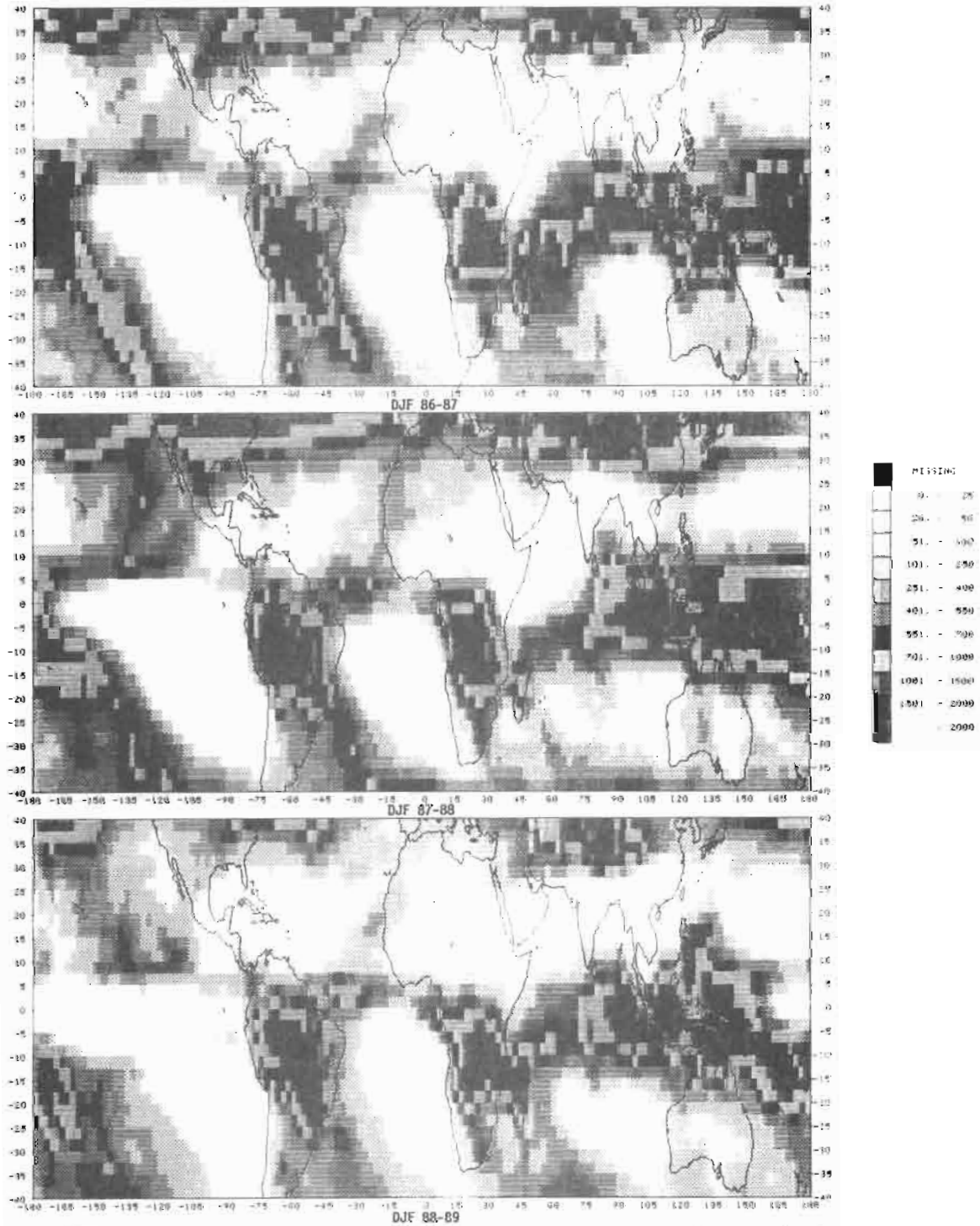

FIG.7. Precipitation estimated by the GPCP using IR data from geostationary and polar-orbiting satellites for the seasons DJF 1986-87 (top), DJF 1987-88 (middle) and DJF 1988-89 (bottom). Values are total accumulations in mm; estimates are quantitatively valid only in the tropics.

4. Conclusions

The GPCP of the WCPR is in operation and is producing analyses of tropical rainfall for the TOGA period. It uses a variety of satellite data and algorithms but, for the tropical oceans, presently relies primarily on estimates from geostationary satellite observations. Seasonal rainfall totals for the period 1986-88 show that the large interannual change in oceanic precipitation associated with the change from warm to cold episode conditions was qualitatively quite well depicted in these analyses.

In order to improve our confidence in the quantitative accuracy of the estimates, a variety of calibration/validation activities are planned. Of these, the Algorithm Intercomparison Program is of particular significance for TOGA/COARE. It is hoped that high-quality, quantitatively-accurate rainfall analyses for COARE can be obtained using a combination of radar and satellite data, and that improved estimation techniques can be developed with these products.

REFERENCES

Reynolds, R.W., 1988: A real-time global sea surface temperature analysis. *J. Climate,* **1**, 75-86.

World Climate Research Programme, 1986: Global Large-Scale Precipitation Data Sets for he WCPR. Report of the workshop held July 24-26, 1985, Camp Springs, MD, USA, WCP-111, WMO/TD - N° 94, 50 pp.

World Climate Research Programme, 1988: Validation of Satellite-Derived Precipitation Estimates for the Global Precipitation Climatology Project of the WCPR. Report of the workshop held November 17-20, 1987, Washington, DC, USA, WCRP-1, WMO/TD - N° 203.

Surface Radiation Processes in the Tropical Pacific

Catherine GAUTIER and Robert FROUIN

California Space Institute, A-021
Scripps Institution of Oceanography
La Jolla, CA 92093 - U.S.A.

This short article is a summary of the results contained in a forthcoming article (Gautier and Frouin, 1989) investigating net surface solar irradiance variability in the central and eastern tropical Pacific from GOES satellite data for the period 1982-1985. This period covers the 1982-1983 El Niño event during which major changes took place in the coupled atmosphere-ocean system. The satellite estimates provide an unprecedented and accurate description of the spatial and temporal variability of the surface solar radiation on a daily (to monthly) basis and a 50 km spatial scale.

The first result of the study was a preliminary assessment (see Fig. 1) of existing climatologies by comparing them with the mean annual satellite estimates (over the October 1983 to September 1985 period), which are expected to be accurate to better than 15 Wm^{-2}. In Fig. 1 the climatological val-

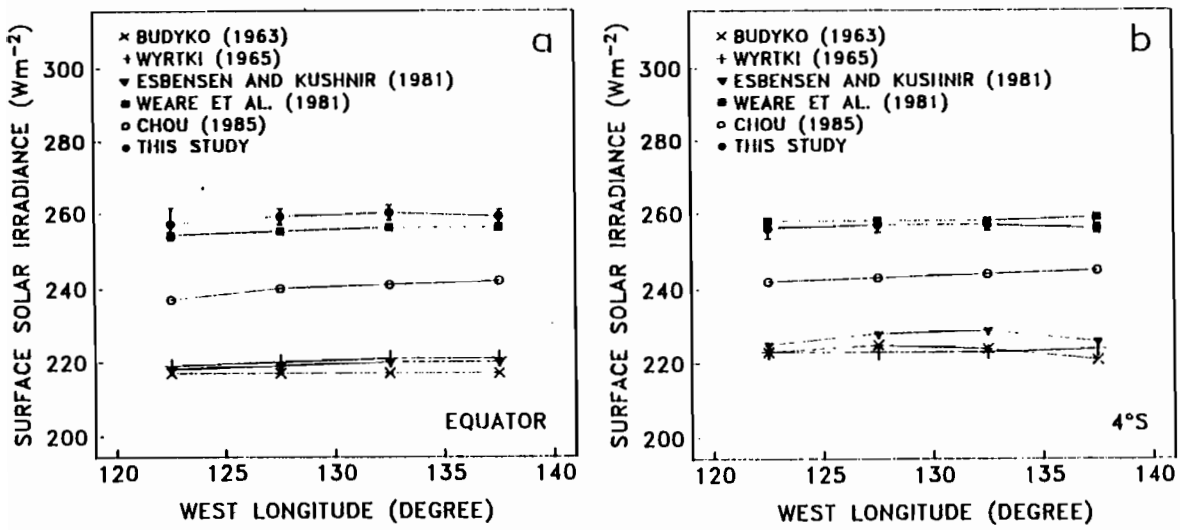

Fig. 1 Comparison of annually-averaged net surface solar irradiance obtained by various authors and computed with the satellite technique of Gautier et al. (1980) in regions centered at the equator (a) and at 4° S(b). Each point corresponds to 4° lat. by 5° lon. averages. The vertical bars (satellite technique only) represent the spatial standard deviation in the 4° lat. by 5° lon. areas.

ues at the equator computed by Budyko (1963), Chou (1985), Esbensen and Kushnir (1981), and Wyrtki (1965) all appear to underestimate solar irradiance

ORSTOM
CENTRE DOCUMENTATION
Montpellier

F 30244

at the surface by about 20 to 40 Wm^{-2}, whereas those computed by Weare et al. (1981) are very close (within 1 to 2 Wm^{-2}) to the satellite estimations. When the annual mean is computed by including the El Niño conditions, the satellite estimations are reduced by only 8 Wm^{-2}, suggesting that most climatologies underestimate solar irradiance at the surface.

The spatial variability of the annual net solar irradiance depicted from the satellite data is illustrated in Fig. 2a and b for the periods Oct. 1982 – Sept. 1983 and Oct. 1983 – Sept. 1984. Also included in Fig. 2a and b are the corresponding temporal standard deviation fields. During non-El Niño periods (Fig 2b), the annually averaged net solar irradiance field is dominated by very weak zonal gradients (1 to 2 Wm^{-2} over 2000 km) and stronger meridional ones (up to 20 Wm^{-2} over 200 km) in the region of the ITCZ. The standard deviation field also has weak zonal gradients and its maximum values (about 25 Wm^{-2}) are found in the southern part of the study area. During the El Niño period (Fig 2a), the zonal variability becomes as large as the meridional variability, particularly in the central Pacific, where intense convection dominates the atmospheric state. The standard deviation from the annual mean reaches 40 Wm^{-2} in that region, much larger than that observed within the ITCZ region during non-El Niño years. A difference of more than 150 Wm^{-2} in surface solar irradiance takes place in the equatorial region between 140° and 180° W between January 1981 and January 1983, where the largest SST anomaly is observed. The variability of the standard deviation reflects the large changes in surface solar irradiance occurring during the El Niño year. Its maximum values (about 45 Wm^{-2}) are found in the western part of the study area.

A general view of the seasonal and interannual variations of the net surface solar irradiance is obtained by condensing the data into diagrams of latitude (and longitude) versus time. Such diagrams, illustrated in Fig. 3a and b, have been obtained by averaging the data longitudinally (and meridionally) over the entire domain. The latitude versus time diagram (Fig. 3a) shows the meridional extension of low net surface solar irradiance values (less than 160 Wm^{-2}) covering the entire study area starting in November 1982 and retreating in May 1983. These low values are associated in the north with the ITCZ, but their large meridional extent suggests that they are also related to processes other than ITCZ displacements. The longitude versus time diagram (Fig. 3b) supports this statement and shows a large zonal extension of the low net surface solar irradiance values. This extension is associated with the eastward displacement of the main region of convection/precipitation, as mentioned above.

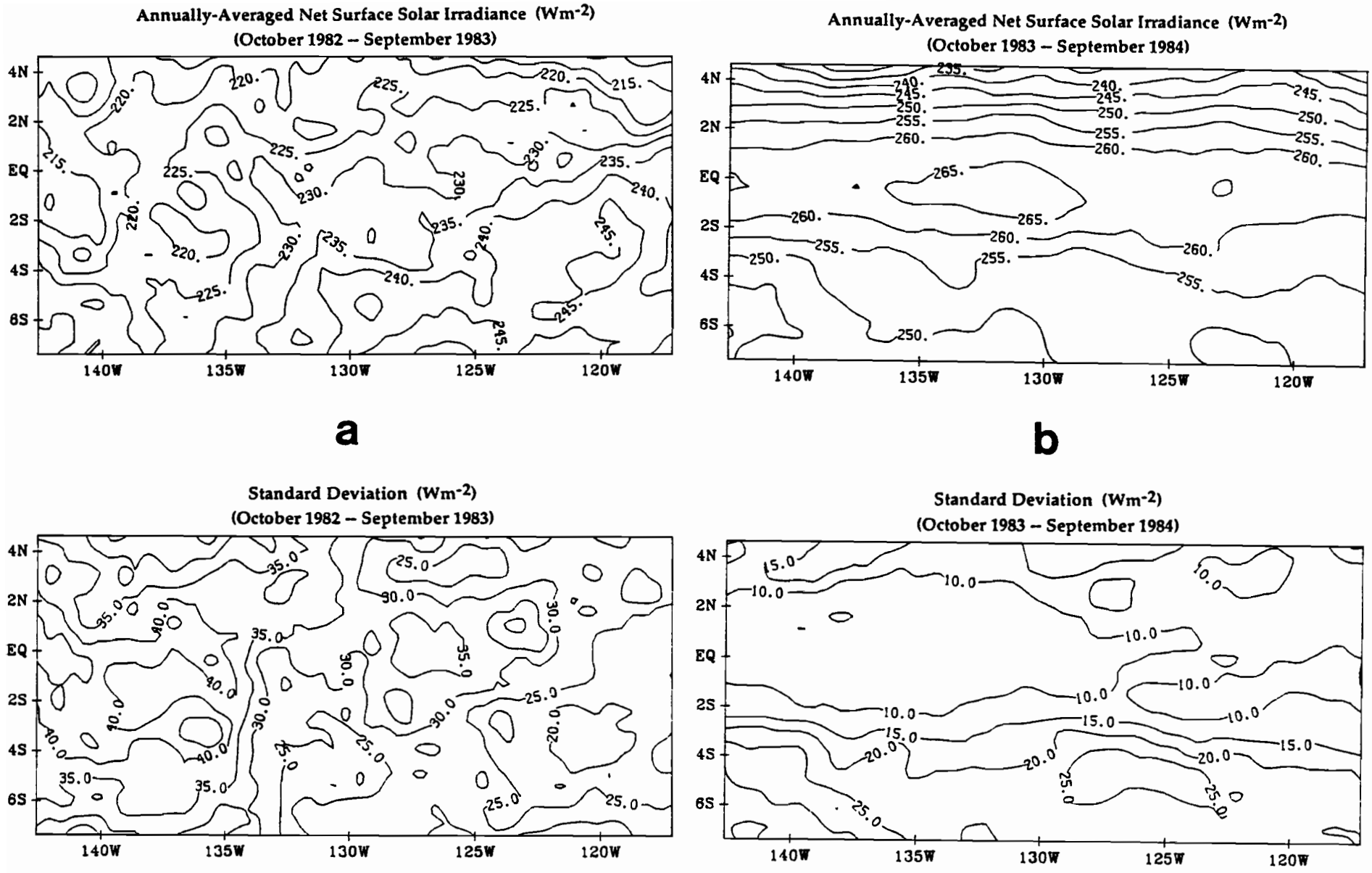

Fig. 2 Spatial distribution of annually-averaged net surface solar irradiance (computed with the satellite technique of Gautier et al., 1980) for the periods October 1982—September 1983 (a) and October 1983—September 1984 (b). The corresponding temporal standard deviation fields are also shown below.

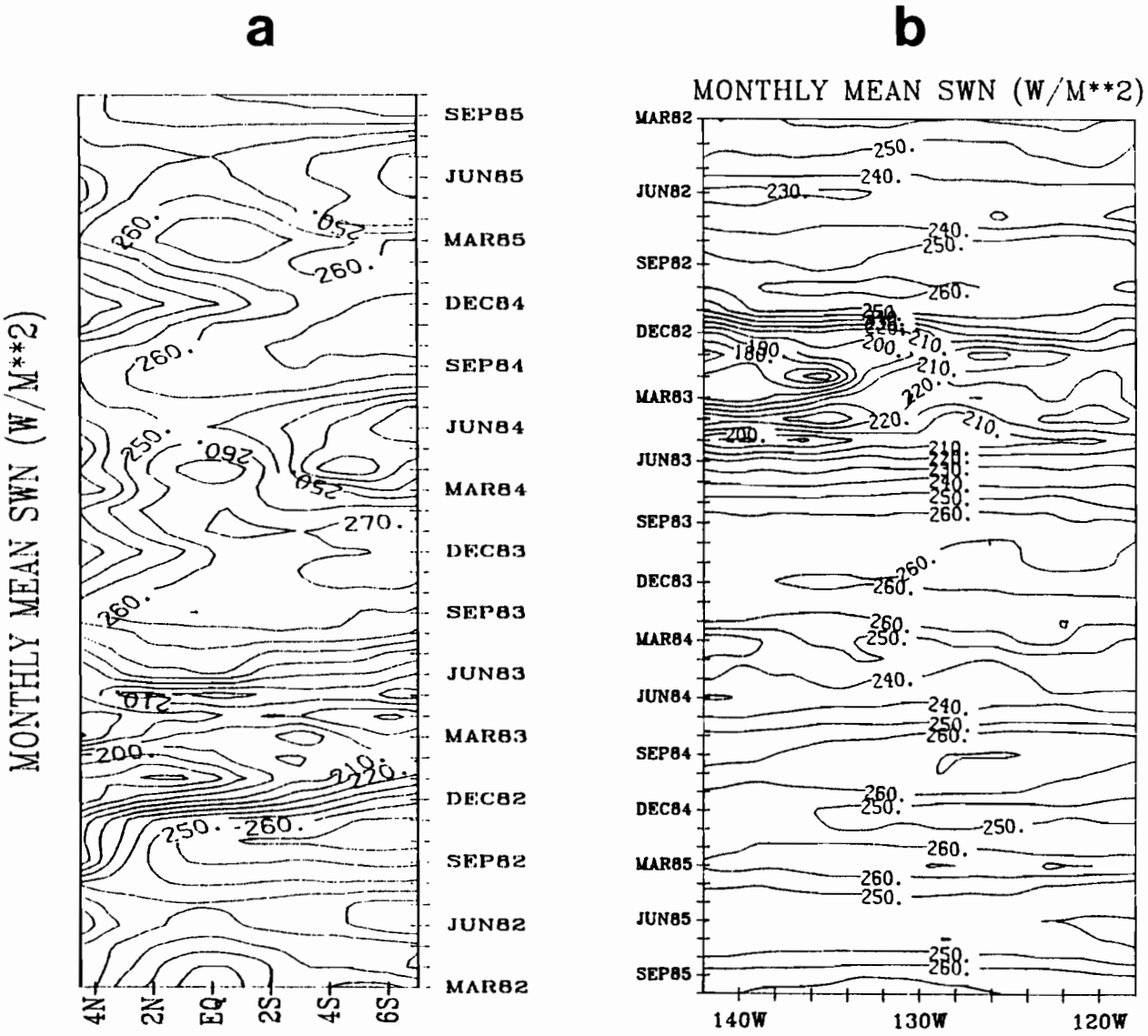

Fig. 3 Diagrams of time vs latitude (a) and time vs longitude (b)

The spatial and temporal variability of the net solar irradiance fields can be further quantified using empirical orthogonal function (EOF) analysis. An EOF analysis has been applied to two types of fields including and excluding the seasonal cycle: (1) difference fields from an annual mean (October 1984 to September 1985) and (2) difference fields from the monthly mean for each month of that same year. The annual mean removed from the first data set is shown in Fig. 4a and the square root of the variance (standard deviation) analyzed is illustrated Fig. 4b. The standard deviation field exhibits values ranging from 15 Wm^{-2} to 32 Wm^{-2} and a very high spatial variability (no direction is privileged).

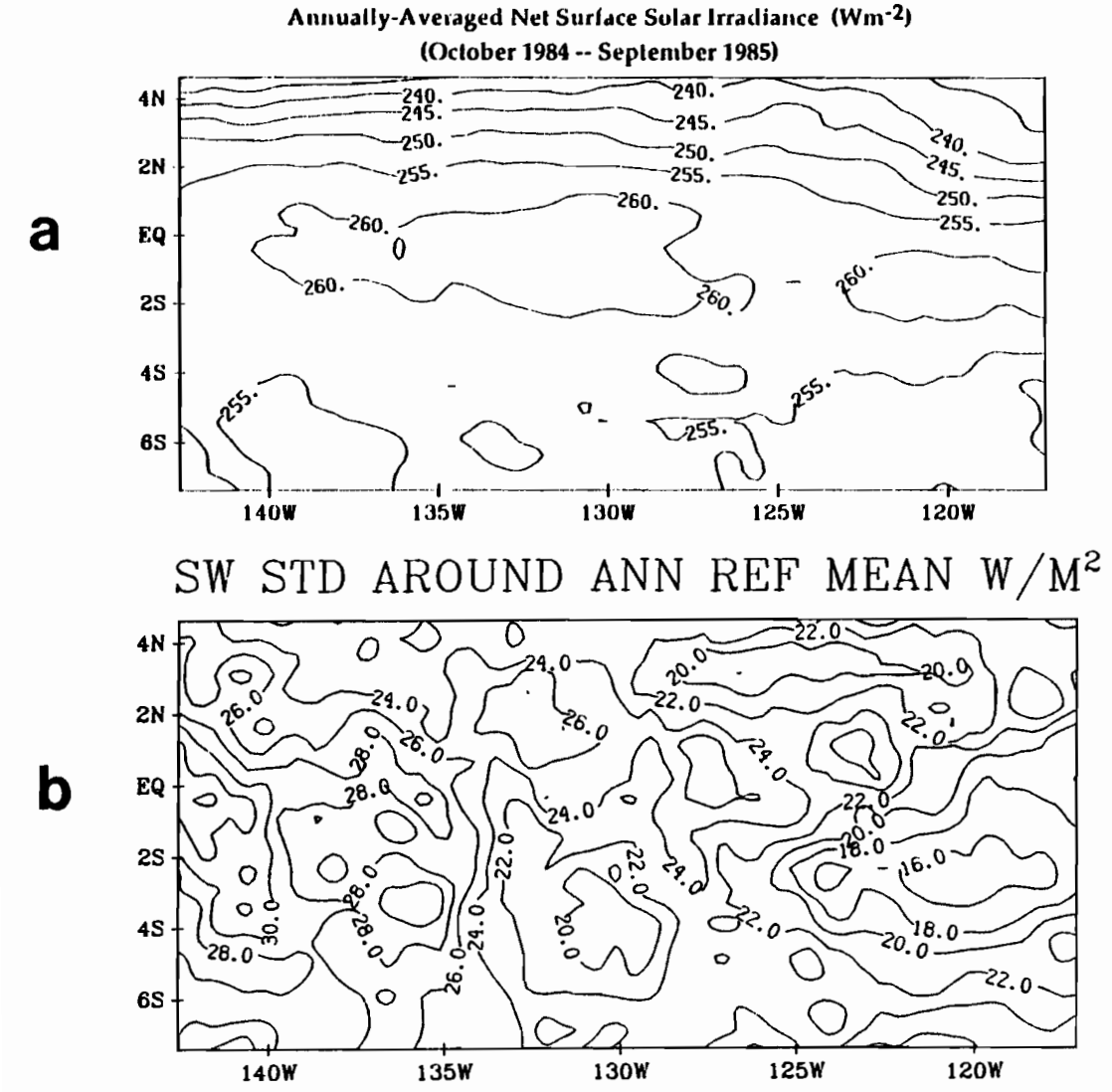

Fig. 4 Annually averaged net surface solar irradiance used for computing the anomalies (a) and the standard deviation around this mean of data used in the EOF analysis (b).

The EOF analysis of the first data set provides us with mostly the seasonal signals: semi-annual and annual. The first two EOFs explain 62.2 and 16.1 % of the variance (78.3 % cumulative), respectively, whereas the two subsequent EOFs each explain less than 5 % of the variance. The remaining EOFs each account for less than 2% of the variance. The first eigenfunction is presented together with its corresponding time varying amplitude coefficient in Fig. 5a. The values of this eigenfunction are small (3×10^{-2}) and negative everywhere; the spatial variability is small and a weak maximum exists in the equatorial region, centered around 2.5° S. The time variability of the amplitude coefficient is dominated by a semi-annual signal (cf. clear net surface solar irradiance plotted on the same graph with scaled amplitude). The semi-annual cycle is strongly perturbed by the El Niño event. The secondary maximum of December is strongly enhanced and delayed by a month whereas the primary maximum of June occurs earlier, after a much reduced minimum. These effects obviously result from cloud variations which counteract the normal sun variation effects and perturb the

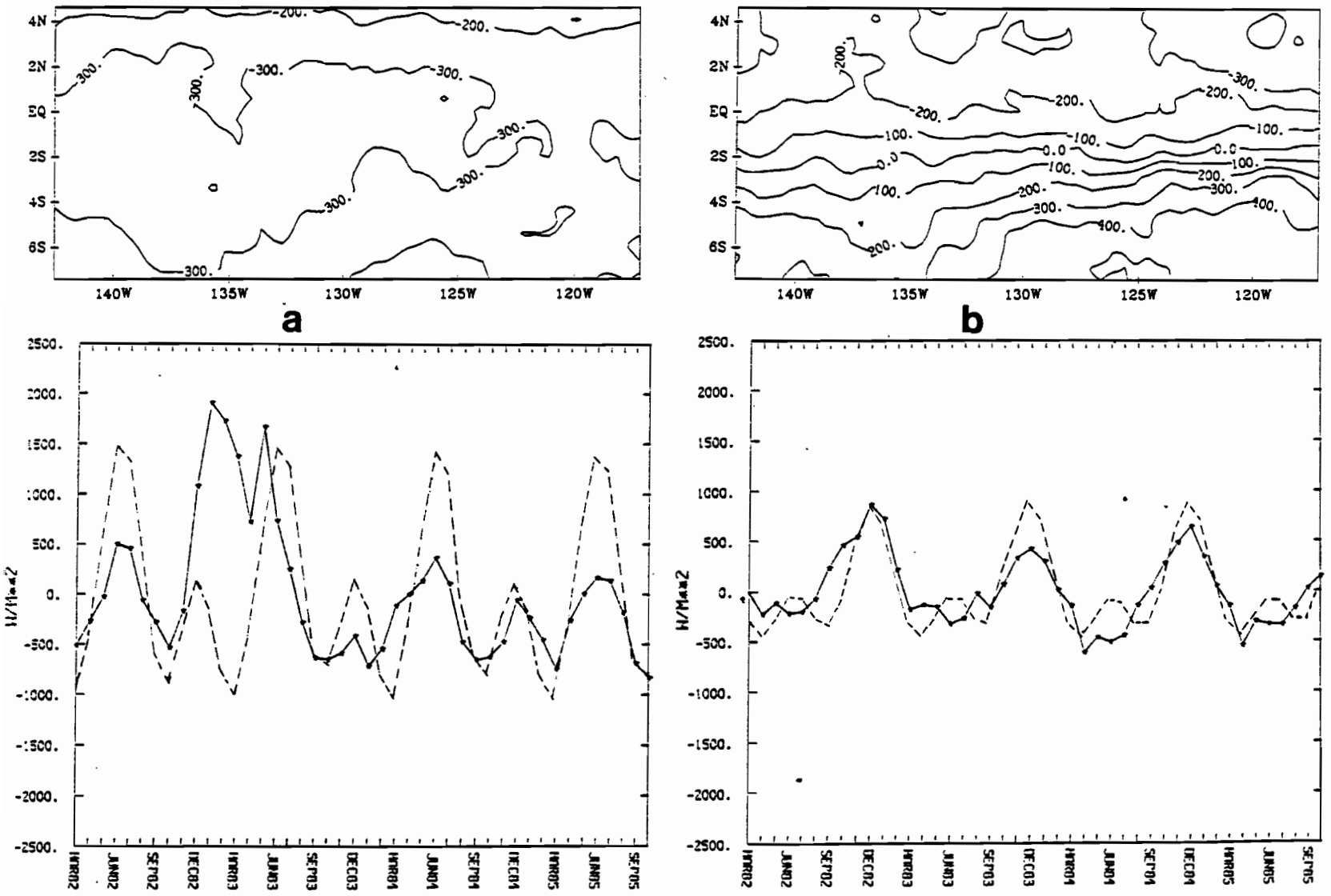

Fig. 5. The first (a) and second (b) empirical orthogonal functions (EOFs) of the seasonal data set. The top figures represent the eigenfunctions, and the bottom figures depict the time variations of associated amplitude coefficient (continuous line) and equivalent coefficient for clear-sky conditions (dashed line).

semi-annual cycle. The amplitude of the semi-annual signal for the area studied is about 30 Wm^{-2} during the years preceding and following El Niño.

The second eigenfunction and its corresponding time varying coefficient are presented in Fig 5b. The function field is very zonal and composed of negative values north of about 2.5° S and positive values south of 2.5 °S. Because of the non-symmetry of the studied area, the zero isoline is located at about 2.5° S, instead of the equator, where it should be since this function represents the annual variations of the field. The amplitude coefficient has a strong annual signal with a marked maximum in November–December and a flat minimum around April–July, indicating that the north-south gradient changes sign annually. The El Niño appears to only slightly modify the annual signal (plotted on the same graph) by broadening the period of minimum from March to September 1983 and reducing the maximum. The amplitude of this annual signal varies with latitude; at about 5°S, it is about 30 Wm^{-2} and very similar to the semi-annual signal.

The first EOF of the non-seasonal data set is presented in Fig. 6a. It represents 67% of the total variance, while all the remaining EOFs represent less than 5 %. The spatial variability of the field is very similar to that of the first eigenfunction of the seasonal data set, with the largest value of the coefficients in the western equatorial region. The corresponding amplitude is presented in Fig 6b. It clearly shows the El Niño effect from December 1982 to June 1983. The maximum variation of net solar irradiance during that period was about -75 Wm^{-2} for about 3 months and less than -50 Wm^{-2} for another three months in the western equatorial region. An important aspect to note is the negative values of the amplitude coefficient (corresponding to 10 to 40 Wm^{-2} depending on the region) for most of the time after June 1983, suggesting anomalously clear sky conditions. These conditions were indeed noticed in our analysis of the anomaly fields not presented here.

The results presented above clearly indicate the strong effect the 1982-83 El Niño had on the net solar irradiance of the central equatorial Pacific. The western part of the area studied was in an anomalous state from September 1982 to August 1983. The reduction of net solar irradiance was more than 50 Wm^{-2} for several months. Such a large reduction of net solar irradiance over such a long time period suggests a possible feedback mechanism on the anomalously warm sea surface temperature then existing in the central equatorial Pacific. Whereas the warm sea surface temperature appears to precede the reduction of net solar irradiance, it can be expected that the lasting low values of net solar irradiance might induce a reduction of the warm anomaly during the subsequent months.

A study of the entire tropical Pacific solar irradiance has been recently initiated using data from two geostationary satellites to cover the entire width of the basin. The GMS satellite data have been used to complement the GOES data and compute solar irradiance in the eastern Pacific. The region of the warm pool is found to be dominated by deep convection of a similar nature to that observed in the central Pacific during El Niño.

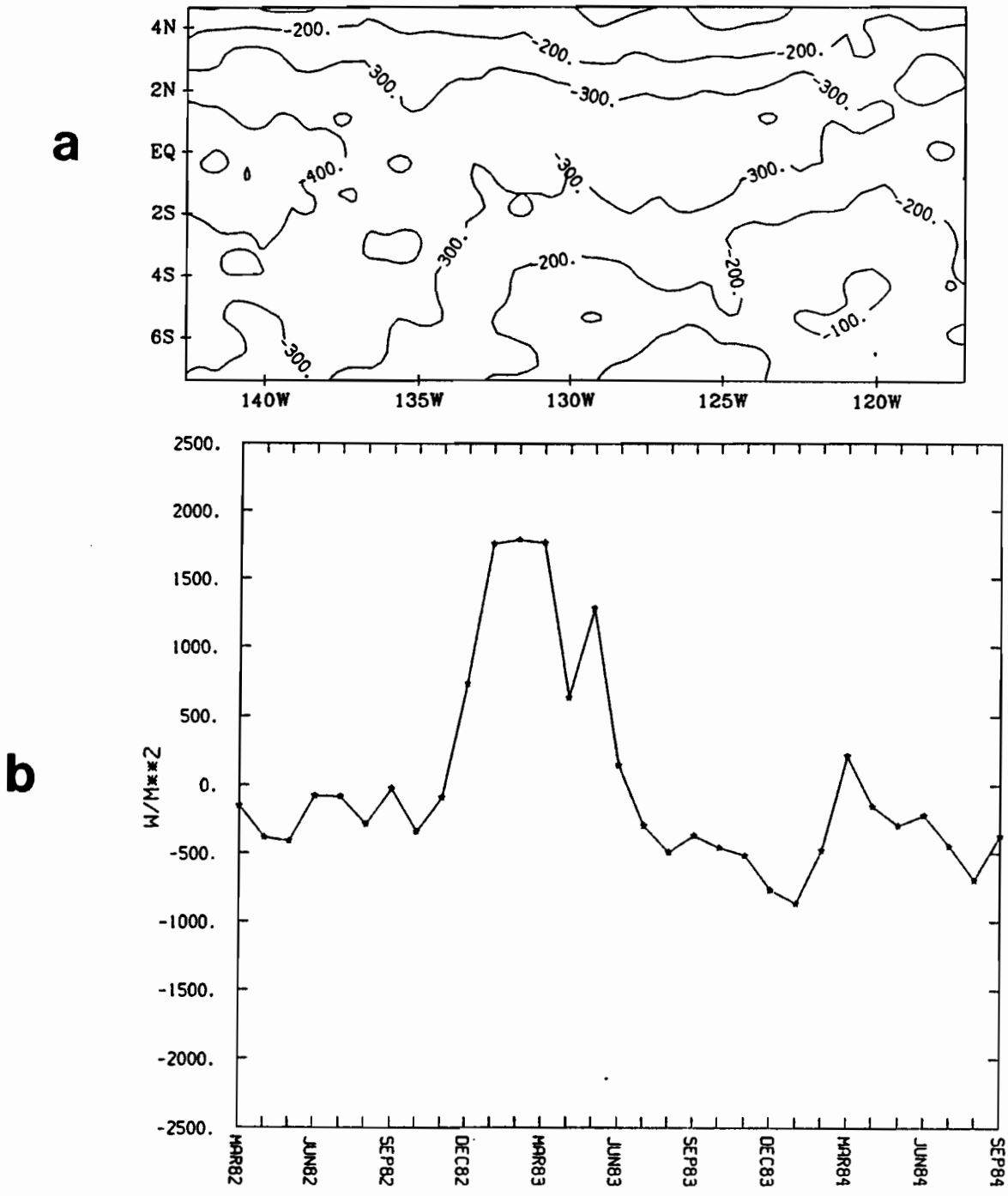

Fig. 6 First empirical orthogonal function of the non-seasonal data set (a) and time variations of associated amplitude coefficient (b).

Acknowledgments

This work has been supported by the National Oceanic and Atmospheric Administration's TOGA Project Office (NA86AA-DAC051) and through a research grant from the National Science Foundation (OCE-8717654). We are grateful for the technical support provided by Mr. Bob Wylie, Ms. Beth DiGiulio, and Mr. Brian Bloomfield.

References

Budyko, M. L., 1963: Atlas of the Heat Balance of the Earth, (in Russian). Kartfabrika Gosgeoltekhizdata, Leningrad.

Chou, M. D., 1985: Surface radiation in the tropical Pacific. *J. of Clim. and Appl. Meteorol.*, **24**, 83–92.

Esbensen, S. K., and Y. Kushnir, 1981: The heat budget of the global oceans: An atlas based on surface marine observations. Rep. 29, Clim. Res. Inst., Oreg. State Univ., Corvallis.

Gautier, C., G. Diak, and S. Masse, 1980: A simple physical model to estimate incident solar radiation at the surface from GOES satellite data. *J. Appl. Meteorol.*, **19**, 1005–1012.

Gautier, C., and R. Frouin, 1989: Net surface solar irradiance variability in the central tropical Pacific. (In preparation).

Weare, B. C., P.T. Strub, and M. D. Samuel, 1981: Annual mean surface heat fluxes in the tropical Pacific Ocean. *J. Phys. Oceanogr.*, **11**, 705–717.

Wyrtki, K, 1965: The average annual heat balance of the North Pacific Ocean and its relation to ocean circulation. *J. Gephys. Res.*, **70**, 4547–4559.

Mechanisms of Subsurface Thermal Structure and Sea Surface Thermo-Haline Variabilities in the South Western Tropical Pacific during 1979-85 - A Preliminary Report

Thierry DELCROIX and Christian HENIN

Groupe SURTROPAC, Centre ORSTOM de Nouméa, Nouméa, New Caledonia

ABSTRACT

Major features of the South Western Tropical Pacific, defined between 160°E-140°W and 24°S-10°S, are brought to light through analysis of surface water samples (23000) and temperature profiles (8500) gathered during the 1979-85 period.

Mean vertical thermal structure, sea surface temperature (SST) and salinity (SSS) are first portrayed, to further quantify their 1979-85 respective variability. It is demonstrated that the observed seasonal and interannual variabilities, the latter being associated with the strong 1982-83 El Nino, are mostly governed by specific mechanisms involving varying wind field and rainfall regime.

During the non ENSO period (1979-81+1984-85), SST annual cycle and 0-100m thermal structure changes are tied to the seasonal variations of the sun position (minimum SST in August). Below the mean position of the SPCZ is a marked seasonal SSS cycle (minimum SSS in March). This minimum occurs 2-3 months after minimum E-P whose variations suffice to explain SSS changes, assuming a 28±7m mixed layer depth, in agreement with sporadic density profile observations. It suggests that SSS annual cycle is mostly driven by the E-P regime associated with the SPCZ intensity and meridional migration. Noteworthy, the seasonal meridional migration of the SPCZ also causes alternation of cyclonic and anticyclonic wind stress curls west of 175°W and between 13°S-17°S. Such migration governs the seasonal thermocline depth variations through the Ekman pumping mechanism.

During the ENSO period (1982-83), notable changes in the vertical temperature distribution were perceivable between 10°S-15°S, in the upper 100m. These changes occured in response to the anomalous wind stress field that strongly uplifted the thermocline through local Ekman pumping (as much as 70m in May 1983). In the northern part of the studied region (i.e., in the warm pool area) , the thermocline shoaling modified the whole water column all the way to the surface, and was thus responsible for the observed SST cooling anomaly (-0.5°C to -1°C). In the southern part, similar SST cooling anomaly were concomitant with positive latent heat flux anomaly (>20Wm^{-2}) related to an increase in the northward wind component. At the mean SPCZ position, the drastic +1 SSS increase mainly resulted from a rainfall deficit associated with the equatorward shift of the SPCZ.

1. Introduction

In the frame of the international TOGA and COARE programmes, the poorly documented South Western Tropical Pacific ocean (Fig.1) is of main interest to study. Indeed,

- it is situated below the mean position of the South Pacific Convergence Zone (SPCZ), i.e., under the influence of its related wind stress, rainfall regime and convective activity,
- its northern part belongs to the warm pool area (SST > 28°C), and it is located in the rainiest part of the tropical Pacific ocean,
- it lies in between Tahiti and Darwin where the sea level pressure records define the usual Southern Oscillation Index (SOI).

ORSTOM
CENTRE DOCUMENTATION
Montpellier

F 30245

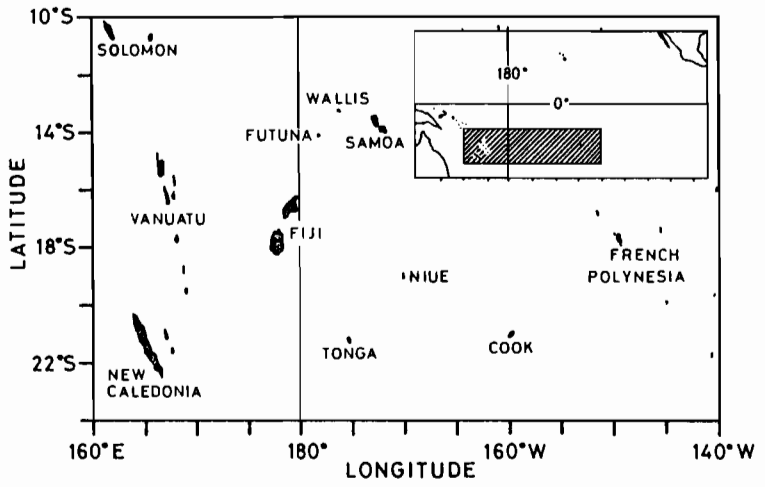

FIG.1. Location of the south western tropical Pacific in relation to the Pacific ocean.

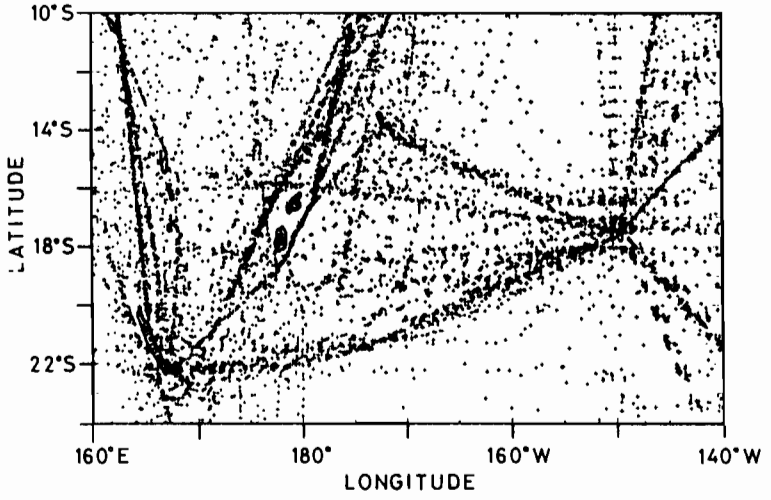

FIG.2. Spatial distribution of temperature/depth observations deployed during 1979-85 in the south western tropical Pacific.

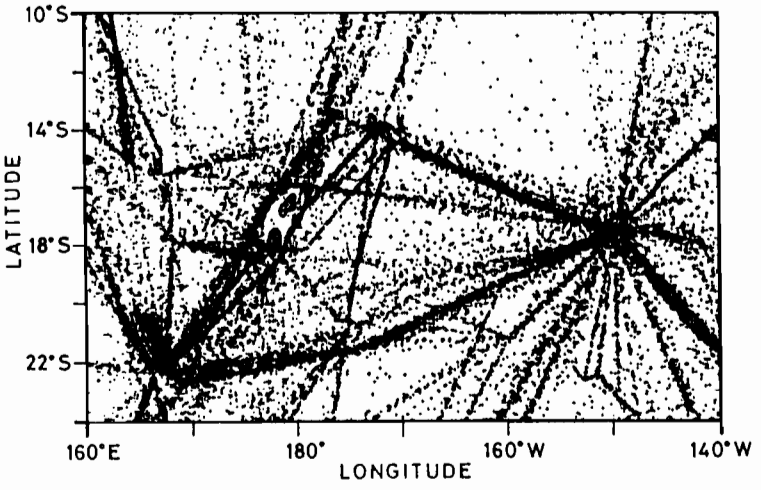

FIG.3. Spatial distribution of SSS observations deployed during 1979-85 in the south western tropical Pacific.

Thanks to a subsurface and surface monitoring, a basic description of the mean hydrological structures and of the 1979-85 variability was undertaken. Specific mechanisms responsible for this variability were identified and tested.

2. The data

Subsurface data (Fig.2) are mainly issued from an ORSTOM-SIO ship of opportunity network, and are complemented with data collected in different data banks. They consist of 8500 XBT temperature profiles (0-400m) during the 1979-85 period, i.e., about 125 XBT month^{-1}. The entire set of sea surface samples (T and S) comes from a ship of opportunity programme operated jointly by the ORSTOM centres in Nouméa and Papeete. The Sea Surface Salinity (SSS) data set (Fig.3) is composed of about 23000 observations (1979-85), i.e., about 240 SSS month^{-1}.

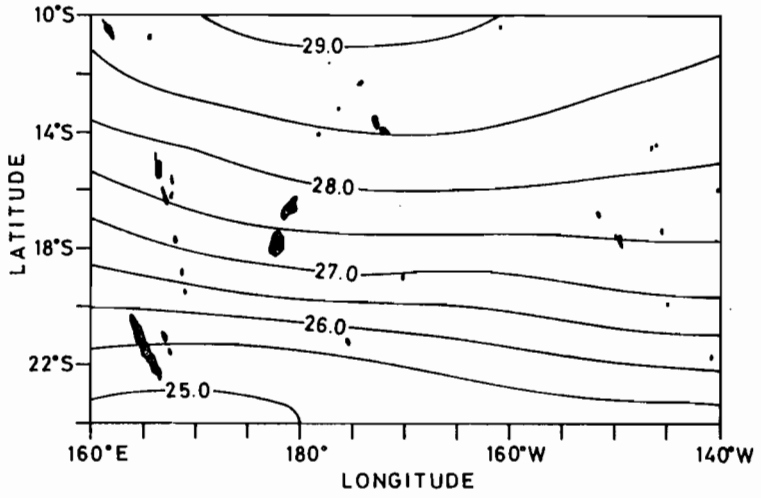

FIG.4. Mean sea surface temperature with contours at 0.5°C intervals.

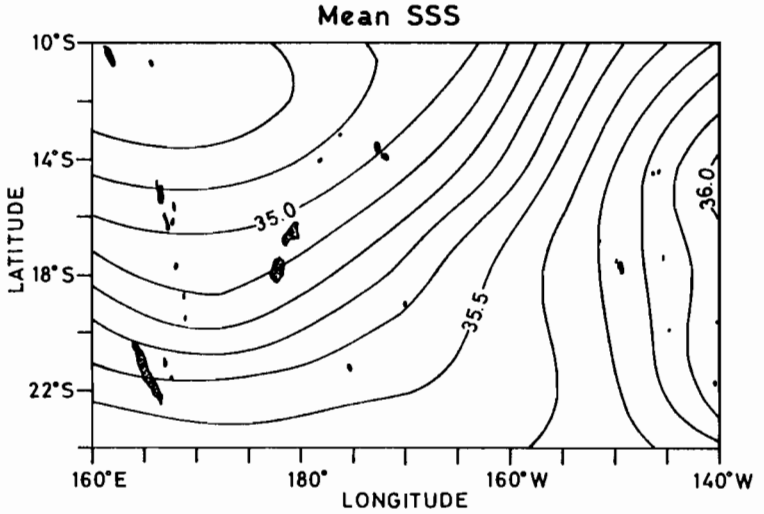

FIG.5. Mean sea surface salinity with contours at 0.1 intervals.

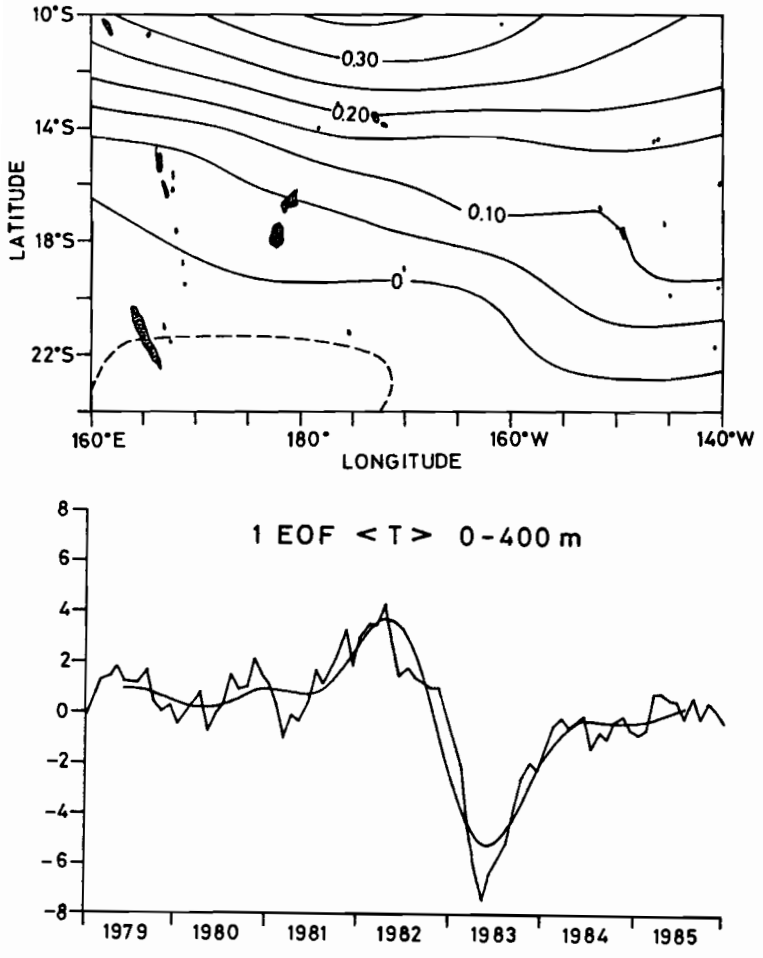

FIG.6. First empirical orthogonal function of the 0-400m average temperature with spatial pattern and time function. The broken line in the top panel denotes negative values. The low-frequency curve in the bottom panel is a result of a Fourier low pass filter removing period < 14 months.

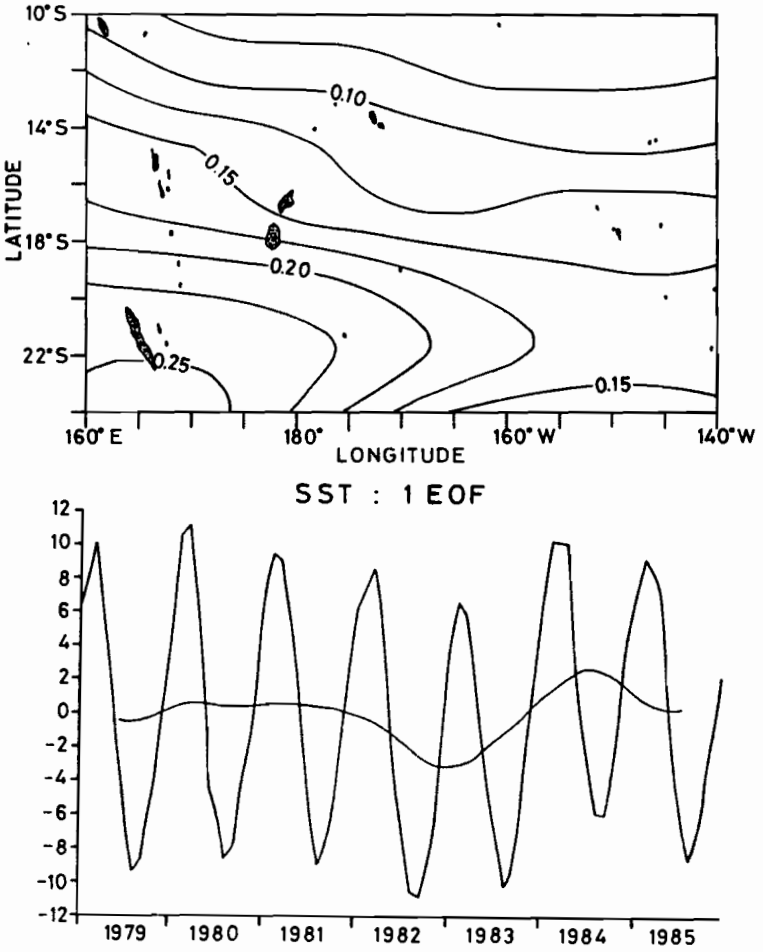

FIG.7. First empirical orthogonal function of the sea surface temperature with spatial pattern and time function. The low-frequency curve as in Fig.6.

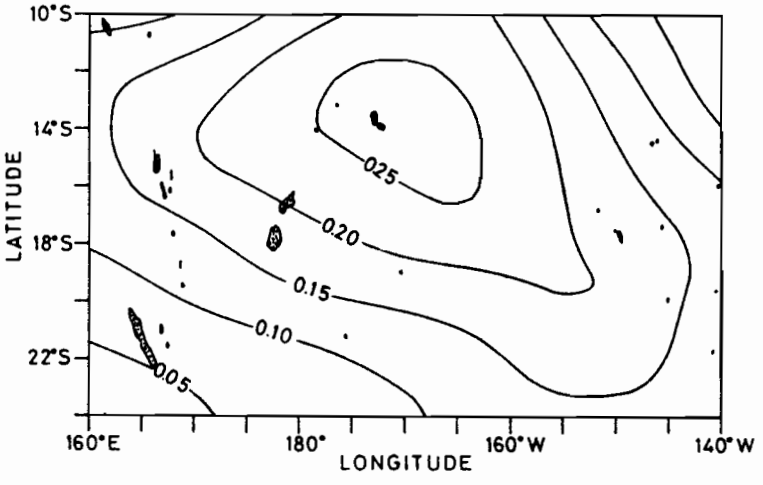

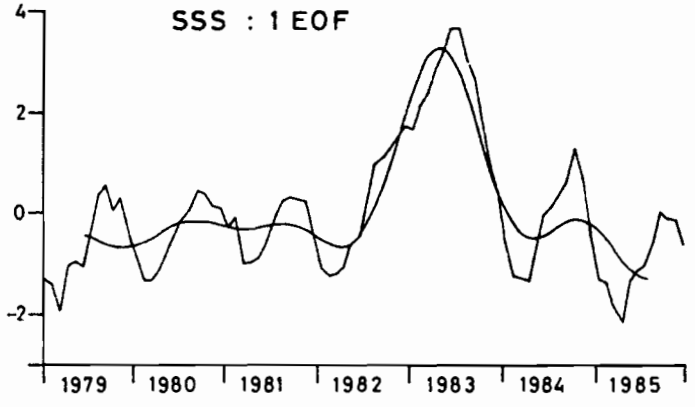

FIG.8. First empirical orthogonal function of the sea surface salinity with spatial pattern and time function. The low-frequency curve as in Fig.6.

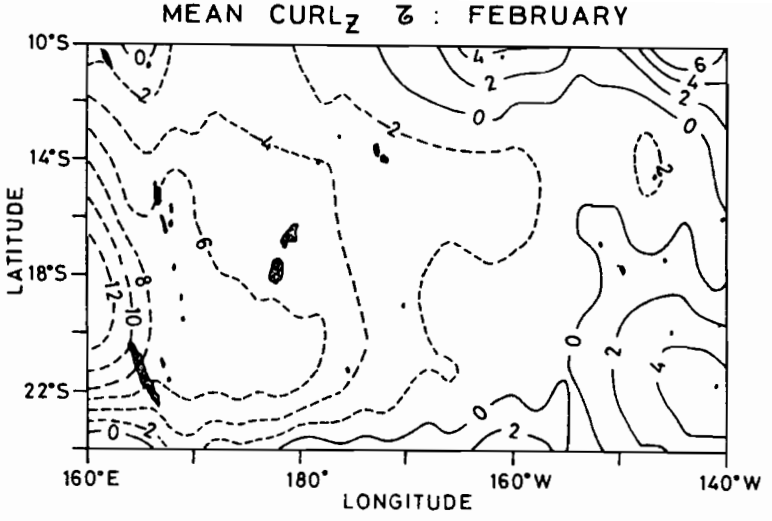

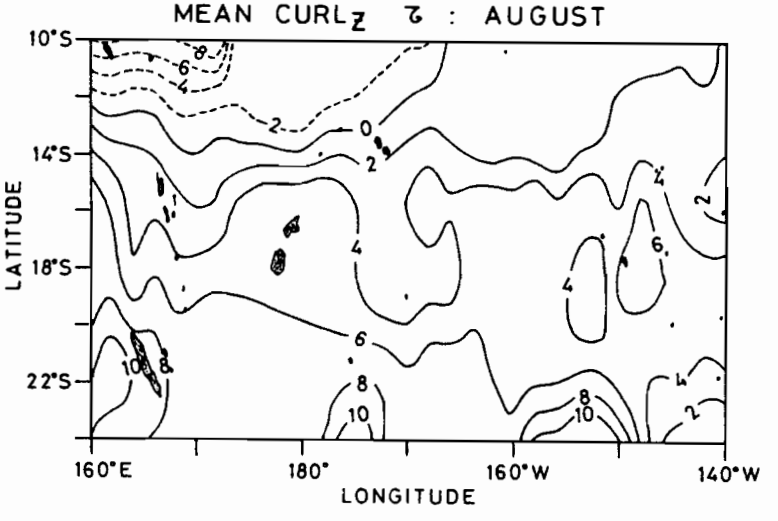

FIG.9. Mean (1979-81+1984-85) February and August wind stress curl. Contours are at 2.10^{-8}N.m^{-3} intervals and the broken lines denote negative values.

3. The mean structures

The mean meridional temperature-depth structure, and the mean SST and SSS distributions were computed over the 1979-81+1984-85 years, in order to exclude the 1982-83 El Nino period.

The mean meridional temperature section (not shown here; cf Delcroix and Hénin, 1989) evidences the gradual southward disappearance of the thermocline, with spreading of the isotherms south of 15°S. Schematically, the region is in the transition zone between the vertical temperature distribution of the equatorial band and the one of the extra-tropical region.

The mean SST map (Fig.4) shows zonally oriented isotherms ranging from 25°C to 29°C. North of 15°S is the southern part of the equatorial Pacific warm pool (SST > 28°C), which migrates to about 12°S and 20°S during the austral winter and summer, respectively.

The mean SSS map (Fig.5) exibits an almost SE/NW gradient between the high salinity waters (S > 35.9) of central south tropical Pacific and the low salinity ones (S < 34.8) south of the Solomon Islands. Minimum SSS coincides with evaporation minus precipitation (E-P) minimum (cf Weare et al., 1981) where rainfall can reach as much as 5 m $year^{-1}$ (Taylor, 1973).

4. The 1979-85 variability

The 1979-85 variability is described here through EOF analysis of the average temperature of the upper 400m and, SST and SSS. The presentation is restricted to only the first EOF.

The first EOF on heat content (Fig.6) accounts for 43% of the variance. The corresponding time function may be decomposed into: a) an accumulation of warm water from mid-1981 to March 1982, b) a net release of heat between April 1982 and May 1983, which constitutes the strong ENSO signal, and c) a return to a "normal" situation only reached in 1984. The space function points out that the ENSO signal is mostly restricted north of 15°S.

The first EOF on SST (Fig.7) accounts for 82% of the variance and primarily represents the seasonal cycle with minimum SST in August (austral winter). The interannual variability is depicted by the low frequency curve, evidencing that SST reaches maximum cooling anomaly at the end of 1982 and early 1983. Note the preponderance of the SST annual signal versus the interannual change related to the 1982-83 El Nino.

The first EOF on SSS (Fig.8) accounts for 46% of the variance. The pattern of the eigenvector is maximum along a SE/NW axis representative of the mean SPCZ location. The time function depicts both the seasonal cycle during the "normal" 1979-81+1984-85 period (minimum SSS in March) and the interannual variability associated with the 1982-83 ENSO phenomenon. It shows that maximum SSS annual amplitude is +0.25 below the SPCZ, as compared with the large + 1 SSS increase during the El Nino period.

5. The mechanisms

Mechanisms involving varying wind field and rainfall regimes accounts for the observed sub-surface and surface changes. In the South Western Tropical Pacific, Ekman pumping, evaporation and precipitation are the main processes that all contribute to the normal seasonal cycle and/or are related to the strong ENSO effects. The role of water advection and vertical mixing will not be examined here.

a. The Ekman pumping

In off-equatorial region, the simplest dynamical mechanism that can affect the vertical thermal structure is Ekman pumping. The Ekman pumping balance is written as:

$$-\partial h/\partial t = curl_z(\tau/\rho.f)) \quad (1)$$

or $$-\partial h/\partial t = (curl_z(\tau) + (\beta/f).\tau^x) / (\rho.f) \quad (2)$$

where h is the depth of the thermocline (>0 down) and the other variables state for their usual meaning. The equation evidences that the relative magnitude of the two right-hand side terms of Eq.(2) determines the sign of Ekman pumping. A qualitative description of these two terms is therefore presented first.

During a "normal" year, the zonal component of the wind stress is always negative (westward), whereas the seasonal meridional migration of the SPCZ induces alternation of negative (cyclonic) and positive wind stress curl, in the course of the year (Fig.9). Hence, the two terms of the equation add or balance , so the South Western Tropical Pacific may be sliced into regions: a) weakly affected by Ekman pumping, b) favourable to upwelling, c) favourable to downwelling, and d) propitious to alternation of upwelling and downwelling depending on the period of the year.

During the "abnormal" 1982-83 period, drastic wind field changes were observed. Of main interest is the reversal of the zonal component of the wind stress in early 1983 between about 13°S and 2°N, as reported in atlases (Leetmaa and Witte, 1984), papers (Kessler and Taft, 1987), and deduced here from the FSU wind field analysis. At this time, both τ^x and $curl_z\tau$ act in the same way, leading to a strong positive (upward) Ekman pumping velocity in the northern part of the studied region. The effect upon the vertical thermal structure distribution is exemplified in Fig.10.

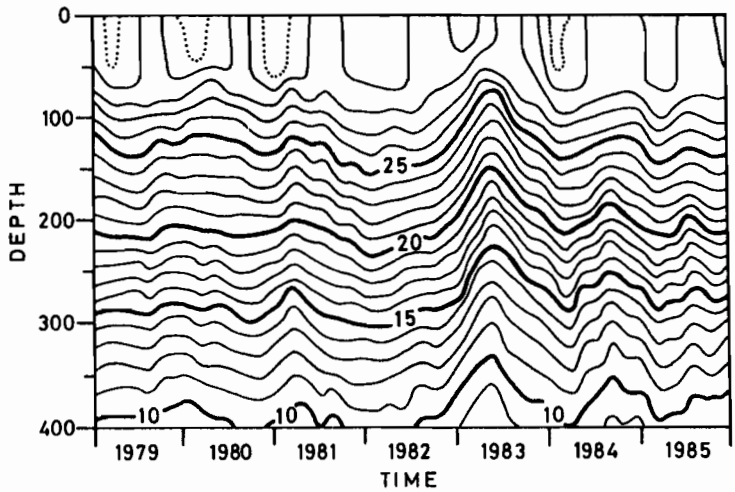

FIG.10. 1979-85 time series of isotherm depth distribution in the (10°S-12°S; 180°-170°W) box. Contours are at 1°C intervals, except for the dotted line which is the 29.5°C isotherm.

Besides the previous qualitative approach, a quantitative comparison between the two terms of the Ekman pumping equation has been performed. It is presented in Fig.11 for selected locations, and it confirms the preceding qualitative discussion.

b. Evaporation and precipitation

Evaporation and/or precipitation are related to the SPCZ which overspreads the studied region, and contributes to SST and SSS changes.

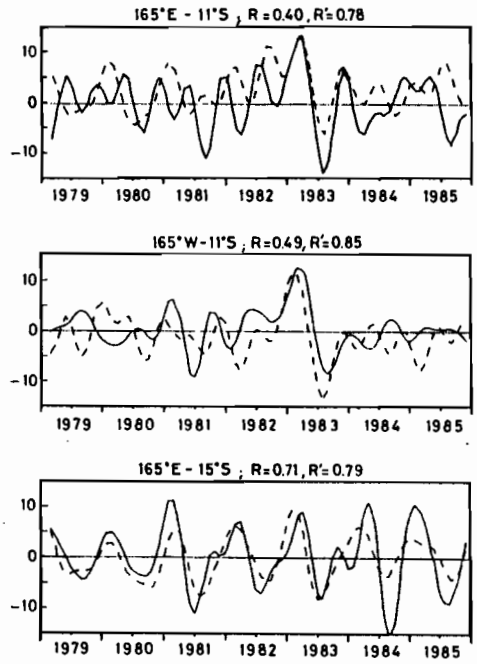

FIG.11. 1979-85 time series of the two terms of the Ekman pumping balance (see Eq. 1), at different reported locations. Solid line is $-\partial h/\partial t$, broken line is $curl_z(\tau/\rho.f)$ in m.month^{-1} (the upward motion is positive). R and R' are, respectively, the correlation coefficients between the two terms during the 1979-81+1984-85 and 1982-83 periods.

During a normal year, mean monthly values of SSS were compared with mean monthly values of E-P (Fig.12). Evaporation was calculated from Weare et al.(1981)'s formulae, and precipitation data derived from the maps of Taylor (1973). Significant correlations (R > .7) are best obtained below the mean SPCZ position, for 2-3 month lag between the twelve month series (i.e., minimum SSS 2-3 months after minimum E-P). Note that similar result is obtained when comparing SSS with only P (i.e., minimum SSS 2-3 months after maximum P). Since E-P may be reasonably written as:

$$E\text{-}P = (E\text{-}P)_0.\cos(\omega.t-\theta) \qquad (3)$$

where $(E\text{-}P)_0$ is the annual mean amplitude, ω the annual frequency and θ is one month (January), the necessary condition for only E-P governs SSS is satisfied (Hires and Montgomery, 1972). In fact, SSS minimum occurs a quarter cycle (3-months) after minimum E-P. The thickness of the mixed layer (in density) that would be required to explain that only E-P variations account for annual SSS variations was thus computed over the R>.7 area. The results show that it is 28±7 m, i.e., in agreement with sparse density measurements. This suggests that, during a normal year, mostly E-P governs SSS below the mean SPCZ position.

The drastic SSS change associated with the 1982-83 El Nino was shown in Fig.8. An estimate of the possible responsible mechanisms was performed. Although horizontal advection and vertical mixing are consistent with the 1982-83 SSS change, we found that such SSS change was mainly governed by the equatorward shift of the SPCZ (Ardanuy et al., 1987), leading to a rainfall deficit below its usual position. For example, at 12°S-170°W, assuming that rainfall linearly decreased from 0.2 m month^{-1} in mid-1982 (the mean June value) to 0 in mid-1983 (Ardanuy et al., 1987), we obtain a -1.2 m fresh water deficit over a one year period. Alone, such deficit would induce a 0.8 SSS rise over

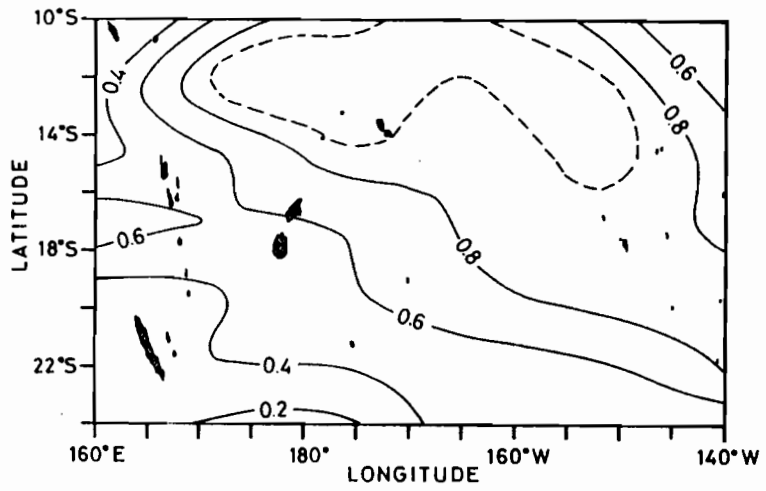

FIG.12. Correlation coefficients between sea surface salinity and evaporation minus precipitation mean years for a 2-month lag. Contour intervals at 0.2 except for the broken line which denotes the 0.9 value.

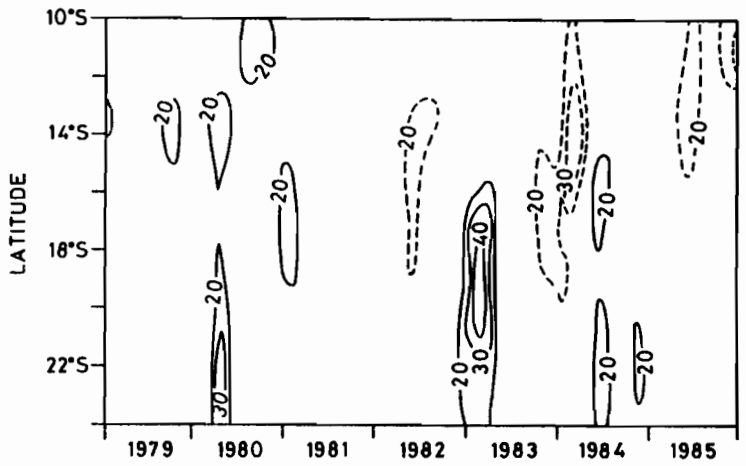

FIG.13. Zonal mean (160°E-140°W) latent heat flux anomalies (W m^{-2}) with reference to the (1979-81+1984-85) mean year, as a function of time and latitude.

a 50 m mixed layer, i.e., the same order of magnitude as observed in mid-1983. Rainfall deficit thus appears to be the dominant factor influencing SSS during the 1982-83 period.

As reported before (cf. Fig.10), Ekman pumping strongly uplift the thermocline in the northern part of the studied region. It modifies the whole water column all the way to the surface, perturbating the normal SST cycle. Figure 13 evidences that the latent heat flux anomalies which occured in early 1983, may also contribute to the abnormal SST cooling observed south of about 16°S.

6. Conclusions

The above findings suggest that most of the oceanic variability observed in the South Western Tropical Pacific is related to the SPCZ which, in turn, is affected by the surface oceanic conditions (Kiladis and Van Loon, 1988). Quantifying the role of such air-sea interactions over the whole warm pool is therefore of great interest. This is the challenge of the future COARE programme.

REFERENCES

Ardanuy P., P. Cuddapah and H. Lee Kyle, 1987: Remote sensing of water vapor convergence, deep convection and precipitation over the tropical Pacific ocean during the 1982-83 El Nino. *J. Geophys. Res.*, **92,** 14204-14216.

Delcroix T. and C. Hénin, 1989: Atlas océanographique du pacifique tropical sud-ouest. Centre ORSTOM de Nouméa, New Caledonia. *Serie Sciences de la mer. Océanographie physique,* **2.** 68 pages.

Hires R. and R. Montgomery, 1972: Navifacial temperature and salinity along the track from Samoa to Hawai. *J. Mar. Res.*, **30,** 177-200.

Kessler W. and B. Taft, 1987: Dynamic heights and zonal geostrophic transports in the central tropical Pacific during 1979-84. *J. Phys. Oceanogr.*, **17,** 97-122.

Kiladis G. and H. van Loon, 1988: The southern oscillation. Part VII: meteorological anomalies over the Indian and Pacific sectors associated with the extremes of the oscillation. *Mon. Wea. Rev.*, **116,** 120-136.

Leetmaa A. and J. Witte, 1984: El Nino atlas 1982-83. Leetmaa and Witte editors, NOAA/ADML, Miami, Florida. 159 pages.

Taylor R., 1973: An atlas of Pacific island rainfall. HIG 73-9, University of Hawai, Honolulu, USA.

Weare B., P. Strub and M. Samuel, 1981: Annual mean surface heat fluxes in the tropical Pacific ocean. *J. Phys. Oceanogr.*, **12,** 705-717.

Observations from the Maritime Continent : Darwin, Australia

Greg. J. HOLLAND, T.D. KEENAN, M.J. MANTON

Bureau of Meteorology Research Centre (BMRC),
Melbourne - Australia

ABSTRACT

A major observational and research program is being undertaken in Darwin, Australia as part of the Tropical Ocean and Global Atmosphere (TOGA) and the National Aeronautics and Space Administration (NASA) Tropical Rainfall Measuring Mission (TRMM). Darwin is situated in northern Australia and experiences a monsoon environment typical of the Maritime Continent region, together with break and transition periods when continental systems are predominant. The Darwin initiative follows the recent Australian Monsoon Experiment (AMEX) and Equatorial Mesoscale Experiment (EMEX) and represents a continuing effort to gather data on the nature of convection in this strategic tropical location.

1. Introduction.

Darwin's strategic location in on the southern edge of the Maritime Continent and at the western extremity of the Pacific Walker circulation, together with its long period of established observations, has made it one of the most well known of all tropical observing sites. The SOI is based on Darwin pressure records that extend back to the last century and Darwin was the base for the recent AMEX/EMEX and Stratosphere/Troposphere Exchange Project (STEP) experiments.

The Bureau of Meteorology Research Centre has continued this tradition by promoting an extensive upgrading of the observing capacity in collaboration with NOAA, NASA, NCAR, NSF, the Northern Territory Regional Office of the Bureau of Meteorology, and a number of United States and Australian universities. We describe the observing system in section 2 and the climatological features of the region in section 3. Some recent experimental and research results are presented in sections 4-6.

2. The Darwin observing system.

The current Darwin observing system, shown in Fig. 1, covers a comprehensive array of mesoscale observations. A NOAA/TOGA Doppler radar has provided extensive Doppler coverage since 1988. This will be removed in 1990 and replaced by a Bureau of Meteorology radar in 1991. For the 1988/89 and 1989/90 wet seasons, dual Doppler observations are being taken in conjunction with the NSF funded MIT radar. MIT also have installed a network of coronal point discharge and could-to-ground lightning detectors for 1988-1990.

Full tropospheric wind and thermal soundings are taken every 12 hours and additional wind soundings are made at the intervening 6 hours. A 50 Mhz Doppler profiler is being installed this year by BMRC in collaboration with the NOAA Aeronomy Laboratory. This will contain one vertical beam for 1989/90 and then be upgraded to a three beam system. A 915 Mhz profiler also will be installed to provide detailed boundary layer observations during special observing periods.

A mesonet of 26 surface raingauges was installed in 1987 and this is being upgraded to include complete surface observations from automatic weather stations at about five sites. A surface radiation monitoring station is being installed this year.

ORSTOM
CENTRE DOCUMENTATION
Montpellier

F 30246

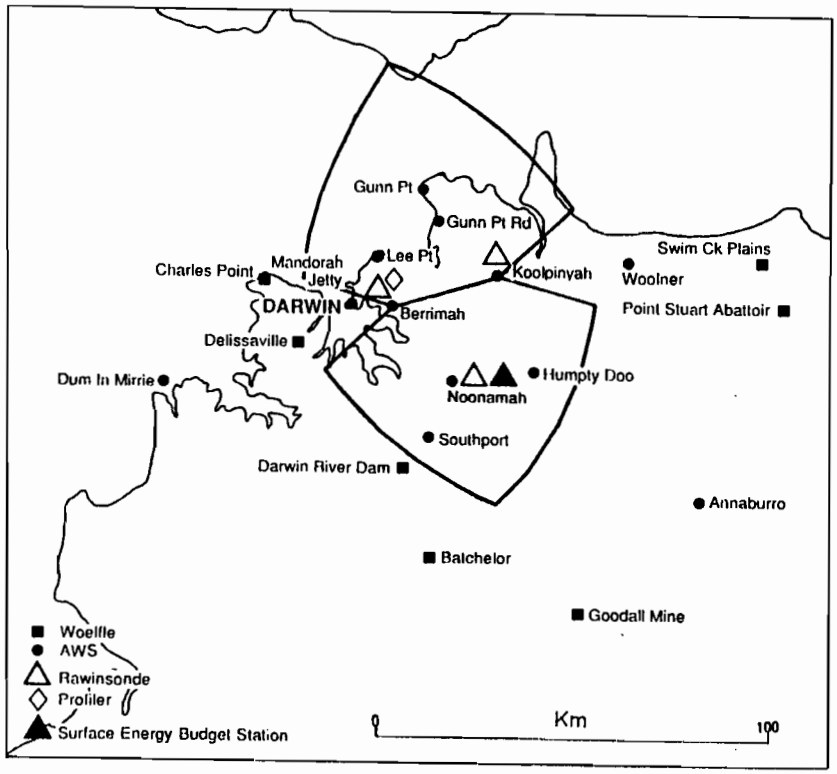

FIG.1. The Darwin observing system for the 1989/90 wet season.

3. Climatological features of the Darwin region.

Darwin lies at the southern edge of the Maritime Continent, within the world's largest source of latent heating. It experiences a classical monsoon climate described in detail by Holland (1986). The onset of the active period, when rainfall and low level equatorial westerly flow occur, is normally during late December, with the retreat to easterly flow and dry conditions usually occurring during late February or early March. Break periods, when low level subtropical esterly flow is again established, occur for around 20% of the summer monsoon season. As a result, there are two to three active westerly flow phases per season, with a mean period between active phases of 40 days. There is a close relationship between low-level westerly flow at Darwin and rainfall over northern Australia (Holland, 1986). In the Darwin region, however, thunderstom and squall line activity during the pre-monsoon October to December transition season contribute up to 30% of the total rainfall (Nicholls et al. 1982).

It is seen from Fig. 1 that within 150 km of Darwin approximately 48% of the area is oceanic, 43% is continental, and 9% is tropical islands. This diverse range of environments provides a rich variety of weather systems. The rain-producing systems during both the transition and wet season include oceanic monsoon cloud clusters and equatorial cloud bands, maritime-continent island thunderstoms, "pop-corn" cumuli and mesoscale convective complexes from the tropical continent, north Australian cloud lines and tropical squall lines, monsoon depressions and tropical cyclones. Theses continental and maritime systems have a variety of convective and mesoscale structures and undergo distinct lifecycles ranging from diurnal to those associated with synoptic scale organization. An indication of the frequency of storm occurrence, and their diurnal shift from land to ocean is shown in Fig.2.

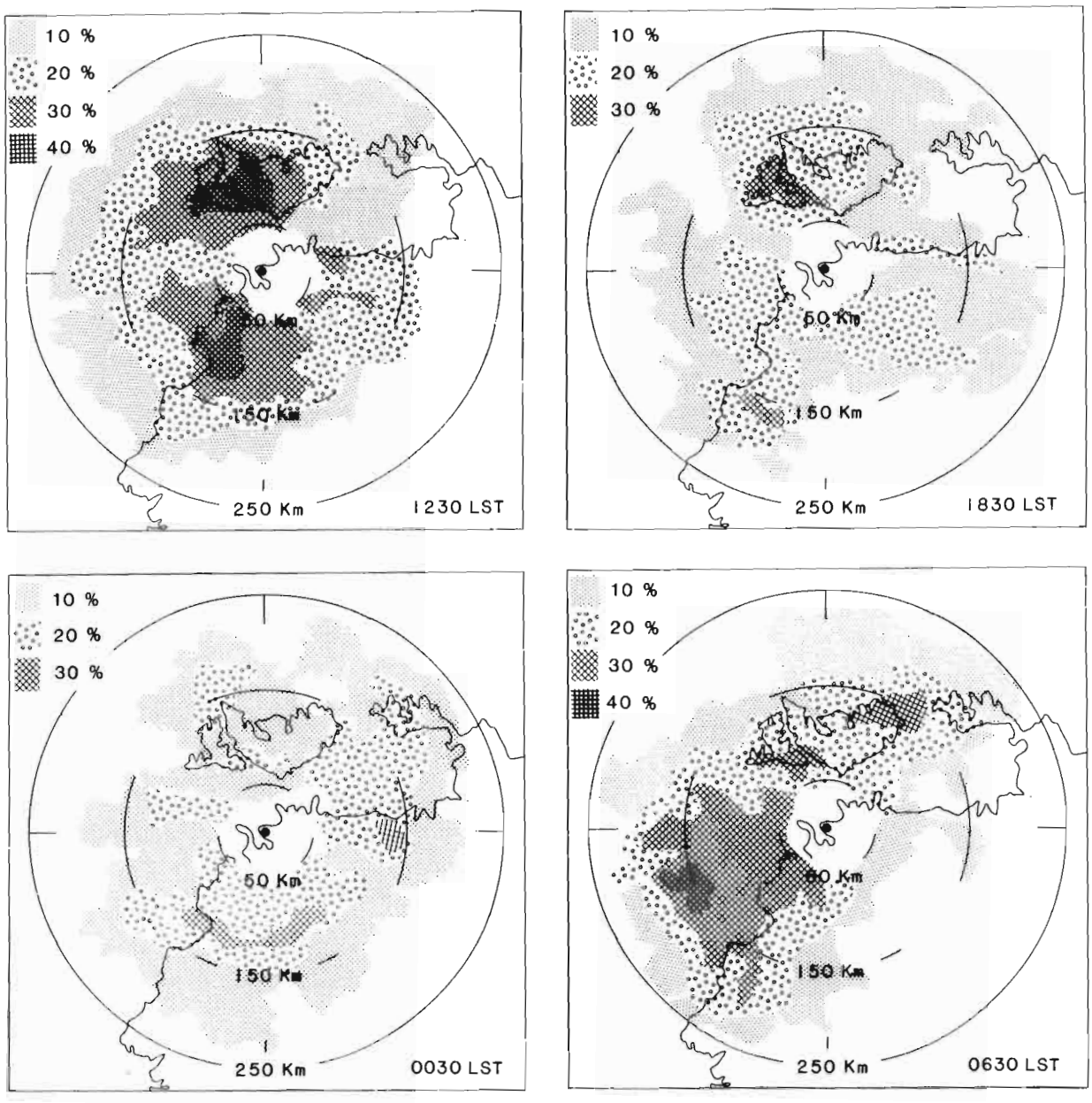

FIG.2. Percentage occurrence of radar echoes greater than 15 dBz at darwin during Phase II of AMEX at 1230, 1830, 0030 and 0630 LST.

Considerable interannual variability is observed in the strenght and duration of the summer monsoon at Darwin. The average daily rainfall is related to the SOI, but the length of the monsoon season is not (Holland, 1986). This may be because the length of the heavy rain and westerly monsoon bursts are very sensitive to the phase of the 30-50 day oscillation (Holland, 1986). There also is considerable variability in the occurrence of the different types of weather system from season to season. During a weak summer monsoon year, squall-lines and island thunderstoms are predominant. During a very active summer monsoon, the rain tends to fall from large-scale upslope flow associated with the well-developed monsoon through. Although tropical cyclones rarely pass over Darwin, rainbands from these systems and from monsoon depressions often occur. Interactions with subtropical flow appear to be particularly important in determining the scale and nature of the convection at Darwin (Keenan and Brody, 1988).

3. The Tropical Rainfall Measuring Mission (TRMM).

TRMM is a US and Japanese program to obtain a minimum three-year data set of 500x500 km^2 scale monthly averaged estimated rainfall rate probabilities in tropical regions (Thiele, 1987). The satellite based instrument package is planned for launching in the mid 1990s. The program involves development of new rainfall measuring techniques using both satellite and ground-based approaches and gathering of data sets suitable for diabatic initialization of weather forecast models. The program is being supported by comprehensive ground-truth observations taken in collaboration with TOGA.

The TRMM ground truth project (Thiele, 1987) includes the objective of determining the three-dimensional structure of tropical precipitation and rainfall amounts from spatial scales less than 1 km up to a 100,000 km^2 area for a one month time period. To date, ground truth data on tropical rainfall have been limited to short period field experiments, e.g. GATE and AMEX/EMEX. In addition, these data have not been collected at locations representative of the entire global regime. NASA, NOAA and BMRC therefore have established a TRMM ground truth station at Darwin to obtain a climatology of convection and total rainfall indicative of the monsoon climate and the maritime continent.

The data collected in Darwin are being used initially in support of pre-TRMM studies. The aim of these pre-TRMM ground measurement studies are to :
1) Undertake rainfall measurement comparisons relevant to spaceborne radar/radiometer techniques, and
2) Undertake rainfall measurements on the scales relevant to the satellite mission.

The mode of operation is to mix a long-term climatological monitoring of the rainfall in the vicinity of Darwin with data obtained during intensive special observing periods. The operation has fulfilled the following objectives:
1) Quantitative estimation of precipitation rates using the high accuracy, 5 minute base scan data available on pseudo constant altitude surfaces,
2) Monitoring of the convective components of precipitation for echo tracking (5 minute base scan data),
3) Three dimensional structure of the precipitating systems from the convective to mesoscale using the 5-15 minute interval volumetric scan data,
4) Monitoring of the stratiform component of precipitation at 15-60 minute hourly intervals using the Extended Velocity Azimuth Display (EVAD) method of Srivastaval et al. (1986).
5) Deriving statistics of vertical motion using EVAD and vertical sounding data.

Further information on the TRMM ground truth mission at Darwin may be found in Keenan et al. (1988).

4. The Island Thunderstorm Experiment (ITEX).

Tropical convective activity within the maritime continent region is dominated by local thunderstorms generated on a diurnal basis over the many tropical islands. Examination of satellite data by Holland and Keenan (1980) showed that this deep, geographically fixed, tropical convection is the basic source of convection within the so called "boiler-box" of the tropics. Disturbances often exist and can be associated with widespread convective activity but these local ephemeral thunderstorms emerge as the basic convective element of the maritime continent.

Houze et al. (1981), Williams and Houze (1987) and Keenan et al. (1989b) have documented some diurnal variations that occur over the maritime continent region. And several experiments (EMEX, WMONEX) have examined the structure of convective

disturbances over the ocean. The ITEX objective (Keenan et al. 1989a) was to complement these studies by gathering detailed information on the thunderstorm complexes that regurlarly form over Bathurst and Melville Islands to the north of Australia (Fig.1). The observing system shown in Fig.1 was complemented by additional rawinsonde stations on Melville Island and at Cape Don, and by an array of surface anemometers which were established on the islands together with a radiation budget and surface flux station. An instrumented aircraft was used to obtain photographic and thermal data in the vicinity of the developing storms.

ITEX was a collaborative effort between BMRC, the Centre for Dynamical Meteorology at Monash University, and NASA. The aims were to obtain the first comprehensive data set of these Maritime Continent thunderstorms and to carry out physical and numerical studies on their structure, generation and evolution. Particular attention was given to the mechanisms of generation, to the evolution, to the structure, the quasi-steady location over the islands and to the causes of decay. Studies are underway that focus on the surface energy budget, the role of sea breeze circulations and their interaction with thunderstorm scale circulations, the role of the large-scale environment and the larger-scale modification by the thunderstorms. Future studies are planned on analytic and numerical examination of tropical cumulus convection and on comparative tests of existing convective cloud models.

Further information on this experiment and on the climatology of thunderstorms over the islands may be found in Keenan et al., (1988, 1989a).

5. Squall-line and continental convection.

Tropical convection in the vicinity of Darwin has been shown by Keenan and Carbone (1989) to exist in a surprisingly large variety of modes. Bulk Richardson number classification and radar derived structure indicated the existence of storm conditions ranging from the high shear, moderate buoyancy range of tornadic type disturbances to the low stability moderate shear of hurricane rainbands. Darwin squalls encompassed the dynamic regime of severe squalls found in the US to the low stability/shear encountered in the oceanic and monsoon regimes. Important differences in the propagation mechanisms on the squalls were evident and recent observational data collected at Darwin have indicated the frequent occurrence of microbursts in association with this deep convective activity.

Tropical squalls during transition and break periods of the Darwin wet season result primarily from storms generated along the sea breeze front, from continental type squalls generated over the escarpment region 250 km to the east, or from continental storms to the east and south-east. A preliminary climatology indicates that during the 1500-0200 LST period, sea breeze front storms occur on 77% of days and major squalls from the east on 60% of days.

Oceanic convection occurs during monsoon conditions. The maritime systems are different in structure from the continental storms with generally weaker convective activity and a greater proportion of stratiform precipitation. However, very large CAPE is observed prior to the development of rainbands. In addition, squall-like lines develop within the massive stratiform decks.

An intensive examination of these tropical squalls, deep convection and monsoon convection will be carried out in the 1989/90 season by collaboration between the following institutions: Bureau of Meteorology Research Centre, Monash University Centre for Dynamical Meteorology, NASA Goddard Space Flight Center, Colorado State University, Massachusetts Institute of Technology, National Center for Atmospheric Research, NOAA Aeronomy Laboratory and the Northern Territory Regional Office, Bureau of Meteorology.

The aims are to investigate :

1. **The convective to mesoscale structure, motion and evolution of storms affecting Darwin and their interaction with environment.** Attention will be directed to comparisons with midlatitude systems, the generation and maintenance of the stratiform precipitation, the coupling between the horizontal and vertical flow within the trailing anvils and differences between oceanic and continental systems.

2. **The relationship between planetary boundary layer flow and the initiation, maintenance and propagation of tropical convection.** Convergent boundaries caused by the interaction between the sea breeze front, storm outflow and variations in surface heating will be investigated in relation to the propagation and initiation of the convective systems. Recent work by Rotunno et al. (1988) suggests that the structure and longevity of squalls is determined by the interaction between the environmental low level shear and the cold pool outlow from the convective cells. In addition, propagation of the squalls seems to be related to the speed of cold pool outflow.

3. **The development of microbursts in a tropical environment.** Previous observational data from the NOAA/TOGA radar has indicated that microbursts occur 4-5 times per day between 1230 and 1930 LST within 60 km of Darwin during break or transition season flow. The evolution of these tropical microbursts will be investigated in a contrasting regime to that of the dry continental sub cloud air; an environment in which most microbursts have been studied.

4. **The investigation of the lightning characteristics of continental and monsoon convection.** Preliminary investigations by E. Williams (MIT) and S. Rutledge (CSU) during the last two wet seasons in Darwin indicate that convective clouds in the vicinity of Darwin are indeed electrified highly with lightning rates in some clouds (those in an environment of large CAPE) equalling that observed at mid-latitudes. Observations indicate that in-cloud lightning (IC) rates dominate cloud-to-ground (CG) rates with ratios about 30 to 1. Investigations will continue on the electrical properties of both continental and monsoon convection with emphasis on relating electrical characteristics to cloud dynamics and cloud vertical development.

5. **Mesoscale Forecasting Experiments.** An intensive, mesoscale forecasting program will be mounted to evaluate the use of Doppler radar in aviation forecasting and to develop a climatology of gust fronts and convective downbursts in a tropical environment.

The observational network will be based on the NOAA/TOGA and MIT Doppler radars for convective scale data, an associated mesoscale network of surface weather stations, three rawinsonde stations, a surface energy budget station, a wind profiler and a tipping bucket raingauge network. The enhanced network will be concentrated about the dual Doppler lobes of the two radars, as shown in Fig. 1. These lobes are in a favourable location for observation of both squalls initiated along the sea-breeze front and continental squalls propagating to the west from the escarpment. Smaller sea breeze front and locally generated squalls can be found in either or both lobes whereas escarpment squalls typically encompass both lobes.

6. Summary.

The enhanced observing system at Darwin is providing valuable data to support a wide variety of studies into convective and mesoscale phenomena in the Maritime Continent regime. These studies include : (i) provision of ground truth information for the Tropical Rainfall Measuring Mission; (ii) the first comprehensive examination of the island thunderstorms that comprise the bulk of the "boiler box" convection; (iii) a detailed examination of the structure of tropical squall-lines from a wide range of dynamical regimes; and, (iv) experiments on mesoscale forecasting in a tropical environment.

A number of these studies are TOGA process studies are all are contributing valuable data and understanding of the tropical heat engine.

REFERENCES

Holland, G.J., 1986: Interannual Variability of the Australian summer Monsoon at Darwin : 1952-82. *Mon. Wea. Rev.,* **114**, 594-604.

Holland, G.J. and T.D. Keenan, 1980: Diurnal Variations of Convection over the "Maritime Continent". *Mon. Wea. Rev.,* **108**, 223-225.

Houze, R.A. Jr., S.G. Geotis, F.D. Marks and A.K. West, 1981: Winter monsoon convection in the vicinity of North Borneo. Part I: Structure and Time Variation of the clouds and precipitation. *Mon. Wea. Rev.,* **108**, 1595-1614.

Keenan, T.D. and L.R. Brody, 1988: Synoptic Scale Modulation of Convection during the Australian Summer Monsoon. *Mon. Wea. Rev.,* **116**, 71-85.

Keenan, T..D., G.J. Holland, M.J. Manton and J. Simpson, 1988: TRMM Ground Truth in a Monsoon Environment : Darwin, Australia. *Aust. Meteor. Mag.*, **36**, 91-90.

Keenan, T.D. and R. Carbone, 1989: A preliminary morphology of convective systems in tropical northern Australia. Paper presented at 24th Conference on Radar Meteorology, Tallahassee, Florida, March 27-31.

Keenan, T.D., B.R. Morton, M.J. Manton, G.J. Holland 1989a: The Island Thunderstorm Experiment (ITEX) - A study of Tropical Thunderstorms in the Maritime Continent. *Bull. Amer. Met. Soc.*, **70**, 152-159.

Keenan, T.D., J. McBride, G.J; Holland, N. Davidson, B. Gunn, 1989b: Diurnal variations during the Australian Monsoon Experiment (AMEX) Phase II. *Mon. Wea. Rev.,* (to appear).

Nicholls, N., J.L. McBride and R.J. Ormerod, 1982: On predicting the onset of the Australian wet season at Darwin. *Mon. Wea. Rev.,* **110**, 14-17.

Rotunno, R., J.B. Klemp, M.L. Weissman, 1988: A Theory for Strong, Long-Lived Squall Lines. *J. Atmos. Sci.*, **45**, 463-485.

Srivastava, R.C., T.J. Matejka and T.J. Lorello, 1986: Doppler radar Study of the Trailing Anvil Region Associated with a Squall Line. *J. Atmos. Res.,* **43**, 356-377.

Thiele, O.W., 1987: On Requirements for a Satellite Mission to Measure Tropical Rainfall. *NASA Reference Publication,* **1183**, 49 pp.

Williams, M. and R.A. Houze, Jr., 1987: Satellite-Observed Characteristics of Winter Monsoon Cloud Clusters. *Mon. Wea. Rev.*,**115**, 505-519.

Observations of Air-Sea Interactions in the Western Pacific Warm Pool During WEPOCS

Roger LUKAS

Joint Institute for Marine and Atmospheric Research
University of Hawaii, 1000 Pope Road
Honolulu, Hawaii, 96822 - U.S.A.

I. Introduction

The meteorological observations made during the Western Equatorial Pacific Ocean Circulation Study (WEPOCS) show the complex nature of air-sea interaction occurring in the western equatorial Pacific warm pool. The winds in the core of the western Pacific warm pool are usually light (cf. Sadler *et al.*, 1987). During these low mean wind speed conditions, a radiative-convective equilibrium (cf. Sarachik, 1978; Betts and Ridgeway, 1988) seems to hold in which the strong coupling between atmosphere and ocean, controlled by local convective processes, provides a negative feedback that stabilizes the system with near-zero net heat flux. Recently, the importance of the hydrological cycle in this coupling has become apparent, both in observations (Lukas, 1989) and in simple models (Garwood and Chu, 1989; Stevens *et al.*, 1989).

Strong winds, associated with synoptic disturbances such as monsoon surges and westerly wind bursts, appear to be responsible for most of the transfer of heat from the western Pacific Ocean to the atmosphere. The character of the convection and air-sea interaction during these disturbances is different from the low mean wind speed conditions (Keen, 1988; Lander and Morrissey, 1988; Lau *et al.*, 1988; Lukas, 1988), involving spatial scales of thousands of kilometers, versus the 10-100 km scales seen during the low mean wind speed conditions. The transition from the local 1-dimensional balance to the fully 3-dimensional interaction of the ocean and atmosphere in the western equatorial Pacific is of particular interest, as the latter thermodynamics is relevant to ENSO onset.

ORSTOM
CENTRE DOCUMENTATION
Montpellier

F30247

II. Data

A. WEPOCS

WEPOCS is a joint U.S.-Australian program to study the low-latitude western boundary currents of the Pacific Ocean, and to study the response of the warm pool of the western equatorial Pacific to the Northwest Monsoon (Lindstrom *et al.*, 1987). Figure 1 shows the cruise tracks from WEPOCS I, II, and III, conducted in June-August 1985, January-February 1986, and June-July 1988 respectively.

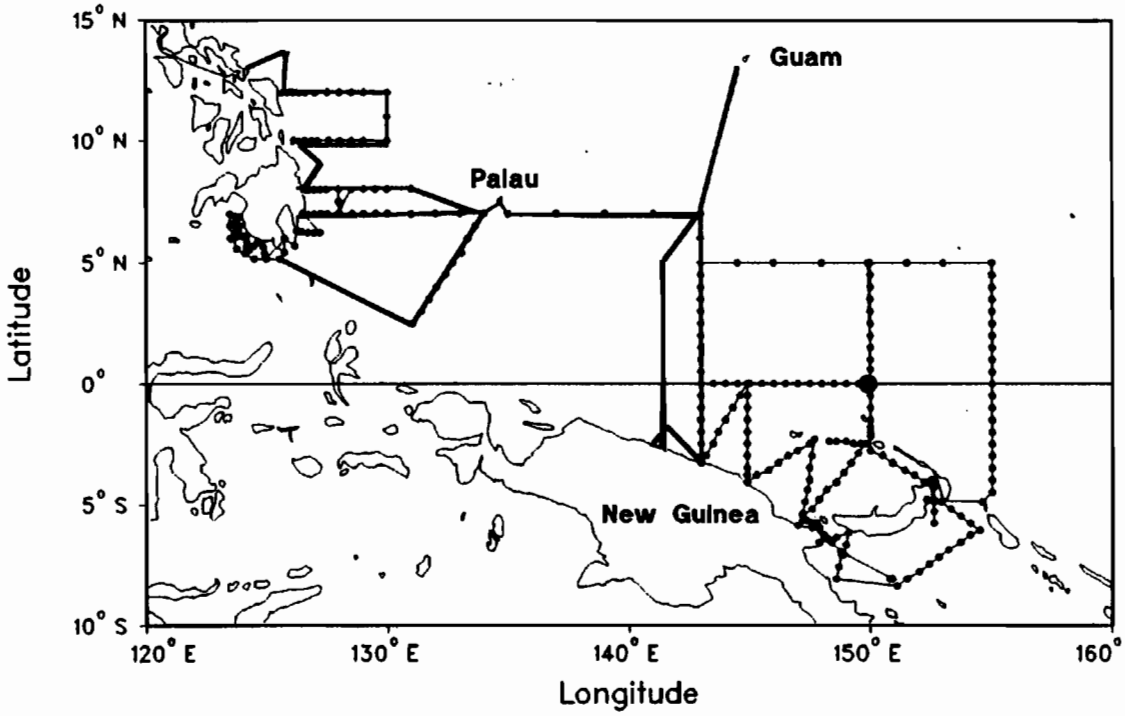

Figure 1. Cruise tracks from the three WEPOCS expeditions. The heavy line is the track of R/V MOANA WAVE during WEPOCS III (19 June - 30 July, 1988). Leg 1 is that portion to the east of Palau and north of New Guinea; the portion around Mindanao and west of Palau is Leg 2. The large sold circle indicates the location of the equatorial surface mooring during WEPOCS I, and the small sold circles indicate hydrographic station positions.

B. Observations

During WEPOCS III, hourly shipboard observations were made of sea surface temperature (SST) at 0.5 m depth, wet- and dry-bulb air temperature (from sling psychrometer at 3 m height), and wind speed and direction at 10 m (Fig. 2). Cloudiness observations were made every 3 hours and during hydrographic stations.

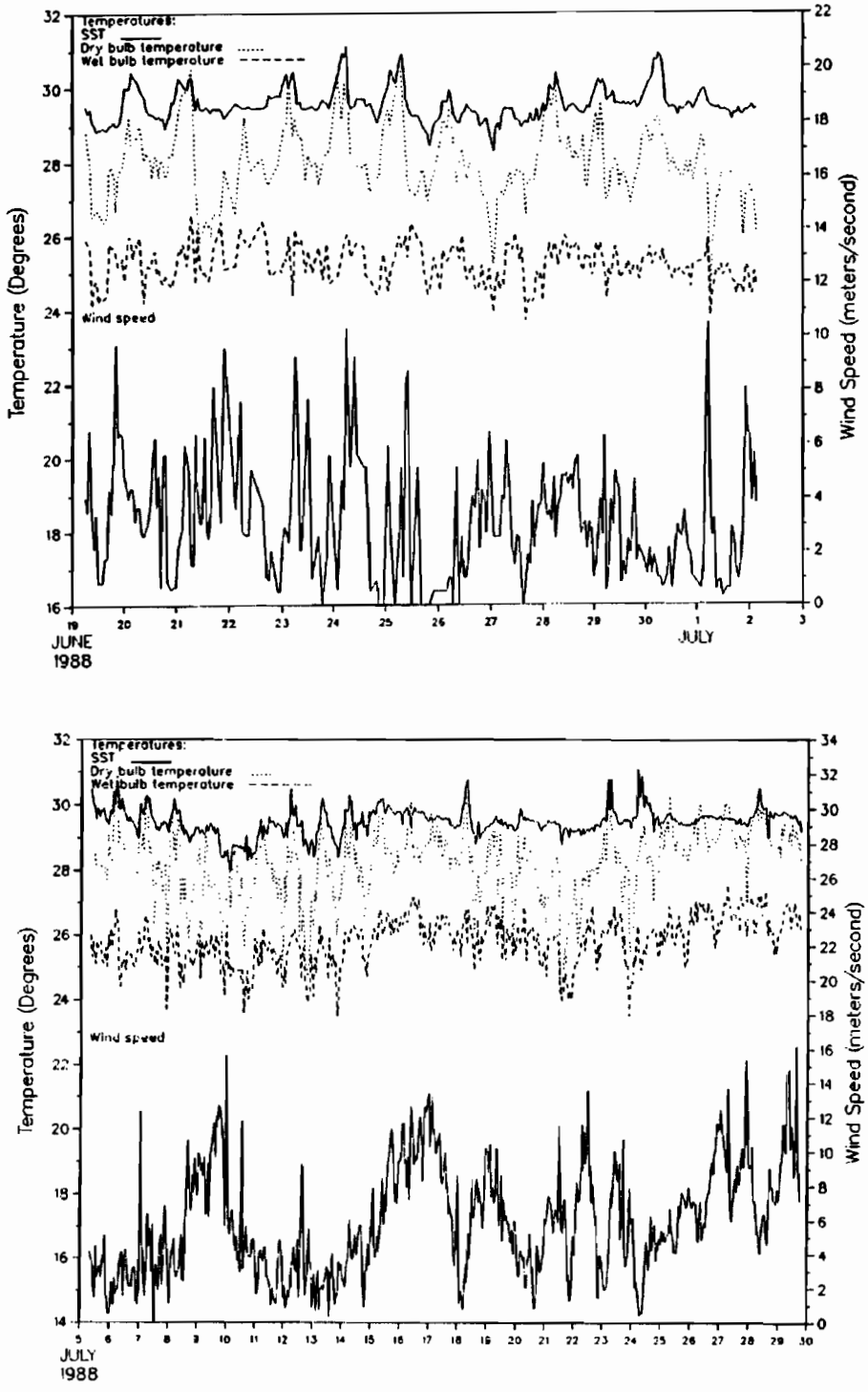

Figure 2. Hourly shipboard meteorological observations made during WEPOCS III, Leg 1 (top) and Leg 2 (bottom).

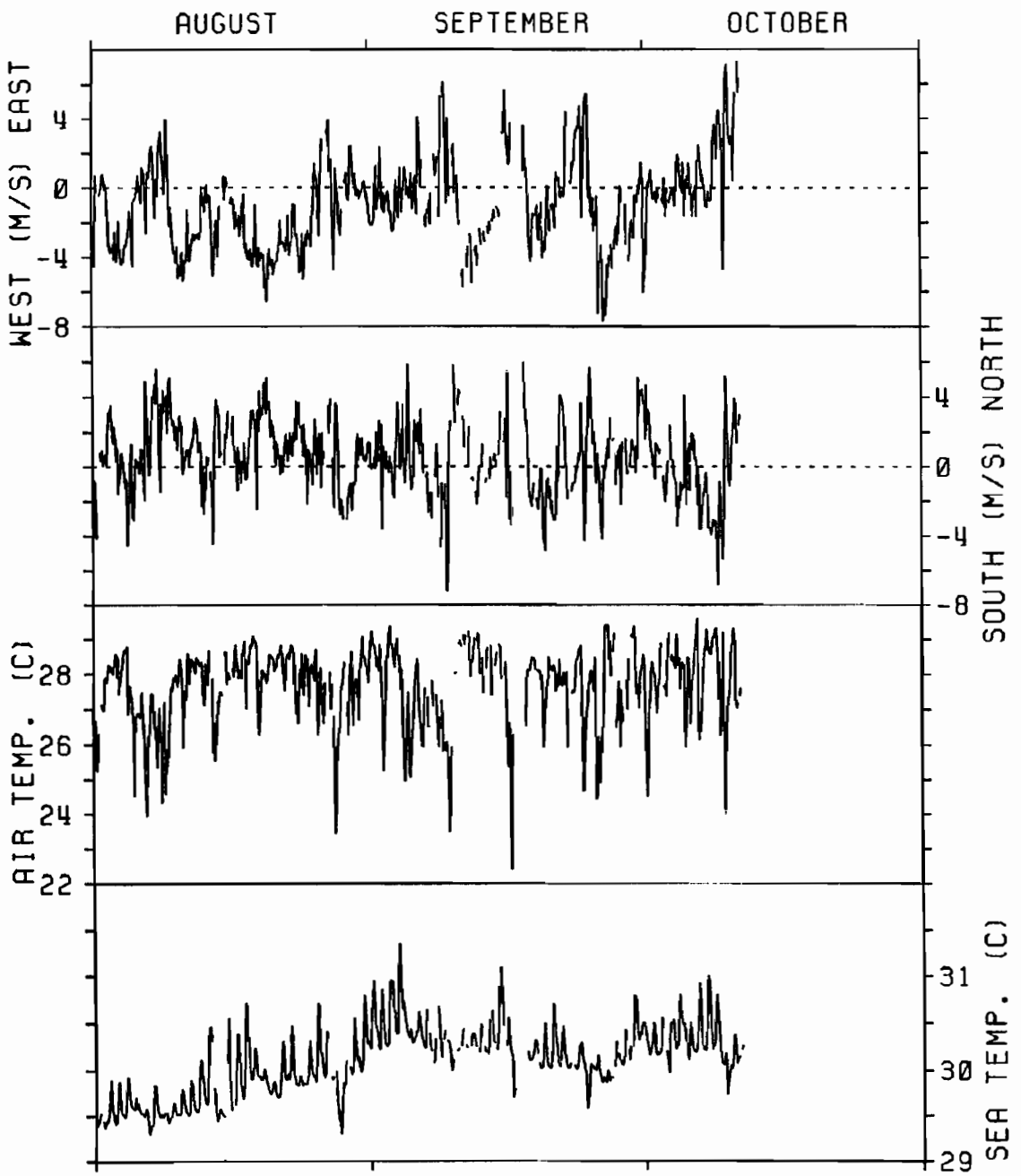

Figure 3. Time series of wind, air temperature, and sea surface temperature from the WEPOCS equatorial surface mooring of the equator at 150°E.

An Eppley full-sky radiometer was mounted on the ship's stern A-frame, and data were recorded at 1 minute intervals, but only a partial record was obtained because of data logging problems.

Wind and temperature measurements were also made from the surface buoy on the equatorial current meter mooring deployed during WEPOCS I in 1985 (Fig. 3). Winds and air temperature are from a height of 3 m, and SST is from 1 m below the surface.

During WEPOCS II and III, R/V MOANA WAVE was equipped with a thermosalinograph in the intake to the cooling pump for the hydrographic winch. The water was drawn continuously from a depth of 4 m. Seabird temperature and conductivity sensors were used, and the system sampled every 20 seconds. After editing, and calibration of salinity against water samples, the data were smoothed and subsampled at 1 minute intervals.

C. Heat flux computations

The components of the net heat flux were computed from the hourly meteorological observations using the bulk formulae as per Stevenson and Niiler (1982) and Large and Pond (1982), and with direct measurements of solar radiation. When daily averages of these fluxes were compared to fluxes calculated using daily averaged variables (Table 1), the differences were generally small. Thus, heat fluxes from daily means are presented below, using cloudiness observations to estimate insolation because the radiometer records were not complete. Note that the net insolation parameterization used in these estimates was checked against the radiometer data and the calculated insolation is biased high by -26 W/m^2 for the 24 days of data. The insolation and net heat flux were not corrected for this bias. Also, low wind-speed modifications (Liu *et al.*, 1979) were not made to the exchange coefficients. These computations will be made in the near future.

Table 1.

Difference of heat flux components and net heat flux for daily averages calculated as the flux from daily-averaged meteorological variables minus the daily-averaged fluxes calculated from hourly observations.

day	ΔQ_h	ΔQ_e	ΔQ_b	ΔQ(Wm^{-2})
172	-4.7	6.3	.6	-2.2
173	-2.3	4.4	.2	-2.3
174	-.9	11.8	2.0	-12.8
176	-4.9	8.8	.4	-4.2
177	-.5	4.7	.0	-4.2
179	-.3	2.1	.2	-2.0
180	.1	1.2	.2	-1.6
181	-3.9	1.3	.1	2.5
182	2.9	2.0	.1	-5.0
183	-3.1	5.4	-.4	-1.8
189	.1	-.5	-.9	1.3
190	.8	-2.0	-2.8	4.0
192	-1.1	7.7	.9	-7.5
193	4.6	4.4	-.2	-8.8
194	-6.1	1.9	-1.9	6.1
195	2.7	2.0	.2	-4.9
196	5.4	1.4	.6	-7.4
197	-2.5	1.3	-.6	1.8
198	-3.1	1.1	-.3	2.3
199	-7.2	1.3	1.1	4.9
200	2.0	6.6	-.7	-7.9
201	-8.5	1.0	.9	6.5
203	.4	5.6	-.2	-5.8
204	2.4	6.7	.4	-9.5
205	.9	8.8	.4	-10.1
206	-1.5	4.5	-.6	-2.5
207	-1.2	-.1	-.1	1.5
208	-1.8	-4.6	-1.0	7.4
210	-.2	1.2	.3	-1.3
avg	-1.08	3.33	-.05	-2.20
std	3.31	3.57	.91	5.38

III. Results

A. Heat Fluxes

During Leg 1, the winds were usually less than 4 m/s, except during convective downdrafts and squalls (Fig. 2). Note the very high frequency variations in these hourly data, associated with convective activity, that can not be resolved with twice or even four times per day sampling. The mean air-sea temperature difference was 1.6°C during this period, and was as large as 3-4°C during the downdrafts. This large mean air-sea temperature difference is three times larger than climatological estimates for this region (Weare *et al.*, 1981; Esbensen and Kushnir, 1981). This is probably due to biases in merchant ship temperature observations; large air-sea temperature differences have been observed on all three WEPOCS expeditions and from the WEPOCS moored buoy in the warm pool.

The time series from the WEPOCS mooring shows the light mean winds (speed less than 4 m/s most of the time, and variable direction) that are characteristic of the warm pool (Fig. 3). The air temperature is usually in the range 27-29°C, with negative excursions (attributed to convective downdrafts) below 24°C on occasion. The SST shows a strong (0.5°C amplitude) diurnal cycle during light winds (cf. Ostapoff and Worthem, 1974), and SST is usually warmer than the air temperature by 1.5-2.0°C (Lukas, 1987).

During Leg 2, the calm conditions of the warm pool region were disturbed by several surges of the Southwest Monsoon (Fig. 2). During these periods, the large air-sea temperature difference is reduced (cf. 25-30 July), and the diurnal cycle is supressed.

The insolation and latent heat are the largest terms in the net heat flux, and they also have the largest variability (Fig. 4). The sensible heat flux is proportional to the air-sea temperature difference, which varied diurnally but not as much from day to day. Large negative excursions of dry air temperature are associated with convective gust fronts (squall lines) in which the air is cold and saturated. This air is brought rapidly to the surface in downdrafts inside the convective towers. Because of the large air-sea temperature difference at these times, a considerable sensible heat flux from the ocean to the atmosphere is occurring in the region of such downdrafts (eg. Gautier, 1978; Bean and Reinking, 1978).

Both wind and humidity changes were responsible for modulating the daily mean latent heat fluxes during Leg 1 of WEPOCS III, where the mean wind speed was less than 4 m/s. The net heat flux over 11 days was 40 W/m^2, with excursions between +130 and -30 W/m^2 for the daily values. During Leg 2, several surges of the Southwest Monsoon resulted in winds of 8-14 m/s for 2-3 days at a time, and an average wind speed of about 6 m/s. The large latent heat losses (200-270 W/m^2) and reduced insolation during the monsoon surges resulted in net heat losses

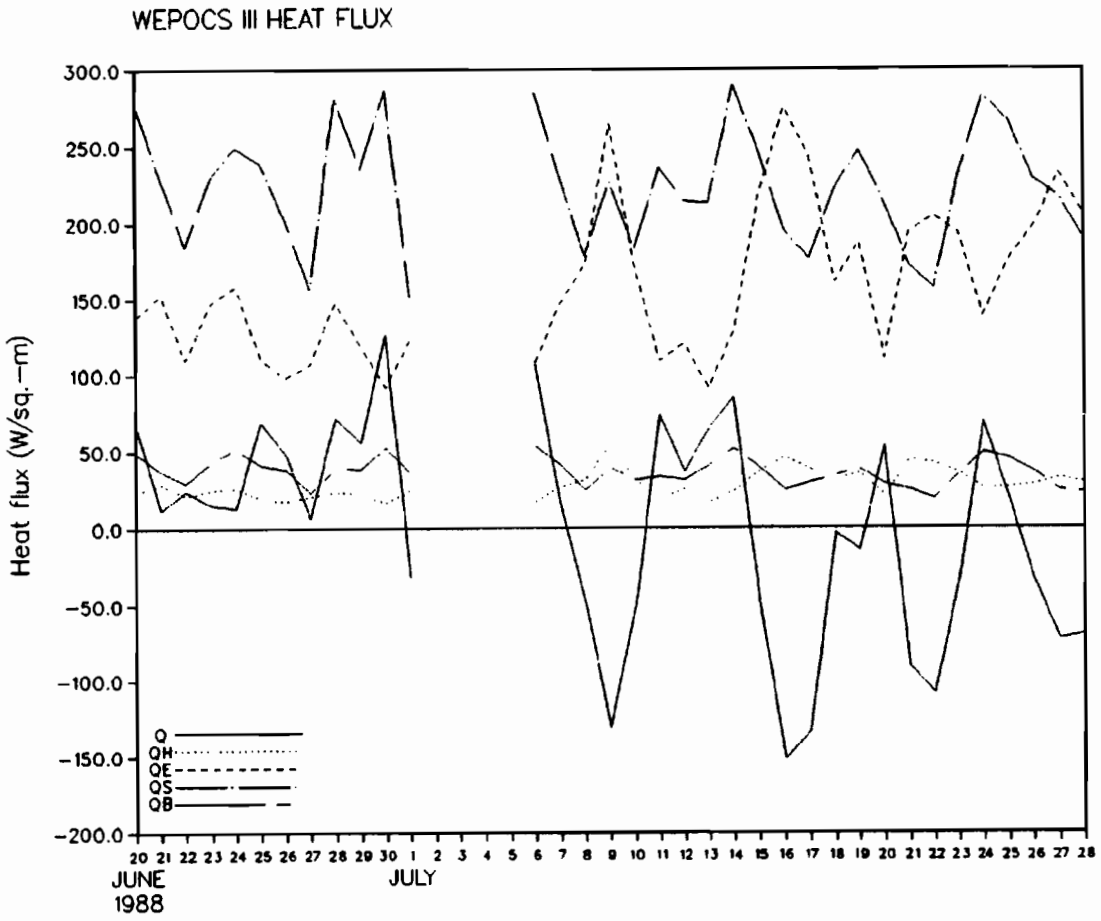

Figure 4. Heat fluxes computed from daily mean meteorological variables observed during WEPOCS III. See text for description.

from the ocean of 100-150 W/m^2 during these periods, and an average over 23 days of -20 W/m^2. Note that these net fluxes may be biased high by 20-30 W/m^2 because the algorithm used to calculate insolation from daily cloud coverage is probably not applicable to the cloud types found in the western tropical Pacific.

B. Precipitation signatures

The thermosalinograph record from 21 July 1988 (near 8°N, 128.5°E), shows the effect of the strong precipitation and convective downdrafts, which is seen in the freshening of sea surface salinity, and the cooling of SST (Fig. 5). The width of this cold, fresh puddle is about 20 km, comparable to the scale of the convection cell. It is not clear whether the cooler water is due to cold rain, or to heat being extracted from the ocean by cold downdrafts, although previous observations (Greenhut, 1978) suggest the latter, which is consistent with the 1-dimensional radiative-convective equilibrium theory.

Temperature and salinity from the thermosalinograph on R/V MOANA WAVE during WEPOCS III Leg 1 show the aggregate effect of the mesoscale convection on the upper ocean temperature and salinity fields (Fig. 6). Individual convective cells freshen and cool the upper ocean as indicated by the heavy vertical lines. The

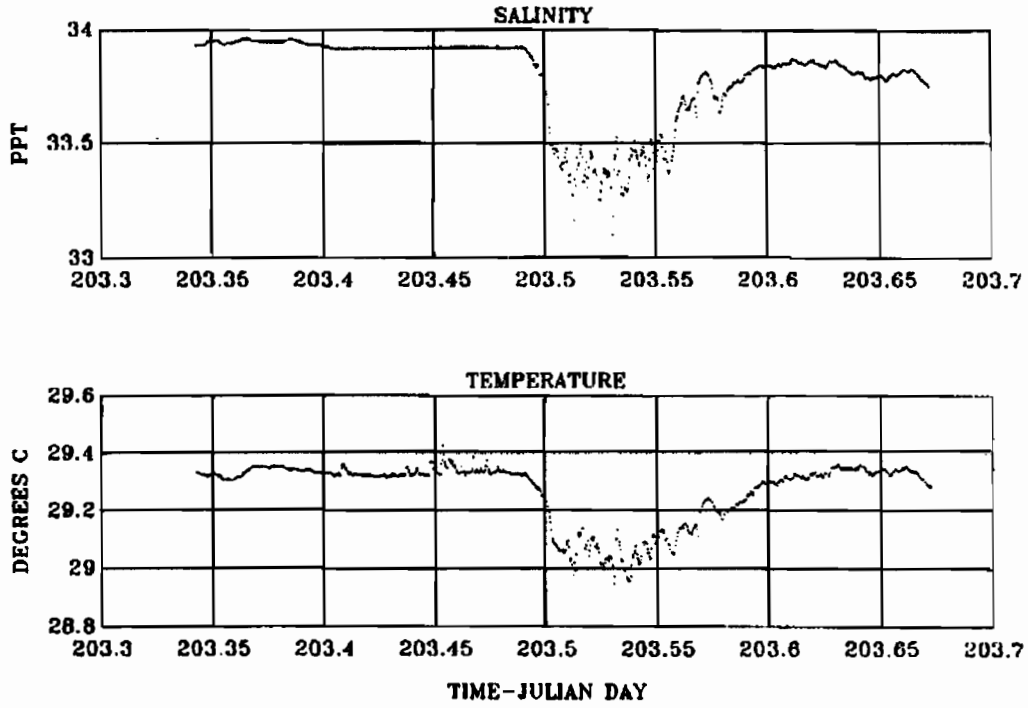

Figure 5. Segment of WEPOCS III thermosalinograph record (salinity at top, temperature at bottom) showing the depression of salinity and temperature as R/V MOANA WAVE passed through a convective cell. Approximate length scale associated with this large freshwater input is 20 km.

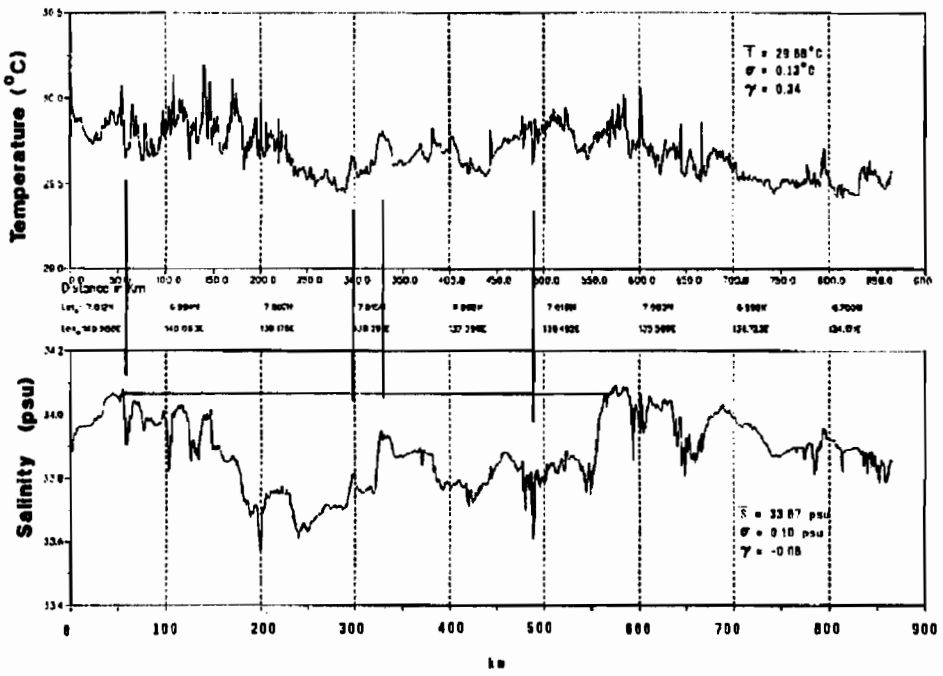

Figure 6. A two-day segment of the thermosalinograph record from R/V MOANA WAVE during the WEPOCS III expedition showing temperature (top) and salinity (bottom) at a depth of 4 m versus distance (km) along track. Note the general depression of salinity between 50 km and 550 km, as well as the more localized depressions (eg. 250-300 km).

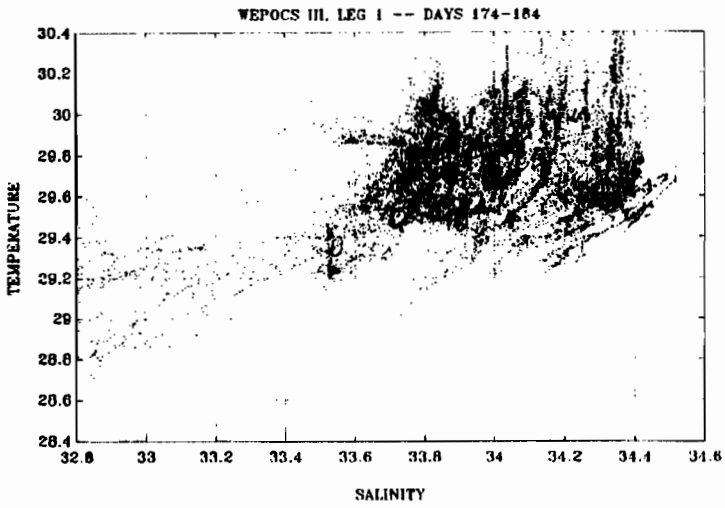

Figure 7. Temperature-salinity diagram for thermosalinograph data from WEPOCS III for the same period as the observations in Fig. 6. Note the general tendency for low salinity to be associated with lower temperature.

freshening of the sea surface between 100 and 550 km along track is attributable to a mesoscale convective complex of this spatial extent. The diurnal cycle in SST is seen in the apparent long wavelength variation.

A surface temperature-salinity diagram (Fig. 7) shows the strong correlation of SST and surface salinity variations, with cold, fresh "puddles" from mesoscale convection mixing with warmer, saltier waters. This good correlation suggests that the buoyancy forcing of the warm pool is dominated by mesoscale convection during the time of these observations. Elliot (1974) did not find such a good correlation during BOMEX, probably because the relative influence of wind and buoyancy forcing was so different from the western equatorial Pacific.

IV. Discussion

From the WEPOCS observations, it is clear that air-sea fluxes in the warm pool are dominated by processes associated with mesoscale convection. Thus, it is appropriate to review these processes here. The view of the tropical convective cell that arose from the intensive GATE observations is summarized by Bean and Reinking (1978). The complexity of the circulation and the vertical fluxes is substantial; a complete description is given by Leary and Houze (1979).

The heaviest rain occurs in the convective tower, but when weighted by area, the stratiform anvil contributes as much as 50% of the precipitation. Within the tower, strong downdrafts occur leading to the formation of gust fronts, and because of the rapid sinking, this air remains cold. Because of the very thick and dark cloud in the tower, incoming solar radiation is severely attenuated. In the regions outside of the convective cell, the cloud cover is generally thin stratocirrus cloud,

permitting solar radiation to reach the sea surface without much attenuation. This region is where cooler, drier air from the outflow regions of the convective cells returns to the near-surface layers (Betts and Ridgway, 1988).

The incoming solar radiation is primarily modulated by the diurnal cycle, and by the clouds associated with mesoscale convection. When the winds are light, and the skies are clear, the SST responds rapidly to the heating (Ostapoff and Worthem, 1974), as does the overlying atmosphere. This can be seen in Figs. 2 and 3, where the diurnal cycle of SST is as large as 1°C, and the diurnal cycle of air temperature is about 2°C.

According to bulk parameterizations, the latent heat flux depends on the vapor pressure difference between air at the sea surface temperature and that of the air above the sea surface, and on the wind speed. For the case of no wind, the bulk formula predicts no moisture flux. Liu *et al.* (1979) suggest that this is not the case, and that the exchange coefficient in this formula varies strongly with wind speed at low wind speeds, especially when the air-sea temperature difference is large. The subsiding air outside the convective towers is relatively dry (see the large difference between dry bulb and wet bulb air temperatures in Fig. 2), and is thus capable of picking up substantial moisture.

The heat flux depends on SST, but changes of SST depend strongly on mixed layer thermodynamics. The momentum and buoyancy fluxes at the sea surface, combined with the initial buoyancy profile, determine the evolution of the mixed layer and its heat budget. Thus, precipitation and salinity effects, through their influence on the buoyancy flux and the buoyancy profile, may exert a control on the mixed layer heat budget (Ostapoff *et al.*, 1973; Miller, 1976), and thus on the flux of heat to the atmosphere.

V. Conclusions

The fluxes of heat and moisture in the western Pacific warm pool are generally controlled by mesoscale convection, with a quasi-one-dimensional radiative-convective equilibrium in which there is near-zero net heat flux on time scales longer than about one day (Godfrey and Lindstrom, 1989). This equilibrium is occasionally disturbed by synoptic scale atmospheric events; it is during these times that heat is effectively extracted from the warm pool by the atmosphere (Meyers *et al.*, 1986). The horizontal scales of SST and sea surface salinity variability are controlled by the convective processes and the synoptic scale forcing.

Scale interactions occur when processes on at a particular time or space scale modulate the energy of processes on different time or space scales. This can arise only from nonlinear thermodynamics. The turbulent fluxes of heat, moisture, and momentum between the upper ocean and the lower atmosphere are nonlinear, and

are dependent on one another. Synoptic scale forcing modulates the atmospheric convection, and thus substantially modulates the air-sea fluxes (eg. Seguin and Kidwell, 1980). It is this synoptic atmospheric forcing which can change the warm pool system from a nearly one-dimensional radiative-convective equilibrium into a fully three-dimensional system.

Acknowledgements

Mr. Toshiaki Shinoda computed the heat fluxes from WEPOCS III meteorological observations. Mrs. Mimi Baker processed and plotted the meteorological and thermosalinograph data. The author gratefully acknowledges the support of the National Science Foundation under grants OCE-8610458 and OCE-8716510 for the Western Equatorial Pacific Ocean Circulation Study (WEPOCS). This is Joint Institute for Marine and Atmospheric Research contribution No. 89-0177 and Hawaii Institute of Geophysics contribution No. HIG-2156.

REFERENCES

Bean, B.R. and R.F. Reinking, 1978: Marine turbulent boundary layers fluxes of water vapor, sensible heat, and momentum during GATE. in Turbulent Fluxes Through The Sea Surface, Wave Dynamics, and Prediction. A. Favre and K. Hasselmann, eds. Plenum Press, New York, 21-33.

Betts, A.K. and W. Ridgway, 1988: Coupling of the radiative, convective, and surface fluxes over the equatorial Pacific. J. Atm. Sci., 45, 522-536.

Elliot, G.W., 1974: Precipitation signatures in sea-surface-layer conditions during BOMEX. J. Phys. Oceanogr., 4, 498-501.

Esbensen, S.K. and Y. Kushnir, 1981: The heat budget of the global ocean: An atlas based on estimates from surface marine observations. Climate Research Institute Rept. #29, Oregon State University, 27 pp + figs.

Gautier, C., 1978: Some evidence of cool surface water pools associated with mesoscale downdrafts during GATE. J. Phys. Oceanogr., 8, 162-166.

Garwood, R.W. and P.C. Chu, 1989: Hydrological effects on the air-sea coupled system. This volume.

Godfrey, J.S. and E. Lindstrom, 1989: On the heat budget of the equatorial West Pacific surface mixed layer. J. Geophys. Res., 94, 8007-8017.

Greenhut, G.K., 1978: Correlations between rainfall and sea surface temperature during GATE. J. Phys. Oceanogr., 8, 1135-1138.

Keen, R., 1988: Equatorial westerlies and the Southern Oscillation. in Proceedings of the U.S. TOGA Western Pacific Air-sea Interaction Workshop, R. Lukas and P. Webster, eds., USTOGA 8, U. Corp. Atmos. Res., 121-140.

Lander, M.A. and M.L. Morrissey, 1988: Genesis of twin typhoons associated with a west wind burst in the equatorial western Pacific: A case study. in Proceedings of the U.S. TOGA Western Pacific Air-sea Interaction Workshop, R. Lukas and P. Webster, eds., USTOGA 8, U. Corp. Atmos. Res., 163-174.

Large, W.G. and S. Pond, 1982: Sensible and latent heat flux measurements over the ocean. J. Phys. Oceanogr., 8, 1135-1138.

Lau, K.-M., L. Peng, C.H. Sui, and T. Nakazawa, 1988: Dynamics of super cloud clusters, westerly wind bursts, 30-60 day oscillations and ENSO: An unified view. J. Met. Soc. Japan, submitted.

Leary, C.A. and R.A. Houze, Jr., 1979: The structure and evolution of convection in a tropical cloud cluster. J. Atmos. Sci., 36, 437-457.

Lindstrom, E., R. Lukas, R. Fine, E. Firing, S. Godfrey, G. Meyers, and M. Tsuchiya, 1987: The Western Equatorial Pacific Ocean Circulation Study. Nature, 330, 533-537.

Liu, W.T., K.B. Katsoros, and J.A. Businger, 1979: Bulk parameterization of air-sea exchanges of heat and water vapor including the molecular constraints at the interface. J. Atm. Sci., 36, 1722-1735.

Lukas, R., 1987: WEPOCS and the US-PRC Bilateral: Western Pacific air-sea interaction studies. in Further Progress in Equatorial Dynamics, E. Katz and J. Witte, eds., Nova University Press, 71-85.

Lukas, R., 1988: On the role of western Pacific air-sea interaction in the El Niño-Southern Oscillation Phenomenon. in Proceedings of the U.S. TOGA Western Pacific Air-sea Interaction Workshop, R. Lukas and P. Webster, eds., USTOGA 8, U. Corp. Atmos. Res., 43-69.

Lukas, R., 1989: Freshwater input to the western equatorial Pacific Ocean and air-sea interaction. In: Proceedings of the Symposium on Western Tropical Pacific Air-Sea Interactions, Beijing, People's Republic of China, 15-17 November 1988.

Lukas, R. and E. Lindstrom, 1987: The mixed layer of the western equatorial Pacific Ocean. in Proceedings of the 'Aha Huliko'a Hawaiian Winter Workshop on The Dynamics of the Oceanic Surface Mixed Layer, Honolulu, January 1987, P.Muller and D.Henderson, eds., 67-94.

Meyers, G., J.-R. Donguy, and R.K. Reed, 1986: Evaporative cooling of the western equatorial Pacific Ocean by anomalous winds. Nature, 323, 523-526.

Miller, J., 1976: The salinity effect in a mixed layer ocean model. J. Phys. Oceanogr., 6, 29-35.

Ostapoff, F., Y.Tarbeyev, and S. Worthem, 1973: Heat flux and precipitation estimates from oceanographic observations. Science, 180, 960-962.

Ostapoff, F. and S. Worthem, 1974: The intradiurnal temperature variation in the upper ocean layer. J. Phys. Oceanogr., 4, 601-612.

Sadler, J.C., M.A. Lander, A.M. Hori, and L.K. Oda, 1987: Tropical marine climatic atlas, Volume II, Pacific Ocean. UHMET87-02, Department of Meteorology, University of Hawaii, 27 pp.

Sarachik, E.S., 1978: Tropical sea surface temperature: An interactive one-dimensional atmosphere-ocean model. Dyn. Atm. Oceans, 2, 455-469.

Seguin, W.R. and K.B. Kidwell, 1980: Influence of synoptic scale disturbances on surface fluxes of latent and sensible heat. Deep-Sea Res., 26(suppl. I), 51-64.

Stevens, D., Q. Hu, and G. Stephens, 1989: The hydrological cycle of the intraseasonal oscillation. This volume.

Stevenson, J., and P.P. Niiler, 1983: Upper Ocean Heat Budget During the Hawaii-to-Tahiti Shuttle Experiment. J. Phys. Oceanogr., 13, 1894-1907.

Weare, B.C., P.T. Strub, and M.D. Samuel, 1981: Annual mean surface heat fluxes in the tropical Pacific Ocean. J. Phys. Oceanogr., 11, 705-717.

Satellite Derivation of Ocean-Atmosphere Heat Fluxes in a Tropical Environment

M. NUNEZ and K. MICHAEL

Department of Geography and Environmental Studies,
University of Tasmania,
Hobart, Tasmania - Australia

ABSTRACT

Satellite estimates of ocean/atmosphere heat fluxes were compared with surface measurements taken at John Brewer Reef (18°38'S, 147°E) located 80 km NNE of Townsville, Australia. For a 45 week period all the components of the surface heat fluxes : net radiation, sensible and latent heat fluxes, were estimated from surface observations and averaged on a weekly basis. Concurrent satellite observations in the vicinity of John Brewer Reef consisted of GMS visible reflectance data, NOAA-9 soundings of temperature and humidity, and sea surface temperatures derived from a blend of ship observations and NOAA-9 data. Wind estimates were derived from the Darwin Tropical Analysis. All satellite data were tested for their ability to reproduce surface heat fluxes.

The rms differences (measured versus modeled) between the weekly averaged values of net radiation, the turbulent heat flux (sensible plus latent) and the total ocean/atmosphere heat flux were 16 Wm^{-2}, 45 Wm^{-2} and 48 Wm^{-2} respectively. Averaged over the 45 week period, a mean difference of 9 Wm^{-2} (measured-modeled) was obtained for the total ocean-atmosphere heat exchange.

1. Introduction

Large scale studies of ocean/atmosphere heat fluxes are traditionally based upon marine weather reports. However these data sets are scarce in many ocean areas not covered by shipping routes. The reliability of monthly mean fluxes has been questioned in these areas, as biases may result from the inclusion of temporally and/or spatially sparse data (Ramage, 1984; Sarachik, 1984).

It is within this framework that satellite data offer distinct advantages. Geostationary and polar-orbiting satellites cover large areas of the globe at regular intervals, providing information on the state of the atmosphere and ocean. In this study we assess the applicability of satellite data to provide estimates of ocean/atmosphere heat fluxes at a location in the tropical western Pacific ocean. The emphasis has been placed on long term high quality surface measurements as opposed to short term ship estimates from a variety of geographic locations.

The total ocean/atmosphere heat flux (Q_A) may be partitioned into its component fluxes consisting in net radiation (Q^*) and sensible (Q_H) and latent (Q_E) heat fluxes :

$$Q_A = Q^* + Q_H + Q_E \qquad (1)$$

In turn the net radiation can be written in terms of the incoming (K_D) and reflected (K_U) solar radiations fluxes and the incoming (L_D) and emitted plus reflected longwave radiation fluxes (L_U) :

$$Q^* = K_D + L_D - K_U - L_U \qquad (2)$$

ORSTOM
CENTRE DOCUMENTATION
Montpellier

F 30248

In this study all the terms in equations (1) and (2) with exception of K_U were obtained from direct surface measurements. Similarly satellite data, or satellite related data, were used to estimate all the component fluxes in the above equations.

2. Data acquisition

The measurement period encompassed the dates 1 June 1985 to 1 April 1986 (Figure 1). Measurements were taken from a wooden floating pontoon, anchored to the reef bottom (~7m depth). A tower was constructed on the pontoon and all atmospheric sensors were located free from obstructions and 4.5 m above the platform and 5.5 m above the water. A Campbell CR21X micrologger was used to record all data at a frequency of 0.5 seconds. Table 1 provides details on all the meteorological variables that were measured.

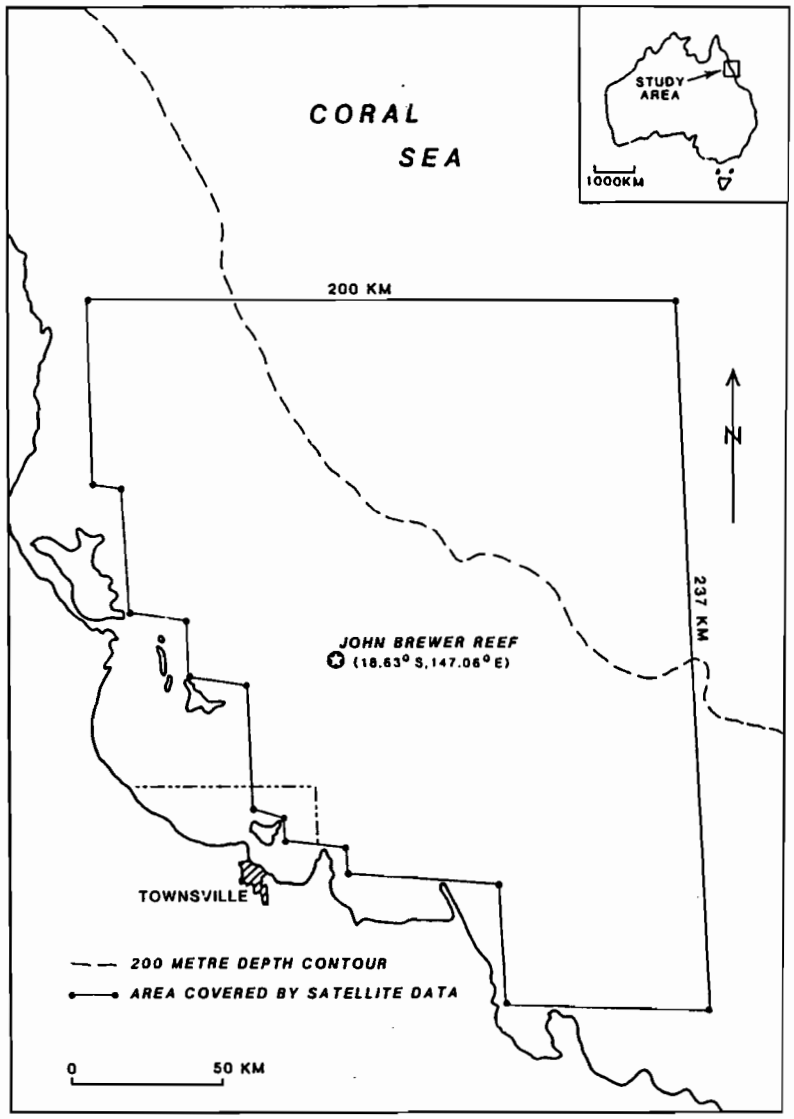

FIG.1. Location of the study region showing the area of GMS coverage and the location of John Brewer Reef.

During the course of the measurement period, there were no weeks with predominantly westerly of southerly winds which would have indicated the presence of air masses of

continental origin. The reef coral was only partially exposed (<10 percent) at extremely low tides which occurred infrequently. Measurements of surface water temperature with an infrared radiometer (J. Hacker, Flinders University of South Australia, pers. comm.) have shown the lagoon to be occasionally 0.1 to 0.3°C warmer than surrounding waters.

TABLE 1 Instruments used to measure ocean-atmosphere heat fluxes at John Brewer Reef : 1 June 1985 - 1 April 1986

Instrument	Measured Meteorological Variable	Days Available
Kipp & Zonen pyranometer	(a) incoming solar radiation	225
Eppley precision pyrgeometer	(b) incoming longwave radiation	107
copper/constantan thermocouples	(c) air temperature	225
copper/constantan thermocouples	(d) sea surface temperature	173
Vaisala humidy sensor	(e) relative humidity	225
Met One (3 cup) anemometer and locally built (4 cup) anemometer	(f) wind speed	225

Calculated Fluxes	Relevant Meteorological Variable(s)	Days Available
incoming global radiation	(a)	225
outgoing global radiation	(a)	225
incoming longwave radiation	(b)	107
outgoing longwave radiation	(d)	107
latent heat	(c),(d),(e),(f)	173
sensible heat	(c),(d),(e),(f)	173

Table 2 provides details on satellite and related data that were used to derive the surface heat fluxes. A continuous data set with no missing values would imply a total of 315 days with GMS and NOAA/TOVS and NOAA/AVHRR data. This was not achieved.

Data for the GMS pixel closest to John Brewer Reef was manually retrieved on a daily basis. NOAA/TOVS data containing three levels of precipitable water vapor and 15 levels of air temperature, was obtained from NOAA-NESDIS (Washington, DC) as a TOVS sounding data product. These data were retrieved in a box of 4° x 4° square with John Brewer Reef being located in the southwest corner. On each day all soundings in the square were averaged, with larger weighting applied to those soundings closest to John Brewer Reef.

Sea surface temperatures were extracted from a monthly averaged data set consisting of a blend of ship reports and NOAA-9 multi-channel sea surface temperatures (Reynolds, 1988). An average monthly sea surface temperature was estimated for the study area as a weighted average of the three closest grid points, which were spaced at two degree intervals. These monthly values were temporarily interpolated to provide mean weekly sea surface temperatures. No satellite-derived estimates of near-surface wind were available. In the absence of this important parameter, data from the Darwin Tropical Wind Analysis were substituted. Values from the grid point at 17.5°S, 147.5°E were averaged to estimate at mean weekly wind speed for the study area.

TABLE 2 Satellite and ancillary data used to estimate ocean-atmosphere heat fluxes near John Brewer Reef : 1 June 1985 - 1 April 1986

Data Type	Frequency	Spatial Resolution	Days with at least one observation	Related Heat Fluxe(es)
GMS visible	3 times daily	2.5 x 3 km	303	K_D,K_U,L_D
NOAA/ TOVS	2 times daily	300 x 300 km	209	L_D,Q_E,Q_H
NOAA/ AVHRR plus ship SSTs	monthly	1° x 1°	interpolated weekly	L_U
Darwin Tropical wind Analysis	2 times daily	2.5° x 2.5°	315	Q_E,Q_H

3. Analysis

The following relationships were derived to estimate surface heat fluxes from satellite data.

a. Incoming Global Radiation

A relationship was defined between the daily transmissivity of global radiation (τ) and the satellite-determined earth-atmosphere reflectivity (αE_A). When applied to half the data set the following relationship was obtained :

$$\tau = K_D/K_O = 0.773 - 1.037\ \alpha E_A; \quad \gamma^2 = 0.89 \quad ; \quad S.E. = 0.052 \qquad (3)$$

where K_O is the extra terrestrial global radiation, a function of latitude and time of year. When tested on the remainder of the data, this relation could estimate K_D on a daily basis with a mean difference of -2 Wm^{-2} (measured-predicted) and a rms difference of 28 Wm^{-2}. This rms difference represents an error of 11 percent in the mean measured value of 246 Wm^{-2}.

b. Reflected Solar radiation

The upwelling solar radiation from the water surface (K_U) can be written as :

$$K_U = \alpha_W K_D \qquad (4)$$

Due to measurement problems and the relative insensitivity of this term (Nunez et al., 1972), the albedo term α_W was determined from the tables of Payne (1972) corresponding to a latitude of 20°S. The resulting α_W daily values were 0.07 for May through August and 0.06 for all other months.

c. Incoming Longwave Radiation

The LOWTRAN 6 model for atmospheric transmittance and radiance (Kneizys et al., 1983) was applied on the daily TOVS data for the estimation of L_D.

Reconstruction of the temperature and humidity profiles from TOVS data was based upon the technique of Darnell et al. (1983), modified to include a well mixed planetary boundary layer capped by an inversion. It is physically reasonable to treat the atmospheric structure in this fashion since the area is subjected to winds with large oceanic fetches for most of the study period. No distinction was drawn between winds of northerly and winds of south-easterly origin. Below the inversion the atmospheric features constant potential temperature and specific humidity, except in the surface boundary layer where the air temperature and specific humidity, change to take the characteristics of the ocean surface. Further details are provided in Michael and Nunez (1989).

The LOWTRAN 6 model solves for L_D for totally cloudy (L_{DC}) and cloudless (L_{DO}) conditions. The actual longwave radiation can then be given as :

$$L_D = (1\text{-}C)\, L_{DO} + C L_{DC} \tag{5}$$

Values of C were derived using GMS visible data and tables presented by Taylor and Stowe (1984) on low level and middle level cloud albedo. Denoting α_L as the minimum satellite reflectivity for the month, and α_H as the threshold reflectance value for totally overcast conditions, the following relations is obtained :

$$C = \begin{cases} 0 & \alpha_{EA} < \alpha_L \\ (\alpha_{EA} - \alpha_L)/(\alpha_H - \alpha_L) & \alpha_L < \alpha_{EA} < \alpha_H \\ 1 & \alpha_H < \alpha_{EA} \end{cases} \tag{6}$$

Cloud heights were derived from the TOVS cloud top pressure, and assigned fixed pressures of 850 hPa and 750 hPa for low and middle clouds respectively. No TOVS cloud top pressures were consistent with the presence of clouds.

Pyrgeometer measurements were available during the summer and autumn period for a total of 125 days. Of these, there were 107 days with concurrent pyrgeometer and GMS data, and 57 days with additional TOVS data. For this 57 days period, the mean difference produced by the model just described is 5 Wm^{-2} (the model under-predicts) and the rms difference in the daily estimates of L_D is 14 Wm^{-2}.

d. Outgoing Longwave Radiation

This term is mainly dependent on the satellite derived sea surface temperature. Best agreement with surface measurements were obtained from the Reynolds blended shipboard/NOAA AVHRR data set (Reynolds, 1988). The outgoing longwave radiation can be written as :

$$L_U = \varepsilon\theta T_S^4 + (1\text{-}\varepsilon) L_D \tag{7}$$

where T_S is the surface temperature, θ is the Stefan-Boltzmann constant and ε is the surface emissivity which was taken as 0.97 (Davies et al., 1971).

e. Turbulent Fluxes

Both surface estimates and the satellite technique use the bulk aerodynamic formulae, with stability-dependent bulk transfer coefficients as described by Large and Pond (1982) :

$$Q_E = \rho\, L C_E\, U_a (q_s - q_a); \qquad Q_H = \rho\, C_P C_H U_a (T_s - T_a) \tag{8}$$

where ρ is the air density, L is the latent heat of vaporization of water, C_P is the specific heat of air at constant pressure, C_E and C_H are the bulk transfer coefficients for sensible and latent heat flux respectively, q and T are the specific humidity and temperature at the water

surface (subscript "s") and 10 meter height (subscript "a") and U_a is the wind speed at 10 meters.

Using the satellite technique Qs can be readily derived from the surface temperature, and U_a is given by the Darwin Tropical Wind Analysis. The problems is to derive q_a in terms of the precipitable water vapor as obtained from TOVS. Various relationships were tested, including that described in Liu (1986) for 40 stations in the mid-latitude and tropics. Also tested was a simple linear relationship between W (precipitable water vapor) and $q_a$for John Brewer Breef. The best relationship was obtained by a plot of q_a versus Δ q where $\Delta q = q_s - q_a$ is treated as a dependent variable

$$\Delta q = 0.012 - 0.00018W_o; \qquad r^2 = 0.27; \quad S.E. = 0.002 \tag{9}$$

This relationship is statistically significant at the 1 percent level. Equations 8 and 9 were applied for the 26 weeks in which Q_E values were available from measurements at John Brewer Reef. The rms weekly difference is 40 Wm^{-2}, which is considerably lower than the value using the Liu (1988) technique (104 Wm^{-2}) and the W versus q_a linear regression (69 Wm^{-2}).

The lack of success of the polynomial regressions technique of Liu is probably a result of fundamental differences between W supplied by NOAA-9/TOVS and by Nimbus-7/SMMR. To ensure compatibility with radiosonde data, Liu (1988) describes how empirical correction formulae for SMMR W data were determined for monthly or yearly intervals. The TOVS data underwent no similar treatment so that it is possible that they were not representative of the field of W which would have resulted from a network of radiosondes in the study region. However comparison of our TOVS data with radiosonde data from Willis Island (16°8'S; 149°59'E) gave good results. Nevertheless there is need to subject the TOVS data to the same spatial and temporal scales as that applied by Liu to the Nimbus-7 SMMR data. It is likely that a similar relationship will be derived.

The sensible heat flux is a small term in the marine environment. The satellite technique cannot be applied in equation 8 since near surface air temperatures are not available from satellite data. Instead the Bowen ratio technique, which is deemed to be a function of surface temperature (Priestl and Taylor, 1972; Hicks and Hess, 1977) was used. The Bowen ratio can be described as :

$$\beta = 0.79\,(C_p/L_s) - 0.21 \tag{10}$$

where S is the slope of the saturation specific humidity/temperature curve. The temperature dependence of β comes mainly through S. The sensible heat QH can be given as

$$Q_H = \beta Q_E \tag{11}$$

For each week, the blended sea surface temperature was used to determine the ratio C_p/L_s. β was obtained from equation 10 and applied in equation 11 to determine Q_H.

Few Q_H values exceed 10 Wm^{-2} in magnitude. The mean difference between surface measurements and the predictions was -1.6 Wm^{-2}, and the rms difference was 8.5 Wm^{-2}, of the same magnitude as the average weekly sensible heat flux. At this time scale Q_H are not meaningful, although they are useful in providing an estimate of the correct order of magnitude for the heat balance.

f. Time Series of Weekly Heat Fluxes

Figure 2 shows how the weekly satellite estimates of the turbulent heat fluxes compare with surface measurements. In deriving the net solar radiation flux, equations 3 and 4 were applied to the entire data set. As may be noticed, both measurements and models agree closely in the overall seasonal trend. The net longwave radiation flux is a conservative quantity which does not show a seasonal trend.

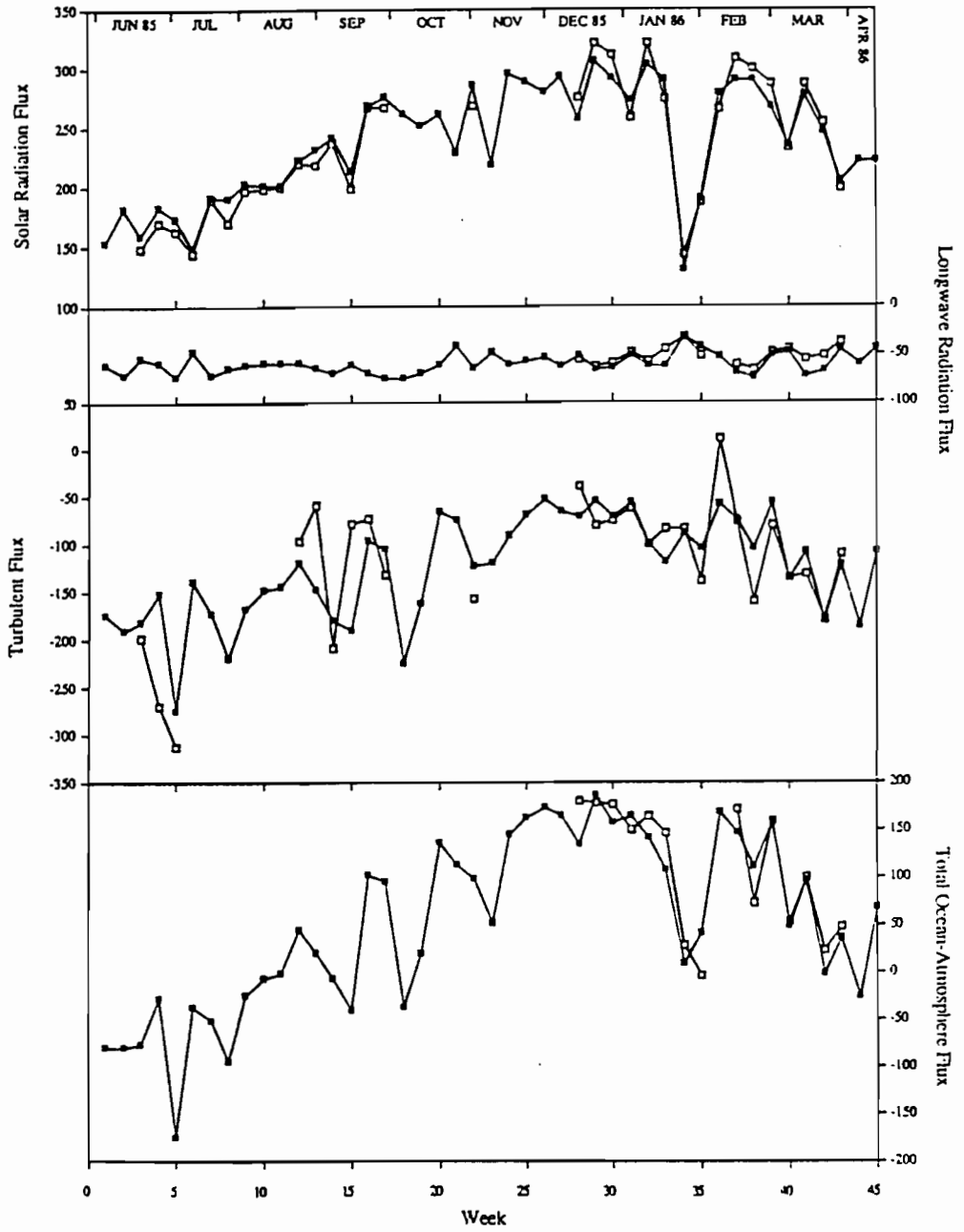

FIG.2. Weekly time series of net solar radiation flux (K*), net longwave radiation flux (L*), total turbulent heat flux (Q_t) and the total ocean-atmosphere heat flux (Q_a). Surface measurements are represented by open squares, and the satellite-derived estimates are drawn as filled squares. Negative heat fluxes imply a heat loss by the ocean. All units are Wm^{-2}.

The form of the variations in outgoing turbulent flux (Q_T) indicate that wind speed is the dominant influence. In winter (June-August) the south-easterly trade winds are strong and the latent heat flux often exceeds 200 Wm^{-2} in magnitude. In summer the northerly winds are moister and lighter; the magnitude of Q_E drops. In March as the winds strengthen, the correspondence between the surface and satellite-bases fluxes is limited, a consequence of the difficulty in reproducing the 10 meter specific humidity.

The total ocean/atmosphere heat flux is dominated by the energy gain by solar radiation and loss by latent heat flux. In winter Q_E is large and Q* is low so that the ocean is loosing energy. By mid-August the ocean starts gaining energy. This pattern persists until mid-December when a maximum heat gain of 180 Wm^{-2} is reported.

4. Conclusion

In summary, the rms differences (measured versus modeled) between the weekly averaged values of net radiation, the latent heat flux and sensible heat flux were 16, 40 and 21 Wm^{-2} respectively. Combining all these terms, and assuming independence of errors, a rms difference of approximately 48 Wm^{-2} was obtained in the weekly estimate of the total ocean-atmosphere heat flux.

This paper demonstrates that is is feasible to estimate weekly ocean-atmosphere heat fluxes at a point in the ocean based on satellite-derived quantities. Shorter time scales were inaccessible, due to limitations imposed by the sea surface temperature and atmospheric sounding data.

We conclude by advising of the need to test these empirical relationships in other environments and synoptic situations. A general satellite-based method, well calibrated in a number of locations would be a practical and powerful analysis tool.

Acknowledgments. The authors wish to thank Gary Meyers of the CSIRO Division of Oceanography for advice, and Doug Tarca who allowed the establishment of the meteorological station at John Brewer Reef. Support and assistance provided by the Geography Department, James Cook University, and the crew of the Reef-Link is gratefully acknowledged. This work was funded by a CSIRO/University of Tasmania cooperative research grant.

REFERENCES

Darnell, W.L., S. K. Gupta and W.F. Staylor, 1983: Downward longwave radiation at the surface from satellite measurements. *J. Clim. Appl. Meteorol.*, **22**, 1956-1960.

Davies, J.A., P.J. Robinson and M. Nunez, 1971: field determinations of surface emissivity and temperature for Lake Ontario. *J. Appl. Meteorol.*, **10**, 811-819.

Hicks, B.B. and G.D., Hess, 1977: On the Bowen ratio and temperature at sea. *J. Phys. Ocean.*, **7**, 141-145.

Kneizys, F.X., J. H. Chetwynd Jnr., S.A. Clough, E.P. Shettle, L.W. Abreu, R.W. Fenn, W.O. Gallery and J.E.A. Selby, 1983: Atmospheric Transmittance/Radiance : Computer Code LOWTRAN 6, Rep. No. AFGL-TR-83-0187, p. 200, Air Force Geophysics Laboratory, Hanscom AFB, Massachusetts, USA.

Large, W.G. and S. Pond, 1982: Sensible and latent heat flux measurements over the ocean. *J. Phys. Oceanogr.*, **12**, 464-482.

Liu, W.T., 1988: Moisture and latent heat flux variabilities in the tropical Pacific derived from satellite data. *J. Geophys. Res.*, (Oceans) **93**, 6749-6760.

Michael, K. and M. Nunez, 1989: Satellite derivation of ocean-atmosphere heat fluxes in a tropical environment. Submitted to *J. Geophys. Res.*, (Oceans).

Nunez, M., J.A. Davies, and P.J., Robinson, 1972: Surface albedo at a tower site in Lake Ontario. *Boundary-Layer Meteorol.*, **3**, 77-86.

Payne, R.E., 1972: Albedo of the sea surface. *J. Atmos. Sci.*, **29**, 959-970.

Priestley, C.H.B. and R.J. Taylor, 1972: On the assessment of surface heat flux and evaporation using large scale parameters. *Mon. Weather Rev.*, **100**, 81-92.

Ramage, C.S., 1984: Can shipboard measurements reveal secular changes in tropical air-sea heat flux ? *J. Clim. Appl. Meteorol.*, **23**, 187-193.

Reynolds, R.W., 1988: A real-time global sea surface temperature analysis. *J. Climate*, **1**, 75-86.

Sarachik, E.S., 1984: Large-scale surface heat fluxes. In : Gautier, C. and Fieux, M. (Eds.). Large Scale Oceanographic Experiments and Satellites, Reidel, Dordrecht, pp. 288.

Taylor, V.R. and L.L. Stowe, 1984: Atlas of reflectance patterns for uniform earth and cloud surfaces (NIMBUS-7 ERB-61 days), *NOAA Technical Report NESDIS*, **10**, pp. 88.

EMPIRICAL STUDIES OF ENSO AND SHORT-TERM CLIMATE VARIABILITY

Convection and Circulation Anomalies over the Oceanic Warm Pool during 1981-1982

Klaus M. WEICKMANN

NOAA/ERL/CRD
325 Broadway
Boulder, CO 80303 - U.S.A.

ABSTRACT

An important issue in understanding the low frequency evolution of the atmospheric circulation and the ocean-atmosphere system is the role of transients during individual events. We examine this question from an observational point-of-view for two different time scales and speculate on the importance of transients from these two different perspectives. Our analysis period covers September 1981 - April 1982 which includes the development phase of the 1982-83 El Nino Southern Oscillation (ENSO) as well as six Madden-Julian (30-60 day) Oscillations (MJO). The latter include a strong event during December 1981 that is studied in detail. The self-similarity of these two time scales (Webster, 1989) is also highlighted.

1. Introduction

Intensive research in the last decade on the composite characteristics of El Nino/Southern Oscillation (ENSO) and the Madden-Julian (30-60 day) Oscillation (MJO) have been followed in recent years by attempts to forecast and understand individual events. A major issue for both oscillations concerns the relative importance of organized transient activity whose structure and evolution resembles aspects of the oscillation's life cycle (Weickmann, 1983; Lau and Chan, 1985; Nakazawa, 1986). For ENSO, the MJO and the annual cycle are the most prominent quasi-periodic and periodic transients. For the MJO, transients of 1-2 days (individual cloud clusters), 4-5 days (easterly waves) and 10-15 days (superclusters) populate the envelop of convective activity as it "moves" east. The role of this transient activity is the subject of numerous observational and modeling studies for both oscillations.

The results to be presented in this paper will focus primarily on the development phase of the 1982-83 ENSO, i.e., northern fall and winter 1981-82. This is well before any coupled instability of the type postulated for example by Philander (1985), van Loon and Shea (1987), Trenberth and Shea (1987), Lau and Shen (1988) is apparent. The SST anomalies are generally small at this time although systematic behavior of ocean and atmosphere anomalies is observed in composite studies. We report on an apparent link between a strong MJO, a change in western Pacific SSTs and the evolving warm event. The same MJO will then be investigated in more detail. The primary focus on this time scale will be on the shift of convection from the eastern Indian Ocean (EIO) to the western Pacific Ocean (WPO) which involves an equatorial transient feature, a re-distribution of low level moisture and possibly a CISK-type instability. We note that for both oscillations, eastward shifts of convection involve transient activity. The eastward shift of convection is linked with SST variability during ENSO and with low level moisture variations during MJO.

ORSTOM
CENTRE DOCUMENTATION
Montpellier

F 30249

2. Composite life cycles

a. The El Nino/Southern Oscillation

The Southern Oscillation involves an ocean-atmosphere interaction having a broad period range from 2-7 years. During the development phase of a warm event (northern summer/fall of year-1; notation follows Rasmusson and Carpenter, 1982), small positive SST anomalies are observed in the Indian Ocean and extreme western Pacific which then shift east to the central Pacific during the northern winter of year 0 (Fu et al. 1986). The movement east has been ascribed to air-sea interaction over the western Pacific (e.g., Lau and Shen, 1988) and in vicinity of the South Pacific Convergence Zone (Van Loon and Shea, 1987). In composites of warm events, the SSTs gradually cool in the Indian Ocean and near Indonesia (Kiladis and Diaz, 1989) during the northern winter of year 0. The mature phase of ENSO is manifested by large SSTA in the central and eastern Pacific that develop rapidly during or after northern spring of year 0. As documented by Barnett (1984), van Loon and Shea (1987) and Kiladis and van Loon (1988), there is a systematic eastward shift of negative sea level pressure anomalies from Australia to the central South Pacific during this time. The largest anomalies in eastern Pacific SSTs (i.e., the El Nino region; see Wallace et al., 1987; Deser and Wallace, 1987) tend to occur in northern spring of year +1.

Many other oceanic and atmospheric precursors are observed prior to the development of a warm or cold event and it is now generally recognized that years preceding warm events tend to have cold event characteristics (and *vice versa*; Meehl, 1987; Ropelewski and Halpert, 1989; Kiladis and van Loon, 1988; Kiladis and Diaz, 1989). This result has been synthesized for the atmosphere by Meehl (1987) who noted a biennial tendency in the intensity of the annual cycle of convection and circulation, i.e., a strong annual cycle in one year reverses to a weak annual cycle in the following year. Hackert and Hastenrath (1986) demonstrate how anomalous air-sea interaction over the Indonesian region can lead to a reversal of sea level pressure (SLP) anomalies at the western pole of the Southern Oscillation Index. For example, given a positive SOI (negative SLP, positive SST anomalies near Indonesia), the implied surface wind anomalies would tend to increase SSTs and keep SLP low during May-October but decrease SSTs and increase pressure during November-April. Anomalies in latent heat flux, ocean stirring and cloud-radiation feedbacks may be involved. Similar positive and negative feedbacks between the atmosphere and ocean anomalies are postulated to take place all along the path followed by the tropical convective maximum (Meehl, 1987).

In this perspective, warm events tend to be extreme examples of weak annual cycles (convection suppressed over Indonesia) while cold events are extreme examples of strong annual cycles (convection enhanced over Indonesia). These results are in agreement with Gutzler and Harrison (1987) who showed that the northern fall (year -1) before a warm event is characterized by enhanced vertical motion over the eastern Indian ocean and Indonesia. The enhanced vertical motion then shifts east to the western Pacific during northern winter. This evolution is precisely that followed by the normal annual cycle and leads to the interpretation of a strong annual cycle before a warm event. The following northern winter is then characterized by weak vertical motion over the region. This alternating signal during adjacent years is also very pronounced in SLP, precipitation and cloudiness (Meehl, 1987; Kiladis and van Loon, 1988) although Trenberth and Shea (1987) show that this "biennial tendency" is not always present in the pre-1950 period.

The intensity of the air-sea interaction postulated by Hackert and Hastenrath (1986) could be one relevant factor for determining the occurrence of a warm event. MJOs represent strong transient perturbations within the annual cycle whose characteristics (e.g., through wind-evaporation feedback; Emanuel, 1987; Neelin et al.,

1987) could be systematically affected by the strong annual cycle base state. These short-period oscillations may contribute (in large part) to local air-sea interaction through wind-stress forcing, radiational effects and changes in surface fluxes.

Alternatively, the MJO has been implicated in triggering ENSO or conditioning the eastern Pacific through remote oceanic responses to wind stress forcing. The actual trigger mechanism is ascribed to short period westerly wind bursts (5-10 day duration) that may be clustered at a certain phase of the oscillation. These wind stress bursts generate downwelling oceanic Kelvin waves that can affect the depth of the thermocline and sea level in the central and eastern tropical Pacific Ocean (Lukas, et al., 1984). Anomalous currents induced by the bursts can also give rise to warmer SSTs via zonal advection (Harrison and Schopf, 1984). The effect that the convectively active and suppressed phases of a strong MJO have on the ocean is poorly known and will be an area of research within TOGA-COARE.

We have emphasized the meteorological viewpoint in the preceding discussion, although other oceanic precursors to warm events besides SSTs are also prominent. Unfortunately, a synthesis of the ocean-atmosphere features has not been attempted. In the western Pacific Ocean, the period before a warm event is usually characterized by positive anomalies in oceanic heat content (high sea level, deep thermocline) whose source is a matter of debate. Downwelling Rossby waves reflecting off the western boundary or net heat inflow from the west are some mechanisms under consideration. Low frequency, quasi-periodic (3-4 year periods) oscillations involving equatorial Rossby and Kelvin modes are also believed important. The strong annual cycle with its embedded MJOs may provide atmospheric perturbations that - in conjunction with an anomalous oceanic state - help shift the warm waters in the western Pacific Ocean eastward.

b. The Madden-Julian Oscillation

The Madden-Julian Oscillation is primarily an atmospheric phenomenon having a broad period range from 30-60 days. During an oscillation, convection intensifies over the Indian Ocean and shifts eastward discontinuously, eventually reaching the central Pacific Ocean. Over the oceanic warm pool, convection "moves" east at an average speed of 4-6 $m.s^{-1}$ and is associated with regional circulation anomalies over southeast China and the western North Pacific (Knutson and Weickmann, 1987). Over the remainder of the globe, a remote dynamical component (e.g., Rossby wave dispersion, equatorial Kelvin wave, etc.) is observed that moves eastward at 10-15 m/s. This component appears to be excited as convection shifts into the western Pacific and while the transition in the regional circulation is underway. Possible transient interaction between the regional and remote circulation anomalies may give rise to the observed wavenumber 1 and 0 spatial structures.

Similar qualitative arguments can be made for the role of transients in MJOs as were made above for MJOs in ENSO. Rather than speculating on intraseasonal transients in ENSO, we now consider 1-10 day transients in the MJO. In ENSO we seek to understand the mechanisms that give rise to oceanic anomalies over the western Pacific and those that shift the anomalies east. In the MJO we seek mechanisms that give rise to convective anomalies over the Indian Ocean and those that shift these anomalies east. In both cases, the eastward shift of oceanic or convective anomalies is preceded by amplification of an atmospheric circulation pattern (Indian Ocean subtropical anticyclones, Pacific Ocean subtropical cyclones) that resembles the annual mean. This pattern may favor anomalous transient activity that eventually helps bring about a reversal (or eastward shift) of the pattern. Viewed from this perspective, the transients

serve primarily a timing (and possibly catalytic) role in the evolution of the low frequency modes and thus are important at least for forecasting purposes. We will provide a specific example of these ideas in the next section.

3. Results from 1981-82

a. The developing warm event and the MJO

Figure 1 shows selected 3-month running means of the anomalous 150 mb winds (1979-1987 base period) during the development phase of the 1982-83 warm event. ORL anomalies for the same period are superimposed on each map. During October-November-December 1981 (OND 81, Fig. 1a), twin anticyclones are prominent north and south of Indonesia with easterly anomalies extending into the Indian Ocean. Westerly anomalies cover the remainder of the equatorial belt. The OLR anomalies indicate enhanced equatorial convection from the eastern Indian Ocean to north of New Guinea. This general pattern of equatorially symmetric anomalies (i.e., small meridional components) is also present during NDJ (Fig. 1b) and represents an example of the enhanced convection and circulation that accompany a strong annual cycle. At this time, positive sea surface temperature anomalies between 0.5-1.0° C cover the tropics from the Indian Ocean to 140°E (Arkin et al., 1983) and presumably help force the anomalous convection and circulation.

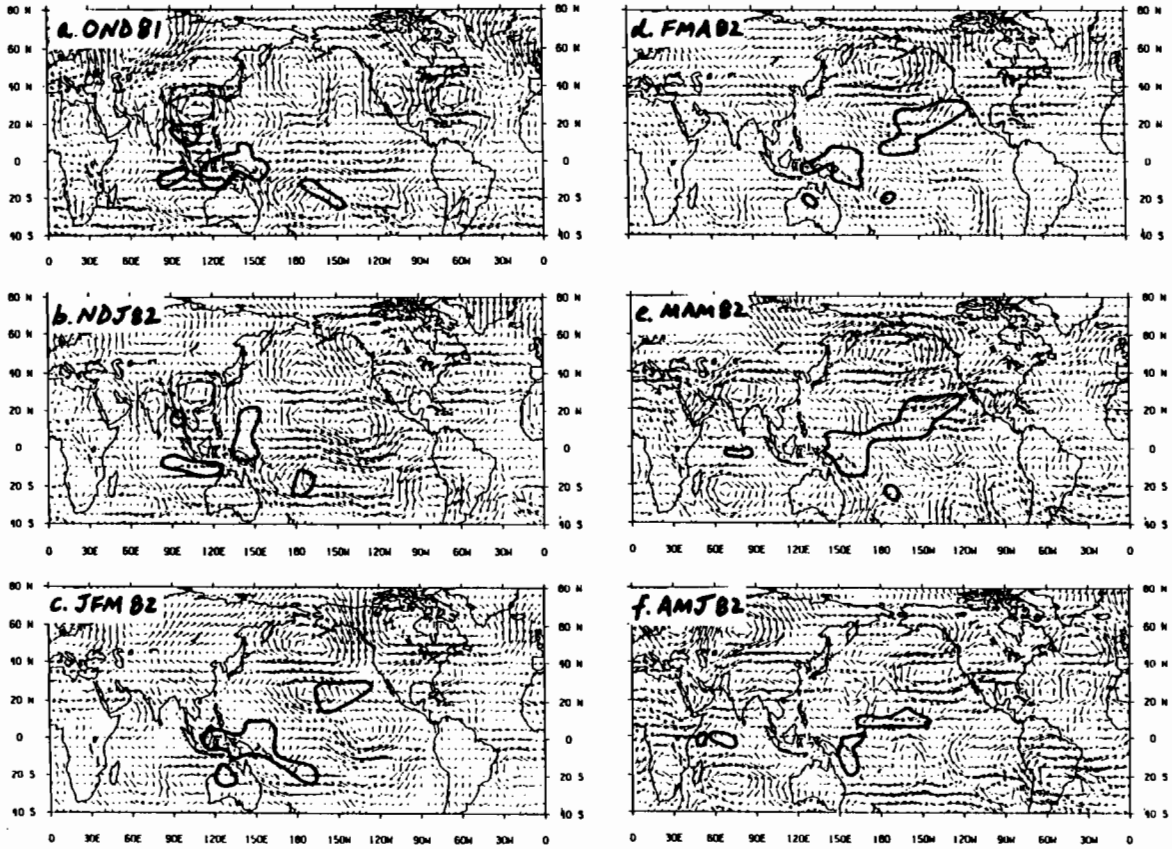

FIG. 1. Wind anomalies at 150 mb relative to 1979-87 base period: a) October-November 1981, b) November-January 1982, c) January-March 1982, d) February-April 1982, e) March-May 1982 and f) April-June 1982. The arrows are scaled by the largest wind magnitude on each map which are : a) 10.5m.s^{-1}, b) 11.8 m.s^{-1}, c) 16.6 m.s^{-1}, d) 15 m.s^{-1}, e) 9 m.s^{-1} and f) 8 m.s^{-1}. Corresponding OLR anomalies < -10 W.m^{-2} are superimposed on each map.

By northern winter (DJF 82, Fig. 1c), the subtropical circulation anomalies have developed a distinctly asymmetric or monsoonal structure. Anomalous convection has shifted eastward to the western Pacific Ocean and strong twin cyclones have developed over the central-eastern Pacific indicating an enhanced Walker Circulation. This transition in the circulation represents a typical precursor in the development of a warm event as shown by Gutzler and Harrison (1987) as well as continuation of the strong annual cycle patterns postulated by Meehl (1987). It is accompanied by a cooling of SSTs from the Indian Ocean to Indonesia and an eastward shift of positive SST anomalies (~1°C) to west of the dateline. Intensified convection is located near 150°E and extends southeast in the SPCZ.

Figure 2 shows a detailed picture of the convection and 30-60 day variability during the period September 1981 to April 1982. The interannual transition described above occurs rapidly in association with a strong 30-60 day oscillation during December 1981 (Fig. 2a). This oscillation appears to be embedded within a more slowly evolving zonal circulation cell moving out of the Indian Ocean at about 2 $m.s^{-1}$ (not shown). The cell starts over the western Indian Ocean following the September 1981 MJO (Fig. 2a) and has the November and December 1981 MJOs embedded within it. The convective activity associated with this slower-moving cell is more clearly defined in the southern tropics (5°S-15°S) than in equatorial regions. Several westerly wind bursts were observed along the equator during the December 1981 period of more rapid eastward shift of convection.

Figure 3 shows the monthly mean SSTs before, during and after the strong MJO (November, December 1981 and January 1982 respectively). Prominent features include the retreat of 29°C water from 100°E to 150°E, the strong cooling over the South China Sea and the southward shift of 29°C water from near the equator to 5°S. These are features of the normal annual cycle but monthly and seasonal (e.g., from September-November to December-February; Arkin et al., 1983) SST anomalies show a similar cooling in western and warming in eastern portions of the region in Figure 3. The anomalous SLP fields also undergo a large change from November 1981 to January 1982 as shown by Barnett (1985). We postulate that the strong MJO contributed substantially to the evolving SST and SLP anomaly features.

Returning to Figure 1, the next major transition in the anomalous 150 mb wind begins over the South Pacific Ocean to the northeast of New Zealand during MAM 82 (Fig. 1e) and becomes well-defined in equatorial regions during AMJ 82 (Fig. 1f). The latter includes the first upper level easterly anomalies over the central equatorial Pacific which increase dramatically during MJJ 82 (not shown). By this time, the warm event is well underway as the monthly mean SOI falls abruptly from -0.6 in May 1982 to -2.5 in June 1982.

This transition is again closely linked with a strong 30-60 day oscillation that develops over the Indian Ocean in late May 1982 and propagates into the western Pacific in June 1982. The equatorial OLR anomalies shown in Fig. 4 for September 1981 through September 1983 indicate that this event may have initiated (or provided the perturbation for) an ocean-atmosphere instability that evolved into the slow eastward propagating mode characteristic of the 1982-83 ENSO event.

We have presented qualitative evidence that a strong 30-60 day oscillation, occurring at a transition time in the seasonal cycle, probably contributed to cooling of SSTs over the extreme western Pacific and possibly to warming of SSTs west of the dateline. The phase of oceanic waves both in equatorial and subtropical regions as well as sea level and ocean current anomalies did not display simple patterns during this time although a further comparisons and a synthesis is required. We speculate that the perturbation to the ocean-atmosphere system from the warmest SSTs shifting east provided the conditions for an instability that was realized during northern spring of

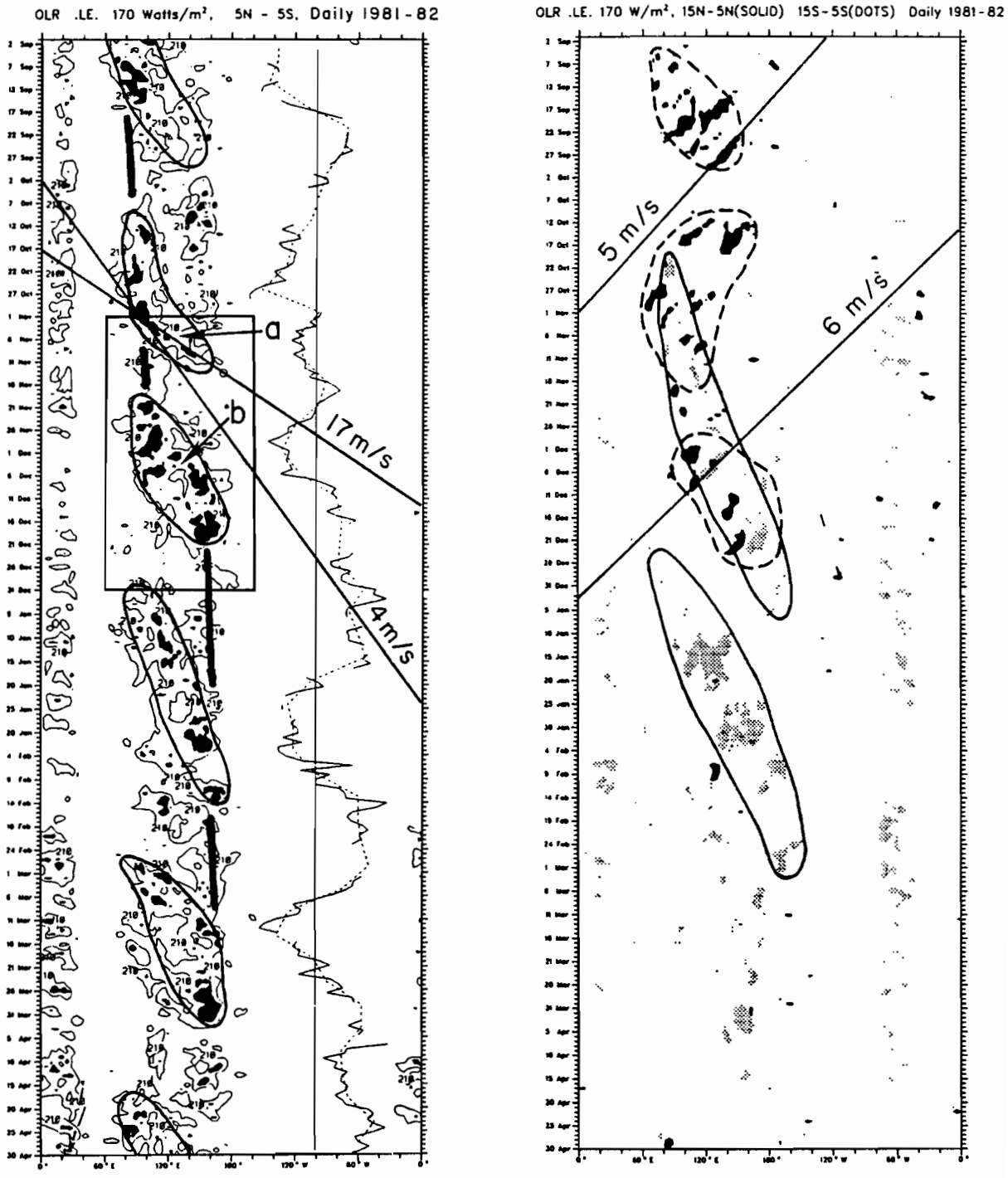

FIG. 2. Hovmollers of daily outgoing longwave radiation (OLR) for 1 September 1981 to 30 April 1982 averaged for a) 5°N-5°S and b) 5°N-15°N (solid) and 5°S-15°S (dots). In a) the 210 W.m^{-2} contour is shown and OLR < 170° W.m^{-2} is darkly shaded. In b) only OLR < 170 W.m^{-2} is shown. Envelopes of low OLR (most intense convection) are highlighted with solid lines. The time series on Fig. 2a represent Northern Hemisphere angular momentum anomalies for both daily and pentad averages. The sloping lines represent the speed of movement of individual OLR elements or of the envelop of OLR activity. The rectangle shows the region that will be studied in detail. The heavy solid line segments highlight the shift east of the most intense convection from the Indian ocean to the western Pacific Ocean. (From Weickmann et al., 1989).

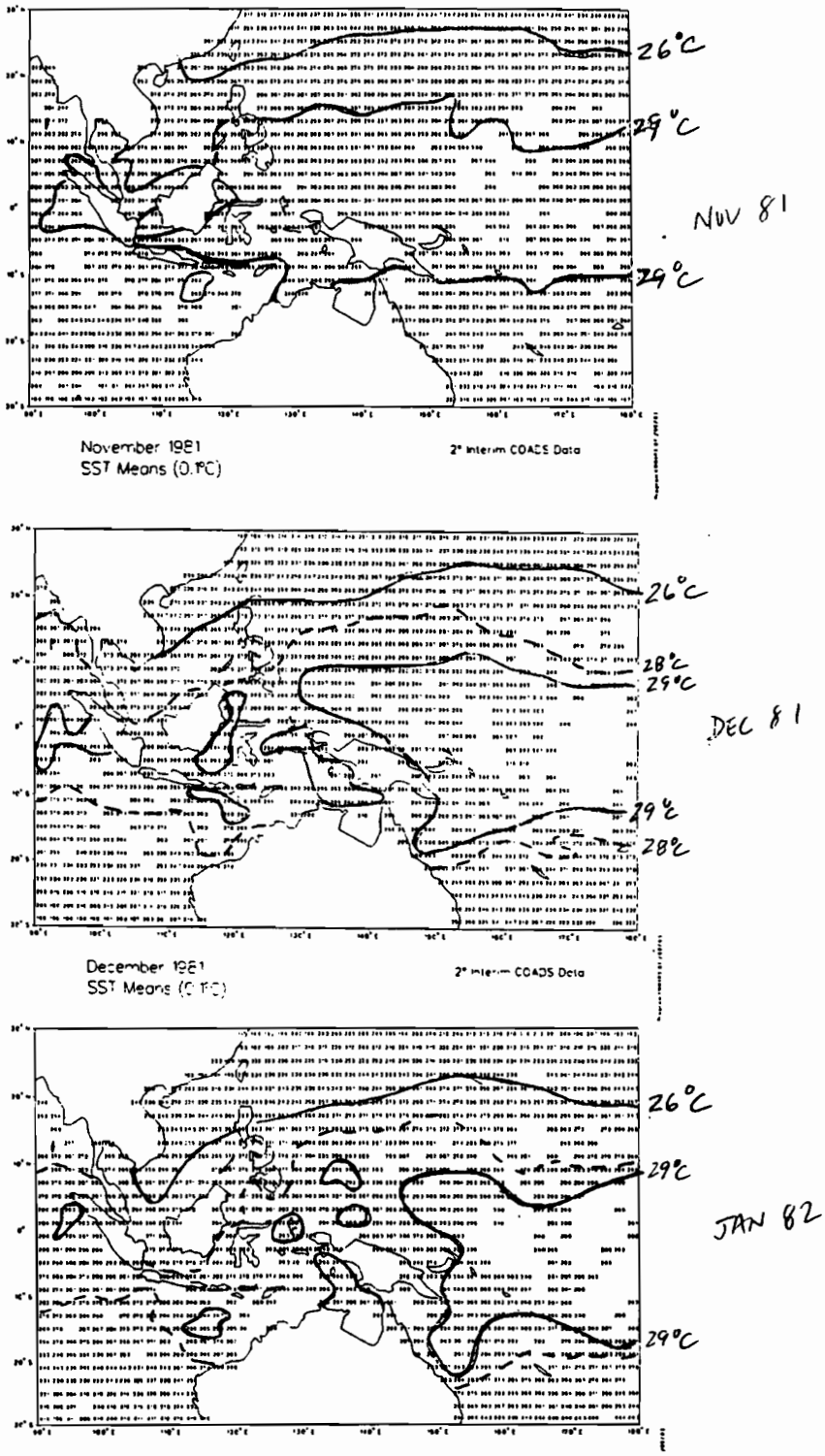

FIG. 3. Sea surface temperature in 2° squares from COADS for November 1981, December 1981 and January 1982. Selected contours have been drawn at 29°C, 28°C and 26°C.

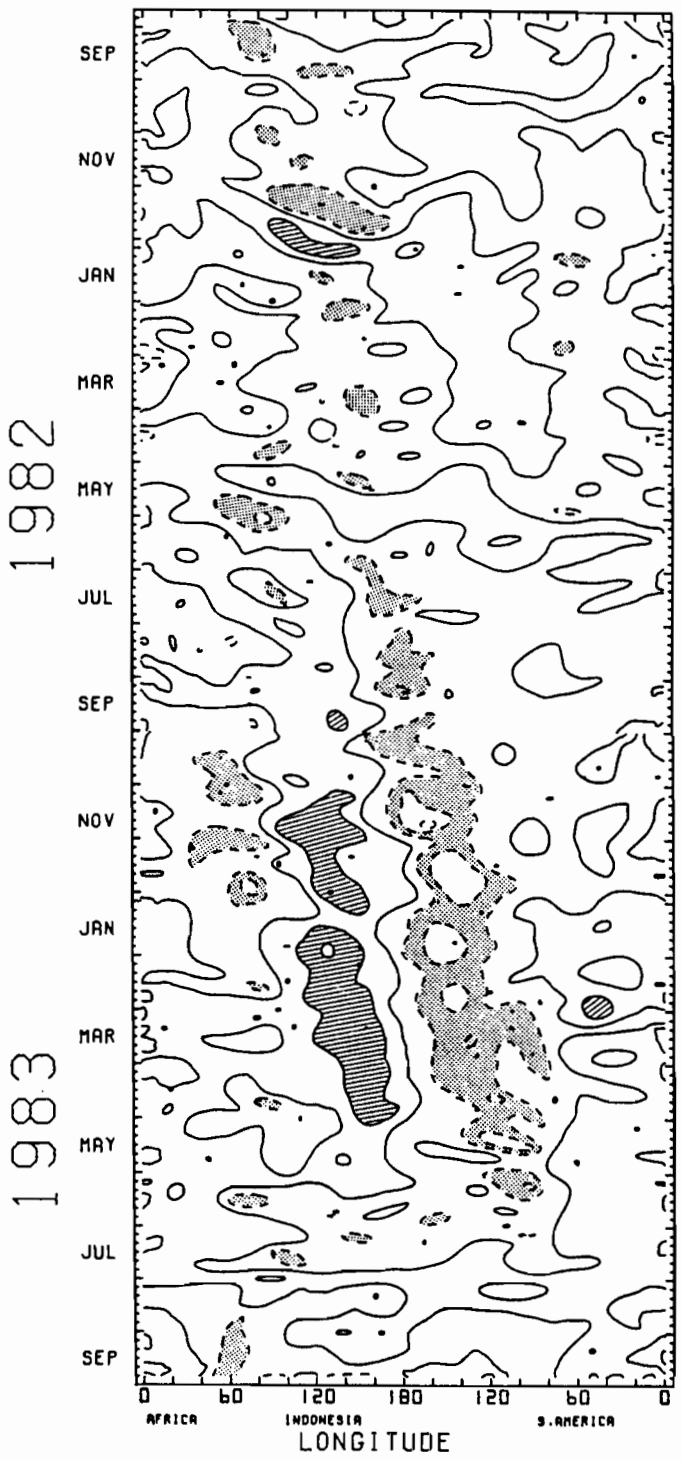

FIG. 4. Pentad OLR anomalies averaged between 10°N- 10°S for September 1981 to September 1983. Negative (positive) anomalies between 20 and 40 W.m^{-2} are stippled (hatched).

1982 and resulted in the 1982-83 warm event (Lau and Shen, 1988). Such an SST perturbation (i.e., cooling the western edge of the warm pool and warming the eastern edge) may lead to more direct coupling between deep convection, zonal surface wind and SSTs over the central Pacific as suggested by Gutzler and Wood (1989).

b. The December 1981 Madden-Julian Oscillation

In the previous section, one transition in the chain of events leading to the 1982-1983 warm event and the possible role of a strong MJO in the evolution of ENSO-related SST anomalies was described. In this section, we show that a much higher frequency transient may have played an analogous role in a chain of events normally observed during a strong MJO; namely, the shift of convection from the EIO to the WPO. Rather than influencing the pattern of SSTs as with the MJO in ENSO, the transients within the MJO influence the pattern of low level moisture. In both cases perturbations to the pattern of convection result.

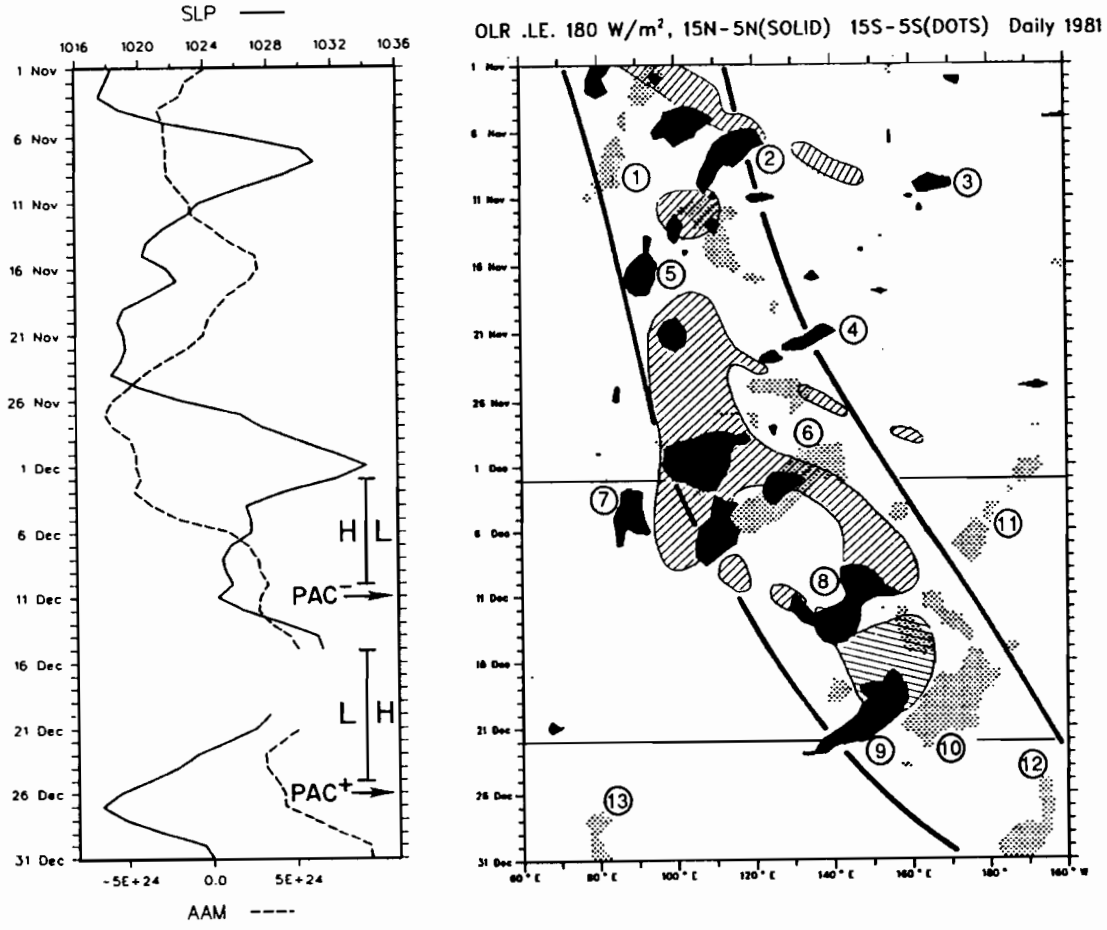

FIG. 5. a) an enlargement of Fig. 2b with the most intense convection (OLR < 170 W.m^{-2}) from Fig. 2a schematically superimposed (hatched areas). OLR < 180 W.m^{-2} is shown in the northern 15°N-5°N, solid) and southern (5°S-15°S) tropics. The circled numbers refer to tropical storms and other synoptic features. See text. b) sea level pressure over southeast China (25-35°N, 100-120°E; solid line, top axis) and Northern Hemisphere atmospheric angular momentum anomalies (dashed line, bottom axis). The time series have been smoothed with a 3-day running mean. The phase and duration of the regional circulation anomalies are shown by H/L and vertical lines, respectively. PAC$^-$ and PAC$^+$ refer to the onset of persistent extratropical circulation anomalies over the North Pacific.

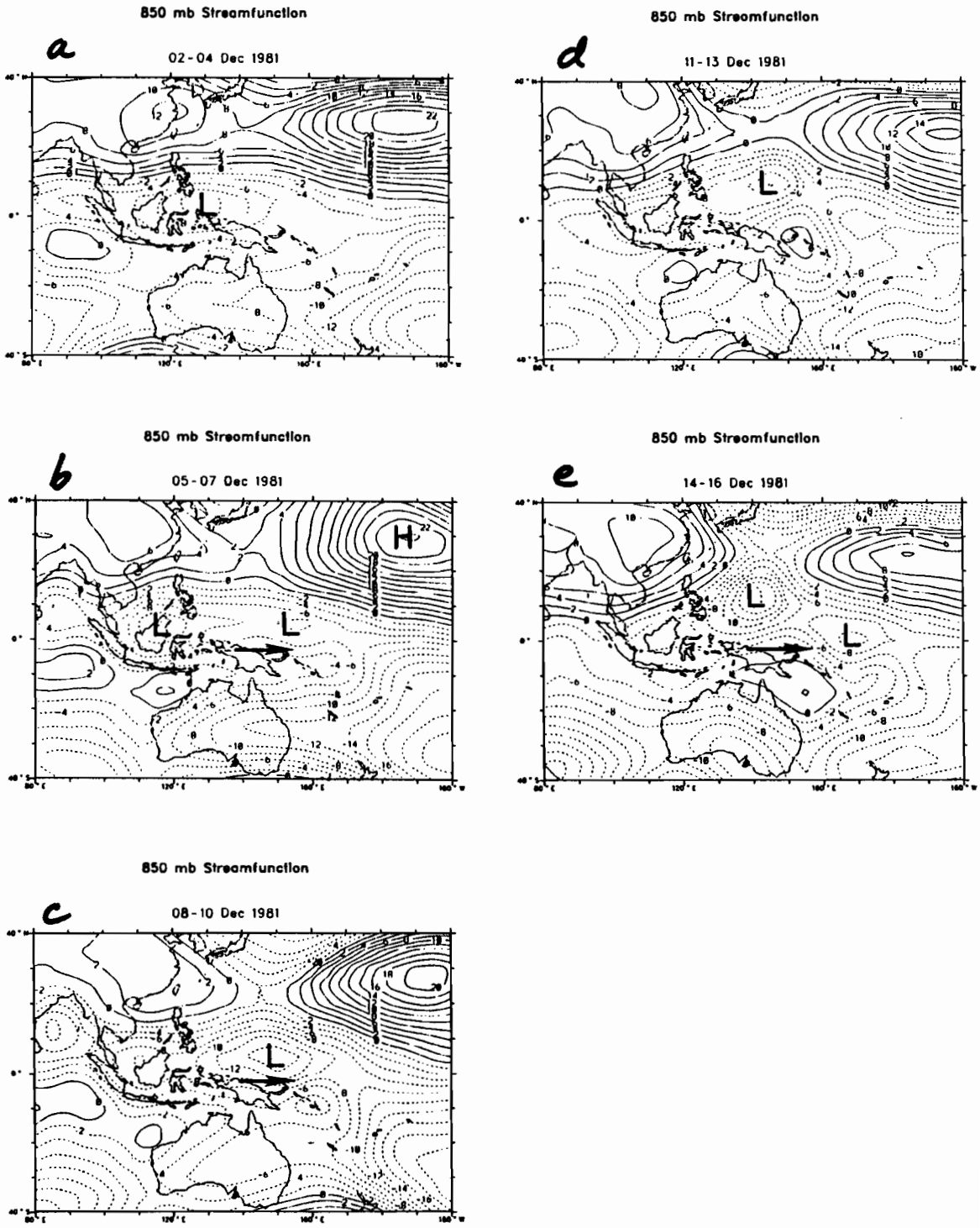

FIG. 6. Total streamfunction at 850 mb for five 3-day averages from 2-4 December (a) through 14-16 December 1981 (e). The contour interval is $2.0 \times 10^5 m^2.s^{-1}$ and negative contours are dashed. Hs and Ls highlight anticyclonic and cyclonis circulation features respectively. The arrows represent the location of westerly wind bursts based on the definition used by Keen (1982).

Figure 5a shows an enlargement of the Hovmoller shown in Figure 2b with the Figure 2a Hovmoller schematically superimposed. Although the picture is complex, the gross features of the combined Hovmoller show quasi-stationary convection near 100°E before early December 1981, a rapid shift east to 150°E during mid-December 1981 and then suppressed convection over the warm pool region after 22 December 1981. The most prominent transients during the period display eastward phase propagation in equatorial regions (hatched areas) and westward phase propagation in off-equatorial regions (dotted and solid areas). A large portion of the off-equatorial convective activity can be attributed to tropical storms (the circled numbers on Fig. 5a).

Important events in the general circulation of the region are shown in Figure 5b (see Weickmann et al., 1989 for a detailed discussion); the time series represent Northern Hemisphere atmospheric angular momentum and southeast China sea level pressure. An outstanding feature of Figure 4 is the link between the strong cold surge that peaks on 1 December 1981, the convective increase in the northern tropics near 105°E (solid areas) and the subsequent intensification of the regional subtropical circulation over southeast China and the western North Pacific. An eastward moving equatorial convective mode (hatched area connecting EIO and WPO convection from 1-6 december 1981) appears to emanate from the tropical region south of the cold surge following the convective increase over the northern tropics (Fig. 5). Low level westerly winds accompany the mode as it moves to the east.

The synoptic evolution of the 850 mb streamfunction for five 3-day averages following the cold surge and convective flareup near 100°E is shown in Figure 6. The downstream regional response to the convection near 100°E involves an intensification and amplification of the 850 mb anticyclone at 30°N, 175°W (Figs. 6 a,b). This development may be linked with an equivalent barotropic Rossby wavetrain that either emanates from the subtropical North Pacific or develops through barotropic interactions over the mid-latitude North Pacific (Weickmann, et al., 1989). In either case, the 850 mb anticyclone is accompanied by a surge in equatorial trades during an 8-day period following the 100°E convective flareup.

Over the western Pacific, an eastward surge of equatorial westerlies occurs during the same period as the trade surge (Fig. 6b; also see OLR signature on Fig. 5a). These westerlies, in conjunction with the surging trades produce strong low level moisture convergence and provide favorable conditions for intensifing convection near 150-160°E (see Weickmann, et al., for more details). The westerly winds intensify as convection increases and westerly wind bursts are observed on 5-10 and 14-18 December 1981. An interplay between the bursts and tropical cyclone formation is also evident in Figures 6 d,e.

4. Summary

We have presented synoptic evidence that the convectively active phase of a strong Madden-Julian (30-60 day) Oscillation is linked with a pattern of cooling/warming SSTs similar to that observed during the development phase of a warm event. The phasing of the various components (winds, OLR, SST) resembles Lau and Shen's advective mode although zonal SST gradients are small from the eastern Indian Ocean to the western Pacific Ocean. Similarly, for the Madden-Julian Oscillation an equatorial transient provides partial forcing for a low level drying/moistening pattern that precedes the shift of convection from the eastern Indian to the western Pacific Ocean. In both cases, these interactions occur within an anomalous basic state (strong annual cycle for ENSO, regional circulation enhancement for the MJO) that subsequently shifts east or reverses when convection shifts east. Additional analyses of individual events are required to substantiate these results.

REFERENCES

Arkin, P.A., J.D. Kopman and R.W. Reynolds, 1983: 1982-83 El Nino/Southern Oscillation event quick look atlas. (available from : NOAA/NWS, NMC, Climate Analysis Center, Washington, D.C., 20233.)

Barnett, T.P., 1984: Interaction of the monsoon and Pacific trade wind system at interannual time scales; Part III: A partial anatomy of the Southern Oscillation. *Mon. Wea. Rev.*, **112**, 2388-2400.

Barnett, T.P., 1985: Three-dimensional structure of low frequency pressure variations in the tropical atmosphere. *J. Atmos. Sci.*, **42**, 2798-2803.

Deser, C., and J.M. Wallace, 1987: El Nino events and their relation to the Southern Oscillation: 1925-1986. *J. Geophys. Res.*, **92**, 14,189-14,196.

Emanuel, L.A., 1987: An air-sea interaction model of intraseasonal oscillation in the tropics. *J. Atmos. Sci.*, **44**, 2324-2340.

Fu, C., H.F. Diaz, and J.O. Fletcher, 1986: Characteristics of the response of sea surface temperature in the central Pacific associated with warm episodes of the Southern Oscillation. *Mon. Wea. Rev.*, **114**, 1716-1738.

Gutzler, D.S., and D.E. Harrison, 1987: The structure and evolution of seasonal wind anomalies over the near-equatorial eastern Indian and western Pacific Oceans. *Mon. Wea. Rev.*, **115**, 169-192.

Gutzler, D.S. and T.M. Wood, 1989: Structure of large-scale convective anomalies over tropical oceans. *J. Climate*, submitted.

Hackert, E.C. and S. Hastenrath, 1986: Mechanisms of Java rainfall anomalies. *Mon. Wea. Rev.*, **114**, 745-757.

Harrison, D.E., and P.S. Schopf, 1984: Kevin-wave-induced anomalous advection and the onset of surface warming in El Nino events. *Mon. Wea. Rev.*, **112**, 923-933.

Kiladis, G.N. and H. Diaz, 1989: Climatic anomalies associated with the extremes of the Southern Oscillation. *J. Climate*, (in press).

Kiladis, G.N., and H. van Loon, 1988: The Southern Oscillation. Part VII: Meteorological anomalies over the Indian and Pacific sectors associated with the extremes of the oscillation. *Mon. Wea. Rev.*, **116**, 120-136.

Knutson, T., and K.M. Weikmann, 1987: The 30-60 day atmospheric oscillations: Composite life cycles of convection and circulation anomalies. *Mon. Wea. Rev.*, **115**, 1407-1436.

Lau, K.M. and P.H. Chan, 1985: Aspects of the 40-50 day oscillation during the northern winter as inferred from outgoing longwave radiation. *Mon. Wea. Rev.*, **113**, 1889-1909.

Lau, K.M., and S. Shen, 1988: On the Dynamics of intraseasonal oscillations and ENSO. *J. Atmos. Sci.*, **45**, 1781-1797.

Lukas, R., S.P. Hayes and K. Wyrtki, 1984: Equatorial sea level response during the 1982-83 El Nino. *J. Geophys. Res.*, **89** 425-430

Meehl, G.A., 1987: The annual cycle and interannual variability in the tropical Pacific and Indian Ocean regions. *Mon. Wea. Rev.*, **115**, 27-50

Nakazawa, T., 1986: Mean features of 30-60 day variations as infrerred from 8-year OLR data. *J. Met. Soc. Japan*, **64**, 777-786.

Neelin, J.D., I.M. Held, and K.H. Cook, 1987: Evaporation-wind feedback and low frequency variability. *J. Atmos. Sci.*, **44**, 2341-2348.

Philander, S.G.H., 1985: El Nino and La Nina. *J. Atmos. Sci.*, **42**, 2652-2662.

Rasmusson, E.M., and T.H. Carpenter, 1982: Variations in tropical sea surface temperature and surface wind fields associated with the Southern Oscillation/ El Nino. *Mon., Wea. Rev.*, **110**, 354-384.

Ropelewski, C.F., and M.S. Halpert, 1989: Precipitation patterns associated with the high index phase of the Southern Oscillation. *J. Climate* (in press).

Trenberth, K.E. and D.J. Shea, 1987: On the evolution of the Southern Oscillation. *Mon. Wea. Rev.*, **115**, 3078-3096.

Van Loon, H., and D.J. Shea, 1987: The Southern Oscillation. Part VI: Anomalies of sea level pressure on the Southern Hemisphere and of Pacific sea surface temperature during the development of a Warm Event. *Mon. Wea. Rev.*, **115**, 370-379.

Weickmann, K.M., 1983: Intraseasonal circulation and outgoing longwave radiation modes during Northern Hemisphere winter. *Mon. Wea. Rev.*, **111**, 1838-1858.

Wright, P.B., J.M. Wallace, T.P. Mitchell, and C. Deser, 1987: Correlation structure of the El Nino/Southern Oscillation Phenomenon. *J. Climate*, **1**, 609-625.

Instability Waves in the Tropical Pacific Observed with GEOSAT

Claire PERIGAUD

Jet Propulsion laboratory, MS 300/323
4800 Oak Grove Drive
Pasadena, CA 91109, U.S.A.

ABSTRACT

Sea level variations for periods between 20 to 50 days are examined in the tropical Pacific ocean from Geosat data which have been processed and analyzed weekly during the first 13 months of the Exact Repeat Mission. Based on comparison with twice daily tide-gage data, sea level variations can be determined with an rms accuracy of 6 cm for time scales of a week. Subsampling by the satellite and smoothing introduced by the analysis aliase the frequency spectra by introducing artificial secondary peaks and reducing the energy level of significant peaks. However the synopticity of the satellite observations give significance to the energy peaks detected locally and allows a detailed description of the 20 to 50 days oceanic variations during 1 year. Along the equator, sea level spectra show low energy. The highest energy is found in the Northeastern Pacific along 5ºN for 25 to 45 day periods, 1000 to 1500 km wavelengths, and a westward 40 km/day phase velocity. The signal filtered in this band of wavelengths and periods shows the strongest amplitude East of 160ºW and the weakest amplitude along 2000 km in the Central Pacific. Waves are propagating energy eastward and are seasonally modulated in high correlation with the shear-strength of the zonal flows. West of the central zone of minimum amplitude however, the signal is no longer well correlated with the shear-strength variations. The signals at 5ºN and 5ºS are not antisymetric with respect to the equator but positively correlated.

I INTRODUCTION

Instability waves have been observed and simulated as wavelike oscillations in the meridional velocity along the equator and in the sea surface temperature about 2º north of the equator in the Northeastern tropical Pacific. Weisberg (1987) provides a synopsis of their theoretical and observational history. These oscillations are narrow-band in frequency and wavenumber with time and zonal length scales centered about 30 days and 1000 km respectively. Their phase speed is westward and their apparent group velocity is eastward. These characteristics fit the Rossby-gravity wave ones. The pressure field of such a theoretical wave is antisymetric with respect to the equator. Maximum of wave amplitude in the dynamic topography has been observed in the Northeastern tropical Pacific with inverted echo sounders (Miller et al, 1985) and with Seasat altimeter data (Malarde et al, 1987). The packet duration of these oscillations is seasonnaly modulated and these waves seem to be generated by the (zonal or vertical) shear instabilities of the zonal equatorial currents (Cox, 1980). It seems clear that these instability waves play a primary role in the momentum balance of the near surface near equatorial mean currents. It is suggested that they may have similar importance for the near surface heat balance through meridional heat convergence towards the equator (Hansen and Paul, 1984).

The generation and decay of these energetic oscillations and the relation of their spatial and temporal distributions with the variations of the equatorial currents are addressed in this work. The Geosat altimeter data from the first year of exact repeat mission are processed and analyzed in the 20º band across the Pacific. Results are validated by

ORSTOM
CENTRE DOCUMENTATION
Montpellier

F 30250

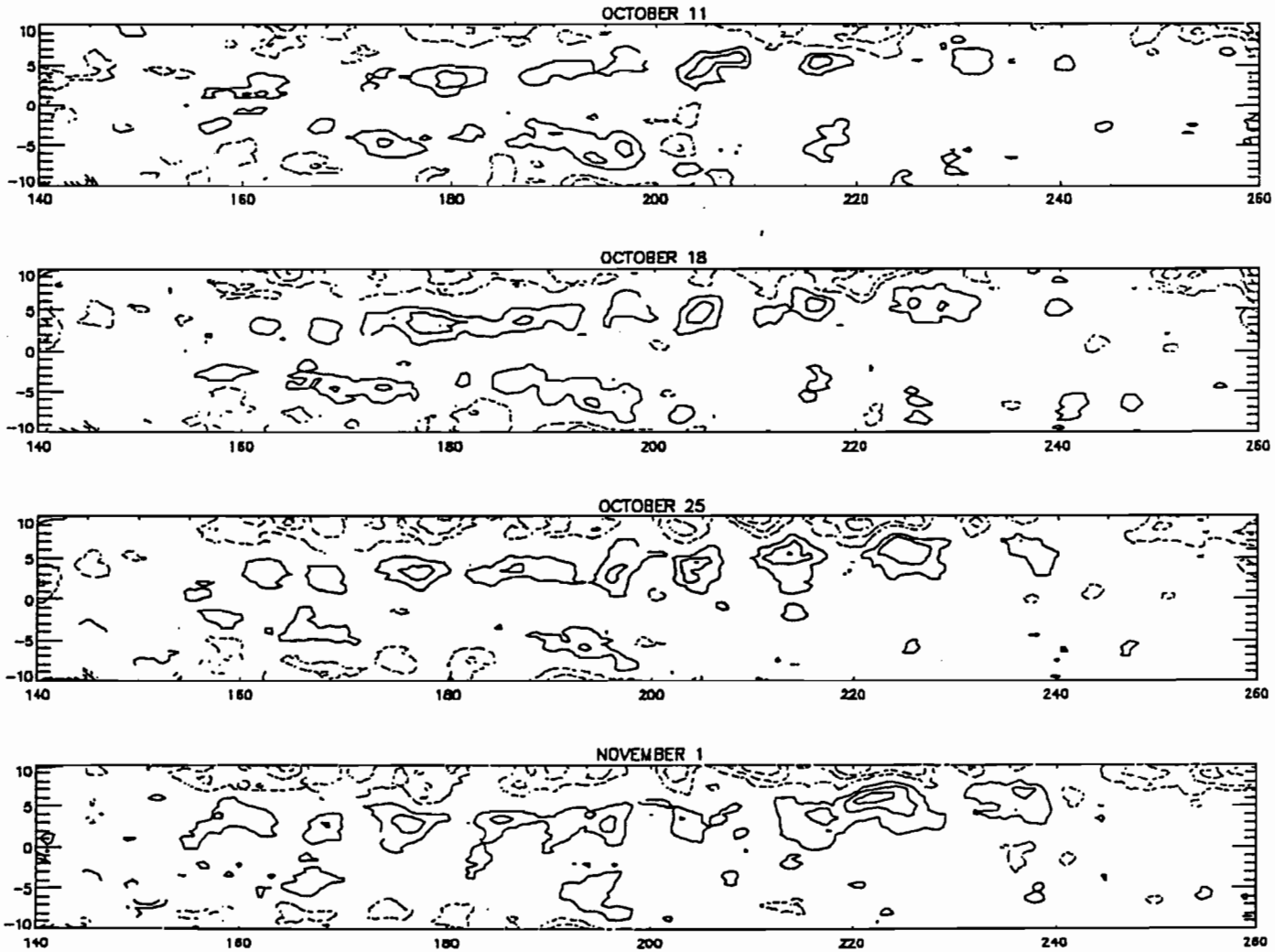

FIG.1. Weekly maps of sea level anomalies (relative to the 13 month mean) analyzed from GEOSAT altimeter data. Isocontours are 5 cm with continuous lines for positive and dotted lines for negative values. Zero contour is not drawn for more clarity.

comparison with tide-gage data. Frequency-wavenumber spectra are given as a function of latitude and altimeter signal filtered at the wave energy peaks is examined.

II ALTIMETER DATA PROCESSING AND ANALYZING

The Geophysical Data Record computed by NOAA's National Geodetic Survey (Cheney et al, 1988) are corrected for earth and ocean tide, inverse barometer response of sea level to atmospheric pressure, wet (FNOC) and dry tropospoheric path delays. Spikes are eliminated and data are gridded as a function of latitude along repetitive tracks of one ground "pass". Orbit errors are then corrected by applying to each repeat of each pass, a second degree polynom between 20ºS and 20ºN, using the mean of the differences to the most complete pass (as used in Zlotnicki et al, 1989). The mean is taken from November 8 1986 to December 20 1987 (first 24 cycles).

Residual orbit error is negligible over a narrow latitudinal band as studied here. Presence of wet tropospheric signal is surely effective in the tropical band (Emery et al, 1988). However, little contribution of this signal is expected in the range of wavelengths, periods and propagation speeds typical of the oceanic variations that are investigated in the present study.

Residual alongtrack altimetric differences are then analyzed using a successive correction method, as formerly used in meteorology (Tripoli and Krishnamurti, 1975). The spatial resolution chosen is d= 0.5 degree in latitude and longitude. This fine resolution results from a choice between the satellite crosstrack sampling (between 0 and 170 km at worst) and alongtrack sampling (7 km). The correlation function used in space is the Cressman function:
$(r^2-R^2)/(r^2+R^2)$ where r is the distance between the data point and the analyzed point and R is the correlation distance. Different sets of values for R have been chosen ranging from (4d, 3d, 2d, d) to (8d, 6d, 4d, 2d). An influence time of 34 days and an e-folding time of 5 to 7 days are applied on the weekly analyses performed over the 13 months of data. The time resolution (7 days) is chosen better than the satellite repetitive period (17 days) because oceanic information can be gained from neighbouring tracks within the satellite subcycle (3 days) This analysis is not optimal. It does not impose a westward phase speed as done with optimal analysis in (Malarde et al, 1987), nor any dynamical constraint as done with Kalman filter in (Gaspar and Wunsch, 1989). The present method certainly can be improved when the knowledge about the kinematics and physics of these waves becomes better.

A series of the sea level anomaly maps resulting from the Geosat analysis is presented in autumn 1987 (figure 1) showing succession of positive anomalies in the 3ºN to 8ºN latitudinal band. Some of them can be followed to migrate westward from week to week. Indeed the axis along which the anomalies are aligned, is not purely zonal but has a prevailing southwest-northeast orientation as has the axis of maximum shear-strength between the North Equatorial Counter Current and the South Equatorial Current (Kendall, 1970). However it is difficult from these results to characterize the waves involved in those variations as the anomaly maps represent the sum of the short-term, seasonnal and interannual variations for this particular year. Taking monthly averages and spatial smoothing over 1º latitude and 4º longitude of these series allow us to recover the sea level variations that have been described for the year 1986-1987 (Cheney and Miller, 1987). The present series enhances the important contribution of the short-term events in the seasonal variations of the tropical Pacific Ocean. These short-term variations detected by the satellite are validated in the next section.

III COMPARISON WITH TIDE-GAGE DATA

Tide gage data have been provided by Klaus Wyrtki on four island sites in the Central Tropical Pacific. These are twice daily data from November 1 1986 till December

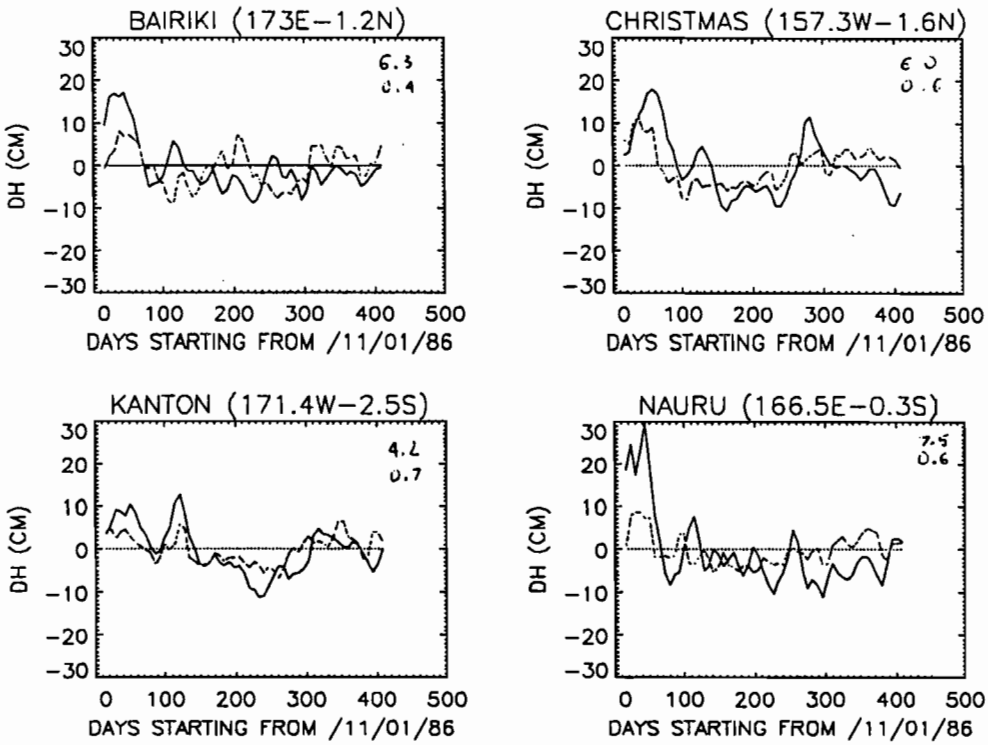

FIG.2. Variations of sea level relative to the 13 month mean derived from tide gage (continuous line) or from GEOSAT data (dotted line). The top value is the RMS difference between the 2 curves. The bottom value is the correlation coefficient.

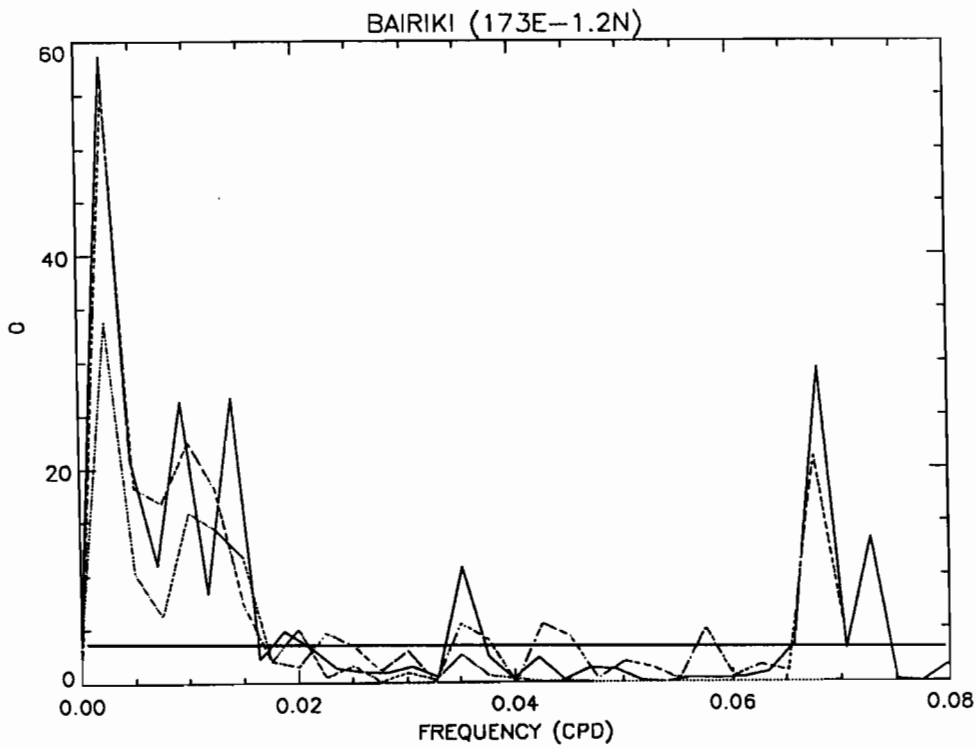

FIG.3. Frequency energy spectrum at Bairiki island derived from tide-gage data, with twice-daily data (continuous line), weekly subsampled data (dashed line) or 14 day averaged data (dotted line). The 95% level of confidence is given for the twice-daily data.

31 1987. The same 13 months mean is removed from these data and a 14 day running average is applied to remove the fortnight tidal signal. Then a weekly binning at the times corresponding to Geosat analyzed series is performed. The closest point within a 0.5 degree box around the island is extracted from the Geosat field for comparison. The time series (fig 2) agree within a mean RMS of 5.2 cm and a correlation coefficient ranging from 0.4 to 0.7. When the monthly mean is taken from both these series, the agreement is slightly better (mean RMS of 3.6 cm and correlation ranging from 0.1 to 0.8) and is a little less good than what Cheney et al (1989) found when comparing 16 sites of monthly averaged tide-gage data with Geosat over 18 months in 1985-1986 (respectively 3.7cm and 0.69). The energy spectrum of the non-smoothed non-subsampled tide-gage sea level presents 2 significant peaks at 14 days and 28 days. The former peak corresponds to a fortnightly tidal signal as found in Mitchum and Lukas (1987). The spectrum is modified by subsampling and smoothing (fig 3). Weekly subsampling twice-daily tide-gage data shifts energy from the higher frequencies into the lower ones so that artificial peaks show up in the 10 to 30 day range. Running a 14 day average on the twice-daily tide-gage data zeroes the fortnightly tidal signal but also reduces the 28 day signal just below the 95% level of confidence. These effects explain the differences between tide-gage and Geosat spectra (fig 4). Geosat peak has the energy level as the smoothed tide-gage peak, which has 50% less energy than the original one. Geosat spectra show secondary peaks between 10 and 30 days consistant with the subsampling aliasing. It is surely unfair to derive conclusions from these ponctual comparisons all the more as these islands happen to be in the Central Pacific where the variance is the smallest (Wyrtki, 1975). However Geosat series provide 300 grid points in longitude over which frequency spectra can be computed. Therefore the spatial consistency of the Geosat spectra can be examined.

IV WAVENUMBER-FREQUENCY SPECTRUM

Frequency spectra have been averaged in the Eastern (100ºW to 160ºW) and in the Western (140ºE to 160ºW) basins along zonal sections of the Geosat weekly series (fig 5). These basins have the same spectra along the equator, with a low of energy between 30 and 50 days, the highest energy level of all the spectra at the lowest frequencies and a secondary peak at 22 days just above the 95% level of confidence. The eastern basin presents significant peaks in the 25 to 45 day band both North and South of the equator. The peak maxima are centered on 33 days at 5ºN and 40 days at 5ºS and the secondary maxima centered at 7.5ºN and 7.5ºS with a wider frequency band shifted to the longer 40 day periods. The energy level is about twice larger in the North than in the South. The 25 to 45 day peak may be due to instability and will be studied in the next section.

The equator presents a minimum of energy in the 30 to 50 days as the Rossby-gravity wave has a zero sea level amplitude along the equator. The secondary peak at 22 day can be due to subsampling of the highest frequency waves which energy is concentrated in the equatorial wave guide.

In the western basin, significant peaks show up between 40 and 60 days but little energy is found below 35 days. The structure looks more complex than in the East and is certainly resulting from the superposition of different events. The increase in the periods from East to West has been observed in current measurements (Halpern et al, 1988) and tide-gage data (Chriswell and Lukas, 1989) and corresponds to the eastward dispersion of the Rossby-gravity wave. Two main differences appear between these spectra and those derived from 730 days of 17 tide-gage stations in the central and western 10ºS to 10ºN Pacific (Mitchum and Lukas, 1987). No 40 to 50 day peak is found along the equator and the 20 to 40 day peak is centered higher than 30 days rather than lower. The peak, which corresponds to sea level response to atmospheric oscillations (Enfield, 1987) may be absent on 1986-1987; indeed it has not either been observed in the Western Pacific Ocean for 1986-1987 (McPhaden et al, 1989).

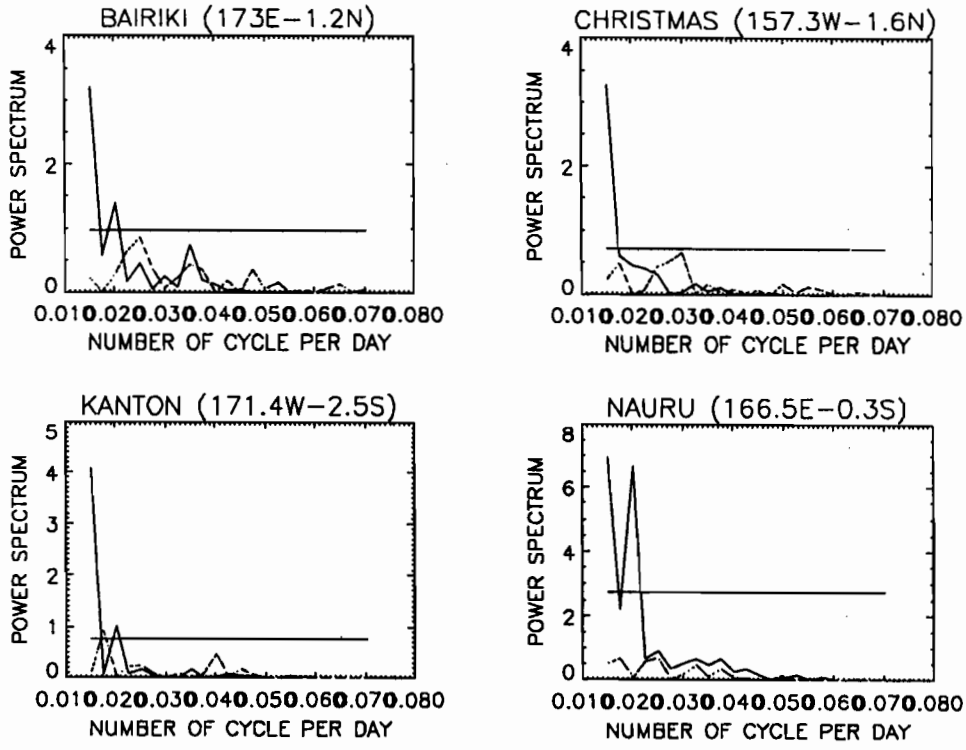

FIG.4. Frequency power spectra in cm²/cycle per day derived from tide-gage smoothed data (continuous line) and from GEOSAT data (dotted line). The 95% level of confidence is given for the twice-daily tide-gage data.

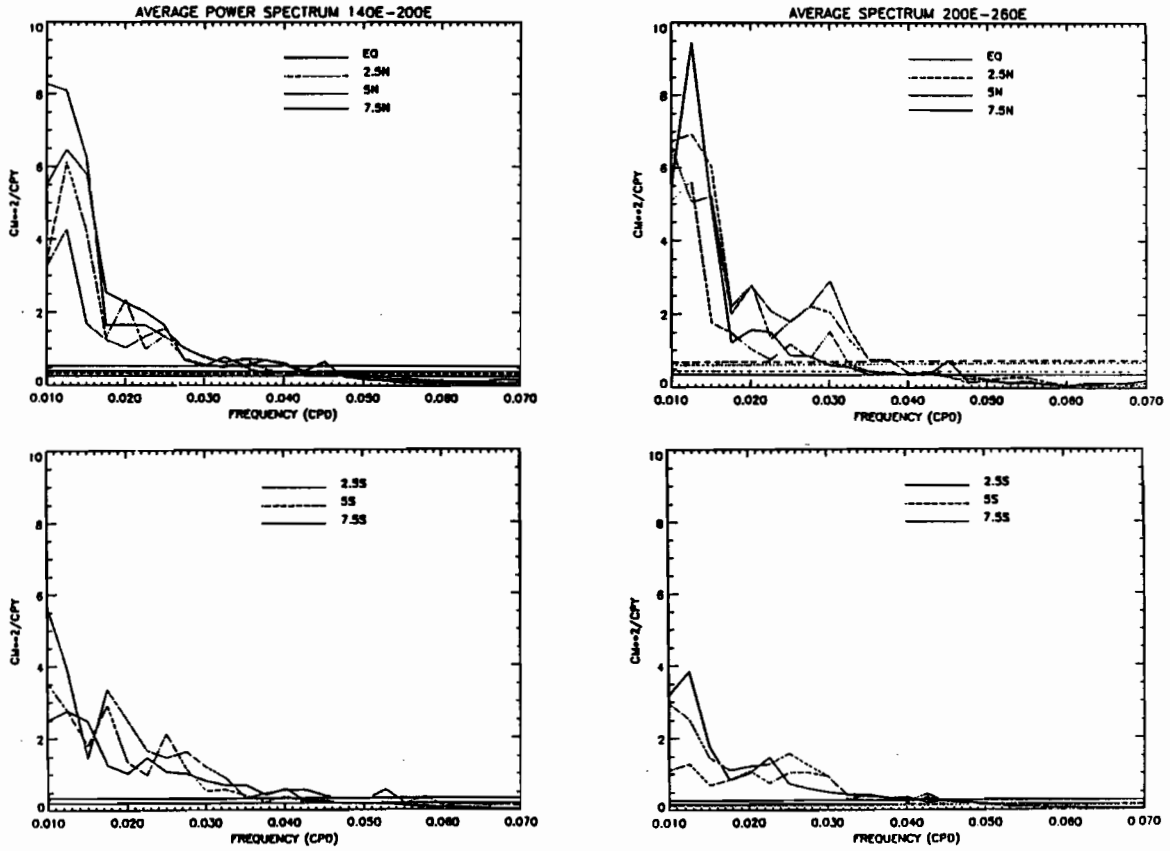

FIG.5. GEOSAT frequency power spectra averaged along zonal sections in the western and eastern Pacific. Units are cycle per day for frequencies and cm² per (cycle per year) for power.

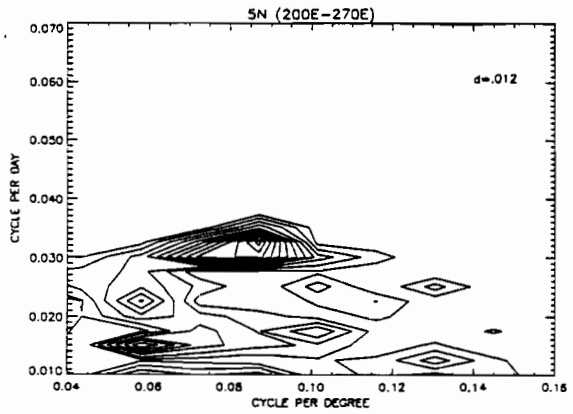

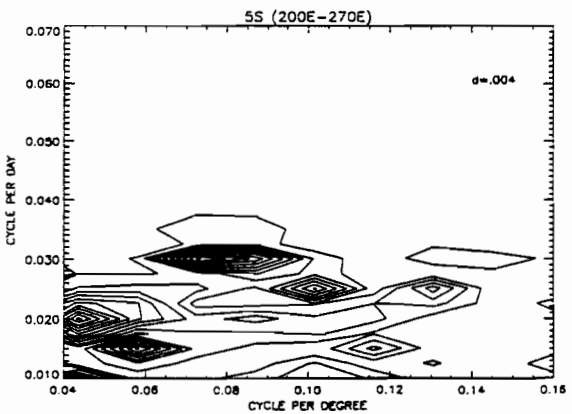

FIG.6. Wavenumber-frequency spectra derived at 5°N and 5°S zonal sections of GEOSAT anomaly maps. Units of isocontours are in cm^2 per (cycle per year) per (cycle per km).

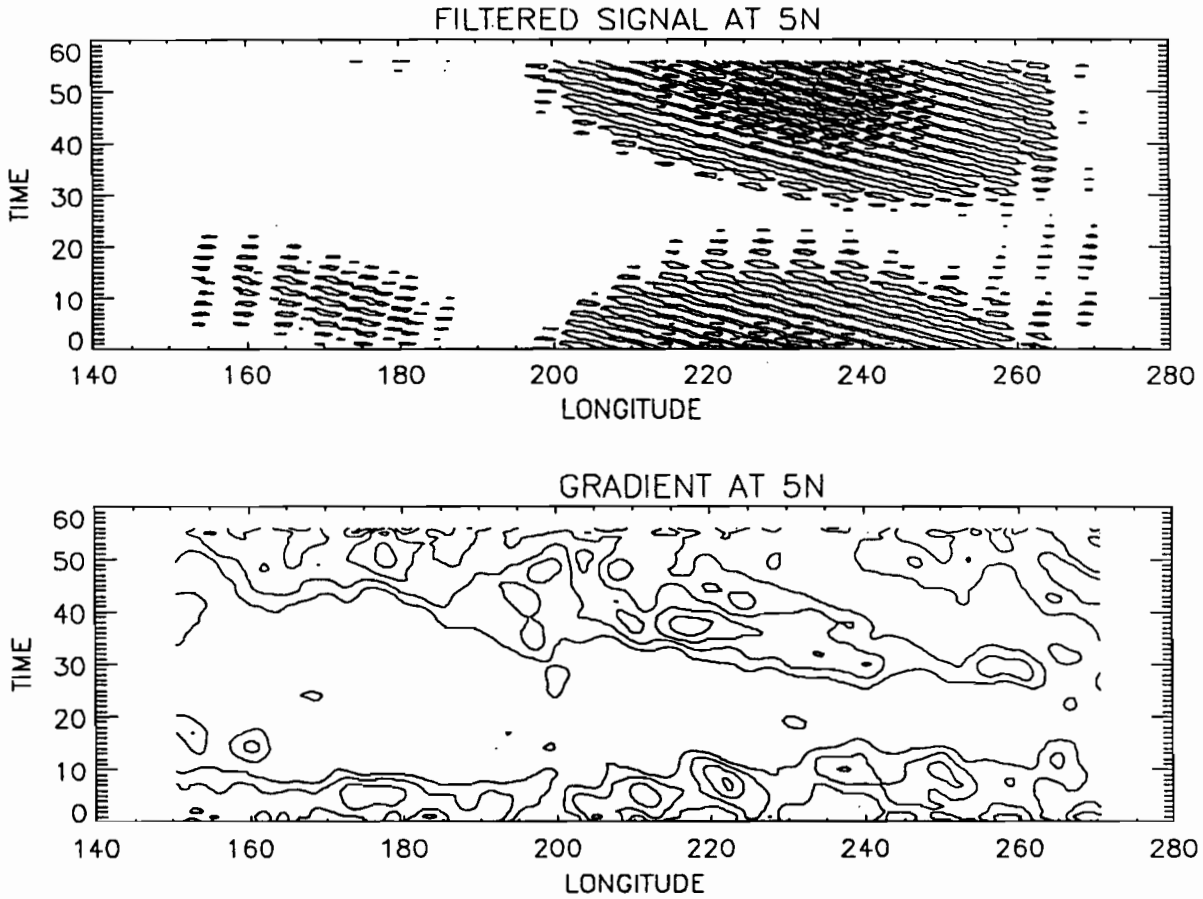

FIG.7. Top: Amplitude of GEOSAT filtered sea level variations at 5°N as a function of longitude and time (units of time axis are week starting on November 16 1986 and isocontours are 0.5 cm).

Bottom: meridional sea level gradient (relative to the 13 month mean): only the negative values increasing the shear-strength are contoured. Isocontour is 2 cm per degree of latitude.

Wavenumber frequency spectra are then given at 5ºN and 5ºS (fig 6). The 25 ot 45 day band corresponds to the 1000-1500 km zonal wavelength range. Some symetry relative to the equator is found as well in these wavelength band, but with less energy in the Southern than in the North.

V FILTERED SIGNALS

Geosat analyzed residuals are filtered within 25 to 45 days and 1000 to 1500 km. The filtered signal (fig 7 top) clearly shows a westward phase speed of 40 km/day. From November 1986 to February 1987, waves are present in the western and eastern Pacific with the strongest amplitude in the East and the weakest amplitude in the Central Pacific between 160ºW and 180º. The maximum amplitude in time is 4 cm East of 180º and 2 cm in the West. The eastern and the western packets of waves are disconnected. Waves are the weakest between February and June and become active again in the East from 120ºW in June to 160ºW in August. Very little wave activity is found in the West after February 1987.

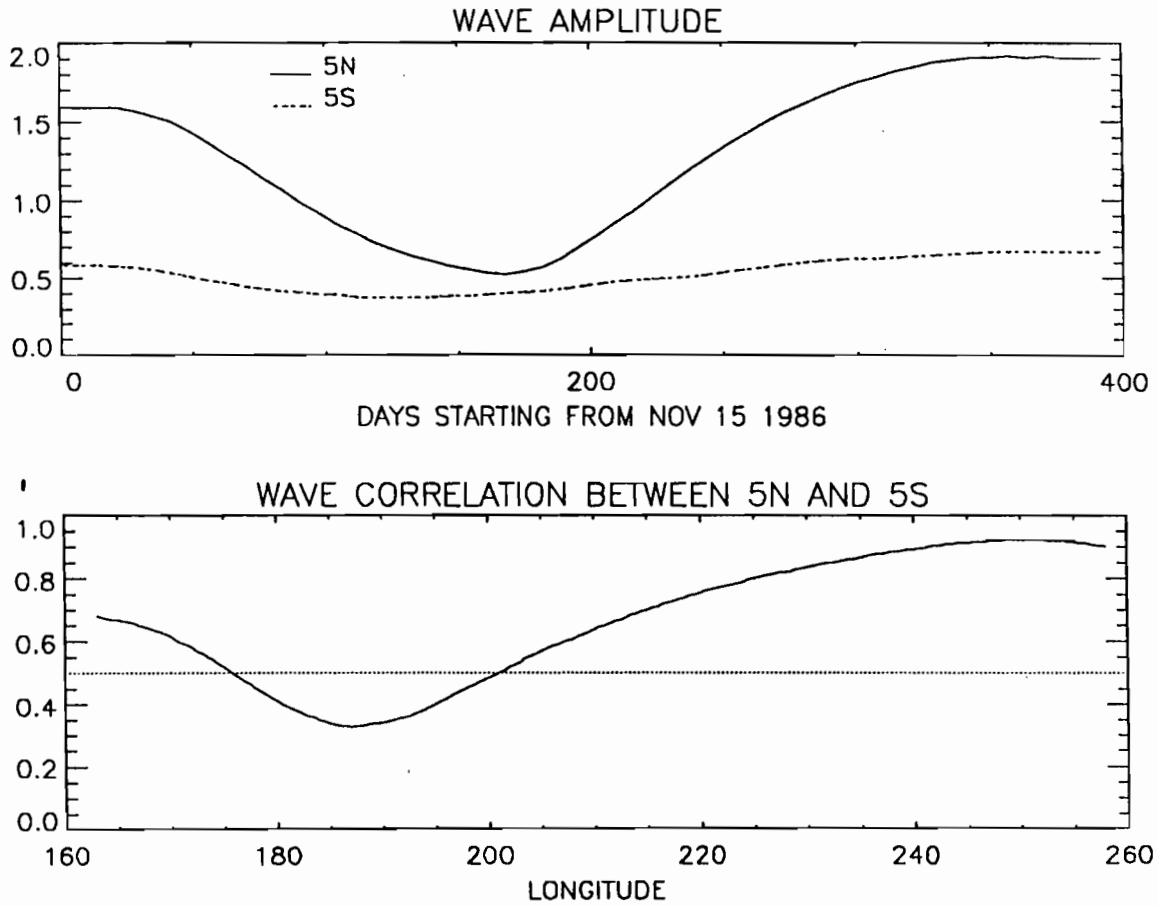

FIG.8. Top: Zonally averaged wave amplitude as a function of time.
Bottom: correlation in time between wave at 5°N and at 5°S as a function of longitude.

In the East, energy is transported eastward at 35 km/day. Furthermore the strong seasonal modulation is strongly correlated with the increase of shear strength between the South Equatorial Current and the North Equatorial Counter Current as measured by the meridional gradient of sea level derived from Geosat smoothed time series (fig 7 bottom). Indeed the axis along which the shear-strength increases in time by 2 cm per degree of latitude is tilted with time corresponding to a 40 km/day westward migration and its longitude-time location is well correlated with the strengthening of the waves as filtered above.

In the West, the phenomenon look different. The shear strength is increased in winter 1986-1987 when the waves are present but in summer 1987, the shear-strength continues to increase with time as in the East and the waves do not strengthen again before late 1987. Indeed 20 to 30 day oscillations of meridional velocity have been observed in the western Pacific in 1986-1987 with current measurements along the equator and have been correlated with meridional wind fluctuations (McPhaden et al, 1989).

The same filter in frequency and wavenumber has been applied along 5ºS. Then no clear eastward nor westward propagation of energy is found. The waves at 5ºS show similar seasonal modulation and longitudinal dependency (fig 8 top) but the correlation between 5ºN and 5ºS is always positive and shows significant symetry with respect to the equator (fig 8 bottom). The strongest signal in the North with a dominant symetry can be explained if the waves generated by instability are a superposition of Rossby-Gravity waves and Rossby waves. Similar mechanisms have been invoked in the superposition of Kelvin waves and Rossby waves (Busalacchi et al, 1983).

No evidence for Rossby-gravity wave nor link to the shear-current is demonstrated all across the Pacific. From figure 1 however, the positive anomalies are aligned all across the Pacific along the tilted axis of maximum sheared flow. The filtering zonally applied as previously precludes equatorial convergence of the waves (Schopf et al, 1981). This is why the same frequency-wavenumber band filtering has been applied within a 4º latitudinal band along a tilted axis. Then some energy is gained in the West compared to the previous results but the same time-longitudinal characteristics are found as well.

VI DISCUSSION

Geosat residuals have been analyzed with different space and time correlation parameters. The different Geosat analyzed series give similar mean RMS differences and similar range of correlation with the tide-gage data, although individual plots show significant differences with the previous ones. Nevertheless negligible difference is found in the spectra in the 10 to 50 day range, as well as in the filtered signal. Thus the previous results are not sensitive to the analysis parameters. This is consistent with the large zonal extent of the tropical waves. However the method used in this study is certainly not optimal to quantify the energy of the instability waves. Both the subsampling of the satellite and the smoothing of the analysis aliase the spectra. We must also keep in mind that water vapor content is not properly corrected in Geosat data and that the contribution of the atmospheric signal has not been examined in the present results.

With 13 months of Geosat data, it is possible to describe the time-longitude-latitude extent of the sea level anomaly due to instability waves. Waves with 1000-1500 km, 25 to 45 day, westward 40 km/day phase propagation and eastward 35 km/day energy propagation are clearly present along 5ºN East of 160ºW all year long except between February and June 1987. Compared to September 1978 as detected from Seasat altimeter (Malarde et al, 1987), these waves are less strong in September 1987. This is consistent with the weaker shear-strength present during the El-Nino 1986-1987 event. Furthermore, altimeter also provides the anomaly of shear-strength of the zonal flow. It is found that for the year 1986-1987, these waves are correlated with an increase of zonal shear East of the dateline and have a more complex latitudinal structure than the Rossby-Gravity wave.

ACKNOWLEGEMENTS

The author wants to thank Klaus Wyrtki (University of Hawai, Honolulu) who provided the tide-gage data in the Pacific, Victor Zlotnicki (JPL, Pasadena) who provided the program for orbit error correction, Akiko Hayashi (JPL, Pasadena) who gridded the Geosat GDR along track, and Stuart Pilorz (JPL, Pasadena) who was most helpful in the mathematical analysis. The research described in this paper was carried out by the Jet Propulsion Laboratory, California Institude of Technology, under a contract with the National Aeronautics and Space Administration.

BIBLIOGRAPHY

BUSALACCHI A.J., TAKEUCHI K. and O'BRIEN J.J., 1983: "Interannual Variability of the Equatorial Pacific - Revisited", J. Geophys. Res., 88, 7551-7562.

CHENEY R.E., DOUGLAS B.C., AGREEN R.W., MILLER L.L., DOYL N.S., 1988: "The NOAA Geosat Geophysical Data Records: summary of the first year of Exact Repeat Mission", NOAA Tech. Memo., NOS-NGS-48, Rockville, MD.

CHENEY R.E., DOUGLAS B.C. and MILLER L., 1989: "Evaluation of Geosat altimeter Data. With application to Tropical Pacific Sea Level Variability", submitted to J. Geophys. Res.

CHENEY R.E. and MILLER L, 1987.: "Geosat Altimeter Pacific Ocean Sea Level Anomalies", Climate Diagnostics Bulletin, NOAA, Ed: Kousky

COX M.D., 1980: " Generation and Propagation of 30-day waves in a numerical model of the Pacific", J. Phys. Oceanog, 10, 1168-1186.

CRISWELL S.M. and LUKAS R., 1989: "Rossby-gravity Waves in the Central Equatorial Pacific Ocean Durind the NORPAX Hawaii-to-Tahiti Shuttle Experiment", J. Geosphys. Res., 2091-2098.

EMERY W., BORN G., BALDWIN D., NORRIS C., 1988: "Satellite based tropospheric water vapor corrections for Geosat altimetry; a comparison btween Microwave and Infrared measurements ", EOS, 69, 44, 1274.

ENFIELD D., 1987: "The intraseasonal oscillation in eastern Pacific sea levels: How is it forced?", J. Phys. Oceanog., 17,

GASPAR P. and WUNSCH C., 1989: "Estimates from altimeter data of Barotropic Rossby Waves in the Northwestern Atlantic Ocean", submitted to J. Geophys. Res.

HALPERN D., KNOX R.A. and LUTHER D.S., 1988: "Observations of 20-day period Meridional current Oscillations in the upper Ocean along the Pacific Equator", J. Phys. Oceanog.

HANSON D.V. and PAUL C.A., 1984: "Genesis and effects of long waves in the equatorial Pacific", J. Geosphys. Res., 39, 10431-10440.

KENDALL, 1970: "The Pacific Equatorial Countercurrent", Ph D, Nova University.

MALARDE J.P., DE MEY P., PERIGAUD C. and MINSTER J.F., 1987: " The oceanic dynamic topography associated with long equatorial waves", J. Phys. Oceanog., 17, 2273-2279.

McPHADEN M.J., HAYES S.P, MANGUM L.J. and TOOLE J.M., 1989: "Variability in the western Equatorial Pacific Ocean During the 1986-1987 El-Nino/Southern Oscillation Event", submitted to J. Phys. Oceanog.

MILLER L., CHENEY R.E. and DOUGLAS B.C., 1988: "Geosat altimeter observations of Kelvin waves and the 1986-1987 El-Nino", Science, 239, 52-54.

MILLER L., WATTS D.R. and WIMBUSH M., 1985: "Oscillations of Dynamic topography in the Eastern Equatorial Pacific", J. Phys. Oceanog., 15, 1759-1770.

MITCHUM G.T. and LUKAS R., 1987: "The Latitude-Frequency Structure of Pacific Sea Level Variance", J. Phys. Oceanog., 17, 2362-2365.

SCHOPF P.S., ANDERSON D. and SMITH J., 1981: "Beta Dispersion of low frequency Rossby waves", Dynamics of Oceans and Atmospheres, 5, 187-214.

TRIPOLI G.J., and KRISHNAMURTI T.N., 1975: "Low-level flows over the Gate Area during Summer 1972", Mon. Wea. Rev., 197-209.

WEISBERG R.H., 1987: "Observations pertinent to instability waves in the equatorial oceans", Further Progress in Equatorial Oceanography, Nova University Press, Edited by Katz and Witte, 335-350.

WEISBERG R.H. and WEINGARTER T.J., 1988: "Instability waves in the equatorial Atlantic Ocean", J. Phys. Oceanog., 1641-1657.

WYRTKI K., 1975: "Fluctuations of the Dynamic Topography in the Pacific Ocean", J. Phys. Oceanog., 5, 450-459.

ZLOTNICKI V., FU L.L., PATZERT W., 1989: "Seasonal variability in global sea level", submitted to Jour. Geophys. Res.

Intraseasonal and Interannual Modes of Atmosphere-Ocean System Over the Tropical Western Pacific

Ryuichi KAWAMURA

Environmental Research Center
University of Tsukuba
Tsukuba, Ibaraki 305 - Japan

1. Introduction

The importance of the wave-CISK mechanism on the 30-60 day oscillation has been verified by the results of numerical models (Hayashi and Sumi, 1986; Hayashi and Golder, 1986; Lau and Peng, 1987; Yamagata, 1987, *etc.*). Since the intraseasonal oscillation was fairly well simulated using numerical models in which the sea surface temperature (SST) was fixed, it has been understood that this oscillation is an atmospheric phenomenon which is excited by the dynamics of the tropical atmosphere itself and there is no need to regard it as being an air-sea coupled system. However, there still remain some differences between the simulated and observed oscillations. One of them is the shift of simulated intraseasonal oscillations toward higher frequencies as compared to those observed. In recent numerical model studies, Miyahara (1987) estimated the effect of SST on tropical intraseasonal oscillation by varying the CISK parameter as functions of longitude and latitude. Sui and Lau (1989) shows that the lower boundary forcing due to heat flux from the ocean surface destabilizes the mobile wave-CISK mode. Thus some studies focus on the role of tropical SST as a lower boundary in destabilizing the intraseasonal mode.

The existence of the intraseasonal variations of tropical SST is already reported by Krishnamurti *et al.* (1988) and so on. We further found that the tropical SST exhibits a coupling with outgoing longwave radiation (OLR) on the same time scale with a phase difference of 10-20 days (Murakami, 1988; Kawamura, 1988). This fact is suggestive of not only the importance of the dependence of the 30-60 day oscillation on SST but also air-sea interaction in this time scale. It is still uncertain, however, how the air-sea coupling in the intraseasonal time scale is different from that in the interannual time scale which is represented by the ENSO and QBO.

The objective of this research, therefore, is to investigate phase relationships among SST, zonal wind at 850mb and high-cloud cover (HCC), providing a measure of active convection similar to OLR, in the warm pool region of the western Pacific on intraseasonal and interannual time scales. We extracted dominant phase relationship of the air-sea coupling in two time scales, using the complex EOF (CEOF) analysis.

2. SST and eastward-propagating intraseasonal mode

We first examine the relationships between the SST over the western Pacific and the eastward-propagating large-scale disturbance having an 30-60 day mode. The 10-day averaged SST data used were regularly collected by the Japan Meteorological Agency. Figure 1a indicates the climatological mean OLR field, which was obtained from the NMC/NOAA, for the northern summer (May-

ORSTOM
CENTRE DOCUMENTATION
Montpellier

F 30251

October) over the period from 1979 through 1984. Deep convective areas are observed in a belt extending from the Indian to the western Pacific Ocean. We divide the equatorial western Pacific sector (0°-10°N, 130°E-180°), where SST is very warm, into five blocks (10°latitude by 10°longitude) as shown in Fig. 1b and compute lag-correlations between 10-day mean SST and OLR averaged over each region during the above period. Figure 2 depicts the spatial distributions of lag-correlation coefficients between the tropical OLR anomalies from the Indian Ocean through the central Pacific and the SST in a key region (0°-10°N, 130-160°E), where significant correlations were detected. Here negative lag denotes that the variation in OLR precedes that in SST and one lag is equivalent to 10 days. Weak positive OLR anomalies cover the key region and extend to the central Pacific at lags of -2 and -1. On the other hand, negative anomalies are located in the region from the Indian Ocean to the maritime continent and progress eastward from negative through positive lags. At a lag of +2 (20 days), significant negative anomalies expand into the equatorial western Pacific. The above results show that the SST over the equatorial western Pacific and the eastward-propagating disturbance interact with an intraseasonal time scale, and that the SST is above normal to the east of the eastward-propagating 30-60 day mode disturbances.

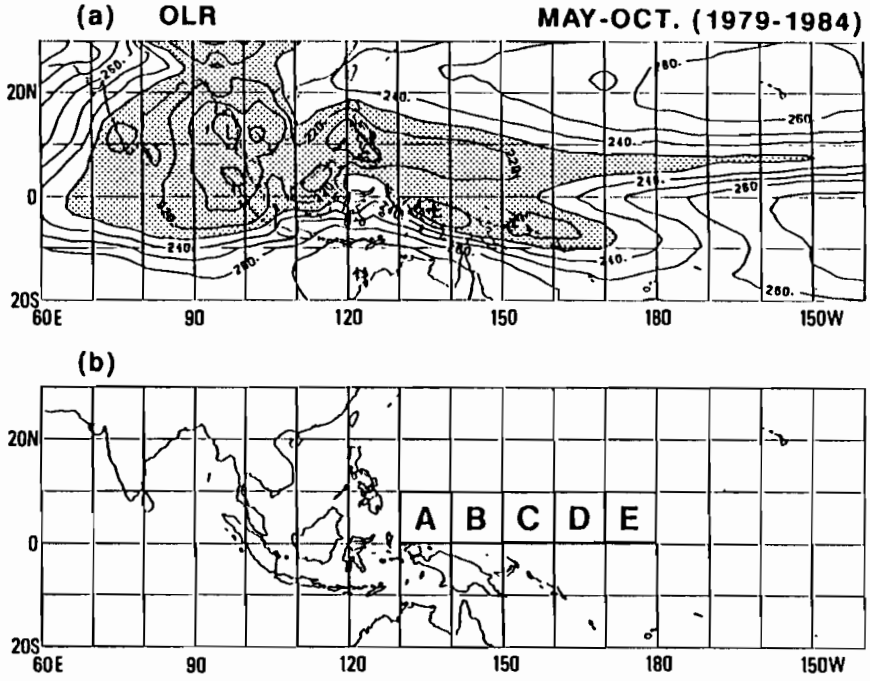

Fig. 1 (a) Climatological mean OLR field for the northern summer over the period from 1979 through 1984. The contour interval is 10Wm^{-2} and areas less than 230 Wm^{-2} are shaded, indicating the most active convection. (b) Location of five regions selected in computing lag-correlations between the 10-day mean SST and OLR.

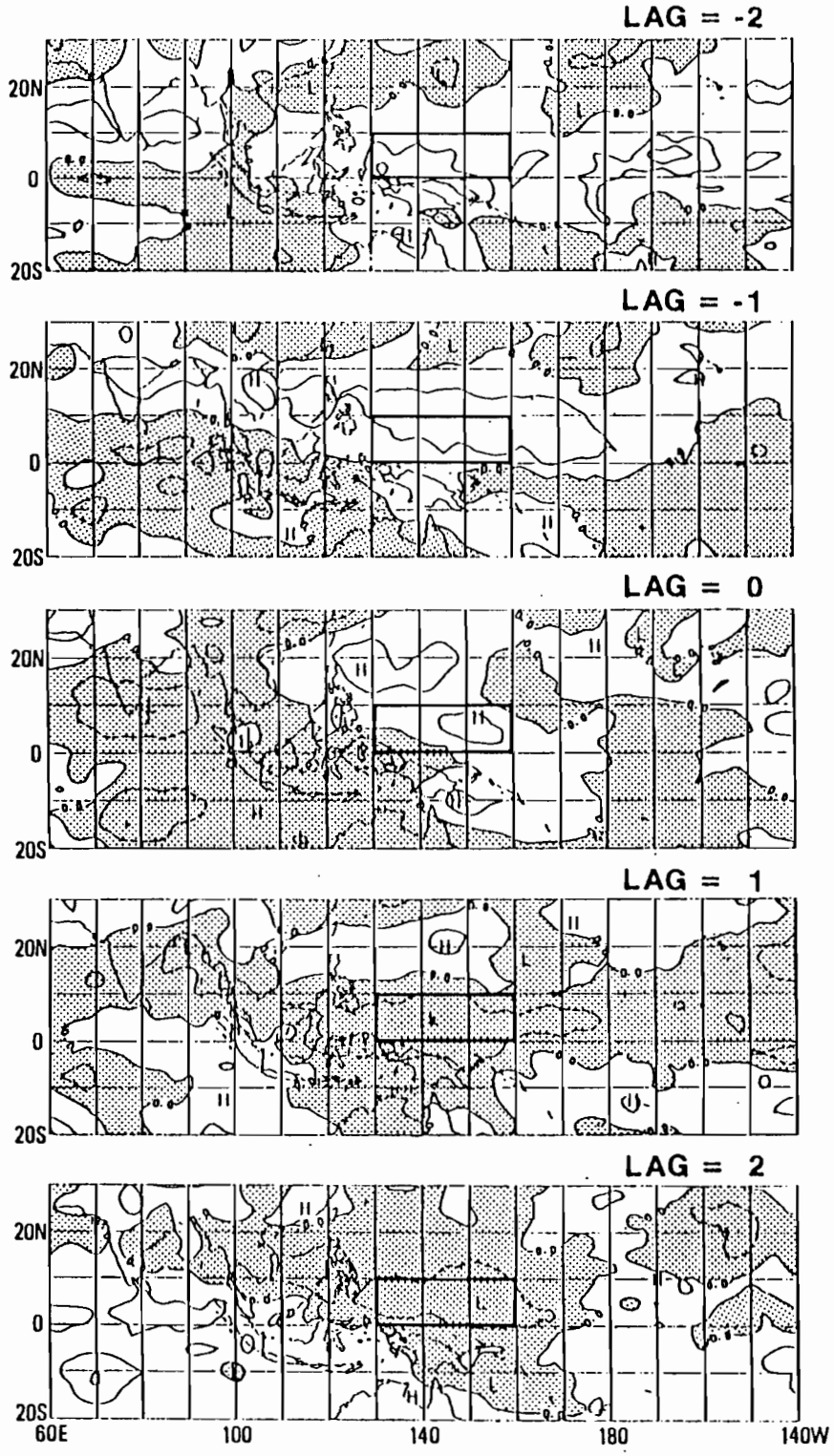

Fig. 2 Lag-correlation patterns between the OLR anomalies in tropical regions and SST anomalies in the key region (0°-10°N, 130-160°E) shown by the rectangle. Positive lag implies that the variation in SST precedes that in OLR and one lag is equivalent to 10 days. The contour interval is 0.2 and negative values are shaded.

Although Emanuel (1987) and Neelin *et al.* (1987) suggested that evaporation-wind feedback mechanism leads to the eastward propagation of intraseasonal disturbance using numerical model which SST is fixed, the high SST located to the east of eastward-propagating disturbance also provides a favorable condition for the disturbance to propagate eastward. It can be considered that the intraseasonal variations are easily modified by air-sea interaction and as a result have spectral peaks in wide (30 to 60 day) period range if we take account of such an air-sea interaction as the reduced incoming solar radiation and active turbulent mixing accompanying the large-scale disturbance result in a decrease of SST.

Figure 3 displays the time series of the 10-day mean SST (solid line) and OLR (dashed line) averaged over the key region for the northern summer (May-October) during the 6 year period (1979-1984). The coupling of SST and OLR on the intraseasonal time scale is more notable in the northern summer during 1979 when the 30-60 day oscillation of tropical convection was dominant. The SST in the key region fluctuates between 29.0 and 29.5°C during this period. In contrast, although the SST was above 29.5°C during 1981, the 30-60 day oscillations in both the OLR and SST were not very dominant. Rather, the SST in the equatorial western Pacific exhibited a 20-30 day oscillation and fluctuated in phase with OLR during the northern summer of this year. Thus the air-sea coupling in the 30-60 day time scale seems to be weak during the northern summer of 1981. It is of interest that the periodicity in the intraseasonal oscillation tends to be short for the 1981 when the air-sea coupling appears to be weak.

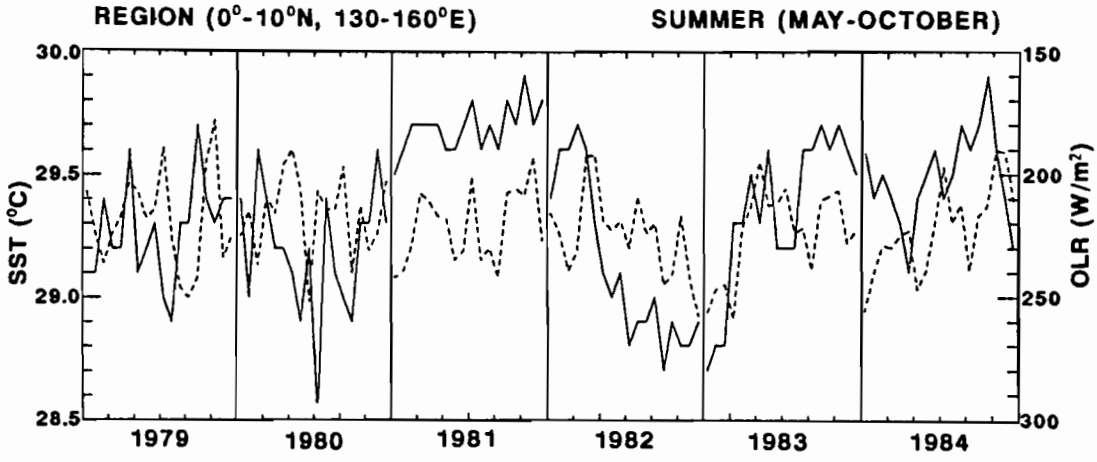

Fig. 3 Time series of the 10-day mean SST (solid line) and OLR (dashed line) in the key region (0°-10°N, 130-160°E) during the northern summer (May-October) for the period from 1979 through 1984.

3. Phase relationships among SST, HCC and zonal wind at 850mb

Figure 4 shows time series of HCC, SST and 850mb*u* for two time scales in the key region during the 7 year period 1980-1986. We utilize the GMS high-cloud cover data defined as a fractional ratio of cloud pixels at a 1°latitude by 1°longitude area, whose top height is above 400mb. The maximum value of HCC is 10.0. Daily 850mbu data are derived from global analyses by ECMWF. The intraseasonal component is here evaluated as departures from the smoothed data (interannual component) using a 90-day weighted running mean. It is deduced that the amplitudes and phases of SST, HCC and 850mb*u* vary with longitude even over the tropical western Pacific, though both components have a general nature of propagating eastward. Hence time series of the three variables (SST, HCC and 850mb*u*) in two time scales in regions A and E are also indicated in Figs. 5 and 6, respectively. For the intraseasonal component in region A, the periods of large amplitude of all three variables are the 1979 period and 1984/85 period. The amplitude of the intraseasonal component in region E is smaller than that in region A. In contrast, the amplitude of the interannual component in region E tends to be larger than that in region A. Thus it is observed that the regions where two components are dominant are different each other.

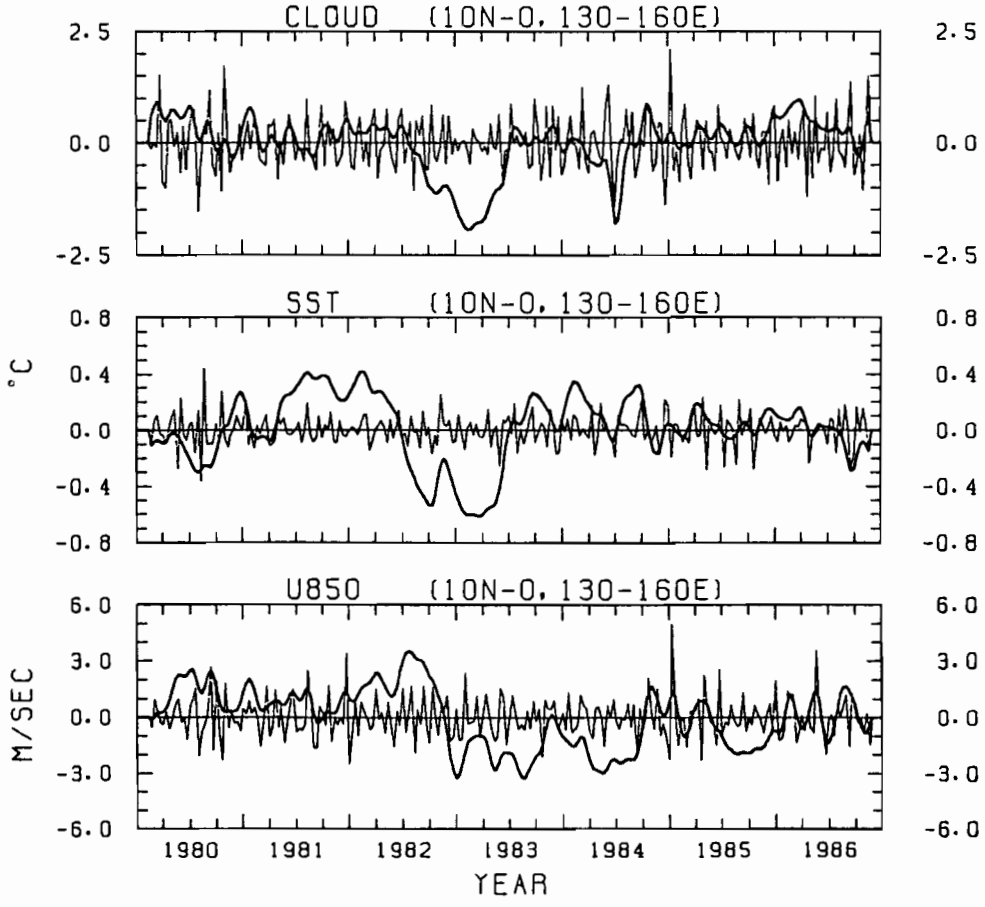

Fig. 4 Time series of HCC, SST and 850mb*u* in the key region for intraseasonal component (thin line) and interannual component (thick line).

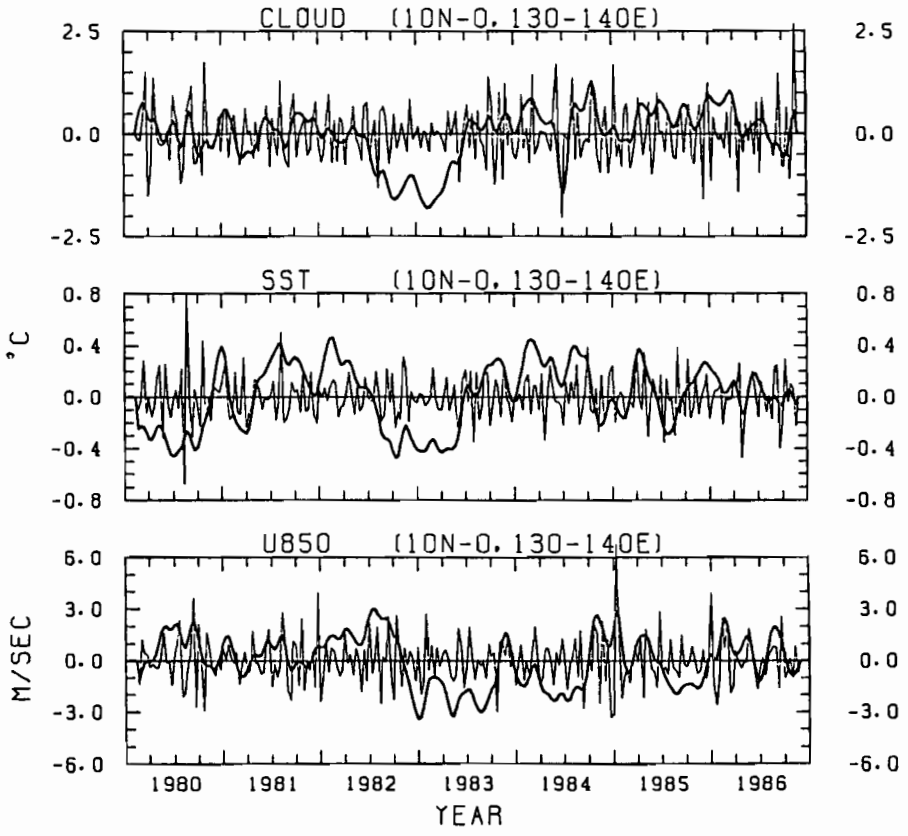

Fig. 5 As in Fig. 4, but for region A.

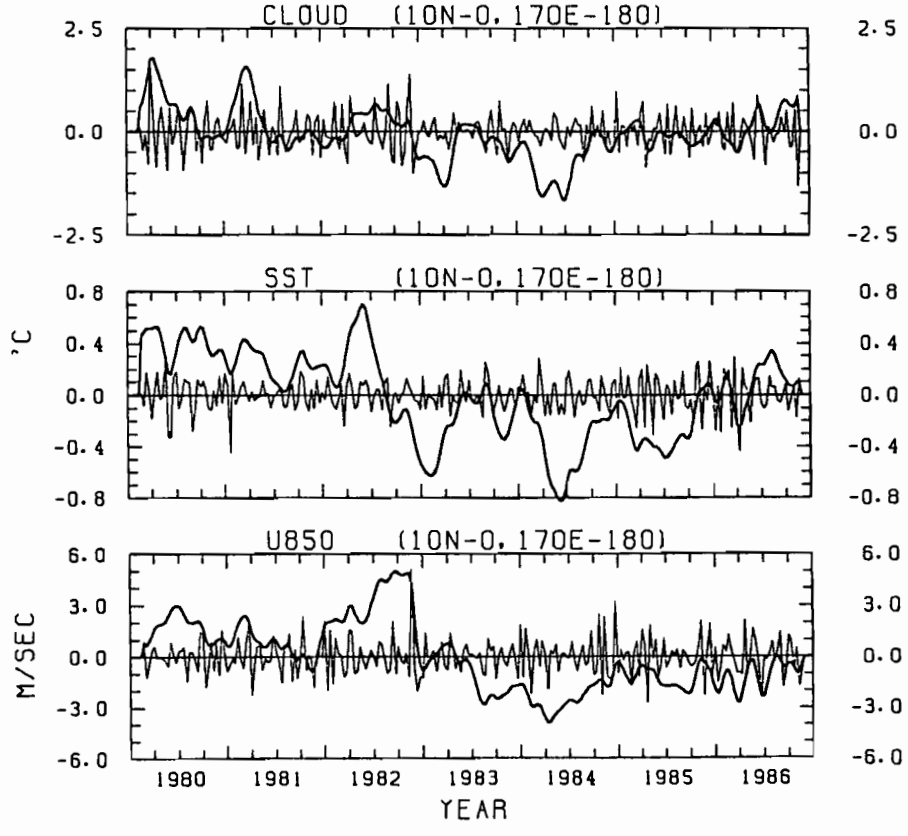

Fig. 6 As in Fig. 4, but for region E.

We next examined statistically phase relationships among three variables on each time scale in regions A, E and key region, using the CEOF analysis. Complex time series $X(j,t)$ is obtained by Hilbert transform of $x(j,t)$, the normalized time series of each variable j. $X(j,t)$ is expand into the sum of EOFs as follows.

$$X(j,t) = \sum_{m=1}^{3} Fmt\, Bm^*(j)$$

where the asterisk implies complex conjugation, $Bm(j)$ represents the complex eigenvector of the j-th variable for the m-th mode, and Fmt is the complex coefficient for $Bm(j)$. Considering only three variables, we solve the eigenvalue problem of the 3x3 complex correlation matrix (Hermite matrix). We should refer to Barnett (1983) if more detailed explanation is needed. The amplitudes $A(j)$ and phases $P(j)$ of the first CEOF modes for the intraseasonal and interannual time scales in each region are shown in Fig. 7. We can obtain $A(j)$ and $P(j)$ as

$$A(j) = [Bm(j)\, Bm^*(j)]^{1/2},$$
$$P(j) = \tan^{-1} [\mathrm{Im}\ Bm(j) / \mathrm{Re}\ Bm(j)].$$

Here the first CEOF modes for the intraseasonal and interannual time scales are called the intraseasonal mode and interannual mode, respectively.

The intraseasonal mode has a similar tendency in all regions. In this mode the HCC is almost in phase with 850mb$u$, that is, the maximum of HCC is in accord with that of westerly wind at 850mb, while the SST leads HCC by around 140°-170°. If we notice the key region where the variance is largest in all regions, it can be seen that the amplitude of SST is somewhat smaller than that of HCC or 850mb$u$ and phase difference between SST and HCC is about 140°. This means that in the intraseasonal time scale the HCC (or westerly wind at 850mb) couples with SST with a phase shift of 10-20 days. The above result is consistent with the results of previous observational studies (Kawamura, 1988; Murakami, 1988).

On the other hand, in the interannual mode the amplitude of SST is almost as large as that of HCC and the SST leads HCC by around 10°-30°. Further it is seen that the phase of 850mb$u$ shifts obviously from regions A to E, that is, in region A the phase lag between SST and 850mb$u$ is about 80°, whereas in region E the 850mb$u$ comes to lag SST by only about 20°. Since the interannual mode includes the time scales of the ENSO and QBO, it is inferred that the SST over the western Pacific is anomalously high and then the HCC reaches its maximum about 1-3 months later. The maximum of westerlies at 850mb lags that of HCC by 3-7 months for the key region and by within 1 month for region E. The variance of the interannual mode tends to become large from the western Pacific eastward to the dateline. The above results are summarized as a schematic diagram as shown in Fig. 8.

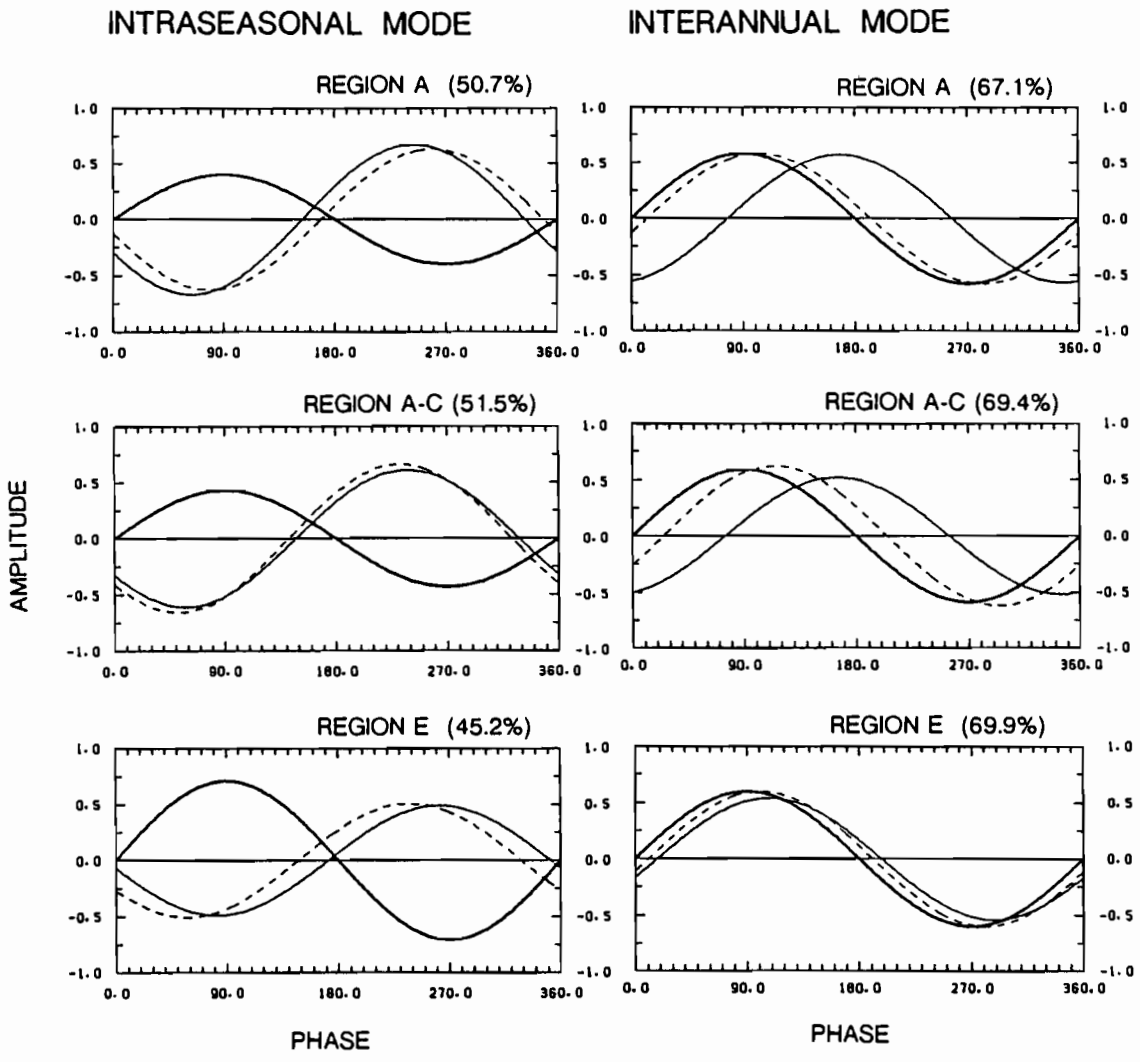

Fig. 7 The amplitudes and phases (degrees) of SST, HCC and zonal wind at 850mb on the intraseasonal and interannual modes. The SST, HCC and 850mb*u* are denoted by thick, dashed and thin lines, respectively. Note that the ratio of the explained variance of the total variance, expressed as percentages, is also shown for each region.

4. Summary and discussion

This paper addresses the question of air-sea coupling in the warm pool region of the western Pacific on intraseasonal and interannual time scales. We make investigation into phase relationships among SST, HCC and zonal wind at 850mb in two time scales using the CEOF analysis.

It is first found that there exist the remarkable differences of air-sea coupling in intraseasonal time scale from in interannual time scale. The intraseasonal mode reveals similar tendencies over the tropical western Pacific. In this mode the SST is approximately out of phase with HCC and

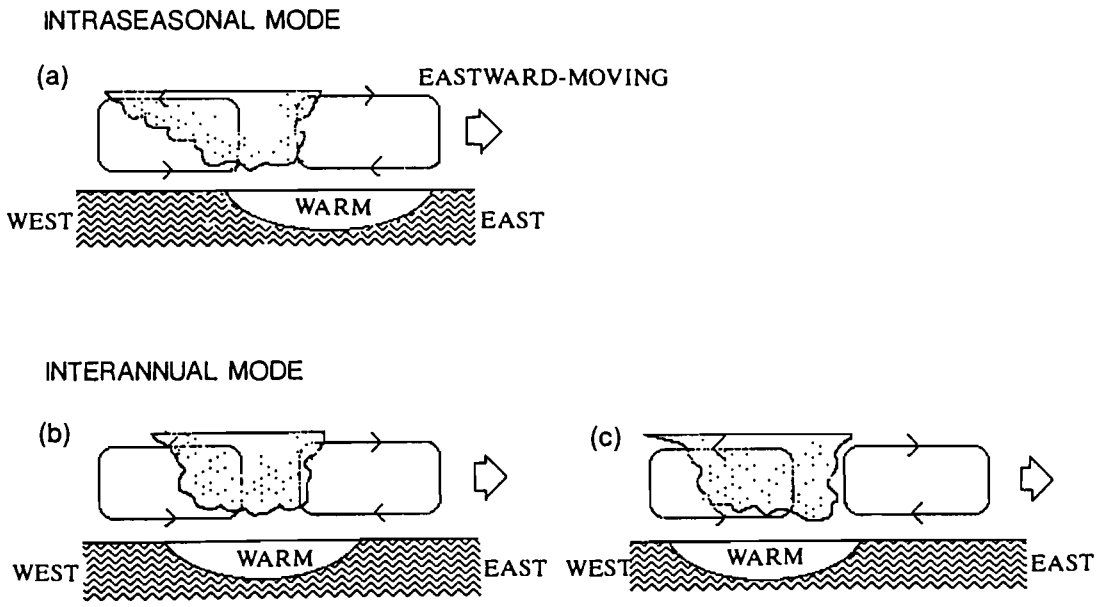

Fig. 8 Schematic diagrams displaying the phase relationship of air-sea coupling on (a) the intraseasonal mode for the key region and on the interannual mode for (b) the key region and (c) region E.

850mb*u*. The existence of high SST located to the east of eastward-propagating 30-60 day disturbance favors its further eastward propagation. This mode is very similar to the advective mode presented by Lau and Shen (1988) with respect to phase relationship. Their mode requires an east-west SST gradient. However, the intraseasonal mode defined in this paper exists in the warm pool region where the east-west SST gradient is so small. The intraseasonal variations of SST in the warm pool region, therefore, are probably caused by the mechanism of incoming short-wave radiation and turbulent mixing in ocean mixed layer rather than east-west SST advection. The importance of air-sea interaction for intraseasonal oscillations cannot be denied, though the amplitude of SST is somewhat smaller than of the other variables.

It is also found that the air-sea coupling in interannual time scale varies with longitude over the tropical western Pacific. The interannual mode is that the SST leads HCC by about 20° but the phase of 850mb*u* is different in each region. The SST-HCC negative feedback may not be essential to this mode because the SST and HCC tend to be in phase. Since the variances of this mode are large from the western Pacific eastward to the dateline, it is understood that an atmospheric interannual mode propagating eastward over the western Pacific gradually intensifies large-scale air-sea coupling. Although the variances of interannual mode are larger than those of intraseasonal mode, it may be natural that the air-sea coupling like the ENSO event is stronger than that in intraseasonal time scale.

Although we examined statistically phase relationships of air-sea couplings on two time scales only over the western Pacific, we will further understand the air-sea couplings of eastward-propagating modes in two time scales if a similar analysis is applied in the eastern Pacific and Indian Oceans.

References

Barnett, T.P., 1983: Interaction of the monsoon and Pacific trade wind system at interannual time scales, Part I: The equatorial zone. *Mon.Wea.Rev.*, 111, 756-773.

Emanuel, K.A., 1987: An air-sea interaction model of intraseasonal oscillations in the tropics. *J.Atmos.Sci.*, 44, 2324-2340.

Hayashi, Y. and D.G. Golder, 1986: Tropical intraseasonal oscillations appearing in a GFDL general circulation model and FGGE data, Part I: Phase propagation. *J.Atmos.Sci.*, 43, 3058-3067.

Hayashi, Y.Y. and A. Sumi, 1986: The 30-40 day oscillations simulated in an "aqua planet" model. *J.Meteor.Soc.Japan*, 64, 451-467.

Kawamura, R., 1988: Intraseasonal variability of sea surface temperature over the tropical western Pacific. *J.Meteor.Soc.Japan*, 66, 1007-1012.

Krishnamurti, T.N., D.K. Oosterhof and A.V. Mehta, 1988: Air-sea interaction on the time scale of 30 to 50 days. *J.Atmos.Sci.*, 45, 1304-1322.

Lau, K.-M. and L. Peng, 1987: Origin of low frequency (intraseasonal) oscillations in the tropical atmosphere, Part I: The basic theory. *J.Atmos.Sci.*, 44, 950-972.

Lau, K.-M. and S. Shen, 1988: On the dynamics of intraseasonal oscillations and ENSO. *J.Atmos.Sci.*, 45, 1781-1797.

Miyahara, S., 1987: A simple model of the tropical intraseasonal oscillation. *J.Meteor.Soc.Japan*, 65, 341-351.

Murakami, T., 1988: Relationship between sea surface temperatures and outgoing longwave radiation on intraseasonal time scale (*in Japanese*). *Bull.Meteor.Soc.Japan (Tenki)*, 35, 715-722.

Neelin, J.D., I.M. Held and K.H. Cook, 1987: Evaporation-wind feedback and low-frequency variability in the tropical atmosphere. *J.Atmos.Sci.*, 44, 2341-2348.

Sui, C.-H. and K.-M. Lau, 1989: Origin of low frequency (intraseasonal) oscillations in the tropical atmosphere, Part II: Structure and propagation of mobile wave-CISK modes and their modification by lower boundary forcings. *J.Atmos.Sci.*, 46, 37-56.

Yamagata, T., 1987: A simple moist model relevant to the origin of intraseasonal disturbances in the tropics. *J.Meteor.Soc. Japan*, 65, 153-165.

Observed Structure of Convective Anomalies

David GUTZLER and Tamara M. WOOD

Atmospheric and Environmental Research, Inc.
840 Memorial Dr.
Cambridge, MA 02139 - U.S.A.

1. Introduction

One of the major thrusts of TOGA, and of COARE in particular, is to improve our understanding of the mechanisms by which variations of sea surface temperature (SST) force perturbations in the overlying atmosphere. Several different forcing mechanisms have been developed for use in simple models. The purpose of this study is to compare variance and correlation statistics derived from observed wind, SST, and convection data to try to diagnose the relative importance of some of these mechanisms.

Three coupling mechanisms will be considered. Gill (1980) developed a simple model in which the low-level atmospheric circulation is driven by deep convection, a mechanism we refer to as "interior heating". Zebiak (1986) adapted and extended this model by parameterizing the link between SST and convection in terms of anomalous latent heat flux from the ocean surface over warm SST anomalies, which acts as a trigger for the convection that provides most of the heating. Using a different approach, Neelin and Held (1987) parameterized the effect of variations in SST on the overlying atmosphere in terms of changes in the gross moist static stability, which governs deep convection and low-level convergence. In this model the ocean-atmosphere coupling is local and thermodynamic in nature. A third, entirely different ocean-atmosphere coupling mechanism was explored by Lindzen and Nigam (1987), who proposed that the atmospheric boundary layer could be approximated by a homogenous slab and SST gradients are dynamically equivalent to surface pressure gradients, which then drive the low-level circulation directly. In this model deep convection is a dynamically passive byproduct of pressure gradient-driven low-level convergence whereas convection plays a fundamental role forcing the circulation in the other models.

Comparison of these different mechanisms suggests how they might be differentiated in observed data, although it seems plausible that each of the mechanisms is operative to some extent. The static stability scheme should results in high local correlation between fluctuations of SST and deep convection. The interior heating and surface gradient schemes can be differentiated if there is significant vertical structure in the convergence field, since surface temperature gradients ought to be relatively more effective at forcing the wind field right at the ocean surface, and interior heating ought to be relatively more effective at forcing winds well above the surface in the lower troposphere. We therefore base this study on a comparison of the geographical distribution of variance and correlations among SST, outgoing longwave radiation (OLR; a proxy for deep convection), and convergence at the surface and at 850 mb.

2. Data and analysis procedure

We use monthly mean fields of SST, OLR, NMC-analyzed 850 mb winds, and surface winds analyzed subjectively from ship reports, for the 9-year period January 1979- December 1987 (108 months). The surface wind data were derived from wind stress analyses produced at Florida State University and the other fields were provided

ORSTOM
CENTRE DOCUMENTATION
Montpellier

F30252

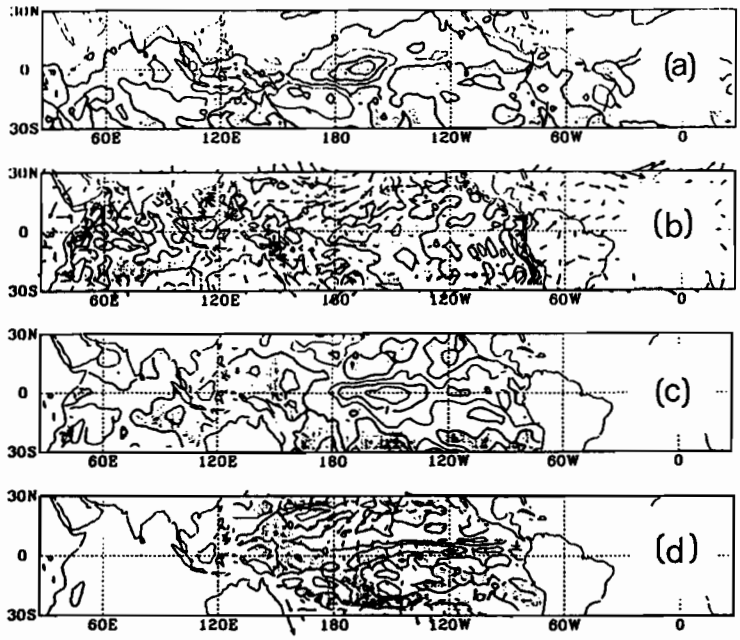

FIG.1. Monthly mean anomalies for January 1987, defined relative to the January average at each gridpoint for years 1979-1987 (negative values shaded). (a) OLR, (b) v_{850} and $\nabla \cdot v_{850}$, (c) SST, (d) v_s and $\nabla \cdot v_s$.

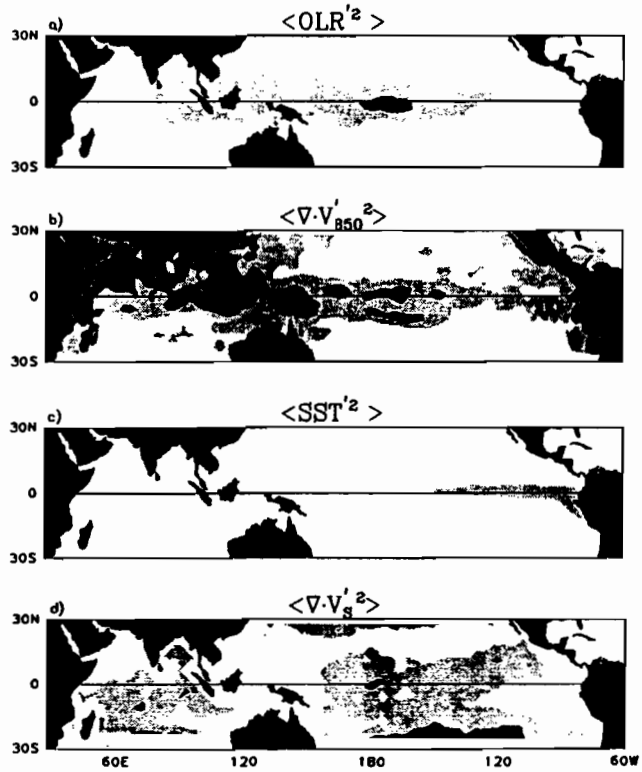

FIG.2. Variance of monthly anomalies for the period Jan. 1979 - Dec. 1987. (a) OLR : variance > 200 $W^2.m^{-4}$ lightly stippled, > 400 heavily stippled. (b) $\nabla \cdot v_{850}$: variance > 1×10^{-12} s^{-2} lightly stippled, > 2×10^{-12} heavily stippled. (c) SST : variance > 1 K^2 lightly stippled. (d) $\nabla \cdot v_s$: variance > 10×10^{-12} s^{-2} lightly stippled, > 20×10^{-12} heavily stippled.

by the NMC Climate Analyses Center. All data have been interpolated to a common 2.5°x2.5° latitude-longitude (ϕ, λ) grid extending from 30°N to 30°S across the Indian and Pacific Oceans (Indian Ocean surface wind analyses were available only through December 1986). The surface and 850 mb wind fields chosen for this study were derived completely independently from each other so there is no inherent vertical coupling between them.

Climatological monthly means were calculated at each gridpoint by averaging over the nine-year period, and monthly anomalies were then formed by subtracting the monthly climatological value from each gridpoint. Wind divergence fields were derived from the centered difference calculation

$$\nabla\cdot v = (1/a\cos\phi)\,\partial u/\partial\lambda + (1/a\cos\phi)\,\partial(v\cos\phi)/\partial\phi$$

(where a is the radius of the earth) without additional smoothing.

3. An example: January 1987

Figure 1 shows anomalies of OLR, SST, and the surface and 850 mb wind and divergence fields for January 1987 (during the mature phase of the 1986-87 ENSO warm event). These plots illustrate the significant vertical structure that can be present in the low-level convergence field. The upper panels show the OLR and v_{850} anomaly fields. The largest negative OLR anomaly (indicative of enhanced convection) is centered on the equator between 160°E and 150°W, coincident with a broad 850 mb convergence anomaly. The warm SST and $\nabla\cdot v_s$ anomalies, in the lower two panels, are also coincident but they extend between the date line and the South American coast, distinctly to the east of the OLR and $\nabla\cdot v_{850}$ anomalies. The impression given by the plots in figure 1 is that, at least for this particular month, the near-equatorial surface convergence anomaly is coupled to the SST anomaly, whereas the convergence anomaly at 850 mb is more closely associated with the OLR anomaly.

4. Variance and cross-correlation of SST, OLR, and convergence

Figure 2 shows plots of the local variance of monthly anomalies of OLR, SST, $\nabla\cdot v_{850}$ and $\nabla\cdot v_s$ about monthly climatological averages (the annual cycle has been removed). Variance maxima in OLR and 850 mb divergence are nearly coincident across the near-equatorial Pacific to the west of about 120°W. SST and $\nabla\cdot v_s$ variance maxima are located east of the dateline extending to the South American coast. Note that the variance of $\nabla\cdot v_s$ is generally much greater than the variance of $\nabla\cdot v_{850}$ but the spatial distributions of these variances are very different. We divide the near-equatorial Pacific into three longitudinal zones based on these anomaly variance calculations : in the west (from the maritime continent to the dateline) OLR and $\nabla\cdot v_{850}$ variances are large and SST and $\nabla\cdot v_s$ variances are small; in the east (120°W to South America) OLR and $\nabla\cdot v_{850}$ variances are small and SST and $\nabla\cdot v_s$ variances are large; in the mid-Pacific (between the dateline and 120°W) the variances of all these fields are large.

Geographical variations of pointwise correlations between monthly anomalies of OLR and $\nabla\cdot v_{850}$ or $\nabla\cdot v_s$ (Fig.3) underscore the distinctions implied by the previous two figures. The only region of significant local correlation (exceeding 0.4) of SST and OLR anomalies lies along the equator between the dateline and the South American coast, nearly coincident with the region of maximum variance of SST anomalies. The OLR-$\nabla\cdot v_{850}$ correlation exceeds 0.4 in a band across the western and central Pacific as far east as about 120°W. In contrast, significant OLR-$\nabla\cdot v_s$ correlations are located along the equator from the South American coast westward only to the dateline. Hence surface

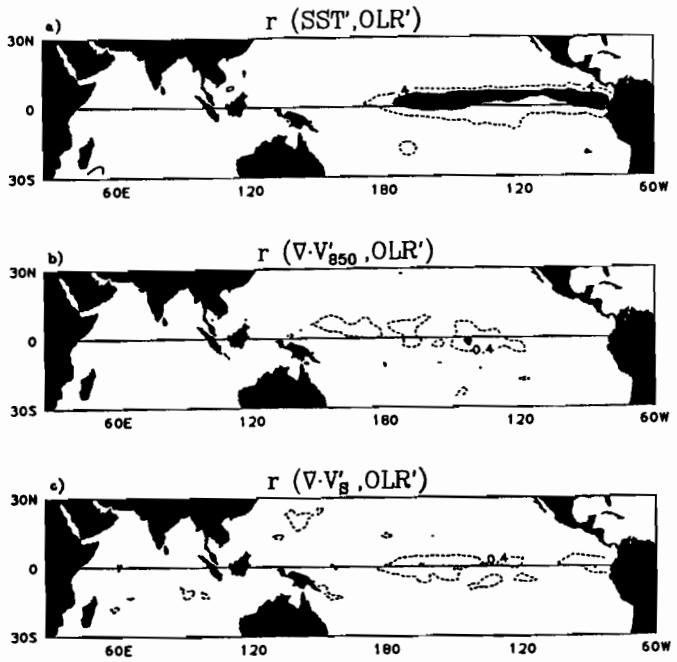

FIG.3. Pointwise correlation between monthly anomalies of OLR and monthly anomalies of (a) SST, (b) $\nabla \cdot v_{850}$, (c) $\nabla \cdot v_s$. In (a), -0.4 contours are dashed and correlations less than -0.6 are stippled; +0.4 contours are solid and correlations greater than +0.6 are hatched. Sign convention is reversed in (b) and (c).

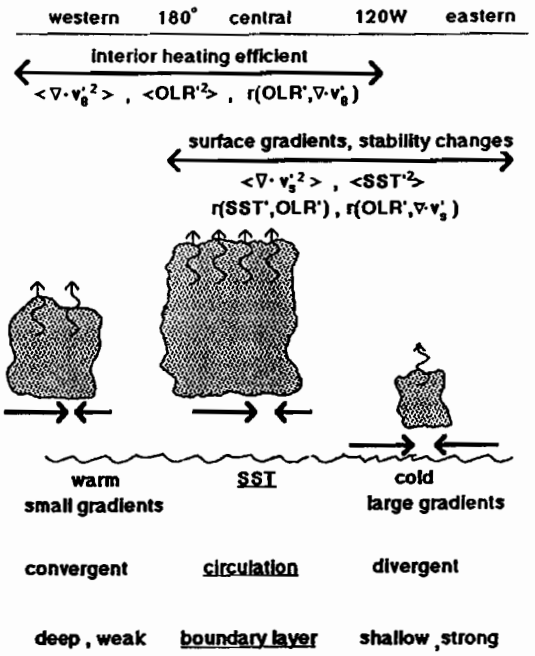

FIG.4. Schematic depiction of longitudinal variations of SST-OLR-wind relationships across the near-equatorial Pacific.

convergence and OLR anomalies are highly correlated over the eastern Pacific despite the low variance of OLR anomalies there; conversely the correlation is nearly zero over the western Pacific despite the high OLR variance there.

5. Discussion and recommendations for COARE

Our results and interpretation are summarized in figure 4 by a schematic depiction of longitudinal variations in the relationships among monthly anomalies of SST, convection and low-level wind convergence across the near-equatorial Pacific.

. *West of the dateline* (Including the proposed COARE domain), where the mean SST field features warm temperatures and small temperature gradients and the mean low-level atmospheric circulation is convergent, monthly anomalies of SST and $\nabla \cdot v_s$ are small and anomalies of OLR and $\nabla \cdot v_{850}$ are large (as determined by the variances of the anomaly time series). OLR anomalies are better correlated with $\nabla \cdot v_{850}$ anomalies than with $\nabla \cdot v_s$ anomalies. SST and OLR anomalies are not significantly correlated.

. *From 120°W eastward to the South American coast,* in contrast, the mean SST field is cold with large temperature gradients and the mean low-level atmospheric circulation is divergent. Monthly anomalies of SST and $\nabla \cdot v_s$ are large and anomalies of OLR and $\nabla \cdot v_{850}$ are small. OLR anomalies are better correlated with $\nabla \cdot v_s$ anomalies than with $\nabla \cdot v_{850}$ anomalies, and the correlation between OLR and SST is high.

. *In the central Pacific between the dateline and 120°W*, anomaly variances of all these quantities are relatively large. Anomalies of SST and convergence at both the surface and 850 mb are significantly correlated with OLR anomalies.

Taken together these results support the following comparison of the coupling mechanisms discussed in the introduction: forcing of the low-level wind field (particularly at 850 mb) by *interior heating* is relatively effective over the western Pacific (the proposed COARE domain), whereas forcings by *stability changes* and *surface gradients* are relatively more effective over the *eastern* Pacific. It seems likely that the central Pacific is a regime in which all of these forcing mechanisms are effective.

Several additional conclusions follow from the results. First, it must be emphasized that the convergence of the surface wind field is significantly different from the convergence at 850 mb, reinforcing the results of a previous comparison of u and v winds derived from individual station data (Harrison and Gutzler, 1986). Winds from these two levels should therefore not be used interchangeably, particularly for purposes of vertically extrapolating the horizontal wind convergence. Second, our results imply that *none* of the forcing mechanisms considered can individually provide a satisfactory parameterization of large-scale ocean-atmosphere coupling over the entire Pacific. Furthermore it appears that vertical structure beyond a single layer is required to simulate correctly the low-level convergence field.

The results confirm that the proposed COARE domain is well-situated to examine interior heat-forced circulations - as it was designed to be, of course. Perhaps not so obvious is the suggestion made here that the other coupling mechanisms considered may be much more effective across the central Pacific. The variances of monthly-mean SST and OLR anomalies increase eastward across the dateline, so extending the COARE domain eastward (even by just 10° or so) would capture more of the low-frequency variability of these fields and might allow an examination of other

ocean-atmosphere coupling mechanisms as well. The interaction and feedbacks among different mechanisms at the eastern edge of the warm pool would be extremely interesting to study.

Intensive examination of the near-surface vertical structure of convergence (and more generally, the vertical structure of the boundary layer) should be an important component of COARE data collection and analysis efforts. SST and OLR fluctuations across the COARE domain are not well-correlated and 850 mb convergence is better correlated with OLR than surface convergence. We interpret this to mean that the 850 mb convergence is a better indicator of vertical motion that the larger convergence at the surface, i.e. the 850 mb circulation is representative of a thicker layer of convergence (more mass convergence) than the surface wind. Alternative interpretations could be made, including the possibility that significant tilts exist in the upward motion associated with large-scale, deep convection. The local pointwise statistics calculated here would not capture such tilts; this study is now being generalized to examine questions like this.

Other uncertainties in this study will require special data sets to address. For example, in Zebiak's (1986) model the initial forcing for convection comes from enhanced latent flux associated with a warm SST anomaly, yet SST-OLR correlations are nearly zero over the western Pacific. Perhaps the SST anomalies in the western Pacific are too subtle to be depicted properly in the data, or perhaps some other mechanism (such as destabilization of the tropospheric column from cold-air incursions in the upper troposphere) provides the initial convective trigger. It is hoped that COARE can provide sufficiently accurate and dense three-dimensional circulation and thermodynamic data to provide some definitive answers to these questions.

Acknowledgment. This material is based upon work supported by the U.S. TOGA Project Office under NOAA contract NA88AA-D-AC038. Data for the study were generously provided by D. Legler at Florida State, and by J. Janowiak and R. Reynolds at the NOAA Climate Analysis Center.

REFERENCES

Gill, A.E., 1980: Some simple solutions for heat-induced tropical circulation. *Quart. J. Roy. Meteor. Soc.*, **106**, 447-462.

Harrison, D.E., and D.S. Gutzler, 1986: Variability of monthly-averaged surface and 850 mb winds at tropical Pacific islands. *Mon. Wea. Rev.*, **114**, 285-294.

Lindzen, R.S., and S. Nigam, 1987: On the role of sea surface temperature gradients in forcing low level winds and convergence in the tropics. *J. Atmos. Sci.*, **44**, 2418-2435.

Neelin, J.D., and I.M. Held, 1987: Modeling tropical convergence based on the moist static energy budget. *Mon. Wea. Rev*, **115**, 3-12.

Zebiak, S.E., 1986: Atmospheric convergence feedback in a simple model for El Nino. *Mon. Wea. Rev.*, **114**, 1263-1271.

Remote Sensing of Atmospheric Thermodynamics in the Tropics

Siri Jodha KHALSA

Cooperative Institute for Research in Environmental Sciences,
University of Colorado,
Boulder, CO 80309 - U.S.A.

1. Introduction.

Successful diagnosis and prognosis of coupling between the tropical oceans and global atmosphere requires knowledge of the thermodynamic state of the atmosphere. The horizontal and vertical distribution of heat and moisture is important in the evolution of cloud clusters and tropical cyclones, and it is tied to the redistribution of convection during El Nino events. The propagation of convection associated with the 30-60 day oscillation depends upon, among other things, the thermodynamic basic state of the atmosphere. The lower tropospheric temperature and humidity are important in determining the magnitude of the latent, sensible and longwave radiative fluxes at the air-sea interface. And, of course, moisture in the form of clouds is important in determining insolation and freshwater flux into the ocean. Owing to the poor coverage of the tropics by radiosonde stations, remote sensing from space is the only practical means of obtaining the required thermodynamic information over the broad regions of the tropical oceans.

I briefly review the principal satellite sensors that have been used to measure thermodynamical variables in the tropics and mention some of the studies that have been done with these instruments. I then describe work that has been done at CIRES with a gridded TOVS data set. This work encompasses studies of interannual (ENSO), intraseasonal (30-60 day), and high-frequency (synoptic) variability in the tropics. Finally, I discuss current and proposed methods of estimating latent and perhaps sensible heat fluxes using satellite data.

2. Previous and current satellites used to measure tropical thermodynamics.

In this review only instruments that are on polar orbiting platforms are discussed. Geostationary satellites have the advantage of being able to sample the same location on the earth many times in a day but at present only the U.S. geostationary satellites (GOES) have the multi-channel radiometers on them necessary for atmospheric sounding.

Remote sensing of atmospheric temperature and moisture is accomplished by measuring upwelling radiances at specific frequencies, either in the infrared or microwave portions of the spectrum. Among the first to work with remote sensing of atmospheric variables over the ocean were Prabhakara et al. (1979), who used data from the Infrared Interferometer Spectrometer, IRIS, on Nimbus-4 to map seasonal distributions of precipitable water vapor. Chang and Wilheit (1979) used data from Nimbus-5 to estimate water vapor, liquid water and surface wind speed. Grody et al. (1980) used data from the Scanning Microwave Spectrometer on Nimbus-6 to examine atmospheric water vapor over the tropical Pacific. Kidder and Shyu (1984) examined data from the same instrument for its potential use in forecasting tropical cyclone motion.

The two instruments with the longest history and greatest use in remote sensing of atmospheric variables are the scanning multi-channel microwave radiometer, SMMR,

ORSTOM
CENTRE DOCUMENTATION
Montpellier

F 30253

carried by the Nimbus-7 satellite, and the TIROS operational vertical sounder, TOVS, flown on the TIROS (now called NOAA) series of satellites.

SMMR measured microwave radiation at five frequencies from which a number of geophysical parameters could be derived. This data has been used to estimate sea surface temperature, ocean surface wind speed, total column water vapor, and liquid water or rainrate. Data are available from 1978 to 1986. Limitations of this instrument include low (250 km) horizontal resolution, incomplete sampling of the globe in a day, problems with shifting calibration, and the fact that no parameters could be derived within 600 km of land due to sidelobe contamination. Nominal rms errors are 1-1.5°C for SST, 1.5-2 $m.s^{-1}$ for wind speed, and 0.2 $g.cm^{-2}$ for precipitable water. (Gloersen et al., 1984)

Prabhakara et al. (1982) used SMMR data to estimate water vapor over the oceans. Chang et al. (1984) produced monthly maps of precipitable water from SMMR data. Prabhakara et al. (1985) examined variations in global water vapor distribution associated with El Nino.

Liu (1984) described a method to estimate surface latent heat flux using a bulk parametrization with SMMR data. He derived relationship between total column water vapor and surface-level humidity and used this in conjunction with SMMR-derived wind speed and surface temperature. In Liu (1988), monthly averages of latent heat flux for the period 1980 - 1983 were examined.

TOVS consists of three separate instruments: a 20 channel high-resolution infrared sounder (HIRS-2), a four channel microwave sounder (MSU), and a three channel stratospheric sounder (SSU). NOAA polar orbiters have carried a TOVS since 1979 with two normally in orbit, providing six hourly coverage of most points on the earth. Its primary mission is to provide sounding information for assimilation into numerical forecast models.

TOVS is a sounder, it gives the vertical distribution of temperature and moisture, albeit at a lower resolution than radiosondes. The effective horizontal resolution of the soundings was 250 km until 1986 when improvements in the retrieval techniques increased this to 50 km (the resolution of the instruments did not change, only the manner in which data from the instruments was processed). Moisture information is derived solely from the IR channels and is thus unavailable in completely cloudy situations although the microwave sounder gives temperature information under these circumstances. In comparisons with monthly tropical radiosonde data, TOVS had rms errors in the troposphere of roughly 0.5°C in temperature and 1-2 mm in precipitable water (Khalsa and Steiner, 1988)

Early applications of TOVS data to tropical studies focused on data from the FGGE. Cadet (1983) combined TOVS precipitable water data with ECMWF Level II-b humidity data in a study of the summer Indian monsoon. Reyes and Cadet (1988) used the same technique to examine horizontal moisture flux for the Mexican monsoon.

A new generation of microwave instruments is proving to be quite valuable in tropical studies. These are the Special Sensor Microwave Imager, SSM/I, and Special Sensor Microwave, Temperature, SSM/T, aboard the Defense Meteorological Satellite Program (DMSP) polar orbiters.

The SSM/I, a seven channel, four frequency, linearly polarized microwave radiometer, can measure a number of atmospheric, oceanographic and land parameters with a nominal resolution of 25 km. It is currently flying on the F8 satellite which has a 6:10 local ascending node equatorial crossing time. The 1400 km wide conical scan pattern and 102 minute orbital period requires at least 2.5 days for complete coverage in the tropics. Surface wind speed and total column water vapor content can be derived under cloudy conditions but not under regions of heavy rain (drop sizes greater than 100 μm). Where it is raining, cloud liquid water and rainrate can be derived. Evaluations of instrument accuracy place rms errors in wind speed at approximately 2 m s^{-1} (Goodberlet, 1989), precipitable water at 4 mm (Alishouse, et al., 1989a), and cloud liquid water at 0.02 Kg m^{-2} (Alishouse et al., 1989b). SMMR cannot resolve wind speeds below 3 m s^{-1}.

The SSM/T is a seven channel temperature sounder with a resolution of 174 km at nadir. It is currently flying on both the F7 and F8 DMSP satellites which both having morning ascending equatorial crossing times. Sounding products are being produced and archived by the National Environmental Satellite, Data, and Information Service, NESDIS. With a 1600 km wide, cross-track scan, a two satellite system is capable of providing nearly complete global coverage in a 24 hour period, producing 18,900 views per day. Comparisons with tropical radiosonde data gives rms errors in the 2-3°C range (Maiden et al., 1989).

Data from the SSM/I and SSM/T will be part of the program that we are proposing for remote sensing of latent and sensible heat flux. This will be discussed in Section 4.

3. Studies with TOVS.

The archived TOVS product has been obtained by CIRES from NESDIS for the years 1981-1988. Slightly over six years (October 1981 - December 1987) of data have been interpolated onto daily 5° latitude x 5° longitude grids. The gridded data include seven levels of temperature up to 100 mb (stratospheric data are not included) and 3 levels of precipitable water up to 300 mb.

The first use of TOVS data at CIRES was in a study of changes in the thermodynamic structure of the eastern Pacific troposphere during the 1982-83 El Nino (Garcia et al., 1986). TOVS data helped establish that the lower troposphere in the eastern Pacific became warm and moist several months prior to the arrival of deep convection.

Monthly averages of SST, HRC (a proxy for deep convection) and low-level precipitable water from TOVS for the period 1982 - 1985 were examined for the tropical equatorial Pacific in Steiner and Khalsa (1987). Fig. 1 shows the longitudinal variation in the correlation between these three variables. El Nino-induced variability in the eastern Pacific is responsible for a high correlation between all three variables there. West of 160°W the correlation between HRC and SST falls off rapidly. The only correlation that remains significant at the 95% level out to 150°E is that between low-level precipitable water (LLPW) and HRC. This implies that over the western Pacific, changes in convection on monthly time scales are more closely tied to changes in moisture supply, perhaps related to low-level wind convergence, than to sea surface temperature.

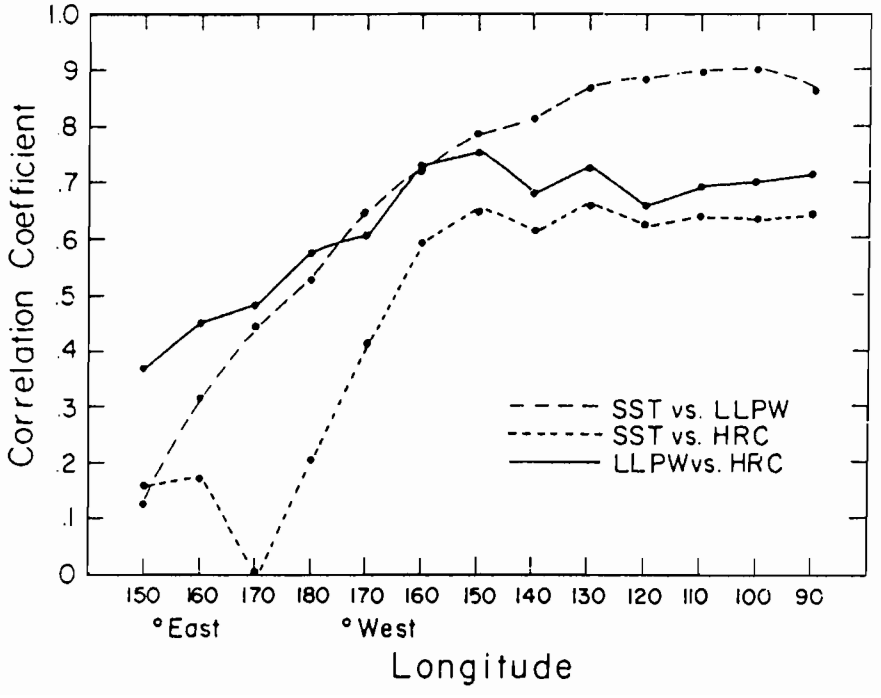

Fig.1. Simple correlation coefficients between sea surface temperature, low-level precipitable water and highly reflective cloud as a function of longitude.

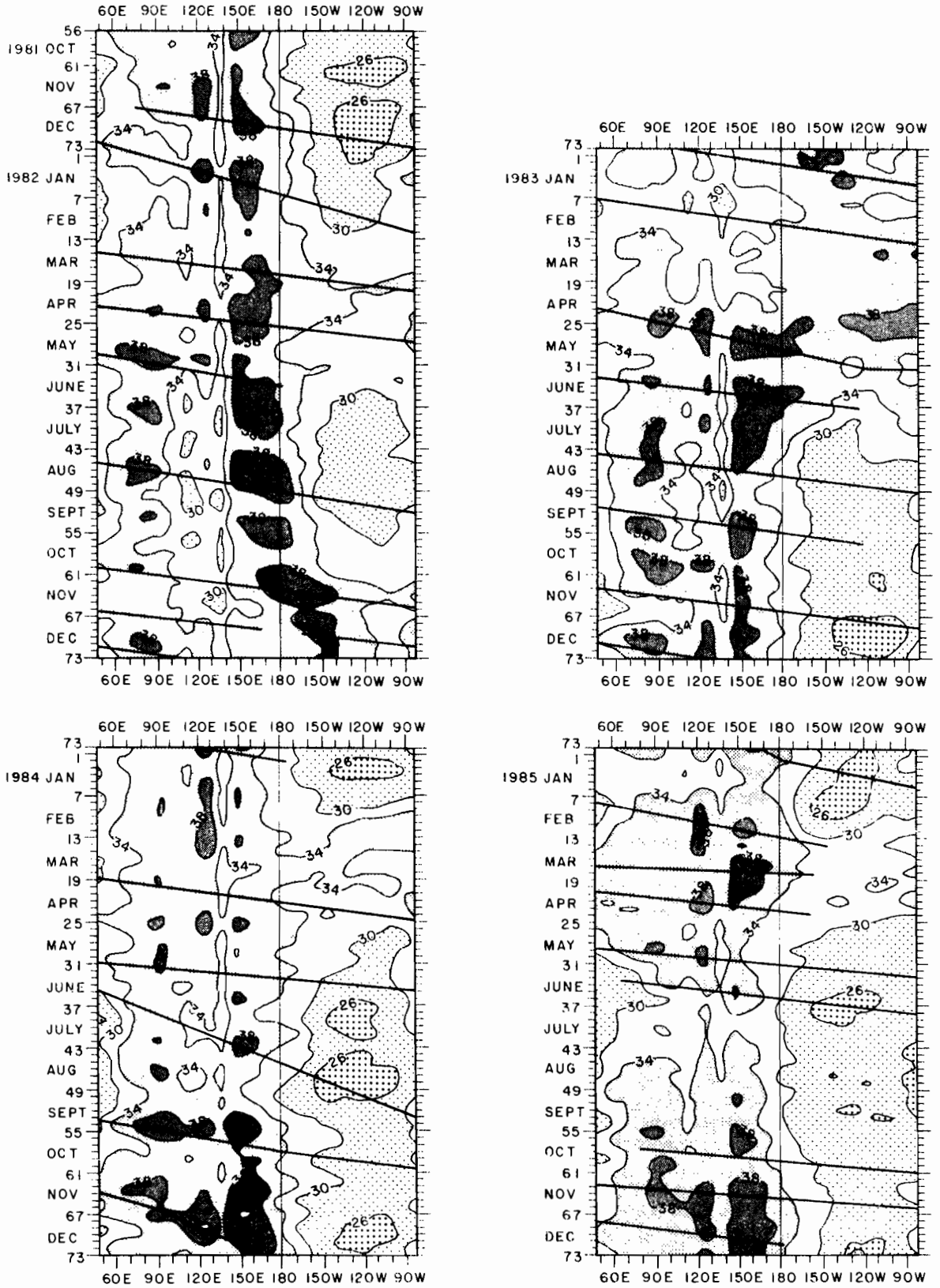

Fig.2. Time-longitude diagram of precipitable water (1000-700 mb) in millimeters for the 0°-5°S strip across the Indian and Pacific oceans from 3 October 1981 through 31 December 1985. Data are 5-day, 5° averages.Bold lines on the plot indicate axes of minima in filtered 250 mb velocity potential.

TOVS has proved valuable in studies of tropical phenomena on shorter time scales as well. Fig. 2 shows a time-longitude diagram of LLPW at 2.5°S latitude in the Indian and Pacific oceans for the period October 1981 through December 1985. In addition to the major changes in moisture distribution during the 1982-83 El Nino, higher frequency variations are evident. Superimposed on the plot are axes of filtered 250 mb velocity potential showing propagating 30-60 day oscillations. It will be noted that in most cases where there is an eastward extension of the 38 mm contour of LLPW there is a coincident passage of a 30-60 day wave.

In a case study of a 30-60 day oscillation (Weickmann et al., 1989, see also Weickmann and Khalsa, this volume), TOVS revealed that an increase in low-level moisture preceded the eastward movement of the bulk of convection from the Indian ocean to near the dateline (Fig. 3). This moisture increase coincided with strengthened easterlies and enhanced convergence (Steiner, 1989).

Low level moisture represents only part of the thermodynamic conditions that determine the potential for deep convection. A stability index, representing the buoyant forcing on a low level parcel when lifted to the middle troposphere, has been derived for use with TOVS data. This stability index is expressed as:

$$SI = \Theta_{es}(700\text{-}500 \text{ mb}) - \Theta_{e}(1000\text{-}850 \text{ mb})$$

where Θ_e (Θ_{es}) is the (saturated) equivalent potential temperature. Because of the coarse vertical resolution of the operational TOVS product this measure is not perfect. However, comparisons with in situ data show that SI is usually a good indicator of static stability in the tropics (Khalsa, 1989). Because of large diurnal changes in stability over continents, current investigations are limited to oceanic areas.

Five day, non-overlapping averages (pentads) were computed for the period of record. The annual cycle was removed by subtraction of the long-term (6 year) pentad mean at each grid point. To study interannual variability, a 12 month (73 pentad) running mean was computed. To isolate intraseasonal variability, a band pass filter with half power points at 28 and 72 days was applied to the data. The outgoing longwave radiation (OLR) data set, which measures cloud top temperatures, is used as a proxy for deep convection.

The character of the time variability in SI for the grid point at 2.5°S, 172.5°E is shown in Fig. 4. In this example the annual cycle has not been removed. Variations across a broad range of time scales are evident. In the latter half of 1982 stability was low and quasi-periodic fluctuations with a 40-50 day time scale are seen. These oscillations were followed by a rapid change to stable conditions in early 1983. The cause of this change was the movement of the warmest waters and bulk of convection to east of the dateline during El Nino. The lowest values of stability occurred in 1987, another El Nino year, and were followed, as in 1983, by a rapid change to large values of
SI, at the end of the record.

The 1981-1987 December through February means of SI and OLR are shown in Fig.5. There is a good correspondence of negative stability index and low OLR (high clouds, deep convection) in the western Pacific/Indonesian region and in the South Pacific Convergence Zone. Lower SI values in the eastern Pacific and Atlantic Intertropical Convergence Zones are also evident. High values of SI off the western coasts of the continents, where oceanic upwelling produces stable conditions, are also clearly seen.

The variances of Θ_{e1} (TOVS level 1 = 1000-850 mb) and Θ_{es3} (level 3 = 700-500 mb) for the intraseasonal (28-72 day) time scale are shown in Fig.6. The greatest variability in these quantities occurs at latitudes poleward of 20° where midlatitude waves produce fluctuations in temperature throughout the troposphere. When Fig.6 and Fig. 7, which shows the intraseasonal variance in SI, are compared it is evident that the large fluctuations in the subtropics generally occur simultaneously at most levels in the troposphere, resulting in a small net effect on SI. In contrast to Θ_{e1} and Θ_{es3}, the maxima in SI variance occur in

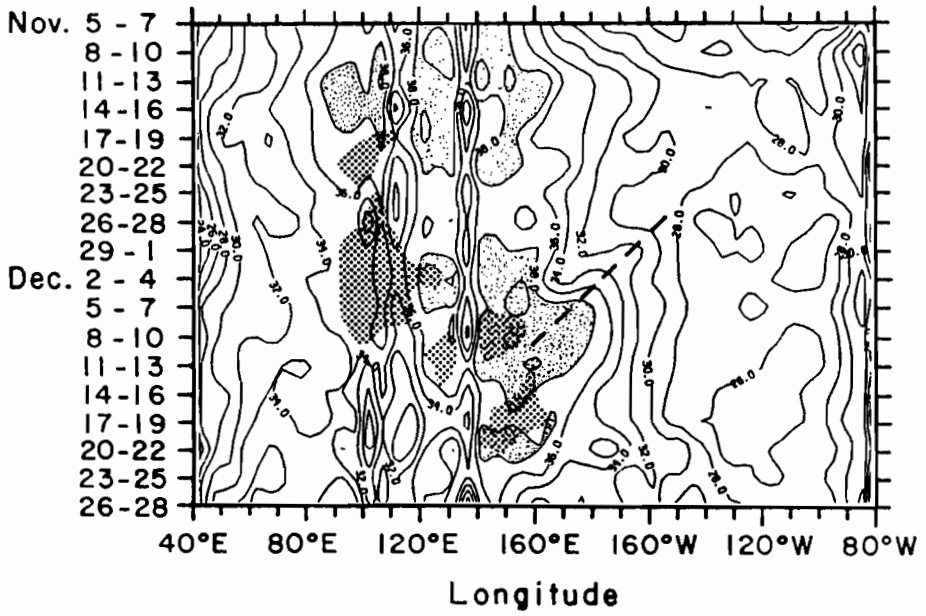

Fig.3. Time-longitude diagram of 3-day averaged low-level precipitable water averaged from 2.5°N-2.5°S for 5-7 November 1981 through 26-28 December 1981. The contour interval is 2 mm and values greater than 38 mm and stippled. Dotted areas indicate values of OLR < 180 $W.m^{-2}$.

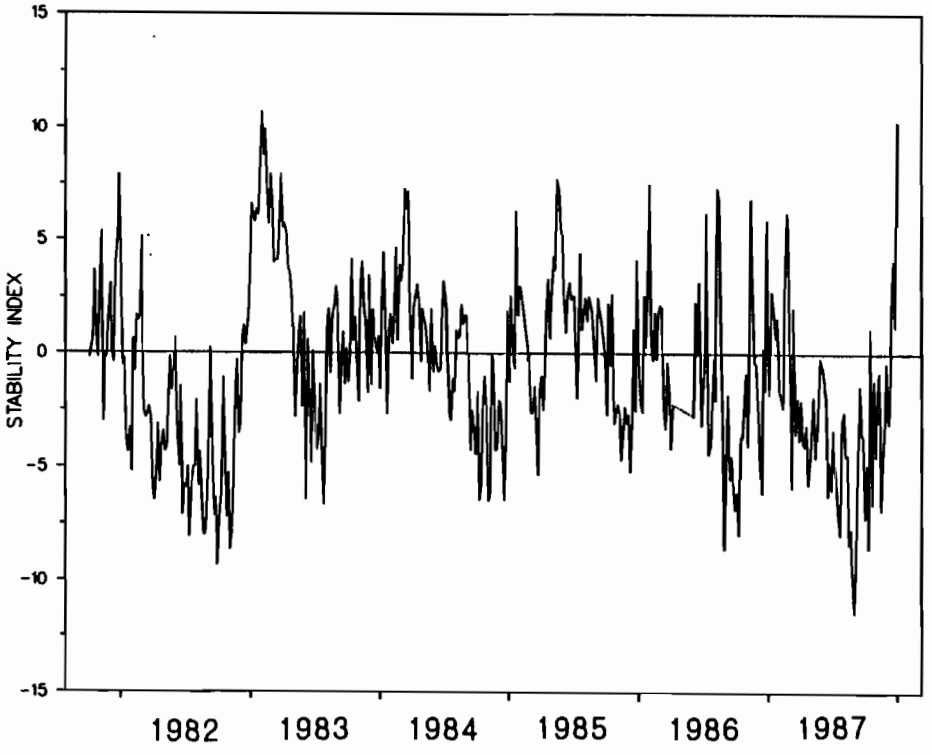

Fig.4. Time series of the stability index at 2.5°S, 172.5°E for the period of record.

specific regions known to be affected by the Madden and Julian (30-60 day) oscillation, i.e. the Indian and western Pacific oceans. The maximum off the coast of east Asia may arise from cold surges coming off the Asian land mass. These events have been shown to be coupled to the Madden and Julian Oscillation (Weickmann et al., 1989).

What is unusual about Fig. 7 is that SI variance in the equatorial Indian and far western Pacific oceans is relatively small. This is a region of strong intraseasonal variance in convection as shown in Fig. 8 (Lau and Chan, 1988). This is also the region of warmest sea surface temperatures. Over these very warm waters the stability is always low and the changes in stability associated with the onset and cessation of convection are small.

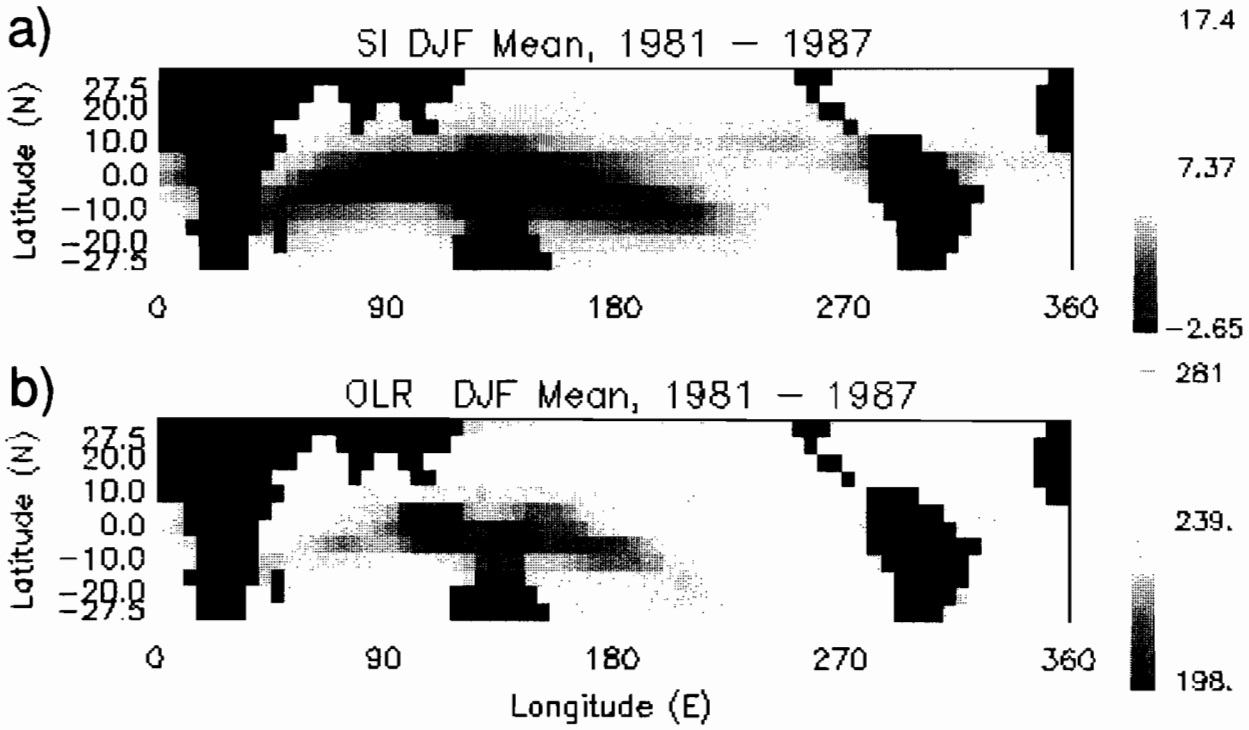

Fig.5. December-February means of a) stability index, and b) outgoing longwave radiation, for the global tropics (±30° latitude) from the years 1971-1987.

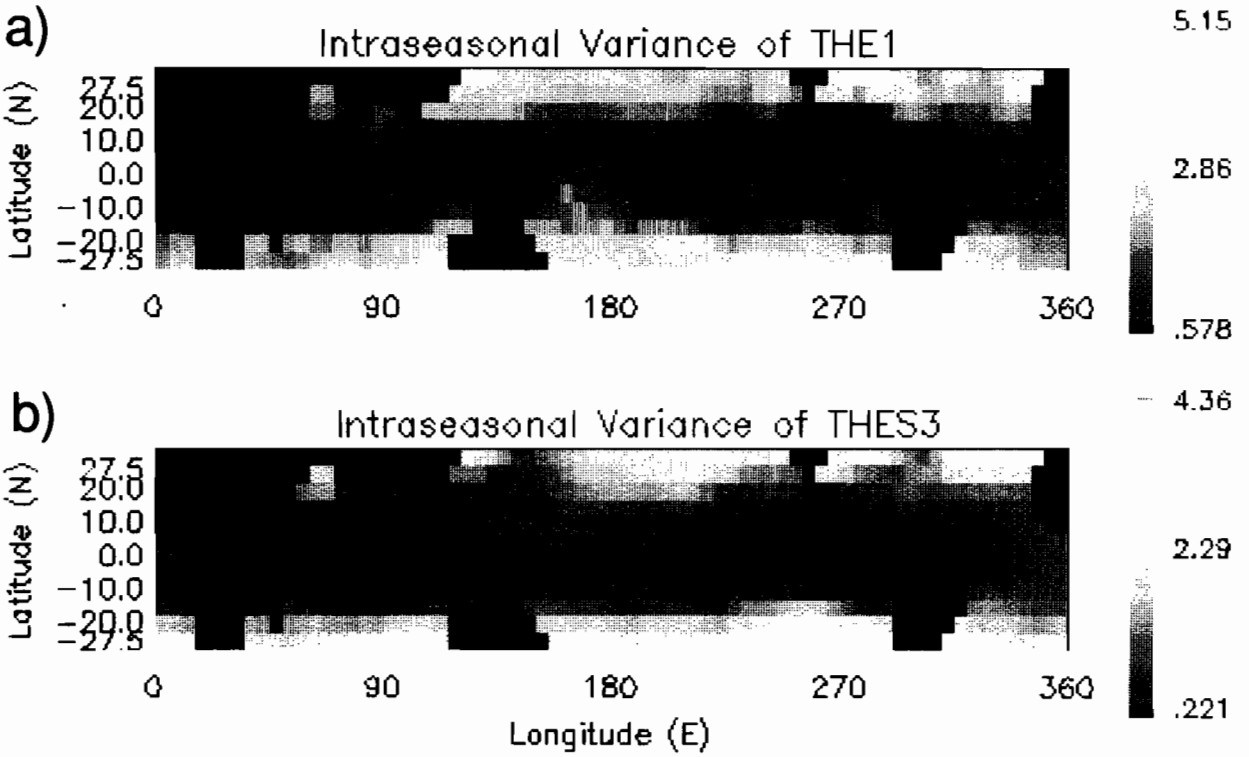

Fig.6. Intraseasonal variance of a) Θ_e (1000-850 mb), and b) Θ_{es} (700-500 mb) from the period October 1981 through December 1987.

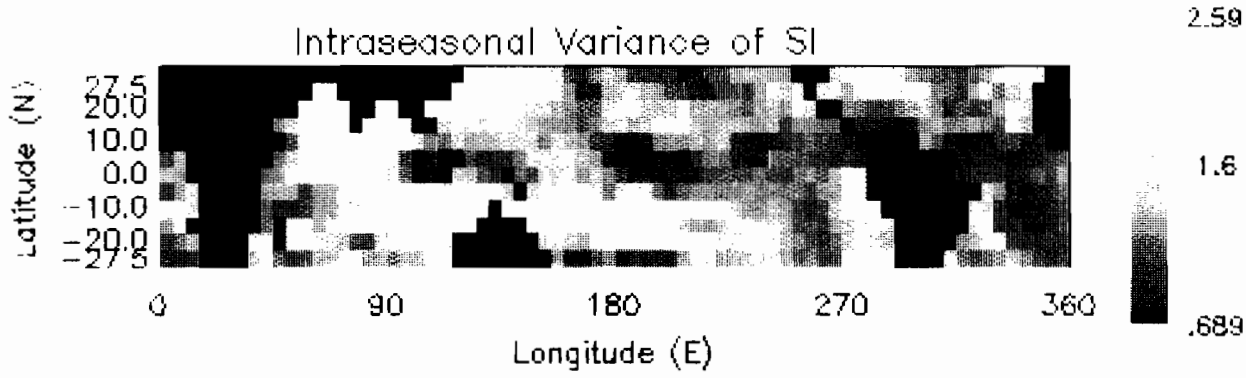

Fig.7. Same as for Fig.6 but for the stability index.

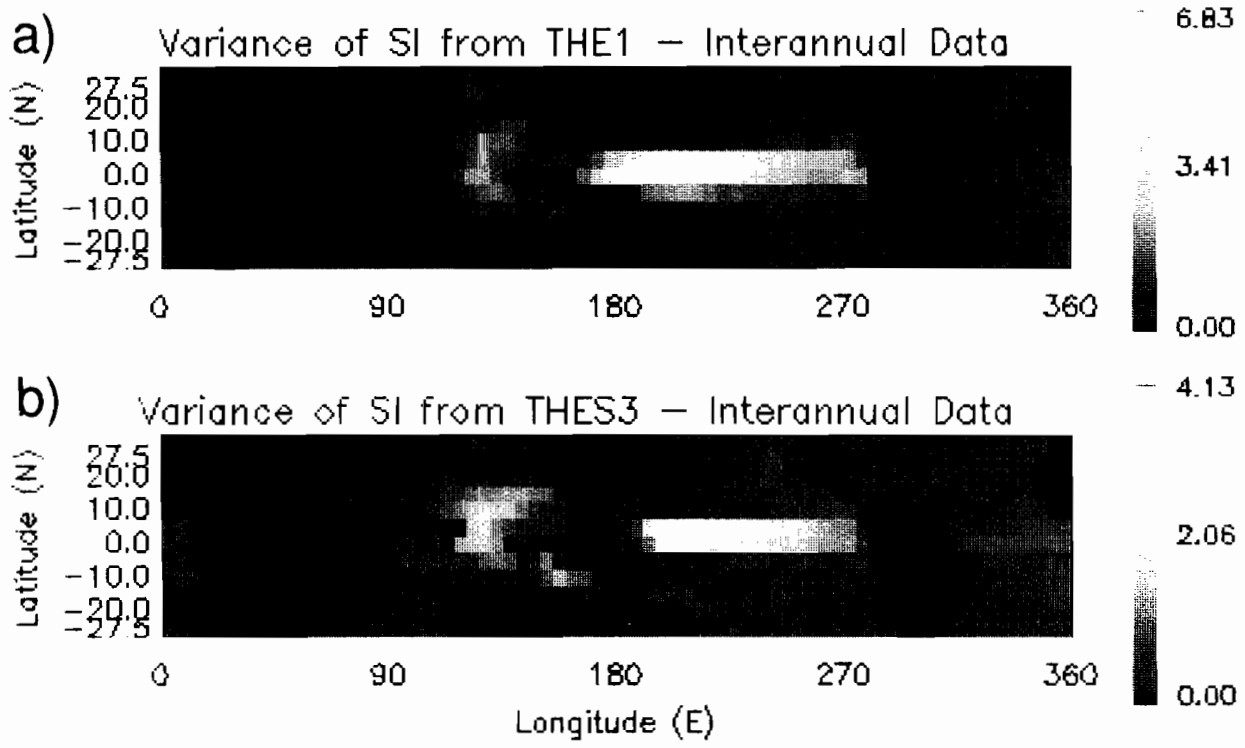

Fig.9. Magnitude of the interannual variance of the stability index explained by a) Θ_e (1000-850 mb), and b) Θ_{es} (700-500 mb).

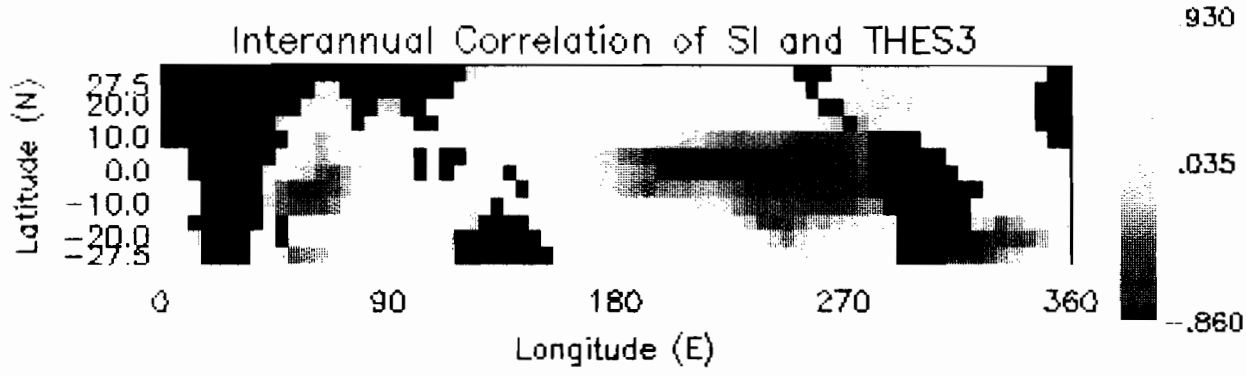

Fig.10. Correlation between the stability index and Θ_{es} (700-500 mb) for interannual time scales.

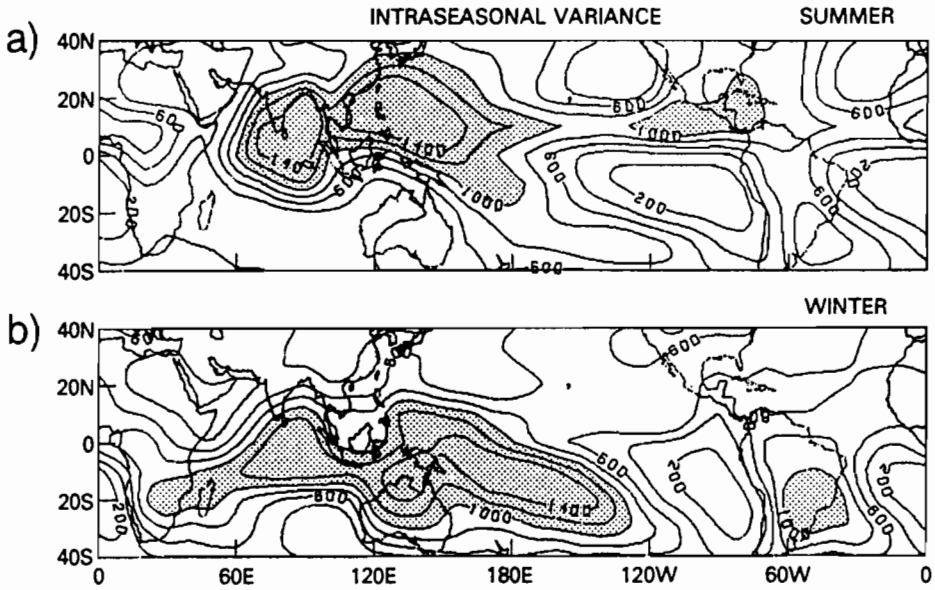

Fig.8. Intraseasonal variance of OLR for a) northern summer (May-October) and winter (November-April) from Lau and Chan (1988).

Interannual variance during the period of record is dominated by the 1982-83 El Nino. In Fig. 9 the magnitudes of the variance in SI that are produced by Θ_{e1} and Θ_{es3} (defined as the product of the variance in SI and the square of the correlation coefficient between SI and Θ_{e1} or Θ_{es3}) are shown. The largest variance in SI occurs where the sea surface temperature (SST) anomaly during El Nino is greatest. In the Indonesian region the magnitude of the contribution from Θ_{es3}, compared with the central Pacific maximum, is greater than that from Θ_{e1}. In other words, the warming of the middle troposphere in the Indonesian region contributes at least as much to the stabilization of the atmosphere during El Nino as low level drying. Fig. 10 shows the correlation of SI and Θ_{es3}. Negative values over the central and eastern Pacific Ocean mean that there the tendency for stabilization due to middle troposphere warming is completely overwhelmed by the destabilization produced by the warming and moistening of the lower layers due to SST anomalies.

4. Remote sensing of latent and sensible heat flux.

The method proposed by Liu (1984) to estimate surface latent heat flux from space relies on an empirical relationship between total column water vapor, W, and specific humidity, Q, at some level near the surface. This relationship is based on monthly mean radiosonde data. Its validity on shorter time scales is questionable. As an example, Fig. 11a shows the mixing ratio deviation for various stages of a tropical cloud cluster development derived from a large number of radiosonde stations in the western Pacific (Lee, 1986). Deviations of greater than 2 $g.kg^{-1}$ occur in the middle troposphere while at the surface the deviations are less than 0.5 $g.kg^{-1}$. Clearly, in this case changes in total column water vapor are not simply related to changes is surface mixing ratio. The corresponding deviations in atmospheric temperature are shown in Fig.11b.

The variability in the vertical distribution of heat and water vapor on synoptic time scales poses a challenge in any effort at remotely sensing surface heat fluxes. To the degree that the atmospheric perturbations associated with convective disturbances, such as those represented in Fig.11, can be classified, it may be possible to define a set of Q-W relationships that could be used in a bulk parametrization formulation. This set of reference profiles would also be used in an improved retrieval algorithm for SSM/T.

If for each perturbation temperature profile in this reference set there is an associated perturbation humidity profile, then SSM/T could be used to identify the reference

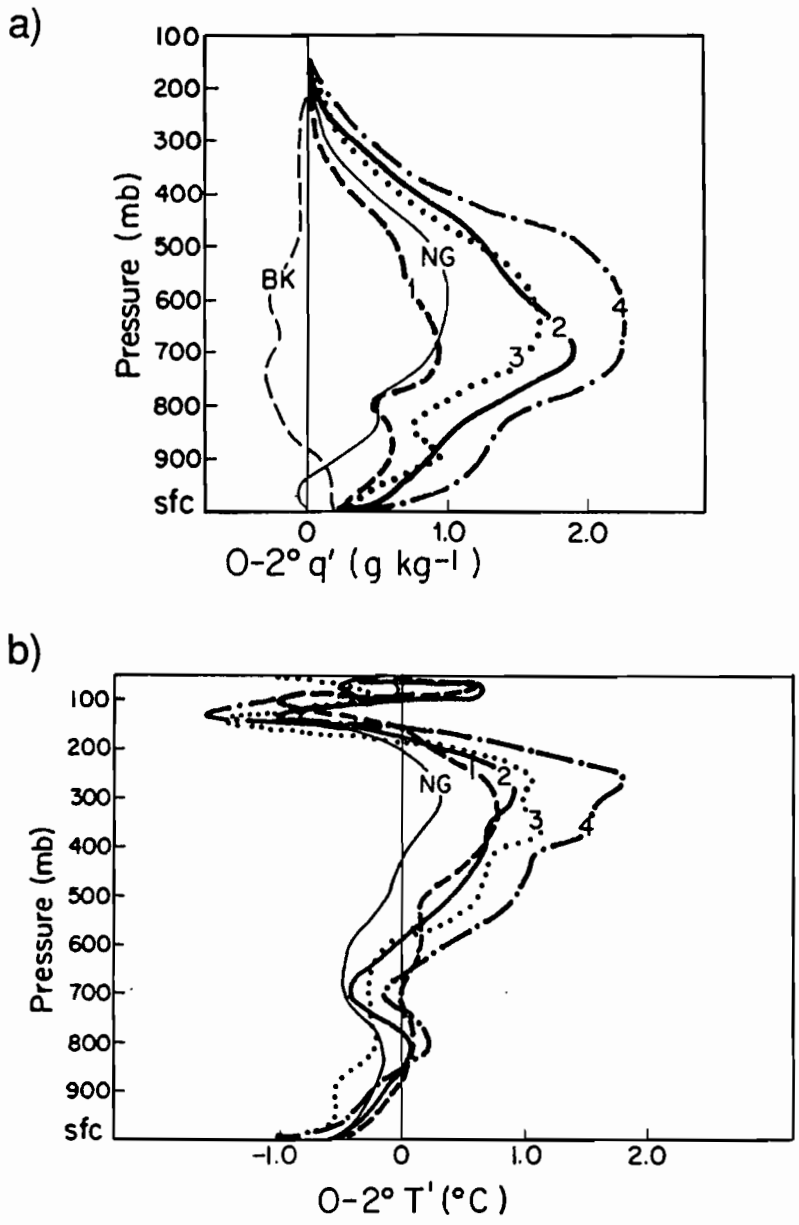

Fig.11. Deviations in the vertical profiles of a) mixing ratio and b) temperature for 4 stages of a developing tropical cyclone, the non-genesis (NG) cloud cluster case and the background (BK) composite. All profiles derived from a large number of island radiosonde reports.

Fig.11. Deviations in the vertical profiles of a) mixing ratio and b) temperature for 4 stages of a developing tropical cyclone, the non-genesis (NG) cloud cluster case and the background (BK) composite. All profiles derived from a large number of island radiosonde reports.

temperature profile and SSM/I could be used to scale the reference humidity profile to give the corresponding total column water vapor. The Q-W relationship for this humidity profile would then give the surface mixing ratio to be used in the bulk formulation. Wind speed would be obtained from SSM/I but SST would have to be obtained from another source, probably AVHRR.

Remote sensing of sensible heat flux can be more problematic, especially in the warm pool region where the air-sea temperature difference is small. However, as shown by Fig. 11b, surface air is cooler in disturbed conditions, probably due to convectively driven downdrafts, increasing air-sea temperature differences and sensible heat flux. It may be possible to parametrize the sensible heat flux for these circumstances using the method proposed above for latent heat flux. This might capture a large fraction of the time-averaged flux. The contribution from undisturbed periods could be estimated from climatology.

The proposed method for estimating fluxes depends on the identification of appropriate

perturbation temperature and humidity profiles from which near-surface values can be derived for use in bulk parametrization formulae. Satellite sounders do not work under conditions of heavy rain and so cannot be used for this purpose. It may be possible, however, to associate thermodynamic profiles, or more directly, near-surface temperature and humidity perturbations, with a given convective state as identified by visible and broad band IR imagery. The stages of evolution of a convective cloud cluster may characterized by texture and other higher order spatial moments derived from imagery. The magnitudes of the perturbations might be related to the coldest cloud tops identified by IR emissions.

5. Conclusions.

Remote sensing can add greatly to our knowledge of the thermodynamic processes governing ocean-atmosphere coupling. New approaches to remote sensing of air-sea heat fluxes await development and testing with field programs such as TOGA COARE.

REFERENCES

Alishouse, J. C., S. Snyder and J. Vongsathorn, 1989a: Determination of total precipitable water in the tropics from the SSM/I. *Preprints of the Fourth Conference on Satellite Meteorology and Oceanography,* May 16-19, San Diego, Calif., American Meteorological Society, pp. 221-223.

Alishouse, J. C., C. Swift, C. Ruf, S. Snyder and J. Vongsathorn, 1989b: Determinations of cloud liquid water in the tropics from the SSM/I. *Preprints of the Fourth Conference on Satellite Meteorology and Oceanography,* May 16-19, San Diego, Calif., American Meteorological Society, pp. 187-189.

Cadet, D. L., 1983: Mean fields of precipitable water over the Indian Ocean during the 1979 summer monsoon from TIROS-N soundings and FGGE data. Tellus, **35B**, 329-345.

Chang, A. T. C., and T. T. Wilheit, 1979: Remote sensing of atmospheric water vapor, liquid water, and wind speed at the ocean surface by passive microwave techniques from Nimbus 5 satellite. *Radio Sci.*, **14**, 793-803.

Chang, H. D., P. H. Hwang, T. T. Wilheit, A. T. C. Change, D. H. Staelin and P. W. Rosenkrans, 1984: Monthly distributions of precipitable water from the Nimbus 7 SMMR data. *J. Geophys. Res.*, **89**, 5328-5334.

Garcia, O., S. J. S. Khalsa and E. Steiner, 1986: Atmospheric characteristics of the eastern equatorial Pacific during the 1982-83 El Nino, deduced from satellite and aircraft measurements. *J. Geophys. Res.*, **91**, 13,217-13,231.

Gloersen, P., D. J. Cavalieri, A. T. C. Chang, T. T. Wilheit, W. J. Campbell, O. M. Joannessen, K. B. Katsaros, K. F. Kunzi, D. B. Ross, D. Staelin, E. P. L. Windsor, F. T. Barath, P. Gudmandsen, E. Langham and R. O. Ramseier, 1984: A summary of results from the first Nimbus 7 SMMR observations. *J. Geophys. Res.*, **89**, 5335-5344.

Goodberlet, M. A., 1989: Remote sensing of ocean surface winds with the Special Sensor Microwave/Imager (SSM/I). *Preprints of the Fourth Conference on Satellite Meteorology and Oceanography,* May 16-19, San Diego, Calif., American Meteorological Society, pp. J42-45.

Grody, N. C., A. Gruber and W. C. Chen, 1980: Atmospheric water vapor content over the tropical pacific derived from the Nimbus-6 Scanning Microwave Spectrometer. *J. Appl. Meteor.*, **19**, 986-996.

Khalsa, S. J. S. and E. J. Steiner, 1988: A TOVS data set for study of the tropical atmosphere. *J. Appl. Meteor.*, **27**, 851-862.

Khalsa, S. J. S., 1989: Atmospheric stability over the tropical oceans, derived from TOVS. *J. Appl. Meteor.*, August issue.

Kidder, S. Q. and K. Shyu, 1984: On the potential use of satellite sounder data in forecasting tropical cyclone motion. *Mon. Wea. Rev.*, **112**, 1977-1984.

Lau, K. M. and P. H. Chan, 1988: Intraseasonal and interannual variations of tropical convection: a possible link between the 40-50 day oscillation and ENSO ? *J. Atmos. Sci.*, **45**, 506-521.

Lee, C.-S., 1986: An observational study of tropical cloud cluster evolution and cyclogenesis in the western north Pacific. Dept. Atmos. Sci. Paper No. 403, Colorado State University, Fort Collins, Colorado, 80523.

Liu, W. T., 1984: Determination of monthly mean humidity in the atmospheric surface layer over oceans from satellite data. *J. Phys. Oceanogr.*, **14**, 1451-1457.

Liu, W. T., 1988: Moisture and latent heat flux variabilities in the tropical Pacific derived from satellite data. *J. Geophys. Res.*, **93**, 6749-6760.

Maiden, M. E., M. V. Piepgrass, D. R. Donahue, M. Sylva, H. F. Drahos, Jr., 1989: Atmospheric temperature retrieval from satellite microwave measurements. *Preprints of the Fourth Conference on Satellite Meteorology and Oceanography*, May 16-19, San Diego, Calif., American Meteorological Society, pp. 204-207.

Prabhakara, C., G. Dalu, R. C. Lo and N. R. Nath, 1979: Remote sensing of seasonal distribution of precipitable water over the oceans and the inference of boundary layer structure. *Mon. Wea. Rev.*, **107**, 1388-1401.

Prabhakara, C., H. D. Chang and A. T. C. Chang, 1982: Remote sensing of precipitable water over the oceans from Nimbus 7 microwave measurements. *J. Appl. Meteor.*, **21**, 59-68.

Prabhakara, C., D. A. Short and B. E. Vollmer, 1985: El Nino and atmospheric water vapor observations from Nimbus 7 SMMR. *J. Climate Appl. Meteor.*, **24**, 1311-1324.

Reyes, S. and D. L. Cadet, 1988: The southwest branch of the North American monsoon during summer 1979. *Mon. Wea. Rev.*, **116**, 1175-1187.

Steiner, E. J. and S. J. S. Khalsa, 1987: Sea surface temperature, low-level moisture, and convection in the tropical Pacific, 1982-1985. *J. Geophys. Res.*, **92**, 14,217-14,224.

Steiner, E. J., 1989: Moisture convergence during a convective flare-up in the tropics. *Preprints of the Fourth Conference on Satellite Meteorology and Oceanography*, May 16-19, San Diego, Calif., American Meteorological Society, pp. 154-157.

Weickmann, K. M., S. J. S. Khalsa and E. J. Steiner, 1989: The shift of convection from the Indian Ocean to the western Pacific Ocean during a 30-60 day oscillation. *Mon. Wea. Rev.*, in review.

Some Features of the Western Tropical Pacific: Surface Wind Field and its Influence on the Upper Ocean Thermal Structure

Bingrong XU

Second Institute of Oceanography, SOA
Hangzhou, Zhejiang 310012
People's Republic of China

1. Introduction

Wyrtki (1974) and Meyers (1982) have indicated that the seasonal variation of the thermocline depth and the sea level in the tropical Pacific Ocean, which can represent the strength of major oceanic currents, are strongly influenced by the position of the trade wind. Affected by the East Asian Monsoon, sea surface wind field has apparently seasonal displacements in the western tropical Pacific. It appears that the position of the Inter-Tropical Convergence Zone of the wind (ITCZ) has large seasonal oscillation from about 15°S (February-March) to 10°N (September-October) as shown in Donguy et al (1982). Responding to the seasonal oscillation of the ITCZ, some oceanic thermal elements may have corresponding seasonal variations. Recently some research works, e.g. Donguy et al. (1982) and White et al. (1985), showed the sea surface wind field and the upper ocean thermal structure in the western tropical Pacific have interannual variations corresponding with El Nino-Southern Oscillation phenomenon (ENSO). Usually, anomalies of the wind field are leading ENSO by several months. Due to a lack of wind field and subsurface temperature data sets, the effects of surface wind field seasonal variations on the upper ocean thermal structure have not been clearly described in the western tropical Pacific.

In this study, seasonal and interannual variations of sea the surface wind field over the western tropical Pacific are described, using mean monthly sea surface pseudo wind stress data series from Jan. 1962 to Jan. 1980, and mean seasonal subsurface temperature data series from spring 1964 to winter 1980 (kindly provided by W. White and sea-air interaction group, Second Institute of Oceanography, SOA). The effects of the wind field on the upper ocean thermal structure are primarily analyzed.

2. Seasonal and interannual variations of the sea surface wind field

a. Seasonal variations.

The long-term monthly mean (1964-1980) zonal and meridional components of pseudo wind stress along 155°E are shown in Fig.1a-b. The zonal and meridional components of pseudo wind stress are represented by

$$\tau^x = u\,(u^2+v^2)^{1/2}; \qquad \tau^y = v\,(u^2+v^2)^{1/2} \tag{1}$$

where u and v, are the surface wind velocity components. From these figures it is apparent that the northeast and southeast trade winds are stronger in February to March and August to September respectively. The interface of the opposite zonal and meridional wind components may indicate the mean position of the ITCZ. The dashed

ORSTOM
CENTRE DOCUMENTATION
Montpellier

F 30254

line in Fig. 1 is the interface of the wind components and show that the mean position of the ITCZ is near 13°S during January to February and near 10°N during August to September, i.e., consistent with the indication of Donguy et al. (1982).

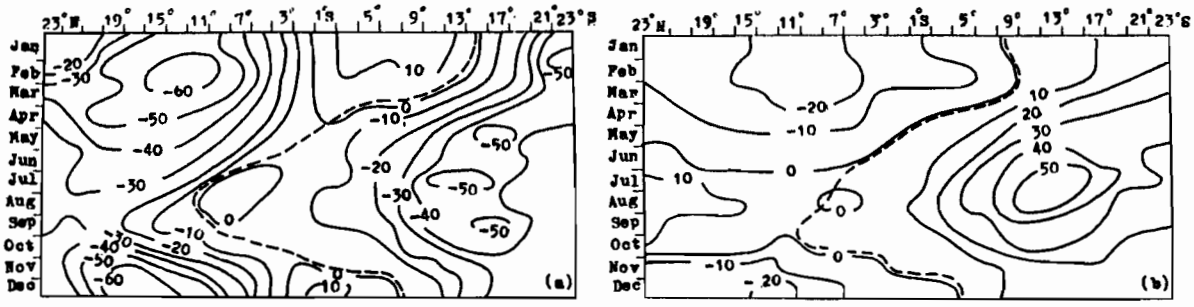

FIG.1. Long-term monthly mean of the zonal (a) and meridional (b) components of the pseudo wind stress along 155°E. (in $m^2.s^{-2}$). The dashed lines are the interface of the opposite wind components.

Monthly mean zonal and meridional wind stresses (τ') can be represented by its first and second harmonic coefficient,

$$\tau' = \langle\tau\rangle + a_1 \cos \omega_1 t + b_1 \sin \omega_1 t + a_2 \cos \omega_2 t + b_2 \sin \omega_2 t \qquad (2)$$

where a_1, b_1 and a_2, b_2 are the first and second harmonic coefficients, respectively, $\omega_1=2\pi/12$, $\omega 2=2\pi/6$, t is the time in month, and $\langle\tau\rangle$ denotes the annual mean value of the pseudo wind stress components. The harmonic coefficients together with the standard error of estimate (σ) and ratio of amplitude (s6/s12) of the pseudo wind stress in the latitude bands of 0°-4°N and 8°-12°N along 155°E are shown in table 1 where σ, s6 and s12 are defined as:

$$\sigma = [(1/12) \sum_{1}^{12} (\tau_t^1 - \tau_t)^2]^{1/2} \qquad (3)$$

$$s6 = (a_2^2+b_2^2)^{1/2} \qquad s12 = (a_1^2+b_1^2)^{1/2} \qquad (4)$$

here τ_t are the monthly mean values of the pseudo wind stress components.

		a1	b1	a2	b2	σ	s6/s12	$\langle\tau\rangle$
0°-4°N	τ^x	- 3.3	- 5.2	0.7	-4.0	0.5	0.67	- 6.4
	τ^y	- 8.6	- 4.0	-2.3	-0.8	4.9	0.26	- 1.3
0°-8°N	τ^x	-22.7	-17.1	-1.5	5.3	11.7	0.19	-35.4
	τ^y	-14.7	- 8.2	-1.7	-0.4	12.1	0.11	-10.5

Table 1. Harmonic coefficients (a_1, a_2, b_1, b_2), σ and s6/s12 of the pseudo wind stress along 155°E (see text for definition).

The standard errors (σ) are smaller than the largest harmonic coefficient in both latitude bands. The ratios of the second to the first harmonic amplitudes (s6/s12) in the 0°-4°N band are not negligible, particular for τ^x. It shows that the semiannual variation is apparently near the equator.

Fig. 2 represents the seasonal variations of the zonal pseudo wind stress (τ^x) as calculated from equation (2). Near the equator (Fig.2a), the surface wind has apparent semiannual variation. When the ITCZ shifts across 2°N during May to June and October to November, it causes a decrease of the easterly wind. But near 10°N there is a marked anuual cycle (Fig. 2b), because the ITCZ arrives nearly 10°N once a year.

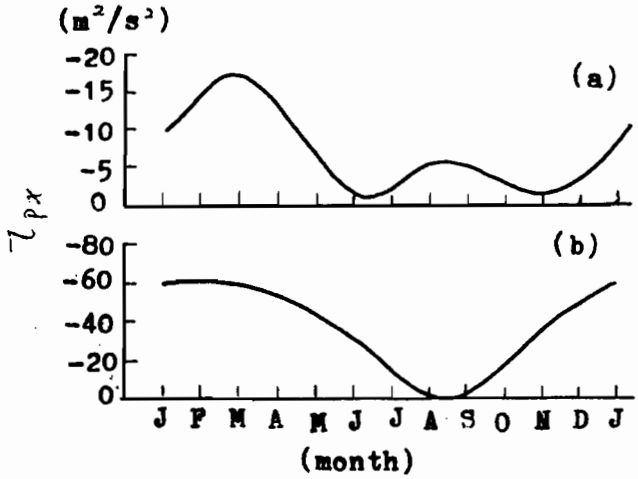

FIG.2. Seasonal variation of zonal pseudo wind stress calculated from harmonic coefficients at 2°N 155°E (a) and 10°N 155°E (b).

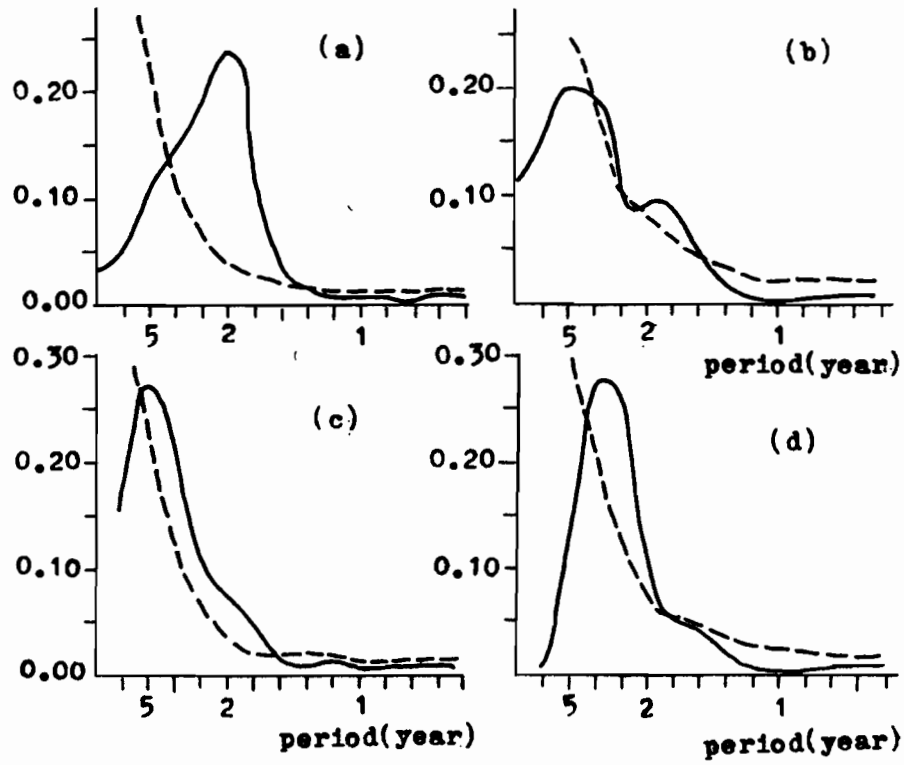

FIG.3. Power spectra of monthly anomalies of the zonal pseudo wind stress for four latitude bands, along 155°E. The dashed lines are confidence limit of 95% red noise.

b. Interannual variations.

Power spectrum of monthly anomalies of the zonal pseudo wind stress (τ^x) for four latitude bands (0°-10°S, 10°-20°S, 0°-10°N and 10°-20°N) along 155°E are displayed in Fig.3. These spectra curves have a marked peak at 2-4 year period, it indicates that the zonal wind over the western tropical Pacific has a main 2-4 year period of variation, corresponding to that of ENSO events.

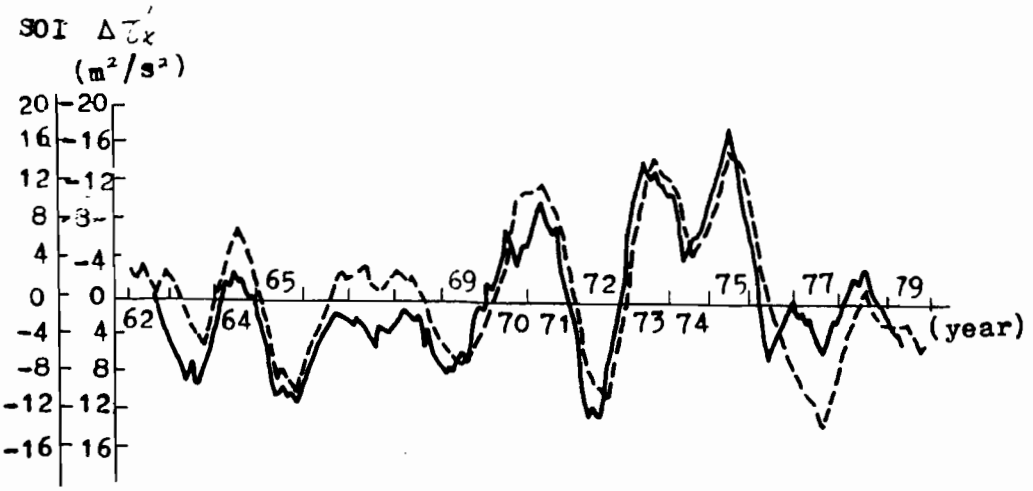

FIG.4. Time series of the average zonal pseudo wind stress anomalies over 3°N-3°S; 140°E-170°W (solid line) and Southern Oscillation Index (dashed line). Both curves have been smoothed with an 11-month running mean.

The solid line in Fig.4 is the time series of the zonal pseudo wind stress anomalies over 3°S-3°N and 140°E-170°W ($\pm 3^\circ\Delta\tau^x$). The curve shows that there is a strong westerly wind anomaly ($>5 m^2.s^{-2}$) during ENSO years. The dotted line in Fig.4 is the time series of the Southern Oscillation Index (SOI, taken from Parker (1983). Wind anomalies ($\Delta\tau^x$) over ±3° area closely related to SOI. The monthly correlation coefficient of these two time series is -.87.

c. Surface wind field anomalies during the ENSO period.

The time-longitude section of the composite monthly zonal wind stress anomalies along the equator for four El Nino years (1965, 1969, 1972, 1976) is shown in Fig.5. The composite span 36 months beginning 12 months before and ending 12 months after a given El Nino year. Fig.5 shows anomalous variations of the surface wind field in the period of ENSO event. Several months prior El Nino years, easterly winds are stronger than normal, but in October to November preceding El Nino years, westerly wind anomalies replaced easterly wind anomalies over the western edge of the tropical Pacific, migrating eastward gradually. During March to April of El Nino years the westerly anomalies covered all area of the western equatorial Pacific and the magnitude can be above 20 $m^2.s^{-2}$. At the end of El Nino years, easterly wind anomalies are present again.

The time-latitude section of the difference between τ^x for four El Nino years (1965, 1969, 1972, 1976) and that of the long term monthly mean (1964-1980) along 155°E, is displayed in Fig.6. From Fig.6 it is apparent that during El Nino year westerly wind anomalies are prevailing over the western tropical Pacific, particularly in the 10°S-10°N. band. There are two periods in which westerly wind anomalies strengthen, one is in the northern hemisphere during February to April, and the other is in the southern hemisphere during August to October.

3. Effects of the wind field on upper ocean thermal structure

a. Effect of the wind stress curl on the depth of thermocline.

Meyers (1975) used the following formula to approximately estimate the seasonal variation of the depth of 14°C isotherm

$$W_b = \nabla \times (\tau/\rho f) + \nabla . M_g \qquad (5)$$

where τ is the wind stress vector, f the coriolis parameter, ρ the density of the mixed layer, ∇M_g the vector of horizontal geostrophic transport in the layer between the surface and depth B, and W_b the vertical velocity at depth B. Donguy et al. (1982) used Eq.5 and estimated and analyzed the seasonal and interannual variations of the depth of the thermocline in the central tropical Pacific.

In our case, for lack of long-term salinity data, the term of the divergence of geostrophic transport ($\nabla . M_g$) is neglected. Since τ^y_x is much smaller than τ^x_y (see Table 2.) except at 16°N, during April to May, where both are small, equation (5) can be reduced to:

$$Wb = -(\tau^x/\rho f)_y \qquad (6)$$

According to long-term monthly mean (1964-1980) τ^x, one can estimate the seasonal variations of the depth of the thermocline. The integrated curves of W_b calculated by equation (6) are shown in Fig.7. At 8°N-155°E, the thermocline depth displays semiannual variations that can be explained by seasonal oscillations of the position of the ITCZ. In September-October, the ITCZ is situated in the 8°N band. Therefore, zonal wind stress and its curl near 8°N are weaker than annual mean values. The thermocline (or the isotherm in upper layer) descends from annual mean depth, responding to weaker Ekman pumping. During June to July and November to December, the ITCZ is south of 8°N, so the wind stress curl at 8°N is stronger than the annual mean, the thermocline (also the isotherm line) is rising in response to stronger Ekman pumping. In March the ITCZ is at its southernmost position (near 15°S), northeast trade are strong but uniform near 8°N. So the thermocline descends in response to weaker wind stress curl. Because sea level and thermocline depth are 180° out of phase in the equatorial ocean, sea level data taken at station near the equator permit a test of the analyzed thermocline (also isotherm depth in upper layer ocean). The dashed line in Fig.7 is Truk island (7°28'N, 151°51'E) monthly mean sea level (after Meyers, 1982). It shows 180° out of phase with the solid line (computed curve). The dotted line in Fig.7 is observed long-term mean (1964-1974) seasonal variations of the 20°C isotherm depth, which is similar to the computed curve.

		1	2	3	4	5	6
8°N	τ^x_y	14.2	13.8	7.2	19.3	15.3	14.9
	τ^y_x	2.6	0.9	2.8	0.7	1.5	0.7
16°N	τ^x_y	17.1	13.1	25.2	1.1	0.0	4.4
	τ^y_x	1.8	1.3	1.5	0.7	1.1	0.2

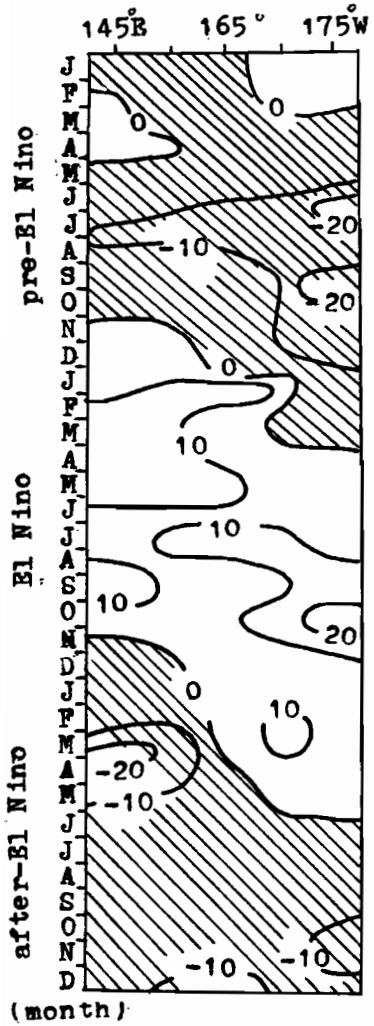

FIG.5. Time-longitude section of composite monthly zonal pseudo wind stress anomalies (in $m^2.s^{-2}$) along the equator for four El Nino years (1965, 1969, 1972, 1976). Shaded areas indicate east wind anomalies.

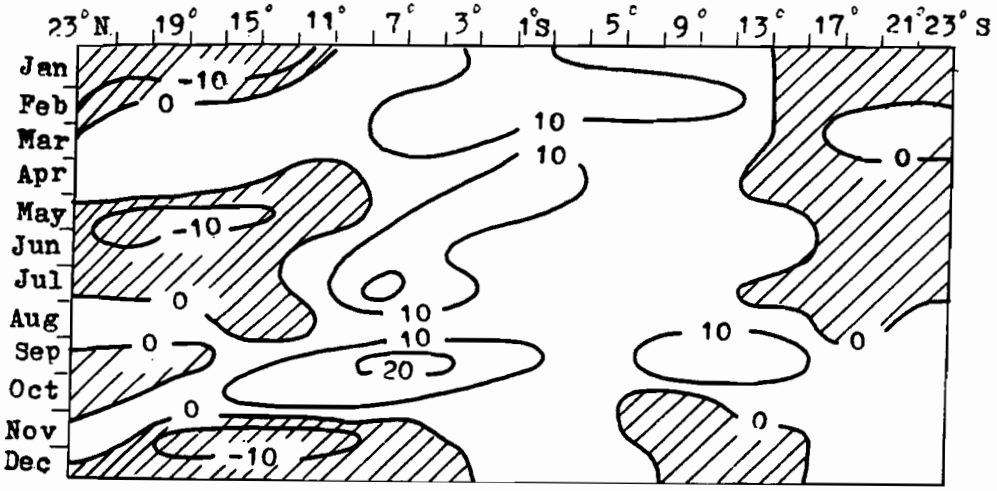

FIG.6. Time-latitude section of the difference between the monthly mean (zonal pseudo wind stress) for four El Nino years (1965, 1969, 1972 and 1976) and that of long term (1964-1980) monthly mean.

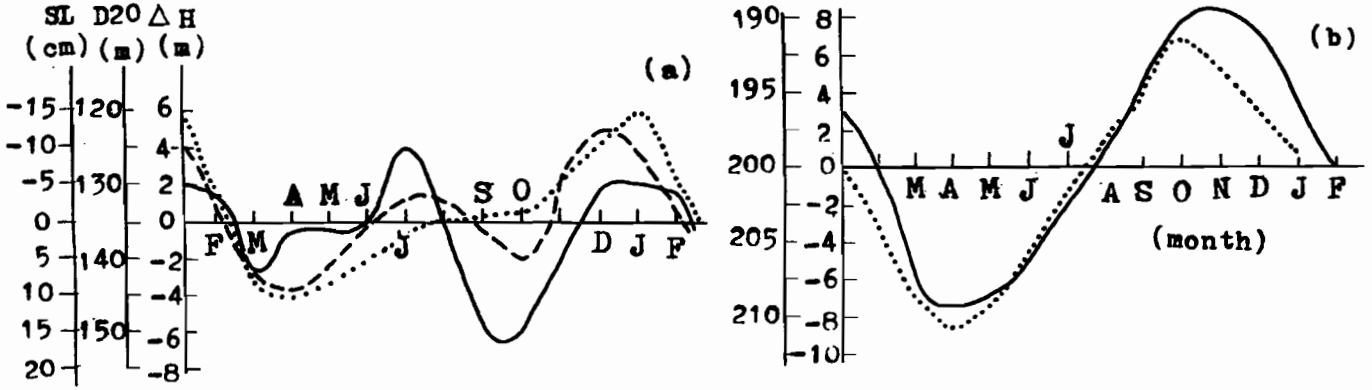

FIG.7. Seasonal variation of the thermocline depth at (a) at 8°N-155°E, (b) 16°N-155°E, as calculated by equation 6 (solid line). The dotted line denotes the long-term mean depth of the 20°C isotherm. The dashed line denotes the long-term mean sea level at Truk Island (7°28'N- 151°51'E), after Meyers (1982).

		7	8	9	10	11	12
8°N	τ^x_y	21.9	6.1	3.1	5.9	20.8	24.1
	τ^y_x	0.2	0.7	0.0	0.0	1.1	1.5
16°N	τ^x_y	7.2	10.5	12.0	14.2	2.2	3.9
	τ^y_x	0.4	2.2	0.4	0.2	1.3	0.0

Table 2. Monthly mean value of τ^x_y and τ^y_x at 8°N-155°E and 16°N-155°E (in cm.day^{-1})

At 16°N-155°E, both computed and observed thermocline depth have only one cycle per year (Fig.7b). During September to October the ITCZ reaches its northeast position, and at 16°N the wind stress curl is stronger: isotherms rise in response to the stronger Ekman pumping. In March, the ITCZ reaching its at the southeasternmost position, wind stress curl is weaker at 16°N due to uniform wind field, and the isotherms descend.

As described above, the effects of Ekman pumping produced by wind stress curl on the upper ocean thermal structure are visible. It can explained mean seasonal variations of the thermocline depth in the Western Tropical Pacific.

b. Effect of zonal wind stress on the Western Pacific Warm Pool.

In this section seasonal wind stress anomalies $\Delta\tau^x$ computed over ±3° area (defined as in section 2), represent variations of zonal wind stress in the western equatorial Pacific. We use the number of grid points at which the mean temperature from sea surface to 100m depth are warmer or equal to 28°C (west of 180° and north of the equator), to represent the volume of the Western Pacific Warm Pool (the T28 time series was taken from Lin, 1989). Its variations appear to be related to the equatorial zonal wind stress. The correlation coefficient of these two seasonal mean time series is -0.70 (n=52 seasons).

c. Relationship between zonal wind stress and other thermal indexes of the western tropical Pacific.

As indicated in Katz et al (1977), it is generally assumed in theoretical work that the vertically integrated zonal pressure gradient (in the upper ocean) can be equated to the zonal component of the wind stress. After analyzing the GATE's data, they showed strong correlation between zonal pressure gradient and simultaneously observed zonal wind stress. Donguy et al (1984) use zonal slope of thermocline to represent the zonal pressure gradient, and analyze its relation to zonal wind stress in the central Pacific. In the present study, zonal slope of the 20°C isotherm between 140°E and 180° in the 3°N-3°S band (D20), from 1964-1974, is calculated. D20 seasonal time series appear to be related to zonal wind stress anomalies (as calculated above), the correlation coefficient between the two series is -0.52 (n=38 seasons).

We also use seasonal difference of the 20°C isotherm depth between 7.5°N and 2.5°N, along 155°E, to indicate the strength of the NECC. We define T27 as T28 except for mean temperature higher or equal to 27°C, to indicate the mixed layer heat content in the western tropical Pacific. All of these upper ocean thermal indexes are related to the

wind field. Their cross correlation coefficients are shown in table 3. From table 3, it is apparent that the sea surface wind field over the western equatorial Pacific plays an important role in changing the upper layer ocean thermal structure.

($\pm 3^{\circ}\Delta\tau^{x}$	-.86* (62,0)	-.45 (31,1)	-.52* (38,1)	-.58* (52,0)	-.70 (52,0)
T28	-.70* (52,0)	-.56* (31.0)	.43 (38,0)	.83 (52,0)	
T27	-.62* (38,0)	-.62* (31,0)	.51* (38,0)		
D20	-.37 (38,0)	-.14 (30,0)			
NECC	-.21 (30,0)				

Table 3. Cross correlation coefficients between the wind field and the upper ocean thermal indexes (numbers in parentheses are the seasons of time series and lag). Stars denote significance at the 1% level.

4. Conclusion

The primary results of the present study are:

(1) The surface wind field over the western tropical Pacific have apparent annual cycle. Near the equator, it has apparent semiannual variations, because the ITCZ crosses the equator twice a year.

(2) The interannual variations of the surface wind field over the western tropical Pacific present a main variation of 2-4 years, consistent with that of the ENSO event. The zonal wind over the western equatorial Pacific is closely related to SOI (correlation coefficient is -0.87).

(3) In the western tropical Pacific mean seasonal variations of the thermocline depth, and of sea level near the equator can be explained by displacement of the surface wind field (indicated by the ITCZ position).

(4) From correlation analysis of long-term historical data, it is apparent that the sea surface wind field over the western equatorial Pacific plays an important role in changing the upper layer thermal structure of the ocean.

The data sets used in this study have poor resolution but the interannual variations of the wind field and the thermal structure are strongly related to ENSO events. Therefore some primary results can be obtained as above. More complete data sets are necessary to analyze more details. Wind field and upper ocean thermal structure data sets will be greatly improve within the international TOGA programme.

REFERENCES

Donguy, J.R. and C. Hénin, 1981: Two types of hydroclimatic conditions in the south-western Pacific. *Ocean. Acta*, **4**, 57-62.

Donguy, J.R., C. Hénin, A. Morliere and J.P. Rébert, 1982: Thermal changes in the western tropical Pacific in relation to the wind field, *Deep-sea Res.*, **29**, 869-882.

Donguy, J.R., A. Dessier, G. Eldin, A. Morliere and G. Meyers, 1984: Wind and thermal conditions along the equatorial Pacific. *J. Mar. Res.*, **42**, 103-121.

Katz, E.J. and Collaborators, 1977: Zonal pressure gradient along the equatorial Atlantic. *J. Mar. Res.*, **35**, 293-307.

Lin Chuanlan, 1989: Some features of the heat content changes of the ocean upper layer in the Northwest Pacific during period 1964-1982. Submitted to Tropical ocean. (in Chinese)

Meyers, G., 1975: Seasonal variation in transport of the Pacific North Equatorial Current relative to the wind field. *J. Phys. Oceanogr.*, **5**, 442-449.

Meyers, G., 1982: Interannual variation in sea level near Truk Island: a bimodal seasonal cycle. *J. Phys. Oceanogr.*, **12**, 1161-1168.

Parker, D.E., 1983: Documentation of a Southern Oscillation Index. *Meteoro. Mag.*, **112**, 184-188.

White, E.B., G. Meyers, J.R. Donguy and S.E. Pazan, 1985: Short-term climate variability in the thermal structure of the Pacific Ocean during 1979-1982, *J. Phys. Oceanogr.*, **15**, 917-935.

Wyrtki, K., 1974: Equatorial current in the Pacific 1950-1970 and their relations of the trade wind. *J. Phys. Oceanogr.*, **4**, 372-380.

Influence of Southern Oscillation on New Zealand Weather

Bret A. MULLAN

New Zealand Meteorological Service
P.O. Box 722, Wellington - New Zealand

ABSTRACT

The Southern Oscillation is known to have a significant effect on New Zealand weather. In general, during the negative (El Niño) phase of the Oscillation, New Zealand experiences an increased frequency of cold southwesterly airstreams that result in more rain in the southwest of the country, and dry conditions in the north and east. During the positive (La Niña) phase, there is a tendency for increased cyclonic activity in the North Tasman and more slow-moving or blocking anticyclones to the southeast of New Zealand. This results in frequent warm moist northerly or northeasterly airstreams over the country, with warmer than normal temperatures nationwide and wetter conditions in parts of the North Island exposed to these prevailing winds.

The pressure anomalies in the New Zealand region associated with extremes of the Southern Oscillation Index show some seasonal variation. The anomalies are also not entirely linear with respect to the value of the SOI. This paper examines differences between El Niño and La Niña conditions as they affect New Zealand, and then discusses the predicted and observed anomalies in New Zealand weather associated with the 1988/89 La Niña episode.

1. Introduction

Interest in the Southern Oscillation and its regional effects has been high since the 1972–73 El Niño event that devastated the Peruvian anchovy fisheries, and particularly intense since the dramatic 1982–83 episode. Although the existence of the Southern Oscillation (SO) has been known for many years (Walker, 1923), it took some time for the link between the SO and periodic ocean warming off the Peruvian coast to be appreciated. However, the term ENSO, for El Niño–Southern Oscillation, quickly became accepted. More recently, the term La Niña has become popular for describing the opposite extreme to El Niño conditions.

There is a considerable recent literature on regional weather changes associated with fluctuations in the Southern Oscillation. In the Australasian region, for example, McBride and Nicholls (1983) have examined seasonal relationships between Australian rainfall and the Southern Oscillation Index (SOI). Some of the lag correlations they found are sufficiently promising that the Australian Bureau of Meteorology plans to start issuing regular seasonal outlooks to the public from mid-1989 (National Climate Centre, 1988). Gordon (1985, 1986) discussed how the seasonal patterns of rainfall and temperature over New Zealand are related to the SOI. These relationships, along with further work, enabled the New Zealand Meteorological Service to make statements about the long-range weather prospects during the 1986–87 El Niño and the more recent 1988–89 La Niña.

A good start has thus been made to documenting general SO–weather relationships. However, much more attention now needs to be paid to the differences from one ENSO event to another: the reasons for the different evolution of the anomaly patterns, and the regional implications. This paper is a contribution to this need, essentially from a New Zealand point of view. Our particular interest is to examine anomalies associated with La Niña and El Niño, and see whether the anomalies vary linearly with the SOI. Predicted and observed anomalies in New Zealand during the 1988/89 La Niña summer are used as an example.

2. Data

The Southern Oscillation Index data used here cover the period May 1851 to December 1988. Parker's (1983) monthly values from January 1935 to March 1983 were updated using the standard 6-hourly pressure readings (at 0000, 0600, 1200 and 1800 GMT) at Tahiti and Darwin. The base period 1941–80 was used to normalize the Tahiti–Darwin pressure difference to form the so-called "Troup" Index (McBride and Nicholls, 1983). The SOI time series was extended back to 1851 using the seasonal Index values published by Wright (1975). Regression equations were calculated for each month of the year (N.D. Gordon, pers. comm.) relating the monthly Tahiti–Darwin pressure difference to Wright's Index values of the surrounding three seasons. The period 1935–1974 was used to generate the regression equations, which were then applied to Wright's values to extend the SOI time series back to 1851.

Although the basic SOI time series consists of monthly values, running three-monthly means are used throughout the analyses of this paper.

The pressure anomaly calculations (Section 4) use monthly mean sea level pressures determined from daily grid-point values on a 5° by 10° latitude–longitude grid over the New Zealand–Australia region (Gordon, 1986). These data cover the period July 1957 to September 1988. In the verification of the 1988–89 anomalies, the pressure time series was updated to February 1989 using the daily ECMWF analyses over the Southern Hemisphere from 20°S to 90°S that are received operationally by the New Zealand Meteorological Service. In addition, time series of monthly temperature and rainfall at selected New Zealand stations were used.

3. Persistence

a. *SOI AUTOCORRELATION*

The SOI time series shows considerable persistence from month to month. Conventional wisdom has it that the autocorrelation is highest during May–July and there is a "break" in persistence about March–April. Hence, Gordon (1986) recommended that the 12-month period May–April, rather than the calendar year, be used when calculating annually averaged relationships with the SOI. The break in persistence occurs because there is a tendency for new ENSO events to become established in May–June and also for existing events to weaken during February–March (at least in so far as ENSO behaviour is represented by the SOI).

Fig. 1 shows the seasonal variation in autocorrelation of the 3-month running mean SOI at lags up to 12 months. The lag autocorrelations were calculated separately according to whether the starting 3-month mean SOI was positive (1a) or negative (1b). Gordon (1986) calculated lag correlations that included all starting SOI values irrespective of sign, and his Fig. 2 is very similar to our Fig. 1b. It appears then that the autocorrelation structure of "all SOI" is dominated by that for "negative SOI" (Fig. 1b). The pattern for a starting "positive SOI" is somewhat different, with slightly greater persistence for starting months January–March and reduced persistence for the remainder of the year. The "positive SOI" result is also much noisier, particularly in March–May, the southern autumn, although the sample size is similar for each month (at slightly over 40% of the total).

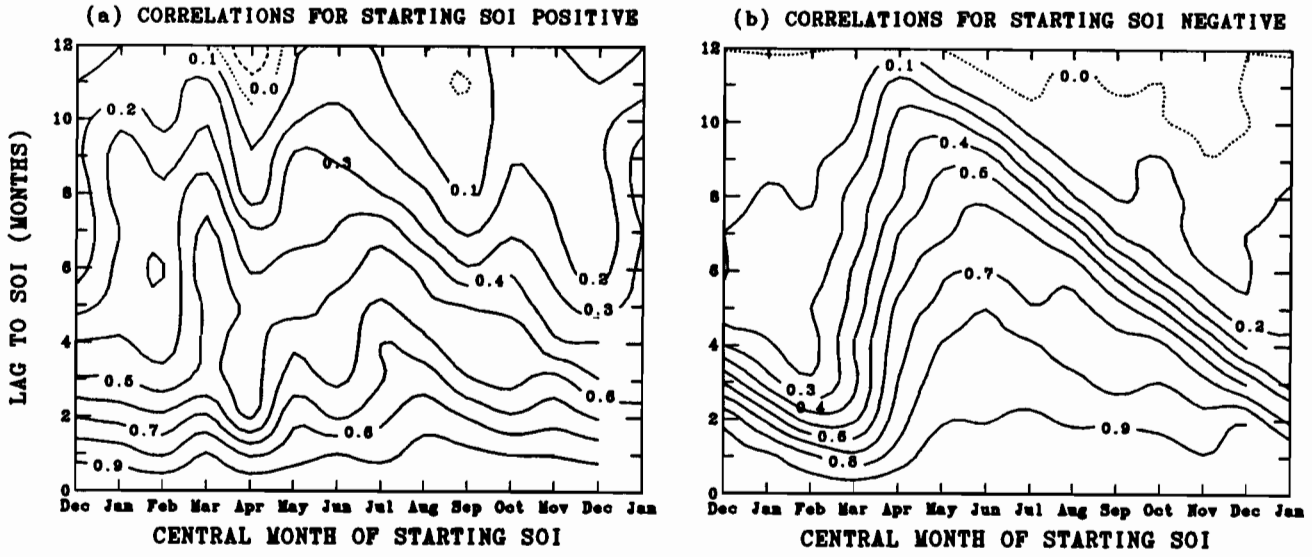

FIG. 1. SOI autocorrelation between the 3-month average centered on the given starting month and the 3-month average for 1–12 months later. Results cover the period May 1851 to December 1988 for 3-month average starting SOI positive (a), and for 3-month average starting SOI negative (b).

b. *LA NIÑA/EL NIÑO EVENTS*

In an attempt to identify further characteristics of La Niña and El Niño events, an objective definition of these events in terms of the SOI time series was applied. "Positive"/"negative" events (identified with La Niña/El Niño events, respectively) were defined to start when the 3-month running average SOI became at least S_0 above/below zero and remained that way for at least three consecutive months. The event continued until the 3-month running average SOI became smaller than S_1 above/below zero.

Various combinations of S_0 and S_1 were tried and the final values decided upon were $S_0 = 10$ and $S_1 = 5$ (in units of 0.1 standard deviation). The events identified by this choice agreed reasonably well with ENSO events identified by other authors (such as van Loon, 1984, and Rasmusson and Carpenter, 1982). Taking $S_1 = S_0$, for example, often resulted in breaking up what should have been single events into two or more parts.

Over the period of record, 11 positive (La Niña) events were identified, excluding the one apparently in progress in 1851 where the starting month could not be determined and the 1988–89 event that had not finished. The length varied from 10 to 23 months, with a mean of 14.0 months. Of the negative (El Niño) events, 29 were identified, of which 3 were of less than six-months duration (in 1857/58, 1957/58 and 1963/64). The length of the negative events varied from 3 to 47 months, with a mean of 13.7 months. Table 1 shows the distribution of the start and end months of the events selected. The reason for the seasonal break in persistence seen in Fig. 1 is quite obvious.

A relationship between the "intensity" of an event and its duration was also sought. Defining the starting intensity I_n of an event as the mean of the unsmoothed SOI values over the first n months, I_n was correlated against duration. While nothing useful was found for negative events, quite large correlations were found for positive events, which maximised at $n = 5$ ($r = +0.90$). Fig. 2 shows a scatter plot of La Niña starting intensity (average SOI over first 5 months) against duration.

TABLE 1. Start and end months of the 11 La Niña and 29 El Niño events identified in the period 1851–1988.

	J	F	M	A	M	J	J	A	S	O	N	D
Start month:												
La Niña	1	0	1	2	2	1	1	0	0	1	1	1
El Niño	1	3	3	7	2	1	3	3	1	2	1	3
End month:												
La Niña	1	2	1	2	0	0	0	0	2	1	1	1
El Niño	2	5	10	2	3	0	0	0	1	2	4	0

The 1988–89 La Niña event began strongly (I_5 = 16.8), and on the basis of Fig. 2 would be estimated to last for about 19–20 months from the start of August 1988; i.e., to about February–March 1990 before the 3-month running average SOI fell below +5. This prediction may not be too successful, as according to the latest observations (March 1989 Climate Diagnostics Bulletin) the current "cold episode conditions continued to show signs of weakening". Various U.S. modellers (e.g., Cane and Barnett, as reported in The New York Times, 1989) also seem to agree that the current La Niña event should be over by mid-1989.

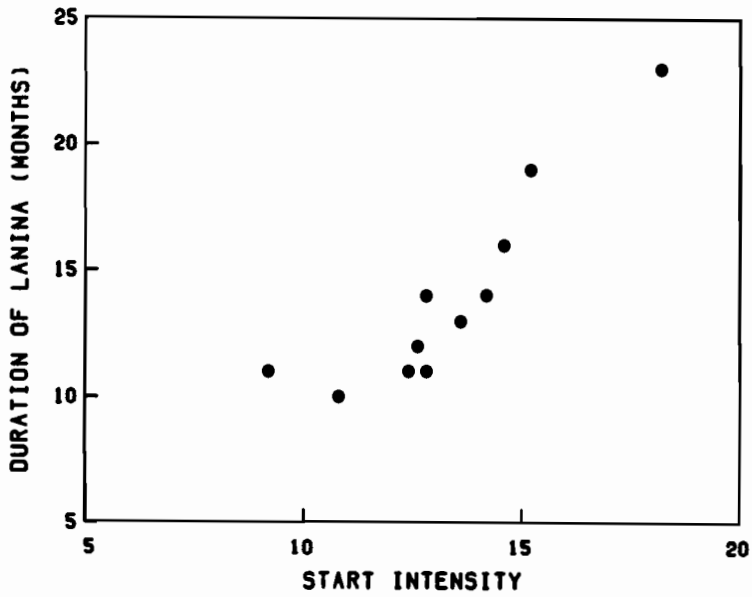

FIG. 2. Scatter plot of La Niña starting intensity (5-month average SOI, in units of 0.1 standard deviation) against calculated duration in months.

4. Pressure Anomaly Composites

a. *METHOD*

Gordon (1985,1986) calculated seasonal correlation maps of mean sea level pressure against SOI for an area covering Australia and New Zealand . Both positive and negative Index events were

included in the correlations. Overall, he found that positive SOI was associated with anomalous northeasterly flow over New Zealand (and, conversely, anomalous southwesterly flow during negative SOI periods). There was some seasonal variation in this pattern, with the flow anomalies displaying a more east/west direction in summer and more north/south in winter (for positive/negative SOI respectively).

In this section we will analyse the pressure variations not by a correlation pattern but by compositing seasonal pressure anomalies, weighted by the 3-month mean SOI for that season. Thus, if the array Y_i is the seasonal msl pressure anomaly over the Australia–New Zealand area, and x_i the seasonal SOI, we have:

$$Y_i = R\,x_i + C + E_i$$

where R is a "response" matrix, C a constant matrix, and E_i a random field for season i. Assuming that E_i has zero mean and is uncorrelated with the Index (i.e., $\bar{E}_i = 0$ and $\overline{x_i E_i} = 0$), we find:

$$R = \left(\frac{\overline{x_i Y_i} - \overline{x_i}\,\overline{Y_i}}{\overline{x_i^2} - \overline{x_i}^2} \right)$$

and $C = \bar{Y}_i - R\,\overline{x_i}$.

If the pressure field (Y_i) and SOI (x_i) time series were both normalised over the same base period as the composites are calculated for, then C would be zero. The pattern shown by the response matrix R is of course very similar to that of the correlation matrix. Thus, when displaying the pressure anomaly patterns associated with "all SOI", it is equivalent to show either the correlation field (as in Gordon, 1986) or the predicted $\hat{Y}$ (evaluated for some nominal Index value $x_i = 1$, say). Since our interest here is in the pressure pattern for subsets of the SOI data (in particular, positive and negative periods), it is more convenient to display the results in terms of the predictand $\hat{Y}$.

The significance of the resulting composite field was assessed by a Monte Carlo randomisation procedure. For the same season (e.g., summer) and period (1957-88) as the field in question, 1000 *sets* of composited response fields were calculated for randomly generated SOI series (with the same mean and standard as observed). The mean random response $\bar{\bar{R}}$ is essentially zero, but the standard deviation $S_{\bar{\bar{R}}}$ of the random response allows us to calculate the significance of the initial composite. We thus normalise the composite by evaluating:

$$R_N = 100 \left(\frac{R - \bar{\bar{R}}}{1.64\, S_{\bar{\bar{R}}}} \right)$$

Values of $|R_N|$ greater than 100 denote regions where the pressure response is significantly different from random at the 90% level (2-sided test).

b. *RESULTS*

Weighted composites of seasonal pressure anomaly fields were calculated for each season for three cases: using the whole sample regardless of the sign of the SOI ("all"), compositing only those seasons when the SOI was positive ("+"), and compositing only those seasons when the SOI was negative ("-"). The linearity of the pressure response with respect to the sign of the SOI could thus be assessed. Calculations showed that the linearity was good through December–May (Southern Hemisphere summer and autumn), but relatively poor in the June–November (winter and spring) period. Hence, using the seasonal correlation patterns of Gordon (1985,1986) to predict flow

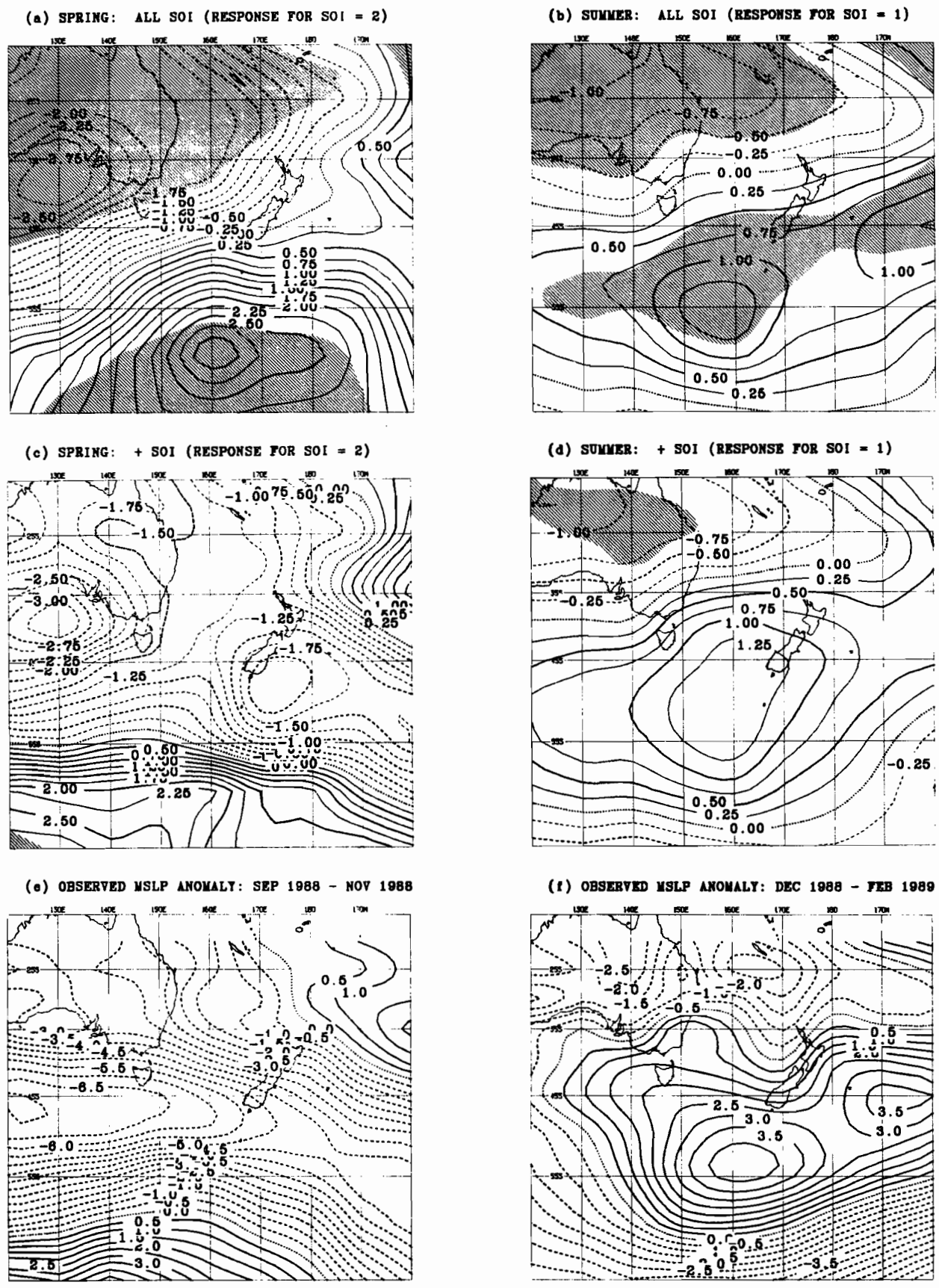

FIG. 3. Seasonal pressure anomaly patterns. Predicted anomaly, based on sample of "all" seasons, for a spring SOI of 20 (3a) and a summer SOI of 10 (3b). Predicted anomaly, based on sample of "+" SOI seasons, for a spring SOI of 2.0 (3c) and a summer SOI of 1.0 (3d). Observed anomaly for spring 1988 (3e), and for summer 1988/89 (3f). Shading indicates the composite response is significantly different from random at 90% level.

anomalies during both La Niña and El Niño periods could be expected to be reasonably successful in summer and autumn, but less so in winter and spring. Further discussion here is restricted to the spring (September–November) and summer (December–February) seasons.

Fig. 3 shows examples of calculated and observed seasonal pressure anomalies (in millibars) for the spring (Fig. 3a, c, e) and summer (Fig. 3b, d, f) seasons. The periods used to calculate the composites did not include the verification period September 1988–February 1989. The observed anomalies (Fig. 3e, f) cover a period of the current La Niña event. The 3-month running average SOI (Fig. 4) reached a maximum of 2.0 for the September–November (spring) 1988 period and decreased to an average of 1.1 over December–February (summer) 1988/89. (Note the change in contour interval from 0.25 mb in the composites to 0.50 mb in the observed fields.)

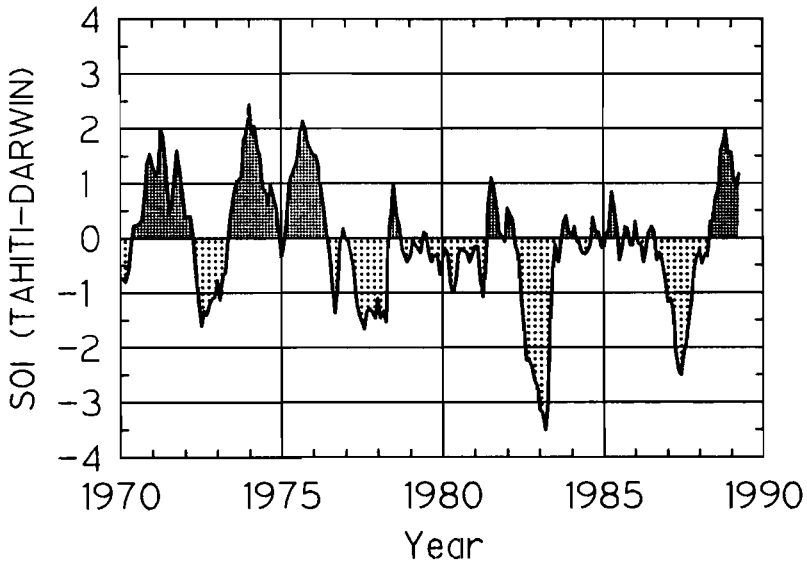

FIG. 4. Three-month running average SOI from January 1970 to April 1989 (in standard deviation units).

New Zealand was affected by stronger than normal westerlies throughout the 1988 winter and much of spring. This caused high rainfalls and some severe flooding on the west coast of the South Island, while drought conditions developed on the eastern side of the South Island mountain range. A sudden breakdown of the strong westerly flow occurred in early November, and a succession of persistent slow-moving anticyclones crossed the South Island during the summer, which served to further aggravate the drought there. Fig. 3e, f show the seasonal pressure anomaly patterns over this spring and summer period.

The predicted spring pressure anomaly, evaluated for the observed SOI of 2.0, is shown in Fig. 3a, c. It is clear that developing the composite using all spring seasons (Fig. 3a), and therefore the standard correlation approach too, completely fails to capture the stronger westerlies that affected New Zealand during the 1988 spring. The composite developed from only those spring seasons where the SOI was positive (Fig. 3c) is much more successful. Since Fig. 3c uses only about half the data set of Fig. 3a, the significance levels are lower, as indicated by the shading changes. The predicted summer pressure anomaly associated with Southern Oscillation changes is shown in Fig. 3b, d, evaluated for an SOI of 1.0, close to that observed. As mentioned above, the relationship between the flow anomaly over New Zealand and the SOI is more linear in summer than spring, so Fig. 3b, d are quite similar. The main difference is that in Fig. 3d the anticyclone is stronger and extends over more of the country.

5. 1988/89 Summer

The observed temperature and rainfall anomalies in New Zealand during the 1988/89 summer (December 1988–February 1989) are shown in Fig. 5a, b. The maps are based on daily temperature and rainfall observations from 46 stations evenly distributed around the country. Fig. 5c indicates the locations of places mentioned in the text. Temperatures were above normal over the whole country, with the largest anomalies occurring in the South Island and the southwestern half of the North Island. Rainfall was below normal in almost all eastern districts from Dunedin to East Cape.

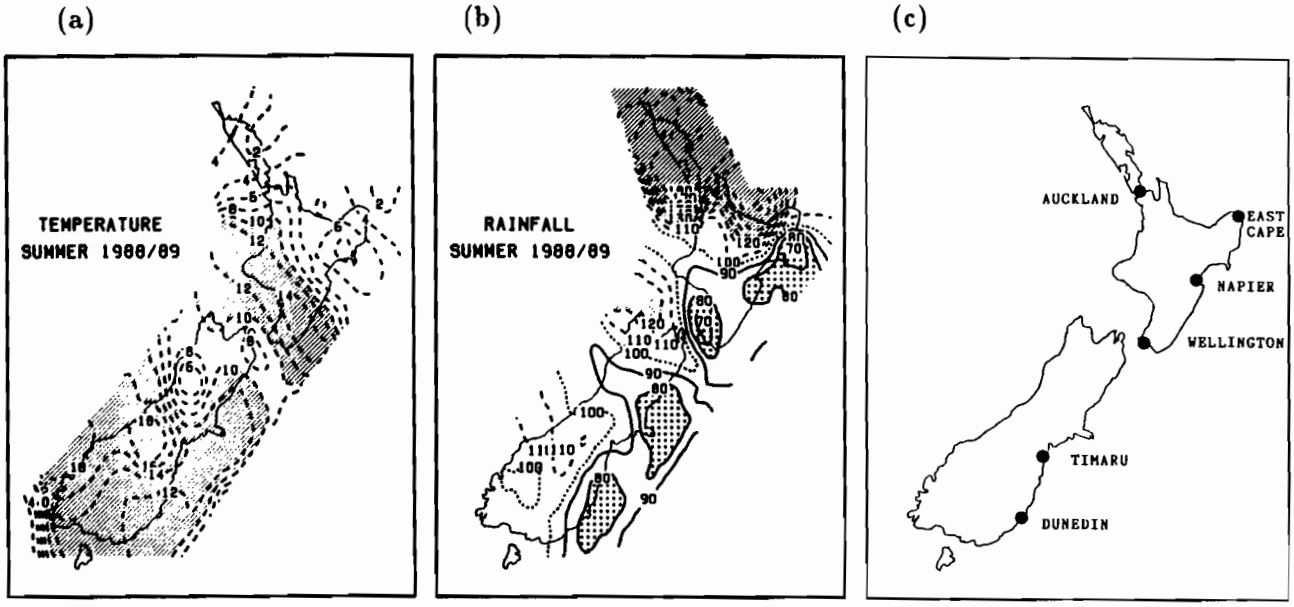

FIG. 5. Observed temperature anomalies (a, in 0.1°C) and rainfall (b, as % normal) over New Zealand during the 1988/89 summer season. Temperature anomalies greater than 1.0°C are shaded. Rainfall greater than 120% normal shaded and less than 80% stippled. (c) Map of New Zealand, showing some places mentioned in text.

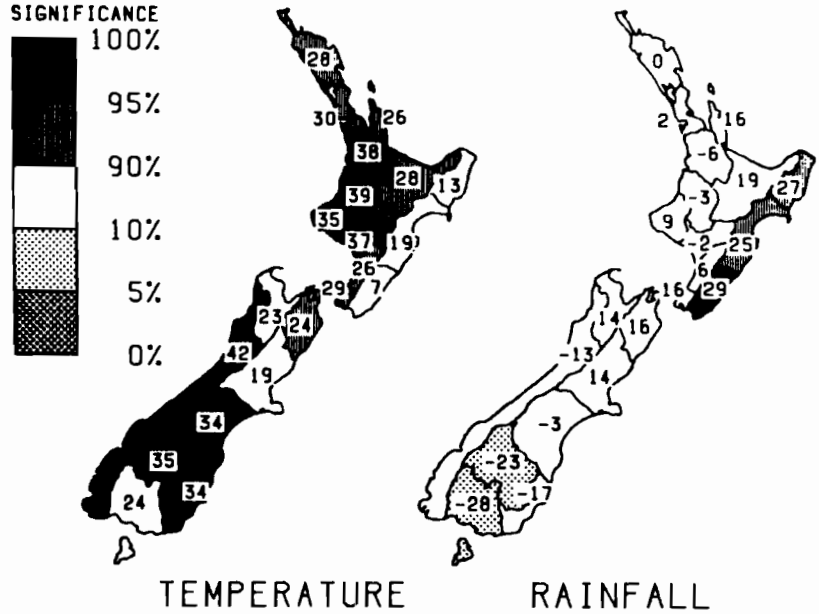

FIG. 6. Correlations ($x100$) between summer temperature and rainfall anomalies and the summer SOI, for various subregions of New Zealand. Significance levels indicated by shading (from Gordon, 1985).

Over the summer the drought that had previously affected only southeastern South Island areas extended up into eastern districts of the North Island as well. On the other hand, much above normal rainfall was experienced in the northern part of the North Island. Many places from Auckland northward received almost twice their normal summer rainfall. January was a particularly wet month, with rainfall in these northern areas being three to five times normal.

The pattern of temperature and rainfall anomalies over the country can be compared to the correlation patterns found by Gordon (1985), based on 30–34 years of data (Fig. 6). The main discrepancies with the observed patterns over the 1988/89 summer occur in the north and east of the North Island. In the north there was more rainfall, greater cloudiness and smaller (but still positive) temperatures anomalies than might have been anticipated. In the east of the North Island, rainfall was below normal (presumably as a result of the more intense anticyclonic anomaly over the country with a ridge extending up the east coast, Fig. 3f), and not above normal as Fig. 6 would indicate for significantly positive SOI.

6. Analogue Prediction

A comparison of Fig. 5 and Fig. 6 shows some features of (particularly) the rainfall distribution over New Zealand where the correlation pattern does not agree too well with that observed during the La Niña summer of 1988/89. Thus, we attempt again to separate the effects of La Niña and El Niño in the rainfall pattern as was done with the pressure anomaly. In this case. however, a somewhat different approach was taken: namely, the selection of analogues. (This analysis was actually done prior to the 1988/89 summer season, and was part of the background information used by the New Zealand Meteorological Service in issuing a long-range weather outlook for the summer on 19 October 1988.)

Analogues of 1988 were selected subjectively from examination of the 3-month running average SOI series. We selected La Niña start years (years zero, in the terminology of Rasmusson and Carpenter, 1982) to be those where the SOI rose from essentially zero at the beginning of the year to a positive value of at least one standard deviation above zero in the middle part of the year. Analogue years after 1900 were 1909, 1916, 1938, 1950, 1955, 1964, 1970, 1973, and 1975. Earlier events were not relevant since, in general, the station data sets do not extend back beyond the early years of the century. The only difference between this set of years and those chosen more objectively in Section 3b was the inclusion of 1964 which did not appear in the earlier set. The temperature and rainfall distribution during the winter and spring of year zero and during the following summer were then examined. Only the results for summer rainfall will be discussed here.

Monthly rainfall over the summer season at a number of representative long-record stations was allocated to categories of "dry", "near normal" and "wet", where for the examples shown here we take "near normal" to mean 81–119% of the normal monthly rainfall. Doing this for all years in the period of record, we could calculate an *a priori* probability that a summer month would be "dry" or "wet". The actual number of "dry" and "wet" summer months for the La Niña analogue seasons were counted, and the binomial test applied to assess the significance of the result. Fig. 7 shows the result in histogram form for the stations of Auckland and Timaru.

The changed temperature and rainfall category distribution in La Niña analogue years generally supported the correlation maps shown in Fig. 6, although there were some differences. Fig. 7a gives a stronger indication than Fig. 6 of Auckland being wet during a La Niña summer, although the results do not quite come up to the 90% significance level. (For example, the *a priori* probability of

a "dry" summer month in Auckland is $p = 0.460$, but during past analogue La Niña summers only 9 of 27 months have been "dry", which has a probability of 0.13 of occurring by the binomial test.) The analogue approach also predicted the east coast of the North Island (Napier, not shown) should not be as dry in La Niña summers as "all" summers, a result that supports Fig. 6 but conflicts with the observations (Fig. 5b).

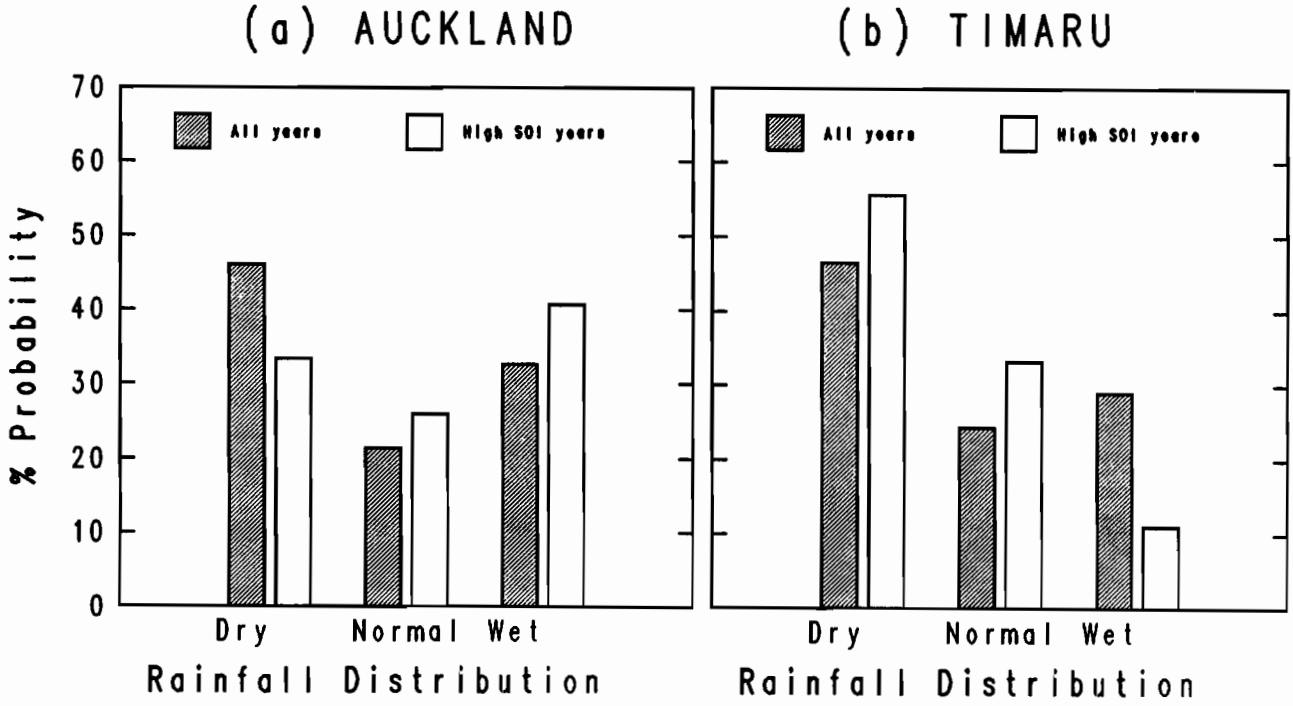

FIG. 7. Probability of Auckland (a) and Timaru (b) rainfall falling into one of three categories, comparing all years of record with La Niña analogue years.

7. Conclusions

Although New Zealand is not near the centres of action of the Southern Oscillation, it is nevertheless affected by this phenomenon. Significant anomalies in the seasonal pressure distribution around New Zealand do occur, and these result in temperature and rainfall anomalies over the country. The general pattern of the anomalies and their seasonal variation have been documented previously in terms of correlation maps. This procedure implicitly assumes a linearity of the response to the forcing.

We have shown that this assumption of linearity is not always valid. In particular, over the period September–November 1988 when the SOI reached a positive extreme, it seems necessary to take account of *nonlinearity* in the response in order to explain the observed pressure distribution. The summer case is not as obvious although, even here when the SOI value was less extreme, there was some improvement in the predicted anomalies using only that part of the historical record when the SOI was positive.

Acknowledgments

The extended SOI series and Fig. 6 was provided by Neil Gordon. I would also like to thank John Marsh, Director of International TOGA Project Office, for financial assistance that made possible my participation in the Noumea TOGA Conference.

REFERENCES

Gordon, N.D., 1985: The Southern Oscillation: a New Zealand perspective. *J. Royal Soc. of New Zealand 15:* 137–155.

Gordon, N.D., 1986: The Southern Oscillation and New Zealand weather. *Mon. Wea. Rev. 114:* 371–387.

McBride, J.L., and Nicholls, N., 1983: Seasonal relationships between Australian rainfall and the Southern Oscillation. *Mon. Wea. Rev. 111:* 1998–2004.

National Climate Centre, 1988: Seasonal outlooks (Based on El Niño/Southern Oscillation (ENSO) Relationships). Australian Bureau of Meteorology, August 1988, 46 p.

Parker, D.E., 1983: Documentation of a Southern Oscillation index. *Meteor. Mag., 112:* 184–188.

Rasmusson, E.M., and Carpenter, T.H., 1982: Variations in tropical sea surface temperature and surface wind fields associated with the Southern Oscillation/El Niño. *Mon. Wea. Rev., 110:* 354–384.

The New York Times, 1989: *Science Times*, Tuesday, January 3, 1989.

van Loon, H., 1984: The Southern Oscillation. Part III: Associations with the trades and with the trough in the westerlies of the South Pacific Ocean. *Mon. Wea. Rev., 112:* 947–954.

U.S. Dept. of Commerce, 1989: Climate Diagnostics Bulletin. March 1989. Climate Analysis Center, Washington.

Walker, G.T., 1923: Correlation in seasonal variations of weather, VIII. *Mem. Indian Meteor. Dept. 24:* 75–131.

Wright, P.B., 1975: An index of the Southen Oscillation. Climatic Research Unit Rep., CRU RP4, University of East Anglia, Norwich, NR4 7TJ, England, 22 pp.

Wind Profiler Related Research in the Tropical Pacific

Kenneth GAGE, Ben BASLEY, Warner ECKLUND
D.A. CARTER and J.R. McAFEE

Aeronomy Laboratory
NOAA, Boulder, CO 80303 - U.S.A.

ABSTRACT

This paper is broadly concerned with the application of wind profiling Doppler radar technology to tropical atmospheric research. Examples of the use of wind profilers in the tropics are drawn from the Aeronomy Laboratory's wind profilers located on Pohnpei (7°N, 158°E) and Christmas Island (2°N, 157°W). The Pohnpei wind profiler was constructed in 1984 and has been used exclusively to observe vertical motions. The Christmas Island wind profiler has observed horizontal and vertical velocities routinely since 1986. These two wind profilers form part of a planned trans-Pacific network of wind-profiling radars that will eventually span the tropical Pacific.

1. Introduction

The past decade has seen a rapid increase in the use of wind-profiling Doppler radars in atmospheric research (Gage, 1989). With a few notable exceptions most atmospheric research using wind profilers has been carried out with individual radars. With the current wide-spread acceptance of clear-air radar wind-profiling technology, field programs are increasingly taking advantage of the continuous wind observations available from wind profilers. While much of the wind profiler research community has been focused on mid-latitude atmospheric research, the Aeronomy Laboratory's Tropical Dynamics and Climate Program has focused its attention on the use of wind profilers in the tropics to study the scale interactions that take place between tropical convection and large-scale atmospheric circulation systems. Because the wind profilers observe vertical as well as horizontal motions, the relationship between atmospheric vertical motions and convective systems in the tropics can now be examined directly.

The wind observations from the new wind profilers augment the existing base of conventional observations available in the tropics. For example, wind observations from Christmas Island are routinely transmitted via GOES satellite and input into the Global Telecommunications System (GTS) for world-wide dissemination. These observations are already being used routinely by the National Meteorological Center (NMC) and the European Center for Medium Range Weather Forecasts (ECMWF) in their analysis and forecast products (Gage et al., 1988).

This paper is broadly concerned with the application of wind profiling technology to tropical atmospheric research. Specifically, we will present some preliminary results of wind profiler studies of tropical convection using observations of vertical motions from the Pohnpei wind profiler and present some sample of wind observations made by the Christmas Island wind profiler. We conclude the paper with a discussion of plans to construct a trans-Pacific wind profiler network designed to support studies of equatorial waves and large-scale atmospheric circulation systems associated with El Nino-Southern Oscillation (ENSO) phenomena.

ORSTOM
CENTRE DOCUMENTATION
Montpellier

F 30255

2. Studies of tropical convection using the Pohnpei profiler

The Aeronomy Laboratory has pioneered the use of wind profilers in the tropics since 1984 when the Pohnpei wind profiler was installed. The Pohnpei profiler has been used to measure continuously vertical velocities over Pohnpei. These vertical motions have been related to convective storms and rainfall by Balsley et al (1988) and the influence of topography at Pohnpei on the observed vertical motions has been considered by Balsley and Carter (1989).

The ability of wind-profiling Doppler radars to measure directly vertical motions provides a useful technique for observing tropical convective systems. Figure 1 shows the signature of a deep convective system as it passed over the Pohnpei radar on 20 November 1984. Strong updrafts as shown here probably represent the first direct measurement of the convective "hot towers" discussed by Riehl and Malkus (1958). These convective storms are invariably associated with heavy rain as recorded at the surface.

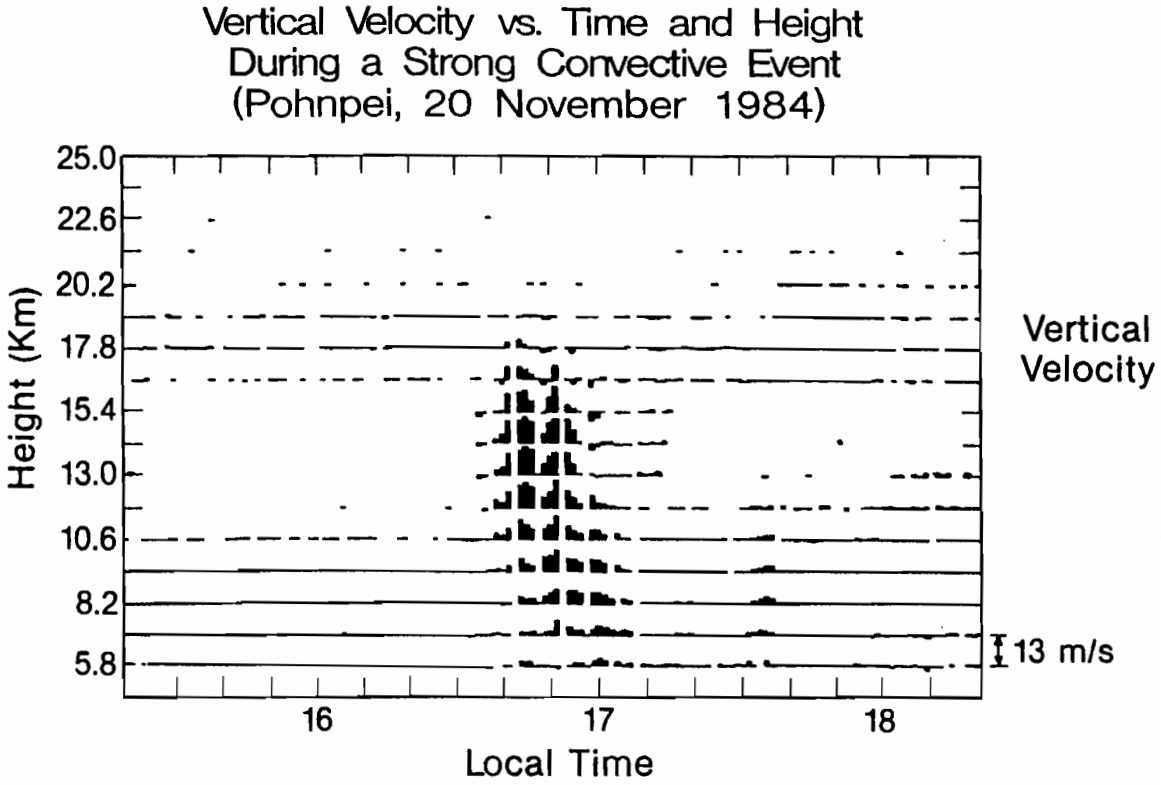

FIG.1. Signature of convective "hot tower" as seen by the Pohnpei wind profiler.

Average vertical motions seen by the Pohnpei wind profiler during its first two years or operation have been stratified by rainfall rate from surface measurements to reveal how the vertical motion field is affected by the presence or absence of convection. The results of this study published by Balsley et al (1988) are shown in Figures 2-4. Figure 2 shows the results obtained when the heaviest rainfall periods are averaged. The most intense vertical motion of magnitude 100 cm s^{-1} are observed in the height range of 8-14 km. Also shown in Figure 2 is the vertical velocity profile deduced by Gamache and Houze (1982) for the eastern Atlantic during GATE. The direct measurements are seen to yield peak velocities to considerably higher altitudes than for Gamache and Houze's result. Indirect measurements of average vertical motions in convective systems

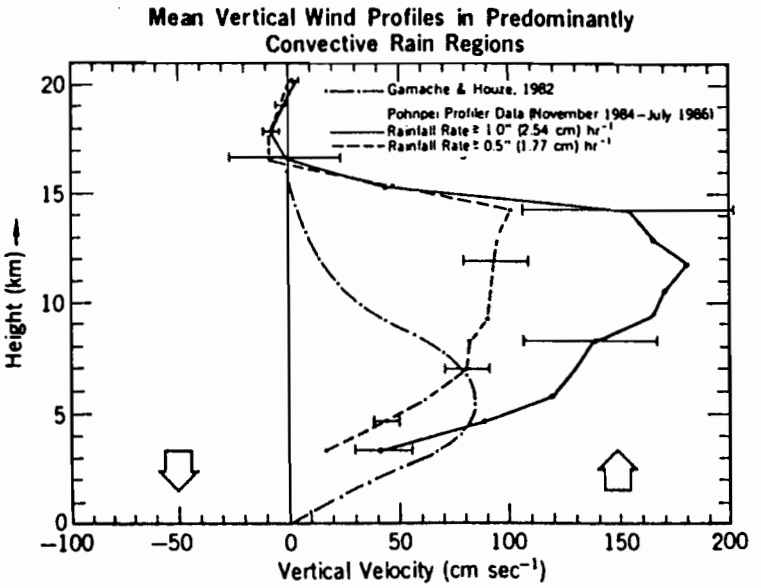

Fig. 2. Average vertical wind profiles from the Pohnpei profiler for rainfall rates corresponding as closely as possible to convective conditions. (After Balsley et al, 1988.)

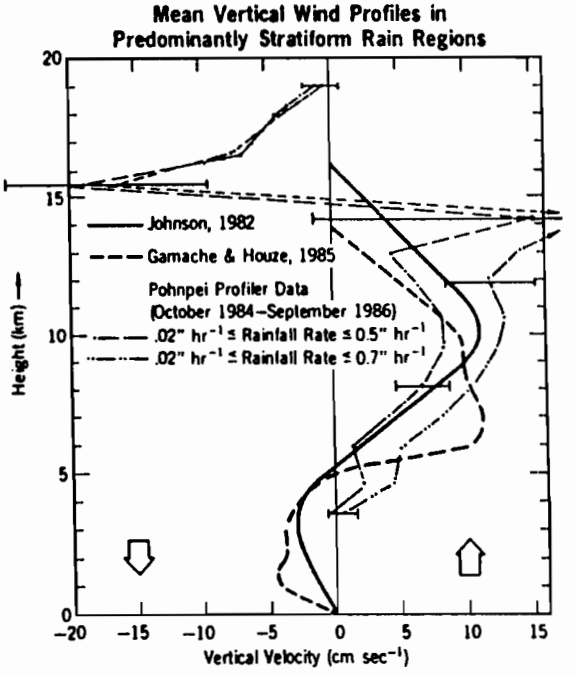

Fig. 3. Average vertical wind profiles from the Pohnpei profiler between Oct. 1984 and Sept. 1986 for rainfall rates corresponding as closely as possible to stratiform conditions. (After Balsley et al, 1988.)

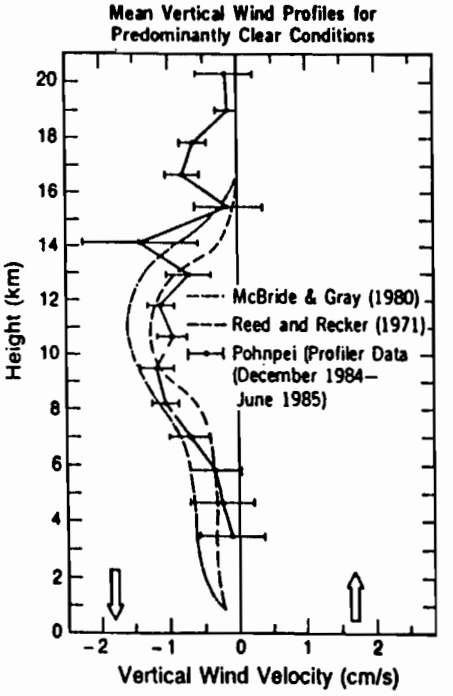

Fig. 4. Average vertical wind profile determined by the Pohnpei wind profiler for 250 hourly periods between Dec. 1984 and June 1985, when the sky cover was ≤ 30% as determined by the Pohnpei weather station. (After Balsley et al, 1988.)

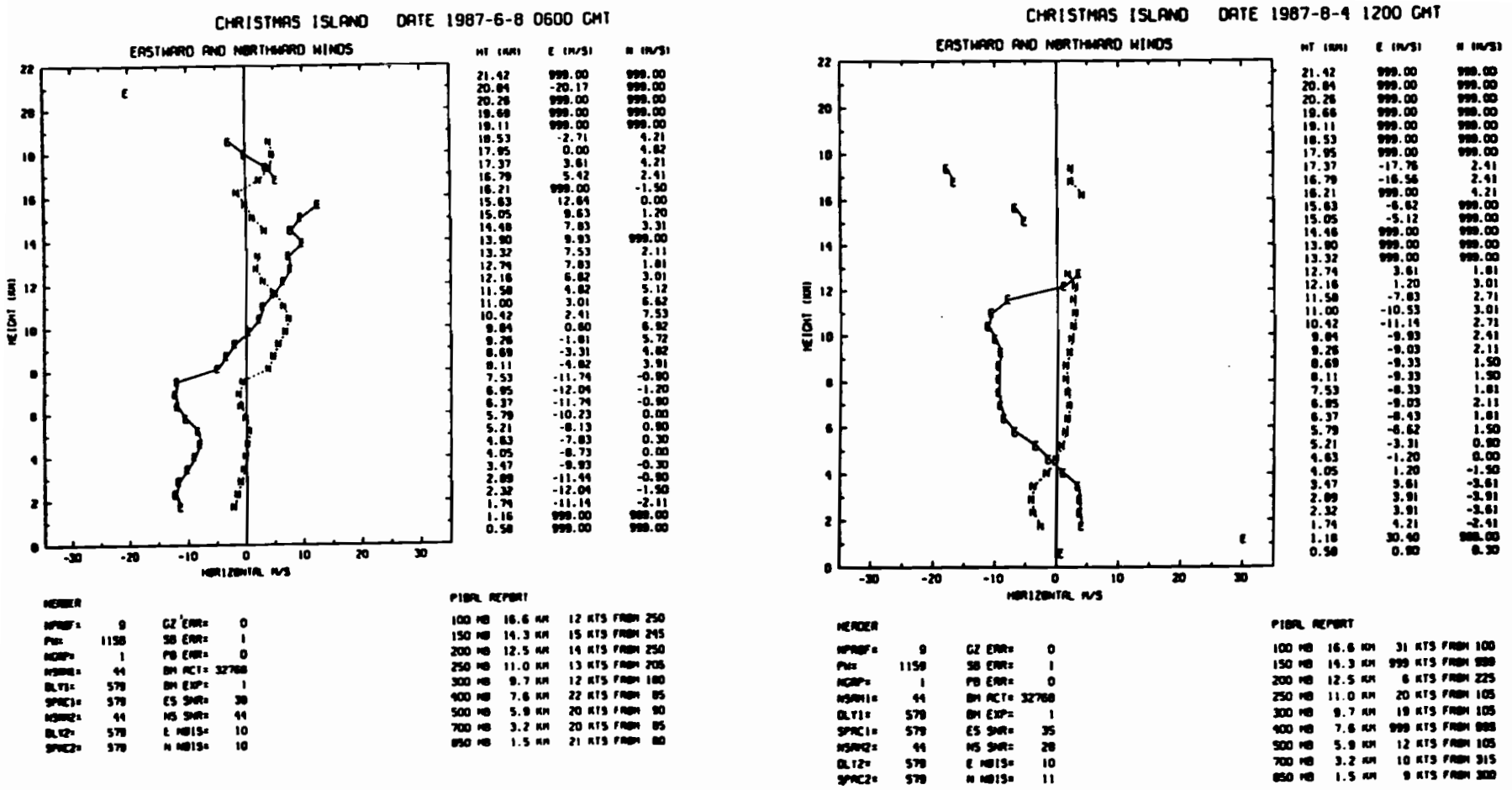

Fig. 5. Sample wind profiles as transmitted via GOES. A typical profile with easterly trades is shown in (a). A profile with westerly low-level winds during the 1986-1987 El Niño is shown in (b).

have been determined by Reed and Recker (1971) and these also show a similar disparity with the GATE results. The vertical profile of condensation heating is related to the vertical motion profile. As pointed out by Hartmann et al (1984), the vertical distribution of diabatic heating in the tropics is important for the parameterization of global climate models.

Much of the rain that falls in the tropics is now thought to be associated with mesoscale convective systems. Rainfall in the tropical convective systems is comprised of heavy showers of limited duration and lighter more persistent rainfall. The persistent rainfall is called stratiform rain and is inherent to the mesoscale convective system. Figure 3 shows average vertical motions in predominantly stratiform rainfall regions as deduced from the direct vertical velocity measurements using the Pohnpei wind profiler. The observed profile at Pohnpei is very consistent with the profile determined for GATE by Gamache and Houze (1985). The downward velocity at the lowest heights is commonly associated with stratiform rain in mesoscale convective systems.

For predominantly clear conditions at Pohnpei, average vertical motion is observed to be downward at all heights as shown in Figure 4. The magnitude of the mean descending motion is what is required to balance the radiative cooling to space. In magnitude and shape the Pohnpei measurements agree well with indirect determinations by Reed and Recker (1971) and McBride and Gray (1980).

3. Observations of tropical winds using the Christmas Island wind profiler

The Christmas Island wind profiler was constructed by the Aeronomy Laboratory in 1985 and became operational in March 1986. The Christmas Island wind profiler has three fixed beams and routinely measures horizontal and vertical velocities. Hourly-averaged wind observations from the Christmas Island profiler are routinely transmitted four times daily via satellite and input onto the GTS. Examples of the wind profiles as transmitted over satellite and received in our laboratory are reproduced in Figure 5. In addition to the summaries of wind transmitted via satellite, detailed horizontal and vertical velocities are recorded at the profiler site on christmas Island and archived in our laboratory.

Wind observations from Christmas Island are routinely used by NMC and ECMWF in their operational analysis and forecast products. Gage et al (1988) compared the Christmas Island observations with the analyses of both centers. A sample comparison for zonal winds at 500 mb is shown in Figure 6. Statistics of the standard deviation and bias of the observed winds relative to the analyses is show, in Figure 7 and Figure 8, respectively. Improvement is considerable in both standard deviation and bias after the introduction of the winds into the analyses. The Christmas island winds were first used in the NMC analyses in mid-January 1987 and in the ECMWF analyses in April 1987.

Monthly summaries of Christmas Island winds are published in NOAA's Climate Diagnostics Bulletin. A sample monthly vector plot of Christmas island winds for April 1989 is reproduced in Figure 9. The monthly summaries are useful for detecting the presence of intraseasonal wind oscillations. Such oscillations are very common in the Christmas Island winds especially in the upper troposphere.

Zonal wind profiles for Christmas Island are shown as annual summaries in Figure 10 and Figure 11. These figures show clearly low-frequency variations associated with the changing phase of the Southern Oscillation. Much of 1987 shows fairly deep weak easterlies during the El Nino. In marked contrast 1988 shows strong low-level easterlies and strong upper tropospheric westerlies. Unfortunately, the length of wind observations at Christmas Island is too short to permit us to define the annual mean winds.

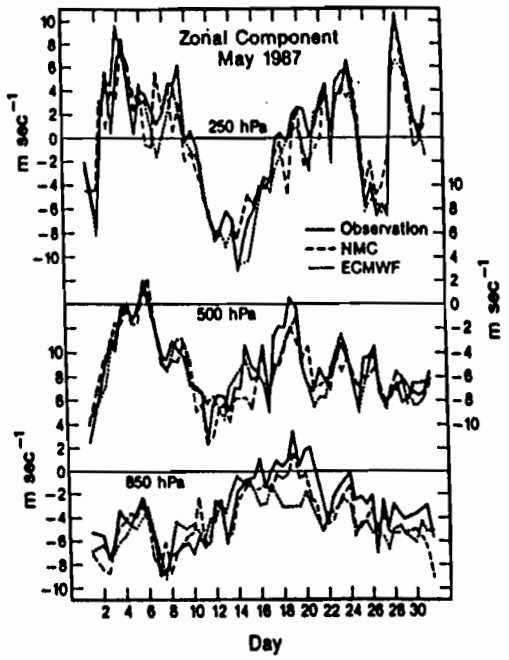

Fig. 6. Multi-height time series of zonal winds observed at Christmas Island for the month of May 1987. Interpolated NMC and ECMWF analyses are shown for comparison. (After Gage et al. 1988).

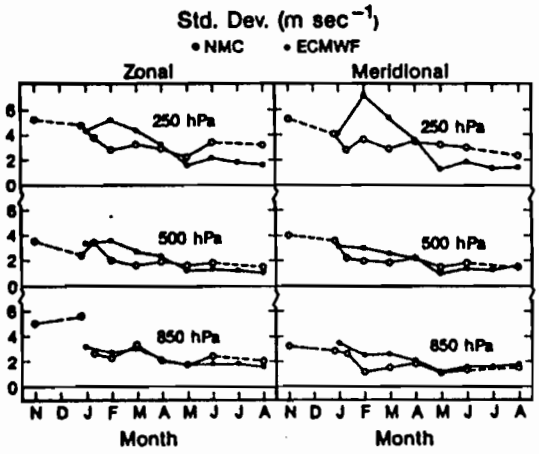

Fig. 7. Time series of monthly standard deviation of Christmas Island winds compared to NMC and ECMWF analyses. (After Gage et al, 1988.)

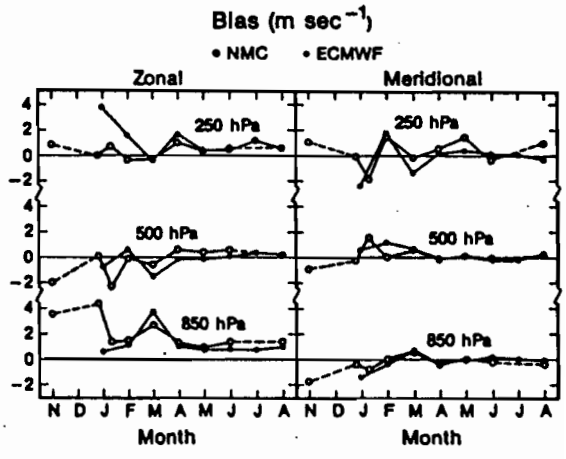

Fig. 8. Time series of monthly bias of Christmas Island winds compared to NMC and ECMWF analyses. (After Gage et al, 1988.)

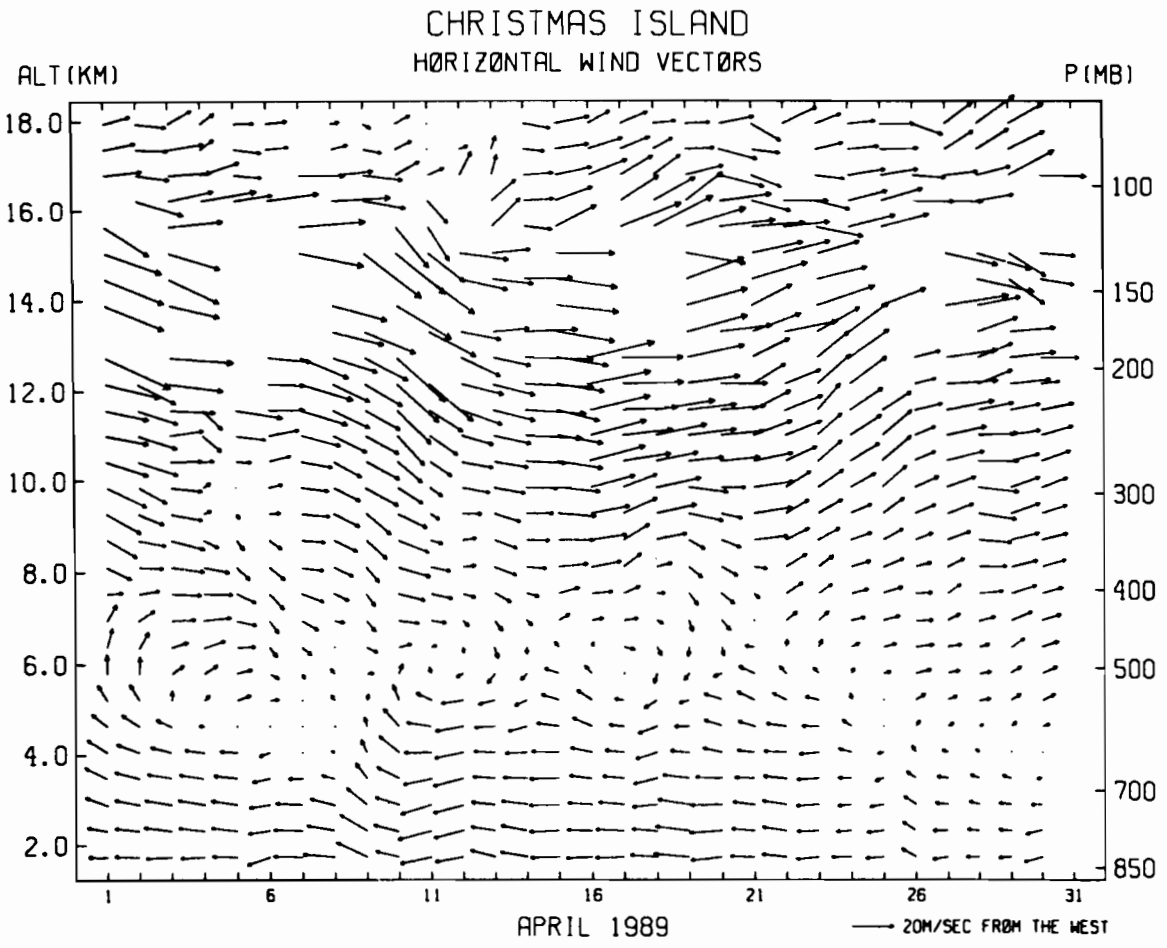

FIG.9. Monthly summary plot of Christmas Island wind vectors for April 1989.

4. A trans-Pacific network of wind profilers

As is well known, the atmosphere across the tropical Pacific is far from uniform. Sea surface temperatures are typically much warmer in the western Pacific than they are in the central and eastern Pacific. Convection tends to be concentrated over the warm water which normally resides in the western Pacific. As shown in Figure 12, large-scale ascent typically occurs centered over the western Pacific and Indonesian maritime continent. This zonal Walker Circulation is most pronounced during the anti-El Nino phase of the Southern Oscillation which represents the quasi periodic interannual variation of the Walker circulation (Rasmusson and Wallace, 1983).

The intraseasonal, seasonal, and interannual variations in tropical sea surface temperature, tropical convection and atmospheric circulation systems is a subject of much contemporary research. Variations in the longitudinal distribution of tropical convection are evident in patterns of outgoing long-wave radiation measured by satellite (Lau and Chan, 1985). Systematic patterns of low-level convergence and upper-level divergence are clearly associated with the regions of most intense convection (Weikmann, 1983). The influence of the non-uniform distribution of tropical convection across the Pacific basin is evident in the longitudinal variation of tropopause properties as discussed by Gage et al (1987). Recent diagnostic studies by Reid et al (1989) show

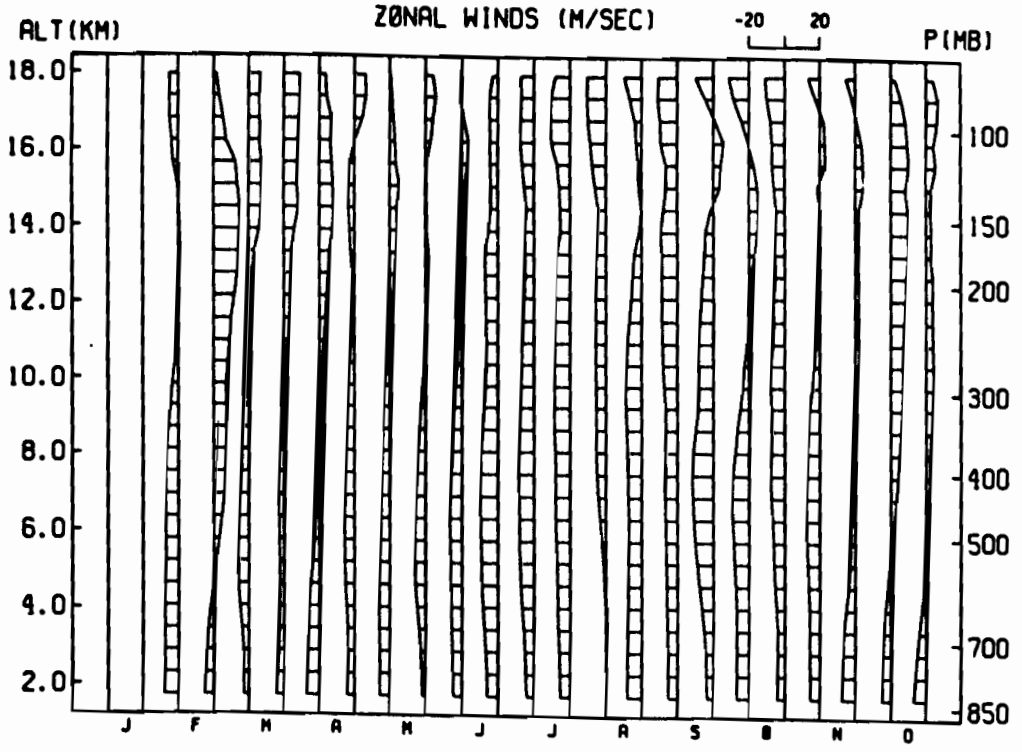

FIG.10. Annual summary of Christmas Island zonal winds for 1987.

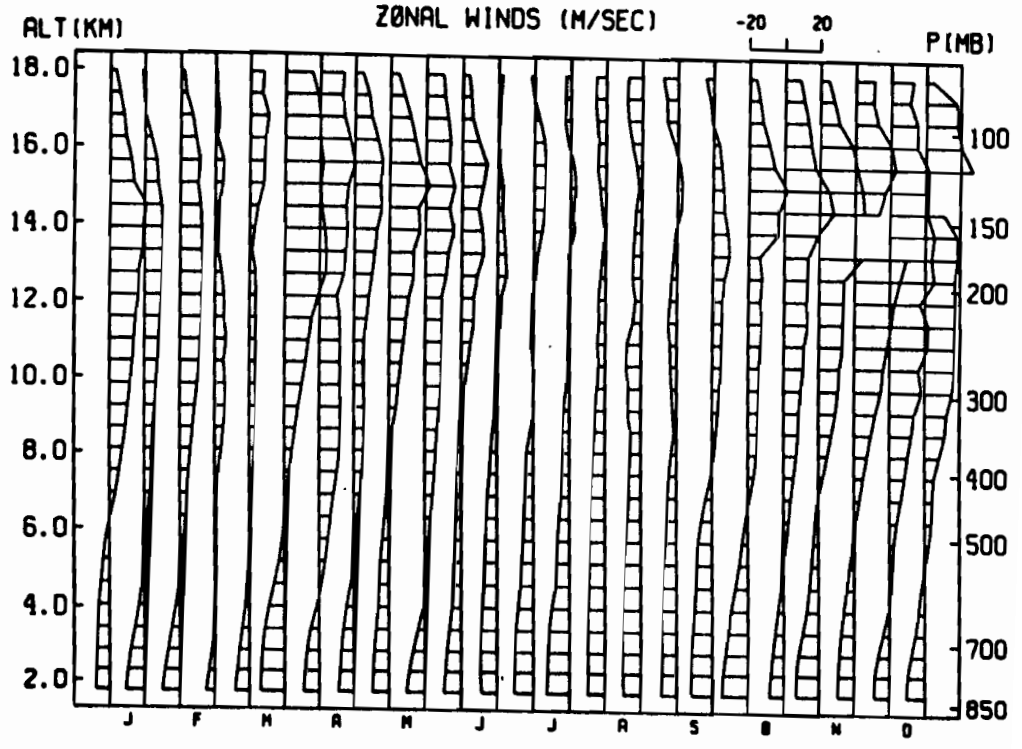

FIG.11. Annual summary of Christmas Island zonal winds for 1988.

that the influence of the ENSO signal can be seen at least into the lower stratosphere. It is thought that the influence of the varying tropical heating patterns create global teleconnections that influence weather around the globe (Horel and Wallace, 1981).

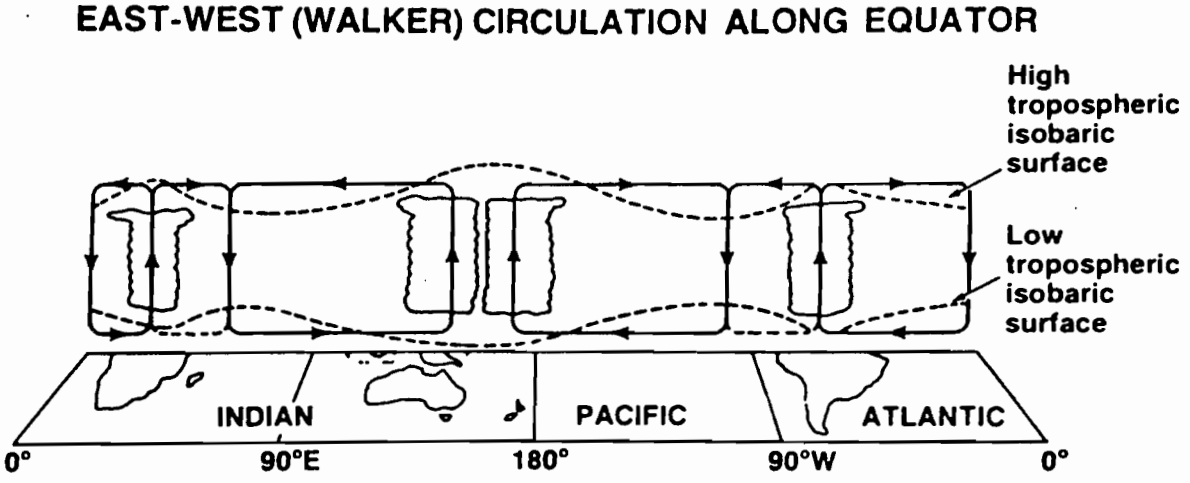

FIG.12. Walker circulation along the equator. (After Webster, 1983).

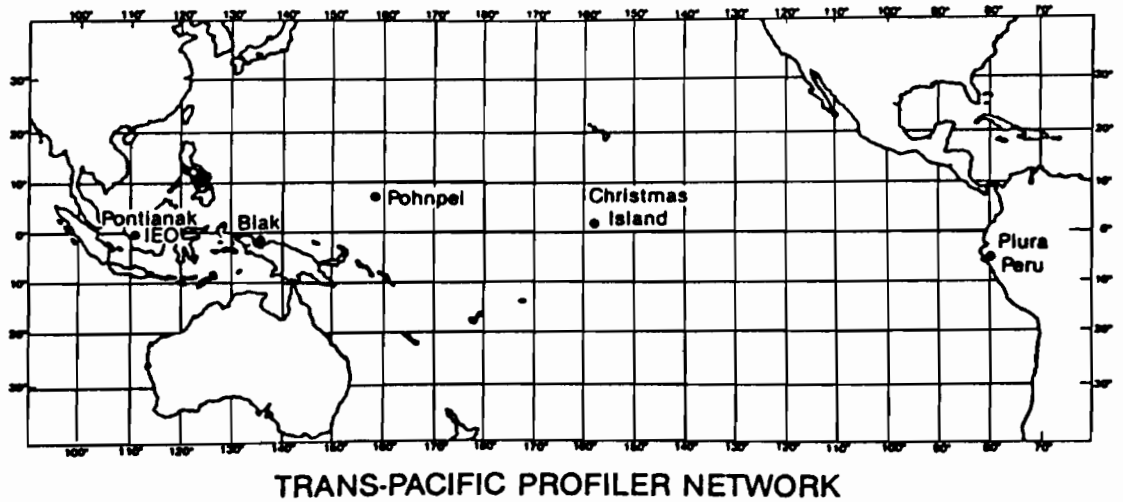

FIG.13. Planned trans-Pacific network of tropical wind profilers.

Clearly, an understanding of the coupled ocean atmosphere dynamics that governs the ENSO phenomena is of prime importance in making further progress in climate forecasting. The Tropical Ocean Global Atmosphere (TOGA) Program is an international program designed to develop an understanding of the coupled ocean atmosphere system over the tropics. An important part of the TOGA effort is an intensive ten-year monitoring program to observe the tropical oceans and atmosphere.

Evidence is accumulating that the western Pacific region plays a key role in the initiation of ENSO events (Lukas, 1988). Since the processes that give rise to the El Nino are so poorly understood, a coordinated effort is needed in the western Pacific to develop the requisite understanding to make further progress (Lukas and Webster, 1988). The TOGA Coupled Ocean Atmosphere Response Experiment (COARE) is planned for the early 1990's.

Figure 13 shows the Pacific ocean basin and the location of the proposed network of wind profilers. Profilers are already located at Pohnpei and Christmas Island. At the eastern end of the network a wind profiler is under construction at Piura, Peru. At the western end we plan to construct a wind profiler at Biak, Indonesia, in cooperation with the Indonesian National Institute of Aeronautics and Aerospace (LAPAN). When the planned International Equatorial Observatory (IEO) is taken into account, a truly international network of at least five wind profilers will eventually span the equatorial Pacific.

Wind observations from the proposed network should greatly aid the TOGA observational effort and provide a valuable new source of observations to explore a variety of dynamical phenomena in the tropics. The western stations should be well placed to be of use to the TOGA COARE experiment. The proximity of the network stations to the equator and the lack of other near equatorial stations will provide a new source of observations for the study of equatorial waves.

5. Concluding remarks

Consideration of the current base of wind observations that are used in contemporary operational global analyses and forecasts shows major deficiencies over the tropics. Furthermore, owing to the diversity of tropical circulation systems ranging from the scale of convection to the scale of the Walker and Hadley circulations, there is a need to better understand the scale interactions that take place in the tropical atmosphere. At the same time it is important to press forward on research aimed at better understanding of the coupled dynamics of the atmosphere and ocean.

A network of wind profilers spanning the tropical Pacific can contribute substantially to further progress in understanding the dynamics of the tropical atmosphere. Additionally, observations from the wind profilers could be used to overcome deficiencies in the global observation system. Furthermore, long continuous records of wind observations from these stations should prove invaluable in monitoring interannual variations in large-scale atmospheric circulation systems.

The wind profilers described here generally do not observe below about one kilometer. Because of the importance of the tropical boundary layer and the relative lack of observations that are currently available, an intensive effort should be made to complement the large wind profilers with smaller lower tropospheric wind profilers. A lower tropospheric profiler that meets this need has recently been developed (Ecklund et al, 1988). This lower tropospheric wind profiler can be deployed in networks at a fraction of the cost of larger wind profilers, suggesting that eventually nested grids of large and small profilers may be desirable. We are also working together with colleagues at NCAR to develop an Integrated Sounding System (ISS) that would combine surface observations with upper-level balloon soundings of wind and temperature and continuous wind observations using the lower tropospheric wind profiler. This development should satisfy the need for a sounding system capable of monitoring temperature and wind fields.

Acknowledgments. The trans-Pacific wind profiler network is a joint research program of the Aeronomy Laboratory and University of Colorado. This research program is supported primarily by the National Science Foundation under Agreement ATM-8720797. The Christmas Island wind profiler is supported by the U.S. TOGA Program Office.

REFERENCES

Balsley, B.B., W.L. Ecklund, D.A. Carter, A.C. Riddle and K.S. Gage, 1988: Average vertical motions in the tropical atmosphere observed by a radar wind profiler on Pohnpei (7°N latitude, 157°E longitude). *J. Atmos. Sci.*, **45**, 396-405.

Balsley, B.B. and D.A. Carter, 1989: Mountain waves in the tropical Pacific atmosphere: a comparison of vertical wind fluctuations over Pohnpei and Christmas Island using VHF wind profilers. *J. Atmos. Sci.*, in press.

Ecklund, W.L., D.A. Carter and B.B. Balsley, 1988: A UHF wind profiler for the boundary layer : brief description and initial results. *J. Tech.*, **5**, 432-441.

Gage, K.S. and G.C. Reid, 1987: Longitudinal variations in tropical tropopause properties in relation to tropical convection and El Nino Southern Oscillation events. *J. Geophys. Res.*, **92**, 14, 197-14, 203.

Gage, K.S., J.R. McAfee, W.G. Collins, D. Soderman, H. Bottger, A. Radford and B.B. Balsley, 1988: Comparison of winds observed at Christmas Island using a wind-profiling Doppler radar with NMC and ECMWF analyses. *Bull. Amer. Meteorol. Soc.*, **69**, 1041-1046.

Gage, K.S., 1989: The structure and dynamics of the free atmosphere as observed by VHF/UHF radar, Chapter 28a., in Radar in Meteorology, D. Atlas, ed. A.M.S., Boston, in press.

Gage, K.S., B.B. Balsley, W.L. Ecklund, R.F. Woodman and S.K. Avery, 1989: A transpacific network of wind-profiling Doppler radars for tropical atmospheric research. Handbook for MAP, 28, in press.

Gamache, J.F. and R.A. Houze, Jr., 1982: Mesoscale air motions associated with a tropical squall line. *Mon. Wea. Rev.*, **110**, 118-135.

Gamache, J.F. and R.A. Houze, Jr. 1985: Further analysis of the composite wind and thermodynamic structure of the 12 September GATE squall line. *Mon. Wea. Rev.*, **113**, 1241-1259.

Hartmann, D.L., H.H. Hendon and R.A. Houze, Jr., 1984: Some implications of the mesoscale circulations in tropical cloud clusters for large-scale dynamics and climate. *J. Atmos. Sci.*, **41**, 113-121.

Horel, J.D. and J.M. Wallace, 1981: Planetary-scale atmospheric phenomena associated with the Southern Oscillation. *Mon. Wea. Rev..*, **109**, 813-819.

Johnson, R.H., 1982: Vertical Motion in near-equatorial winter monsoon convection. *J. Meteorol. Soc. Japan*, **60**, 682-689.

Lau, K.M. and P.H. Chan, 1985: Aspects of the 40-50 day oscillation during the northern winter as inferred from outgoing longwave radiation. *Mon. Wea. Rev.*, **113**, 1889-1909.

Lukas, R. and P. Webster, 1988: Proc. of the U.S. TOGA Western Pacific Workshop, USTOGA8, U.S. TOGA Program Office, NOAA.

Lukas, R., 1988: On the role of the western Pacific air-sea interaction in the El Nino/Southern Oscillation phenomenon. Proc. of the U.S. TOGA Western Pacific Workshop. USTOGA8, R. Lukas and P. Webster, eds., U.S. TOGA Program Office, NOAA.

McBride, J.L. and W.M. Gray, 1980: Mass divergence in tropical weather systems: paper II. Large-scale controls on convection. *Quart. J. R. Met. Soc.*, **106**, 517-538.

Rasmusson, E.M. and J.M. Wallace, 1983: Meteorological aspects of the El Nino/Southern Oscillation. *Science*, **222**, 1195-1201.

Reed, R.J. and E.E. Recker, 1971: Structure and properties of synoptic-scale wave disturbances in the equatorial western Pacific. *J. Atmos. Sci.*, **28**, 1117-1133.

Reid, G.C., K.S. Gage and J.R. McAfee, 1989: The thermal response of the tropical atmosphere to variations in equatorial Pacific sea-surface temperature. *J. Geophys. Res.*, in press.

Riehl, H. and J.S. Malkus, 1958: On the heat balance in the equatorial trough zone. *Geophysica,* **6**, 503-548.

Webster, P.L., 1983: Large-scale structure of the tropical atmosphere. In Large Scale Dynamical Processes in the Atmosphere, B.J. Hoskins and R.P. Pearce, eds., Academic press, pp. 235-275.

Weickmann, K.M., 1983: Intraseasonal circulation and outgoing longwave radiation modes during the northern hemisphere winter. *Mon. Wea. Rev.*, **111**, 1838-1858.

Signature of a West Wind Convective Event in SSM/I Data

John Joseph BATES

Climate Research Division, NOAA/ERL
325 Broadway
Boulder, CO 80303 - U.S.A.

1. Introduction.

In the western equatorial Pacific, the net heat flux into the ocean is approximately a balance between heat input due to solar flux and heat loss due to evaporative cooling. Climatologies such as Weare et al. (1981) show the region west of the dateline from 10°N to 10°S to be an area of net oceanic surface heating of from 30-60 W m^{-2}. Although much smaller in magnitude than the short-wave and latent heat fluxes, the longwave and sensible heat fluxes can not be ignored, since the net flux is so small. The largest discrepancies between climatologies of net heat flux in the western equatorial Pacific [e.g., between Weare et al. (1981) and Wyrtki (1965)] occur in the estimation of the latent heat flux.

Work by Meyers et al. (1986) has shown that anomalous cooling of the ocean upper mixed layer during the 1982-83 ENSO episode was caused primarily by anomalous evaporative cooling. Their work was confined, however, to a rather limited spatial domain (i.e., 2°S-4°N and 150-170°E). Since the location of deep convection, and the teleconnections to the mid-latitudes that can result in regional short-term climate anomalies, are highly correlated to equatorial sea surface temperature, it is important to monitor the larger temporal and spatial patterns associated with evaporative cooling anomalies. Remote sensing is one means of obtaining the coverage necessary to adequately monitor evaporative cooling anomalies.

2. Remote sensing of moisture and wind speed using SSM/I.

The Special Sensor Microwave Imager (SSM/I) on the Defense Meteorological Satellite Program (DMSP) polar-orbiting spacecraft has been operating since July 1987. Similar instruments are planned to fly on all future DMSP spacecraft, offering the possibility of two SSM/I instruments covering the earth in the future. SSM/I scans at four frequencies; 19, 22, 37 and 85 GHz as well as dual polarizations except at 22 GHz (Hollinger et al., 1987). The SSM/I provides improved coverage, spatial resolution, and accuracy over prior passive microwave intruments, but lacks the lower frequency channels that allow sea surface temperature to be retrieved.

The 22 GHz channel is primarily used for estimating integrated water vapor content, since it is located near the center of a weak water vapor absorption line. Dr. J. Alishouse, NESDIS, has performed a statistical regression of co-located radiosonde estimates of integrated water vapor with observed SSM/I brightness temperatures (Alishouse et al., 1989). These statistical results, as well as theoretical results, show that the SSM/I 22 GHz channel has less sensitivity to high moisture concentrations due to a nonlinear relation between moisture and the 22 GHz brightness temperature. This has important consequences for remote sensing of moisture in the TOGA COARE region. For example, using Alishouse et al. (1989) tropical nonlinear algorithm, the error in retrieving moisture due to noise in the 22 GHz channel alone is only 0.6 kg m^{-2} in a

ORSTOM
CENTRE DOCUMENTATION
Montpellier

F30256

typical subtropical atmosphere, while it is 1.22 kg m^{-2} for a moist tropical atmosphere. The actual retrieval error is larger since additional channels are used in the regression to account for attenuation in the atmosphere and emission from the sea surface.

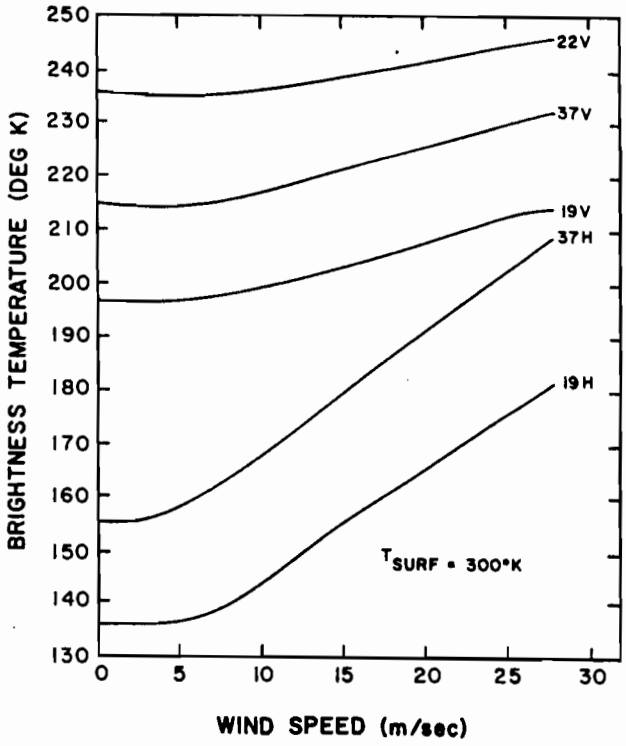

FIG.1. SSM/I brightness temperature as a function of frequency and wind speed.

The physical basis for estimating wind speed from passive microwave data is illustrated in Figure 1. At the SSM/I incidence angle (approximately 54°), vertically and horizontally polarized microwave radiation have a differential sensitivity to wind roughening of the sea surface. The sensitivity is greatest for the 37 GHz channels. The effect on the 37 GHz channels, however, is not apparent until wind speeds are in excess of 3 m s^{-1}. This is important to TOGA COARE since some regions of the equatorial western Pacific have mean wind speeds less than 3 m s^{-1}. It may be possible to classify these low wind speed regions by identifying unique signatures of SSM/I brightness temperature profiles, but this has yet to be shown. Fortunately, we are interested in anomalously large evaporative cooling events for which wind speeds should be great enough for SSM/I to detect. We are using the revised statistical wind speed algorithm of Goodberlet (1989) which was derived from regression of buoy wind speed observations against co-located SSM/I brightness temperature observations.

SSM/I estimates of both integrated water vapor content and surface wind speed are degraded in the presence of large cloud water droplets (>100 microns) and precipitation. Thresholds on the 19 GHz horizontally-polarizeed channel brightness temperature and the difference 37V-37H channel brightness temperatures are used to screen for such conditions. For this study, we have required that 19H < 185 K and that 37V-37H and that 37V-37H > 50 K.

Sixty days of SSM/I data, from mid-January through mid-March 1988, over the western equatorial Pacific has been extracted, calibrated, and geo-located. Goe-locations have been adjusted to agree with know landmarks using a correction algorithm provided

by Dr. C. Swift. The data have also been quality controlled using reasonable bounds on the derived brightness temperatures. The data were binned on a 50 km by 50 km grid daily with only the single most recent sample in the bin being saved. Land areas and areas with no retrievals, due to exceeding the cloud thresholds for all five days, are left blank. The daily and five-day (pentad) average binned data were objectively analyzed using a Barnes two-pass scheme on a 100 km by 100 km grid to produce the contour maps shown.

3. Case study.

Using Outgoing Longwave Radiation (OLR) data, several convective events were found during winter 1987-88 propagating eastward from the Indian Ocean through the Indonesian area and into the western equatorial Pacific. These events were identified as 5-day mean OLR values of less than 200 W m^{-2} (Figure 2) and negative OLR anomaly values of less than 20 W m^{-2}. NMC 850 mb wind analyses showed that westerly winds were associated with the movement of a convective event in late February, with peak wind speeds of up to 15 m s^{-1} located off the northeastern tip of Australia during the pentad of February 20-24. COADs ship data, however, did not show such a dramatic wind burst. SSM/I data were analyzed for the 60-day period in an attempt to capture the characteristics of this event in passive microwave data.

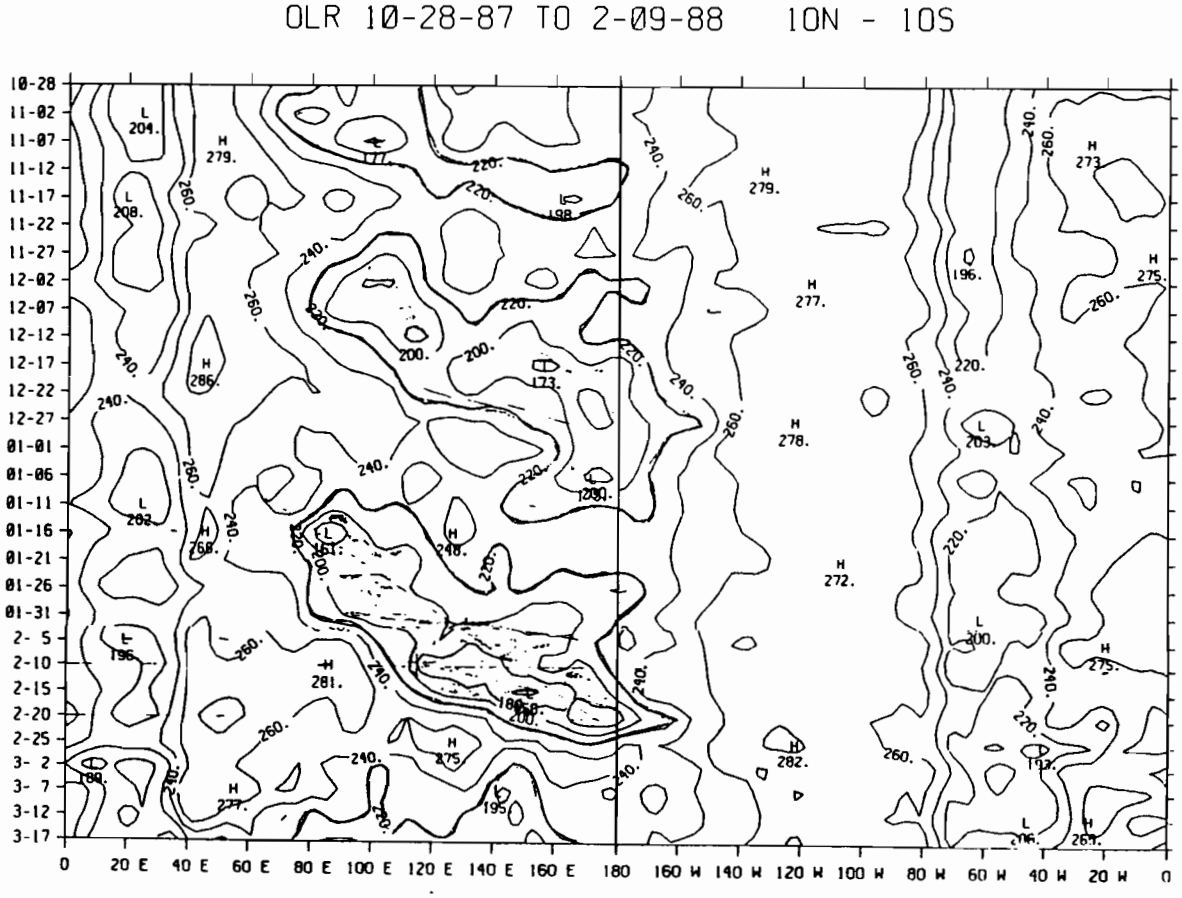

FIG.2. Time-longitude section of outgoing longwave radiation (OLR).

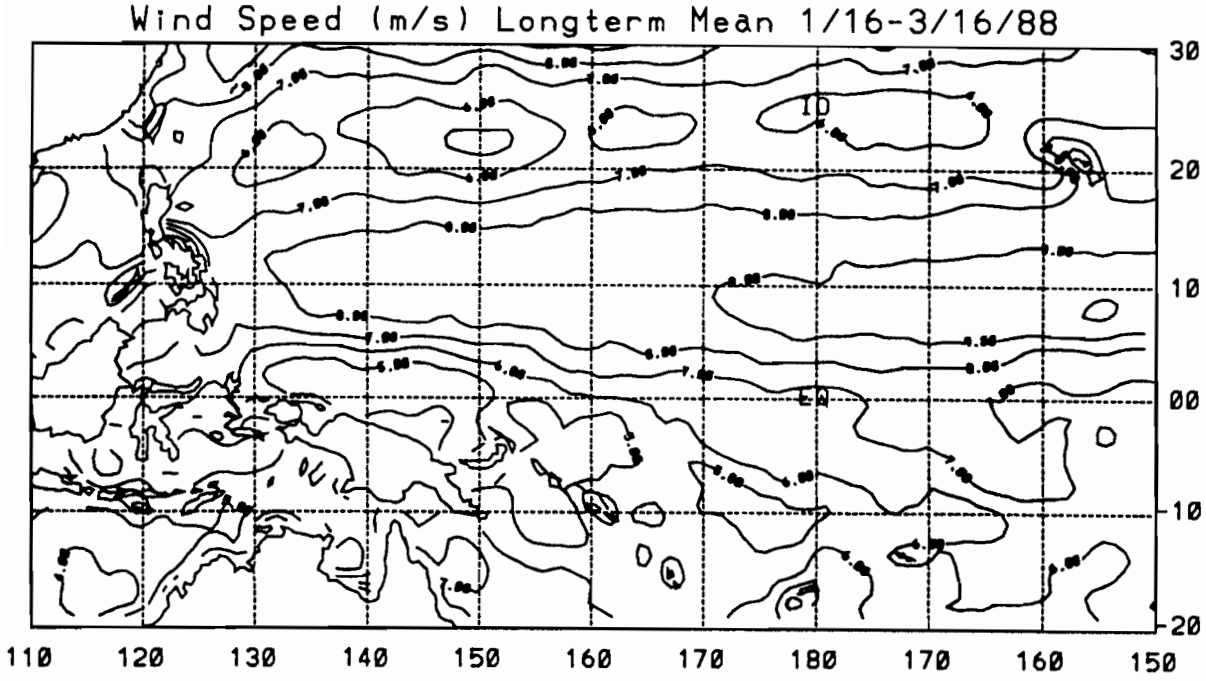

FIG.3. Long-term mean (14 January-14 March 1988) wind speed (m s^{-1}) from SSM/I.

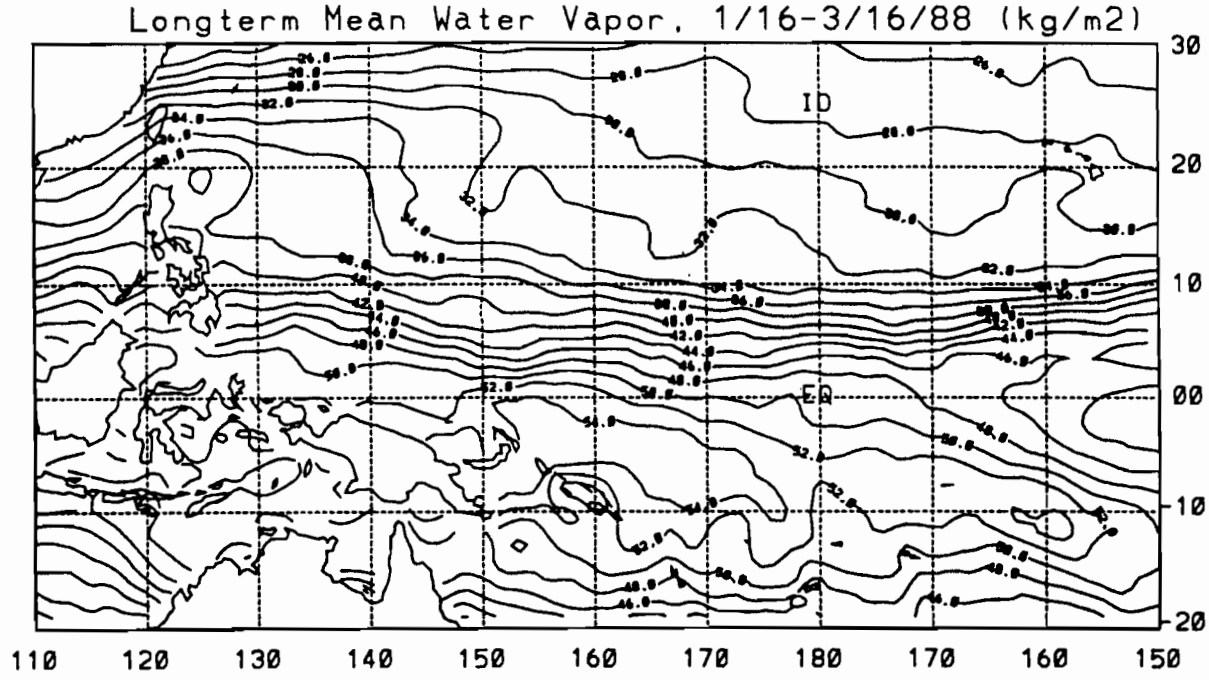

FIG.4. Long-term mean (14 January-14 March 1988) total precipitable water (kg m^{-2}) from SSM/I.

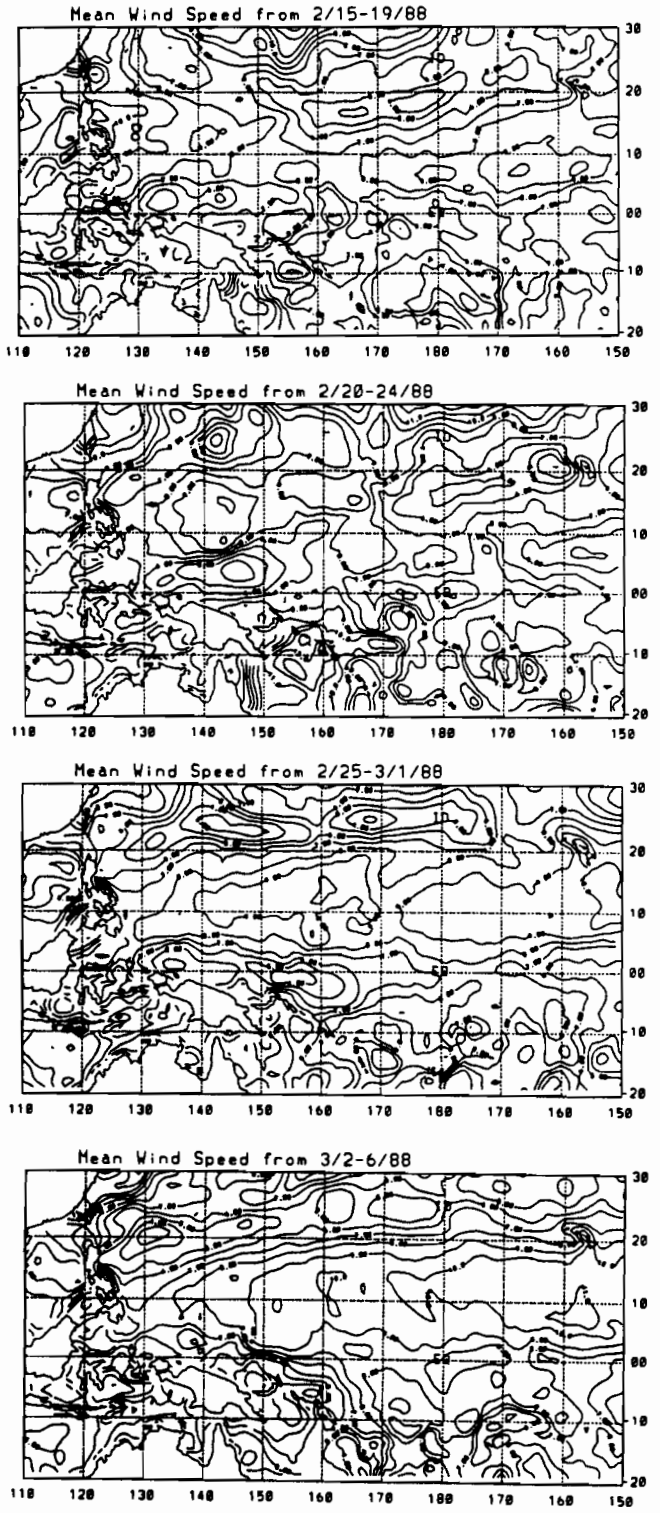

FIG.5. Pentads (5-day means) of wind speed (m s^{-1}) and total precipitable water (Kg m^{-2}) from SSM/I.

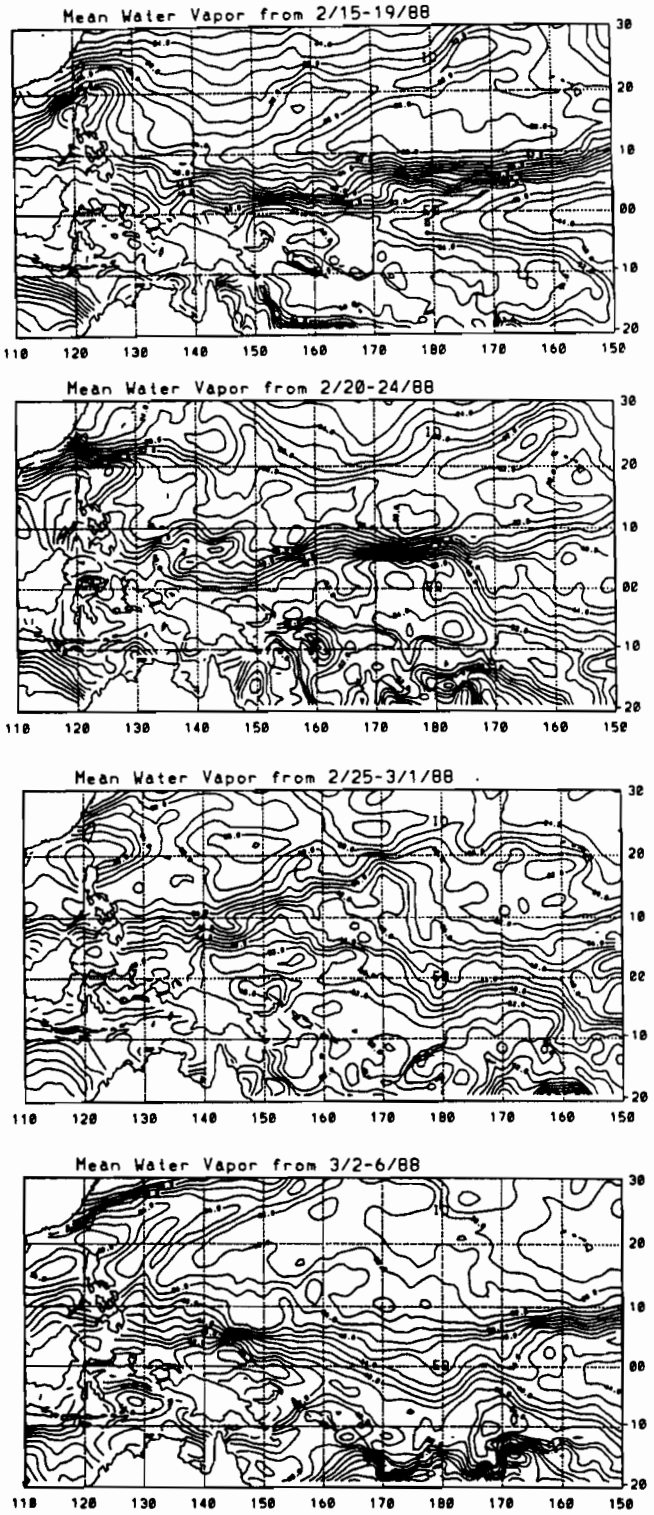

FIG.5. (Continue)

The long-term mean analysis of wind speed derived from SSM/I data (Figure 3) shows a band of high wind speeds along 30°N, extending south along the coast of southeast China toward the Philippines. A band of lower wind speeds is found along 20°N, while a broad zone of high wind speeds extends from 15°N to 5°N. A crescent-shaped region of low wind speeds is seen around Australia. The long-term mean integrated water vapor analysis (figure 4) shows a maximum along and south of the equator with a split into the ITCZ and SPCZ in the eastern edge of the domain. Low values of integrated water vapor are found north of 20°N.

Pentads of wind speed and integrated water vapor imagery, the objective analyses, and the objective analyses of anomalies from the long-term mean are shown in Figure 5. The wind speed analyses show a high degree of spatial variability. The first clear evidence of increased wind speeds associated with the convective event is found in the pentad of February 15-19 off northeastern Australia. In the following pentad, very high winds are found surrounding an area blacked out due to persistent precipitation during the five-day period. Wind speeds in this area are in excess of 11 m s^{-1}. High wind speeds, but not as dramatic, propagate to the east in association with the convective event in the next two pentads. Throughout this 60-day period, the moisture field undergoes a large oscillation. Prior to the convective event, large amounts of integrated water vapor are found associated with the convective region over the western Pacific warm water pool. At the height of and following the passage of the convective event, dramatically less amounts of integrated water vapor are found over the equatorial region.

In order to better quantify the standing oscillation patterns, principal component analysis has been used to examine the daily objectively analyzed fields of wind speed, integrated water vapor, and a latent flux parameter (the wind speed multiplied by the integrated water vapor concentration). Only the first principal component from each variable is shown, and in each case this component is significantly different from random noise at the 95% confidence interval.

The spatial pattern of the first EOF of wind speed (Figure 6) shows positive centers of action located from 10°N to 20°N and 160°E to 190°E and south of the equator from 160°E to 200°E. Negative centers cover much less area and occur off the coast of southeast Asia and near 10°N, 120°E. The amplitude time series that modifies this spatial pattern shows several oscillations over the sixty day period, with the highest values being positive from days 55-65. This corresponds to the time of passage of the west wind burst.

The first EOF integrated water vapor spatial pattern (Figure 7) shows a maxima center of action along the equator, extending north along the Phillipines, and curving back to the east along 20°N. Negative centers are found off the coast of southeast Asia and near 15°N, 160°E. The associated amplitude time series shows an extreme negative excursion between days 50-60, slightly leading the maxima in the wind speed EOF.

In a first attempt at inferring the latent heat flux from these data, an EOF analysis was performed on the flux parameter wind speed times the integrated water vapor content. This field was not standardized prior to calculating the EOF; standardizing does not significantly change the results. Centers of action (Figure 8) are located in two zonal bands; one from 10°N-20°N, the other 5°S-15°S. Positive centers are found between 120°E-140°E, and negative centers are found between 150°E-200°E. the largest amplitudes are reached between days 53-63. This indicates enhanced positive values of the flux parameter in the region of the convective event during the time of its passage. There also seems to be a symmetric response in the northern hemisphere, although the convective event was largely confined to the southern hemisphere.

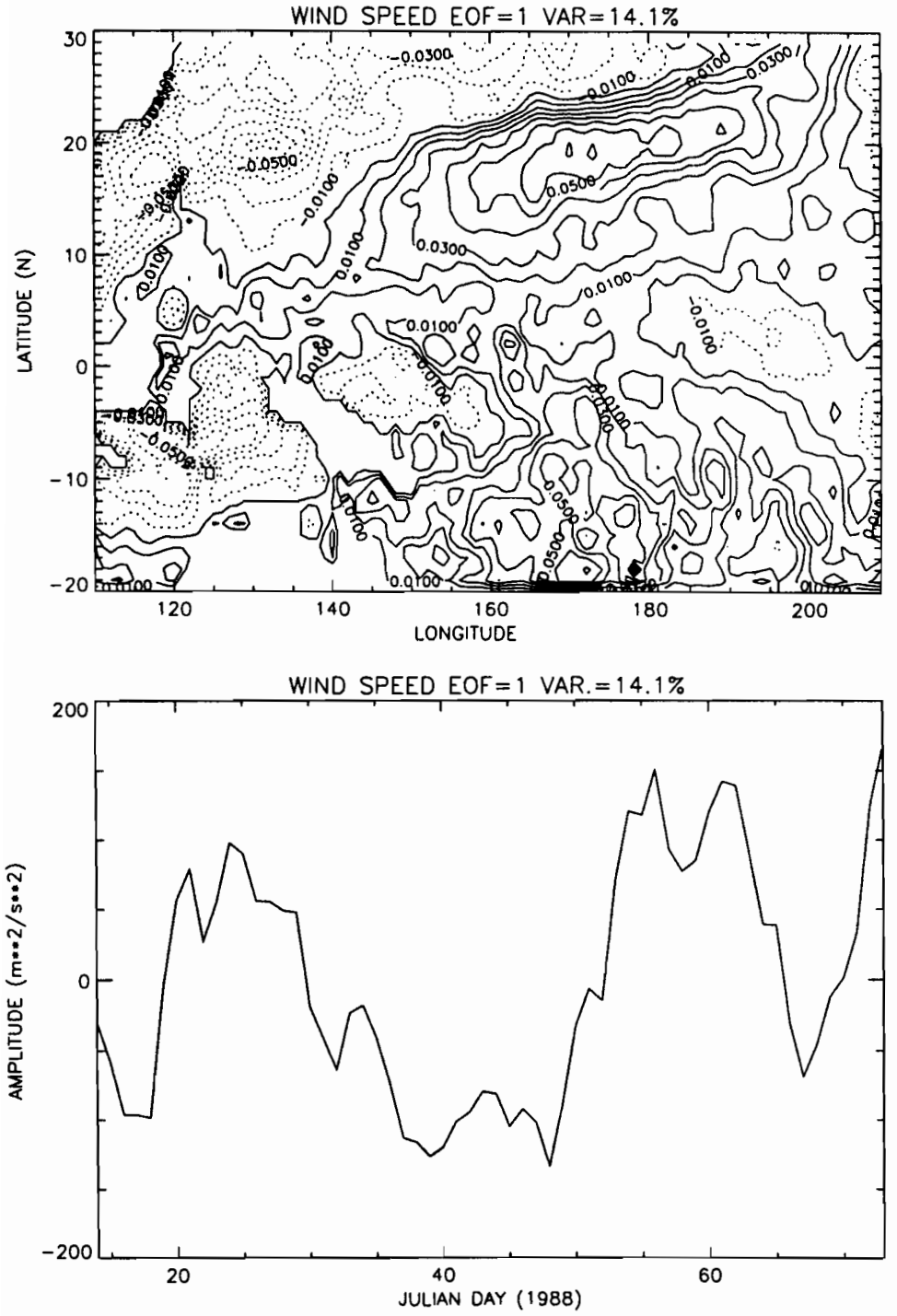

FIG.6. First EOF of SSM/I daily wind speeds.

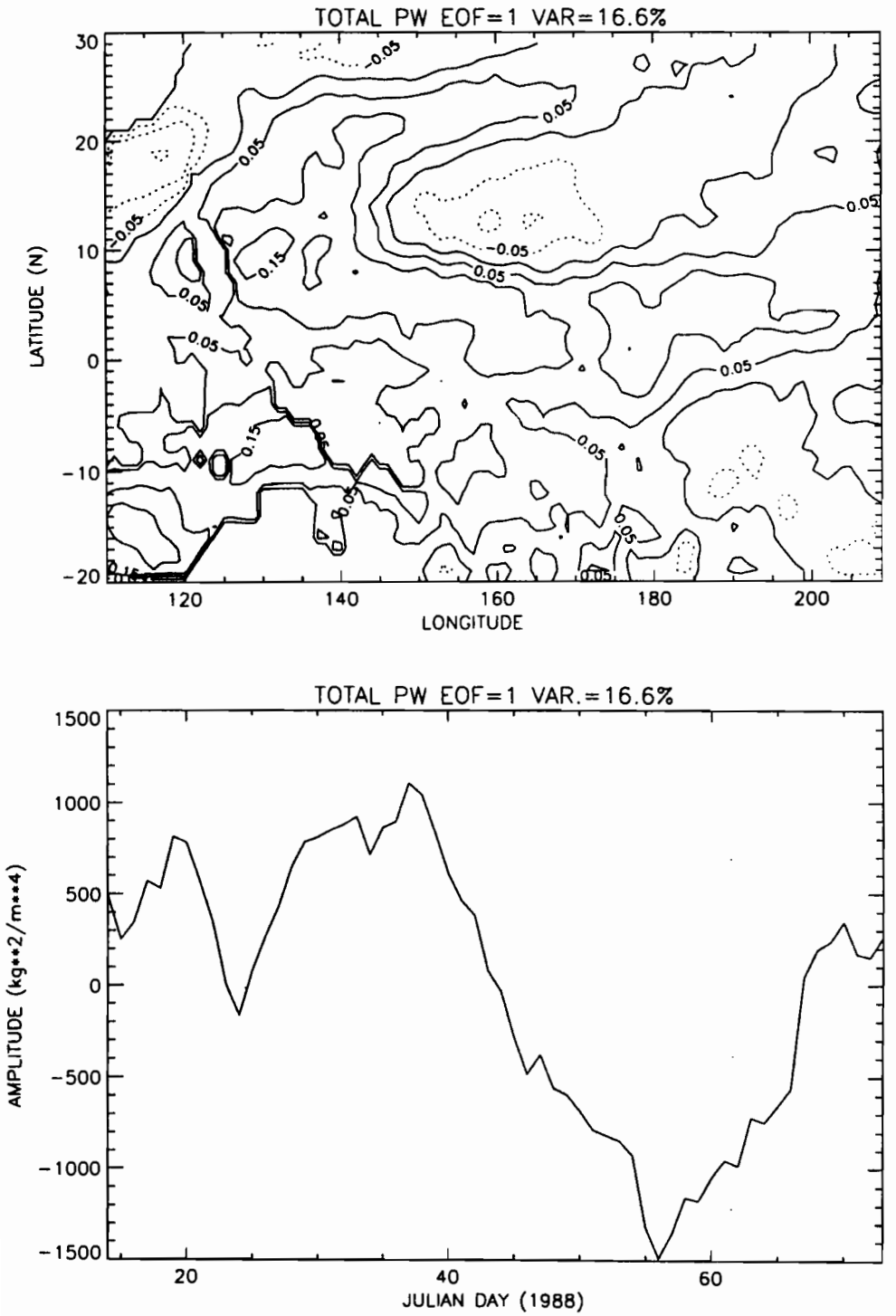

FIG.7. First EOF of SSM/I daily total precipitable water.

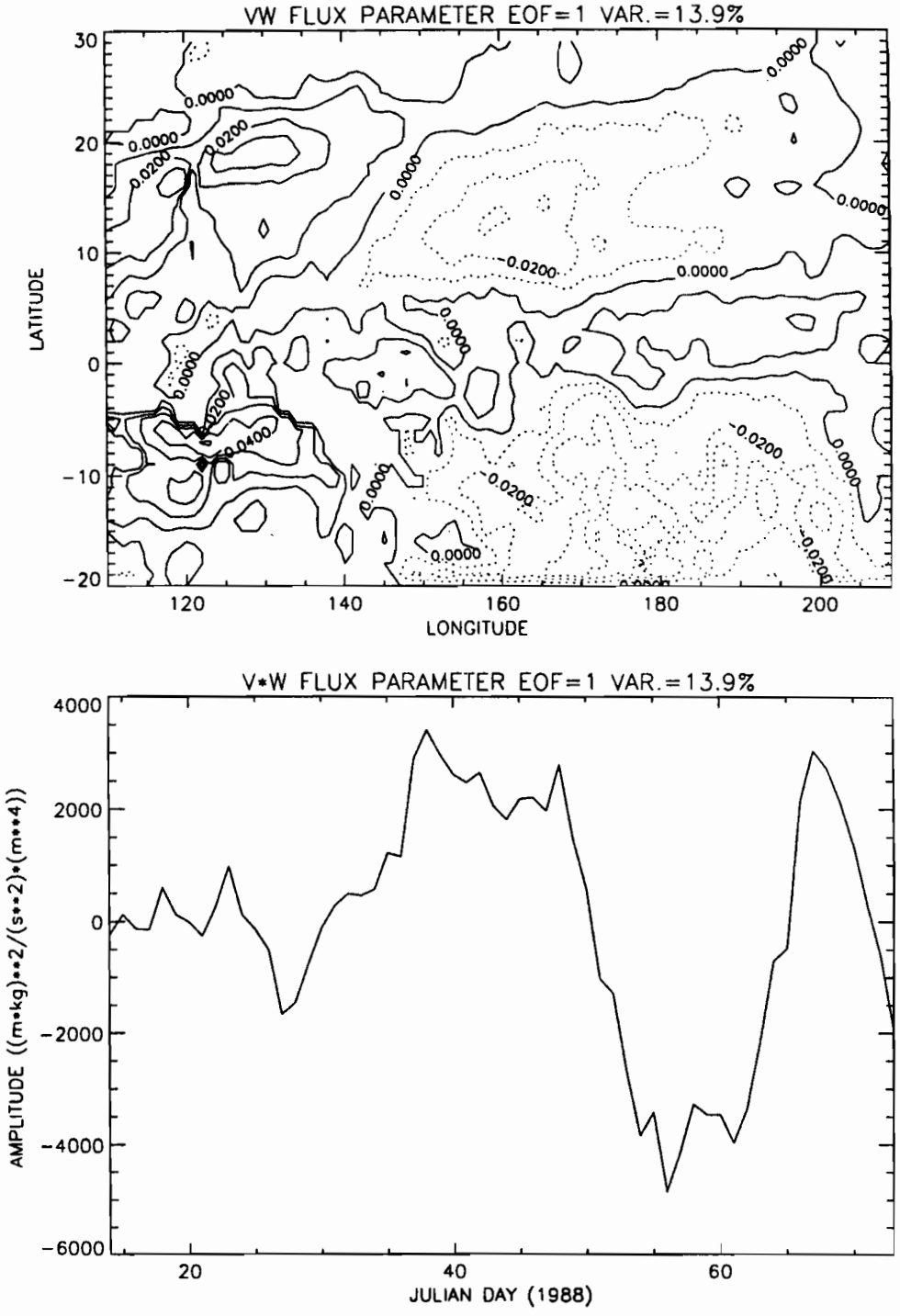

FIG.8. First EOF of SSM/I flux parameter.

4. Continuing work and TOGA COARE pilot studies.

The objective of this work is to analyze moisture and latent heat flux variability starting with a case study of a single convective event, but eventually we hope to extend the analysis to the entire tropical oceans, using a method similar to Liu (1988). While the improved accuracy and coverage of data provided by the SSM/I hold great promise, several significant roadblocks remain. First, to estimate the latent heat flux on daily or weekly time scales, a relationship between integrated water vapor content and surface specific humidity, similar to that of Liu (1986) for monthly time scales, must be established for the shorter time scales. Second, we must find a parameterization for the latent heat flux in disturbed, convective regimes where precipitation interferes with microwave observations of wind speed and integrated water vapor. Finally, since SSM/I does not contain low frequency microwave channels, we must rely on other remote sensing and *in situ* observations of sea surface temperature. We are continuing to work on all theses issues.

I would hope that this work could be continued as part of a pilot study of moisture and latent heat flux variability over the TOGA COARE region. For such a study, the region should be expanded longitudinally in both directions to include all of the Pacific and Indian oceans. The Indian ocean has been identified as being intimately connected to atmospheric oscillations in the western equatorial Pacific.

Acknowledgments. This research has been funded by the Equatorial Pacific ocean Climate Studies (EPOCS) program. Drs. C. Swift and J. Alishouse kindly provided their updated algorithms for retrieval of wind speed and integrated water vapor from SSM/I data.

REFERENCES

Alishouse, J.C., S. Snyder, and J. Vongsathorn, 1989: Determinations of total precipitable water in the tropics from the SSM/I. *Preprints Forth Conference on Satellite Meteorology and Oceanography,* San Diego, CA, .

Goodberlet, M., 1989: Remote sensing of ocean surface winds with the SSM/I, 1989: *Preprints Forth Conference on Satellite Meteorology and Oceanography,* San Diego, CA, .

Hollinger, J., R. Lo, G. Poe, R. Savage, and J. Peirce, 1987: *Special Sensor Microwavel/Imager User's Guide,* Naval Research Laboratory, Washington, D.C., 119 pp..

Liu, W.T., 1986: Statistical relation between monthly precipitable water and surface-level humidity over global oceans, *Mon. Weather Rev.*, **114**, 1591-1602.

Liu, W.T., 1988: Moisture and latent heat flux variabilities in the tropical Pacific derived from satellite data, *J. Geophys. Res.*, **93**, 6749-6760.

Meyers, G., J.R. Donguy, and R.K. Reed, 1986: Evaporative cooling of the western equatorial Pacific Ocean by anomalous winds, *Nature,* **323**, 523-526.

Weare, B.C., P.T. Strub and M.D. Samuel, 1981: Annual mean surface heat fluxes in the tropical Pacific Ocean, *J. Phys. Oceanogr.*, **11**, 705-717.

Wyrtki, K., 1965: The average annual heat balance of the North Pacific ocean and its relation to ocean circulation. *J. Geophys. Res.*, **70**, 4547-4559.

Seasonal and Interannual Variability of the Madden-Julian Oscillation

David S. GUTZLER

Atmospheric and Environmental Research Inc.
840 Memorial Dr.
Cambridge, MA, 02139, U.S.A.

1. Introduction.

Several recent studies have examined the seasonal variability of the "40-50 day" or "Madden-Julian oscillation" (hereafter denoted MJO) in near-equatorial wind and rainfall data (Madden 1986; Hartmann and Gross 1988; Gutzler and Madden 1989). These studies related observed seasonal differences in the variance and presence or absence of a 40-50 day spectral peak to seasonal shifts in the position of convective maxima and the mean wind field. The present study examines the sensitivity of intraseasonal zonal wind variance at near-equatorial rawinsonde stations in the eastern Indian and western Pacific Oceans to interannual shifts in convection and mean winds associated with the Southern Oscillation (SO). As with most SO-related phenomena, the interannual signals are best understood within the context of seasonal variability.

2. Data and analysis procedure.

Daily time series of 200 mb and 850 mb zonal winds from six rawinsonde stations are considered (Table 1 and Fig.1). The stations are all within 10° latitude of the equator and are distributed in longitude between the southern tip of India and the mid-Pacific. Truk and Majuro are located within the COARE domain; Koror and Canton are less than 10° from the proposed western and eastern boundaries of the COARE domain. Daily surface wind time series from the three easternmost stations (Truk, Majuro and Canton) are also considered.

The seasonal cycle (defined as the sum of the Fourier harmonics with periods one year, 6 months, 4 months, and 3 months) was removed from each time series to form time series of anomalies, which were then passed through a band-pass filter with half-power cutoff periods of 31 and 66 days and a central period of 42 days. Each 31-66 day filtered time series is chopped into seasonal segments (Dec.-Jan.-Feb., etc.) and the variance within each seasonal segment is calculated, thus creating seasonal time series of filtered zonal wind variance, denoted σ_{BP}^2, for each station and level. Seasonal values of the variance of unfiltered anomalies about the individual seasonal means σ_A^2, are calculated over the same seasonal segments; σ_A^2 thus represents the total intraseasonal variance. A third variance quantity, $\langle\sigma_I^2\rangle$, is calculated from the time series of seasonal mean anomalies, i.e. $\langle\sigma_I^2\rangle$ is the interannual variance of zonal winds for each season. Brackets denote an average over all years (instead of the average over a single season implicit in σ_{BP}^2 and σ_A^2).

The time series of σ_{BP}^2 and σ_A^2 provide a local measure of low-frequency (seasonal) variations in the amplitude of the MJO, and of variability on all intraseasonal time scales, respectively. The climatological averages of these variances are calculated for each season and compared with $\langle\sigma_I^2\rangle$. The seasonal time series are correlated with seasonal values of the Southern Oscillation Index (the difference between normalized sea level pressure anomalies at Tahiti and Darwin).

ORSTOM
CENTRE DOCUMENTATION
Montpellier

F 30257

TABLE 1

Rawinsonde stations used in the analysis. The beginning and ending dates are the first and last seasons considered in the calculation of seasonal time series of 31-66 day variance; the actual filtered time series are somewhat longer.

Station name	Abbrev	lat	long	begin/end seasons
Trivandrum	TRV	8°N	77°E	MAM 1965 - SON 1977[1]
Singapore	SIN	1°N	104°E	JJA 1963 - SON 1985
Koror	KOR	7°N	134°E	JJA 1963 - SON 1985
Truk	TRU	8°N	152°E	JJA 1963 - SON 1985[2]
Majuro	MAJ	7°N	171°E	JJA 1963 - SON 1985[2]
Canton	CAN	3°S	172°W	JJA 1955 - SON 1966[3]

[1]DJF 1968 - DJF 1970 seasons missing
[2]begin/end seasons for surface wind: JJA 1956 - SON 1978
[3]begin/end seasons for surface wind: JJA 1955 - SON 1966

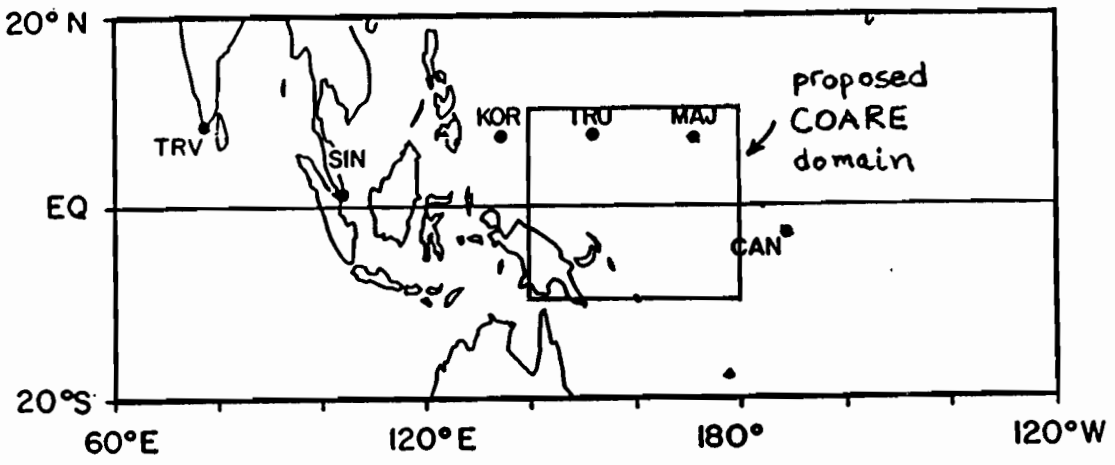

FIG.1. Map of rawinsonde and surface wind stations (see table 1 for key to station abbreviations).

3. Variance and correlation statistics.

Table 2 shows the climatological average values of 31-66 day filtered variance $\langle\sigma_{BP}^2\rangle$ and the total anomaly variance $\langle\sigma_A^2\rangle$, and the interannual variance $\langle\sigma_I^2\rangle$, for u_{200}, u_{850}, and (where available) u_s for each of the stations, stratified by season (DJF, MAM, JJA, and SON). We begin by discussing the 31-66 day variances, the middle number of the entry for each station and level.

The seasonal and geographical distribution of $\langle\sigma_{BP}^2\rangle$ for u_{200}, u_{850} shown in Table 2 reproduce and confirm previous results of Madden (1986), Hartmann and Gross (1988), and Gutzler and Madden (1989). The 31-66 day variance of u_{200}, is much greater than that of u_{850}, or u_s, and seasonal variations of $\langle\sigma_{BP}^2\rangle$ are also greatest in the upper troposphere. The value of $\langle\sigma_{BP}^2\rangle$ at 200 mb is greatest over the Indian Ocean and mid-Pacific (Trivandrum, Singapore and Canton) in DJF and $\langle\sigma_{BP}^2\rangle$ at these stations is lowest in JJA. At Koror in the far western Pacific, in contrast, $\langle\sigma_{BP}^2\rangle$ of u_{200} is small in DJF compared to other seasons. The 31-66 day variance is much greater at Canton than at Majuro, but we cannot tell from these data whether the variance gradient is primarily north-south (increasing toward the equator) or east-west (increasing toward the eastern Pacific) between these stations.

The distribution of $\langle\sigma_{BP}^2\rangle$ of u_{850} is considerably different. The DJF maximum is found only at Canton, and the variance at Trivandrum is exceedingly small. Elsewhere $\langle\sigma_{BP}^2\rangle$ is largest in the SON season, and at Koror and Truk the u_{850} value of $\langle\sigma_{BP}^2\rangle$ is smallest in the DJF season.

The 31-66 day variances in surface zonal winds are much smaller than the 850 mb variances. From Table 2 it appears that the MJO has very little amplitude in the surface wind field, except perhaps at Canton in the SON and DJF seasons.

Seasonal variations of $\langle\sigma_{BP}^2\rangle$ must be put in perspective relative to the total variance of intraseasonal anomalies $\langle\sigma_A^2\rangle$. The seasonal variability of $\langle\sigma_A^2\rangle$ is generally smaller than of $\langle\sigma_{BP}^2\rangle$ in relation to the annual average variance. As a consequence, for example, the ratio $\langle\sigma_{BP}^2\rangle$ / $\langle\sigma_A^2\rangle$ for u_{200} at Trivandrum and Canton exceeds 0.25 in DJF and drops to about 0.15 in JJA. At Singapore and Koror this ratio is roughly 0.2 in all seasons at both 200 mb and 850 mb. In contrast, at the surface this variance ratio is less than 0.2 in all cases except at Canton in DJF and SON.

It is also interesting to compare the intraseasonal variances with the interannual variance $\langle\sigma_I^2\rangle$, much of which is associated with fluctuations in the Southern Oscillation. To the west of Truk, $\langle\sigma_{BP}^2\rangle > \langle\sigma_I^2\rangle$, i.e. the MJO typically accounts for more variance than interannual variability, although at Singapore in DJF (both levels) and SON (850 mb) the variances are about equal, and the lower tropospheric intraseasonal variances at Trivandrum are too small to compare meaningfully.

From Truk eastward into the mid-Pacific, interannual variability is proportionately more prominent and the relative amplitude of $\langle\sigma_I^2\rangle$ and $\langle\sigma_{BP}^2\rangle$ is a function of level and season. At 200 mb at Truk and Majuro, $\langle\sigma_{BP}^2\rangle$ is greater in DJF and MAM, but $\langle\sigma_I^2\rangle$ is greater in SON. The transition from mostly $\langle\sigma_{BP}^2\rangle$ to mostly $\langle\sigma_I^2\rangle$ takes place between Majuro and Canton in MAM, and in JJA the variances are about the same. In the lower troposphere, anywhere that either variance is greater than 0.5 $m^2.s^{-2}$ it is the interannual variance that is greater, especially in the surface wind.

Table 3 shows correlations between time series of σ_{BP}^2 and the SOI. Year-round (denoted ALL) and seasonally stratified correlations are tabulated. Formal significance tests are difficult to apply uniformly because the seasonal time series are of different lengths. For convenience, a nominal significance level of 0.4 is adopted and only those correlations exceeding this threshold are discussed. This correlation threshold should be considered a general guide to significance but not a rigorous test thereof.

TABLE 2

Variance ($m^2 s^{-2}$) of (from left to right) $\langle\sigma_I^2\rangle$, $\langle\sigma_{BP}^2\rangle$, and $\langle\sigma_A^2\rangle$, at each station and level. These variances represent interannual variability, 31-66 day filtered variability, and total intraseasonal variability, respectively (see text).

	TRV			SIN			KOR			TRU			MAJ			CAN		
DJF																		
u_{200}	9	24	88	34	37	183	4	6	35	5	8	40	9	11	48	9	21	73
u_{850}	0	1	11	8	9	55	2	6	26	1	2	15	1	2	17	11	8	27
u_s										1.2	0.2	1.1	0.4	0.5	3.0	4.5	2.1	6.7
MAM																		
u_{200}	4	14	53	14	32	143	6	12	52	7	14	56	4	14	63	28	15	75
u_{850}	0	2	13	2	7	40	4	5	20	2	3	17	2	2	14	5	3	15
u_s										1.0	0.3	1.8	0.6	0.4	2.2	1.0	0.5	3.2
JJA																		
u_{200}	6	9	54	15	30	160	4	12	57	8	7	49	8	5	48	8	8	53
u_{850}	1	3	15	4	8	46	5	8	27	5	4	19	2	2	13	1	1	10
u_s										1.0	0.5	2.9	0.4	0.5	3.4	0.5	0.4	2.8
SON																		
u_{200}	7	9	51	16	31	146	5	11	54	14	9	56	18	7	51	22	12	56
u_{850}	2	3	18	12	12	56	5	9	39	5	4	23	5	3	17	5	4	18
u_s										1.0	0.7	4.2	0.7	0.6	4.0	2.0	1.4	5.1

TABLE 3

Correlation coefficients (×100) between seasonal averages of the variance of 31-66 day filtered time series and the Tahiti-Darwin Southern Oscillation Index.

	TRV	SIN	KOR	TRU	MAJ	CAN
ALL						
u_{200}	-01	-18	+02	-06	+11	+25
u_{850}	+02	+07	+11	-12	-12	-34
u_s				-31	-03	-36
DJF						
u_{200}	+09	-20	00	-17	+17	+60
u_{850}	-02	00	+40	+50	+22	-55
u_s				+27	+44	-61
MAM						
u_{200}	-20	-21	+18	+02	+07	-13
u_{850}	-48	+28	+35	+10	+24	-05
u_s				-11	+55	-14
JJA						
u_{200}	-42	-11	+11	-02	+04	+26
u_{850}	+28	+24	+02	-36	-17	+08
u_s				-50	-40	-34
SON						
u_{200}	-22	-23	-23	00	+34	+34
u_{850}	+38	-12	-21	-22	-46	-67
u_s				-53	-48	-52

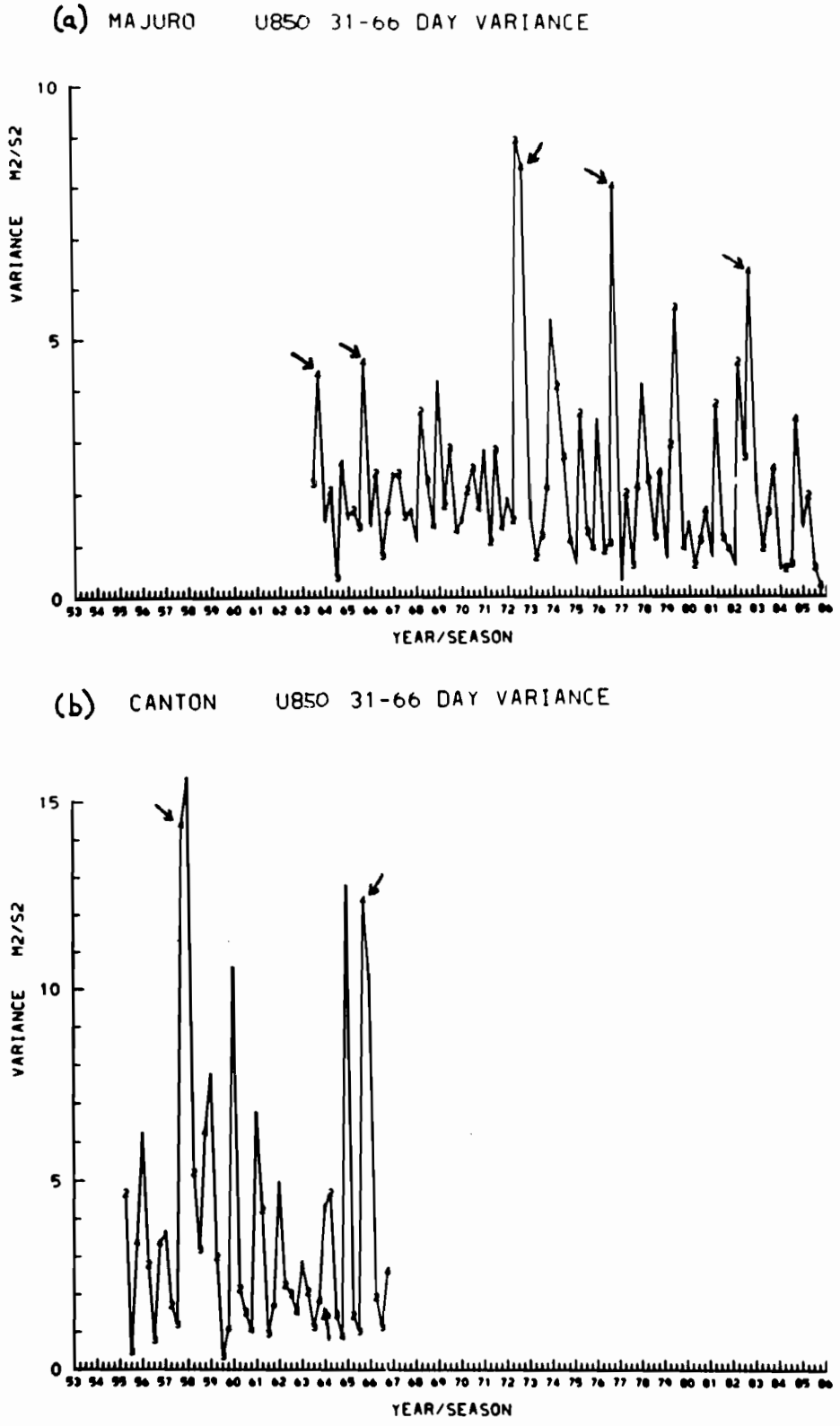

FIG.2. (a) Time series of σ_{BP}^2 of u_{850} at Majuro. DJF, MAM, JJA, and SON seasons are respectively denoted 1, 2, 3, and 4 on the plot. Arrow point to SON seasons in year(0) of SO warm events (1963, 1965, 1972, 1976, and 1982). (b) As in (a), but for u_{850} at Canton. Arrows point to SON season in year(0) of SO warm events (1957, 1963, and 1965).

None of the correlations derived from year-round data exceed 0.4 in magnitude, and most of the year-round correlations are very close to zero. The only significant 200 mb correlations are at canton in DJF and at Trivandrum in JJA. Examination of the time series of σ_{BP}^2 at 200 mb at Trivandrum and Canton (not shown) suggests that the 200 mb correlations exceeding |0.4| at those stations in Table 3 are caused by a few solitary seasons of extremely large variance, and may represent just sampling errors. There seems to be no association between SOI correlations involving σ_{BP}^2 in upper and lower tropospheric zonal winds at the same station.

The seasonally stratified statistics in the lower troposphere exhibit a complex distribution of significant correlations varying not only in magnitude but in the *sign* of the correlation from station to station and season to season. During the DJF season, interannual fluctuations of σ_{BP}^2 in lower tropospheric zonal winds at canton are negatively correlated with the SOI, but stations to the west of Canton exhibit positive correlations between σ_{BP}^2 and the SOI. In MAM the positive correlation between σ_{BP}^2 and the SOI is confined to the surface zonal wind at Majuro. In JJA the values of σ_{BP}^2 of surface zonal winds at Truk and Majuro are negatively correlated with the SOI, and in the SON season negative correlations are found in the lower troposphere between Truk and Canton.

Inspection of the various time series of σ_{BP}^2 sheds light on this complex set of correlations; in this brief report only two time series will be shown. Interannual variability at 200 mb is unsystematic and there is no apparent correspondence between fluctuations of σ_{BP}^2 in the upper and lower tropospheric wind series, a result consistent with the σ_{BP}^2-SOI correlations.

The interannual variability of σ_{BP}^2 in the lower tropospheric series is more systematic. Obvious peaks in the σ_{BP}^2 time series for u_{850} at Majuro (Fig. 2a) are evident in the SON season in years 1963, 1965, 1972, 1976, and 1982; these are SO warm event years (frequently referred to as "year 0"; Rasmusson and Carpenter 1982). SON(0) peaks are also found in the time series for the variance of the surface wind at Majuro and for surface and 850 mb winds at Truk (not shown), and for surface and 850mb winds at Canton (the latter shown in Fig. 2b), where the signature of the 1957-58 warm event is particularly prominent. Other peaks during non-warm event years are also found in the time series, but the tendency for large σ_{BP}^2 in lower tropospheric zonal winds at central Pacific stations during the second half of warm event years(0) is striking. This relationship is actually much clearer than suggested by the correlation statistics in Table 2, because the absence of a correspondingly strong "cold event"/highs SOI signature dilutes the overall correlation between the SOI and the time series of σ_{BP}^2.

At Majuro each of the SON(0) peaks is followed by an abrupt drop of σ_{BP}^2 to values below the seasonal average during the next two seasons, DJF(+1) and MAM (+1). The SOI tends to remain negative (and sea surface temperatures remain warm) during these seasons, which accounts for the change in sign of the correlation between σ_{BP}^2 and SOI between SON and DJF at 850mb at Majuro in Table 3. The time series of σ_{BP}^2 for u_s at Majuro (not shown) has similar peaks during warm events, but because the intraseasonal variance is generally small at the surface (Table 2), warm events account for almost all the seasons in which σ_{BP}^2 exceeds 1 $m^2.s^{-2}$. To the southeast, at Canton, σ_{BP}^2 at 850mb does not diminish between SON(0) in 1957 and 1965 and DJF(+1), but remains large. Therefore the SOI-σ_{BP}^2 correlation also remains negative, in contrast to the change in sign at Majuro and Truk.

Figure 3 contains a summary schematic of the geographical distribution of σ_{BP}^2 anomalies in lower tropospheric zonal winds during JJA(0)-DJF(+1) seasons of warm events, derived from statistics such as the correlations in Table 3 and from inspection of

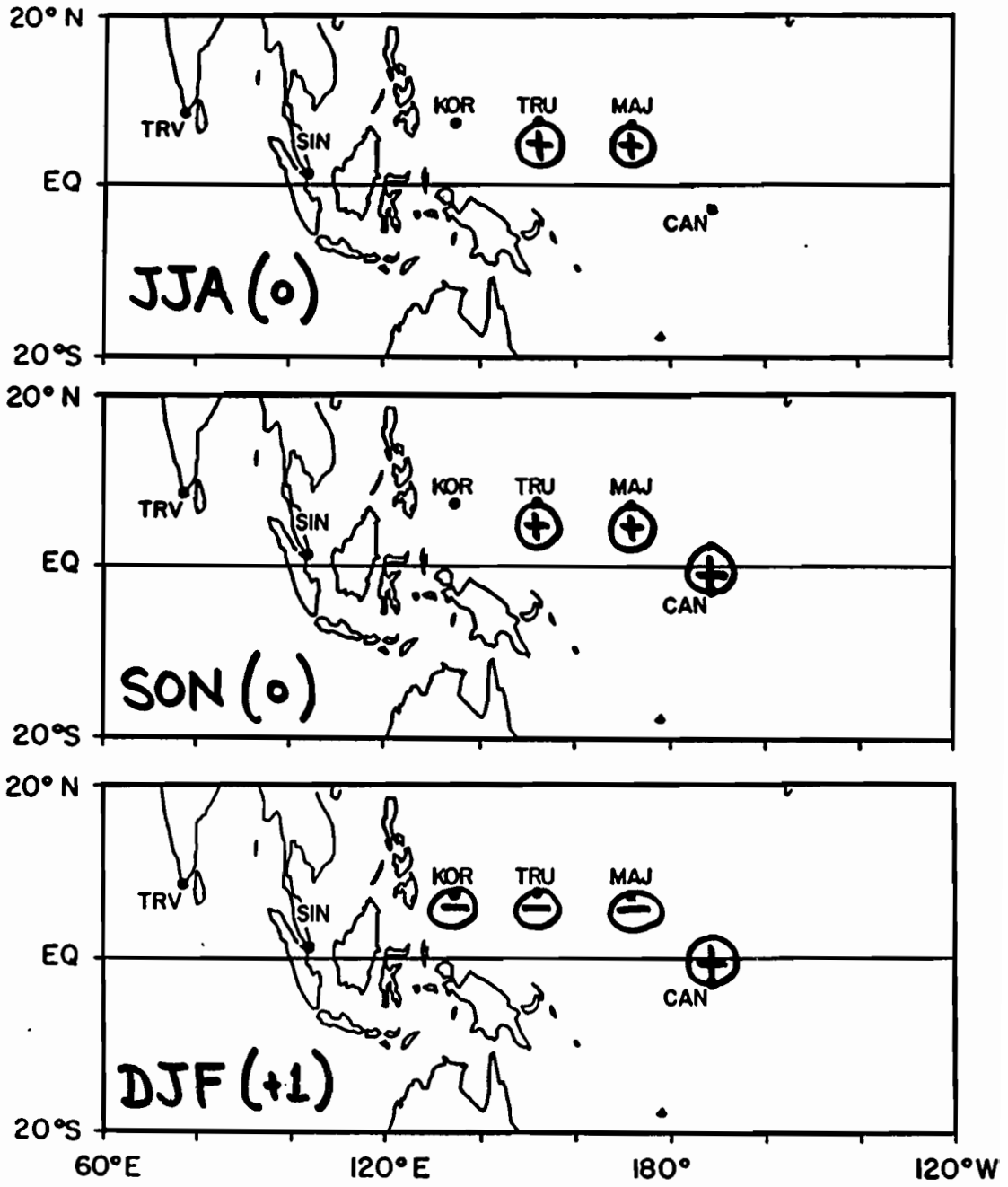

FIG.3. Summary schematic of the modulation of σ_{BP}^2 of lower tropospheric zonal winds during the JJA(0)-DJF(+1) period of SO warm events. Stations exhibiting enhanced of depressed 31-66 day variance are indicated by + and - symbols, respectively.

time series of σ_{BP}^2 at other stations (not shown). The region of enhanced intraseasonal variance shifts eastward from JJA(0) to SON(0), then abruptly shifts either eastward or southward in DJF(+1).

The aforementioned modulation of intraseasonal zonal wind variance during SO warm events, inferred from the seasonal time series of σ_{BP}^2, is evident in the time series of u_{200}, u_{850} and u_s wind anomalies at Canton during the 1965 warm event (Fig. 4). These plots show the output of the 31-66 day filter (with the seasonal cycle removed) superimposed on the bi-daily anomalies. At 200mb (Fig. 4a) the 31-66 day filter provides the best fit to the time series of unfiltered anomalies in the DJF seasons. In DJF 1965/66 a particularly intense episode of intraseasonal variability interrupts the lower-frequency seasonal average westerly anomalies. There is no apparent relationship between seasonal fluctuations of σ_{BP}^2 or σ_A^2 and the mean wind anomaly or the development of the warm event in late 1965.

The 31-66 day time series at 850mb (Fig. 4b) is clearly out-of-phase with its 200 mb counterpart, but there is no systematic correspondence between the amplitudes of the fluctuations in the two time series. Both the 31-66 day variance and the unfiltered variance increase during the period of largest mean westerly anomalies in SON 1965 and DJF 1965/66 (this is also the period of maximum SST anomalies in the central Pacific during this event; Rasmusson and Carpenter, 1982). There is an isolated 31-66 day event in January 1965, which is exceptional for a non-warm event period (cf. Fig. 2b). The surface wind time series (Fig. 4c) is highly coherent with the 850mb time series, but has less variability on all time scales.

Both of the lower tropospheric time series exhibit burst-like behavior not noticeable at 200 mb, with episodes of large positive (westerly) anomalies capping the crests of the westerly phases of the 31-66 day time series. The bursts are organized on MJO time scales during SON 1965 and DJF 1965/66, as demonstrated by the variance ratio σ_{BP}^2/σ_A^2, which is approximately one-third in those seasons. Other isolated bursts of a few days' duration occur (e.g. in April 1965), which are not visibly associated with large variance on MJO time scales. The amplitude of 31-66 day variability during SON and DJF is as large as the magnitude of the seasonal anomalies. Both the seasonal-average westerlies and the large amplitude 31-66 day events cease in MAM 1966.

The effects of the MJO and burst-like variability on the total zonal wind are illustrated in Fig.5, which shows the actual bi-daily u_s values together with the sum of the seasonal cycle, the output from the 31-66 day filters, and the output from a low-pass filter. The latter is designed so that the two filters in combination approximate the effect of a low-pass filter whose half-power point is also 31 days, so the residual time series after implementation of these filters is high-pass filtered to isolate variability on sub-MJO time scales. It is apparent that the bursts are responsible for most of the periods of absolute westerly winds during this warm episode. Note the absence of "easterly bursts" of comparable magnitude during easterly phases of 31-66 day fluctuations (or any other time). The figures suggest that the bursts and the MJO are indeed coupled. Time series of σ_{BP}^2 of the surface wind at Canton during the 1957-58 warm event (not shown) show behavior consistent with these conclusions.

4. Discussion and recommendations for COARE.

The principal systematic interannual modulation of the amplitude of the Madden-Julian oscillation in near-equatorial zonal winds is an increase in the lower troposphere across the western Pacific during the second half of "year 0" of ENSO warm events. This is followed by an abrupt drop in intraseasonal variability during the DJF(+1) and MAM(+1) seasons at stations north of the equator and west of the dateline, but the

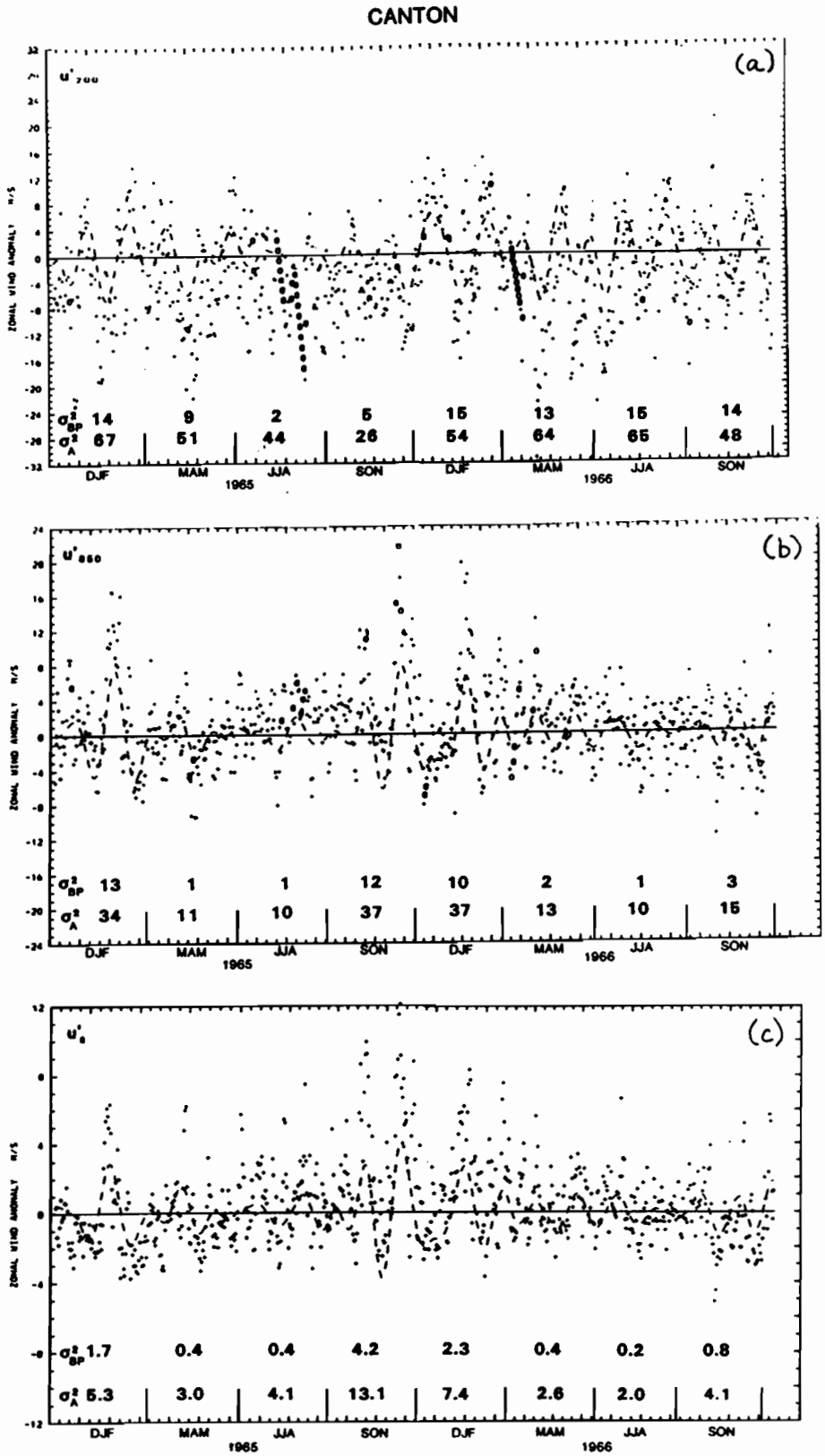

FIG.4. (a) Time series of anomalies (daily value minus the seasonal cycle) at Canton and output of the 31-66 day filter for the period 1 December 1964 - 30 November 1966, for u_{200} at Canton. Every second day of the daily time series is plotted for clarity; ticks on the abscissa are spaced ten days apart. Small crosses denote observed values; zeros are plotted for missing data that have been linearly interpolated. The short horizontal solid lines are monthly mean anomalies. Seasonal values of σ_{BP}^2 and σ_A^2 are plotted for each season. (b) As in (a), but for u_{850}. (c) As in (a), but for u_s.

variance to the south and east remains high during that season and the following MAM(+1) season as well. Correlations between seasonal values of σ_{BP}^2 and the Southern Oscillation Index are generally insignificant everywhere in upper tropospheric zonal winds and from Singapore westward in lower tropospheric winds.

Considering just the lower tropospheric zonal wind, the increase in 31-66 day filtered variance during the second half of years (0) at Truk, Majuro, and Canton is consistent with the more general result that the seasonal variability of intraseasonal zonal wind variance in the lower troposphere shifts north and south along with the region of most intense convection (Gutzler and Madden, 1989; Table 2). The center of mean convective activity shifts eastward across the western Pacific during the second half of year(0) (Rasmusson and Carpenter 1982), during the seasons when intraseasonal zonal wind variance at stations in this region increases. The SON(0)→DJF(+1) transition in the distribution of intraseasonal zonal wind variance may represent an amplification of the seasonal cycle transition, as the anomalous convection and associated mean westerly surface anomalies shift south across the equator from SON(0) to DJF(+1) (Rasmusson and Carpenter 1982), following the seasonal cycle. Here again, it would be very interesting to know whether the important gradient of intraseasonal variance between Majuro and Canton during DJF(+1) is meridional or zonal.

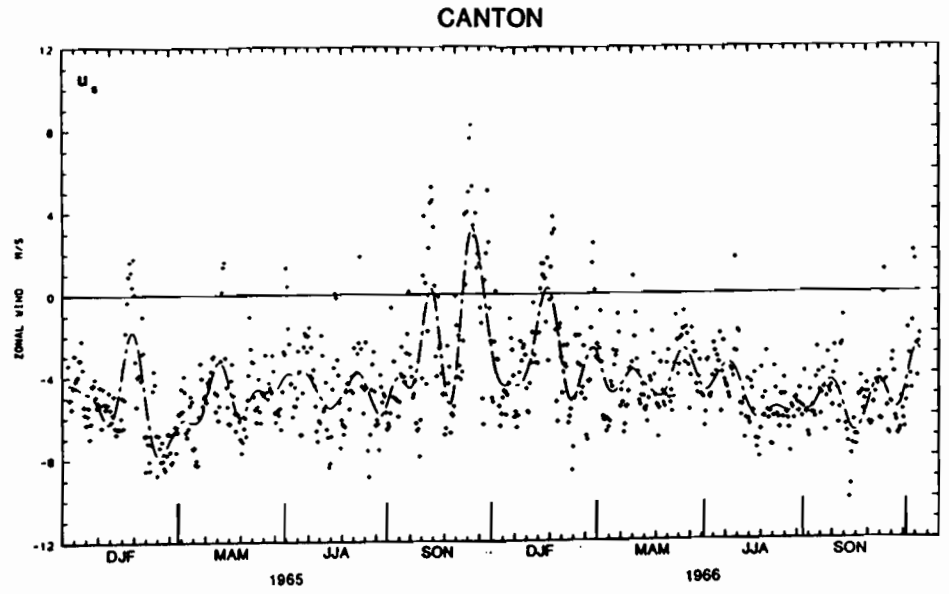

FIG.5. Time series of u_s (not anomalies) at Canton, corresponding to Fig. 4(c). The solid curve is the sum of the seasonal cycle and the outputs of the band-pass filter and a low-pass filter (see text); the sum of these filter outputs is approximately equivalent to a low-pass filter whose high-frequency cutoff is the same as that of the band-pass filter.

Modulation of intraseasonal variance by SO-related interannual variability is observed only in lower tropospheric winds. There is no correlation between the amplitude of 31-66 day anomalies in the upper and lower troposphere, suggesting that the enhancement of lower tropospheric wind variance is not the results of a convective feedback, which ought to affect the amplitude of wind fluctuations in the upper troposphere as well. This results adds to previous evidence for some degree of vertical decoupling of wind fluctuations on 40-50 day time scales, including seasonal variations in the coherence between 150 mb and 850 mb fluctuations (Madden, 1986) and the

different geographical structure of the seasonal cycle of 40-50 day zonal wind variance (Gutzler and Madden, 1989). Initial analysis of the filtered surface wind time series suggests that high-frequency westerly bursts are associated with the westerly phase of MJO variability on 40-50 day time scales. These bursts are already known to occur preferentially during SO warm event periods (Keen, 1982; Luther et al., 1983), a result confirmed by the present analysis.

Significant variance of surface zonal winds on intraseasonal time scales (both on 31-66 day time scales and higher frequency bursts) occurs during SO warm phases. The time scale of the MJO is particularly awkward, because monthly means are the standard archival period for most surface wind data sets. Unfortunately, monthly-averaged data contains considerable aliased variance in the presence of a 40-50 day signal (Gray and Madden, 1986). They noted that the use of seasonal averaging reduces the aliasing of variance in this frequency range, but only by eliminating 40-50 day variance almost completely. The time series in Figs. 4 and 5 suggest that enhanced intraseasonal variance is a fundamental component of the atmospheric response to warm event conditions, perhaps more important energetically than the quasi-stationary westerly wind response.

The questions raised by this study are central to the goals of the TOGA program and are highly relevant to COARE. The study is limited by the extremely small sample of six stations, only four of which are located over the Pacific Ocean. There are several other island stations within the COARE domain whose historical surface wind records could be used to augment the present results, but the network of rawinsonde stations over this region is quite sparse. Effort should be directed toward increasing the density of observations during pilot studies and the proposed COARE intensive observation period. The results indicate that there is a sharp increase in intraseasonal zonal wind variance between Majuro and Canton, across the proposed eastern boundary of the COARE domain. If possible it would be worthwhile to extend the eastern boundary of the COARE domain eastward to at least 170°W.

These results also suggest themes for future modeling studies. The effect of intraseasonal surface stress variability on ocean circulation should be evaluated. In the absence of comprehensive wind stress data with sufficient temporal resolution, a good first step would be sensitivity studies with artificial data. The Canton time series suggest that amplitudes of up to 5 $m.s^{-1}$ for quasiperiodic anomalies with periods of about 40 days occur during warm events. Additional studies could superimpose westerly bursts on the 40 day periodic anomalies.

*Acknowledgments.*This material is based upon work supported by the U.S. National Science Foundation under Grants ATM-8613060 and ATM-8819825 awarded to AER. The advice and assistance of Dr. R.A. Madden of NCAR is gratefully acknowledged. Dr. D.E. Harrison of the NOAA Pacific Marine Environmental Laboratory provided the surface wind data.

REFERENCES

Gray, B.M., and R.A. Madden, 1986: Aliasing in time-averaged tropical pressure data. *Mon. Wea. Rev.*, **114**, 1618-1622.

Gutzler, D.S., and R.A. Madden, 1989: Seasonal variations in the spatial structure of intraseasonal tropical wind fluctuations. *J. Atmos. Sci.*, **46**, 641-660.

Hartmann, D.L., and J.R. Gross, 1988: Seasonal variability of the 40-50 day oscillation in wind and rainfall in the tropics. *J. Atmos. Sci.*, **45**, 2680-2702.

Keen, R.A., 1982: The role of cross-equatorial tropical cyclone pairs in the Southern Oscillation. *Mon. Wea. Rev.*, **110**, 1405-1416.

Luther, D.S., D.E. Harrison, and R.A. Knox, 1983: Zonal winds in the central equatorial Pacific and El Nino. *Science*, **22**, 327-330.

Madden, R.A., 1986: Seasonal variations of the 40-50 day oscillation in the tropics, *J. Atmos. Sci.*, **43**, 3138-3158.

Rasmusson, E.M., and T.H. carpenter, 1982: Variations in tropical sea surface temperature and surface wind fields associated with the Southern Oscillation/El Nino. *Mon. Wea. Rev.*, **110**, 354-384.

Fine structure variability

in the equatorial Western Pacific Ocean

Marie-Hélène RADENAC

Groupe PROPPAC, ORSTOM - BP A5,
Nouméa - New Calédonia

ABSTRACT

CTD and velocity measurements were carried out in the western equatorial Pacific ocean at 165°E in April 1988. Large-scale structures along this meridian are first described. Then, preliminary results of an 8-day long station at the equator are used to locate layers of high variability.

1. Presentation and data

The specific goals and scientific objectives of PROPPAC (PROduction Pélagique dans le PACifique) program are to study relations between physical processes and biological production. Main physical interest is to locate possible areas of vertical mixing. We will then establish how this local mixing interacts with large-scale hydrographic and velocity structures.

In the framework of this program, three cruises have been carried out along 165°E (20°S-6°N). Along the transect, every degree of latitude, a velocity profile is made down to 600 db and, at the same time, a CTD cast is done to 1000 db (Delcroix et al, 1987). Afterward, position for an eight-day long station is chosen in order to study variability of a specific situation.

We present here preliminary results of the cruise undertaken in April 1988:

1. Large-scale structures encountered from 5°S to 5°N along 165°E track (from April 3rd to 7th) are described using temperature, salinity, and velocity sections. Mean and standard deviation profiles are constructed from density data of the 8-day station (April 12th to 19th) in order to locate strong variability layers at the equator.
2. Then, a fine-scale variability study in the upper 400 m is initiated at the equator from the 8-day time series. Väisäla frequency, zonal vertical shear and zonal Richardson number are contour-plotted as functions of depth and time. The 29 profiles of zonal velocity, Väisäla frequency, zonal vertical shear, and zonal Richardson number measured during the 8-day long station have been averaged and are also presented. A mean "activity index" profile is compared to the averaged zonal Richardson number profile.

2. Large scale structures

As potential density section and temperature section look similar, only temperature section is presented here. However, salinity effect on the density field must be taken into account in areas where vertical temperature gradients are weak and vertical salinity gradients are strong (North Subsurface Countercurrent : 2°N-3°N).

A structure evidenced by the three sections shown in Figures 1a to 1c is an unusually strong equatorial upwelling. Delcroix et al (1987) only mentionned weak upwellings detected on temperature and salinity sections of the SURTROPAC cruises of January and August 1984.

ORSTOM
CENTRE DOCUMENTATION
Montpellier

F 30 268

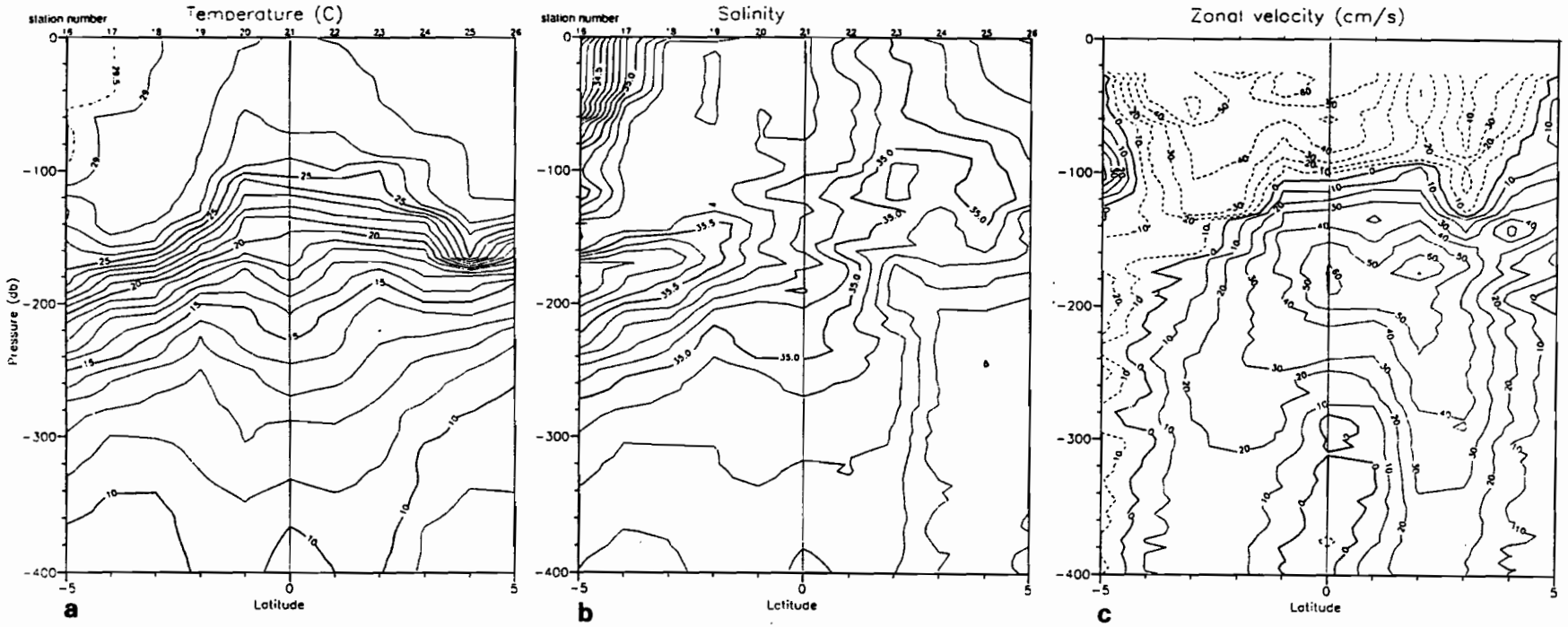

FIG.1. Large-scale stuctures of (a) temperature, (b) salinity, and (c) measured zonal current (ref. 600db) along 165°E.

In April 1988, we observe:

- a decrease in sea surface temperature (SST) from 28.6°C at 2°N and 2°N to 27.7°C at the equator;
- a strong meridional salinity gradient from the surface down to 100 m limiting the southern boundary of the upwelling at 4°S: | 0.5 (ppt) per degree of latitude;
- a strong South Equatorial Current (SEC) (Umax > 50 cm.s^{-1}) from 5°S to 5°N and down to 100 m. This strong westward flow has also been observed during the SURTROPAC cruise in January 1988 (Eldin, 1989) but it was not associated with an equatorial upwelling. SST between January and April cruises is measured by equatorial mooring (McPhaden and Freitag, 1988). It indicates a sharp fall in March 1988 and SST reaches value as low as 1°C below climatology at the end of the month.

Other main features have been observed during most cruises:

- isotherm spreading associated with Equatorial Undercurrent (EUC);
- vertical temperature gradient weakens under 300 m depth;
- EUC core is located in the area of maximum meridional salinity gradient (| 0.4 per degree of latitude at 170 m) situated at the northern edge of the high salinity tongue;
- under 300 m, westward Equatorial Intermediate Current (EIC) is hardly detected because of weak zonal velocity (5 to 10 cm.s^{-1}) and narrow meridional extension.

Layers of strong variations (in a statistical sense) are deduced from standard deviation profile of potential density (Fig. 2).

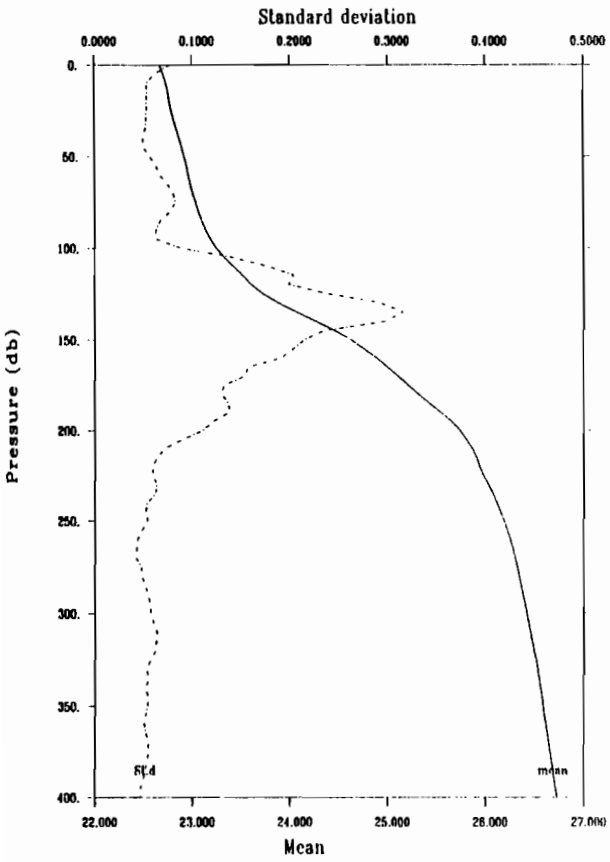

FIG.2. Mean and standard deviation profiles of potential density.

- The mixed layer down to 100 m is associated with small variations except a low maximum at 70 m.
- Strong variations are observed in the thermocline.
- Under the thermocline, there are small variations in the weakly stratified layer but a slight peak around 300 m.

This variability is not caused only by vertical displacements or shear instabilities.

Lateral advection of nearby water masses (which is not studied here) should be taken into account too.

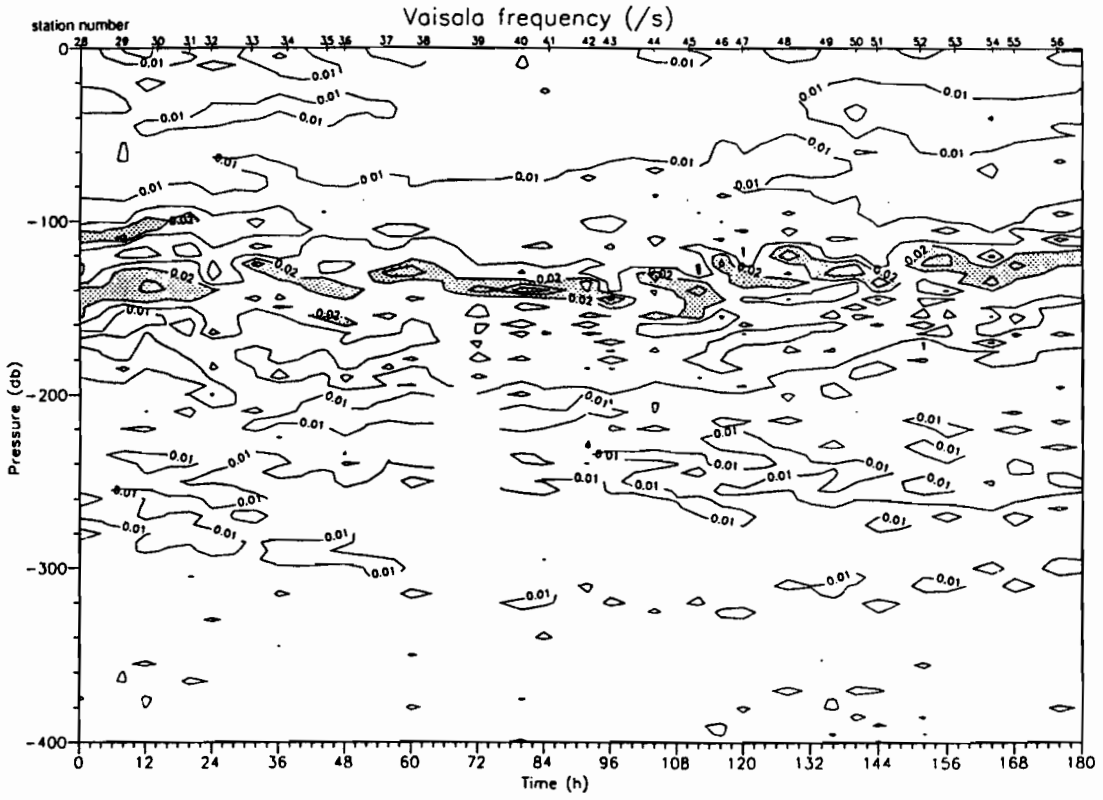

FIG.3a. Evolution of Väisälä frequency during the equatorial 8-day station.

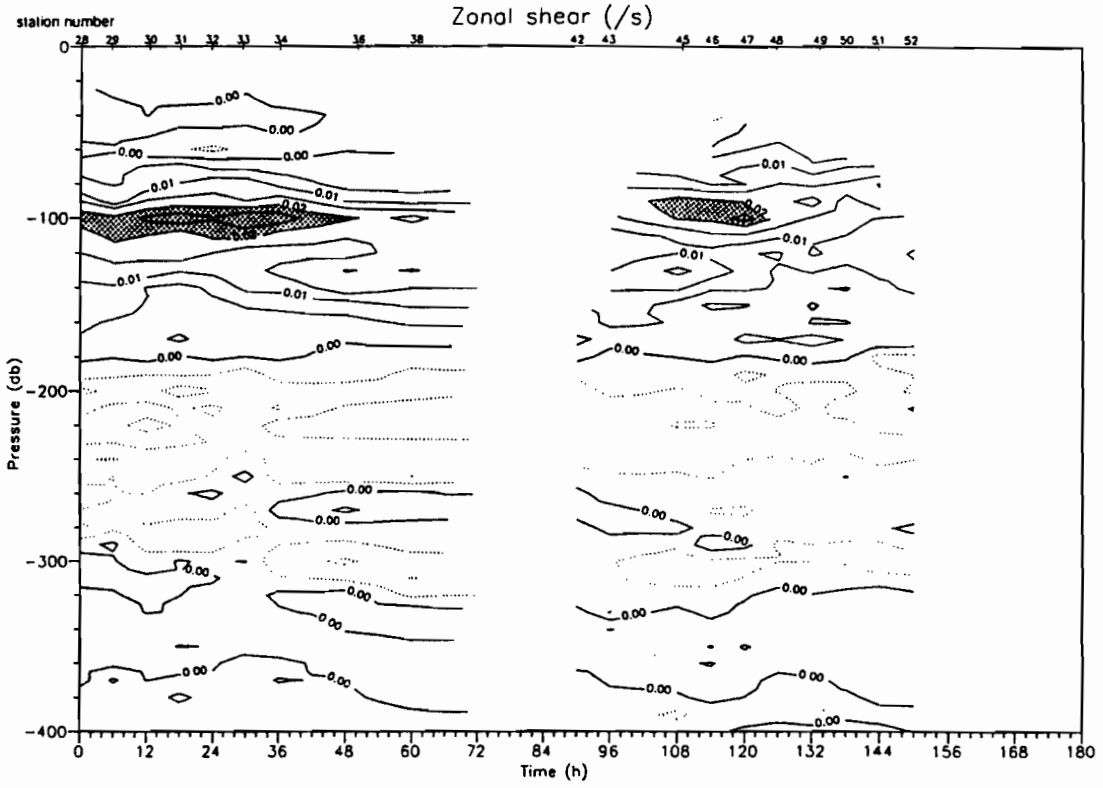

FIG.3b. Evolution of zonal vertical shear during the equatorial 8-day station.

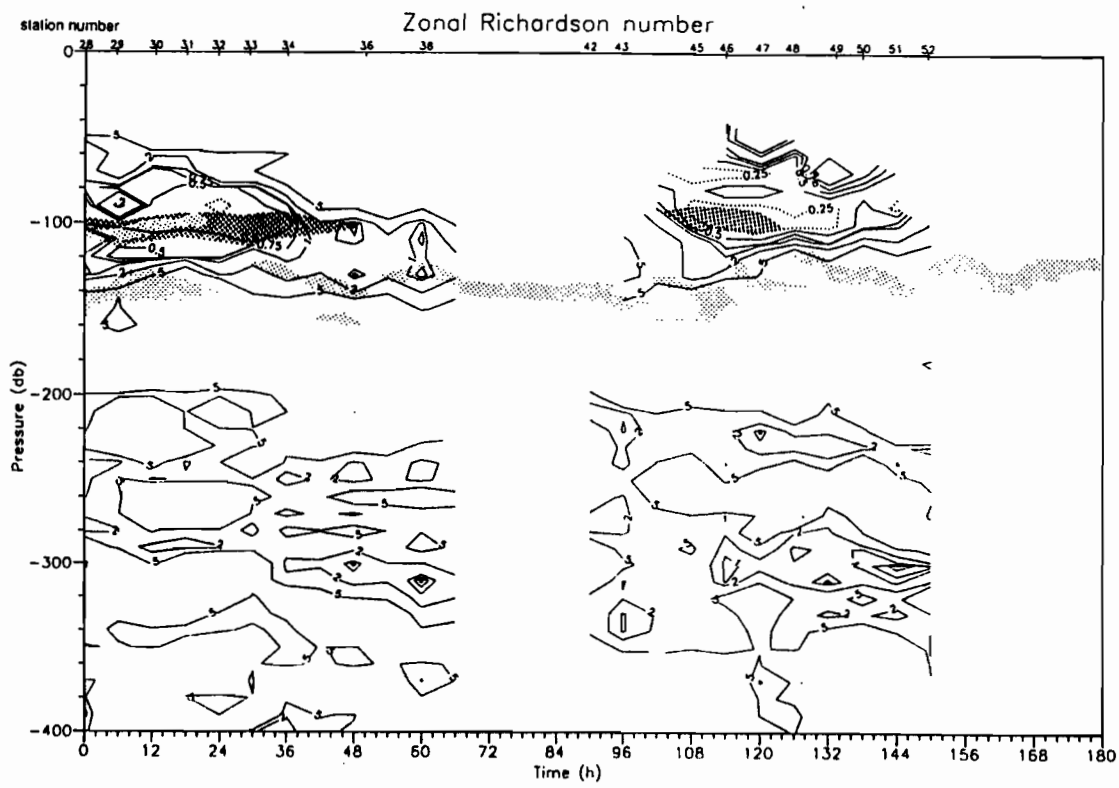

FIG.3c. Evolution of zonal Richardson number during the equatorial 8-day station.

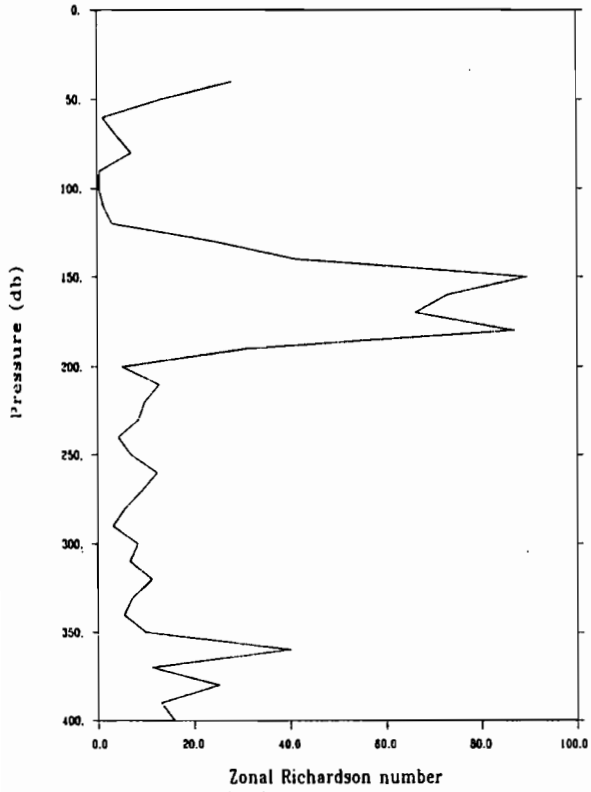

FIG.4a. Mean zonal Richardson number during the equatorial 8-day station.

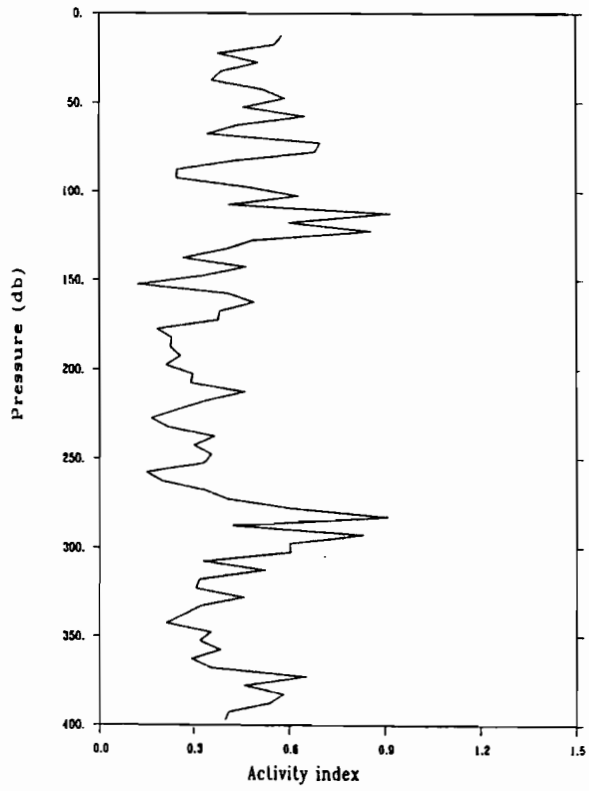

FIG.4b. Activity index computed from the potential density profiles of the equatorial 8-day station.

3. Fine scale variability

In this section, we identify layers of strong static stability and layers of large vertical shear of zonal current component and compare them to a statistical activity index. We also calculate Richardson numbers. Richardson numbers greater than 1. indicate a high stability regim in contrast to values smaller than 1. which represent destabilized system. If it is smaller than .25, the regim is considered as turbulent.

During all the 8-day station, the upper part of the thermocline constitutes the layer of strongest static stability (Fig. 3a).

The EUC core (evidenced in Figure 3b as the zero zonal shear value) is associated with a high Richardson number band (Fig. 3c).

Above the core, lowest Richardson numbers are confined in a layer closely linked to the highest shear region between 60 and 80 m. The critical value of 0.25 is reached during about 24 hours (it matches an intensive shear period) at the end of the station in a 15 m thick layer.

Around 300 m, between EUC and EIC, we find a layer where, although being bigger than 1., Richardson number is significantly lower than in the surrounding layers.

An activity index has been calculated from the potential density data of the 8-day station. It is defined as:

$$A = \mathrm{Var}\left(|\sigma/|z \right) / \left(\langle |\sigma/|z \rangle \right)^2$$

where the sign < > indicates mean value. It is equal to the square of activity index used in McPhaden (1985).

Comparing the profile of averaged Richardson numbers (Fig. 4a) and the profile of activity index (Fig. 4b), two different regims are detected.

- Around 100 m, high activity index is associated with low Richardson number (< 1.). In this layer, part of the variability observed from the mean density profile may be caused by shear instabilities between SEC and EUC.
- At 300 m, there is also a high activity index peak (as well as a small standard deviation maximum in potential density) which lies in a layer where Richardson number remains high (> 1). It is not clear that this variability only results from vertical shear because of the weakness of the shear between EUC and EIC. We still have to remember that, even if it is weak, this layer lies in a discontinuity zone for temperature or salinity gradients, as well as for velocity. Mechanisms other than shear instabilities are probably related to this high activity. They may be associated with this weak discontinuity property.

REFERENCES

Chereskin, T.K., J.N. Moum, P.J. Stabeno, D.R. Caldwell, C.A. Paulson, L.A. Regier, and D. Halpern, 1986: Fine-scale variability at 140°W in the Equatorial Pacific, *J. Geophys. Res.*, 91, 12887-13091.

Delcroix, T., G. Eldin, and C. Hénin, 1987: Upper ocean water masses and transports in the Western Tropical Pacific (165°E), *J. Phys. Oceanogr.*, **17**, 2248-2262.

Eldin, G., 1989: Coupes verticales des structures océaniques à 165°E observées au cours de dix campagnes SURTROPAC, 1984-1988, *Rapports Scientifiques et Techniques, Océanographie Physique* 1, ORSTOM, 130 pages.

McPhaden, M.J., 1985: Fine-structure variability observed in CTD measurements from the Central Equatorial Pacific, *J. Geophys. Res.*, **90**, 11726-11740.

McPhaden, M.J. and H.P. Freitag, 1988: November-December Equatorial SST, surface wind and current, Climate Diagnostics Bulletin, Delayed mode analyses ocean/atmosphere.

Toole, J.M., H. Peters, and M. Gregg, 1987: Upper ocean shear and density variability at the Equator during TROPIC HEAT, *J. Phys. Oceanogr.*, **17**, 1397-1406.

The Climatology of the Western Tropical Pacific: Analysis of the Radiosonde Data Base

G.C. REID, K.S. GAGE and J.R. McAFEE

Aeronomy Laboratory
National Oceanic and Atmospheric Administration
Boulder, CO 80303 - U.S.A.

ORSTOM
CENTRE DOCUMENTATION
Montpellier

INTRODUCTION

Upper air data are available from several radiosonde stations in the western tropical Pacific at daily or twice-daily intervals for a period of over 30 years, beginning in the early 1950s. Three of these stations (Ponape, Truk, and Majuro) lie within the TOGA COARE domain, and several others (Koror, Yap, Guam, Eniwetok, and Pago Pago) are closely adjacent. Analysis of this data base is in principle capable of providing important information on the height and time structure of atmospheric variability over the warm pool region.

As a preliminary study, we have used the temperature records from three of these stations (Yap, Majuro, and Pago Pago), together with two more distant stations (Wake Island and Curacao) to examine the development in time of the ENSO-related anomalies at 30 pressure levels from 1000 hPa to 15 hPa (about 28 km) during the 17-year period 1966-1982. The analysis is described in detail in Reid et al. (1989).

THE RELATIONSHIP OF OCEANIC AND ATMOSPHERIC TEMPERATURE ANOMALIES

The El Nino time series of SST anomalies used was that derived by Weare et al. (1976) and updated by Weare (1986). It is the amplitude of the dominant interannual mode found in an EOF analysis of SSTs over a wide region of the Pacific north of 20°S, and the time series of monthly values is shown in Figure 1. The only pre-treatment of the time series was the removal of a weak linear trend, shown in the figure.

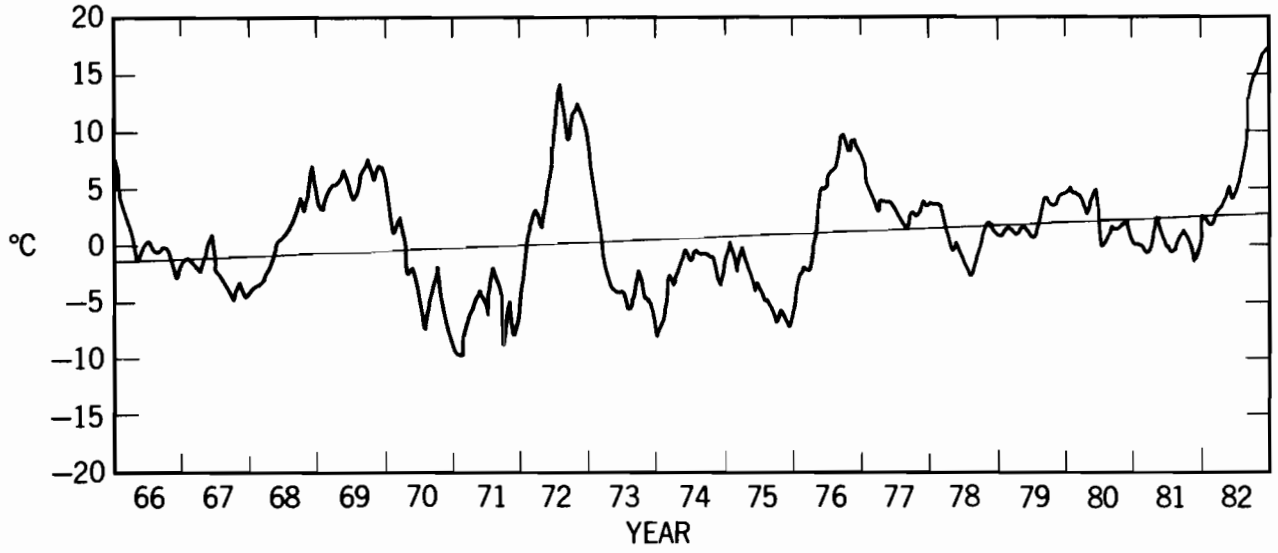

Figure 1. Pacific SST anomaly time series (after Weare [1986]).

F 30259

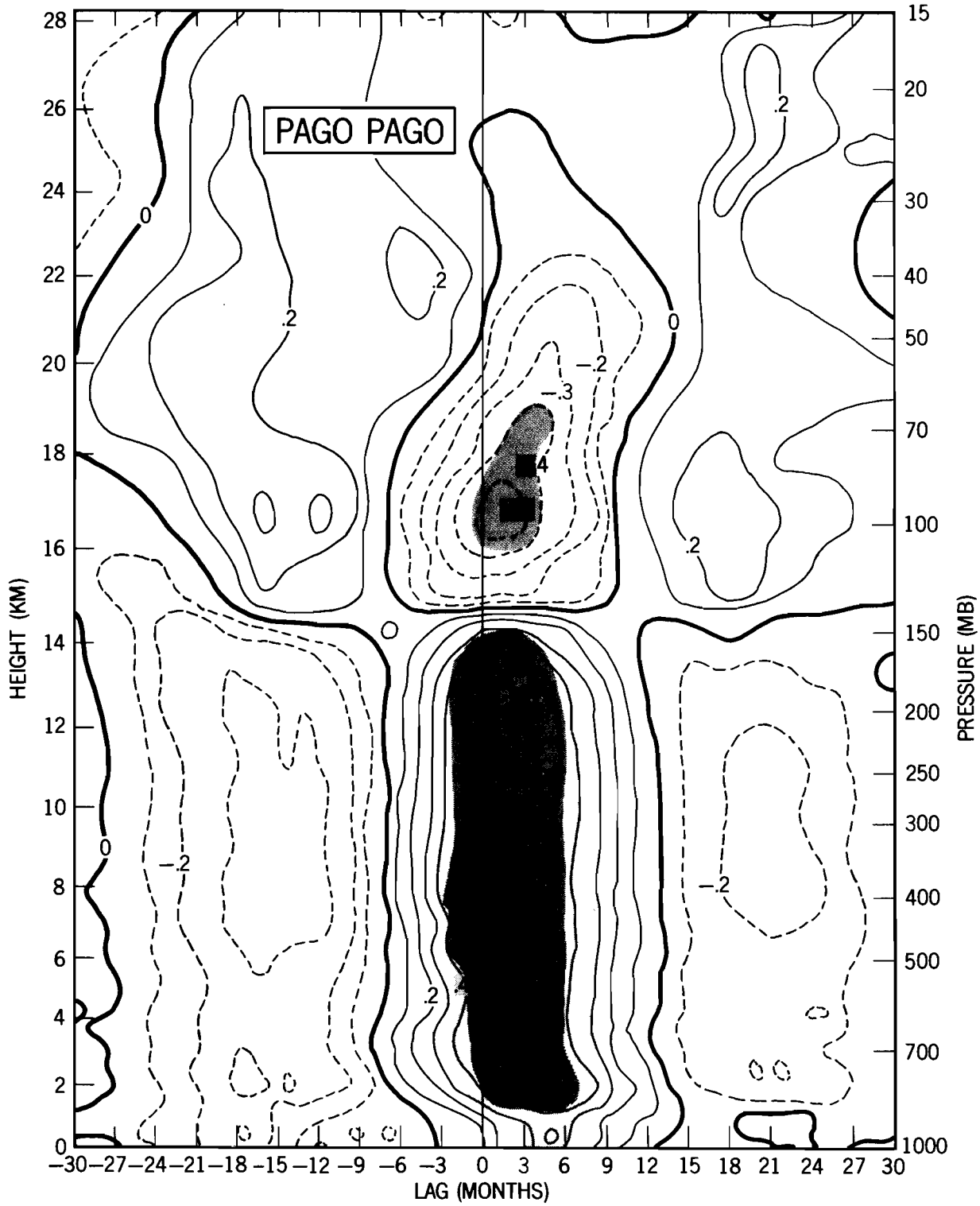

Figure 2. Contour plot of cross-correlation coefficients between time series of Figure 1 and monthly mean atmospheric temperature anomalies at Pago Pago. The ocean leads the atmosphere for positive lags.

The atmospheric temperature time series for each of the 5 stations and for each of the 30 pressure levels (nearly 2 million individual measurements in all) were reduced to monthly means, and anomaly series were formed by subtracting the 17-year mean for each calendar month from the individual values. Fairly pronounced trends were evident at all levels, and were removed before carrying out the analysis. The trends and their significance are discussed below.

For each station, the temperature anomalies at each pressure level were cross-correlated with the SST anomaly time series for lags of ± 30 months (positive lag means SST leads the atmosphere). Figure 2 shows the result for Pago Pago in the form of contours of equal cross-correlation coefficient. Dark and light shading indicate correlation significant at the 99% and 95% levels respectively, taking autocorrelation in the individual time series into account.

The main features are:

(1) Strong positive correlation in the main troposphere, from 850 hPa to 150 hPa, with the atmosphere lagging the ocean by about 2 months.
(2) Strong negative correlation between 100 hPa and 60 hPa, with a similar lag.
(3) A transition region between 150 hPa and the tropopause at about 100 hPa.
(4) A surface layer below 850 hPa, with little significant correlation.
(5) Disappearance of the signal above about 40 hPa (22 km).

A generally similar picture is seen at the other four stations, but with interesting differences from station to station, and with a systematic variation in lag.

Figure 3 shows the lag in the mid-troposphere as a function of longitude of the station, and indicates that the signal appears to propagate slowly outward from a center near 135°W, where the lag would probably be close to zero (if there were a station to observe it). The zonal propagation speed is about 0.8 meters per second, considerably less than typical wind speeds.

INTERPRETATION

The slow propagation speed, and the close similarity of the speeds in the troposphere and stratosphere, suggest that the mechanism is not simply the advection of air from a region of enhanced convective activity. Two other possibilities are:

(1) Enhancement of the large-scale tropospheric subsidence and stratospheric upwelling resulting from increased convective activity centered near 135°W. In this case, the tropospheric subsidence can be considered as a sign of an enhanced and displaced Walker circulation accompanying El Nino events, while the stratospheric upwelling can be considered as a sign of an enhanced Hadley circulation.
(2) An increase in the extent of optically thick mesoscale cirrus sheets in the upper troposphere resulting from enhanced convective activity, leading to radiative warming of the troposphere below and radiative cooling of the stratosphere above.

Both of these mechanisms may be contributing to the effect, and some effort is needed to try to devise ways of estimating their relative effectiveness.

ATMOSPHERIC TEMPERATURE TRENDS

Significant trends were found in the 1966-1982 atmospheric temperature anomaly time series at all pressure levels. Figure 4 shows the slope of a least-squares straight-line fit to the trend at each of the five stations for several pressure levels. The station trends all show similar characteristics - a warming below the 150 hPa level, which continues into the lower stratosphere only at the near-equatorial stations of Yap and Majuro. The other stations show a transition to a cooling trend near the tropopause and at the base of the stratosphere, weakening with increasing height and becoming irregular above about 40 hPa.

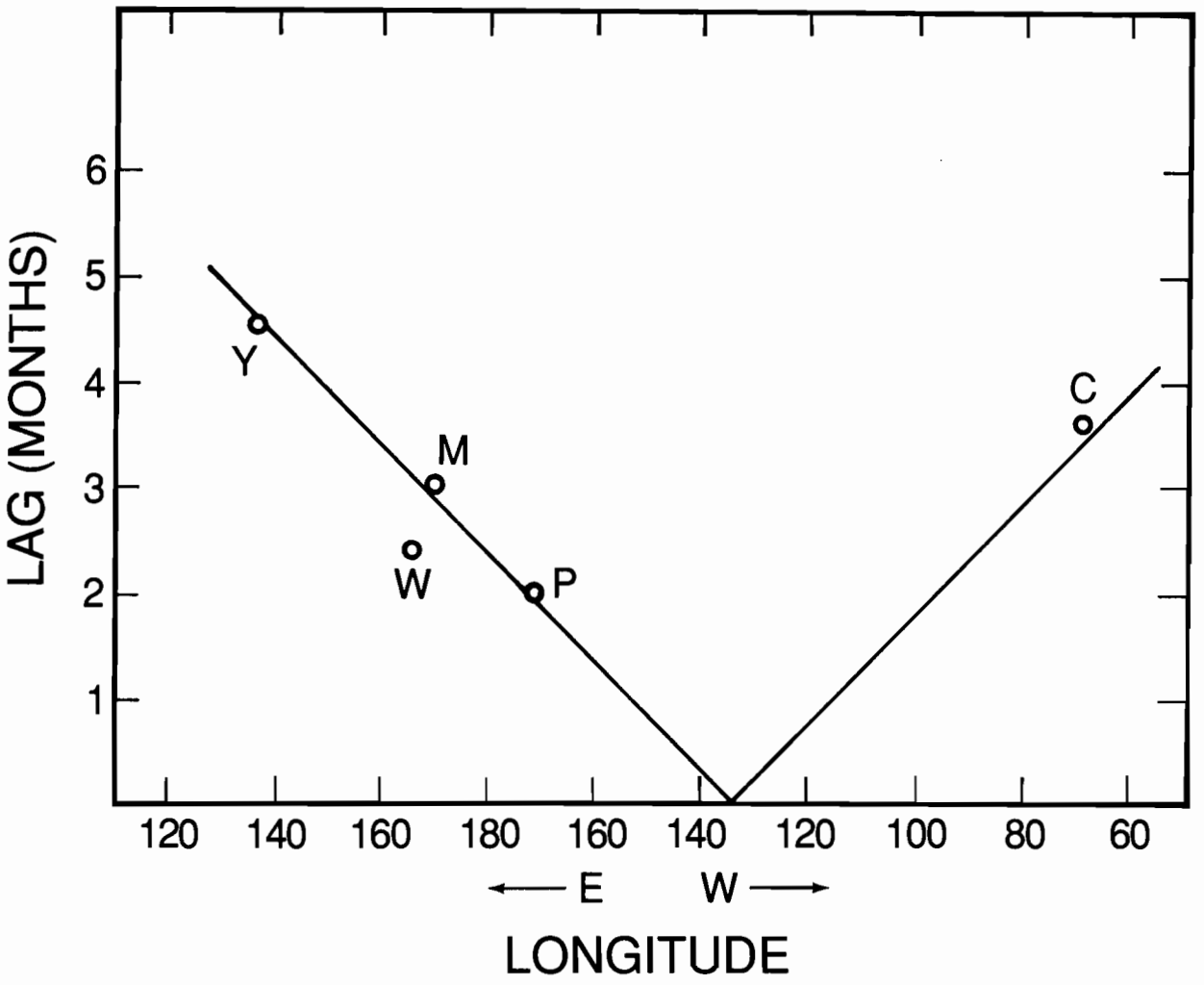

Figure 3. Lag of maximum correlation in the mid-troposphere as a function of station longitude for Yap, Majuro, Wake Island, Pago Pago, and Curacao. The straight lines have slopes of 0.8 meters per second at the equator.

The variation with height is somewhat similar to the height variation of the correlation patterns illustrated in Figure 2, and suggests that the trends seen in the atmosphere may reflect a warming trend in the tropical Pacific during the 1966-82 time period. The cause of such a warming is a matter for speculation.

CONCLUSIONS

(1) The signals of tropospheric warming and stratospheric cooling that accompany El Nino events are clearly evident in tropical radiosonde data, and appear to propagate both westward and eastward from a center near 135°W at a speed of about 0.8 m s^{-1}.

(2) The relative importance of dynamical (Walker and Hadley circulations) and radiative (extensive cirrus sheets) effects in producing the signal needs to be determined.

(3) Long-term trends in atmospheric temperature over the period 1966 to 1982 are consistent with an overall warming of the tropical Pacific.

(4) Extension of the analysis to study (a) the characteristics of the signal at other tropical

and extratropical locations, (b) the behavior of the signal at earlier times, before 1966, and (c) the existence of a corresponding signal at intraseasonal frequencies, is being planned.

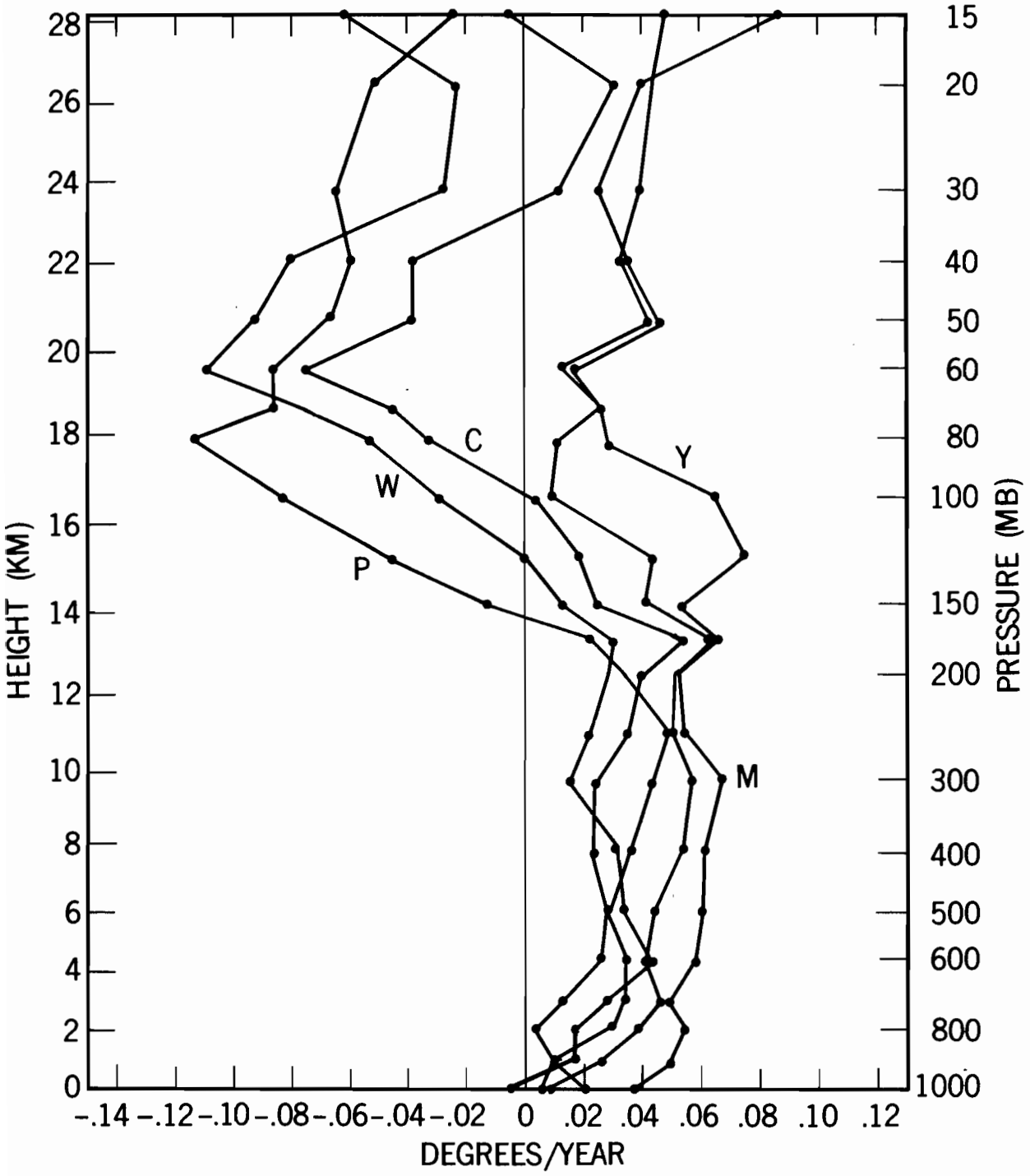

Figure 4. Slopes of the linear trend in temperature anomaly at the 5 stations during 1966-82.

REFERENCES

Reid, G.C., K.S. Gage, and J.R. McAfee, The thermal response of the tropical atmosphere to variations in equatorial Pacific sea-surface temperature, *J. Geophys. Res.*, in press, 1989.

Weare, B.C., An extension of an El Nino index, *Mon. Wea. Rev.* **114**, 644-647, 1986.

Weare, B.C., A.R. Navato, and R.E. Newell, Empirical orthogonal analysis of Pacific sea surface temperatures, *J. Phys. Oceanogr.* **6**, 671-678, 1976.

Multi-scale Processes in the Equatorial Western Pacific

Chung-Hsiung SUI[1] and Ka-Ming LAU

Laboratory for Atmosphere, NASA/Goddard Space Flight Center
Greenbelt, MD 20771 - U.S.A.

1. Introduction.

Recent modeling and observational studies reveal that intraseasonal oscillation (ISO) in the tropical atmosphere contains higher frequency components. Nakazawa (1989) found that convection associated with intraseasonal oscillation tends to appear in organized synoptic-scale complex systems (or called super cloud clusters SCCs). It is also known that the surface easterly trade winds over the western and central Pacific often reverse to fluctuating strong westerlies. These energetic fluctuations are known as "westerly wind bursts" (WWB). Studies by Keen (1982, 1987), Luther et al. (1983) and Murakami and Sumathipala (1988) showed that WWBs tend to be modulated by annual as well as interannual variabilities.

Lau and Chan (1988) suggested that the ISOs may act as a trigger to the development of ENSO. On the other hand, it has also been speculated that energetic WWB over the western and central Pacific may play an important role at the onset stage of ENSO (e.g. Keen, 1982, 1987; Luther et al., 1983; *etc.*). Based on the above and other studies, Lau et al. (1989) proposed that a unifying theory of the tropical climate system should include ISO, SCC and WWB as the intermediate to high frequency components. Their results show that the intermediate to high frequency variabilities are linked to the warm water region of the open ocean of the western Pacific.

The general goal of this study is to seek a better understanding of the multi-scale processes involved in the western equatorial Pacific. The results can provide an observational basis for the design of the implementation phase of the upcoming Tropical Ocean Global Atmosphere/Coupled Ocean-Atmosphere Response Experiment (TOGA/COARE) planned in 1992-1993. Most of the results of the present paper are based on data obtained from the first Special Observing Period (5 January to 4 March 1979) of the First GARP Global Experiment (FGGE).

2. Seasonal variations.

Monthly mean maps of convection and SST for December 1978, January and February 1979 are shown in figure 1. The deepest convection (represented by averaged Ic>2) forms in the equatorial belt (shaded areas) and is generally found over the areas of warmest SST which are located slightly south of the equator. There are broad agreement between the area of warmest SST (>29°C) and regions of deep convection over the open ocean regions (160°E-170°W). The region of warmest SST over the western Pacific expand eastward in concert with the increased area of deep convection from December to January. The center of Ic near 130°-140°E shifts over the Gulf of Carpentaria signalling the development of the Australian monsoon.

1. NCR-NASA Resident Research Associate

ORSTOM
CENTRE DOCUMENTATION
Montpellier

F 30260

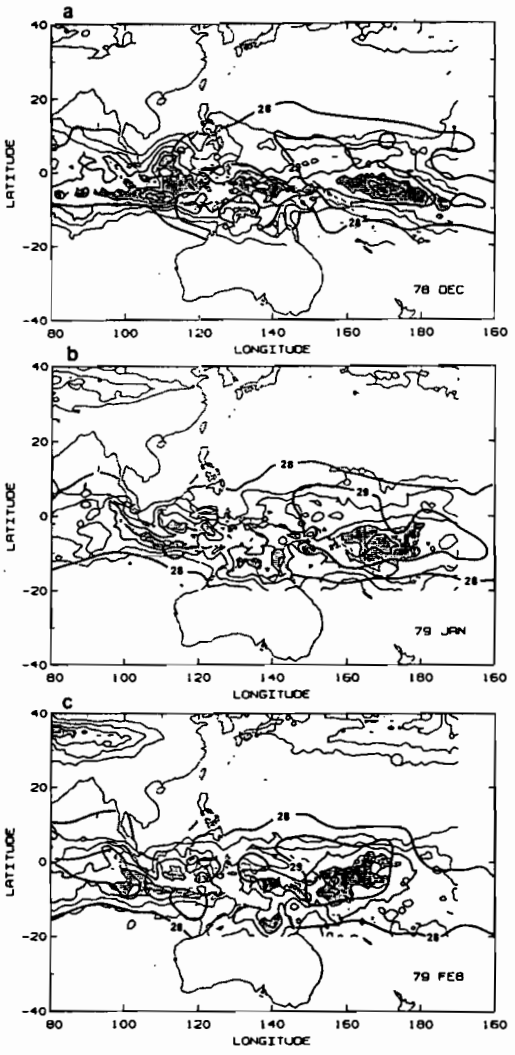

FIG.1. Monthly mean SST (heavy contour lines, interval is 1°C) and convection index, Ic (contour interval is 0.5 and the shaded regions indicate Ic ≥ 2) for (a) December, 1978; (b) January, 1979; and (c) February, 1979.

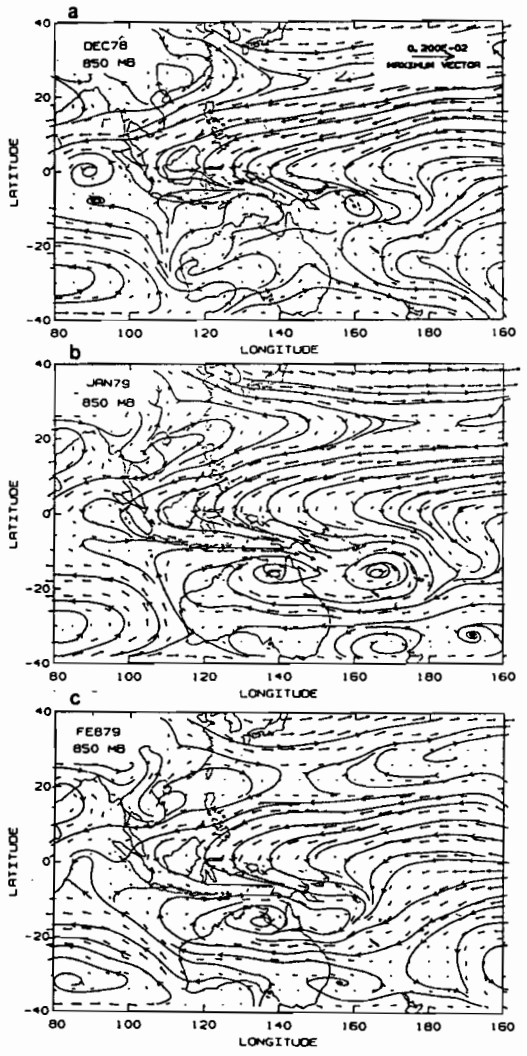

FIG.2. Monthly mean horizontal wind and streamline at 850 mb for (a) December, 1978; (b) January, 1979; and (c) February, 1979.

Corresponding to the strong convective heating, centers of equatorial cyclonic flow are formed at 850 mb (Fig.2). The 850 mb flow indicates very strong and persistent easterly wind over the western Pacific from the equator to 20°N throughout the season. The cyclonic circulation with centers over the gulf of Carpentaria and the western Pacific are most conspicuous during January associated with the development of Australian monsoon.

The onset of the Australian monsoon is often characterized by a sudden development of low-level westerlies between the equator and 10°S during late December or early January. This is clearly illustrated in figure 3 which shows the time-height distribution of averaged zonal wind between 110° and 140°E at 10°S. The sudden establishment of westerly winds in the lower troposphere started around December 22. The westerly winds persisted for over two months with a break from February 10 to 16. Easterly winds prevailed in the upper troposphere after the onset of monsoon.

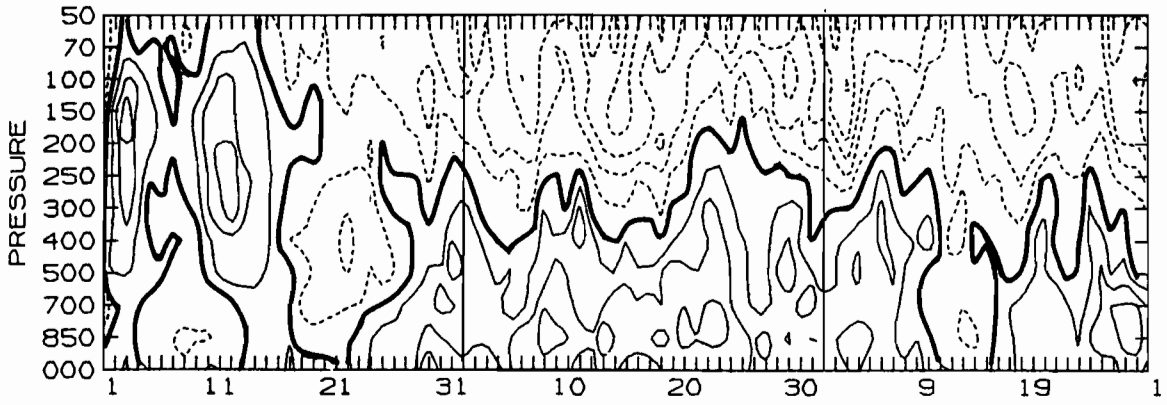

FIG.3. Time-height distribution of averaged zonal wind between 110° and 140°E at 10°S. Contour interval is 4 m s^{-1}.

Once westerlies are established in the near-equatorial trough (0°-10°S), strong convective systems tend to develop in this area. The accumulative rainfall rate at Darwin shown in figure 4 indicates that a large part of monsoon rainfall is due to a few heavy precipitation events. The first heavy precipitation occurred at December 26 at the time of the onset followed by a second event near January 2. A third event occurred around January 7 and lasted for several days. During the monsoon break (February 10-18), the cumulative curve remained essentially flat indicating very little precipitation occurred during this period.

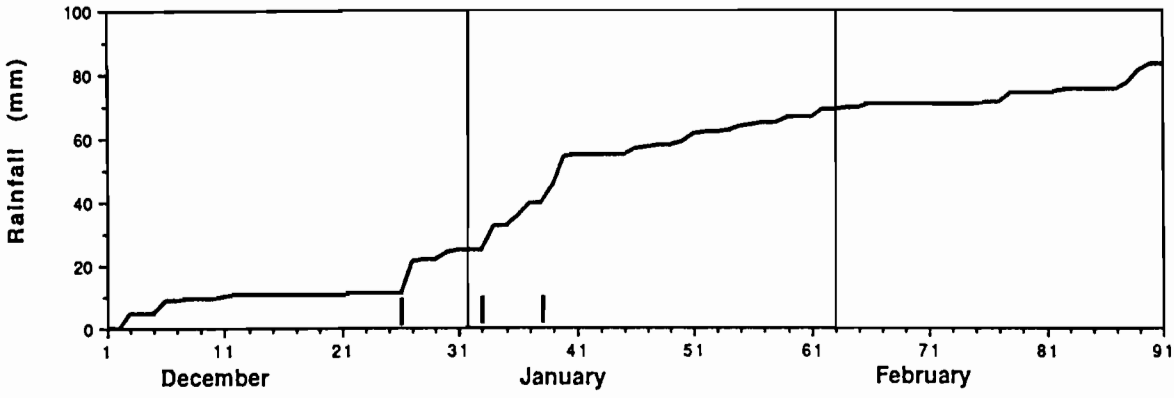

FIG.4. Accumulative rainfall at Darwin (12.42°S, 130.87°E).

3. Subseasonal scale variabilities.

During the three-month period, there are two predominant eastward-moving intraseasonal signals shown in the time-longitude section of the averaged Ic (over 4° latitude by 5° longitude grid boxes) centered at 10°S (Fig.5). These two intraseasonal disturbances consist of several "super cloud clusters". Here a SCC is loosely defined as an ensemble of deep convective clouds represented by the averaged Ic larger than certain threshold value. The threshold value is chosen as 3.5 in figure 5.

During mid-December of 1978, the first SCC is detected over the Indian Ocean near 90°E longitude (labeled A1). The disturbance moved eastward to northern Australia (120°-140°E) where a strong SCC (labeled A2 associated with the Australian monsoon developed in late December. The average eastward-moving speed of SCC A2 is about 3.75° longitude day^{-1}. The intraseasonal disturbance was interrupted by a westward-moving SCC (labeled B1) near 160°E at January 5. The latter is first observed

near the date line and propagates westward with a phase speed of approximately 6° longitude day^{-1}. There appears to be an apparent enhancement in the convection as the two SCCs meet near 160°E. The two disturbances re-emerge after their brief encounter. SCC B1 moves westward rapidly and disappeared near 120°E after January 10 while SCC A2 continues its eastward migration while a new SCC (labeled A3) is developed downstream near the date line from 10 to 20 of January.

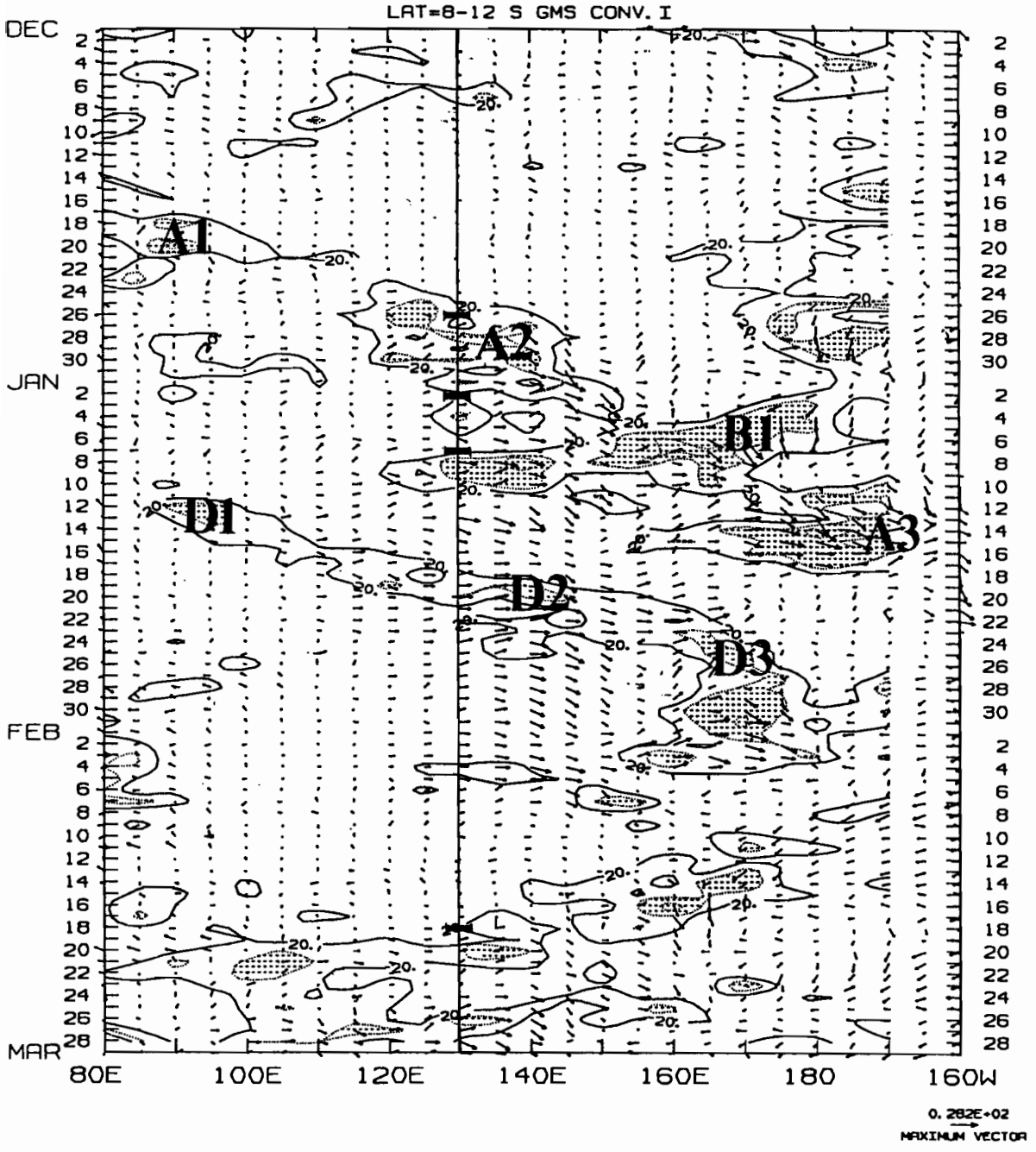

FIG.5. Time-longitude distribution of Ic and 850 mb wind at 10°S. Data resolution is 4° latitude by 5° longitude and 24 hourly. The minimum Ic plotted is 2 and contour interval is 1.5. Dotted regions indicate Ic ≥ 3.5.

The second intraseasonal disturbance appeared at 90°E about 20 days following the first disturbance (around January 12). It maintained a continuous band of moderate convective activity from the Indian ocean to 170°E from its first inception to late January and early February. The average speed is about 6.15° longitude day^{-1}. A stationary SCC (labeled D3) was fully developed by February 1. From here on to the end of February, the centers of convection retreated westward to the maritime continent. This large scale east-west migration of convection from December to February seems to be consistent with the seasonal variation of the warm SST noted in figure 1. Thus it appears that while the ISO possesses low frequency variation of its own, it seems to be phase locked to the SST seasonal variation.

The relationship of the ISOs and the phase of the Australian monsoon is particularly interesting. A vertical line drawn along 130°E in figure 5 intersects the 2.0 Ic contour near December 26, January 2, January 7 and February 18 which coincides remarkably with the abrupt steep slopes in the cumulative rainfall time series in the vicinity of Darwin (Fig.4). Thus the large fluctuation in rain fall over Darwin during the monsoon season is not entirely a local phenomena but rather should be considered as a local manifestation of a large scale phenomenon which possesses many spatial and temporal scales.

We next examine the lower tropospheric circulation associated with the SCCs. The time-longitude section of 850 mb zonal wind at 10°S is also shown in figure 5. Over the region 120° E to 180° westerly winds were found after the onset of the Australian monsoon near the last week of December to the end of February. These westerly winds fluctuate in accord with the passage of SCCs over the region. Most notably is the episodic eastward extension of a tongue of strong westerly winds to the western Pacific during January 12-18 and January 30 to February 4 respectively. The location and duration of these westerly events are consistent with those for WWBs defined by Keen (1987). These two events will be referred to as WWB1 and WWB2 hereafter. Maximum westerly winds of over 25 ms^{-1} are found during the peak for both events. The region of maximum westerly wind appear to agree very well with centers of the SCCs. The westerly wind leading up to the WWB1 can be traced to the onset of the Australian monsoon. For WWB2 the westerly wind axis can be tracked to 110°E near January 16. One of the most important message from figure 5 is that the WWBs and SCCs are not isolated or random events that all happen to be found in the western Pacific, but rather they are parts of a closely related and interacting system of many different scales.

4. Propagation and structure of ISO in relation to WWB.

In this section we investigate the large scale circulation and convection pattern associated with the ISOs leading up to the maximum low level westerly wind in WWB1 and WWB2. The important features of sequence of events for WWB1 and WWB2 are similar. For brevity, only the WWB2 is discussed here. Figures 6 a-d show the horizontal distribution of Ic and 850 mb wind at every 5 day intervals starting from January 15 till January 30. A five-day equal-weight averaging is applied to the data to emphasize the ISO signal.

The systematic eastward propagation of SCCs D1, D2, D3 from 100°E at January 15 (Fig. 6a) to 165°E at January 25 (Fig.6c) is obvious. Between January 25-30, the SCC appears quasi-stationary. This sequence should be compared with that shown in figure 5. Strong westerly winds are often found along 10°S sandwiched between two cyclonic inflow regions to the west of the SCC. It is noted that the region of westerly wind is quite extensive in longitude but the convection appear to be confined mostly to the eastern terminus of the region of westerlies.

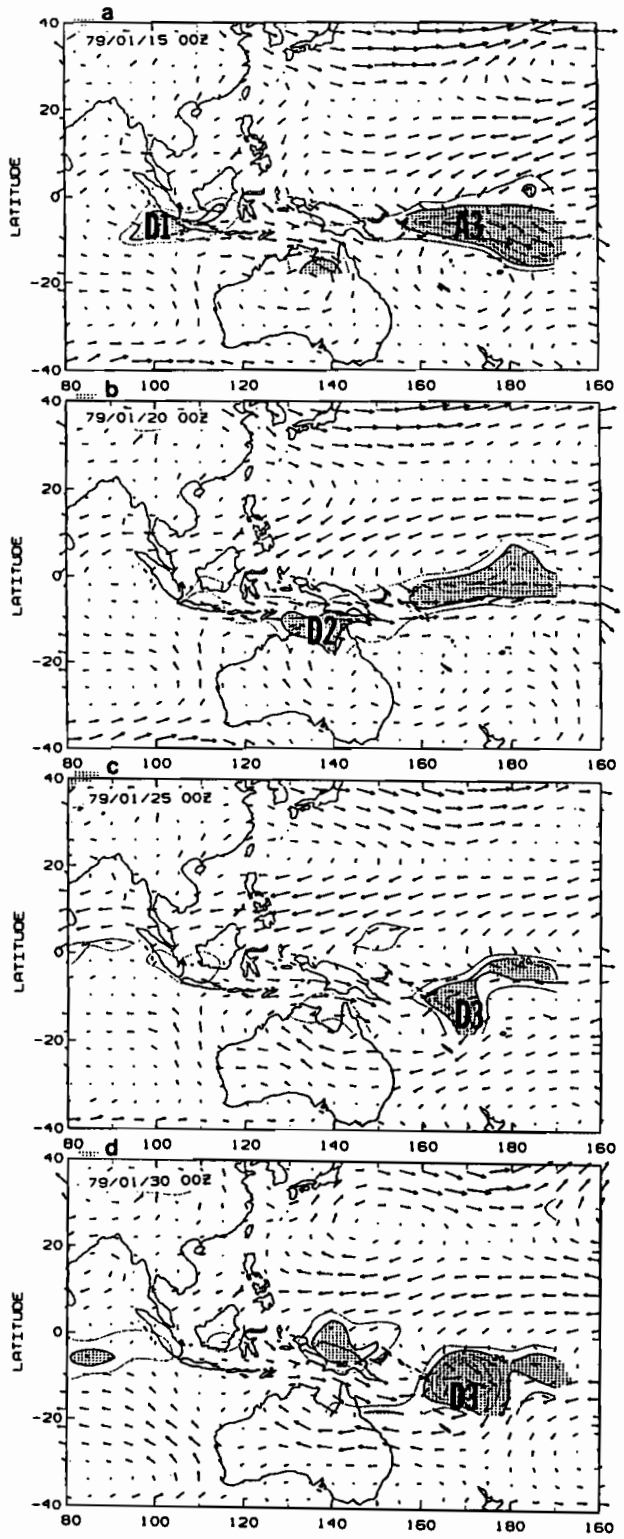

FIG.6. Horizontal distributions of Ic and 850 mb wind averaged over five day periods centered at (a) 00Z 15 January, 1979; (b) 00Z 20 January, 1979; (c) 00Z 25 January, 1979; and (d) 00Z 30 January, 1979. Contour interval of Ic is 0.5 and the shaded regions indicate Ic $\geq$ 2.

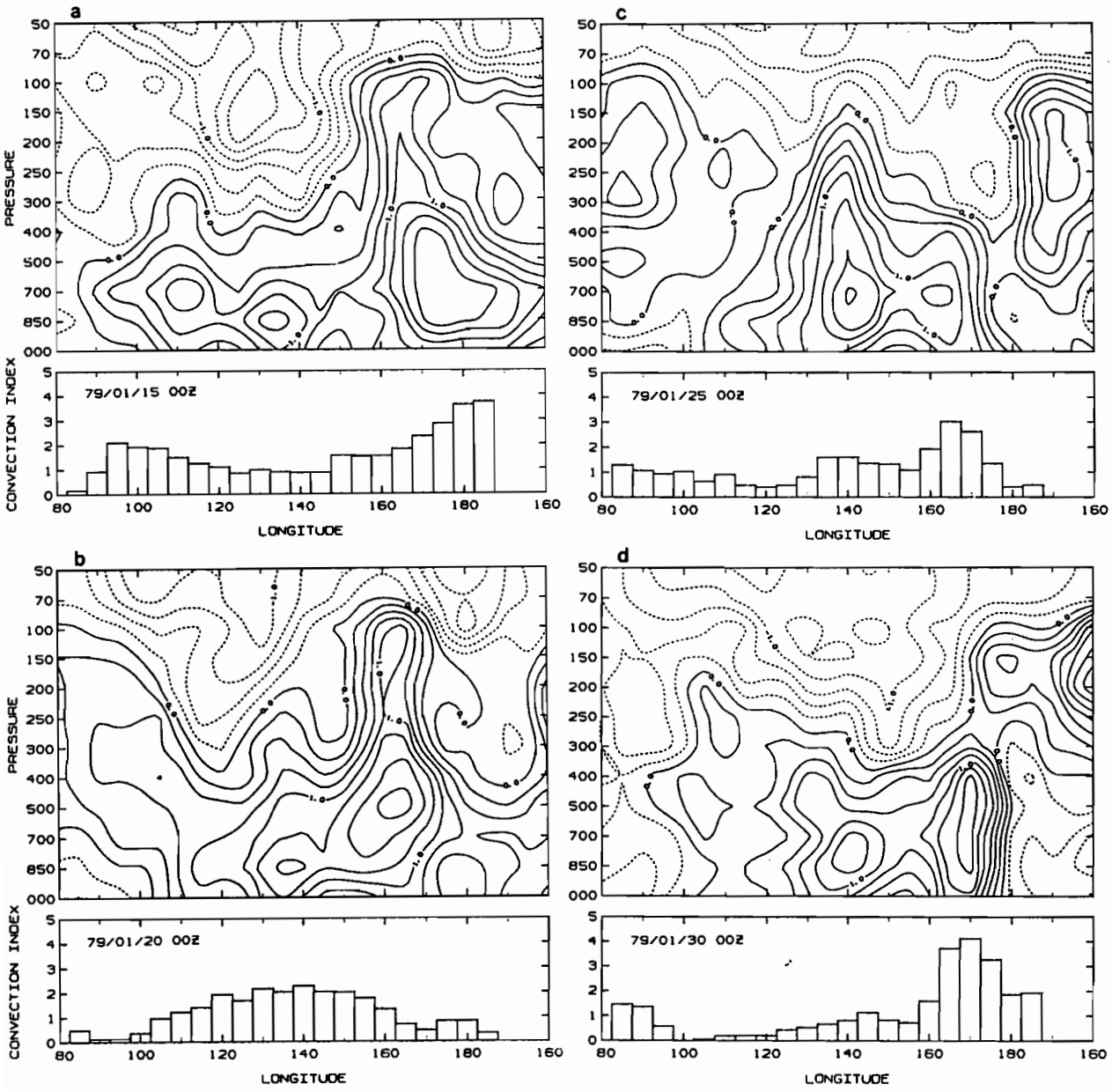

FIG.7. Vertical-zonal distribution of five-day mean zonal wind (upper) and zonal distribution of Ic (lower) along 10°S, respectively, for (a) 00Z 15 January, 1979; (b) 00Z 20 January, 1979; (c) 00Z 25 January, 1979; and (d) 00Z 30 January, 1979.

The vertical distribution of zonal wind along 10°S for WWB2 is shown in figures 7 a-d. The most conspicuous feature shown in figure 7 is the eastward moving baroclinic structure associated with the ISO. As noted before on January 15, major convective centers (D1 and A3) are found in the two extreme ends of the westerly wind belt. This period corresponds to the maximum development of WWB1 and the beginning phase of WWB2. We shall focus on the development associated with D1 in the following

discussions. The strong westerly wind in the lower troposphere is capped by easterly wind above 400 mb near 110° (Fig. 7a). The convective center D1 moves to 140° E at January 20 with the low level westerlies consolidating over a rather extensive region of above-normal convection. At about 160°E, the westerly wind extends throughout the troposphere and appears to have an equivalent barotropic structure above 700 mb with the upper troposphere westerlies. At this point, while the convection appears to be related to the low level westerly wind, it does not appear to have a strong control on the large scale circulation as evidenced by the presence of the transient barotropic structure of the disturbance decoupled from the region of enhanced convection. As the convection moves to 165°E 5 days later, it begins to intensify. The direct control of convection on the circulation can be seen by the marked change in the vertical structure of the zonal wind. Here, maximum low-level westerly wind is found at low level and to the west of the convection center D3. The low level westerlies has a wavy structure with two maxima separated by about 20° in longitude. A region of weak easterly wind appears below 700 mb east of the date line indicating strong low level convergence near 170°E. The upper level easterly wind over the region of the SCC suggests a first baroclinic mode with a weak westward tilt with height. This strongly signals an interaction between the circulation and latent heating for propagating unstable modes as discussed in Lau and Peng (1987)'s theory of ISO. At the peak of WWB2 (Fig. 7d), ISO becomes stationary (see Fig.5). The vertical structure of the zonal wind indicates a very strong low level convergence with the strongest westerly wind over the center of the SCC D3 near the date line. The distribution of zonal wind in the vertical plane and the absence of a vertical tilt in the wave axis are consistent with the appearance of stationary modes forced by latent heating (cf. Chang and Lim, 1988).

5. Summary and Discussion.

In this study, we have systematically analyzed the features of multi-scale processes over the western Pacific region using observations collected during winter of the FGGE year. Generally speaking, intraseasonal oscillations are composed of a series of cloud clusters. These cloud clusters tend to organize into a synoptic scale (called super cloud clusters) when subject to favorable large-scale conditions like in the monsoon trough region or over the warm pool of the ocean. The circulation induced by convective heating is characterized by strong low-level convergent flow with asymmetric zonal winds, i.e. stronger westerly flow to the west of heating and weaker easterly flow to the east of heating.

Approaching the warm pool of the western Pacific, eastward-moving SCCs tend to slow down and intensify. Besides eastward-moving SCCs, westward-moving SCCs are also excited over the warm pool in the western Pacific. These SCCs have strong low-level cyclonic vorticity and dissipate quickly once move out of the source region. These features are consistent with the "Rossby wave-shed off" within the mobile Wave-CISK mechanism as suggested in Lau et al. (1989).

The frequency and intensity of SCCs and westerly wind bursts revealed in this study suggest that it is important to include them in the study of low-frequency climate variability. It is also essential to understand and simulate the basic equilibrium state of the oceanic mixed layer and their changes to the impact of SCCs and westerly wind bursts in order to obtain a realistic feedback between the ocean and the atmosphere.

REFERENCES

Chang, C.P., and H. Lim, 1988: Kelvin wave-CISK: a possible mechanism for the 30-50 day oscillations. *J. Atmos. Sci.*, **45**, 1709-1720.

Keen, R.A., 1982: The role of cross-equatorial tropical cyclone pairs in the southern oscillation. *Mon. Wea. Rev.*, **110**, 1405-1416.

Keen, R.A., 1987: Equatorial westerlies and Southern Oscillation. Proceedings of the US TOGA western Pacific air-sea interaction workshop. September 16-18, Honolulu, Hawaii.

Lau, K.M., and P. Chan, 1988: Intraseasonal and interannual variations of tropical convection: A possible link between the 40-50 day oscillation and ENSO? *Mon. Wea. Rev.*, **45**, 506-521.

Lau, K.M., and L. Peng, 1987: Origin of low frequency (intraseasonal) oscillations in the tropical atmosphere. Part. I: the basic theory. *J. Atmos. Sci.*, **44**, 950-972.

Lau, K.M., L. Peng, C.H. Sui and T. Nakazawa, 1989: Super cloud clusters, westerly wind burst, 30-60 day oscillations and ENSO: An emerging unified theory. (submitted to *J. Meteor. Soc. Japan).*

Luther, D.S., D.E. Harrison and R.A. Knox, 1983: Zonal winds in the central equatorial Pacific and El Nino. *Science*, **222**, 327-330.

Murakami, T., L.X. Chen and A. Xie, 1986: Relationship among seasonal cycles, low-frequency oscillations and transient disturbances as revealed from Outgoing Longwave radiation data. *Mon. Wea. Rev.*, **114**, 1456-1465.

Murakami, T., and W.L. Sumathipala, 1988: Westerly bursts during the 1982/1983 ENSO. To be submitted to *J. of Climate.*

Nakazawa, T. 1988: Tropical super clusters with intraseasonal variations over the western Pacific. *J. Meteor. Soc. Japan.*, **66**, 823-839.

Diagnostic Studies of Pacific Surface Winds

Stephen E. ZEBIAK

Lamont-Doherty Geological Observatory
Palisades NY 10964 - U.S.A.

ABSTRACT

Analyses are performed using surface winds derived from the FSU Pacific pseudo-stress fields. Vorticity budget calculations reveal the relative contributions of various terms, and allow simplification of the full momentum equations. Based on the simplified equations, a procedure is developed for estimating surface pressure, and then adjusting the winds. Finally, the winds and pressure are used to infer boundary layer and upper level forcing, within the context of particular model formulations. The results reveal deficiencies in these models, and suggest a convective heating structure different from what is often assumed.

1. Introduction

The importance of surface winds has long been appreciated in the context of the general circulation of the world's oceans, but recently has been underscored by developments in the theory and modeling of tropical ocean-atmosphere interaction. As the primary agent of communication between atmosphere and ocean, surface winds must be considered an essential component of all long-term climate variability. Yet, until recently, the surface wind field over the oceans has received relatively little attention. Fortunately, recent efforts have resulted in substantial improvements in operational surface wind analyses (Trenberth and Olsen,1988), and also in the reworking of historical ship winds using more complete data sets and new analysis procedures. The problems are still many: evidence of artificial trends (Ramage,1987; Wright,1988; Posmentier et al.,1989; Cardone et al.,1989), and large data gaps in both space and time, even in current analyses. Despite such difficulties, many of these products have been used to drive ocean model simulations with notable success (e.g.,Philander and Seigel,1985; Seager,1989; Harrison et al,1989), implying that they are indeed capturing salient features of the real variability.

We might then expect that the same products, even with their limitations, could be useful in evaluating different conceptual scenarios represented in recent atmospheric modeling studies. We could ask, for example, whether some of the simplifications of these models are justified in the context of "observed" surface winds. If so, then perhaps something can be learned about systematic model errors in terms of parameterized forcing functions. These were the motivations for the present study. The data source is the FSU tropical Pacific analysis product (Goldenberg and O'Brien, 1981), which spans the period from 1961 to present. The choice is arbitrary; other products could (and ultimately should) be used for the same purpose. Since most of the results appear to depend on very general properties of the wind fields, and not details, it seems likely that similar findings would be obtained with other products.

The study consists of three parts. First, a vorticity budget calculation is done, as a means to evaluate the relative importance of various terms, especially those that are neglected in most simple models. This calculation also affords the opportunity to make an indirect assessment of the

ORSTOM
CENTRE DOCUMENTATION
Montpellier

F 30264

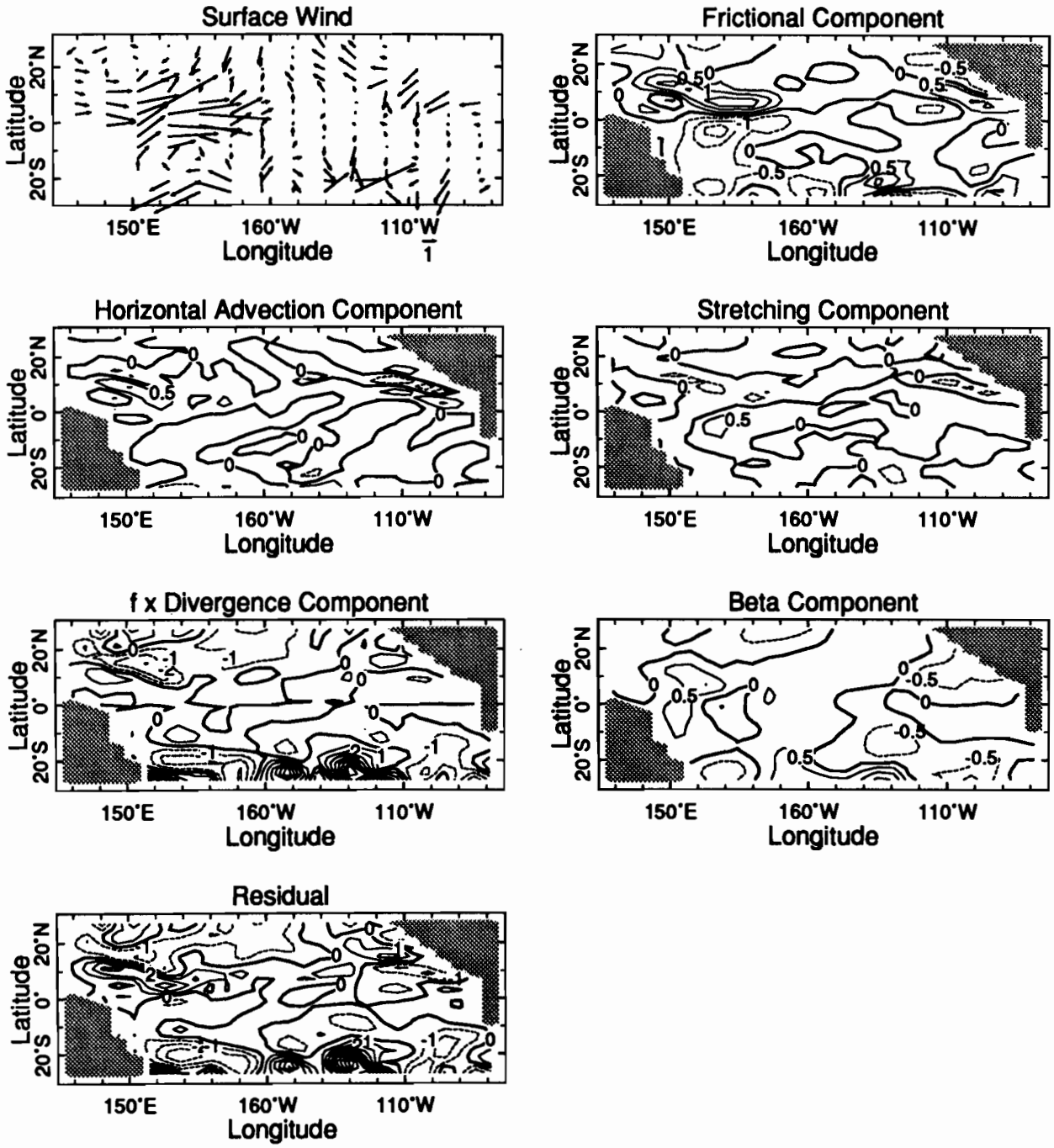

Fig. 1. Surface wind anomalies, and the component terms of the vorticity budget (Eq. 1), for July 1982.

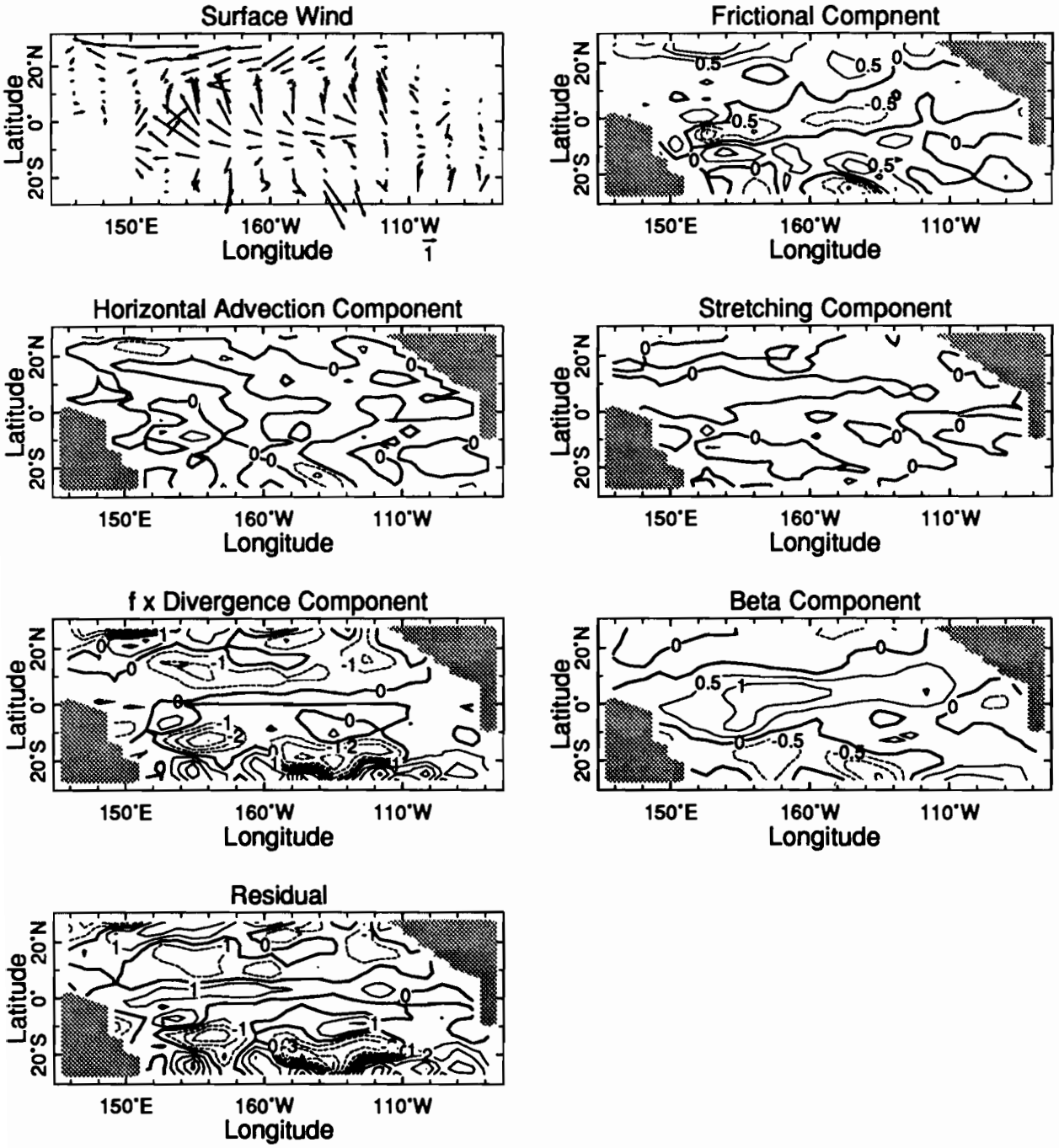

Fig. 2. As in Fig. 1, except for March 1985.

data quality, as will be shown below. Secondly, we present an algorithm for estimating surface pressure fields from the winds, and make some comparisons with observed surface pressure. From the pressure field, it is posible to calculate a modified, and dynamically consistent wind field. This procedure selectively filters out certain "noisy" (and unrealistic) features in the divergent component of the winds, while reproducing most other characteristics closely. Thirdly, the combined wind and pressure fields are used to test particular models, and to infer the structure of forcing functions that would give the "correct" surface winds. The study focuses primarily on (monthly) anomalies; ENSO variability is thus the dominant signal being analyzed.

2. Vorticity Budget

We start with the vorticity equation in the following form:

$$u\zeta_x + v\zeta_y + \zeta\delta + f\delta + \beta v + F = R, \tag{1}$$

where ζ and δ are the vorticity and divergence, respectively, f is Coriolis parameter, β its latitudinal gradient, F is the curl of the frictional force, and R a residual. In spherical coordinates, $x=a\cos(\theta)\phi$ and $y=a\theta$, where a is the earth's radius and θ and ϕ measure latitude and longitude, respectively. The residual R contains the effects of time dependence and transients, vertical advection, the nonlinear curvature terms, and errors. For the monthly mean fields being analyzed, most of these can safely be regarded as small. The possible exceptions are the error terms, and transient forcing. Note that errors can arise from the parameterization of F, as well as the data itself.

Two forms were investigated for the frictional stresses: a linear and a quadratic drag. The former is commonly used, though the latter is formally better justified. Near the surface, such parameterizations should be appropriate, whereas, if dealing with depth-averaged winds over a deeper layer, the effects of vertical structure within and above the boundary layer would become important. In fact, the results proved to be insensitive to which form was used, so we will describe here the results using the linear form. For this case, $F=\varepsilon\zeta$. Unless stated otherwise, the dissipation time (ε^{-1}) is taken to be 1 day.

The monthly FSU data are produced on a 2° latitude by 2° longitude grid between 29°S and 29°N, 124°E and 70°W. These fields were first smoothed with a 1-2-1 filter in time and space, interpolated to a coarser longitudinal grid (5.625° intervals, as used by the models to be described below), and then the terms in (1) evaluated, for each month of the data set. (As a check, some of the calculations were repeated with unsmoothed fields; none of the results changed significantly.) Representative cases are shown in Figs. 1-2.

July 1982 (Fig. 1) represents the beginning phase of the major warm event of 1982-1983. As is typical of antecedent periods, strong westerly anomalies appear in the western Pacific, from the equator northward. There is little signal in the eastern Pacific, and a rather incoherent pattern of anomalies in the southern subtropics. The frictional stress curl (which in the linear case is proportional to the vorticity anomaly) features a large dipole pattern in the west Pacific in the vicinity of the westerlies, and smaller, less coherent pattern elsewhere. In comparison, the zonal and meridional advection terms (displayed together in Fig. 1c) are small, and rather "noisy". The same is true for the $\zeta\delta$, or stretching term. On the other hand, the $f\delta$ term is very large, especially in the subtropical latitudes, where already sizeable divergence anomalies are amplified most. In the equatorial region the field is more coherent, and roughly in quadrature with the vorticity field, as might be expected. The βv term is slightly smaller in magnitude than the frictional term, but larger than the nonlinear terms; moreover, its spatial structure is unique in being coherent over large meridional regions spanning the equator. Unfortunately, the residual term is as large or larger than any other, but inspection reveals that its structure is almost identical to the $f\delta$ term. A reasonable hypothesis is that the divergence field contains spurious features that cannot be

balanced by the remaining terms.

March 1985 represents approximately the opposite phase of ENSO; there were anomalously cold sea surface temperatures and strong equatorial easterlies (Fig. 2). Southerly anomalies across the normal ITCZ position indicate its northward displacement. Despite the very different conditions, the same conclusions follow with respect to the relative contributions of vorticity budget terms. The nonlinear terms are small, and the $f\,\delta$ term is largely unbalanced.

In order to make a more general assessment of the vorticity budget, the root-mean-square (RMS) of the various terms were computed, based on all spatial points and all months between 1970 and 1988. Once again, the nonlinear terms are seen to be the smallest contributions, and the $f\,\delta$ and residual terms are more than twice as large as the next largest terms (Table 1). As a test, the residual was recomputed with the nonlinear terms removed; this resulted in a *reduction* of the residual. Our interpretation is that these terms are incorrectly represented due to the data quality combined with the amplifying effect of second order differentiation. In any case, it is clear that they play a minor role in the budget.

The size of the residuals in these calculations is alarming. The fact that the structure of the residual field is very similar to that of $f\,\delta$ suggests that the source of the imbalance is data errors, and not some other term excluded from the budget. This is reinforced by additional calculations with the $f\,\delta$ term artificially reduced. In all cases, this resulted in a proportional reduction in the residual, as would be expected if this term were largely unbalanced by any other. We note that similar calculations were carried out with other terms suppressed: the residuals either increased or were unchanged. Also, the frictional parameter ε was varied over a considerable range. Probably due to the overwhelming imbalances from other sources, the sensitivity of the residual to this parameter was rather low, but the "best" values were in the range of $1 day^{-1}$. Replacing the linear frictional form by a quadratic one produced no detectable difference.

3. Pressure Field Estimation

The results so far indicate that the nonlinear terms of the surface momentum balance are of secondary importance. On the other hand, the remaining linear terms do not balance, even approximately, based on the wind data. Is the problem just data errors, or something more? One way to attack this question is to assimilate the data into a model based on the linear equations, and determine whether the differences between the two are within expected limits of uncertainty. We did this by using the winds to estimate the surface pressure field, and then reconstructing the winds from the pressure in accordance with the governing equations. This approach, by definition, yields a dynamically consistent combined wind-pressure set.

The linear momentum equations may be written as follows:

$$\varepsilon u - f v = -p_x/\rho \tag{2a}$$

$$\varepsilon v + f u = -p_y/\rho, \tag{2b}$$

where p is the surface pressure and ρ the density. These equations imply a particular relation between the wind components which does not hold in the data, due to errors and neglected terms. Thus the pressure field is not uniquely determined. Our approach was to compute many estimates of the pressure field by integrating (2a-b) along different paths, and average them. The individual estimates were calculated as follows: for a particular latitude of the grid (the reference latitude), (2a) was integrated along the entire longitude range. Then, for each longitude, (2b) was integrated from the reference latitude northward and southward to the limits of the grid. By choosing all possible reference latitudes, 30 separate versions of the pressure field were produced. The final pressure field was then calculated as a weighted average of these, with the weighting proportional to $1/\sin\theta$. This was important because of the general increase of pressure

Data source	$\varepsilon\zeta$	$u\zeta_x+v\zeta_y$	$\zeta\delta$	$f\delta$	βv	R
Original winds	.50	.30	.15	1.28	.49	1.39
Adjusted winds	.47	.13	.06	.49	.39	.05

Table 1. Root-mean-square contributions of vorticity budget terms based on original and adjusted winds.

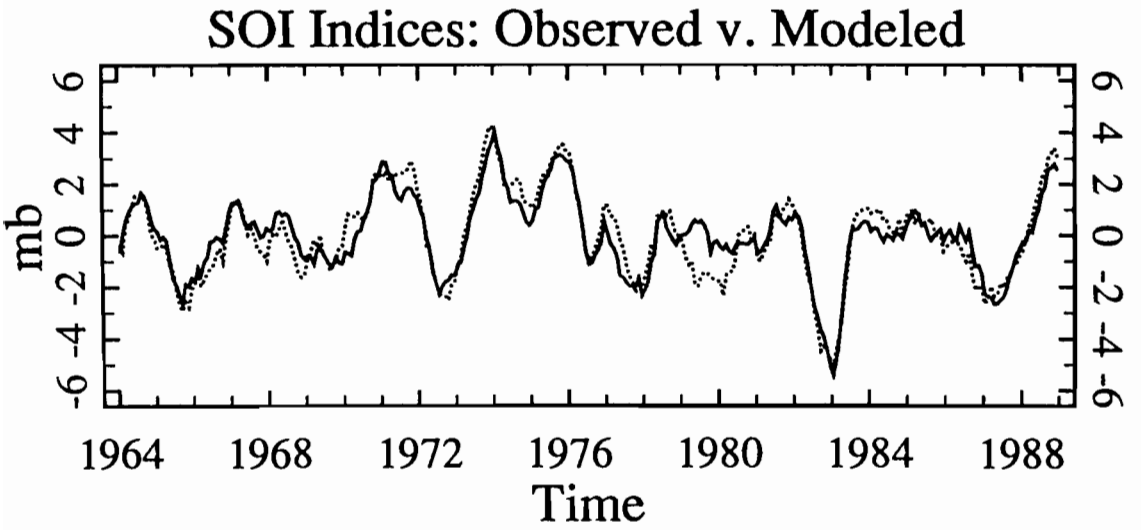

Fig. 3. Southern Oscillation Indices for the period 1964-1988, from pressure observations (solid line) and from pressure estimates based on surface winds (dotted line).

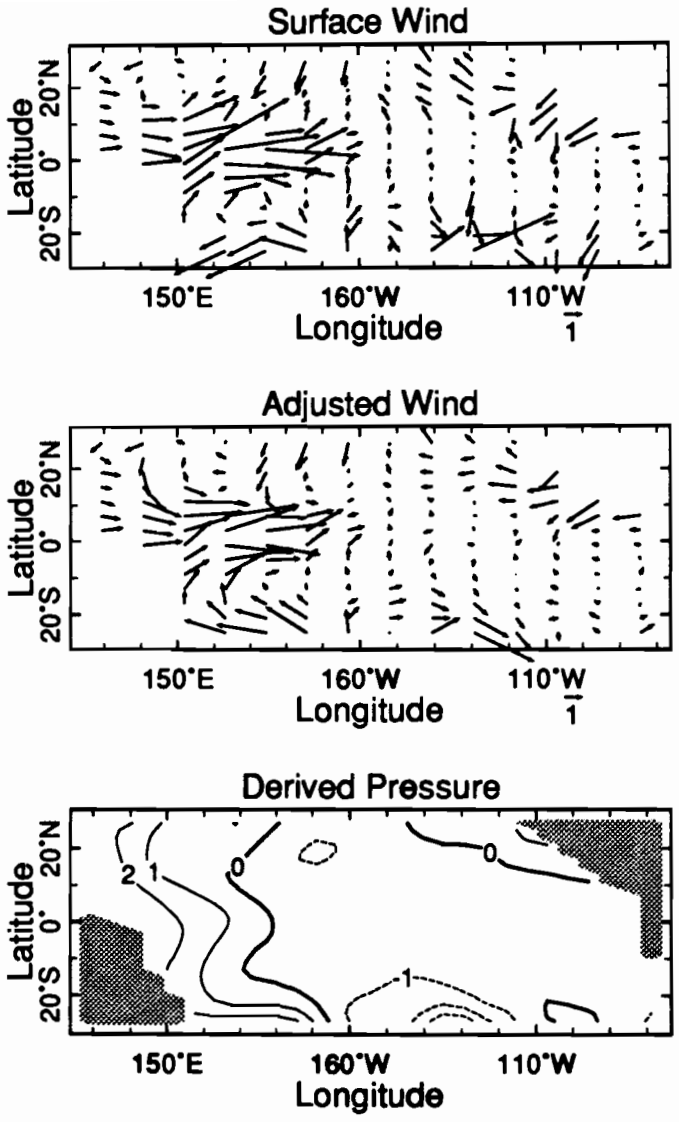

Fig. 4. Surface wind anomalies, estimated pressure anomalies, and adjusted wind anomalies for July 1982, derived using the procedure described in the text.

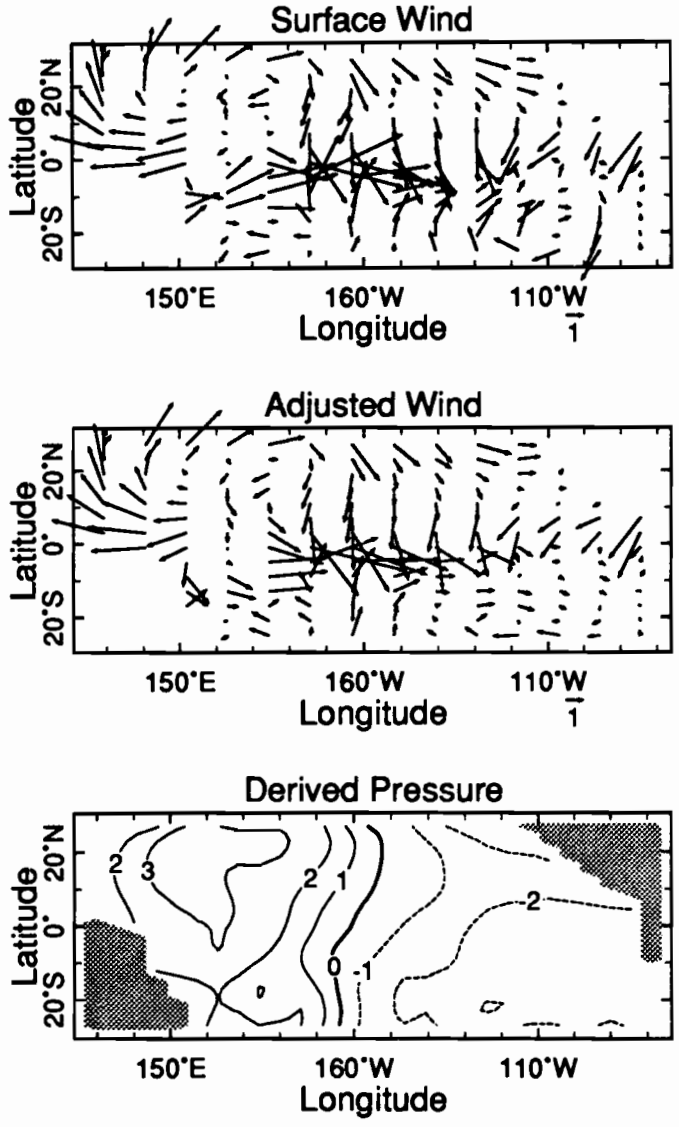

Fig. 5. As in Fig. 4, except for December 1982.

perturbations relative to wind perturbations at higher latitudes (in accordance with geostrophy). The normalization effectively gives equal weight to winds at all latitudes, and is consistent with a given uncertainty in the wind data, independent of position. Also, as the area-mean pressure is not determined by the wind field, it was arbitrarily set to zero.

Other schemes could easily be imagined for estimating the pressure field. For example, one could derive an equation for the Laplacian of pressure, and invert it. The advantage of the present scheme is that it relies on averaging and integrating: fundamentally stable operations that are not scale-sensitive. One expects such a procedure to minimize individual errors quite effectively in producing a "best guess" field.

An obvious test for the derived pressure fields is direct comparison with pressure data. We computed a Southern Oscillation Index based on derived pressure for the period 1964-1988 (Fig. 3). For the present purposes the index was defined simply as the monthly anomaly at Tahiti minus that at Darwin, with no normalization (thus it is an anomalous pressure difference). Comparison with the same index computed from observations shows a very close relationship. The only arguably significant discrepancy occurs in the 1979-1980 period, when the derived index shows a drop that is absent in the observed one.

Another means of testing the pressure fields is through reconstructing the associated wind fields. That is, using (2) and the derived pressure, one can calculate a modified wind field. This modified field will satisfy the linear vorticity balance, and will therefore differ from the original winds in certain ways. In order to judge the whole analysis reasonable, it should happen that the two wind fields show generally good agreement to within the uncertainty of the data, and that the differences are not strongly biased with respect to location (except possibly in very data poor regions).

The reconstructed winds were calculated for all months of the data set. They are presented along with the original winds and derived pressure fields for selected months in Figs. 4-7. For July 1982 (Fig. 4) the pressure field shows a strong zonal gradient in the equatorial west Pacific, extending poleward into the subtropics of both hemispheres. Also featured is a localized low in the vicinity of the cyclonic circulation in the southeastern region. The reconstructed winds are generally similar to the data, with all major features reproduced. The strength of the equatorial westerly anomalies are reduced slightly, as is the divergent component of v to the north. A notably large change is at the center of the cyclonic circulation near 25°S and 130°W: whereas the original wind field shows a somewhat chaotic and strongly divergent flow superimposed on a more coherent cyclonic circulation, the reconstructed field retains only the latter. This is typical of the sorts of changes found in the reconstructed fields; in many (but not all) instances, the changes are obvious improvements.

A mature warm event pattern is found in December 1982 (Fig. 5). The derived pressure field shows the quintessential Southern Oscillation pattern: a very large-scale dipole with centers in the western Pacific and southeastern Pacific. The two wind fields are similar except for the region near 10°S and 160°E, where the reconstructed anomalies are much weaker, and the meridional component is reversed. Also, the meridional component is generally weaker in the southeastern region; our guess is that the reconstructed version underestimates it in this case.

January 1984 presents a very different scenario: strong easterlies in the equatorial west Pacific, continued westerlies in the east, and very strong subtropical anomalies in both hemispheres (Fig. 6). The pressure field depicts a band of low pressure stretching across most of the subtropical southern region, extending all the way to the northern subtropics west of the dateline, with high pressure prevailing in the rest of the domain, and especially strong in the northeastern region. In this case, as the previous ones, the reconstructed winds match the original winds rather closely, with a slightly "cleaner" appearance due to the suppression of strongly divergent and incoherent features.

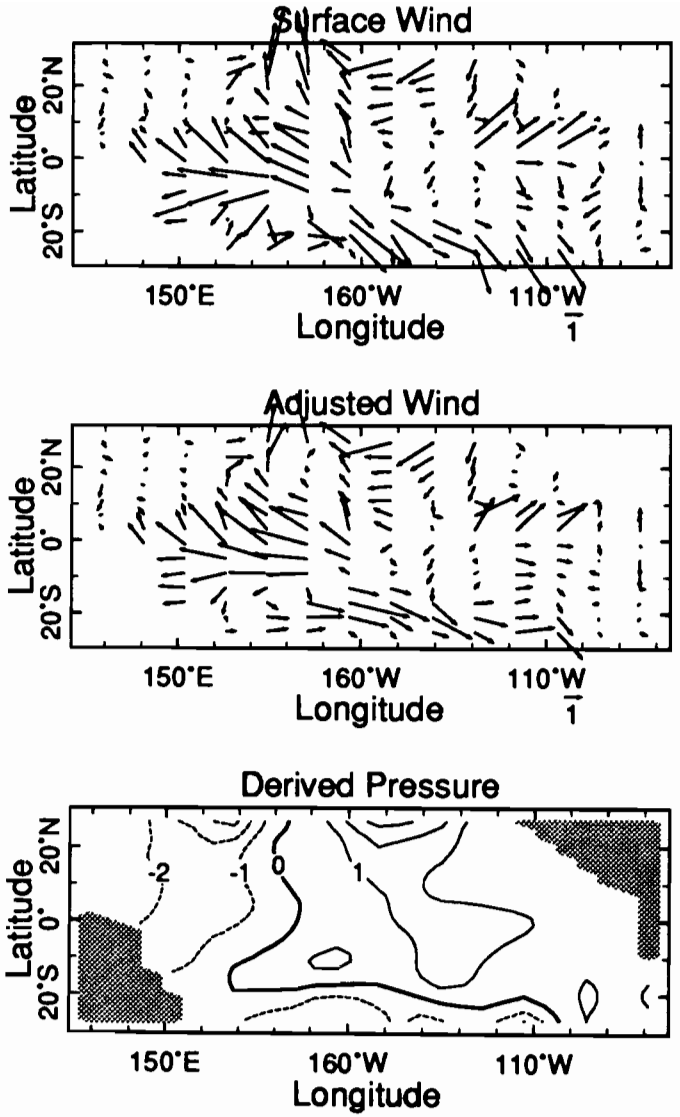

Fig. 6. As in Fig. 4, except for January 1984.

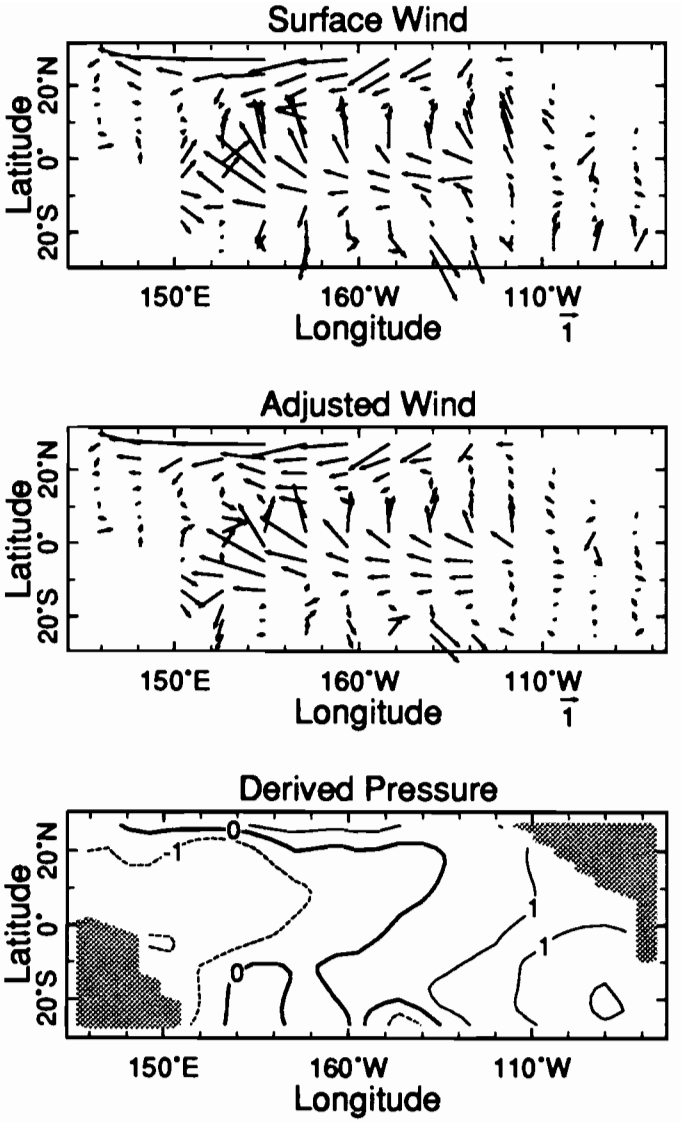

Fig. 7. As in Fig. 4, except for March 1985.

Yet another pattern obtains in March 1985 (Fig. 7). This is a "cold event" scenario; that is, anomalously cold SST in the equatorial east Pacific. Along with this are found strong easterly anomalies in the central equatorial region, and especially strong northward flow to the north, resulting in very strong near-equatorial divergence. Interestingly, the anomalies remain large but become easterly again further to the north, so that a strong convergence results at about 10°N. (A more typical pattern is found in the south: a general reduction or reversal of the zonal component between the equatorial zone and the subtropics.) The pressure field resembles the Southern Oscillation pattern (opposite phase from Dec 1982), except for the band of rapidly increasing pressure in the northernmost latitudes. This is the counterpart to the subtropical easterlies here; the more characteristic pattern tends to have relatively little meridional gradient in the subtropics. The easterlies, and divergence/convergence zones are all reproduced well in the reconstructed wind field.

The examples shown give the impression that the procedure for calculating pressure, and then modifying the winds, results in generally minor changes of the original wind field. To quantify this more precisely, we computed the RMS difference in u and v between the two wind fields, based on all spatial points and all months. The results for both were roughly 0.5 m/s. Thus the adjustments are well below the uncertainty of the data itself, which is roughly 2m/s (Reynolds et al.,1989). Moreover, by construction, the adjusted winds are consistent with the pressure field, and they satisfy the vorticity balance that was not even approximately satisfied in the original wind field. We consider that this alone is sufficient reason to warrant using the adjusted data in subsequent modeling applications. For comparison, the RMS values of the vorticity budget terms based on the reconstructed winds are given in Table 1. The residual term in this case is based only on the linear terms (it is not exactly zero because of differences in the numerical methods used for integration and differentiation). It can be seen that, as before, the nonlinear components are relatively small, but now the linear components are all roughly equal in magnitude. Among these, the divergence term is by far the most changed from the original data.

4. Model Applications

Having a consistent surface wind-pressure data set based on the linear momentum equations affords a good oportunity to evaluate models. Two classes of simple models have been applied to simulating surface winds: one based on a single mode baroclinic structure forced by internal heating (Gill,1980; Zebiak,1982,1986; hereafter Z), and another based on a boundary layer structure forced by buoyancy perturbations associated with surface fluxes (Lindzen and Nigam,1988; hereafter LN). For quite different reasons, both models assume the form of the steady linear shallow water equations, but the forcing is different. Neelin (1989) has shown that the boundary layer model can be written in such a way that the forcing appears in the "thermal" equation, as it does with the baroclinic model, but the theory assigns its structure directly to the SST field. For the baroclinic model, the forcing is assumed to be associated with organized convection. Though this has been parameterized in terms of SST frequently, it clearly has an important dependence on the circulation itself, and particularly the boundary layer convergence (see Z).

How well does either of these models square with observations? This question can now be addressed, since for either model, the combined surface wind and pressure data are sufficient to determine a forcing field uniquely. This "inverted" forcing field is the one that would, in either case, produce the correct circulation (as approximated by the adjusted wind fields). The extent to which this forcing satisfies the theoretical constraints of the models can be taken as an indication of their validity.

The thermal (or mass) equation for either model can be written in the following (nondimensional) form:

$$\varepsilon p + \gamma(u_x + v_y) = -Q\,, \tag{3}$$

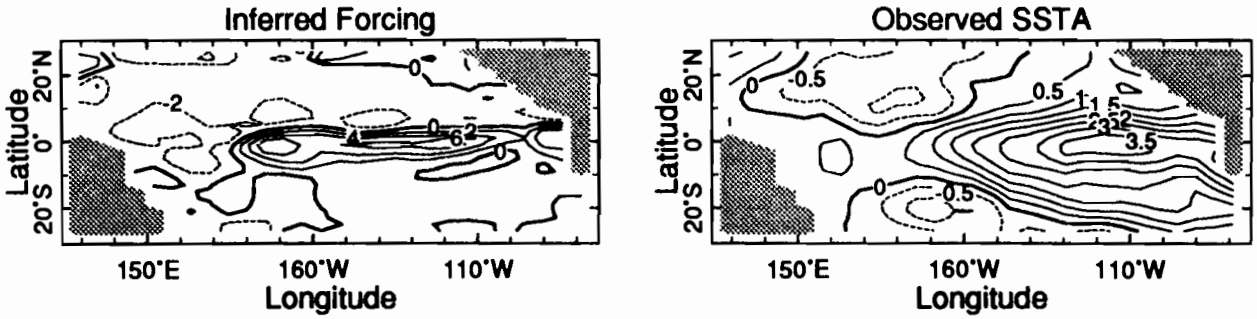

Fig. 8. Inferred forcing (from Eq. 3), and observed sea surface temperature anomalies for December 1982.

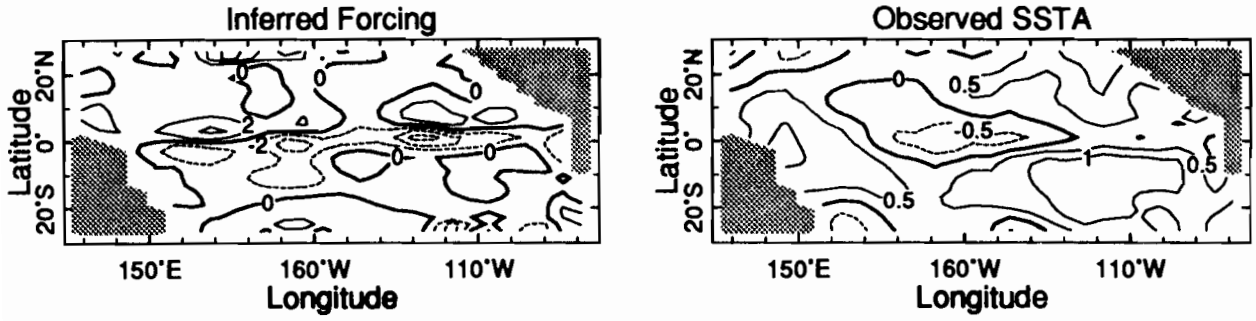

Fig. 9. As in Fig. 8, except for January 1984.

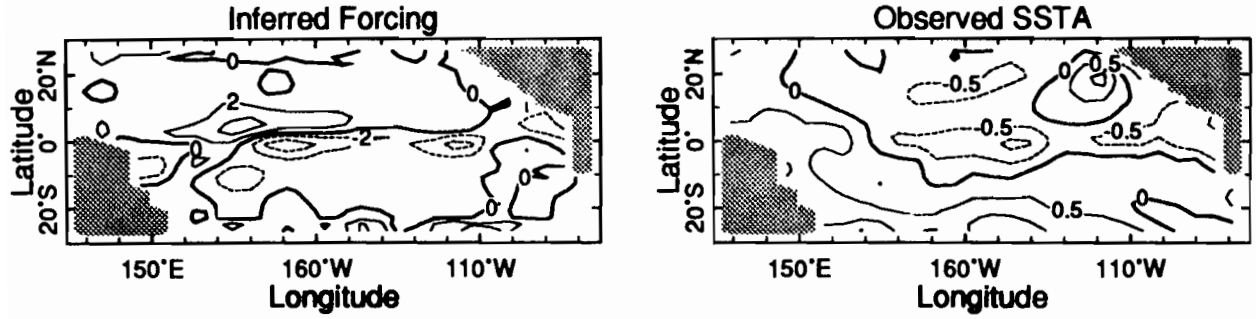

Fig. 10. As in Fig 8, except for March 1985.

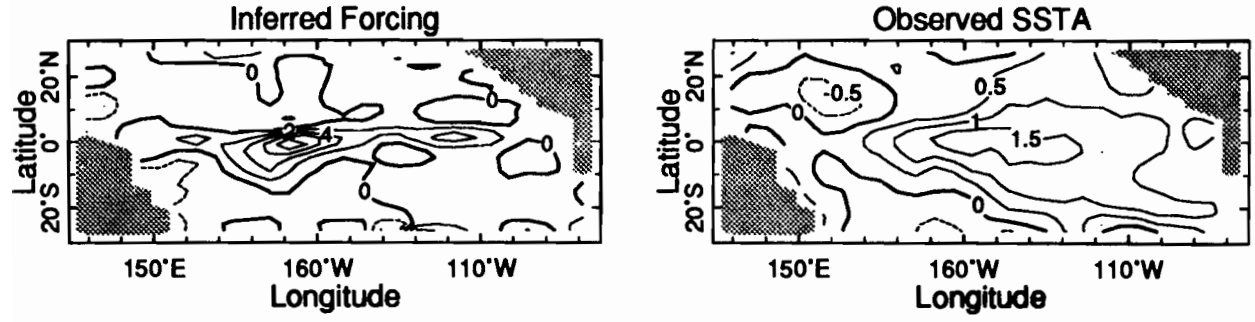

Fig. 11. As in Fig 8, except for December 1986.

with the value of γ and the form of Q depending on the choice of model. For the baroclinic model, Z assumed an internal (Kelvin) wave speed (c_a) of 60 m/s, and nondimensionalized such that γ had a value of unity. The parameterized heating, meant to represent mainly convective latent heat release, depended partly on the local SST anomaly, and partly on low level convergence. However, for the chosen parameters, the SST dependence was strong enough to control the character of the response.

The reader is referred to LN and Neelin (1989) for a detailed description of the boundary layer model. From the latter paper, combined with the nondimensionalization of Z, one can determine that $\gamma=\varepsilon H_0 g/\varepsilon_T c_a^2$, where g is the acceleration of gravity, H_0 is the boundary layer height, and ε_T^{-1} is a "cumulus uptake time". LN chose ε_T^{-1} to be 30 minutes, and H_0 to be 3 km, which gives $\gamma=.68\varepsilon$. The forcing in this model depends only on the SST field; for the LN parameter values, the result is $Q=.85\varepsilon T'$, where T' is the SST anomaly in ° K. Finally, the nondimensional value of ε corresponding to a 1 day dissipation time is 0.25.

It is apparent that the ratio of Q and γ for the baroclinic model is close to the ratio of T' and γ for the boundary layer model. Given that the divergence term tends to dominate the left-hand side of (3), this means that the structure and magnitude of Q and T' from the respective models will be very similar. In fact, we found them to be nearly identical in all cases, and only the baroclinic model heating will be presented here. In dimensional terms, a unit value of Q corresponds approximately to 1.5 mm/day of rainfall. For the boundary layer model, it corresponds to a 1 °C SST anomaly.

The derived forcing field, together with the observed SST anomaly field (CAC analysis), for December 1982 are shown in Fig. 8. Two important points are immediately evident: first, the structure of the two fields is very different -- the forcing has a much smaller meridional scale; and second, the magnitude of the forcing is too large to be explained by the boundary layer model alone. Notice that the heating anomaly changes sign at about 5°N, whereas large positive SST anomalies extend to nearly 15°N in the eastern Pacific. A cautionary note is required here: because the area-mean pressure anomaly is undetermined, and set to zero, the same is true of the derived heating field. Any fluctuation of the net heating over the entire domain that may occur in nature cannot be captured here. In any case, the issues of spatial structure are unaffected by this uncertainty.

For January 1984 (Fig. 9), there is again a conspicuous mismatch in spatial structure between the SST anomaly and derived forcing fields. The forcing field shows intense negative anomalies along the equator in the central and east Pacific, and large positive anomalies to the north. Disregarding the overall mean, there is in this case an identifiable correspondence between the two fields in the equatorial east Pacific, but not in the central and western sectors. Furthermore, it is implausible that such negative anomalies in the eastern Pacific could arise solely from convective sources, as there is too little convective activity in this region to begin with. Thus, in agreement with Gutzler and Wood (1989), there is the suggestion of boundary layer mechanisms being important in the eastern region, and perhaps less so elsewhere. Similar conclusions could be drawn from the March 1985 fields (Fig. 10). In this case the scale difference between SST and heating in the central Pacific is unmistakable.

December 1986 was an instance of a moderate warm event (Fig. 11). Equatorial westerly anomalies were large in the western and central regions, with equatorward flow to the north and south, but little response to the east. This typical pattern was discussed by Z as problematical; the model response for mature phase ENSO conditions tends to resemble the familiar pattern of Gill (1980), with broad easterlies to the east of the heat source. Many models, including some GCMs, tend to do this; yet the observed pattern shows the westerlies and cyclonic circulations in the heating region without the easterlies to the east. Neelin and Held (1987) achieved a more realistic simulation by specifying the vertical motion from a GCM calculation, suggesting that

the problem in other models may be in the parameterized forcing. The "inverted" forcing field shows, once again, a substantial scale reduction relative to the SST anomaly field, especially in the eastern sector. Positive heating anomalies are situated in the equatorial central Pacific, and along a very narrow band farther to the east, with predominantly negative anomalies in western Pacific. The general pattern is not unlike what is inferred from OLR anomalies during ENSO events (with the possible exception of the eastern equatorial region), but tends to show even smaller scales. This difference could easily arise from the extensive smoothing of OLR data.

The origin of the "easterly problem" discussed in Z is now evident: the parameterized heating is too strongly tied to the SST field. Whereas the prescribed heating tends to have the broad structure of the SST anomaly field, the required forcing is much more confined, with a tendency for nearby compensation (that is, anomalies of the opposite sign). The impact on the easterlies is dramatic, since they arise from the Kelvin wave component, as discussed by Gill (1980). This component is forced at a given longitude by the projection of the heating onto the first Hermite function, which has the form of a Gaussian (centered on the equator) with y-scale of order 10° latitude. A function with the structure of the SST anomaly field of Fig. 11, for example, projects strongly onto the Kelvin component, whereas one like the inferred heating field projects very weakly. On the other hand, the projection onto the gravest Rossby modes, those responsible for the equatorial westerlies, is if anything stronger with the more confined forcing.

5. Conclusions

Starting from the FSU wind analyses for the tropical Pacific, we have performed several calculations. First, a vorticity budget for the surface layer was computed. It reveals the relative unimportance of the nonlinear components, but is not even approximately balanced. Based on the former result, and an hypothesis that the latter is largely due to data errors, an algorithm was developed to estimate the surface pressure field from the wind observations and the linear momentum equations. The estimated surface pressure agrees well with direct observations in terms of the SOI variability over the past 25 years, and also matches closely recent operational analyses that were examined.

Using the same linear equations, and the derived pressure field, a revised wind field was determined. This wind field, by construction, is consistent with the pressure field, and satisfies the linear vorticity budget. We feel confident that the modified winds are superior to the original data since the adjustments amount to only about .5 m/s in a root-mean-square sense, well below the uncertainty of the data, and yet a dynamical balance is achieved. This result is very dependent on a carefully chosen method of pressure field construction. Rather than using a method involving derivatives of the data, we adopted an integral technique, and one that further allowed for preferential weighting of information in the very sensitive equatorial zone.

The combined surface wind and pressure fields were then used to infer forcing fields within the context of two simple atmospheric models, one based on a tropospheric scale baroclinic circulation forced by internal heating, and the other based on a boundary layer circulation forced by buoyancy perturbations associated with surface fluxes. Both have been presented as relevant to the variability of tropical surface winds. We found that the structure of the inferred forcing for the two models was nearly identical, within reasonable parameter ranges. This might be taken as evidence that the two models are indistinguishable, except for the fact that the derived forcing differs importantly from the SST anomaly fields. The buoyancy forced model is based on the theory that the flow is driven by pressure gradients set up hydrostatically by temperature perturbations tied to SST. Thus, for the model to be validated, it should happen that the derived forcing has the SST anomaly structure. There is some evidence of this relationship holding in the eastern tropical Pacific, but not elsewhere.

On the other hand, the baroclinic model as presented in Zebiak (1986) is also shown to be wrong, as its parameterized heating depends heavily on the SST field. The most systematic failure of this model in simulating ENSO is the fictitious easterlies it produces in the eastern Pacific. This problem vanishes when the forcing assumes a smaller-scale structure as in the inferred heating fields.

It might be argued that the boundary layer calculations are incorrect, since the model really applies to layer-averaged winds, rather than the surface winds used to infer forcing. It is certainly true that the meridional component of winds at the surface, with associated strong convergence, is largely absent at 850 mb. Thus the more appropriate layer-averaged convergence will typically be smaller than that implied by the surface wind. This might account for the discrepancy in amplitude between inferred and observed SST fields. Nonetheless, even allowing boundary layer turning and deceleration, one cannot account for the needed scale reduction -- additional mechanisms seem to be required. Fundamentally, the problem for this model is that the surface pressure and SST anomaly fields do not closely match.

What mechanism could be responsible for forcing at such small scales? The most plausible candidate is cumulus convection. Our results are not inconsistent with OLR analyses, considering the resolution and degree of smoothing typically applied to such fields. If convective heating is indeed the mechanism, then it follows that the large scale dynamics minimally represented by the Gill (1980) model must be included in order to simulate the real variability accurately. On the other hand, the results for the eastern Pacific are suggestive of the importance of boundary layer dynamics. In such convectively suppressed regions, this is the most likely mechanism controlling surface winds.

These results should be verified with other wind products, but it is hard to imagine that the major conclusions could change, as they depend on rather striking and consistent features. Apparently, what is needed (even for simple models) is a reasonable parameterization of organized convection, based on the large scale circulation and SST. Unfortunately, a satisfactory theory for this is lacking; issues such as what controls the scale of convective complexes, and the interaction and competition of convectively active regions, and the modulating influence of SST, are poorly understood. Nonetheless, it appears that the benefits of further progress in this area could be great. An additional implication of this work is that a rather fine resolution is required to simulate the real atmosphere faithfully. The scale of heating anomalies that should be resolved appears to be 2-3 degrees of latitude. This may be the explanation for why several low resolution models, including GCMs, show some of the same spurious easterlies as described above in ENSO simulations. If this is true, then only an increase in resolution can remedy what has frequently proven to be a devastating effect in coupled models.

ACKNOWLEDGEMENTS

This work was supported by the National Science Foundation under grant ATM-8612570, and by NOAA under grant NA-84-AA-D-00031.

REFERENCES

Cardone, V. J., J. G. Greenwood, and M. A. Cane, 1989: On trends in historical marine wind data. *J. Climate* In press.

Gill, A. E., 1980: Some simple solutions for heat induced tropical circulation. *Quart. J. Roy. Met. Soc.* **106**, 447-462

Goldenberg, S. B., and J. J. O'Brien, 1981: Time and space variability of tropical Pacific wind stress. *Mon. Wea. Rev.*, **109**, 1190-1207

Gutzler, D. S., and T. M. Wood, 1989: Structure of large-scale convective anomalies over tropical oceans. *J. Climate*

Harrison, D. E., W. S. Kessler, and B. S. Giese, 1989: Ocean circulation model hindcasts of the 1982-1983 El Niño: thermal variablity along the ship-of opportunity tracks. *J. Phys. Oceanogr.* **19**, 397-418

Lindzen, R. S., and S. Nigam, 1987: On the role of sea surface temperature gradients in forcing low level winds and convergence in the tropics. *J. Atmos. Sci.* **45**, 2440-2458

Neelin, J. D., 1989: A note on the interpretation of the Gill model. *J. Atmos. Sci.*

Neelin, J. D., and I. M. Held, 1987: Modelling tropical convergence based on the moist static energy budget. *Mon. Wea. Rev.* **115**, 3-12

Philander, S. G. H., and A. D. Seigel, 1985: Simulation of the El Niño of 1982-1983. *Coupled Ocean-Atmosphere Models*. J. Nihoul, Ed., Elsevier Publishers, Amsterdam, 517-541

Posmentier, E. S., M. A. Cane, and S. E. Zebiak, 1989: Tropical Pacific climate trends since 1960. *J. Climate* In press.

Ramage, C. S., 1987: Secular change in reported surface wind speeds over the ocean. *J. Clim. Appl. Meteorol.* **26**, 525-528

Reynolds, R. W., K. Arpe, C. Gordon, S. P. Hayes, A. Leetmaa, and M. J. McPhaden, 1989: A comparison of tropical Pacific surface wind analyses. *J. Climate* **2**, 105-111

Seager, R. S., 1989: Modeling tropical Pacific sea surface temperature: 1970-87. *J. Phys. Oceanogr.* **19**, 419-434

Trenberth, K. E., and J. G. Olsen, 1988: An evaluation and intercomparison of global analyses from the National Meteorological Center and the European Centre for Medium Rnage Weather Forecasts. *Bull. Amer. Meteor. Soc.* **69**, 1047-1057

Wright, P. B., 1988: On the realiaty of climatic changes in wind over the Pacific. *J. Climatol.* **8**, 521-527

Zebiak, S. E., 1982: A simple atmospheric model of relevance to El Niño. *J. Atmos. Sci.* **39**, 2017-2027

Zebiak, S. E., 1986: Atmospheric convergence feedback in a simple model for El Niño. *Mon. Wea. Rev.* **114**, 1263-1271

MISCELLANEOUS

Relevance to TOGA of Systematic XBT Errors

R.J. BAILEY, H.E. PHILLIPS, G. MEYERS

CSIRO / Division of Oceanography
GPO Box 1538
Hobart, Tasmania - Australia

Introduction

Over recent years expendable bathythermographs (XBTs) have become increasingly relied upon in large-scale oceanographic research programs. An assessment of the accuracy of XBTs, and the systems used to drive them, is therefore essential.

The depth accuracy of XBTs has been the subject of many studies [1, 2, 3, 4]. These studies have proposed alternative fall-rate equations to the one specified by the manufacturer on the basis of the errors observed in the depth of the XBT. Other investigators [5, 6] have concentrated on the temperature calibration of the probe thermistors in an effort to improve the accuracy of XBTs.

The aims of this study are to:

- provide further calibrations of XBTs and XBT systems by comparing them with conductivity-temperature-depth (CTD) sensors.
- evaluate the applicability of the various depth-correction algorithms mentioned above.
- examine the implications of the observed depth and temperature errors to a large-scale research program such as TOGA (Tropical Ocean and Global Atmosphere).

Instrumentation and Methods

Two types of digital XBT systems were calibrated against the RV *Franklin*'s Neil Brown CTD Profiler during separate voyages in 1987 (Table 1). Both types of XBT system are used in the CSIRO's Ship-of-Opportunity Program (SOOP). The MK–9 XBT system was used in two configurations for the calibration experiments; with the *Franklin*'s PDP–11 data logging system, and with an HP–85 microcomputer as deployed on ships-of-opportunity. Deep Blue XBTs, from the same batch, were used throughout the calibrations.

The CTD station positions are shown in Fig. 1. Typically, XBTs were dropped 10–20 minutes prior to the descent of the CTD profiler at each station.

The temperature profiles recorded by the CTD Profiler for both voyages are shown in Fig. 2.

ORSTOM
CENTRE DOCUMENTATION
Montpellier

F 30262

Table 1

Calibration Experiment #	Voyage	XBT System Description	XBT Type	Number of XBTs	Number of Corresponding CTDs
1	FR0487	SEAS II/Bathy Systems SA-810 (HP-85)	Deep Blue	17	17
2	FR1087	Sippican MK-9 (HP-85)	Deep Blue	14	3
3	FR1087	Sippican MK-9 (PDP-11)	Deep Blue	12	3

Table 2

DYNAMIC HEIGHT ERROR

Voyage	XBT System	Error in Dynamic Height Relative to 200 m (dyn m)		Error in Dynamic Height Relative to 400 m (dyn m)		Error in Dynamic Height Relative to 700 m (dyn m)	
		Mean	Standard Dev.	Mean	Standard Dev.	Mean	Standard Dev.
FR0487	SEAS II/Bathy Systems SA-810 (HP-85)	0.001 (0.007)	0.007 (0.008)	-0.009 (0.010)	0.013 (0.013)	-0.012 (0.020)	0.013 (0.014)
FR1087	Sippican MK-9 (HP-85)	-0.011 (0.004)	0.007 (0.006)	-0.012 (0.011)	0.009 (0.009)	-0.016 (0.012)	0.011 (0.011)
FR1087	Sippican MK-9 (PDP-11)	-0.011 (0.003)	0.008 (0.009)	-0.013 (0.008)	0.008 (0.008)	-0.019 (0.009)	0.012 (0.011)

( ) after XBT depth correction according to Hanawa and Yoritaka[4].

Table 3

SEAS II MIXED LAYER ANOMALY ANALYSIS 1987
(Estimate)

Index = $T_{max} - T_{5\ metres}$

Total number of drops = 1739
Total number of anomalous drops = 1223
Mean Index for anomalous drops = 0.22

Index Bin	Index >	Range ≤	Frequency	Percentage of Total Drops
0.1	0.05	0.15	625	35.94
0.2	0.15	0.25	315	18.12
0.3	0.25	0.35	133	7.65
0.4	0.35	0.45	44	2.53
≥0.5	0.45	—	106	6.10
			TOTAL = 1223	TOTAL = 70.34

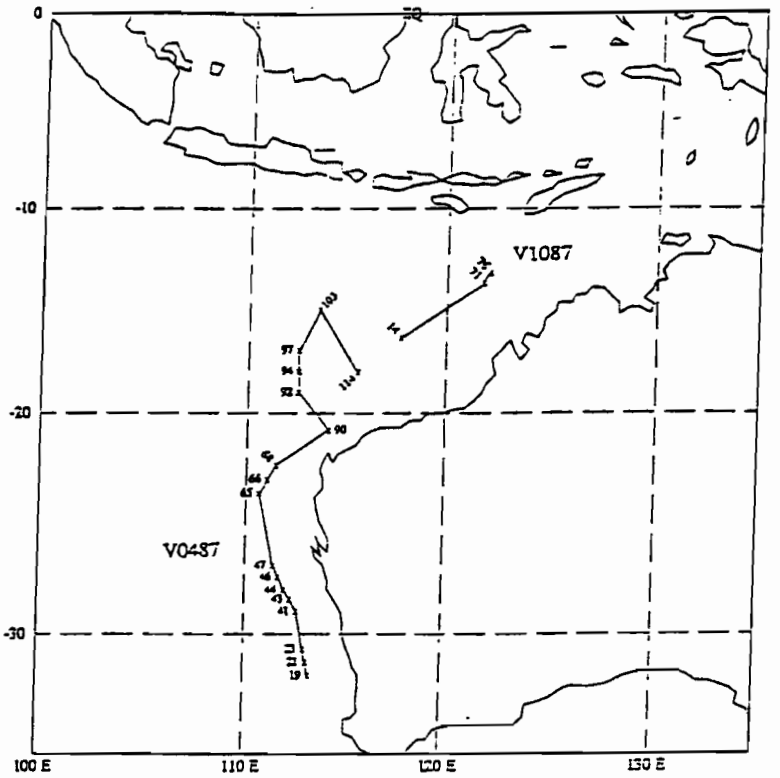

FIG.1. RV Franklin V0487 and V1087 station positions.

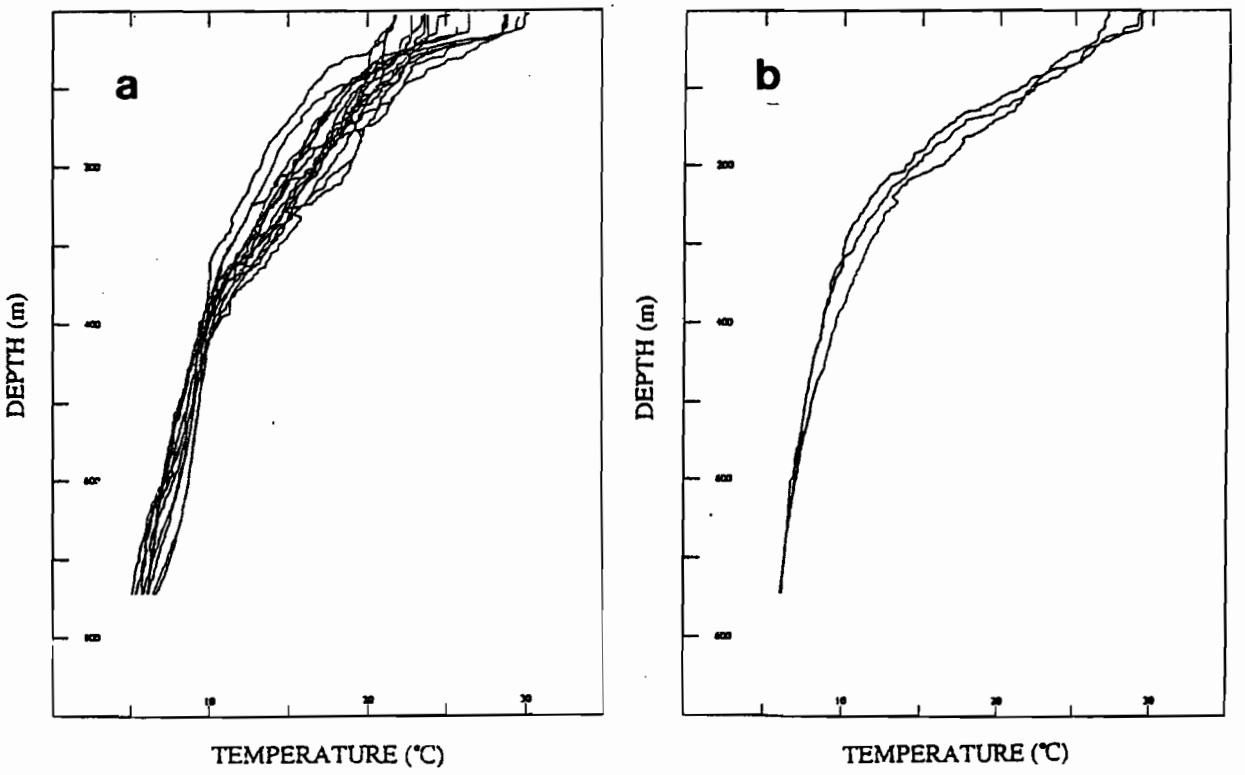

FIG.2. CTD temperature profiles: (a) FR0487, (b) FR1087

Depth and Temperature Errors

(a) Depth Errors

Figs. 3(a) and 4(a) give examples of the average temperature error (T_{XBT}–T_{CTD}) as a function of depth for two of the XBT System/CTD calibration experiments. The characteristic shape of both profiles of temperature error is similar to that found in the experiments of Hanawa and Yoritaka[4]. They found the negative errors in temperature to be mainly due to the errors in depth that result from the XBT falling faster than specified by the manufacturer's fall-rate equation. The largest errors in temperature correspond to the depths of large temperature gradient in the temperature profiles (cf Fig. 2). This is where the depth error due to an incorrect fall-rate has its largest effect.

Figs 3(b) and 4(b) give examples of the average temperature error (T_{XBT}–T_{CTD}) as a function of depth for the same two calibration experiments, however, the depths of the XBTs have been corrected according to the depth-correction algorithm developed by Hanawa and Yoritaka[4]. This algorithm proved to be the most successful at reducing the mean and rms temperature errors for each of the three calibration experiments. The rms temperature error was consistently reduced from above to below the accuracy of the XBT (±0.15°C). The depth-correction algorithm according to Heinmiller et al.[1], on the other hand, actually increased the rms temperature error for each case.

Unfortunately, some errors in temperature still remain at depths corresponding to large temperature gradients, even after the data has been corrected according to Hanawa and Yoritaka[4]. The fall-rate correction of Hanawa and Yoritaka[4] is therefore not totally applicable in the waters of this study, although it does improve the data.

(b) Temperature Errors

Start-up Transients: Large start-up transients in the upper 4 m were observed for the SEAS II XBT System (Fig. 5), and to a lesser extent for the MK–9 XBT System. The mean difference between the first temperature digitisation (0.6 m) and the temperature at 3.9 m (commonly used as the sea surface temperature due to such transients) was –9.50 ± 10.08°C for the SEAS II XBT System, compared to 0.41 ± 0.30°C for the MK–9 XBT System.

SEAS II Mixed Layer Anomaly (Bowing): The need for the comparison of XBT data with a precision CTD sensor was first invoked by the observation of anomalies in the mixed layer temperature profiles recorded by SEAS II XBT Systems deployed in the CSIRO SOOP in the western tropical Pacific. A gradual increase, or "bowing", in temperature was observed as opposed to an isothermal profile. An example is given in Fig. 6. Such anomalies were not present in the data recorded by the MK–9 XBT Systems.

The upper 200 m of the temperature profiles recorded by the SEAS II XBT System and the CTD Profiler during FR0487 are shown in Figs 7(a) and 7(b) respectively. The gradient in temperature in the mixed layer for a single XBT and its corresponding CTD are highlighted to emphasize the "bowing" problem. The corresponding average error in temperature (T_{XBT}–T_{CTD}) in the mixed layer as a function of depth is shown in Fig. 7(c). The mean SEAS II XBT temperature in the mixed layer starts less than and finishes greater than the mixed layer temperature given by the CTD. On examination of each individual XBT/CTD

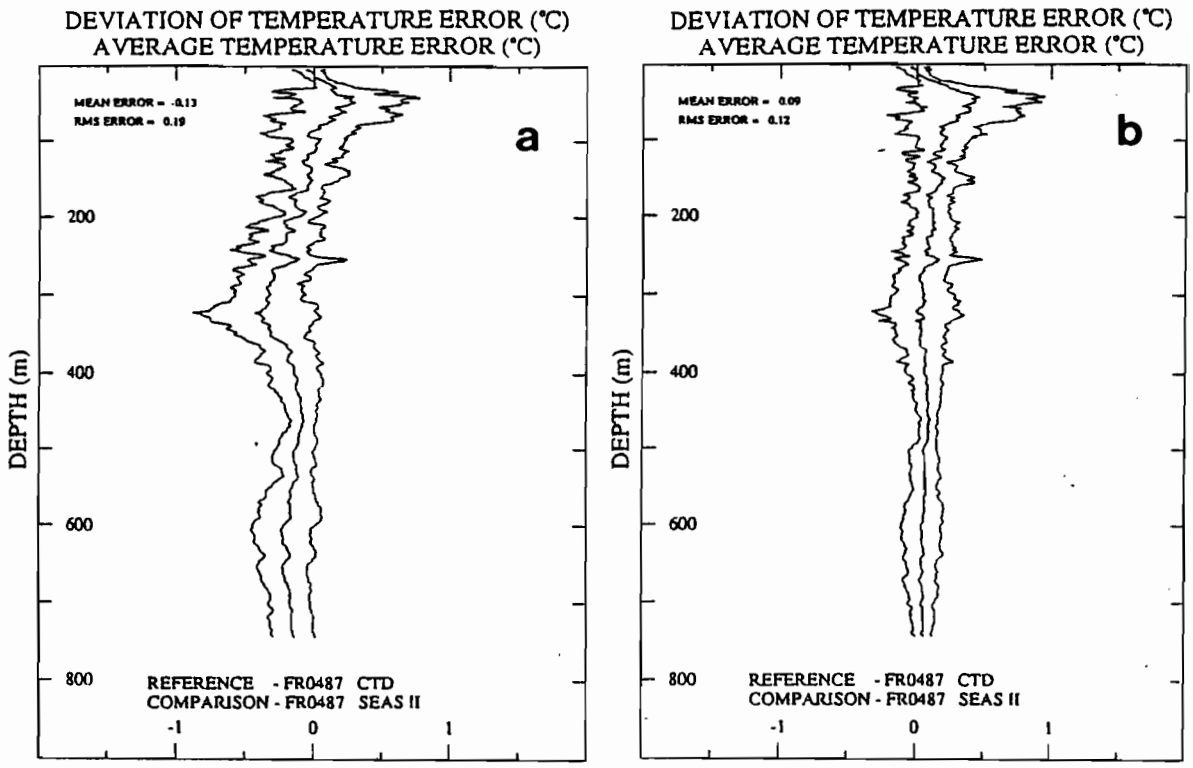

FIG.3. Average temperature error profiles (TXBT-TCTD) for the XBT/CTD comparisons on FR0487 using the SEAS II XBT system; (a) depth uncorrected, (b) depth corrected according to Hanawa and Yoritaka4.

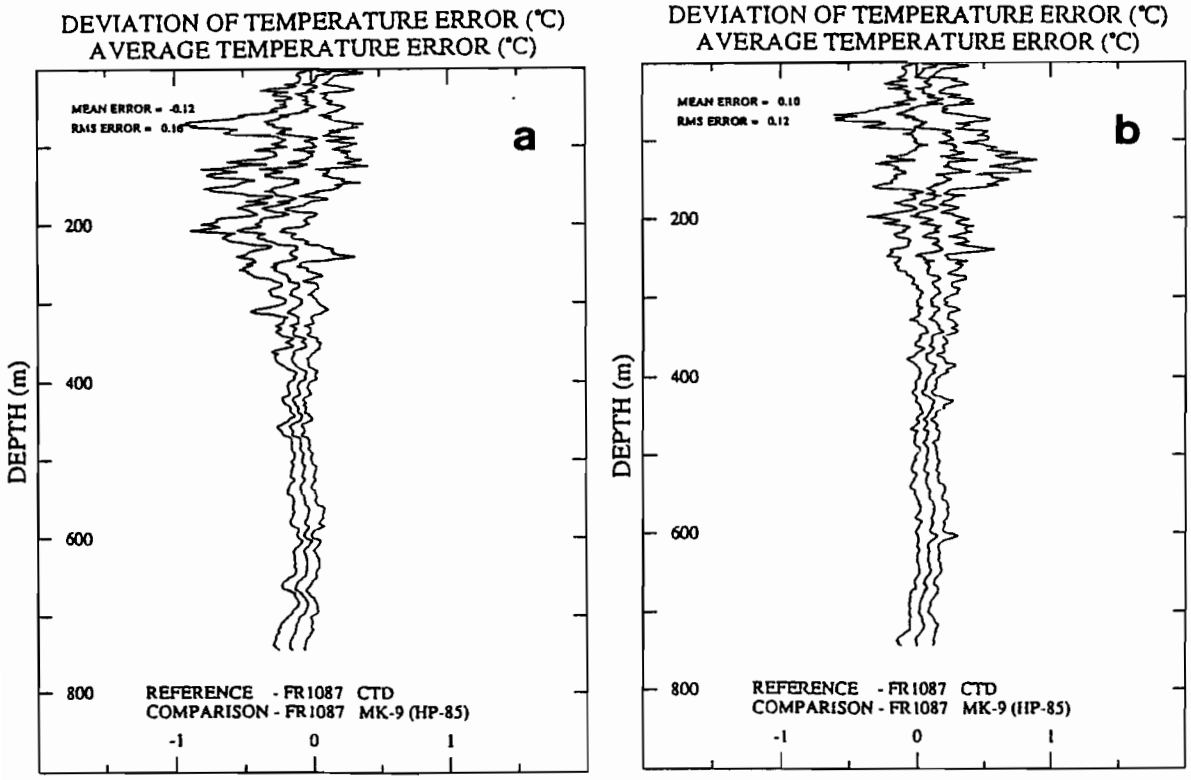

FIG.4. Average temperature error profiles (TXBT-TCTD) for the XBT/CTD comparisons on FR1087 using the MK-9 XBT system; (a) depth uncorrected, (b) depth corrected according to Hanawa and Yoritaka4.

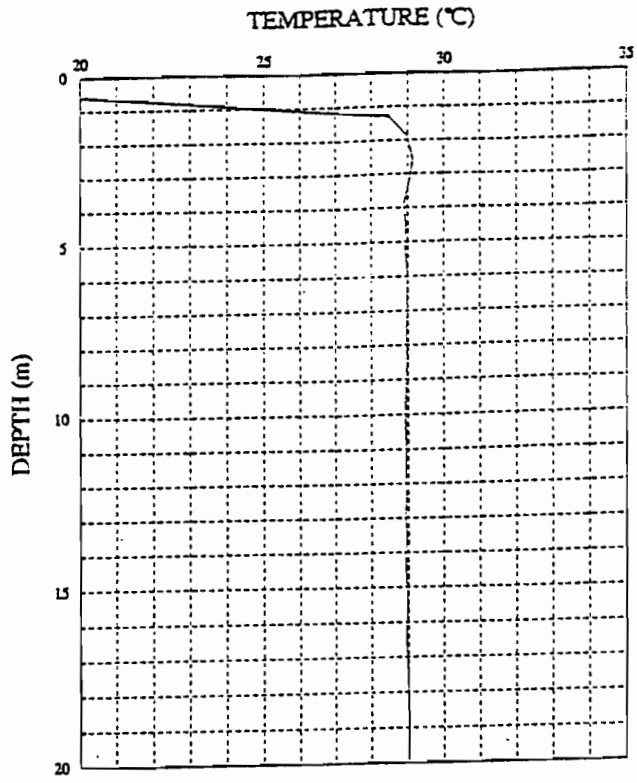

FIG.5. Example of a start-up transient from a SEAS II XBT system.

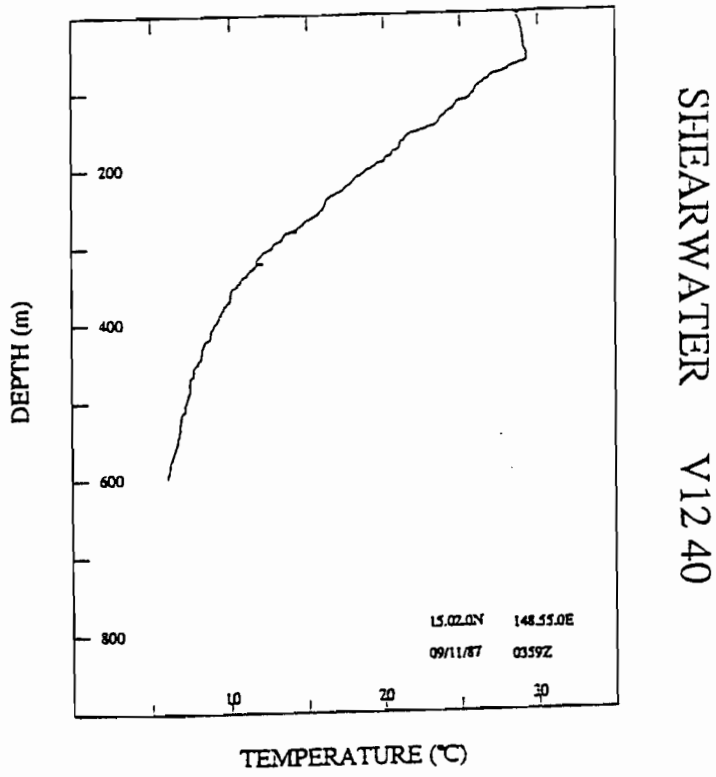

FIG.6. Example of a mixed layer anomaly recorded by a SEAS II XBT system.

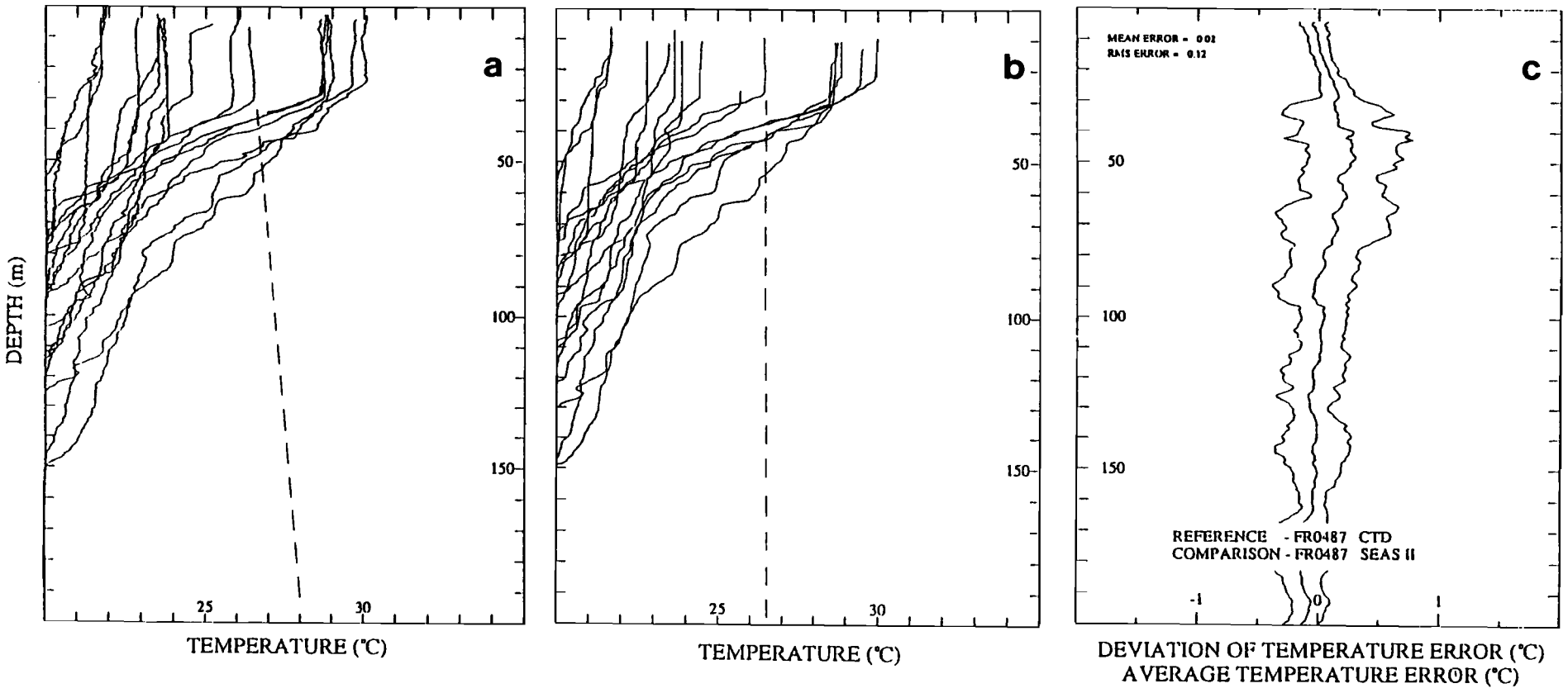

Fig. 7. (a) SEAS II temperature profiles (upper 200 m) for FR0487; (b) CTD temperature profiles (upper 200 m) for FR0487; (c) corresponding average temperature error profile (upper 200 m)

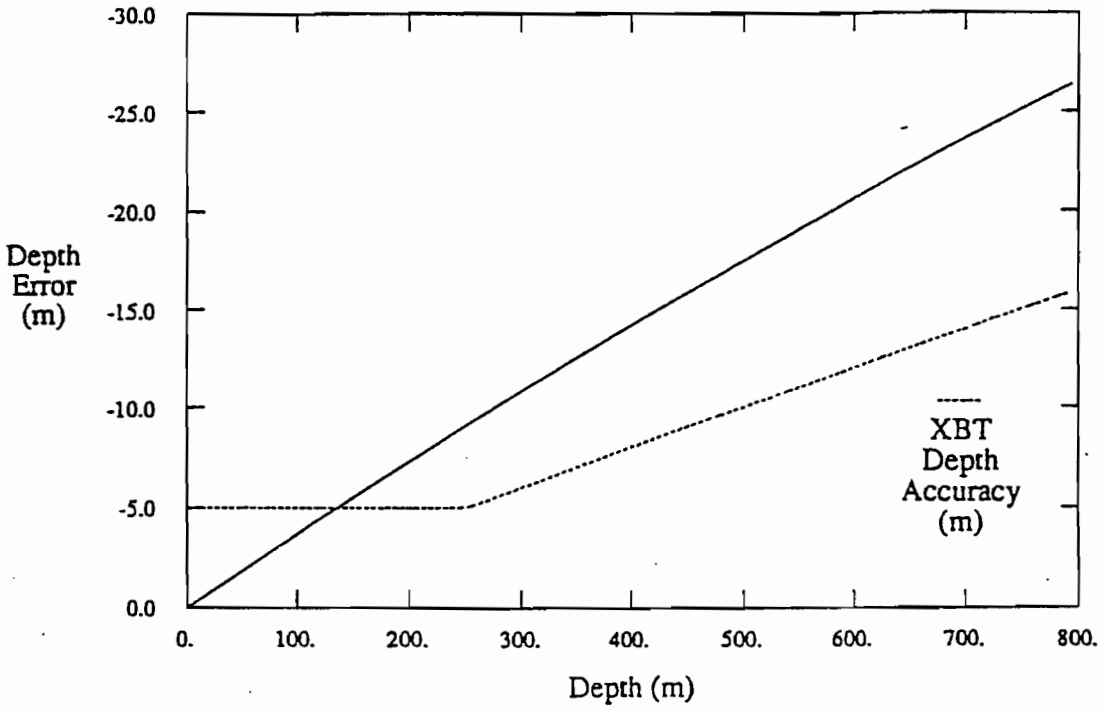

FIG.8. Depth error of the XBT as a function of depth.

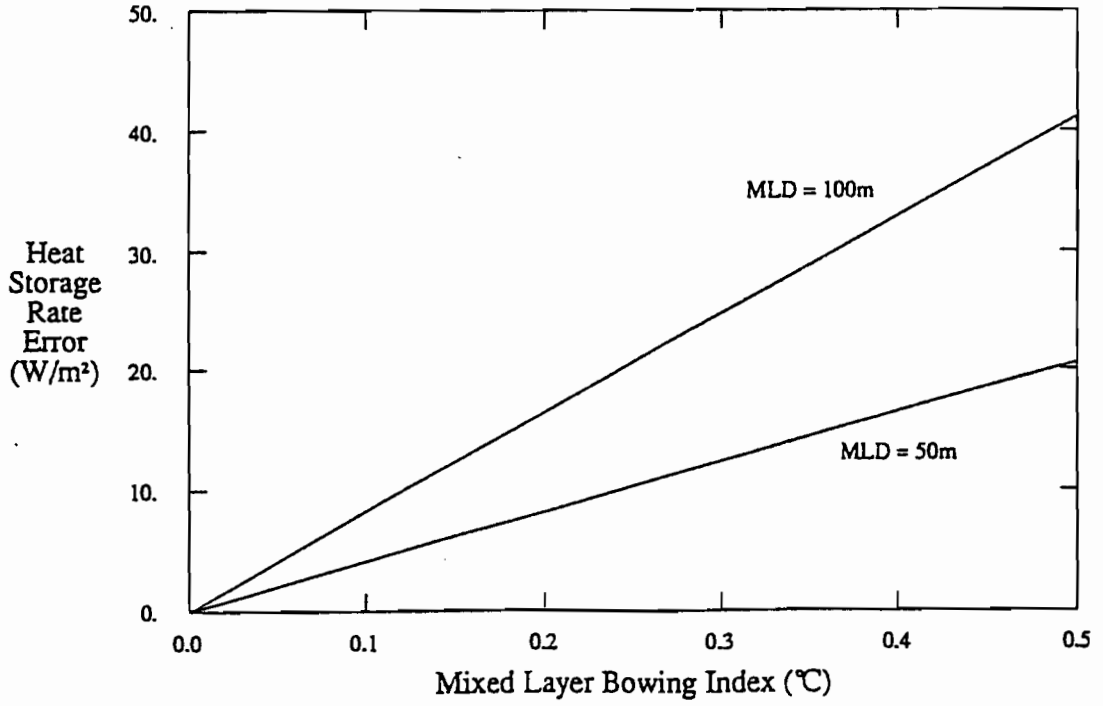

FIG.9. Error in monthly heat storage rate due to the "bowing" problem of the SEAS II XBT system.

comparison, however, the start and finish temperatures of the SEAS II XBT System were found to be randomly distributed in relation to the CTD mixed layer temperature. In some cases the SEAS II temperature starts above the CTD mixed layer temperature and finishes further above it. In other cases, it may start below it and finish equal to it.

The above results indicate a possible drift problem with the electronics of the SEAS II XBT System. The temperature errors may also extend deeper than the mixed layer. We can only distinguish the problem in the mixed layer where the real temperature gradient is zero.

Implications for TOGA

(a) Isotherm Depth Errors

If we assume the corrected depth (z') from Hanawa and Yoritaka[4] to be the true depth of the XBT, then Fig. 8 shows the depth error ($z-z'$) as a function of depth, where z is the depth of the XBT given by the manufacturer. The depth accuracy of the XBT at any given depth is also shown. A 20°C isotherm depth of 200 m, for example, will be measured by an XBT as occurring at a depth of approximately 192.5 m — an error of 7.5 m. The depth error exceeds 25 m at a depth of 800 m, and exceeds the depth accuracy of the XBT (5 m or 2% of the depth, whichever is greater) at a depth of approximately 135 m.

(b) Dynamic Height Errors

Table 2 shows the mean error in dynamic height ($D_{XBT}-D_{CTD}$) relative to 200 m, 400 m and 700 m for the three calibration experiments. The errors are small both before and after the correction for depth of the XBT. Values range from –0.019 dyn m to 0.001 dyn m. Fortunately, the largest temperature gradients in the tropics are shallow enough for errors in temperature, which affect the dynamic height, to be small. The error in depth, which affects the temperature error, is relatively small at these shallower depths.

The depth correction from Hanawa and Yoritaka[4] successfully reduces the error in dynamic height for the MK–9 XBT System, but increases it for the SEAS II XBT System. The additional positive errors in temperature caused by the "bowing" problem of the SEAS II XBT System are possibly cancelling some of the negative errors in temperature that result from errors in depth. The dynamic height error, which depends on temperature, is therefore reduced for the SEAS II XBT System.

(c) Mixed Layer Temperature Errors

A mixed layer bowing index, defined as the maximum temperature of a profile minus the temperature at 5 m, was used to estimate the typical magnitude and frequency of the mixed layer anomaly recorded by the SEAS II XBT Systems deployed in the CSIRO SOOP. The results for the XBT data recorded in 1987 are given in Table 3. Potentially, 34.4% of the data had errors greater than the temperature accuracy of the XBT (±0.15°C). Some profiles recorded indexes of 0.7°C (Fig. 6) and above.

Fig. 9 shows the error in monthly heat storage rates as a function of the potential error in mixed layer temperature due to "bowing". The errors are shown for two characteristic mixed layer depths (MLD). Given the mean index for 1987 from Table 3 of 0.22°C, the corresponding error in the monthly heat storage rate is approximately 18 W/m^2 for a mixed layer depth of 100 m. This is an unacceptable source of error in heat budget studies.

(d) Sea Surface Temperature Errors

The shallowest depth that should be used to estimate sea surface temperature (SST) from an XBT is 3.9 m due to start-up transients. Large errors in SST will be observed otherwise.

Conclusions

- The depth-correction algorithm according to Hanawa and Yoritaka[4] proved the most effective in reducing the mean and rms temperature errors for this data set. However, as neither this correction nor the other corrections that were applied completely reduced the temperature errors observed between the XBTs and CTD Profiler, further studies on the factors that vary the fall-rate of XBTs between different locations will need to be undertaken before a generally applicable depth-correction algorithm will be found. This will have to be done for each type of XBT probe.

- Temperature errors observed in the mixed layer, due to the "bowing" problem associated with the SEAS II XBT System, are a significant source of error for TOGA. A thorough engineering analysis of the electronics of this system is recommended before future use of the system. On the results of this study, CSIRO has replaced the SEAS II units in its SOOP with MK–9 XBT Systems.

References

1. Heinmiller, R., C. Ebbesmeyer, B. Taft, D. Olson and O. Nikitin (1983): Systematic errors in expendable bathythermograph (XBT) profiles. *Deep-sea Research* **30**, 1185–1196.

2. Seaver, G., and S. Kuleshov (1982): Experimental and analytical error of the expendable bathythermograph. *Journal of Physical Oceanography* **12**, 592–600.

3. Green, A. (1984): Bulk dynamics of the expendable bathythermograph (XBT). *Deep-sea Research* **31**, 415–426.

4. Hanawa, K. and H. Yoritaka (1987): Detection of systematic errors in XBT data and their correction. *Journal of the Oceanographical Society of Japan* **43**, 68–76.

5. Georgi, D., J. Dean and J. Chase (1980): Temperature calibration of expendable bathythermographs. *Ocean Engineering* **7**, 491–499.

6. Roemmich, D. and B. Cornuelle (1987): Digitisation and calibration of the expendable bathythermograph. *Deep-sea Research* **34**, 299–307.

ENSO Events and Consequences on Nutrient, Planktonic Biomass, and Production in the Western Tropical Pacific Ocean.

Jean BLANCHOT, Robert LE BORGNE, Aubert LE BOUTEILLER
and Martine RODIER

Groupe PROPPAC, Centre ORSTOM,
Nouméa, New Caledonia

ABSTRACT

ENSO events change the hydrographical structures and the planktonic biomass and production particularly in the low latitude region of the Pacific Ocean. We compare here the consequences of these variations at 165°E, in two opposite situations, i.e. during an ENSO event in September 1987 and during an non ENSO event in September 1988.
Preliminary conclusions show: (i) for the **nutrients** in September 1987, a thick nutrient-depleted mixed layer (under detectable limits) along the transect, except at 10°S and 9°S and in September 1988, a wide upwelling between 5°S and 2°N with surface nitrate concentrations ranging between 0.3 and 2 mM; (ii) for **phytoplankton**, the abundance of cyanobacteria (procaryotes) and microalgae (eucaryotes) shows large changes both in cells abundance and depth distribution between the two periods. Overall, there is a close relationship between upwelling and increase of phytoplankton abundance and chlorophyll biomass. The integrated values over 0-120m are higher in September 1988 than in September 1987: 5 times for cyanobacteria cells, 3 times for microalgae and 1.4 times for chlorophyll between 6-5°S and 2°N; (iii) **primary** production maximum is deeper during ENSO event whereas it is shallow in the upwelling situation. The level of production increased during the upwelling: the integrated value in the 0-120 m averaged (n=7), about 150 versus 59 $mgCm^{-2}h^{-1}$; (iv) for zooplankton (200-2000 mm), there is a significant increase due to the equatorial upwelling in non-ENSO period and none in ENSO event, although a biomass peak appears around 10°S together with the nutrient enrichment.

1. Introduction

14 transects were undertaken on the 165°E meridian between 20°S and 6°-10°N, from 1984 to 1989, within time frames of 3 to 6 months, under 2 ORSTOM programs PROPPAC and SURTROPAC. These cruises occured during the El Nino/Southern Oscillation (ENSO) event and non-El Nino periods. Data collected in the 200m upper layer provide an important basis for the study of effects of long-term hydroclimatic variations on the chemical and biological stuctures in the open western tropical Pacific Ocean. We restrict our study here, to the comparison of two opposite situations, the first in September 1987 (PROPPAC 1 cruise) during an ENSO event, the second in September 1988 (PROPPAC 3 cruise) during a non-ENSO event.

2. Results

a. Physical and chemical environment

The main physical and chemical features during the two periods are presented Figure 1. In September 1987, low salinity waters water (<35.0) originating from the north of New Guinea and the Solomon islands were at the surface north of 14°S, associated with an eastward current. Deeper water originating from the south central Pacific between Tahiti and Easter island formed a tongue of high salinity (>35.5) between 20°S and 2°S. The core (>35.5) was located at 120 m at 8°S. The nutrients were absent at the surface along the

ORSTOM
CENTRE DOCUMENTATION
Montpellier
F 30263

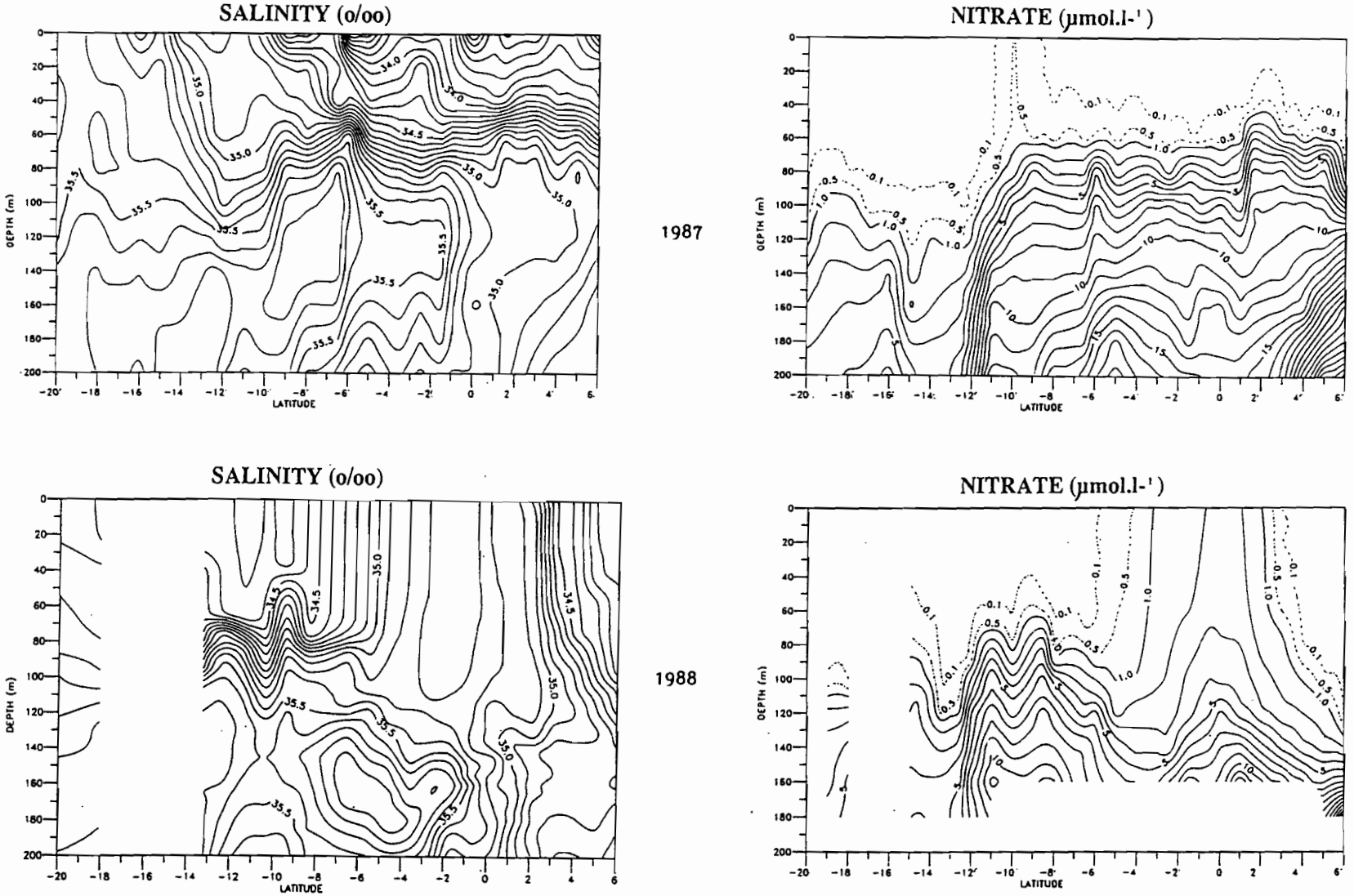

FIG.1. Meridional profiles of salinity and nitrate along 165°E from 20°S to 6°N in September 1987 (top) and September 1988 (bottom).

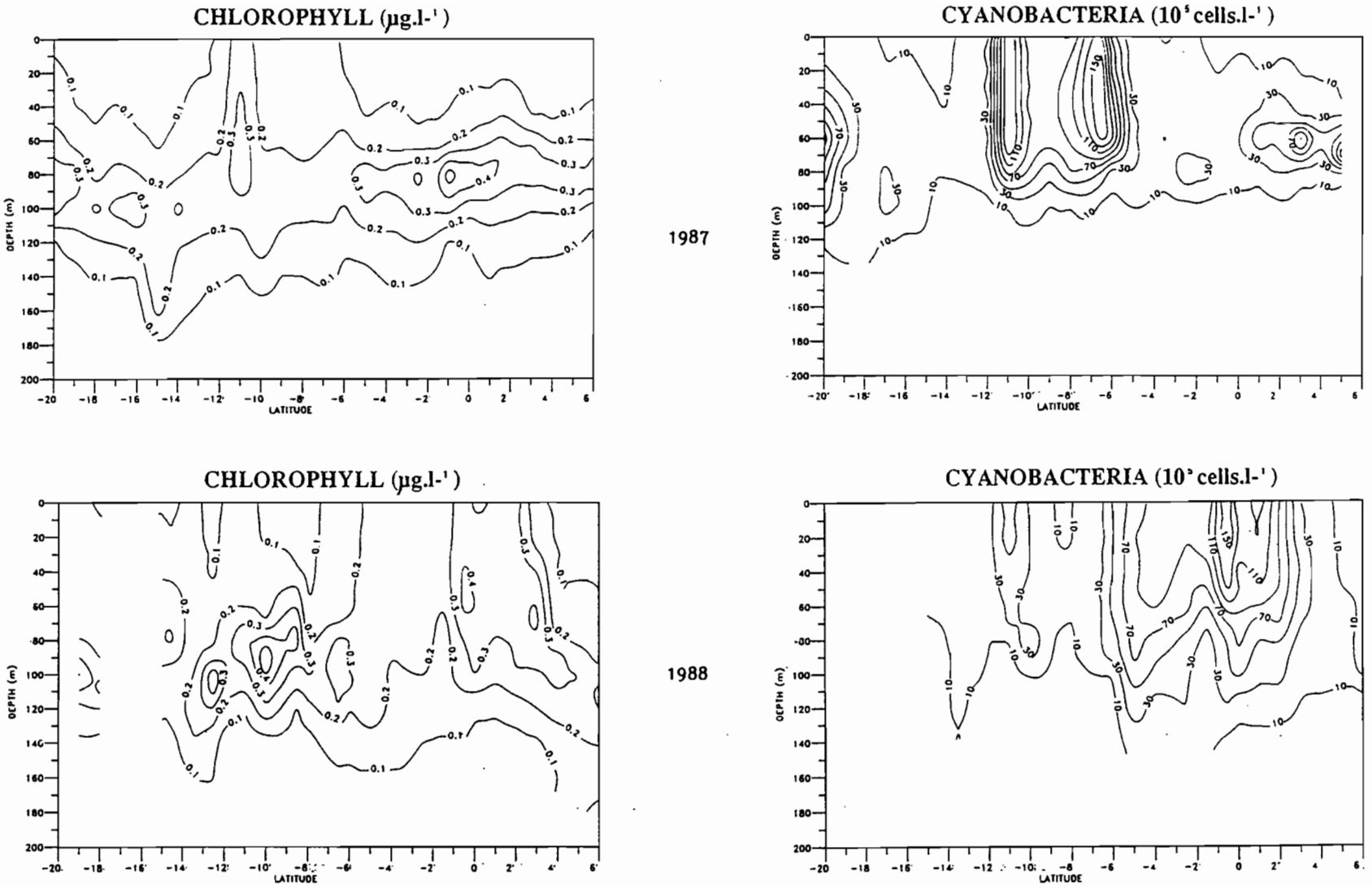

FIG.2. Meridional profiles of chlorophyll and cyanobacteria along 165°E from 20°S to 6°N in September 1987 (top) and September 1988 (bottom).

whole transect except at 10°-9°S where a slight enrichment, a consequence of the divergence between the South Equatorial Current (SEC) and the South Equatorial Counter-Current (SECC), could be observed.

In opposition with the above situation, high salinity surface waters (>35) were present between 5°S and 2°N in September 1988. This drastic change in sea surface salinity was the direct consequence of the equatorial upwelling. However below 100 m, high salinity waters from the central Pacific (S>35.8), were observed as in the opposite situation. The 35.5 isohaline crossed 2°S as previously. Linked with high surface salinity, the nutrients concentration were important from 5°S to 2°N, with values up to 2.29 mM at 1°S.

b. Biological consequences

* Chlorophyll concentrations

In September 87, surface values >0.2 $\mu g l^{-1}$ were observed in the divergence zone around 12°S-10°S. A deep chlorophyll maximum >0.3 $\mu g l^{-1}$ near 90m, occurred from 6°S to 6°N. In September 88, maximum chlorophyll concentrations were found in the equatorial upwelling, with concentrations higher than 0.2$\mu g.l^{-1}$ in the whole photic zone (Fig.2).

* Distribution and abundances of procaryotic chrococcoïd cyanobacteria and eucaryotic microalgae.

The maximum abundance of phytoplankton cells always occurred at the same location as the maximum biomass of chlorophyll *a*. In September 87, the maximum cell abundances of cyanobacteria (>7 10^6 cells l^{-1}) occurred from the surface to 80-90m, between 11°S and 6°S (Fig.2). The eucaryotes abundances were weak and located at several stations only at the bottom of the euphotic zone (Fig.3). In September 88, the maximum occurence of cyanobacteria was observed in the equatorial area from 5°S to 2°N (Fig.2) coincident with increase of cyanobacteria abundances, one important zone of great abundance of microalgae occurred from the surface to the bottom of the euphotic zone in the equatorial upwelling (Fig.3).

* Primary production in the equatorial zone

Vertical profiles of dawn-to-dusk rates of in situ primary production showed that in the equatorial area, during EL NINO events, the maximum rate was observed at 60 m. Observations made in the equatorial upwelling in April 1988 (PROPPAC 2 cruise) showed that the maximum rate of primary production was just below the surface at 20 m (Fig.4)

* Zooplankton biomasses

In September 87, the zooplankton biomasses were weak and rather uniform (less than 1000 $mg.m^{-2}$) except at 12°S where a slight enrichment was measured (Fig.3). A year later, a strong increase was measured between 5°S to 2°N. The maximum zooplankton biomass was 2500 $mg.m^{-2}$ at 1°N (Fig.3).

3. Discussion

Looking at all transects, a slight enrichment is often observed around 10°S in the SEC-SECC divergence zone. However, temporary surface nutrients are unusual and are observed only once in September 1987. This enrichment seems to be higher during ENSO events, and has a direct consequence on the increase of phytoplankton abundance.

During PROPPAC 3 (September 1988), when nitrates were present from the surface to the bottom of the photic zone, maximum chlorophyll concentrations were in this case at the same level than the maximum cell counts. Inputs of nutrients in the photic layer allow higher vegetal production and biomass-increases in upper levels of the food-web (here, zooplankton). Such inputs are very important during the NON-ENSO period, when the equatorial upwelling is present. No such a phenomenon, which may be seen on surface salinity nitrate or chlorophyll occurs during ENSO at the equator.

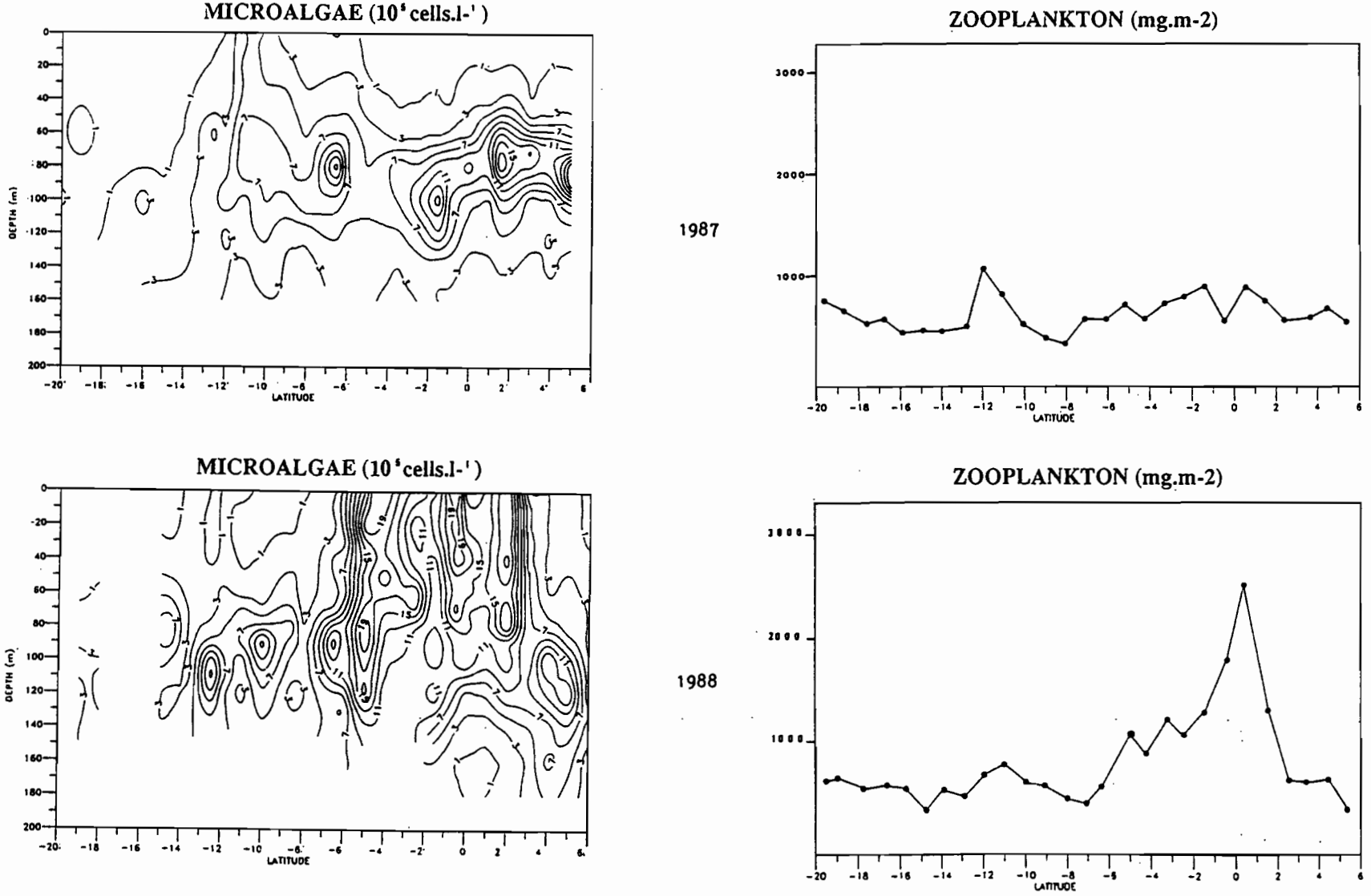

FIG.3. Meridional profiles of microalgae and zooplankton along 165°E from 20°S to 6°N in September 1987 (top) and September 1988 (bottom).

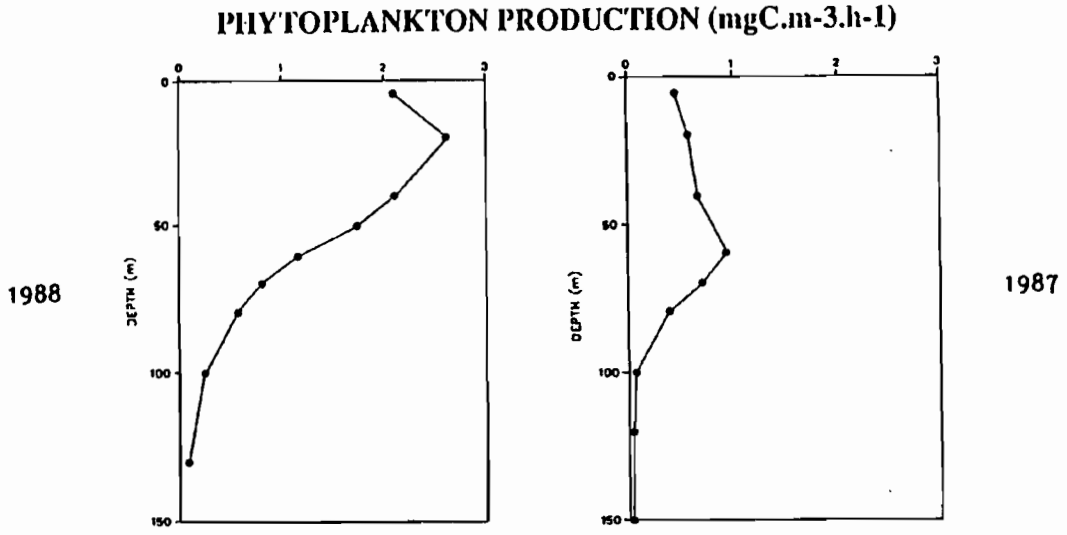

FIG.4. Depth distribution of in situ rates of carbon fixation at the equator in September 1988 and 1989.

The upwelling consequences are between 5°S and 2°N to 5°N:

- an increase of integrated chlorophyll (1.4 times), numbers of phytoplankton cells (5 times increase for cyanobacteria and 3 times for microalgae) and zooplankton biomass (2.5 times);
- a change of vertical profile of in situ primary production (most of phytoplankton production is achieved in upper layers);
- an increase of integrated primary production (2.5 times).

Nevertheless, equatorial upwelling in the western Pacific is not a general feature of NON-ENSO periods. Since SURTROPAC and PROPPAC transects started in January 1984, it has only been observed for the different parameters in April, July, September 1988 (Blanchot et al. 1988a,b) and January 1989. However in January and August 1984 a change of the salinity structure was reported (Delcroix et al., 1987; Eldin, 1989) and in February 1986 a chlorophyll signature was described by Barber and Kogelschatz, 1989. Intermediate situations during NON-ENSO periods are characterized by different increases of planktonic biomasses. The increases are directly dependent on the depth of the nutricline.

REFERENCES

Barber, R.T. and J.E. Kogelschatz, 1989: Nutrients and productivity during the 1982/83 El Nino. In: Global ecological consequences of the 1982-1983 El Nino - southern oscillation, ed. P.W. Glynn. Elsevier, Amsterdam. (In press.)

Blanchot, J., R. Le Borgne, A. Le Bouteiller and M.-H. Radenac, 1988a: Rapport de la cam pagne PROPPAC 03 du N.O. "CORIOLIS" 27 mars - 27 avril 1988. Rapports de mission, Sciences de la mer, Océanographie, Centre de Nouméa, 13 pp.

Blanchot, J., R. Le Borgne, A. Le Bouteiller, M.-H. Radenac, and M. Rodier, 1988b: Rap port de la campagne PROPPAC 03 du N.O. "CORIOLIS" 11 septembre - 11 octobre 1988. Rapports de missions, Sciences de la mer, Océanographie, Centre de Nouméa, 54 pp.

Delcroix,T., G. Eldin and C. Hénin, 1987: Upper ocean water masses and transports in the western tropical Pacific (165°E). *J. Phys. Oceanogr.*, **17**, 2248-2262.

Eldin, G., 1989: Coupes verticales des structures océaniques physiques à 165°E observées au cours de dix campagnes SURTROPAC, 1984 - 1988. Rapports scientifiques et techniques, Sciences de la mer, Océanographie physique, 1, 130 pp.

Abnormal Bloom of Phytoplankton around 10°N in the Western Pacific during the 1982-83 ENSO.

Yves DANDONNEAU

Groupe SURTROPAC, ORSTOM BP A5
Nouméa, New Caledonia

ABSTRACT

The chlorophyll concentration at the surface of the tropical Pacific has been monitored through the 1982-83 ENSO, owing to the SURTROPAC ships of opportunity network. The event was characterized by a decrease in chlorophyll concentrations at the equator, where a belt of relatively rich water however persisted. The most striking anomaly was observed in the western Pacific between 5°N and 15°N. In this region, chlorophyll at the surface is generally less than 0.07 mg m^{-3}, caused by a mixed layer exhausted in nutrients and by strong density gradient in the thermocline. From October 1982 to March 1983, higher concentrations up to 0.70 mg m^{-3} have been recorded by the network. This is consistent with the shallowing of the thermocline which characterizes all ENSO events and was especially well marked in 1982-83. This bloom can be explained by nutrients supplied to the surface mixed layer through the thermocline. Turbulent vertical mixing was indeed made easier during this ENSO event by shallow thermocline, abnormally strong winds, and mixed layer cooler than usual by 2°C. NO_3 data from this region show that 0.07 moles m^{-2} of nitrates have been consumed between January 1982 and January 1983; this value which does not take horizontal advection into account is probably underestimated.

1. Introduction

It is generally considered that ENSO events cause a pronounced decrease in the primary production of the equatorial Pacific Ocean, where upwelling conditions which usually prevail are favourable to the growth of phytoplankton. This is shown by lower than normal direct measurements of primary production (Barber and Chavez, 1986) and by low nutrients concentration at the equator (Feely, et al., 1987). For logistic reasons however (i.e. existing observational networks, availability of research vessels, distance from oceanographic institutes), the Galapagos region and the Peruvian coast have received much more attention than the Central and Western Equatorial Pacific Ocean (Cowles, et al., 1977 ; Barber and Chavez, 1983 ; Feldman, 1986). Furthermore, oceanographic research was focused on the Peruvian anchovies fishery problems (Walsh, 1981), and interest for large scale open ocean primary production has grown up only since a few years, in relation with ocean - climate interactions studies (Chavez et al., 1984 ; Chavez and Barber, 1987). In this scope, a major challenge for oceanographers is to routinely estimate (for instance : on a monthly basis) how much carbon is globally fixed by photosynthesis and buried into the deep sediments. This task is out of reach if undertaken using time consuming *in situ* fourteen carbon experiments, and even if undertaken using proxies such as precise laboratory chlorophyll determinations. Only satellites equipped with sea color sensors today would permit a global survey of a parameter in close relation with photosynthesis (Smith, 1984). The Coastal Zone Color Scanner (CZCS) onboard of Nimbus 6 was still active during the 1982-83 El Nino (Feldman, 1986), but intense cloudiness during most of this warm episode in the equatorial region (Gill and Rasmusson, 1983) prevented teledetection of the sea color most of the time. The only, while rudimentary, global view of the phytoplankton biomass in the

ORSTOM
CENTRE DOCUMENTATION
Montpellier

F 30264

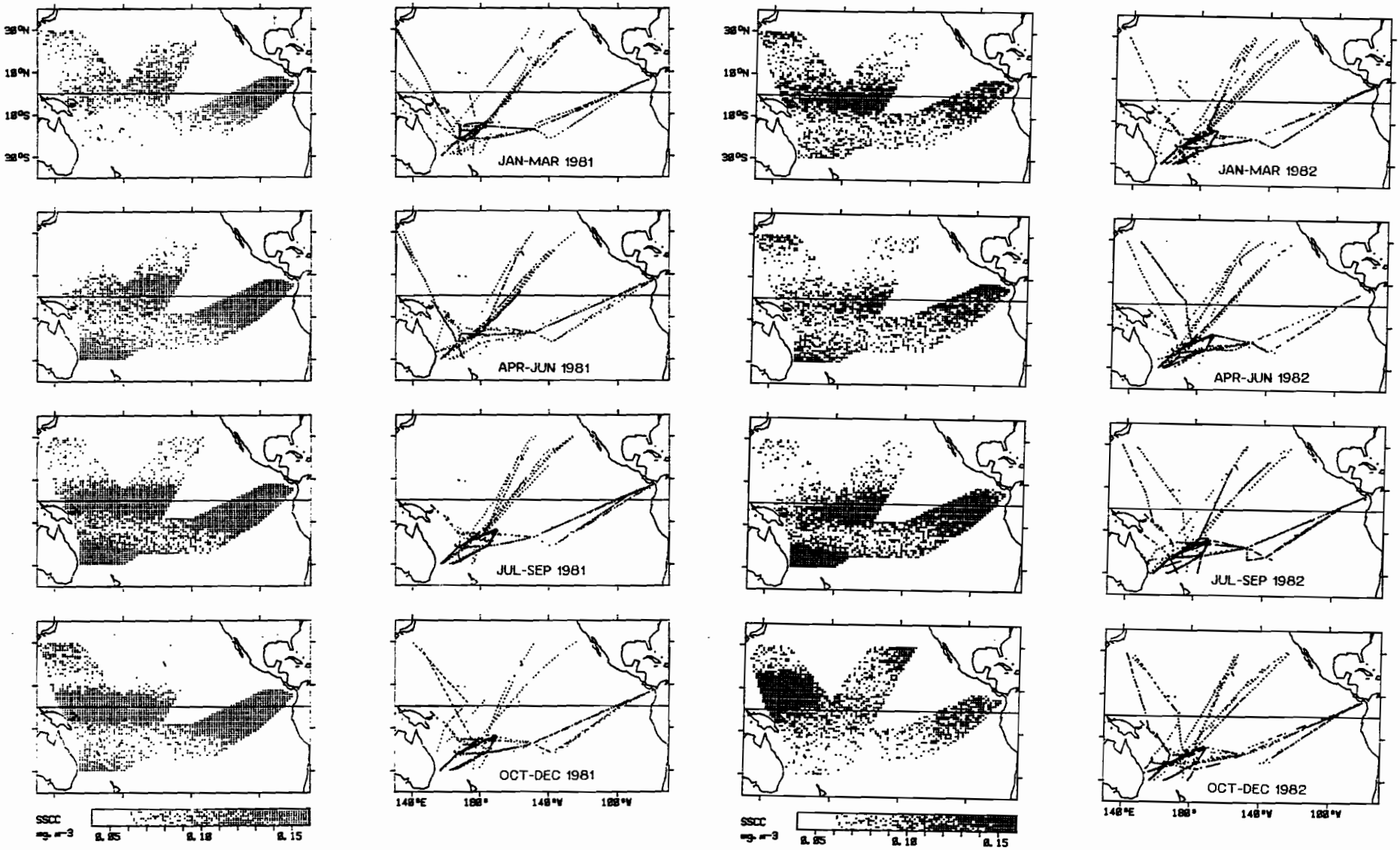

FIG.1.Odd columns : quarterly charts of sea surface chlorophyll concentration (SSCC) in the tropical Pacific (shaded), from 1981 to 1984. Even columns: position of the data collected by the SURTROPAC merchant ships network during each quarter.

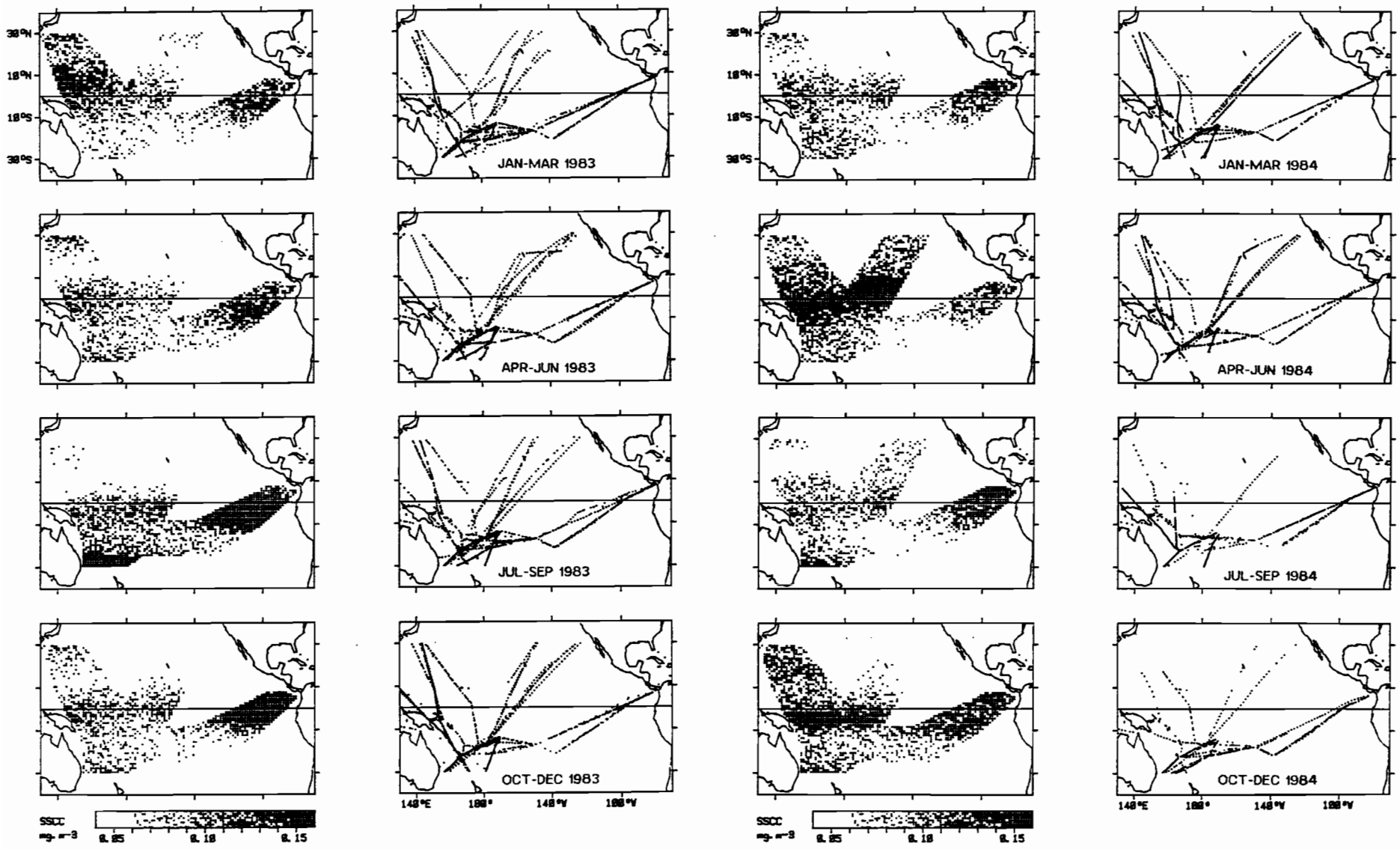

FIG.1. (Continue)

Tropical Pacific Ocean has thus been provided by the SURTROPAC network of merchant ships (ORSTOM, New Caledonia) : chlorophyll measurements are included in the routine observations made from these ships, and the period from 1982 to 1983 was an especially well sampled one (Dandonneau, 1986). The variations of the phytoplankton biomass at the surface of the Pacific Ocean during this exceptional warm event are described using the chlorophyll data from the merchant ships network. Attention is called on a phytoplankton bloom which developed in the western Pacific between the equator and 15°N, and which had never been detected in the past. Quality of the data, and possible mechanisms, are examined in order to establish the reality of this bloom.

2. Methods

Chlorophyll measurements are made according to a specially adapted technique (Dandonneau, 1982), which was developed in order to face the difficulties inherent in sampling, filtration, and filter storage made by voluntary observers. The main constraint arises from the volume of filtered water, which must be small, so that filtration does not take too much time. Filtration is made with a syringe on 13 mm in diameter Millipore HA type filters (porosity : 0.46µ). Filtered volume has been reduced to 10 cm^3, entailing a second constraint : measurement technique must be very sensitive (usual techniques based on the fluorescence of chlorophyll in acetone or methanol require 100 to 500 cm^3 of sea water). Fluorescence is thus measured directly on the surface of the filters, without extraction of the chlorophyll by a solvent. This procedure multiplies the sensitivity by a factor 10. The instrumental error, and causes of chlorophyll data rejection, have been discussed in previous papers (Dandonneau, 1986 ; Dandonneau and Eldin, 1987).

3. Results

The observations collected by the SURTROPAC merchant ships network are distributed along three main shipping tracks : from New Caledonia to Japan, from Australia to North America, and from New Caledonia to Panama. All three tracks were regularly sampled from 1981 to 1984 (at least two or three voyages at each quarter, except in July to September 1981 for the New Caledonia to Japan track), ensuring a reasonably good coverage during the 1982-83 El Nino (Fig. 1). Large scale chlorophyll concentration patterns in the Pacific are dominated by the equatorial belt of rich waters which corresponds to the equatorial upwelling.

Chlorophyll concentrations greater than 0.15 mg m^{-3} spread along the equator westwards to 180° (Fig. 1) during the first half of 1981, and across the entire Pacific ocean until March 1982. Such a large spreading of chlorophyll concentrations greater than 0.15 mg m^{-3} along the equator from America to New Guinea will not be seen until march 1984; only from april to june 1984, and from october to december 1984 does the equatorial enrichment appear again like a long even stripe through the entire Pacific Ocean. Most of the time, the equatorial enrichment is weak in the western Pacific.

From October 1982 to June 1983, the equatorial enrichment is still weaker, with lowest values in April-June 1983, but persists through the El Nino event, with chlorophyll concentrations lesser than 0.10 mg m^{-3} in the central Pacific, and lesser than 0.13 mg m^{-3} in the eastern Pacific. During the northern hemisphere 1982-83 winter, a large bloom of phytoplankton develops west of the dateline, between the equator and 15°N. The position of this bloom, centered at about 10°N, makes it different from a consequence of equatorial upwelling. Furthermore, westerly winds which prevailed in this region during the 1982-83 El Nino did not favour equatorial upwelling. This bloom is very uncommon in this area, as shown on Figure 2 : the mean conditions from October to March (derived from the data collected from 1979 to June 1982, and from July 1983 to 1985) show low chlorophyll

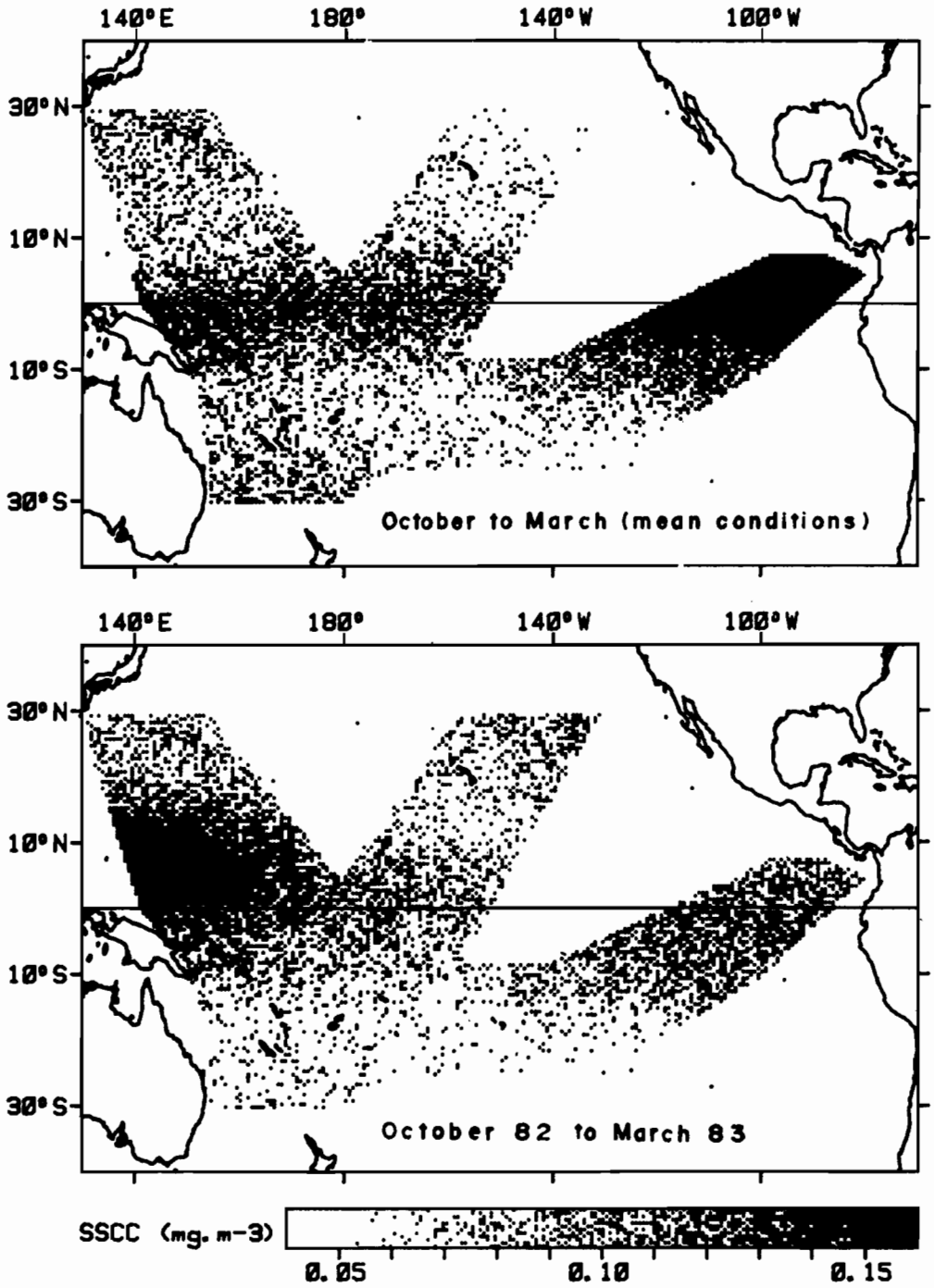

FIG.2. Top : mean chlorophyll concentration at the surface of the tropical Pacific in northern winter (October to March) from 1979 to 1985 (1982-83 winter excluded). Bottom : mean chlorophyll concentration during the 1982-83 northern winter.

concentrations at 10°N, which are typical of tropical waters with a nutrient-exhausted mixed layer (Figure 2, top). The patterns shown for the same months during the 1982-83 El Nino are strikingly different (Fig. 2, bottom), the main difference being the very large bloom which occurred in the northwestern tropical Pacific.

These equatorial or near equatorial large scale features account for most of the variance shown on the quarterly charts from 1981 to 1984 (Fig. 1). A winter increase in chlorophyll concentrations south of about 20°S (austral winter : April to September) can also be seen on these charts. This winter enrichment has been explained as the result of a cooling of the surface mixed layer which thickens and incorporates deep nutrients from the thermocline (Dandonneau and Gohin, 1984). It is much more pronounced in the southern hemisphere near Australia than at the same latitude in the northern hemisphere near Japan.

4. Discussion

Consequences of El Nino on the marine primary production have only been described in the eastern and equatorial Pacific (Walsh, 1981 ; Barber and Chavez, 1983, among other papers cited here). The bloom which developed in the western Pacific at about 10°N during the 1982-83 El Nino (Fig. 1: October 1982 to March 1983) had never been observed on previous El Ninos, nor has it been observed by the Coastal Zone Color Scanner which was still active in 1982-83. The SURTROPAC merchant ships network furthermore did not detect any chlorophyll enrichment in this region before nor after the 1982-83 El Nino. The observation reported here thus has the character of an exceptional one. Low precision and risk of bias inherent to this chlorophyll measurement technique (Dandonneau, 1982, 1986) call for prudence, and arguments must be presented showing that the observed enrichment does not result from measurements errors.

The chlorophyll data from the northwestern tropical Pacific during the 1982-83 El Nino have been collected by two merchant ships : M.S. Pacific Islander, and M.S. Mosel; the first one is part of the SURTROPAC network of merchant ships since 1981, and is still continuing; the second one has been sampling from February 1983 to December 1984. Both were careful observers, and ensured the monitoring of the sea surface chlorophyll in this region after the 1982-83 warm event. The chlorophyll enrichment was detected by both ships from November 1982 to February 1983 (Figure 3). Later, the highest chlorophyll concentrations at each voyage shifted toward the equator. Mean chlorophyll concentrations in the northwestern tropical Pacific never exceeded 0.10 mg m^{-3} during the period from January 1981 to December 1983 (Fig. 1), as well as during the entire monitoring experiment (Fig. 2, bottom), except during the 1982-83 ENSO; higher chlorophyll values were then detected at each voyage between November 1982 and February 1983 by two different merchant ships. Such a coincidence being the result of measurements errors is very unlikely.

Under normal conditions, the western tropical Pacific is generally characterized by high chlorophyll values at the equator, and low ones on the northern and southern sides (Fig. 1; Fig. 2, bottom). At the end of 1982 and the beginning of 1983, the highest chlorophyll concentrations were centered at about 10°N, instead of the equator. This can be seen at each ship's voyage from November 1982 to February 1983 (Fig. 3) ; the chlorophyll data collected during these voyages all show the highest values neatly shifted to the north of the equator, and embedded between lower values to the south and to the north. The most frequent measurement errors in this experiment are systematic errors (overestimates, or, more frequently, underestimates) ; when these errors are obvious, the data from the entire voyage are rejected (Dandonneau, 1986). But even in such cases, the spatial structure of the chlorophyll distribution is still visible. An extra equatorial enrichment in the western tropical Pacific is then an exceptional feature which can hardly result from measurement errors. The chlorophyll-latitude plots from individual voyages shown in Fig. 3 reveal a

high, undersampled spatial variability. It cannot be said here if this variability, which throws some uncertainty on our conclusions, results from the measurement errors, or reflects the intrinsic variability of the chlorophyll field, which can be high too, as shown by precise shipboard measurements made during an oceanographic cruise (Fig. 4).

The shift of the western tropical Pacific enriched area from the equator to about 10°N implies that the physical processes which maintained the enrichment are distinct from equatorial upwelling. The western Pacific between 5°N and 15°N is characterized by a thick mixed layer, exhausted in nutrients, and corresponds thus to the "typical tropical structure" described by Herbland and Voituriez (1979); such tropical waters have a low chlorophyll content. In 1982, after the onset of El Nino, the mean depth of the thermocline decreased by 50 meters at 6 - 8°N (Meyers and Donguy, 1984). Furthermore, the sea surface temperature cooled by 2°C in this region, which Meyers et al. (1986) related to intense evaporation caused by anomalous strong winds. Cooling of the surface mixed layer causes the water immediately below the thermocline to have a lesser density than the mixed layer, and so, to be entrained into the mixed layer. Nutrients from below the thermocline can thus be transferred to the surface and be available to photosynthesis. The data from the Ryofu Maru cruises at 137°E (Masuzawa and Nagazaka, 1975) indicate that the nitrate - temperature relationship is a straight line which intercepts $[NO_3]=0.0$ at T | 24 to 26°C (Dandonneau, 1986). The upper layer temperature decreased to below 26°C north of 15°N in January 1983 (Meyers and Donguy, 1984) so that a small quantity of nitrates could have been injected into the mixed layer. Furthermore, the rise of the thermocline, and the cooling of the mixed layer both are likely to favour turbulent vertical mixing. The typical tropical structure which usually prevails in the western Pacific Ocean between 5°N and 15°N could thus have been replaced by a regime of nitrates pulses, causing the observed phytoplankton bloom. The data from the Ryofu Maru indeed show a shift in the nitrate - temperature relationship between January 1982 and January 1983, corresponding to a 2 μmole l^{-1} drop of $[NO_3]$ at a given temperature (Dandonneau, 1986). This shift was observed on a 35 m thick layer, and if horizontal advection is neglected, the upward flux of nitrates through the thermocline can be estimated to 70 mmoles m^{-2}, i.e. 980 mg m^{-2}. A C/N ratio in the phytoplankton equal to 9.01 (Sharp et al. 1980) gives 8.83 g m^{-2} of new organic carbon production from January 1982 to January 1983, most of which probably occurred after the onset of El Nino. If this result is applied to the area limited by 5°N-15°N, 130°E-170°E (i.e. about 4.8 10^6 km^2), carbon fixation by new production is 0.04 Gt. Advection however cannot be neglected in this region, especially during the 1982-83 El Nino, when the North Equatorial Countercurrent was intensified (Tournier and Picaut, this volume). An error can thus be made when assuming that the January 1982 to January 1983 nitrate decrease was caused only by photosynthetic production. It has been shown indeed that the phosphate - temperature relationship in this region undergoes interannual variations which are not completely explained by the ENSO cycle (Dandonneau, 1988).

No positive anomaly of the chlorophyll concentration at the sea surface was observed in the northwestern tropical Pacific during the 1986-87 El Nino (unpublished data from the SURTROPAC network). Previous warm events, in 1957, 1965, 1972 and 1976 have occurred while no observing network or satellite existed for the sea surface chlorophyll, so that possible phytoplankton blooms could not be detected. The global compilation of data made by Koblentz-Mishke et al. (1970) does not show any sign of such blooms in the western tropical Pacific. The 1982-83 El Nino was a very strong one (Quinn et al. 1987). During this event, the sea surface temperature between 5°N and 15°N was the coldest recorded since 1969 (unpublished data from the SURTROPAC network). The anomaly of the 20°C isotherm depth (observation minus mean annual cycle) at 13°N in the western Pacific reached a peak value, which was only surpassed in 1957 and 1972 (Kessler, this volume). The sea level at Truk Island (7°27'N, 151°51'E) in January 1983 was 25 cm below the mean value (Wyrtki, 1985), which was only (and briefly) surpassed in January 1977

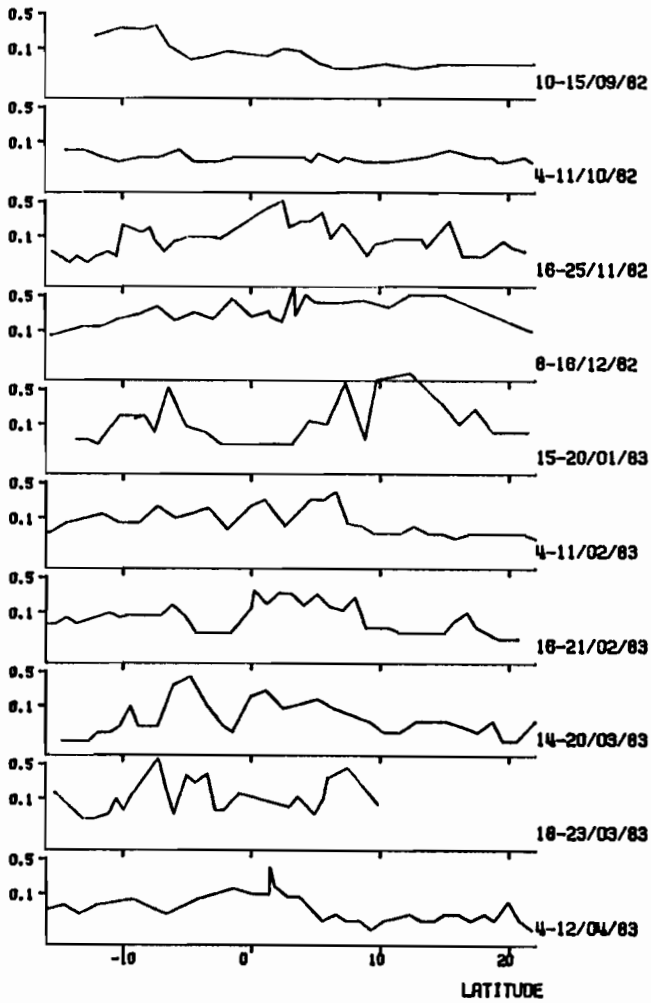

FIG.3. Surface chlorophyll on the New Caledonia to Japan shipping track (logarithmic scale). All the merchant ships voyages from September 1982 to April 1983 are represented here.

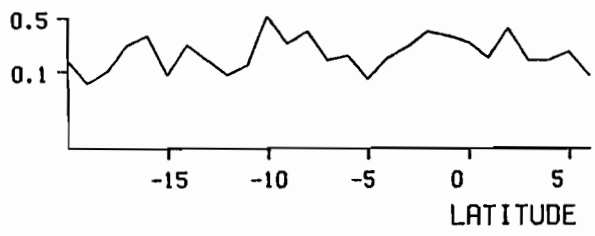

FIG. 4. Chlorophyll concentration (logarithmic scale) at the surface along 165°E, from precise shipboard laboratory measurements during cruise PROPPAC 2 in April 1988 (ORSTOM, Nouméa, courtesy of Aubert Le Bouteiller). Mesoscale variability is as high as shown by the data collected by merchant ships (Figure 3).

(Meyers, 1982). Wyrtki (1985) indeed found that the upper layer volume of the tropical Pacific was much smaller in 1983 than in previous years. Such a low sea level is indicative of low heat content (low sea surface temperature, and/or shallow thermocline) in the upper oceanic layers (Rébert et al., 1985 ; Delcroix and Gautier, 1987) and is favourable to vertical mixing of nutrients and to enhanced photosynthesis. The phytoplankton bloom which we have observed between November 1982 and February 1983 then could be an abnormal feature, which only occurs during very strong El Ninos, when threshold conditions are surpassed.

The equatorial upwelling did not completely vanish during the 1982-83 El Nino. A slightly enriched zone persists at the equator through the warm event, east of the dateline, even in April-June 1983 when chlorophyll concentrations were remarkably weak over most of the Pacific (Fig. 1). Most papers dealing with the consequences of El Nino indeed mention a decrease in productivity rather than a complete pause of the equatorial upwelling (Barber and Chavez, 1986). Existing information on nitrates concentration at the equator in the central Pacific during El Ninos generally shows concentrations significantly different from zero : 6.47 µmole l^{-1} at 150°W in February 1965 (Hisard, 1985); 2 µmole l^{-1} at 160°W in May, 1987 (Wong, personal communication); but | 0 µmole l^{-1} at 158°W in April, 1983 (Feely et al., 1987). The map of chlorophyll distribution in April-June, 1983 (Fig. 1) indeed shows a quasi null influence of the equatorial upwelling in the central Pacific. Permanence of an equatorial enrichment during El Ninos at the equator in the eastern Pacific has been shown on a time series of observing merchant ships voyages from 1979 to 1985 (Dandonneau and Eldin, 1987) : in spite of a decrease of the chlorophyll concentration in the equatorial zone, the limit between enriched equatorial waters and oligotrophic waters in the south only shifted from about 15°S to about 12°S during the 1982-83 El Nino. This limit could be located for each voyage, except on two occasions, in December 1982 and in April 1983.

5. Conclusions

The network of observing merchant ships managed by the SURTROPAC Group in Nouméa has allowed to gather chlorophyll data which provide a unique view of the tropical Pacific Ocean before, during and after the 1982-83 El Nino. It has thus been possible to draw quarterly charts of the chlorophyll distribution at the surface of the Pacific ; in spite of the limited number of available data (about 1000 for each chart), of the high variability which generally characterizes the biological fields, and of the coarseness of the measurement technique, these charts agree reasonably well with current knowledge of the consequences of El Nino. Furthermore, they reveal the occurrence of a large phytoplankton bloom which occurred between 5°N and 15°N from November 1982 to February 1983. Such a bloom in this region had never been detected on previous El Ninos, and has no more been detected during the 1986-87 event. This bloom can however be explained by the extreme conditions (abnormally low sea surface temperature, shallow thermocline) which occurred during the 82-83 warm event, and would thus be a characteristic feature of very strong El Ninos.

Acknowledgments : The officers who carefully sample the surface of the Pacific Ocean and make the filtrations for the chlorophyll measurements took a very large part in this work. I wish to pay homage to their benevolent contribution.

REFERENCES

Barber, R. T. and F. P. Chavez, 1983 : Biological consequences of El Nino. *Science*, **222**, 1203-1210.

Barber, R. T. and F. P. Chavez, 1986 : Ocean variability in relation to living resources during the 1982-83 El Nino. *Nature*, **319**, 279-285.

Chavez, F. P., R. T. Barber, J. E. Kogelschatz, V. G. Thayer and B. Cai, 1984 : El Nino and primary productivity : potential effects on atmospheric carbon dioxide and fish production. *Trop. Ocean Atmos. Newsl.*, **28**, 1-2.

Chavez, F. P. and R. T. Barber, 1987 : An estimate of new production in the equatorial Pacific. *Deep Sea Res.*, **34** : 1229-1243.

Cowles, T. J., R. T. Barber and O. Guillen, 1977 : Biological consequences of the 1975 El Nino. *Science*, **195**, 285-287.

Dandonneau, Y., 1982 : A method for the rapid determination of chlorophyll plus phaeopigments in samples collected by merchant ships. *Deep Sea Res.*, **29**, 647-654.

Dandonneau, Y., 1986 : Monitoring the sea surface chlorophyll concentration in the tropical Pacific : consequences of the 1982-83 El Nino. *U. S. Fish. Bull.*, **84**, 687-695.

Dandonneau, Y., 1988 : La chlorophylle dans le Pacifique : un essai d'océanographie à partir de mesures à la surface de l'océan. Thesis, University of Aix-Marseille II, Oceanography, 68 p.

Dandonneau, Y. and G. Eldin, 1987 : Southwestward extent of chlorophyll-enriched waters from the Peruvian and equatorial upwellings between Tahiti and Panama. *Mar. Ecol. Prog. Ser.*, **38**, 283-294.

Dandonneau, Y. and F. Gohin, 1984 : Meridional and seasonal variations of the sea surface chlorophyll concentration in the southwestern tropical Pacific (14 to 32°S, 160 to 175°E). *Deep Sea Res.*, **31**, 1377-1393.

Delcroix, T. and C. Gautier, 1987 : Estimates of heat content variations from sea level measurements in the central and western tropical Pacific from 1979 to 1985. *J. Phys. Oceanogr.*, **17**, 725-734.

Feely, R. A., R. H. Gammon, B. A. Taft, P. E. Pullen, L. S. Waterman, T. H. Conway, J. F. Gendron and D. P. Wisegarder, 1987 : Distribution of chemical tracers in the Eastern Equatorial Pacific during and after the 1982-83 El Nino / Southern Oscillation event. *J. Geophys. Res.*, **92**, 6545-6558.

Feldman, G. C., 1986 : Patterns of phytoplankton production around the Galapagos islands. In : Bowmnan, J., Yentsch, M., Peterson, W. T. (eds.), Tidal mixing and plankton dynamics. Springer-Verlag, Heidelberg, p 77-106.

Herbland, A. and B. Voituriez, 1979 :Hydrological structure analysis for estimating the primary production in the tropical Atlantic Ocean. *J. Mar. Res.*, **37**, 87-101.

Gill, A. E. and E. M. Rasmusson, 1983 : The 1982-83 climate anomaly in the equatorial Pacific. *Nature*, **306**, 229-234.

Hisard, P., 1985 : La structure thermique équatoriale de l'Océan Pacifique de l'hiver 1965 reconsidérée par référence à El Nino. *Océanogr. Trop.*, **20**, 135-150.

Kessler, W. S., 1989 : Observations of long Rossby waves in the Northern Tropical Pacific. (This volume).

Koblentz-Mishke, O. J., V. V. Volkovinsky, and J. G. Kabanova, 1970 : Plankton primary production of the world ocean. In : W. S. Wooster ed., Scientific exploration of the southern Pacific, National Academy of Science, Washington, D. C., 183-193.

Masuzawa, J. and K. Nagasaka, 1975 : The 137°E oceanographic section. *J. Mar. Res.*, **33** (sup.), 109-116.

Meyers, G., 1982 : Interannual variation in sea level near Truk Island - a bimodal seasonal

cycle. *J. Phys. Oceanogr.*, **12**, 1161-1168.
Meyers, G. and J. R. Donguy, 1984 : The North Equatorial Countercurrent and heat storage in the western Pacific Ocean during 1982-83. *Nature*, **312**, 258-260.
Meyers, G., J. R. Donguy and R. K. Reed, 1986 : Evaporative cooling of the western equatorial Pacific Ocean by anomalous winds. *Nature*, **323**, 523-526.
Quinn, W. H., V. T. Neal and S. E. Antunez de Mayolo, 1987 : El Nino occurrences over the past four and a half centuries. *J. Geophys. Res.*, **92**, 14449-14461.
Rébert, J. P., J. R. Donguy, G. Eldin and K. Wyrtki, 1985 : Relations between sea level, thermocline depth, heat content and dynamic height in the tropical Pacific Ocean. *J. Geophys. Res.*, **90**, 11719-11725.
Sharp, J. H., M. J. Perry, E. H. Renger, and R. W. Eppley, 1980 :Phytoplankton rate processes of the oligotrophic waters of the Central North Pacific Ocean. *J. Plank. Res.*, **2**, 335-353.
Smith, R. C., 1984 : Ocean color for the estimation of global marine productivity. In : Global Ocean Fluxes Study, Proceedings of a workshop, Nat. Acad Press, Washington D.C., pp 103-124.
Tournier, R. and J. Picaut, 1989 : Thermal and current structure variabilities in the western and central tropical Pacific during 1979-85. (This volume).
Walsh, J. J., 1981 : A carbon budget for overfishing off Peru. *Nature*, **290**, 300-304.
Wyrtki, K., 1985 : Water displacements in the Pacific and the Genesis of El Nino cycles. *J. Geophys. Res.*, **90**, 7129-7132

Sea Surface Chlorophyll Concentration in the South Western Tropical Pacific, as seen from NIMBUS Coastal Zone Color Scanner from 1979 to 1984

(New Caledonia and Vanuatu).

Cécile DUPOUY

Center ORSTOM of Noumea
BP A 5 Nouméa New Caledonia

ABSTRACT

Examination of 40 processed cloud-free NIMBUS CZCS images over New Caledonia and Loyalty Islands provides a first view of the remotely sensed near-surface chlorophyll distribution. The major pattern of the phytoplankton abundance is the same as the one detected from the SURTROPAC survey: in winter, enrichment in the south of New Caledonia; in summer, extensive *Trichodesmium* blooms in the north east of New Caledonia. Much newer is the detection of mesoscale gyres trapped on the coast, narrow island mass effects, and generally detailed observations on the small and mesoscale variability around the islands.

1. Introduction.

The South Western Tropical Pacific ocean (SWTP) is considered as an oligotrophic region because of the generalization of the Deep Chlorophyll Maximum (Dandonneau, 1979). When the stratification is disturbed, nutrients usually blocked below the thermocline become available for the phytoplankton of the euphotic layer, leading to increases of the near-surface phytoplankton concentrations which can be remotely sensed from satellite platforms (ocean color) or detected from merchant ships surveys (SURTROPAC). Different possible causes of thermocline disturbances exist in the SWTP. The region (Fig.1) is rich in islands and the bathymetry is complicated by ridges (Norfolk and Fairway) and shoals above coral reefs, which enhance the vertical instability. The vertical mixing is high throughout the year, except from december to march, when a seasonal thermocline forms (Hénin et al., 1984).

Though, increases in Sea Surface Chlorophyll Concentrations (SSCC) towards the islands are not systematically observed by Dandonneau and Charpy, (1985). At the difference of Hawaiian Islands (Gilmartin and Revelante, 1974), no "island mass effect" was detected towards the island of Mare (Loyalties) (LeBorgne et al., 1985). Much strongly identified from the SURTROPAC survey, are the major SSCC increases north and south of the main island linked to the meteorological conditions (Dandonneau and Gohin, 1984).

Our goal is to describe the distribution and quantify the phytoplankton abundance in the region of New Caledonia with help of the ocean color remote sensing. As the NIMBUS-Coastal Zone Color Scanner measures the sea-irradiance in the blue light (Hovis et al., 1980), it allows the rapid and synoptic determination of the photosynthetic pigment distribution. If the cases of coastal upwellings and continental shelves are until now subjects of long-term interest in remote sensing, (Pelaez and McGowan, 1986,

ORSTOM
CENTRE DOCUMENTATION
Montpellier

F 30265

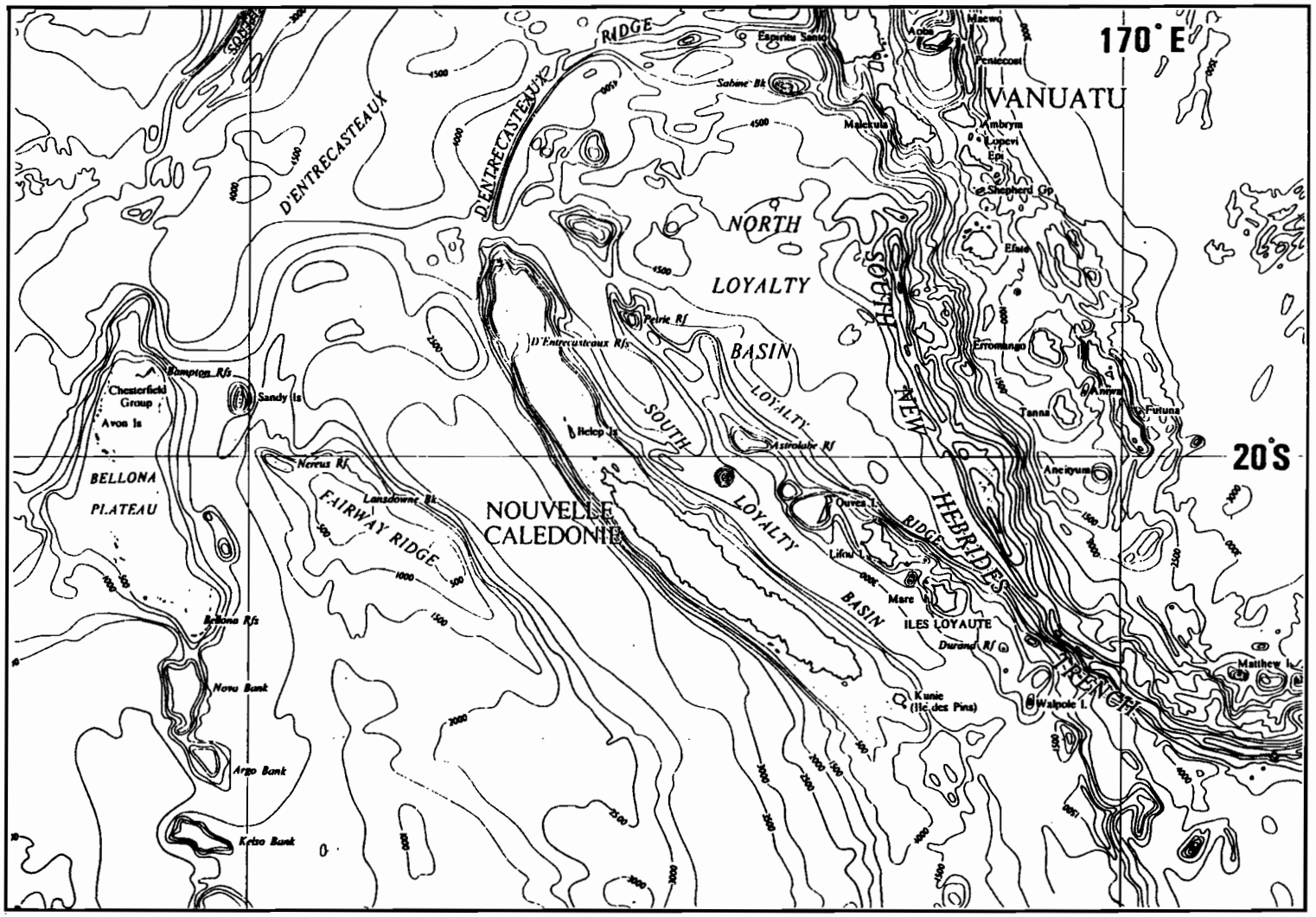

FIG.1. Detailed bathymetric map of the region around New Caledonia, Loyalty Islands and Vanuatu (from CCOP-SOPAC map, 1983 Fairway Ridge and Landsdowne Bank at 20°S, 164°E, Norfolk Ridge at 22°S, 165°E, Chesterfield Group at 19°S, 162°E.

Bricaud et al., 1987, Dupouy and Demarcq, 1987, Gordon et al., 1983, Viollier et al., 1988, Mueller-Karger et al., 1988), only a few studies were devoted to oligotrophic areas and islands rich regions.

2. Results.

The most cloud-free images from CZCS were selected over the area for the period 1979-1984. A fixed common geographic area was chosen and all the images were resampled on a Mercator projection onto this frame (160°E-170°E and 15°S-20°S ; 20°S-25°S). In this region, the chlorophyll is sensed over a depth of 20 meters (determined from the attenuation coefficient of the visible light, Gordon and McCluney, 1975). The deep chlorophyl maximum is never detected, which does not allow to estimate the total chlorophyll content of the water column from the ocean color sensor signal.

The results will be described (figures 2,3,4) by extracting the boundaries of the chlorophyll enrichments determined from the spatial gradients of the CZCS data.

a. Strong signal.

The strong signal of the data set is defined as high values of CZCS chlorophyll concentrations, detected more than once in the data set. Recurrent patterns have been observed at different dates, representative of the winter and summer conditions around New Caledonia.

* Winter conditions.

The 0.3 $mg.m^{-3}$ satellite chlorophyll isopleth (figure 2) shows the limit at 22°S between rich southern waters, and the poorer northern ones, in winters 1981 (April, May, June, July), 1983 (April and September) and 1984 (September 7 and 15). This frontal zone can be narrow in longitude (following the Norfolk ridge in May and September) or continuous over 5 or more degrees (July). The color fronts are indented by smaller eddies. As a strong thermal front was already detected during classical cruises (Jarrige et al., 1980), color and thermal fronts are probably coincident. In this case, the information is not new, as this latitude has been already described from the merchant ship survey (Dandonneau and Gohin, 1984) as the northward limit of the southern enrichment due to cooling and overturning by trades.

* Summer conditions.

The 0.2 $mg.m^{-3}$ CZCS chlorophyll isopleth delineates conspicuous features (figure 3), in December 1979, December 1980 and January 1982. Large patches of richer waters extend as far as 400 km between New Caledonia and the Vanuatu. They originate at the northern Loyalty Islands or New Caledonian northern lagoon. The pattern of January is remarkably well structured (large cyclonic vortex ending south in a arrow shape). Though no coincident measurements are available, the CZCS most probably detects three realizations of *Trichodesmium* blooms. As these algae are known to float at the surface and concentrate along convergence lines (positive buoyancy from gas vacuoles), observations of meanders on the CZCS images are not surprising. They are regularly made at sea or from aerial surveys when red tides of *Trichodesmium* are developed. An estimation of the nitrogen amount fixed by the bloom (these algae can fix the atmospheric nitrogen) has been made; according that the algae are *Trichodesmium sp.*, taking a mean fixation rate (Carpenter and Price, 1976), and assuming a duration of 10 days, the bloom of January 1982 could fix one ton of nitrogen (Dupouy et al., 1988). These irregular blooms of *Trichodesmium* were already identified as summer increase factors of SSCC, north of 22°S (Dandonneau and Gohin, 1984). The CZCS is the only tool to delineate the boundaries of such blooms, and then give an estimation of the nitrogen input in the upper layer.

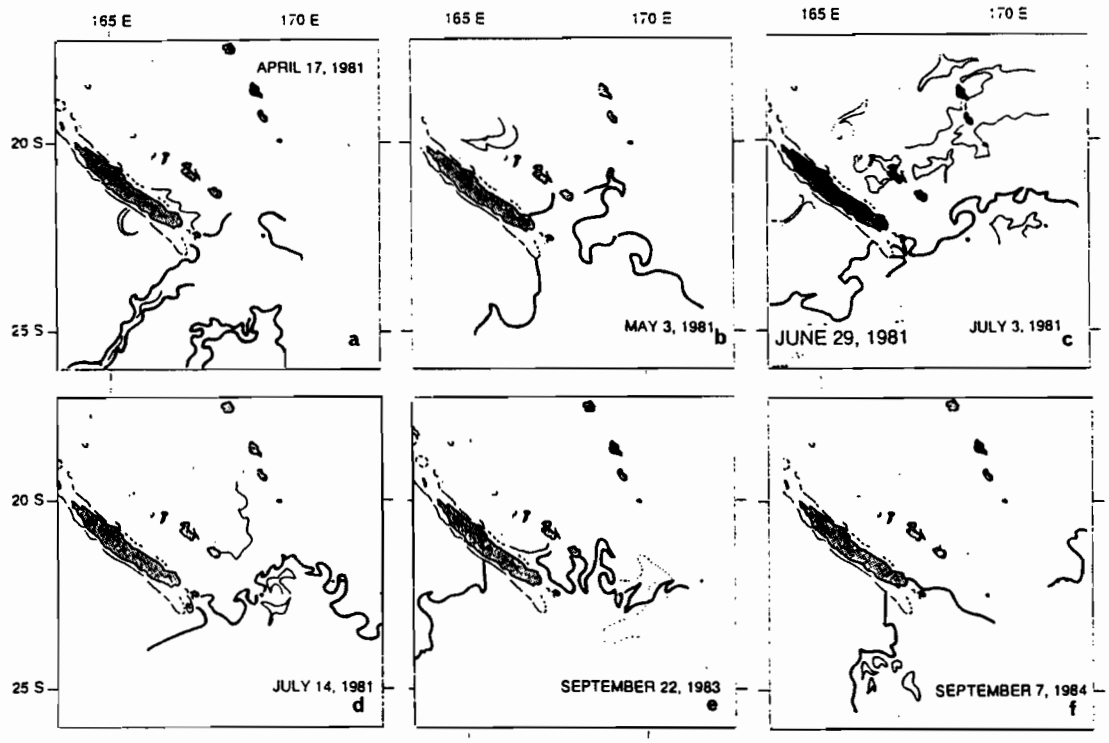

FIG.2. Schematic representation of the limit between pigment rich waters in the south, and poorer ones north of New Caledonia for 1981, 1983 and 1984 winter conditions. The CZCS pigment contour follows aproximately the 0.3 mg.m^{-3} isopleth and was smoothened for clarity (see III.1). a) April 17, 1981. b) May 31, 1981. c) June 29 and July 3, 1981. d) July 14, 1981. e) September 22, 1983. f) September 7, 1984.

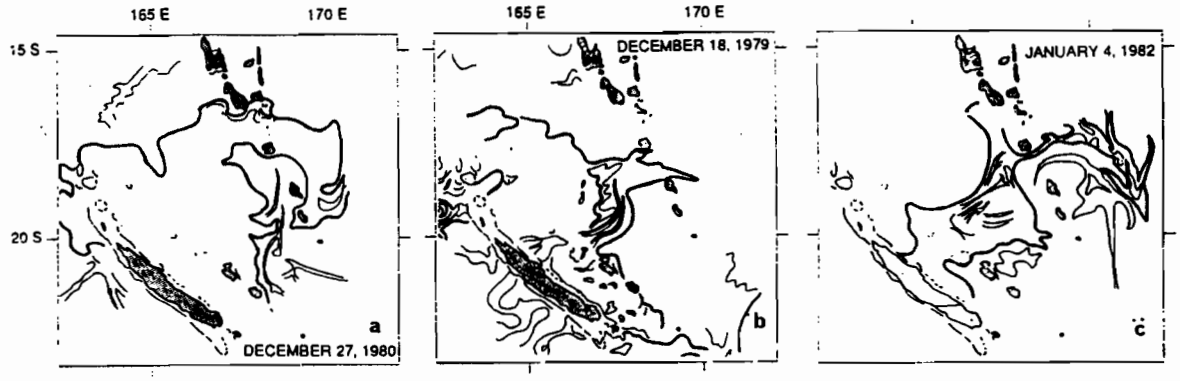

Fig.3. Schematic representation of the pigment rich waters for 1979, 1980 and 1982 summer conditions, showing the extension of Trichodesmium blooms. The CZCS pigment contour follows approximately the 0.2 mg.m^{-3} isopleth. a) December 27, 1980. b) December 18, 1979. c) January 4, 1982.

b. Secondary signal.

This secondary signal is defined as low chlorophyll patterns delineated by the 0.1 $mg.m^{-3}$ CZCS chlorophyll isopleth.

The swadth of the CZCS (1600 km) allows to show that the region surrounding the islands is, all over the year, richer than the more oligotrophic waters found north of 15°S or west of New Caledonia. This enrichment (low chlorophyll value), rather spatially continuous and constant over the year, was not previously evidenced.

The 0.1 $mg.m^{-3}$ CZCS chlorophyll isopleth delineates interesting features. The majority of these patterns are not observed with regularity in the data set. For example, plumes of rich chlorophyll waters originating in the lagoon, and extending along hundreds of kilometers offshore (northern and southern passages of the lagoon barrier). The northwestern coast of the main island is the site of eddies of great diameter (100km-200km) in November 1980 and April 1981 (see figure 4). The gyre of November is spatially coincident with an eddy of warm waters identified in the infrared (Petit and Gohin, 1982). Around the Loyalty Islands (Lifou and Mare), narrow plumelike meanders appear to be entrained from the coasts in winter 1983 (April and September) and winter 1981 (June to July), which agree with the G.E.K. current measurements (same dates). A bathymetric effect, defined as a chlorophyll rich patch surrounded by poorer waters, was detected many times above the Chesterfield lagoons, and twice above the Landsdowne Bank in the Fairway ridge (at 20°S, 164°E see map), in June 1981 and December 1979.

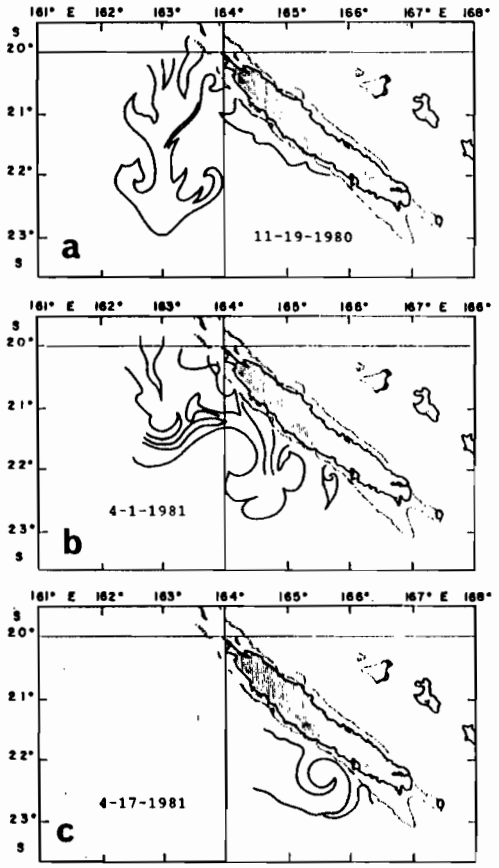

FIG.4. Schematic representation of the low chlorophyll patterns. The CZCS pigment contour follows the 0.1 $mg.m^{-3}$ isopleth. Best examples of trapped mesoscale eddies on the northwestern coast of New Caledonia. a) November 19, 1980. b) April 4, 1981 c) April 17, 1981.

3. Conclusions.

The strong signal defined as recurrent features (high chlorophyll enrichments) detected by CZCS, confirms the conclusions made from the observations of merchant ships during the SURTROPAC survey.

The secondary signal defined as low chlorophyll enrichments is interesting as it reveals new features, never detected from sea-measurements. These near-surface chlorophylls are related to the superficial circulation (eddies, 2-D turbulence, Ekman drift) which has been described as variable and low in this region (Hénin et al., 1984, Le Borgne et al., 1985). The island mass effects are shown by the CZCS, but they are difficult to isolate from the "archipelago" continuous enrichment. As this chlorophyll enrichment is rather continuous between lands, the total amount of pigment biomass, by taking into account the covered surfaces, should be compared to the other source of phytoplankton biomass in the Western Tropical Pacific (equatorial upwelling).

REFERENCES

Bricaud, A., A. Morel, and J.M. André, 1987: Spatial/temporal variability of algal biomass and potential productivity in the Mauritanian upwelling zone, as estimated from CZCS data. *Adv. in Space Res.*, **7**, 2-12.

Carpenter, E.J. and C.C. Price, 1976: Marine Oscillatoria (*Trichodesmium*): explanation for aerobic nitrogen fixation without heterocysts. *Science*, **191**, 1278-1280.

Dandonneau, Y., 1979: Concentrations en chlorophylle dans le Pacifique Tropical sud-ouest: comparaison avec d'autres aires océaniques. *Oceanol. Acta*, **2**, 133-142.

Dandonneau, Y. and F. Gohin, 1984: Meridional and seasonal variations of the sea surface chlorophyll concentration in the southwestern Tropical Pacific, (14° to 32°S, 160 to 175°E). *Deep Sea Res.*, **31**, 1377-1393.

Dandonneau, Y. and L. Charpy, 1985: An empirical approach to the island mass effect in the south tropical Pacific based on sea surface chlorophyll concentrations. *Deep Sea Res.*, **32** (6), 707-721.

Dupouy, C. and H. Demarcq, 1987: CZCS as an aid for understanding modalities of the phytoplankton productivity during upwelling off Senegal. *Advances in Space Res.*, **7**, 2, 63-71.

Dupouy, C., M. Petit and Y. Dandonneau, 1988: Satellite detected cyanobacteria bloom in the SouthWestern Tropical Pacific: implication for nitrogen fixation. Intern. *J. Remote Sensing*, **9**, (3), 389-396.

Gilmartin, M. and N. Revelante, 1974: The "island mass" effect on the phytoplankton and primary production of the Hawaiian islands. *J. Exp. Mar. Biol. Ecol.*, **16**, 181-204.

Gordon, J.R. and McCluney, 1975: Estimation of the depth of sunlight penetration in the sea for remote sensing. *Appl. Opt.*, **14**, 413-416.

Gordon, J.R. and Others, 1983: Phytoplankton pigment concentrations in the Middle Atlantic Bight: Comparison of ship determinations and CZCS estimates. *Appl. Opt.*, **22**, 20-36.

Hénin, C., J.M. Guillerm and L. Chabert, 1984: Circulation superficielle autour de la Nouvelle Calédonie. *Océanogr. trop.*, **19** (2), 113-126.

Holligan, P., M. Viollier, D.S. Harbour, P. Camus M. Champagne-Philippe, 1983: Satellite and ship studies of coccolithophore production along a continental shelf edge, *Nature*, **304**, 339-342.

Hovis, W., D.K. Clark, R.W. Anderson, W.H. Austin, E.T. Wilson, K.D. Baker, D. Ball, , H.R. Gordon, J.L. Mueller, S.Z. El-Sayed, B. Sturm, R.C. Wrigley, and C.S. Yentsch, 1980: NIMBUS-7 Coastal Zone Color Scanner: System description and initial imagery. *Science*, **210**, 60-63.

Jarrige, F., P. Bourret and J.M. Guillerm, 1979: Observations d'une zone de frontière thermique dans le sud ouest Pacifique. Rapport Scientifique et Technique, **5**, Centre ORSTOM de Nouméa. New Caledonia

Le Borgne, R., Y. Dandonneau, and L. Lemasson, 1985: The problem of island mass effect on chlorophyll and zooplankton standing crops around Mare (Loyalty Islands) and New Caledonia. *Bull. Mar. Science*, **37** (2), 450-459.

Mueller-Karger, F.E, C.R. McClain and P. Richardson, 1988: The dispersal of the Amazon's water. *Nature*, **333**, 56-59.

Petit, M. and F. Gohin, 1982: Radiométrie aérienne et prospection thonière. Rapport de Convention ORSTOM Nouméa, 94p.

Pelaez, J., and J.A. McGowan, 1986: Phytoplankton pigment patterns in the Californian Current as determined by satellite. *Limnol. Oceanogr.*, **31**, 5, 927-950.

Viollier, M., A. Sournia, J.L. Birrien, M.J. Chretiennot-Dinet, R. Leborgne, P. Le Corre, P. Morin and J.P. Olry, (GREPMA Group), 1988: Satellite (AVHRR/NOAA9) and ship studies of a coccolithophorid bloom in the Western English Channel. *Marine Nature*, **1**, 1, 1-14.

Field Evaluation of Real-Time XBT Systems

Michael SZABADOS and Darren WRIGHT

National Ocean Service, NOAA
6001 Executive Blvd
Rockville, MD 20852 - U.S.A.

INTRODUCTION

The use of XBT's to measure the ocean's subsurface temperature has significantly increased over the past decade. NOAA is actively participating in an international effort to increase the number of subsurface temperature observations in support of global oceanographic and climate studies. NOAA's XBT program currently supports more than one hundred voluntary observing ships (VOS). These vessels are responsible for more than 12,000 XBT observations each year. Determining the field performance of XBT data systems is an importance step in the quality control of these data. The purpose of this field test was to evaluate the performance of four XBT systems under field conditions. The systems evaluated were a SEAS III (Sippican's MK-9), a Bathy Systems' 810 XBT Controller, an ARGOS XBT system, and Oregon State University's (OSU) XBT Data Box. In addition, the capability of both the ARGOS and GOES satellite systems to transmit XBT data in the JJXX format were evaluated. The SEAS III and ARGOS systems were used to evaluate the satellite transmission process for GOES and ARGOS respectively.

METHODS AND PROCEDURES

All XBT data were evaluated relative to a field standard. The field standard used was a Neil-Brown Instrument Systems Mark III CTD. Each XBT system and the Neil-Brown CTD were calibrated before and after the test. A decade box and XBT test canister were used to evaluate the XBT systems over a range of eleven resistance (temperature) values. The results of the XBT calibration check are presented in Table 1. Initially the OSU system failed the calibration test at temperatures below 5 degrees Celsius. The system was returned to the manufacturer for adjustments. The values from the OSU system in Table 1 were taken from a second calibration check of the OSU system after adjustments were made by the manufacturer.

The XBT Field Evaluation took place on board the NOAA Ship WHITING during July 1988. The WHITING was participating in studies of the current and water mass structure in the Southwestern North Atlantic Ocean in the context of the Subtropical Atlantic Climate Studies (STACS) Program. The evaluation occurred during the Barbados-Barbados leg of the cruise when thirty-three CTD casts were taken. Station locations are shown in Figure 1. During each CTD cast, two XBT's were released from each system. One was released during the descent of the CTD and one was released during the ascent of the CTD. Each XBT system was set up for an XBT drop prior to the

ORSTOM
CENTRE DOCUMENTATION
Montpellier

F 30266

descent of the CTD. To minimize the influence of internal waves, XBT's were released from each system at the same time when the CTD was located in the thermocline. Similar procedures were repeated during the ascent of the CTD. XBT's released during the ascent of the CTD were used to help indicate the temporal variability of the thermal structure while on station. Only XBT's released during the descent of the CTD were used for the XBT-CTD comparison. A total of 250 XBT's were released during the evaluation. Of these, 126 were released during the descent of the CTD. Table 2 presents the total number and type of XBT probe released for each system during the descent of the CTD. No T-5 or T-10 probes were used with the OSU and ARGOS system since these systems were not programmed with the corresponding depth coefficients.

Table 1. XBT SYSTEM CALIBRATION CHECK
(Temperature in Degrees Celsius)

		XBT System Temp - Calibration temp			
Resistance	(Calibration Temp)	MK-9	BATHY	OSU	ARGOS
3193	(35.55)	0.00	-0.06	-0.05	**N/A
3350	(34.44)	-0.05	0.08	-0.08	**N/A
4024	(30.00)	0.02	0.13	-0.01	-0.03
5000	(25.00)	-0.01	0.08	-0.04	-0.06
6247	(20.00)	0.00	0.06	-0.05	-0.06
7274	(16.66)	0.01	0.05	-0.05	-0.06
9948	(10.00)	0.02	0.04	-0.05	-0.06
12679	(5.00)	0.03	0.04	-0.02	-0.03
16329	(0.00)	0.01	0.00	-0.05	-0.06
17287	(-1.10)	0.00	0.01	-0.06	-0.07
18094	(-2.00)	0.01	0.00	-0.04	-0.05

** - The ARGOS system does not handle temperatures in these two ranges.

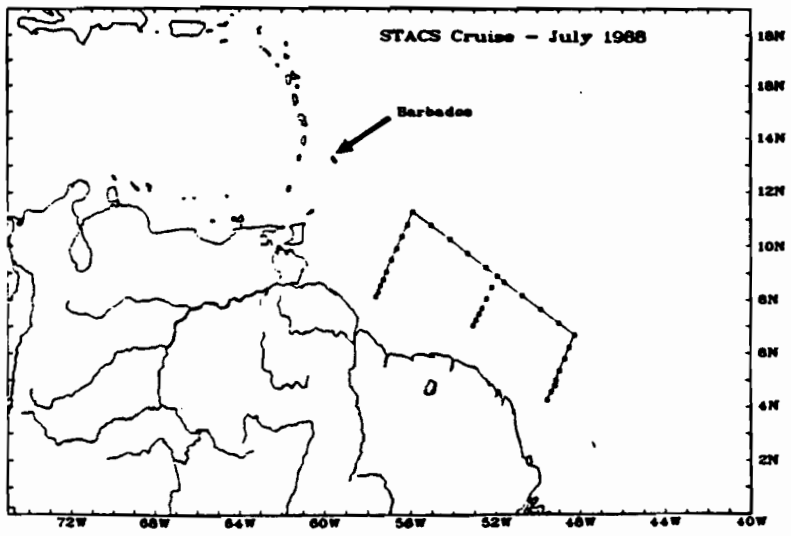

Figure 1. Cruise Track and XBT/CTD Stations

Table 2. PROBE TYPE AND NUMBER RELEASED FOR EACH XBT SYSTEM DURING DESCENT OF CTD

PROBE TYPE	MK-9	BATHY	OSU	ARGOS
T-10	7	7	0	0
T-7	7	7	7	7
T-6	7	7	15	15
T-5	5	5	0	0
T-4	7	7	8	8

Out of the 250 XBT's released, there were a total of five probe failures (2%). A summary of common XBT malfunctions is presented in Kroner and Blumenthal, 1978. The BATHY system had one probe failure, while the OSU and ARGOS systems each had two probe failures. Five software/system crashes occurred with the OSU system. These failures were attributed to incompatibility between the OSU software and the PC clone (televideo XL computer) used. All XBT data collected by the SEAS III and the ARGOS systems were transmitted in real-time contingent on available space in the satellite transmission window.

Before comparing the XBT data to the CTD data, XBT depth-temperature pairs were computed using a linear interpolation scheme so as to have the XBT depth coincide with the CTD depth. Except for the profile plots comparing the XBT and CTD traces, analysis was based on the interpolated XBT data.

RESULTS

Several factors must be considered in the evaluation of XBT - CTD temperature comparisons. Some of the important factors are the methods used to determine the depth of the XBT and the CTD, thermistor errors, and environmental factors such as the stability of the water column. Differences between a temperature measured by the CTD and an XBT can in part be attributed to the computation of the XBT probe depth. The depth of the XBT is determined by using a depth equation based on the fall rate of the probe, while the CTD depth is measured using a pressure transducer. In addition, the XBT descends at a faster rate than the CTD (6.5 m/sec, XBT; 0.5 m/sec, CTD). The XBT and CTD will therefore measure temperature simultaneously at the same depth and time only once. Any changes in the thermal structure of the water column during the descent of the CTD due to internal waves will appear as a temperature difference between the CTD and XBT. Temperature differences between an XBT system and the CTD can also be attributed to the individual thermistor in each XBT probe. While each XBT system and the CTD thermistor were calibrated, the actual thermistor in each XBT probe were not.

The mean of the absolute temperature difference between the CTD and each XBT system over the total XBT profile for each probe type is provided in Table 3. These results show differences greater than the +/- 0.15 degree Celsius specification for XBT probes. To interpret these results it is important to identify the factors which contribute to these differences between the XBT and CTD measurements.

Table 3. MEAN OF THE ABSOLUTE DIFFERENCE BETWEEN THE XBT AND CTD TEMPERATURE (Degrees Celsius)

	Probe Type									
SYSTEM	T-04		T-05		T-06		T-07		T-10	
	Mean	SD	Mean	SD	Mean	SD	Mean	SD	Mean	SD
MK-9	.36	.14	.11	.06	.33	.13	.34	.24	.30	.21
BATHY	.30	.15	.24	.17	.26	.11	.30	.19	.33	.18
OSU	.19	.19			.14	.06	.18	.07		
ARGOS	.38	.22			.39	.11	.42	.33		

To isolate the contributions of the XBT thermistor error to the results shown in Table 3, temperature differences in the isothermal portion of the mixed layers were analyzed. This was done because temperature differences due to depth errors, instrument response, and internal waves would be minimized by these conditions. Thus, as shown in Table 4, when comparing only temperatures in the isothermal portion of the mixed layers, the temperature difference between the CTD and all four systems was reduced by an order of magnitude. The mean departure of the XBT temperature from that of the CTD is well within the XBT specifications. These results also agree well with the XBT system calibration check in Table 1.

Table 4. MEAN TEMPERATURE DIFFERENCES BETWEEN THE XBT AND CTD IN THE MIXED LAYERS (DEGREES CELSIUS)

SYSTEM	MEAN	STANDARD DEVIATION
MK-9	.029	.046
BATHY	.106	.064
OSU	-.074	.083
ARGOS	.016	.055

Errors in XBT depth can also contribute to the differences found between the XBT and CTD temperatures. The temperature profiles in Figure 2 show a depth offset between the XBT and CTD data. To determine the associated XBT temperature error due to an offset in XBT depth, the XBT data was shifted in depth to find a best fit with the CTD data. A best fit of the XBT profile to the CTD was found by shifting the XBT data in 50 meter segments by one-meter increments up and down until the least mean difference between the XBT and CTD temperatures was determined. The depth error was then

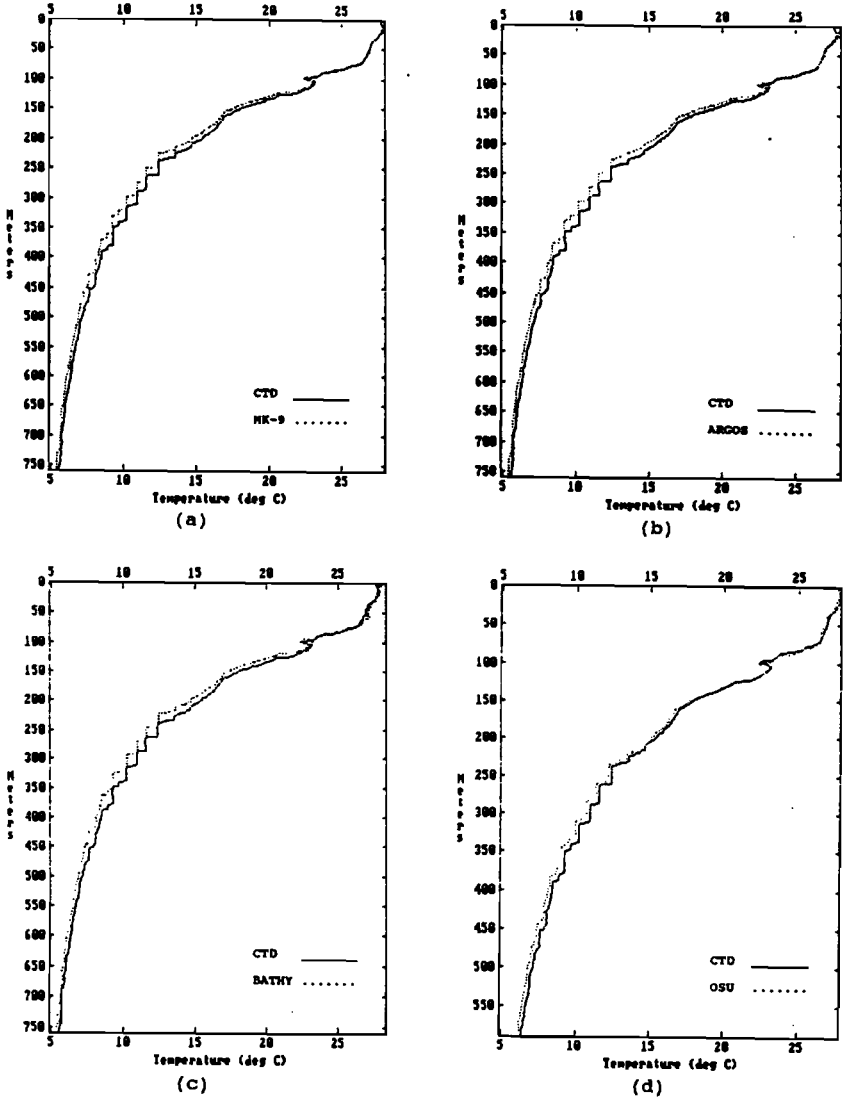

Figure 2. XBT - CTD Temperature Profiles, XBT Drop 25.
(a) MK-9 (b) ARGOS (c) BATHY (d) OSU

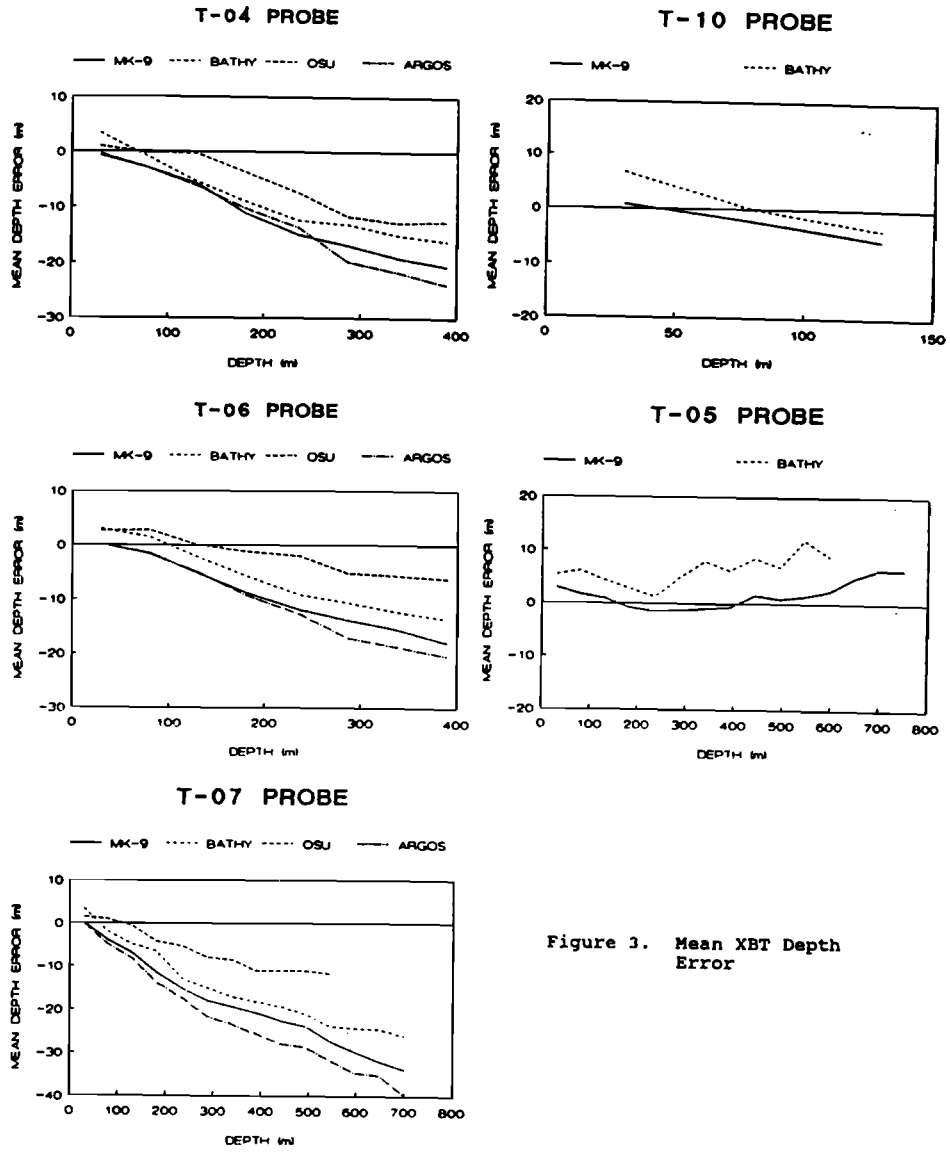

Figure 3. Mean XBT Depth Error

computed from how many meters the original XBT data was moved to best fit the CTD data. Table 5 provides a sample output from this analysis. As is shown in Table 5, by shifting the XBT depth the temperature difference between the XBT and CTD can be reduced by an order of magnitude. The mean temperature difference with a depth correction agrees well with the temperature difference found in the mixed layers and those from the calibration check.

For each of the XBT systems, the mean depth error in 50 meter segments is shown in Figure 3 by probe type. While there appears to be some bias between different XBT systems, it is important to note that for all the XBT systems the depth error for probe types T-4, T-6, and T-7 show a similar trend. This trend indicates that these XBT probe types are falling at a faster rate than calculated by the XBT depth equation, using the standard coefficients. The standard depth equation and coefficients are provided in Table 6 (Sippican, 1973). Similarly, the T-10 probes are falling at a faster rate, while the T-5 probes are falling at the proper rate. The OSU system depth error, as shown in Figure 3, was less than the other systems. This resulted in a smaller temperature difference from the CTD data as was indicated in Table 3.

Table 5. BEST-FIT ANALYSIS

System type: MK-9 Drop Number 27 Probe Type T-07

Depth Range (meters)	Depth Error (meters)	Mean Temp. Error w/ Depth Corrected (C)	Mean Temp. Error w/ Depth Uncorr. (C)
5.0 to 52.7	- 0.99	0.05 +/- 0.03	0.07 +/- 0.04
56.7 to 104.4	- 3.98	0.09 +/- 0.05	0.45 +/- 0.10
108.4 to 156.1	- 6.96	0.11 +/- 0.07	0.63 +/- 0.08
160.0 to 207.7	-10.93	0.05 +/- 0.05	0.62 +/- 0.10
211.7 to 259.4	-17.88	0.04 +/- 0.04	0.68 +/- 0.14
263.4 to 311.0	-19.86	0.02 +/- 0.03	0.49 +/- 0.10
315.0 to 362.7	-21.84	0.03 +/- 0.02	0.37 +/- 0.12
366.6 to 414.3	-24.82	0.03 +/- 0.02	0.48 +/- 0.07
418.2 to 465.9	-27.79	0.04 +/- 0.02	0.32 +/- 0.07
469.8 to 517.5	-30.76	0.04 +/- 0.02	0.32 +/- 0.03
521.4 to 569.0	-33.73	0.04 +/- 0.02	0.35 +/- 0.04
573.0 to 620.6	-41.65	0.03 +/- 0.02	0.35 +/- 0.02
624.6 to 672.2	-48.58	0.01 +/- 0.02	0.31 +/- 0.02
676.1 to 723.7	-49.56	0.03 +/- 0.02	0.22 +/- 0.02

Table 6. STANDARD FORM OF THE DROP EQUATION

Probe type	Coefficients A	B	
T-4	6.472	.00216	$Depth = A*T - B*T^2$ (meters)
T-5	6.828	.00182	T= sample rate * sample no.
T-6	6.472	.00216	
T-7	6.472	.00216	
T-10	6.301	.00216	

To determine if the XBT depth for the T-4, T-6, and T-7 probes could be corrected by modifying the coefficient in the depth equation, a regression analysis was employed to revise the coefficients using the MK-9 data. This was accomplished by first calculating what the sample interval would have to be to provide the correct depth as determined by the best fit analysis. This sample interval was found to be 0.105 seconds. The actual MK-9 sample interval is 0.1 seconds. The revised coefficients A' and B' were then determined by the following method:

$$A' = (6.472 * 0.105) / 0.1 = 6.796$$

$$B' = (0.00216 * (0.105)^2) / 0.01 = 0.00238$$

New temperature and depth pairs for the T-4, T-6, and T-7 probes using the revised coefficients were then computed. Scatter plots comparing the XBT and CTD using the standard and revised coefficients are presented in Figure 4. As shown in these plots the revised coefficients improve the agreement between the XBT and CTD temperature data. Using the same revised coefficients, the ARGOS and BATHY data had similar results. The temperature profiles that were shown in Figure 2 are replotted in Figure 5 using the revised coefficients. Most of the temperature errors associated with the depth offset (previously characterized by the temperature profiles in Figure 2) are now reduced or eliminated. The exception is the OSU XBT data which has better agreement with the CTD data using the standard coefficients.

To determine the temporal variability of the water column during the XBT-CTD comparison, XBT's were launched from each system during the ascent of the CTD. This provided a measure of the variability on the scale of one hour. Any variability on this time scale is likely a result of internal waves. While a few stations exhibited variability in the thermocline of about 10 meters, typically the variability was less than 2 meters. To quantitatively determine the influence of internal waves on the CTD - XBT comparison, several more XBT drops are required during the descent of the CTD. Although variability of the water column due to internal waves can influence the comparison between the XBT and CTD, it should be minimal since it takes approximately 16 minutes for the CTD to reach 500 meters.

The real-time transmission of XBT data is crucial to the optimum utilization of these data sets by the oceanographic and climatological communities. The alternative is retrospective data submission to national data archives which historically can take months, years or even worse never. During the field test the ARGOS and GOES satellite systems were evaluated for their XBT data transmission capability using the SEAS III and ARGOS XBT systems, respectively. For both these systems, data received was disseminated to the community on the Global Telecommunication System (GTS).

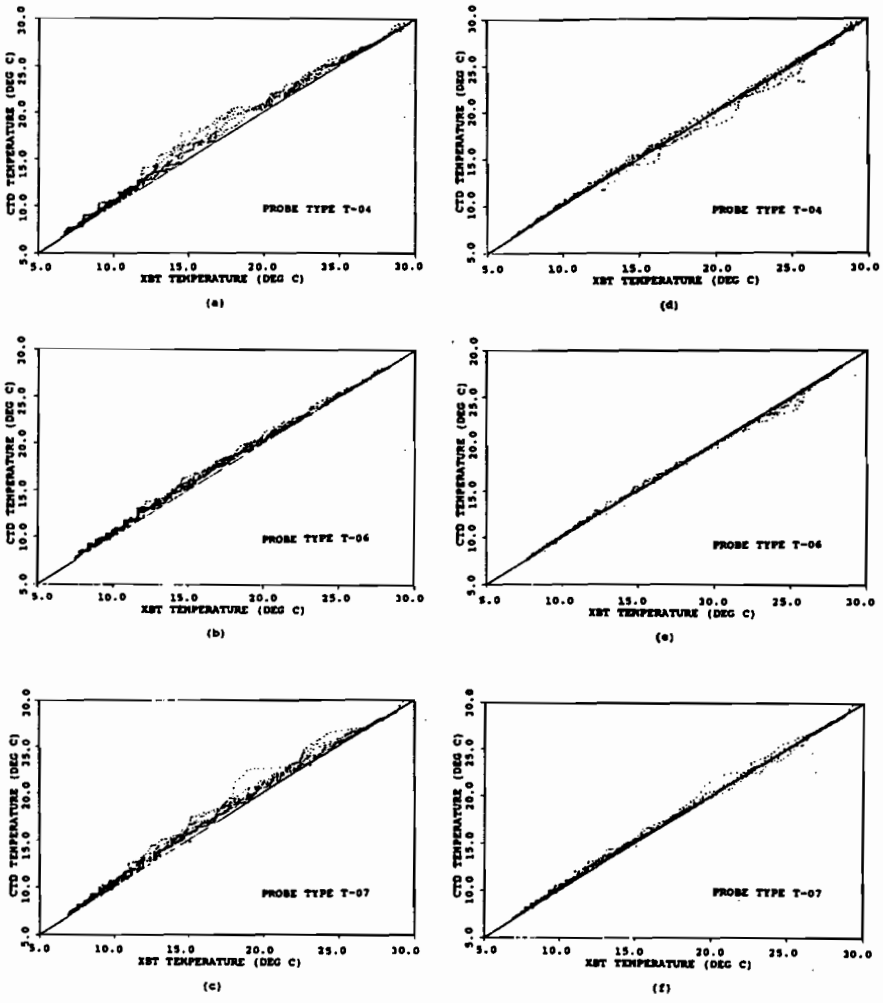

Figure 4. Scatter Plots of MK-9 XBT Data vs. Ctd Data
(a-c) Standard Depth Coefficients
(d-f) Revised Depth Coefficients

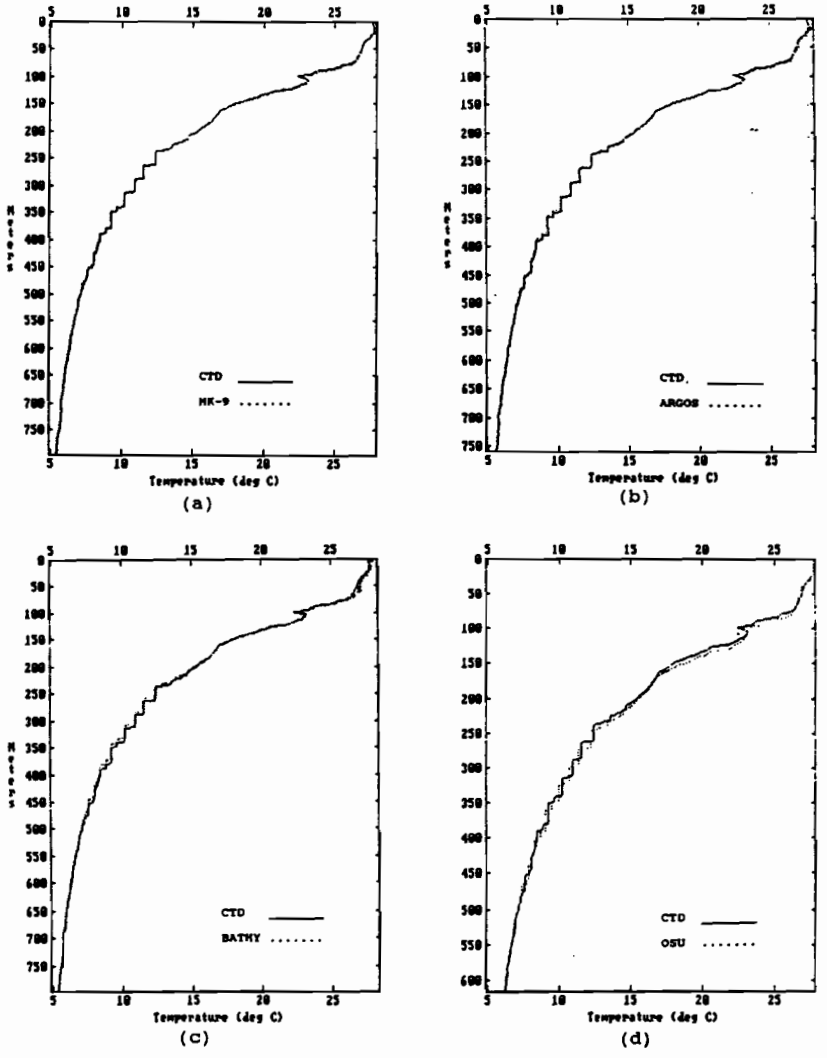

Figure 5. XBT -CTD Temperature Profiles, XBT Drop 25
with Revised Depth Coefficients.
(a) MK-9 (b) ARGOS (c) BATHY (d) OSU

Table 7 summarizes the results from evaluating the real-time data transmissions. Of the 60 XBT's dropped using the ARGOS XBT system, 48 XBT messages were transmitted. Ten were not transmitted because of the 15 iteration limit, imposed by the software in version 1.0, to compute the 15 inflection points. This limitation has been corrected in version 2.0. Two XBT messages were not transmitted because of faulty probes. The high launch frequency, sometimes generating a message every hour, resulted in 11 of the 48 messages not being generated into GTS bulletins. The bulletins were not generated because of the required two transmission receptions not being received. This should not be considered a limitation of the system since most oceanographic surveys do not require the high XBT launch frequency used during this field test. Of the 65 XBT's dropped using the SEAS III system, 58 XBT messages were transmitted and entered onto the GTS. Seven of the XBT drops were not transmitted because of the high frequency of XBT launches. The XBT buffer in the GOES transmitter allows for 3 XBT messages. Since the GOES satellite assignment permitted a transmission every 4 hours, the XBT transmitter rejected seven XBT drops. Again, most oceanographic surveys do not require this high frequency of XBT launches. If necessary, the data can be stored on floppy disk and transmitted at a later time.

TABLE 7 SUMMARY OF REAL-TIME DATA TRANSMISSION

SYSTEM	XBT's DROPPED	TRANSMISSION STATUS	DATA DISSEMINATION STATUS
ARGOS	60	Transmitted - 48	Data Bulletins - 37
		Not Transmitted - 10 (1)	Not Disseminated - 11 (3)
		Not Transmitted - 2 (2)	
SEAS III	65	Transmitted - 58	Data Bulletins - 58
		Not Transmitted - 7 (3)	

(1) Ten XBT messages not generated because criteria for obtaining 15 inflections points were too strict. This limitation is corrected in latest software, Version 2.0.

(2) Two XBT messages not generated because of XBT probe failure.

(3) Eleven from the ARGOS XBT system and 7 from the SEAS III system were neither transmitted or disseminated in real-time because of the high launch frequency during field evaluation.

SUMMARY

This field test evaluated both the performance of XBT systems under field conditions and the capability of the ARGOS and GOES satellite systems to transmit XBT data in the JJXX format. Results show that the mean temperature differences between the CTD and each XBT system over the total XBT profile were greater than the +/- 0.15 degrees Celsius specification for XBT probes. In the isothermal portion of the mixed layer where the temperature differences between the XBT and CTD are minimized due to depth, instrument response, and internal waves, the temperature differences between the XBT's and CTD were reduced by an order of magnitude. From these results, it was determined that temperature error due to the XBT's thermistor is small. The major contributing factor for the differences in temperature is an error in the computation of the XBT probe depth. The error in depth for the T-4, T-6, and T-7 probe types was found to be greater than allowable by the manufacturer's specifications (+/- 5 meters or +/- 2% of depth, whichever is greater). It was determined that these probes are falling at a faster rate than calculated by the standard coefficient of the drop equation. This depth error has been previously identified by Heinmiller et al.(1983) and Seaver and Kuleshov (1982). The depth errors can be reduced by revising the coefficients in the depth equation. While all XBT systems indicated a depth error, there was a system bias among the systems, some showing a greater error than others. This bias among system requires further analysis. Transmission results demonstrated that both ARGOS and GOES satellite based XBT systems provided adequate capability to transmit data in real-time. Together, ARGOS and GOES provide the necessary data communications for a global ocean observation program.

ACKNOWLEDGEMENTS

We would like to express our sincere thanks to Sonny Richardson for help making this evaluation possible and for all his helpful suggestions. We'd like to thank Yvonne Newmen for helping with the data processing and preparation of this report. Also we appreciate the help, suggestions, and support of the following people, Archie Shaw and Mitch Tiger of Argos, Rod Mesecar and Jim Wagner of Oregon State University, Jim Hannon of Sippican, Don Dorson of Bathy Systems, Mike Miyake of the Institute of Ocean Sciences and Bob Molinari of NOAA/AOML.

REFERENCES

Seaver, G.A., Kuleshov, S., "Experimental and Analytical Error of the Expendable Bathythermograph." Journal of Physics and Oceanography, 12, 592-600, 1982.

Heinmiller, R.H., Ebbesmeyer, C.C., Taft, B.A., Olson, D.B. and Nikitin, O.P., "Systematic Errors in Expendable Bathythermograph (XBT) Profiles." Deep Sea Research, 30, 1185-1197, 1983.

Kroner, S.M., Blumenthal, B.P., "Guide to Common Shipboard Expendable Bathythermograph (SXBT) Recording Malfunctions." Naval Oceanographic Office, August 1978.

Sippican Ocean Systems, "Operation/Maintenance Manual MK-9 Digital XBT/XSV System." September 1983.

For a Better XBT Bathy-message: Onboard Quality Control, plus a New Data Reduction Method

Pierre RUAL

ORSTOM, Centre de Noumea, BP A5,
Noumea, New Caledonia

ABSTRACT

To improve the quality of the bathy-messages, sent to the Global Transmission System of the World Weather Watch via the Argos satellite, by ORSTOM - C.L.S. service Argos software onboard ships of opportunity, the following operations are implemented: *i)* a combination of a nonlinear median filter in order to despike the eXpandable BathyThermogramme profile prior to onboard quality control, *ii)* plus a linear Hanning filter, to filter out the small scale features before using the Broken stick data reduction method (that gives directly the required number of significant data point without iteration), *iii)* and a final regression fit. Only bathy-messages from temperature profiles that passed the onboard quality control, are sent to the satellite transmitter and the bathy-messages are computed only to the depth of the deepest "good" data point. So very few bathymessages are rejected later on, during the successive quality controls.

1. Introduction.

In order to improve the quality of the XBT (eXpandable BathyThermogramme) bathy-message sent to the GTS (Global Transmission System) of the World Weather Watch, an onboard quality control of the XBT temperature profile is necessary. The number of significant points constituting the bathy-message is limited (15 to 30), so it is important to use the best data reduction method to calculate the significant points. The bathy-message being used by meteorologists but also by atmosphere or ocean modelers, it is necessary to produce a bathy-message not only representing correctly the temperature profile but also representing with a good accuracy the integrated parameters such as the heat content. Dynamic height and geostrophic currents are deduced from the integrated density profile calculated by adding a temperature-salinity relation.

2. Onboard Quality Control.

Prior to any bathy-message calculation, a set of tests is applied to the temperature profile in order to know if it is worth doing.

All the test parameters given here are those used by ORSTOM for the TOGA (Tropical Ocean and Global Atmosphere) program in the tropical oceans, and they are to be modified according to the area of observation.

i) If the maximum depth of the profile is less then 90 meters, the profile is considered too short to be useful, and another launch is asked to the operator.

ii) If the profile is deeper than 200 meters, but its deepest temperature is higher than the 10 meters temperature minus 2°C, the profile is considered to have failed probably due to probe nose breakage, so that the probe thermistor instead of falling with its nominal speed, is floating in the mixed layer. This error is possible due to the fact that the probe depth is not measured but computed from the time elapsed since the probe

ORSTOM
CENTRE DOCUMENTATION
Montpellier

F 30267

contact with the sea surface. This test is a good example of a regional test that should be modified if the measuring area contain a region of deep water formation, where the water is mixed from the surface to a very great depth, as it is the case in the Antarctic Ocean.

If these two tests have been passed then the bathy-message is considered worth computing, but the question of its maximum depth is raised.

3. Bathy-message Depth.

The number of significant points (15-30) constituting a bathy-message is much reduced compared to the data points number of a profile (generally one to two per meter). So it is important to try to know the depth of the deepest "good" data point. If this depth becomes the maximum depth of the bathy-message then the later will make use of all its significant points to describe the "good" part of the profile, and the accuracy of the description will be the best obtainable with a given data reduction method.

A series of test are conducted to determine that maximum depth. Again the test parameters are those used by ORSTOM for the TOGA tropical ocean region, and should be modified if necessary.

i) In the first 10 meters, no tests are conducted as it is a region where there is a great variability both due to the ocean or to the instrument. For instance, large temperature change may be due to ice melting or cold rain or to a big difference between the storage temperature of the probe and the sea surface temperature.

ii) Starting from 10 meter, the profile is downward tested until the first of the following is met :

- the end of the profile,
- the preset maximum depth of the bathy-message (512 m with the Argos transmission,
- the first outside range temperature (-2°C, 32°C),
- the first temperature gradient above 3°C/meter, positive or negative,
- the first temperature inversion greater than 1.5°C in the first 200 meters or 0.5°C below.

iii) The temperature minimum of the profile above the data point under test, is kept in memory. The depth of the deepest data point where the temperature is less or equal to the temperature minimum plus 5/100°C (white noise value of an XBT temperature profile) is also kept in memory. This point is considered as the last "good" point of the profile and its depth is taken as the maximum depth of the bathy-message. This point may be several meters above the last data point under test.

4. Data Reduction Methods.

Once determined the fraction of the temperature profile used to compute the bathy-message, the question is, what kind of data reduction method will give the best results in the less possible processing time.

Until recently, with the strip chart recorders, this was made by hand, by skilled observers, but on ships of opportunity, where the operators are volunteers but not specialists, it is better to use an automatic method. The base for all these methods is that the profile is reasonably linear, between two successive significant points, but depending upon the premises, they are divided into two different groups:

i) A tolerance is given in the adjustment of the bathy-message to the full profile, and a certain number of significant points is deduced. If there are too many or not enough points, the tolerance may be modified and the process repeated.

ii) A number of significant points is given and the maximum deviation of the bathy-message to the profile is deduced. If that deviation is too big, then the process may be resumed adding more significant points.

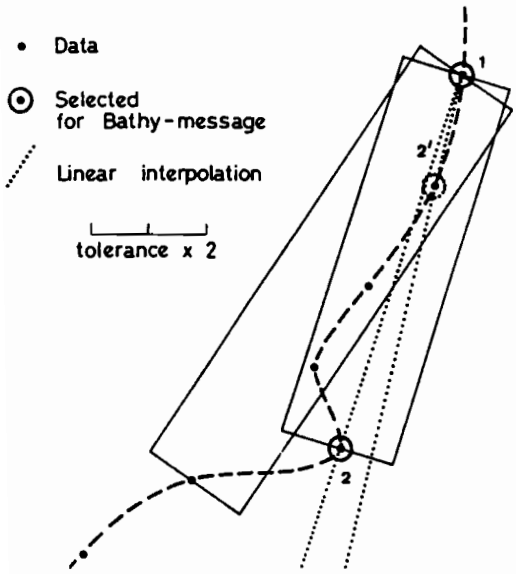

FIG.1. PIPE data reduction method.
a) Select a temperature tolerance.
b) Between 1 and 2 build a pipe with a radius equal to the tolerance.
c) Test all the data points between both ends of the pipe.
d) All of them are inside, so proceed to the data point following 2 and do again b) and c).
e) If any data point outside the pipe (here, data point 2), then select as the new significant point, either the bottom end of the previous pipe (point 2), or the data point opposite to the exit side (point 2').
f) When reaching the last data point, there is N+1 significant points. If it is too much or not enough, start again from a) with another temperature tolerance.

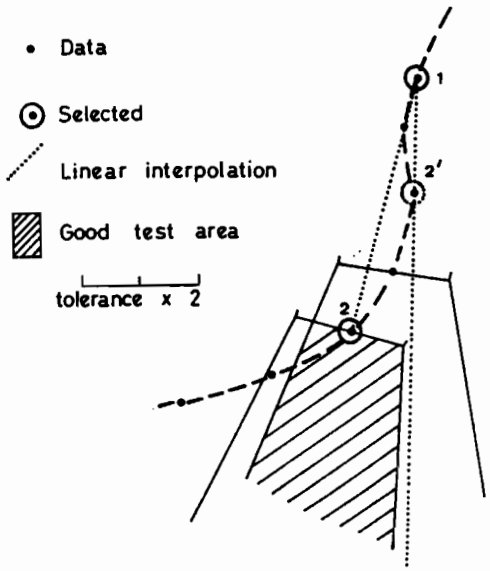

FIG.2. CONE data reduction method.
a) Select a temperature tolerance.
b) Between 1 and 2 build a cone with a base equal to twice the tolerance.
c) Test if the data point following point 2 is inside the intersection of the cone (1,2) with the previous cone.
d) If it is inside, then use it as the base of a new cone and start again b) and c).
e) If it is outside (as it is here), then select as the new significant point, either the cone base (point 2), or the data point opposite to the exit side (point 2').
f) When reaching the last data point, there is N+1 significant points. If it is too much or not enough, start again from a) with another temperature tolerance.

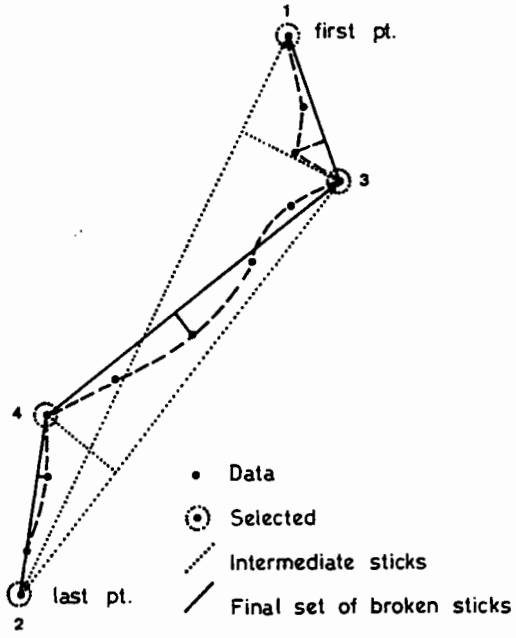

FIG.3. BROKEN STICK data reduction method.
a) Fix the number of significant points needed.
b) Draw a straight line (the stick) between the first and the last data points (1 and 2).
c) Calculate the distance between all the data points and the stick.
d) Break the stick at the data point where the distance is the greatest (point 3).
e) Having now 2 shorter sticks. Calculate the distances to the new sticks.
f) Break the stick, of all the sticks, with the data point the furthest from it (point 4).
g) Start again from b) until the selected number of significant points is reached.
Remark: Attention must be paid when breaking a stick, to check that the 2 new sticks created are not collinear with the preceding or the following stick. If so, then the intermediate point is deselected.

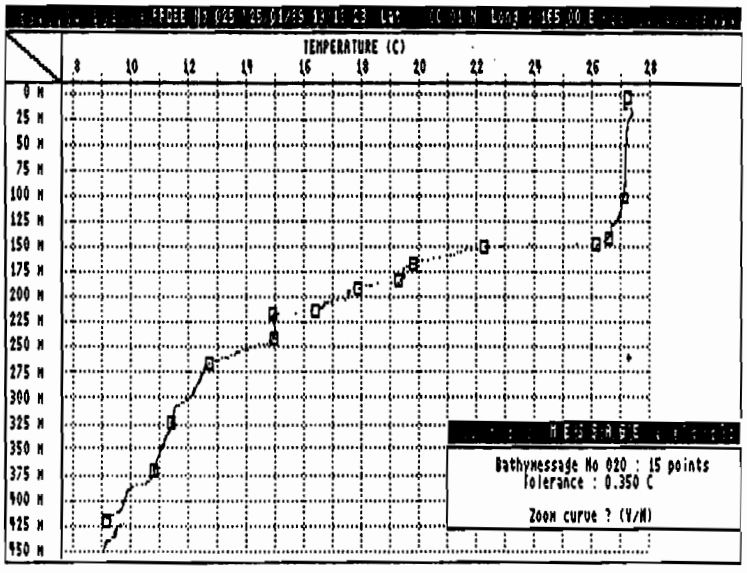

FIG.4. Bathy-message significant points. The squares represent the 15 significant points selected in 18 seconds by the Broken stick data reduction method out of a 500 data points XBT temperature profile. The maximum depth of the calculation was set to 420 meters by onboard quality control, because the temperature inversion below it, is considered too big, higher than half a degree.

a) Methods.

1) Pipe and Cone methods.

There are at least two methods in which the tolerance is given (Frachon 1987), the basic Pipe method, and the more controversial but also more rapid Cone method.

The Pipe method (Fig.1) (Siess, 1982) is equivalent to a rigid pipe with a diameter twice the tolerance, pushed around the profile, each time the profile breaks trough the pipe's wall, a significant point is found in the preceding data point or in the preceding point the most opposite to the exit. The process is then iterated starting with the new significant point. This method is very slow due to the fact that each time a new pipe is build between two points, the position of all the data points, in between, must be tested to check if they are inside or outside the pipe.

The Cone method (Fig.2) (Mesecar and Wagner, 1980; Frachon, 1987) is less satisfactory theoretically but seems to give comparable results and is very rapid as there is no backward control. The last significant point is the summit of the cone, the following point is its base, with a width twice the tolerance. If the third point is within the extrapolation of the cone, then this point is used for the base of a new cone and the next point is tested. There is one restriction, the next cone must always be inside the preceding cone, so if they intersect, only the intersection of the two cones is considered as the new cone (otherwise, it may be possible to mistake a large circle for a straight line!). When the following point is outside the cone then, as with the pipe method, a new significant point is found in the base point or in the preceding point the most opposite to the exit.

2) Broken Stick method.

The Broken Stick method (Fig.3) (Frachon, 1987; Kerr, 1984) is the only method that suppose a preset number of significant data points. Its basis is very different from the first two methods. A straight line (the stick) is drawn between the first and the last points of the profile. The distance between all the data points and the stick is computed and the stick is broken into two pieces at the data point the furthest from the stick. This point becomes a new significant point and the process is repeated, until the given number of significant points is reached. Each stick has a data point the furthest from it, but only one stick is broken at a given time, the stick containing the data point, the furthest of all the furthest data points. At the end of the process the remaining maximum distance of the furthest data point is a measure of the quality of the method and is equivalent to the tolerance of the previous methods. This method is more rapid than the Pipe method but less than the Cone method.

b) Bathy-message problem.

The GTS bathy-message format as well as most of the satellite messages, imposes a maximum length message. In order to make the best use of a message, it is best to fix the maximum number of significant points that fits into a message. The number of significant points being fixed, the obvious method to use is the Broken Stick method (Fig.4). When using one of the other methods, one has to iterate them, and to change the tolerance, until the number of significant points falls within a given range. These iterations may take a long time even with the very rapid Cone method. The empirical relation between the tolerance and the number of significant points in an XBT temperature profile, is nearly hyperbolic. Using an hyperbolic interpolation reduce a lot the number of iterations, but even then, for a 500 data points temperature profile, with a Personal Computer, the mean time to compute a 15 point bathy-message is 18 seconds with the Broken Stick method (+/- 1 second and no iteration), 45 seconds with the Cone method (9 to 90 seconds, with 9 seconds/iteration), and 2.5 minutes with the best dichotomic Pipe method (0.5 to 5 minutes, with 0.5 minute/iteration).

CRUISE : SURTROPAC 09 JAN. 88

50 Drops / 46 Bathymessage CORIOLIS

Method	$\overline{\text{Heat Content}}$ (Mean temperature)	$\overline{\lvert\text{Error}\rvert}$ Mean temperature	$\overline{\sigma}$ (profiles)	$\overline{\lvert\text{Error Max}\rvert}$ (profiles)
Cone	17.557°C	.043°C	.138°C	.404°C
Broken Stick		.032°C	.125°C	.362°C
BS + Regression		.004°C	.087°C	.314°C

TAB.1. Errors between the full XBT temperature profile and the bathy-messages computed using the Cone or the Broken stick method. On the third line, was added to the later a regression fit. A pseudo heat content is given in the first column, the mean of the amplitude of its error is given in the second column. The third and fourth columns present the mean of the temperature standard deviation and the mean amplitude of the maximum temperature error.

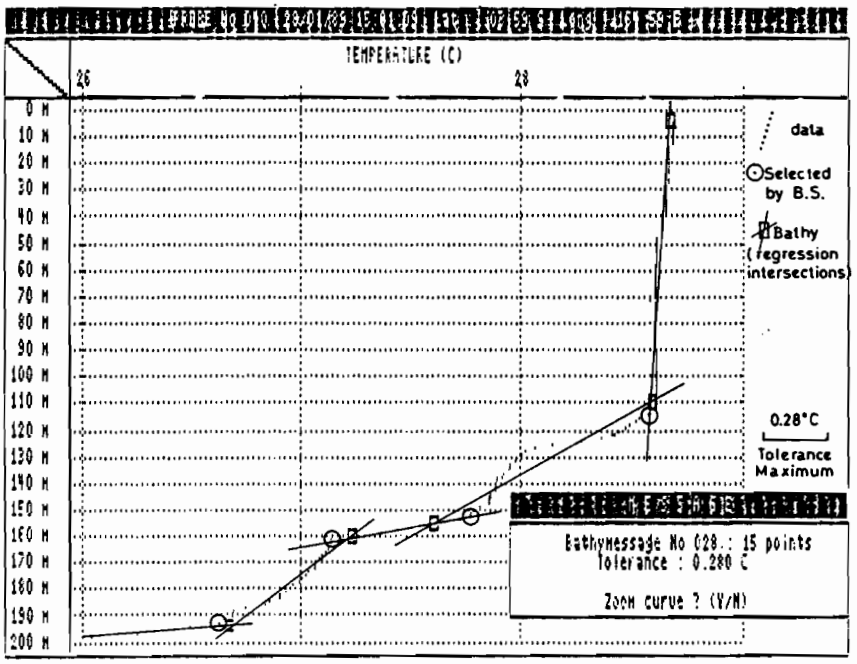

FIG.5. Linear regression fit. The open circles are the significant data points selected by a data reduction method. The squares are the intersections of the regression fit segments constructed from all the data points between two successive significant data points. The straight lines drawn between the squares are a better fit to the curve than the lines between the open circles so the regression lines intersections are chosen as new significant points.

The Broken Stick method is not only quicker but also better, as shown in Table 1, according to a study based on more than 50 temperature profiles and 46 bathy-messages. It results in a mean standard deviation and a mean maximum deviation 10% better than those of the Cone method. The mean heat content itself is 25% better. The Pipe method being too long, was not considered in this case, but its results are very close to the Cone method as seen in a previous study on a few profiles.

c) Final tests.

The final tests purpose is to verify the quality of the data reduction.

1) Pipe and Cone methods.

If the first pass with a standard tolerance does not give the right number of points, another test pass is made using the tolerance maximum (minimum) if the number of significant points is too large (too small). This will determine if it is possible to calculate the right number of points. If the resulting number of significant data points is too small (too large), then hyperbolic interpolations may converge to the required range. In the other case, the bathy-message can not be computed.

2) Broken Stick method.

After each stick breakage, the new maximum deviation between the profile and the bathy-message is computed and is checked against the tolerance minimum (generally, the white noise of the profile). If it is below then the computation stops prematurely, and if the final number of significant points is below the minimum number of points, the bathy-message is considered bad and not sent or recorded. When this is not the case, at the end of the computation, the bathy-message has the optimum number of significant data points, but its maximum deviation from the profile is checked against the tolerance maximum. If it is above then the computation is resumed till the maximum deviation is below the tolerance maximum or till the maximum number of points is reached. In this later case the bathy-message is considered bad and not sent or recorded.

Generally (Mesecar and Wagner, 1980), the tolerance maximum is 1°C and the minimum is 5/100°C, the white noise of the XBT profiles. For the GTS bathy-message format the optimum number of significant points is 20, for an Argos transmitted bathy-message it is 15. The minimum number of points is often 50% of the optimum number, and the maximum number is 10% to 20 % higher. In the case of an Argos transmission, they are respectively, 9 and 17 points, but no more than 15 points are actually transmitted because this is not possible, due to the short length of the Argos messages.

5. Improvements.

a) Linear Regression Fit .

We now have a number of significant data points belonging to the profile, and in between, a certain number of points, per definition, more or less linearly positioned. Then why not replacing these segments of curve by their linear regression fit, and use as new significant points, the intersections of the regression lines (Fig.5).

A test on more than a 150 profiles, shows in Table 2 a drastic improvement, the mean standard deviation is reduced by 30%, the mean maximum error is reduced by 13%, but more important for the modelers, the error in the integrated parameters, as the mean heat content, is reduced by an order of magnitude.

The only problem encountered while using the regression fit is when two successive regression segments are nearly parallel (Fig.6). In that case their intersection may be far from the curve and the solution is to eliminate the intersection as a significant point and to keep the significant data point.

CRUISE : ACT 9 JUL-AUG 88

105 Drops / 78 Bathymessage

Method	Heat Content (Mean temperature)	|Error| Mean temperature	$\bar{\sigma}$ (profiles)	|Error Max (profiles)
Cone	17.098°C	.030°C	.111°C	.339°C
Broken Stick + Regression		.002°C	.068°C	.243°C

TAB.2. Same as Table 1 for another cruise, but only with the results of the Cone method or the Broken stick plus regression fit method.

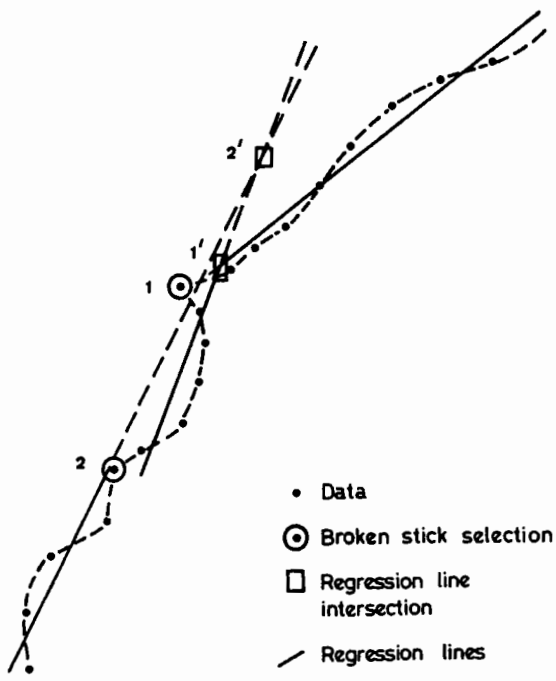

FIG.6. Quasi parallel regression lines problem. Data points 1 and 2 have been selected as significant points by some data reduction method. Points 1' and 2' are the intersections of the regression lines constructed using all the data points between two significant points. Point 1' is a better representation of the local curve and will replace the data point 1 as significant point. The two following regression segments are almost parallel. Point 2' is above 1' or 1 and is very far from the curve, so point 2' is abandoned and point 2 is kept as a significant point.

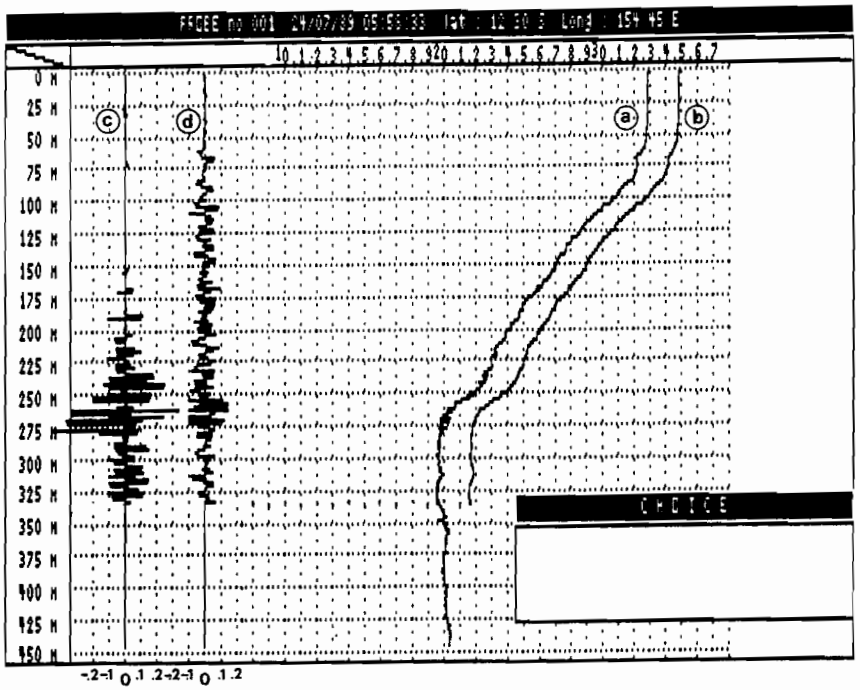

FIG.7. Median and Hanning filter effect on a temperature profile. Profile *a* is the original profile, profile *b* is the filtered profile, offset by 2°C, used to calculate the bathy-message down to 333 meters (temperature minimum). Curve *c* shows the effect of the despiking nonlinear median filter over a window of 5 points, and curve *d* the effect (offset by 5°C) of the low pass linear Hanning filter over a window of 11 points. The scales of the last two curves are multiplied by 10.

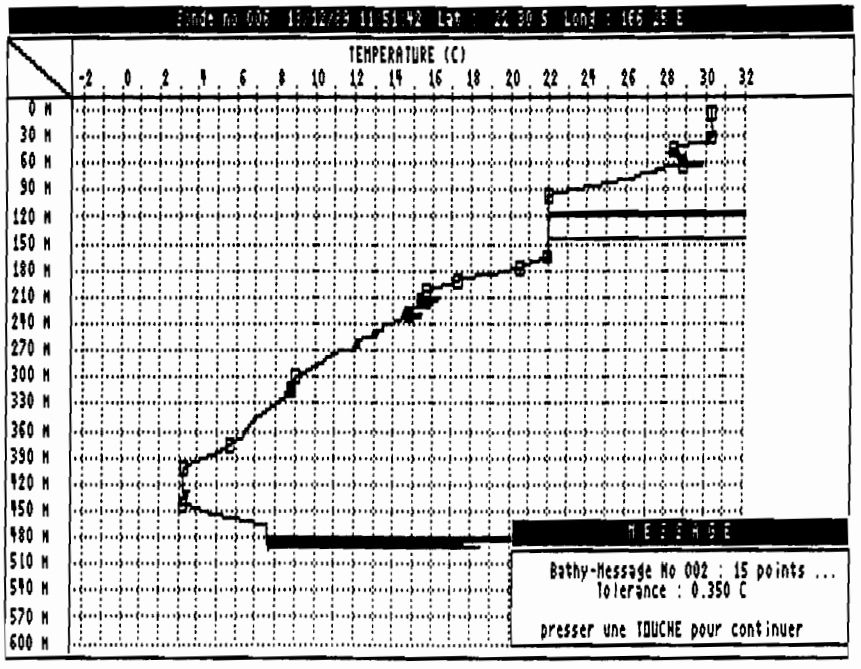

FIG.8. Improved bathy-message. Significant points are represented by the squares on that dummy temperature profile were spikes and contact problems have been amplified. Without despiking, the onboard quality control would have declared the last good data point at 118 meters and the bathy-message would have stopped at that depth. Moreover, Hanning filtering has reduced the effect of small scale features and no significant points are lost to describe them. The regression fit has also adjusted the significant points so that the vertically integrated mean temperature error is less than 2/1000°C.

b) Data Filtering.

1) Median filter.

Due to temporary defective electrical contacts, or any other cause such as radio transmission while launching, more or less isolated spikes may occur during a launch. As the search for the bathy-message maximum depth stops at the first large temperature gradient (>3°C/m), it is useful to use a despiking filter prior to the test. The nonlinear median filter (Sy, 1985) is adequate as it completely filters out the spikes with a width less than the half window, but leaves intact the data as long as the data is monotonous. A 5 meters window seems to be adequate for an XBT profile, it cuts out any spike 2 meters wide or below. A more elaborate median filter with a threshold (Brock, 1986) may also be used in order not to modify any data if it is not a spike above a given amplitude.

2) Hanning Filter.

To describe as well as possible a 500 point curve with 30 significant points or less, one wants to represent the major characteristics of the curve, leaving out the small scale features. At our disposal, now is an efficient bathy-message computing method, but it has a tendency to privilege angular points, as all data reduction methods do. So, prior to the bathy-message computation small scale features should be filtered out by a linear filter such as the Hanning filter (Fig.7) (Etienne, 1970). It is a cosine pondered running mean, a kind of Tukey filter (Matushevskiy and Prival'skiy, 1968) which has almost no secondary maximum. After comparison with CTD profiles, the best filter window seems to be 10-20 meters.

6. Conclusion.

Using a median filter (5 meters window) prior to the first quality control test, then a Hanning filter, (11 meters window) prior to the Broken stick data reduction method, and finally applying a linear regression greatly improves the bathy-message fit with the profile (Fig.8). Temperature errors are reduced by at least 40%, and errors on integrated parameters, such as the heat content, are reduced by an order of magnitude. The maximum depth of the bathy-message may also be increased by the median filter despiking. All these improvements are included in the software developed by ORSTOM and C.L.S. service Argos, for the XBT-ST Argos transmission equipment, that has been on use for more than a year on most of the French TOGA Voluntary Observing Ships network.

Furthermore, when using the Argos satellite transmission system (Table 3), the ratio between the bathy-message sent and transmitted to the GTS is very high (99%), as very few bad profiles pass the onboard quality control, and as the C.L.S. service Argos insert itself the messages, directly onto the GTS, after a rapid quality control. In the TOGA Subsurface Temperature Data Bank, the ratio between the GTS received and archived messages is also very high (99%), as most of the quality control was made during the first steps of the transmission link.

TOGA-VOS, ORSTOM PACIFIC network

January-September 1989

	Number	Step ratio	Global ratio
Probes launched	1945	-	-
Good Profiles (Noumea)	1520	78%	78%
Bathy-messages (service Argos)	1501	99%	77%
Bathy-messages (TOGA Bank)	1486	99%	76%

TAB.3. TOGA-VOS ORSTOM XBT Pacific network efficiency. The 8 ships were equipped with C.L.S.-ARGOS XBT-ST satellite transmission equipment. The second column represents the success rate between two successive lines, the third column, the global success rate between the number of probes launched and the data locally received and archived. The second line indicates the number of XBT profiles received in delayed mode in Noumea, manually quality controlled and archived. the third and fourth lines represent the real time bathy-messages received and archived after quality control, in Toulouse Argos center and in Brest TOGA subsurface temperature data bank.

Acknowledgments. This work has been possible, due to the help of the SURTROPAC ORSTOM Noumea group for the TOGA XBT Voluntary Observing Ship program, and the Toulouse based C.L.S.- service ARGOS group. The Sippican probes were funded by the US TOGA Office under an agreement with the French TOGA Representative.

REFERENCES

Brock, F.V., 1986: A Nonlinear Filter to Remove Impulse Noise from Meteorological Data. *J. Atm. Ocean. Tech.*, **3**, 51-58.

Etienne, A., 1970: Etude Spectrale des Ondes Internes et de la Turbulence, Filtrage des données. *Cahiers du COEC*, **22**, 7, 661-664.

Frachon, I.A., 1987: Réduction des Sondages bathythermiques. Service Hydrographique et Océanographique de la Marine, EPSHOM/E/OC/NP, Report N° 449, 38 pp.

Kerr, G., 1984: Chords: a New Temperature or Sound Speed Profile Thinning Algorithm. NORDA, Technical Note 272.

Mesecar, R. and J. Wagner, 1980: Instruction Manual for XBT Digital Recording and Display System, Model 791. Oregon State University Tech. Planning and Development Group, School of Oceanography. 43-112

Matushevskiy, G.V. and V.Ye. Prival'skiy, 1968: The Use of Filters in Time Series in Hydrometeorology. *Oceanology, Methods and Instruments*, **8**, 3, 401-411.

Siess, J., 1982: Algorithme des Secteurs Emboités. Service Hydrographique et Océanographique de la Marine, EPSHOM/E/OC/NP. Report

Sy, A., 1985: An Alternative Editing Technique for Oceanographic data. *Deep Sea Research*, **32**, 12, 1591-1599.

Centre ORSTOM de Nouméa
B.P. A5 Nouméa Cédex Nouvelle-Calédonie
© 1989